

**Solid Freeform Fabrication Symposium  
1998**

**Proceedings  
August 10-12, 1998**

**Edited by  
David L. Bourell, Joseph J. Beaman  
Richard H. Crawford, Harris L. Marcus  
and Joel W. Barlow**

**The University of Texas at Austin  
Austin, Texas**

DISTRIBUTION STATEMENT A  
Approved for Public Release -  
Distribution Unlimited

# Solid Freeform Fabrication Proceedings

August, 1998

Solid Freeform Fabrication as an important and totally integrated approach to design, materials processing and manufacturing research results related to it is contained in this proceedings of the SFF Symposium held in Austin, Texas on August 10-12, 1998

SFF Topics covered in the Symposium include:

Machine Design  
Computer Sectioning  
Reverse Engineering  
Materials Processing  
Applications

Harris L. Marcus, Joseph J. Beaman,  
David L. Bourell, Joel W. Barlow,  
and Richard H. Crawford, Editors

© 1998 The University of Texas at Austin

All rights of reproduction in any form are protected by U.S. Copyright Laws.  
Permission to copy all or portions of the proceedings contents must be obtained  
from the authors and The University of Texas at Austin.

Library of Congress ISSN 1053-2153

**DISTRIBUTION STATEMENT A**  
**Approved for Public Release**  
**Distribution Unlimited**

**DTIC QUALITY INSPECTED 4**

19990504 143

## Table of Contents

	<u>Page</u>
Preface-----	ix
Organizing/Advisory Committee-----	x
<b><i>Process Development</i></b>	
<b>Direct Laser Fabrication of a Gas Turbine Engine Component- Microstructure and Properties (Part I and II)</b> <i>Suman Das<sup>a</sup>, Timothy P. Fuesting<sup>b</sup>, Gregory Danyo<sup>a</sup>, Lawrence E. Brown<sup>b</sup>, Joseph J. Beaman<sup>a</sup>, David L. Bourell<sup>a</sup>, Kathleen Sargent<sup>c</sup>, <sup>c</sup>The University of Texas at Austin, <sup>b</sup>Allison Engine Company, <sup>c</sup>Wright Laboratories</i> -----	1
<b>Geometry Processing for SLS/HIP</b> <i>Ravi Venkataramani, Suman Das, Joseph J. Beaman, The University of Texas at Austin</i> -----	19
<b>Surface Finishing of Selective Laser Sintering Parts with Robot</b> <i>Dongping Shi, Ian Gibson, University of Hong Kong</i> -----	27
<b>Laser Polishing of Silica Rods</b> <i>Hongyun Wang, David Bourell, Joseph J. Beaman, The University of Texas at Austin</i> -----	37
<b>Enhanced Controlling of the SLS Process During a Build</b> <i>Alexandre L. Papadatos, Kenneth Stanley Jr., Said Ahzi, Frank W. Paul, Clemson University</i> -----	47
<b>Process Control of 3D Welding as a Droplet-Based Rapid Prototyping Technique</b> <i>R. Kovacevic<sup>a</sup>, H. Beardsley<sup>b</sup>, <sup>a</sup>Southern Methodist University, <sup>b</sup>University of Kentucky</i> -----	57
<b>Study of Ejection Forces in the AIM™ Process</b> <i>Neil Hopkinson, Phil Dickens, De Montfort University</i> -----	65
<b>Thermal Behavior of Parts Made by Direct Metal Laser Sintering</b> <i>N. P. Karapatis, Y. Guidoux, P. E. Gyax, R. Glardon, Swiss Federal Institute of Technology</i> -----	79
<b>Thermal Behavior in the LENS Process</b> <i>M. L. Griffith, M. E. Schlienger, L. D. Harwell, M. S. Oliver, M. D. Baldwin, M. T. Ensz, J. E. Smugeresky, M. Essien, J. Brooks, C. V. Robino, W. H. Hofmeister, M. J. Wert, D. V. Nelson, Sandia National Labs</i> -----	89
<b>Prototyping Large-Sized Objects Using Freeform Thick Layers of Plastic Foam</b> <i>A. F. Lennings, J. J. Broek, I. Horváth, A. de Smit, J. S. M. Vergeest, Delft University of Technology</i> -----	97
<b>Direct Rapid Prototyping of Tools</b> <i>K. P. Karunakaran<sup>a</sup>, P. Vivekananda Shanmuganathan<sup>a</sup>, Sabine Roth- Koch<sup>b</sup>, Kai Uwe Koch<sup>b</sup>, <sup>a</sup>Indian Institute of Technology Bombay, <sup>b</sup>Fraunhofer Institut Produktionstechnik und Automatisierung</i> -----	105

<b>Real Time Video Microscopy for the Fused Deposition Method</b> <i>Evan Bossett, Lorna Rivera, Dan Qui, Ryan McCuiston, Noshir Langrana, Sriram Rangarajan, Natesan Venkataraman, Stephen Danforth, Ahmad Safari, Rutgers, The State University of New Jersey</i> -----	113
<b>Bevel Cutting Methods and Cutting Trajectory Control for Steel Laminations Used in Tooling</b> <i>Daniel F. Walczyk, Rensselaer Polytechnic Institute</i> -----	121
<b>Designing Conformal Cooling Channels for Tooling</b> <i>Xiaorong Xu, Emanuel Sachs, Samuel Allen, Michael Cima, Massachusetts Institute of Technology</i> -----	131
<b>Investigation of Short Pulse Nd: YAG Laser Interaction with Stainless Steel Powder Beds</b> <i>W. O'Neill, C.J. Sutcliffe, R. Morgan, K.K.B. Hon, University of Liverpool</i> -----	147
<b>EFAB: Batch Production of Functional, Fully-Dense Metal Parts with Micron-Scale Features</b> <i>Adam Cohen, Gang Zhang, Fan-Gang Tseng, Florian Mansfeld, Uri Frodis, Peter Will, University of Southern California</i> -----	161
<b>Powder Deposition and Sintering for a Two-Powder Approach to Solid Freeform Fabrication</b> <i>Ashok V. Kumar, University of Florida</i> -----	169
<b>Effective Mechanisms of Multiple LED Photographic Curing</b> <i>Kai Loose, Toshiaki Niino, Takeo Nakagawa, University of Tokyo</i> -----	177
<b>Rapid Freezing Prototyping with Water</b> <i>Wei Zhang<sup>a</sup>, Ming C. Leu<sup>a</sup>, Zhiming Ji<sup>a</sup>, Yongnian Yan<sup>b</sup>, <sup>a</sup>New Jersey Institute of Technology, <sup>b</sup>Tsinghua University</i> -----	185
<b>Reducing the Surface Deviation of Stereolithography Using an Alternative Build Strategy</b> <i>P. E. Reeves<sup>a</sup>, R. C. Cobb<sup>b</sup>, <sup>a</sup>De Montfort University, <sup>b</sup>The University of Nottingham</i> -----	193
<b>Sacrificial Materials for the Fabrication of Complex Geometries With Lens</b> <i>E. Schlienger, M. Griffith, M. Oliver, J. A. Romero, J. Smugeresky, Sandia National Labs</i> -----	205
<b>Rapid Prototyping Based on 2D Photographic Images</b> <i>Jianguo Wang<sup>a</sup>, Y.S. Wong<sup>a</sup>, Jerry Fuh<sup>a</sup>, H.T. Loh<sup>a</sup>, ZhaoHui Du<sup>b</sup>, GuoDong Hong<sup>b</sup>, YongNian Yan<sup>b</sup>, <sup>a</sup>National University of Singapore, <sup>b</sup>Tsinghua University</i> -----	211
<b>Art to Engineering: Pervasive RP Activities at Arizona State University</b> <i>Anshuman Razdan, Mark R. Henderson, Dan Collins, Arizona State University/PRISM</i> -----	221
<b>Solid Freeform Fabrication Research in Engineering Education</b> <i>R. S. Crockett, V. R. Gervasi, Milwaukee School of Engineering</i> -----	229

## ***Computational Modeling***

<b>Parametric Based Controller for Rapid Prototyping Applications</b> <i>Georges Fadel, Ravi Ganti, Clemson University</i>	236
<b>Process Planning and Automation for Additive-Subtractive Solid Freeform Fabrication</b> <i>J. Miguel Pinilla, Ju-Hsien Kao, Fritz B. Prinz, Stanford University</i>	245
<b>Modeling and Designing Components with Locally Controlled Composition</b> <i>Todd R. Jackson, Nicholas M. Patrikalakis, Emanuel M. Sachs, Michael J. Cima, MIT</i>	259
<b>Domain Decomposition and Space Filling Curves in Toolpath Planning and Generation</b> <i>Bertoldi M., Yardimci M. A., Pistor C. M., Guceri S. I., University of Illinois at Chicago</i>	267
<b>Reverse Engineering Trimmed NURB Surfaces From Laser Scanned Data</b> <i>Ben Steinberg, Anshuman Razdan, Gerald Farin, Arizona State University</i>	277
<b>Stereometric Design for Desk-Top SFF Fabrication</b> <i>Zbigniew M. Bzymek, Scott Theis, Tariq Manzur, Chandra Roychaudhuri, Lianchao Sun, Leon L. Shaw, University of Connecticut at Storrs</i>	285
<b>A Process Planning Method and Data Format for Achieving Tolerances in Stereolithography</b> <i>Charity M. Lynn, Aaron West, David W. Rosen, Georgia Institute of Technology</i>	293
<b>Dimensional Issues in Stereolithography</b> <i>David L. Winmill, David M. Hoopes, Suresh S. Jayanthi, DuPont Somos</i>	303
<b>Variable Thickness Ruled Edge Slice Generation and Three-Dimensional Graphical Error Visualization</b> <i>Peter B. Chamberlain, Mark D. Van Roosendaal, Charles L. Thomas, University of Utah</i>	311
<b>Topology Driven Improvement of FDC Build Parameters</b> <i>Vikram R. Jamalabad, Jeffrey A. Chard, Charles Gasdaska, Richard B. Clancy, AlliedSignal Research &amp; Technology</i>	319
<b>A Visual Tool to Improve Layered Manufacturing Part Quality</b> <i>Gautham Kattethota, Mark Henderson, Arizona State University</i>	327
<b>Machine Design, Control and Performance of Automated Computer-Aided Manufacturing of Laminated Engineering Materials</b> <i>Brian B. Mathewson<sup>a</sup>, Ravi Hebbar<sup>b</sup>, Sangeun Choi<sup>b</sup>, Wyatt S. Newman<sup>b</sup>, James D. Cawley<sup>b</sup>, Arthur H. Heuer<sup>b</sup>, <sup>a</sup>CAM-LEM, Inc., <sup>b</sup>Case Western Reserve University</i>	335
<b>Build Time Estimations for Large Scale Modelling</b> <i>G. Mensing, I. Gibson, University of Hong Kong</i>	343
<b>Reverse Engineering of Polymeric Solid Models Using Refractive Index Matching (RIM)</b> <i>Jon Christensen, Amit Bandyopadhyay, Washington State University</i>	351

<b>Software Development for Laser Engineered Net Shaping</b> <i>M. T. Ensz, M. L. Griffith, L. D. Harwell, Sandia National Labs</i>	359
--	-----

**Physical Modeling**

<b>Measurement and Modeling Of Residual Stress-Induced Warping in Direct Metal Deposition Processes</b> <i>N. W. Klingbeil, J. L. Beuth, R. K. Chin, C. H. Amon, Carnegie Mellon University</i>	367
--	-----

<b>FDM Systems and Local Adaptive Slicing</b> <i>Justin Tyberg, Jan Helge Bøhn, Virginia Tech</i>	375
--	-----

<b>Virtual Design and Fabrication in Layered Manufacturing</b> <i>Kathryn B. Higgins, Noshir A. Langrana, Rutgers, The State University of New Jersey</i>	383
--	-----

<b>Influence of Rheology on Deposition Behavior of Ceramic Pastes in Direct Fabrication Systems</b> <i>Bruce H. King, Sherry L. Morissette, Hugh Denham, Joseph Cesarano, III, Duane Dimos, Sandia National Laboratories</i>	391
---	-----

<b>A Theoretical Model for Optimization of SALD Parameters</b> <i>Zbigniew M. Bzymek<sup>a</sup>, Leon L. Shaw<sup>a</sup>, Wojciech Marks<sup>b</sup>, <sup>a</sup>University of Connecticut, <sup>b</sup>Inst. of Fundamental Technical Problems-PAS</i>	399
---	-----

<b>Simulation of Laminated Object Manufacturing (LOM) with Variation of Process Parameters</b> <i>Lawrance Flach, Michelle A. Jacobs, Donald A. Klosterman, Richard P. Chartoff, University of Dayton</i>	407
--	-----

<b>Dimensional Variability Analysis in Post-Processing of Rapid Tooling</b> <i>Wanlong Wang, James G. Conley, Henry W. Stoll, Northwestern University</i>	417
--	-----

<b>Shell Cracking in Investment Casting with Laser Stereolithography Patterns</b> <i>W. L. Yao, Ming C. Leu, New Jersey Institute of Technology</i>	427
--	-----

<b>2-D Wavelet Analysis of Solid Objects: Applications in Layered Manufacturing</b> <i>Mark D. Van Roosendaal, Peter Chamberlain, CharlesL. Thomas, University of Utah</i>	435
---	-----

**Materials**

<b>Strength of the DTM RapidSteel 1.0 Material</b> <i>T. D. Stewart, K. W. Dalgarno, T.H.C. Childs, J. Perkins, The University of Leeds</i>	443
--	-----

<b>Direct Injection Molding Tooling Inserts from the SLS Process with Copper Polyamide</b> <i>Christian Nelson, Jason Kepler, Rick Booth, Phillip Conner, DTM Corporation</i>	451
--	-----

<b>Rapid Steel Tooling via Solid Freeform Fabrication</b> <i>Timothy J. Weaver, Julian A. Thomas, Sundar V. Atre, Randall M. German, Pennsylvania State University</i> -----	461
<b>Processing of Titanium Net Shapes by SLS/HIP</b> <i>Suman Das, Martin Wohler, Joseph J. Beaman, David L. Bourell, The University of Texas at Austin</i> -----	469
<b>Feasibility of Fabricating Metal Parts from 17-4PH Stainless Steel Powder</b> <i>Guohua Wu, Noshir Langrana, Sriram Rangarajan, Rajendra Sadangi, Ahmad Safari, Stephen C. Danforth, Rutgers, The State University of New Jersey</i> -----	479
<b>Industrial Use of Direct Metal Laser Sintering</b> <i>Olli Nyrhila, Juha Kotila, Jan-Erik Lind, Tatu Syvanen, Electrolux Rapid Development</i> -----	487
<b>3D Welding and Milling for Direct Prototyping of Metallic Parts</b> <i>Yong-Ak Song<sup>a</sup>, Sehyung Park<sup>a</sup>, Kyunghyun Hwang<sup>b</sup>, Doosun Choi<sup>b</sup>, Haeseong Jee<sup>c</sup>, <sup>a</sup>Korea Institute of Science &amp; Technology, <sup>b</sup>Korea Institute of Machinery and Metals, <sup>c</sup>Hongik University</i> -----	495
<b>Materials Issues in Laminated Object Manufacturing of Powder-Based Systems</b> <i>J. D. Cawley, Z. Liu, J. Mou, A. H. Heuer, Case Western Reserve University</i> -----	503
<b>Issues Associated with the Development of a Water Soluble Support Material for Use in Extrusion Freeforming &amp; Fused Deposition Modelling</b> <i>John L. Lombardi<sup>a</sup>, Gregory J. Artz<sup>a</sup>, Dragan Popovich<sup>a</sup>, Ranji Vaidyanathan<sup>a</sup>, Sajiv Boggavarapu<sup>b</sup>, <sup>a</sup>Advanced Ceramics Research Inc., <sup>b</sup>University of Arizona</i> -----	511
<b>Thermal-Expansion and Fracture Toughness Properties of Parts made from Liquid Crystal Stereolithography Resins</b> <i>J. S. Ullett<sup>a</sup>, T. Benson-Tolle<sup>c</sup>, J. W. Schultz<sup>b</sup>, R. P. Chartoff<sup>a</sup>, <sup>a</sup>University of Dayton, <sup>b</sup>Georgia Tech Research Institute, <sup>c</sup>United States Air Force - Materials Directorate</i> -----	519
<b>Rapid Prototyping of Functional Three-Dimensional Microsolenoids and Electromagnets by High-Pressure Laser Chemical Vapor Deposition</b> <i>J. Maxwell<sup>a</sup>, K. Larsson<sup>a</sup>, M. Boman<sup>a</sup>, P. Hooge<sup>b</sup>, Kirk Williams<sup>b</sup>, P. Coane<sup>b</sup>, Uppsala University, <sup>b</sup>Louisiana Tech University</i> -----	529
<b>Gas-Phase Selective Area Laser Deposition (SALD) Joining of SiC Tubes with SiC Filler Material</b> <i>S. Harrison, H. L. Marcus, University of Connecticut at Storrs</i> -----	537
<b>Preparation and Properties of In-Situ Devices Using the SALD and SALDVI Techniques</b> <i>James E. Crocker, Lianchao Sun, Leon L. Shaw, Harris L. Marcus, University of Connecticut at Storrs</i> -----	543

<b>Temperature Dependent Optical Properties of Polymers as a Basis for Laser Process Modeling</b> <i>Bernd Keller, Rolf Pfeifer, Wei-Nien Su, Peter Eyerer, Inst. of Polymer Testing &amp; Polymer Science</i> -----	549
<b>Mechanical Characterization of Parts Processed via Fused Deposition</b> <i>Bertoldi M., Yardimci M. A., Pistor C. M., Guceri S. I., Sala G., University of Illinois at Chicago</i> -----	557
<b>Material Strength in Polymer Shape Deposition Manufacturing</b> <i>J. W. Kietzman, F. B. Prinz, Stanford University</i> -----	567
<b>Rapid Prototyping of Titanium Nitride Using Three-Dimensional Laser Chemical Vapor Deposition</b> <i>James Maxwell, Jubin Shah, Terry Webster, Jason Mock, Louisiana Tech University</i> -----	575
 <i>Ceramic Materials</i>	
<b>Si/SiC-Ceramic – Low Process Shrinkage - High Temperature Material for the Laser Sinter Process</b> <i>Peter Stierlen<sup>a</sup>, Peter Schanz<sup>b</sup>, Peter Eyerer<sup>a</sup>, <sup>a</sup>Inst. for Polymer Testing &amp; Polymer Science, <sup>b</sup>DLR</i> -----	581
<b>Mechanical Behavior of Robocast Alumina</b> <i>Hugh B. Denham<sup>a</sup>, Joe Cesarano III<sup>a</sup>, Bruce H. King<sup>a</sup>, Paul Calvert<sup>b</sup>, <sup>a</sup>Sandia National Laboratories, <sup>b</sup>University of Arizona</i> -----	589
<b>Titanium Casting Molds via Selective Laser Sintering</b> <i>Nicole Harlan, David Bourell, Joe Beaman, The University of Texas at Austin</i> -----	597
<b>Selective Laser Sintering of Zirconium Silicate</b> <i>F. Klocke, H. Wirtz, Fraunhofer Inst. of Production Technology</i> -----	605
<b>Development of a Binder Formulation for Fused Deposition of Ceramics</b> <i>Thomas F. McNulty, Ivan Cornejo, Farhad Mohammadi, Stephen C. Danforth, Ahmad Safari, Rutgers, The State University of New Jersey</i> -----	613
<b>Materials for Biomedical Applications</b> <i>N. K. Vail<sup>a</sup>, L. D. Swain<sup>a</sup>, W. C. Fox<sup>a</sup>, T. B. Aufdemorte<sup>b</sup>, G. Lee<sup>c</sup>, J. W. Barlow<sup>c</sup>, <sup>a</sup>BioMedical Enterprises, Inc., <sup>b</sup> University of Texas Health Science Center at San Antonio, <sup>c</sup>University of Texas at Austin</i> -----	621
<b>Processing of Bioceramic Implants via Fused Deposition Process</b> <i>Susmita Bose, Marisol Avila, Amit Bandyopadhyay, Washington State University</i> -----	629
<b>Automated Fabrication of Nonresorbable Bone Implants Using Laminated Object Manufacturing (LOM)</b> <i>Cheri Steidle, Don Klosterman, Nora Osborne, George Graves, Richard Chartoff, University of Dayton</i> -----	437
<b>Generation of Porous Structures Using Fused Deposition</b> <i>Bertoldi M<sup>a</sup>., Yardimci<sup>a</sup> M. A., Pistor<sup>a</sup> C. M., Guceri S. I<sup>a</sup>., Danforth S. C<sup>b</sup>., <sup>a</sup>University of Illinois at Chicago, <sup>b</sup>Rutgers, The State University of New Jersey</i> -----	639

<b>A Study on Weight Loss Rate Controlled Binder Removal from Parts Produced by FDC</b> <i>Senol Pekin<sup>a</sup>, John Bukowski<sup>a</sup>, Avigdor Zangvil<sup>a</sup>, <sup>a</sup>University of Illinois at U-C, <sup>b</sup>Argonne National Laboratory</i> -----	651
<b>Binder Formulation in EVA-wax System for Fused Deposition of Ceramics</b> <i>Senol Pekin<sup>a</sup>, Avigdor Zangvil<sup>a</sup>, William Ellingson<sup>b</sup>, <sup>a</sup>University of Illinois at U-C, <sup>b</sup>Argonne National Laboratory</i> -----	661
<b>Curved Layer LOM of Ceramics and Composites</b> <i>Donald A. Klosterman<sup>a</sup>, Richard P. Chartoff<sup>a</sup>, Nora R. Osborne<sup>a</sup>, George A. Graves<sup>a</sup>, Allan Lightman<sup>a</sup>, Gyoowan Han<sup>a</sup>, Akos Bezeredi<sup>a</sup>, Stan Rodrigues<sup>a</sup>, Sung Pak<sup>b</sup>, Gary Kalmanovich<sup>b</sup>, Leon Dodin<sup>b</sup>, Song Tu<sup>b</sup>, <sup>a</sup>University of Dayton, <sup>b</sup>Helisys, Inc.</i> -----	671
 <b>Multiple Materials</b>	
<b>Virtual Simulation for Multi-material LM Process</b> <i>Dan Qiu, Noshir A. Langrana, Stephen C. Danforth, Ahmad Safari, Mohson Jafari, Rutgers, The State University of New Jersey</i> -----	681
<b>Features in Layered Manufacturing of Heterogeneous Objects</b> <i>Xiaoping Qian, Debasish Dutta, University of Michigan</i> -----	689
<b>Recent Developments in Robocasting of Ceramics and Multimaterial Deposition</b> <i>Joseph Cesarano III, Bruce H. King, Hugh B. Denham, Sandia National Laboratories</i> -----	697
<b>Functionally Optimized Ceramic Structures</b> <i>C. Gasdaska<sup>a</sup>, R. Clancy<sup>a</sup>, M. Ortiz<sup>a</sup>, V. Jamalabad<sup>a</sup>, Anil Virkar<sup>b</sup>, Dragan Popovitch<sup>c</sup>, <sup>a</sup>AlliedSignal, Inc., <sup>b</sup>University of Utah, <sup>c</sup>University of Tucson</i> -----	705
<b>Fabrication of Curved Ceramic/Polymer Composite Transducers for Ultrasonic Imaging Applications by Fused Deposition of Ceramics</b> <i>G. M. Lous, I. A. Cornejo, T. F. McNulty, A. Safari, S. C. Danforth, Rutgers, The State University of New Jersey</i> -----	713
<b>Automated Fabrication of Complex Molded Parts Using Mold SDM</b> <i>A. G. Cooper<sup>1</sup>, S. Kang<sup>1</sup>, J. W. Kietzman<sup>1</sup>, F. B. Prinz<sup>1</sup>, J. L. Lombardi<sup>2</sup>, L. Weiss<sup>3</sup>, <sup>1</sup>Stanford University, <sup>2</sup>University of Tucson, <sup>3</sup>Carnegie Mellon University</i> -----	721
<b>Composites With Gradient Properties from Solid Freeform Fabrication</b> <i>V. R. Gervasi, R. S. Crockett, Milwaukee School of Engineering</i> -----	789
<b>Properties of a High Temperature Liquid Crystal Stereolithography Resin</b> <i>R. P. Chartoff<sup>a</sup>, J. W. Schultz<sup>b</sup>, J. Bhatt<sup>c</sup>, J. S. Ullett<sup>a</sup>, <sup>a</sup>University of Dayton, <sup>b</sup>Georgia Tech Research Institute, <sup>c</sup>Polaroid Corporation</i> -----	737

**Net Shape Fabrication of SiC and SiC/SiC Components Using  
Laminated Object Manufacturing (LOM)**  
*Don Klosterman, Richard Chartoff, Nora Osborne, George Graves, Allan  
Lightman, Akos Bezeredi, University of Dayton*----- 745

**Keyword Index**----- 747

**Author/Attendee List**----- 756

## PREFACE

The Ninth Solid Freeform Fabrication (SFF) Symposium, held at The University of Texas in Austin on August 10-12, 1998, was attended by over 150 national and international researchers. Papers addressed SFF issues in computer software, machine design, materials synthesis and processing, and integrated manufacturing. New sessions on ceramic materials and multiple materials SFF were added to this year's program. The diverse domestic and foreign attendees included industrial users, SFF machine manufacturers, university researchers and representatives from the government. We are pleased once again with the strong showing of university students. The excitement generated at the Symposium reflects the participants' total involvement in SFF and the future technical health of this growing technology. The Symposium organizers look forward to its being a continuing forum for technical exchange among the expanding body of researchers involved in SFF.

The Symposium was again organized in a manner to allow the multi-disciplinary nature of the SFF research to be presented coherently, with various sessions emphasizing computer issues, machine topics, and the variety of materials aspects of SFF. We believe that documenting the changing state of SFF art as represented by these Proceedings will serve both the people presently involved in this fruitful technical area as well as new researchers and users entering the field.

The editors would like to extend a warm "Thank You" to Gloria Gutches for her detailed handling of the logistics of the meeting and the Proceedings, as well as her excellent performance as registrar and problem solver during the meeting. We would like to thank the organizing committee, the session chairmen, the attendees for their enthusiastic contributions, and the speakers both for their significant contribution to the meeting and for the relatively prompt delivery of the manuscripts comprising this volume. We look forward to the continued close cooperation of the SFF community in organizing the Symposium. We also want to thank the Office of Naval Research (Grant No. N00014-96-1-0441) and the National Science Foundation (Grant DMI-9812084) for supporting this meeting financially. Other co-sponsors included DARPA, The Rapid Prototyping Association of the Society of Manufacturing Engineers, The Minerals, Metals and Materials Society, and the University of Connecticut at Storrs along with the Mechanical Engineering Department, Laboratory for Freeform Fabrication and the Texas Materials Institute at The University of Texas at Austin.

The editors.



## Organizing Committee

Joel Barlow	University of Texas at Austin
Joseph Beaman	University of Texas at Austin
David Bourell	University of Texas at Austin
Richard Crawford	University of Texas at Austin
Harris Marcus	University of Connecticut at Storrs

## Advisory Committee

Clint Atwood	Sandia National Labs
Robert Brown	The Gillette Company
Richard Chartoff	University of Dayton
Michael Cima	Massachusetts Institute of Technology
Stephen Danforth	Rutgers-The State University of New Jersey
Steve Fishman	Office of Naval Research
Jim Maxwell	Louisiana Tech University
Kesh Narayanan	National Science Foundation
Thomas Pang	Ciba Specialty Chemicals Corporation
Fritz Prinz	Stanford University
Eli Sachs	Massachusetts Institute of Technology
Ralph Wachter	Office of Naval Research
Lee Weiss	Carnegie Mellon University



## Direct Laser Fabrication of a Gas Turbine Engine Component - Microstructure and Properties - Part I

Suman Das<sup>†</sup>, Timothy P. Fuesting<sup>‡</sup>, Gregory Danyo<sup>†</sup>, Lawrence E. Brown<sup>†</sup>, Joseph J. Beaman<sup>†</sup>, David L. Bourell<sup>†</sup>, and Kathleen Sargent<sup>§</sup>

<sup>†</sup>Laboratory for Freeform Fabrication  
University of Texas at Austin

<sup>‡</sup>Allison Engine Company, Inc.  
Indianapolis, Indiana

<sup>§</sup>Air Force Research Laboratory  
Wright Patterson AFB, Ohio

### Abstract

This paper presents the development of a new technique for the production of abrasive turbine blade tips by direct laser processing. This superalloy cermet component is an integral part of the low pressure turbine sealing system in a demonstrator engine. Direct laser fabrication of this component from a bed of loose powder results in significant cost savings and improved performance over the currently employed production technique. The technology has been demonstrated by fabricating a prototype lot of 100 blade tips, which will be subjected to an engine test. This is the first instance of a direct fabrication method applied to the production of functional engine hardware. This research was funded by the United States Air Force contract F33615-94-C-2424 titled "Affordable Turbine Blade Tips".

### SUMMARY

This program has contributed significantly towards meeting the Advanced Technology affordability goals for turbine engine acquisition. These goals require engines to be developed and maintained at a reduced cost. To meet some of these cost reduction goals, advanced manufacturing methods such as solid freeform fabrication (SFF) must be applied. Although only one small turbine engine component is being discussed here, SFF in general has great potential for impacting cost reduction goals. The work performed is developmental, which means fewer parts are produced regardless of the component. Since SFF costs are nearly independent of the number of parts<sup>1</sup>, it will allow components to be fabricated at reduced cost. Since SFF has the potential to significantly reduce time from design conception to fabrication, it will also allow more design iterations to take place.

The use of SFF to directly produce functional components eliminates the costs and time associated with raw material acquisition, conversion and manufacture. The final goal of developing such a process would be to have the ability to control the microstructure with respect to precipitate size, density, porosity size and distribution, grain size, crystallographic texture and solidification modes. Such process control would allow production of components tailored with functionally graded microstructures to enhance properties and performance in specific regions of

the component. This would represent the pinnacle of life and performance enhancement, and cost and schedule reduction.

SFF can also be applied to tooling production applications such as investment castings. Investment castings are used for complex geometries such as airfoils, where SFF can provide a means for prototyping tooling or patterns. These prototypes assist in production trials and iterations that are necessary to finalize geometry and processing<sup>2</sup>. Whether it is used for component or tooling manufacture, SFF is a critical area and a technology that is required to reduce the cost and lead time for producing turbine engine components.

## INTRODUCTION

Until recently, no work was reported on direct selective laser sintering (SLS) of high performance materials such as Nickel and Cobalt base superalloys, superalloy cermets<sup>9</sup>, Titanium base alloys<sup>3</sup> and monolithic high temperature metals such as Molybdenum<sup>4</sup>. These materials are used for high performance components that typically experience high operating temperatures, high stresses and severe oxidizing or corrosive environments. Direct SLS, with its ability to produce components in such materials is especially useful for functional prototype, low volume or "one of a kind" production runs. To manufacture a typical prototype lot of 100 superalloy cermet abrasive turbine blade tips, direct SLS was shown<sup>9</sup> to achieve acceptable microstructure and properties with 80% cost savings over the traditional method. Automotive and aerospace industries face typical lead times of several weeks for functional, metallurgical quality prototypes. Direct SLS fabrication can lower cost and drastically reduce lead times by eliminating pre-processing and post-processing steps, and by eliminating the need for specialized tooling.

Since its inception in the 1930's, the gas turbine engine has grown to be the workhorse power plant of modern aircraft. Advanced technology propulsion systems are very important from an overall system affordability viewpoint since higher engine performance can result in a smaller airframe. SFF technologies are advanced manufacturing methods that can significantly impact cost reduction of engine components. SFF is striving towards decoupling cost from volume<sup>5</sup> by making it possible to produce the first unit at a recurring cost equal to the hundredth unit<sup>6</sup>. To demonstrate SFF's cost-effectiveness, a superalloy cermet abrasive blade tip (ABT) was chosen for direct fabrication technology development and demonstration.

Gas turbine efficiency is highly dependent upon minimizing leakage of the gas away from and around the working gas path. Therefore, clearance between rotating and static parts is critical. This clearance changes with component expansion and contraction due to the thermal cycling experienced in gas turbines. One of the primary methods developed to compensate for this expansion and contraction is an abradable seal system<sup>7,8</sup>. This seal system works by attaching an ABT to the tips of the turbine blades. The stationary turbine shroud is coated with an abradable ceramic, which is abraded by the abrasive blade tip during engine operation to form a gas path seal around the rotating component. The abradable ceramic liner is relatively inexpensive and simple to manufacture. However, the abrasive cermet (0.9-1.5 mm thickness) is difficult to manufacture on a production scale and contains expensive components. The cost of the raw

materials makes scrap highly undesirable. Due to the difficulties encountered<sup>9</sup>, a more reliable method for producing this material is desired. A direct SLS process for producing the cermet abrasive can provide a uniform, repeatable manufacturing process that would eliminate much of the manual labor, reduce scrap and make all unsintered surplus materials reusable.

## **OBJECTIVES**

Prior research<sup>9</sup> in direct laser processing ABT cermet material had shown the capability of directly laser processing cermet material to obtain microstructure and properties that were consistent with production specifications. The ultimate goal of ongoing research was to complete technology development and demonstration of a direct laser manufacturing process capable of repeatably producing the ABT component to dimensional specifications, with microstructure and properties equivalent or superior to current production material. A prototype lot of 100 turbine blade tips would be manufactured to demonstrate the developed process and the associated efficiency.

During process development, the objectives were fourfold. The first objective was to investigate and establish a variety of material composition variants and processing conditions, and their effects on solidification microstructure, and mechanical properties. The second objective pertained to identification and specification of optimal processing windows for manufacturing the ABT component in a single pass laser scan. Under this objective, the optimal processing conditions would result in fully dense, fully melted and rapidly resolidified material free of solidification defects such as hot tearing, pinholing, entrapped porosity, grit floating or segregation. A third objective was to demonstrate reusability of unprocessed material. Attaining this objective would directly impact cost effectiveness of the laser based manufacturing process by eliminating scrap of expensive material constituents. The fourth and final objective was to prove consistency and repeatability of the laser process by producing a large number of ABT components in several experimental runs under identical processing conditions.

## **MATERIALS AND METHODS**

### **Cermet Specifications**

The cermet in production is vacuum sintered using a Silicon and Boron containing Cobalt based braze alloy (Amdry 788) and subsequently bonded to the blade using a similar braze. Elimination of the low melting point braze constituent could extend oxidation life and possibly allow higher operating temperatures. Higher operating temperatures could be achieved by replacing the braze used for bonding the ABT to the blade by a higher temperature diffusion braze. Currently, interactions between the component braze and the bonding braze prevent the use of a diffusion braze alloy. The goal of developing a brazeless cermet composition for direct laser processing was achieved during previous work<sup>9</sup>. This cermet is composed of Mar-M-247 nickel superalloy matrix (Table 1), GE Borazon 510 (titanium coated cubic boron nitride) and Alundum 90 (titanium coated alumina). The thickness and chemical quality of the titanium coating on the abrasive grit is critical. Poor chemical quality of the coating causes contamination of the molten matrix alloy either through dissolution alone or in combination with spallation. A

titanium coating of non-uniform or insufficient thickness results in poor metallurgical bonding with the nickel matrix, and grit floating out of the melt due to large density and surface energy differences.

To meet homogeneity requirements, the sintered material must exhibit no discrete layering or agglomeration of abrasive particles which would result in grit pullout and associated decrease in seal efficiency. Porosity requirements allow for no more than 20% linear porosity as determined from a metallographic montage using a line intercept method. If the material meets these specifications, coupons are removed and brazed into the gauge section of a CMSX-4 single crystal test bar conforming to ASTM-E139 and subjected to an application specific stress-rupture test.

Material	Ni	Co	Cr	Al	Ti	W	Si	B	Mo	Ta	Hf
MAR-M-247	Bal	10.0	8.4	5.5	1.0	10.0		0.01	0.7	3.1	1.4

Table 1. Nominal composition of matrix material used in the cermet.

### Process Apparatus and Methods

A laser processing machine dedicated to the production of ABTs was designed jointly by the University of Texas and Allison Engine Company. The principle of operation of this machine is similar to a generic SLS machine. However, it has a few distinguishing features. Since one objective of ABT process development was to produce the full thickness (0.9-1.5 mm) in a single laser pass, this machine does not provide multiple layer powder delivery. This machine is equipped with a 250 Watt CW Nd:YAG laser, high temperature powder heating capability and controlled atmosphere. Metal powders can be heated up to 1000°C in this workstation. This workstation has the capability of maintaining high vacuum ( $< 10^{-5}$  Torr) as well as high purity atmospheres of select gases. Custom software for CAD geometry processing was used to convert the electronic drawing of the demonstration ABT component into the desired laser scanning sequence. The machine control software allows the user to control and set processing parameters including preheat temperature cycle and setpoint, laser power, scan speed and scan spacing.

Material preparation for the direct SLS method consists of combining by weight 73% superalloy, 18% Ti coated alumina, and 9 % CBN. This mixture is blended for 4-6 hours prior to loading in the SLS chamber. The blended mixture is poured into a 4" diameter, 0.060-0.100" deep processing dish and leveled to produce a uniform thickness powder layer. The powder mixture was then baked out under high vacuum ( $< 5 \times 10^{-5}$  Torr) and with 25° C to 875° C temperature ramp over 30 minutes prior to SLS processing.

Direct SLS involves directly melting and consolidating selected regions of a powder bed to form a desired shape having full density. This method of fabrication involves melting the component matrix and obtaining the appropriate amount of flow from the molten material. The appropriate amount of flow is critical. It can be described as the flow that eliminates porosity, produces a highly dense part maintaining dimensional tolerances and minimizes other defects such as hot tearing, pitting, pinholing and solidification cracking. A number of experiments were

conducted to evaluate the influence of the most important SLS process parameters on the solidification behavior of this material composition. These parameters are atmosphere, preheat temperature, scanning sequence and energy density<sup>9</sup>. The appropriate amount of flow is controlled by several factors such as atmosphere, degree of preheat and three characteristic variables affecting laser energy density: laser power, scan spacing and scan speed.

Rectangular coupons 1" long X 0.5" wide were produced by raster scanning across the width. These samples were used for process parameter development and mechanical testing. Tip shape processing was done by two alternate methods. The first method involved raster scanning the shape of a tip on a powder bed container. The second method was to laser process a rail shaped tip out of powder contained in a mold. The mold material directly affects the thermal profile generated and thus can be used in conjunction with preheat and laser scanning preheat to assist in control of the solidification microstructure of the component. The physical properties of the powder container influence the microstructure of the part dramatically. A ceramic powder container insulates the bottom surface of the powder bed and sets up a fairly uniform thermal gradient which results in partial directional solidification or epitaxial growth. A more conductive powder, *e.g.* a steel or superalloy container can produce a very fine dendrite spacing in the solidification microstructure.

The laser scanning sequence significantly affects the thermal profile of the part during processing, therefore it will have a significant affect on tendency of the material to tear, crack and separate. The scanning sequence incorporated on actual parts will be dependent upon part geometry and modified in an attempt to provide a uniform thermal profile. This experiment involved only two variables on rectangular coupons, rastering the beam on continuously back and forth, and intermittently shutting the laser off and only rastering left to right. Scanning sequence can dramatically affect local solidification time, which affects dendrite spacing or solidification mode.

Traditional metallurgy practices dictate that the superalloy cermet material requires processing in a high vacuum atmosphere. However, a quick evaluation of the affects of different atmospheres was performed to document the degree of degradation. This consisted of performing trials in different types of atmospheres that included rough vacuum (of order 30mTorr), rough vacuum purged with argon, high vacuum ( $< 5 \times 10^{-5}$  Torr) and high vacuum followed by argon-2% hydrogen backfill.

Experiments were conducted to determine the affects of preheating the powder bed in the range of 350°C to 1000°C vs. no preheat. The experimental results provided two findings. First, preheat was beneficial in that it hastened outgassing of the powder. Second, if a well outgassed powder was placed in the powder bed, the preheat improved the surface characteristics, wetting and flow, and minimized hot tearing or cracking. In general the components manufactured were more consistent in surface texture quality if a preheat is applied. Preheat could also be used to manipulate the thermal gradient during solidification which affects dendrite spacing and the mode of solidification.

## RESULTS AND DISCUSSION

### Component Demonstration

During the course of this research program solid blade tips were manufactured by laser scanning the shape on a powder bed. The ABT component for technology demonstration is a hollow, rail type tip which is brazed to a projecting outline at the blade top surface. The component drawing called for  $\pm 0.001$ " variation in the dimensional outline. The fully solid tips did not have the dimensional control needed to meet this specification. Thus, a series of ceramic and metallic molds were manufactured. The tip shown in Figure 1 is a typical tip produced from a mold. The outline drawing above it represents the part according to the print showing a direct match up between the drawing and the tip.

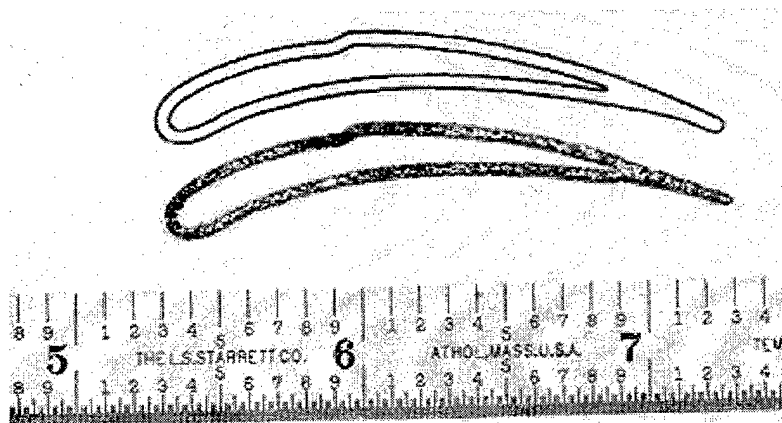


Figure 1. Typical abrasive blade tip produced by direct laser processing.

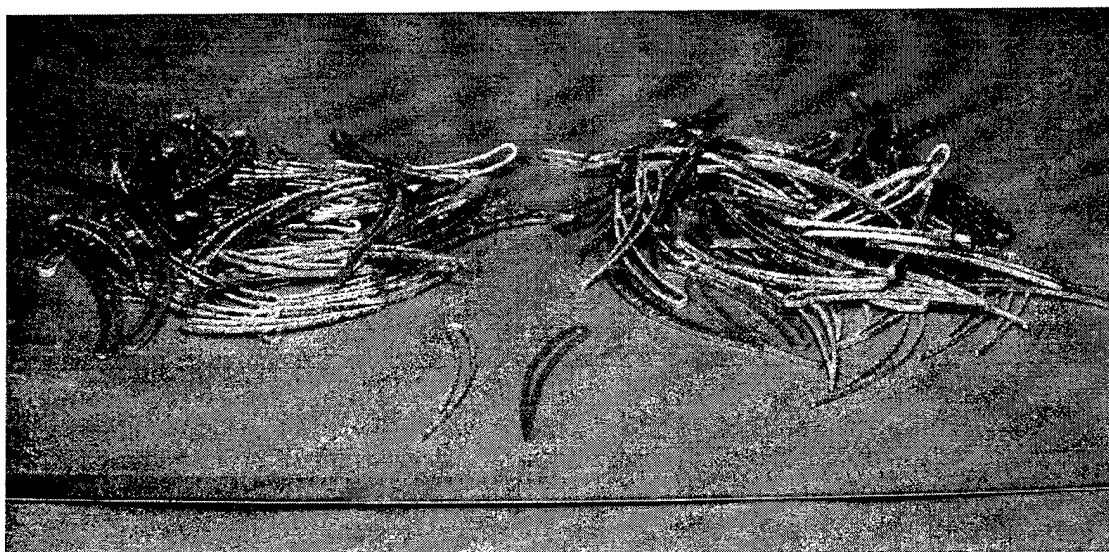


Figure 2. Prototype production lot of abrasive blade tips.

The life of the ceramic mold was not as long as desired, therefore a metallic mold was used to produce the components. A partial production lot of ABTs produced via this method is shown in Figure 2. The production yield was excellent, in excess of 95%. The mold was 0.090" deep and yielded parts that were in the 0.077 to 0.084" thick range. Subsequently, one surface was ground flat for bonding. The tips attained a final thickness in the 0.073 to 0.077" range.

### **Process Parameters for Production**

Precipitate strengthened nickel base superalloys are considered difficult to weld or work with in the molten state due to their tendency to strain age crack<sup>10,11</sup>. Therefore, SLS processing parameters should be aimed at attaining the most uniform thermal profile possible during processing to minimize the tendency for hot tearing and solidification cracking due to residual stresses and stresses resulting from aging during processing. This implies that a very fine scan spacing with a high scan speed should be incorporated. These two parameters also affect the surface roughness of the sintered coupon. A fine scan spacing will provide a relatively uniform smooth surface. Scan speed effects on surface roughness are dependent upon the overall energy density and the associated residence time in the molten region. For a given material a high scan speed with a high energy density which would produce extensive superheat or a long molten residence time will produce a poor surface finish. The same scan speed with a lower energy density and thus a lower degree of superheat will produce a better surface finish. In general excessive superheat will allow growth of morphological instabilities in solidification fronts that produce non-uniform surface finish. Controlled heating, superheat, and cooling rate will produce a uniform solidification front thus producing a uniform surface appearance and microstructure. In general a fine scan spacing was chosen with the power and scan speed being variables used to deliver different energy densities. The goal was to produce a short molten residence time with full through thickness melting.

Prior process development<sup>9</sup> resulted in manufacture of test coupons (1 inch long, 0.5 inches wide and 0.060 inches thick) with acceptable microstructures for mechanical property characterization. The energy density used for producing these specimens was 3202 J/cm<sup>2</sup>. In order to develop acceptable processing parameters for the ABT geometry, a number of experiments were conducted investigating a wide array of energy densities. These tests proved that the ABT component having acceptable microstructure and surface finish could be produced in the 2400 J/cm<sup>2</sup> to 3878 J/cm<sup>2</sup> range. The microstructure produced at 2400 J/cm<sup>2</sup> is shown in Figure 3.

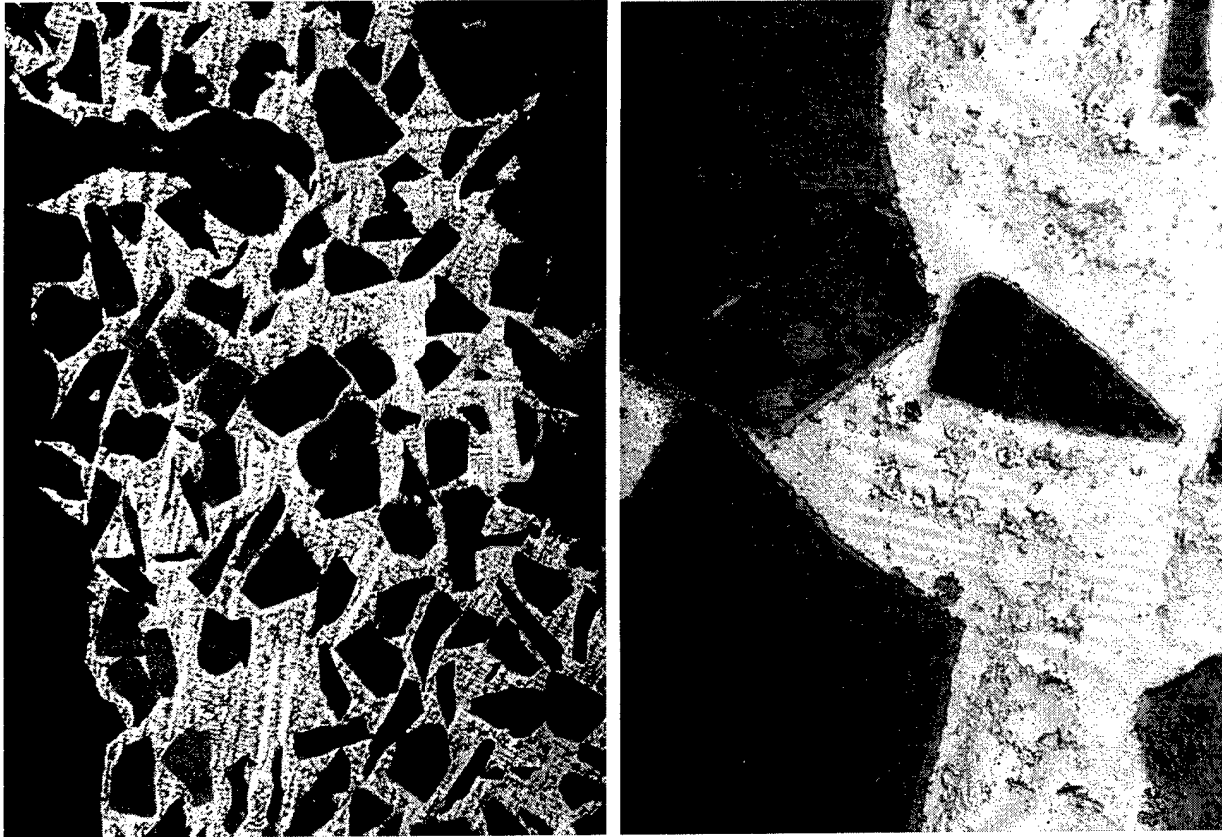


Figure 3. Microstructure of ABT produced at 2400 J/cm<sup>2</sup>, 50X (left) and 500X (right).

### Thermal Boundary Effects

Experimentation with different mold materials, energy densities, and preheats indicated that the solidification microstructure in a component can be controlled. This implies that the mechanical properties of a component can also be controlled or tailored through region specific manipulation of the microstructure. The variables listed above were manipulated to alter the cooling rate and thermal gradient and thus the solidification rate. The solidification dendrite arm spacing  $d$  can be described as a function of local solidification time  $t_f$  or the average cooling rate  $\dot{\epsilon}_{avg}$  during solidification as<sup>12</sup>

$$d = at_f^n = b\dot{\epsilon}_{avg}^{-n}$$

where  $a$  and  $b$  are constants, the exponent  $n$  is usually 0.3 to 0.5 for secondary spacings and nearly 0.5 for primary spacings.

The constants  $a$  and  $b$  are related because the local solidification time  $t_f$  is a function of the average cooling rate  $\dot{\epsilon}_{avg}$  during solidification and the solidification temperature range  $\Delta T$ , which is a physical property of the alloy. Thus,

$$\dot{\epsilon}_{avg} = \frac{\Delta T}{t_f}$$

The average cooling rate in turn is the product of the temperature gradient at the solid-liquid interface  $G$  and the velocity of the solidification front  $R$ . Thus,

$$\dot{\epsilon}_{avg} = \frac{\partial T}{\partial t} = \frac{\partial T}{\partial x} \times \frac{\partial x}{\partial t} = G \cdot R$$

It is evident that the temperature gradient and the solidification rate are easily manipulated through preheat, laser power density, scan speed, scan spacing and thermal boundary conditions at the mold-melt interface. Therefore the dendrite spacing as well as the solidification mode can be controlled through control of these parameters. For example, it has been shown<sup>9</sup> that the solidification microstructure of SLS processed MAR-M-247 superalloy is a function of laser energy density and thermal boundary conditions, ranging from fine-grain equiaxed to dendritic and directionally solidified. Mechanical properties such as fatigue can be improved through dendrite arm spacing refinement.

The solidification mode, *i.e.* plane front, cellular, dendritic or equiaxed as well as the types of defects that can form such as shrink and entrapped broken dendrite tips are known to depend on the cooling rate  $GR$  and the ratio  $G/R$ <sup>13</sup>. Increasing  $G/R$  results in progressive transition from equiaxed to dendritic towards cellular onto planar front growth. Increasing the cooling rate  $GR$  results in finer structures. Thus  $G/R$  influences the type of structure whereas  $GR$  controls the scale of the structure. In laser surface remelting, the velocity of the solidification front is known to be related to the velocity of the moving heat source via the epitaxial growth angle<sup>14</sup>. Therefore, by appropriate control of process parameters in direct laser processing such as preheat temperature, laser power density, scan speed, scan spacing and thermal boundary conditions, it is indeed possible to locally control the type, scale and directionality of the solidification microstructure. An example of process control to obtain epitaxial growth is shown in Figure 4.

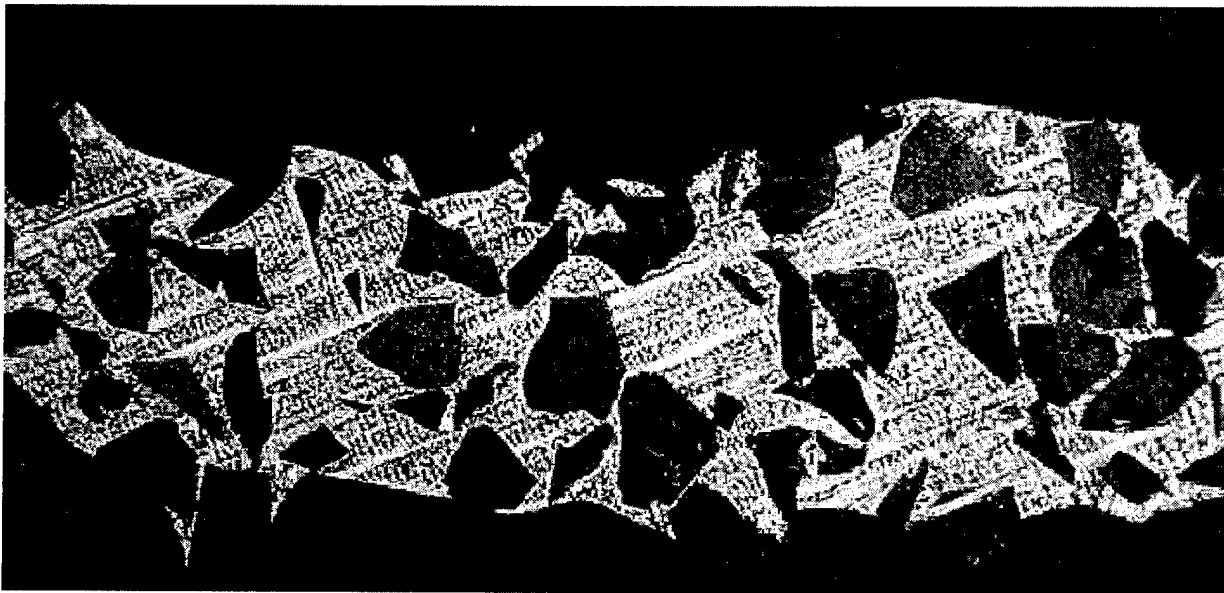


Figure 4. Directional solidification (DS) by imposing insulating boundary condition at mold surface, 50X.

## **Direct Laser Fabrication of a Gas Turbine Engine Component - Microstructure and Properties – Part II**

### **Processing Atmosphere**

Both rough vacuum and the purged argon contained sufficient oxygen to oxidize the molten alloy thus causing balling, separation, and tearing due to surface tension effects. The high vacuum atmosphere resulted in relatively uniform surface features, no cracking, tearing or separation when experimentation was conducted within an acceptable window of parameters. Volatilization of low vaporization temperature elements may be a concern depending upon preheat temperature and alloy composition. Volatilization can lead to problems with alloy depletion and or laser energy inconsistencies over long periods of time.

### **Reactive metal coating thickness and quality**

Two vendors were evaluated for depositing the reactive metal coating on the abrasive ceramic grit. Significant differences were noted in how the product performed when subjected to the SLS process. In some instances the SLS preform would simply disintegrate while in other instances the preform was not sufficiently strong to withstand surface grinding. Internal contamination of the superalloy matrix was noted on the microstructure of these specimens. In other cases the components performed flawlessly in all aspects. An analysis of the coating deposited on the abrasive grits explained the differences.

Coated grit from two vendors were metallographically analyzed for coating thickness and uniformity. The photomicrographs shown in Figure 5 illustrate the difference in coating thickness and uniformity. The titanium coating thickness on Brand B is greater and much more uniform than of Brand A. Consequently, the Brand B material always performed better. However it was also noted that when the Brand A coating thickness was increased, the performance of Brand A still did not compare to that of Brand B. It was also noted that when only the Borazon 510 CBN (titanium coated cubic boron nitride) was used in the powder mixture the results were excellent. Therefore, chemical analysis of the Ti coating on both Brand A and Brand B titanium coated alumina as well as the Borazon 510 CBN was performed. The contaminants C, O, and N were of interest. Significant levels of these contaminants could dramatically diminish the performance of the Ti coating and consequently the overall integrity of the laser processed cermet.

Two types of analyses were conducted in order to determine the contaminant content in the Ti coating. Auger analysis with intermittent ion milling from the surface of the particle provided data at different depths of the coatings. The data from this analysis is shown in Table 2 and Figure 5, Figure 6 and Figure 7. The tabular data at different depths indicates that the surface layers of all coatings analyzed were severely contaminated. A significant drop in contaminant level was noted at 1000 Å on all coatings, however the levels were still extremely high. At 1000 Å a large drop to relatively pure material was noted on the CBN coating while both the Brand A and Brand B dropped to near similar levels with Brand A having the highest overall contaminant level. At 5000 Å only the CBN still possessed coating. The CBN's titanium coating at 5000 Å was relatively pure. The data from the Auger Analysis indicated that the overall thickness and uniformity as well as purity at depths of approximately 1000 Å is of high importance in

performance. Auger analysis could not discern nitrogen from titanium because of peak overlap. Therefore microprobe analysis was conducted on cross-sectioned samples.

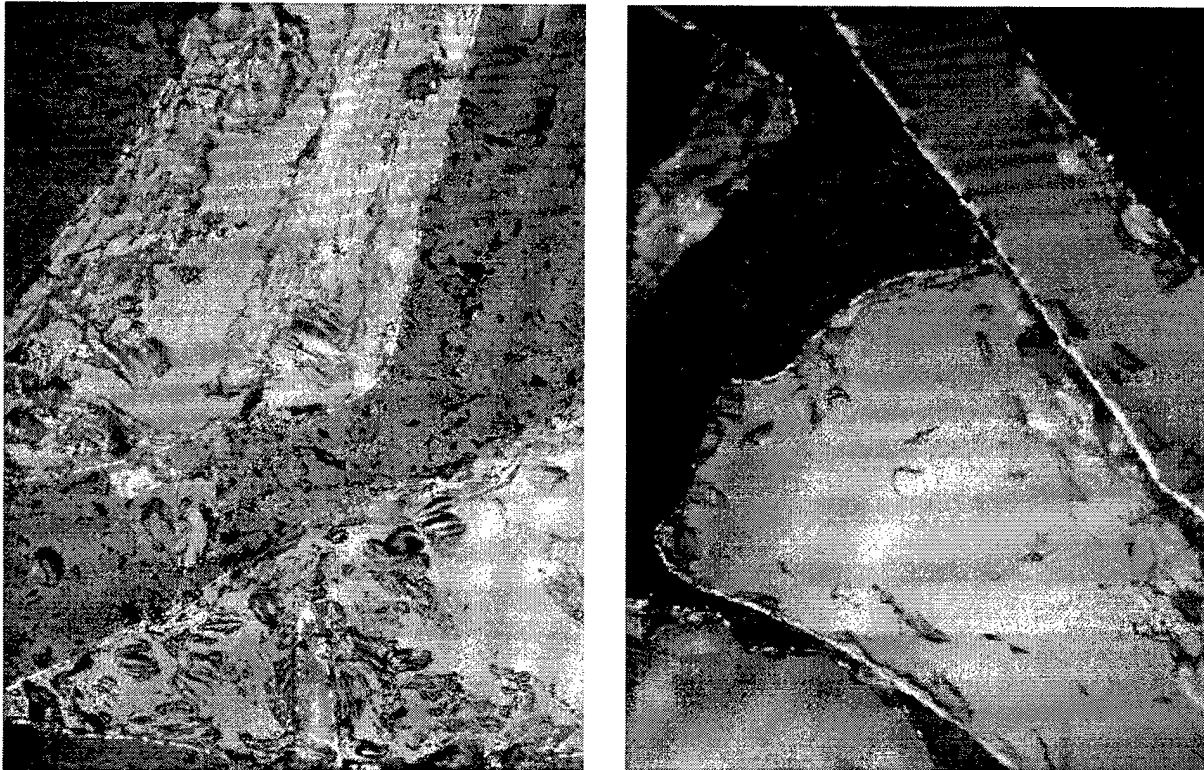


Figure 5. Titanium coating thickness and uniformity, Brand A (left) and Brand B (right), 500 X.

Atomic % Concentrations

	<u>Surface</u>			<u>100 Angstroms</u>			<u>1000 Angstroms</u>			<u>5000 Angstroms</u>		
	Ti	O	C	Ti	O	C	Ti	O	C	Ti	O	C
CBN	35.6	33.8	30.6	72.7	16.0	11.3	92.0	3.1	4.9	92.7	1.5	5.8
Brand B - 5.2 wt %		#		78.0	12.7	9.3	79.8	13.0	7.2		*	
Brand A - 5.2 wt %		#		56.1	20.6	23.3	73.7	10.1	16.2		*	
Brand A - 2.4 wt. %	21.1	23.8	55.1	50.7	32.2	17.1		*			*	

# - Surface was charging too much to obtain data.

This indicates that there was no free titanium or carbon

\* - Lack of data indicates that base particle had been exposed by ion milling.

Note: Nitrogen cannot be discerned because nitrogen peak overlaps with titanium peak.

Table 2. Auger chemical analysis of titanium coating.

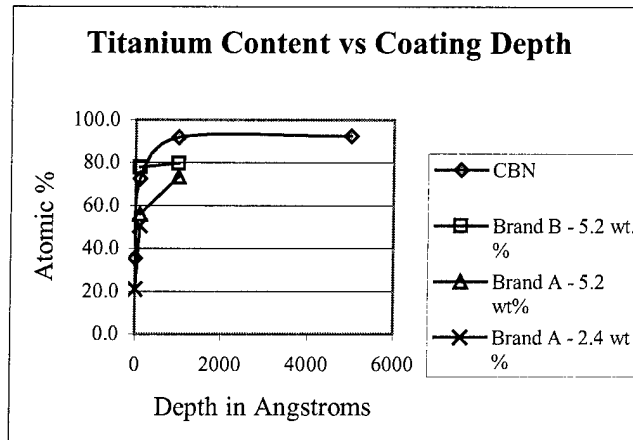


Figure 6. Titanium coating purity vs. coating depth.

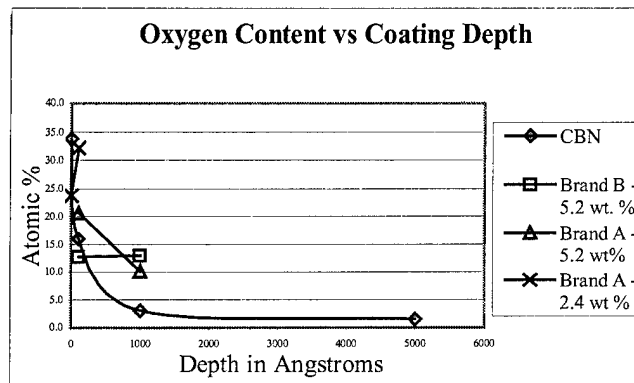


Figure 7. Oxygen content vs. titanium coating depth.

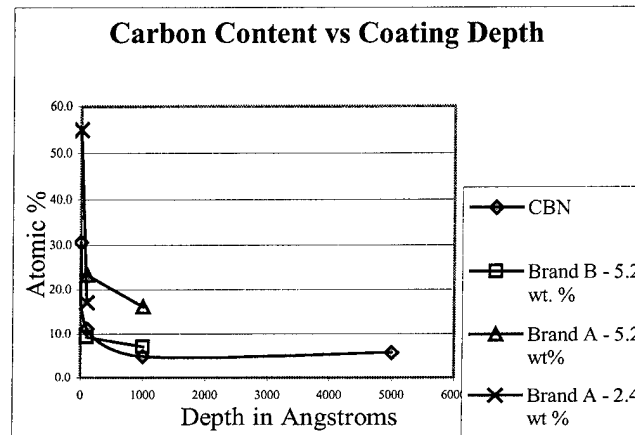


Figure 8 Carbon content vs. titanium coating depth.

The results of microprobe analysis are shown in Table 3. The microprobe analysis also suggested that the CBN had the purest titanium coating. Brand A coating did have a much higher nitrogen content than Brand B with the overall contaminant content being similar. When a composite contaminant level is calculated for each of the abrasive grits using the C and O Auger data at 1000 Angstroms and the N levels from the microprobe analysis, a clearer picture of the performance is evident. The CBN composite contaminant content is approximately 28 atomic %, The Brand B Ti coated alumina is approximately 42%, While that of Brand A is approximately 63%. The chemical analysis data indicates that there is a significant difference in the coating purity of the three different grits. The results of the SLS trials combined with the chemical and metallurgical analysis indicated that the coating's uniformity and overall chemical purity are all equally important. The coating thickness is also important. However, the presence of significant residual coating on SLS processed specimens such as that shown earlier in Figure 3 indicate that the coating's thickness is not as important as uniformity or chemical purity.

<b>Microprobe Data for Cross - Sectioned Grit Samples</b>				
Weight %	CBN	Brand B - 5.2 wt. %	Brand A - 5.2 wt%	Brand A - 2.4 wt %
	Avg.	Avg.	Avg.	
Ti	86.3	72.0	69.2	39.0
Al	0.0	0.6	4.3	14.3
O	5.9	17.1	7.5	43.5
N	7.9	10.4	19.0	3.2
	100.0	100.0	100.0	100.0
Atomic %	CBN	Brand B - 5.2 wt. %	Brand A - 5.2 wt%	Brand A - 2.4 wt %
	Avg.	Avg.	Avg.	
Ti	66.1	48.7	43.3	19.0
Al	0.0	0.6	6.7	12.3
O	13.5	30.2	13.6	63.4
N	20.4	20.5	36.4	5.3
	100.0	100.0	100.0	100.0

Table 3. Microprobe data for cross-sectioned grit samples.

### Effect of Dopants

Due to some of the processing difficulties encountered because of the coating uniformity and purity, an experiment involving doping was performed. Doping consists of adding a material to the cermet mixture that would assist in scrubbing and breaking down the highly contaminated surface of the Ti coating on the grit particle and also assist in cleaning the remainder of the melt. Scrubbing of the Ti coating is necessary in order to clean the refractory type surface and activate the more pure underlying Ti in order to improve the wetting and bonding with the superalloy matrix. Different methods were evaluated for adding various levels of free Ti to the melt. Other elements that have been evaluated as dopants are F and Y. Both methods yielded promising results. In addition to Ti doping, multiple coatings were also evaluated. The coating in this case

was a very thin Ni overcoat with minor addition of dopant type elements. Both the Ti doping and the multiple coating provided dramatically improved SLS results.

The initial trial of an addition of 1 to 2 wt.% Ti provided an exceptional cermet coupon. However, when the coupon was metallurgically analyzed, it was noted to have Topologically Close Packed (TCP) phases, shown in Figure 9 as the light cross hatched needle phases nucleating off the interdendritic eutectic phase. TCP phases result in Ni base superalloys as a result of improper chemistries or chemical imbalances. TCP phases typically have an acicular or needle like morphology and are very hard. These phases are deleterious to high temperature mechanical properties such as stress rupture, tensile, and creep<sup>11</sup>, and are therefore not desirable. An additional effect of the Ti addition that can be noted in the low magnification micrograph is the excessive amount of interdendritic eutectic that forms as compared to previous samples without the Ti addition.

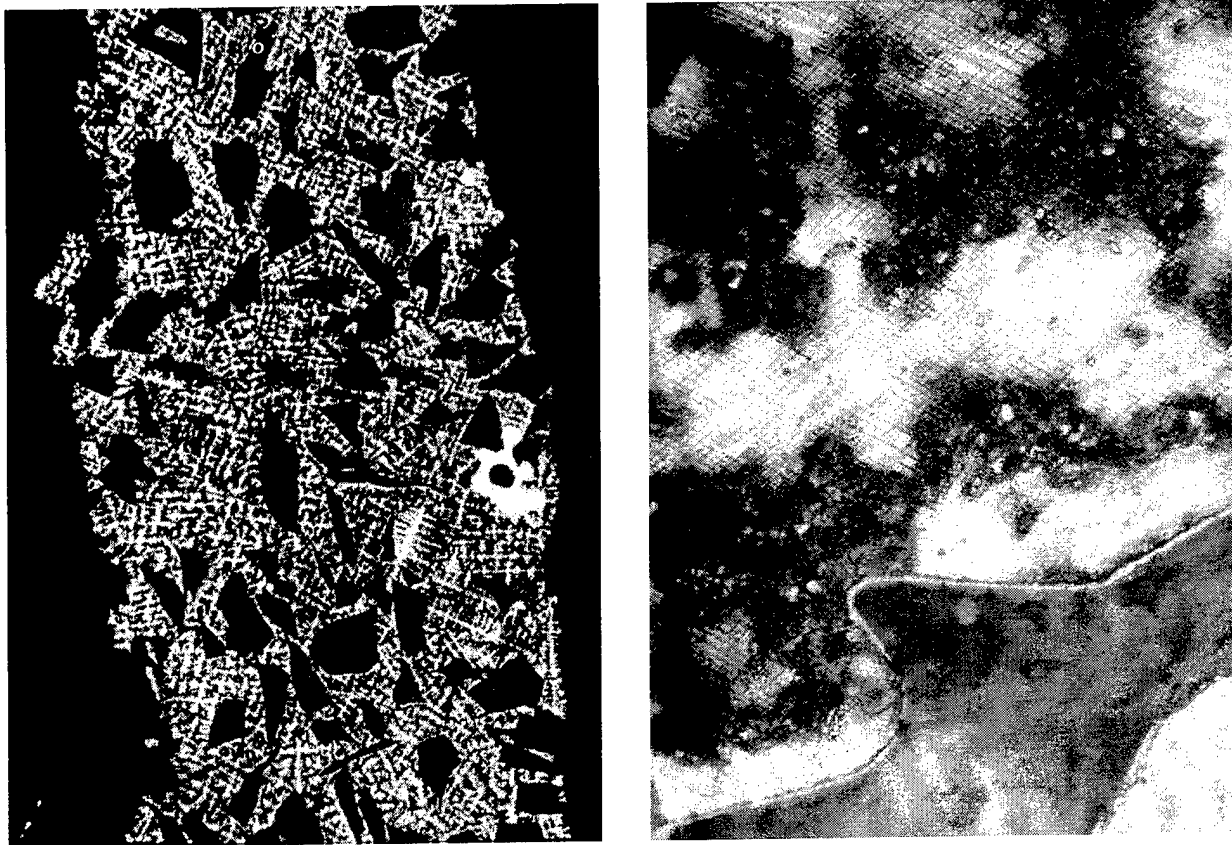


Figure 9. Topologically Closed Packed (TCP) phases resulting from 1 wt.% free Ti addition, 50X (left) and 500X (right).

### **Mechanical Properties**

Stress-rupture and rub-testing of SLS processed ABT cermet material have been reported previously<sup>9</sup>. The stress rupture samples were divided into two distinct groups: ABT specimens with uniform surface appearance and ABT specimens with some “acceptable” levels of pitting and

porosity. The surface condition did not produce any difference in stress rupture properties. An additional variable involved eliminating the 2150°F/32 hour standard diffusion cycle from some of the specimens. Elimination of the braze diffusion heat treat cycle significantly improves the properties of the CMSX-4 base material. The stress-rupture data in Larson Miller form is shown in Figure 10. The testing was conducted in the temperature range of 1900°F to 2200°F with some of the samples tested in excess of 500 hrs. The samples brazed without the diffusion heat treat cycle exhibited slightly reduced life. All samples failed in the braze joint and did not traverse the SLS material. This indicates that the plot of Figure 10 is actually a representation of the braze bond strength. Standard production material exhibits failures that traverse through the center of the cermet because of the braze component in the standard mixture. Therefore this difference in failure mode indicates an improvement in temperature capability of the laser processed cermet. These results imply that the brazeless material composition processed by direct SLS is superior to the standard cermet.

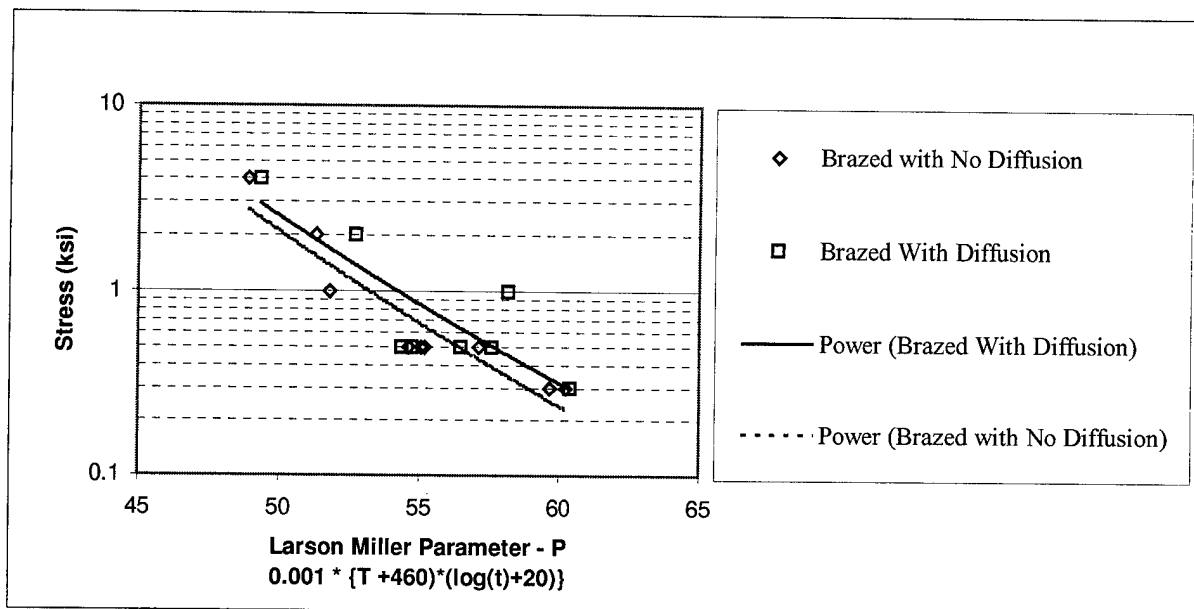


Figure 10. Stress-Rupture of CMSX-4 bar with ABT brazed in-gage.

## FUTURE WORK

The primary goal of future work is to develop a laser process for direct tipping. Direct tipping is performing SLS on top of the turbine blade and actually bonding the cermet layer to the blade at the same time that melting and densification is occurring. A laser based process that fabricates abrasive tips directly onto turbine blades will yield three important benefits. The first and most important potential benefit is that the base material of the blade will have substantially better mechanical properties since it will not be exposed to either the braze or diffusion thermal cycles. Both the braze and diffusion cycles involve high temperatures and long times which degrade the microstructure and mechanical properties of the base material. Elimination of these degrading thermal cycles will allow higher design mechanical properties and higher operating temperatures, potentially resulting in designs that improve efficiency. Second, the need for

tooling and the intensive labor associated with preparing and brazing tips to blades will be eliminated. Third, mechanical properties of the tip-blade bond interface will be improved as a result of epitaxial solidification of the tip material off the blade base material.

Additional goals of the future include incorporating process understanding and control such that region specific or tailored microstructures can be produced. This ability could significantly improve the performance of a given region or component overall thus increasing expected life. Such achievements may also allow the repair of single crystal turbine hardware to original conditions or the production of super plastically formable components of a given alloy which were not available previously. The total control over processing environment should favor technological breakthroughs in the manufacture of net shape components in extremely difficult to process high performance materials such as refractories, in-situ composites, and intermetallics.

## CONCLUSIONS

A successful direct SLS process was developed and approximately 100 tips produced. The process developed achieved all of the objectives and goals originally set forth. The goals are listed below.

1. Raw material input is proportional to quantity of tips needed.
2. Fall off materials are reusable.
3. Majority of processing steps of standard production process eliminated.
4. Process produces the fully dense component in a single pass by achieving full through thickness melting.
5. Mechanical properties were improved by eliminating the cobalt braze material from the cermet composition .
6. Elimination of Processing steps, scrap, fall off, and input stock required produced cost savings in excess of that originally calculated.
7. Microstructure, properties and performance are superior to that of the standard production material.

In addition to achieving all of the original program goals and outlining parametric windows, important information was noted concerning the effects of preheat temperature, processing atmosphere, thermal boundary effects, energy density, dopants, and reactive metal coating quality on ceramic grit in cermets. Some of these effects are summarized as follows.

Preheating the powder bed has been shown to be beneficial by outgassing the powder thus preventing further contamination during processing. Preheat was also noted to improve the uniformity of flow and solidification of the molten material, thus enhancing the surface finish

uniformity of the final component. It is also known that preheat to appropriate temperatures also reduces hot tearing, hot cracking, and balling of the molten material.

Energy density and the associated parameters of laser power, scan spacing, and scan speed were crucial in minimizing hot tearing, balling and cracking. Without the proper selection of energy density parameters significant porosity, incomplete through thickness melting, and very poor surface finish may result.

The SLS apparatus developed during this program allows total process control. The extent of process control capability allows the manipulation of thermal boundary effects and solidification rates. This in turn may be used in the future to tailor region specific microstructures. Experiments conducted during this program illustrate that it is possible to dramatically manipulate the microstructure of the material.

The experimentation with different types of abrasive grit, Ti coatings and contaminant analysis revealed the importance of uniformity and purity of the reactive metal coating in the processability, performance and properties of cermets produced by direct SLS. High quality coatings can result in the difference between failure and success.

Dopants were evaluated in an attempt to overcome the detrimental affects of the poor quality reactive metal coatings. The usefulness of dopants to improve melt cleanliness and activate the reactive metal coating on the abrasive grit to enhance bonding was demonstrated. However, caution should be exercised with dopants due to secondary affects resulting from alloy chemistry modification. The coated grits used for production were of sufficient quality that a dopant was not necessary to provide a robust production process. However, dopants may be very beneficial if one were to produce a very large part or multiple layer part.

## **ACKNOWLEDGEMENTS**

Partial funding for this work was provided by the United States Air Force, Contract No. F33615-94-C-2424. The remainder of resources were provided by Allison Engine Company and the University of Texas at Austin.

## **REFERENCES**

- <sup>1</sup> Marcus, H.L and D. L. Bourell, Solid Freeform Fabrication Finds New Applications, Advanced Materials & Processes, Volume 144, No.3, September 1993.
- <sup>2</sup> Proceedings of a Technical Interchange Meeting on "Metals/Processing for Engine Affordability", 9-10 April 1996, Williamsburg, VA.
- <sup>3</sup> Das, S. et al., Processing of Titanium Net Shapes by SLS/HIP, 1998 Solid Freeform Fabrication Symposium Proceedings.

- <sup>4</sup> Das, S. et al., Selective Laser Sintering of High Temperature High Performance Materials, 1996 Solid Freeform Fabrication Symposium Proceedings.
- <sup>5</sup> Proceedings of the First Air Force, Wright Laboratory S&T Affordability Exit Criteria Workshop.
- <sup>6</sup> Dix, D.M. and Riddell, F.R., *Projecting Cost-Performance Trade-offs for Military Vehicles*, Attachment to Anita Jones letter to JAST program office on IHPTET AFFORDABILITY, dated 31 August 1994, Aeronautics & Astronautics, September 1976.
- <sup>7</sup> Yeaple, F., Gas Turbine Rotor Grinds Own Tip Seals, *Design News*, 1-5-87, pp. 106-107.
- <sup>8</sup> Helms, Harold E. et al., *Ceramic Applications in Turbine Engines*, Noyes Publications, Park Ridge, New Jersey, 1986, pp. 131-137.
- <sup>9</sup> Fuesting, T. et al., Development of Direct SLS Processing for Production of Cermet Composite Turbine Sealing Components, 1996 Solid Freeform Fabrication Symposium Proceedings.
- <sup>10</sup> *Welding Handbook - Materials and Applications Part 1*, American Welding Institute, 550 N.W. Lejeune Road, Miami, FL.
- <sup>11</sup> Sims, Chester T., Norman S. Stoloff and William C. Hagel, eds., *Superalloys II - High Temperature Materials for Aerospace and Industrial Power*, Wiley-Interscience, 1987.
- <sup>12</sup> Flemings, M.C., *Solidification Processing*, McGraw-Hill, 1974, pp. 148.
- <sup>13</sup> Breinan, E.M. and B. H. Kear, Rapid Solidification Laser Processing at High Power Density, in *Laser Materials Processing*, Vol. 3 of Materials Processing Theory and Practices, North-Holland, 1983, pp. 239-255.
- <sup>14</sup> Carrupt, B., M. Rappaz and M. Zimmerman, in *Modeling of Casting and Welding Processes IV*, TMS, 1988, p. 581.

## Geometry Processing for SLS/HIP

Ravi Venkataramani, Suman Das, Joseph J. Beaman  
Laboratory for Freeform Fabrication  
University of Texas at Austin

### Abstract

SLS/HIP is a new net shape manufacturing method that combines the strengths of direct selective laser sintering and hot isostatic pressing. Direct selective laser sintering is a rapid manufacturing technique that can produce high density metal parts of complex geometry with an integral, gas impermeable skin. These parts can then be directly post-processed by containerless HIP. Sophisticated processing of the part geometry is required to facilitate the desired results from SLS/HIP. This paper presents geometry processing algorithms being developed for *in-situ* canning of SLS/HIP components. This research is funded by DARPA/ONR contract N00014-95-C-0139 titled "Low Cost Metal Processing Using SLS/HIP".

## INTRODUCTION

Selective laser sintering (SLS) is a layered manufacturing technique that can produce freeform three-dimensional objects directly from their CAD models without part specific tooling or human intervention. Parts are built by selectively fusing layers of a powder material using a scanning laser beam. Details on this process are described elsewhere<sup>1,2</sup>. The next generation of selective laser sintering i.e. direct fabrication of functional metal and cermet components and tooling is under development at the University of Texas<sup>3,4</sup>. To produce full density metal parts having complex geometry, a novel net shape manufacturing technique called SLS/HIP<sup>5,6</sup> has been developed at the University of Texas. The idea is to consolidate the interior of a component to 80% or higher density and to fabricate an integral gas impermeable skin or "can" at the part boundary *in-situ*. Sophisticated geometry processing is required to obtain the desired results. It is proposed to develop parametric representations of the part contours at the slice level. These parametric curves will then be offset in a suitable direction, to grow or shrink the curves, to generate skins. This parametric representation will also enable local shape change to compensate for any changes in dimension or shape that might occur after HIP post-processing for a specific part. These parametric representations for each layer are then used as the contours for SLS processing. The SLS processed part can then be directly post-processed by containerless HIP to full density. The optimal thickness of the skin will depend on the HIP deformation model and the tolerance requirements. A final machining step will result in a part having the desired geometry, mechanical properties and tolerance.

## BACKGROUND

In the SLS/HIP process (Figure 1), the component is produced by selectively consolidating a metal powder with a laser beam layer by layer. While producing each layer, a gas impermeable high-density skin (> 98% density) is formed at the boundaries

of the part. The interior of the part is laser processed to a high density typically exceeding 80%. Thus, the part is shaped and canned *in-situ*. The encapsulated part is evacuated, sealed and post-processed by containerless HIP to full density. A final machining step may be applied if necessary.

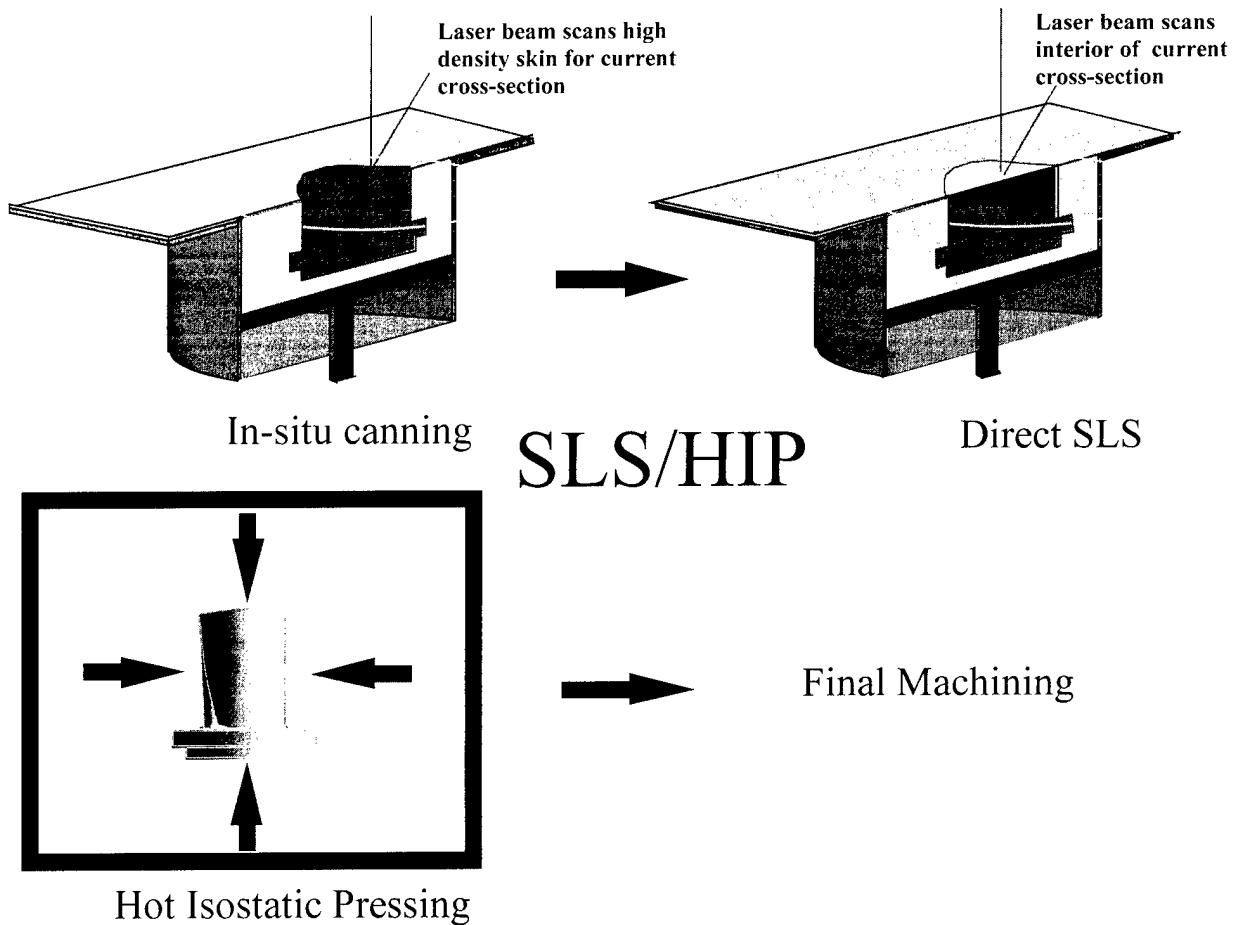


**Figure 1** The SLS/HIP Process

Offset curves have been used in industry for a range of applications some of which are mold design, NC path planning, tolerance analysis and CAD in the automobile industry. An offset curve is a curve parallel to the original curve at some offset distance. Offsets can be generated for implicit curves as well as freeform curves. Offset techniques have been well established for a series of parametric curves like Hermite curves<sup>7</sup>, B-splines<sup>8</sup>, NURBS<sup>9</sup>, Pythagorean Hodograph curves<sup>10</sup> etc. It is proposed to use B-splines and NURBS for the considered application.

B-splines have been chosen because they are used widely in industry and have been well documented. However they cannot represent regular or implicit curves like conics precisely. NURBS, being rational, are more versatile in representing both freeform and regular curves precisely. One of the drawbacks of using NURBS is that the offsets generated will not be rational requiring the use of special polynomial parametric curves like Pythagorean Hodograph curves, which surmount this problem.

## GOALS

This research proposes to address the following issues:

Generation of skins for each slice contour data, modification of part geometry based on part-specific HIP deformation models, development of intelligent scan patterns to produce an integral, gas impermeable skin by SLS, and to incorporate the above in intelligent process control.

## PROCEDURE

The sliced CAD data file of the component considered gives the contours along each layer. A B-spline or a NURB is fit to the slice data points. Details on the formulation of B-splines and NURBS can be found elsewhere<sup>11,12</sup>. This parametric curve is then used to generate the offset. Depending on the relative location of the part contours at the slice level it may be required to grow or shrink the curve, thus denoting a positive or negative offset respectively.

### *Offset Procedure*

Let  $(x(t), y(t))$  be a point on a parametric curve  $C$ . Then, the curve  $C_0$  offset a distance  $\pm d$  has points  $(x_0(t), y_0(t))$  that satisfy the equations<sup>13</sup>

$$x_0(t) = x(t) \mp d \frac{\dot{y}(t)}{\sqrt{\dot{x}(t)^2 + \dot{y}(t)^2}}$$
$$y_0(t) = y(t) \pm d \frac{\dot{x}(t)}{\sqrt{\dot{x}(t)^2 + \dot{y}(t)^2}}$$

where  $(\dot{x}(t), \dot{y}(t))$  is the tangent vector at  $(x(t), y(t))$ . This is illustrated in Figure 2.

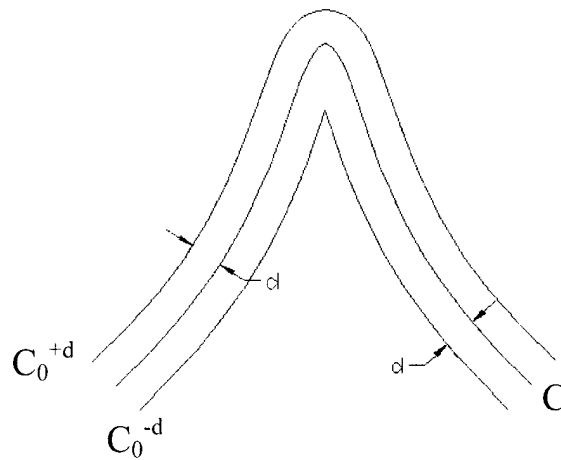


**Figure 2** Offset Procedure

Some of these offset curves may have self-intersections forming loops as shown in Figure 3. These loops need to be removed to get an intersection-free contour, giving the offset.

#### *Loop Removal*

In order to remove loop that may occur in the offset generated the following sequence of operations may be performed

- 1) Analyze the offset for self-intersections<sup>13</sup>. Self-intersections define multiple closed loops<sup>14</sup>.
- 2) If the direction of rotation of such a loop is inconsistent with the direction of rotation of the original contour, it is removed.
- 3) For loops whose direction of rotation is consistent, check the span of the remaining part of the offset.
- 4) If the span of the remainder is greater, discard the loop.
- 5) If the span of the loop is greater, keep the loop and discard the rest of the offset.

The result of the given set of operations on an offset curve with self-intersections is shown in Figure 4.

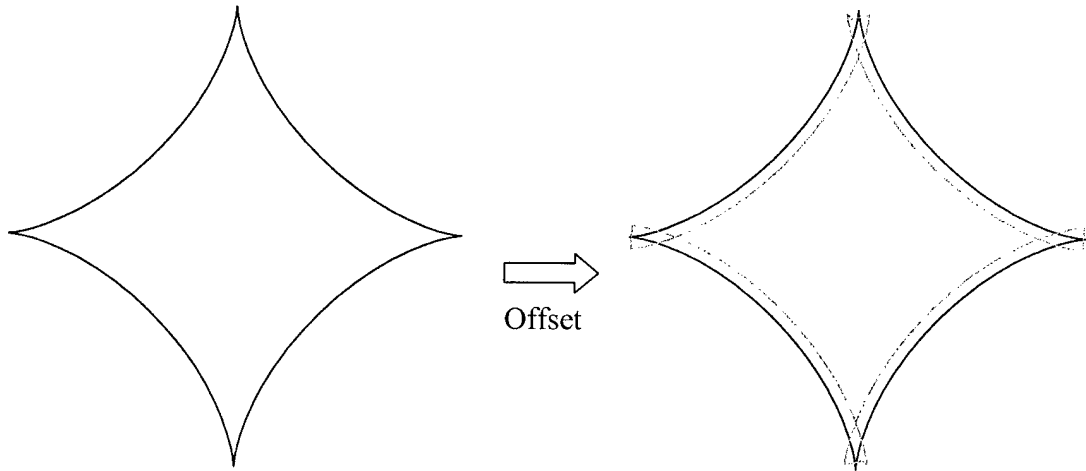


**Figure 3** Offset with loops

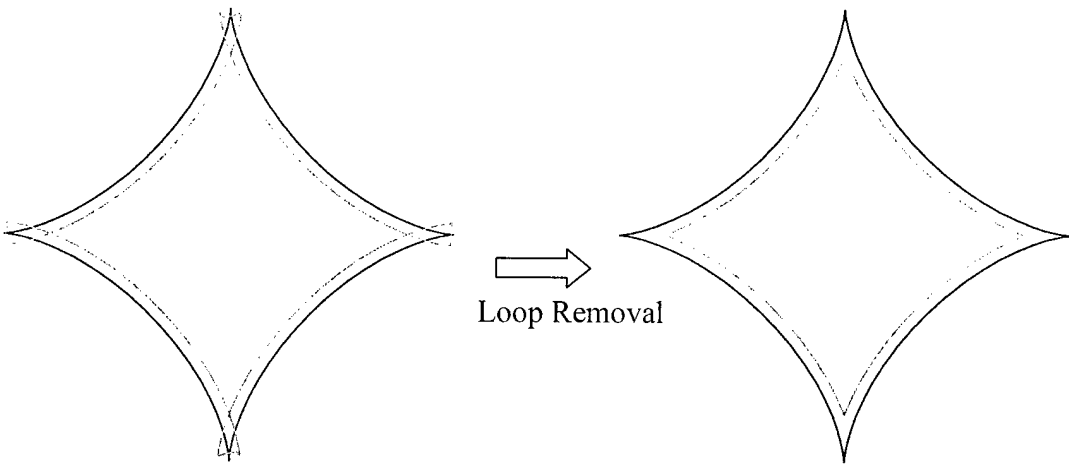


**Figure 4** Loop Removal

## RESULTS

Two test cases were considered to validate the algorithm, one for a freeform contour and the other for a regular or implicit contour.

### *Case 1 : Slice Contour of a Stator Vane*

This is one of the candidate components chosen to demonstrate the capabilities of SLS/HIP.

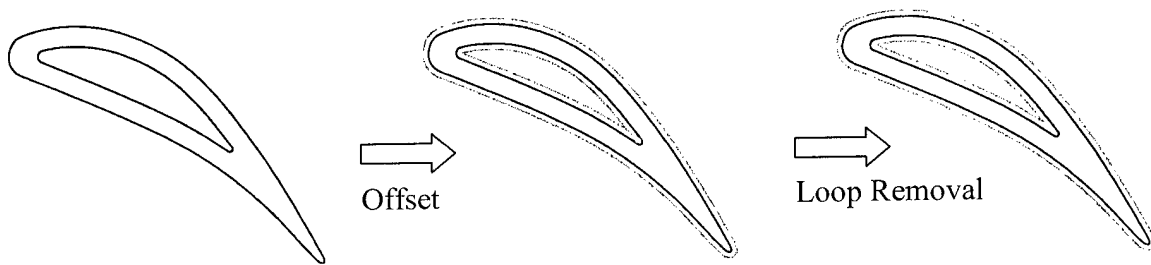


**Figure 5** Growing of the Stator Vane

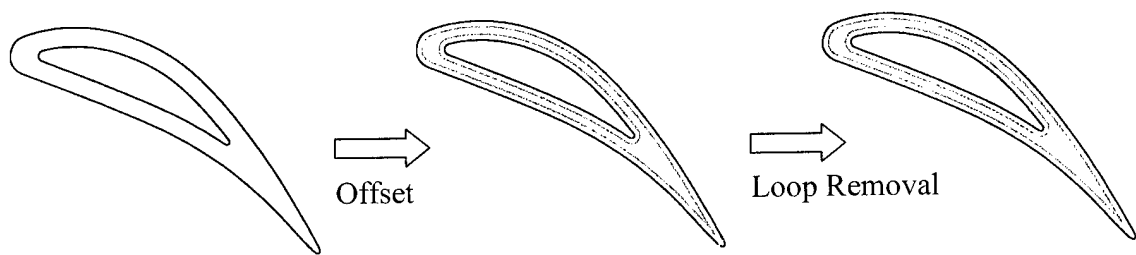


**Figure 6** Shrinking of the Stator Vane

*Case 2 : Curve with Convexities*

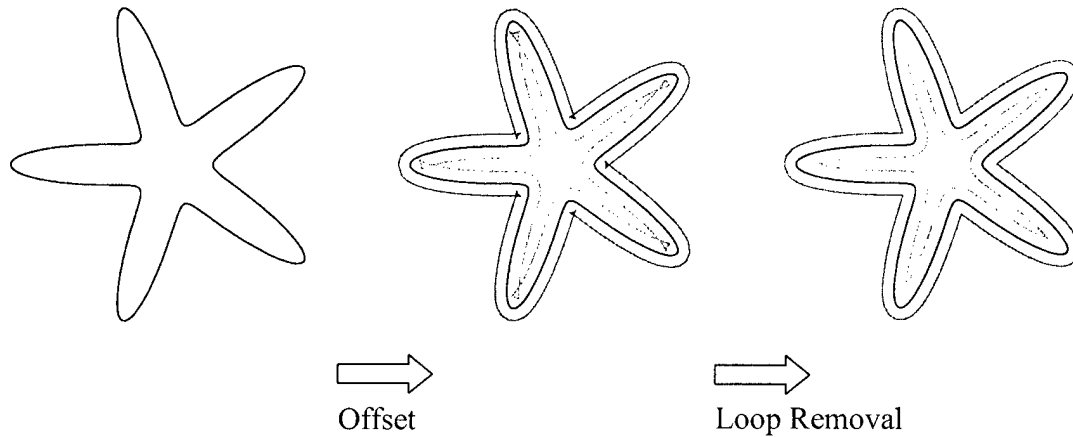


**Figure 7** Offset of an Implicit Curve

The polar form of the curve of Figure 7 is given by

$$\rho = \frac{p}{1 + \epsilon \cos(m\varphi)}$$
$$p > 0, \quad 0 < \epsilon < 1, \quad m \in \mathbf{N}, m > 1$$

**SUMMARY**

An offset technique for B-splines was developed and tested for a series of curves. This technique will be validated by producing an SLS/HIP component. A similar technique for NURBS should be developed to optimize contour specific processing. Part geometry re-engineering will be performed based on HIP deformation models.

**ACKNOWLEDGEMENTS**

This research is supported by DARPA/ONR contract #N00014-95-C-0139 titled "Low Cost Metal Processing Using SLS/HIP".

## REFERENCES

- <sup>1</sup>Beaman, Joseph J. and Deckard, Carl R., *Solid Freeform Fabrication and Selective Powder Sintering*, 15<sup>th</sup> NAMRC, North American Manufacturing Research Conference Proceedings, 1987, pp. 636-640.
- <sup>2</sup>Deckard, C.R., Ph.D. Dissertation, Department of Mechanical Engineering, The University of Texas at Austin, 1988.
- <sup>3</sup>Fuesting, et al, *Development of Direct SLS Processing for Production of Cermet Composite Turbine Sealing Components-Part I*, Solid Freeform Fabrication Symposium 1996 Proceedings, pp. 39-46.
- <sup>4</sup>Das, S., et al, *Selective Laser Sintering of High Performance High Temperature Metals*, Solid Freeform Fabrication Symposium 1996 Proceedings, pp. 89-95.
- <sup>5</sup>Das, S., et al, *Direct Selective Laser Sintering and Containerless Hot Isostatic Pressing for High Performance Metal Components*, Solid Freeform Fabrication Symposium 1997 Proceedings, pp. 81-90.
- <sup>6</sup>Das, S. et al, *Processing of Titanium Net Shapes by SLS/HIP*, Solid Freeform Fabrication Symposium 1998 Proceedings.
- <sup>7</sup>Klass, R., *An offset spline approximation for plane cubic splines*, Computer Aided-Design, Vol. 15 No. 4, 1983, pp. 297-299.
- <sup>8</sup>Pham, B., *Offset approximation of uniform B-splines*, Computer Aided-Design, Vol. 20, 1988, pp. 471-474.
- <sup>9</sup>Tiller, W., and Hanson, E.G., *Offsets of Two-Dimensional Profiles*, IEEE Computer Graphics and Applications, Vol. 4 No. 9, 1984, pp. 36-46.
- <sup>10</sup>Pham, B., *Offset curves in Layered Manufacturing*, ASME Manufacturing Science and Engineering, Vol. 2, 1994, pp. 557-568.
- <sup>11</sup>Rogers, D.F., and Adams, J.A., *Mathematical Elements for Computer Graphics*, 2nd ed., New York: McGraw-Hill, 1990.
- <sup>12</sup>Piegl, L., and Tiller, W., *The NURBS Book*, Berlin: Springer-Verlag, 1995.
- <sup>13</sup>Hoschek, J., *Offset curves in the plane*, Computer Aided-Design, Vol. 17 No. 2, 1985, pp. 77-82.
- <sup>14</sup>Choi, S., et al, *CAD and Control Technologies for computer-Aided Manufacturing of Laminated Engineering Materials*, Solid Freeform Fabrication Symposium 1997 Proceedings, pp. 643-651.

# Surface Finishing of Selective Laser Sintering Parts with Robot

Dongping Shi and Ian Gibson

Centre for Advanced Product Development Technologies  
Department of Mechanical Engineering  
The University of Hong Kong  
Pokfulam Road, Hong Kong

## ABSTRACT

Compared with conventional subtractive manufacturing technologies, RP has great benefits in shortening the design-manufacture cycle time of a product. Even if mechanical properties are not considered, most RP products still cannot be directly used in applications until the requirements for overall surface quality are satisfied. To improve the overall surface quality of Selective Laser Sintering parts, a robotic finishing system has been developed as a part of an ongoing research project. A finishing tool is held by a robot and moved according to programmed paths generated from the original CAD model data. This paper describes the experimental system in detail and shows that the surface roughness, dimensional accuracy, and geometrical accuracy can be improved.

Keywords: Rapid Prototyping (RP), Selective Laser Sintering (SLS), Surface Finishing, Robot.

## INTRODUCTION

Rapid prototyping is now widely regarded as a major technological breakthrough similar to the development of computer numerical control (CNC) technology. Compared with conventional subtractive manufacturing technologies, RP has demonstrated benefits in shortening the design-manufacturing cycle time. Over the last decade, RP has been developed quickly and is widely used in industries such as automotive, aerospace, medical and consumer electronics. As users become experienced, they seek more functional and practical RP parts in which the overall surface quality must compare with products manufactured by conventional technologies.

According to Wohlers in 1997 [1], almost one-third of all RP parts are being used for fit and functional applications, also more than one-quarter are being used as patterns for secondary tooling. These applications require RP parts to have a good overall quality, which includes surface quality and quality of mechanical properties. With the development of RP technologies and material science, the quality on mechanical properties of RP parts is improving and will continue to improve in future. But the surface quality is always influenced by some factors such as stair-steps and shrinkage since RP parts are produced layer by layer. Looking through all RP technologies at present, it is difficult to find a suitable RP technology by which the surface quality of parts produced can be comparable with CNC machining or precision machining. Without finishing or polishing in post-processing, RP parts can not be directly used in industries due to their poor surface quality.

With many materials capable of being processed, nearly any RP application can use a suitable SLS part as the required prototype. It is therefore important to improve the surface quality on SLS parts. Considering the combined characteristics of SLS and industrial robotics, an ongoing project in which a robotic finishing system has been developed for improving the

surface quality on SLS parts. Experiment results have shown that the surface roughness, dimensional accuracy, and geometrical accuracy can be improved.

### THE OVERALL SURFACE QUALITY ON SLS PARTS

In the field of manufacturing engineering, the exact degree of overall surface quality, which affects the functioning of a component and also its cost, is considerably important [2]. Usually, the overall surface quality includes surface roughness, dimensional accuracy, and geometrical accuracy. Surface roughness is the recurrent irregularities of a surface, which are inherent in the production process. The most common indicator of surface roughness is  $R_a$ , the arithmetic average roughness value over one sampling length. Accuracy is the correctness of dimension or geometry. Different manufacturing processes can obtain different overall surface quality [3]. For design engineers or production process planning engineers, the most important thing they should be concerned with is determining a set of suitable manufacturing processes in the shortest lead time for satisfying the application requirements on the overall surface quality.

In SLS, the overall surface quality of parts is influenced by many factors, some of which are shown in figure 1.

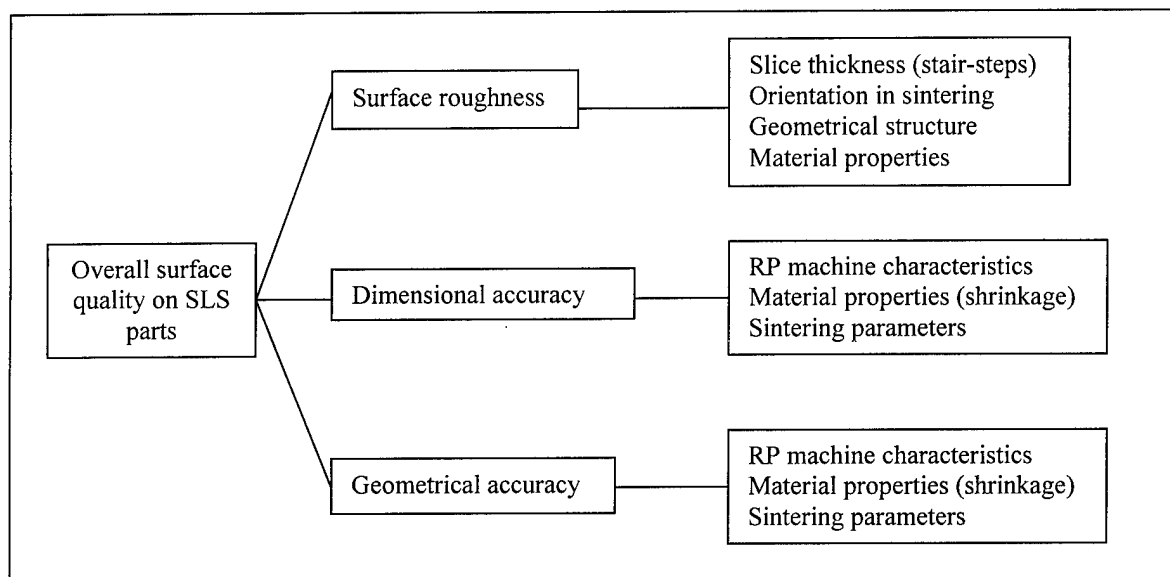


Figure 1 Influence factors of overall surface quality on SLS parts

To improve the overall surface quality on SLS parts, some efforts should be carried out on improving RP machine characteristics, optimizing sintering parameters, decreasing slice thickness, and improving material properties. At present, the minimum slice thickness in DTM SinterStation 2000 or 2500 systems is 0.003". The shrinkage of material is also unavoidable in the sintering process. Most SLS parts still have need of surface finishing or polishing to obtain a good surface quality. An industrial robot, with its programming flexibility and advanced kinematic structure, can assist in performing this finishing task.

### ARCHITECTURE OF ROBOTIC FINISHING SYSTEM

To improve the overall surface quality of SLS parts, a robotic finishing system has been developed. The architecture of the system is shown in Figure 2

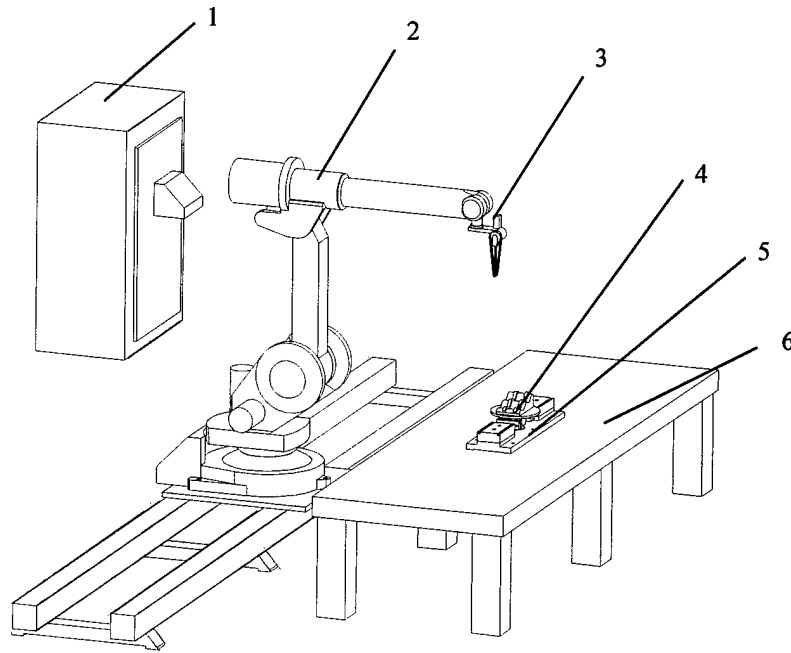


Figure 2 The architecture of the robotic finishing system: 1-controller; 2-articulated manipulator; 3-finishing tool; 4-SLS part; 5-fixture; 6-platform.

In the 3D modelling stage, a design part is produced using EDS Unigraphics (UG) software, which outputs a STL file to a SinterStation 2000 machine. If needed, a base fitting is added to the part. After the sintering process, the SLS part is placed in a fixture that is compatible with the base fitting. The position and orientation of the part relative to the robotic system is determined in the calibration process. The robot holds a high-speed finishing tool and moves over the surfaces according to a programmed path.

#### **ABB IRB1400 Robot**

This system uses an ABB IRB1400 robot, an industrial robot with 6-axis articulated movement and a linear external axis [4]. The robot is programmed using the machine-specific RAPID language [5]. In order to finish a part, the robot holds a finishing tool as its end-effector. Using a high-speed finishing tool, combined with the complex motion of the robot, results in a fine finish on the surfaces of the SLS part.

#### **Finishing Tool**

To achieve a smooth surface in the shortest time, the finishing tool should be changed according to the RP material, finished surfaces and surface requirements. The finishing tools used in this research include abrasive belts, ballnose endmills, spiral endmills, polishing bobs and special end brushes. Currently, finishing tool change is not automatic. Suitable finishing tools result in good surface quality.

#### **Fixture and the Base Fitting**

To be finished by the robot system, the SLS part should first be placed on a fixture. Since RP caters for different geometries, it is impossible to design a general fixture that is suitable for fixing all parts. It is therefore necessary to add a standard base fitting to the part at the design stage, which is fabricated during the sintering process. Some parts, such as injection rapid

tooling molds, have their own base fitting and do not need this additional feature. Using this method, many designs can be placed on a single fixture. The base fitting can also be designed to aid the position and orientation of the part relative to the robotic system during the calibration process.

### CALIBRATION AND ROBOTIC PATH PROGRAMMING

Co-ordinate systems exist within the robot system for the tool, user, object, base and world. It is necessary to define these correctly by calibration. The calibration procedure is divided into two steps: tool data calibration and base fitting calibration. Tool data calibration expresses co-ordinates in terms of the tool centre point (TCP). Base fitting calibration relates the position and orientation of the part relative to the base co-ordinates. Both calibration data are needed in programming robotic finishing paths.

The robotic paths are programmed using the ABB RAPID language. A software module was developed for generating robotic finishing paths. It was programmed using Visual C++ on a PC platform. The principle is based on the corresponding relationships between the RAPID language and the cutter location source file (CLSF) generated using UG software. The CLSF is a tool path file that describes machining processes in a UG manufacturing application [6].

### EXPERIMENTAL STUDY

With a DTM SinterStation 2000 system, SLS parts were produced using polycarbonate, nylon composite, fine nylon, true form and rapidsteel powders. After sintered or infiltrated with copper, some parts were then finished with the robot. Experimental results are shown in table 1 to table 3, figure 3 to figure 9. The surface roughness and surface profile were measured with a TAYLOR HOBSON surface texture-measuring machine (Form-Talysurf Series 2). The flatness was measured with a MITUTOYO coordinate-measuring machine (BLN122).

	Polycarbonate	Nylon Composite	Fine Nylon	True Form
Slope-planar surface (up 15°)	30~35µm	28~35µm	28~35µm	22~24µm
Slope-Planar surface (down 15°)	24~28µm	15~18µm	12~16µm	13~15µm
Planar surface (up)	18~22µm	14~17µm	12~16µm	7~10µm
Curved surface	32~36µm	32~36µm	32~36µm	30~34µm

Table 1 Surface roughness ( $R_a$ ) in the unfinished SLS parts (slice thickness=0.1mm, other parameters are default)

In table 1, it is very clear to see that surface roughness in the unfinished SLS parts is very poor especially in slope-planar surfaces and curved surfaces. It is also shown that surface roughness is varied with material types, geometrical structures and orientations.

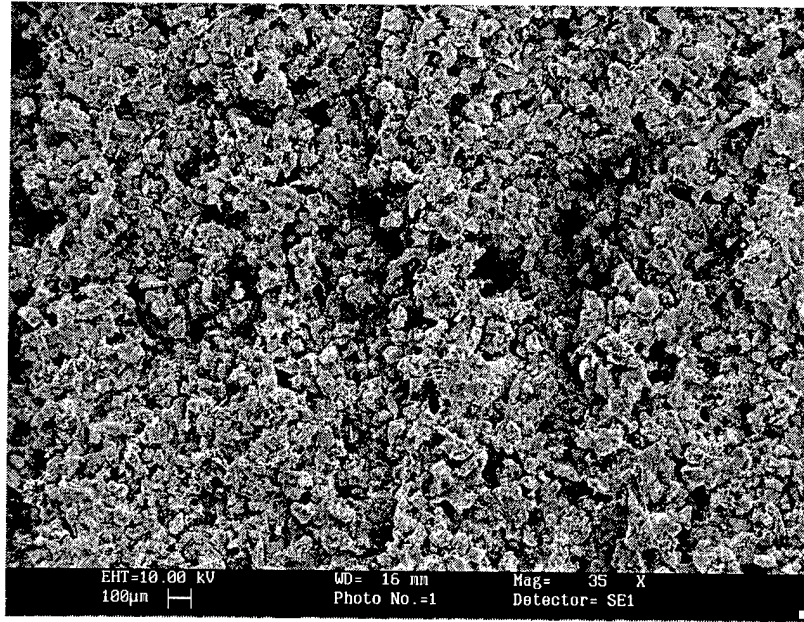


Figure 3 A microstructure of an unfinished slope-planar surface (material: fine nylon, slice thickness=0.1mm, slope angle=15<sup>0</sup> (upward), other parameters are default).

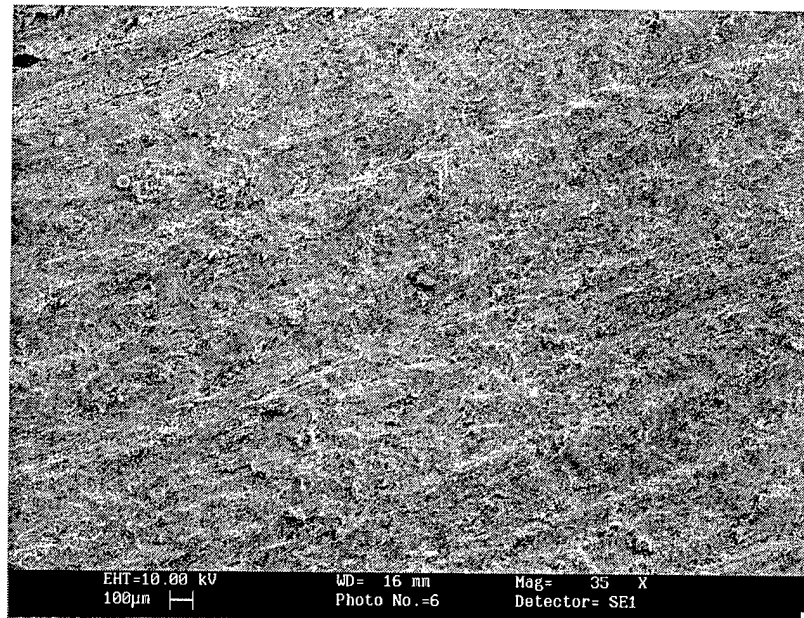


Figure 4 A microstructure of a finished slope-planar surface (material: fine nylon, slice thickness=0.1mm, slope angle=15<sup>0</sup> (upward), other parameters are default; finishing tool: abrasive belt, type: Zirconia, grit: Z#120).

In figure 3, we can see that particles adhered to adjacent surfaces. Stair-stepping can be seen clearly in this figure. When finished with abrasive belt, stair-steps were diminished and some grit marks were left on the surface in figure 4. Therefore, the surface roughness is

decreased after finishing. Figure 5 and figure 6 are surface roughness profiles on an unfinished curved surface and a finished curved surface.  $R_t$  is the vertical height between the highest and lowest points of the profile within the sampling length. Comparing figure 5 with figure 6, it is shown that both  $R_a$  and  $R_t$  are greatly decreased after robotic finishing.

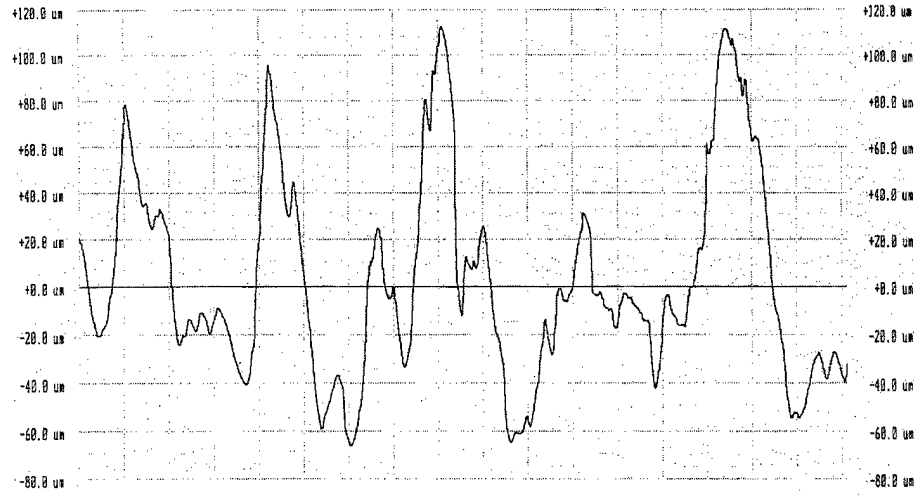


Figure 5 Surface roughness profile on an unfinished curved surface (material: fine nylon, slice thickness=0.1mm, other parameters are default,  $R_a=33.9250\mu\text{m}$ ,  $R_t=179.0299\mu\text{m}$ ; horizontal scale:  $200\mu\text{m}/\text{division}$ ).

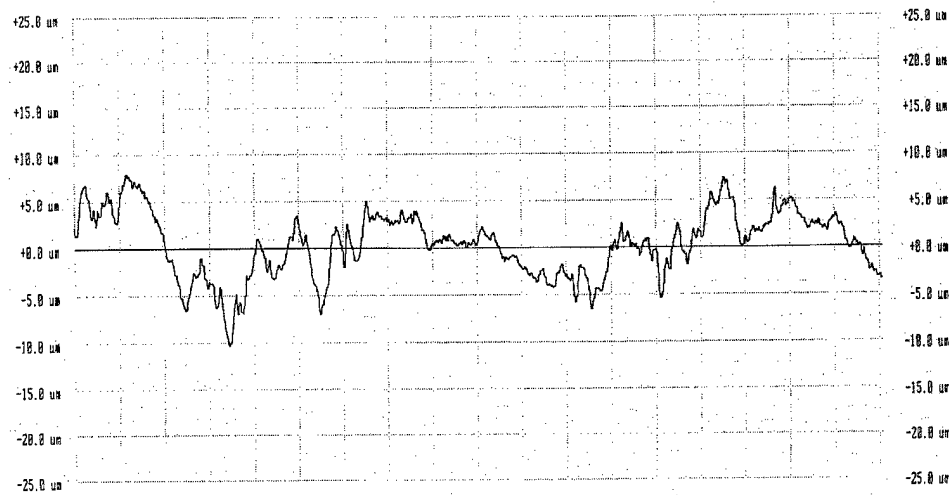


Figure 6 Surface roughness profile on a finished curved surface (material: fine nylon, slice thickness=0.1mm, other parameters are default; finishing tool: abrasive belt, type: Zirconia, grit: Z#120;  $R_a=2.7754\mu\text{m}$ ,  $R_t=18.3384\mu\text{m}$ ; horizontal scale:  $200\mu\text{m}/\text{division}$ ).

During finishing, some particles on the surface were melted due to machining temperature. Since the main defects on the surface are grit marks from tools, which influence the surface roughness, with the change of finishing tools it is possible to obtain different surface roughness as shown in table 2.

	Abrasive belt (type: Zirconia)			Ballnose endmill	Spiral endmill
	Z#80	Z#120	Z#180		
Fine nylon	6.0~10 $\mu$ m	2.8~4.5 $\mu$ m	2.5~3.8 $\mu$ m	3.2~4.8 $\mu$ m	3.5~4.2 $\mu$ m
RapidSteel	2.0~5.2 $\mu$ m	1.5~4.0 $\mu$ m	1.0~1.8 $\mu$ m	2.0~3.2 $\mu$ m	1.5~2.0 $\mu$ m

Table 2 Surface roughness  $R_a$  obtained by different finishing tools.

Another finishing example is on two RapidSteel molds. The two molds in figure 7 were made with RapidSteel at the same time. After furnace treatment, only one mold was finished by robot. Some experimental results are shown in table 3, figure 8 and figure 9.

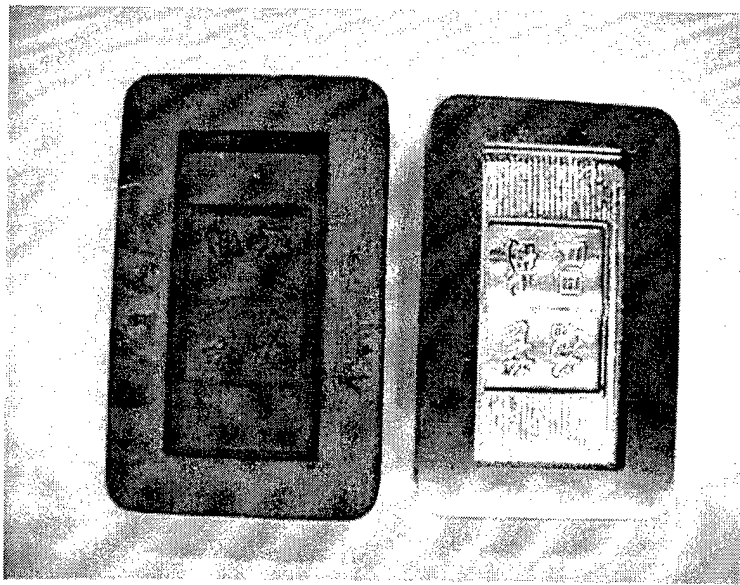


Figure 7 The two injection molds of HKU badge: left-unfinished (A); right-finished (B).

	Surface roughness		Dimensional accuracy		Flatness
	Curved surface	Planar surface	Length 50.25mm	Length 102.50mm	
Mold A (unfinished)	$Ra:14.5\sim15.5\mu\text{m}$ $Rt:165\sim220\mu\text{m}$	$Ra:8.5\sim9.5\mu\text{m}$ $Rt:128\sim135\mu\text{m}$	$49.38\pm 0.10\text{mm}$	$101.65\pm 0.15\text{mm}$	0.20mm/ 100mm
Mold B (finished)	$Ra:5.0\sim7.0\mu\text{m}$ $Rt:73.8\sim75.0\mu\text{m}$	$Ra:1.2\sim1.5\mu\text{m}$ $Rt:17\sim20\mu\text{m}$	$50.35\pm 0.05\text{mm}$	$102.65\pm 0.10\text{mm}$	0.05mm/ 100mm

Table 3 Surface quality comparison between the two injection molds.

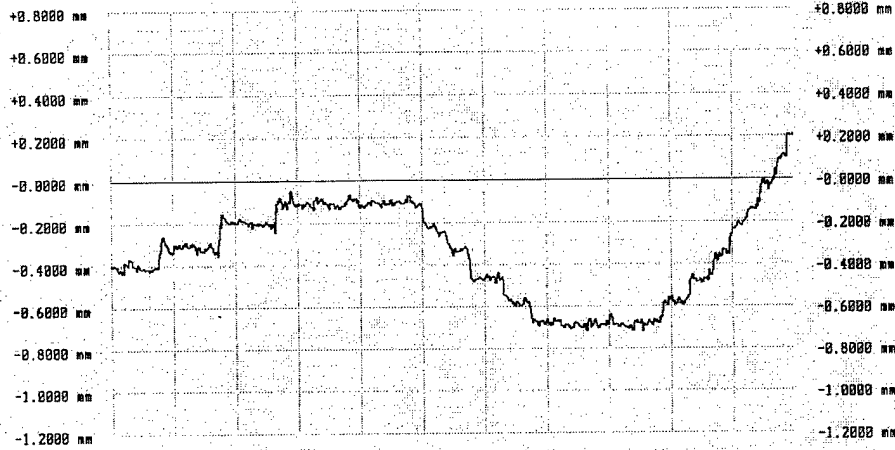


Figure 8 A section surface profile of mold A (horizontal scale: 2.0mm/division)

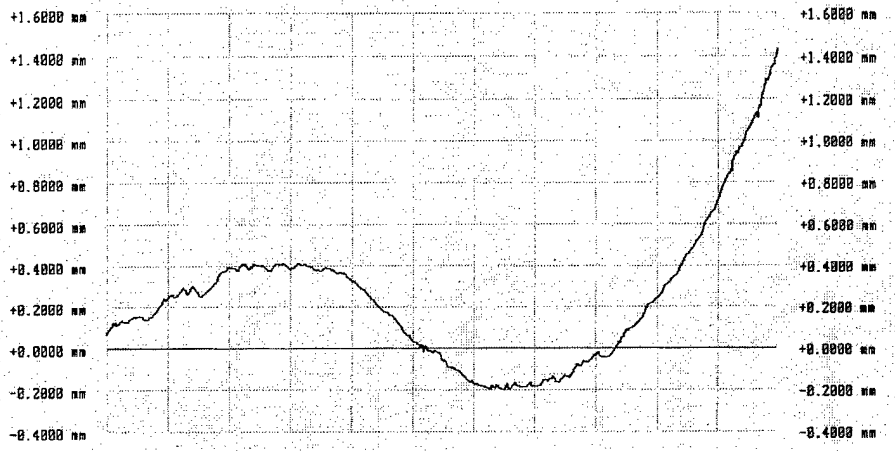


Figure 9 A section surface profile of mold B (horizontal scale: 2.0mm/division)

Table 3 is the surface quality comparison between the two injection molds. It is shown that surface roughness, dimensional accuracy and flatness are improved after the mold was finished. In mold A, it is very clear to see the stair-steps on the curved surface in figure 8. The top and bottom area of the curved surface appears planar due to lamination. After finished with the robot, we can see in figure 9 that stair-steps were diminished but their fragments still left on the surface profile. Because the robotic finishing paths are generated from the original CAD data, the geometrical accuracy of the surface profile was improved after the mold was finished. The overall surface quality of the injection mold will directly determine the surface quality of the final injected products.

## CONCLUSIONS

The overall surface quality of SLS parts is influenced by many factors. To improve the surface quality, some efforts should be carried out on improving RP machine characteristics, optimizing sintering parameters, decreasing slice thickness, and improving material properties. Due to stair-steps and shrinkage, surface finishing on SLS parts is needed.

The overall surface quality of SLS parts can be improved using a robotic finishing system. Because the robotic finishing paths are generated from the original CAD model data, the finishing process can eliminate the influences of stair-steps and shrinkage in the finished parts. Experimental results have demonstrated that surface roughness, dimensional accuracy and geometrical accuracy are improved in the finished SLS parts.

With the change of finishing tools, different surface roughness can be obtained. But dimensional accuracy and geometrical accuracy of the finished parts are mainly dependent on the robot accuracy. Further research will include continued experiments with different geometry parts, decision support for suitable finishing tools, development of an intelligent calibration technique and changing the open-loop control mode to a tool-based closed-loop mode.

## REFERENCES

1. Terry Wohlers, *Rapid Prototyping: State of the Industry—1997 Worldwide Progress Report*, Wohler Associates, Inc., 1997
2. H. Dagnall, *Exploring Surface Texture*, Rank Taylor Hobson Limited, 1986
3. B. H. Amstead, P. F. Ostwald, M. L. Begeman, *Manufacturing Processes*, John Wiley & Sons, Inc., 1986
4. ABB Robotics Products, *Product Manual IRB 1400*, 1995
5. ABB Robotics Products, *User's Guide*, 1995
6. EDS Unigraphics, *Manufacturing User Manual-Volume 2*, 1996



# Laser Polishing of Silica Rods

Hongyun Wang David Bourell Joseph J. Beaman  
Texas Materials Institute  
Laboratory of Solid Freeform Fabrication  
The University of Texas at Austin

## Abstract

Lasers have been widely used in surface modification. In this research a CO<sub>2</sub> continuous wave laser has been used to polish the slot surface of the silica rods. The strong absorption of the 10.6 μm CO<sub>2</sub> radiation by the silica surface promotes the softening of a very thin layer of material that flows under the action of surface tension. As a result, a mirror smooth glassy surface has been formed which decreases the surface roughness without any substantial change in the surface geometries. The effect of laser to surface inclination angle on the requisite power requirement was assessed experimentally and theoretically. With laser beam scanning controlled by a computer-aided design (CAD) database without specific tooling or human intervention, reliability and reproducibility of this process have been greatly improved compared to conventional fire polishing. The potential use of laser polishing as a post-processing step for freeform-fabricated parts is very promising.

## Introduction

Lasers have been widely used in surface modification. The properties of a surface layer of a metal or semiconductor are modified by changing its composition or microstructures using focused radiant energy. Laser-driven heating processes can also be used to enhance the resistance of crystal and glass surfaces to laser damage<sup>[1,2]</sup>. Recently, laser beams have been used to polish glass in the optics industry<sup>[3]</sup>. It has been suggested that preheating the bulk to a point above glass transformation temperature before starting the laser-driven surface heating process can help avoid the generation of undesirable thermal stress.

Surface finish is a critical and, for some applications, limiting feature of parts produced using Solid Freeform Fabrication (SFF). Selective laser sintering (SLS) uses a laser and scanning system, so the possibility of laser polishing SFF parts is a logical approach to surface finish improvement. It is most desirable to present the laser to a part without regard to part geometry specifics. That is, the most robust laser polishing process would not require "on the fly" changes in laser parameters such as laser power or the inclination of the laser onto the part surface. The purpose of this investigation was to assess the feasibility of laser polishing of a part with simple surface features and constant initial surface roughness. Specially, we have chosen a silica rod with slots mechanically cut into the periphery.

A conventional polishing process is fire polishing, which requires technicians to sweep a hand-torch over the silica slots. This process can smooth the edges of the slots, but because of the relatively narrow space between adjacent slots, about 0.07 inch wide, fire polishing cannot polish the inside surface. Obtaining reliable and reproducible surfaces by fire polishing is difficult because the process is highly dependent on the skill and technique of the technicians.

The disadvantages related to fire polishing are effectively overcome by irradiating the slot surface with a laser beam as discussed in this paper. The results of this work are directly applicable to surface finishing of freeform-fabricated parts produced both from silica and from other materials amenable to laser surface polishing.

This work was done at the laboratory of SFF at University of Texas at Austin, where the SFF approach was first invented, originally conceived as a shortcut to making models and

prototype parts. Solid Freeform Fabrication is now expanding its potential applications into short-run production, mold/die manufacturing, and smart laser processing.

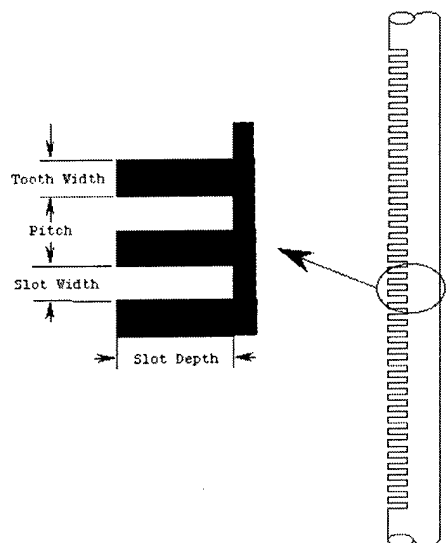
### CO<sub>2</sub> Processing Apparatus

Mechanically cut silica rod slots were used during the experiments. The geometry of the silica rods is shown in Figure 1. The silica slots were cut normal to the rod surface. The material was fused quartz, which is an amorphous phase of silica.

The absorptance of 10.6 μm radiation is about 80% for quartz<sup>[4]</sup>, which is one of the crystalline state of silica. This is a high level of absorption. There is no available absorptance data for fused quartz. Since the wavelength of CO<sub>2</sub> radiation is much longer than the wavelength of the absorption edge of fused quartz, fused quartz has very strong absorption of the 10.6 μm radiation also<sup>[2,3]</sup>. Fused silica does not reflect CO<sub>2</sub> laser significantly<sup>[4]</sup>.

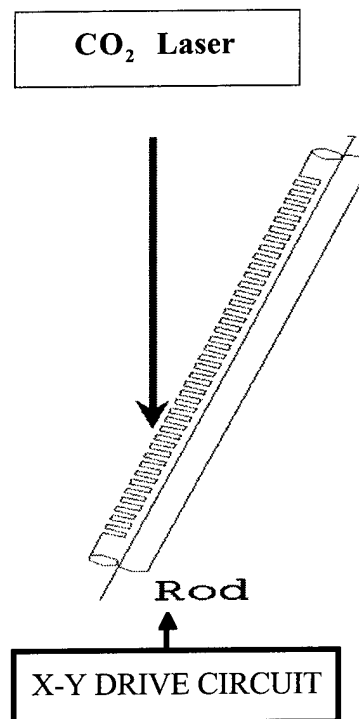
In Figure 2, a schematic drawing of the laser polishing process is shown. A CO<sub>2</sub> continuous wave laser, with a maximum beam power of 50 W, was incident on the rod with angle φ after passing through the optical system. The inclination angle φ has been defined to be the angle (in degrees) between laser beam and the normal to the slot surfaces. φ can be changed to accommodate different slot geometries. For this work, the silica rods were moved by a motor in the X-Y plane, and the angle φ had been set up manually by geometrical measurement.

### Quartz Rod Geometry



Diameter: 15 mm; Length: 50 cm  
 Tooth width: 0.07 inch; Slot width: 0.07 inch  
 Slot depth: 0.22 inch; Slots per rod: ~ 150

Figure 1. Schematic drawing of quartz rod



CO<sub>2</sub> Laser; φ: inclination angle

Figure 2. Schematic drawing of laser polishing

## Experimental

To facilitate the effects of polishing, initially large, flat surfaces were made by bisecting silica rods using the same method as the slot cutting. Two sets of experiments were set up. Test I was carried out using 32 and 40 watt laser beam power on the bisecting surfaces with  $\phi$  fixed at  $0^\circ$ . Test II was carried out using slot surfaces with various laser powers and angles,  $\phi$ . The test results were studied by using Scanning Electron Microscopy (SEM), optical microscopy, a profilometer and a beamscanner.

Laser scanning for this work was a single-pass set up, which is shown in Figure 3. During this process,  $\text{CO}_2$  laser radiation was incident on surfaces with different inclination angles,  $\phi$ .

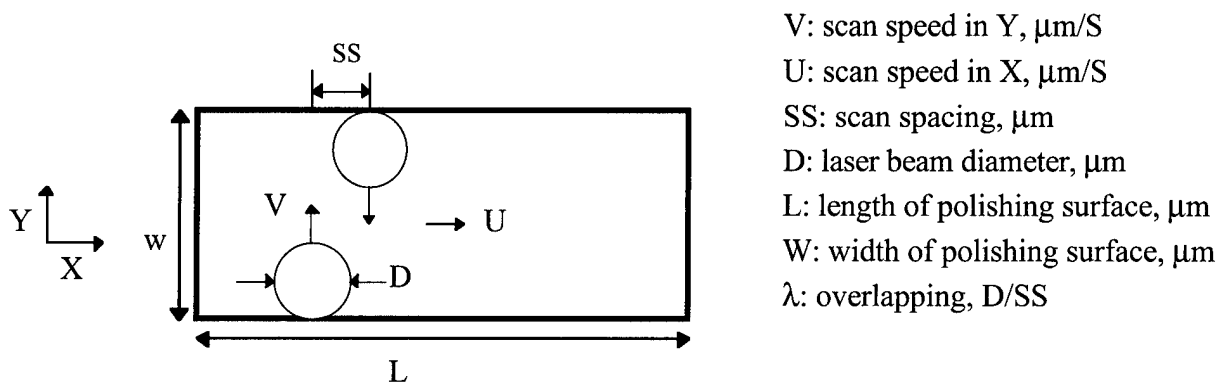


Figure 3. Plan view of single pass polishing

## Results and Discussion

### Laser Beam Energy Distribution

In Table I, D was defined to be 50% cliplevel of the laser beam energy density E, which in theory should obey a Gaussian distribution as shown in Figure 4. By using a beamscanner, the beam energy distribution was recorded, which is shown in Figure 5. It has been found that the energy distribution for the  $\text{CO}_2$  laser used in this work did not conform to the Gaussian form. In the X direction, E is uniformly distributed across the beam diameter. In the Y direction, the distribution was skewed. The energy distribution varied according to working conditions such as the laser cooling condition, power supply stability, beam power, etc. For simplicity, D was taken to be the 50% cliplevel of the Gaussian distribution in the Y direction for every laser power used in this work. E was taken to be uniformly distributed across the whole beam area.

Because of the non-uniform distribution of E, overlapping ( $\lambda$ ) was introduced into this work to be the ratio of D and SS, to accommodate the lower energy density at the edge of the laser beam. The importance of  $\lambda$  will be discussed in detail later.

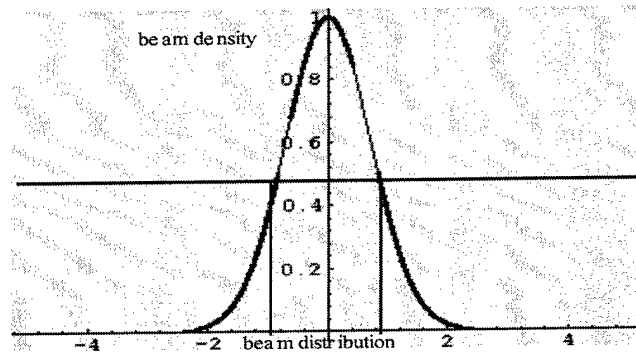


Figure 4. Gaussian distribution and 50% clipping level for laser beam energy distribution  
(Beam distribution for X axis is not based on this results)

Test	D (50%) (um)	scan spacing(um)	E( J/ cm**2 )	$\lambda$ (overlappg)
<b>Laser Polishing</b>				
<b>32 watts</b>				
1	1000	50	4.08	20
2	1000	100	4.08	10
3	350	50	4.29	20
4	350	100	4.29	10
5	300	50	5.10	16
6	300	100	5.10	8
7	300	50	6.79	12
8	300	100	6.79	6
9	300	200	6.79	3
10	450	100	9.06	4.5
11	450	200	9.06	2.25
12	450	300	9.06	1.5
13	250	200	163.1	1.25
14	250	300	163.1	0.8
15	250	400	163.1	0.6
16	200	400	203.8	0.5
17	200	500	203.8	0.25
<b>40 watts</b>				
1	1000	50	5.10	20
2	1000	100	5.10	10
3	350	100	5.36	9.5
4	350	200	5.36	4.75
5	300	100	6.37	8
6	300	200	6.37	4
7	300	300	6.37	2.67
8	300	300	8.49	2
9	300	400	8.49	1.5
10	300	500	8.49	1.2
11	300	600	8.49	1.0
12	300	800	8.49	0.75
13	450	400	113.2	1.13
14	450	600	113.2	0.75
15	250	300	203.8	0.83
16	250	800	203.8	0.31
17	200	800	254.8	0.25

Table I. Different Experimental parameters for Test I and E (Energy density)

Test	Laser power	Inclination angle(degree)	Scan speed	Scan spacing(um)	Overlapping( $\lambda$ )	Beam size( um)
1	11.8~30	0	1 cm/s	85	3	250
2	5.85~15	0	0.5 cm/s	85	3	250
3	13.5~33.75	30	1 cm/s	85	3	250
4	16.5~41.25	45	1 cm/s	85	3	250
5	8.33~20	45	0.5 cm/s	85	3	250
6	17~41	70	0.5 cm/s	85	3	250

Table II. Different Experimental parameters for Test II

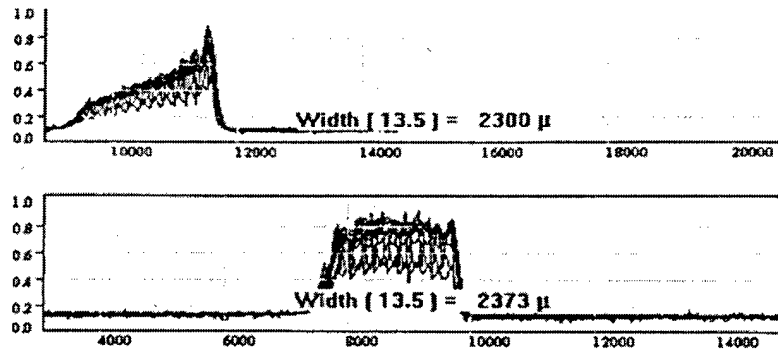


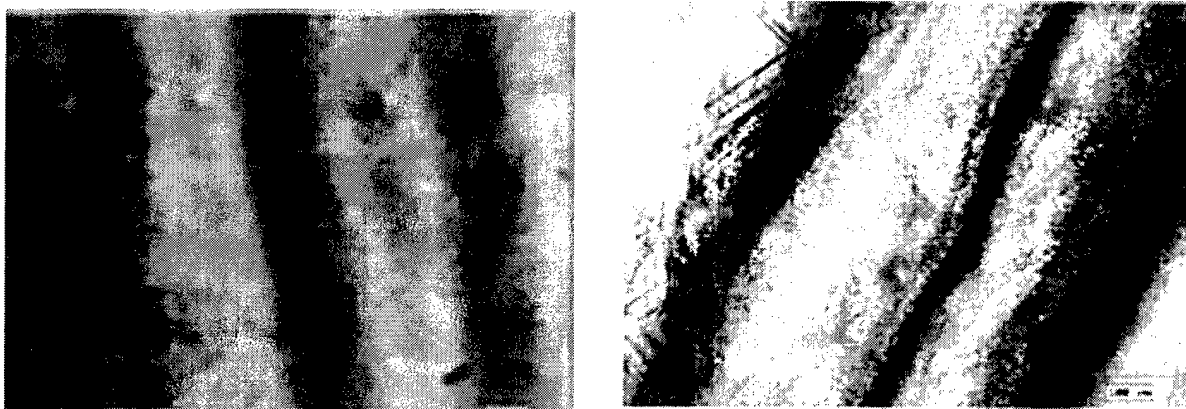
Figure 5. Beam profiles for 40 watt laser (Upper: Y direction; Lower: X direction)

### Laser Polishing Working Window

The effects of a variety of important laser polishing parameters have been studied. These include laser power, beam diameter, scan speed, scan spacing and inclination angle  $\phi$ .

The scan speed of the polishing process was restricted to be less than 1 cm/s. Laser beam diameter can be adjusted according to the laser power that has been used. By using higher laser power, larger beams can be used which will cover more surface at one time. This will decrease polishing times greatly.

From experiments, we found that there was a laser beam energy density range for polishing: the Laser Polishing Working Window. Too low a laser energy density didn't cause any obvious polishing for the slots. If too much laser power or slower scan speed was used, the surface was cut into grooves or covered by a layer of white powder. The grooves are shown in Figure 6.



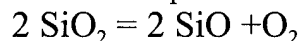
(a) 32 watt, Test I #14

(b) 40 watt, Test I #15

Figure 6. Grooves and cuttings on the polished surfaces

To smooth the slot surfaces, the surface temperature needs to reach the softening point of the material. Beyond that point a thin layer of material can flow under the action of the surface tension. If the laser energy is too low, the heat provided by the laser beam is not enough to raise the sample surface to the softening point where the viscous flow of silica can happen, and there is no smoothing effect.

At higher laser power or slower scan speed,  $\text{SiO}_2$  evaporated from the irradiated region followed by decomposition. The resulting  $\text{SiO}$  can only exit as vapor phase. It redeposited as white loose particles of  $\text{SiO}_2$  on the cooler parts of the sample.



This redeposition should be avoided by maintaining the slots surface temperature below the vaporization point. The depth of the damage increased with laser power density.

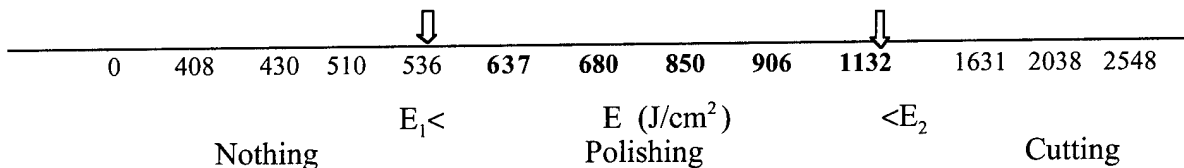


Figure 7. Laser Polishing Working Window for Test I

The results for Test I is shown in Figure 7. The working laser energy densities are from  $E_1$  to  $E_2$ . The results for Test II are shown in Figure 8. The polishing windows have been shifted according to different inclination angles. Changes in the scan speed did not cause obvious deviations in these windows. The effect of surface roughness before polishing is not clear from this work.

### Laser Beam Energy Density (E)

E for this work has been defined as following,

$$E = \frac{Pt}{A} \quad (2)$$

Where P is the laser power (watt), t is the duration time of the laser beam on the surface at any given point and A is the area of laser beam ( $\mu\text{m}^2$ ). By changing  $\phi$ , beam shape changes from a circle with diameter D to an ellipse with D (semimajor axis) and  $D\cos\phi$  (semiminor axis).

Substituting t, which is shown as following in Equation 3, and A into Equation 2, produces Equation 4,

$$t = \frac{D}{v} \quad (3) \quad E = \frac{\pi D^2}{4 \cos \phi} \quad (4)$$

Temple produced similar surface smoothing results [2], although for a different laser application. His laser beam energy was calculated out to be  $796 \text{ J/cm}^2$  when using Equation 4. It is just inside the laser polishing density range from our work.

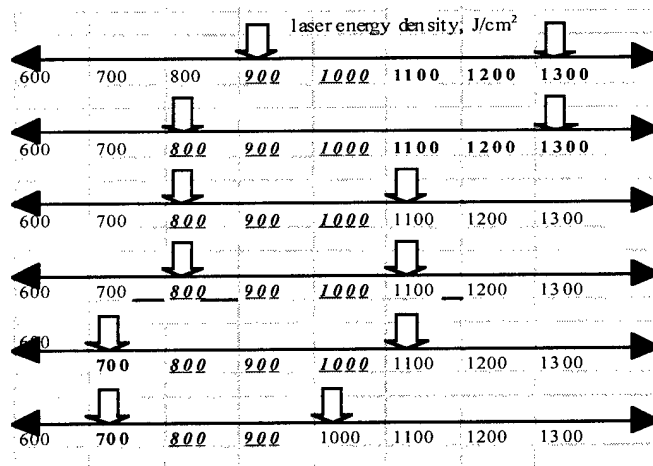


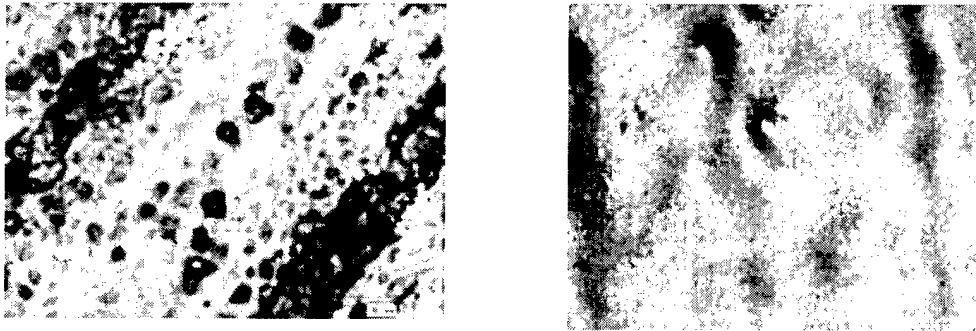
Figure 8. Polishing Working Windows of laser beam energy density for Test II (Listed in the same order as Table II)

## Surface Morphology

The surface profiles of silica slots before and after fire and laser polishing are shown in Figure 9. The as-cut surface is very rough with a lot of loose particles adhering to it. After fire polishing, some of the loose particles have been removed and the surface roughness is improved. In comparison, laser polishing created a mirror-smooth surface without any loose particles sticking on it. There are distinct differences between the fire and laser polished surfaces. Laser polishing can guarantee the reproductivity and reliability by computer controlling the whole process.

Figure 10 shows the features of slot edges after different processes. Both fire and laser polishing can deburr the edge without changing the feature of the edge. Although fire polishing can smooth the edge of the slot, it can not reach the inside because fire is blocked from entering into the narrow space between adjacent slots. By changing  $\phi$ , laser beam can reach any point deep inside the slots, provided the laser has line-of-sight to all the areas of the surfaces. So, the surface inside the slot can be smoothed also as shown in Figure 10 (c).

Different overlapping had been used for Test I. Some results are shown in Figure 11. Surface (a) and (b) in Figure 11 both had the same laser power but different scan spacing. Between the polished areas, there was an unpolished space left in Figure 12(a).  $\lambda$  for both tests was greater than unity, which meant that beam overlapping occurred. But the lower energy density distributed at the brim of the laser beam did not provide enough heat to raise the surface temperature to the softening point of the materials. The larger laser beam size decreased the beam energy density also in Test I #12. So viscous flow was not sufficient for polishing.



(a) partially polished surface, Test I # 12      (b) continuous polished surface, Test II, #4

Figure 11. Overlapping effect for polishing at 32 watt laser power

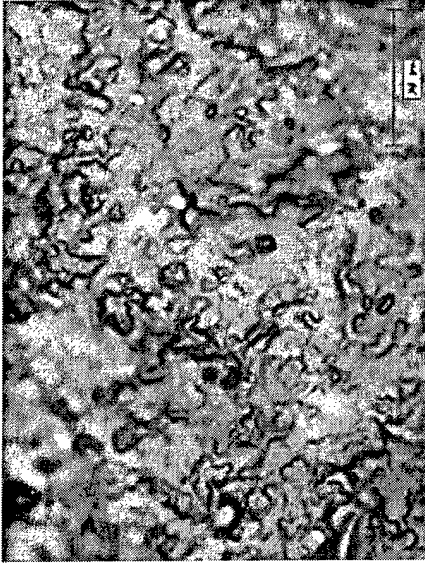
A surface profilometer was used to record the surface profiles for as-cut and after fire and laser polished slots. The results are shown in Figure 12. The surface roughness for an as cut surface is about  $2\mu\text{m}$  for the peak to valley height. After fire polishing, it reduced to about  $1\mu\text{m}$ . Laser polishing can reduce the surface roughness to  $0.05\mu\text{m}$ .

## Summary and Conclusions

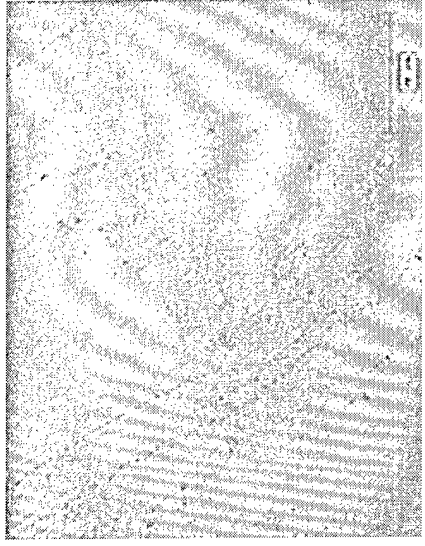
The materials studied for this project is amorphous silica, which does not exhibit a well-defined fusion phase transition. By absorbing laser energy, the surface temperature was raised to the softening point and the softened silica flowed under the action of surface tension and cooled before recrystallization could take place. The resulting surface was a mirror-smooth glassy film without any significant change in surface geometry.



(a) surface as cut, 200x



(b) surface after fire polishing, 200x



(c) surface after laser polishing, 200x

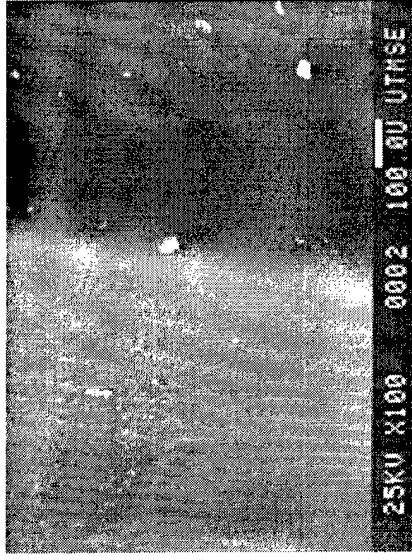
Figure 9. Surface comparison for as cut, after fire and laser polishing (optical microscope)



(a) edge as cut, 200x

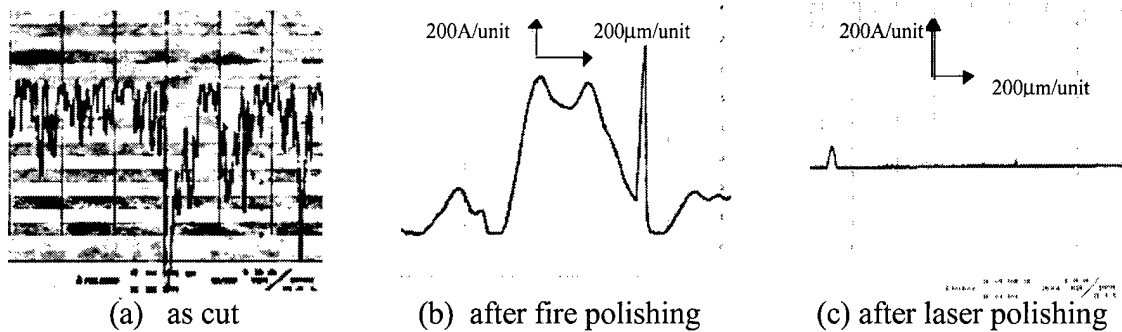


(b) edge after fire polishing, 200x



(c) edge after laser polishing, 200x

Figure 10. Edge comparison for as cut, after fire and laser polishing (SEM)



[Plot (a) has the same X unit, but twice the unit in Y direction as in (b) and (c).]

Figure 12. Surface roughness profiles for as-cut and after-polished surfaces

Laser polishing process can potentially benefit a lot of materials. According to materials parameters such as absorptivity and reflectivity, different wavelengths can be chosen for laser polishing to provide the necessary energy.

We offer the following conclusions:

1. CO<sub>2</sub> laser polishing can create mirror-smooth surfaces on mechanically cut silica.
2. There is a laser polishing working window for silica surfaces. Below this power density range, there is no obvious surface roughness decrease; above this range, vaporization of SiO<sub>2</sub> to SiO occurred. SiO redeposited back on the surface producing a thin layer of white, loose particles of SiO<sub>2</sub>.
3. The pre-polished surface roughness affects the required laser beam energy density. The rougher the initial surface, the higher the required beam energy density.
4. Based on the physical properties (heat capacity, absorptivity, reflectivity, etc.) of the materials to be processed, different wavelength lasers can be chosen to provide the energy required for surface polishing.
5. Laser polishing can work on different surface geometries under the condition that laser has a line-of-sight to all areas that need to be polished.
6. Overlapping of laser beam was required for continuous surface polishing because of the non-uniform distribution of the beam energy density.
7. The potential use of laser polishing as a post-processing step for freeform-fabricated parts is very promising.

### Acknowledgment

The authors wish to thank Cryco Co., Austin, TX for funding this research.

### References

- [1] P.A. Temple, D. Milam, and W.H. Lowdermilk, "CO<sub>2</sub>-Laser Polishing of Fused Silica Surfaces for Increased Laser Damage Resistance at 1.06 μm," Natl. Bur. Stand. (U.S.) Spec. Pub. 568(1979), Pp229
- [2] Temple, P. A.; Milam, D.; W. H. "Carbon dioxide Laser polishing of fused silica surfaces for increased laser damage resistance at 1064 nm", Applied Optics, Vol. 21, 3249-3255, 1982
- [3] F. Laguarda, N. Lupon, and J. Armengol "Optical glass polishing by controlled laser surface-heat treatment," in Applied Optics, Vol. 33, 6508-6513, 1994
- [4] Touloukian, Y.S. "Thermophysical Properties of Materials", Vol. 8, New York, IFI/Plenum, 1972



Enhanced controlling of the SLS Process during a build.

Alexandre L. Papadatos, Kenneth Stanley Jr., Said Ahzi and Frank W. Paul

Center for Advanced Manufacturing  
Department of Mechanical Engineering, Clemson University, Clemson, SC 29634

### Abstract

Current commercial Rapid Prototyping (RP) systems like Stereolithography (3D Systems Corporation) and Selective Laser Sintering (DTM Corporation) use galvanometers from General Scanning Inc. (GSI) for the positioning of the laser beam. The GSI scanners are delivered as a "black box". Operating Consoles which are usually Personal Computers (PC) have very few feedback from the performance of the GSI scanners. Therefore, the PC spends 90% or more of its time waiting for the GSI scanners to be over with the building of the current layer before sending the information regarding the next layer. Also, very little process control can be performed during the scanning of a layer using the GSI scanners. This kind of setup prevents any dynamic controlling of the process that could prevent building errors like burning, warping etc.

At Clemson University, our team has developed both hardware and software components that allows a dynamic control of the building process. New features like scanning one vector with laser power as a function of position and/or time are now possible. Both hardware and software issues will be presented.

### Background

To create objects using the Selective Laser Sintering process, an X Y optical scanner using CAD solid model data, guides or directs the laser beam to target points requiring sintering. The SLS system employs the General Scanning Incorporated (GSI) optical scanner, the DE series 2000 scanner controller and two G325 DT galvanometers with mirrors (1,3). The objective of Stanley's work (1) has been to identify the technological limitations of the GSI optical scanner, as related to the scanning requirements of SLS, and present a new optical scanner design based on digital signal (DSP) control theory. One important accomplishment of the research done by Stanley is the use of information derived from the closed loop position control of the galvanometers to trigger the laser on/off function. This functionality has been enhanced and constitutes one of the main components for the dynamic optical scanning controller.

The GSI system has always been used as a "black box", and a very small amount of data is returned to the operating console. We will describe how the build of an object is managed: the software that supervises the SLS process (the *main* software) downloads the informations required to build one single layer into the GSI system. When the downloading is over, the main software orders the GSI system to go ahead and build (scan) the layer. The main software then waits for the GSI system to finish. When over, the GSI system sends an "OK" command back to the main software. Then the main software becomes aware of the fact that scanning operations are over for that layer. It then spreads a new layer of powder and downloads to the GSI system the informations required for the processing of the next layer.

In the GSI system, the laser controlling software that processes the scanning of a layer cannot be willingly modified. It is a property of General Scanning Inc., and it is engraved in a memory chip. However, the new controller developed by Stanley (1), uses a

Texas Instrument digital signal processor board (4), which is capable of implementing both digital control of the scanning system and supervisory control of the SLS process. A main software is still required in order to read the commands for the layers, to perform the management of the controller operation and as a user interface with the system. This is mainly because the Texas Instrument board cannot access devices such as the hard drive, the communication ports and the monitor. Therefore, an interface between the board and these devices is needed, and this is the primary function of the main program in the new controller system: the dynamic scanning controller. The main difference with the GSI system is that the software controlling the laser position, speed and intensity can now be modified to meet our needs.

### Hardware Design for the Dynamic Optical Scanning Controller

The optical scanner developed by Stanley (1) utilizes the actuators and sensors of the GSI scanning system, but provides a new controller based on digital signal processing (DSP). With the DSP based controller, control of the laser tracking is accomplished with software and control algorithms instead of the hardware controller from the GSI system. This technique provides the user with a flexible control environment for laser tracking and also allows control of laser on/off and laser intensity signals based on the galvanometer's position. The sensors and actuators have been retained by Stanley in his DSP based system because they were the best technology available to move the mirrors with the required performances for rapid prototyping optical scanning.

The controller of the DSP optical scanner uses a C30 digital signal processor system from Spectrum Signal Processing, Inc. of Westborough, Massachusetts (3). The C30 system board is designed to coexist in an IBM compatible PC. Data transfer between the DSP and PC is accomplished through the ISA-AT bus. The C30 system board has 64K of 32 bit RAM memory that is accessible by both the PC and DSP. These 64K of memory will be split into two memory banks of 32K each, in order to speed up the process. This feature will be discussed later in this chapter. More detailed information on the board itself can be found in (1,3,4).

Since the DPS system uses the same sensors and actuators as the GSI system, an interface board was required. It has been successfully designed and developed by Stanley (1). The interface board hooks on the GSI system and allows the control of the SLS process either with the GSI system or the newer DSP system. All the signal of the DSP/GSI interface board are designed on one circuit board that is sized appropriately to fit in the EURO Card Frame of the DE 2000 series controller from General Scanning. A schematic for the DSP/GSI interface board and further technical information can be found in Appendix A of (1).

## Software Design for the Dynamic Optical Scanning Controller

Terala (2) and Stanley (1) initially developed the control program developed for the CLEMSON SLS project, using the GSI controller. The new controller program incorporates some of the control software developed by Terala and Stanley. Our contribution consists of further testing the software, correcting some problems due to communications problem between the DSP and the PC, and also enhancing the capability of the DSP system by featuring the variation of the laser intensity while scanning a vector.

The software developed for this research, uses scan commands with the same format as the GSI controller, in order to provide compatibility with previously generated scan files. One new command is added, called the Laser Setting. The syntax is LSxxxxx where "xxxxx" is an integer number from 0 to 65535. Each vector can now be scanned with a particular laser intensity pattern. While being scanned, each vector is divided into ten zones, each equal in length. One laser intensity can be specified for each of these ten zones. Eight different levels define the laser intensity. The first level (level "0") represents 2% of the maximum laser intensity (i.e. 1 Watt for a 50W CO2 laser). The second level (level "1") represents 16% of the maximum laser intensity, and so on. At the end, level "7" represents the maximum intensity that can be provided by the laser apparatus. This configuration was chosen in order to be able to code the pattern in an octal form. The octal format has been retained since the decimal format would require the use of three LS commands for each scan vector, making a total of five commands required to build a single vector. Choosing a smaller base would not provide such a wide range of power levers. The use of the octal format requires only two LS commands to describe the way a vector should be scanned, bringing the total to four commands for each scan vector. Figure 1 shows five vectors, scanned each with an independent scanning pattern. We have scanned these vectors on paper in order to keep a visual track of the change in laser intensity. The five vectors are horizontal and all are equal in length. On the top of each vector we have added the laser intensity level for each of the laser zones. The zones are shown at the top.

Zone #0	Zone #1	Zone #2	Zone #3	Zone #4	Zone #5	Zone #6	Zone #7	Zone #8	Zone #9
7	7	7	7	7	7	7	7	7	7
0	1	2	3	4	5	6	7	7	7
7	6	5	4	3	2	1	0	0	0
0	2	4	6	7	7	6	4	2	0
7	0	7	0	7	0	7	0	7	7

Figure 1. Horizontal vectors with different scanning laser pattern.

In the encoding of the scanning pattern describing these five vectors, two LS commands are used for each of the vectors. The numbers following the two LS commands describe the pattern. For instance, the two first LS commands found in the script file are "LS16383" and "LS65535". They correspond to the first vector, the one on the top of Figure 1. In order to derive these numbers, we first choose the desired pattern. For the first vector the desired pattern was vector with maximum and uniform laser intensity. The maximum intensity is level 7; therefore all the ten zones are assigned level 7. In an octal form we have

777777777 describing the desired pattern. If we subdivide this octal number in two integer numbers, of 16 bit each, we get in binary form 111111111111 for the first integer number (i.e. 16383 in decimal) and 11111111111111 for the second one (i.e. 65535 in decimal).

For the second vector, the desired pattern is 0123456777 in octal form or 000001010011100101110111111111 in binary form. We divide this binary number into two integer 16 bit numbers: 00000101001110 (i.e. 334) and 1011101111111111 (i.e. 24063). Thus, the LS commands for the second vector are "LS334" and "LS 24063".

### Computer Implementation

The control software of the DSP controller has two parts due to the design of the system (1). The DSP processor requires the support of a host computer for data storage, user interface and communication with the SLS machine. Stanley named the program for the host PC "PCBUILD.C" and for the DSP system "DSPBUILD.C". The PC program has been written using Borland™ C++ v4.5. When the program starts, a menu is displayed on the screen. The user can perform from there several actions. In order to start building a part, the user needs to initialize the DSP system by selecting the first option of the menu. Detailed instructions on how to use the PC program can be found in (6). The DSP program has been written in C using a text editor and the special compiler provided by Texas Instrument. Most of the program is similar to the version written by Stanley. However, some communication problems between the PC and the DSP had risen as the entire system was used and tested. In order to prevent communication problems, we have enhanced the protocol used for the DSP and the PC, by adding stages during the communication, where the DSP and PC processors have acknowledge of each other's status: The DSP waits on the PC to acknowledge its status, before continuing. Then the PC waits its turn on the DSP to acknowledge its status. Due to this added checkings, the time for initialization and data transfer has been slightly increased compared to Stanley's version. However, communication problems that caused the system to freeze, have virtually disappeared.

Another enhancement over Stanley's version of the DSP program, is the addition of the laser intensity monitoring. Since the DSP system supervises the scanning of each vector, the system is also capable on setting the appropriate laser intensity during the scan of a vector. The actions corresponding to the LS commands have been implemented. The system monitors the scan of a vector and sets the laser intensity accordingly to the value specified after the two LS commands. In order for the LS commands to be considered, the commands "LP0" and "LR0" need to be previously specified. This restriction was chosen to prevent confusion of the system by opposite commands: LP and LR commands specify scanning of vectors with uniform laser intensity, while LS commands specify vectors with variable laser intensity.

An optimization concerning the time required for data transfer from the PC to the DSP has been initially designed by Stanley. The 64 kilobytes of memory that the DSP is equipped in order to store data have been divided into two banks of 32 kilobytes each. The reason that led us to this decision is that the informations for one layer are seldom larger than 32 kilobytes. This division of the DSP memory allows us to fill one memory bank with data from one layer, while we process the data of the previous layer stored in the other memory bank. Therefore, in the ideal context where the time to process a layer is equal to the time to transfer the data into the DSP memory, the data transferring time is reduced by half. Practically, the laser is always scanning faster the layers than with the GSI system, since most of the informations for the next layer have already been transferred in the available memory bank when the laser ends a layer.

## Dynamic Controller Results

In order to test the ability of the new controller, we took an existing scan file and added manually LS commands for each of the vectors. We then proceeded to the build using the DSP controller. Figure 2 displays the result of the dynamic scanning of one layer of a dogbone sample. We used paper as a medium in order to visually track the dynamic scanning.

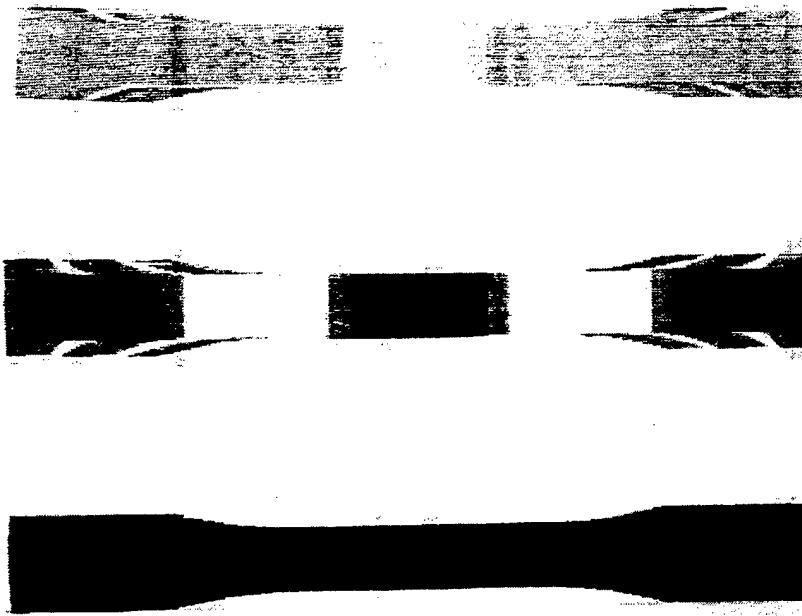


Figure 2. Dynamic scanning

In Figure 2, we can clearly see where the laser intensity changes. The bottom "dogbone" used a constant laser intensity to prove that dynamic scanning can behave similarly as when using the GSI controller. The three dogbones have been scanned using horizontal vectors. The dynamic controller takes each of these vectors and divide them into ten equal-in-length zones. The largest the vector, the largest the zones will be and the worst the resolution will get since we can only specify one laser setting per zone. There are two ways to remedy to this problem:

- 1) Increase the number of zones per vector. This would result in a direct increase of the length of the script file since more LS commands will be necessary. A major update of the software is required in this case, including code programming.
- 2) Scan the part in a different way. For instance, the use of vertical vectors instead of horizontal, will result in shorter vectors. Therefore, the zones will be shorter and the resolution will also be better. This will lead to an increase of the length of the scan and script files, since more vectors will be generated. In this latter case however, no update of the software is required.

## The Building Script

At Clemson University, a program simulating the SLS process has been developed and implemented (5,7). Once a simulation has been performed, we are in possession of data representing the powder bed after the build that can be displayed on a computer screen as a visual representation of the powder bed. These visual representations already provide the SLS user with important informations on how the build will actually look like. Among these informations are burning (thermal degradation of the material), bonus z and low sintering (5). However, without a tool that would modify dynamically the building parameters, the user can do very little in order to prevent these unwanted phenomena.

The dynamic controller allows supervising the entire SLS process. The dynamic controller also allows varying the laser intensity settings while scanning a vector. Each vector can therefore have its individual laser power setting depending on the geometry. However, due to the amount of vectors required to build an entire geometry, specifying manually the laser setting for each vector becomes an impossible task. This difficulty is the main reason that led us towards the development of a new tool. We will present the analysis software that uses the results from the simulation software in order to automatically<sup>1</sup> generate a script file (an improved scan file) which will use the new features of the dynamic controller.

### Automatic Generation of a Scan File

For a machine to perform a task automatically, it is necessary to give the machine certain guidelines on how to perform in different situations it will encounter. The set of the guidelines is what we will be calling the "*analysis rules*" and depending on them, the machine will perform accordingly in the analysis of the simulation results. The analysis rule we have adopted as a testbed for our system is based on the maximum temperature reached in the powder bed. We have been referring to the scan file used by the simulator and the GSI scanners as the "*scan file*". We will be referring to the new scan file that is generated by the analysis software as the "*script file*", since it also includes informations regarding the improvement of the build. The scan file and the script file are describing the same geometry. However, the scan file uses two commands to define a vector, whereas the script file describes a vector using four commands; the two additional commands describe the laser power settings for a given vector. The result is that the script file is close to double the size of the scan file.

For each scan vector describing the geometry, the following procedure is followed:

- 1) We initialize all the vector zones with the laser setting specified in the input file. For the sake of simplicity, we have assumed that the laser setting is higher than needed. Therefore, the laser setting can only be decreased and the phenomenon of low sintering is not taken into consideration in the analysis rule presented here.
- 2) We make sure to identify the vector zone we are currently in, depending on the progression of the vector scanning. As we saw, there are ten vector zones, which are equal in length for each vector and seven laser power settings.
- 3) We call the subroutine *Analyze()* which can be found in the module *models.c*. This subroutine will decrease the laser setting in each vector zone according to the information from the simulation data on this region of the powder bed.

---

<sup>1</sup> By "automatically" we understand "with minimum user intervention"

- 4) Once a vector has been analyzed, we derive the two attributes that will be specified by the two "LS" commands.
- 5) Unless we are dealing with a scan vector, we copy the same command we read in the scan file into the script file. However, if we are dealing with a scan vector, we first write the two "LS" commands for the scan vector in the script file and then we copy the "NX" and "NY" command. This is in order for the dynamic controller to know a priori what laser setting is required to scan the given scan vector.

### Performance and Limits

The analysis rule we have used for testing the system is based on the maximum temperature reached in the powder bed. The script file that is generated based on this analysis will only have an effect on the burning. This is mainly due to the simplicity of the analysis that we have used. In order to take into consideration other problems, a more extended analysis is required, and more complex analysis rules need to be implemented. With a better-detailed analysis, the system including the simulation software, the analysis software and the dynamic controller will provide better quality of the parts made using the SLS process. However, the goal of the research presented in this thesis has been to prove the feasibility of such a system, and this is the reason we have used a simple analysis as a testbed. Figure 3 shows the part built with the GSI controller using a constant laser intensity setting. Figure 4 shows the same part built using the dynamic controller in conjunction with the simulation and analysis software.

When using the GSI controller, the laser delivers too much energy into the powder bed as the length of the vector decreases at the edges. We can see that the burning at the edges is eliminated when using the dynamic controller. The burning was predicted by the simulation software, and the analysis software created a script file in such a way that the laser intensity is decreased, as the vectors become shorter.



Figure 3. Part built using the GSI controller.

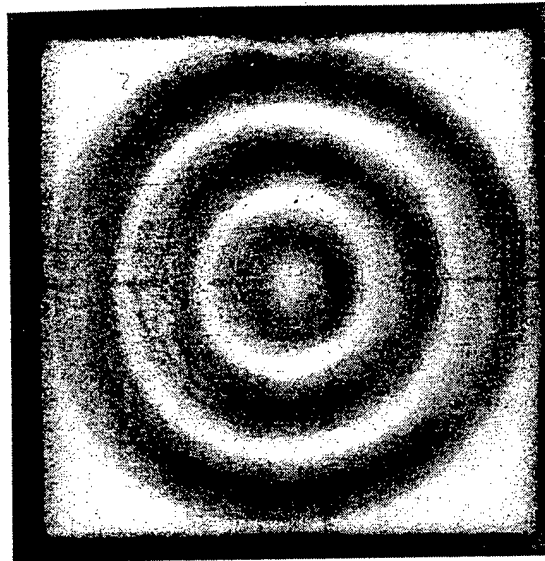


Figure 4. Part built using the DSP controller.

### Conclusion

The DSP system developed at Clemson University has been improved in two major ways. Some problems caused by faulty communication between the DSP and PC programs have been corrected, and controlling the laser intensity defined by a new command has been implemented. One single vector can be scanned using its own laser intensity pattern, independently of previous or next configurations. This feature allows to reduce the intensity when burning occurs specially at the edges, or to increase the intensity if the sintering is not enough. However, when one considers the number of vectors describing a three dimensional CAD object, a manual editing of the scan file becomes an impossible task. Our idea is to couple the results provided by the simulator to this new feature, and automatically generate a script file that would correct problems like burning, bonus Z or inadequate sintering. The coupling of the simulation results and generation of the script files has been discussed in this paper.

Literature cited

1. Stanley, K., "Using Digital Signal Processing to Enhance the Optical Scanner System of Selective Laser Sintering", MS Thesis, Clemson University, Clemson, SC, 1997.
2. Terala, K. M., "Feed Forward Geometric Compensation for Selective Laser Sintering", MS thesis, Clemson University, Clemson, SC, 1996.
3. General Scanning Incorporated. "DE Series: 2000, 3000 Digital Electronics User Manual", General Scanning, Watertown, MA. 1991
4. Spectrum Signal Processing Incorporated, "TMS320-C30 System Board Technical Reference Manual." Spectrum Signal, Westborough, MA 1992
5. Papadatos A. L., Ahzi, S., Deckard, C.R., Paul, F. W. "On Dimensional stabilities: Modeling of the Bonus-Z During the SLS Process ", SFF Symp. Proc., 8, pp. 709-716, 1997
6. Davis A.L., "User's Manual", Clemson University Mechanical Engineering Department, SLS Laboratory, version 1.01, June 1998
7. Papadatos A.L., "Computer Simulation and Dynamic Control of the SLS Process", Clemson University Mechanical Engineering Department, SLS Laboratory, August 1998



## Process Control of 3D Welding as a Droplet-Based Rapid Prototyping Technique

R. Kovacevic and H. Beardsley, Southern Methodist University, Dallas, TX

### Abstract

Three-dimensional welding is investigated as a rapid prototyping technique for the production of real metallic parts using gas metal arc welding principles. A high speed machine vision system is used to study the correlation between droplet transfer parameters and resultant weld penetration characteristics. Experimental work is conducted to determine how droplet transfer frequency, droplet size, and number of passes affect the geometrical and metallurgical properties of the weld penetration. A finite element analysis is performed in order to study what influence additional layering has on the cooling characteristics and resultant penetration profile.

### Introduction

Current rapid prototyping techniques such as stereolithography, laminated object manufacturing, fused deposition modeling, and selective laser sintering can produce parts made from wax, plastic, nylon, and polycarbonate materials. The processes are useful for creating 3D models for visualization purposes or feasibility studies, however, industry has expressed interest to expand the current rapid prototyping techniques or create new ones to enable the direct production of metallic parts. With this goal in mind, much effort has been focused on using the principles of traditional welding processes for the direct fabrication of metallic parts. For many years welding techniques have been used to repair damaged components or to build up surfaces to resist wear and abrasion, but it was only during the last three decades that scientists began investigating the possibility of manufacturing complete metal parts using the controlled deposition of filler metal. The use of welding for creating free standing shapes was established in Germany in the 1960's. This led to companies such as Krupp, Thyssen, and Shulzer developing welding techniques for the fabrication of large components of simple geometry, such as pressure vessels which could weigh up to 500 tons. Other work in this area has been undertaken by Babcock and Wilcox who have been working mainly on large components produced in austenitic material. Also, work by Rolls-Royce has centered on investigating the technique as a means of reducing the waste levels of expensive high performance alloys which can occur in conventional processing. They have successfully produced various aircraft parts of nickel based and titanium based alloys. Work on 3D welding has also been in progress at the University of Nottingham, United Kingdom [1]. All of these attempts to use 3D welding for building metal parts failed to incorporate a feedback control system between the robot controller and the welding system. Sensory feedback is a necessary requirement for improvement of the system quality through process monitoring and for post inspection purposes. Attention must also be given to the use of sensors to prevent possible collapse of the part caused by temperature build-up as well as to avoid build-up of metal along the layer caused by the change in the welding speed. Recently, a sensing system based on machine vision and high speed image processing has been developed for controlling the metal transfer process in a 3D welding operation [2,3]. Production of complete parts using welding principles can offer the following major advantages over conventional techniques: 1) A wide variety of shapes and sizes is possible when the torch is robotically controlled., 2) The produced parts have good isotropic

characteristics., 3) The process is very fast so development lead times are significantly shorter., 3) There is very little material waste., and 4) A very highly automated system can be developed.

While initial work in the area of 3D welding has already shown that complex shapes can be formed, the results are not perfect. The problems associated with rapid prototyping metallic parts can be attributed to many different factors. Heat build-up due to the welding processes can cause part malformation or collapse of the structure. Inaccuracies in the welding and robot parameters can cause cumulative errors, resulting in the torch being too close or too far away from the surface. Solid layers cannot be formed accurately enough to form a smooth surface. This means that gaps can occur inside solid objects. It is evident from these problems that some form of sensing is required to control the process. In conventional gas metal arc welding, the manner in which metal is transferred from the consumable electrode into the weld pool plays a major role in the formation of the bead and penetration characteristics, as well as the final microstructure of the solidified metal. Thus, developing a sensing system based on the metal transfer process should advance the potential for applying GMA welding principles to a rapid prototyping process capable of producing metallic parts.

### Experimental Setup

The welding power supply used for the experimental work uses a 24 V constant voltage wire feeder capable of providing wire feed speeds in the range of 127-1981 cm/min. A high speed digital camera is used for acquiring images of the metal transfer process. The images have a resolution of 128X128 pixels and a gray scale range of 0-255. The maximum possible frame rate of the camera is 800 frames per second with a data transfer rate of 16 MHz. The images are captured by a frame grabber capable of on-line image acquisition and real-time image processing. The frame grabber is equipped with its own DSP chip which allows for asynchronous processing so the time required for image acquisition and processing can also be used for monitoring other process parameters. A laser backlighting technique is used to filter out the arc light and produce shadowgraph images of the metal transfer process. The lighting source and optical components are shown in Fig. 1. During welding, the welding torch and machine vision components remain stationary and the workpiece traverses along a linear path beneath the torch. A photograph of the experimental setup can be seen in Fig. 2.

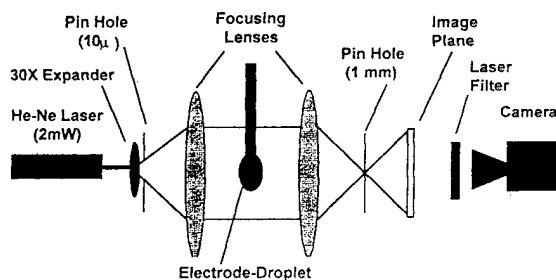


**Fig. 1** Schematic presentation of the laser optics and high speed camera system.

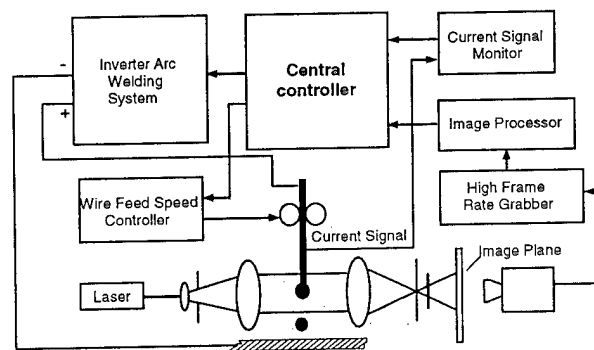


**Fig. 2** Experimental setup.

## Experimental Work

The welding experiments are performed with direct current-electrode positive (DCEP) gas metal arc welding. Coupons of 1015 mild steel with dimensions of 7.62 X 25.4 X 0.3 cm are used as workpieces. An ER 70S-6 automatically fed electrode wire with a diameter of 1.2 mm serves as the filler material. The contact tube-to-workpiece distance is 25 mm for all welds. A constant electrode extension of 20 mm is used for all experiments. A mixture of 95% argon and 5% carbon dioxide is employed as the shielding gas, and traverse speed is fixed at 6.4 mm/sec.

## Controlling the Metal Transfer Process

Regulating the metal transfer process can best be accomplished by controlling the total heat input. The process parameter that is primarily responsible for heat input is the average welding current. Once a droplet reaches a desired size, switching the current from the peak level to the base level will initiate an oscillation of the droplet at the tip of the electrode. When the droplet is on a downward stroke, a signal is sent to the power source controller to raise the current to the peak level, which increases the electromagnetic force. The downward momentum of the droplet in combination with the increased electromagnetic force generates a large enough detachment force to detach the droplet from the electrode. Fig. 3 shows an idealized shape of the current waveforms employed in this work for controlling the metal transfer process. In addition to detaching the droplet, the welding current must be controlled to achieve the desired heat input. In order to allow a certain degree of control over the average current level, the current waveform in the droplet growth period, i.e., the interval between the detachment instant of the previous droplet and the oscillation initiation of the present droplet, should be designed based on the desired average current and the required drop in current necessary to initiate the droplet oscillation. (See Fig. 4.) Immediately following the detachment instant, the current should be returned back to the base level for a pre-set duration, and then smoothly increased back to the peak level. Using this approach, the height to width ratio of a bead layer generated by GMA welding can be controlled.

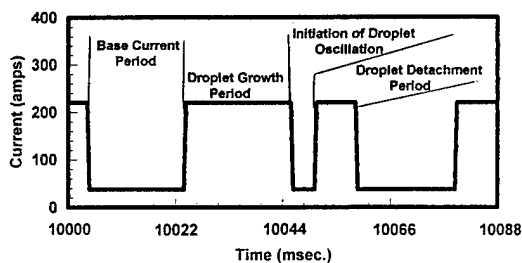


Fig. 3 Idealized shape of pulsed current waveform.

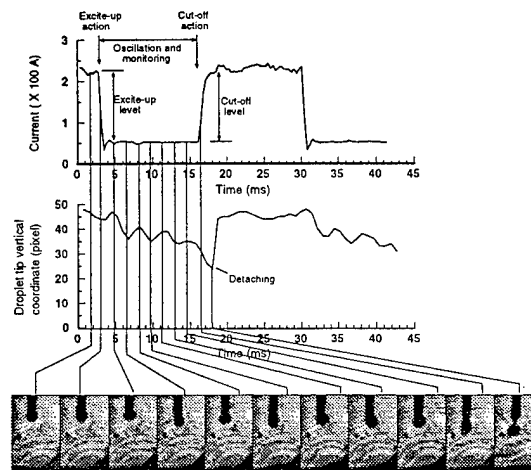
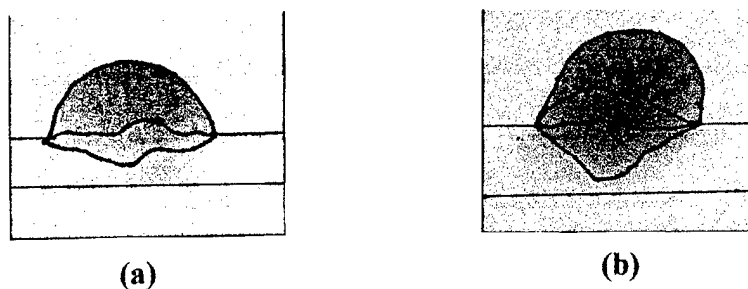
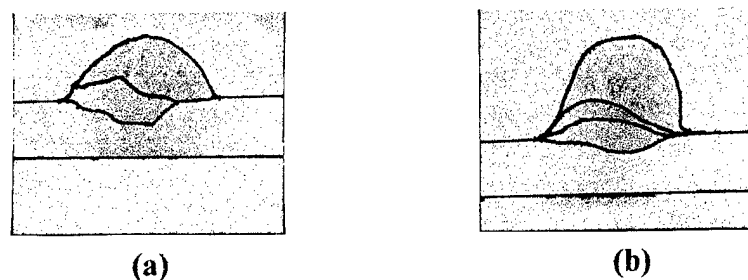


Fig. 4 Experimental observation of the excited droplet oscillation and detachment.

When building a layered structure it is required that the heat input be much less than the amount required for a welding process. Important factors in the production of high quality layered structures are the creation of metallurgical bonding through substrate remelting, the control of cooling rates of both the substrate and deposited material, and the minimization of residual stresses. Figs. 5(a and b) respectively show cross-sectional views of the double and triple layering results produced with an average current of 170 A and a long droplet growth period. Use of a larger droplet size will contribute more heat to the substrate and result in a more pronounced finger-shaped penetration. This is supported by the bead cross-sections, and is especially evident for the triple-layer case represented in Fig. 5(b). Excessive remelting of the previously deposited layers will also occur. Applying additional layers will introduce more heat into the substrate and make it more difficult to provide the conditions for building a straight wall layered structure. By shortening the droplet growth time period and by decreasing the level of average current to 150 A, the amount of heat contained in the deposited droplets will be reduced, and the depth of layer penetration into the substrate can be controlled as illustrated in Figs. 6(a and b) for the case of double and triple layer deposition. The photographs of the bead cross-sections depict much smoother penetration boundaries free of the central finger-like penetration that is inherently characteristic of a GMA welding process.



**Fig. 5 Bead cross-sections of a double-pass (a) and triple-pass (b) weld formed with an average current of 170 A.**



**Fig. 6 Bead cross-sections of a double-pass (a) and triple-pass (b) weld formed with an average current of 150 A.**

## Finite-Element Modeling of 3D Welding

Almost as quickly as welding emerged as one of the most popular and widely used joining processes, engineers and physicists began their theoretical journey into the field of welding to understand the physics of the process and the interactions of the different phenomena involved. Efforts in this area were strongly motivated from the start by the clearly visible and rapidly growing potential for the application of the welding processes. To avoid the tedious approach of endless trial-and-error experimentation for establishing reliable data bases, accurate theoretical models were needed to predict the critical welding results, such as weld bead width and depth of penetration. However, after decades of intense research in this area, precisely predicting process results for such a complex process as welding has proven to be a very difficult task. Regardless, these models have saved both time and resources by serving as tools for narrowing the ranges of feasible operating parameters. Likewise, if a rapid prototyping process is to be developed based on the principles of welding, theoretical models must be developed which provide information pertinent to the layered fabrication of metallic parts. The mathematical models previously developed for the welding processes are not applicable for droplet-based rapid prototyping due to the many different requirements of the two processes. The finite element technique is employed to perform a thermal analysis of a droplet-based rapid prototyping operation and model the depth of bead penetration into the base plate.

Designing a feasible 3D welding operation requires a thorough understanding of how the part will respond to the repeated heating and cooling cycles. The maximum and minimum temperatures play a major role in determining the final microstructure, as do the heating and cooling rates of the process. Important factors in the production of high quality layered structures are the creation of metallurgical bonding through substrate remelting, control of cooling rates of both the substrate and the deposited material, and the minimization of residual stresses. For building a layered structure, it is required that the heat input will be much less than in the case of a welding process. In the layer building process the bonding thickness between two layers has to be large enough to provide sound bonding mechanical strength. However, excessive remelting of the previously deposited metal can disrupt the geometry of the earlier formed layers. Therefore, it is critical that the selected heat input level be suitable for the given part geometry and process conditions. Also, the cooling rate must be considered since it affects not only the microstructure, but also the shape of the solidified bead. If the newly deposited molten metal cools rapidly, a high and narrow bead will form. Whereas, a low cooling rate will allow time for the molten metal to spread over the previously deposited layer before solidification occurs. The resultant bead will be wide and more flattened.

The finite element model for 3D welding is designed based on the welding conditions and experimental parameters employed for the experimental work. They include the geometrical dimensions of the workpiece and newly formed weld bead, fixturing, composition of the workpiece and filler metal, weld path, traverse speed, initial temperatures, ambient conditions, composition and flow rate of the shielding gas, welding current, voltage, and properties of the metal transfer process such as droplet size and transfer rate.

The outcome of any welding process is predominantly determined by the heat that is input to the workpiece to produce melting. Simulating the heat source is a critical step in the

development of a numerical model designed to predict the outcome of a welding operation. Both the magnitude and distribution of the heat source are of significant importance, and thus can have a profound effect on the process results. The finite-element method has developed into a powerful tool to solve complex thermal analysis problems [4,5]. While the technique has been fairly successful in simulating the gas tungsten arc welding process [6-11], very few attempts have been made to model a gas metal arc welding process [12] owing to the additional complexity caused by the introduction of filler metal during the operation.

Due to the nature of the energy transfer to the workpiece, analytically modeling the welding heat source is complex. For numerical modeling purposes, heat input to the weldment can be represented as a distribution of surface flux, but this approach introduces some arbitrariness into the defined heat source. In a few works, major simplifications have been made and the thermal energy supplied by the heat source is assumed to be input at a point or line source, depending on the geometry of the weldment [13]. These types of idealized solutions are only valid for simple geometries and for regions far away from the fusion and heat affected zones.

Determining the losses that occur between the solid electrode and the workpiece is extremely difficult. A portion of the arc heat is spent to melt the continuously fed filler wire. Part is lost to the environment before it ever reaches the base plate. Heat from the arc and heat contributed by the molten metal droplets deposited onto the workpiece induces heat flow in all directions in the workpiece. In an attempt to quantify the portion of arc energy that is actually absorbed by the workpiece, a term referred to as the arc efficiency ( $\eta$ ) has been developed. Compared to GTAW, radiation and conduction from the arc plasma make much more minor contributions to the total amount of heat input to the weldment [14]. The major source of heat energy is the mass of molten material provided by the consumable electrode to the workpiece in the form of metal droplets. Therefore, two sources of thermal energy should be included when modeling a GMAW heat source, i.e., the energy from the arc generated at the workpiece and the heat energy contained in the metal drops transferred from the filler wire. It has been shown that the energy contribution from the arc primarily affects the width of the weld pool while the amount of energy contained in the molten metal droplets primarily controls the melting rate of the workpiece material [15]. Consequently, the depth of pool penetration into the base material is predominantly governed by the amount of heat energy supplied to the workpiece by the molten droplets. Also, it has been reported that the degree of weld penetration can be influenced by the impingement of the metal droplets on the weld pool [16].

Idealistically, in order to accurately model a GMAW heat source, effects from the following phenomena should be included: radiation and conduction from the arc, positive ion impingement on the workpiece, heat input from the filler metal droplets, influence of the additional mass of material from the consumable electrode, and effects of weld pool indentation caused by the impinging metal drops. Numerically representing any one of these phenomena would be a very complex task. Furthermore, attempting to quantify the cumulative effect of these factors coupled together would be even more challenging, and nearly impossible to verify.

In an effort to take advantage of the results from previous works and also minimize the chances of making erroneous assumptions, the procedure of modeling the GMAW heat source

for the present work is divided into two phases: 1) Evaluate the magnitude of the total heat energy input to the workpiece, and 2) Determine the manner in which the heat energy is supplied to the workpiece.

Calculating input thermal energy will be based on an estimated arc efficiency ( $\eta$ ). The works that have addressed the topic of arc efficiency for the GMAW process have reported values ranging from 66% up to 71% [17,18]. Since it is known that very small changes in the welding parameters can significantly alter the arc efficiency, estimating an exact value for  $\eta$  is unrealistic given the knowledge available to date. However, a reasonable estimation for  $\eta$  can be assumed by comparing the current experimental conditions with those in previous studies. For this work, an efficiency value of  $\eta=74\%$  is assumed for modeling the GMAW heat source. The amount of energy supplied by the arc to the base plate is calculated using the formula:  $q = \eta \cdot V \cdot I$  where  $q$ (Watts) is heat transfer rate,  $\eta$  is arc efficiency,  $V$ (volts) is voltage, and  $I$ (amperes) is welding current.

Before the heat transfer rate can be incorporated into the finite-element model, it needs to be converted into a heat flux  $q''$  having units of  $W/m^2$ . Thus, phase II of modeling the heat source must be completed in order to determine over what surface area the heat will be input and how it will be distributed over the area. Various approaches have been taken to simulate a GMAW heat source, including input at a point or line [14], input over a circular area having a uniform, ramped, triangular, or Gaussian distribution [19], and supplying the heat internally within a spheroidal or ellipsoidal region [20]. Recent works have shown that in a GMAW process, the majority of the heat energy supplied to the workpiece comes from the mass of molten material deposited into the weld pool, and that radiation and conduction from the arc plasma contribute very little thermal energy to the weldment [20]. Based on this information, the molten droplet is selected as the object of focus for modeling the heat source. It will be assumed that the weldment receives heat energy solely from the molten droplets depositing into the weld pool. An average maximum droplet diameter value of 1.82 mm has been calculated for the range of process parameters values employed for the experimental work. Taking 1.82 mm as the diameter, a projected area for droplet impact on the pool is calculated and used to convert the heat transfer rate  $q$  (Watts) into a value for heat flux  $q''$  ( $W/m^2$ ).

The finite-element results for modeling a double- and triple-layer 3D welding process are presented in Figs. 7-8 for average welding currents of 170 A and 150 A. It can be observed that the higher current yields a slightly deeper penetration depth. However, melting of the original base plate, distinguishable by the larger mesh elements, does not occur in either case.

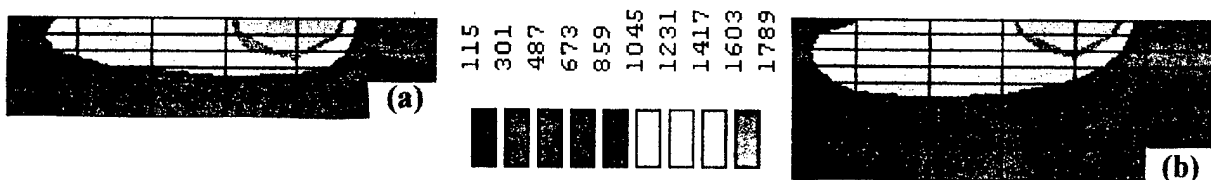


**Fig. 7 Isotherm plot of an FEM simulated double (a) and triple (b) pass weld formed with an average current of 170 A (view of the weld path cross-section)**

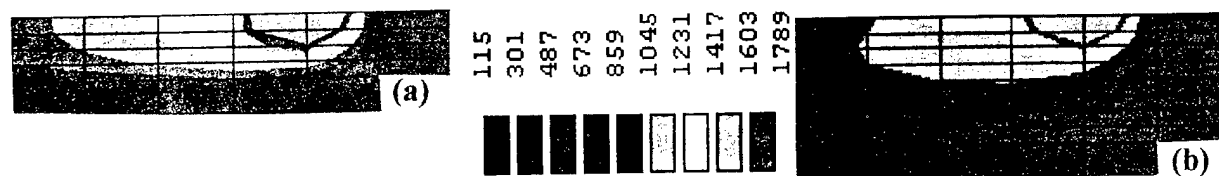


**Fig. 8 Isotherm plot of an FEM simulated double (a) and triple (b) pass weld formed with an average current of 150 A (view of the weld path cross-section)**

## Conclusions

Machine vision sensing can be used for monitoring and controlling the metal transfer process in a 3D welding operation. By precisely controlling the droplet growth process and instant of detachment, the maximum depth of weld penetration as well as the shape of the bead penetration profile can be controlled. Isotherm plots of simulated bead cross-sections demonstrated that the finite-element modeling technique can accurately predict the weld penetration results of a 3D welding operation.

## Acknowledgements

The authors would like to gratefully acknowledge the funding support provided by National Science Foundation (Project No. DMI-9732848), Texas Advanced Technology Program (Grant No. 003613-005), Raytheon Systems in Dallas, TX, and Raytheon E-Systems in Waco, TX.

## References

- [1] P. Dickens, R. Cobb, Gibson, M. Pridham, "Rapid Prototyping Using 3D Welding", *J. of Design and Mfg* 1993.
- [2] H. Beardsley and R. Kovacevic, "Controlling Heat Input and Metal Transfer for 3D Welding-Based Rapid Prototyping", Proc. of the 5<sup>th</sup> Int'l Conf. on Trends in Welding Research, June 1-5, 1998, Pine Mountain, GA.
- [3] H. Beardsley and R. Kovacevic, "New Rapid Prototyping Technique based on 3-D Welding", Proceedings of the 31<sup>st</sup> CIRP International Seminar on Manufacturing Systems, May, 26-28, 1998, Berkeley, CA.
- [4] O. C. Zienkiewicz and C. J. Parekh, 1970. *International J. of Num. Meth. Engr.*, 2:61-71.
- [5] E. L. Wilson and R. E. Nickell, 1966. *Nuclear Engr. And Design*, 4:276-286.
- [6] E. Friedman, 1975. *Journal Pressure Vessel Technology*, Trans. ASME, 8:206-213.
- [7] E. Friedman and S. S. Glickstein, *Welding Journal*, 55(12):408-s to 420-s.
- [8] E. Friedman, Jan. 1980. DOE Research and Development Report. Bettis Atomic Power Lab., West Mifflin, PA.
- [9] G. W. Krutz and L. J. Segerlind, 1978. *Welding Journal*, 57(7):211-s to 216-s.
- [10] P. Tekriwal, M. Stitt, and J. Mazumder, 1987. *Metal Construction*, 19(10):599R-606R.
- [11] K. W. Mahin, A Shapiro, and J. Hallquist, May 1986. Int. Conf. on Trends in Welding Res., Gatlinburg, TN.
- [12] H. D. Hibbitt and P. V. Marcal, 1973. *Computers and Structures*, 3(9):1145-1174.
- [13] P. S. Myers, et al., July 1967. Fund. of Heat Flow in Welding, Welding Research Council Bulletin, No. 123.
- [14] J. H. Waszink and G. J. P. M. Van Der Heuval, Aug. 1982. Heat Generation and Heat Flow in the Filler Metal in GMA Welding, *Welding Journal Research Supplement*, Vol. 61, p. 269-s to 282-s.
- [15] W. G. Essers and R. Walter, Feb. 1981. Heat Transfer and Penetration Mechanisms With GMA and Plasma-GMA Welding, *Welding J. Research. Supp.*, Vol. 60, p.37-s to 42-s.
- [16] K. Tsao, C. Wu, 1988. Fluid Flow and Heat Transfer in GMA Weld Pools, *Welding J.Res. Supp.*, V67(70-75s).
- [17] N. Christensen, V. de L. Davies, and K. Gjermundsen, 1965. *British Welding J.*, (2):54-75.
- [18] W. G. Essers and R. Walter, 1981. *Welding Journal*, 60(2):37-s to 42-s.
- [19] P. Tekriwal and J. Mazumder, 1988. Finite-Element Analysis of Three-Dimensional Transient Heat Transfer in GMA Welding, *Welding Journal Research Supplement*, Vol. 67 (No. 7), p. 150-s to 156-s.
- [20] J. Goldak et al., Sept. 1986. Computer Modeling of Heat Flow in Welds, *Metall. Trans. B*, Vol. 17, p.587-600.

# Study of Ejection Forces In The AIM<sup>TM</sup> Process

Neil Hopkinson and Phil Dickens

Department of Mechanical & Manufacturing Engineering, De Montfort University,  
Leicester, UK, LE1 9BH Tel: 0116 2551551 x8093

## 1 Abstract

The AIM<sup>TM</sup> process has been used to successfully produce short runs of injection moulded parts. One of the main drawbacks of the process is the tendency of the tools to be damaged during part ejection<sup>1</sup>.

At De Montfort University a successful AIM<sup>TM</sup> moulding cycle has been developed in which simple shapes from polypropylene are produced and the ejection forces required are measured. Two different ejection methods are used; one uses conventional ejector pins and the other uses a conformal ejector pad. The tool surface roughness is measured before and after moulding to observe any changes caused by ejection. Results show that ejector pins require a lower ejection force than a conformal ejector pad and this may contribute to longer tool life for the AIM<sup>TM</sup> process. Possible reasons for the results are discussed along with recommendations for further work.

## 2 Background

### 2.1 The Direct AIM<sup>TM</sup> Process

The SL process is a proven technique for the rapid manufacture of parts from CAD designs and it has been used successfully in the production of short run injection moulding inserts<sup>1,2,3,4</sup>. SL tooling inserts are used during the prototyping stage of new product development when parts made from the final materials and using the final production technique are required. The AIM<sup>TM</sup> process may also be used to manufacture end use parts, however relatively low yields and long moulding cycles limit its use.

With non-aggressive moulding materials and favourable geometries, SL tools are capable of producing hundreds of parts when used correctly<sup>3,4</sup>. The aim of the research currently being carried out at De Montfort University is to investigate the limits on tool life caused by more difficult moulding geometries, as it is with these geometries that the SL process has its most distinct advantage over traditional tool manufacturing methods.

## 2.2 Mould Failure During Part Ejection in the Direct AIM™ Process

The most common source of failure in SL moulds has been described as the result of the moulding cooling onto features in the core causing it to break during ejection<sup>1</sup> (see Figure 1).

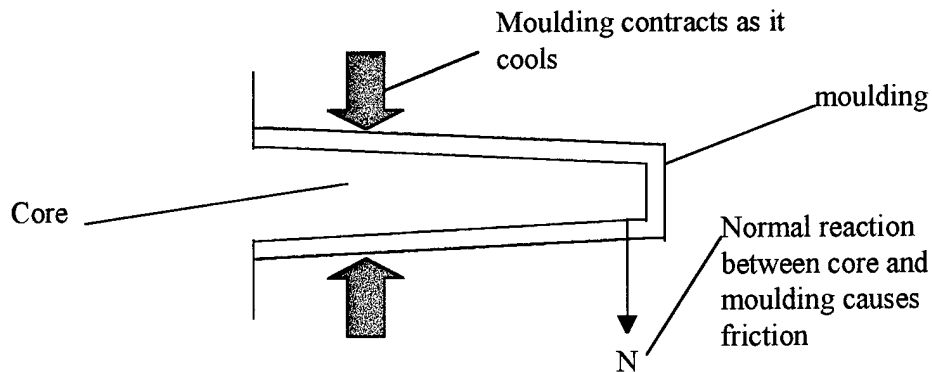


Figure 1. As the Moulding Cools it Contracts onto the Core

It can be seen from Figure 1 that as the part cools it contracts onto the core. It is this contraction along with the surface roughness of the core which leads to high ejection forces and therefore tool failure during ejection. Previous work in this area using steel tools has investigated the sources of high ejection forces and their effect on the quality of the moulded part<sup>5</sup>. In the case of direct AIM™ tooling, the ejection forces are even more important as it is the tool itself which may be damaged.

## 2.3 The Study of Ejection Forces in Injection Moulding

As mentioned above, previous work in this area has been carried out with a view to minimising damage to the moulded part. In the case of direct AIM™ tooling the emphasis for the research is different but many of the principles of ejection in conventional injection moulding still apply.

An equation predicting the ejection force based on various material properties of the mould and moulding has been developed by Glanvill and Denton<sup>5</sup>. The equation is based on ejecting a tube from a core. The use of a tube rather than a closed cylinder like the one used in this research is significant as the ejection force will not need to overcome a partial vacuum between the mould and moulding.

The equation is given as:

$$F_e = \frac{\alpha \cdot (T_m - T_e) \cdot D \cdot E \cdot A \cdot \mu}{D \left[ \frac{D}{2t} - \left( \frac{D \cdot \gamma}{4t} \right) \right]}$$

Where:

$F_e$  = Ejection Force

$\alpha$  = coefficient of thermal expansion of moulding material

$T_m$  = melting temperature of moulding material

$T_e$  = ejection temperature of moulding material  
 $D$  = diameter of core  
 $E$  = Young's Modulus of moulding material at  $T_e$   
 $A$  = Area of contact between core and moulding in direction of ejection  
 $\mu$  = coefficient of friction between moulding material and core  
 $t$  = thickness of moulding  
 $\gamma$  = Poisson's ratio for moulding material

## 2.4 Different Methods of Part Ejection

A number of alternative methods are used for part ejection in the injection moulding process. The simplest and most common method uses ejection pins, however in some cases ejection may be performed using ejector pads, air ejection, sprue pulling or combinations of these <sup>6</sup>. In this research the use of ejector pins and pads are investigated. The reason for assessing pad ejection is because the production of an ejection pad should be relatively simple using stereolithography.

### 2.4.1 Pin Ejection

During the design of an injection moulding tool, ejector pins are positioned in a way to allow a clean ejection from the mould without damaging the moulding. The addition of ejector pins to a mould adds complexity, lead time and cost and is generally kept to a minimum.

After a part has been moulded and allowed to cool, the mould opens and the ejector pins are pushed forward to free the part from the mould. Ejector pins are generally evenly spaced within a mould to provide an even ejection, however extra pins may be required where ejection is more difficult such as with deep features in the mould.

### 2.4.2 Pad Ejection

Pad ejection is very similar to pin ejection except that whole areas of the part are pushed by the pad as opposed to scattered points with pins. This provides a more even ejection and is preferred for larger parts which may be damaged by pins.

A major drawback of using ejector pads is the increased complexity in their manufacture. However with the flexibility of stereolithography, a conformal ejector pad could easily be produced and fixed to ejector pins to provide a more even ejection.

## 3 Research Methodology

The purpose of this research is to investigate the process of part ejection in the direct AIM<sup>TM</sup> process by observing any changes in surface roughness of tools. Also, any effects of ejection method were studied by measuring the ejection forces required.

### 3.1 Tool Design

The basic tool design was based on investigating the principle of failure during ejection as shown in Figure 1. Two factors which required attention were the possibility of using both pin and pad ejection for the same tool and also to ensure that the core would be able to withstand the ejection forces without breaking.

#### 3.1.1 Allowing Both Pin and Pad Ejection

To allow both pin and pad ejection the closed cylinder shape (shown in Figure 1) had a collar added to its base as shown in Figure 2. This design also allows the use of thinner cores with the same ejection set up.

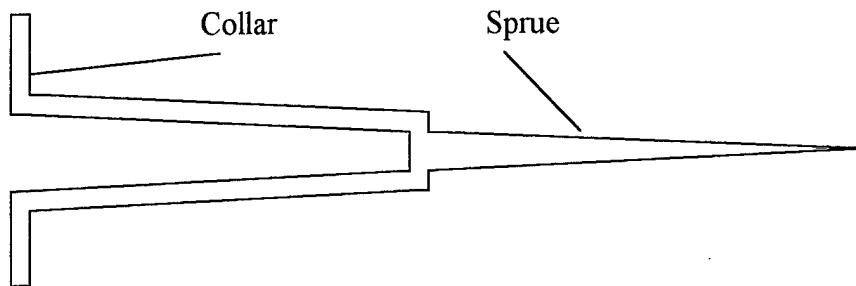


Figure 2. Cross Section of Test Mouldings Produced

#### 3.1.2 Ensuring that the Core Would Not Break During Ejection

In order to produce a number of mouldings and perform a number of tests it was important to ensure that the core would not break off during ejection. Using the equation described earlier to predict the ejection forces along with estimates of material properties and temperatures an acceptable core design was found. Appendix 1 shows the estimates of material properties and tool temperatures based on previous work. These data are fed into Glanvill and Denton's equation and tool dimensions which may result in failure are calculated. Based on these calculations it was decided to use a core with an overall length of 40mm and diameter of 20mm with a 2mm wall thickness.

### 3.2 Equipment

The equipment required for this research is described briefly below.

#### 3.2.1 Injection Moulding machine

A Battenfeld 600 CDC 60 ton injection moulding machine was used. This was controlled by a UNILOG4000 text based programming language which allows easy changing of the many parameters involved in the injection moulding process.

#### 3.2.2 Injection Moulding tools

The tools used were made from solid SL5170 resin using the ACES<sup>TM</sup> build style on an SLA250 machine (see Figure 3). The mould design included a single round core feature to ensure an even shrinkage of the moulding onto the core. The core was 38mm long with a base diameter of 16mm and a 1.5° taper. A 40mm diameter flange

at the base provided an area for ejection and all wall thicknesses were 2mm. The design of the tool with no large flat areas ensured that part distortion after an early ejection would not occur.

The parts were built so that the direction of ejection would be parallel to the z build axis, this maximised the effects of stair stepping on part ejection but is commonplace in the production of SL injection moulding tools. To maintain repeatability between different moulds each insert was thoroughly cleaned between part building and post curing. No other form of finishing was used. Equally spaced steel ejector pins were used to eject the mouldings.



Figure 3: ACES™ Injection Moulding Inserts Used

### 3.2.3 Measurement of Surface Roughness of Cores

The surface roughness of the cores were measured using a Taylor Hobson Talysurf machine. The Talysurf drags a stylus over a surface, plots its profile and calculates the roughness average (Ra).

### 3.2.4 Measurement of Ejection Forces

The ejection forces were measured using 3 load cells each of which consisted of a 4 arm wheatstone bridge. The load cells were mounted behind the ejector pins to measure forces in the direction of ejection (see Figure 4).

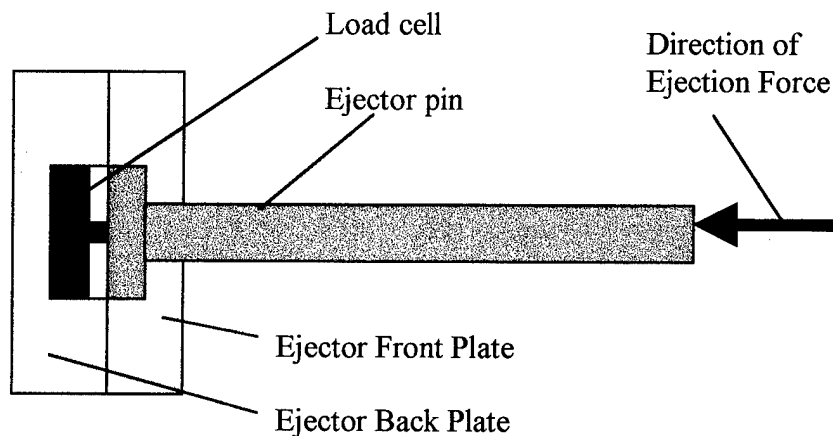


Figure 4. The Load Cells Housed Behind the Ejector Pins

### 3.2.5 Measurement of Tool Temperatures

The tool temperature was measured from the centre of the core using a K Type thermocouple. The SL core had a 2mm hole from the base to the centre of the core. After part building, the thermocouple was inserted into the hole and then SL5170 resin was injected into the hole ensuring that no air was trapped. The core was then post cured in the normal way for 1 ½ hours.

### 3.2.6 Data Acquisition with Visual Programming

The signals from the load cells and the thermocouple were fed into an analogue signal conditioning unit. This unit, which was controlled by HPVee visual programming software, was used to amplify the analogue signals before sending them to the host computer; it also provided excitation for load cells.

The HPVee programming language allowed a great deal of flexibility in terms of acquisition and manipulation of the data. For example, the effects of friction recorded when actuating the ejector pins could be simply measured and automatically subtracted from the ejection reading each time a moulding was ejected.

## 3.3 Experimental Conditions

### 3.3.1. Measurement of Surface Roughness

Measurements of surface roughness were made at 12 fixed positions to ensure repeatability between results. At a distance of 7mm from the base of the core, 6 equally spaced points were measured for surface roughness. Similar readings were taken at a distance of 7mm from the top of the core.

### 3.3.2 Injection Moulding Machine Parameters

Melt injection was performed at the lowest speed possible on the machine which was 5% of full speed. The peak injection pressure measured by the load cells through the ejector pins was 2000 psi (14MPa) and no packing pressure was applied as no surface ripples due to cooling in the mould could be seen.

### 3.3.3 Cycle Times and Tool Cooling

Cooling times were varied as these would greatly affect the melt temperature at ejection ( $T_e$ ) which, according to Glanvill and Denton's equation will affect the ejection force ( $F_e$ ). The longest cooling time used was 480 seconds and the shortest time was 20 seconds.

For each moulding, the core temperature was allowed to cool to 55 degrees C before the next shot was performed. This ensured that the tool was below its glass transition ( $T_g$ ) at the start of each cycle.

### 3.3.4 Data Acquisition Parameters

Measurement of the ejection forces required a quick sampling rate of 1000Hz to catch the peak values. The raw signal included some noise and was smoothed to compensate. The rate of change of tool temperature was much slower and a sampling rate of only 1Hz was required for this.

## 4 Results

### 4.1 Surface Roughness

Surface roughness measurements were taken to assist with estimating the ejection forces and to observe any changes caused by running the tools.

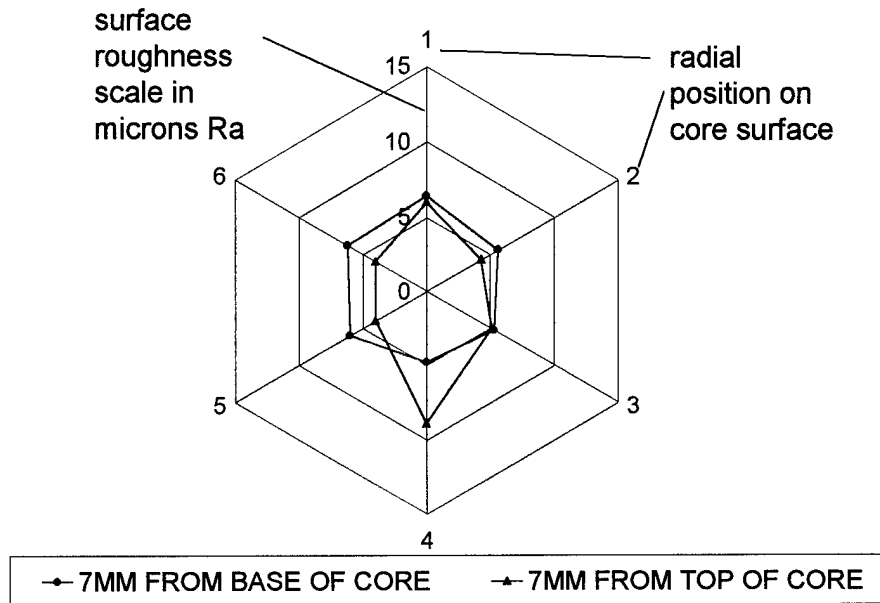


Figure 5. Polar Plot of Surface Roughness of Core Used with Ejector Pins Before use.

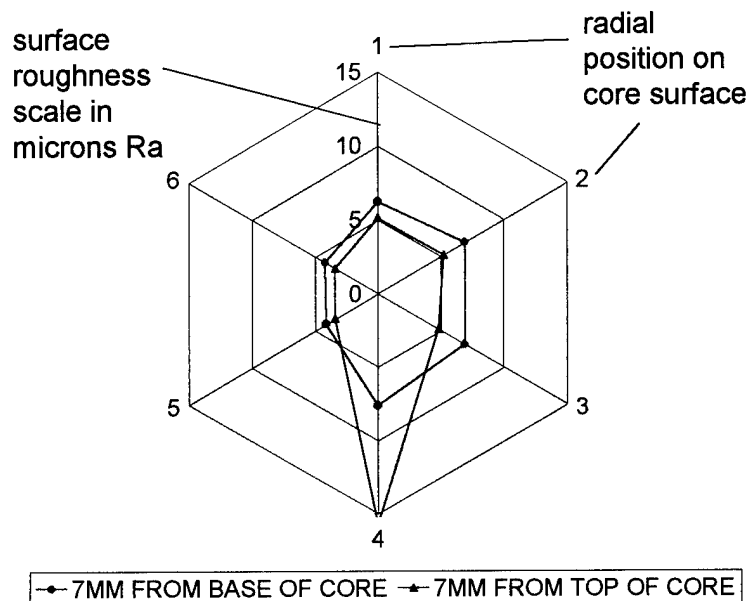


Figure 6. Polar Plot of Surface Roughness of Core Used with Ejector Pad Before use.

#### 4.1.1 Roughness Average Values

Figure 5 shows a polar plot of the surface roughness of the tool which was used with ejector pins before any mouldings were taken. Figure 6 shows a similar plot for the tool which was due to be used with an aluminium ejector ring. Both plots show that the surface roughness measured was between 3 and 7 microns Ra except for position number 4, 7mm from the top of each core. Bubbles could be seen on these parts at this position which explains the higher Ra values.

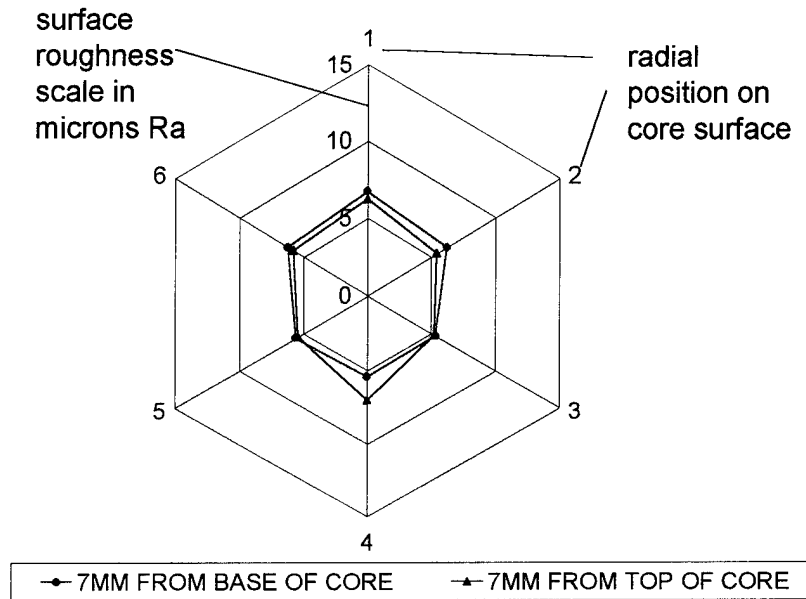


Figure 7. Polar Plot of Surface Roughness of Core Used with Ejector Pins After 50 Shots

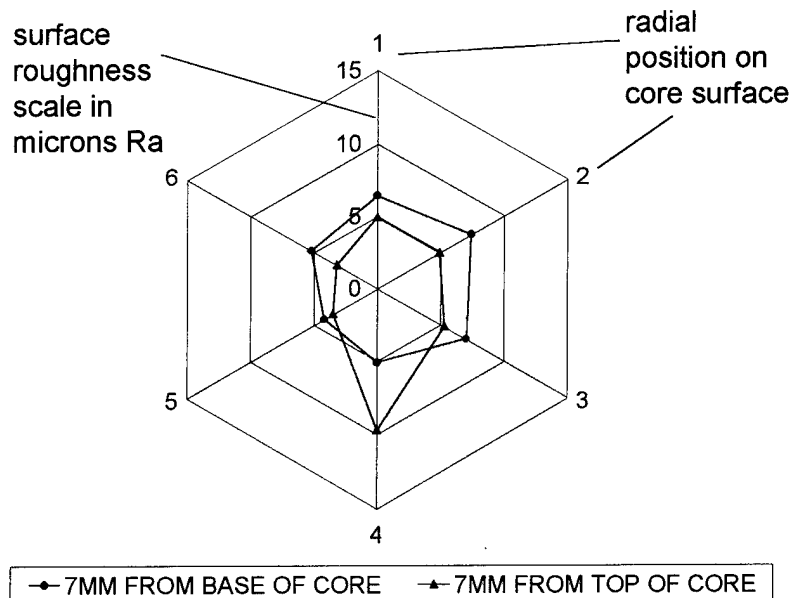


Figure 8. Polar Plot of Surface Roughness of Core Used with Ejector Pad After 50 Shots

Figures 7 and 8 show the polar plots for the cores shown in Figures 5 and 6 after 50 shots had been taken. There appears to be no real change in surface roughness after 50 mouldings for 11 of the 12 points measured. The roughest point on the original plots appears to have been smoothed after 50 mouldings.

#### 4.1.2 Surface Profile Traces

Figure 9 shows a typical surface profile from the core used with pin ejection before any mouldings had been made. As expected, a regular “shark tooth” profile can be seen. Figure 10 shows the surface profile from the same point on the same core after 50 shots. There appears to be no change in the profile of the surface roughness and this is consistent with the results which showed no change in Ra values.

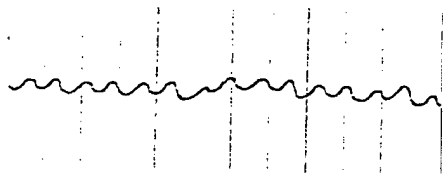


Figure 9. Surface Roughness Profile of Core Before Being Used with Pin Ejection

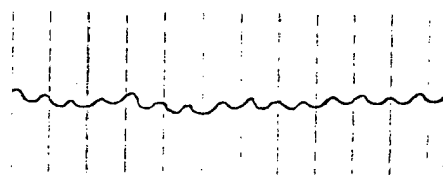


Figure 10. Surface Roughness Profile of Core After 50 Shots had been produced with Pin Ejection

#### 4.2 Pin Ejection

Figure 11 shows the ejection forces recorded against cooling time for mouldings ejected with ejector pins. The graph shows that as cooling time is increased (and therefore melt temperature at ejection is decreased) ejection force is increased. This is consistent with Glanvill and Denton’s equation as are the magnitudes of forces which are up to 300 Newtons.

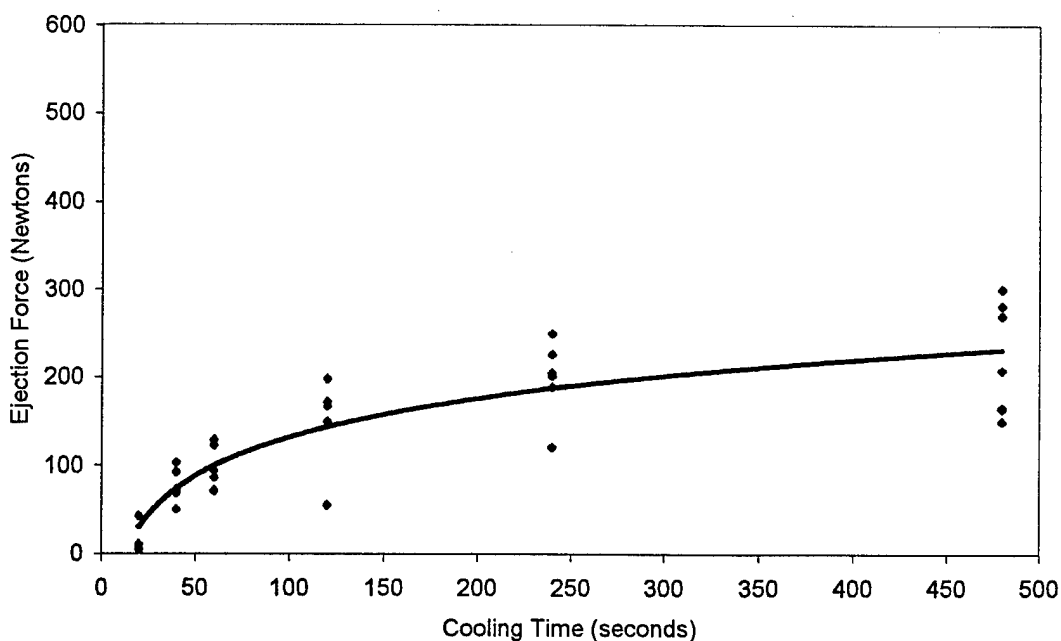


Figure 11. Graph of Ejection Force against Cooling Time Using Ejector Pins

For each specified cooling period there appears to be a significant range of ejection forces measured. The reason for this may be that the temperature of the moulding varies when the ejection time is kept the same. The temperature measured inside the core appears to be consistent with the ejection times, however the core material is an insulator so the temperature at the centre of the core may only give a rough indication of the moulding temperature. It is important to remember that it is the temperature of the moulding rather than the temperature of the centre of the core which will dictate the ejection force.

### 4.3 Aluminium Ring Ejection

Figure 12 shows the ejection forces plotted against cooling time for parts ejected using an aluminium ejector pad. Unlike the graph for ejector pins there is no discernible difference when ejecting after longer cooling times. Also, the forces measured are higher (up to 500 Newtons) than those found with ejector pins. The reason for higher ejection forces was thought to be due to greater cooling at the base of the core due to the aluminium ejector pad acting as a heat sink. In order to test this theory, an ejector pad made from Nylon with a much lower thermal conductivity was used and tested.

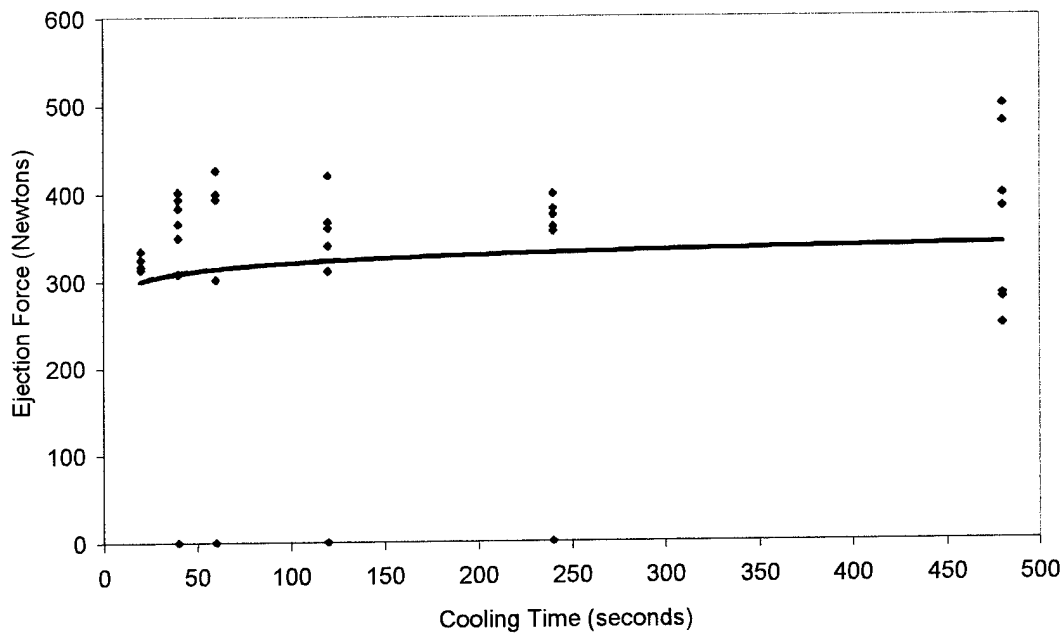


Figure 12. Graph of Ejection Force against Cooling Time Using Aluminium Ejector Pad

### 4.4 Nylon Ring Ejection

Figure 13 shows the ejection forces plotted against cooling time for parts ejected using a Nylon ejector pad. The graph is almost identical to that for the aluminium ejector pad. This suggests that the higher ejection forces are caused by the method of ejection rather than any local cooling caused by heat sinks in the tool.

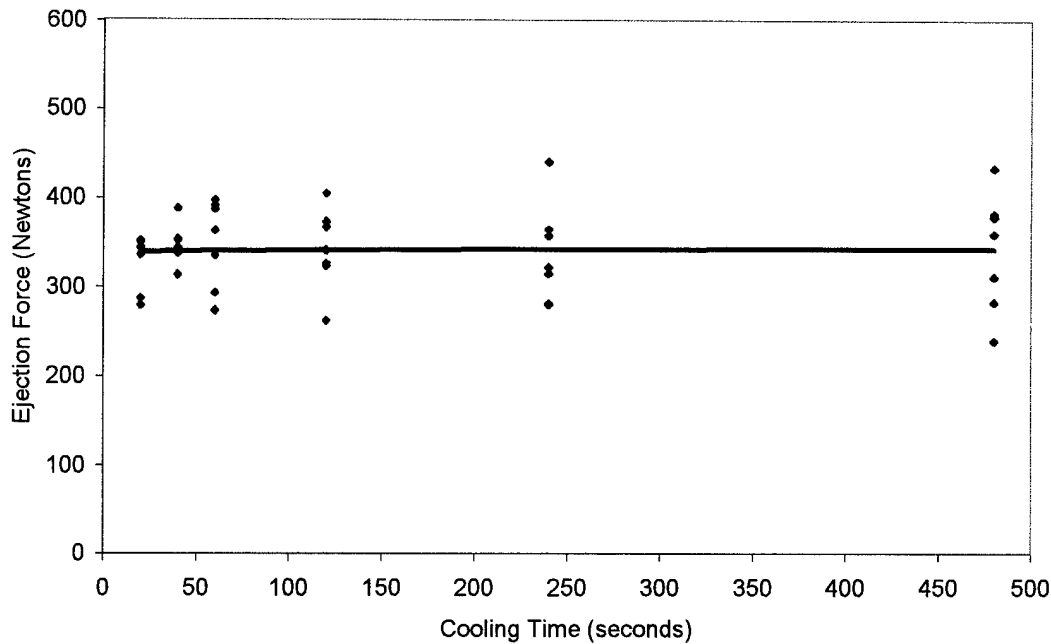


Figure 13. Graph of Ejection Force against Cooling Time Using Nylon Ejector Pad

## 5 Conclusions and Discussion

### 5.1 Surface Roughness of Cores

The measurements taken after 50 shots showed that for most parts of the tool surface there was no change in surface roughness. This suggests that there is no plastic deformation of the tool surface and measurements of roughness taken from the mouldings are similar to those of the tool. This indicates that during ejection, either the tool or the moulding or both are able to deform elastically before returning to their original state.

### 5.2 Ejection Forces

All of the ejection forces measured were within the range which might be expected from the equation provided by Glanvill and Denton. The forces recorded using ejector pins increased as expected with longer cooling times however this was not the case with pad ejectors. One possible reason for the higher ejection forces using pads is that air is not able to fill the void between the mould and moulding at the early stages of ejection. If this is the reason for higher ejection forces, then it suggests that the use of pins allows air to fill the gap between mould and moulding thus reducing the ejection force. It is possible that using pins causes the moulding to bend while still on the core thus allowing air between the mould and moulding. Indeed, given that the ejection force versus cooling time graph profile using pins is similar to that predicted by

Glanvill and Denton's equation using an open cylinder, this theory would seem reasonable.

Another possible reason for higher ejection forces using pads is that the ejection profile using pads is steeper than that using pins. This suggests that the moulding is pushed off more quickly using pads and therefore the acceleration applied is greater which requires a higher force.

### **5.3 Further Work**

The results presented above showed two areas which are difficult to explain and therefore require closer attention. Firstly the higher ejection forces using ejector pads may be investigated by performing tests with different ejector methods. For example ejection with 2 ejector pins could be compared to that with 6 ejector pins. If a more even ejection results in a higher force then it could significantly ease mould design with fewer pins.

Secondly, the variation in ejection forces after the same cooling time may be explained by some variation in the actual temperature at ejection. Further tests should be performed with the temperature of the moulding being recorded rather than the temperature of the centre of the core.

## **6 References**

1. Jacobs, P.F. Recent Advances in Rapid Tooling from Stereolithography. Proceeding of the 2nd National Conference on Rapid Prototyping and Tooling Research. Buckinghamshire College 1996. ISBN: 085298 982 2
2. Decelles, P. and Barrit, M. Direct AIMTM Prototype Tooling, Procedural Guide 3D Systems, Valencia, CA, USA P/N 70275/11-12-96
3. Rahmati, S. and Dickens, P.M. Stereolithography Injection Moulding Tooling 6<sup>th</sup> European Conference on Rapid Prototyping and Manufacturing Nottingham UK July 1997 ISBN 0 9519759 7 8
4. Jayanthi, S. Hokuf, B. McConnell, R. Speer, R.J. and Fussell, P.S. Stereolithographic Injection Moulds for Direct Tooling 8<sup>th</sup> SFF Proceedings Austin Texas September 97 ISSN 1053-2153
5. Glanvill, A and Denton, E Injection Mould Design Fundamentals. Industrial Press, NY 1965
6. Pye, R.G.W. Injection Mould Design 2<sup>nd</sup> Edition The Plastics and Rubber Institute 1978 ISBN 0 7114 3906 0

## Appendix 1

Glanvill and Denton's equation for ejection force is:

$$F_e = \frac{\alpha \cdot (T_m - T_e) \cdot D \cdot E \cdot A \cdot \mu}{D[(D/2t) - (D \cdot \gamma / 4t)]}$$

The equation can be re-written as:

$$F_e = \frac{D^2 \alpha (T_m - T_e) \cdot E \cdot \pi \cdot L \cdot \mu}{D^2 \cdot (1/2t - \gamma/4t)}$$

Where L is the core length.

The  $D^2$  cancels out on top and bottom so the theoretical ejection force  $F_e$  is independent of core diameter.

Using the following figures, ejection forces for different core diameters can be evaluated.

$$\alpha = 6.8 \times 10^{-5} \text{ K}^{-1} \text{ (linear)}$$

$$T_m = 160^\circ\text{C}$$

$$E = 245 \text{ MPa}$$

$$A = \pi \cdot D \cdot L$$

$$\mu = 0.5$$

$$t = 2\text{mm}$$

$$\gamma = 0.35$$

$$\text{Length of Tool (L)} = 40\text{mm}$$

Using an ejection temperature ( $T_e$ ) of  $100^\circ\text{C}$  gives an ejection force of 289N

Using an ejection temperature ( $T_e$ ) of  $60^\circ\text{C}$  gives an ejection force of 482N

These predicted forces (remembering that a trapped vacuum has not been accounted for) can be compared with the predicted tool strength which is governed by cross sectional area and tool temperature.

$$\text{Max Temp of Tool} = 80^\circ\text{C}$$

$$\text{Tensile Strength of Tool at } 80^\circ\text{C} = 12\text{MPa}$$

Therefore for failure at  $80^\circ\text{C}$ :

$$F_e > 12 \cdot \pi (D/2)^2$$

$$\text{For a 10mm diameter tool } 12 \cdot \pi (D/2)^2 = 942\text{N}$$

$$\text{For a 20mm diameter tool } 12 \cdot \pi (D/2)^2 = 3768\text{N}$$

These calculations show that both a 10mm and 20mm diameter core should be strong enough to resist tensile failure assuming no vacuum exists between the mould and moulding.



# THERMAL BEHAVIOR OF PARTS MADE BY DIRECT METAL LASER SINTERING

N. P. Karapatis, Y. Guidoux, P. E. Gyax, R. Glardon

Laboratory for Production Management and Processes

Department of Mechanical Engineering, Swiss Federal Institute of Technology, Lausanne

---

## Abstract

The Direct Metal Laser Sintering (DMLS) manufacturing technique induces thermal stresses in parts. When such parts are used at elevated temperatures, residual stresses are relaxed and the part can suffer significant distortion. This study presents values of geometrical distortion for two laser exposure strategies and for different heat treatment temperatures and durations. Surface and bulk hardness data are provided as well as porosity measurements. At temperatures above 300 °C, the geometrical changes become important. A stabilization treatment at 600 °C can help reduce distortions.

## 1. INTRODUCTION

Freeform fabrication is most often based on the generative manufacturing of parts. In the case of Selective Laser Sintering (SLS), and particularly when fully metallic powders are considered, the heating and cooling of the layers induce heterogeneous dimensional changes of the part. Due to the temperature gradients, residual stresses are generated in the part [1]. These stresses can be very high and cause compact warping, cracking and/or failure. Furthermore, when the sintered part is exposed to relatively high temperatures, residual stresses are relaxed, leading to geometrical deformations and loss of tolerances. The purpose of this paper is to present an experimental observation of the behavior of DMLS parts under several heating conditions. Dimensional variations are provided, together with hardness data and porosity values.

## 2. EXPERIMENTAL METHOD

### 2.1. Specimens

The test samples were DMLS plates 20x30x4 mm<sup>3</sup>, made of conventional EOS MCu 3201 Nickel-Bronze powder. Two standard EOS exposures were used to fabricate the specimens: the Skin and Core strategy (see below) and a usual strategy where the whole layer is sintered with the same parameters (skin parameters). The upper face (z direction) was milled (-0.5 mm) to create an initial planarity before thermal treatments.

#### 2.1.1. The Skin & Core strategy

With the Skin & Core strategy (SK), the outer region (skin) of the part is sintered with a greater laser energy concentration and has a higher sintered density. The bulk of the part (core) is exposed to a lower energy concentration and has a lower density (Figure 1). Different stripe widths are used for the skin and for the core. Moreover, the core zones are sintered every second layer. Reportedly, buildup time can be reduced by about 10%, and residual stresses are decreased [2].

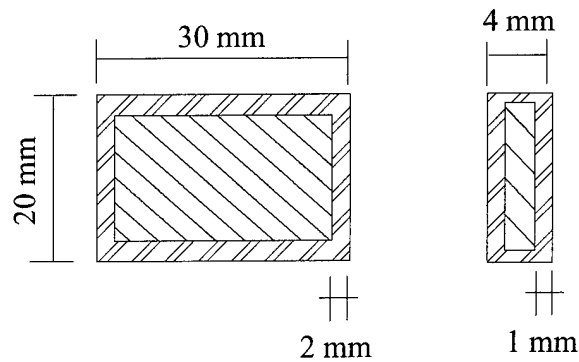


Figure 1: schematic of the SK samples, with skin depths.

## 2.2. Thermal treatments

### 2.2.1. One-step treatments

The DMLS specimens were put into a conventional, pre-heated oven, at temperatures ranging from 200 °C to 700 °C, for 2 and 4 hours. After treatment, the samples were cooled in air. Thermal treatment conditions are summarized in Table I.

Table I: treatment conditions for the one-step experiments.

Sample	Temperatures (°C)	Duration (hours)
High density (skin - S)	200, 300, 400, 500, 600, 700	2 and 4
Low density (skin/core - SK)	200, 300, 400, 500, 600, 700	2 and 4

### 2.2.2. Two-step treatments

Some specimens were treated in two steps to study a possible stabilization by a first thermal treatment (similar to post-sintering). The stabilization treatment consisted of 2 hours at 600 °C. The second treatment lasted 2 hours at 200, 300 and 400 °C (Table II).

Table II: treatment conditions for the two-step experiments.

Sample		Temperatures (°C)	Duration (hours)
High density (skin - S)	First treatment	600	2
	Second treatment	200, 300, 400	2
Low density (skin/core - SK)	First treatment	600	2
	Second treatment	200, 300, 400	2

## 2.3. Measurements and characterization

### 2.3.1. Geometry

Pre-defined points were measured on a coordinate measuring machine (CMM), according to Figure 2, in order to determine the planarity of the horizontal upper face of the platens, before and after thermal treatment. The planarity is defined as the distance between the two remotest points in the z direction, as shown in Figure 2.

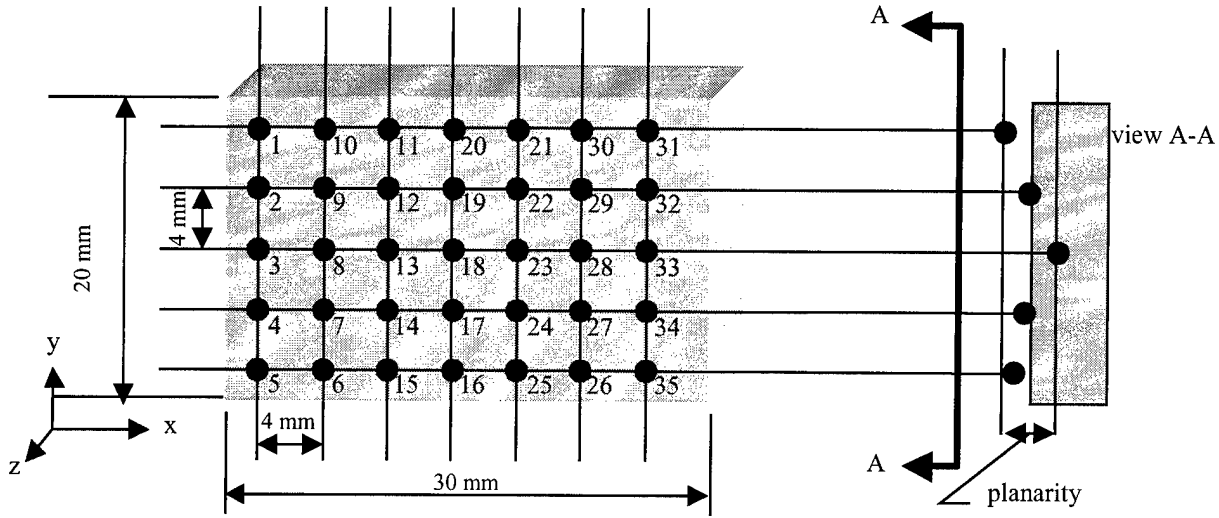


Figure 2: measurement locations at the sample surface and definition of planarity.

The curvature was measured at the plates center (point 18) according to:

$$\frac{1}{\rho_x} = \frac{z_{13} + z_{23} - 2 \cdot z_{18}}{\Delta x^2}, \quad \frac{1}{\rho_y} = \frac{z_{17} + z_{19} - 2 \cdot z_{18}}{\Delta y^2}$$

Where:  $z_i$  = coordinate measured at location  $i$

$\Delta x, \Delta y$  = spacing between measurement points in the x, respectively y direction

$\rho_x, \rho_y$  = radius of curvature in the x, respectively y direction.

### 2.3.2. Hardness

Hardness measurements were carried out according to ISO 4498/1. Five stamps were performed on the upper face of each plate with a load of 50 N (HV 5).

### 2.3.3. Microstructure

Cross-sections (perpendicular to the x axis, Figure 2) were prepared and micrographs (50 x and 500 x) taken in order to measure porosity. The micrographs were systematically taken in the middle of the section. Therefore, these porosity measurements may not be representative of the whole sample. This is important, especially in the case of low density samples, where the core zones are much less dense than the skin.

### 3. RESULTS

#### 3.1. Planarity and curvature

##### 3.1.1. One-step treatments

Figure 3 shows important variations of planarity and curvature at temperatures around 400 °C, for all strategies and treatment durations. Above and below this point, the variations are much smaller. Variation of planarity is significantly lower for the S sample treated for four hours. The other samples exhibit a similar behavior.

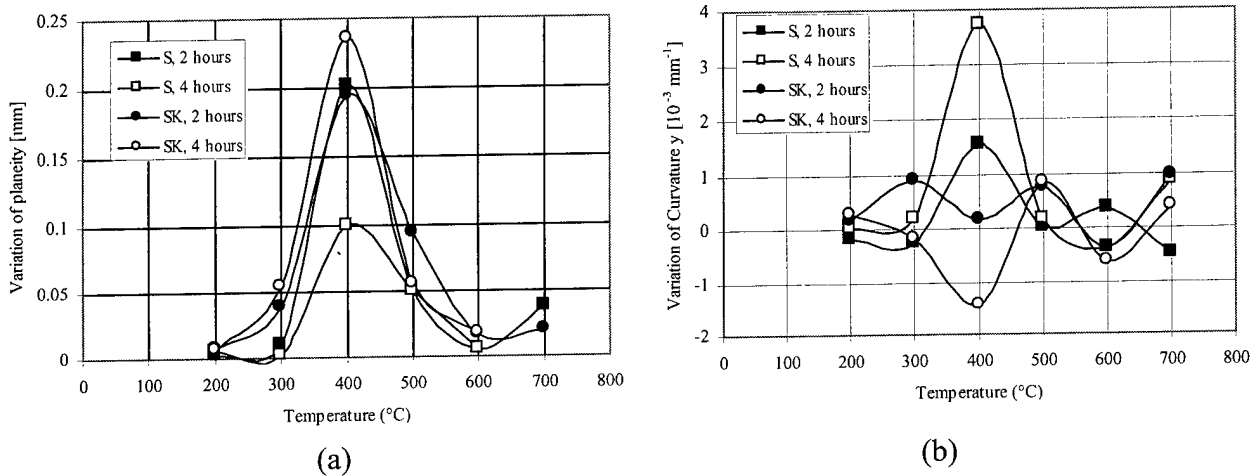


Figure 3: variations of (a) planarity and (b) curvature in the y direction, as a function of the treatment temperature, for the different treatment durations and strategies.

##### 3.1.2. Two-step treatments

After a first stabilizing treatment of 2 hours at 600 °C, the variation of planarity observed at temperatures ranging from 200 to 400 °C are approximately 25 to 50 times smaller than without a stabilizing heat treatment (Figure 4a).

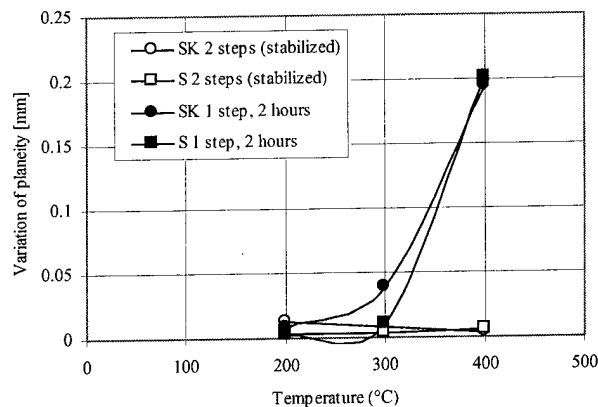
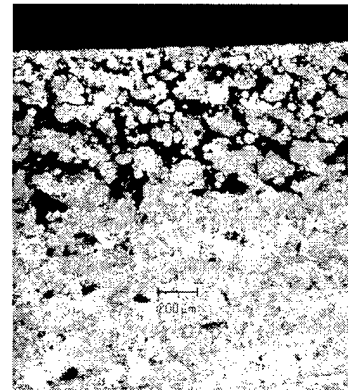
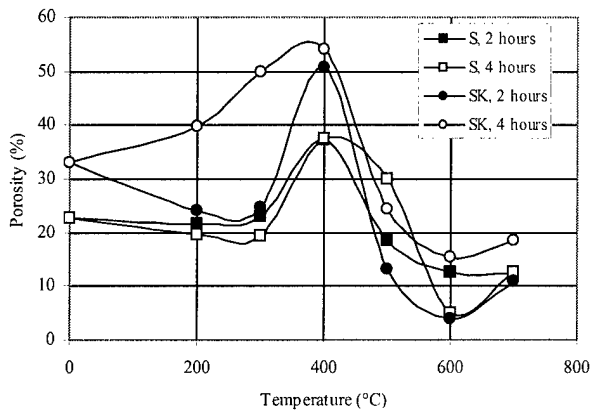


Figure 4: Variation of planarity due to the second step heat treatment after a first stabilization treatment (2 hours at 600 °C).

### 3.2. Porosity

#### 3.2.1. One-step treatments

The porosity measurements (Figure 5) reveal a similar behavior to the geometrical variations presented above. They exhibit a local maximum at 400 °C, regardless of the treatment duration and sample initial density and then drop below 20 % at 600 °C and 700 °C.



(a)

(b)

Figure 5: (a) bulk porosity of the one-step samples, measured at the center of the cross-section, as a function of temperature, for the different durations and exposures. (b) Microstructure indicating a porosity increase at the surface on an SK specimen after 2 hours at 600 °C.

#### 3.2.2. Two-step treatments

After a stabilizing treatment of 2 hours at 600 °C, the porosity observed at 200 °C is about 2 to 3 times lower than without stabilization (Figure 6). However, at 300 °C and 400 °C, similar values are measured for the less dense SK specimens. For the more dense S specimens, the porosity remains about half of its value without previous stabilization.

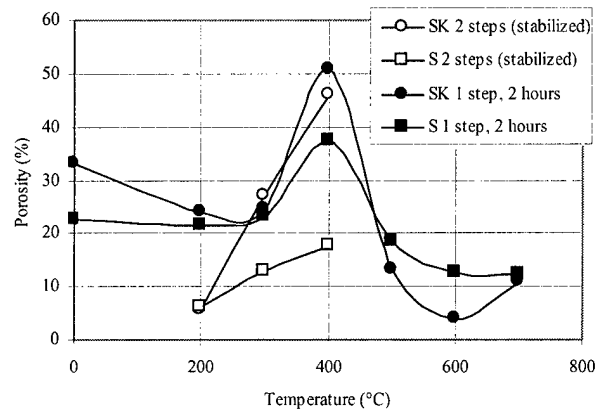


Figure 6: effect of a stabilization heat treatment (2 hours at 600 °C) on the porosity.

### 3.3. Hardness

Figure 7a presents the surface hardness of the various samples. The values of the S and SK samples treated for two hours decrease from about 60 HV for temperatures up to 400 °C down to 30 HV at 600 °C and 700 °C. For the longer treatment durations, a hardness increase can be observed at 300 °C, followed by a rapid decrease down to about 30 HV at 600 °C. At 700 °C, the hardness of these samples increases again up to around 50 HV, while the two hours values remain at about 30 HV.

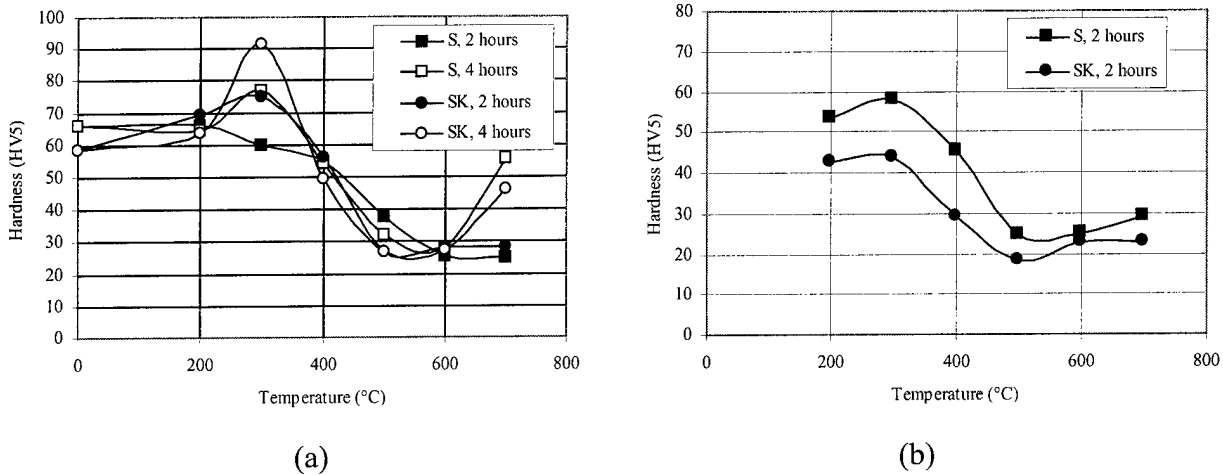


Figure 7: (a) surface hardness as a function of treatment temperature, for different treatment times. (b) Bulk hardness of the one-step samples treated 2 hours, measured in the cross-section.

Figure 7b shows the hardness values measured in the transverse cross-sections, in the middle of the samples, for the two hours treatments. Roughly the same behavior can be observed as for the surface hardness (Figure 7). The denser S structure exhibits a higher hardness at all treatment temperatures. Figure 8 compares the hardness values at the surface and in the sample for the less dense SK samples. The hardness inside the SK samples is lower than at the surface, for treatment temperatures up to 400 °C, as expected according to the laser scanning strategy (Figure 1). However, from 500 °C up to 700 °C, surface and inside values come closer together.

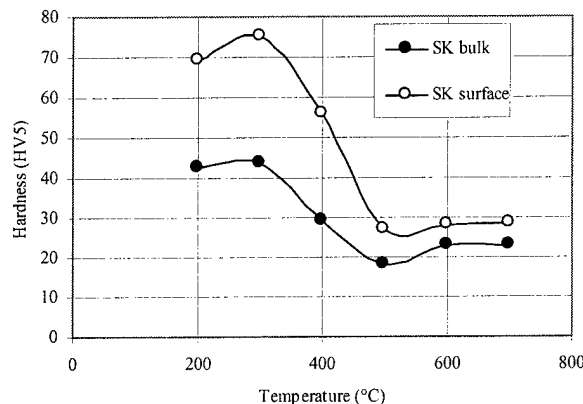


Figure 8: surface and bulk hardness (measured in the middle of the sample), for SK specimens.

In all two-step experiments (Figure 9), the hardness remains at low values similar to those observed after the first treatment at 600 °C. This indicates that the material has been partially stabilized.

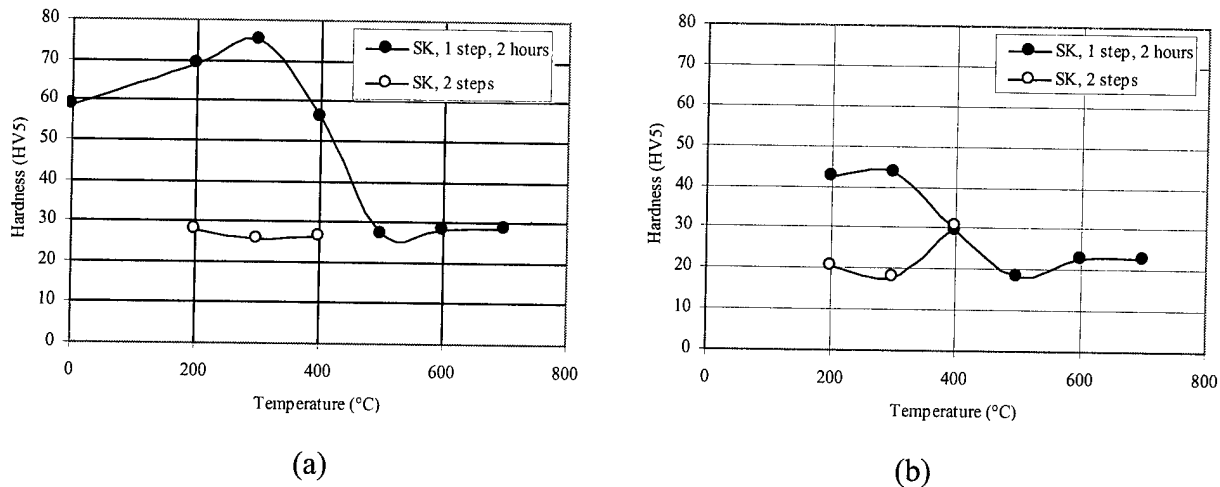


Figure 9: (a) surface and (b) bulk hardness for the one-step samples and after the two-step treatment (stabilization).

## 4. DISCUSSION

### 4.1. Geometrical variations

Figure 3 shows an important variation of planarity at around 400 °C, for both sample densities and treatment durations. Curvature looks roughly the same, although the SK samples exhibit smaller curvature change. This could be explained by a lower level of residual stresses in SK samples, leading to less severe distortion. 400 °C appears to be a critical temperature for dimensional variations. Above and below 400 °C, the variations of planarity and curvature are much smaller. Further investigations are required here to understand the observed behavior. This could be done by testing the effect of time and temperature more extensively or by differential thermal analysis measurements. The diffusion coefficients and activation energy may also give a clue for the observed phenomena. Looking at the geometrical changes occurring in the two-step treatment, the variation of planarity in both S and SK samples is 25 to 50 times smaller than in the one-step experiments, indicating a possible stabilization of the structure by the 600 °C treatment.

### 4.2. Porosity

All porosity values must be taken with care since they were measured in a single location in the transverse cross-section of the samples. The porosity of the one-step samples appears to increase up to 400 °C (Figure 5), with the maximum value reached by the SK samples. At higher temperatures, porosity decreases to a value lower than the initial porosity, for all samples. Looking at Figure 5b, the decrease in porosity observed at 600 °C may be due to a diffusion of matter toward the inside of the sample, leading to a densification of its inner part. For the two-step experiments, the porosity of both samples type (S and SK) increases, with a steeper slope for the SK samples. No satisfactory explanation has been found for this behavior at this stage of the study.

### 4.3. Hardness

Considering the bulk hardness of the samples (Figure 7b), all values of the S samples are above those of the SK samples, in conformity with the higher porosity of the SK structure. The comparison between the surface and bulk hardness (Figure 8) of the SK samples shows a higher surface hardness than in the bulk, as the surface of SK samples is sintered similarly to the S samples. At higher temperatures, this difference is less important, probably because of the surface porosity increase observed in Figure 5b. The decrease by a factor 2 of the bulk hardness between 300°C and 600 °C indicates a reduction in the mechanical strength that could explain the recovery of the geometry observed at high temperatures (Figure 3). The curves obtained for the two-step experiments (Figure 9) show that little hardness changes occur at the different temperatures, for both the S and SK curves. This indicates that the material has been partially stabilized by the first thermal treatment.

## 5. CONCLUSIONS

According to these preliminary results, 300 °C appears to constitute an upper temperature limit for practical use. This can be of significance as DMLS is a potential technology for the rapid manufacturing of complex tools like injection molds [3]. However, if structural and geometrical changes occur at temperatures normally reached in these processes, this could strongly limit the use of this material/process combination for Rapid Tooling. The present results indicate that a stabilization heat treatment around 600 °C may somewhat improve this situation. Still, additional work is required to confirm and extend the present results, as well as to better understand the physical and metallurgical phenomena governing the observed behavior.

## 6. REFERENCES

- [1] A. Coremans, D. Groot, "Residual stresses and thermal stability of laser beam sintered metal parts", *Proceeding of Lane '97*, pp. 577-588.
- [2] J. Weilhammer, EOS GmbH, personal communication.
- [3] N. Karapatis, J.-P. van Griethuysen, R. Glardon, "Direct rapid tooling: a review of current research", *Rapid Prototyping Journal*, Vol. 4 No 2, 1998, pp. 77 – 89.

Keywords : SLS, DMLS, rapid tooling, residual stresses, dimensional changes, hardness, porosity.



## THERMAL BEHAVIOR IN THE LENS PROCESS

M. L. Griffith, M. E. Schlienger,  
L. D. Harwell, M. S. Oliver, M. D. Baldwin, M. T. Ensz,  
J. E. Smugeresky\*, M. Essien, J. Brooks, and C. V. Robino  
Sandia National Laboratories<sup>#</sup>, Albuquerque, NM, \*Livermore, CA

W. H. Hofmeister and M. J. Wert  
Vanderbilt University, Memphis, TN

D. V. Nelson  
Stanford University, Stanford, CA

### Introduction

Direct laser metal deposition processing is a promising manufacturing technology which could significantly impact the length of time between initial concept and finished part. For adoption of this technology in the manufacturing environment, further understanding is required to ensure robust components with appropriate properties are routinely fabricated. This requires a complete understanding of the thermal history during part fabrication and control of this behavior. This paper will describe our research to understand the thermal behavior for the Laser Engineered Net Shaping (LENS) process<sup>1</sup>, where a component is fabricated by focusing a laser beam onto a substrate to create a molten pool in which powder particles are simultaneously injected to build each layer. The substrate is moved beneath the laser beam to deposit a thin cross section, thereby creating the desired geometry for each layer. After deposition of each layer, the powder delivery nozzle and focusing lens assembly is incremented in the positive Z-direction, thereby building a three dimensional component layer additively.

It is important to control the thermal behavior to reproducibly fabricate parts. The ultimate intent is to monitor the thermal signatures and to incorporate sensors and feedback algorithms to control part fabrication. With appropriate control, the geometric properties (accuracy, surface finish, low warpage) as well as the materials' properties (e.g. strength, ductility) of a component can be dialed into the part through the fabrication parameters. Thermal monitoring techniques will be described, and their particular benefits highlighted. Preliminary details in correlating thermal behavior with processing results will be discussed.

### Case Study with H13 Tool Steel

#### *I. Thermocouple Measurements*

A relatively easy way to obtain a thermal signature during processing is by inserting thermocouples directly into the sample during fabrication. Hollow, one line width wide shell boxes were fabricated from H13 tool steel with varying laser powers and traverse velocities (see Table I). Fine diameter (10  $\mu\text{m}$ ) Type C thermocouple wire was used for the measurements to ensure no reaction during deposition.

---

<sup>#</sup> This work supported by the U. S. Department of Energy under contract DE-AC04-94AL85000. Sandia is a multiprogram laboratory operated by Sandia Corporation, a Lockheed Martin Company, for the United States Department of Energy.

**Table I. Parameters of fabrication for H13 tool steel shell box.**

Parameter	Value
Material	H13 tool steel
Layer Thickness	0.125 mm
Traverse Velocity	6.0 and 9.3 mm/s
Power	200 and 300 W
X, Y Dimension	62.5 mm

Figure 1 shows the in-situ temperature readings from a representative thermocouple inserted during fabrication of a shell box processed at 200W and 6 mm/s. Each peak represents the thermocouple response as the laser passes over the thermocouple, from initial insertion to subsequent layer depositions. The data acquisition time is 0.3 seconds, so each spike represents many individual measurements during fabrication\*. After the initial peak in temperature, the heat is quickly conducted away in about 40 seconds to a nominal value of 150 °C. Typically, this would result in a solidification process producing a high hardness, martensitic microstructure. However, for LENS processing, each subsequent pass reheats the previous layers, such that even after seven layers, the part receives a thermal 'hit' of 800 °C, and after eleven subsequent layers the thermocouple still receives a thermal excursion of 600 °C. Even after forty two deposition layers, the thermocouple reads a maximum temperature of 300 °C. After each deposition pass, the part cools down to 150 °C, but the part has received an integrated reheat which can adversely affect the material's properties including residual stress and mechanical strength due to tempering or aging effects.

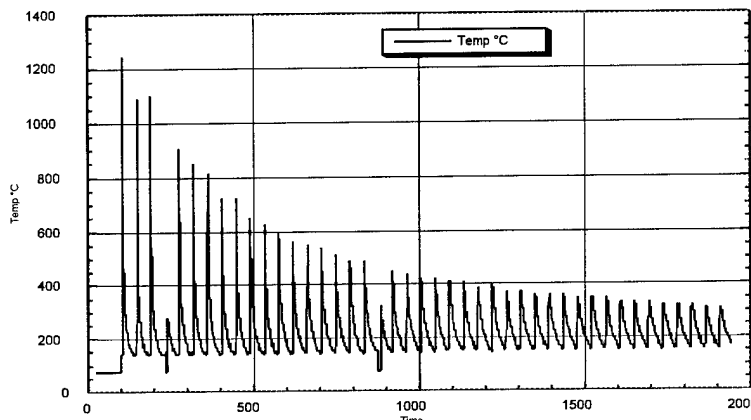


**Figure 1. Thermocouple response (°C) versus time (seconds) during fabrication of H13 shell box.**

## *II. Correlation between Thermal Behavior and Hardness for H13 Tool Steel*

Figure 2 shows a cross-section of the top layers in the H13 hollow part processed at 200W with a 9.3 mm/s traverse velocity. The light area represents the last five layers of deposition (or approximately 870  $\mu\text{m}$ ), whereas the dark area represents the integrated temperature reheat or thermal cycling region. There is a definite change in microstructure between these two zones, as shown in Figure 3 with a dramatic decrease in hardness as the sample

\* Absolute peak temperatures are higher than recorded because the thermocouple response time has not been incorporated.

is probed from the top region into the dark zone. The last five layers do not receive the integrated heat treatment and retain the martensitic phase with a high hardness value of 59 Rockwell C. The subsequent layers undergo many thermal excursions. Thermal cycles above 800 °C can re-austenize the material, and at 900 °C, this can happen in a matter of seconds. With many thermal cycles above 600 °C, it is possible to age or temper the material through reprecipitation or coarsening of the carbide distribution.

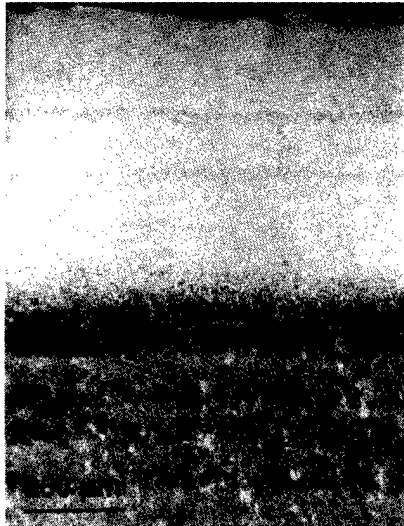


Figure 2. Cross-section micrograph of H13 tool steel thin wall.

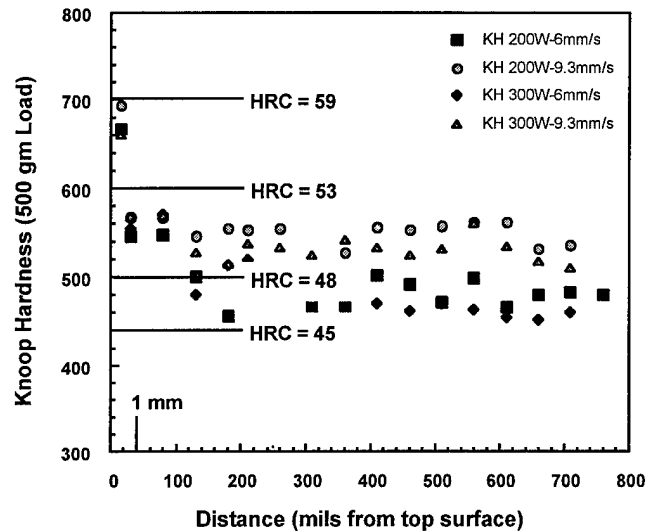


Figure 3. Hardness values (Knoop and Rockwell C, HRC) versus distance from top of wall for four processing conditions.

Even though these are preliminary results, these types of effects are evident from the microstructure shown in Figure 2. In the dark zone, the sample has experienced many thermal excursions above 600 °C, which corresponds to a reasonable amount of tempering or aging, where the expected hardness value, in the range of 50 Rockwell C (HRC)<sup>2</sup>, is observed in our data (Fig 3). Fully understanding and controlling this transition is important for tailoring material properties.

In Figure 3, it is apparent that process parameters directly affect the properties, with traverse velocities having the greatest effect on the final hardness of the tool steel material. At a traverse velocity of 6 mm/s, the hardness ranges from 45 to 48 HRC; whereas at 9.3 mm/s, the hardness has a slightly higher value between 50 and 52 HRC. At increased speeds, the previous layers receive a shorter time excursion at the elevated temperatures producing reduced aging effects.

### III. Residual Stress in H13 Tool Steel

Knowledge of the magnitude and distribution of residual stresses is often important because of their effect on structural behavior. A holographic-hole drilling technique<sup>3</sup> was used to determine the residual stress state in the shell samples. In the holographic-hole drilling method, a region of a test object containing stress is illuminated with laser light using an optical setup. A hologram of the region is made by exposing a recording plate in a commercially available holocamera to the light of a reference beam and that of the object beam as reflected from the test

object. The hologram is recorded electrostatically on an erasable, re-useable thermoplastic medium. Then a small square-bottomed hole is milled into the region of interest to a depth that can be varied, but which is generally a fraction of the hole diameter. The hole releases residual stresses locally, causing material surrounding the hole to deform in response to the stress relief. The resulting surface deformations, which are both in-plane and out-of-plane, alter the path length of the light reflected from the region, immediately creating a pattern of optical interference fringes on the hologram. The interference fringe pattern can then be analyzed to determine the residual stresses that existed prior to the introduction of the hole.

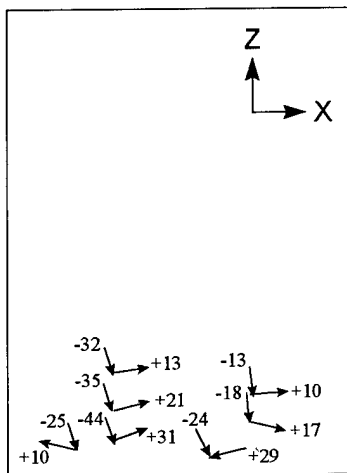


**Figure 4. Principal residual stresses along H13 wall (magnitude and direction).**

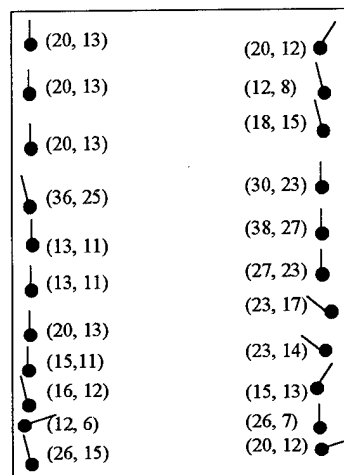


**Figure 5. Principal residual stresses on surface of H13 solid part (depth=1mm).**

Figure 4 shows the residual stress distribution along a wall processed at a laser power of 200W with a 6 mm/s traverse velocity. For these thin walled hollow shapes, the stress was only measured near the base of the sample to minimizing any distortions created during the drilling sequence. An unusual biaxial stress state was measured, where in the fabrication plane (X direction) the principal stress state is positive, or in tension, with values ranging from 10 to 31 ksi. However, in the through-layer condition (Z direction), the stress state is negative, or in compression, with values ranging from -13 to -44 ksi. It should be mention this material has a yield strength of 180 ksi, so the residual stress values are quite low with respect to the strength of the as-processed material (~20%). Further work is required to understand the biaxial stress state condition in these shell samples.

To clarify the effect of geometric influence on residual stress manifestation for H13 tool steel, a solid H13 tool steel sample was fabricated (6.4 cm x 1.0 cm x 11.4 cm). Figure 5 shows the distribution of principal stresses and their direction along one side measured in the as-processed material. The residual stress near the surface is in tension and has a low value ranging from 6-38 ksi, well below the yield strength of the material (180 ksi). In complex part fabrication, it is expected the overall residual stress state would be low for this alloy.

Initial evidence suggests that H13 solidification may occur as primary austenite or ferrite. If it occurs as ferrite, then it must undergo a transformation to austenite during cooling and this transformation would likely proceed in such a way as to reduce some of the stress. If

solidification occurs as primary austenite there would not be any stress relieving effect. However, at lower temperatures, the austenite (whether it is primary austenite or austenite formed from ferrite) transforms to martensite in this alloy (which has a high hardenability) rather than the diffusional decomposition products of ferrite and pearlite. This transformation to martensite is known to be affected by stress, and might act to reduce the stress (i.e. the dilatation that occurs during the transformation might reduce the residual stresses from differential thermal contractions). Moreover, each reheat cycle from subsequent deposition layers which heat the alloy back into the austenite phase field (say then next four or five layers based on the thermocouple data) will result in the formation of austenite. Here again, stresses which are present may tend to be relieved by the transformation dilatations. Finally, the tempering (alloy carbide precipitation) which occurs during reheats to peak temperatures below 900 °C also results in a dimensional change. It is conceivable that this tempering would also act in such a way that the dimension change would help to reduce the residual stresses.

### **Non-invasive Thermal Imaging Techniques**

As discussed earlier, it is known intuitively that a thermal gradient exists across the molten pool and into the bulk material created by the LENS process. The nature and extent of this gradient has not been fully characterized. Since mechanical properties are dependent upon the microstructure of the material, which in turn is a function of the thermal history of solidification, an understanding of the temperature gradient induced by LENS processing is of special interest. It would be particularly beneficial to use non-invasive thermal imaging to measure the temperature profile and gradients and to use these thermal profiles in feedback control. Preliminary results for two techniques will be discussed: 1) infrared imaging for bulk temperature measurements plus gradients, and 2) high speed visible imaging to measure the molten pool temperature and its corresponding gradients. With these two techniques, it is possible to obtain a complete picture of the thermal behavior, near and far from the molten pool, during LENS processing. Initial experiments were conducted using stainless steel 316 powders.

#### *I. Temperature Measurement Using Digital IR Imaging*

In-situ temperature measurements were performed during LENS processing using a digital infrared camera, (Flir Systems, Prism DS). The camera's recording element is a 320 x 244 pixel platinum silicide CCD array, with a spectral range from 3.6 to 5 mm. The system records the infrared radiation emitted by a heated object, and, using various filters, may record the emission from objects with temperatures ranging from -10 °C to 1700 °C. Absolute temperature measurements require knowledge of the emissivity of the object. Since no emissivity values for metal objects fabricated using laser deposition are known, only relative temperature measurements have been performed. A discussion of a procedure for performing absolute temperature measurements, without knowledge of the object's emissivity will be discussed.

Figure 6 shows a thermal image taken with the digital camera. The laser is incident from the top of the frame, and the part is rastered from left to right to form a thin, one line width wide wall in stainless steel 316. The image shows the laser weld pool and the heat conduction into the surrounding metal.

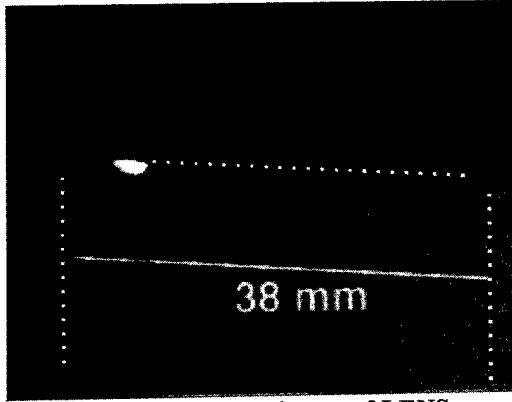


Figure 6. In-situ thermal image of LENS process for stainless steel 316 alloy.

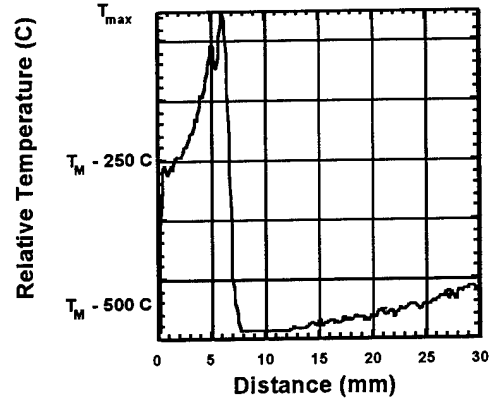


Figure 7. In-situ thermal profile of wall along the direction of travel (Fig. 6).

Figure 7 shows the thermal profile of Fig. 6 taken along to the direction of travel. Since the quantitative temperature is not known at this time, the relative temperature  $T_{max}$  is plotted as the maximum temperature measured by the IR camera near the weld pool region. The rest of the temperatures plotted are the values below this maximum temperature. The trace shows a steep profile in the region surrounding the molten pool ( $\sim 36$  K/mm), a cooler region to the right with a thermal signature that is not detectable, and another detectable heated region at the right corner of the part where the laser had completed the previous layer four second ago. The effect of the thermal profile on the previous layers is not shown in this figure. Figure 6 shows a large thermal tail as well a large thermal region of conduction into the previously deposited layers. With more analysis, a complete thermal picture will be developed for processing stainless steel 316 alloy.

In order to develop a procedure for determining absolute temperature using an infrared imager without knowledge of the object's emissivity, it is necessary to consider Planck's radiation law. The monochromatic energy density radiated by a blackbody is given by the Planck relation,

$$W(\lambda) = \frac{c_1 \lambda^{-5}}{e^{-c_2/\lambda T} - 1} \quad [1]$$

where  $c_1$  and  $c_2$  are constants,  $\lambda$  is the wavelength, and  $T$  is the temperature of the object<sup>4</sup>. An approximation to equation [1] is given by Wien's law,

$$W(\lambda) = c_1 \lambda^{-5} e^{-c_2/\lambda T} \quad [2]$$

The signal recorded by a detector element in the camera's focal plane is

$$S_i = \int_{\lambda_1}^{\lambda_2} \varepsilon W(\lambda) R(\lambda) d\lambda \quad [3]$$

where  $\varepsilon$  is the emissivity of the object and  $R(\lambda)$  is the detector response. As a further approximation,

$$S_i = \varepsilon c_1 \lambda_e (T)^{-5} e^{-c_2/\lambda T} R(\lambda) \quad [4]$$

where  $\lambda_e(T)$  is the temperature dependent effective wavelength. If an independent measurement of temperature is made at  $T_0$ , then the temperature  $T$  recorded by the  $i$ th detector element is related to the signal  $S_{i,0}$  by

$$\frac{1}{T} = \frac{1}{T_0} + \frac{\lambda_e(T)}{c_2} \ln \frac{S_i}{S_{i,0}} \quad [5]$$

where  $S_{i,0}$  is the signal recorded by the  $i$ th detector from an object at temperature  $T_0$ . Therefore, with a valid expression for  $\lambda_e(T)$ , the ratio of the signal at an unknown temperature to that at a known temperature may be used to obtain absolute temperature measurements without knowledge of the emissivity of the object. The set of experiments to calibrate the infrared camera is currently underway.

## II. Temperature Measurement Using High Speed Visible Imaging

Preliminary experiments were conducted using ultra high speed digital imaging techniques<sup>5</sup> during LENS processing to provide insight as to the size of the molten pool and the thermal gradient in 316 stainless steel (SS316) samples fabricated using the LENS process. Digital images were obtained directly through a CaFl viewport in the LENS glovebox using a 12 bit digital camera equipped with a telephoto lens and 650nm broad band filter. A total of 2048 frames/run were recorded at a rate of 1.4 ms/frame. Temperatures were obtained using standard pyrometric techniques. The results shown are for SS316 material built using coarse powder (-150/+325 mesh) at a nominal laser power of 260W. A single, one line width wide wall was fabricated with 250 micron layer increments, where the traverse direction is from left to right.

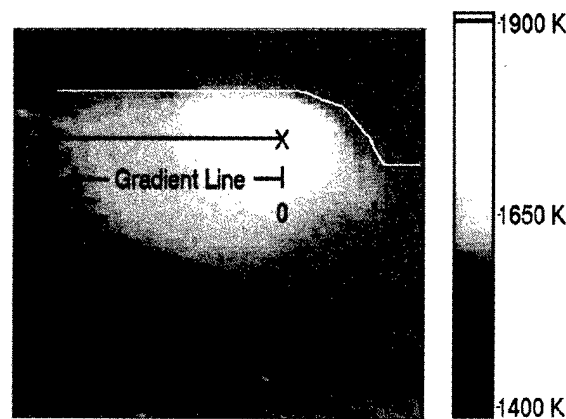


Figure 8. Digital image of molten pool and bulk material during LENS processing of SS316.

Figure 8 is a digital image of the molten pool and the adjacent bulk material created during processing. The field of view encompasses approximately 5 mm. A white line has been superimposed on the image to indicate material boundaries (i.e.; the top layer is being deposited on the previous layer with a curved profile in the region of the molten pool).

The temperature profile shown in Figure 9 and thermal gradient shown in Figure 10 correspond to the gradient line indicated in the digital image. Figure 9 shows that the molten pool reaches temperatures on the order of 1875 K (reasonably large superheat) with a linear decrease in temperature until thermal arrest (solidification) occurs at approximately 1650 K. Upon solidification, bulk material continues to cool similar to the thermocouple measurements. In Figure 10, the gradient at the center of the molten pool is zero, where immediately adjacent (~0.25 mm), the gradient is 150 K/mm. A maximum gradient of 160 K/mm is indicated in the region approximately 1 mm from the molten pool. The gradient decreases sharply with distance from the molten pool until solidification occurs, at which point the gradient levels out to approximately 20–30 K/mm. This agrees with the infrared data which measured approximately 36 K/mm near but not within the melt region of the molten pool.

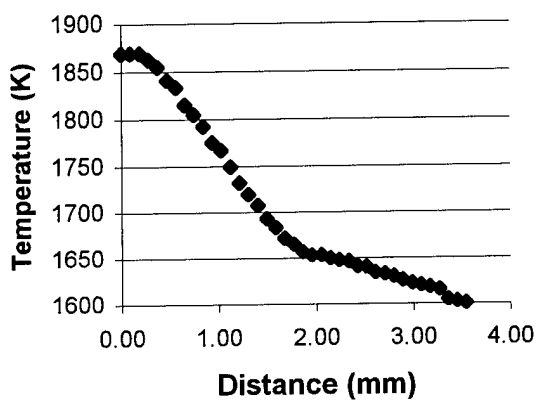


Figure 9. Temperature profile across gradient line indicated in Fig 8.

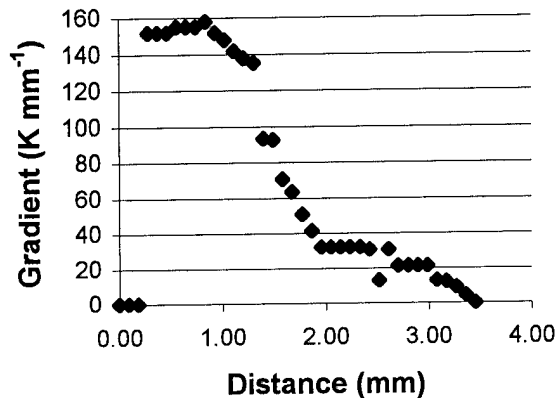


Figure 10. Thermal gradient across gradient line indicated in Fig 8.

## Summary

Knowledge of the thermal behavior is critical to reliable and repeatable fabrication during LENS processing. Our initial thermal experiments show promise in both monitoring as well as understanding the thermal behavior. With in-situ, calibrated real time monitoring, it will be possible to use these thermal signals for feedback control. Preliminary results show there is a significant effect on the microstructural evolution during fabrication of hollow H13 tool steel parts, where the integrated temperature reheat tempers the material.

## References

- <sup>1</sup> M. L. Griffith et. al., *Free Form Fabrication of Metallic Components using Laser Engineered Net Shaping (LENS)*, Proceedings of the Solid Freeform Fabrication Symposium, August 12-14, 1996, Austin, TX.
- <sup>2</sup> G. Roberts, G. Krauss, R. Kennedy, Editors, *Tool Steels*, Fifth Ed., ASM International, Chapter 13, 1998.
- <sup>3</sup> A. Makino and D. V. Nelson, E. A. Fuchs, D. R. Williams, *Determination of Biaxial Residual Stresses by Holographic-Hole Drilling Technique*, J. of Engineering Materials and Technology, Vol. 118, 1996, p.583.
- <sup>4</sup> M. R. Wehr. *Physics of the Atom*. Addison-Wesley:Reading, 1984, p.82.
- <sup>5</sup> W.H. Hofmeister, R.J. Bayuzick, M.B. Robinson, *Noncontact Temperature Measurement of a Falling Drop*, International Journal of Thermophysics, Vol. 10, No. 1, 279 - 292.

# Prototyping large-sized objects using freeform thick layers of plastic foam.

A.F. Lennings, J.J. Broek, I. Horváth, A. de Smit, J.S.M. Vergeest

Delft University of Technology  
Subfaculty of Industrial Design Engineering  
Jaffalaan 9, 2628 BX Delft, The Netherlands  
Email [a.f.lennings@io.tudelft.nl](mailto:a.f.lennings@io.tudelft.nl)

## ABSTRACT.

Current Rapid Prototyping systems are primarily aimed at small-sized objects containing many shape details. In this paper a Rapid Prototyping technology is presented that is aimed at large-sized objects having a complex, freeform outer shape. This new technology builds the model out of thick layers, each having freeform outside faces. The paper will present: an overview of current methods to produce large prototypes, the basics of the new method, the technology used to produce the layers, the toolpath planning and finally the overall system design.

## 1. INTRODUCTION.

Most Rapid Prototyping systems build a model by stacking a large number of thin layers. Each of these layers has vertical front faces, which results in a so-called staircase effect on the surface of the object (zero order approximation). The thickness of each consecutive layer has to be very small in order to achieve a model of sufficient preciseness. This thin layer technology is well suited for prototypes of small-sized objects. For larger products however, the time and cost involved are far too high: a different approach is needed. A number of solutions to this problem that have been proposed are discussed in section 2. One of these being the combination of layers with ruled front faces (first order approximation) and a higher layer thickness, to enhance speed without losing preciseness.

In section 3 of this paper we will present our new approach: a prototyping system based on higher order approximation (e.g. second order, i.e. circular, or better). Using this technology consecutive layers can be produced with outer surfaces that smoothly fit together. This way very high quality models can be produced at moderate cost. The actual technology to be used is based on cutting polystyrene slabs using a flexible (hot) blade as a cutting device. The shape of the cutter can be controlled during the cutting process, for which the theoretical base is given in section 4. Section 5 describes the method to calculate the toolpath and the shape of the cutter for every tool position. The overall system design is presented in section 6, and finally in section 7 the results will be discussed and conclusions will be given.

## 2. RELATED RESEARCH.

Rapid Prototyping is the process of automatically creating a physical prototype, based on a 3D CAD model, and within a short time. For this automatic creation of physical models three fundamentally different methods are possible [Kruth, 1995]:

- Incremental (adding material), commercially available in LMT systems.
  - Decremental (removing material), commercially available in CNC systems
  - Deforming (changing the shape of flexible material), no commercial RP systems available.
- Next to these three base methods a number of hybrid methods have been developed too, for instance stacking layers (incremental) that have been cut out (decremental).

Incremental processes are mainly used for relatively small but complex (many shape details) models. A large advantage of these processes is that the price of the prototype is (almost) independent of its complexity. However, when the desired model has to be large, like one or more cubic meters, incremental techniques tend to be slow, complicated because of the small working envelope of these systems, and very expensive. So for the production of large models decremental methods are better suited, using large CNC milling machines. Currently easy-to-use CAM software is available, especially developed for Rapid Prototyping purposes [Lennings, 1997]. This approach is best suited for styling block models: detailed inside geometry is more suited for incremental processes. Thus, for the creation of models that both are large and contain many details no solution is available yet.

In recent years some steps forward were made in the field of large shape prototyping. Recently a system called Topographic Shell Fabrication (TSF) became commercially available, based on the incremental principle [Formus, 1997]. It uses sand as the building material, which is then bound using wax. This system is able to build models up to about 3.6 x 2 x 1.3 meters. The models produced by this technique are quite heavy and can melt by sunlight because of the wax used. The main application of the technique is to create molds for lay up techniques.

Furthermore, some new hybrid techniques have been developed or described. Research projects on the Universities of Utah [Thomas ea., 1996], Queensland [Hope ea., 1996, 1997a] and Delft [de Jager ea., 1996, 1997a, 1998] have delivered systems, algorithms and techniques that can be used to create large shapes out of thick layers. The main problems to be solved here were: how to build the shapes with as few layers as

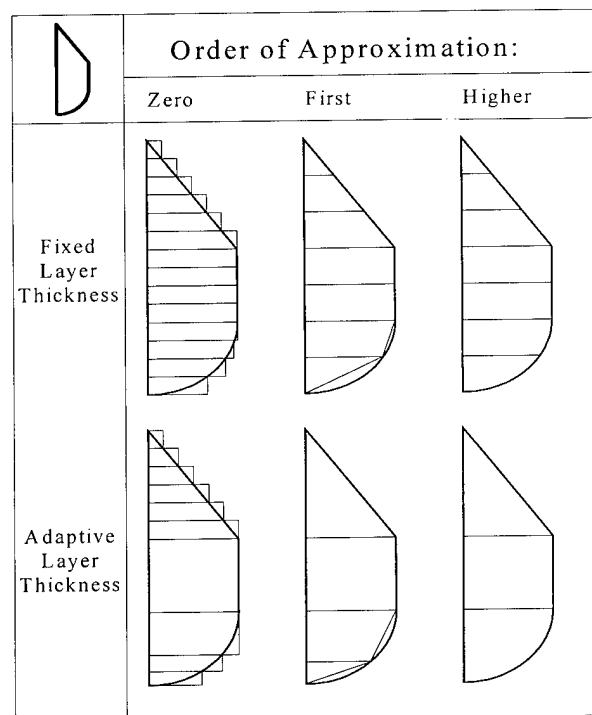


**Figure 1: Available slicing techniques.**

possible, and how to avoid the staircase effect which also exists in thin layer systems but is of much more importance in thick layer systems.

The solution for the first problem is adaptive slicing. Several algorithms have been developed [Hope ea., 1997b], [de Jager ea., 1997b] and [Marsan ea., 1996] that are able to generate layers with variable thickness from a CAD model. The thickness of each layer depends on the local shape that has to be approximated and the tolerance that is given. An extruded shape can be produced using one layer or a small number of the thickest possible layers, while a free formed shape of the same height has to be built using many more layers to approximate the shape accurately.

The second problem, on the staircase effect, can be reduced by using layers with sloped front faces (first order approximation) instead of the classical method which uses layers with vertical front faces (zero order approximation) [Hope ea.] and [de Jager ea.]. Production of layers with sloped front faces can be done using existing cutting equipment, like 4 axis hot wire cutters, laser cutters or waterjet cutters. Using these two solutions combined results in fewer layers needed to produce a model at a given accuracy: see the two leftmost columns of figure 1.

### **3. A NEW APPROACH.**

Building a model by stacking a number of layers is in fact a perfect example of a discrete procedure: the layer either is or is not present, causing the staircase effect mentioned before. As said before: sufficient for small models, but very inefficient in case of large models. The use of sloped front faces does offer some improvement here, however is still insufficient for high quality prototypes. In our proposed method we use a higher order approximation for the front faces of each layer, to be created using an analog procedure.

In contrast to discrete methods, analog methods create shape by reproduction of a master, like a mold for injection molding (3D example). The craftsman modelmaker regularly uses 2D analog tools while creating a freeform model: all sorts of 2D templates that are being used as scraping tools [Trudeau, 1995]. A foam model of a sphere can for instance be created by scraping with a circle-formed tool, using one or more layers. In case of a more complex shaped geometry the front faces of the layers can also be created by scraping with circular tools, which is second order approximation. In many cases a better approximation is possible using freeform tools (higher order approximation). The use of analog tools is very efficient: complex shapes can be produced in a short time. Especially when combined with adaptive layer thickness: see figure 1.

However, the disadvantage of using an analog tool is that the tool first has to be created, because an infinite amount of possible toolshapes exists. In our proposal this problem is covered by using a computer controlled flexible tool, that can indeed be set to an infinite number of shapes. This tool is a heated flexible blade: a thin, flexible metal blade that is supported at both ends by active supports. By changing the length of the blade, the position and the orientation of the supports, the shape of the flexible blade can be influenced (figure 2). As the blade is heated it can be used to cut slabs of polystyrene foam, thus producing thick layers with freeform front faces.

These layers have to be stacked (either automatically or by hand) to produce the actual large prototype. At the connection between two layers now a continuous surface is created, with a high order continuity. Where standard LMT methods produce a discontinuous outer surface, and the ruled front face method a zero order continuity (positional), the new method creates a first order continuity (tangential), or even a second order continuity (same curvature). Using this method will result in a large prototype of high quality, produced within a short time and at moderate cost.

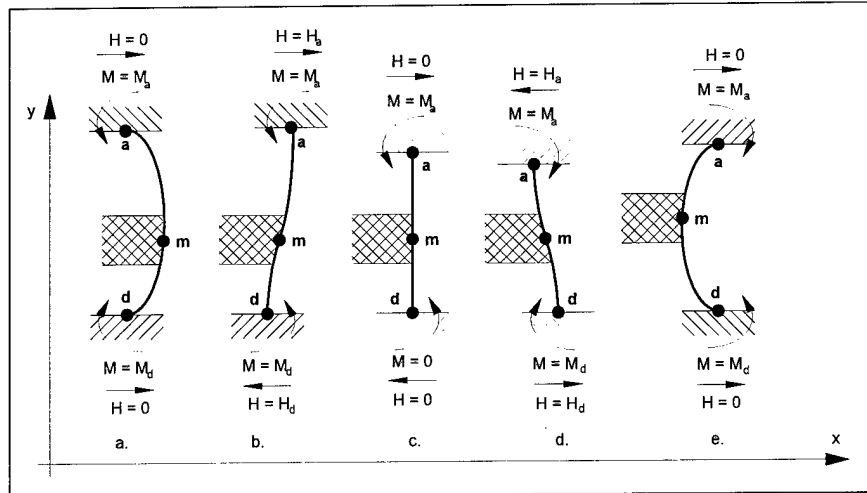


**Figure 2: Possible shapes of the flexible blade.**

#### 4. OVERALL DESIGN OF THE NEW SYSTEM.

Based on the idea of using a heated flexible blade to produce layers with freeform front faces, a complete Rapid Prototyping system has been designed, which is presented in figure 3. It consists of three phases. First the preparation phase, in which the geometry is imported, analyzed and if needed segmented. Segmentation is needed in case the total prototype cannot be manufactured in one piece because of size and/or geometry problems. We will not discuss the process of segmentation in this paper. Next the computing and simulation phase, in which the layers to be manufactured are calculated and the result is simulated. Especially important for a successful system is the layer thickness calculation (slicing), which has to produce layers of variable thickness in such a way that each layer can indeed be produced. For each layer the freeform front face (nominal shape) has to be approximated by curves that can be produced by the flexible blade. Finally the third phase: the physical fabrication phase, in which the prototype is actually built on a real (designed, built and tested) machine.

This overall system design consists of many processes, for all of which methods, algorithms and physical tools have to be developed. It is not possible to treat each of these processes in detail here. In this paper we will discuss the most crucial items of the systems design, which are the modeling of the flexible blade and the curve matching of the blade-curve with the nominal geometry.

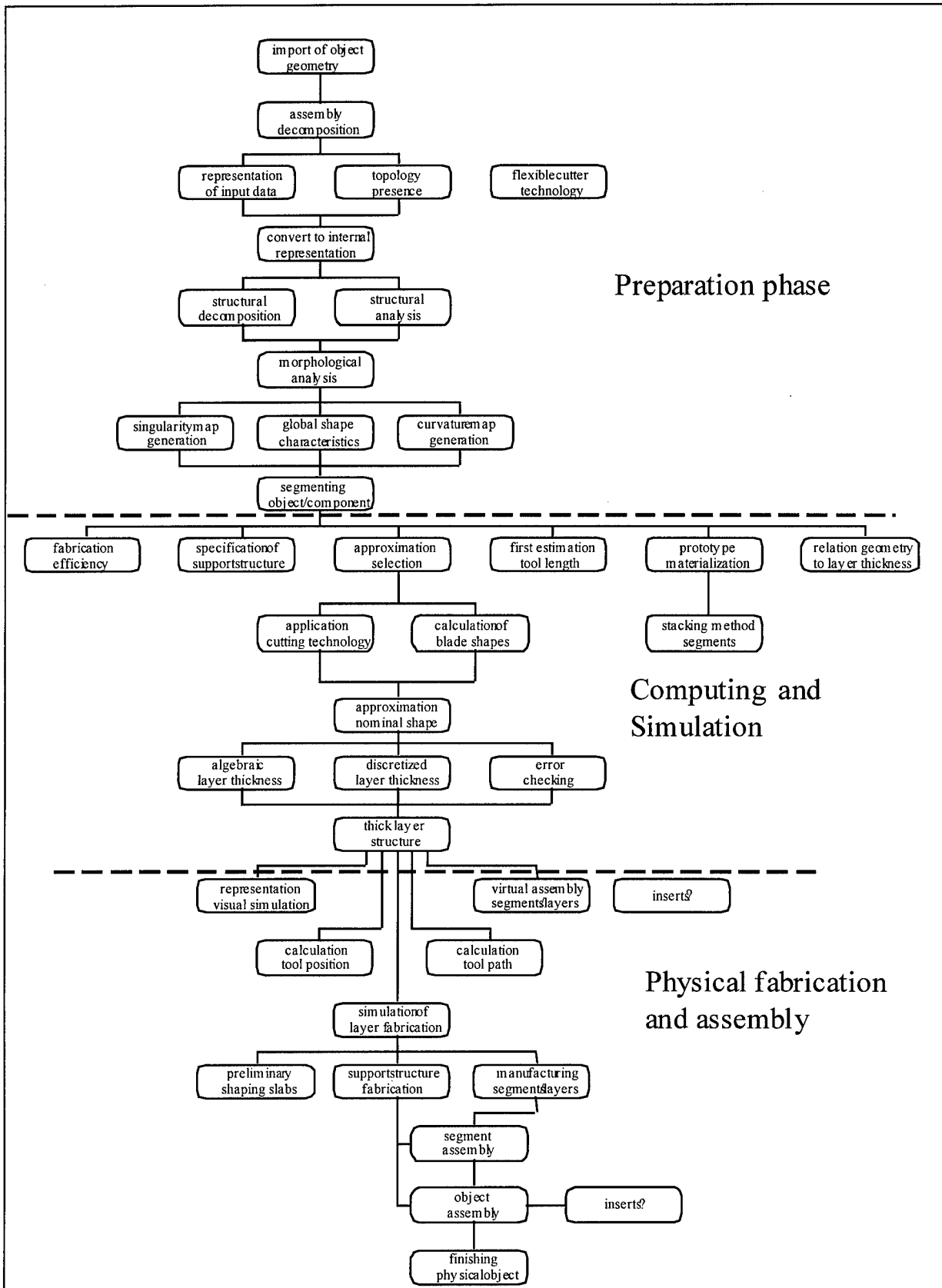


Figure 3: The overall design of the flexible cutting system.

## 5. THE FLEXIBLE CUTTING BLADE.

As mentioned in section 3, the flexible blade is attached to active supports, of which both orientation and position can be changed. A schematic view of cutting blade and supports is given in figure 3. Each support is capable of transferring a winding force (to set the length of the blade), a bending moment (to set the rotation) and a lateral force (to set the position). It must also isolate the heated blade in order not to lose too much energy.

From a mechanical point of view, the flexible blade behaves like a 'physical spline', which takes up its shape following the law of minimum strain energy. For the commonly used blades the ratio between the largest cross sectional dimension and the actual length is very small ( $< 0.01$ ), which means that the blade is in fact a very tender bar. On this basis a physically based model of the flexible blade has been created, resulting in a non-linear differential equation which has no exact analytical solution. Details about these calculations can be found in [Horváth, 1998-a].

The problem could be solved using a geometrically based modeling. Again the issue was to find a curve of a given length that interpolates two points at a certain angle and takes up its minimal strain energy. For this calculation the assumptions are made that, irrespective of its cross section, the curved blade can be substituted by its profile curve, and that the curve is planar. The resulting B-Spline curve  $\mathbf{r}(\mathbf{u})$  is called the profile curve of the flexible blade [Horváth, 1998-b].

## 6. CURVE MATCHING.

As said in section 3, the flexible cutting blade will be used to create layers with freeform front faces, which are used to build the prototype. A geometric description of each layer is derived from the CAD model in a slicing process (see section 6). A cross-section of the freeform front face of the layer at a certain location is given by a curve  $\mathbf{q}(\mathbf{v})$ , called the shape curve. As the geometry of the front face will vary following the layers circumference, an infinite number of shape curves exists for each layer. Obviously only a limited number of curves will be processed, interpolating the front faces geometry in-between.

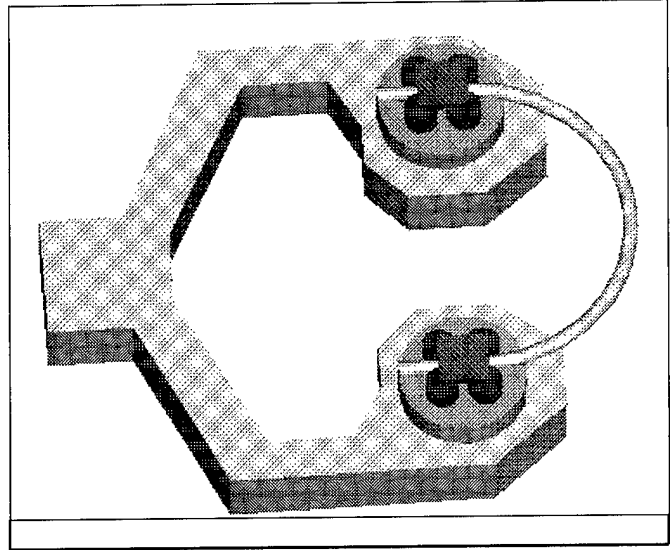


**Figure 4: The cutting unit, consisting of a flexible blade attached to two active supports.**

In order to calculate the toolpath for a certain layer, a number of shape curves  $q$  has to be selected for processing. Next for each shape curve an appropriate profile curve  $r$  has to be found that can be used to manufacture the layer. Curve  $r$  should approximate curve  $q$  within a certain tolerance  $\delta$ . The evaluation of what can be achieved with shape curve  $r$  consists of shifting curve  $q$  along curve  $r$ , in such a way that the start- and endpoints  $b$  and  $c$  of  $q$  remain on  $r$  (see figure 4). For each shifted  $r$  the deviation  $\delta$  between the two curves can be measured by comparing a number of points on each curve. This process is called curve matching. To find a suitable curve  $r$  a number of profile curves that potentially match will have to be evaluated. This can be done by just evaluating profile curves from a library one by one (current project status) or by developing a convergent process to find the desired profile curve in a few iterations. The curve matching process is described in more detail in [Horváth, 1998-b].

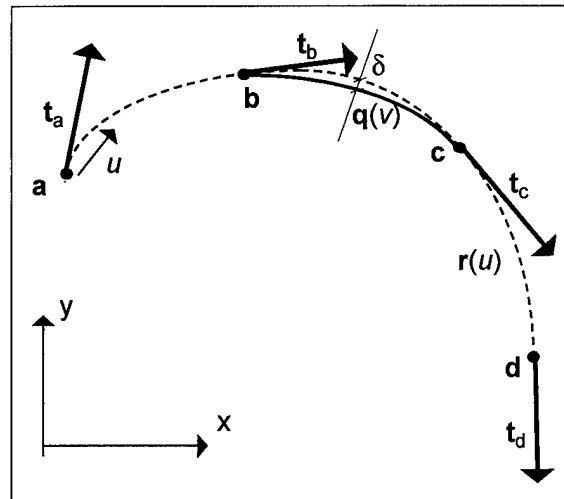


**Figure 5: The given (solid) shape curve  $q(v)$  that describes the CAD geometry needs to be approximated by some portion of the (dashed) profile curve  $r(u)$  that describes the flexible blade.**

## 7. DISCUSSION AND CONCLUSIONS.

The objective of our research and development has been to come up with an effective technology for the fabrication of large-sized, freeform physical models, based on higher order shape approximation. This technology proved to be feasible.

The geometry of the flexible blade can be properly generated/calculated with the assumption of minimum strain energy, specifying as boundary conditions the position and the tangency of each support.

Further work will focus on the slicing algorithms, the optimization of the process parameters and the calculations and the development of the machine to be actually used.

## LITERATURE.

\* **Formus**,  
 "TSF from Formus."  
 Prototyping Technology International, 1997 No 2, pp. 95.

\* **Hope, R.L., Riek, A.T., Roth, R.N.**  
 "Layer Building with Sloped Edges for Rapid Prototyping of Large Objects."

Proceedings 5<sup>th</sup> European Conference on Rapid Prototyping and Manufacturing. , pp. 47-58  
Ed Dickens, P., Helsinki, 1996.

\* **De Jager**, P.J., Broek, J.J. and Vergeest, J.S.M.

“Using adaptive ruled layers for Rapid Prototyping: principles and first results.”

Proceedings 8<sup>th</sup> Solid Freeform Fabrication Symposium, pp. 585-592

Ed. David L. Bourell ea. Univ. of Texas, Austin, 1997, ISSN 1053-2153

\* **De Jager**, P.J.

“Development of a New Slicing Method to Improve Layered Manufacturing.”

Ph.D. thesis, Delft University Press, 1998, ISBN 90-407-1625-0

\* **Horváth**, I., Vergeest, J. S. M., Juhász, I. 1998-a

"Finding the Shape of a Flexible Blade for Free-form Layered Manufacturing of Plastic Foam Objects." Proceeding of the ASME 1998 Design for Manufacturing Conference, Atlanta, Georgia, USA, September 13-16, pp. 25, (Status: Submitted for review).

\* **Horváth**, I., Vergeest, J. S. M., Broek, J. J., de Smit, A., 1998-b

"Tool Profile and Tool Path Calculation for Free-form Thick-layered Fabrication."

Computer Aided Design, Vol. X, No. Y, 1998, pp. 26, (Status: Submitted for review).

\* **Kruth**, J.

“Rapid Prototyping, a New Application of Physical and Chemical Processes for Material Accretion Processes.” Proceedings International Symposium for ElectroMachining, pp. 3-28 EPFL, Lausanne, Switzerland, 1995.

\* **Lennings**, A.F.

“Advantages of using CNC milling for Rapid Prototyping”

Proceedings 30<sup>th</sup> International Symposium on Automotive Technology & Automation (ISATA) Florence, Italy, June 1997, pp. 113-120

Ed D. Roller, Automotive Automation Ltd, Croydon, 1997, ISBN 0 947719 96 2.

\* **Marsan A.**, Dutta, D.,

“Survey of Process Planning Techniques for Layered Manufacturing.”

Proceedings of 1997 ASME Design Engineering Technical Conference. ASME, New York, 1997, CD-ROM #DETC97/DAC3988.

\* **Thomas**, C.L., Gaffney, T.M., Kaza, S., Lee, C.H.

“Rapid Prototyping of Large Scale Aerospace Structures.”

Proceedings 1996 IEEE Aerospace Applications Conference, Vol. 4. IEEE, 1996, ISBN 0-7803-1396-6

\* **Trudeau**, N.

“Professional Model making.”

Watson-Guptill Publications, New York, 1995.

# DIRECT RAPID PROTOTYPING OF TOOLS

K.P. Karunakaran<sup>1</sup>, P. Vivekananda Shanmuganathan<sup>1</sup>,  
Sabine Roth-Koch<sup>2</sup> & Kai Uwe Koch<sup>2</sup>

<sup>1</sup>Indian Institute of Technology, Bombay, INDIA

<sup>2</sup>Fraunhofer Institut für Produktionstechnik und Automatisierung, Stuttgart, GERMANY

## ABSTRACT

Even as several new *Rapid Prototyping* processes are emerging that can build metallic and ceramic tools directly in slices, this new manufacturing concept continues to have an inherent problem of poor accuracy primarily due to the *staircase effect*. To surmount this problem, a new RP process is proposed that makes use of *adaptive slicing*. The edges of these slices need not be vertical unlike the existing RP processes. In manufacturing, one uses a fast but inaccurate roughing process followed by one or more finishing processes which are slow but accurate. The methodology adopted in the proposed RP process also uses this concept of two-level processing, viz., near-net building of the layer and net-shaping it by high-speed machining. This new methodology will result in faster prototyping due to adaptive layer thickness in addition to better accuracy and surface finish since the *staircase effect* is eliminated. The proposed RP process can be used for building both metallic as well as soft prototypes.

## 1. INTRODUCTION

Rapid Prototyping (RP) introduced in 1989 as a design visualization tool has revolutionized the way products are designed and manufactured today. Although the prototypes could be made out of only soft materials, very soon, innovative methods of using them for making the short-run and production tools were developed using the existing technologies. Silicon Rubber Molding, Epoxy Tooling etc. are some of these indirect routes. Selective Laser Sintering (SLS) and Multiphase Jet Solidification (MJS) are some of the RP processes that can produce metallic and ceramic tools. Therefore, these are called *Direct Rapid Tooling Processes*. In these processes, the raw material is the required hard material coated with a soft binder. While selectively sintering during the layer building process, only the soft material melts binding the hard particles around it. The prototype thus obtained is initially in 'green state' which needs to be post-sintered and/or infiltrated with a low melting material to get the desired mechanical properties for the tool. The properties of these tool will be invariably inferior to the conventional tools since the hard particles do not fuse together fully and the density is lower. These processes also suffer from shrinkage-related inaccuracies. Such processes following a "binder-coated powder approach" are suitable for only short runs (Figure 1). Laminated Object Manufacturing (LOM) process has been successfully used to produce tools for sheet metal as well as

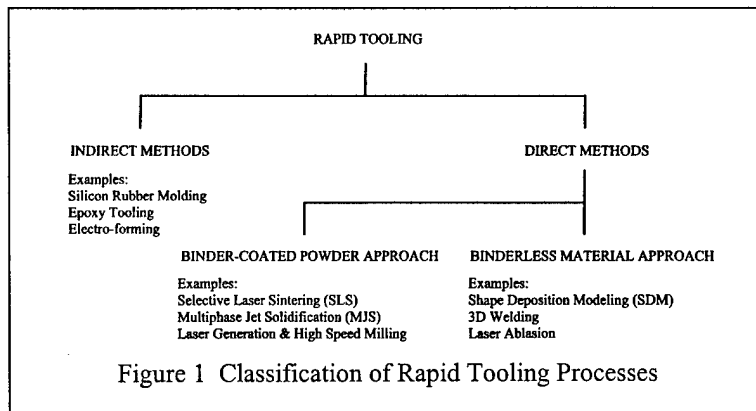


Figure 1 Classification of Rapid Tooling Processes

injection molded parts [Himmer, 1997]. However, LOM tools suffer from poor bonding between the layers due to mechanical fastening and their inherent inability to have adaptive layer thickness.

In order to manufacture tools more accurately and rapidly, the Rapid Tooling process should have the following characteristics:

- Sintering or melting of the hard material directly
- Two-step processing of each layer; the first step yielding the near-net layer and the second step finishing it to the required accuracy
- Adaptive slicing
- Elimination of staircase effect
- High rate of material deposition
- Ability to build support structures.

While research to develop direct sintering/ melting rapid tooling processes is in progress at several places, significant works among them are “Laser Generating and High Speed Milling” [Fritz 1996], “Shape Deposition Manufacturing (SDM)” [Merz 1994] and “3D Welding” [Dickens 1994].

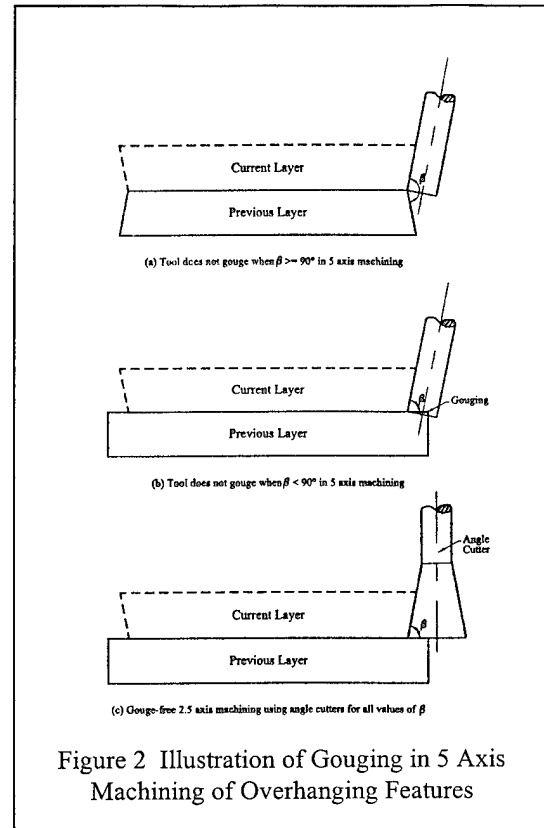


Figure 2 Illustration of Gouging in 5 Axis Machining of Overhanging Features

In “Laser Generating and High Speed Milling” process developed at Fraunhofer Institute for Production Technology (FhG-IPT), Aachen, Germany, the raw material used is binder-coated metallic powder which, when passed through the nozzle, is melted by a laser beam resulting in the deposition of the near-net layer. The layer is then milled to net-shape. As this process uses „binder-coated powder approach“, it suffers from shrinkage-related inaccuracies. Moreover, this process is not free from the staircase effect and does not employ adaptive slicing. The SDM process developed at Carnegie Mellon University (CMU) is principally similar to that of FhG-IPT in the sense that it also uses an additive process to deposit the rough material and a machining process to get the desired accuracy. However, instead of sintering by a laser beam, they use a deposition process called ‘micro-casting’ which is in-between metal spraying and MIG welding. They use 5 axis machining to eliminate the staircase effect. However, 5 axis machining cannot produce gouge-free surface while machining reentrant contours as shown Figure 2. When  $\beta < 90^\circ$ , the ordinary end mill in 5 axis machining gouges the previous layer as shown in Figure 2b. In order to overcome this difficulty, they make use of the fact that a reentrant profile in the model will be a non-reentrant profile in the support. However, this involves complex geometric processing. Machining in 2.5 axis mode using angle cutters will be preferable to this as shown in Figure 2c. “3D Welding” process developed at University of Nottingham uses a MIG welding process to build metallic prototypes. Using a 0.8 mm diameter wire, they report a building speed of 6500 mm/min. the bead size being 4.5 mm wide and 1.4 mm thick. Although the building speed of this process is very attractive, the poor accuracy of 0.5 mm limits its applications. It is seen that none of the existing and emerging RP processes meet all the criterion mentioned in the beginning of this section. The proposed process proposed aims to achieve this goal.

### 3. PROPOSED RP MACHINE FOR RAPID TOOLING

Based on the above discussions, it is proposed to develop a RP machine with the following features:

- It will use an additive process to obtain the near-net layer and machining processes to finish it.
- Adaptive slicing will be made use of.
- The machining process using angle cutters will eliminate the errors due to the 'staircase effect'.
- It will require only a 2.5 axis CNC milling machine with an Automatic Tool Changer (ATC).
- It will be possible to retrofit this RP process to any existing CNC machining center.
- The size of the prototype is independent of its accuracy and is limited by only the table traverse.

The proposed RP machine will have, in addition to the milling head, two additional heads fixed on the same frame (Figure 3). One, called *Modeling Head*, will deposit steel using a MIG welding process. The other head called *Masking Head* will deposit a soft masking material. This will be a suitable electric brazing machine. Copper has been successfully used as masking material for steel prototypes at CMU [Merz 1994]. The dies often have cooling ducts that run close to the mold cavities. The presence of these conformal cooling ducts may introduce reentrant profiles necessitating the use of support structures. In the proposed process, the masking material itself can act as the support structure. The change over among heads can be achieved using *Work Offsets* of any CNC machine. The following steps are used to make the prototype:

1. Deposit the near-net layer of model material.
2. Rough-mill the extreme contours.
3. Finish-mill the extreme contours by one or more angle end mills to eliminate the staircase effect.
4. Deposit the masking material over the machined extreme contours to protect them during the welding of subsequent layers.
5. Surface mill the layer to maintain the required layer thickness accurately.

The above steps will be repeated till the prototype is complete. The prototype thus built will be covered by a skin of the masking material. This skin can be

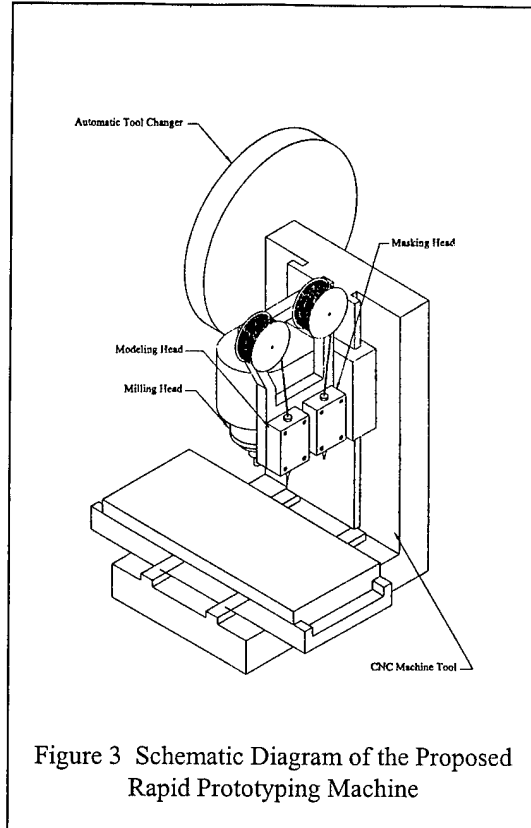


Figure 3 Schematic Diagram of the Proposed Rapid Prototyping Machine

Cutter Number	Cutter Geometry	Operation
$N_p$		<b>Face Milling Cutter:</b> This is used to mill the top surface of the layer to maintain the required thickness accurately.
$N_{p-1}$		<b>End Milling Cutter:</b> This is used to rough mill the edges of the layers leaving adequate allowance for finishing.
1 to $N_s$		<b>Set of Angle Cutters:</b> The angle $\alpha$ of these cutters range from $+\alpha_{max}$ to $-\alpha_{max}$ in steps of $\Delta\alpha$ . These are used for finishing the edges of the layers within the desired accuracy of $\delta_{max}$ . Any layer may require one or more of these cutters depending on the nature of the twist of the rulings of the edge surface.
$N_s+1$		
$N_s+2$ to $2N_s+1$		

Figure 4 Milling Cutters Used in the Proposed RP Machine

simply peeled off if it is wax (for ABS prototypes) or removed by an electrolytic or electro-chemical etching process if it is copper (for steel prototypes).

The modeling head will be a MIG welding head that makes use of a coil of filler wire as the consumable electrode. It will be possible to deposit a cross-section of 4.5mm width x 1.4mm thickness of model material at a speed of 6,500mm/min. [Dickens 1994]. The machining also can take place at 'breakneck' speed, thanks to the combination of machines with linear motors and the latest carbide cutters with ceramic coating. At this speed, the performance of the proposed process in speed and accuracy will surpass all existing RP&T processes in tool making. Although a number of tool changes may be involved, considering a tool change time of as low as 5 seconds on modern machines, this overhead will be considerably small.

The various cutters used in the proposed RP machine are shown in Figure 4. For higher magnitudes of  $\alpha$ , the insert type of angle cutters are used (Figures 5a & 5c) and for lower magnitudes, solid carbide cutters can be used (Figure 5b). Although a constant increment  $\Delta\alpha$  has been used in the illustration, it is preferable to have this also vary adaptively with coarser  $\Delta\alpha$  in the middle of the range of  $\alpha$ . Furthermore, in the final system, the angle, diameter and length of the angle cutter in the tool holder will be measured accurately after assembly using a Tool Presetting Device and stored in a cutter database. Higher the number of ATC stations lower will be  $\Delta\alpha$  resulting in higher layer thicknesses and hence faster building of the prototype (Table 2).

#### 4. DATA PROCESSING FOR THE PROPOSED RP MACHINE

The input to the proposed RP machine is the STL file of the object to be prototyped due to its simplicity [Karunakaran 1998 and Yan 1996]. The STL file has to be converted into NC program that will control the functions of the CNC machine. The NC controlled functions are:

- Movements of all the three heads.
- Invoking appropriate work offsets in order to switch among the three heads using G codes.
- Invoking tool offsets using G/D/H codes.
- Control of switching functions pertaining to the two depositing heads.
- Control of switching functions for the milling process such as tool change, spindle, coolant etc.

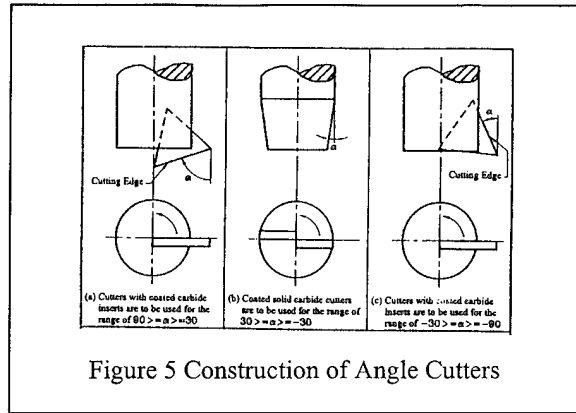


Figure 5 Construction of Angle Cutters

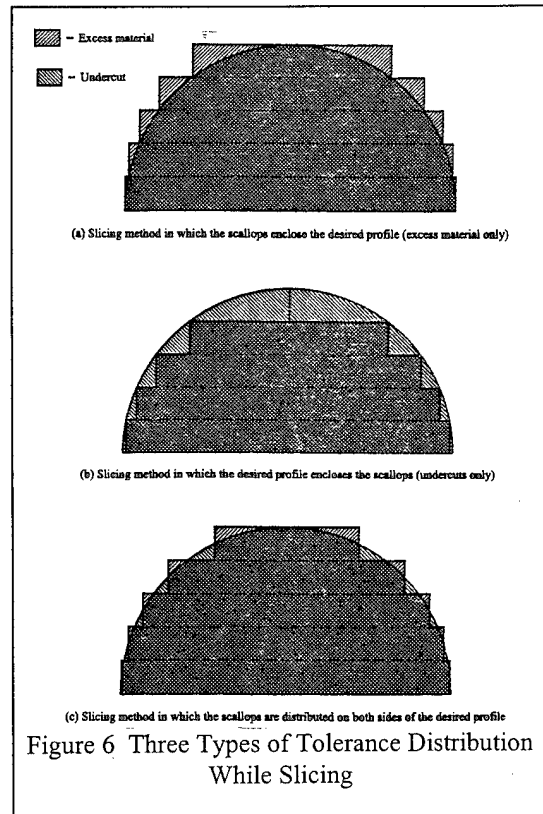


Figure 6 Three Types of Tolerance Distribution While Slicing

In addition to these, there are a few other parameters related to welding and masking processes such as the speed of the welding wire, speed of the masking material etc. These can be fine-tuned and frozen after experimentation. Any further adjustments of these can be done external to the CNC controller. In order to obtain the NC program to control the machine from the STL file of the prototype, the following steps are required:

1. Adaptive slicing,
2. NC program generation for the modeling head,
3. NC program generation for the milling head,
4. NC program generation for the masking head and
5. NC post-processing (to translate the CL data into machine specific code).

#### 4.1 Adaptive Slicing

Slicing is the process of cutting the geometric model of the 3D object by parallel planes so that the 3D object can be approximately represented by several 2D slices. Since this is an approximation, the user

specifies the amount of maximum deviation  $\delta_{max}$  for the slicing process. Three types of slicing processes are illustrated in Figure 6. In the first type of slicing shown in Figure 6a, the union of all the layers contains the required 3D object. This type of slicing is desirable where some allowance is required to finish the prototype. Most die cavities require this type of slicing since often they need to be polished to mirror-finish to ease ejection of part from the cavity. On the other hand, the union of all the layers is fully contained inside the required 3D object in the slicing method shown in Figure 6b. This type of slicing is desirable where the prototype is finished by adding material that fills the scallop cavities. In the third method shown in Figure 6c, the scallops are distributed on both sides of the desired profile. This is preferable if an accurate prototype is required without any finishing operation. For a given number of slices, the last type of slicing gives the most accurate prototype [Martin 1997].

The slicing shown in Figure 6 is called uniform slicing since the thicknesses of all layers are equal. In uniform slicing, the layer thickness is decided by the maximum deviation  $\delta_{max}$  and hence for higher accuracy, one has to use smaller layer thickness throughout resulting in longer processing time. On the other hand, adaptive slicing is the slicing of the 3D object with different layer thicknesses at different places based on the consideration of the local curvature [Kulkarni 1996 and Young 1994]. There are two types of adaptive slicing as illustrated in

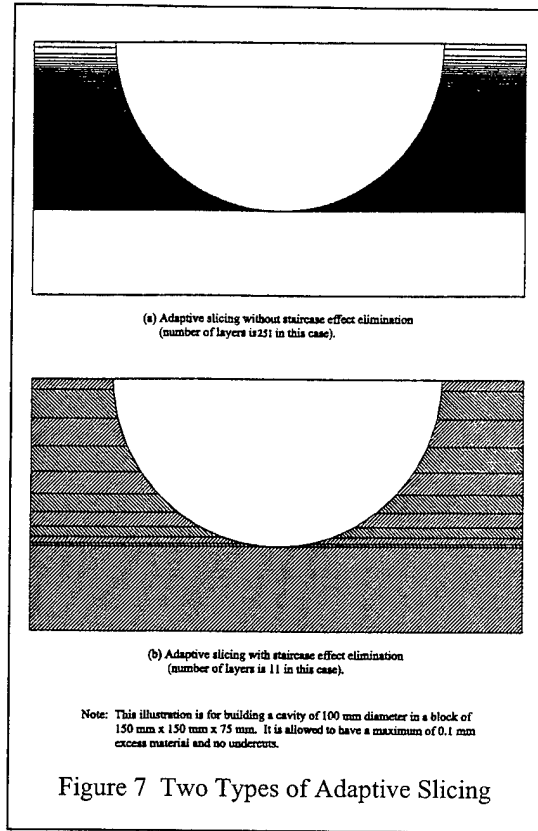


Figure 7 Two Types of Adaptive Slicing

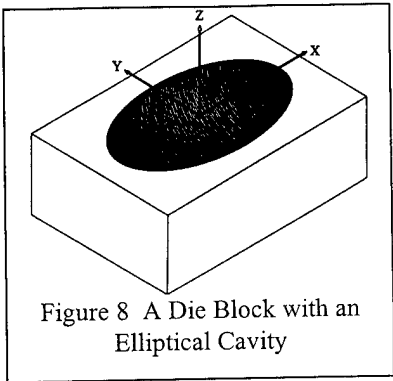
Slicing Type	Number of Layers Required
Uniform slicing	750
Adaptive slicing without staircase elimination	251
Adaptive slicing with staircase elimination	11

**Table 1** Comparison of Various Slicing Methods (This illustration is for building a die block of 150 mm x 150 mm x 75 mm with a hemi-spherical die cavity of 100 mm diameter. The tolerance limits are 0.1 mm excess material and no undercuts.)

Figure 7 for a hemi-spherical die cavity [Hope 1996 and Peter 1996]:

1. Adaptive slicing without staircase elimination and
2. Adaptive slicing with staircase elimination.

Table 1 gives a comparison of these slicing methods. It is obvious that adaptive slicing with staircase elimination requires the least number of layers and is significantly less than the others. The existing RP processes inherently can produce layer edges only in vertical orientations and hence they cannot incorporate adaptive slicing with staircase elimination.



### 4.2 NC Program Generation

The path of the modeling head will be contour parallel, i.e., the deposition starts from inner points and moves outward. In addition to the path, the switching functions for the welding process will also have to be output as user-defined codes. This is followed by rough milling by  $N_p-1^{th}$  cutter and finish milling by the angle cutters along the contour peripheries. However, depending on the slope of the edge surface of the layer, more than one angle cutter may be called for finishing any contour as seen in the illustration. If no angle cutter is found suitable for some part of the edge surface, then the layer thickness should be reduced. The path of the masking head will also be a profiling operation with the deposition of the material sufficient to mask the edges of the layer.

### 5. ILLUSTRATIVE EXAMPLE

In this section, the proposed methodology of calculating adaptive layer thicknesses and finishing the prototype using angle cutters is illustrated. The object considered for this illustration is a die block of size 250 mm length x 170 mm width x 170 mm height with an ellipsoidal cavity as shown in Figure 8. The ellipsoid is obtained by revolving an ellipse  $[a \cos u, b \sin u, 0]$  about X axis where  $a=100$  mm and  $b=60$  mm. Therefore, any point on the surface of the cavity is given by  $[a \cos u, -b \sin u \cos v, -b \sin u \sin v]$ . An excess material of  $\delta_{max}$  is allowed and there shall not be any undercuts. The angle cutters are available at a uniform angle increment of  $\Delta\alpha$ . Let  $t_{max}$  be 15 mm. Table 2a, 2b and 2c give the layer details for three combinations of  $\delta_{max}$  and  $\Delta\alpha$ . For instance, in Table 2a, layer 10 has a thickness of 1.164 mm and its bottom and top Z values are respectively -55.671 and -54.507. The edges of this layer are to be machined by four angle cutters with  $\alpha$  ranging from  $72^\circ$  to  $66^\circ$ , i.e.,  $72^\circ, 70^\circ, 68^\circ$  and  $66^\circ$ .

**Table 2a** Layer Details of the Ellipsoidal Die Cavity for  $\delta_{max} = 0.100$  and  $\Delta\alpha 2.000^\circ$

Layer No.	1	2	3	4	5	6	7	8	9	10
Thickness	15.000	10.100	0.350	0.205	0.555	0.654	0.668	0.911	0.886	1.164
$Z_{top}$	-70.000	-59.900	-59.550	-59.345	-58.790	-58.136	-57.468	-56.557	-55.671	-54.507
$Z_{bottom}$	-85.000	-70.000	-59.900	-59.550	-59.345	-58.790	-58.136	-57.468	-56.557	-55.671
Cutters $\alpha_i$	90	90	86 - 84	84 - 80	82 - 80	80 - 76	78 - 74	76 - 70	74 - 68	72 - 66

Layer No.	11	12	13	14	15	16	17	18	19	20
Thickness	1.100	1.410	1.308	1.651	1.509	1.883	1.704	2.106	1.889	2.319
Z <sub>top</sub>	-53.407	-51.997	-50.689	-49.038	-47.529	-45.646	-43.942	-41.836	-39.947	-37.628
Z <sub>bottom</sub>	-54.507	-53.407	-51.997	-50.689	-49.038	-47.529	-45.646	-43.942	-41.836	-39.947
Cutters $\alpha_i$	70 - 62	68 - 60	66 - 58	64 - 56	62 - 52	60 - 50	58 - 48	56 - 44	54 - 42	52 - 40

Layer No.	21	22	23	24	25	26	27	28	29	30
Thickness	2.067	2.520	2.233	2.709	2.389	2.626	3.059	2.507	3.219	2.627
Z <sub>top</sub>	-35.561	-33.041	-30.808	-28.099	-25.710	-23.084	-20.025	-17.518	-14.299	-11.672
Z <sub>bottom</sub>	-37.628	-35.561	-33.041	-30.808	-28.099	-25.710	-23.084	-20.025	-17.518	-14.299
Cutters $\alpha_i$	50 - 36	48 - 34	46 - 32	44 - 28	42 - 26	40 - 24	38 - 20	36 - 18	34 - 14	32 - 12

Layer No.	31	32	33	34						
Thickness	3.363	2.735	2.779	2.795						
Z <sub>top</sub>	-8.309	-5.574	-2.795	0.000						
Z <sub>bottom</sub>	-11.672	-8.309	-5.574	-2.795						
Cutters $\alpha_i$	30 - 8	28 - 6	26 - 4	24 - 0						

**Table 2b** Layer Details of the Ellipsoidal Die Cavity for  $\delta_{max} = 0.100$  and  $\Delta\alpha = 1.000^\circ$

Layer No.	1	2	3	4	5	6	7	8	9	10
Thickness	15.000	10.100	0.589	0.922	1.234	2.212	2.030	3.095	3.146	3.846
Z <sub>top</sub>	-70.000	-59.900	-59.311	-58.389	-57.155	-54.943	-52.913	-49.818	-46.672	-42.826
Z <sub>bottom</sub>	-85.000	-70.000	-59.900	-59.311	-58.389	-57.155	-54.943	-52.913	-49.818	-46.672
Cutters $\alpha_i$	90	90	85 - 84	81 - 79	78 - 74	74 - 69	70 - 63	66 - 59	62 - 53	58 - 48

Layer No.	11	12	13	14	15	16	17	18	19	20
Thickness	3.892	4.056	4.463	4.494	5.002	4.788	5.295	4.986	5.426	0.424
Z <sub>top</sub>	-38.934	-34.878	-30.415	-25.921	-20.919	-16.131	-10.836	-5.850	-0.424	0.000
Z <sub>bottom</sub>	-42.826	-38.934	-34.878	-30.415	-25.921	-20.919	-16.131	-10.836	-5.850	-0.424
Cutters $\alpha_i$	54 - 43	50 - 38	46 - 33	43 - 28	39 - 23	35 - 18	32 - 13	28 - 8	25 - 3	22 - 0

**Table 2c** Layer Details of the Ellipsoidal Die Cavity for  $\delta_{max} = 0.050$  and  $\Delta\alpha = 1.000^\circ$

Layer No.	1	2	3	4	5	6	7	8	9	10
Thickness	15.000	10.050	0.217	0.247	0.490	0.478	0.749	0.687	1.016	0.893
Z <sub>top</sub>	-70.000	-59.950	-59.733	-59.486	-58.996	-58.518	-57.769	-57.082	-56.066	-55.173
Z <sub>bottom</sub>	-85.000	-70.000	-59.950	-59.733	-59.486	-58.996	-58.518	-57.769	-57.082	-56.066
Cutters $\alpha_i$	90	90	87 - 86	85 - 83	83 - 81	81 - 78	79 - 75	77 - 72	75 - 70	73 - 67

Layer No.	11	12	13	14	15	16	17	18	19	20
Thickness	1.278	1.095	1.534	1.291	1.680	1.692	1.799	1.900	2.003	2.100
Z <sub>top</sub>	-53.895	-52.800	-51.266	-49.975	-48.295	-46.603	-44.804	-42.904	-40.901	-38.801
Z <sub>bottom</sub>	-55.173	-53.895	-52.800	-51.266	-49.975	-48.295	-46.603	-44.804	-42.904	-40.901
Cutters $\alpha_i$	71 - 65	69 - 62	67 - 60	65 - 57	63 - 55	61 - 52	59 - 49	57 - 46	55 - 44	53 - 41

Layer No.	21	22	23	24	25	26	27	28	29	30
Thickness	2.197	2.289	2.381	2.467	2.554	2.634	2.714	2.787	2.860	2.816
Z <sub>top</sub>	-36.604	-34.315	-31.934	-29.467	-26.913	-24.279	-21.566	-18.779	-15.919	-13.103
Z <sub>bottom</sub>	-38.801	-36.604	-34.315	-31.934	-29.467	-26.913	-24.279	-21.566	-18.779	-15.919
Cutters $\alpha_i$	51 - 38	49 - 36	47 - 33	45 - 30	43 - 28	41 - 25	39 - 22	37 - 19	35 - 16	33 - 14

Layer No.	31	32	33	34	35				
Thickness	3.217	2.823	3.344	2.925	0.794				
$Z_{top}$	-9.886	-7.063	-3.719	-0.794	0.000				
$Z_{bottom}$	-13.103	-9.886	-7.063	-3.719	-0.794				
Cutters $\alpha_i$	31 - 11	29 - 8	27 - 5	25 - 2	23 - 0				

It is evident from these tables that increase in  $\delta_{max}$  and/or decrease in  $\Delta\alpha$  decrease the number of layers and hence the build time. Furthermore, the layer thickness in the proposed method is several times higher than those of the existing RP processes which are of the order of 0.050 mm to 0.150 mm. In order to have higher accuracy, the layer thickness in these processes has to be decreased resulting in substantial increase in the build time, whereas in the proposed methodology, the layer thickness need not be decreased to improve accuracy.

## 6. CONCLUSIONS

The new RP process proposed here combines layered manufacturing and conventional machining methods in order to exploit the benefits of both while avoiding their limitations. The two-level processing adopted in realizing each layer using simple processes will result in producing tools economically, accurately and fast. The process does not pose any restriction or loss of accuracy on the prototype as its size grows. Since the size of the part is limited only by the traverse available on the CNC machine, a larger CNC machine can be used to produce large prototypes. If non-metallic prototypes are required, appropriate heads can be mounted to deposit the corresponding modeling and masking materials. For instance, if an ABS prototype is required, wax can be used as the mask. This process can be retrofitted to any existing CNC machine.

## REFERENCES

- Dickens P.M., Pridham M.S., Cobb R.C. and Iqibson, 1994, „3-D Welding”, <http://www.cranfield.ac.uk/coa/rapid/proceeding/dickens1.html>.
- Fritz Klocke and Ulrich Clemens, 1996, „Rapid Tooling Combining Laser Generating and High Speed Milling“, Proceedings of 5th European Conference on RP&M, Finland, pp. 211-221.
- Himmer T., Nakagawa T and Anzai M., 1997, „Lamination of Metal Sheets”, Proceedings of the Conference on Intelligente Produktionssysteme - Solid Freeform Manufacturing, Dresden, Germany, Sept. 25&26, pp. 335-341.
- Hope R.L., Riek A.T. and Roth R.N., 1996, „Layer Building with Sloping Edges for Rapid Prototyping of Large Objects“, Proceedings of 5th European Conference on RP&M, Finland, pp. 47-57.
- Karunakaran K.P., Bapat V.P. and Ravi B., 1998, Rapid Prototyping & Tooling: New Paradigms in Design and Manufacture, Proceedings of Workshop on Rapid Prototyping & Tooling, IIT Bombay, February 6-8.
- Kulkarni P. and Dutta D., 1996, „An Accurate Slicing Procedure for Layered Manufacturing“, CAD, Vol. 28, No. 9, pp. 683-697.
- Martin Geiger and Kai Uwe Koch, 1997, „Data Processing for Additive Fabricators”, IEEE International Symposium on Industrial Electronics, Guimaraes, Portugal, July 7-11, pp. SS190-SS192.
- Merz R., Prinz F.B., Ramaswamy K., Terk M and Weiss L.E., 1994, „Shape Deposition Manufacturing“, Proceedings of Solid FreeForm Fabrication, University of Texas, Austin, pp. 15-29.
- Peter J. de Jager, 1996, „Using Slanted and Ruled Layers for Rapid Prototyping“, Proceedings of 5th European Conference on RP&M, Finland, pp. 1-8.
- Yan X. and Gu P., 1996, „A Review of Rapid Prototyping Technologies and Systems“, CAD, Vol. 28, No. 4, pp. 307-318.
- Young Seok Suh and Michael J. Wozny, 1994, „Adaptive Slicing of Freeform Fabrication Processes”, Proceedings of Solid FreeForm Fabrication, University of Texas, Austin, pp. 404-411.

# **Real Time Video Microscopy for the Fused Deposition Method**

Evan Bossett, Lorna Rivera, Dan Qiu, Ryan McCuiston, Noshir Langrana,  
Shriram Rangarajan, Natesan Venkataraman, Stephen Danforth, Ahmad Safari  
*Mechanical & Aerospace Engineering, Ceramics & Materials Engineering*  
*Rutgers, The State University of New Jersey, Piscataway, NJ, 08854*

## **1. ABSTRACT:**

Fused deposition is a layered manufacturing technology, which is being investigated for fabrication of functional parts. Defects and voids in the build process affect the quality and level of accuracy of components. These occur due to several factors, such as the toolpath contours in a layer, material(s) deposited, and the environmental conditions. For a functional part to be constructed, a perfect green part is critical. To further understand this process, a visualization of the deposition is needed. Therefore, we have developed a real-time video microscopy system. The hardware has been constructed and mounted on the existing liquifier. Real time deposition of layered manufacturing is being recorded. Three materials being investigated are: PZT, silicon nitride, and wax. The contrast in wax layering is not as strong, which makes visual observation extremely hard. However, interaction between the roads of PZT and silicone nitride parts has been successfully quantified. Using the current set up and software, the road width and height have been quantified.

## **2. INTRODUCTION:**

The Fused Deposition Method has been employed as a rapid prototyping technique. Many different materials are being tested, including silicon nitride, lead zirconate titanate (PZT), and metals. Rutgers, The State University of New Jersey is currently developing a multi-material fused deposition fabrication hardware, which could use combinations of different materials[1].

One critical area in the effort of producing a perfect part is that of quality control. Parts produced using FDM which contain voids and imperfections will have a much higher probability of failure. Thus, it is of the utmost importance that the layered deposition is properly understood so weaknesses in the fabrication process can be corrected. A visualization technique is imperative as an aid in understanding the deposition method. The goal has been to create a system by which we could visually observe and then quantify certain aspects of the layering process. This would produce information not only about how the machine was creating the part, but also how different materials behave.

## **3. MOTIVATION:**

At Rutgers University, under ONR (Office of Navy Research) funded MURI program [1], An intelligent layered manufacturing (LM) system for fabrication of multiphase electromechanical parts has been developed. To achieve this multi-materials LM software system, one of the necessary requirements is to perform the virtual simulation of the of the multi-material LM process[2]. In order to make this simulation realistic, the information on layer

deposition is needed. In the present project, a real time video microscopy system is developed. This system provides geometric information on deposited roads and layers which will be used in the virtual simulation.

## **4. PROCEDURE**

### **4.1 HARDWARE CONSIDERATIONS:**

The initial setup included the COHU CCD camera, microscope attachment, and Trinitron monitor. The task was to create a non-obtrusive way to observe the deposition at high magnification without effecting or disturbing the normal build process or environment. This required the equipment to fit into the existing closed FDM chamber and have it mounted in a way that would allow as normal a build as possible.

The choice of hardware was carefully thought out. It was assumed that going from our initial video microscope to a different setup would provide the performance enhancements which were sought since the original hardware was not designed for this task. AEI was selected as a good choice because of the variety of hardware which they carried. The two choices which had to be considered again, were either the boroscope or the fiberscope. Both provided integrated lighting and reduced size. The advantage that the fiberscope seemed to have was that it would be the most flexible in terms of positioning. However, after a sample was sent to AEI for analysis with several of their packages, they strongly suggested the boroscope as a solution for our imaging needs. They felt that the magnification we required would result in compromising image degradation. This degradation was due to the fact that the image would be carried by a bundle of fiberoptic cables. As magnification is increased, each of these cables becomes more visible and the image is fragmented into partitioned areas defined by the individual fibers. This would make analysis virtually impossible. So, based upon the advice from AEI we selected an industrial boroscope.

### **4.2 ATTACHMENT TO THE EXISTING FDM SYSTEM**

The next step attempted was a physical mount to the liquifier head. Again, it was considered imperative to maintain the isolated nature of the build chamber. By mounting an extra piece to the extrusion head, several new problems had to be faced. Since the head would be in motion, the possibility of vibration existed. At such a high level of magnification, even a small vibration can be enough to completely blur the image. In addition, problems of lighting and depth of field were of similar nature to those experienced in the previous static experiments.

The camera attachment to the liquifier head was considered carefully. Two possible locations to attach the camera are: to the carriage in which it rides on, and, to the cooling assembly. To preserve normal function of the machine, the second option of attaching the camera from the top surface of the cooling chamber was chosen. Primarily, this allowed an attachment which changed nothing in the existing FDM system when it was connected, Figure 1. It also gave easy access so the camera assembly could be quickly removed and replaced. Another benefit which was gained was the ability to remove the liquifier and replace it without changing anything of the video setup.

The physical implementation of the mount was two L shaped metal pieces, Figure 1. Sliding channels were left instead of simple screw holes to allow adjustment in the X, Y, and Z directions. This helps to avoiding precise measurements and calculations that would have had to be done in order to place the centerline of the camera exactly along the centerline of the nozzle. Finally, the camera is held firmly in a u-clamp which is mounted to the protruding L bracket (see Figure 1).

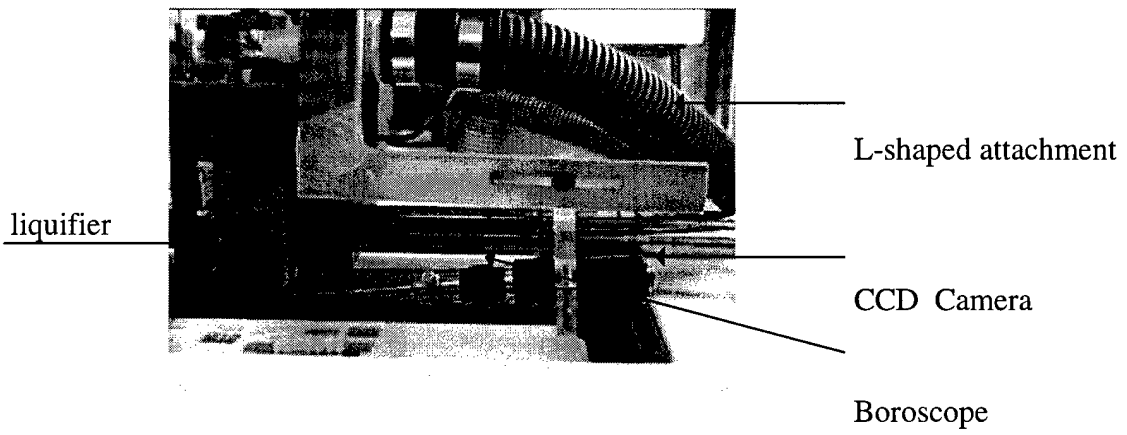


Figure 1: L-shaped mounting bracket with CCD camera

This setup provided a workable solution. One problem with this setup is that there is no way to focus the camera except by manually moving it towards or away from the object. With the small depth of field, this was extremely difficult. Another problem is that the camera and microscope combined are so long that they just barely fit into the confines of the build chamber. This left us only enough room for a quarter inch wide part at the very corner of the build platform. Since the part was so small, the inner contours were such as to require sharp and rapid turning. The vibration induced from this repeated cornering was too much. As shown later on the videos taken, all of the sequences were blurry. Long roads parallel to the camera, however, could be observed.

With minor modifications to the existing implementation, we were able to adapt it to the new hardware, with an attachment that reduced significantly the vibration problem (see Figure 2). The benefits which the boroscope had over our previous equipment was its reduced size, a focusing ring, and an integrated fiber-optic lighting system. This allows a direct beam of high intensity light to be focused on our area of interest.

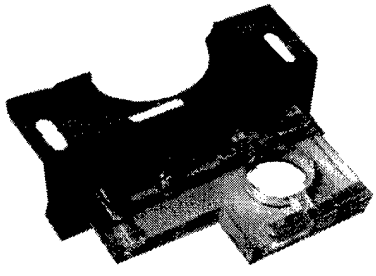


Figure 2: L-shape mounting bracket with camera

The modified set up (see Figure 3) proved to be more efficient and exhibited less vibration than the previous set up.

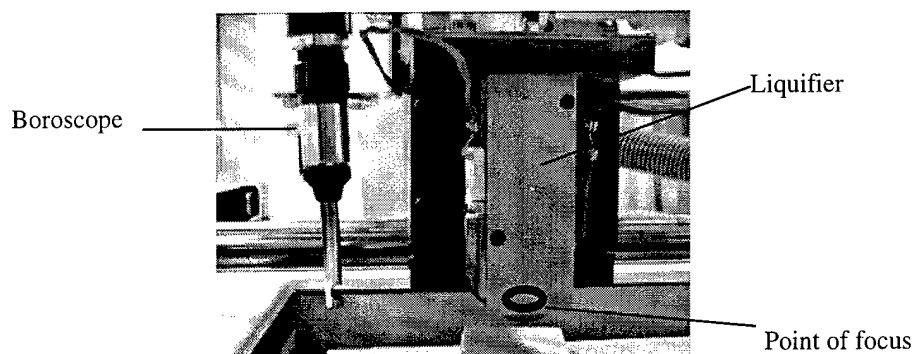


Figure 3: Final set up with attachment #2

As far as calibration, it is impractical to place a scale at the point of focus during operation allowing us to have every frame calibrated automatically by the software on hand. Therefore, another method was sought. The problem was expected to be solved by using the nozzle as a reference. Because the nozzle size is known exactly, it would be an easy reference point to look at in each frame. However, in most of the videos the nozzle is obscured by material build up. It is unclear whether or not the entire bottom of the nozzle is visible, or if some is being obscured by material. What is being done to overcome this is to capture visual data on the nozzle size before the build begins. These initial frames can then be used to calibrate the ones that will follow. In addition, a ruler with 1/16" markers were recorded and the scale factor was computed. These markers were quantified within 5% error. This calibration scheme implies that the results are accurate to  $\pm 75 \mu\text{m}$ .

#### 4.3 QUANTIFICATION:

For analysis and quantification, we are using HL Image software which has several useful capabilities. First and foremost, images can be calibrated using a scale image. Thus, we are able to measure distances and feature sizes directly from the images with good accuracy. It also has a "blob analysis" function, which discerns areas of different coloration. In images of high contrast, this can be very helpful since voids can be "automatically" detected and quantified.

#### 5.0 EXPERIMENTATION:

Experiments were conducted with the modified hardware in an attempt to quantify several aspects of the tool path parameters such as the road shape and road interaction. In these experiments, the voids were intentionally created by using positive offsets. We held the nozzle size constant at 15 mil, the road width at 20 mil, the height at 10 mil and the build speed at 1/2" per second. Then, video sequences of builds being performed with offsets of 0 mil, -4 mil, and +4 mil were recorded. Experiments were conducted with silicon nitride, PZT and wax materials.

An experiment with 5 mil road height on PZT material was for the same set of tool path parameters.

## 6.0 ANALYSIS:

### 6.1 GENERAL OBSERVATIONS:

Various experiments were conducted with wax, silicon nitride and PZT materials. Due to the natural shine of wax, it is very difficult to distinguish each layer under a light source.

To investigate the vibration problem, the machine was allowed to build two parts without the camera. These were compared with the images obtained with the ones produced while recording with the video camera mounted on the machine. Direct visual comparison and inspection revealed that the set up was not disturbing the normal building process. Stacking of the rows and inclination angle was almost identical in both image. Under the light of a micro-camera set up interesting information can be gathered. Several factors were evaluated. They are road shape, bead shape, nozzle location, voids recurrence and alignment of the beads.

### 6.2 SILICON NITRIDE EXPERIMENTS:

Initially, the frames captured from the video on Silicon Nitride revealed rows slightly inclined. The location of the deposited road was changing from layer to layer. The adjacent road shape was altered as new road was deposited for negative offset. Using HL Image software, a point of reference was drawn in one of the frames at the beginning of the process. Looking at successive frames with respect to the point drawn, the nozzle appeared to be in a different location each time it deposited a bead on top of a previous one, creating the alignment problem (Figure 4).



Figure 4: Silicon Nitride +4 mil Offset Layered Fabrication  
(Inclination is due to camera misalignment)

When the deposition process begins, in the current set-up a blob of material is deposited for approximately 3 seconds before the nozzle moves, Figure 4. This blob corresponds to a start

error in the process. However, at the end of each layer there is no blob. The nozzle finishes up clean.

An enlarged image of the stack of 10 rows was analyzed to determine the inclination angle  $\theta$  between the adjacent layers. This angle of inclination  $\theta$  was computed to be  $80 \pm 1.2^\circ$ . In a parallel study, direct measurements were obtained (on cross-sections of 2-2 plates of PZT fabricated by some hardware) using optical micrograph[ 3]. The inclination angles for PZT under the similar set-up were  $80 \pm 13^\circ$ . These two results are in agreement, and they are hardware dependent & independent of material properties.

With the aid of HL Image information on the size and shape of the beads was also obtained. Seven captured frames at random locations and layers, were analyzed and tabulated.

Table-1 Deposited Silicon Nitride Road Width & Height

	<b>CAD</b>	<b>-4 mil Offset</b>	<b>0 mil Offset</b>	<b>+4 mil Offset</b>
<b>Road width(mil)</b>	20	$23.29 \pm 2.28$	$21.88 \pm 1.35$	$27.76 \pm 1.30$
<b>Road height(mil)</b>	10	$13.87 \pm 0.76$	$14.06 \pm 0.89$	$17.23 \pm 1.65$

Table-2 Results of Void Creation in Silicon Nitride Parts

	<b>-4 mil Offset</b>	<b>0 mil Offset</b>
<b>Void Area(mil<sup>2</sup>)</b>	0	$60.06 \pm 39.16$
<b>Equivalent Diameter(mil)</b>	0	$7.74 \pm 4.20$

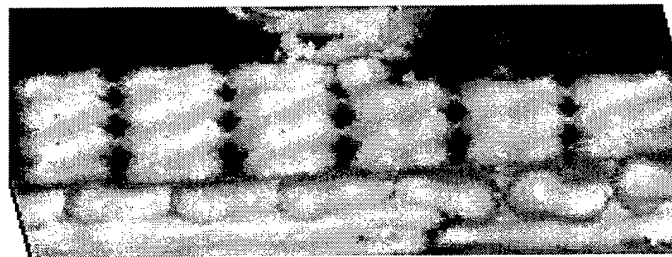


Figure 5: Silicon Nitride 0 mil offset Layered Fabrication

The shape of the deposited road was a truncated ellipse, Figure 5. The width of the deposited roads was slightly larger than what was set by CAD, Table-1. The road height was larger than the set road height, implying that there is a swelling in the vertical direction. Table-2 shows that -4 mil offset eliminated voids, a perfect part was created. With 0 mil offset, the void size was  $7.74 \pm 4.20$  mil diameter.

### 6.3 PZT EXPERIMENTS:

Again, seven frames were captured for each offset and compared against the values set by the hardware. For each of the PZT off sets, the bead size was quantified with HL Image software and a calibrated image. The results are tabulated below.

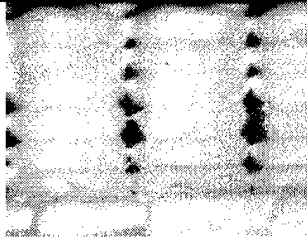
Table 3: Deposited PZT Road Width & Height

CAD Setup		-4 mil Offset	0 mil Offset	+4 mil Offset
Road width(mil)	20.00	19.71 ± 1.20	19.60 ± 1.60	19.94 ± 2.00
Road Height(mil)	10.00	13.71 ± 1.30	14.39 ± 1.35	11.56 ± 0.75

The results from Table-3 indicate that the road width deposited was close to what was set by CAD, with an error of about 10%. Whereas, the road height was always greater than what was set by CAD. This implies that the material was swelling in the vertical direction.

The last aspect to quantify is the voids present in between roads. The entire void area accounts significantly for the defects created in the parts built by the FDM machine. Again, using HL Image software, the void areas were quantified as follows:

Table-4 Results of Voids Creation in PZT Parts

	-4 mil Offset	0 mil Offset
<b>Void Area(mil<sup>2</sup>)</b>	1.52±2.37	40.58± 23.90
<b>Equivalent Diameter(mil)</b>	1.39	7.19
<b>Video Microscopy Image</b>		

In the case of +4 mil offset the void/gap area is largest as expected. However, this is not an error of the process. This gap area is due to a predetermined offset between roads. When looking at the negative offset, the void area is almost negligible compared to the area of the road width. This makes the negative offset part almost void free. However, the zero off set gives a 7.19 mil diameter void size. For the current PZT processing set-up, it appears that for a 15mil nozzle with 20mil road width & 10mil height and -4 mil offset, void occupied less than 5% of the area. Finally, for both PZT & Silicon Nitride materials, the void sizes are very similar.

## 7. CONCLUSIONS:

Video microscopy experiments demonstrated that imperfections in the process can be detected, analyzed and quantified. This study demonstrated that we can make void free parts by selecting appropriate toolpath parameters. Plus this investigation helped us quantify how and when the voids can occur, and this data is useful in making virtual layered manufacturing simulation more realistic.

## 8. ACKNOWLEDGMENTS:

The authors would like to thank the Office of Naval Research (ONR) Drs. R. Wachters and G. Spanos, for the financial support under ONR MURI grant, #N00014-96-1-1175. The authors I would also like to thank Dan Qiu, Lucy Tirado, and Kemi Ladeji-Oasis for their cooperation and support.

## 9. REFERENCES:

1. Office of Naval Research (ONR), #N00014-96-1-1175 Multidisciplinary Research Program of the Univ. Research Initiative (MURI): An Intelligent CAD Based System.
2. Dan Qiu, Noshir Langrana, Stephen Danforth, Ahmad Safari, Mohsen Safari, "Virtual Simulation for Multi-material LM Process.", The Proceedings of the Ninth Annual Solid Freeform Fabrication Symposium., Austin, Texas, Aug. 1998.
3. Stephen C. Danforth, Department of Ceramic and Materials Engineering, Rutgers, "*Fabrication of a Curved Ceramic/Polymer Composite Transducer for Ultrasonic Medical Imaging Applications by Fused Deposition of Ceramics*", Multi-lifecycle Engineering and Manufacturing Program, Final Report: Year One, New Jersey Commission on Science & Technology (NJCSJ) Program, pages 106-112, February, 1998.

### Keywords:

Layered Manufacturing  
Video microscopy  
PZT  
Silicon Nitride

# Bevel Cutting Methods and Cutting Trajectory Control for Steel Laminations Used in Tooling

by Daniel F. Walczyk

Department of Mechanical Engineering, Aeronautical Engineering and Mechanics  
Rensselaer Polytechnic Institute  
Troy, New York

## Abstract

Bevel cutting of steel laminations used in profiled-edge laminated tooling allows for a more accurate representation of the intended die surface, since stair-stepping at the edges is eliminated. Based on experiments involving maximum cutting speed, bevel angle and kerf quality, the three recommended methods for bevel cutting steel are (best to worst) pulsed Nd:YAG laser with hard-optic delivery, abrasive water jet, and machining with the flute edge of an endmill. For each method, bevel angles of up to 80 degrees are possible. Further experimentation was used to determine the optimal process parameters for kerf quality, with constant cutting speed being one of the main requirements. Finally, a new technique to assure constant velocity along the entire lamination cutting trajectory is developed.

## 1. Introduction and Background

All lamination-based RP methods begin with intersecting a finite number of specified parallel planes (usually equally-spaced) with a 3-D solid or surface model. The resulting collection of contour or profile curves define how the laminations are to be machined and assembled. When laminations are cut perpendicular to their surface (i.e., zero-order approximation), the assembled array of laminations has a stair-stepped surface as shown in Figure 1(a). Thin laminations (e.g., 0.05 mm) that are common with some RP methods like Laminated Object manufacturing (LOM), only require surface finishing to remedy this problem. With larger models, thicker layers (e.g., 10 mm) are typically used and the stair stepping problem becomes more troublesome. Common remedies in this latter case are to perform secondary machining on the stair-stepped surface or fill in between lamination edges with some hard material (e.g., epoxy).

Many have recognized the advantages of cutting lamination edges with a varying bevel instead of simply perpendicular to the surface. Essentially, the lamination edge is defined by connecting two adjacent contour (closed curve) or profile (open curve) lines with a bevel. As shown in Figure 1(b), bevel cutting allows for a first-order or piecewise continuous approximation of the tool or model surface between lamination interfaces. Prior work with thick lamination beveling includes [Beyer et al.,1988] making laminated models with a laser; [Weaver,1991] making metal tooling with a laser; [Berman,1991] making models with a routing head; [Glozer et al.,1993] cutting aluminum with an EDM for plastic injection molds; [Walczyk,1994] cutting steel with a laser, AWJ cutter, and machining head for sheet metal forming dies; [Lee et al.,1996] cutting polystyrene foam with a electrically heated wire; [Zheng et al.,1996] making models with a laser; and [Hope et al.,1997] making models with an AWJ cutter (Styrofoam).

As seen in Figure 1(c), bevel cutting of a particular lamination requires line-of-site machining instructions defined by a series of position point and unit directional vector pairs  $(P_i, \vec{V}_i)$ . There are several algorithms that have been developed for defining lamination edge bevels and suitable cutting trajectories. [Keppel,1975] developed a heuristic-based algorithm for obtaining an optimal approximation of the bevel surface defined by randomly distributed points along adjacent contour lines (i.e., contours are defined by co-planar polylines). The surface approximation is made up of a collection of triangular facets that stitch the adjacent contours together. Based on the [Keppel,1975] graph-search technique, [Fuchs et al.,1977] developed a faster algorithm that does not utilize any heuristics, thereby allowing more options for choosing optimizing criteria. A "minimum square span length" between nodes on adjacent contours was used by [Newman et al.,1995] as the cost function in an optimal surface reconstruction. Furthermore, [Newman et al.,1995] used the concept of a *cutting contour*, defined by the midpoints of the spans, to describe a constant velocity cutting trajectory. [Zheng et al.,1996] used a "smoothed" path between two adjacent contours that eliminates the rapid velocity changes corresponding to the transitions between the computed triangular facets. [Lee et al.,1996] simply defined the cutting trajectory as the exact geometry of the two adjacent contours. Instead of defining a lamination by two adjacent contours, [Hope et al.,1997] defines a lamination by its mid-contour curve and the associated surface normal, curvature, and tangency data taken directly from the NURBS surface model. This information is used to establish a linear approximation of the local surface

curvature and, hence, the beveled lamination edge. Furthermore, the user can define the thickness of each lamination.

## 2. Bevel Cutting of Profiled-Edge Laminations

Profiled-Edge Lamination (PEL) tooling (see Figure 2(a)) has been shown to have distinct advantages over contoured lamination tooling (see Figure 2(b)) in terms of automated assembly, registration, securing, and re-machining of the laminations [Walczyk,1998]. Since PEL lamination edges are bevel cut, the issues of developing kinematically and dynamically desirable cutting trajectories for common tooling materials (e.g., steel) must be addressed for successful implementation of this method in industry. Therefore, the focus of this paper is to compare various methods for cutting metal laminations (specifically steel which is arguably the most common tooling material used), discuss the associated cutting trajectory requirements, and describe a cutting trajectory algorithm which fulfills these requirements.

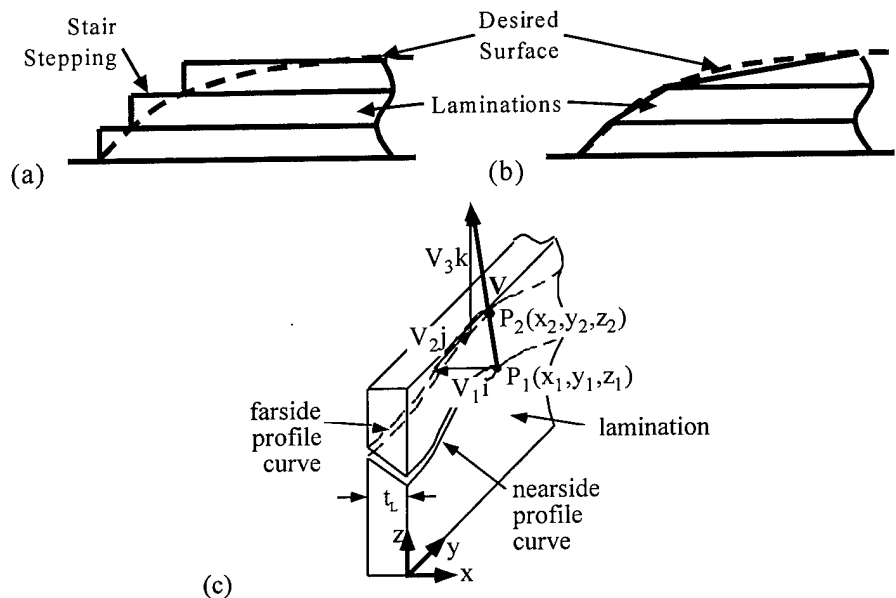


Figure 1 - (a) Stair-stepping of tool surface from perpendicular-cut lamination edges, (b) smoother surface from bevel cutting, and (c) line-of-site machining instructions needed for bevel cutting.

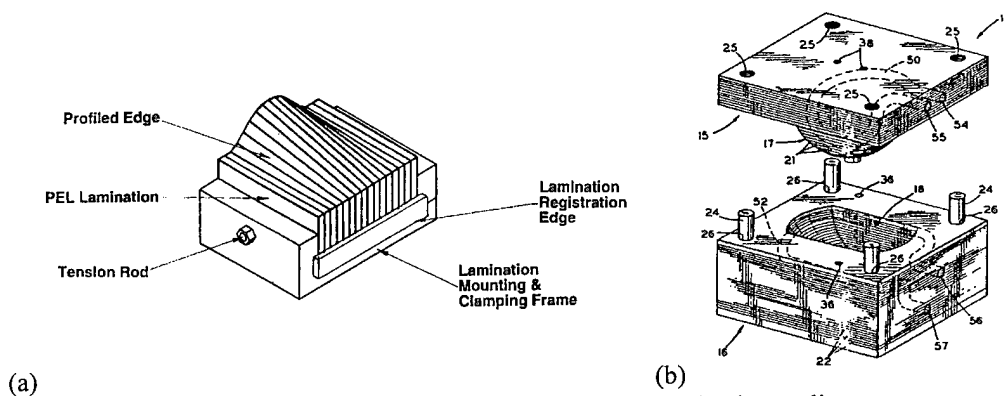


Figure 2 - (a) PEL tooling and (b) contoured lamination tooling.

## 3. Bevel Cutting Methods for Steel Laminations

The most promising methods for bevel cutting steel laminations are machining with the flute-edge of an endmill, abrasive water jet cutting, plasma-arc cutting, and laser cutting [Walczyk,1998]. To determine how rapidly and accurately they will machine steel PEL laminations, each of these methods was investigated through a series of cutting experiments at bevel angles of 0, 30, and 60 degrees. The basis of evaluation for each beveling method will

be the quality characteristics of the bevel cut as defined by Figure 3. A narrow kerf width is desirable so that fine details can be cut into the lamination edge. A low surface roughness of the cut surface is desirable since this will decrease the amount of grinding and polishing time that is necessary for the assembled PEL die forming surface. Minimal or no edge burring on the farside of the kerf is desirable since it must be removed before the die laminations can be assembled into a complete die. Deburring increases the overall fabrication time. The lamination material used for every cutting experiment was 1.5 mm thick SAE 1010 cold drawn steel sheet.

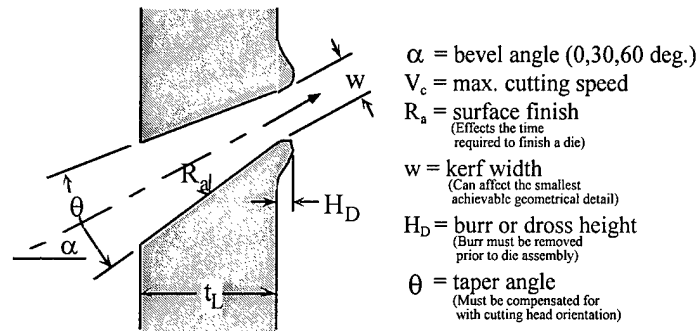


Figure 3 - Quality characteristics of a bevel cut.

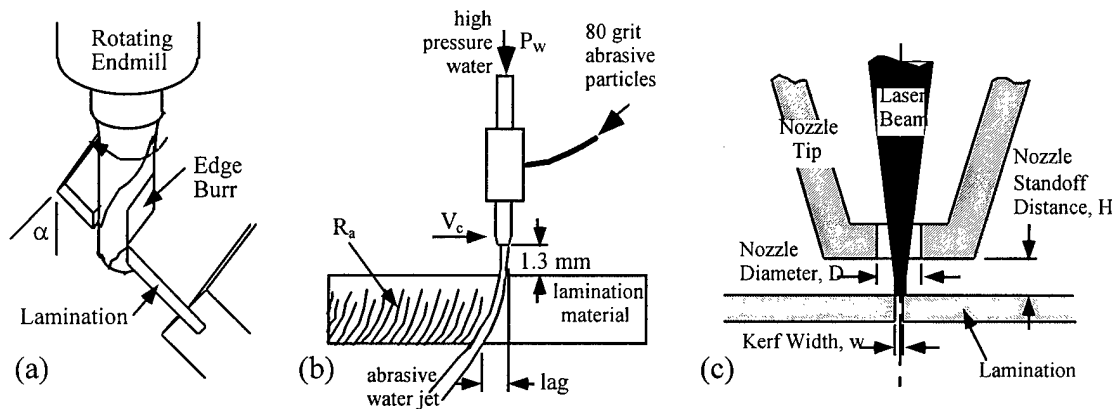


Figure 4 - Lamination cutting methods including (a) machining with an endmill, (b) abrasive waterjet cutting, and (c) laser cutting.

### 3.1 Machining with the Flute-Edge of an Endmill

As seen in Figure 4(a), a profiled-edge with a compound bevel can be machined using the flute-edge of an endmill mounted in a 5-axis machining center. According to a series of bevel cutting experiments using a 6.4 mm diameter endmill, beveling the 1.5 mm thick steel laminations with the endmill's flute-edge leaves very good surface finishes but cutting speeds are relatively low. Slower cutting speeds (denoted as  $V_c$ ) and higher spindle speeds (denoted as  $N$ ) yield the best surface finish ( $R_a$ ) and the smallest burr ( $H_D$ ). The maximum  $V_c$  and  $N$  cutting and spindle speeds for cutting bevels is highly dependent on the material's machinability. Although the presence of coolant did not seem to have any real effect on surface finish and edge burring, it should be used when cutting metal to extend the life of the tool and to minimize the HAZ of the cut. The extent of burring on the climb-milling side of the cut is extensive (see Figure 4a) and it gets longer as the bevel angle increases. Due to the high cutting forces from the large amount of material removed (i.e., width of the tool), there is also significant deflection of the lamination during machining which exacerbates any chattering problem and decreases machining accuracy. For comparison purposes, the average surface roughness, burr height, and maximum cutting speed (and spindle speed used) for each of the bevel angles are listed in Table 1.

**Table 1** - Experimental results for flute-edge endmilling of bevels.

Bevel Angle ( $\alpha$ )	0°	30°	60°
Ave. $R_a$ ( $\mu\text{m}$ )	1.3	4.6	3.1
Ave. $H_D$ (mm)	0.3	2.7	8.6
Max. $V_c$ (m/min)	0.46 (at N=3000 rpm)	0.46 (at N=3000 rpm)	0.25 (at N=2000 rpm)

### 3.2 Abrasive Water Jet (AWJ) Cutting

As seen in Figure 4(b), an abrasive water jet (AWJ) is a non-contact method for cutting bevels into die laminations. The control factors that affect the cut quality are cutting velocity  $V_c$ , upstream water pressure  $P_w$ , and size of the abrasive particles. An OMAX JetMachining System was used for the AWJ cutting experiments. The cutting nozzle diameter and standoff distance from the lamination used for all experiments was 0.76 and 1.27 mm, respectively. Since the AWJ manufacturer strongly recommended that an abrasive particle of particular size be used, specifically 80 grit (0.267 mm average particle size), this was not used as a process parameter.

From the experiments, a number of general effects were noticed. It is difficult to generalize about what effect  $V_c$ ,  $P_w$  and their interaction has on  $R_a$  because the trends vary with every bevel angle. However,  $V_c$  and  $P_w$  have a significant effect on the kerf width  $w$ , but in opposite directions. Specifically,  $w$  tends to increase with higher  $P_w$  and tends to decrease with higher  $V_c$ . The effect that  $V_c$  and  $P_w$  have on  $H_D$  is inconclusive. Since there appear to be no optimal process parameters for bevel cutting with AWJ in terms of  $R_a$  and  $H_D$ , the author suggests using a maximum  $V_c$  and as low a  $P_w$  as is practical. Average values of various quality characteristics from the AWJ experimental bevel cuts are listed in Table 2.

AWJ cutting is a very good non-contact method for machining narrow cuts into die laminations. Because it is non-contact and low forces are imposed on cutting area, there is negligible deflection of the lamination during cutting. Aside from a decrease in the maximum  $V_c$ , AWJ cutting seems to have no problems cutting high bevel angles. According to [Tikhomirov et al.,1992], the maximum  $V_c$  for this process is highly dependent on the yield strength of the material. However, the measured maximum  $V_c$  for 1.5 mm thick thickness lamination material made of mild steel and much harder tool steel are close in value. The surface finish of the bevel cut is slightly rougher than flute-edge endmilling, but more consistent as process parameters change. The burr left on the far edge of the kerf is much less than CNC-machining with an endmill especially at high bevel angles. However, the kerf made with AWJ has a large taper, around 10° for all the bevel angles tested. The kerf taper angle may decrease when thicker laminations are cut and/or when the upstream  $P_w$  is increased.

Even though the cut from an abrasive waterjet introduces error in the cut because of the drag line, taper angle of the kerf, and variable kerf width; [Matsui,1991] has successfully compensated for these errors to increase the precision of the AWJ process as shown in Figure 5. Compensation for these errors involves offsetting the centerline of the kerf by half of it's width which is a function of  $V_c$ , rotating the cutting nozzle slightly about the direction of travel (y-axis) by half the taper angle, and tilting the cutting head backwards (about x-axis) to minimize the effect of the lag line.

**Table 2** - Experimental results for AWJ bevel cutting of 1.5 mm thick steel.

$\alpha$	0°	30°	60°
Ave. $R_a$ ( $\mu\text{m}$ )	4.8	5.1	4.3
Ave. $w$ (mm)	0.62	0.63	0.80
Ave. $H_D$ (mm)	0.061	0.100	0.053
effective thickness of material being cut (mm)	1.47	1.70	2.95
Max. $V_c$ (m/min)	0.34	0.31	0.20
kerf taper	10°	11.5°	9°

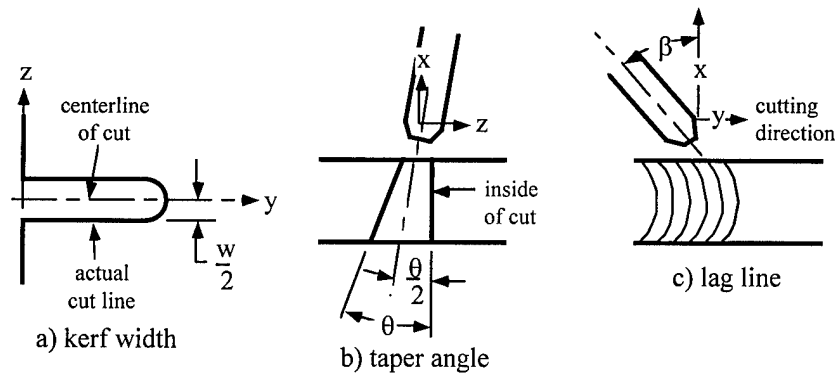


Figure 5 - Compensation methods for AWJ cutting error.

### 3.3 Plasma-Arc Cutting

Using a plasma-arc is another non-contact cutting method that can be used to cut bevels into steel laminations. The system used for the bevel cutting experiments was a Hypertherm HD-1070 HyDefinition Plasma unit. The control variables in plasma-arc cutting are the plasma gas type ( $O_2$  or Air), the plasma gas pressure  $P_G$ , the standoff distance of the cutting nozzle from the lamination  $H_{SD}$ , and the cutting velocity  $V_c$ . Extensive experimentation was abandoned after it became apparent that a plasma-arc was not suitable for beveled cuts. Bevel cuts at angles up to  $45^\circ$  yielded very large tapers ( $>10^\circ$ ) in the kerf, excessive dross ( $H_D=0.9$  mm) that was welded to the metal, and a large heat affected zone (HAZ). The large HAZ caused the cut edge of the lamination to warp slightly. The maximum bevel angle achieved was  $60^\circ$  but the kerf edge closest to the cutting nozzle was consistently obliterated from an over-zealous self-burning<sup>1</sup> of the metal during cutting.

The attractive feature of plasma-arc cutting is the maximum allowable cutting speed which is typically 5 to 10 times faster than that of machining and water-jet cutting. Unfortunately the problems of excessive kerf taper and the tendency of kerf edge nearest to the cutting nozzle to experience self-burning make plasma-arc cutting unsuitable for cutting lamination bevels. The key to plasma-arc's successful usage in cutting bevels will be to solve the edge burning problem, minimize or even eliminate (if possible) the kerf taper, and to reduce the amount of dross. Such an effort will require more than the optimization of process parameters which is beyond the scope of this paper.

### 3.4 Laser Cutting

Laser cutting is another promising non-contact method for machining bevels because of the rapid cutting speeds and steep bevel angles that can be achieved. The main issue to be resolved is what combination of laser type, beam temporal mode, and beam delivery system is best for cutting lamination bevels, particularly in steel. Therefore, a series of experiments were performed with various industrial laser types ( $CO_2$  and Nd:YAG), cutting modes (pulsed and continuous wave), and beam delivery configurations (hard optics and fiber optics) to quantify the ability of a particular laser configuration to cut bevels into lamination material. The object of these experiments was to determine what maximum bevel angles and cutting speeds were achievable.

$CO_2$  laser light can not be delivered by a fiber optic system. Since most glasses, including those used for fiber optic cables, have a high absorptivity at the  $CO_2$  laser wavelength of  $10.6 \mu m$ , fiber optic delivery for a  $CO_2$  laser is not used and is not commercially available [Powell,1993]. A Light beam from a  $CO_2$  laser is almost always delivered with a hard optic system.

$CO_2$  laser cutting tests were performed using a Laser Dyne Model 780 5-axis CNC Machining System with a Rofin-Sinar 1700 SM laser. Using the laser fusion cutting method, a pulsed  $CO_2$  laser beam with hard optic delivery and nitrogen assist gas successfully cut bevels of up to  $45^\circ$  with narrow kerfs (0.18 to 0.30 mm) but with an extensive recast material (a.k.a. adherent dross) that is difficult to remove. Pulsing energies of 2.7 to 6.5 joules were used. For reactive gas cutting (i.e. oxygen assist gas) in pulsed and continuous wave (CW) modes, bevel angles of only  $10^\circ$  were achievable and most of the cuts exhibited self-burning, presumably from an excess of oxygen in the

<sup>1</sup> 'Self burning' is an uncontrolled oxidation reaction caused by an excess flow of oxygen.

the cut, and taper angle  $\theta$ . The control factors that affect these output responses are the focused spot diameter  $d$  which is proportional to the process lens focal length  $F$ , pulse width  $\tau_w$ , pulsing frequency  $f_p$ , cutting speed  $V_c$ , type of assist gas (e.g. O<sub>2</sub>, Air, N<sub>2</sub>), and assist gas pressure  $P_g$ . All of these control factors (actual values used are listed in Table 3) are easily varied with the CNC laser cutter used for the experiments. Since almost all Nd:YAG lasers used for cutting have a tuned resonator, the output power of the laser beam is held constant to minimize the beam divergence. Therefore, the average laser output power was consistently held close to 0.25 kW in this case.

**Table 3 - Control factor values for laser cutting experiments.**

$\alpha$	0°			30°			60°		
	low	med.	high	low	med.	high	low	med.	high
%O <sub>2</sub> in assist gas (mass)	23	-	100	23	-	100	23	-	62
P <sub>g</sub> (kPa)	140	280	410	140	210	280	140	210	280
F (cm)	7.6	12.7	20.3	7.6	12.7	20.3	7.6	12.7	20.3
f <sub>p</sub> (Hz)	30	60	100	30	60	100	22	30	40
V <sub>c</sub> (m/min)	0.13	0.25	0.38	0.13	0.25	0.38	0.13	0.19	0.25
$\tau_w$ (msec)	0.3	0.4	0.5	0.3	0.4	0.5	0.3	0.4	0.5

In the optimization of the laser cutting parameters, the object is to minimize the surface roughness  $R_a$ , kerf width  $w$ , and dross height  $H_D$ . From the experiments,  $R_a$  tends to decrease (i.e., better surface finish) with higher pulsing frequency (except at higher bevel angles), lower cutting speeds, higher percentages of oxygen in the cutting gas, lower assist gas pressure  $P_g$ , and longer laser pulses  $\tau_w$ . The effect of the processing lens focal length  $F$  on surface roughness was not clear from the experimental results. The kerf width  $w$  decreases with lower concentrations of oxygen, higher pulsing frequencies, shorter pulse widths, and shorter processing lens focal lengths. This last effect may be explained by the smaller effective focused beam diameter. No significant effects on kerf width were observed for changes in assist gas pressure or cutting speed. Less dross is noticed with higher oxygen concentrations and cutting speeds. The effects of assist gas pressure, processing lens focal length, laser pulsing frequency, and pulse width on  $H_D$  are either negligible or unclear.

In the following discussion, the parameter values corresponding to the low, medium, and high levels are found in Table 3. For the smoothest surface finish, a low %O<sub>2</sub>, medium  $f_p$ , and high  $\tau_w$  are recommended. For the narrowest kerf, a low %O<sub>2</sub>, high  $f_p$ , and low  $F$  are recommended. For the least amount of dross, a high %O<sub>2</sub>, medium  $P_g$ , and high  $V_c$  are recommended. Depending upon what surface qualities of the bevel cut are most important, the levels of each laser cutting parameter can be set accordingly. The test bevel cuts with the best overall kerf quality and the associated process parameters are listed in Table 4.

**Table 4 - Optimal control factor levels for an Nd:YAG laser cutter.**

$\alpha$	Control Factor Levels						Output Responses		
	%O <sub>2</sub>	P <sub>g</sub>	F	f <sub>p</sub>	V <sub>c</sub>	$\tau_w$	R <sub>a</sub> (μm)	w (mm)	H <sub>D</sub> (mm)
0°	High	High	Low	High	Med.	High	2.6	0.14	0.02
30°	High	High	Low	High	Med.	High	4.4	0.10	0.04
60°	High	High	High	Med.	Low	Med.	5.9	0.07	0.39

With optimal process parameters, lamination cutting with the same general surface finish as flute-edge endmilling and AWJ are possible but surface finish deteriorates with an increase in the bevel angle. The edge-burring due to adherent dross is comparable to AWJ but much less than endmilling. The kerf width is the smallest of all three bevel cutting methods. Although bevels up to ±80° are possible, the range of parameters that yields acceptable cuts narrows with the increase in bevel angle. Since there is a very small mechanical force associated with laser cutting, the fixturing required for lamination being cut is minimal. Furthermore, the HAZ of the laser cut is very small and most of the heat-affected material is blown away during the cutting process.

cut zone. However, the kerfs are narrow; the adherent dross is porous, brittle, and easily removable; and lower pulsing energies of only 0.7 joules were needed. Higher cutting speeds were achievable in the CW cutting mode.

Initial Nd:YAG laser cutting tests were performed using a Lumonics JK701H laser with a fiber-optic delivery. Using O<sub>2</sub> as an assist gas, an Nd:YAG pulsed laser beam delivered with fiber-optics could cut bevels only up to 30°. Kerf widths are also narrow (e.g. 0.33 to 0.40 mm) but the cutting dross increases with the bevel angle. Cutting speeds were slightly lower than for a CO<sub>2</sub> laser of similar power. Pulsing energies of 2.2 joules were used. Cutting in CW mode yielded unacceptable cuts.

With the limited success of fiber-optic delivery, a Lumonics JK704 Nd:YAG laser with hard-optic delivery was used for cutting tests. When air (20% oxygen) was used as the assist gas for a pulsed Nd:YAG laser beam, bevel cuts up to 75° were achieved. Even higher angles may be achievable. Narrow kerf cuts (i.e. 0.15 to 0.30 mm) were observed with a porous dross that remains relatively constant for all bevel angles. The lower cutting speeds are attributable to the low pulsing frequency used. Faster cutting speeds will be achievable at the low bevel angle (i.e. 0 to 40°) if higher pulsing frequencies are used. For cutting experiments involving different lamination thicknesses and laser powers, the maximum cutting speed decreases non-linearly with increasing bevel angle because both the effective material thickness and laser energy absorbtivity of the material surface decreases.

*Summary:* As previously mentioned, a high laser beam energy intensity at the material surface is of prime importance for cutting steep angle bevels. The limited success with the CO<sub>2</sub> laser beam delivered with hard optics is attributable to insufficient energy intensity at these steep angles. The energy absorbtivity of steel and other metals to CO<sub>2</sub> laser light is relatively low compared to Nd:YAG laser light, which contributes to this problem. The theoretical focused beam diameter is 0.102 mm in this case. The better success with Nd:YAG laser beam delivered with hard optics is attributable to the higher absorbtivity of this shorter wavelength light by the metal and a much smaller focused spot diameter, specifically 0.008 mm and 0.013 mm for the low and high powered lasers, respectively. A small focused spot diameter yields a high energy intensity.

The limited beveling success of an Nd:YAG laser beam with fiber optic delivery is due to a large focused diameter and the homogenization of the laser beam within the fiber. The spot diameter of the laser beam delivered through a 1.00 mm diameter fiber is 0.5 mm. Even though the theoretical focused spot diameter is typically 2 to 5 times larger in reality [Powell,1993], the focused spot diameter from the hard optic delivery of an Nd:YAG laser beam is at least an order of magnitude less than the 0.5 mm spot. Furthermore, the laser beam exiting a fiber optic is homogenized as compared to the incoming beam. Homogenization lessens the exiting laser light's quality to a non-gaussian spatial distribution leading to a lower energy density on the material surface.

### 3.4.1 Optimization of Parameters for Pulsed Nd:YAG Laser Cutting with Hard-Optic Delivery

For cutting bevels into steel sheet—the predominant material used for tooling—the optimal configuration is a pulsed Nd:YAG laser with hard-optic beam delivery. A pulsed laser beam creates a scalloped-type kerf (see Figure 6(a)) by overlapping drilled holes (see Figure 6(b)). The process parameters chosen for the previous laser cutting experiments yielded kerfs of generally poor surface finish and geometrical accuracy. In this section, the optimal parameters for better kerf quality from pulsed Nd:YAG laser cutting are determined.

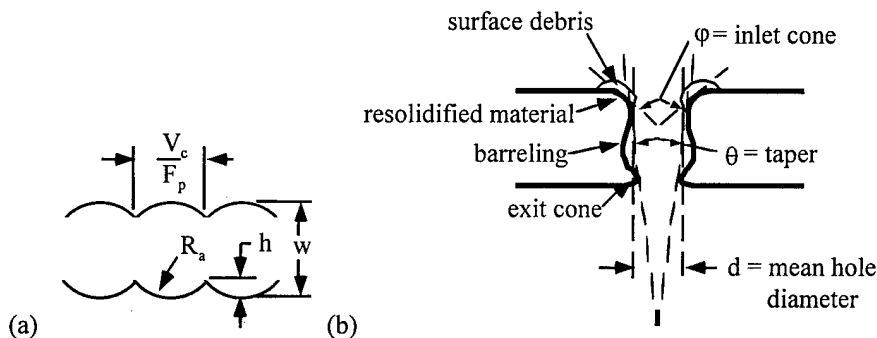


Figure 6 - (a) Top view of a pulsed laser-cut kerf and (b) features of laser-drilled holes.

As shown in Figures 3 and 6, the easily measurable output responses that help to define the kerf quality of the laser cut bevel are the kerf width  $w$ , surface roughness of the kerf  $R_a$ , the height of the burr  $H_D$  on the farside of

### 3.5 Comparison of Bevel Cutting Methods

Based on the previous discussion, some final comparisons can be made between flute-edge endmilling, abrasive water jet cutting and laser cutting (plasma-arc cutting not considered) for beveling steel laminations.

- The higher cutting forces associated with flute-edge endmilling significantly deflect the unsupported portion of a lamination being beveled. AWJ cutting and laser cutting, i.e. non-contact cutting methods, cause negligible deflection to the lamination.
- All three cutting methods are capable of high cutting speeds but the maximum speed is highly dependent upon the steel composition and hardness with flute-edge endmilling and less so with AWJ cutting. The maximum laser cutting speed is only dependent on laser power which means that higher cutting rates are achievable.
- The maximum bevel angle for all three methods is around  $\pm 80^\circ$ .
- The kerf from AWJ cutting has a very large, consistent taper of around  $10^\circ$  for all bevel angles that must be compensated for during bevel cutting. Laser cutting creates only a slight kerf taper. Flute-edge endmilling leaves no appreciable kerf taper unless there is significant deflection of the lamination and cutting tool during beveling.
- The width of the kerf affects the smallest radius of curvature achievable for a PEL's profiled edge. Of the three beveling methods, laser cutting creates the narrowest kerf. The kerf from AWJ cutting is also narrow but not as much as that cut with a laser. The kerf width from endmilling is relatively large since it is the diameter of the cutting tool.
- Flute-edge endmilling leaves a very large machining burr, especially at larger bevel angles. AWJ cutting and laser cutting, on the other hand, yield much smaller machining burrs. Laser cutting with a pure oxygen assist gas yields a porous, brittle edge burr (i.e. iron oxide) which is easily removed from the cut lamination without grinding.
- Flute-edge endmilling yields the smoothest surface finish of all the methods although the finish deteriorates at higher bevel angles from more machining chatter. AWJ cutting offers the most consistent surface finish for all bevel angles.

The author ranks the suitability (best to worst) of these three bevel cutting methods for cutting steel laminations as follows:

1. Nd:YAG laser cutting because cutting speed is only dependent on laser power, tool wear is non-existent, cutting force is negligible and the kerf is the narrowest of all.
2. Abrasive water jet cutting since cutting speed is dependent on material hardness and the kerf taper is the largest among the three methods.
3. Flute-edge endmilling since the cutting force, kerf width, edge burr, and cutting speed's dependency on material hardness is the greatest overall.

### 4. Suitable Cutting Trajectory and Method for Cutting Steel PELs

From the preceding discussion, uniformity in cut quality and geometry of steel laminations is based on the control of cutting process parameters. The main parameter that is controlled by the chosen cutting trajectory is cutting speed. In flute-edge endmilling, the maximum  $V_c$  is constrained by the steel's machinability and the lamination stiffness. Furthermore,  $R_c$  deteriorates with increasing speed. For AWJ cutting, kerf width decreases with increasing speed but the effect of the water jet lag line becomes more pronounced. For laser cutting, surface finish gets better with increasing cutting speed but more extensive deburring is required. The ideal situation for cutting with any of these three cutting methods would be to cut lamination material at a constant speed for the entire cutting trajectory.

While the methods of [Newman et al.,1995], [Zheng et al.,1996], and [Hope et al.,1997] can be used to define a trajectory for cutting the top edge of a PEL at a nearly constant velocity, the author has chosen a more straight-forward procedure. As shown in Figure 7, the lamination's profiled edge is defined by two adjacent profiles resulting from the intersection of a two parallel cutting planes (separated by the lamination thickness) with the tool's CAD surface model (e.g., NURBS surface). Typically, each profile will be B-Spline curve, i.e., a piecewise polynomial made up of Bézier curves. To achieve a cutting trajectory with a nearly constant velocity, both curves are divided into the same number ( $n$ ) of equal length segments using numerical procedures. Points are assigned to the end of each curve segment. This series of corresponding point pairs  $(P_1, P_2)$  are used to define corresponding line-of-site machining instructions, that is, a series of position point and unit directional vector pairs  $(P_i, \vec{V})$  as shown in Figure 1(c). If a constant velocity is prescribed for the point-to-point moves performed by the CNC

machine (e.g., 5-Axis laser cutter), then the cutting means will have a nearly constant velocities along both profile curves.

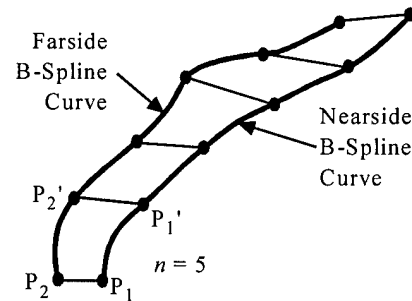


Figure 7 - Lamination's profiled-edge defined by two adjacent B-Spline curves.

### Acknowledgment

This research was partially supported by the National Science Foundation CAREER award DMI-9734231.

### Bibliography

- Beyer, E., Klein, R., and Herziger, G., "Method for the Production of Three Dimensional Models," *German Patent #P 37 11 470.0*, Issued October 27, 1988.
- Fuchs, H., Kedem, Z.M., and Uselton, S.P., "Optimal Surface Reconstruction from Planar Contours," *Communications of the ACM*, Vol. 20, No. 10, Oct. 1977, pp. 693-702.
- Glozer, G.R., and Brevick, J.R., "Laminate tooling for injection moulding," *Journal of Engineering Manufacture*, Vol. 207, No. B1, 1993, pp. 9-14.
- Hope, R.L., Jacobs, P.A., and Roth, R.N., "Rapid Prototyping with Sloping Surfaces," *Rapid Prototyping Journal*, Vol. 3, No. 1, 1997, pp. 12-19.
- Keppel, E., "Approximating Complex Surfaces by Triangulation of Contour Lines," *IBM Journal of Research Developments*, Vol. 19, January 1975, pp. 2-11.
- Lee, C.H., Gaffney, T.M., and Thomas, C.L., "Soft Tooling for Low Production Manufacturing of Large Structures," *Proceedings of the 1996 Solid Freeform Fabrication Conference*, Austin, TX, August, 12-14, 1996, pp. 207-214.
- Matsui, S., Matsumura, H., Ikemoto, Y., and Shimizu, H., "High Precision Cutting Method for Metallic Materials by Abrasive Waterjet," *Proceedings of the 6<sup>th</sup> American Water Jet Conference*, Houston, Texas, Aug. 24-27, 1991, pp. 127-137.
- Newman, W., Zheng, Y., Fong, C., "Trajectory Generation from CAD Models for Computer-Aided Manufacturing of Laminated Engineering Materials," *Proceedings of the 26<sup>th</sup> International Symposium on Industrial Robots*, Singapore, Oct. 4-6, 1995, pp. 153-158.
- Powell, J., *CO2 Laser Cutting*, Springer-Verlag, Inc., New York, 1993.
- Tikhomirov, R.A., Babanin, V.F., Petukhov, E.N., Starikov, I.D., and Kovalev, V.A., *High Pressure Jetcutting*, ASME Press, New York, 1992.
- Walczyk, D.F., and Hardt, D.E., "A New Rapid Tooling Process for Sheet Metal Forming Dies," *5<sup>th</sup> International Conference on Rapid Prototyping*, University of Dayton, Dayton, Ohio, June 12-14, 1994, pp. 275-289.
- Walczyk, D.F., and Hardt, D.E., "Rapid Tooling for Sheet Metal Forming Using Profiled Edge Laminations—Design Principles and Demonstration," *Journal of Manufacturing Science and Engineering*, Vol. 120, No. 3, August, 1998.
- Weaver, W.R., "Process for the Manufacture of Laminated Tooling," *US Patent #5031483*, Issued on July 16, 1991.
- Zheng, Y., Choi, S., Mathewson, B., and Newman, W., "Progress in Computer-Aided Manufacturing of Laminated Engineering Materials Utilizing Thick, Tangent-Cut Layers," *Proceedings of the 1996 Solid Freeform Fabrication Conference*, Austin, TX, August, 12-14, 1996. pp. 355-362.



# DESIGNING CONFORMAL COOLING CHANNELS FOR TOOLING

Xiaorong Xu, Emanuel Sachs, Samuel Allen, Michael Cima

MIT  
Cambridge, MA 02139

Contact:  
Emanuel Sachs  
MIT  
(617) 253-5381  
sachs@mit.edu  
77 Mass Ave  
Cambridge, MA 02139  
Rm 35-134

## Abstract

SFF technologies have demonstrated the potential to produce tooling with cooling channels which are conformal to the molding cavity. 3D Printed tools with conformal cooling channels have demonstrated simultaneous improvements in production rate and part quality as compared with conventional production tools. Conformal Cooling lines of high performance and high complexity can be created, thus presenting a challenge to the tooling designer. This paper presents a systematic, modular, approach to the design of conformal cooling channels. Recognizing that the cooling is local to the surface of the tool, the tool is divided up into geometric regions and a channel system is designed for each region. Each channel system is itself modeled as composed of cooling elements, typically the region spanned by two channels. Six criteria are applied including; a transient heat transfer condition which dictates a maximum distance from mold surface to cooling channel, considerations of pressure and temperature drop along the flow channel and considerations of strength of the mold. These criteria are treated as constraints and successful designs are sought which define windows bounded by these constraints. The methodology is demonstrated in application to a complex core and cavity for injection molding.

## 1. Introduction

### 1.1 Motivation

The cooling of injection molding tooling is crucial to the performance of the tooling influencing both the rate of the process and the resulting quality of the parts produced. However, cooling line design and fabrication has been confined to relatively simple configurations primarily due to the limits of the fabrication methods used to make tools, but also due to the lack of a design methodology appropriate for cooling lines.

For many years mold designers have been struggling for the improvement of the cooling system performance, despite the fact that the cooling system complexity is physically limited by the fabrication capability of the conventional tooling methods. Different methods such as the helical channels, the baffled hole system, the spiral plug system and the heat-pipes have been developed for the uniform and efficient cooling of the part [2]. Some mold manufacturers such as Innova built tools with conformal cooling effect by stacking slices of the tool layer by layer with cooling channels milled on each layer. Other manufacturers such as CITO Products Inc. developed the pulse cooling technique for better control of the mold temperature in order to reduce the energy consumption and enhance uniform cooling condition.

The emergence of Solid Freeform Fabrication (SFF) processes offers injection mold manufacturers new degrees of freedom in mold tooling. The SFF processes are additive processes that construct 3D objects by incrementally building up cross sectional layers of arbitrary complex shapes converted from CAD models. Typical SFF processes include stereolithography, selective laser sintering, three dimensional printing, solid ground curing, laminated object manufacturing, etc. [23]. The ability to fabricate 3D features with almost arbitrary complexity makes these processes extremely useful for fabricating parts and tools that cannot be practically made by other techniques. One example of the applications is to fabricate complex cooling channels inside injection molds in order to improve the uniformity of cooling. The 3D Printing Lab at MIT has been participating in the injection molding tooling project for several years [24, 25, 26]. The industrial application of 3D Printed tools with serpentine conformal cooling channels built inside have achieved the simultaneous improvement of the cycle time by 15% and the part distortion by 9% [26]. With the manufacturing flexibility offered by SFF processes such as 3D Printing, more complex cooling channel systems such as that shown in Figure 1b can be fabricated for the further improvement of the cooling performance.

The emergence of new processes that can be used to create tools with conformal cooling channels placed with almost arbitrary complexity not only offers the designer new degrees of freedom in the design of injection molding tools but also simplifies the methodology used to design cooling channels. The work discussed in this paper seeks to develop a methodology for the design of cooling channels that both simplifies the design and results in substantially improved performance. As you will see from the paper this methodology makes the design of complex cooling channel system for the inserts such as that shown in Figure 1b a handy work.

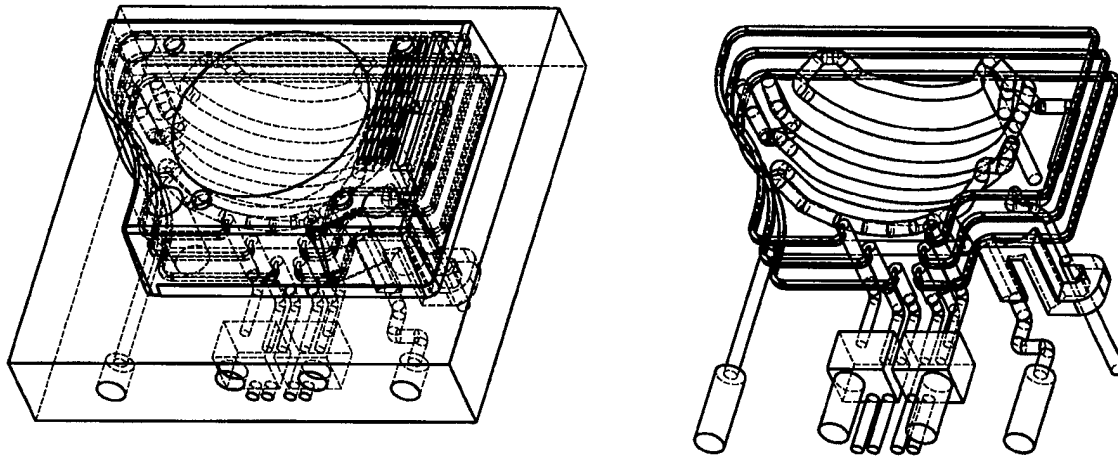


Figure 1. Left: solid model of the core insert with conformal cooling channels built inside. Right: solid model for the conformal cooling channel set

## 1.2 Related Work

Before the scientific analysis was introduced into injection molding, the design of the mold cooling system was dominated by designers' experience and simple formula [1-4]. It is not until early 80's that the mold cooling simulation was paid more and more attention. Different methods were proposed to predict the temperature field for the mold and the part during the cooling stage [5-14]. The cooling related quality issues such as residual stress, shrinkage and warpage were also addressed in [15-22]. Among those simulation algorithms, an iterative hybrid scheme proposed by Cornell Injection Molding Program (CIMP) became a standard scheme for mold cooling analysis due to its computational efficiency [8-12]. Today most of the mold design packages such as C-MOLD are equipped with this analysis scheme. This scheme treats the plastic part as one-dimensional transient heat transfer and the mold as three-dimensional heat transfer. The periodic transient mold temperature field within an injection cycle is separated into a quasi-steady component and a time-varying component. The quasi-steady component reflecting the cycle-averaged temperature field is obtained by solving the Laplace equation for the entire mold using the boundary element method. The solution is then used as the boundary for 1D part temperature field. The iterative reference between the boundary element solution of the cycle-averaged mold temperature field and the finite difference solution of the part temperature field continues until a steady temperature boundary is achieved at the mold-part interface. Compared with the finite element simulation that needs to calculate the internal nodes, the hybrid scheme discussed above significantly reduces the computational time because only the boundary nodes are considered for obtaining the cycle-averaged mold temperature field.

The emerging techniques for freeform fabrication of the injection molding tools place a new challenge to the mold design and analysis strategy due to the increased complexity in cooling channel geometry. This situation motivates us to develop a systematic tool for conformal cooling line design. Compared with the existing cooling analysis software, the methodology

discussed in this paper builds a synthesis tool instead of an analysis tool for the design of the complex conformal cooling channels which take the full advantage of SFF processes.

## 2. Heat transfer model for conformal cooling

As the name implies, conformal cooling is used to signify cooling channels that conform to the surface of the mold cavity. However, in this paper, the term “conformal cooling” has a further significance that is related to the transient heat transfer within the mold. When a mold is started up it takes some time before the mold reaches a steady state operating temperature. Figure 2 shows the mold surface temperature histories recorded by the thermocouples for both the mold with conformal cooling channels and that with straight cooling channels [24]. As one can see from the figure, the mold surface temperature of the core with straight cooling channels tracked over 25 successive injections starting from the coolant temperature of 12° C and reaching a cycle average steady state temperature of approximately 55° C. However, if the cooling lines are placed very close and conformal to the mold surface the steady state condition is reached very quickly. As illustrated in Figure 2 the cycle average temperature of a conformally cooled core reaches its steady state value after one injection cycle. Our operational definition of conformal cooling then is that the cycle average temperature reaches its steady state value within one injection cycle. As shown by experiments, the difference of the mold surface temperature profiles we just discussed above significantly effects the part quality and productivity.

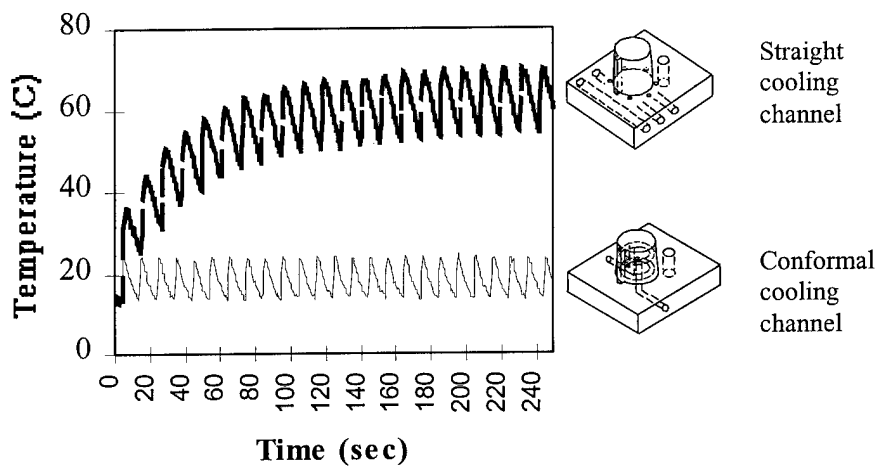


Figure 2. Comparison of mold surface temperature histories for straight channel cooling and conformal channel cooling

The difference between two cases shown in Figure 2 has to do with the rate of the energy transfer into the mold over successive injections and the thermal inertia of the mold. As the hot plastic comes in during each successive injection, heat transfer takes place across the plastic mold interface and a heat pulse is conducted through the mold material itself. This heat pulse warms up the mold material as it propagates toward the cooling channels and is eventually

removed in the cooling water. If the cooling channels are far from the mold's surface, successive heat pulses keep raising the temperature of the mold until the heat pulse propagating in is balanced by heat extraction by the coolant. If the cooling channels are close to the mold surface, the effective thermal mass of the tool is confined to that region between the surface and the cooling channels and is much reduced. In addition, the conduction path from the surface of the tools to the cooling lines is reduced. As a result, the steady state condition is reached much more rapidly and can in fact be attained within one injection cycle.

An energy balance may be written for the active portion of the mold, that is the portion between the surface and the cooling lines. Equation (1) shows the resulting differential equation (see Appendix A for derivation of this equation).

$$\rho_m C_m l_m \frac{dT_m}{dt} + \frac{h\pi DK_m}{2K_m W + h\pi D l_m} (T_m - T_c) = \frac{\rho_p C_p l_p (T_{melt} - T_{eject})}{t_{cycle}} \quad (1)$$

The first term in Equation (1) captures the thermal mass of the tool and the build-up of heat as the temperature of the tool increases. The second term in Equation (1) captures the transfer of heat by conduction through the mold and then convection into the cooling fluid. The right hand side of Equation (1) captures the source of the heat, which is the cooling down of the plastic. This first order differential ordinary differential equation has the solution of the form shown in Equation (2) where  $T_{ms}$  is the cycle averaged mold temperature at steady state and  $\tau$  is the time constant of the system. Equations (3) and (4) give the expressions for cycle averaged mold temperature and the time constant respectively. Our definition of conformal cooling can now be stated formally by requiring that  $\tau$  be less than or equal to one injection cycle time. Figure 3 shows a prediction of Equation (2) superimposed on the experimental results previously shown in Figure 2. As can be seen, there is reasonably good prediction with the cycle average temperature.

$$T_m(t) = T_{m0} + (T_{ms} - T_{m0})e^{-t/\tau} \quad (2)$$

$$T_{ms} = T_c + \frac{\rho_p C_p l_p (2K_m W + h\pi D l_m) (T_{melt} - T_{eject})}{h\pi DK_m t_{cycle}} \quad (3)$$

$$\tau = \frac{\rho_m C_m l_m (h\pi D l_m + 2K_m W)}{h\pi DK_m} \quad (4)$$

A limiting case of Equation (4) is that where the heat transfer to the fluid is very efficient and we can then examine the limiting case where the heat transfer coefficient goes to infinity. In this case, the expression for the time constant reduces to the form shown in Equation (5). In this simplified expression we see that the important material property for the mold is the thermal diffusivity which is  $K_m / \rho_m C_m$ . We also see that the time constant is proportional to the square of the distance between the surface of the mold and the cooling channels. This simplified expression makes clear the importance of considering this as a transient heat transfer calculation. If this were a steady state heat transfer problem then doubling the thermal conductivity of the

mold would allow the channels to be placed twice as far away. However, as we can see from Equation (5) if we double the thermal conductivity and place the channels twice as far away the time constant in fact increases by a factor of 2. Thus, while the material properties are important, the geometry (as seen by the square of the distance of Equation (5)) is even more important.

$$\tau = \frac{\rho_m C_m l_m^2}{K_m} \quad (5)$$

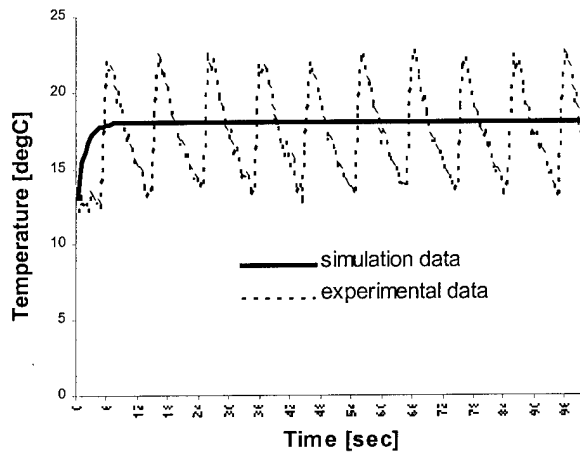


Figure 3. Comparison of the experiment data vs. the simulation data for the mold surface temperature profile during successive injections

### 3. Design methodology

The introduction of conformal cooling significantly simplifies the injection molding cooling system design methodology. In the conformal cooling situation, the heat transfer is localized in a small region between two adjacent cooling channels. This feature suggests that we first design a cooling “cell” composed of the small region between the adjacent cooling lines and then map the solution to the entire mold. The flexibility of SFF processes makes this modular approach possible by minimizing the manufacturing constraint that must be applied. This strategy simplifies the cooling line design by providing a sequential approach which provides a global solution by the addition of many local solutions. While the design process is simplified, the resulting cooling line designs can be quite complex and take full advantage of the flexibility of SFF processes.

Figure 4 illustrates this design strategy by using a generic part with a hemispherical dome and a flat bottom. As shown in the figure, the part is first divided into two cooling zones (a hemisphere and a flat surface) based on its geometry. Then in each cooling zone the conformal cooling surface is constructed and the cooling channel topological structure is defined. After that the system of cooling channels is further decomposed into small elements called cooling cells.

The heat transfer analysis and the cooling system design is based on these cooling cells and is then mapped to the entire mold. This modularized design strategy is not sensitive to the part geometry, therefore it keeps the same design simplicity no matter how complex the part geometry is.

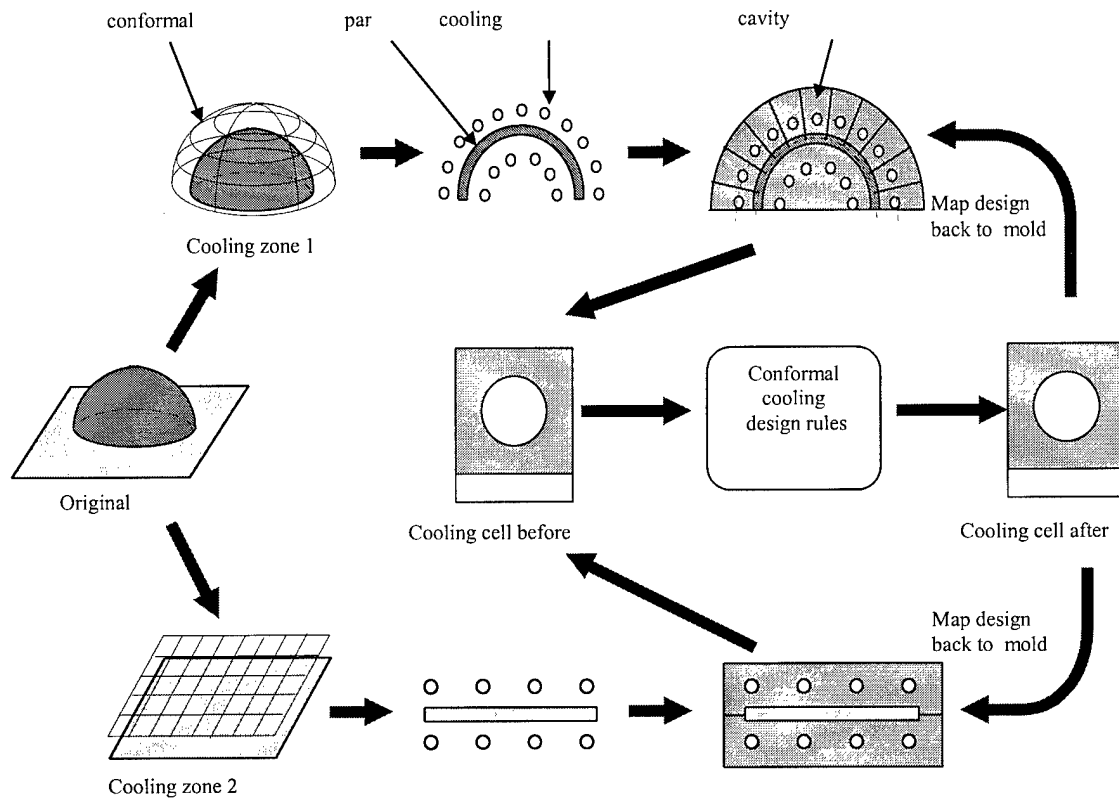


Figure 4 Steps for the modularized cooling line design for a generic part

#### 4. Design rules

After the cooling system has been decomposed into simple cooling cells by the method discussed above, the design rules are applied to these cooling cells in order to obtain cooling channel design parameters and process conditions. In this chapter, six design rules are proposed and design windows are constructed for the cooling line design based on individual cooling cells. These rules include design for conformal cooling condition, design for coolant pressure drop, design for coolant temperature uniformity, design for sufficient cooling, design for uniform cooling and design for mold strength and deflection.

##### 4.1 Design for conformal cooling condition

The conformal cooling condition defined in section 2 must be applied throughout the tooling in order to guarantee the good control of the temperature at the surface of the tool. In order to satisfy this condition, the mold designer can increase the heat transfer coefficient, increase the channel diameter, decrease the distance between the cooling lines and the mold wall

or choose mold material with a high thermal diffusivity. The determination of these design parameters is also constrained by other design rules that will be discussed below.

#### 4.2 Design for coolant pressure drop

The allowable pressure drop of the coolant in the conformal cooling channel is constrained by the available pumping pressure of the chiller. The objective of the cooling line design for pressure drop is to find a proper combination of the coolant flow rate, the cooling channel diameter and the cooling line length so that the resulting total pressure drop is smaller than the given pressure budget. The fluid mechanics of the incompressible flow can be used to predict the coolant pressure drop that is a function of the cooling line length, the cooling line diameter and the coolant flow rate [27].

$$P = \frac{L}{2D} \rho v^2 C_f \quad (6)$$

where  $C_f$  in Equation (6) is the cooling channel surface friction factor which differs for different flow regions:

$$C_f = \frac{16}{R_{eD}} \quad (\text{for laminar flow}) \quad (7)$$

$$C_f = \frac{0.25}{1.8^2} (\log_{10} [(\frac{e}{3.7D})^{1.11} + \frac{6.9}{R_{eD}}])^{-2} \quad (\text{for turbulent flow}) \quad (8)$$

In the above equations,  $R_{eD}$  is the Reynolds number of the coolant flow.  $e$  is the surface roughness of cooling channels.

#### 4.3 Design for coolant temperature uniformity

The objective of the design for the coolant temperature uniformity is to check and make sure that the coolant temperature drop is maintained within a certain range. A simple expression of the coolant temperature drop  $\Delta T$  is obtained by the following equation:

$$\Delta T = \frac{\rho_p C_p l_p w L}{\rho_c C_c Q} \cdot \frac{(T_{melt} - T_{eject})}{t_{cycle}} \quad (9)$$

where  $l_p$  is half the plastic part thickness,  $w$  is the cooling line pitch distance,  $L$  is the cooling line length,  $Q$  is the coolant flow rate and  $t_{cycle}$  is the injection cycle time.  $\rho_c$ ,  $C_c$ ,  $\rho_p$ ,  $C_p$  are the densities and specific heats for coolant and part materials respectively. Equation (9) indicates that during the steady injection cycles the heat pulse due to the cooling down of the plastic part is totally converted to the temperature rise of the coolant flow. In order to reduce the coolant temperature drop, the designer can use the coolant with large thermal mass, increase the coolant flow rate, decrease the pitch distance between two adjacent cooling channels or reduce the length of the cooling line.

#### 4.4 Design for sufficient cooling

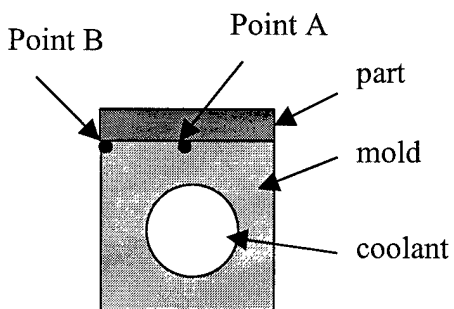
As we have discussed in section 1, the cooling analysis scheme adopted by most of mold design software is computationally expensive and not good for the design and analysis of complex cooling channels. With the concept of conformal cooling, this scheme is much simplified. As the matter of fact, the steady cycle averaged mold temperature can be directly derived from Equation (3). However, this expression requires both the part ejection temperature  $T_{eject}$  and the cycle time  $t_{cycle}$  which can not be both obtained. A simple iteration discussed below finds the cycle time and the steady cyclic mold temperature  $T_{ms}$  based on the required part ejection temperature:

- Step 1. Assume the cycle averaged mold temperature  $T_{ms}$ .
- Step 2. Calculate the cycle time  $t_{cycle}$  for the required part ejection temperature according to 1D part heat transfer.
- Step 3. Calculate the part ejection temperature at the end of  $t_{cycle}$ .
- Step 4. Calculate the cycle averaged mold temperature  $T_{ms}$  based on equation (3).
- Step 5. Replace  $T_{ms}$  in step 1 by the cycle averaged mold temperature value obtained in step 4.
- Step 6. Follow the iterations from step 1 to 5 until the cycle averaged mold temperature  $T_{ms}$  reaches a steady value.

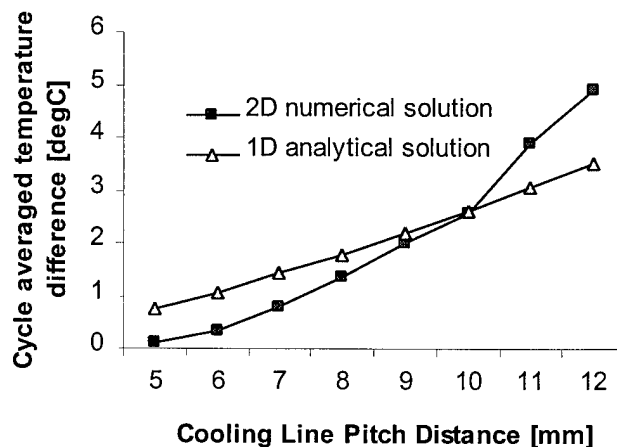
For readers with special interest in detail algorithms, please refer to Appendix B.

#### 4.5 Design for uniform cooling

The “uniform cooling” in this paper has both the global and the local meanings. The global uniformity is the cooling rate variation over the entire mold. It is guaranteed by keeping the coolant temperature uniformity. The local cooling uniformity refers to the variation of the mold surface temperature within the individual cooling cell sketched in Figure 5(a). The local cooling uniformity is defined by the difference of the cycle averaged temperatures on the mold surface right above the cooling channel and at the middle of two adjacent channels, i.e. points A and B in Figure 5(a).



(a)



(b)

Figure 5 (a) Sketch of a cooling cell for cooling uniformity analysis. (b) Comparison of the analytical and numerical solutions for cycle averaged mold surface temperature differences at point A and B

The cycle averaged mold surface temperatures at point A and point B are expressed by the following equations:

$$T_{ma} = T_c + \frac{\rho_p C_p l_p (2K_m W + h\pi D l_a)(T_{melt} - T_{eject}^a)}{h\pi D K_m t_{cycle}} \quad (10)$$

$$T_{mb} = T_c + \frac{\rho_p C_p l_p (2K_m W + h\pi D l_b)(T_{melt} - T_{eject}^b)}{h\pi D K_m t_{cycle}} \quad (11)$$

where  $l_a$  and  $l_b$  are the depth of the heat diffusion into the mold at point A and point B respectively.  $T_{eject}^a$  and  $T_{eject}^b$  are part ejection temperatures at A and B respectively. The cycle averaged temperatures  $T_{ma}$  and  $T_{mb}$  are obtained following the same routine as discussed in section 4.4. The local cooling uniformity of the mold is thereby defined as the absolute value of the cycle averaged temperature difference between point A and point B:

$$\Delta T_{ab} = |T_{ma} - T_{mb}| \quad (12)$$

Figure 5(b) plots the local cooling uniformity and compare it with the numerical solution (see Appendix C for details) for different cooling line pitch distance. The material properties used for this calculation are those of polystyrene (part), 316 stainless steel (mold) and 30 °C water (coolant). The calculation is based on 2mm part thickness, 4mm cooling channel diameter and 3mm vertical distance from cooling line to mold wall. The heat conduction distances  $l_a$  and  $l_b$  in equation (19) and (20) are chosen to be distances from point A and B to the wall of the cooling channel respectively. As one can see from the figure, the analytical and numerical solutions match very well in a certain pitch distance range. More accurate prediction can be achieved by adding adjustment factors to  $l_a$  and  $l_b$ .

#### 4.6 Design for mold strength and deflection

Rao [3] predicted the mold stress and deflection based on the rectangular cooling channel model shown in Figure 6. According to his model, the maximum tensile stress in the mold under a certain injection pressure  $P_m$  is:

$$\sigma_{max} = \frac{0.5P_m D^2}{l_m^2} \quad (13)$$

The maximum shear stress in the mold is:

$$\tau_{max} = \frac{0.75P_m D}{l_m} \quad (14)$$

The maximum mold surface deflection under pressure  $P_m$  is:

$$f_{\max} = \frac{P_m D^2}{l_m} \left( \frac{D^2}{32E_m l_m^2} + \frac{0.15}{G} \right) \quad (15)$$

The above expressions represent the worst case of the loading because the commonly used cooling channels are circular shaped that result in much smaller stress and deflection. The numerical simulation shows that the stress concentration is reduced by over 50% if we choose channels with round corners.

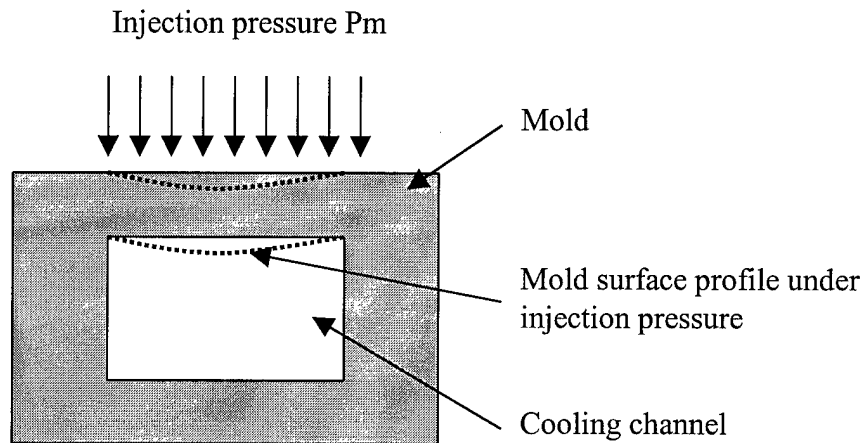


Figure 6 Sketch of a cooling cell under the injection pressure

## 5. Tool design and fabrication with conformal cooling channels

With the help of the conformal cooling line design methodology, the 3D Printing Lab of MIT has successfully designed and fabricated the mold inserts for the part shown in Figure 7. The challenge placed by this part is that the geometric features are so small and so close to each other that it gives the designer little room for the cooling channel placement. In order to proceed the conformal cooling line design for this part, we first divide the part into two cooling zones. For each cooling zone, the cooling line topological structure is defined and different cooling channel cross section shapes are assigned to different sections of the cooling line. Then the cooling system is further decomposed into individual cooling cells and the design rules are applied to these cells to obtain the local solution of the cooling channel parameters. The 2D numerical simulation (see Appendix C for details) is also used for the evaluation of the transient heat transfer in each cooling cell. Figure 9 shows the design results for individual cooling cells. These results include the cooling channel geometry, process condition as well as the evaluation of design rules such as the part ejection temperature, the coolant pressure drop, the mold stress, etc. In addition to the local design of individual cooling cells, the designer is responsible for coordinating between local solutions for the proper global performance. One example of such coordination is to balance the coolant flows between cooling zones. In the table shown in Figure 8 the coolant pressure drops for each section of the cooling zone are summed up so that the total pressure drop through each cooling zone is obtained. In order to maintain the equal coolant flow

between two cooling zones, it is important to make the total pressure drop in each cooling zone as close as possible.

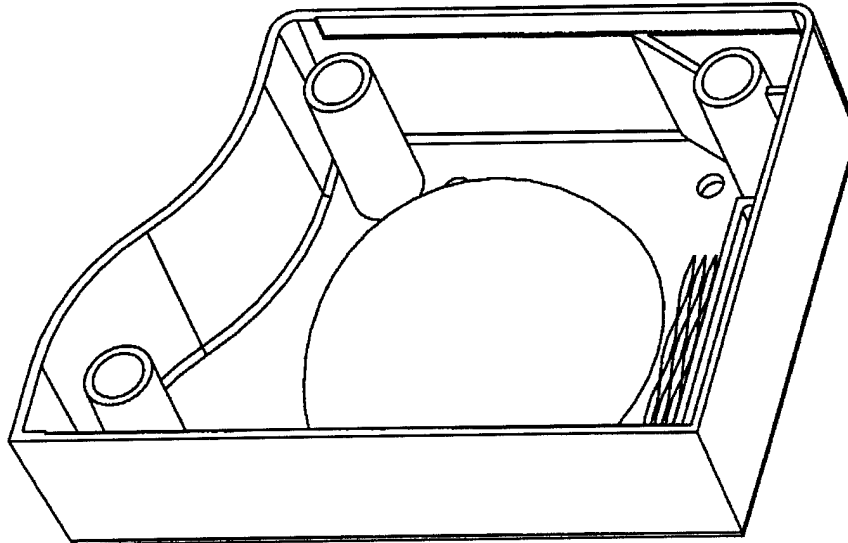


Figure 7 The part we used to demonstrate the conformal cooling design and fabrication ability

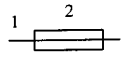
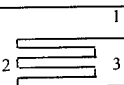
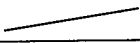
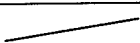
	Cooling zone 1		Cooling zone 2	
Cooling zone Topological Structure		section 1: inlet section 2: 3 parallel line section 3: outlet		section 1: inlet section 2: serpentine cooling lin section 3: outlet
Section No.	1, 3	2	1, 3	2
Cross Section Shape				
Hydraulic Diameter	6.35 mm	2.3 mm	8 mm	4 mm
Cooling Line Length	.03 m	.43 m	.03 m	1.15 m
Pitch Distance	10 mm	10 mm	10 mm	10 mm
Coolant Flow Rate	3 GPM	1 GPM	3 GPM	3 GPM
Reynolds	2800	36,000	2220	62,100
Coolant Pressure Drop	<<1psi	29.6 psi	<<1psi	37.5 psi
Total Pressure Drop	~30 psi		~38 psi	
Vert. Dist. To Mold Wall		2.5 mm		5 mm
Cooling Time		10 sec		10 sec
Max. Stress		< 13,000 psi		< 8094 psi
Part Ave. Temp.		62.95 degC		64.9 degC

Figure 8 Cooling system design results for the 3DP bench mark part

After the design parameters and process conditions for all the cooling cells have been determined, the solutions are mapped back to the entire mold to construct the global cooling system. Figure 1(b) shows the solid model of such a cooling system. The final tool with conformal cooling channels placed is obtained by subtracting the cooling system model from the mold insert and adding the manufacturing tolerance. The .stl file is then created for solid freeform fabrication. Figure 10 shows the resulting green part fabricated by 3D Printing process.

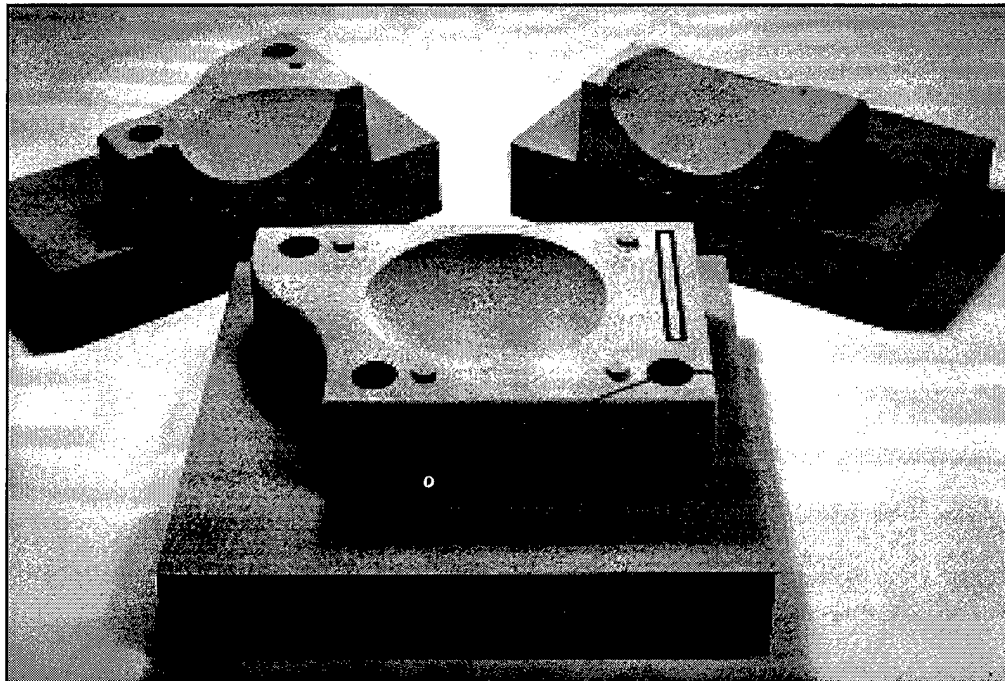


Figure 9 Green part of the insert fabricated by 3D Printing process based on the solid model in Figure 1

## 6. Conclusions

Solid Freeform Fabrication processes such as 3D Printing can create injection molding tooling with complex cooling channels offering the potential for substantial improvement in production rate and part quality. This capability raises the challenge of designing the complex cooling channels required to realize these improvements.

This work presents a systematic method for the design of cooling channels for tooling. First the mold surface is decomposed into manageable sections called cooling zones. Then a system of cooling channels is designed for each cooling zone. This system of cooling channels is further decomposed into smaller elements called cooling cells that are easy to analyze. The cooling cell is a sandwich structure covering the part, the mold and the cooling channel region between two adjacent cooling lines. Six design rules are applied in order to create design windows for the individual cooling cell. These design rules include design for conformal cooling condition, design for coolant temperature drop, design for part ejection temperature, design for

sufficient cooling, design for mold strength and deflection and design for cooling uniformity. After the design for individual cooling cell is finished, the solution is mapped back to the mold in order to build the entire conformal cooling system.

## 7. Acknowledgment

The work discussed in this paper is supported by the Technology Re-Investment Project, Cooperative Agreement (DMI - 9420964) funded by DARPA and administered by NSF, and the 3D Printing Industrial Consortium. The authors thank members of 3DP Consortium and the colleagues of 3DP Lab for their consistent support and encouragement. Special thanks are due to Dick Barlik from Hasbro, who designed the prototype part for the 3DP benchmark tool, David Brancazio and Jim Serdy from 3D Printing Lab of MIT, who took care of most of the work from administration to manufacturing of the conformal cooling project, Dr. K. K. Wang and Dr. Hieber from Cornell Injection Molding Program, who provided generous help and encouragement in mold cooling system design and simulation.

## 8. Nomenclature

$\rho_m, \rho_p, \rho_c$ :	Density of the mold, the plastic part and the coolant
$C_m, C_p, C_c$ :	Specific heat of the mold, the plastic part and the coolant
$K_m, K_p, K_c$ :	Thermal conductivity of the mold, the plastic part and the coolant
$\alpha_m, \alpha_p, \alpha_c$ :	Thermal diffusion of the mold, the plastic and the coolant
$\mu_c$ :	Coolant viscosity
$Re_D$ :	Coolant Reynolds number
$Q$ :	Coolant flow rate
$v$ :	Coolant flow velocity
$h_c$ :	Heat transfer coefficient between mold and coolant
$e$ :	Cooling channel surface roughness
$C_f$ :	Cooling channel surface friction factor
$T_{melt}$ :	Plastic melt processing temperature
$T_{eject}$ :	Plastic ejection temperature
$T_m^s$ :	Cycle averaged mold temperature at steady operation
$T_m(t)$ :	Cycle averaged mold temperature as a function of time
$T_m^s$ :	Cycle averaged mold temperature
$T_c$ :	Coolant temperature
$l_m$ :	Vertical distance from cooling line to mold wall
$l_p$ :	Half the plastic part thickness
$D$ :	Cooling channel diameter
$w$ :	Cooling line pitch distance
$L$ :	Cooling line length
$E_m$ :	Young's modulus of the mold
$G_m$ :	Shear modulus of the mold
$\Delta m$ :	Step length of finite difference nodes for the mold
$\Delta p$ :	Step length of finite difference nodes for the part
$\Delta t$ :	Step length for the simulation time

$t_{cycle}$ : Injection cycle time  
 $\tau$ : mold time constant

## 9. Reference

1. Z. Tadmore, C. Gogos, "Principles of Polymer Processing", Wiley, 1979, p584 - 610
2. R. Pye, "Injection mould design", Longman, 1989
3. N. Rao, "Design formulas for plastics engineers", Hanser, 1991, chapter 6
4. D. Rosato, "Injection Mold Design Handbook", Van Nostrand Reinhold Comp., NY, 1985, Chapter 7, p160 - 234
5. K. Singh, "Design of Mold Cooling System", *Injection and Compression Molding Fundamentals*, A. Isayev Ed., Marcel Dekker, 1991, p567 - 605
6. C. Austin, "Mold cooling", *ANTEC '85*, p764 - 768
7. E. Chu, M. Kamal, S. Goyal, "A Computer Simulation of the Injection Molding Process Including Filling, Packing and Solidification", *ANTEC'89*, p344 - 347
8. T. Kwon, "Application of the Boundary Integral Method to the Nonisothermal Flow of a Polymeric Fluid Advancing in a Thin Cavity of Arbitrary Shape", *CIMP Technical Report*, No. 38 Jan-82
9. T. Kwon, "Mold Cooling System Design Using Boundary Element Method", *ASME Journal of Eng. for Industry*, Vol. 110, p384 - 394
10. L. Turng, "Application of the Boundary Element Method to the Cooling-Line Design for Injection Molds", *CIMP Technical Report*, No. 56, Jan-87
11. L. Turng, K. Wang, "A computer - aided cooling line design system for injection molds", *Journal of engineering for industry*, vol 112, May-90, p161
12. K. Himasekhar, J. Lottey, K. Wang, "CAE of Mold Cooling in Injection Molding Using a Three Dimensional Numerical Simulation", *Journal of Engineering for Industry*, vol. 114, May-92, p213 - 221
13. S. Chen, S. Yu, A. Davidoff, "Hybrid Methods for Injection Mold Cooling Process Simulation and Mold Cooling System Analysis", *ANTEC'91*, p499 - 503
14. S. Hu, N. Cheng, S. Chen, "Effect of Cooling System Design and Process Parameters on Cyclic Variation of Mold Temperatures - Simulation by DRBEM", *Plastics, Rubber and Composites Processing and Applications*, Vol. 23, No. 4, 1995, p221 - 231
15. M. Rezayat, T. Burton, "Combined Boundary-Element and Finite - Difference Simulation of Cooling and Solidification in Injection Molding",
16. Y. Lauze, J. Hetu, "Temperature Prediction of Part and Mold Using Finite Element Simulations", *ANTEC'94*, p809 - 812
17. M. Rezayat, "Numerical Computation of Cooling-Induced Residual Stress and Deformed Shape for Injection-Molded Thermoplastics", *ANTEC'89*, p341 - 343
18. R. Thomas, N. McCaffery, "The Prediction of Real Product Shrinkage Calculated from a Simulation for the Injection Molding Process", *ANTEC'89*, p371 - 375
19. S. Chen, N. Cheng, K. Jeng, "Post-Filling Simulation and Analyses of Shrinkage and Warp of the Injection Molded Parts", *ANTEC'91*, p493 - 498
20. G. Titomanlio, K. Jansen, "In-Mold Shrinkage and Stress Prediction in Injection Molding", *Polymer Engineering and Science*, Vol. 36, No. 15, Aug-96, p2041 - 2049

21. S. Liu, "Modeling and Simulation of Thermally Induced Stress and Warpage in Injection Molded Thermoplastics", *Polymer Engineering and Science*, Vol. 36, No. 6, Mar-96, p807 - 818
22. W. Zoetelief, L. Douven, A. Housz, "Residual Thermal Stresses in Injection Molded Products", *Polymer Engineering and Science*, Vol. 36, No. 14, Jul-96, p1886 - 1896
23. H. L. Marcus, D. L. Bourell, "Solid Freeform Fabrication Finds New Applications", *Advanced Materials & Processes*, Sept - 1993, p28 - 35
24. E. Sachs, M. Cima, P. Willams, D. Brancazio, J. Cornie, "Three dimensional printing: rapid tooling and prototypes directly from a CAD model", *Transactions of the ASME: Journal of Engineering for Industry*, vol 114, no.4, Nov -1992, p481 - 488
25. E. Sachs, E. Wylonis, M. Cima, S. Allen, S. Micheals, E. Sun, H. Tang, H. Guo, "Injection Molding Tooling by Three Dimensional Printing: a Desktop Manufacturing Process", *ANTEC'95*
26. E. Sachs, S. Allen, H. Guo, J. Banos, M. Cima, J. Serdy, D. Brancazio, "Progress on Tooling by 3D Printing: Conformal Cooling, Dimensional Control, Surface Finish and Hardness", *Solid Freeform Fabrication Proceedings*, Sept-1997, p115-123
27. J. Fay, *Introduction to Fluid Mechanics*, MIT Press, 1995
28. Mills, *Heat and Mass Transfer*, Irwin Press, Chicago, 1995

# Investigation of Short Pulse Nd:YAG Laser Interaction with Stainless Steel Powder Beds

W. O'Neill, C.J. Sutcliffe, R. Morgan & K.K.B. Hon

Department of Engineering  
Manufacturing Engineering & Industrial Management  
University of Liverpool  
United Kingdom

## Abstract

The development of metallic object construction has occurred at quite a pace over the last five years with provision of many commercial techniques such as indirect and direct sintering of metal powder beds. Although porosity is still a major problem for metal building a number of notable solutions have been proposed, these include infiltration with low melting point alloys or direct fusing with binary powder mixtures. Neither of these solutions allows one to build components without compromising part strength and functionality. A process route is required that will allow solid parts to be built from a single powder component without requiring time consuming downstream processes. To this end, the present work examines the feasibility of using low energy high peak power laser pulses from a Q-switched Nd:YAG laser to melt stainless steel powder fractions whilst examining the melt displacement through high recoil pressures induced by rapid partial vaporisation of the powder layer. The effect of laser pulse energy, laser beam intensity, pulse frequency, and environmental gas control on the integrity of the fused powder layer is presented.

## 1.0 Introduction

The introduction of Rapid Production Technologies (RPT) into modern manufacturing has been received with great applause from product designers and manufacturing engineers. The use of RPT has facilitated shorter lead times on product development and the ability to produce design iterations without the time and cost penalties associated with traditional product development cycles. Rapid prototyping quickly emerged as a completely new tool for product development tasks which in turn initiated a number of research and development programmes for rapid tooling processes that allowed small batch production to become cost effective. The manufacturing engineer has a wealth of small to medium batch processes such as investment casting, vacuum casting, AIMS<sup>TM</sup> tooling, Keltool<sup>TM</sup> and Rapidtool<sup>TM</sup>. Whilst these processes provide sufficient scope for injection mould tooling certain compromises have to be made with regard to lifetime, lead-time, material properties, accuracy and scale. These compromises must be eradicated if we are to realise true rapid manufacturing for both functional components and tooling.

Of the main RPT processes selective laser sintering provides the widest range of build materials which include a variety of polymers and a number of metal based materials. The accuracy of parts produced by SLS is no greater than that achieved with stereolithography, although the ability to produce functional parts directly from the SLS build chamber gives the SLS process considerable advantages over other RPT. When it comes to metallic object construction there are a number of SLS methods which have been used as shown in Figure 1.

Direct metal sintering relies on laser induced melting to couple powder particles together, significant thermal gradients exist using this route unless the powder bed temperatures are controlled to a value just short of the powder melt temperature. This approach reduces problematic temperature gradients and produces parts with minimum internal stresses. Porosity is still a problem which is normally reduced by post sintering or infiltration.

Indirect sintering of metals relies on melting of the polymer coating on each metal particle, this "green" part can then be handled with subsequent de-binding, sintering and low melting point infiltration stages which are necessary to produce a solid high density part [1,2].

Binary phase sintering has been investigated by a number of workers [3,4,5]. This process involves the illumination of a composite powder mixture such that a particular phase of the powder is melted in preference to the other. Examples of binary mixtures include Cu-Ni; Fe-Co; W-Mo. The low melting point components are employed to effect bonding within the mixture.

Objects built via the above routes are generally not suited for heavy duty functional parts since the majority of infiltrates and binary phase materials are low melting point metals with low mechanical strength. Parts produced thus have the strength and performance characteristics of their weakest composite phase. The production of fully functional parts requires processing routes that result in near 100% density from a single powder, i.e., stainless steel, tool steels, titanium etc. It is clear from the literature that there have been few attempts to condition the laser-material interaction such that laser induced non-thermal effects are generated to aid the melting and densification of powder beds in a single step. To this end, this work presents preliminary results of laser induced high pressure direct sintering of 316 stainless steel powder beds.

## 2.0 Background

The majority of laser based RPT utilise CO<sub>2</sub> gas lasers or in some cases solid-state Nd:YAG lasers. In commercial applications of SLS a 50W or 100 W CO<sub>2</sub> laser are used to thermally activate the powder bed. If melting occurs the process relies on surface tension driven melt displacement to distribute the molten volume and bond nearest particles into a conglomerate that is near full density or significantly less than full density, depending upon the interaction parameters. Fusion based processes of this kind are very susceptible to unwanted thermal gradients which reduce the chance of wetting leading to balling phenomena and poor layer properties. It is useful at this stage to examine the traditional approach to making components from metal powder. Conventional powder metallurgy processes use high temperatures and high pressures to squeeze powder beds into shapes formed by mould cavities or dies [6]. The high pressures ensure high levels of compaction and even at room temperature one can approach the full density of the material when multi-modal powders are used. The application of heat provides the energy necessary for transfer of matter from one particle to the other resulting in a strong diffusion based solid-state bond allowing full densities to be achieved. None of these processes occur in conventional selective laser sintering of metals, the pressures are too low by several orders of magnitude, the laser interaction duration is too short by several hundred orders of magnitude. Table.1 gives typical pressures and temperatures used in the powder metallurgy industry for part forming and sintering.

One can see from Table1 that SLS processes operating at atmospheric pressure are severely handicapped in terms of high density part production. It is for this reason that downstream infiltration and sintering processes are used in conjunction with SLS to increase part functionality and strength.

Attainment of the temperatures presented in Table 1 are not difficult with laser powers even as low as 50W. The SLS systems are capable of melting most materials even ceramics, indeed their ability to fuse materials is the basis of all SLS processes. Interaction times to promote diffusion of matter between particles and promote necking are typically several minutes or longer. Given that the laser

illuminates small areas for definition of part geometry, the dwell time per unit area is generally of the order of milliseconds, much too short to promote solid-state bonding.

It is well known that surface tension forces play an important role in shaping the melt beads that are generated in direct SLS of metals. Cold powder beds will often lead to minimal wetting between the powder bed and the melt bead. Increasing the bed temperature to several hundred degrees Celsius will increase wetting and melt bead balling reduces thereby allowing greater control over part geometry. Unfortunately, there is the possibility that other natural forces are at work which lead to modifications of the melt bead shape, namely Marangoni forces. Marangoni forces are the result of steep temperature gradients across the melt bead that generate surface tension gradients which in turn generate convective mass transfer and local reciprocal stirring of the melt volume. This effect is recognised in laser welding and has a significant effect on the melt geometry. It is likely that under continuous wave laser illumination Marangoni flow may be occurring in the melt bead generated on the surface of the powder bed, although it is not known to what extent it influences the melt bead geometry in this case.

In pulsed laser interactions there is the strong possibility of plasma generation which in turn will lead to forces that allow for modification of the melt pool and hence the shape of the laser generated bead. This is a particularly interesting avenue since it may lead to more controllable bead formation which in turn may increase part accuracy and particularly part density. Consider the situation shown in Figure 2, a pulsed laser interacts with a leveled powder bed over nanosecond time scales such that the peak pulse powers are of the order of several hundred kilo Watts for average powers of around 100W. Rapid heating of the substrate occurs which produces melting, vaporisation and finally partial ionisation of the vapour. The partial ionisation or plasma is fed by vaporised matter leaving the surface of the substrate at velocities up to  $10^5$  m/s. The net result is a shock wave travelling toward the laser beam and a recoil shock travelling away from the laser beam and into the substrate. Recoil pressures of the order of 400 MPa are possible with peak power densities of the order of several  $\text{GWcm}^{-2}$  [7]. This regime is of interest to the authors as it may provide the pressures necessary for localised melt/powder compaction which will produce higher density parts than is possible with continuous wave (CW) laser beams. It is also possible that a second benefit may be the ability of the recoil shocks to overcome surface tension forces and prevent balling of the melt pool (enforced wetting).

It is clear that a balance must be sought between melt production and shock formation, excessive pressures will lead to explosive removal of the powder bed rather than melt displacement. This paper presents the results of a preliminary examination of the interaction characteristics of nanosecond laser pulses and stainless steel powder beds.

### 3.0 Experimental Arrangement

An experimental SLS test facility was constructed consisting of a Rofin Sinar 90W flash-lamp pumped Q-switched Nd:YAG laser with a frequency range of 0 to 60 kHz. Typical pulse energies and pulse widths were in the range 0.2-3 mJ and 80-250 ns respectively. The laser was apertured in order improve the mode quality and therefore focusability of the beam. Plots of laser power output verses pulsing frequency are shown in Figure 3 for a number of lamp currents in the range 12-20 Amps. One can see that continuous wave operation (CW) provides the highest average output power of 15W at 20 Amps lamp current. Powers quoted here are measured at the surface of the powder bed. Line scanning was achieved using a RSG1014 galvanometer scanning head containing 2 thermally regulated S10 galvanometers giving a scanning speed range of 1-500 mm/s over an 80mm by 80mm area. The focal length of the imaging lens was 112mm giving a minimum spot size of  $50\mu\text{m}$ .

Computer control of both laser parameters and scanning is accomplished using an IBM compatible PC running Rofin Sinar's LaserWorkbench software under the OS2 operating system. This software not only allows scanning of many image types but also enables programming of scanning trajectory and the setting of all process variables from within a Pascal based programming language.

The build chamber consists of a build cylinder and powder delivery cylinder each 100 mm diameter powered by 2 linear stepping motors with minimum step size of 0.25 microns and maximum stepping rate of 380 steps per second. 316L Stainless powder with a mode size of 20 $\mu$ m is delivered to the build chamber by a 70 mm diameter counter rotating roller driven by a DC servo motor. The build chamber is computer controlled via a PC based SM30 3-axis stepper motor controller which simultaneously controls powder feeder, build platform and sweeper assembly. In house control software was used to link the laser system with the SLS build chamber thereby effecting full control over the experimental system. This preliminary investigation made no attempt to control powder bed temperatures in order to identify the benefits of the plasma initiated high pressure interaction.

## 4.0 Experimental Procedures

Powder beds some 300 $\mu$ m thick were metered onto the build platform. After a suitable purging operation the chamber was filled with Ar shroud gas (99.999%) in order to minimise oxidation effects. This is particularly important with Stainless Steel powders as the melt temperature of the chromium oxide is substantially higher than that of iron which causes problems when super heated pockets of molten iron are trapped within a "bag" of chromium oxide. Further heating of these oxide "bags" leads to catastrophic failure and explosive release of molten iron which dramatically reduces the controllability of the process.

A series of interaction trials were run to characterise the general nature of the interaction for a number of parameters and classify the interaction site in terms of the observed effects as a function of the value of the parametric variables i.e. crater formation, balling and melting. The parametric variables were: frequency  $f$  0-60kHz; scanning velocity  $v$  100mms<sup>-1</sup>; Lamp current  $I$  0-20Amps; peak power density  $P_p$  2kW-1.4GWcm<sup>-2</sup>, Scan line overlap 25% of line width. The system configuration enabled a matrix of 100 parametric values to be tested at once which made data collection highly efficient and allowed easy comparisons to be made between the data sets. A schematic example of the arrangement is shown in Figure 4. Sintered pads of around 3mmx3mm were produced for a selection of data within the parametric variable range.

## 5.0 Results and Discussion

Figure 5 is a photograph of the undisturbed powder bed at 50x magnification with an insert photograph at 500x magnification. One can see that in general the mode of the powder is lower than the 20 $\mu$ m as given by the manufacturer. Low mode numbers are preferred in this work due to the small laser beam diameters that can be achieved with the experimental arrangement. Although low mode numbers make powder handling more difficult they generally increase laser beam absorption compared to high mode numbers. A full set of single layer interactions were investigated for a range of parameters. Within the grid array described above it is possible to change pulse frequency and laser power and produce a single layer pad for each pair of parameters. The results of these investigations produce a process map which have been analysed by optical and scanning electron microscopy. The following sections discuss the general features of the process maps for three laser spot diameters, 50 $\mu$ m, 150 $\mu$ m and 300 $\mu$ m. We have chosen to view the results obtained at varying spot diameter rather than speed because changes in spot diameter will significantly affect recoil pressures induced on the target powder bed.

### **5.1 Laser Spot Diameter: 50 $\mu$ m**

Using a laser spot diameter of 50 $\mu$ m allows significant recoil pressures to be generated on the powder bed. These are so great that significant levels of powder are blasted from the interaction site preventing samples from fusing. Figure 6 gives the process map for this spot diameter. One can see that a threshold current of 1.9 A is required in order to initiate melting, this is the case throughout the frequency range of 0-60kHz. In the case of the continuous laser beam (CW) pads were produced which could be handled at a current level of 11.9A. Pads produced above this limit suffered an increased surface roughness with current. A distinct region of high recoil pressures is realised above 6.6 kHz with the region extending to high frequencies as the lamp current is increased. Low frequencies give high peak powers per pulse and result in large shock formations accompanied by bright plasma plumes characteristic of an ion plasma. In this region the powder bed was blasted away. Increasing the pulse frequency reduces peak powers and although shock waves are present they are incapable of displacing significant amounts of powder. In this region the pads were melted and could be handled quite easily. Operating above 40kHz and 18.8 Amps produced pads that were fused to the holding platform which was some 300 $\mu$ m below the top of the powder layer.

### **5.2 Laser Spot Diameter: 150 $\mu$ m**

Increasing the spot diameter allows one to change both the given peak power density and the area of the interaction per pulse. In this section the results for a spot diameter of 150 $\mu$ m are presented which represents a substantial decrease in peak power density compared to that at 50 $\mu$ m. This subsequent reduction in peak power density has reduced the scale of powder displacement although lamp currents above 12.5 A and frequencies up to 40kHz produce volumes of powder displacement which prevent the formation of single layer pads. The zone of effective fusion is shown on the top right of Figure 7. Surface roughness scales with lamp current as melt volumes increase and surface tension forces induce slight balling phenomenon.

### **5.3 Laser Spot Diameter: 300 $\mu$ m**

In this section the data for a spot diameter of 300 $\mu$ m is presented. As can be seen from Figure 8 the peak powers have reduced to the point that powder remains in contact with the bed and damaging recoil pressures are absent throughout the range of parameters. The usual threshold for significant particle melting is present at around 12.0 Amps. Increasing the lamp current for a particular pulse frequency serves to raise melt volumes and surface tension forces pull the pads into a rough featured layer. In this data set the effects of curl are beginning to show which is indicative of thermal stresses induced by the temperature gradients within the powder bed. It is interesting to note that the smaller spot diameters produced little evidence of curling.

### **5.4 Scanning Electron Micrographs**

In order to identify specific features in the fused zones it is necessary to use scanning electron microscopy. The density of the layers is important in that the objective of the research is to produce a solid metal build process without the need for downstream processing routes such as infiltration or upstream processing routes such as binary phase mixtures. In this respect the samples were analysed for variations in the observed porosity under high magnification. The results are presented below.

Figure 9 presents photomicrographs at a magnification of 50x for three pads produced with a beam diameter of 150 $\mu$ m and the following beam parameters: 9a) CW @ 20A, 15W; 9b) 40kHz @ 20A, 11W average; 9c) 60kHz @ 20A, 12.6W average. Refer to figure.7 for their position on the process map at 150 $\mu$ m diameter. One can see that the CW sample is exhibiting fusion along the scanning direction (left to right), with high levels of porosity between scans. Figure 9b shows less balling with little evidence of a visible line scan direction. Surface melt would have little time to flow in the pulsed interaction due to the extremely short freeze-out times associated with heating *and* cooling on nanosecond time-scales. Although blast waves from rapid surface heating could conceivably displace the melt during its lifetime. Figure 9c shows the pad surface at a frequency of 60kHz. In this case we have a surface which is less porous than 9a or 9b.

Figure 10 presents photomicrographs at a magnification of 50x for three pads produced with a beam diameter of 300 $\mu$ m and the following beam parameters: 10a) CW @ 20A, 15W; 10b) 20kHz @ 20A, 10W average; 10c) 40kHz @ 20A, 11W average; 10d) 60kHz @ 20A, 12.6W average; Refer to figure.8 for their position on the process map. Figure 10a, the CW sample, shows significant fusion and melt flow with high levels of porosity at the surface still evident. The scan lines in this case are at 45 degrees to the horizontal and can be seen to be the planes of maximum porosity. Figure 10b gives the surface of a pad produced at two thirds the power of sample 10a and is exhibiting less porosity and no evidence of scanning direction. This trend increases with pulse frequency until the maximum at 60 kHz. Here, Figure 10d, shows almost zero surface porosity and has no evidence of the scanning direction.

There is clearly a difference between the interaction of a pulsed laser beam and one operating continuously. We have argued that recoil pressures associated high peak powers may improve the density of laser fused metal powder beds to some degree. The above results, especially those of Figure 10, indicate that melt movement is affected by the pulsed interaction. It is not clear what the mechanism is at this stage of the investigation. All of the above samples have been produced at high lamp currents. The effect of pulsed illumination is shown more clearly in Figure 11 with samples produced at a lamp current of 13.3 Amps at 60 kHz and CW operating modes. It is clear that in Figure 11a that continuous illumination has aided melt displacement through surface tension forces, unlike that of Figure 11b where the melt has been fused in-situ with almost no movement. Greater understanding of this phenomenon requires more data. To this end experiments are in progress to examine the pulsed illumination event in greater detail.

## 6.0 Conclusions

This work has presented preliminary results of the interaction effects of short pulsed Nd:YAG laser light on 316 Stainless Steel powder beds. Results have indicated that improvement in surface quality can be achieved with optimised laser beam interaction parameters. The mechanisms that are at work in the case of pulsed illumination are not fully understood. Further experiments are in hand to gain more information on the means by which pulsed laser light affects the surface of powder beds.

## 7.0 Acknowledgements

The authors would like to thank the EPSRC and Lever Brothers PLC for their support of this program through a ROPA grant, in particular we are indebted to Mr Jim Rait of Lever Brothers PLC for his financial support and encouragement during the course of this work. We would also like to thank Mr. Lawrence Bailey, a technician on the project for his invaluable assistance during the design and fabrication stages of the build chamber.

## 8.0 References

1. Badrinarayan, B. "study of the selective laser sintering of metal-polymer powders", PhD thesis, University of Texas at Austin, Austin, Texas, 1995.
2. Badrinarayan, B., Barlow, J.W., "Prediction of the thermal conductivity of beds which contain polymer coated metal particles", Proc. Solid Freeform Fabrication, University of Texas at Austin, Austin, Texas, pp91-97, 1990.
3. Manriquez-Frayre, J.A., & D.L. Bourell, "Selective laser sintering of binary metallic powder", Proc. Solid Freeform Fabrication, University of Texas at Austin, Austin, Texas, pp99-106, 1990.
4. Manriquez-Frayre, J.A., & D.L. Bourell, "Selective laser sintering of Cu-Pb/Sn solder powders", Proc. Solid Freeform Fabrication, University of Texas at Austin, Austin, Texas, pp252-260, 1991.
5. Nyrhila, O, "Manufacture of dimensionally precise pieces by sintering", US Patent, 5061-439, 1991.
6. Kuhn, H.A., and Ferguson, B.L., "Powder Forging", Princeton, N.J., Metal Powder Industries Federation. 1990.
7. Kyo-Dong, S. and Alexander, D.R., "Propagation velocities of laser produced plasmas from copper wire targets and water droplets", J.App.Phys. 76 (6), 3302-3312, (1994).

Table.1 Typical operating parameters for traditional sintering processes

Material	Pressure (MPa)	Temperature ( $^{\circ}\text{C}$ )	Duration (Min)
Stainless Steels	370-875	1100-1290	30-60
Brass	400-700	760-900	10-45
Bronze	200-275	1100-1290	30-60
Iron	350-800	1000-1150	8-45
Cemented Carbides	140-400	1430-1500	20-30

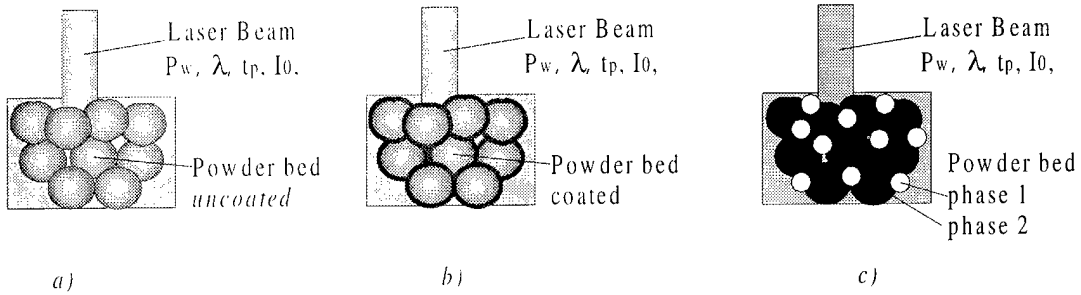


Figure.1 a) direct metal sintering, b) indirect sintering, c) binary phase sintering

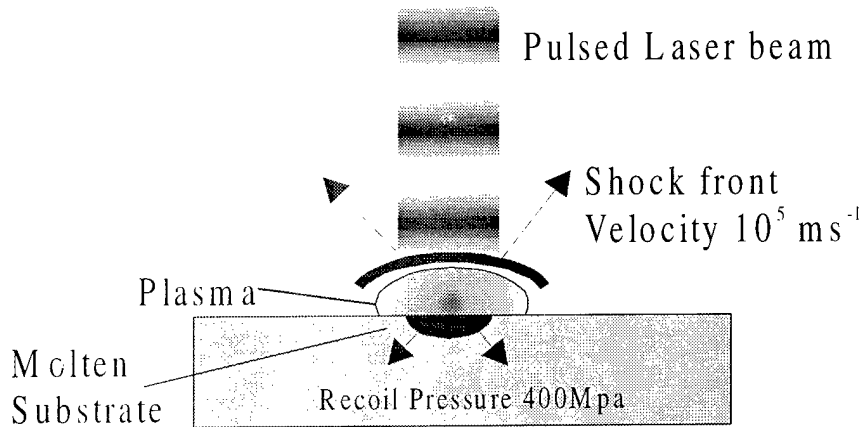


Figure.2 Interaction of a Q-switched laser pulse and the associated shock wave.

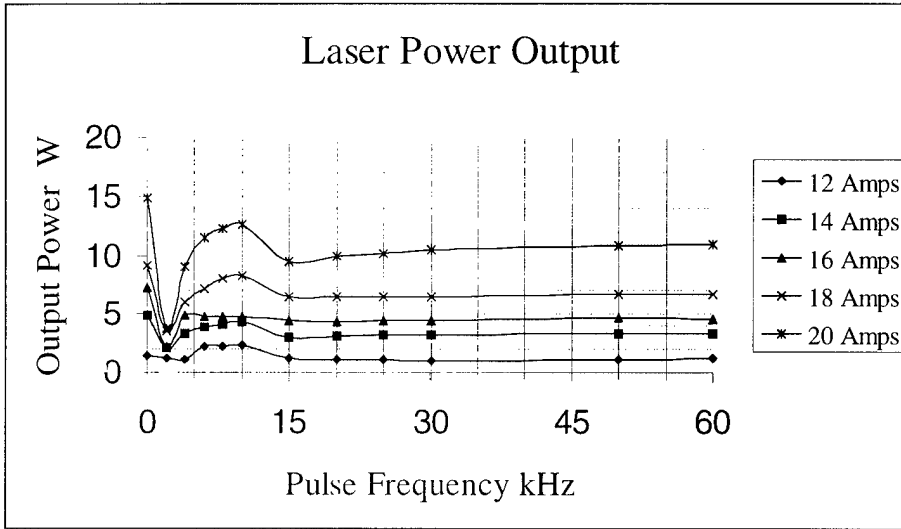


Figure.3 Laser power output characteristics

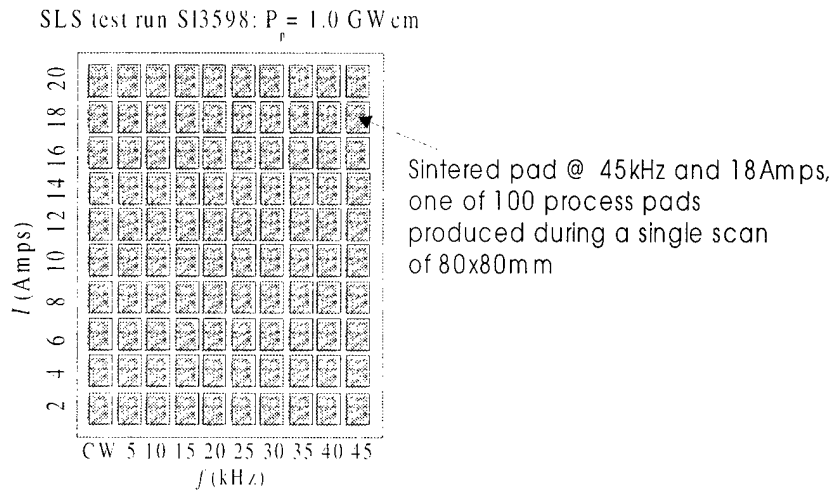


Figure.4 Schematic arrangement of interaction tests showing individual pads.

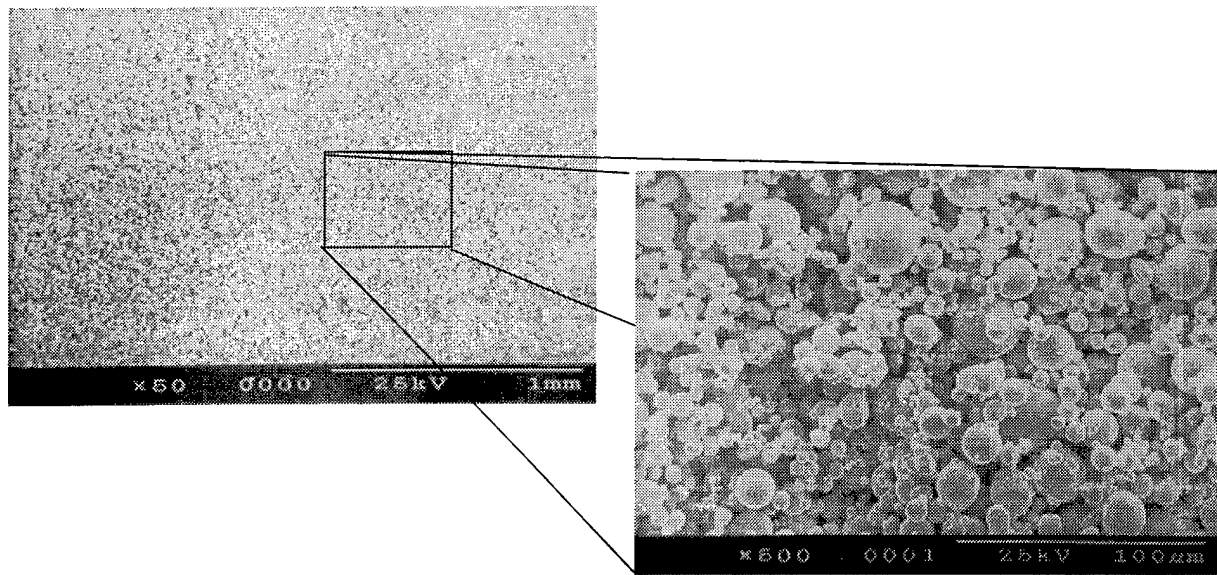


Figure.5 SEM of the unexposed powder bed at 50x magnification with inset at 500x magnification..

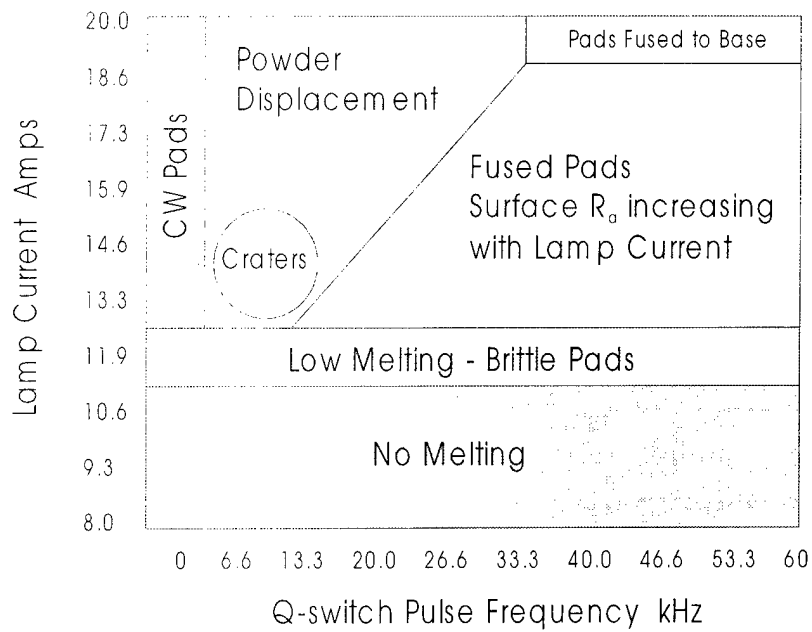


Figure.6 Process map of laser-powder interaction, laser beam diameter 50 $\mu$ m.

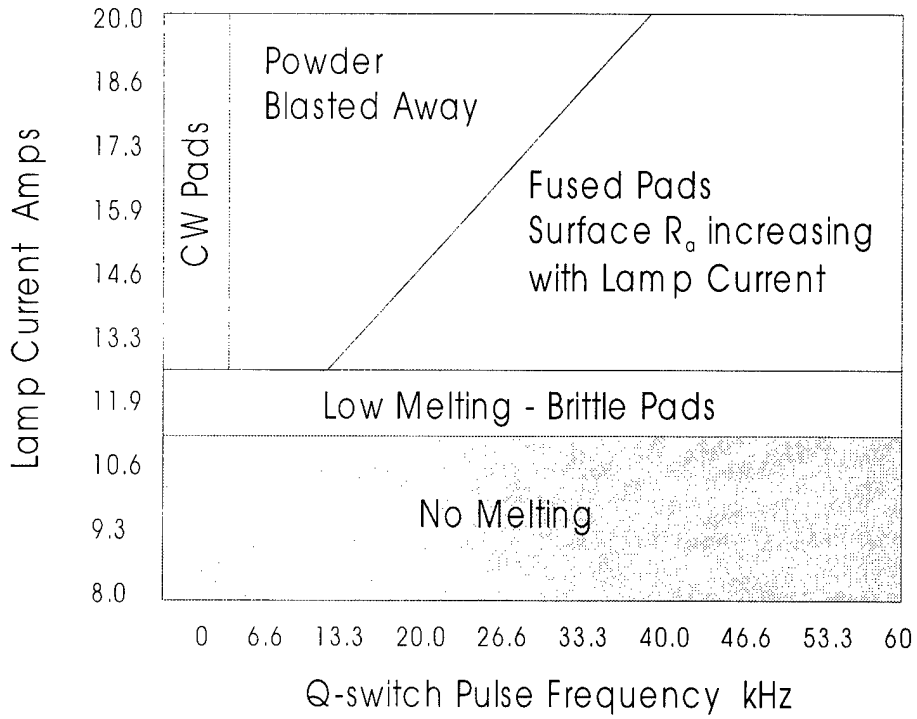


Figure.7 Process map of laser powder interaction, laser beam diameter 150µm.

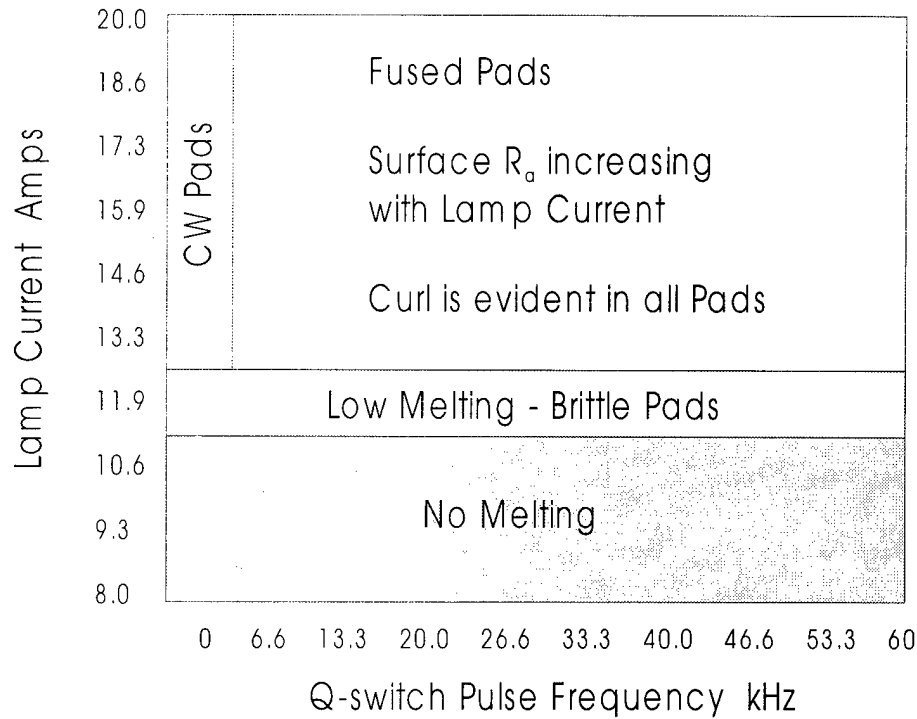
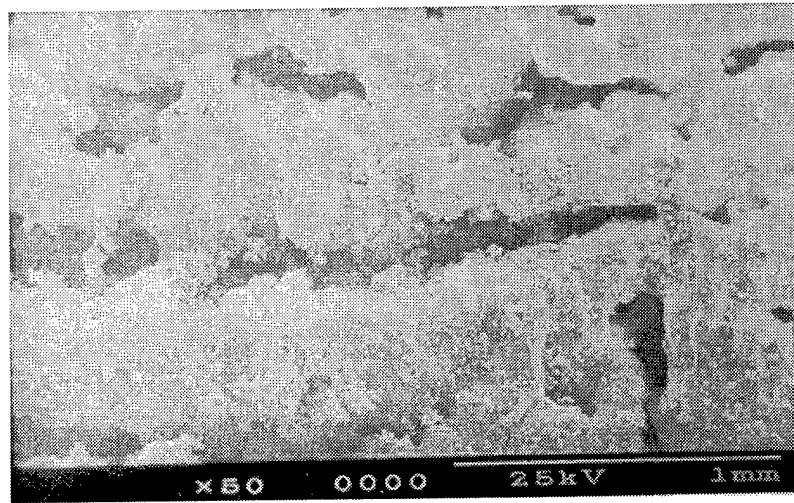
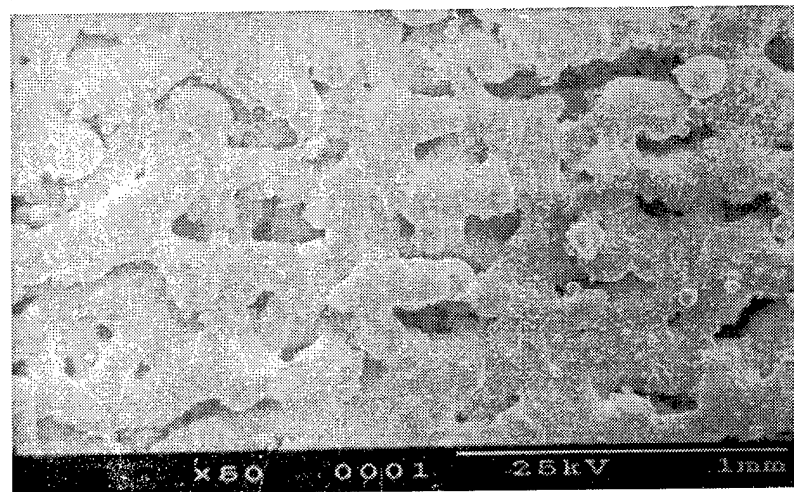


Figure.8 Process map of laser powder interaction, laser beam diameter 300µm

a)



b)



c)

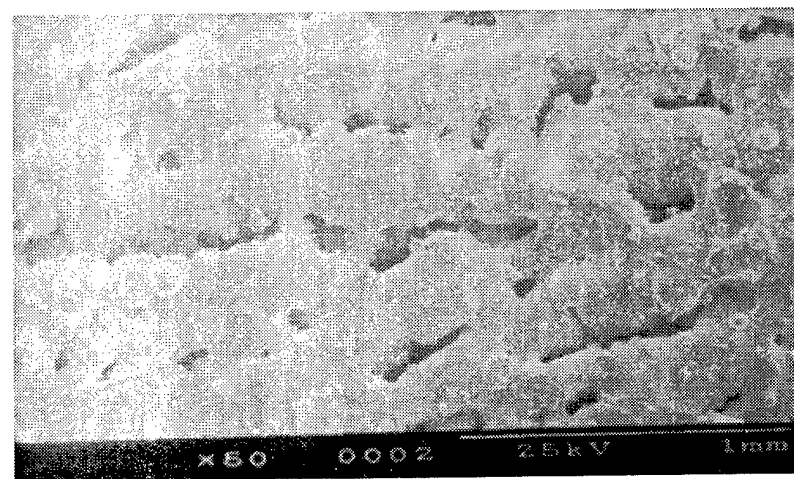
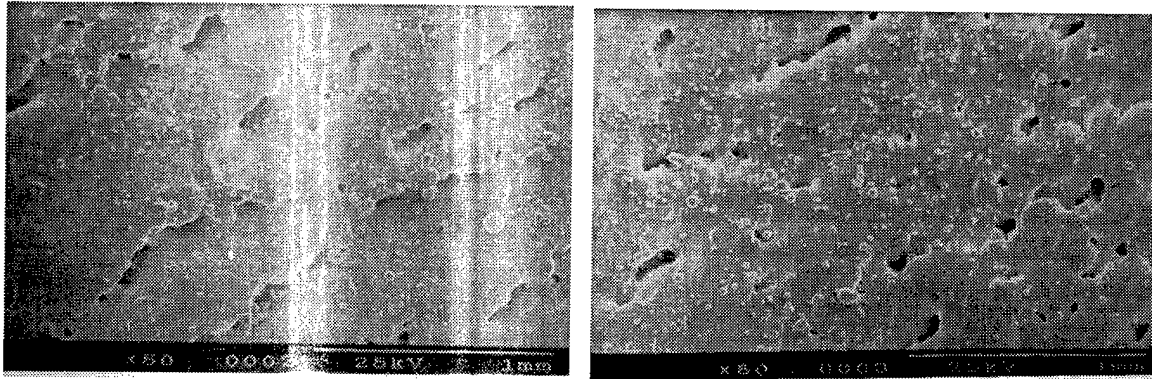
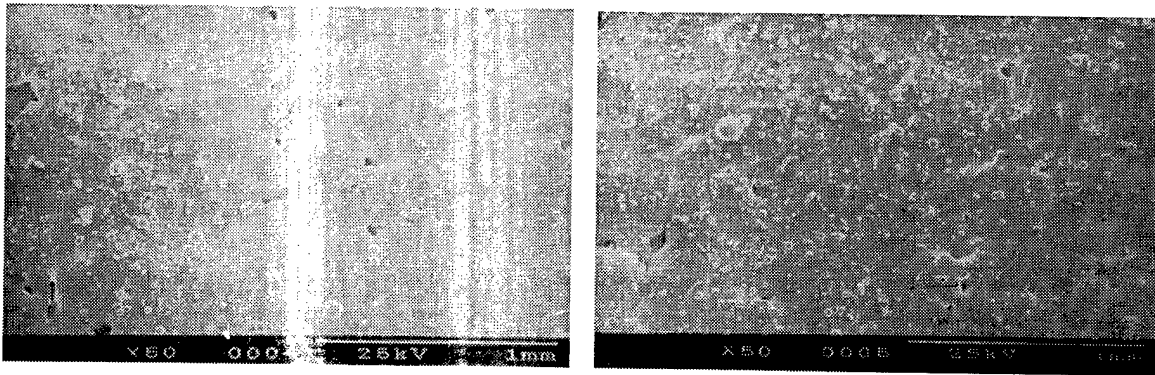


*Figure.9* micrographs of pads produced using a beam diameter of  $150\mu\text{m}$   
a) CW @ 20A and 15W, b) 40kHz @ 20A and 11W, c) 60kHz @ 20A  
and 12.6W.



a)

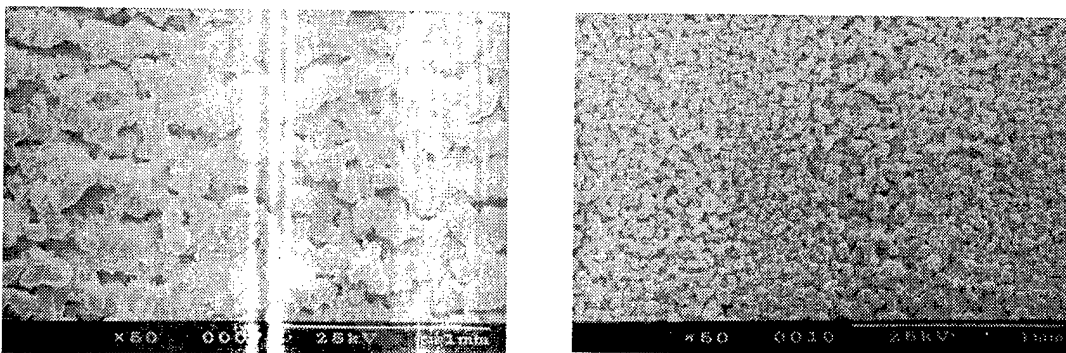
b)



c)

d)

*Figure.10* micrographs of pads produced using a beam diameter of  $300\mu\text{m}$   
 a) CW @ 20A and 15W, b) 20kHz @ 20A and 10W, c) 40kHz @ 20A  
 and 11W, d) 60kHz @ 20A and 12.6W.



a)

b)

*Figure.11* micrographs of pads produced using a beam diameter of  $200\mu\text{m}$   
 a) CW @ 13.3A and 4W, b) 60kHz @ 13.3 A and 4.4W.



# EFAB: Batch Production of Functional, Fully-Dense Metal Parts with Micron-Scale Features

Adam Cohen, Gang Zhang<sup>1</sup>, Fan-Gang Tseng, Florian Mansfeld<sup>1</sup>, Uri Frodis, Peter Will  
USC/Information Sciences Institute, 4676 Admiralty Way, Marina del Rey, CA 90292

## Abstract

EFAB (Electrochemical FABrication) is a new SFF process with the potential to economically fabricate prototypes or mass production quantities of functional, mesoscale-microscale parts and mechanisms. EFAB generates an entire layer simultaneously—versus serially, as with most SFF. Based on electrodeposition, EFAB allows ultra-thin layers (2-10 microns, or even submicron) that minimize stairsteps, and generates a net-shape, fully-dense metal structure that can be homogeneous and isotropic. Minimum feature width is approximately 25 microns, and can be reduced further. EFAB can be used to manufacture micromachines and microelectromechanical systems (MEMS), offering significant advantages over current processes: e.g., true 3-D geometry, IC compatibility, low capital investment, and process automation.

## Background

Microfabrication. During the last decade, there has been extensive worldwide R&D in the field of micromachining/microfabrication. There is much interest in replacing macroscopic devices with micromachines and microelectromechanical systems (MEMS) to reduce size, weight, and cost while often increasing reliability and performance. There is also a desire to create devices offering entirely new capabilities not possible to implement macroscopically (e.g., surgical instruments, mechanical high-resolution displays).

Current microfabrication approaches generally fall into three categories [1]: Bulk micromachining removes material selectively from regions of a substrate (sacrificing precious chip “real estate” and producing very simple shapes); surface micromachining (Fig. 1) deposits thin structural layers and sacrificial layers onto a substrate using semiconductor-type processing; and LIGA generates 2.5-D “extrusions” (Fig. 1) by molding polymers in metal tooling electroplated into apertures in synchrotron-exposed photoresist. All these approaches produce simple geometries (e.g., 1-5 different cross sections), are not standardized or particularly generic (usually requiring a custom process for each new device), and require many manual steps (each using specialized equipment). Moreover, they usually do not permit integrated circuitry to be part of the device, involve large numbers of process variables (often requiring multiple iterations to perfect), are very costly (in facilities, capital equipment, labor, and materials), and involve long lead times.

As a manufacturing paradigm, Solid Freeform Fabrication can potentially overcome the shortcomings of current microfabrication approaches. SFF can offer arbitrary 3-D geometry; short lead times; fully-automated, unattended processing; a single, self-contained machine that produces a huge variety of products; device cost that is largely independent of complexity; high repeatability (few processing variables); and easy device design (few manufacturing constraints). Indeed, in the micro- and mesoscopic

---

<sup>1</sup> University of Southern California, Department of Materials Science & Engineering

(between micro and macro) domain, where there are no existing generic fabrication technologies (such as milling and casting that we take for granted in the macroscopic world), many devices are made with great difficulty or not at all. Here SFF can go far beyond its usual role as a tool to increase speed and reduce cost, becoming instead a tool that makes possible for the first time the manufacture of a entire class of new products.

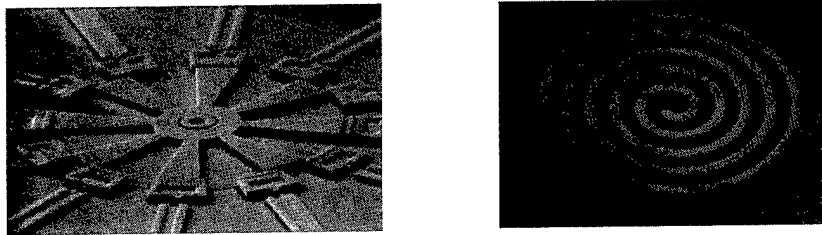


Fig. 1. Typical devices produced by surface micromachining (left) and LIGA (right).

Unfortunately, most SFF processes, intended as they are for producing macroscopic parts, normally cannot produce features less than 50-100  $\mu\text{m}$  wide, or layers less than 50-150  $\mu\text{m}$  thick. Moreover, virtually all SFF processes generate a layer serially (one volume element at a time), so are too slow and costly for quantity production. Nor do materials often allow functional use, due to intrinsic properties or porosity. Some processes are not net-shape, requiring support structures which must be explicitly designed and removed from each device. For example, microstereolithography [2], while succeeding in generating small features and layers, is limited in throughput, produces parts from photopolymer, and requires supports.

Electrodeposition for SFF. If an SFF process could be developed based on selective electrodeposition of material, it might be used for micro- and meso-fabrication, overcoming the limitations of existing microfabrication and SFF processes. Electrodeposition is a tremendously important manufacturing process used to finish metal parts (in the case of electroplating), and also to manufacture metal parts by depositing metal over molds (in the case of electroforming). Electrodeposition takes place in an electrochemical cell consisting of two electrodes, an anode and a cathode (i.e., workpiece or mold) and an electrolyte. Compared with the additive approaches used by most SFF processes, electrodeposition is fundamentally different. The material is “grain-less”, deposited one atomic layer at a time (vs. particle-by-particle or drop-by-drop); and the solid produced can have desirable material properties, since it is fully-dense and relatively homogeneous and isotropic (e.g., inter-layer junctions can be avoided). Moreover, material may be deposited over an entire layer (e.g., hundreds or thousands of parts) simultaneously.

An earlier approach to SFF by electrodeposition, invented at MIT, arranged for deposition to occur preferentially in a localized region due to high current density near a sharpened anode that is moved in a 3-D path [3]. However, even using multiple anodes, this process seems too slow for mass production, is unable to easily create parts with overhangs (since it lacks a support material), and suffers from imprecisely-defined features. More conventional approaches to selective electrodeposition, apparently never attempted for use in SFF, are “brush plating”, in which electrolyte is applied locally to a substrate; and “laser-enhanced plating”, in which the plating rate is locally accelerated by heating. These processes too are essentially serial and therefore slow, and have difficulty producing very small, well-defined features.

The standard approach to high-precision selective electrodeposition—used in the manufacture of PC boards and read-write heads—is known as “through-mask plating”. Through-mask plating can be used to deposit features 1  $\mu\text{m}$  or smaller. With this method, the substrate is prepared, photoresist is applied, the resist

is UV exposed and developed, the substrate is plated through apertures in the insulating resist, and the resist is finally stripped. This entire process involves a total of up to nine separate steps, the use of several different machines (often located in a cleanroom), and multiple liquids. Automation would lead to a machine of great complexity and high cost. Furthermore, total cycle time is large, so repeating these steps hundreds or thousands of times to fabricate a 3-D part would be impractical.

### Instant Masking

A new method of achieving selective electrodeposition is therefore necessary for a viable SFF process. We have devised such a method, which we call "Instant Masking". As with through-mask plating, Instant Masking uses photolithographically-patterned masks, and deposits material simultaneously over the entire layer (which may consist of a batch of discrete devices). Yet unlike through-mask plating, Instant Masking allows the photolithographic process to be performed completely *separate* from the part-building process, and allows *all* of the masks to be generated simultaneously *prior to* part generation, rather than *during* part generation (again and again for every layer). This separation also makes possible a simple, low-cost, automated, self-contained machine that builds devices, while the photolithographic steps can be handled in a traditional cleanroom (e.g., with masks provided by a service bureau).

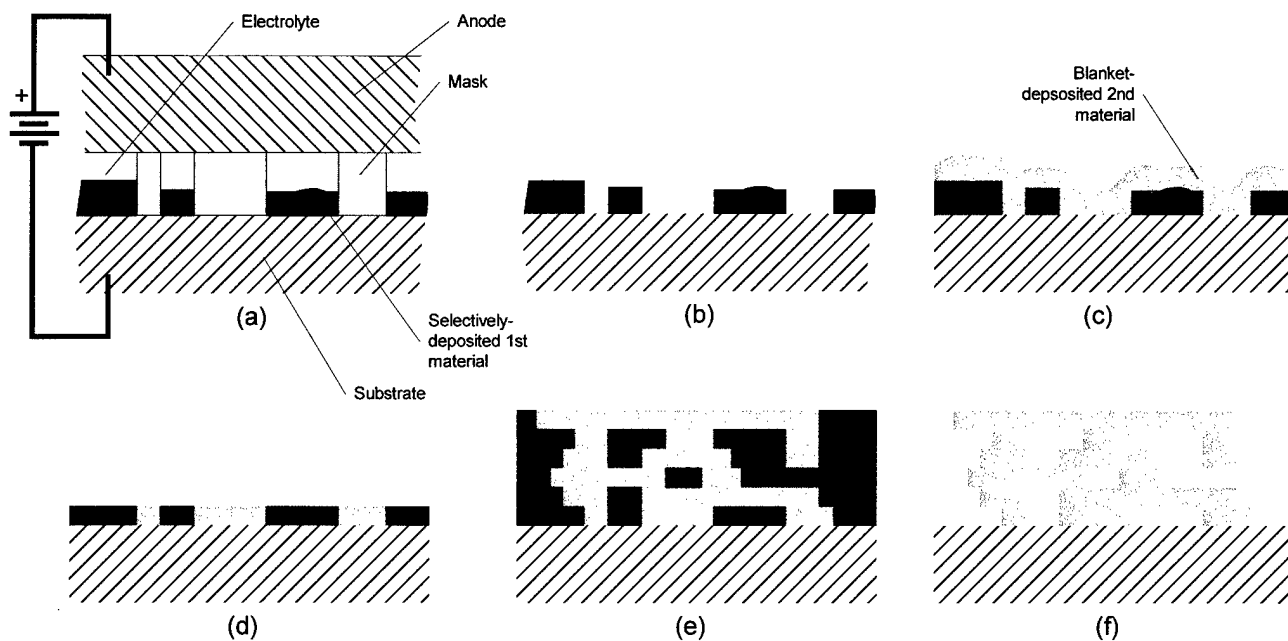


Fig. 2. Stages in the EFAB process.

Instant Masking selectively deposits material onto a substrate (or previous layer) by simply mating a patterned mask against the substrate, depositing material through apertures in the mask, and then un-mating the mask. Since the mask may be topologically complex (e.g., consist of isolated "islands" of masking material), it must be attached to a support structure, which in our current implementation is simply the anode of the electrodeposition cell. This configuration is shown in Fig. 2 (a).

## EFAB

We call the new SFF process we are developing—based on selective electrodeposition using Instant Masking—EFAB (Electrochemical FABrication). A completed layer in EFAB consists of both structural and sacrificial material, as shown in Fig. 3. The block of sacrificial material in which EFAB-built devices are temporarily embedded serves the same purpose as sacrificial material used in SFF processes such as those of Cubital and Sanders Design: mechanical support of structural material. This eliminates most restrictions on device geometry, allowing the structural material on a layer to overhang—and even be disconnected from—that of the previous layer. Such geometrical freedom also makes possible monolithically-fabricated “assemblies” of discrete, interconnected parts (as with Cubital’s Geneva mechanism demonstrated in the early ‘90s). This is a necessity for micro- and mesoscopic devices, for which actual assembly is generally not possible. Furthermore, the placement of the sacrificial material, and its ultimate removal in an automated, batch process, is not device-specific (avoiding the need for explicit support design).

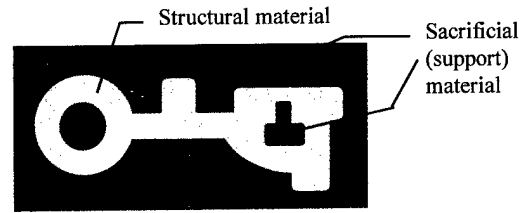


Fig. 3. Plan view of a layer in the EFAB process.

In our current implementation, the process consists of the following steps, repeated on every layer: 1) selectively deposit first material; 2) blanket deposit second material; 3) lap. The process flow is shown in Fig. 2. In Fig. 2 (a), the first material is selectively deposited onto a substrate, producing the (incomplete) layer shown in Fig. 2 (b). In Fig. 2 (c), the second material has been blanket-deposited over this, contacting the substrate in those regions not plated with the first material. Then, as in Fig. 2 (d), the entire two-material layer has been lapped to achieve precise thickness and planarity. After repetition of this process for all layers, the structure shown in Fig. 2 (e) is etched to yield the desired device (Fig. 2 (f)).

While some implementations of EFAB could selectively deposit both structural and sacrificial materials using Instant Masking, we are currently employing lapping in the process for several reasons: 1) it allows the use of blanket deposition of one material, thus requiring only half the masks, and bypassing any alignment of these masks to those used for the other material; 2) neither material needs to be deposited with an extremely uniform thickness to achieve high accuracy and good masking; 3) layer thickness—and thus Z accuracy—can be precisely controlled.

All SFF processes require software to generate cross sectional layer geometry from 3-D CAD geometry. With EFAB, one or more high-resolution (e.g.,  $\pm 1 \mu\text{m}$ ) photomasks must be prepared which include the geometry of all the cross sections of the device. For now, we generate mask files using layout editor software; however, we are developing custom software which will import .STL files and export a 2-D photomask file in a format accepted by commercial photomask-making equipment.

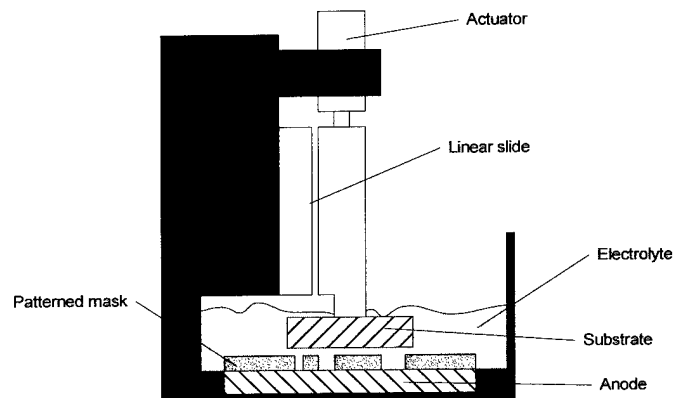


Fig. 4. Schematic of first-generation EFAB machine.

## Experimental

Materials. EFAB can be used to form structures from any electrodepositable metal, with the only constraint being that the accompanying sacrificial metal can be selectively removed (e.g., by chemical etching) after the layers are formed. Nickel and copper form a desirable material system, with copper as the sacrificial material, and it is this system that we have focused on thus far. Nickel has good strength, temperature, and corrosion resistance, and its magnetic properties are useful in electromagnetic devices. Meanwhile, copper can be selectively etched with respect to nickel. We employed commercially-available electrolytes (i.e., plating baths) such as acid copper, cyanide copper, pyrophosphate copper, Watts bath, and nickel sulfamate.

First-generation machine. We constructed the machine shown schematically in Fig. 4 to allow us to investigate the Instant Masking process. This machine uses an interchangeable copper anode, which forms the floor of a plating tank. The substrate, a nickel disk, is pressed against the mask from above using a linear slide and actuator.



Fig. 5. Patterned mask on anode.

Mask. As shown in Fig. 5, the mask consists of a thin layer of material patterned with the desired features on a flat metal disk. This particular mask incorporates several resolution test patterns, in which the smallest bar is 12  $\mu\text{m}$  wide and the largest is 200  $\mu\text{m}$  wide.

Experiments were performed to determine suitable masking conditions with the goal of eliminating “flash” (extraneous deposits).

Second-generation machine. We constructed the machine shown schematically in Fig. 6, to allow fabrication of multi-layer, 3-D parts. The machine consists of several subsystems: the first includes a metal substrate onto which the layers are deposited, a linear slide to move the substrate up and down, an actuator, and an indicator to monitor lapping progress. Another subsystem includes a patterned anode (with multiple masks, one of which is shown in Fig. 7), precision X and Y stages, and a tank to contain the electrolyte. A third subsystem includes an anode and an electrolyte tank.

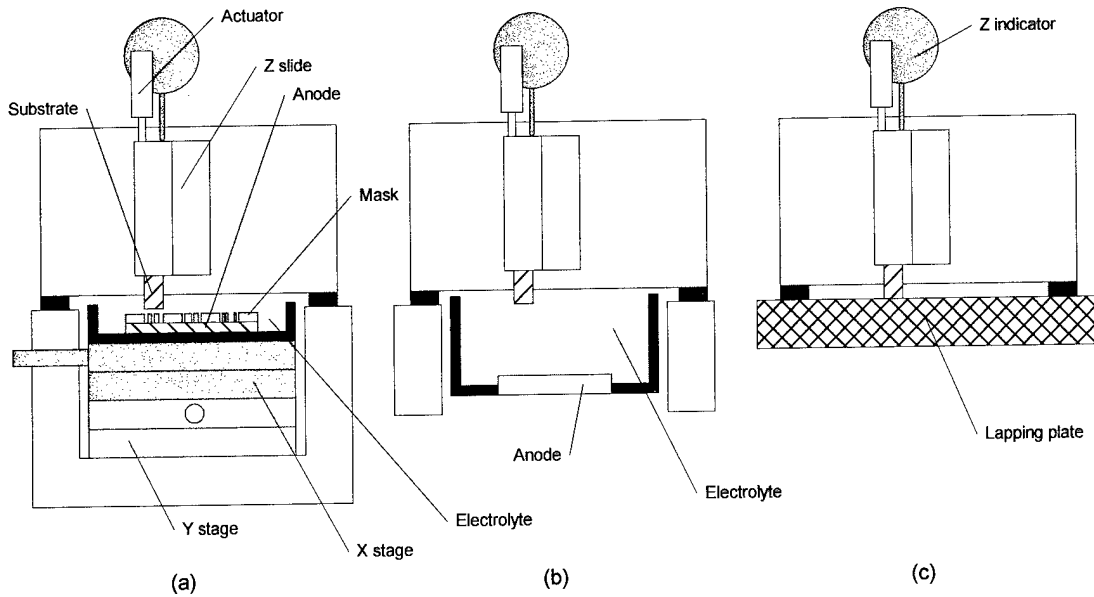


Fig. 6. Schematic of second-generation EFAB machine.

The steps required to make a part are as follows:

1. Lap the substrate to establish a reference/starting plane.
2. Position the anode to place the mask for the current layer below the substrate (Fig. 6(a)), then mate the substrate with the mask and selectively deposit several  $\mu\text{m}$  of the first material.
3. Deposit several  $\mu\text{m}$  of the second material over the first material (Fig. 6(b)).
4. Lap the deposited layer (Fig. 6(c)) until the final desired thickness is reached.
5. Repeat steps 2-4 for remaining layers of the part.
6. Immerse the deposited material in an etchant to remove the sacrificial material.

Cu etching. The ability to remove sacrificial material from narrow and long channels is a potential limitation on part geometry. We artificially created such geometry in advance of having EFAB'd test parts by embedding Cu wires of various diameters in epoxy with only their ends exposed, and immersing these in a commercial Cu etchant. We also immersed Ni wire in the etchant to see if there was any significant effect on Ni.

## Results

Instant Masking. Using the first-generation machine, we were able to obtain excellent definition of the plated deposit: the edges of the deposit were sharp and there was virtually no flash. This is shown in Fig. 9 (traces of electrolyte remain on the substrate in this picture). Rectangular bars down to about  $25\ \mu\text{m}$  width were well defined, although  $12\text{-}\mu\text{m}$  bars showed some definition problems.

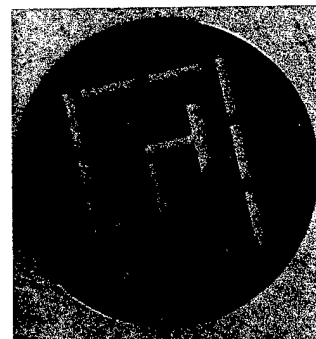


Fig. 7. Mask for selectively depositing sacrificial material on a part layer: the circle is 1.3 mm diameter.

Cu etching. We observed a reasonable etch rate of the epoxy-embedded Cu wires (200-300  $\mu\text{m/hr}$ ), and found that this varied little over a wire diameter range of 40-200  $\mu\text{m}$ . No significant size change of the Ni wire was observed.

Other performance issues. We have not as yet evaluated layer thickness accuracy, mask registration accuracy, residual stress, or material properties (though we expect these to be similar to commercial electroformed Ni).

### EFAB applications

Broadly speaking, EFAB can be used to fabricate microscopic parts, microelectromechanical systems (MEMS), and mesoscopic parts and machines. There is a large and growing market for such devices in such industries as medical, automotive, electronics, and aerospace. Some application examples are:

- Micro- and mesoscopic mechanical machine parts, such as hinges, springs, screws, drive chains, and helical gears;
- Monolithically-manufactured systems such as motors, gearboxes, gas turbines, chemical processors, microsurgical and endoscopic instruments, optical scanners, motion sensors, compressors, pumps, cooling systems, solenoids, and valves;
- Micro- and mesoscopic electrical parts, such as on-chip inductors, transformers, low-loss RF transmission lines, and heat sinks; electronic packaging components, such as interconnects for multichip modules.

In our current program, we plan to use EFAB to produce a functional mesoscopic vibration sensor, shown as a CAD model in Fig. 9.

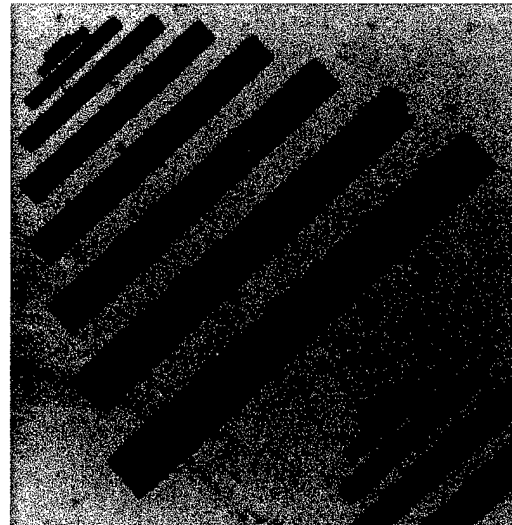


Fig. 8. Deposit produced using Instant Masking using first-generation machine and the mask shown in Fig. 5.

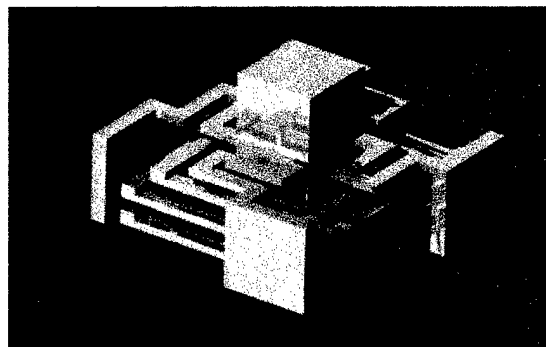


Fig. 9. Preliminary concept of a vibration sensor (overall size 1 x 1 x 0.5 mm)

## EFAB limitations

While well suited for small devices, electrodeposition is too slow (typically 25-100  $\mu\text{m/hr}$ ) a deposition process in most cases for the production of macroscopic devices (e.g., larger than 10 mm in height). Fig. 10 suggests a suitable size range for EFAB devices. Furthermore, there is difficulty using electrodeposition to deposit materials of low conductivity. Also, EFAB also requires part-specific tooling (photomasks), thereby adding to cost and not allowing device fabrication to begin instantly after CAD. Finally, device geometries will not be unlimited: removal of sacrificial material will impose some constraints.

## Conclusions

We are developing a new SFF process and machinery based on selective electrodeposition. We have demonstrated that we can selectively deposit features down to about 25  $\mu\text{m}$  in width with good definition, and we are working to produce multi-layer parts. In developing this process, we hope to provide a capable, generic microfabrication process that will allow functional metal micro- and mesoscopic parts and complex systems to be prototyped and mass-produced by a fixed process that is cost-effective and speedy. We are beginning the development of the next generation machine, which will automate most of the procedures which now must be performed manually using the second-generation machine, and will build parts consisting of many layers unattended.

## Acknowledgements

DARPA/DSO, for primary funding under the Mesoscopic Machines Program (William Warren, Program Manager); Herbert Schorr and Ron Ohlander of ISI, for seed funding; Kan Lee and Victor Jordan of USC for parts fabrication; Jeannine DiCamillo of ISI for administrative support; Mark Messner and Myron Browning, for consulting; Tsung-Hsi Hsieh of USC, for lab assistance; Rebecca Jackman of Harvard and Winston Chan of U. Iowa for information on materials processing; Edward Goo of USC, for use of equipment.

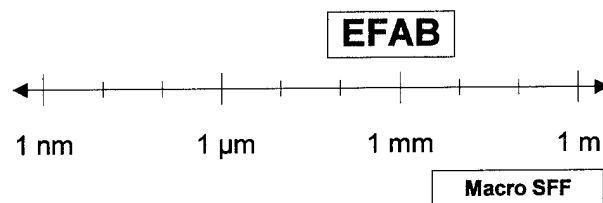


Fig. 10. Possible range of device sizes for EFAB vs. macroscopic SFF.

## References

- [1] M. Madou, *Fundamentals of Microfabrication*, CRC Press (1997).
- [2] See <http://dmtwww.epfl.ch/~abertsch/index.html>
- [3] J. Madden and I. Hunter, *Journal of Microelectromechanical Systems*, vol. 5, no. 1, p. 26 (1996).

# Powder Deposition and Sintering for a Two-Powder Approach to Solid Freeform Fabrication

Ashok V. Kumar

Department of Mechanical Engineering  
University of Florida, Gainesville, FL 32611-6300

## ABSTRACT

A two-powder approach is presented where Fused Deposition modeling (FDM) is used to create a thin shell in the shape of the part to be fabricated. The shell is filled with powder of the part material and surrounded by a support powder that has a high sintering temperature. Upon compressing and sintering the shell/powder system in a uniaxial hot press, the polymer shell burns out and the support powder compresses the part powder. The part powder consolidates into the desired part while the support material remains in powder form and can be easily removed. This paper presents results of initial experimental studies.

## 1. Introduction

Solid Freeform Fabrication (SFF) is a new class of manufacturing technologies that is characterized by layer-by-layer build-up of parts. These technologies promise to revolutionize manufacturing in many ways. Due to the layer-by-layer building approach, it is possible to create significantly more complex parts in one fabrication step than was previously possible. In addition, due to the relatively simple process planning required, the potential has been demonstrated to automatically fabricate a part under computer control given a solid model of the part. The first application of this technology was to create prototypes of designs for visualization and testing purposes. Hence this manufacturing technology is also referred to as *rapid-prototyping* technology. However, more recently the trend has been towards developing layer-by-layer fabrication methods that will directly produce either real parts or the tools / molds necessary to mass produce real parts.

To produce fully functional structural components, powder based approaches to SFF seem to be the most promising. This paper explores the possibility of merging fused deposition technology and powder based SFF technologies to create fully dense metal parts. Section 2 presents a brief overview of the current SFF technologies. The concept of creating parts using two different powders is explained in section 3, while section 4 explains the methodology for depositing powders in the desired fashion using shells created by FDM equipment. Section 5 contains results of experiments on the two-powder concept. Finally, section 6 gives conclusions and looks at challenges that must be overcome for the proposed process to become a viable technology.

## 2. Solid Freeform Fabrication technologies

Over the last decade, many different technologies for Solid Freeform Fabrication have evolved. The common factor that unifies all these methods is that they build parts by adding material layer by layer. This enables very complex shapes to be built in one step with minimal process planning. Therefore, these fabrications methods are able to build parts in a completely automated fashion under computer control. Broadly, the SFF techniques available currently can be classified as stereolithography, solid fusion and solidification, laminated object manufacturing, and powder based techniques (Kochan, 1993). These technologies are briefly described below.

**Stereolithography Apparatus (SLA):** The earliest solid freeform fabrication technology was based on stereolithography. It evolved in the 80s (Kodama, 1981), (Jacobs, 1992) and was first commercialized by 3D systems, Inc. in 1988. Stereolithography builds parts by solidifying a liquid photopolymer using a laser beam. Parts are constructed layer by layer by hardening the photopolymer using a laser beam that is projected in the shape of the cross-section of the part.

**Fusion and Solidification:** Many solid freeform fabrication technologies involve fusing and depositing material layer by layers. The technologies that fall into this category are:

- (i) **Fused Deposition Modeling (FDM):** FDM involves depositing ABS plastic, wax, etc. through a nozzle (Crump, 1992). The raw material comes in the form of spools of wire. The material is heated and extruded through the nozzle so that it comes out in a paste-like fluid form. It solidifies quickly when deposited in a temperature-controlled environment. To construct complex shapes with overhanging features, support structures must be created. The support structures are also made of ABS plastic, but are deposited into shapes that easily peel off. These support structures have to be manually removed.
- (ii) **Ballistic particle manufacturing (BPM):** BPM uses a piezo-electric jetting system to deposit droplets or particles of molten thermoplastic. This method also requires the creation of support structures, which are made perforated to enable easy removal. The BPM jet head is mounted on a 5-axis positioning mechanism and controlled by software to deposit material in the desired shape.
- (iii) **Shape Deposition Manufacturing (SDM):** This method being developed at Carnegie Mellon and Stanford (Weiss, 1995), integrates material deposition and material removal. Layers of part material are deposited and machined to net-shape before additional material and further layers are deposited. Microcasting, a welding process, is used to deposit molten metal droplets for creating fully dense parts. In each layer, the part material is deposited in the shape of the part cross-section and the remaining area is covered using a support material which is etched away after the part is complete. For example, stainless steel parts may be made with copper as the support material.

**Laminated Object Manufacturing (LOM):** This method builds parts by gluing foils or sheets of material on top of one another (Feygin and Hsieh, 1991). A laser beam is used to cut the sheet into the desired shape of the cross-section. The material is stored as rolls of sheet material, which is unwound and routed over a platform on which the part is built. Sheet material is glued to the

layers below by a heated roller. The laser beam then cuts the desired cross-section of the part. The material that is to be removed is cut into a cross-hatch pattern to facilitate easy removal.

In powder-based methods, powder is selectively consolidated into part and the remaining powder can be removed. One of the main advantages of powder based methods is that no support structures are typically required to create complex shapes. The main powder based techniques are:

- (i) Selective Laser Sintering (SLS): In the SLS process (Kimble, 1992),(Nutt, 1991), a thin layer of powder is deposited in a workspace container and heated to just below its melting point. The powder is then fused together using a laser beam that traces the shape of the desired cross-section. The process is repeated by depositing layers of powder thus building the part layer by layer. The area that is not sintered remains as loose powder that can be easily removed after all the layers have been deposited. The materials that can be currently used for building parts are polycarbonates, investment casting wax, PVC, ABS-plastic, Nylon etc. (Nelson et al. 1993).
- (ii) 3D printing: In the 3D printing process (Sachs et al. 1992), a binder material selectively joins powder deposited in layers. Ink-jet printing technology is used to print the binder in the shape of the cross-section of the part on each layer of powder. The powder is deposited on a platform that is lowered after each layer is deposited. After the whole part has been printed, heat treatment is required to consolidate the part. Regions where the binder was not deposited remains as loose powder and can be easily removed after heat treatment.
- (iii) Freeform Powder Molding (FPM): This process is a two-powder method, similar to the one presented in this paper. Although, no specific method for powder deposition has been developed (Rock and Gilman, 1995), deposition of the powders through nozzles has been suggested. Rock and Gilman (1996), have presented application of this process for tool manufacture using metal powders. They use freeze molding to create the part shape where part powder mixed with an aqueous carrier is frozen in a suitable shaped mold. The freeze-molded part is then surrounded using tool powder and sintered.

### 3. Two powder part creation process

In the two-powder process (or FPM), two different powders are used as the part powder and support powder as shown in figure 1. The desired material for the final part is chosen as the part powder. The support powder is chosen such that it has a much higher sintering temperature than the part powder. The two powders are then selectively deposited (into a container or die) layer by layer. On each layer the part powder is deposited in the shape of the cross section of the part while support powder is deposited in the remaining area. Figure 1 shows a sectional view of the powders after deposition.

The part powder can be consolidated in a number of different ways depending on the actual material of the powders. Sintering at a high enough temperature will consolidate part powder due thermal diffusion effects (Rock and Gilman, 1995). This is feasible if the support powder does not sinter at that temperature. Sintering alone may not produce high-density parts. However, if the powders are compressed uniaxially within the die at a high temperature very high density is

achievable as in the powder metallurgy process. Experimental study and theoretical modeling is required to fully understand the compaction and the associated shape change involved. Other ways of consolidating the part powder include mechanical pressure, chemical processes, addition of binder coating on part powder etc.

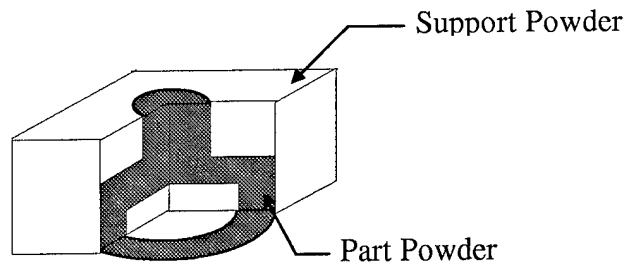


**Figure 1: Two-Powder Based Freeform Fabrication**

In order to experimentally study the feasibility of obtaining high density parts and to understand the shape changes involved we have studied a combination of metal part powder and ceramic support powder. These powders were deposited as shown in figure 1 into a die using a process described in the next section. The powders were then compressed and sintered in a uniaxial hot press at a temperature lower than the sintering temperature of the support powder. The envelope of support powder distributes (albeit not uniformly) the uniaxial pressure in a manner similar to a hot isostatic press (HIP). After cooling, the sintered, fully dense part could be easily removed from the unsintered support powder envelope. The details of the experimental results are described in section 5.

In order for the two-powder SFF process to produce quality parts with good surface quality, the two powders must be deposited with a clear interface separating the two. Typically, when a powder is deposited using a nozzle there is a heaping effect (such as the case in an hourglass). The line of powder tends to have a domed cross-section instead of a flat layer. This heaping effect makes it very difficult to deposit two powders next to each other with clear interface separating the two. In the next section, we describe the use of a polymer shell to separate the two powders during deposition.

#### **4. Implementation of the two-powder process using FDM**

FDM (commercialized by Stratasys Inc.) is a Solid Freeform Fabrication technology that manufactures parts by depositing hot ABS plastic in layers of uniform thickness. The FDM machine consists of a temperature-controlled environment, which contains an extrusion head and a build platform. The extrusion head consists of two temperature-controlled nozzles, one for the part material and one for the support material. It has the capability to move horizontally (in the X-Y plane), while the build platform can move vertically (Z direction). The part nozzle is maintained at 270 F and the support nozzle is maintained at 265 F. Although both part and support material are ABS plastic, the support material is more brittle to facilitate easy removal during post-

processing. The software supplied with the FDM machine slices a CAD model (input as an STL file) into many cross sections at preset uniform distances.

FDM can be used to create a thin shell (approx. 0.015") of the desired part to be manufactured. This shell will serve as a clear interface between the part powder and the support powder. Once this shell is created, the inside of the shell can be filled with part powder and then placed into a container on a bed of support powder. Support powder can then be used to surround the shell to create a two powder - polymer shell system shown in figure 2.

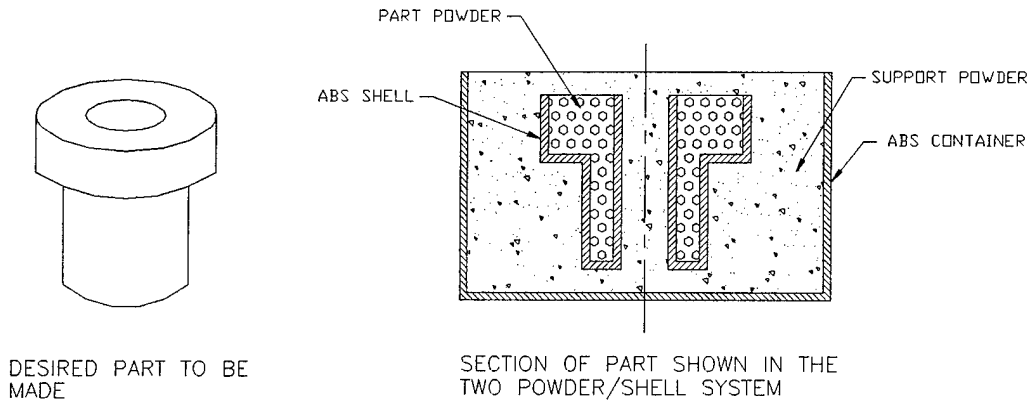


**Figure 2: Two Powder-Polymer Shell System**

The powder-shell system can then be transferred to a uniaxial hot press where it can be compressed and sintered. During the sintering stage, the polymer shell that contains the part powder will burn out and the support powder shifts to fill the void left by the shell. This requires that the support powder should flow readily under compressive stress. After the sintering and cooling process, the fully dense, sintered part can be removed from the unsintered, loose support powder.

If the process described above is automated by installing powder deposition system on to the FDM machine, then the two-powder approach could work as a solid freeform fabrication process. A two-powder delivery device can be fit on the FDM extrusion head so that the powder can be deposited at the same time that the shell is being built. The polymer container (see in fig 2) that holds the support powder would also be built at the same time. Therefore, on each layer, fused deposition modeling technique will be used to deposit polymer in the shape of the cross-section of the shell and the outside container. Then part powder will be deposited inside the shell, while support powder is deposited between the shell and the container. Finally, the powder layer can be made uniform by wiping excess powder off before starting the next layer.

Notice that both the part powder and the support powder can server as support material for holding up the layers of polymer shell. Therefore, polymer support structures are not needed for building the shell using FDM.

## 5. Experimental verification of the two-powder approach

The concept described in section 4 was tested using simple cylindrical shaped shell and container. The shell and container were created on a FDM 1650 rapid prototyping system. The powders were deposited manually. Copper powder of average size 45 microns (100 mesh), was used as the part powder. Titania and Alumina were tested as the support powder. Titania ( $\text{TiO}_2$ ) powder used was approximately 0.25 microns while Alumina powder had an average size of 16 microns.

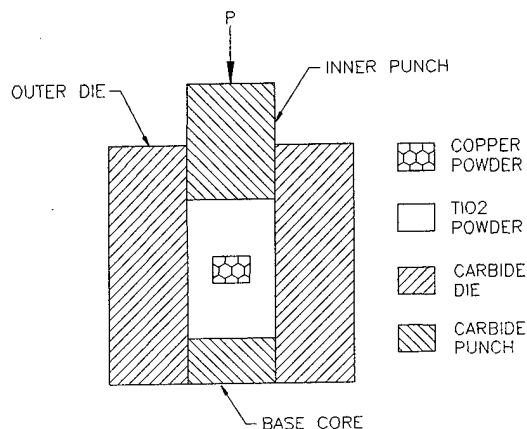


Figure 3: Schematic of Experimental Setup

The die in figure 3 has an inside diameter of 1-1/2" and the shell containing the copper powder was approximately 5/8" in diameter. The die/powder assembly was placed on a solid surface inside a uniaxial hot press. The press is capable of delivering the uniaxial load "P" while simultaneously heating the die using induction coils. A compressive load of 45 MPa was applied through the punch while the temperature of the die was held constant at 700 °C. The system was allowed to sinter for 20 minutes. During the sintering phase, the pressure on the die was maintained constant at 45 MPa. Subsequently, the die/powder system was allowed to cool for approximately three hours.

The compressed copper cylinder was removed and cut in half with a diamond saw. The cross section was then examined at 400X magnification. Although the inter-particle boundaries were slightly visible, the copper was approximately 97-99% dense. This positive result shows that the support powder did in fact transfer the applied load to the part powder effectively.

When titania powder was used as support powder, it did not stay as loose free-flowing powder. Figure 4, shows the image of the  $\text{TiO}_2$  powder after compression and sintering under electron microscope. It can be seen that the support powder had necked and partially sintered. This is due to the extremely small size of the  $\text{TiO}_2$  powder (< 1 micron) that was used, coupled with the large applied pressure. The necking and partial sintering can be greatly reduced through the use of larger sized powder. When large size Alumina powder was used as support powder, it stayed in powder form and was easy to remove. Large, mono-sized spheres deter mechanical locking due to their low packing factor. Spherical powder is also more fluid than irregular shaped

powder due to the minimal contact area between adjacent particles. This will allow the support powder to more efficiently and uniformly distribute the applied load to the part powder. Lowering the sintering temperature will also help in decreasing support powder consolidation.



**Figure 4. TiO<sub>2</sub> powder after compression and sintering**

Significant compaction occurs due to compression and sintering. During this compaction, the part powder not only changes volume but also could change shape. One of the problems to be overcome is to minimize distortion and to be able to accurately predict the change in volume and shape. This is essential to be able to create parts that have desirable dimensional tolerance. Non-uniform deformation occurs in the powder near the die walls due to friction. Therefore, it is necessary to maintain a minimum separation between part powder and the dies walls.

## **6. Conclusions**

The two-powder approach was found to be capable of producing high density copper parts when the powders were subjected to uniaxial compression at high temperature. While this definitely demonstrates the potential of the approach for fabricating high density functional metal parts, it is obvious that much more research is needed to make this a viable process. Experimental studies are required to identify ideal temperature and pressure conditions for various powder combinations. It is also necessary to identify conditions that will ensure that the part powder undergoes uniform deformation during compaction. Methods need to be developed for depositing the powder in uniform layers. To manufacture dimensionally accurate parts, it is necessary to be able to predict deformations caused during compacting and sintering and scale the CAD model for the shell accordingly.

## 7. Acknowledgments

The author would like to acknowledge support from the departments of Mechanical Engineering and Material science and engineering at the University of Florida. Graduate students Aaron Wood and Arfath Pasha helped with the experimental work. Donations from Stratasys, Inc. towards the purchase of FDM equipment is also gratefully acknowledged. This paper has greatly benefited from discussions and help from Dr. Mike Kaufman and Paul Eason of the Material Science department.

## 8. References

- [1] Crump, S., 1992 "The extrusion process of Fused Deposition Modeling", in the Proceedings of the 3rd International conference on Rapid Prototyping, Dayton, OH.
- [2] Feygin, M., Hsieh, B., 1991, "Laminated Object Manufacturing: A simpler process" in *Proceedings of Solid Freeform Fabrication Symposium*, Austin, Texas.
- [3] Jacobs, P. F., 1992, "Rapid Prototyping & Manufacturing Fundamentals of Stereolithography", Dearborn, SME.
- [4] Kimble, L. L., 1992, "The materials advantage of the selective laser sintering process", ", *Proceedings of the 3rd Solid Freeform Fabrication Symposium*, Austin, Texas.
- [5] Kochan, D., 1997, "Solid Freeform Manufacturing: Advanced Rapid Prototyping", Manufacturing research and technology, vol. 19, Elsevier.
- [6] Kodama, 1981, "Display 3 dimensional information to a physical formed model", Trans. of Electronics and Communications Society, vol. 17, no. 6, pp. 237-241.
- [7] Nelson, J.C., Xue S., Barlow, J.W., Beaman, J.J., Marcus, H.L., and Bourell, D.L., "Model of the Selective Laser Sintering of Bisphenol-A Polycarbonate," *Ind. Eng. Chem. Res.*, vol. 32, 1993, pp. 2305-2317.
- [8] Nutt, K., "Selective Laser Sintering as a Rapid Prototyping and Manufacturing technique", 1991, in the *Proceedings of the Solid Freeform Fabrication Symposium*, Austin, Texas.
- [9] *Proceedings of NSF workshop on Design Methodologies for Solid Freeform Fabrication*, June 1995, NSF 96-216.
- [10] Rock, S.J. and Gilman, C.R., 1995, "A New SFF Process for Functional Part Rapid Prototyping and Manufacturing: Freeform Powder Molding," in: *1995 Solid Freeform Fabrication Symposium Proceedings*, H.L. Marcus et al. (eds.), The University of Texas at Austin, (Austin, TX, USA).
- [11] Rock, S.J. and Gilman, C.R., Misiulek, W.Z., and Walczyk, D.F., 1996, "Freeform Powder Molding for Rapid Tooling," in: *1996 Solid Freeform Fabrication Symposium Proceedings*, H.L. Marcus et al. (eds.), The University of Texas at Austin, (Austin, TX, USA).
- [12] Sachs, E., Cima, M., Williams, P., Brancazio, D., and Cornie J., 1992, "Three Dimensional Printing: Rapid Tooling and Prototypes Directly from a CAD Model," *Journal of Engineering for Industry*, vol. 114, pp. 481-488.
- [13] Weiss L. E., "Solid Freeform Fabrication Processes," 1995, *NSF workshop on Design Methodologies for Solid Freeform Fabrication*, June 5-6, 1995.

# Effective Mechanisms of Multiple LED Photographic Curing

Kai Loose, Toshiki Niino  
The Institute of Physical and Chemical Research (RIKEN)

Takeo Nakagawa  
Institute of Industrial Science, University of Tokyo

## Abstract

*Multiple LED Photographic Curing* (MPC) has proven capable of drawing cross sections of three-dimensional objects like printing a sheet of paper. Using raster scanning, however, simultaneously exposing a photopolymer with 1,024 beams of light involves various unknown issues. The aim of this research work was to examine the formation of individual strings and the connecting mechanisms between strings and layers. At light power ranging from 19.0 to 30.3 $\mu$ W and at various scan speeds, string formation perpendicular to scan direction differs greatly from that in scan direction. Curing of plane layers happens by curing strings side-by-side with a constant spacing of 62.5 $\mu$ m.

## 1 Introduction

*Multiple LED photographic curing* (MPC) is based on the concept of exposing a liquid photopolymer through multiple beams of light simultaneously. Unlike Laser Stereolithography (SL), MPC uses light-emitting diodes (LED) as light sources (Loose et al., 1997). Exposure happens through an array of 1,024 beams of light which expose the surface of the liquid resin while using raster scanning. Similar concepts for multiple-spot exposure have been proposed by Ohtsubo et al. (1997) and Marutani et al. (1998). All concepts have successfully shown their practical applicability.

Nevertheless, very little is known about the effective mechanisms in multi-spot exposure. In spite of seemingly principal compatibility between MPC and SL—both processes are essentially an exposure of a liquid photosensitive resin leading to polymerisation, thus to solid objects—there is a number of challenges to be met considering the unique characteristics of the exposure pattern. It can be said that the research on MPC is at the developmental stage, and large number of measurements are required to improve the design. For example, the effective mechanisms when exposing the photopolymer resin surface are unknown. If they are understood to some extent, MPC can be improved to become applicable for rapid concept modelling.

This paper describes the results of the experimental examination of the curing process in MPC. Not only the curing of single strings but also the formation of layers and three-dimensional

objects is studied. Consequently, the authors propose a means to generate an equal cure depth through multiple beams of light and investigate it theoretically and experimentally. In the following, experimental results are presented and the envisaged application explained. The results of this research indicate that MPC is a successful method for faithfully generating three-dimensional objects, and has the potential to aid design evaluation.

## 2 Background of the Examinations

Today, there is a growing demand for cheap and fast concept modelling. Research on MPC carried out at RIKEN aims at combining this application with the unique characteristics of Stereolithography parts, such as transparency. Using inexpensive technology, MPC is an attractive technique to process photopolymers into various shapes.

In the frame of the following examination, the decisive process-technological parameters of influence shall be investigated. **Figure 1** explains that the following examinations focus on the features which are characteristic of the MPC process. Together with an adjusted control software, the way how energy is absorbed in the resin surface is of utmost importance regarding the achievable accuracy to form and shape.

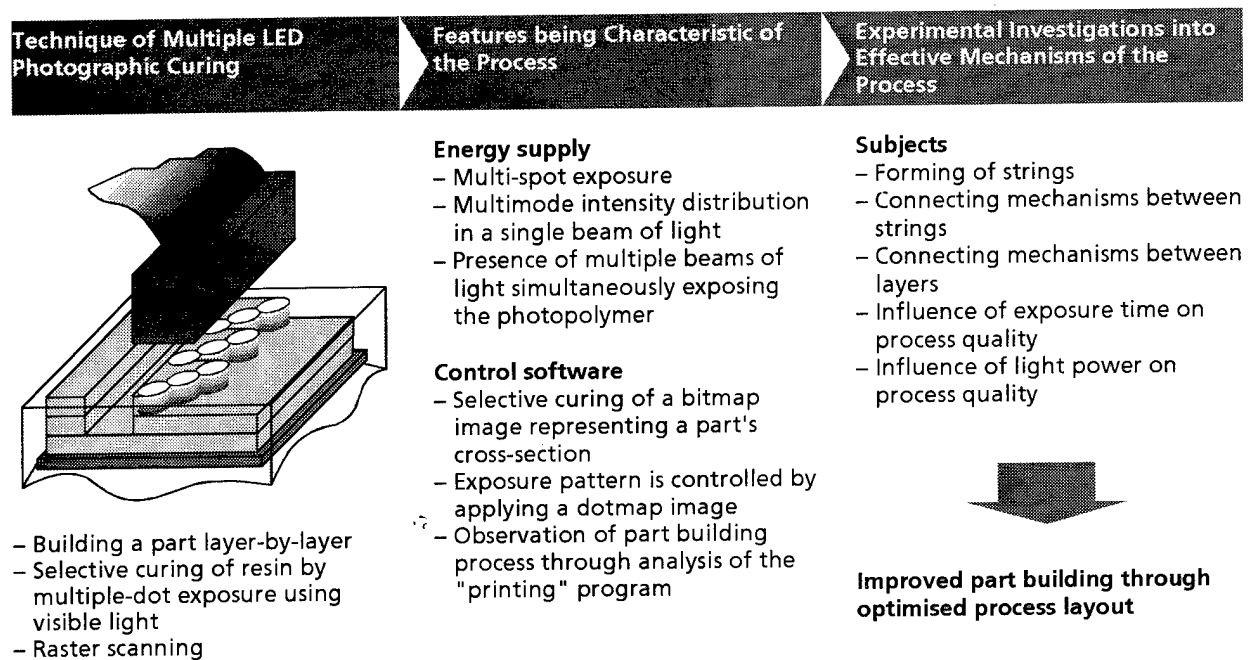


**Figure 1:** Concept of investigating the effective mechanisms of MPC

Besides process technological parameters of influence, the machine is of particular interest. Essentially, the kinematic accuracy of the linear guides and the temperature dependent behaviour of the entire machine must be given in particular. Here, only the motion of the projector scanning the resin surface has direct effect on the exposure quality. Therefore, the influence of the accuracy of the scanner guides is of great importance. The scanner, driven by a step motor, moves with an

accuracy of 70 $\mu$ m per 90mm distance. In the direction perpendicular to the scan direction, the positioning accuracy is 20 $\mu$ m.

The influence of the material on accuracy to form and size, also regarding geometric long-term stability, is often underestimated. The two groups of photopolymers, acrylate- and epoxy-based resins, have some very different characteristics (Jacobs, 1992, Xu, 1997/1). In this context, the influence of the material is not further followed up. These aspects are not a particular characteristic of MPC but they are mentioned here because of their relevance for MPC.

### 3 Experiments into Effective Mechanisms of the Process

For the experiments, all test samples were built using a test facility which has been developed for *Multiple LED photographic curing* at RIKEN. The material is an experimental acrylate-based photopolymer resin, HSX-V-2 (by Asahi Denka). At a constant vat temperature of 30°C, the resin has a viscosity of  $\eta = 3 \times 10^{-5}$ Ns/cm<sup>2</sup>. At the resin surface, the output power in each beam of light is  $P_{L,v} = 29.2\mu$ W. The experiments aid the investigation of the characteristic features when curing a photopolymer using multiple beams of light.

#### 3.1 String Formation

The design of MPC necessitates simultaneous exposure of plane areas and thinnest strings with the same constant scan velocity and LED power. Therefore, in a computer-supported mathematical contemplation the exposure during curing using various numbers of beams of light for the exposure has been calculated. As a result, when exposing a plane area and a thinnest string at the same time, to ensure equal cure depth, the energy of at least five beams of light is necessary for exposing a single string. In this way, an equal level of exposure through superposition of single exposures in one layer is always guaranteed. Only under these conditions, a thin string can be created while a plane area is cured at the same time without overcuring.

For the initial experiments, single strings—exposed by five beam of light—have been chosen for investigating the curing phenomena. A single string is of particular interest because of both their well-known general importance when analysing the exposure process in Stereolithography in general, and investigating the characteristics of MPC in particular. At scan velocities ranging from 0.1 to 1.6mm/s, each string has been exposed by one (L1) to five (L5) beams of light at a fixed hatch distance of 62.5 $\mu$ m. The beam diameter is 0.5mm. Dimensions were measured using an optical microscope and a CCD (charge-coupled device) camera. A comparison of the line widths in scan direction and perpendicular to it at various scan velocities is shown in **Figure 2**. At constant light power at the vat,  $P_{L,v} = 29.2\mu$ W, it can be seen, that in general, the observed line widths decrease with increasing scan velocity. The graphs show, that in X-direction, the same line width can be achieved at higher scan speeds. Besides, perpendicular to scan direction line widths are slightly greater than they are in scan direction. The reason for that may be a not correctly adjusted timer for turning on and off the LEDs. A change in the software should solve this issue. The influence of the different number of beams of light used for exposure is considerable. At five beams of light, thinnest strings can be cured to up to 1.5mm/s and 1.3mm/s, respectively.

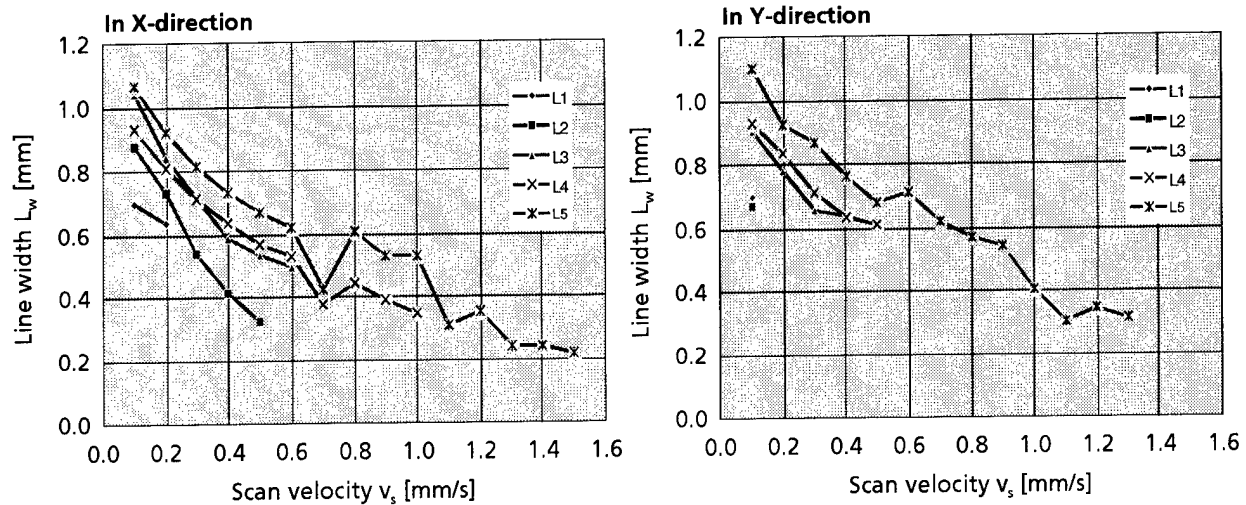


**Figure 2:** Line width in X- and Y- direction at light power  $P_{L,v} = 29.20\mu W$

Perpendicular to the scan direction (Y-direction), at a scan speed of more than 1.3mm/s, no curing occurs. Compared to the exposure in scan direction, to start the polymerisation perpendicular to the scan direction, the scan velocity must be reduced, thus providing more exposure. The lower levels of curing found during exposure in Y-direction may be due to the exposure pattern. Across the scan direction, curing happens gradually and closely spaced. Initially, dots at a distance of 0.5mm are exposed. The energy, however, is not sufficient to connect these individual dots on the resin surface. The next row of beams of light are, therefore, not able to expose the resin anywhere near the previously cured dots. As a result, no strings can be formed at all.

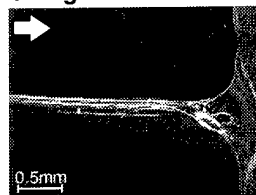
**Cured strings**

- Lines are created by drawing a single line with five beams of light
- Line width increases with lower scanning velocities
- On the free surface, curing dot-by-dot requires more energy than at continuous exposure
- Power  $P_{L,v} = 29.2\mu W$
- Material: acrylate resin HSX-V-2

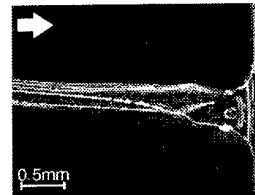
- Scan direction



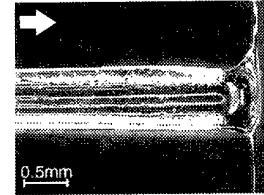
**Strings attached at one end**



$v_s = 1.5\text{mm/s}$



$v_s = 1.0\text{mm/s}$

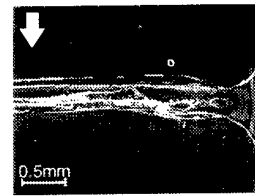


$v_s = 0.5\text{mm/s}$

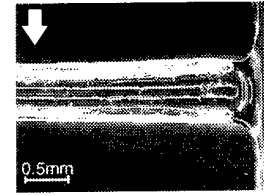
**Strings attached at one end**



$v_s = 1.3\text{mm/s}$



$v_s = 1.0\text{mm/s}$



$v_s = 0.5\text{mm/s}$

**Figure 3:** Formation of strings at various scan velocities  $v_s$  in scan direction and across to it

In scan (X-) direction, at scan velocities between 0.1 and 1.5mm/s, the shape of the strings differs greatly (**Figure 3**). As expected, the line width increases with decreasing scan velocity. At 1.5mm/s, a string has a width of about 0.11mm. Where the string is attached to a frame holding it in position in a right angle, the geometry is unclear. At low exposure, due to the low degree of polymerisation and its position free flowing on the resin surface, the string is rather soft and unstable. Xu et al. (1997/2) found that microscopic flow generated by the process heat could be observed. It is assumed that, during exposure, flow and probably shrinkage cause the string to move slightly on the resin surface. Width increases rapidly up to 0.68mm at 0.5mm/s. At 0.5mm/s, the string has been cured more and, therefore, is stronger and more stable. In Y-direction, at 1.3mm/s, the string is cured at a width of about 0.31mm. At 0.5mm/s, its width increases to about 0.7mm.

### 3.2 Connecting Mechanisms Between Strings

The connections between up to five adjacent lines formation a single string can be observed best at low scan velocities (**Figure 4**). The scan velocity is constant at 0.1mm/s. When exposing with just one beam of light, the shape of the cured string reminds a little bit on a string of pearls. With increasing number of beams, the string becomes smoother. At the same time, however, the line width increases only a little.

#### Cured strings

- Lines are created by drawing a single line with one to five beams of light
- Shape of the line becomes smoother with increasing number of beams of light
- Light power  $P_{LV} = 29.2\mu W$
- Material: acrylate resin HSX-V-2
- When exposing one string with one beam of light, exposure happens in steps caused by the slightly jerky motion of the projector which is driven by a step motor
- With increasing number of beams of light, this effect disappears

- Scan direction

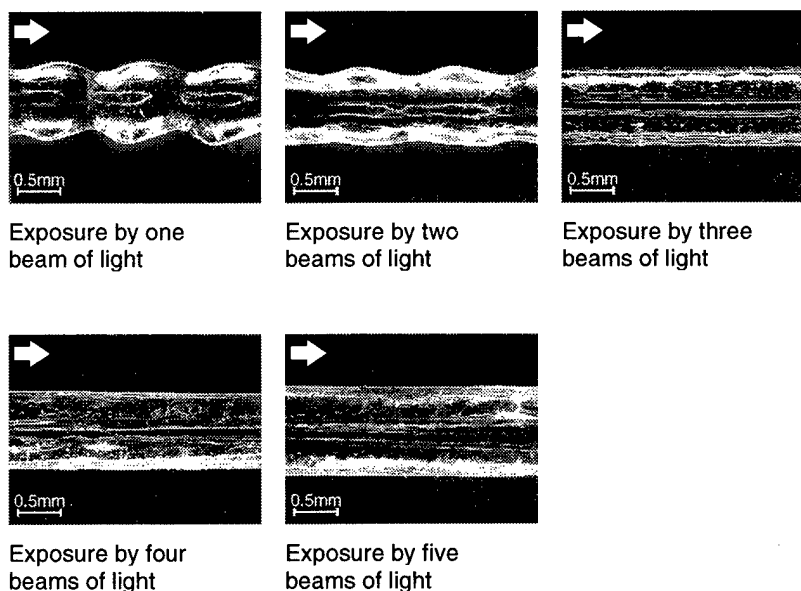


**Figure 4:** Simultaneous multi-beam exposure at a scan velocity  $v_s = 0.1\text{mm/s}$  in scan direction

Uneven curing when exposing at extreme low scan speeds is caused by the motion of the projector. In scan direction, the curing becomes sensitive to the slightest movements of the projector. The exposure happens in steps caused by the slightly jerky motion of the projector, which is driven by a step motor. This effect disappears with increasing number of beams of light expos-

ing the string. Each additional beam of light exposes the same string at a slightly shifted time according to the arrangement of the beam array in the projector. Another observation is, at least three beams of light are necessary for curing one single string. Then, the contour of the string is similar to that of a straight line.

### 3.3 Parameters of Influence "Energy Absorption"

The course of the line widths and cure depths at various scan velocities and light power are shown in **Figure 5**. The data were obtained after curing several strings with three beams of light. In X-direction, line width and cure depth increase with increasing light power. The same result can be found in Y-direction. However, the line width is in average slightly greater than in X-direction. At scan velocities of 0.3 and 0.4mm/s, the increase in cure depth in Y-direction is slightly steeper than that in X-direction. The reason for that may be the initially very low degree of curing at a low exposure dot-by-dot. At higher exposure, the cure depths in X- and in Y-direction are the same.

#### Cured strings

- Data obtained using an optical microscope and CCD camera
- Strings were cured using 3-beam exposure
- In average, line width in scan direction is slightly less than perpendicular to scan direction
- In average, cure depth in scan direction is slightly higher than perpendicular to scan direction
- To get the highest scan velocity process can be operated at a power of 29.2 and 30.3 $\mu$ W

- Scan velocity:
- 0.3mm/s
  - x— 0.4mm/s
  - +— 0.5mm/s
  - 0.6mm/s
  - 0.7mm/s
  - 0.8mm/s

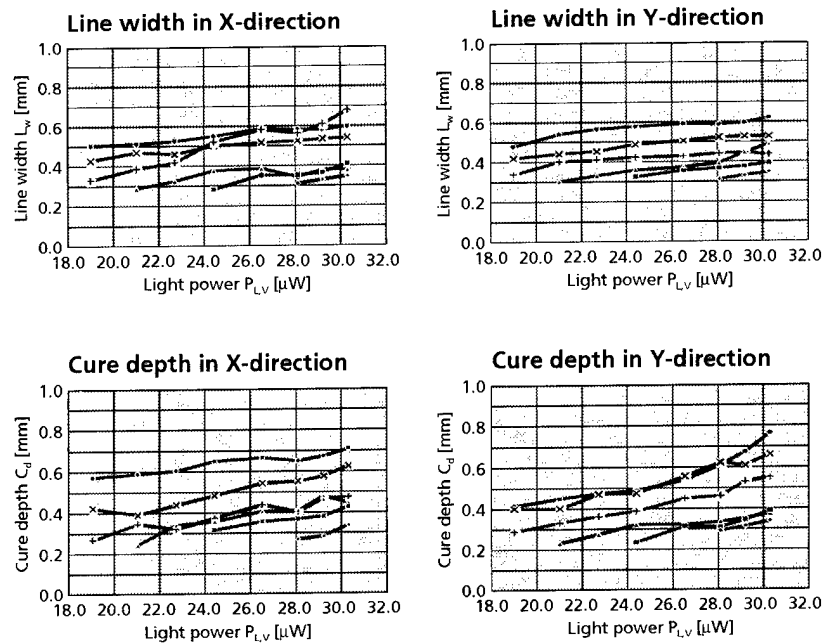


**Figure 5:** Parameters and their influence on curing

### 3.4 Parameter of Influence "Part Geometry"

The process parameters were varied over a wide range to find the optimum combination yielding good surface quality, fine detail, and sharp contours. The tests were carried out using the experimental resin HSX-V-2. The explanations in **Figure 6** focus on the results achieved when building simple geometric objects. A mesh can be build with walls as thin as 0.2mm and in good accuracy in X- and Y-direction as well as at various angles. The effect of multi-spot exposure is

clearly visible in the vertical and the sloping elements. Part quality depends in the part orientation in the X-Y-plane. The vertical surfaces are smooth. It is one characteristic of MPC that strings which form layers lie exactly one above the other. This can not be changed since the arrangement of the lenses in the projector is fixed. MPC is successful for the process parameters for LED power and scan speed which were found above. A top view of the test part's surface shows that the lines from the exposure are clearly visible, even with the naked eye.

**Material**

- Acrylate resin HSX-V-2
- Resin viscosity  $\eta = 3 \times 10^{-5} \text{Ns/cm}^2$

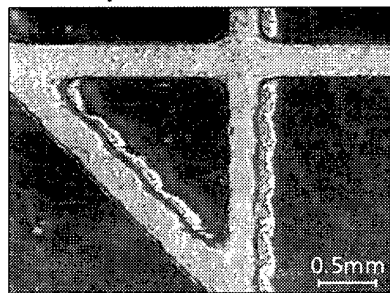
**Process parameters**

- LED power  $P_{L,V} = 29.20 \mu\text{W}$
- Wavelength  $\lambda = 470 \text{nm}$
- Scan velocity  $v_s = 0.75 \text{mm/s}$

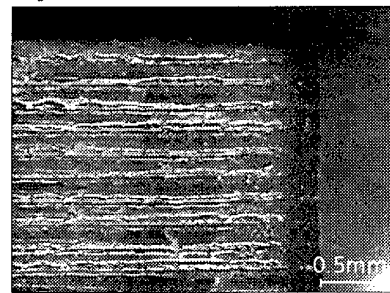
**Test part**

- Size  $45 \times 45 \times 9 \text{mm}^3$
- Build time  $t_b = 81 \text{min}$

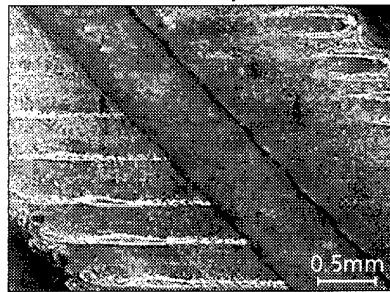
**Mesh, top view**



**Layers, side view**



**Wall and surface, top view**



**Corner, top view**

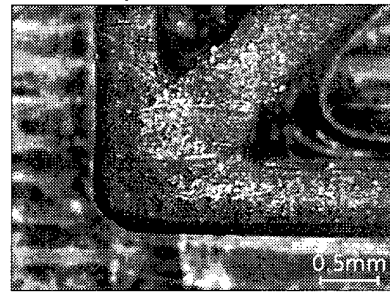


**Figure 6:** Influence of part geometry on surface texture and part quality

## 4 Discussion

The curing process in *Multiple LED photographic curing* (MPC) was experimentally examined. The effects of the parameters of influence on curing of single strings and formation of layers and three-dimensional objects were studied. Previously, theoretical investigations have shown that for the generation of equal cure depths in thin strings and plane areas, the exposure of at least five beams of light is necessary.

The data reported in this paper show that strings can be accurately cured at low light power. Line widths increase at lower scan speeds. In scan direction, strings could be polymerised at a velocity of up to 1.5mm/s. At high scan velocities, the strings are unstable and the geometry is sometimes unclear. One reason could be that microscopic flow causes the strings to move on the free resin surface. Besides, shrinkage may cause the strings to move. Across the scan direction, only up to 1.3mm/s strings could be created. These results can be explained by assuming that gradually and closely spaced exposure is not sufficient for polymerisation. At lower speeds, how-

ever, the exposed dots stick together and start formation strings. At extremely low scan velocity, the process becomes sensitive to slightest jerky movements of the projector when exposing with one beam of light. A jerky motion of the projector creates a line which looks like a string of pearls rather than a continuous line. Adding at least two beams leads to a smoother shape of the string. At high velocities, this effect disappears completely.

Due to the general characteristic of these investigations—strings were examined on a free resin surface—this study is limited to the basic curing process in MPC. It is the basis for further studies on the generation of three-dimensional objects, such as thin walls and other geometric shapes. The heat generation as the assumed reason for moves of the strings on the resin surface has not been examined and is subject of future examinations. The results of this study have implications on further developments of the process and the design of the machine itself.

This study could lead to new important findings about the MPC process. The results of this research indicate that MPC is a successful method for faithfully generating three-dimensional objects, and has the potential to aid design evaluation. Clearly, this technique has promise as a tool to fabricate three-dimensional objects in design evaluation. Future steps will thus include improvements in the light sources to increase process speed and accuracy of Multiple LED photographic curing.

## 5 References

- Jacobs, P.F. (1992) *Rapid Prototyping and Manufacturing—Fundamentals of Stereolithography*, Society of Manufacturing Engineers (SME), Dearborn, MI
- Loose, K., Nakagawa, T., Niino, T. (1997) "Concept modelling using multiple LED photographic curing", *proceedings, 13<sup>th</sup> Rapid Prototyping Symposium*, Yokohama, Japan, pp. 35-40, November 1997.
- Marutani, Y., Kamitani, T. (1996) "Stereolithography system using multiple spot exposure", *Seventh Solid Freeform Fabrication Symposium*, The University of Texas at Austin, TX, pp. 321-326.
- Ohtsubo, Y., Yamamoto, M., Takamori, T., Tadokoro, S. (1997) "Development of microstructure using Stereolithography" (in Japanese), *proceedings, 12<sup>th</sup> Rapid Prototyping Symposium*, Osaka, Japan, pp. 40-45, May 1997.
- Xu, Y. (1997/1) *Studies on curing process of photopolymer in Stereolithography*, Doctoral Thesis, Institute of Industrial Science, University of Tokyo
- Xu, Y., Imamura, M., Nakagawa, T. (1997/2) "Microscopic flow observation of photopolymer by UV-laser beam exposure", *Eighth Solid Freeform Fabrication Symposium*, The University of Texas at Austin, TX, pp. 177-184.

# RAPID FREEZING PROTOTYPING WITH WATER

**Wei Zhang, Ming C. Leu<sup>\*</sup>, Zhiming Ji**

Department of Mechanical Engineering  
New Jersey Institute of Technology, Newark, NJ 07102  
E-mail: zhangwei@oak.njit.edu

**Yongnian Yan<sup>#</sup>**

Department of Mechanical Engineering  
Tsinghua University, Beijing 100084, China  
E-mail: dmeyyn@mail.tsinghua.edu.cn

## ABSTRACT

Rapid Freezing Prototyping (RFP) with water is a novel solid freeform fabrication technique that can generate three-dimensional ice objects by depositing and rapidly freezing water layer by layer. The support where necessary is made of brine whose freezing point is lower than pure water. After building the part, the support can be removed by utilizing the melting temperature difference between brine and water. Preliminary experiments have shown that the ice patterns produced by this technique can be used for design visualization and silicone molding. This paper will present the concept and some experimental results of the RFP process as well as potential applications.

## KEYWORDS

Solid Freeform Fabrication, Rapid Prototyping, Rapid Tooling, Layered Manufacturing, Rapid Freezing Prototyping, Ice Patterns

## 1. INTRODUCTION

Since the late 1980's, several Solid Freeform Fabrication (SFF) techniques have been investigated, and some commercially developed. These techniques allow freeform fabrication of complex-geometry parts directly from their CAD models [1]. By directly or indirectly employing SFF technologies in tool, die and mold fabrication, Rapid Tooling (RT) process is accomplished. These tools may serve the purpose of forming a prototype part in the end use material for design evaluation, or produce a product that only a small quantity need to be manufactured. The direct RT method consists of producing the tools with the SFF techniques and/or some post processing, such as Selective Laser Sintering with post processing technology of low melting point alloy infiltration. The indirect RT method involves secondary steps by integration of SFF and conventional shape duplication technologies. Successfully used indirect RT technologies include RTV (Room Temperature Vulcanization) molding, sand casting, investment casting, metal spraying, Keltool, and electroplating/electroforming based tooling. Currently, it is more widely used than direct RT [2-3].

With the additional shape duplication process in indirect RT, the mechanical properties of

---

<sup>\*</sup> Dr. Ming C. Leu is on-leave at National Science Foundation as the Program Director for Manufacturing Machines and Equipment

<sup>#</sup> Prof. Yongnian Yan is the Director of the Center of Laser Rapid Forming, Tsinghua University, Beijing, China

the prototypes made by SFF techniques are less critical. The materials of the prototypes are not necessarily ABS plastic, ceramic, or metal. However, the following properties are very critical:

- Accuracy: Generally speaking, accuracy for tooling needs to be higher than that for design visualization [4].
- Surface finish: The surface finish of the prototype determines the best achievable surface finish of the final tools. In many cases, the prototype needs to be polished after building in order to obtain better surface finish.
- Easy part removal: This property means less geometry limitation of tooling. If a part is not easy to remove, the mold has to be split into several sections to make. This results in more preparation time and some loss of tooling accuracy.
- Easy part joining: This is an additional desired property for complex geometry tooling. When a part is too complex or impractical to build due to strength or orientation reasons, it is desirable to build the part in several portions and then join them together.

Unfortunately, few SFF techniques satisfy all the above properties. For example, the Stereolithography Apparatus (SLA) can build parts with good accuracy and surface finish; however, the SLA part removal is not easy except for QuickCast parts. On the other hand, wax parts made by Fused Deposition Modeling (FDM) have good properties of easy removal and easy joining, and can be directly used for investment casting, however, the accuracy and surface finish need to be further improved as compared to SLA parts [5].

In terms of Rapid Prototyping or design visualization, techniques which are able to build colored and transparent parts can provide more information about the design result and can give more clear and accurate evaluation. Almost all plastic depositing based SFF techniques can build colored parts with colored material, such as the FDM technique provided by Stratasys and the Model Maker provided by Sanders Prototypes. The parts made by most of the techniques including the FDM and Model Maker are not transparent. They are acceptable in most cases for design visualization. However, in some special cases, such as surgery plan preparation models and very complex one-part subassemblies, these models are not enough. The designer or the surgeon needs more interior information inside the model.

This paper presents the Rapid Freezing Prototyping (RFP) process that is being developed by us to address the above tooling and designing demands. By using water as the material and rapid freezing as the building method, RFP can build ice patterns with good accuracy and surface finish. Easy part removal and joining, colored (different portions in different colors) and transparent parts are additional good properties for both tooling and design visualization. This paper is organized as follows. Section 2 introduces the principle of Rapid Freezing Prototyping. Section 3 discusses the main features of this novel process. Section 4 provides some preliminary application results, and section 5 concludes the paper.

## **2. PRINCIPLE OF RAPID FREEZING PROTOTYPING**

### **2.1 Concept of the Technique**

RFP is a novel SFF process that makes a part by selectively depositing and freezing the material (water or brine) layer by layer [6]. As shown in Figure 1, water is pumped from a reservoir to the nozzle by a peristaltic pump and then deposited onto the previous solidified ice surface or the substrate. The newly deposited material is cooled by both the low temperature environment and the ice surface. As a result the deposited water freezes rapidly and sticks to the

previous layer, forming a new layer of the part. Where necessary, brine is used instead of water to build the support. The nozzle and the transmission pipe are heated and kept at a temperature just above the freezing point of water so that the material may flow smoothly. During the building process, the ratio of the in-nozzle material flow rate to the XY scanning speed is very critical. A too large ratio may cause failure to control its out-nozzle flow along the ice surface. On the other hand, a too small ratio may cause discontinuity of the freezing strands (See Figure 2). The ratio of material flow rate to the XY scanning speed can be kept at the best value by controlling the rotating speed of the peristaltic pump.

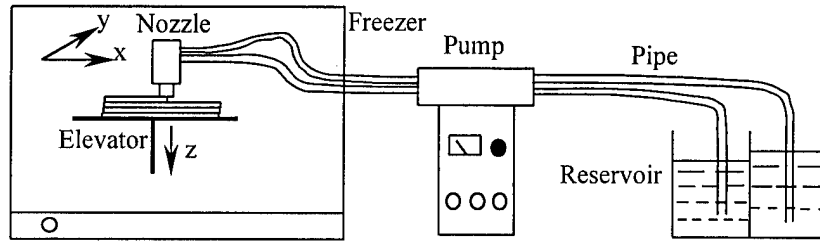


Figure 1. Principle of Rapid Freezing Prototyping

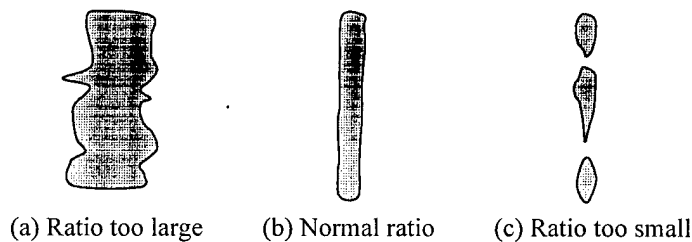


Figure 2. The schematic drawing of strands for different levels of the ratio of material flow rate to XY scanning speed

When the part with support is finished, the next step is to remove the support structure. As shown in Figure 3, there is some special solvent in the tank for removing the support. The solvent is kept at a temperature beyond the melting point of brine ice but under that of the pure ice so that only the support gets melted. The solvent used here must have two basic properties: not soluble with water and a large density difference from water. The first property is to ensure that the brine melt from support is not dissolved in the solvent and has no unexpected influence on the boundary of the ice part. The second property is to let the brine be separated easily from the part and support, either rising up or sinking down easily in the solvent. The blender is applied to accelerate the support removal procedure.

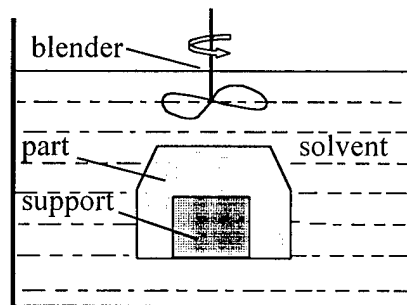


Figure 3. Support removal of Rapid Freezing Prototyping parts

## 2.2 The Current Experimental System

An experimental system is being designed and built for the research and development of the Rapid Freezing Prototyping process. A goal is to be capable of automatically building ice parts from the data provided by CAD software. The main components of the system are (Figure 1):

- 1) Material extruding subsystem
- 2) Material deposition nozzle
- 3) XYZ three-dimensional positioning subsystem
- 4) Support removal subsystem
- 5) Freezing chamber

The material extrusion subsystem pumps repetitively a desired amount of water from the reservoir into the nozzle and then deposits it onto the building surface. This function is achieved by utilizing a peristaltic pump, which uses rollers to squeeze the liquid through a flexible plastic tube. One end of the tube is inserted into the container of the building material, and the other end attached to the nozzle. The advantages of extruding water by a peristaltic pump include: (a) accurate metering of the liquid volume; (b) simplified maintenance due to the fact that there is no contact between the pump mechanism and the liquid; and (c) the pump has multiple channels which can be used for extrusion of building material and support material. The extruding speed of the pump is controlled by the pulses generated by the motion controller.

The material depositing nozzle in this experimental machine will have multiple tips which are designed for depositing building material, support material, and fast material depositing to improve build speed. The tip selection is accomplished by activating a certain electromagnet; see Figure 4. In order to prevent the material in the nozzle and the pipe from overcooling to freeze, some heating components are employed to keep them at a certain temperature, typically around 5°C.

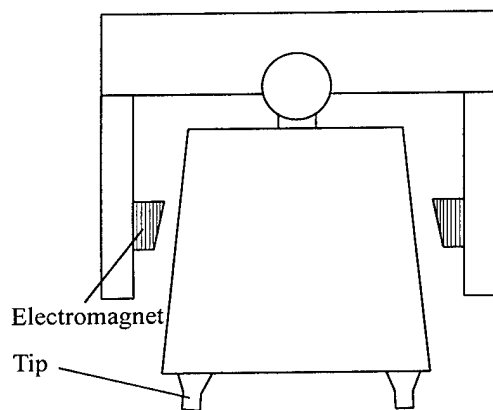


Figure 4. Multiple-tip nozzle

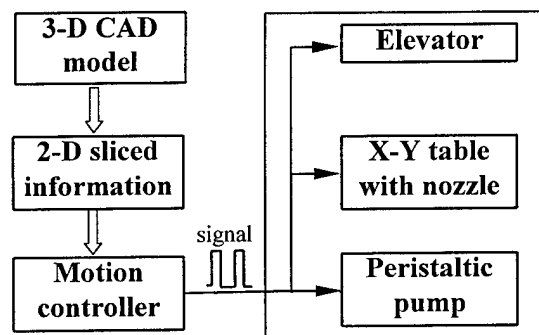


Figure 5. Control system structure of RFP experimental machine

The whole system will be controlled by a personal computer (Pentium-200MHz). The three-axis movement and the peristaltic pump are controlled by a PC-Bus based 4-axis stepping motor controller (OEM AT 6400, by Compumotor Co.). The software to be developed generates the Numerical Control (NC) codes according to the sliced contour information of the CAD model. The stepping motor controller uses the NC codes to control the motion of the elevator in Z direction and the nozzle in X and Y directions. The peristaltic pump is also controlled by this

motion controller. The schematic of controlling is shown in Figure 5.

The support removal subsystem introduced above is shown in Figure 3. The accurate temperature control of the solvent is essential to the success of support removal.

The building mechanism, including the nozzle, the elevator, and part of the XY positioning table, is placed in a temperature controlled freezing chamber. The temperature is controlled by a computer-interfaced controller. The typical chamber temperature is controlled at  $-20^{\circ}\text{C}$ . Generally speaking, lower temperature allows faster building of ice parts.

### 2.3 Building Strategy

Contours and interior fillings of each layer of the ice part are built with different aperture tips. In order to build the ice parts with good accuracy and surface finish, the contours are built by depositing material with a smaller aperture tip, typically 0.3 mm in diameter. However, the interior fillings are built by depositing with a larger aperture tip to improve the building speed; see Figure 6. The properties which make this building strategy possible include almost no heat accumulation, natural binding of layers, and excellent fluidity.

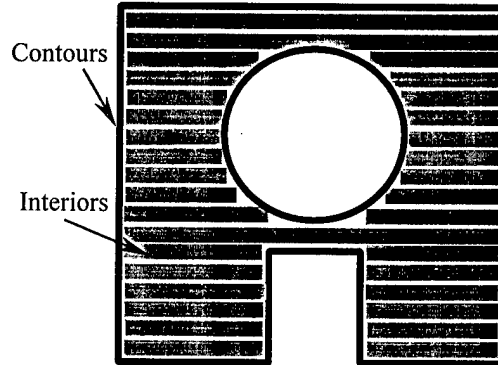


Figure 6. Cross section of an ice pattern

## 3. MAIN FEATURES OF RAPID FREEZING PROTOTYPING

By using water as the building material, RFP distinguishes itself from the current SFF techniques in the following main features.

- (1) RFP is a cheaper and cleaner prototype building technique. The building process and the building material have no negative impact on the operator and the environment. The process has no harmful UV light and does not produce smell, smoke, noise, or garbage.
- (2) RFP has the potential to build accurate ice parts with excellent surface finish although substantial research will be needed to achieve fine part accuracy.
- (3) The ice part made by RFP is easy to remove from a mold simply by warming it up and making the mold dry. There is no residue problem. The ice parts are also easy to join due to its self-welding property. A very complex part can be separated into several portions to make and then join them together.
- (4) RFP does not have the problem of heat accumulation. Water is a kind of crystalloid material and the binding of adjacent layers is accomplished by the hydrogen bond. So the in-nozzle material can be kept in liquid state by keeping its temperature just a little bit above the freezing point. The heat generated during freezing of the deposited material can be easily absorbed by the building surface and the surrounding cold air, thus resulting in no heat accumulation. In other heat related SFF processes, such as FDM, the material is not crystalloid. In order to obtain good fluidity and enough binding strength between adjacent layers, the in-nozzle material must be heated to a fairly high temperature. The environment can not easily absorb the provided heat in time. As a result, the heat will accumulate and affect the accuracy and surface finish of the parts.

- (5) RFP has a much longer binding time than FDM. The temperature of the very thin layer material near the building surface is believed to be most important for the binding property. The schematic temperature change curves of the critical portion of material for RFP and FDM are shown in Figure 7. In RFP, water is a kind of crystalloid material and thus the curve has a flat section which means the material is freezing. The binding between adjacent layers is achieved by hydrogen bond. After freezing, additional cooling by the environment and built part still contributes to better binding. However, in FDM, the curve has no flat section. The binding between adjacent layers is achieved by thermal joining. So only the effective period during which the temperature is higher than the binding point contributes to the binding. This effective period is determined by the nozzle temperature, the environment temperature, and the building speed. Due to limitations of the three factors, the effective period is also limited.
- (6) During the freezing in RFP, the material expands and causes compress stresses in the part. The expansion of the material can be mostly compensated by properly selecting of the interior fill spacing. However, for other depositing SFF techniques, when solidifying, the material shrinks and causes tensile stresses in the part. The shrinkage is much more difficult to compensate due to the material additive building style of SFF. The tensile stress may cause notable distortion, and even cracks or delamination between adjacent layers.
- (7) It is very easy to build colorized parts with RFP process. Different portions of a part can be built with the same material of different colors.

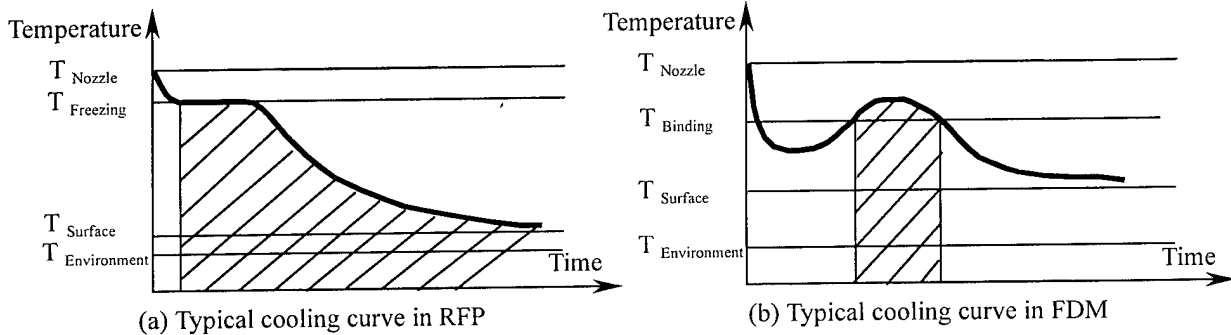


Figure 7. Comparison of typical cooling curves of deposited material in RFP and FDM

#### 4. APPLICATIONS OF ICE PATTERNS

All applications of ice patterns are faced with the problem of low operating temperature. This indeed makes application more difficult. However, in some cases, this problem can be solved or the advantages of RFP are dominant factors. The following describes some of the proper advantageous RFP applications.

##### 4.1 Visualization

RFP can easily build colorized and transparent ice parts. This feature is very important in some cases. For example, a model of diseased organ can help the surgeon to prepare the operation better. By utilizing RFP, a colorized ice model can be made with the CT scanning information, different portions in different colors. This colorized ice model can help the surgeon to get more information and better understanding about a disease focus. The transparent feature

of the ice model makes it possible to see the internal structure of the ice model of the diseased organ.

#### 4.2 Rapid Tooling

RTV silicone rubber molding is one of the most popular Rapid Tooling technologies. Our preliminary experiment shows that silicone molding with ice patterns at low temperatures is feasible. A major disadvantage is that it takes longer time for the silicone (2-composite mixture) to cure (at  $-10^{\circ}\text{C}$ ). However, easy pattern removal is a great advantage of RFP in case the part is very complex and the accuracy is very critical. In this case, after the silicone mold cures, the ice pattern can be removed from the silicone mold by melting instead of physical removal, and thus an accurate complex plastic part can be duplicated very rapidly. The procedure is as shown in Figure 8 and some pictures are given in Figure 9.

Another approach which uses UV curable silicone to replace the 2-composite silicone is being taken. In this approach, the material only reacts to UV radiation. The temperature is no longer an important factor for curing speed. Another advantage of this approach is that the curing speed is much faster than traditional silicone curing systems [7].

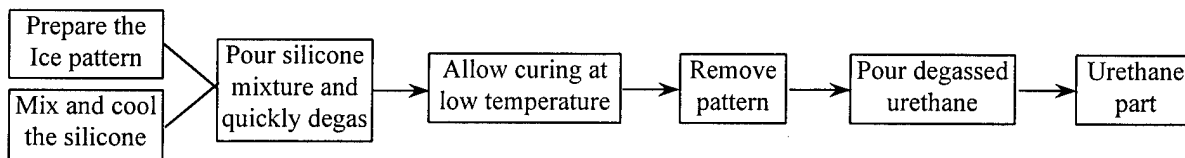


Figure 8. Procedure of silicone molding with ice patterns

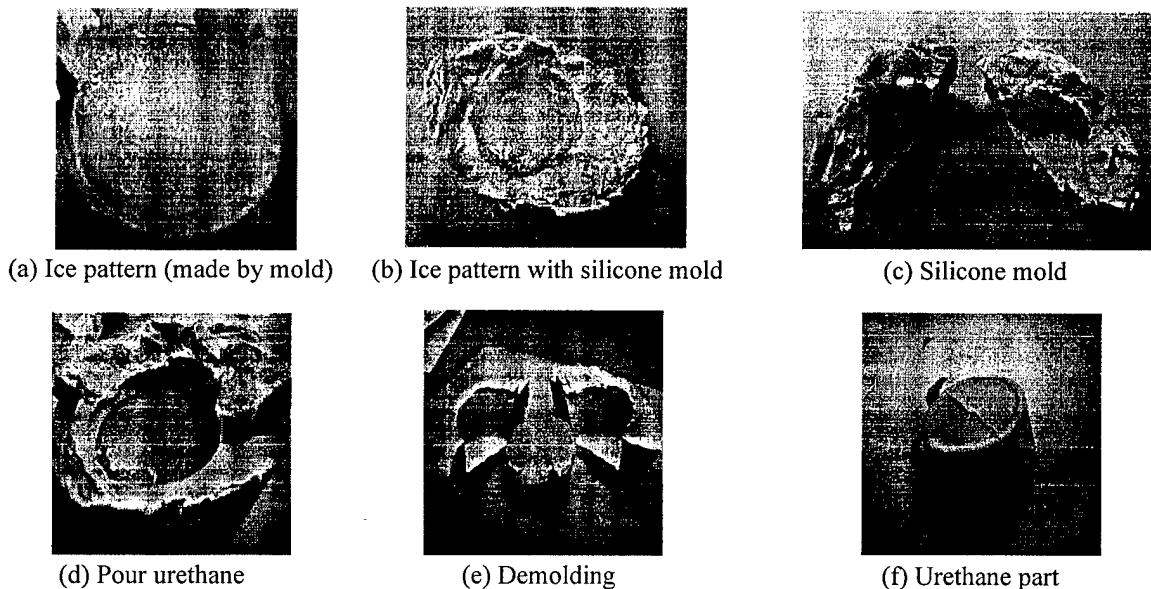


Figure 9. Silicone molding with ice patterns

### 5. CONCLUSION

Rapid Freezing Prototyping is a novel solid freeform fabrication process which has some advantages and disadvantages. The major disadvantage is that it needs low temperature operating environment. However, its advantages including good surface finish, potentially good accuracy, clean and cheap material, easy pattern removal and joining, easy expansion compensation, and

fast building speed makes it a good choice in some application areas. Our preliminary experiment shows that low temperature silicone molding with ice patterns is feasible. Urethane parts have been made with the silicone mold made with ice patterns.

Experiments on tooling application such as UV curable silicone molding and metal casting (including sand casting and investment casting) are needed to validate the application potentials of ice patterns. The building process, including build strategy, process control, and parameter tuning, needs to be developed and physically verified.

#### **ACKNOWLEDGEMENT**

The authors gratefully acknowledge the support of the National Science Foundation and the Multi-lifecycle Engineering Research Center at New Jersey Institute of Technology.

#### **REFERENCES**

1. Schmidt, L. D., "How Chrysler Is Using Stereolithography Rapid Prototyping Survey Results," *Proceedings of the Fifth International Conference on Rapid Prototyping*, Dayton, Ohio, June 1994, pp. 359-370.
2. Leu, M. C. and Zhang, W., "Research and Development in Rapid Prototyping and Tooling in the United States," *Proceedings of the International Conference on Rapid Prototyping and Manufacturing*, Tsinghua University, Beijing, China, July 21-23, 1998.
3. Yang, B., Leu, M. C., and Zhang W., "Rapid Tooling of Dies and Molds through Rapid Fabrication of EDM Electrodes," *Proceedings of the North American Stereolithography Users Group Conference*, San Antonio, Texas, 1998.
4. Jacobs, P. F., "The Effects of Shrinkage Variation on Rapid Tooling Accuracy," *Proceedings of the North American Stereolithography Users Group Conference*, San Antonio, Texas, 1998.
5. Leu, M. C., and Yao, W. L., "An Investigation into the Use of Laser Stereolithography in Rapid Prototyping and Tooling," *Report of the Robotics and Intelligent Manufacturing Laboratory*, New Jersey Institute of Technology, New Jersey, USA, 1997.
6. Zhang, W., "Rapid Freezing Prototyping," *Report of the Robotics and Intelligent Manufacturing Laboratory*, New Jersey Institute of Technology, New Jersey, USA, 1998.
7. Zsysys Inc., "An Innovative, Integrated, UV Cured System for Rapid Tooling," Torrance, CA, 1998.

# REDUCING THE SURFACE DEVIATION OF STEREO LITHOGRAPHY USING AN ALTERNATIVE BUILD STRATEGY

**P.E Reeves \*; R.C. Cobb \*\***

\* Department of Mechanical & Manufacture Engineering, De Montfort University, Queens Building, The Gateway, Leicester, LE1 9BH, UK

\*\* Department of Manufacturing Engineering & Operations Management, The University of Nottingham, Nottingham, NG7 2RD, UK

## 1.0 ABSTRACT

Considerable research has been undertaken to assess the suitability of different post-process finishing techniques, when used to reduce the surface deviation of Stereolithography components. Such techniques are however limited, as irregular roughness on the SL master often results in a loss in geometric integrity before the desired finish is achieved. Hence, removing much of the design intent and traceability within the automated fabrication process. Although a number of research initiatives have been undertaken to design layer manufacturing systems which produce inherently smooth surface, the problem of finishing parts from existing systems remains. The solution currently under investigation by the author is to develop a smooth build cycle within the SL machine, eliminating the need for costly machine modifications.

The solution developed by the author uses a strategy, which relies on both part orientation and a fundamental change to the current SLA build cycle. By orientating parts into an optimum build direction, the paper shows how naturally occurring phenomena within the SL process can be used to produce low roughness over a 50-degree window of surfaces. The paper goes on to demonstrate how, by using a resin meniscus scanned between layers during the build process, this smooth envelope can be extended to encompass 90-degree of surfaces. By scanning fillets between each layer, a reduction in surface roughness of up to 400% can be achieved on some angled planes. The paper concludes that by using this new build algorithm, the roughness of SL tool cavities can be maintained below  $9\mu\text{m Ra}$  on all surfaces. Hence, reducing or even eliminating the need for post-process finishing on all but the most accurate cavities.

## 2.0 INTRODUCTION

The application of layer manufactured components in the product development chain has in recent years extended from the production of simple models, prototypes and pre-production samples into the supply of accurate master patterns and cavities for a range of down-stream Rapid Tooling (RT) systems [1]. Of the available Layer Manufacturing Technologies (LMT), the Stereolithography (SL) process appears to dominate this sector, with the production of master patterns required for processes such as vacuum casting, cast resin tooling, sprayed metal tooling and the emerging Keltool process [2]. Down stream tooling processes now accounts for over 50% of the revenue generated within the RP industry [3]. More recently however, cavities manufactured directly on the SL machine have found applications in both high-pressure injection and reactive injection moulding [4].

Although it is now claimed that the SL process can maintain accuracy and repeatability of +/- 0.075-mm [5], the technique is not without its limitations. In addition to the limited process knowledge and experience of running RT cavities using conventional moulding machines, a question remains over the quality of parts produced from cavities manufactured using layers. Layer manufacturing has always been synonymous with poor surface finish. This being mainly attributed to stair stepping which occurs when the layer edge is not parallel with the part surface. The result is that many SL components require a significant degree of post-process finishing before they can be used as tooling patterns [6].

With the manufacture of master patterns for in-direct rapid tooling, the problems associated with the high surface roughness on the layer manufactured component have been overcome using post-process finishing techniques such as abrasive finishing [7], surface coating [8], or in most cases, a combination of additive and abrasive finishing [9]. These techniques although suited to visual prototypes and masters for components with non-critical dimensions, cannot easily be applied with high accuracy to master pattern or direct RT tool cavities. Hand finishing is both detrimental to part geometry and inverse to the philosophy of Rapid Prototyping. By manually finishing an RP part, all traceability within the manufacturing chain is lost, as geometric problems identified during product appraisal may be a function of the finishing process rather than the initial design.

With direct layer manufactured tooling it is often impractical to undertake manual finishing, as the aspect ratio of many cavities makes hand finishing impossible without the use of specialist finishing equipment. Although research is currently underway to assess the automated finishing of SL tool cavities using process such as Ultrasonic Flow Polishing, such techniques will inevitably increase the lead-time and cost savings associated with rapid tooling systems.

It is the author's opinion that the solution to reducing the surface deviation of the SL process, lies in a fundamental change in the way layer manufactured parts are built, by eliminating stair stepping at source. A number of research teams have addressed this problem, by proposing theoretical solutions such as variable layer thickness parts [10] and the use of variable angled layer edges [11]. The main limitation with previously research is that new hardware must be developed before surface roughness can be reduced. Given that over 1000 SLA machines have now been sold by vendor 3D Systems [12], it is the authors opinion that a new build strategy should be developed which can be use on existing SL hardware, hence eliminating the need for expensive modifications or complete system replacement.

### **3.0 RESEARCH METHODOLOGY**

A research project was started by the author in 1995 and was solely devoted to reducing surface deviation on SL components. The initial stage was to make a comparative analysis of different LMT process, to establish which attributes of the layer manufacturing process produce surface deviation [13]. By comparing eight of the leading RP systems, the research showed that in addition to layer thickness both the fundamental composition of each build layer and the profile of each layer edge have a unique effect on LMT surface topography. It was found that for SL process, particularly with the ACES build style, the composition of each layer has little overall effect on roughness when compared to either layer thickness or layer profile. However, with processes such as Laminated Object Manufacturing (LOM) and Selective Laser Sintering (SLS),

the composition of each layer was found to have a more pronounced affect on surface roughness than layer thickness or layer profile.

By developing a mathematical model of the relationship between layer manufactured surface roughness and build angle, it was demonstrated that significant reductions in SL surface roughness can be achieved by changing either the layer edge profile or the layer thickness. However, by modelling it was also demonstrated that although thinner layers can produce smoother parts, reduced layer thickness will not eliminate stair stepping completely and can increase built time to an uneconomic level.

Research concluded that the most probable solution to the in-process part finishing of SL components is to identify methods of changing layer edge profile within the current SLA technology. If layer edge profile can be optimised, it may be possible to eliminate stair stepping and yield a significant reduction in surface deviation.

### 3.1 Roughness evaluation of SLA parts

Before any changes were made to the existing SL build strategy, a series of test samples were produced to establish a benchmark roughness for each of the commercial SLA systems [14]. Benchmarking was undertaken using an STL file of the geometry shown in Figure 1, which exhibits a range of angled surfaces in 2-degree increments from 0-degrees up facing, through to 180-degrees down facing. Using 3D Systems Maestro™ software, support structure was positioned at the edge of each down facing layer to ensure no witness mark were evident on the surfaces of interest. Part were then manufactured using SLA250, 350, and 500 machines in epoxy resin, in addition to samples manufactured in acrylic resin using the SLA250.

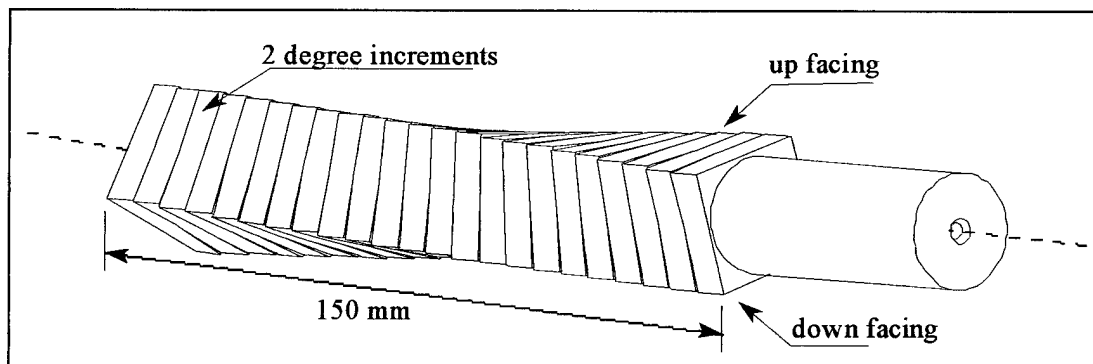


**Figure 1** – Test sample geometry used to determine SLA roughness

By positioning the samples in a dividing head, accurate roughness average data was measured using a contact Taly-surf interfaced to a surface analysis package. Using the average of six-roughness measurement, a comparison between surface angle and roughness was made for each of the test samples. A graphical representation of this comparison is shown in Figure 2.

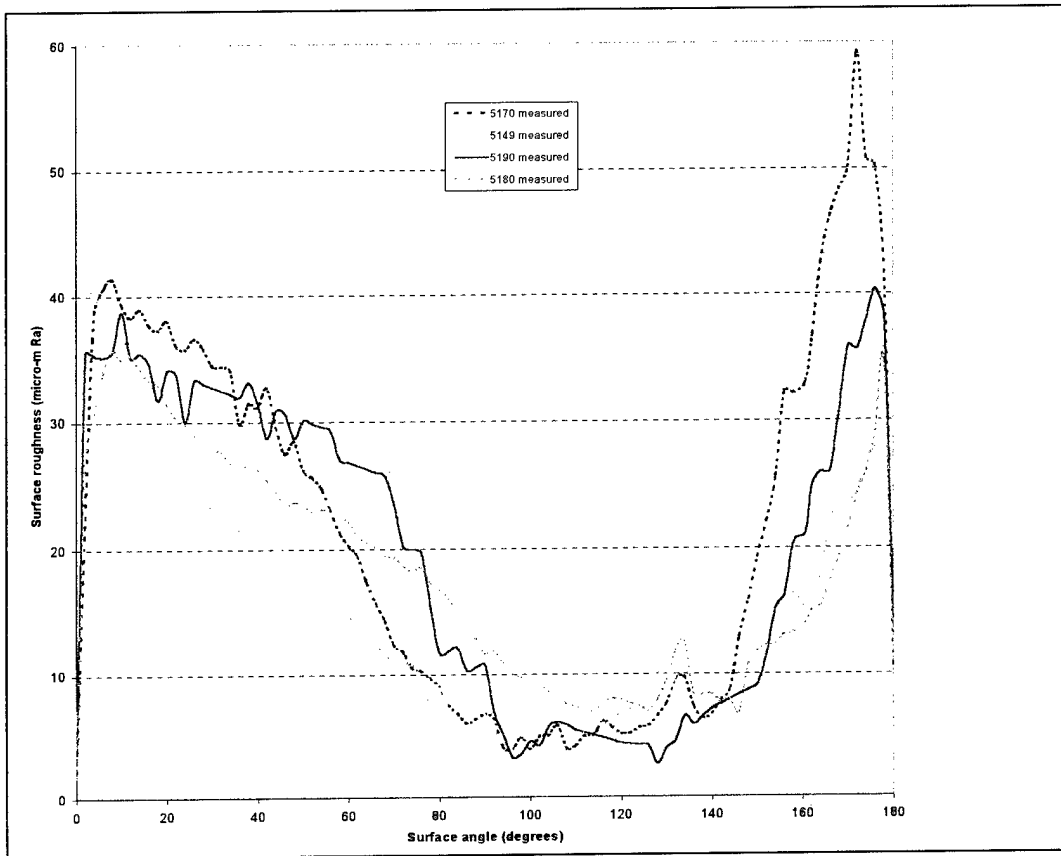


**Figure 2** – Surface roughness comparison of different SLA systems

From Figure 2 a distinct trend can be seen between each of the roughness plots relative to surface angle. As surface angle increases, so surface roughness decreases, as the effects of stair stepping become less prevalent. At 90-degree surface roughness should reach a low point as no stair stepping occurs on vertical planes. After this point, roughness should again increase. It is generally accepted that the roughness of planes between 90 and 180-degrees should mirror those between 90 and 0-degrees. However, in Figure 2 this is not the case, as the roughness of planes between 100 and 150-degrees show a much lower surface roughness than initially expected. This would suggest that some attribute within the build process creates a natural smoothing effects on surfaces within this band of angles. Hence, by orientating the critical surfaces of parts within this smooth envelope a significant reduction in surface deviation can be achieved.

### 3.2 Utilising print-through on down facing surfaces

On investigation, it was found that the smooth surface envelope is the result of partially cured resin at the interface of down facing layers, which continues to cure during the subsequent scanning of the next layer. The result being a fillet of cured resin between the interface of layers producing lower surface deviation. The fillet is now known to be a function of the mechanism by which layers are bonded, known as print-through, and was considered by the author as a possible solution to overall surface improvement on down facing planes [15]. However, the smoothing fillet was only found to improve surface between 100 and 150-degrees. Unfortunately, print-through is a function of both laser power and scan speed and cannot easily be controlled in real-

time by the process user. If print-through is to prove beneficial in reducing surface deviation on SL master patterns and cavities, it must therefore be combined with an additional smoothing strategy for angled surface either greater than 150-degrees or less than 100-degrees.

#### 4.0 MENISCUS SMOOTHING

A method of reducing the surface roughness of SL components within the build envelope has been discussed by both Narahara at the Kyushu institute in Japan [16] and Smalley of SL manufacturer 3D Systems [17]. In Narahara's research, the process called 'lift-up irradiation' stretches a meniscus of liquid resin between each polymerised layer. The resin meniscus is then locked in place using scan data from a previous layer as shown in Figure 3.

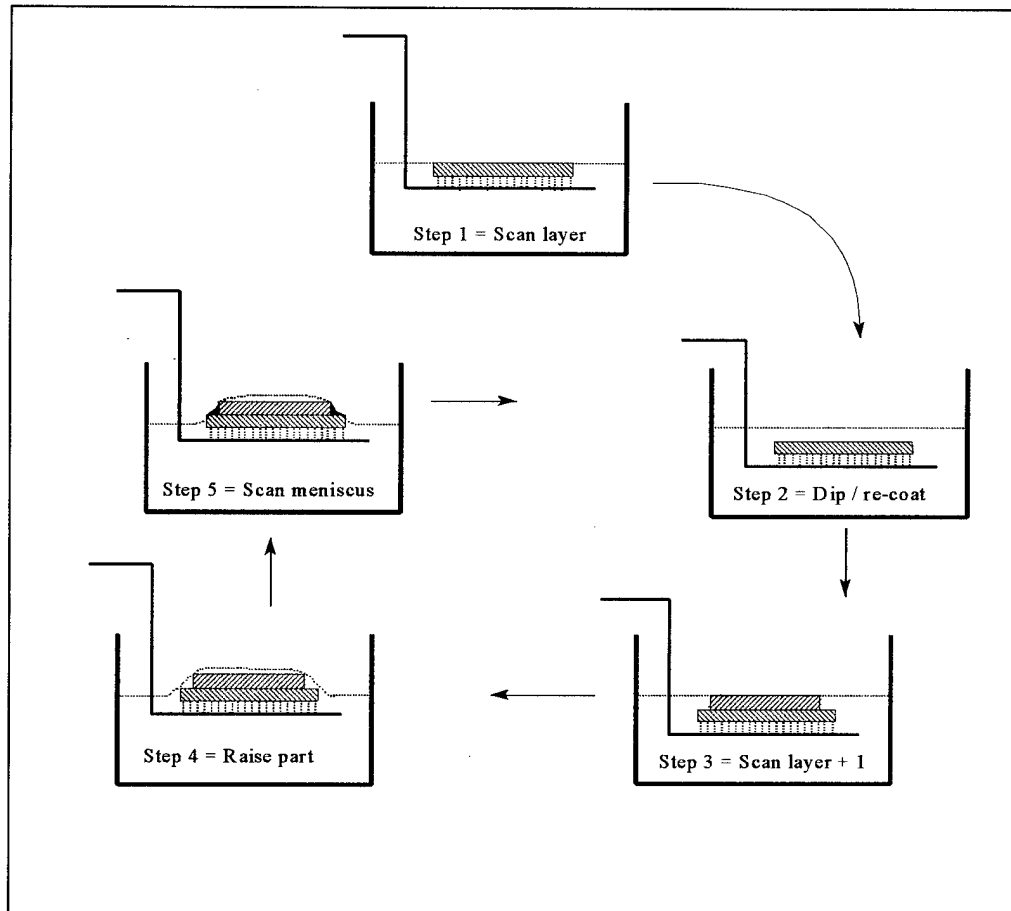


**Figure 3 - Lift-up irradiation or Meniscus smoothing**

Using a SONY JSC 2000 SL machine, with Japanese Synthetic Rubber company resin JSR 200, Narahara was only successful in smoothing surfaces between 10 and 30-degrees. However, successful meniscus were generated between layers ranging from 100 $\mu$ m to 400 $\mu$ m. Narahara concluded that although lift-up irradiation may provide a suitable method of building smooth parts using thick layers, the process is only suited to very limited geometries. Similar research by 3D Systems has also assessed the use of meniscus between layers. However, although 3D Systems hold patents on meniscus smoothing no practical examples of the technique have been shown by the company. 3D System chief executive Chuck Hill claims that meniscus smoothing

is limited to only external surfaces as trapped volumes prevent the generation of meniscus between layers [18]. For this reason 3D Systems have tackled surface smoothing using new thin layer build style [5]. However as previously pointed out, irrespective of layer thickness, stair stepping will always occur unless layer profile is modified. It is the author's opinion that the small range of angled planes found to benefit from Narahara's technique is the result of limited process optimisation. If meniscus smoothing is to be used as a complimentary process alongside print-through, the attributes effecting meniscus shape must be investigated and optimised relative to surface angle.

#### 4.1 Meniscus shape investigation

The shape of a liquid meniscus held between two surfaces is a function of many process attributes, including resin viscosity, temperature, material wetting characteristics and the contact angle of the solid surface interface. All these attributes are however dictated by the SL process and cannot easily be varied during the build cycle. One attribute of meniscus shape, which does vary, is surface angle, which is geometry dependent as shown in Figure 4.

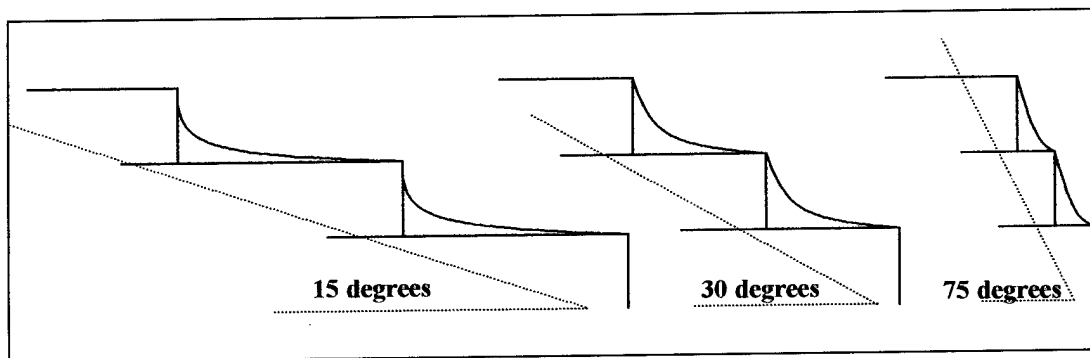


Figure 4 – The effects of surface angle on meniscus shape

In addition to surface angle, the retraction distance used to pull the meniscus above the vat of liquid monomer will also effect the shape of the resulting resin fillet. However, different retraction distances will produce different shaped smoothing fillets on different angled planes, as shown in Figure 5.

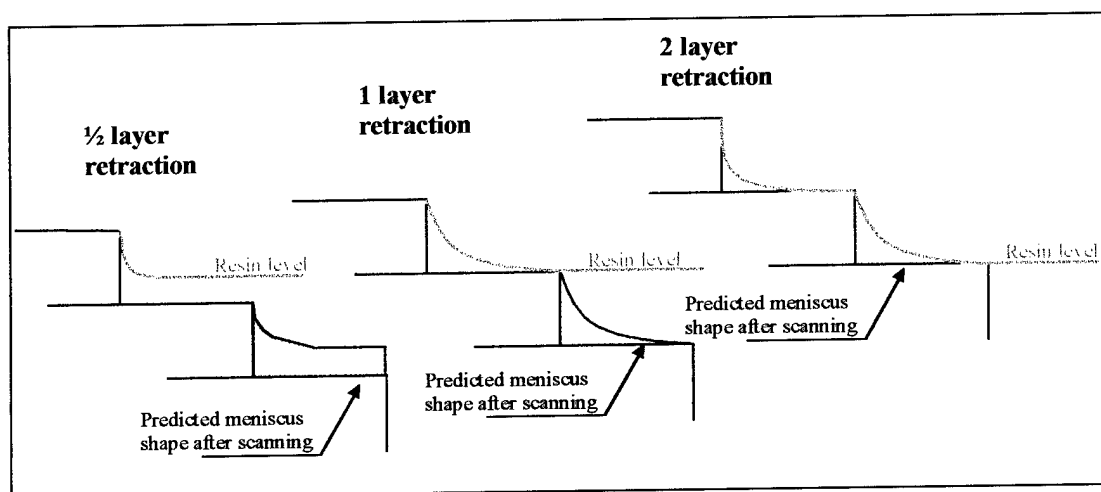


Figure 5 – The effect of retraction distance on meniscus shape

Unfortunately, none of the process attributes effecting meniscus shape can be modified using the current 3D-Systems Build-station™ software. For this reason a new control algorithm has been written to perform the meniscus smoothing cycle detailed in Figure 3. The software has then been run within the operating system of a standard SLA-250/40 machine. Using the new configuration, a series of optimisation experiments were undertaken to assess the effects of different shaped meniscus on different angled planes.

### 5.0 MENISCUS SMOOTHING RESULTS

Using a test sample with up-facing surfaces ranging between 0 and 90-degrees, in 10-degree increments, a range of 0.15-mm layer, ACES components were produced using the new build algorithm. Using the new control software, retraction distances of ½, 1 and 2-layer thickness were used to produce meniscus over each of the angled planes. Figure 6 shows the measured roughness of each sample relative to surface angle for each of the 3 retraction distances in addition to a standard 3D Systems 0.15-mm layer ACES part.

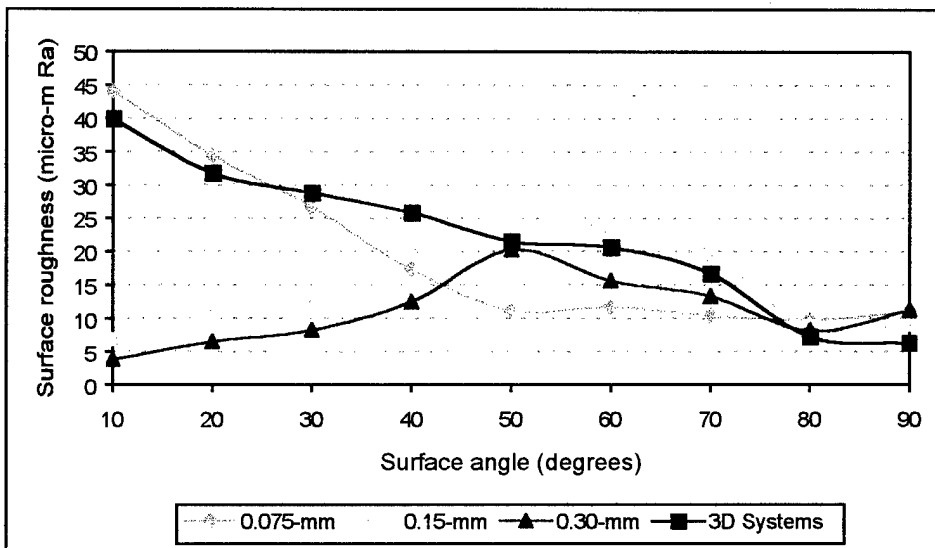
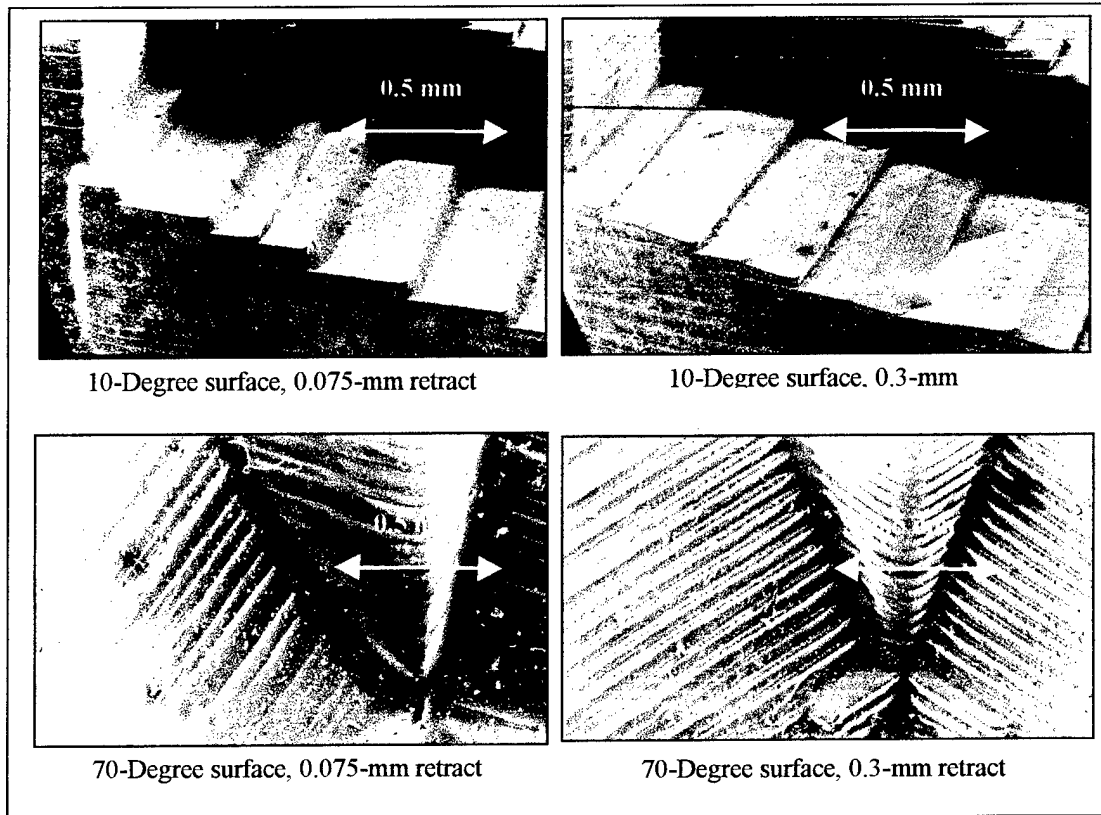


Figure 6 – The effects of meniscus shape on surface roughness

From Figure 6, it can be seen that on a 10-degree manufactured with a 0.3-mm retraction meniscus, surface deviation is below 10% measured on the part manufactured using the standard 3D Systems software. However, as surface angle increases, the effects of meniscus appear less prominent with surfaces between 50 and 70-degrees being reduced by only 60%. Between 80 and 90-degrees meniscus smoothing produces little improvement and can be detrimental in some cases. The effects of different retraction distance on surface deviation can be seen on the micrograph images in Figure 7.



**Figure 7** – The effects of different meniscus shape on 10 and 70-degree surfaces

From Figure 7 it is clearly evident that the 0.3-mm retraction benefits the low angles planes whilst the 0.075-mm retraction is more beneficial to the high angled surfaces. This would suggest that if meniscus smoothing were to be used as a complimentary process in addition to print-through a retraction distance of 0.075-mm would be most suitable as this produces the lowest surface deviation on angled planes between 50 and 100-degree.

## 6.0 SUMMARY

It is now possible to compare the effects of print-through produced by orientation and the reduction in surface roughness using optimised meniscus smoothing with the surface roughness of part produced using the standard 3D Systems software. Figure 8, shows the surface roughness of a standard 3D Systems 0.15-mm ACES sample over a 90-degree build envelope compared to a 90-degree build envelope produced using the new build strategy.

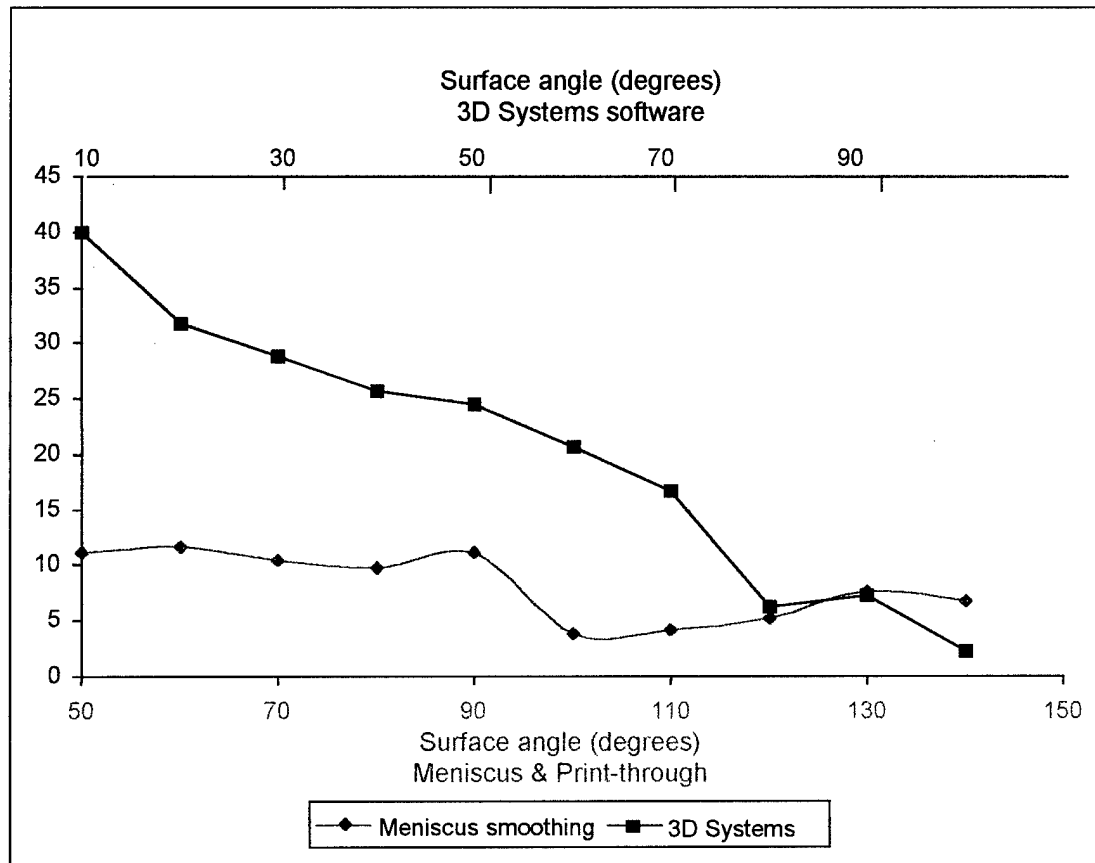


**Figure 8** – Roughness deviation of 3D Systems software compared to new algorithm

## 7.0 CONCLUSIONS

In conclusion it can be said that using the new build strategy a reduction in surface deviation can be achieved on 0.15-mm ACES components of up to 400%. In addition all surfaces within a 90-degree build envelope can be maintained below 10 $\mu$ m Ra, with a uniform roughness distribution. Using the standard 3D Systems software, the difference between the roughest and smoothest surface is 38 $\mu$ m. Using the new build strategy, this is reduced to only 6 $\mu$ m Ra. Hence, for application where a low surface deviation is required, such as tooling, post-process finishing will be less random as all surface on the model now require a similar level of post-processing, if at all.

Although the new smoothing algorithm requires both additional steps within the build cycle and for part be orientating into positions which will inevitable increase built time, it is the authors opinion that such limitations should not detract from the benefits of meniscus smoothing. The speed of the SL process has increased dramatically in recent years from the early 20mW He/Cd laser used on the SLA-1 to the 216mW Solid State Diode Pumped laser used on the new SLA-5000. In addition, the formulation of new resins has made scanning at much higher speeds increasingly possible. However, the cost of skilled labour used to finish parts has also increase, yet the consumer desire for lower price produces necessitates lower cost SL models. Hence,

automated in-process finishing is imperative if the process is to develop further into new applications. By further automating meniscus smoothing, many of the process limitation associated with geometries such as trapped volumes and increased build time could be eliminated, resulting in direct parts produced on SL machines which require no post process finishing at all.

## 8.0 REFERENCES

- [1] SFERRO, P.R. Integrating Time-Compression Technology into existing management Infrastructure, Proceeding of the 2<sup>nd</sup> Time compression Technology conference, 29-30 September 1997, pp163 – 170, Rapid News Publications Plc.
- [2] INNOVATIVE MANUFACTURING CENTRE, Rapid Prototyping workshop, High Field Science Park, Nottingham, UK, 12<sup>th</sup> – 13<sup>th</sup> November 1997
- [3] WOHLERS, T. Rapid Prototyping State of the Industry – 1997 world wide progress report Executive summary, published by Wohlers associates Inc Colorado, USA
- [4] GREAVES, T. HORODYSKY, M. Using Stereolithography to directly develop rapid injection mould tooling, Rapid News, Volume 5, Number 7, December 1997, publishes by rapid news publications Plc, UK
- [5] 3D SYSTEMS SLA-35000 sales literature, Valencia, CA, USA, P/N 70309, 31<sup>st</sup> August 1997
- [6] CHADWICK, A.L. Surface finishing of Stereolithography models used as patterns for Rapid Tooling techniques, BEng dissertation supervised by Dr R.C. Cobb, Department of Manufacturing Engineering and Operations Management, University of Nottingham, June 1996
- [7] RAPID FINISHING & TOOLING, EPSRC Grant GR/J97748, final summary report, June 1997, The University of Nottingham, Dept of Manufacturing Engineering.
- [8] REEVES, P.E. COBB, R.C. The finishing of Stereolithography models using resin based coatings, Solid freeform fabrication symposium, University of Texas at Austin, August 7<sup>th</sup> - 9<sup>th</sup>, 1995 pp 96 - 107
- [9] FLINT, B. ProtoTech Engineering applies finishing touch to Stereolithography, Unigraphics Centre line, Volume 7, Number 2, 1994
- [10] CAWLEY, J.D. WEI, Z.E. LIU, W.S. NEWMAN, B.B. Al<sub>2</sub>O<sub>3</sub> Ceramic made by CAM-LEM (Computer-aided manufacturing of laminated materials technology), Solid Freeform Fabrication Symposium, University of Texas at Austin, August 7<sup>th</sup> - 9<sup>th</sup>, 1995, pp 9 - 17

- [11] DeJAGER, P.J. Using Slanted and ruled layers for rapid prototyping, 5<sup>th</sup> European conference on Rapid Prototyping and Manufacturing, The Dipoli Conference centre, Finland, 4 – 6<sup>th</sup> June 1996, ISBN 0 9519759 5 1
- [12] CHANTRELL, A. Personal communication with director of sales for 3D Systems UK Ltd, 20<sup>th</sup> April 1998
- [13] REEVES, P.E. COBB, R.C. Improvements in the Surface Finish of Stereolithography Models for Manufacturing Applications, 1st National Conference in Rapid Prototyping and Tooling Research, Great Missenden, Buck's, Buckinghamshire College, 6th & 7th November 1995, ISBN 0 85298 982 2
- [14] REEVES, P.E. COBB, R.C. Surface deviation modelling of LMT processes - A comparative analysis, 5th European conference on Rapid Prototyping & Manufacturing, Dipoli conference centre, Helsinki, Finland, June 4th - 6th, 1996 pp 59 - 77, ISBN 0 9519759 5 1
- [15] REEVES, P.E. COBB, R.C. Reducing the surface deviation of Stereolithography using in-process techniques, Rapid Prototyping Journal, Volume 3, Number 1, 1997, ISSN 1355-2546
- [16] NARAHARA, H. A new method for improving performance and surface roughness in Stereolithography, Proceedings of: - The 2nd Korea-Japan Die & Mould workshop, Pusan National University, Pusan, Korea, June 28-30, 1995
- [17] SMALLEY, D.R. et al. Surface resolution in three-dimensional objects by inclusion of thin fill layers, US patent 5,209,878 May 11, 1993
- [18] HULL, C. 3D Systems, Chief Executive, Personal communication, July 15<sup>th</sup> 1997



# Sacrificial Materials for the Fabrication of Complex Geometries with LENS

E. Schlienger, M. Griffith, M. Oliver, J.A. Romero, J. Smugeresky\*

Sandia National Laboratories

Albuquerque, NM

\*Livermore, CA

The direct additive manufacturing of metallic components can present several process challenges. At present, there are several techniques for the accomplishment of this goal<sup>1,2</sup>, each with its own set of strong points and limitations. At Sandia, Laser Engineered Net Shaping, or LENS, is a process which has been developed for the direct additive manufacturing of fully dense three dimensional parts. In LENS, a Nd-YAG laser is focused onto a metallic substrate or onto previously deposited material. The laser melts the metal and a small pool of metal forms. Powder is injected into the pool and a bead forms. By rastering an x-y table to which the part is affixed in a controlled fashion, the bead is pulled and a fully dense metal part is formed. As currently configured, LENS is a 2<sup>1/2</sup> D process.

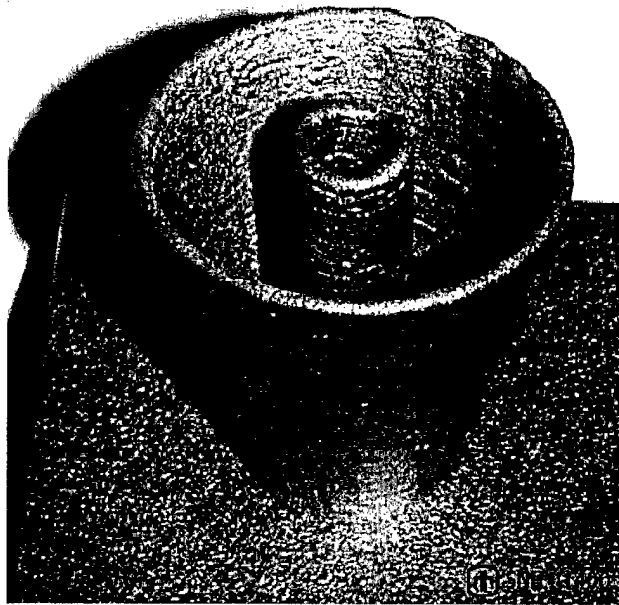


Figure 1  
Example of Overhang Capability in a 2<sup>1/2</sup>D LENS System

A potential drawback of this technique is that in order for deposition to occur, a substrate must be present. This limitation defines the degree of overhang that can be achieved with this

process. Since LENS deposition is based within an orthogonal coordinate system, the degree of overhang that can be achieved seems to be related to surface tension issues. At present, an overhang of about 15° is what may be readily achieved, and Figure 1 is an example of the sort of geometries that may be produced.

Although similar processes utilizing movable deposition heads<sup>3</sup> are more effective at producing overhangs, there will always be applications where some form of support structure is required to produce the desired geometry. One example of such a geometry might be injection molding tools with conformal cooling passages. In such a case, closing off the top of the cooling channel represents a process challenge. However, there are several ways of accomplishing this task. In Figure 2, the image on the left illustrates the manner in which cooling passages may be built into a part simply by utilizing the overhang capacity inherent in the system. Whereas the picture on the right demonstrates that tubing can be readily incorporated into LENS produced components.

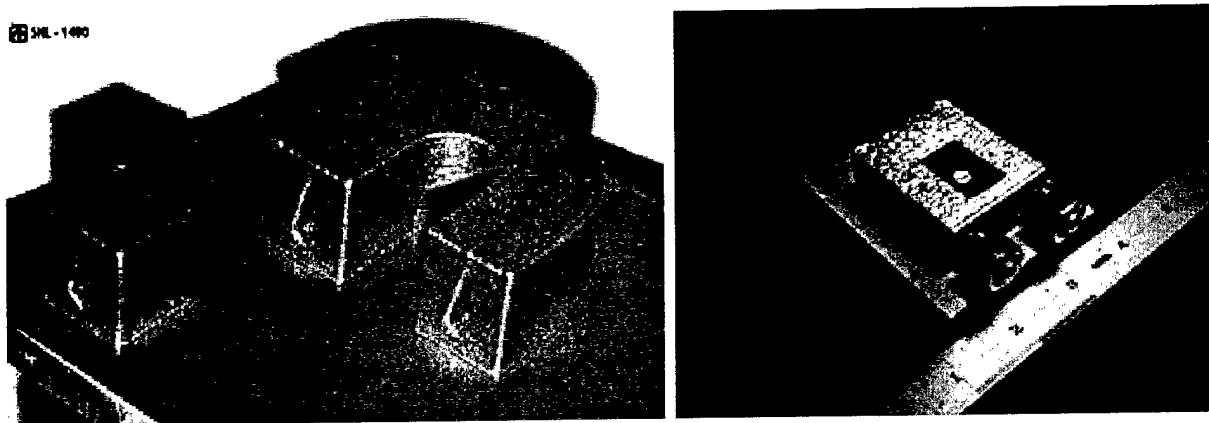


Figure 2  
Cooling channels built with overhang and inserted tube.

Both of these techniques have applications in the production of many different types of parts. Further, manipulation of the deposition head can provide an even greater overhang capability and further extend the ability of the process to produce enclosed shapes. However, even with these various capabilities, some shapes are most readily produced if some form of underlying support is available.

Such a capability is typically achieved by using a sacrificial material. The requirement for such a material is that it must be readily placed, and easily removed from the finished part. Typically, this means that the sacrificial material must not bond to the main structure, or it must be readily removed through some process such as acid etching. Finding a material that is readily deposited via LENS, can withstand molten metal deposition, and not bond to such a deposition is a challenge. The removal of support structures via acid also has some complications associated with it, and since LENS is a melting process, acid etching is not expected to produce good interfaces at the boundary of the sacrificial material.

These problems have been addressed by using powder of the parent material as the necessary support structure. The mechanics of this process are shown in Figure 3. Typically, a part is built up to the point where a support structure is needed. In the case of cooling passages or internal voids, this leaves a cavity in the part. For other types of structures, a form is required to

hold the powder in place. Once a cavity is available, it is filled with powder up to the level of the existing deposition. At this time, the laser is defocused (by increasing the standoff) and the beam is then played over the entire part. This action sinters the powder, resulting in a thin sintered surface layer on the top of the powder bed. This surface layer serves two purposes. First, it delivers the obvious advantage of providing a substrate for subsequent deposition. Additionally, it provides a protective layer that prevents the powder from being blown away by the argon gas used to deliver the powder to the laser spot during the deposition operation. It should be noted that the deposition process after sintering fully melts the sintered layer.

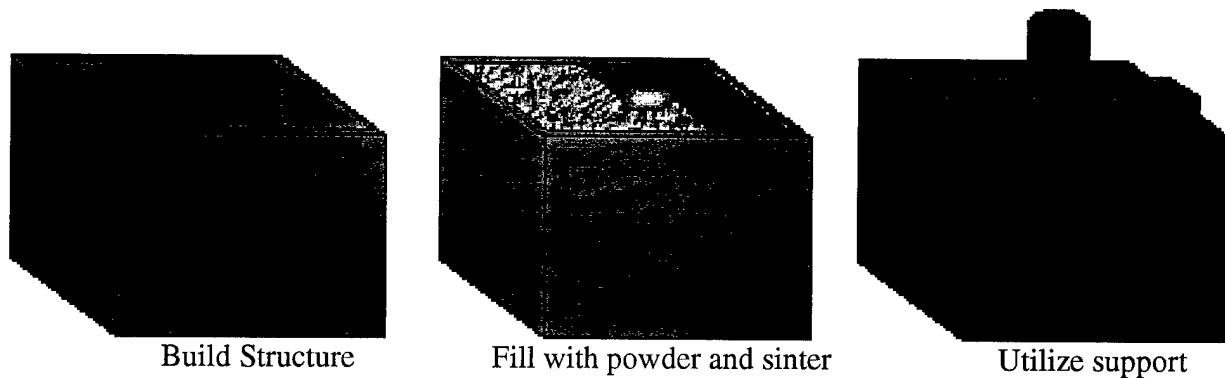


Figure 3  
Using Sintered Powder as a Support

Initial experiments were conducted using simple shapes as shown in Figure 3. The initial material used for these experiments was stainless steel, with subsequent experiments conducted using titanium. Typical processing parameters for stainless steel were 380 watts, 500 mm per minute travel speed, .5mm hatch spacing and .5mm vertical slice thickness.

During the initial experiments, it was found that the sintering operation needed to be conducted with care lest the sintered layer curl up. Typically, such conditions occur when too much power is applied and the powders begin to melt. Subsequent solidification then pulls the top surface, causing the sintered layer to raise upward. Once the sintered layer curls, powder, which resides beneath it, can be blown away by the deposition process. This action results in a void below the sintered surface. When such a void occurs, the sintered layer no longer has a heat sink beneath it and the passage of the laser burns a hole into the cavity beneath. Subsequent deposition passes fill this void. This results in a finished structure that looks fine from the exterior, but has a significant irregularity in the internal cavity.

Similar experiments, conducted using titanium, indicated that titanium served as a better support than stainless steel. During the sintering operation, the titanium seemed to form a more robust sintered layer that was less prone to curling. The titanium was processed at 450 watts, 500 mm per minute travel speed, .5mm hatch spacing and a .5mm vertical slice thickness. The higher power has been found to be necessary in order to obtain sufficient melting, however, it is not responsible for the better sintering behavior. This is born out by experiments with stainless steel that illustrated that above a certain power level, the sintered layer began to curl and actually burn off. As a result, increasing the power during the sintering operation actually proved to be detrimental to the production of a good substrate for subsequent deposition operations.

The results of the titanium experiments are shown in figure 4. These hollows were built using the above processing parameters and were produced via a process similar to that illustrated in Figure 3. Once the parts were built, the ends were cut off to allow the powder to be removed and the internal cavity to be observed. Although the top surfaces are not completely flat, they do demonstrate the ability to produce a fairly regular cap.

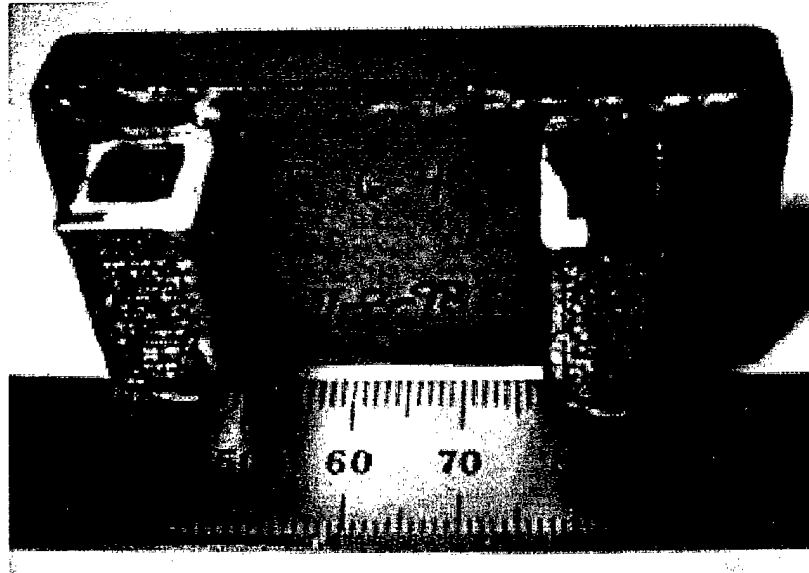


Figure 4  
Titanium hollows produced using powder as a sacrificial material.

Once confidence had been gained that small structures could be produced, a larger item was designed. As a demonstration, a backwards “S” shaped tube was built out of stainless steel.

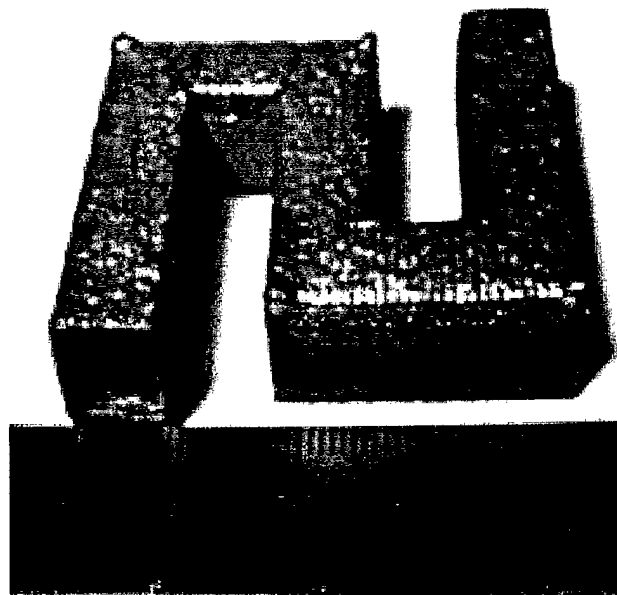


Figure 5  
Stainless steel S-Tube built using powder as a sacrificial material

As may be seen in Figure 5, this technique is suitable for producing internal passages of moderately complex geometry. The most significant challenge is adherence of the sintered layer to the object side walls. If there is a gap between the sintered cap and the part wall, powder is blown out from underneath. Without the heat sinking capacity of the powder, the sintered surface layer burns through and the integrity of the cavity is compromised.

In summary, the capability of LENS and similar processes can be extended by using powder as a sacrificial support material. Since the sintered layer becomes fully melted during subsequent deposition the resultant microstructure maintains the fully dense and melted aspect that is characteristic of this process.

Sandia is a multi-program laboratory operated by Sandia Corporation, a Lockheed Martin Company, for the United States Department of Energy under Contract DE-AC04-94AL85000.

- 
- <sup>1</sup> D.M. Keicher, J.L. Jellison, L.P. Schanwald, J.A. Romero and D.H. Abbott, "Towards a Reliable Laser Powder Deposition System Through Process Characterization", 27<sup>th</sup> International SAMPE Technical Conference, Vol. 27, Diversity into the Next Century, Proc., of SAMPE '95, Albuquerque, NM, Oct. 12-14, 1995, p. 1029.
  - <sup>2</sup> J.L. Koch, J. Mazumder, "Rapid Prototyping by Laser Cladding" presented at ICALEO 1993, Orlando FL, 1993.
  - <sup>3</sup> G.K. Lewis, J.O. Milewski, R.B. Nemec, D.J. Thoma, M Barbe, D. Cremers, "Directed Light Fabrication", Los Alamos Laboratory Publication LA-UR-95-2845, Los Alamos, NM, 1995.



# Rapid Prototyping Based on 2D Photographic Images

Jianguo Wang, Y.S. Wong, Jerry Fuh and H.T.Loh,  
MPE Department, National University of Singapore  
10 Kent Ridge Crescent, Singapore 119260

ZhaoHui Du, GuoDong Hong and YongNianYan  
Center for Laser Rapid Forming, Tsinghua University  
Beijing, P.R.China, 100084

## Abstract

Generally it is difficult to get a 3D model from its 2D images. However, if the object is symmetric and its photograph is taken in appropriate perspective, then it is possible to extract pertinent 3D information from its 2D images. In this paper, a reverse engineering method to derive the 3D surface model from 2D photographs is introduced. Through a case study, the entire process from photo taking to 3D model making and subsequent rapid prototyping of a model car is introduced. The techniques and related problems of reverse engineering and rapid prototyping are discussed and the future research direction is proposed.

## **Introduction**

By combining reverse engineering, CAD system and rapid prototyping technology together, a rapid product development system can be formed. This system can accelerate the iterative design process from initial conceptual and aesthetic design, product prototyping, and performance testing to model modification. Much work has been done in the area of reverse engineering, such as techniques using laser scanner, CMM, structured lighting, moiré interferometers, etc. A comprehensive summary on these approaches can be found in [1].

There are two ways to reconstruct a 3D model from its 2D images according to the types or different features of 2D images. One approach uses 2D images from medical CT, MRI or industrial CT systems. Each of these images presents one intersection layer of the 3D object. The 3D solid model of an object can be reconstructed from a large amount of this type of 2D images. The 3D model obtained possesses both exterior and interior features of the object. Extensive research has been done using this approach<sup>[2][3]</sup>. Another approach employs 2D photographic images or images of an object taken for different angles. The 3D model can be reconstructed based on one or more of this type of photographic or perspective images. In this case, only the surface or external features of the object can be captured.

Generally it is impossible to get a unique 3D model from the 2D images because of inadequate information. However, if the object is symmetric and its photographic image is taken from a perspective view, it is possible to extract necessary 3D information from its 2D image. In this paper, a 3D-model reconstruction process based on the 2D photographic images is introduced. The integration of the reverse engineering method and rapid prototyping technology

is also discussed. Through a case study, the entire process from photo taking to 3D surface model reconstructing and rapid prototyping of a model car is presented.

The approach of creating 3D model out of one or more 2D photographic images has many applications. There are many situations where conventional reverse engineering methods cannot be used. One typical application is tourist souvenir product design and fabrication. This kind of design is often a miniature size of the original object based on existing buildings, statue, old car, etc. Normally this kind of applications does not require high accuracy and serves just as a basis for further modification.

### **3D reconstruction based on 2D photograph:**

Perspective drawings are commonly used as a tool to express and record the objects in 3D space in architecture and mechanical engineering field. A photograph quite resembles perspective drawing if the photograph is taken in a perspective view. Theoretically it is possible to reconstruct 3D model of the object from the photographs of it from different angles or perspectives. The major difficulty is the determination of the corresponding coordinate systems and the unification of them into one coordinate system. If there is only one photograph, the reconstruction will be much more difficult. It requires additional information. The symmetry of the object can double the information obtainable from the photograph. In addition, manual input from an expert is also required to interpret vague information, rendering the reconstruction of the 3D surface model tedious and difficult.

There are numerous texts on methods to construct a perspective drawing to describe the 3D features of an object<sup>[4][5]</sup>. The process presented here is reversed. We already have the perspective photographs or images. The goal is to get the 3D features from these images. The reconstruction process is introduced as follows, assuming that the photograph is already scanned into the computer using a normal flat scanner.

- *Vanishing points and object coordinate system:*

Select two parallel lines on the object and extend them in the perspective view to meet in one point, called the vanishing point. For a two-point perspective there are two vanishing points,  $V_x$  and  $V_y$ , as shown in Fig.1

Select any point  $Q$  on the object as the origin of the object coordinate system. Through the origin, establish the two lines towards the two vanishing points. Then a right-hand object coordinate system can be established (Fig.1).

- *Station Point:*

If the station point is shifted, the vanishing points will also be shifted. The station point can be determined by the vanishing points.

In the Fig.1,  $PP$  is the picture plane.  $V_x$  and  $V_y$  are the left vanishing and right vanishing point respectively. Build a semi-circle based on the segment  $V_xV_y$ . Make a line that passes the

middle point of the object in the image and is perpendicular to the  $V_xV_y$ . This line will intersect the semi-circle at point E, which is the station point.

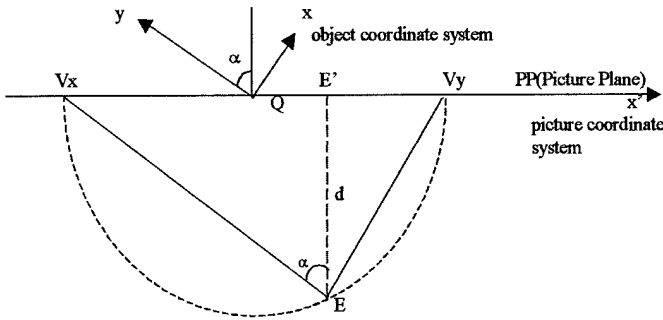


Fig.1 Building of Coordinate System and Station Point

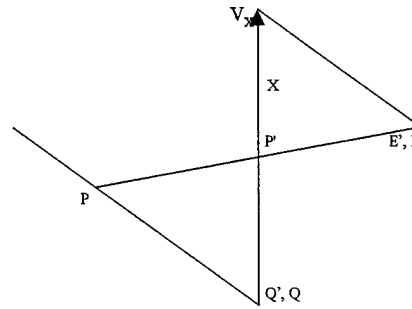


Fig.2. Calculation of symmetry plane

The distance  $d$  between the station point E and picture plane PP can be calculated by the following equations:

$$d = |EE'| = \text{sqrt}(V_xE' * E'V_y) = \text{sqrt} ( |x'_{V_x} - x'_{E'}| * |x'_{E'} - x'_{V_y}| ) \quad (1)$$

$$\sin \alpha = |x'_{E'} - x'_{V_y}| / \text{sqrt} ( d^2 + |x'_{E'} - x'_{V_y}|^2 ) \quad (2)$$

$$\cos \alpha = d / \text{sqrt} ( d^2 + |x'_{E'} - x'_{V_y}|^2 ) \quad (3)$$

Where the  $x'_{V_x}$ ,  $x'_{V_y}$  and  $x'_{E'}$  are the coordinates of points  $V_x$ ,  $V_y$  and  $E'$  in the picture coordinate system.

Then the coordinate E ( $x_E, y_E, z_E$ ) is:

$$\begin{bmatrix} x_E \\ y_E \\ z_E \end{bmatrix} = \begin{bmatrix} -d * \sin \alpha + x_{E'} \\ -d * \cos \alpha + y_{E'} \\ z_{E'} \end{bmatrix} \quad (4)$$

• *Symmetry plane of the object:*

When the object to be reconstructed is symmetric, the symmetry plane can be calculated. The symmetry plane should be the plane where all the middle points of the two symmetry points of the object lie. The normal of the symmetry plane is assumed to be in the direction of the  $x$  axis. Using the coordinate origin Q and its symmetry point P, the equation of the symmetry plane can be calculated as  $x = x_P/2$ , where  $x_P$  is the coordinate of point P.

The determination of  $x_P$  is in Fig.2.  $V_x$  is the vanishing point in the  $x$  axis direction.  $E'$  is the orthographic projection of the station point E on the image. Q is the origin of the coordinate system. Notice that only the  $x$  axis is drawn.  $P'$  is the perspective projection of point P, which is the symmetry point of the origin Q.

$$|QP| = x_p = |Q'P'| / |P'V_X| * |EV_X| \quad (5)$$

Here  $|EV_X| = \text{sqrt}(d^2 + |E'V_X|^2)$

Thus the equation of the symmetry plane is:

$$x = |Q'P'| / (2 * |P'V_X|) * \text{sqrt}(d^2 + |E'V_X|^2) \quad (6)$$

- *Feature points retrieving from surface of object:*

Based on the above principles, the points on the surface of the object can be uniquely determined. According to the symmetry characteristics, two points can be obtained at the same time. These feature points are selected interactively. The coordinates of the feature points and their corresponding points can be calculated using equation (1)-(6). For straight lines, two points are enough to reconstruct them. For curves and free surfaces, more feature points are necessary.

- *Reconstruction of surface model*

After extracting the feature points, different kinds of curves can be chosen to interpolate the feature points and form the boundary lines of the surface patch. Four boundary lines that form a closed loop can be used to interpolate the freeform surface. The surface model can then be derived from these free surface patches<sup>[6]</sup>.

The TDS (Three Dimensional Surface) modelling system is developed based on above principles.

### Integration with RP system

The surface model derived from the TDS modeling system consists of a set of surface patches. There exist two major problems in its application in RP technology. Firstly, the surface model often has zero-thickness and open surfaces. This is not suitable for rapid prototyping, which requires the model to be solid or closed surface model. There are three ways to generate a solid or closed model from an open surface model.

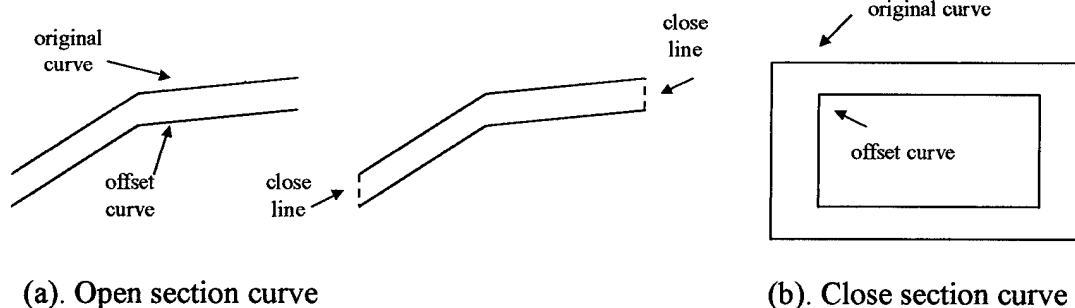


Fig.3. Get a shell by offsetting the 2D sliced section of STL model.

- To close the surface manually by including additional surface patches to close the open surfaces.
- To offset the open surface model so as to create a shell model with a certain thickness.
- Using the layer manufacturing features of the rapid prototyping technology, instead of generating a 3D offset to create the shell model, it is possible to first determine the 2D sliced section of the model, offset the curve and then close the open ends of the curve and its offset to form a 2D closed path, as shown in Fig.3. This will be much simpler than 3D offset.

STL file generation is another problem. By meshing the surface model the STL file can be generated. The problem is that in many cases the boundary curves of the two neighbouring surface patches do not match exactly. There exist some cracks and holes on the surface model. These small cracks cause no problems for rendering and display, but become critical if the models are used for rapid prototyping. The STL files generated from this kind of surface model will also have cracks and holes. Thus sliced layer curves maybe not be closed or continuous and this results in cross-section raster filling errors and ruins the fabricated parts. It is necessary to inspect and modify the STL model. This involves using flat plane to fill the gaps and holes in the STL model. Hence the missing freeform surface patches are replaced by flat planes, rendering the model less accurate.

Above method can not generate an error-free STL model because of the lack of topological information of the surface model. Once its topological information is reconstructed, the surface model can be transferred into a solid model. Then the error-free STL file can be generated. At present only few articles discuss this approach<sup>[7]</sup>.

Besides STL file, another way to bridge the surface model and rapid prototyping is to slice surface model directly. Direct slicing is more accurate and also easier to be converted into an RP slicing file format, such as the CLI or SLC file format<sup>[8]</sup>.

In our case study, two transfer methods are considered. One is to generate, check and repair the STL output. Another is direct slicing of the surface model and then converts it into CLI or SLC format.

The above processes can be summarized in the Fig.4.

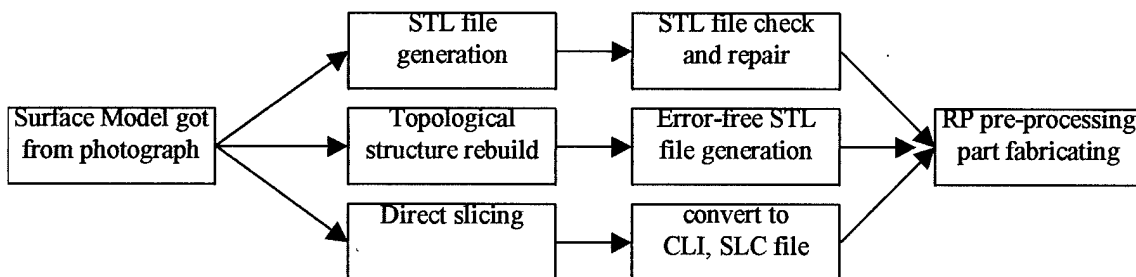


Fig.4. Process from surface modeling to part fabricating

**Case study:**

In this case study the integration of the TDS modeling system and MRPMS (Multi-functional Rapid Prototyping Manufacturing System) machine of Tsinghua University is investigated. The entire process is introduced from photo taking and scanning, feature point selection, curve reconstruction, surface reconstruction, STL file generation, inspection, modification and final rapid prototyping fabrication.

- Photographic image capture

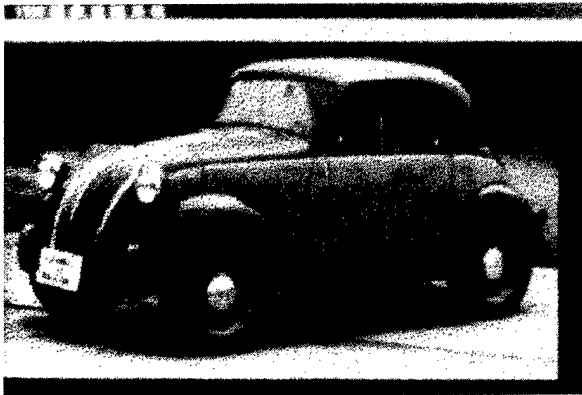


Fig.5. Photograph of the car

Take photo of the object according to different perspective requirements. For a symmetric object, generally only one photograph is needed. Use a normal flat scanner to scan the photo into the computer.

- Feature points selection and the construction of the surfaces.

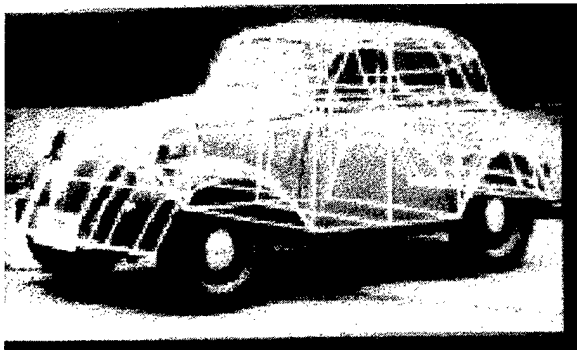


Fig.6. Feature point selection

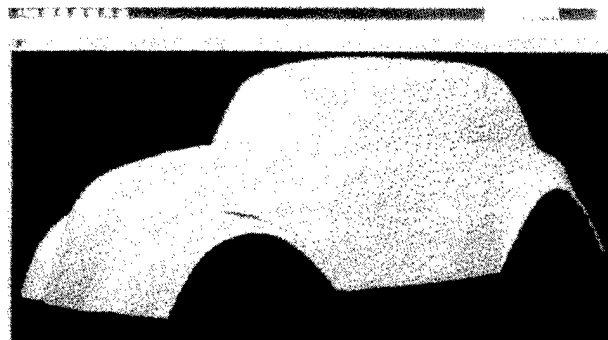


Fig.7. Rendering of surface model

The feature points are selected interactively. According to symmetry, two points can be obtained at one time. Appropriate curves can be determined based on the selected feature points and the corresponding surface can then be computed. Good knowledge and understanding of perspective are required in the selection of the feature points.

- STL file generation:

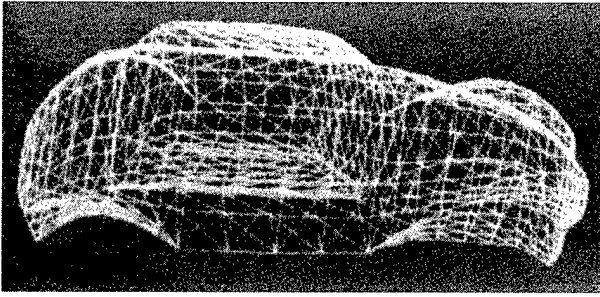


Fig.8. Generated STL model

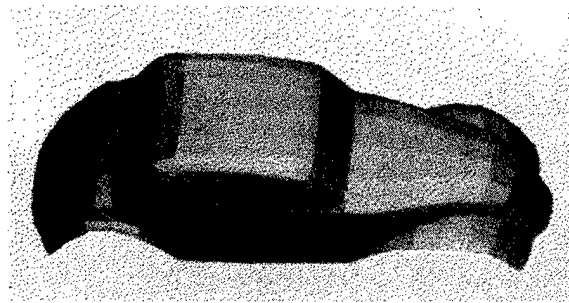


Fig.9. Rendering of the STL model

The STL model can be generated based on the surface model. Fig. 9 is the shaded display of the STL model.



Fig.10. Model of the car fabricated by MRPMS machine

- STL file inspection, repair and slicing

The STL file generated directly from surface model is not error-free. Before slicing, the topological structure must be reconstructed to record the topological relations of vertices, edges and facets in the STL file. Then the errors of STL file can be checked according to the topological structure and be repaired.

- RP fabrication of the model.

Once the error-free solid STL model is obtained, the STL file can be used for various kinds of rapid prototyping fabricating. In this case study, the MRPMS machine developed in Tsinghua University is used. See Fig.10.

Direct slicing is also tested. The sliced data are converted into CLI or SLC file format for rapid prototyping fabricating. Fig.11 shows the directly sliced contour in the TDS modeling system.

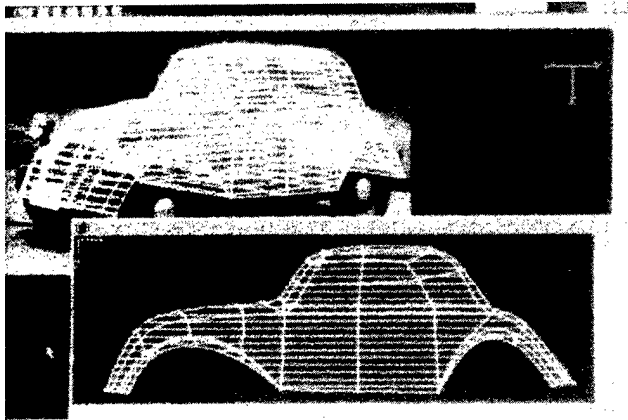


Fig. 11. Direct slicing of the surface model in TDS modeling system

### Conclusion and Future Research

This paper presents a reverse engineering method to reconstruct a 3D surface model based on the 2D perspective photographic images. The case study illustrates the feasibility of getting the approximate RP model of a car from its photographic image. It can be applied to tourist souvenir product design or similar application when other reverse engineering methods are difficult to use.

This work is still in a primary stage. The feature points are selected manually. For the complex object, the process is troublesome and tedious. The details are difficult to capture using a point. This will cause the inaccuracy of the model.

To improve the process, advanced image processing and pattern recognition techniques can be used to detect the feature points automatically. Besides the perspective and symmetry information, other parameters such as colour, shade, materials appearance, etc can also be included to improve the accuracy of the feature point selection.

### Reference:

1. Bidanda, B. and Hosni, Y.A. Reverse Engineering and its relevance to industrial engineering: a critical review. *Computers and Industrial Engineering*, 26(2), 343-348, 1994
2. Lim, C.T., Ensz, M.T. Ganter, M.A., Storti, D.W. Object Reconstruction from Layered Data using Implicit Solid Modeling. *J. of Manufacturing Systems*, 16(4), 260-272, 1997
3. Hirsch, B.E. Reconstruction of Volume Boundary from Layers by Triangulation. *J. of Manufacturing Systems*, 16(4), 249-259, 1997
4. Jefferis, A. and Madsen, D. A. *Architectural Drafting & Design*. Chapter 40, 627-639, Third Edition, Delman Publishers, 1995
5. Pare, E.G. etc. *Descriptive Geometry*. 9<sup>th</sup> edition, Prentice-Hall, 1997
6. Shun JiaGuang, Yang ChangGui, *Computer Graphics*, Tsinghua University Press, 1995
7. Sheng, X. and Meier, I.R. Generating Topological Structures for Surface Models. *IEEE Computer Graphics and Application* 35-41, Nov. 1995
8. Chua C.K. and Leong K.F. *Rapid Prototyping: Principles and Applications in Manufacturing* John Wiley & Sons, 1997

Fig.5

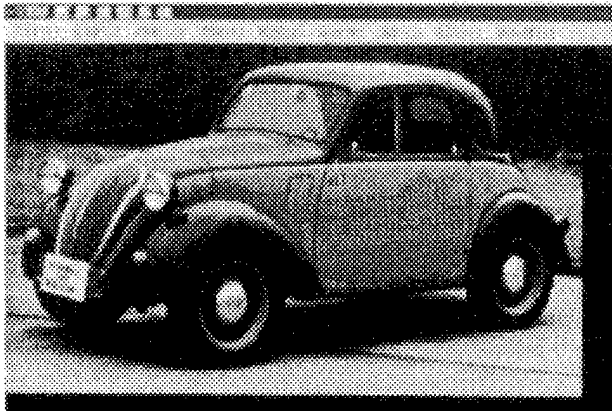


Fig.6

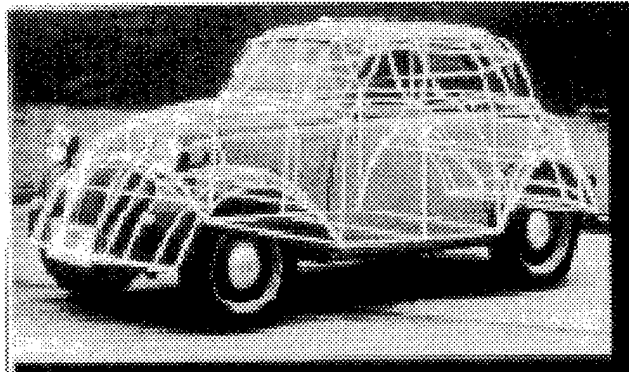


Fig.7

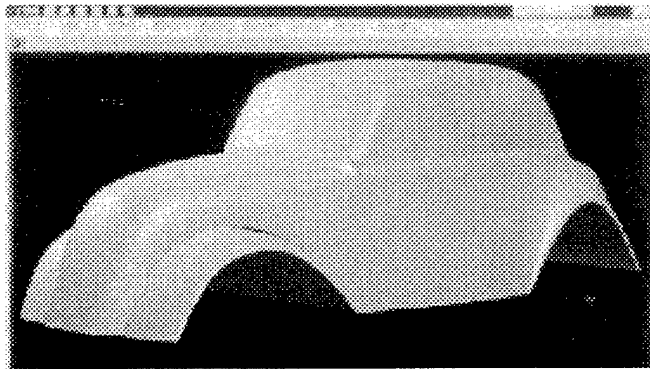


Fig.8

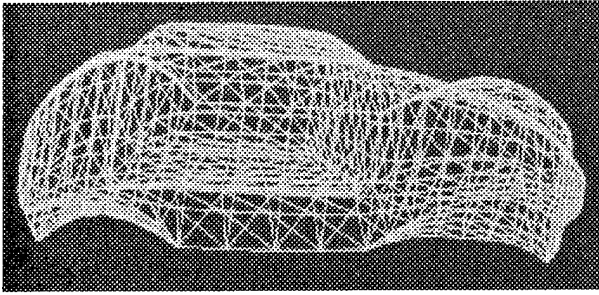


Fig.9

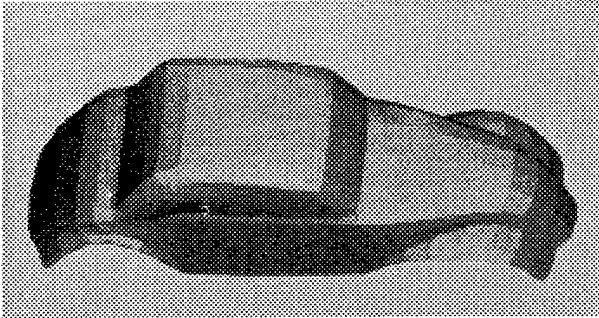


Fig.10

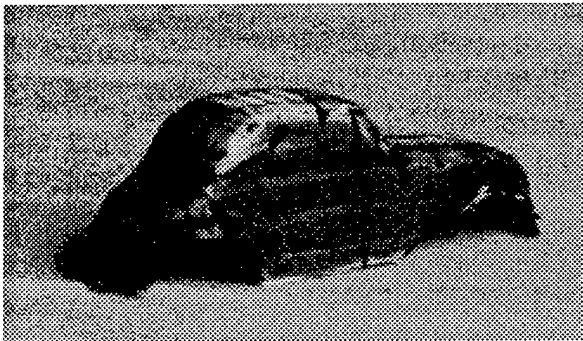
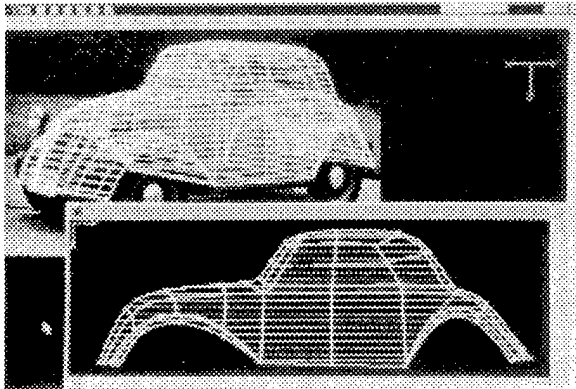


Fig.11



# Art to Engineering: Pervasive RP activities at Arizona State University

Anshuman Razdan, Mark R. Henderson and Dan Collins  
MC5106, PRISM,  
Arizona State University, Tempe, AZ-85287-5106  
prism@asu.edu

## Abstract

We present a sampling of widely diverse Rapid Prototyping activities at ASU. Through the interdisciplinary PRISM project, RP is firmly involved in three areas: education, research and outreach. Two courses have been developed, one teaches RP over the web and the other Visualization and RP as applied technologies aimed at interdisciplinary graduates and seniors. Researchers and students from Engineering, Architecture and Industrial Design, Fine Arts and Liberal Arts and Sciences and Business actively use RP. A recent formation of the PARfC (PRISM Advanced Rapid-fabrication Consortium) Consortium with local industry will create a local and formal center for research, education, service and training in Rapid Fabrication.

## Introduction

### *Description of PRISM*

PRISM stands for Partnership for Research In Stereo Modeling. PRISM was established over two years ago at ASU to promote interdisciplinary research in the areas of 3D Data acquisition, Visualization and Modeling, and Form realization. PRISM researchers come from diverse backgrounds such as Biology, Fine Arts, Archaeology, Anthropology, Computer Science, Mechanical and Industrial Engineering to name a few. The common interest among various disciplines in 3D and higher dimensional data sets is the key motivation for PRISM.

### *Description of PARfC*

Many rounds of discussions and need for a joint Rapid Prototyping and Fabrication research between local companies such as Motorola, Allied Signal, Boeing, PADT, Raytheon and Toy Time Inc., led to the formation of the PRISM Advanced Rapid-fabrication Consortium. The goals of the PARfC consortium are three fold, i.e. Education, Research and Outreach.

### *Equipment and Lab setup*

PRISM currently operates one lab in the Goldwater Center and is in the process of establishing two more labs including the Rapid Fabrication Consortium facility. The lab is equipped with high end SGI and NT workstations, Virtual Reality setup, 2 Cyberware laser digitizers and three rapid prototyping machines including the Genisys (plastic), FDM1650 (ABS and wax) and a JP5 (manual feed paper). The lab is equipped with commercial software such as I-DEAS, PRO-E, Maya (Alias) etc. and also in house software. With the formation of the consortium, we are looking to add a DTM machine to our lab.

We describe in this paper various interdisciplinary activities at PRISM and Arizona State University concerning RP. These are categorized below under Education, Research and Outreach.

## Education

The education component includes providing opportunities for all students from college freshmen through life-long learners. It means learning both on and off campus, with university and industrial teaching and mentoring. For education in Rapid Fabrication (RF) to be effective it needs both theory and practice. The capabilities must be cutting edge in pedagogy and technology. The result will be graduates and practitioners who can bring the most recent ideas and techniques to industry and continue to push the RF envelope. We have several RF education programs already in place. They are as follows:

### Courses

Three courses were offered specifically in rapid prototyping during the 1997-98 academic year.

- IEE591C - Industrial engineering course combining one-third RP and two-thirds mechatronics. A full version of the Rapid Prototyping course will be offered on campus in the fall 1998 as IEE591A.
- IEE591 - Web based version of the RP course offered to students on the web at Oklahoma State University, Allied-Signal and Boeing Helicopter.
- ART591 – VIZProto, Interdisciplinary 3D visualization and rapid prototyping course offered to students across disciplines. Students applied the technology in 3D scanning, modeling and rapid prototyping. Student projects are available at <http://surdas.eas.asu.edu/~razdan/Class/3dvizrp>.

We give three examples from the student projects. The first project was to design and make a functional prototype for a tape measure. The model was designed on Form-Z CAD package and various design parameters were noted. These were compared against the dimensions measured from the rapid prototyped model (see Table 1). The model was built on a Genisys. The differences were attributed to resolution limitation of the RP machine. After only minor finishing the tape measure was functional. Figure 1 is the concept design and Figure 2 is a picture of the actual model. The comparison resulted in characterization of the Genisys machine.

	Part	Form-Z Model	Stratasys Model
A	Total width	3.3350	3.3700
B	Total height	2.7100	2.7050
C	Shell thickness	0.1000	0.1170
D	Shell at thinnest	0.0450	0.0680
E	Rail's diameter	1.5000	1.5120
F	Rail's thickness	0.0625	0.0705
G	Tape mount	0.3200	0.3350
H	Post height	0.9800	0.9755
I	Post diameter	0.1600	0.1630
J	Pin diameter	0.1800	0.1970
K	Pin base diameter	0.3000	0.3200
L	Shell height	0.6250	0.6320
M	Pin height	0.8250	0.8335

N	Mini-Pin diameter	0.0900	0.1000
O	Mini-Pin hole	0.0900	0.0800
P	Screw hole	0.0800	0.0800
Q	Pin hole	0.1800	0.1690

**Table 1: Part design parameters and as measured from the prototyped model**

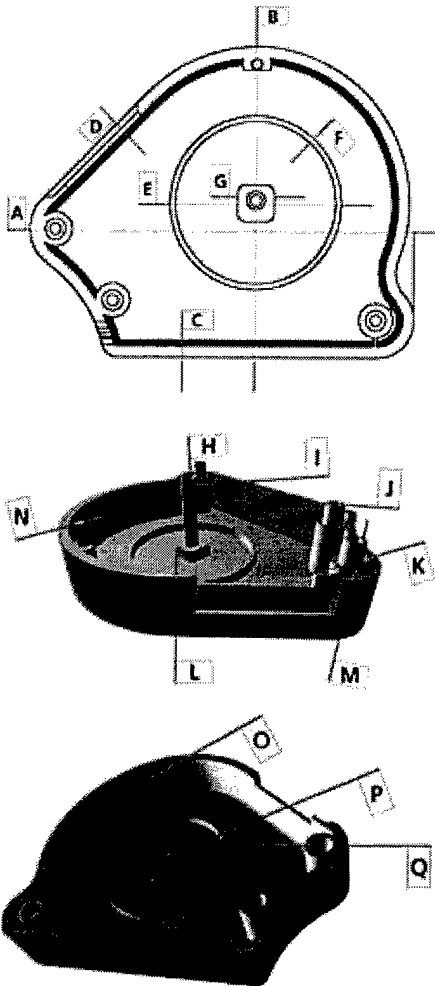


**Figure 1: Concept Design for the tape measure**

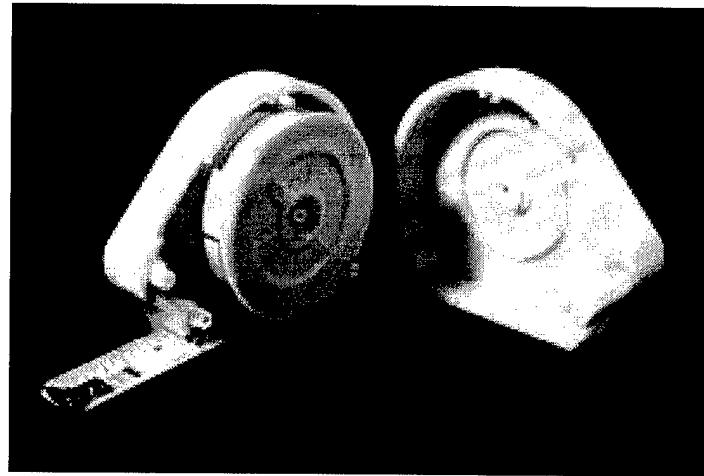


**Figure 2: Picture of the tape measure model**



**Figure 3: Scaled prototype of the tooth**

The second project involved making a scaled prototype. This project combined the high technology of 3D scanning with a more low-tech approach to sculptural prototyping. Initially, an extracted wisdom tooth was scanned using a Cyberware 3D Laser Digitizer. Although much of the tooth scanned with surprising clarity of detail for an object so small, certain problem areas lacked accurate data. The most notable of these areas was where 2 of the roots were quite close together, creating a visual overlap from the digitizer. Using QuickSlice, the proprietary software from Stratasys, the three-dimensional computer model was first repaired, and then *sliced* at even intervals. Each of these 40 layers was projected onto styrofoam and the outlines were traced by

hand. The layers were hand-cut with a hot wire and assembled to form an enlarged replica of the original object. See Figure 3. Not clearly visible, but the original tooth is in the glass case on the top left of the image.

**Design Projects**

The lab was used by students in both the courses listed above and other course projects offered throughout the year. A large number of student design projects were built in the RP lab during the spring 1998 Semester. The table below shows the number of parts and amount of material used. It should be kept in mind that even though the activity is fairly high, this year was the first to have these two machines and their availability was not generally publicized. One notable senior design project was the assembly of the 48 piece articulated landing gear (See Figure 4). Table 2 notes the RP activity during the spring 1998 semester.

RP Machine	Capabilities	No. of Parts	Material Used
Stratasys Genisys	Lower resolution, faster, polyethylene parts	70-80	25(*\$100) cartridges
Stratasys FDM1650	Higher resolution, slower build, ABS, wax and support structure materials	88	2 spools each of modeling (\$153/spool) & support material (\$75/spool)

Table 2: RP Production at ASU, Spring 98

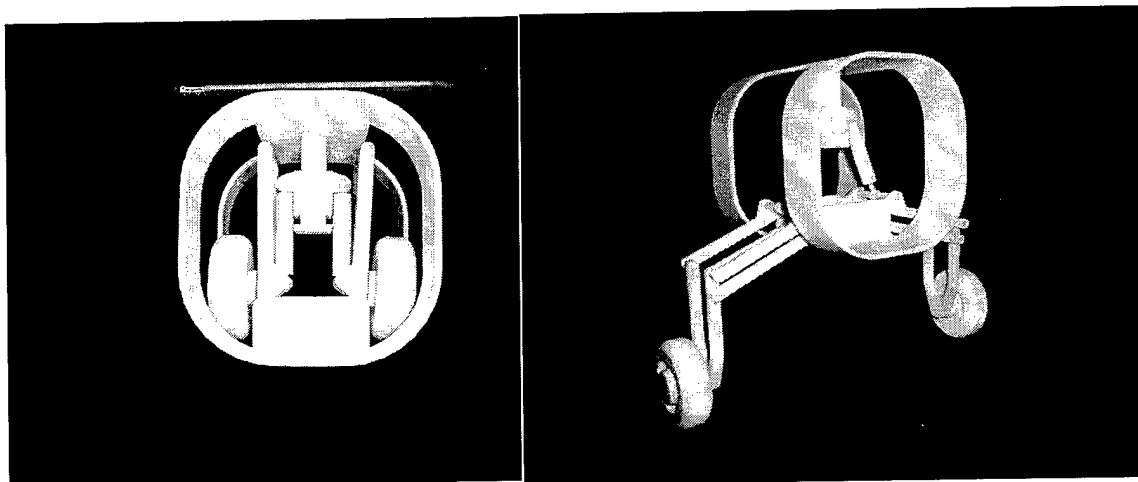


Figure 4: Two views of the 48-Piece Articulated landing gear

**Programs Under Development**

We are proposing to develop the following programs as part of the educational offerings. These include Industry Internships, ASU Internships and Seminars/Conferences. These would facilitate exchange of ideas and rich experience for the students and industry alike.

## Research

### *Current Projects*

The following paragraphs describe ongoing and completed research projects both within and outside of PRISM in the area of Rapid Fabrication. These activities form the basis for research in PAR<sub>r</sub>C.

- 1) Optimizing Part Orientation for Surface Finish, Gautham Kattethota and Mark Henderson.

We are developing a software tool to calculate the expected surface finish quality of all surfaces on a RP model during the build process. Sample RP parts were fabricated with a variety of surface orientations. The surface finishes were characterized using a Sheffield Surface Scanner at Allied Signal (Tempe). Data have shown an unexpected, yet predictable surface finish based on several build factors. The software tool will allow the user, through the use of color codes, to compare desired and possible surface finish specifications during interactive part orientation and to select the optimal build orientation. A paper on this is presented at the SFF 98 conference.

- 2) Reverse Engineering From Scanned Data, Ben Steinberg, Anshuman Razdan, Gerald Farin, NSF

The goal is to reduce and convert the data from a digital laser scan into a NURBS surface for reverse engineering and to create a parametric solid model. A paper on this is being presented at the SFF 98 conference.

- 3) Scientific Visualization Using Tactile Feedback, Anshuman Razdan, NSF.

This is the second year of the two-year NSF funded project to make RP models of microscopic and mathematical images to help visually impaired visualize scientific data. Work continues on transforming various 3D data to RP and incorporating surface texture.

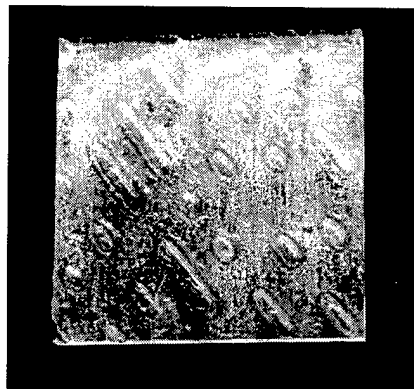
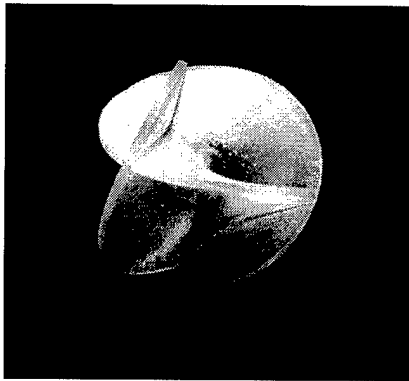


**Figure 5: An enneper surface and CDROM microscope sample**

Figure 5 shows two samples from the project (<http://surdas.eas.asu.edu/~tactile>).

- 4) Virtual Sculpting (HERA Project), Carl Dahl, Alyn Rockwood, Geoff Duke, Jeff Dorman, Mark Henderson.

Interactive shape modification through 3D input to a virtual lump of modeling material creates geometric solids, which can be viewed and prototyped. The user can morph the shape through hand gestures and produce a plastic prototype or solid model as output. This project is aimed at conceptual design (Figure 6).

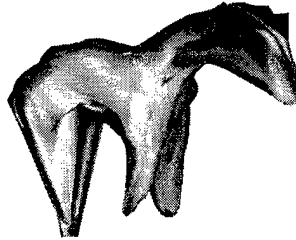


**Figure 6: A shape of a horse using Virtual Sculpting**

- 5) STL File Repair, Surya Suluh, Mark Henderson and Anshuman Razdan.

Using algorithms for redundant vertices, missing and overlapping facets, flipped surface normals and unmatched facet edges, a program was developed to repair damaged or problematic STL files automatically and to review both the errors and results graphically. This was a M.S.E. project (finished May 1998).

- 6) Process Planning For Rapid Machining, Norma Hubele, Chell Roberts, Mark Henderson, NSF

The second 3-year phase of this NSF funded research will develop a tool to provide manufacturing advice to a designer in order to achieve minimum NC machining time, minimum cost or maximum part quality. NC machining is another way to do rapid fabrication.

- 7) Metal Spray Deposition for Rapid Fabrication, Ampere Tseng, Various agencies

A new, patentable process is being developed to create quick metallic prototypes using metal spray.

- 8) Preserving the past in 3D

A recent collaboration has brought the Archaeological Research Institute (ARI) at ASU in partnership with PRISM to create three-dimensional database of archeological artifacts. The ARI at ASU has been the keeper of Native American artifacts that were excavated during the Central Arizona Project. Recently, Congress passed the Repatriation Act, which entitles the Native American tribes to gain possession of these artifacts and rebury them. This will result in the permanent loss of a great amount of scientific data whose only record would be through photographs and subjective description. However, with the joint effort all the artifacts will be digitally scanned before returning to tribes thus preserving true 3D data set. We have successfully reproduced scaled model replicas using the RP equipment at PRISM (see Figure 7).

9) The Capitol Project.

The original idea to create a model of the State Capitol Building came out of recent

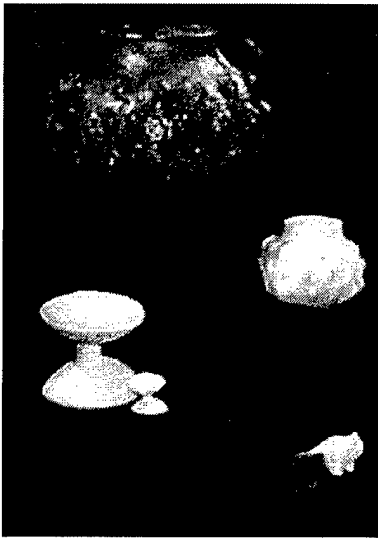


**Figure 7: Archaeological artifacts reproduced**

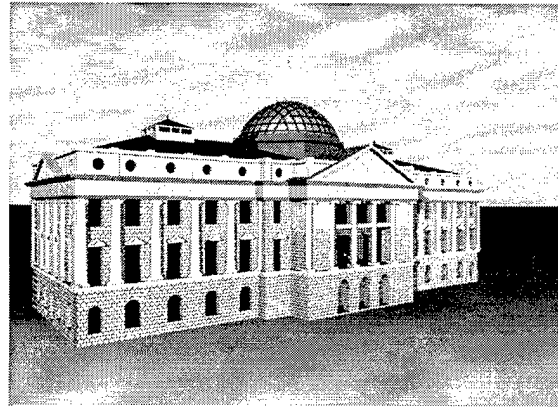


**Figure 8: The Capitol Project**

investigations into the Capitol Mall district and possible urban renewal projects. The Capitol Building model was built to symbolize a renewed commitment and to celebrate its 100 year anniversary. Architectural plans from 1898 were loaned by the Arizona Department of Administration. Details that could not be translated from the plans were digitally photographed or measured directly off the building. The computer model was created using FormZ solid modeling software. Several iterations of the model were produced on the two rapid prototyping machines. A scale model of the original Winged Victory figure that adorns the top of the Capitol was made available by the Arizona State Archives and was scanned in and prototyped. The two models were then translated into bronze casting via silica shell casting at the ASU Art foundry.

***The Research Roadmap***

The following high impact areas have been recognized for emphasis on RF research: Metal fabrication, Non-metal Fabrication, Hybrid Materials, Geometry issues and Prototype Size/Scale. The following table (Table 4) includes an attempt to categorize the ongoing projects enumerated in section Current Projects.

Rank	Research Topic (Top 5)	Specific Issues for Each Topic	Ongoing Projects
1	Metal Fabrication and Rapid Tooling	Precision tooling; direct injection molding tools; dimensional stability and accuracy, material uniformity and properties	7,8
2	Issues of Scale	Ability to produce nano- through mega-size parts; minimum feature	1,3,4

		sizes; part joining; removing need for segmentation	
3	Non-metal part materials including ceramics	Predictable and tunable material properties; Increased range of materials; Dimensional stability and accuracy	3,4,6,7,8
4	Hybrid and composite materials	Fabricating non-homogenous materials; intentional inclusion of varied material features; combining fabrication and assembly	
5	Geometry/CAD and file format issues	Self-repairing STL files; Pursuit of STL alternative format; Optimal discretization; Software for optimal fabrication parameters including orientation	1,2,4,5

**Table 1: The High Priority Research Issues**

### **Outreach**

Outreach is the process in which ASU shares knowledge and technology transfer with the consortium members and other partners. We envision the consortium to have an effective outreach program with the complete supply chain including Large Corporations, Small and Medium Sized Companies, Company Vendors, Rapid Fabrication Equipment Manufacturers and the university. The service is centered around both Large Corporate Members (LCM) who have already invested and adopted RP and Small and Medium size Enterprises (SME) who want to become involved. Service Bureaus are also important in PAR<sub>f</sub>C. Many SMEs are interested in the technology but are turned off by the investment, both financial and staff costs.

Many industries in the region are involved in manufacturing and other activities that could benefit from incorporating RF. Some are not yet aware of the capabilities or the basics of the technology. For example, Toy Time Toys, Inc., a small entertainment concept design company recently interacted with PAR<sub>f</sub>C to create the next generation of a sporting item to be unveiled during SuperBowl 1999. The design and prototype were taken on as a student project. This was the company's first experience with 3D CAD design and RP. The company is convinced of the advantages the technology provides.

### **Acknowledgements**

We wish to acknowledge the supporters of PRISM and PAR<sub>f</sub>C. In particular, John Macintosh, Mary Bates, Mary Marzke, Ben Steinberg, Gerald Farin, the HERA team, Gautham Kattethota, Jacob, Shay and ARI. Thanks to Allied Signal (Don Benjamin, Doug Deye and Don Deptowicz) and other corporate members.

## SOLID FREEFORM FABRICATION RESEARCH IN ENGINEERING EDUCATION

R.S. Crockett, V.R. Gervasi

Rapid Prototyping Center  
Milwaukee School of Engineering, Milwaukee, WI

Milwaukee School of Engineering (MSOE) has been using Solid Freeform Fabrication technologies as a means to provide stimulating, multi-disciplinary research topics for undergraduate engineering students. SLA, LOM, and FDM have enabled undergraduate research in disciplines including *Architecture*: using SFF for preservation, archiving, and reproduction of historical features; *Microelectromechanical Systems*: producing packaging and interconnects for MEMS devices through a combination of stereolithography and photolithography; and *Biomedical Engineering*: creating forensic, research, and educational models of anatomical features and pathology development from MRI images. In addition, MSOE is currently involved in a joint program with the Milwaukee Discovery World Museum to create a SFF experiment that will fly on the Space Shuttle as a *Get Away Special* payload.

### Introduction

Because Solid Freeform Fabrication (SFF) has an extremely wide range of potential applications, crossing traditional engineering and science boundaries, it is a technology that lends itself to multi-disciplinary activities and projects. SFF is an ideal mechanism to present scientific concepts including materials science and mechanics, as well as larger-scope engineering topics such as agile manufacturing. At Milwaukee School of Engineering (MSOE), we are using SFF technologies as a means to teach engineering concepts to undergraduate students through multi-disciplinary research.

MSOE was awarded a five-year grant under the NSF Research Experiences for Undergraduates Program (EEC-9619715) to facilitate student exploration in the field of Solid Freeform Fabrication. Sixty undergraduates will participate in summer and academic year programs by the year 2001. Eighteen students from around the country have participated in the program to date, bringing with them a diverse background of university experience, skill level, and interests. Working closely with a faculty advisor possessing expertise in a particular research area, they have performed research on Solid Freeform Fabrication applications in the biomedical, aerospace, architectural, manufacturing, and electronics industries.

Some of the keys to the success of this program include:

- Hands-on access to Solid Freeform Fabrication equipment through the facilities of the MSOE Rapid Prototyping Center (SLA 250, LOM 2030, and FDM 1650).
- Close partnerships of the students with faculty and industry mentors in specialized areas of expertise.
- Teaming with other educational institutions.

- Significant cross-pollination between projects; faculty from diverse departments.
- Encouraging students to publish and present results at national conferences and symposia.

## Recent Research Projects

### *Architecture*

There are potentially numerous applications for Solid Freeform Fabrication in the architectural field. One example is the restoration, archiving, and duplicating of historical architectural features such as rosettes or gargoyles -- tasks that are currently performed by labor-intensive hand operations. While architects may not talk in terms of “reverse engineering, parametric data archival, and low-volume production”, these are all problems that have been addressed for the manufacturing industry using SFF techniques.

This project applies SFF to the restoration and replication of architectural pieces and artwork. This is especially challenging in that it requires the three-dimensional input of existing objects in multiple scales: from entire buildings to very small detail features. An additional challenge is in making digital input compatible with the paradigms of the architectural field, such as existing software and processes. This project analyzes the feasibility of obtaining three-dimensional data using methods of *photogrammetry*, compatible with standard photographic techniques, to quickly and easily archive and reproduce architectural features.

A set of digital photos was taken of architectural details from different angles. Commercial software (3D Builder Pro) was used to triangulate common reference points from these photos, resulting in a surface mesh which is output directly to an .stl file. A LOM part was created from this file, which served as a pattern for a silicone mold to create multiple reproductions in plaster (Figure 1). The computer surface model can remain with the architectural firm, to be retrieved and modified (size, mirror-image, negative mold, etc.) for any future client.

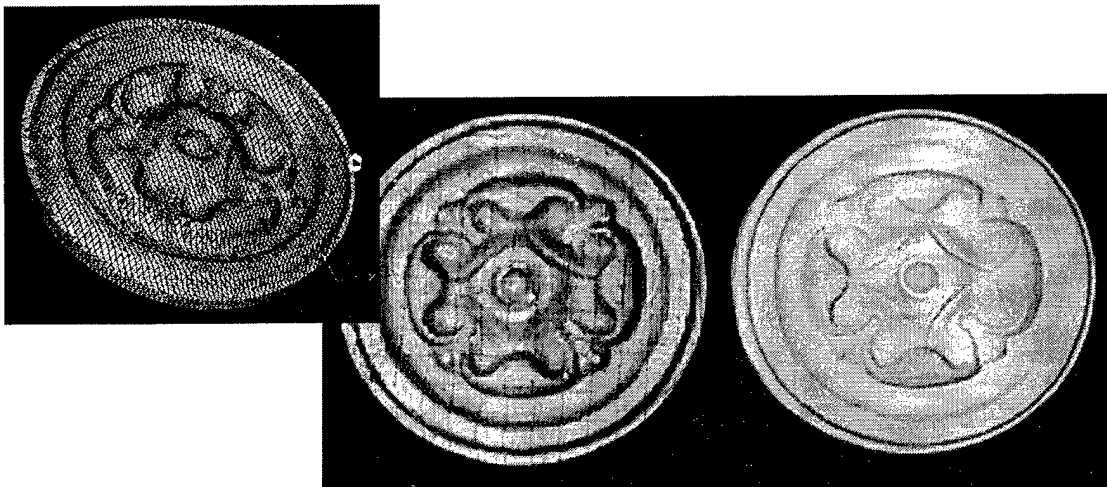


Figure 1. Computer file (inset) obtained from Photogrammetry techniques. LOM master pattern (left), original plaster item (right).

## Microelectromechanical Systems

Microelectromechanical systems (MEMS) are devices containing gears, levers, and pumps etched onto a silicon wafer with features as small as 1-2  $\mu\text{m}$ . Interfacing these extremely small systems with the outside world is the most costly part of a MEMS design. This project endeavors to reduce costs by using a modified stereolithography technique. Currently, stereolithography has planar resolutions on the order of 500  $\mu\text{m}$ , which is not precise enough to create MEMS features. Increasing the resolution by combining stereolithography with a masking technique allows a single manufacturing system to construct not only the MEMS sensors, but also the interfaces and protective packages.

Figure 2 shows the results of initial exploration into using a micron-detail photo mask with stereolithography resin. Working with Process Technologies, Inc. of Milwaukee, multiple-layer parts were prepared by shining UV light through a mask that contained a test pattern typically used in the semiconductor industry. Features as small as 5  $\mu\text{m}$  in-plane were achieved, and the creation of multiple layers was only limited by the positioning accuracy of the physical apparatus used to hold the mask. With a more precise mechanism, multiple layers at this resolution can be manufactured, creating what are in effect high-aspect-ratio MEMS devices. As aspect ratio is a key limitation in current MEMS manufacturing technology, SFF techniques can potentially offer some significant advantages.

The ultimate goal of this project is to create objects that have features spanning multiple orders of magnitude. By building larger-scale features with the scanning stereolithography laser, then inserting a photo mask in the beam path as required, this goal should be achievable. It should thus be possible to use a modified stereolithography apparatus to create 10 cm objects that contain features on the order of 1  $\mu\text{m}$ .

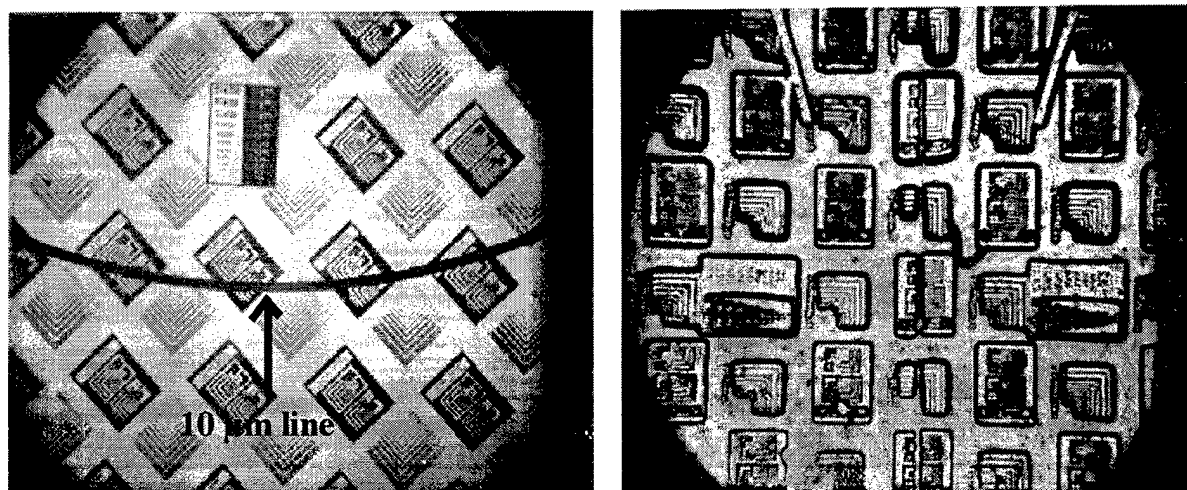


Figure 2. Mask (left). SLA model (right). Feature resolution is as small as 5  $\mu\text{m}$ .

## Biomedical Engineering

The Medical College of Wisconsin has served as a partner in the exploration of a variety of Biomedical applications of Solid Freeform Fabrication. Current efforts focus on constructing solid model data from combined medical imaging modalities such as MRI and CT scans, and then using this information to create complex composites that accurately replicate the non-homogeneous mechanical properties of bone.

One student project is working on automating methods to distinguish the boundaries of anatomical structures in MRI images. Because MRI images are not homogeneous, much manual effort is required to select the desired anatomical structure using software such as MIMICS (Materialize, Inc.). Figure 3, top left shows the original MRI image of a knee. A threshold level must be set within the software to isolate desired features. As Figure 3, bottom left shows, a single threshold level is generally not sufficient to correctly identify a desired structure throughout the scan. In this picture, the bone was the target structure; most of the material meeting the threshold criteria was non-bone, thus an operator must manually isolate the structure slice-by-slice.

A computer program was developed by the student that uses a K-mean segmentation algorithm to analyze and “homogenize” pixel values associated with different structures in MRI images. This program uses data from the MIMICS format as an input, reduces the total number of pixel values from 4095 levels of gray to a user-defined, more manageable set (usually 3-20), and then re-introduces the data back into the MIMICS software for display, structure selection, and .stl

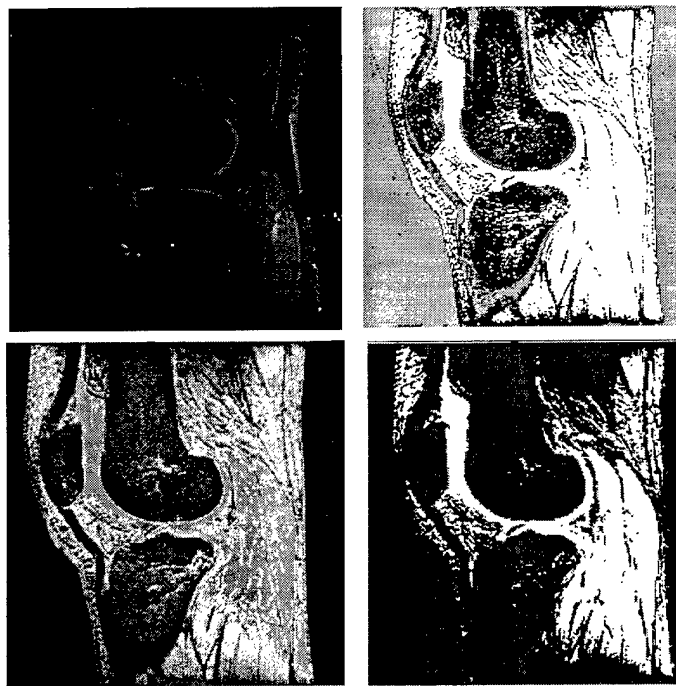


**Figure 3.** Top left: Original MRI image; top right: homogenized image; bottom left: thresholding on original image misses bone; bottom right: correct features are captured in homogenized image.

file construction. Figure 3 shows the results of initial efforts. The figure in the upper right is the same MRI image homogenized to 3 grayscale values. The figure in the lower right is the result after this data has been imported back into MIMICS and an appropriate threshold value has been applied. In this example, the desired bone structure has been correctly identified with minimum manual manipulation.

Whereas this project concentrates on making complex 3-D input more usable, a second undergraduate project in Biomedical applications of SFF is exploring the output side of the problem. Physical models are extremely useful in pre-surgery planning as well as the teaching of anatomy and pathology, and SFF techniques have been used in this area with great success. Human bone replicas to date show only the exterior overall structure of bone, however, and none of the minute interior tissues and structures. This project involves using SFF to build cross-sectional models of fine-detailed interior structures of bone.

Although this project is in the early stages of development, the eventual goal will be to replicate not only the internal physical geometry, but also the non-homogenous mechanical properties of bone. This will require the "borrowing" of techniques developed by a previous project in the area of composites. Stereolithography patterns consisting of open cellular structures inside a surface shell are used as a host for filler materials; regions within a single object may be separated by thin barriers, allowing filling with different matrix materials to create regions of differing local properties. The internal structure can also be continually gradated in thickness to produce composites with properties ranging from that of the filler material to that of the Stereolithography epoxy. Current fillers include epoxy matrices loaded with glass microspheres, as well as hydraulically-bonded ceramic mixtures with bulk properties matched to various bone structures. The long-term goal of this project is to create a composite spinal cord model for mechanical testing, such as automobile crash tests (Figure 4).

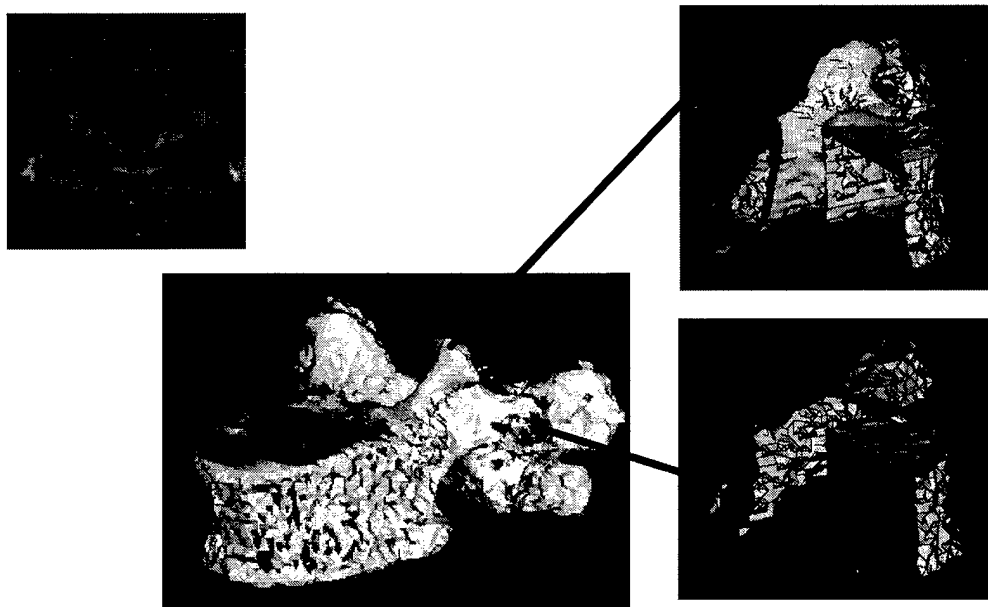


**Figure 4.** Inset: Original MRI image; composite model representing outside shell of dense bone and inside spongy bone. Composite model is constructed to allow filling of different materials to create non-homogeneous final product.

## Space Shuttle Get Away Special Payload

The objective of this project is to demonstrate some of the key technologies required for Solid Freeform Fabrication (SFF) and other automated manufacturing processes in a microgravity environment. Because of the manufacturing flexibility offered by Solid Freeform Fabrication, these techniques have the potential to be of enormous value to continued habitation of humans in space; SFF could eventually serve the International Space Station as an on-orbit system for producing new and replacement components, as well as tools. In the absence of gravity, there is the potential for rapidly creating extremely complex shapes, as supports are not required. The absence of gravity also presents some significant challenges associated with placing a liquid to build an object, however. For example, in depositing a bead of liquid into free space (i.e. without a substrate), interfacial tension will tend to cause the bead to break apart and ball up before it can solidify into a layer. Placing a liquid with a slow solidification rate in a planar arrangement thus becomes a significant challenge.

Two students have prepared a preliminary design for a Get Away Special (GAS) payload to be flown on the Space Shuttle in September 1999 (Figure 5). This payload has been donated to MSOE by the Gammex Corporation through the Discovery World Museum of Milwaukee, WI. This set of GAS experiments will explore a number of the core scientific principles behind the deposition, material flow, and solidification of fluids absent of a gravitational field.

Two types of liquids will be deposited in test patterns that evaluate the relationship between the liquid and the surface onto which it is deposited. In one set of experiments, beads of a rapidly solidifying thermoplastic (ABS) will be deposited onto a rigid substrate, into free space, and onto previously deposited, unsupported beads. In another set of experiments using the same apparatus, a low viscosity photopolymer will be deposited onto a fiber mesh to create a planar

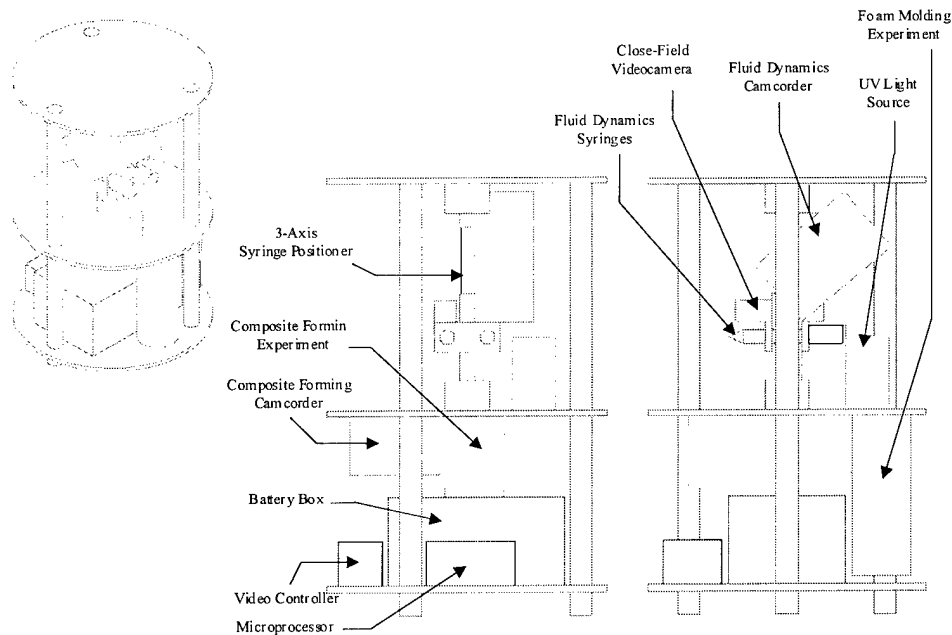


**Figure 5.** Preliminary design for SFF in Microgravity Get Away Special (GAS) payload.

sheet of liquid. This liquid will be cured by ultraviolet light after deposition.

In a separate experimental apparatus, carbon-fiber composite tubes of varying diameter will be constructed from prepreg material without any support structure. Two heated pinch rollers will feed a prepreg strip past a guide roller, which will change the trajectory of the strip such that it feeds back through the pinch rollers after circling through a set diameter. A composite tube with multiple (3-5) layers will be produced during this experiment.

The final experimental apparatus will create and mold a polymer foam. This apparatus consists of a double syringe: Part A is polymeric diphenylmethane diisocyanate and part B is a polyether type of a polypropylene glycol mixture. Parts A and B will be mixed mechanically at the end of the syringe and expand into a mold where the foam will set.

### **Benefits of SFF Research in Engineering Education**

Whereas textbooks have traditionally defined the *boundaries* between engineering principles, modern engineering education requires packages that *integrate* diverse concepts – “containers” providing the resources for student-initiated, project-based learning. These containers must be constructed around a topic that captures the imagination of students and encourages them to view technology in a holistic perspective. They must enable mentor relationships between educators and students, whereby the learning process is a non-linear, joint exploration that includes collaboration with colleagues and industry. Few technologies offer a scope of applications as broad as Solid Freeform Fabrication. Because of this, SFF is a topic that can become the ideal tool for modern engineering education; an education container built around SFF can provide the foundation for an entirely new engineering education paradigm.

### **ACKNOWLEDGEMENTS**

The authors would like to acknowledge the work of the following undergraduate students, who, under mentorship from faculty advisors, performed all of the research presented in this paper:

#### *REU STUDENTS*

Steven Gerritsma  
Rebecca Zick  
Sarah Vickman  
Kevin Tetz  
James Canino  
Kristin Powell

#### *ADVISORS*

Dr. Robert Crockett  
Vito Gervasi  
Dr. Lisa Milkowski  
Prof. Mike McGeen  
Brian Stemper  
Ann Bloor

We also gratefully acknowledge the financial support of the National Science Foundation and the MSOE Rapid Prototyping Consortium, as well as the facilities and expertise provided by the staff of the MSOE Rapid Prototyping Center. The Shuttle experiment was made possible by support from the Discovery World of Milwaukee, WI, the Gammex Corporation, the Wisconsin Space Grant Consortium, and Danfoss Fluid Power, Inc.

# PARAMETRIC BASED CONTROLLER FOR RAPID PROTOTYPING APPLICATIONS

**Georges Fadel**  
Associate Professor

**Ravi Ganti**  
Graduate Student

Center for Advanced Manufacturing  
Mechanical Engineering Department  
Clemson University

## ABSTRACT

A methodology aiming at reproducing in Rapid Prototyping applications, exact parametric curves from CAD data is presented. The approach consists of converting the space-based parametric curves from the CAD system into time-base, such that the equations of the curve in terms of time are then fed to a controller directly. Optimization is used to solve the problem, which has both Rapid Prototyping process and scanning constraints. With information such as the equation of the curve, its first and second derivatives with respect to time, a real-time trajectory controller can be designed. The trajectory displays an increase in accuracy over traditional approaches using STL files, which is of the order of the chordal tolerance used to generate tessellations. The system model involves electrical and mechanical dynamics of the galvanometers and sensors. The controller, which acts on two mirrors, deflecting the laser beam of a stereolithography machine in the x and y directions respectively, should be easily substituted for current systems. Application of the methodology to freeform curves shows acceptable tracking and can be improved by judicious selection of the equation representing the spatial parameter as a function of time.

## KEYWORDS

Controller, rapid prototyping, optimization, time parameterization, optimal control, galvanometers.

## 1. INTRODUCTION

All commercially available Rapid Prototyping (RP) machines are based on a process that converts CAD drawings to machine instructions. The latter drive some mechanism that works mostly by material addition and creates the prototype. All are layered-based processes, and the only control mechanism used to either drive a laser beam or a nozzle, is vector based. The advantages of such a controller are obvious: (1) Two points define the start and the end of the vector; (2) CAD software inherently generates vectors to drive plotters, and it is relatively easy to convert arbitrary surfaces to triangles which are sliced to form a series of vectors.

However, since accuracy of the prototype is becoming a major concern for the users of rapid prototyping hardware who aim at producing finished parts, or molds to produce finished parts, the vector based approach is a limiting factor when curved features are replaced by vectors. Furthermore, most CAD vendors have migrated to a parametric based representation of surfaces, and the ability to draw exact curves would significantly improve surface quality. Clemson University and others have developed algorithms to slice parametric surfaces and generate parametric curves. Presently, these parametric-curves are approximated by vectors, and the improvement in accuracy is already visible over triangle based tessellations. The next step is to directly draw the parametric curves to close the page on the accuracy question in a plane.

This paper illustrates the approach selected to perform the conversion from a space-based parameterization to time-base. A representative curve is illustrated, and the strengths and limitations of the approach are exposed.

## 2. LITERATURE SURVEY

Previous work related to geometric contour following for scanning control in solid freeform fabrication is by researchers at the University of Texas, Austin (Wu and Beaman, 1990). Their

approach utilizes the arc length as a parameter to represent a general geometric path. The reason for using arc length is that the first and second derivatives of the arc length represent the tangential velocity and acceleration respectively. Their approach is applied to standard curve shapes such as a circle or an ellipse. Moreover, the control strategy adopted is based on a simple dynamic model of the system. This does not include all the external and internal factors affecting the dynamics of the system but it is straightforward and can be tailored to consider process based constraints as well as galvanometer constraints

An adaptive slicing algorithm (Vouzelaud, 1993) that makes use of AutoCAD slicing routines to obtain 2-D contours from a 3-D CAD model was developed at Clemson University. Vuyyuru (1994), and Ganesan (1994) also at Clemson, developed a process to slice solid models from I-DEAS directly. This results in the two-dimensional cross sections of the solid model.

The motion of the laser beam in two-dimensional space is analogous to the robot path-planning problem, in which the robot is constrained to follow an arbitrary path in space. This problem, subjected to different motion constraints, has been solved by several researchers (Shiller and Dubowsky, 1989; Bobrow *et al.*, 1985; Shin and McKay, 1985). However, these researchers consider only one type of constraints (limits on the actuation torque) while neglecting the constraints on velocity, which are process-dependent. The method of Van Willigenburg, (1991) uses optimal control strategies, which take into consideration the constraints on actuation torque and process dependent velocities in both directions. In this method, the path of the robot is given by a set of coordinate pairs  $(x_p, y_p)$ , not by any continuous function, and is ultimately a collection of discrete line segments between two successive points. The time taken to travel from one point to the other is obtained by solving the time optimal control problem.

This paper presents an alternative methodology to generate parametric curve equations as function of time, which can then be used to drive a controller.

### 3. PROPOSED METHODOLOGY

The proposed methodology can be applied to most RP technologies, but is applied in this paper to stereolithography. We first derive the necessary equations that are process dependent and that quantify the process constraints, then explain the optimization method used to generate the conversion from space-based to time-based parameterization.

The scanning systems of stereolithography machines consist of a single laser beam, which is deflected by mirrors to draw 2D curves on the resin vat and solidify the liquid. In current scanning systems, two mirrors, actuated by DC motors, deflect the laser beam in one direction each (X or Y), and the combination of the two provides the full required motion range of the laser beam. The dynamics of the DC motors can be represented by

$$U = L di / dt + RI + K\omega \quad (1a)$$

$$T = KI \quad (1b)$$

where

L = motor inductance (Henrys)

R = motor electrical resistance (Ohms)

I = motor current (Amperes)

U = voltage applied to motor (Volts)

$\omega$  = motor angular speed (rad /s)

T = motor generated torque (N. m/rad)

K = motor voltage constant (Vs /rad)

The heat generation and the dissipation characteristics mainly contribute to limiting the capabilities of a DC motor. Heat generation is represented by the second term in equation (1a) and thus is proportional to the motor current. Furthermore, conventional DC motor controllers are built around a motor current controller, which is used to limit the motor current to prevent overheating. Thus, from both a practical and modeling viewpoint, it is convenient to choose the motor currents as the control variables for the dynamic system especially when assuming the motor current controller to

be ideal. Also, assuming an ideal transmission from the DC motor to the galvanometer scanners, the motor current can be considered proportional to the torque (1b). Both these conditions can be translated into acceleration constraints on the DC motors, and have to be taken into account in our analysis.

The other critical process constraint is the scanning speed of the laser. Stereolithography machines typical scanning speeds are in the range of 80 to 90 cm/sec or 30 to 35 in/sec. The scanning velocity depends directly on the power of the laser beam and resin material properties. The laser power varies from laser to laser and varies with time and age of the laser; hence, the velocity is a machine dependent factor. Note that the velocity referred to is the absolute scanning velocity.

The above-presented constraints are the main process constraints that have to be considered in the model for Stereolithography. However, to ensure convergence, and to add general process constraints such as the ones related to nozzle movement, minimum and maximum velocity constraints in the X and Y directions are also added.

### 3.1 Solving the Time Optimal Control Problem using the Method of Optimization

The problem of converting the equations from space-based parameterization to time-base is formulated as a standard optimization problem wherein the function to be minimized is the total time taken to track the desired trajectory subjected to desired velocity and acceleration constraints.

The path, as resolved from the CAD system slicing program, is a parametric curve representation (more and more NURBS based). Such a representation expresses Cartesian coordinates in two-dimensional space as a function of a spatial parameter P. A simpler parametric representation upon which much of the solid geometry has been built is the parametric-cubic representation. This representation is used in this paper without loss of generality. Hence, the equations of motion in terms of the spatial parameter P are:

$$\begin{aligned} x_p &= f(P) = k_1 P^3 + k_2 P^2 + k_3 P + k_4, \\ y_p &= g(P) = k_5 P^3 + k_6 P^2 + k_7 P + k_8 \end{aligned} \quad 0 \leq P \leq P_{\max} \quad (2)$$

To build complex paths, the functions  $f$  and  $g$  (2) are assembled piecewise with other 3<sup>rd</sup> degree polynomials (parametric cubic) in terms of P and are continuous along with their derivatives. The derivation presented below does not consider the multiple segments, rather a single segment in which the parameter P varies between 0 and 1 (normalized).

With the equations of motion in the spatial parameter space (2) and the constraints above, the time optimal control problem boils down to determining a function of the parameter P in terms of time given by

$$P(t) \quad 0 \leq t \leq t_{\max} \quad (3a)$$

This relation should be a non-decreasing continuous function of time as the normalized parameter P goes from 0.0 to 1.0 i.e.,

$$\dot{P}(t) \geq 0 \quad 0 \leq t \leq t_{\max} \quad (3b)$$

The initial and final conditions are given by

$$P(0) = 0 \quad 0 \leq t \leq t_{\max} \quad (3c)$$

$$P(t_{\max}) = 1 \quad (3d)$$

such that  $t_{\max}$  is optimal. Once (3) is known, the time optimal trajectory is given by:

$$x_p = f(P(t)) \quad 0 \leq t \leq t_{\max}, \quad (4a)$$

$$y_p = g(P(t)) \quad 0 \leq t \leq t_{\max}. \quad (4b)$$

Note that when  $\dot{P}(t) = 0$ , the laser beam comes to a stand still. At these points we may split the path in two parts by demanding the laser beam to stand still at the end of the first path, as well as at the start of the second path. Therefore, except for possibly the initial and final time,  $\dot{P} > 0$ .

Since  $P(t)$  in (3a) is a non-decreasing function of time, minimizing  $t_{\max}$  is equivalent to maximizing  $dP/dt$  at all times  $t$ ,  $0 \leq t \leq t_{\max}$ . From the first rules of differentiation, we adopt the following notation:

$$\begin{aligned} f_1 &= df/dP, & f_2 &= d^2f/dP^2, \\ g_1 &= dg/dP, & g_2 &= d^2g/dP^2, \\ \dot{P} &= dP/dt, & \ddot{P} &= d^2P/dt^2. \end{aligned} \quad (5)$$

From (2) and (5), the following relations are derived from the fundamental rules of differentiation:

$$\begin{aligned} \dot{x}_p &= f_1\dot{P}, & \dot{y}_p &= g_1\dot{P}, \\ \ddot{x}_p &= f_1\ddot{P} + f_2\dot{P}^2, & \ddot{y}_p &= g_1\ddot{P} + g_2\dot{P}^2. \end{aligned} \quad (6)$$

The quantity  $\dot{P}$  is referred to as the path velocity, because from the expressions, it is clear that the velocity with which the path is traveled in a given time is directly proportional to the slope of the curve with respect to the parameter at that point and  $\dot{P}$ . Since the slope of the curve is specified by the equation of the curve in space,  $\dot{P}$  is the only variable. Similarly, the quantity  $\ddot{P}$  is referred to as the path acceleration.

A state trajectory determined by  $x_p(t), y_p(t)$ ,  $t_0 \leq t \leq t_{\max}$ , can only be realized if both time domain functions are continuous and have continuous first derivatives. Now from (6), given the properties of  $f$ ,  $g$ , and  $P(t)$  we observe that all of them are continuous functions.

The constraints imposed on the actuators, which supply the necessary power to the system, affect the acceleration of the laser beam in both directions. These constraint relations are obtained from the model of the laser beam in which the acceleration imparted to the beam is directly proportional to the torque supplied.

$$\ddot{x}_p = b_x\tau_x \quad \ddot{y}_p = b_y\tau_y \quad (7)$$

The above expressions denote acceleration in the X and Y directions, where  $b_x$  and  $b_y$  are the coefficients associated with the mass and radius about which the torque is applied,  $\tau_x$  and  $\tau_y$  are the torque in the X and Y directions respectively.

To ensure the satisfaction of the constraints everywhere along the trajectory, the entire curve is divided into a finite number of segments, and the constraints are imposed on all the segments. The optimization problem is solved by assuming an arbitrary relation between parameter  $P$  and time  $t$ . In this study, this relation is assumed to be a sixth degree equation in time  $t$  without the constant term, which has been eliminated because of the initial condition. The following is the relation assumed to exist between parameter and time in this work.

$$P(t) = a_0t^6 + a_1t^5 + a_2t^4 + a_3t^3 + a_4t^2 + a_5t \quad (8)$$

The sixth degree is selected in order to prevent the derivatives from vanishing by differentiation.

The objective of this problem is two folds. The time taken to complete the path is to be minimized and, at the same time, we need to resolve a best fit to find the coefficients of the expression (8) using a least squares method. The curve representing the path in parameter space should be identical to the curve in time space for a successful mapping. Hence, the relation between parameter and time should be such that the value of the parameter corresponding to any time should be equal to its true parametric value. The error can be defined as the difference between the parametric value corresponding to the time and the true parametric value. Hence the objective function is chosen such that the error obtained from calculating the value of the relation (8) and the value of P, over all the parametric locations from P = 0.0 to P = 1.0 should be minimum.

The optimization problem can be stated as follows:

Minimize :

$$f(t_i) = t_{\max} + \sum_{i=0}^k (a_0 t_i^6 + a_1 t_i^5 + a_2 t_i^4 + a_3 t_i^3 + a_4 t_i^2 + a_5 t_i - P_i)^2$$

where  $f_i$  is the function to be minimized,

$k$  is the number of segments into which the spatial curve is divided,

$t_i$  is the time corresponding to the parametric value of  $P_i$ ,

$a_{i=0..5}$  are the coefficients to be determined by the optimizer.

Subject To:

1. Minimum and maximum absolute velocities given by

$$-(\sqrt{f_1^2 + g_1^2} * \dot{P}) / V_{\min} + 1.0 \leq 0.0 \quad \text{and} \quad (\sqrt{f_1^2 + g_1^2} * \dot{P}) / V_{\max} - 1.0 \leq 0.0$$

which are  $(\sqrt{f_1^2 + g_1^2} * \dot{P}) \geq V_{\min}$  and  $(\sqrt{f_1^2 + g_1^2} * \dot{P}) \leq V_{\max}$  normalized.

2. Minimum and maximum velocities in the X and Y are given by

$$-(f_1 * \dot{P}) / V_{x\min} + 1.0 \leq 0.0, \quad (f_1 * \dot{P}) / V_{x\max} - 1.0 \leq 0.0 \quad \text{and}$$

$$-(g_1 * \dot{P}) / V_{y\min} + 1.0 \leq 0.0, \quad (g_1 * \dot{P}) / V_{y\max} - 1.0 \leq 0.0 \quad (\text{also normalized})$$

3. Minimum and maximum accelerations in the X and Y directions

$$\text{given by } -(f_1 \ddot{P} + f_2 \dot{P}^2) / A_{x\min} + 1.0 \leq 0.0, \quad (f_1 \ddot{P} + f_2 \dot{P}^2) / A_{x\max} - 1.0 \leq 0.0,$$

$$-(g_1 \ddot{P} + g_2 \dot{P}^2) / A_{y\min} + 1.0 \leq 0.0 \quad \text{and} \quad (g_1 \ddot{P} + g_2 \dot{P}^2) / A_{y\max} - 1.0 \leq 0.0.$$

The optimizer used is CONMIN (Vanderplaat, 1973), a commercial code based on the feasible directions method. It requires the calculation of gradients, which are automatically generated by the program using finite differences.

#### 4. APPLICATION

The approach presented above is applied to the following parametric cubic curve. Additional examples were generated but cannot be presented because of space limitations.

$$x(P) = 32.0 * (P^3) - 48.0 * (P^2) + 18.0 * (P) \quad (9)$$

$$y(P) = (32.0/3.0) * (P^3) - (56.0/3.0) * (P) + 12.0 * (P) \quad (10)$$

The above equations are normalized such that the curve in the XY plane is completely described when the parameter P varies from zero to one. The number of segments into which the curve is divided is arbitrarily set to one hundred. The number of design variables is thus 107 with 6

variables representing the  $a_i$  parameters of equation (8) and the remaining accounting for the time increments, i.e. the time  $t$  values at each spatial P value.

The constraints applied in this example are: absolute velocity between 2 and 30 cm/s, acceleration between  $-2600$  and  $2600$  cm/s<sup>2</sup> and individual velocities between + and  $-80$  cm/s.

Figure 1 shows the displacements in X and Y direction in space domain for the curve selected. Figure 2 shows the results of the optimization, which is the illustration of the spatial parameter P as a function of time  $t$ . Figure 3 illustrates the parametric cubic with tic marks representing equal time steps. This figure clearly shows how the algorithm slows the laser down towards its minimum absolute velocity at regions of high curvatures, and speeds it up at regions of lower curvature. Figure 4 further illustrates the individual velocities in the X and Y directions and the absolute velocity as a function of time elapsed.

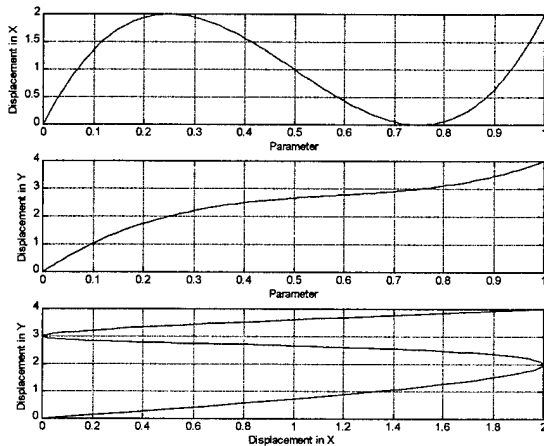


Figure 1. Displacements in X and Y Directions in Parametric Domain

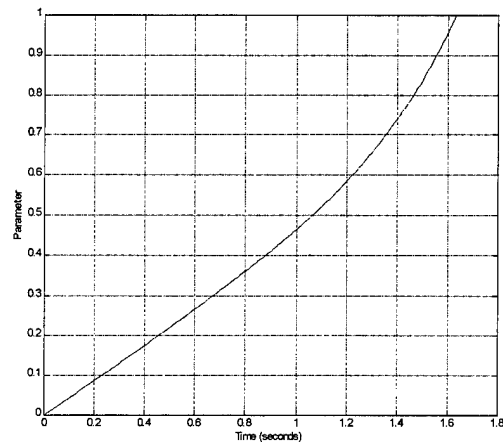


Figure 2. Parameter P versus Time

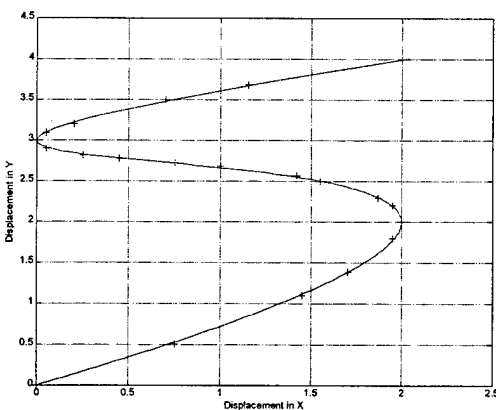


Figure 3. Cubic Spline Curve in Time Domain with (+) Signs Showing Trajectory Covered During Equal Intervals of Time.

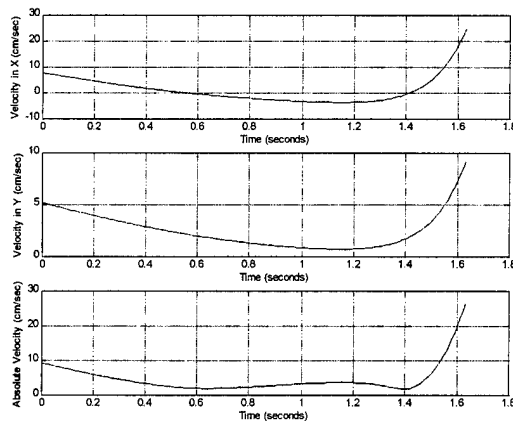


Figure 4. Absolute Velocity and Individual Velocities

This profile shows very well the expected behavior during the first lower part of the trajectory, but does not show as significant change in absolute velocity between the two changes in curvature when the trajectory becomes practically a straight line. The reasons may be the selection of the relation between parameter and time and the pressure of the optimizer to reduce the overall time.

The absolute velocity profile described above shows that the absolute velocity is within the bounds prescribed of 2 cm/sec and 30 cm/sec. The absolute and individual velocity profiles show an increase in the last portion of the trajectory. This is probably due to the pressures of the optimizer to reduce overall time. We would have liked figure 2 to show the monotonous increasing relationship between spatial parameter P and time t, which it did, but were expecting wiggles around the high curvature areas. The choice of a sixth order expression prevented this from clearly happening. Figure 5 shows again the increase in acceleration at the end of the trajectory, again in response to the pressures of the optimizer.

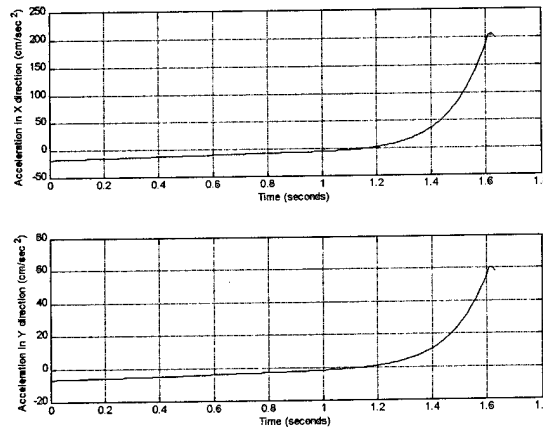


Figure 5. Individual Accelerations in X and Y Directions

Three different cases were tested on each of the curves selected. Table I shows that the time taken to track the trajectory reduces with the increase in velocity. The time taken to track the desired trajectory goes down from 1.65 seconds to 1.00 second with an increase in maximum absolute velocity from 30 cm/sec to 120 cm/sec.

Table I. Results of Maximum Velocity variation

Minimum Velocity (cm/sec)	Maximum Velocity (cm/sec)	Time (sec)
2	30	1.65
2	50	1.63089
2	120	1.00

#### 4.1 Observations

The solution obtained in some of the cases is not in accordance with the desired philosophy of tracking the regions of low curvature at the maximum possible velocity and regions of high curvature with the lowest possible speed. The reasons for this behavior can be attributed to many factors. First and foremost, is the assumption of a relation between parameter and time. In this work, we assumed a polynomial expression of sixth order, this probably has some bearing on the solution. The initial conditions and the bounds on the design variables also effect the solution. The curvature is not explicitly tied to the solution.

Other practical issues such as sharp angle turns have not yet been considered. Also, the start and end velocities of the trajectories, as well as possible starts and stops, have not been incorporated

as constraints but could be readily accomplished. These are issues for continued research especially when migrating to piecewise parametric representations and NURBS.

## 5. CONCLUSIONS

The traditional approach of vector scanning is replaced in this work by continuous parametric curves. The accuracy of tracking by time-based parametric representations is predicted to increase drastically due to the exact nature of the parametric curves fed to the controller. The approach presented in this paper is one of solving a dynamics and controls problem using a commercial optimization package. The previous approaches that attempted to solve the problem did not result in a continuous relation between parameter and time nor in a time-based parameterization of the original CAD drawing. The procedure developed and presented in this work converts parametric curves from a spatial parameter to a time parameter. The proposed approach has been tested on simple curves and curves with large radius of curvature. The results show that the relation can be found for different feasible and reasonable velocity limits. The solution obtained depends on factors like the selection of a relation between parameter and time and initial conditions. The methodology can be applied to a different combination of relations such as a linear superimposed by a sinusoidal or any higher order polynomial.

The time taken to track the desired trajectory is in the order of few seconds considering realistic process parameters. Reducing the time scale to milliseconds could better the results. Furthermore, scaling the objective function and considering multi-objective issues may produce even better results. Other considerations for the method include the significant reduction in data required to draw complex curves and better control ability. The parameters themselves are the only needed information, and, by providing the controller with an equation of a curve as a function of time, its velocity and acceleration at any point, a controller can be designed to accurately track the curve.

Present work is dealing with the following issues: piecewise parameterization, NURBS application, controller development, interface with CAD directly, and implementation in a stereolithography machine.

## BIBLIOGRAPHY

- Bobrow, J.E., Dubowsky, S., and Gibson, J.S., 1985, "Time-optimal control of robotic manipulators along the specified path," *The International Journal of Robotics Research*, 4.3, pp. 3-17.
- Ganesan, M.K., 1992, "Offsetting of NURBS curves for CAD applications," M. S Thesis Report, Clemson University, South Carolina.
- Shiller, Z., and Dubowsky, S., 1989, "Robot path planning with obstacles: Actuator, gripper and payload constraints," *The International Journal of Robotics Research*, 8.6, pp. 3-18.
- Shin, K.G and McKay, N., 1985, "Minimum-time control of robotic manipulators with geometric path constraints," *IEEE Transactions on Automatic Control*, 30. 6, pp. 531-541.
- Vanderplaats, G. N., 1973, "CONMIN, a FORTRAN program for constrained function minimization. User's Manual." NASA Technical Memorandum, TM-X-62, 282.
- Van Willigenburg, L. G., 1993, "Computation and Implementation of Digital Time Optimal Feedback Controllers for an Industrial X-Y Robot subjected to Path, Torque, and Velocity constraints," *The International Journal of Robotics Research*, 12.5, pp.126-134.
- Vouzelaud, F. and Bagchi, A., 1993, "Offset of two-dimensional contours: finish machining." Clemson University ASME WAM and Journal of Mechanical Engineering for Industry.
- Vuyyuru, P. *et Al.*, 1994, "A NURBS based approach for rapid product realization," Fifth International Rapid Prototyping Conference, Dayton, OH.
- Wu, Ying-Jeng Engin and Beaman, J. J., 1990, "Control Following for Scanning Control SFF Publications: Control Trajectory Planning," *Solid Freeform Fabrication Symposium*, Austin, TX, pp. 126-134.







# Process Planning and Automation for Additive-Subtractive Solid Freeform Fabrication

J. Miguel Pinilla, Ju-Hsien Kao, Fritz B. Prinz

[jmp@Stanford.edu](mailto:jmp@Stanford.edu), [jhkao@Stanford.edu](mailto:jhkao@Stanford.edu), [fbp@cdr.stanford.edu](mailto:fbp@cdr.stanford.edu)

Department of Mechanical Engineering, Stanford University

## Abstract

*New additive-subtractive processes promise to enhance SFF capability from prototyping to true low-volume production. However, to maintain the same degree of process automation as in currently available processes like SLA or SLS, more sophisticated planning and execution systems need to be developed.*

*The system we present in this paper consists of two parts. The first is an off-line planner that decomposes a CAD model into 3D manufacturable volumes called "single-step geometries", arranges these geometries into a graph representation called "adjacency graphs", and automatically generates deposition and machining codes for each single-step geometry. The second is an on-line system that handles asynchronous multi-part building, job-shop scheduling, process control and run-time execution. Communication between these two stages is through a "process description language".*

*The goal of this paper is to present a framework for planning and execution for additive/subtractive processes, outline the issues involved in developing such an environment, and report on the progress made in this direction at the Rapid Prototyping Laboratory of Stanford University.*

## 1. Introduction

The demand in industry for fast, accurate renditions of designs is not new, and a whole community of specialized model makers and craftsmen has traditionally catered to this demand. This community has adopted new technology, like CNC machining, as it has become available. Nevertheless, the process of creating a model or a prototype of a design remained labor- and skill- intensive until the set of processes known collectively as Solid Free form Fabrication became feasible.

SFF processes have overcome this skill and labor requirement by simplifying the elementary geometry to be built. The simplification is achieved by decomposing any complex geometry into simple 2-dimensional slices. These processes also sacrifice tolerances, surface finish, and the use of engineering materials for the sake of automatic planning and execution of parts. This trade-off, while acceptable for "look-and-feel" prototypes, is becoming a liability for current processes. Industry is requiring functional prototypes and CNC shops are shortening their lead times, making them competitive with RP bureaus.

The processes currently used in the SFF industry are purely additive, where material is progressively added to the part being built in the final position and shape. Newer processes coming out of the research laboratories are using engineering materials (hard metals, ceramics), and are combining addition and subtraction of material as a way to shape more precisely the part. A comprehensive review of the available processes can be found in [Prinz, Atwood et al. 1997].

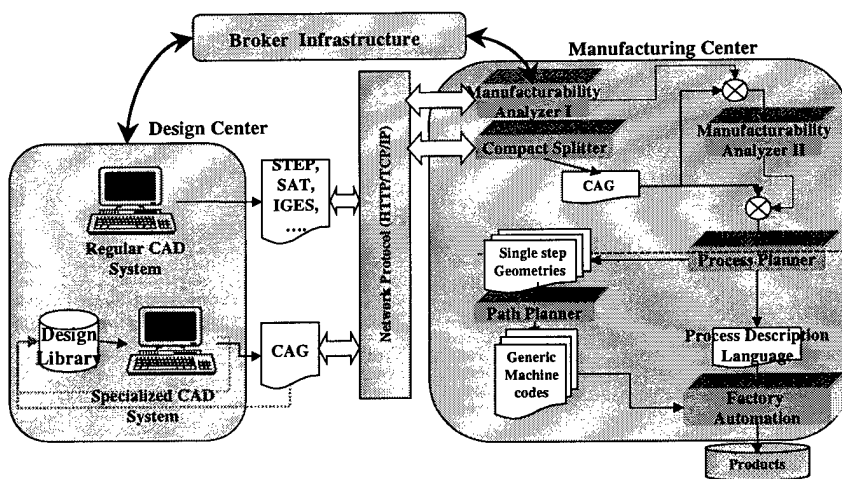
Additive/Subtractive processes improve on purely additive ones in the range of materials they handle and the accuracy they provide. They are also proving to accept more sophisticated design with multiple and graded materials in a single part [Weiss, Merz et al. 1997], as well as integrating whole assemblies in one single fabrication unit. The downside to all these

improvements is that additive/subtractive processes require a substantially more sophisticated process planning and part execution control. This increased difficulty is the result of the use of CNC machining or similar material removal processes and the need to coordinate several different unit processes.

The goal of this paper is to present a planning and execution framework for additive/subtractive processes, outline the issues involved in developing such an environment, and report on the progress made in this direction at the Rapid Prototyping Laboratory at Stanford University. We take the SDM process [Merz, Prinz et al. 1994] developed at Stanford as the case study to apply the concepts developed in planning and execution for this class of additive/subtractive SFF processes.

## 2. Design/Manufacturing interface

The first step towards automated manufacturing is to establish efficient communication between design clients and manufacturing centers. A design client can be equipped with regular CAD packages or with specialized design software [Binnard and Cutkosky 1998] where process-specific knowledge is embedded to facilitate down-stream planning tasks. On the other hand, manufacturing centers should provide manufacturability analyzers, automated process planning software and on-line execution systems. The manufacturability analyzers, for example, examine



tolerance requirement of a design and verify it with their facility and process capabilities. The process planner generates sequences of process plans and associated operations and machine codes for building given parts. Execution systems read in several alternate process plans (possibly for many different parts), and determine subsequent operations and machines based on on-line job-shop

configurations.

Communication between designers and manufacturers can be accomplished by Internet-based process brokers [Tan, Pinilla et al. 1998]. These brokers receive designs and check with available manufacturing centers for accessing turn-around time, material availability, facility capability, and dimensional accuracy. They then select manufacturers that best fit designers' requirements. Figure 1 shows a framework architecture that includes the concepts outlined here.

In the following sections, we will only address issues related to process planning and execution for additive/subtractive SFF processes.

### **3. Challenges and needs in process automation**

#### **3.1. Planning needs and challenges**

The first requirement for a realistic planning and execution system for any manufacturing system is to be able to interface existing CAD systems. The supplied solid models must support free-form surfaces for the sake of geometrical reasoning and path planning required for additive/subtractive processes and for the required levels of accuracy. Further development of CAD systems to be able to represent multi-material parts and graded material parts is an active area of research that will have substantial impact on these processes [Kumar and Dutta 1997, Aug].

The required functionality for a planning system can be summarized as follows:

- Planning for finding a building orientation [Hur and Lee 1998] has to account for the fact that additive/subtractive processes can deposit and shape full 3D shapes and is not limited to thin 2D layers.
- Part shape needs to be decomposed in volumes that are readily manufacturable with the process considered. Decomposition is substantially more complex to take full advantage of the non-planar capabilities.
- Planning each of the decomposed volumes in the two phases of the process: planning the deposition of material [Kao 1998], [Farouki, Koenig et al. 1995] and the machining of the final shape for each surface. In additive/subtractive SFF, geometry simplification due to decomposition avoids most of the tool interference, and tool access problems characteristic of path planning, offering a better chance to achieve automation.

#### **3.2. Execution needs and challenges**

SDM and other additive/subtractive processes present a substantial increase in sophistication compared with pure additive ones regarding its execution environment. The main issues that should be considered are:

- SDM is a multistage process: Multistage processes require or should allow multiple processing stations and transfer of parts between stations. An industrial SDM shop needs to determine scheduling of parts and operations, floor layout, assignment of jobs to machines, etc.
- As soon as multiple machines are considered, the manufacture of several parts will want to take advantage of parallel processing in different stations to maximize equipment utilization. Each part can be built following several alternative sequences. The execution system should be able to take advantage of this flexibility to optimize cost and turn-around time.
- The execution system should coordinate activities of machines and transfer of parts, and track and balance the state of load of each machine in the shop to achieve a smooth flow.

These characteristics make the process somewhat similar to VLSI manufacturing, where an array of processes work in sequence to produce a wafer. A wafer's route travels through a variable number of machines depending on its process plan, and it is very cyclic (Lithography-Etch-

Implant). In a similar fashion to VLSI manufacturing, the execution system will have to cover the handling of partially built parts and intermediate buffers.

#### **4. Process planning**

Process planning takes full 3D geometric models as inputs and outputs process description that specifies contents and sequences of operations that are necessary to produce the input parts. The contents contain machine-understandable codes for driving designated machines to perform desired operations where as sequences specify all possible orders of operations that are valid to manufacture the input parts.

Basic planning steps involve determining building directions, decomposing a part into manufacturable volumes (called single-step geometry), representing these sub-models in a structured format for allowing optimizing building sequences, depositing materials on each single-step geometry, and shaping decomposed entities. The goals of these tasks are to generate process plans that are of low-cost, high-quality, high-precision, and fast turn-around time. We will first define the constituent of the additive/subtractive process: single-step geometry.

##### **Single-step geometry**

Additive/subtractive SFF processes involve iterative material deposition, shaping and other secondary operations. Each of such operations is associated with a part component or a decomposed geometry, which together represent a final product. The characteristics of such decomposed geometry (a set of single-step geometries) are that all supports for its undercut features are previously built, and no interference should occur in depositing or shaping processes from the top with respect to the building direction. In other words, any ray cast along the growth direction should not intersect a single-step geometry more than once.

Operations associated with each single-step geometry may include deposition with different types of material or machines, machining operations using CNC machines, or electrical discharge machining. Or it could be simple operations such as automatic insertion of pre-fabricated components.

The following describes issues related to automatic and optimal planning for additive/subtractive processes.

##### **Building direction**

The approaches are not dissimilar with other pure-additive SFF processes in determining building directions. However, there are some more issues to be considered for additive/subtractive processes:

- The number of decomposed single-step geometries reflects time for part building. In a typical additive/subtractive process, shaping operations usually need deposited materials to be conditioned (in the case of plastics, cured/hardened; in the metal cases, cooled). The more the steps, the more the building time is consumed in the conditioning procedures.
- To facilitate machining tasks, it is preferred that a part has as many as possible flat or vertical surfaces with respect to the building direction. In the cases of free-form surface designs, an orientation that minimizes the number of undercut-nonundercut transitions is most desirable since a surface without being split can be machined in one single operation which eliminates marks resulting from the layer interfaces.

An approach that maps surface normals to a unit sphere and determines the orientation that results in the minimum number of undercut-nonundercut transitions is described in [Rajagopalan, Pinilla et al. 1998].

### Part decomposition

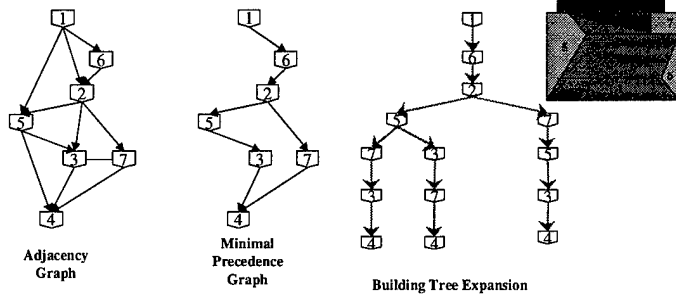


Figure 2 Adjacency graph and building tree for a sample part

An algorithm that finds a feasible solution for this decomposition is described in [Ramaswami, Yamaguchi et al. 1997]. In short, once a building direction has been determined, this approach identifies all silhouette edges that denote transitions from non-undercut surfaces to undercut features or vice versa. A collection of these silhouette edges together with existing edges form a loop, which is used to split the surfaces. Models

are then decomposed and support structures are generated with the help of several extrusion operations. Although this approach gives a solution of decomposition, the following issues need to be addressed to achieve a better solution:

- Parts may be decomposed to several smaller features or may result in sharp cavities that do not exist in the original design. These features increase difficulty in machining and may require more expensive and time-consuming processes, e.g., electrical discharge machining (EDM) for metal parts.
- When a part is decomposed into several sub-volumes, their shared surfaces need not be defined exactly unless they consist of different materials. This is due to the fact that the newly introduced surfaces resulted from decomposition are internal to the part and need not be machined, since subsequent operations will deposit same types of material adjacent to these surfaces.

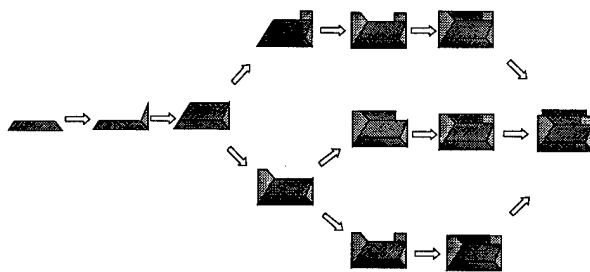


Figure 3 Alternative building sequences.

The results of decomposition are structured in an **adjacency graph** where nodes represent single-step geometries or other components to be embedded, and edges represent the adjacency relationship between connected nodes. After considering part building order, a directed graph that represents the precedence relationship among single-step geometries can be constructed. From this **precedence graph**, one can identify in what order the single-step

models should be built.

With the precedence graph, a set of alternative building plans can be generated. Each plan represents a possible building sequence on the decomposed geometry and can be chosen

optimally depending upon machine availability or other criteria such as minimum building time, or best possible surface finishing, etc. These building alternatives are passed to job shops for run-time job-shop scheduling. The adjacency graph, precedence graph, and the **building alternative tree** of an example part are shown in figure 3.

### **Material deposition**

Material is usually deposited in consecutive 2D layers until a single-step geometry is completely built. The advantages of additive/subtractive processes are that deposition may not need to be net-shaped since material removal processes are involved. This helps reduce stress concentration and warpage problems and improve deposition path optimality that could reduce voids during deposition. An algorithm that describes a method of relaxing 2D-layer geometry based on its medial axis transform can be found in [Kao 1998]. With this approach, original 2D-layer geometry is "fixed" to reduce sharp corners and narrow passages, and to optimize the deposition path for smoothness.

### **Machining**

In additive/subtractive SFF processes, there exist no tool accessibility problems if appropriate machine tools are selected. This is because any supports for undercut features of a single-step geometry have been built in earlier stages and parts can be further decomposed according to machining constraints. Therefore, planning for machining operations need not consider interference problems.

In additive/subtractive processes, automatic machining path generation is crucial due to the number of machining operations involved. These tasks include determining surfaces to be machined, selecting appropriate cutter sizes, retrieving corresponding cutting parameters from database, using the best cutting strategies for given surfaces, and generating tool paths for target machines.

## **5. Execution system**

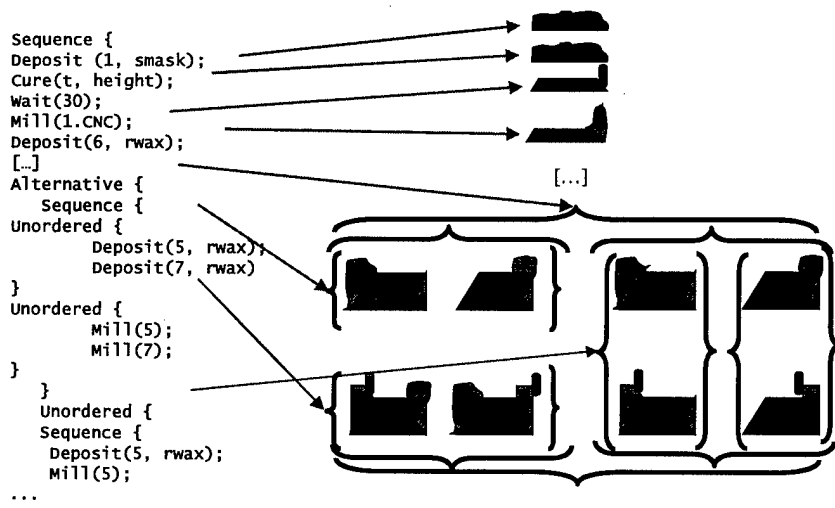
We take the SDM process as a case study for the more general case of SFF additive/subtractive processes. SDM has two levels of operation at the shop level: executing each individual operation and building complete parts.

### **Operations**

SDM relies on a limited set of primitive operations to build the parts. The execution system dedicated to machine operations must provide such primitives. These primitives are **load/unload, mill/shape, deposit, cure, preheat, and cool**. Other auxiliary operations may be needed that act as a bridge between primary operations. These may include **wash, sandblast, shot-peen**, or special operations such as **embed** components, **inspect**, etc.

### **Part building and process description language (PDL)**

Parts are built by a sequence of operations. Each part to be built is characterized by a process plan that is built in terms of the primitive operations presented above. Required operations are described allowing flexibility in the allocation of its execution to a particular machine as late as



possible. No specific machine characteristics are built into the part plan description.

The process plan determines sequences of operations to build the part only to the extent necessary for correct completion of the part. The plan should leave as much flexibility as

possible to the execution system for possible build-time optimizations. As an example of this, in

Figure 4 Process Description Language

figure 2 single step geometries 3 and 7

do not require any special ordering between them to build a correct part. The process plan should reflect this flexibility and not over constrain the execution system by imposing an artificial order between them. A process description language has been designed to accommodate this requirement.

The language in its current implementation has the operations described above as primitives, and provides three higher level constructs to group them:

- Sequence: Describes a set of operations that need to be executed in sequence.
- Unordered: Describes a set of operations that can be executed in any order and still yield a valid part.
- Alternative: Contains a set of operations such that executing one of them is enough to complete this step.

These constructs can be arbitrarily nested to express the full range of possibilities that result from expanding the building tree. In figure 4 a portion of such process description is given to show how this language can be used to express the building options for a sample part.

**Shop scheduling**

For an industrial setting, SDM shops will be composed of differentiated machines to perform each operation. For each part and for each operation, it needs to be decided which machine to use. A first step is to match the operation requirements to the machine capabilities. In the system being built at Stanford, machine capabilities are described parametrically by

- Type of operation they support from the list of operations needed by SDM.
- Some general characteristics like maximum part size or weight.

- Operation specific parameters: materials available for deposition, tools available in a CNC mill tool magazine, achievable accuracy, 3 or 5 axis, etc.

With this information, the pool of machines available for a particular operation is identified. The selection of which machine to use within this pool will be determined by the cost and speed of the machine and by the operating conditions of the machine and the shop.

### **Information system**

Shop scheduling activities and the manufacturing operation implementation at the machine level are implemented in a shop information system with on line access to the status and control of the machines, and can be accessed on-line to submit parts for construction.

SFF shop operation is likely to work with lot sizes of one or very few parts. The execution system has to support a very high part mix, where each part has its own process plan. The shop control system

- Keeps track of the state of construction of each part. In our current implementation, the state of construction is represented by a sort of “program counter” in the process description language.
- Knows the state of load of the shop and each machine. Dynamic dispatching of operations to machines is not possible otherwise. The architecture of the system keeps most of this information distributed in the agents that control each of the machines.
- Can compute an estimate of cost and processing time. This will be used to determine which machine, among the available ones, is the best fit to perform an operation.

Current research in manufacturing executions systems [Motavalli 1995; Gowan 1996] point to information system architectures using a distributed computing system [Whiteside, Pancarella et al. ; No-author 1997]. This type of system supports a multiplicity of agents that collaborate to control production [Maturana and Norrie 1995; Ramos 1996; Gong 1997]. The approach that we will be taking in building a SDM shop control will comprise a network of agents that will use bidding to coordinate estimates and bid for the next operation to be performed.

Bidding among a set of competing agents has already been explored as a way for scheduling and assigning production resources to jobs or making design resources in [Baker 1996; Tilley 1996; Parunak 1997]. This framework is adaptable to SDM given the parametrization of building operations and machine capabilities outlined above.

Currently at Stanford’s RPL, a first prototype of such system is being built using a CNC mill as the basis for an integrated SDM machine tool. The overall shop control will be tested on a simulated set of such machines. A web-based interface is being built on top of the execution software to provide access to the fabrication of parts from other sites than the RPL at Stanford and to provide a design/manufacturing interface.

## **6. Implementation for Shape Deposition Manufacturing**

### **6.1. Planning**

The current process planner being developed at Stanford Rapid Prototyping Laboratory is based on the Unigraphics system and its API’s. Models are imported in STEP format and are

decomposed into single-step models. These sub-models are structured in the adjacency graph, precedence graph and building alternative tree, which are implemented in C++. Deposition and machining codes are generated automatically within UG/Open API and UG/Open GRIP programming environment.

### 6.2. Execution system

The current execution system is implemented on a single real machine. A simulated multi-machine shop is being built to test the scheduling and information support systems.

The SDM machine is based on a Haas CNC mill with additional equipment to enable it to perform the deposition of three different materials, curing, preheating, and cooling. A detailed description of the machine hardware is given in [Cooper, Kang et al. 1998]. The controlling software is written in Java and controls the machine through two serial ports, one to interface the Haas CNC controller and another to control the digital and analog I/O boards.

The software has three main parts: The machine control in charge of hardware interface, an interpreter/scheduler of the process description language, and an interface towards the network that will allow for job submission remotely over the network to facilitate the design and manufacturing scenario described in [Rajagopalan, Pinilla et al. 1998; Tan, Pinilla et al. 1998].

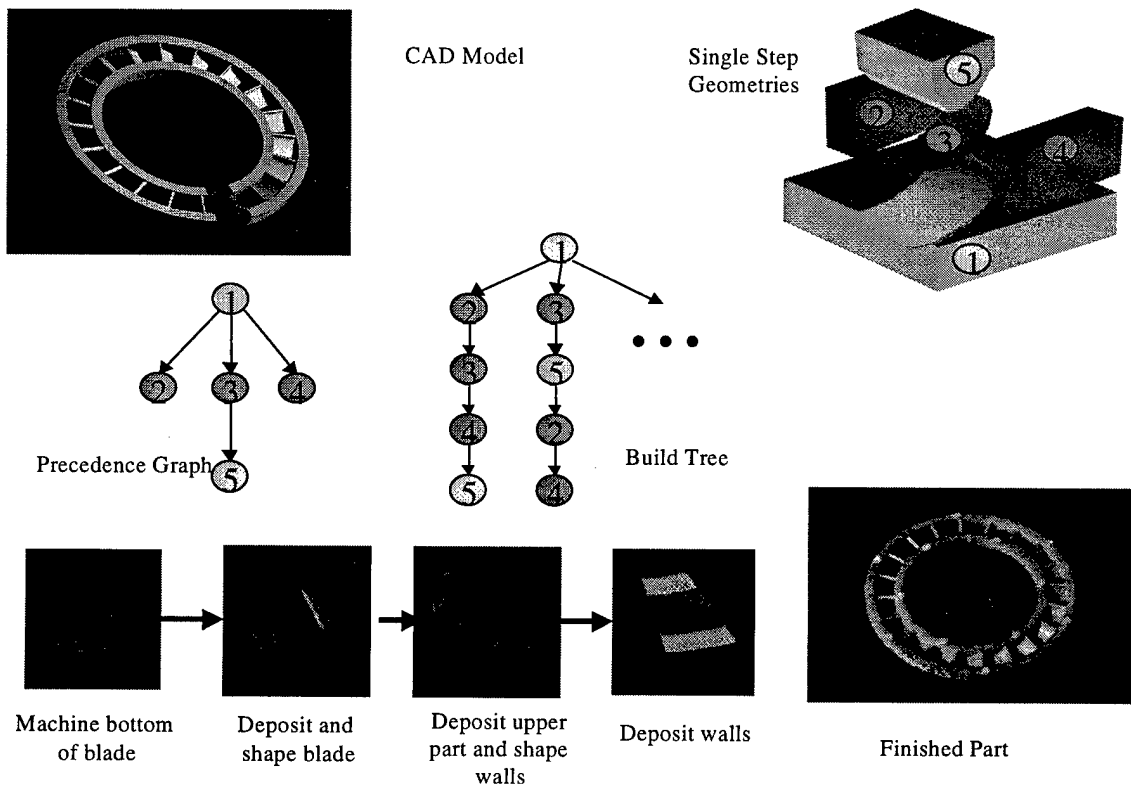


Figure 5 Construction of a shrouded fan from a CAD model

### **6.3. CAD to Part process**

Figure 5 shows an example of a part building plan of a shrouded fan. The CAD model is decomposed into five single-step geometries. These geometries hold precedence relationships that are represented in a precedence graph. This graph completely represents their building constraints. Deposition and machining code is then generated for each single-step geometry. This process code is used to directly drive machine tools.

The overall part plan is codified in the Process Description Language that encodes all possible building sequences derived from the building tree and their associated manufacturing information.

The encoded process description is interpreted by the execution system that controls and monitors all the part building activities. A building sequence is then chosen in real time depending on machine availability, job-shop scheduling, and other criteria. Figure 5 shows the steps of a particular building sequence that completes the part, and the finished part.

## **7. Conclusions.**

We have presented the main issues that need to be solved to make additive/subtractive SFF processes amenable to industrialization. While the basic technology for these processes is well developed, the supporting planning and execution aspects are not well understood.

Planning defines how to achieve a feasible plan to build a design from its geometrical representation. The main tasks are to decompose the model into manufacturable elements, plan the deposition of material and its shaping. Algorithms are being developed to address each of these tasks, and a representation formalism to support them has been presented.

Execution is a somewhat looser term that comprises aspects from shop organization to control of machines looking into commercial use of the technology. In this framework a flexible shop is envisioned supported by an information system to track each part and to dynamically assign tasks to the different machines.

This set of technologies are being explored at Stanford's Rapid Prototyping Laboratory, building prototypes of both a planner and an execution environment as a test bed for pre-industrial deployment of SDM opening the facilities to part submission over the network.

## **8. Acknowledgements**

This work was supported by Air Force Research Laboratory AFRL/MLKT under contract F33615-95-C-5560-P00004 and the Future Professors of Manufacturing program at Stanford University. The authors thank the contributions of their colleagues at the Rapid Prototyping Laboratory for providing experimental support and critique to the ideas presented here, and especially to Falk Kaehny, Jianpeng Dong and Yu-Chi Chang for their contribution to the software implementation, and their thorough knowledge of Unigraphics environment.

## 9. References

- Baker, A. D. (1996). Metaphor or Reality: A case study where agents bid with actual costs to schedule a factory. Market Based Control. S. H. Clearwater. Singapore, World Scientific: 184-223.
- Binnard, M. and M. Cutkosky (1998). Building Block design for Layered Shape Manufacturing. ASME DFM 1998, Atlanta, ASME.
- Cooper, A. G., S. Kang, et al. (1998). Automated Fabrication of Complex Molded Parts Using Mold SDM. SFF Symposium 1998, Austin, Tx.
- Farouki, R. T., T. Koenig, et al. (1995). "Path planning with offset curves for layered fabrication processes." Journal of Manufacturing Systems 14(5): 355-368.
- Gong, D. C. (1997). "A decision-making perspective on hybrid manufacturing system control." International Journal of Production Research 35(7): 1945-1959.
- Gowan, J. A., Mathieu, R.G. (1996). "Critical Factors in information system development for a flexible manufacturing system." Computers in Industry 28 : 173-183.
- Hur, J. and K. Lee (1998). "The Development of a CAD Environment to Determine the Preferred Buildup Direction for Layered Manufacturing." International Journal of Advanced Manufacturing Technology 14(4): 247-254.
- Kao, J. H. (1998). Optimal Motion Planning for Material Deposition in Layered Manufacturing. DETC'98 18th Computers in Engineering Conference, Atlanta, GA.
- Kumar, V. and D. Dutta (1997. Aug). An Approach to Modeling Heterogeneous Objects. Proceedings of the Solid Freeform Fabrication Symposium 1997, Austin, TX.
- Maturana, F. P. and D. H. Norrie (1995). A Generic mediator for Multi-Agent Coordination in a Distributed Manufacturing system. International conference on Systems, Man and Cybernetics.
- Merz, R., F. B. Prinz, et al. (1994). Shape Deposition Manufacturing. Solid Freeform Fabrication Symposium, University of Texas at Austin, Austin TX.
- Motavalli, S. e. A. (1995). "A Proposed Framework and a survey of reserarch Issues in Manufacturing Information Systems." Computers in Industrial Engineering 31(3/4): 551-554.
- No-author (1997). Manufacturing Domain Task Force RFI-3 Manufacturing Execution Systems (MES). Framinham, MA, Object Management Group.
- Parunak, H. V. D. W., A.; Fleischer, M.;Sauter, J. (1997). A Marketplace of Design Agents for Distributed Concurrent Set-Based Design. Fourth Ispe International COnference on Concurrent Engineering: Research and Applications, Troy, Michigan.
- Prinz, F. B., C. L. Atwood, et al. (1997). JTEC/WTEC Panel Report on Rapid Prototyping in Europe and Japan Volume I Analytical Chapters. Baltimore, MD, Rapid Prototyping Association of the Society of Manufacturing Engineers/NSF.
- Rajagopalan, S., J. M. Pinilla, et al. (1998). Integrated Design and Rapid Manufacturing over the Internet. 1998 ASME DETC/CIE Conference, Atlanta, GA.
- Ramaswami, K., Y. Yamaguchi, et al. (1997). Spatial Partitioning of solids for Solid Freeform Fabrication. ACM/SIGGRAPH Symposium on Solid Modeling and Applications.
- Ramos, C. (1996). A Holonic Approach for Task Scheduling in Manufacturing Systems. International Conference on Robotics and Automation, Minneapolis, Minnesota, IEEE.
- Tan, S., J. M. Pinilla, et al. (1998). TRADEWIND: A Prototype Internet Marketplace for Solid Free-form Fabrication. 1998 ASME DETC/CIE Conference, Atlanta, GA.
- Tilley, K. J. (1996). Machining Task Allocation in Discrete Manufacturing Systems. Market Based Control.
- Weiss, L., R. Merz, et al. (1997). "Shape Deposition Manufacturing of Heterogeneous Structures." Journal of Manufacturing Systems 16(4): Journal of Manufacturing Systems.
- Whiteside, R. A., C. M. Pancerella, et al. "A CORBA-Based Manufacturing Environment." Sandia National Laboratories.



# Modeling and Designing Components with Locally Controlled Composition

Todd R. Jackson, Nicholas M. Patrikalakis, Emanuel M. Sachs, and Michael J. Cima, MIT

## Abstract

SFF processes have demonstrated the ability to produce parts with locally controlled composition. In the limit, processes such as 3D Printing can create parts with composition control on the length scale of 100 microns. To exploit this potential, new methods to model, exchange, and process parts with local composition need to be developed. An approach to modeling a part's geometry, topology, and composition will be presented. This approach is based on subdividing the solid model into sub-regions and associating analytic composition blending functions with each region. These blending functions define the composition throughout the model as mixtures of the primary materials available to the SFF machine. Various design tools will also be presented, for example, specification of composition as a function of the distance from the surface of a part. Finally, the role of design rules specifying maximum concentrations and concentration gradients will be discussed.

## Introduction

This research into modeling and designing components with locally controlled composition is part of a larger project funded by the National Science Foundation titled "The Distributed Design and Fabrication of Metal Parts and Tools by 3D Printing." The overall goal of this project is to identify the barriers preventing designers from accessing the unique and useful capabilities of SFF processes such as 3DP and provide solutions. One of the identified barriers is the inability for designers and manufacturers to work with models of graded compositions. To address this issue, we are researching methods to represent, design, exchange, and process these models with the intention of promoting the use and research of Local Composition Control through 3DP by a wider audience.

## Background: Local Composition Control (LCC) through 3D-Printing (3DP)

Solid Freeform Fabrication (SFF) refers to a class of manufacturing processes that build objects in an additive fashion directly from a computer model. Although most build from a single material and in layers, a few SFF processes possess the capability to fabricate objects from multiple materials in a near point-wise fashion. The combination of these two features allows for the possibility of Local Composition Control (LCC) through which graded compositions can be manufactured from the base materials available to the SFF machine<sup>1,2</sup>. One such SFF process capable of LCC is 3D Printing<sup>1</sup>.

Conventional 3DP manufactures a part by selectively binding powder together according to a computer model. The build cycle begins by spreading a layer of powder over the print bed. A print head then traverses the bed, selectively depositing binder over the regions corresponding to the interior of a slice of the

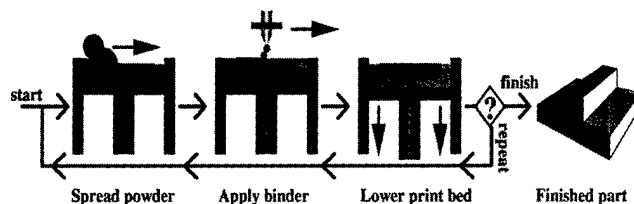


Figure 1. Conventional 3DPrinting process.

computer model. After the binder dries, the print bed is lowered and another layer of powder is spread. The process of spreading powder, depositing binder, and lowering the print bed is repeated, as shown in Figure 1, until the entire volume of the object is printed. At the end of the process, the bound powder becomes the manufactured object, effectively rendering the computer model as a physical object. Currently, metal and ceramic parts are being manufactured through 3DP, but the potential exists to build with any material supplied in powder form.

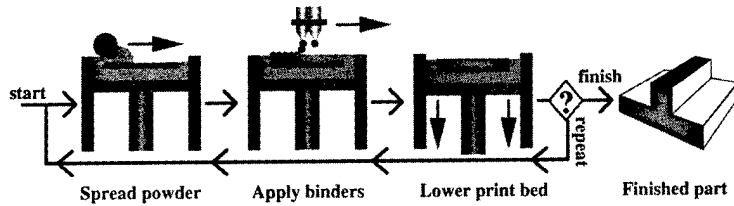


Figure 2. LCC through 3D Printing of multiple binders.

Similar to how an ink-jet printer prints color documents, 3DP can achieve LCC with multiple materials. This is accomplished by using a print-head with several jets, each depositing binders and /or slurries of unique material. By varying the pattern in which the jets deposit material on the powder-bed,

the material composition can be controlled on the scale of the binder droplets ( $\cong 100\mu\text{m}$ ). Regions of uniform and graded compositions can be created in a manner analogous to how continuous tone images are rendered on a hard-copy device from primary colors. With this capability, graded compositions can be designed along with the geometry of the part, tailoring the part's physical properties for a specific purpose or function. Such compositions have become known as Functionally Graded Materials (FGMs).

The capability of producing FGM could be utilized by a wide variety of industries. Some applications being studied at MIT include:

1. Wear resistance and increased strength of a mechanical part through the controlled variation of its FGM composition<sup>3</sup>.
2. Design of electrical components by controlling the electrical properties on a local scale.
3. Variation of medicine placement within an FGM pill to optimally deliver drugs to a patient through the "controlled release" of the drug over time<sup>4</sup>.

### ***Information Flow of FGM Solid Models***

Despite the advanced capabilities of SFF machines, access to this new technology is limited by how information is represented, exchanged, and processed. Designers need new CAD tools to capture their ideas for FGM parts and manufacturers need algorithms capable of converting these models into machine instructions for their fabrication. To address these shortcomings and make LCC processes like 3D Printing available to the design community, this project is developing new methods for the design, representation, exchange, and processing of FGM models.

In current SFF practice, a model is communicated between the designer and manufacturer in terms of a tessellation of the model's boundary, usually in the form of a .STL file<sup>5</sup>. Only communicating information about the bounding surfaces, material information about the model is not conveyed, presenting a barrier to designers who wish to use LCC to create parts graded compositions.

Similar to how computer users regularly use desktop printers to produce hardcopy of their documents, 3DP can potentially permit a clean separation between the design of a part and its manufacture. For this to happen, a method for completely representing a part must be

established, allowing its neutral exchange between designers and manufacturers. For traditional CAD models, this can be accomplished through the use of the IGES or STEP formats. For models consisting of FGM, however, the representation must go one step further and allow the representation of graded material compositions. This representation, along with tools for the design, inspection, and processing of FGM models, will increase access to SFF manufacturing with LCC by allowing more efficient flow of information between designers, manufacturers, and researchers.

### Representation of FGM Models

In order to represent an object within the computer, a data structure representing all of the relevant information for its fabrication must be established. In traditional CAD systems, solid modeling methods maintain information about an object's geometry (shape) and topology (adjacency relationship between the geometric elements of its surface)<sup>6</sup>. Some CAD systems also provide the capability to associate material information with regions, facilitating the representation of composite structures. With the possibility of fabrication with LCC, a solid modeling method for 3DP must go one step further and represent smoothly varying compositions. Similar to how sculpted geometry can be represented as analytic functions (such as NURBS surfaces) methods to analytically describe how an FGM composition varies within a part need to be established. To provide this capability, an FGM solid modeling method must decompose the interior of the object into simpler sub-regions, each of which references information about the composition variation over its domain. To accomplish this goal, an FGM solid modeling method based on a representation known as the cell-tuple data structure<sup>7</sup> is under development. This structure naturally lends itself to the representation of models in terms of sub-regions over which the FGM information can be incorporated, similar to how the geometric information is maintained.

In the traditional cell-tuple structure, a model is decomposed into a set of cells with each cell representing a topological feature in the model, such as a vertex, edge, face or region. The topology of the model (or how the cells are connected together) is maintained by a graph of cells. The shape, position, and orientation of the model are determined by geometric information associated with each cell. Figure 3 illustrates this concept for a simple model of a tetrahedron with cells representing the different topological elements. For larger models, the interior may be decomposed into a single region, as in the .STL file, or subdivided into many smaller regions, similar to a finite element mesh.

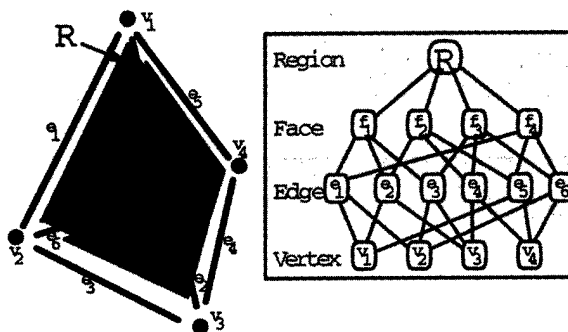


Figure 3. Model of a tetrahedron and its graph of cells.

To represent a FGM model within the cell-tuple structure, composition information, as well as geometric information, is associated with each cell. This information begins with the concept of a material system consisting of the primary materials available to an SFF machine capable of LCC:  $\vec{S} = \{m^1, \dots, m^N\}$ . The composition of the model  $M$  is represented as a vector valued function  $\vec{C}$  defined over the model's interior:  $\vec{C} = \vec{C}(\vec{x})$  for  $\vec{x} \subseteq M$ . Each component of

$\bar{C}$  represents the volume fraction of the corresponding material in the material system  $\bar{S}$  present at point  $\bar{x}$  within the model.

There are many possible approaches to defining the composition function  $\bar{C}(\bar{x})$ . For parts similar to traditional composite structures, constant values can be associated with each sub-region within the model. For graded compositions, however, analytic functions must be defined, capable of representing smooth variations in the volume fractions of the materials over the domain of each sub-region.

With the cell-tuple structure's capability to represent models as subdivided manifolds, models can be arbitrarily subdivided into topologically simpler domains over which composition functions can be defined. In our approach, we are simplifying the problem by beginning with models subdivided into tetrahedral meshes, permitting the use of standard meshing algorithms to convert solid models to our cell-tuple representation. Over each tetrahedral domain, the composition is formulated in terms of a set of *control compositions*  $\bar{c}_{\bar{i}}$  (see Figure 4) and basis functions  $B_{\bar{i}}^n(\bar{u})$ , where  $\bar{i} = (i, j, k, l)$  is the index of the control composition,  $B_{\bar{i}}^n$  is the Bernstein polynomial of degree  $n$  corresponding to index  $\bar{i}$ , and  $\bar{u} = (u, v, w, t)$  is the barycentric coordinate within the tetrahedron<sup>8</sup>:

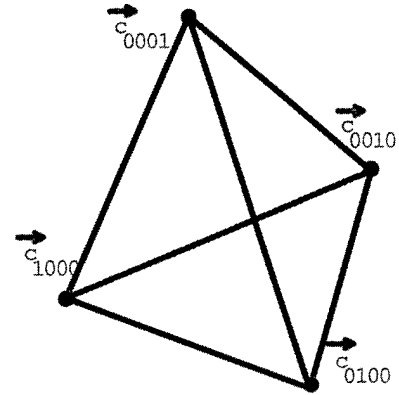


Figure 4. Wireframe view of a linear FGM tetrahedron with control compositions.

$$\bar{C} = \bar{C}(\bar{u}) = \sum_{|\bar{i}|=n} \bar{c}_{\bar{i}} B_{\bar{i}}^n(\bar{u}), \quad B_{\bar{i}}^n(\bar{u}) = \frac{n!}{i!j!k!l!} u^i v^j w^k t^l, \quad \text{and } |\bar{i}| = i + j + k + l.$$

Conceptually, the composition at a point can be considered as a blend of the control compositions with their influence determined by the value of their basis functions, analogous to the representation of NURBS surfaces with a mesh of control points. By defining compositions in terms of the Bernstein polynomials, the degree of composition variation is arbitrary, permitting the representation of regions of piece-wise uniform composition as well as higher order graded composition, as shown in Figures 5 and 6.

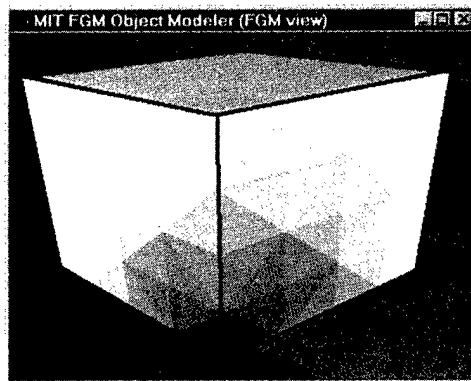


Figure 5. Cube consisting of 320 piece-wise constant FGM tetrahedra.

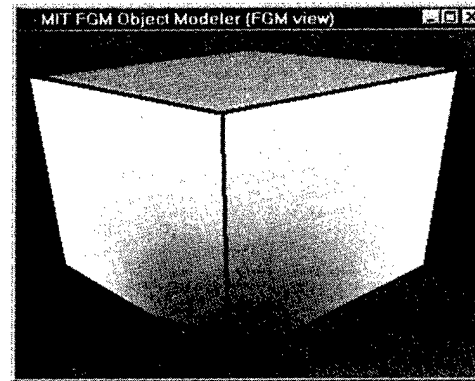


Figure 6. Cube consisting of 320 piece-wise linear FGM tetrahedra.

Although beginning with meshed tetrahedral models, the cell-tuple data structure is sufficiently general to represent a model as any valid subdivided manifold. This will permit FGM objects to be efficiently and accurately modeled from a suitable collection of FGM cells. Regions of uniform composition, for example, could be represented with a single region cell of constant composition, bounded by an arbitrary number of faces (similar to the traditional Boundary Representation and .STL representation). For graded regions, a collection of FGM cells starting with the tetrahedron can be defined, permitting different subdivision schemes of the object's interior. Hexahedral, wedge, and pyramid finite elements, for example, could eventually be defined with formulations for their geometry and graded composition in terms of tensor product B-splines or mixed tensor product B-splines and barycentric polynomials<sup>9</sup>. These formulations permit specification of continuous compositions at the interface of the cells using elementary properties of Bernstein polynomials and B-splines. However, specification of compositions with higher order derivative continuity is more complex and is not addressed in this paper.

The main components of our FGM solid modeling system are shown in Figure 7. Models created on a commercial CAD system are meshed into finite elements and then loaded into the data

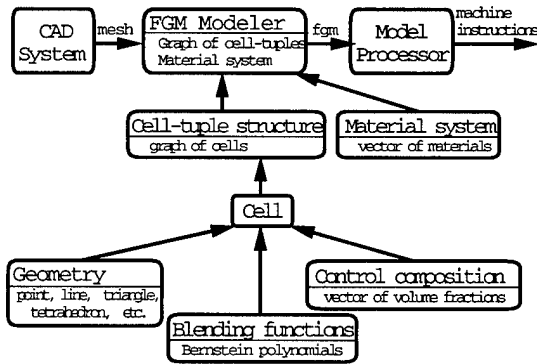


Figure 7. Components of FGM object modeler.

structure. As described above, model's topology is maintained by the cell-tuple structure as a graph of cells. Each cell in the model references information about its own geometry, a set of control compositions, and blending functions to define the variation in composition. The material system is composed of the primary materials available to the SFF machine. The SFF machine is assumed to have the capability to selectively place primitive of each material during the build process. Similar to how an ink-jet printer strategically places drops of the primary colors on a page to represent continuous tones, the model processor will generate the machine instructions to accurately fabricate the desired compositions. The processing of FGM models for fabrication will be based on halftoning algorithms similar to those used in image processing<sup>10</sup>.

### Methods for Designing FGM Models

With each *control composition* in our data structure representing a degree of freedom, the task of designing the FGM can be non-intuitive and confusing at the very least, if not impossible considering that a model may have millions of FGM sub-regions. To aid the designer, tools for simplifying and automating the design of FGM compositions are being developed. One approach being explored is the design of compositions in terms of distance functions.

The design of FGM compositions in terms of distance functions begins with the selection of a feature from which the composition will be designed. This may be a fixed reference in the coordinate system of the model, such as a point, line, or plane, or a feature of the model, such as its boundary or a particular face. Next, the designer specifies a variation for the FGM in terms of distance from the feature:  $\vec{C}_{design} = \vec{C}(r)$ , where  $r$  is the distance of a point from the reference feature. With a reference feature selected and a FGM variation designed, an algorithm automatically assigns values to the model's control compositions to define its FGM.

*Design example 1: FGM design of a pulley.*

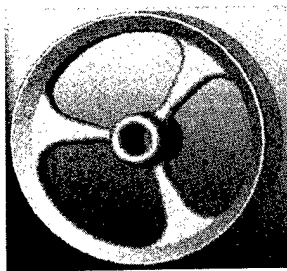


Figure 8. Pulley model.

To illustrate the concept of designing FGM as a function of distance from a line, consider the FGM design of a pulley in Figure 8. The designer, using a 3DP machine capable of building stainless steel parts with local control over the concentration of carbide wishes to optimally design an FGM composition resistant to wear. First, the CAD model is meshed into tetrahedral domains and loaded into the composition design system. The designer then specifies the pulley's axis of rotation as the reference feature from which the composition will vary. The final step in

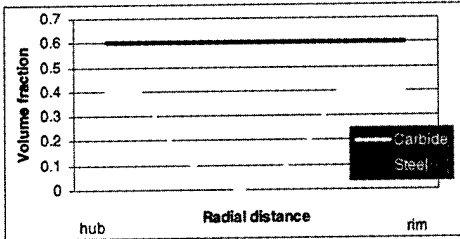


Figure 9. Variation of carbide concentration in pulley.

the design process is the design of the composition variation of the pulley as a function of distance from the axis. In this case, the concentration of carbide is greatest near the hub and rim where wear is greatest, as shown in Figure 9. The control compositions are then automatically assigned to the model, creating the desired FGM pulley as shown in Figure 10. A view of a pulley spoke showing the FGM tetrahedra is given in Figure 11, illustrating how the composition is defined over tetrahedral sub-regions.

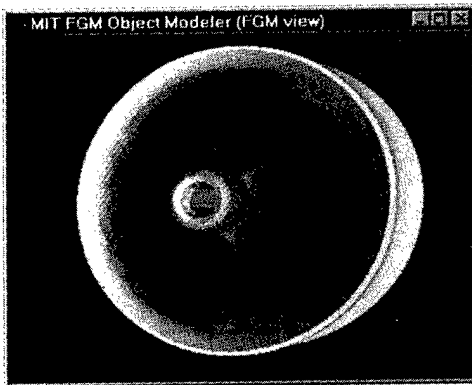


Figure 10. Composition variation over pulley with increased hardness at rim and

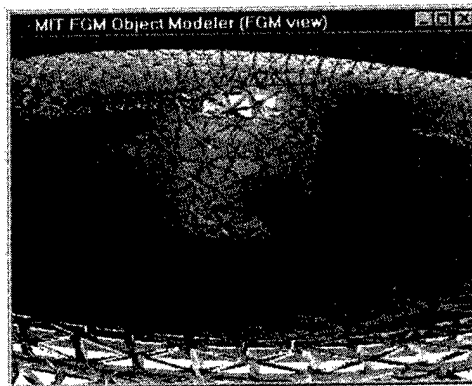


Figure 11. View of spoke decomposed into FGM tetrahedra.

*Design example 2: FGM design of a drug delivery device for controlled release.*



Figure 14. Model of pill.

With the ability to rapidly build objects through LCC, customized drug delivery devices can be created, optimally tailoring the release of drugs into the body. The design of the pill's FGM involves the controlled placement of medicine as a function of distance from its boundary. Knowing that the rate at which medicine is released into the body is governed by the rate at which the pill dissolves, the medicine concentration profile within the pill can be tailored

for optimal release<sup>4</sup>. In this case, the powder bed is the pill matrix and the drug placement is controlled by the print-head. Figure 14 shows the initial model of a pill

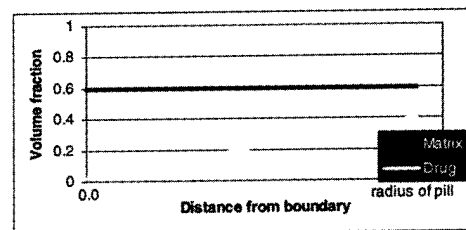


Figure 15. Design of drug concentration profile from the pill boundary.

before it is meshed into tetrahedra. The designer then specifies the concentration profile of the drug as a function of distance from the boundary, as given in Figure 15. The control compositions are then assigned, with each one's concentration determined by its distance to the nearest exterior boundary of the pill. Figure 16 shows a sliced view of the FGM pill with the variation in composition represented as colors on the internal surfaces of the tetrahedra. Figure 17 is the same pill but rendered with shrunken tetrahedra.

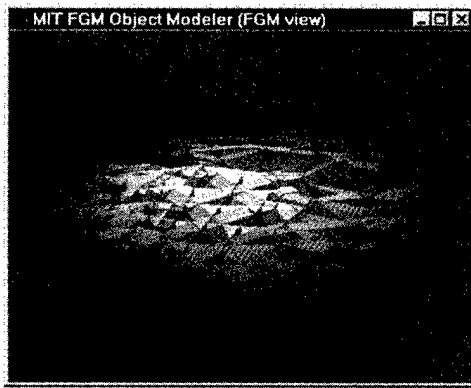


Figure 16. Clipped view of FGM pill.

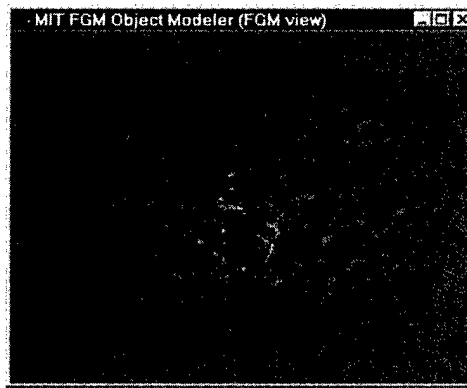


Figure 17. Decomposed view of pill.

### ***Design Rules for FGM Models***

The ability to represent complex FGMs does not guarantee the ability to manufacture the part. Due to the limited accuracy and resolution inherent in any process, some FGM models may not be fabricated to the designer's satisfaction. To avoid this situation, a set of "Design Rules" governing the design of FGMs need to be established. These Design Rules will be based upon the limitations in the manufacturing process (resolution, accuracy, layer thickness, etc.) and will inform the designer about the model's manufacturability. If the CAD model violates the Design Rules, the designer will be informed of the violation and will have the opportunity to redesign the object without the costly and disappointing process of manufacturing an unacceptable product. By providing tools to enforce Design Rule checking, some of the burden of ensuring part quality is reduced, allowing the designer to work with FGMs without being an expert in the manufacturing capabilities of the machine. Similar concepts involving minimum feature size were explored for macro-texturing for 3DP<sup>11</sup>. For FGM models, two Design Rules are being explored, governing the model's composition and its rate of change. Only the former is described here.

#### ***Design Rule limiting maximum and minimum composition.***

Depending upon the material system used to fabricate the part, there is a limitation to the maximum and minimum volume fraction of each material that can be present and still guarantee successful fabrication. Hence, the first foreseen Design Rule would limit the maximum and minimum concentration of each material in an FGM model.

In 3DP, the material system is composed of the powder in the print-bed and several different binders and/or slurries (solutions without binding properties) jetted from the print-head. In order to form the print-bed a minimum amount of powder must be present, thereby imposing a lower limit on the amount of the powder in the FGM. Likewise, the maximum packing density will

limit the maximum concentration of powder's material. During printing, the voids left in the print-bed are filled with material jetted from the print-head. Its porosity places a limit on the maximum total amount of jetted material it can hold. In addition, to form a solid part, a minimum amount of binder is required to hold the powder particles together, placing a lower limit on the amount of binder throughout the interior of the model.

Enforcement of the Design Rules involves restricting the assignment of the FGM  $\vec{C}(\vec{x})$  such that  $DR^{\min,j} \leq C^j(\vec{x}) \leq DR^{\max,j}$ , where  $j$  is the material index and  $C^j$  is the corresponding volume fraction of material. For a system of three materials (powder, binder, slurry), a sample set of Design Rules governing the permissible compositions is given in Table 1. These Design Rules are applied to the hypothetical FGM model in Figure 18. For this example, the composition grades from powder and slurry at the top and bottom faces to powder and binder at the mid-plane. Due to the requirement of a minimum amount of binder, the compositions at the top and bottom need to be redesigned in order to guarantee a solid part.

Material system	$DR^{\min,j}$	$DR^{\max,j}$
$m^1 = \text{Powder}$	0.7	0.8
$m^2 = \text{Binder}$	0.1	0.3
$m^3 = \text{Slurry}$	0.0	0.3

Table 1. Design rule limiting volume fractions of material.

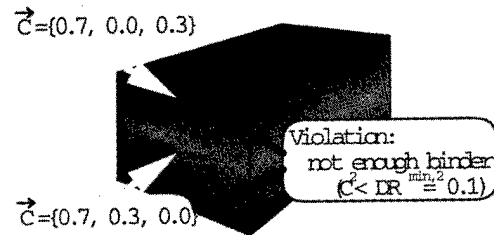


Figure 18. Extreme volume fraction of materials in FGM violate design rules.

### Acknowledgements.

This authors gratefully acknowledge the National Science Foundation (#DMI-9617750) for their support of this research. CAD models for the illustrations for this paper were originally generated with SolidWorks and then meshed with Algor.

<sup>1</sup> E. Sachs, J. Haggerty, M. Cima, and P. Williams. Three-Dimensional Printing Techniques. U.S. Patent No. 5,204,055.

<sup>2</sup> J. Fessler, A. Nickel, G. Link, F. Prinz. *Functional Gradient Metallic Prototypes through Shape Deposition Manufacturing*. In D. L. Bourell, J. J. Beaman, H. L. Marcus, R. H. Crawford, and J. W. Barlow, editors, *Solid Freeform Fabrication Proceedings '96*, Austin, TX, September 1997. The University of Texas at Austin.

<sup>3</sup> J. Yoo, K. Cho, W. S. Bae, M. Cima, and S. Suresh. Transformation-Toughened Ceramic Multilayers with Compositional Gradients. *Journal of American Ceramic Society*, 81(1) 21-32, January 1998.

<sup>4</sup> B. Wu, S. Borland, R. Giordano, L. Cima, E. Sachs, and M. Cima. Solid Free-form Fabrication of Drug Delivery Devices. *Journal of Controlled Releases*, 40(1-2); 77-87, June 1996.

<sup>5</sup> V. Kumar and D. Dutta. An Assessment of Data Formats for Layered Manufacturing. *Advances in Engineering Software*, 28(3) 151-164, April 1995.

<sup>6</sup> M. Mäntylä. *An Introduction to Solid Modeling*. Computer Science Press, Rockville, Maryland, 1988.

<sup>7</sup> E. Brisson. Representing Geometric Structures in D Dimensions: Topology and Order. *Discrete and Computational Geometry*, 9:387-426, 1993.

<sup>8</sup> J. Hoschek and D. Lasser. *Fundamentals of Computer Aided Geometric Design*. A. K. Peters, Wellesley, MA, 1993.

<sup>9</sup> S. T. Tuohy and N. M. Patrikalakis. Nonlinear Data Representation for Ocean Exploration and Visualization. *Journal of Visualization and Computer Animation*, 7(3);125-139, July-September 1996.

<sup>10</sup> R. Ulichney. *Digital Halftoning*. MIT Press, Cambridge, MA 1987.

<sup>11</sup> H. Jee. *Computer-Aided Design of Surface Macro-Textures for Three Dimensional Printing*. PhD thesis, Massachusetts Institute of Technology, Cambridge, MA, April 1996.

# Domain Decomposition and Space Filling Curves in Toolpath Planning and Generation

Bertoldi M., Yardimci M. A., Pistor C. M., Güçeri S. I.  
University of Illinois at Chicago

## *ABSTRACT*

Ever increasing computer performance, along with significant developments in CAD/CAM technology and high precision digital motion controllers lead to rapid and significant developments in the field of rapid prototyping/fabrication. Together, these elements offer a wide range of possible approaches in the toolpath planning issue; two main sets have been analyzed and applied to Fused Deposition Modeling process.

Domain decomposition is a frequently used technique in computational methods. Within the context of present study, this approach is used to divide arbitrary layer geometries into smaller regions of simpler shape. A foreseeable advantage in such an approach is maximizing strength characteristics through thermal management. This is achieved by utilizing space filling curves which are mathematical entities that offer the possibility of building a wide range of structures, covering the surface of a single layer with one continuous curve. To evaluate the proposed concepts, ABS structures and ceramic green bodies have been successfully built.

## *OVERVIEW*

The term toolpath planning is defined here as the collection of operations performed to provide the Rapid Prototyping hardware with the set of building commands.

Although computer-controlled machines are now commonly available, the algorithms for driving them automatically are still subject of research. In CNC machining for example, human intervention and ingenuity are still necessary to design and build the necessary jigs for clamping of the workpiece. The integration of RP equipment with PC-based controllers offers the possibility of using common software development tools and resources for toolpath planning.

Fused Deposition hardware is very similar to basic operation of pen-plotters and the machine level controllers are based on the same language. As a result, they can work more efficiently with patterns (i.e. porous structures) that have "polylines" as the basic geometric features, compared to the current mode of operation, which works on filled polygons (monolithic models).

The algorithms that have been developed and applied to the Fused Deposition can be considered in two main categories:

- Slice level manipulation
  - Domain decomposition is a common technique in computational methods, used here to divide arbitrary layer geometries into smaller regions of simpler shape.
- Machine level manipulation
  - Space filling curves are mathematical entities that offer the possibility of building a wide range of structures, covering the surface of a single layer with one continuous curve.

### *SLICE LEVEL MANIPULATION*

In the current study domain decomposition was demonstrated using a Stratasys 1650 modeler. The standard Stratasys software (QuickSlice™) performs the translation from the 3D CAD model to the 2½D model through a slicing algorithm. At this point, the geometry of the part is described with a finite set of 2D layers, in order to match the SFF building paradigm. For certain applications, it can be more useful to directly generate or modify the geometry of the desired structure at slice level, i.e. in modeling of three dimensional objects from medical images where the original data is a set of 2D images. Furthermore, working on 2D contours allows the use of simpler and more common algorithms.

The slice information is contained in a SSL file, where it is described as a contour representing a closed planar surface. In the standard software processing, the slices are subsequently filled with a set of parallel lines, representing the roads. At the SSL level, the slice represents the building unit and it belongs to a different “group” to which the following properties can be assigned:

- Material
- Build style
- Contour (yes/no)
- Road width
- Air gap between roads
- Raster orientation, which is usually set to [+45 -45] for two consecutive levels.

The main constraint is the fixed nature of the raster, which is always made of straight parallel roads. This affects the physical structure of the part and all its characteristics, including mechanical properties, void contents, surface and bonding quality and accuracy. Furthermore, the topology of the parts that can be created is limited to standard solid structures.

A set of routines and programs has been developed in a combined FORTRAN/MATLAB environment, in order to explore the possibilities of the process.

## DOMAIN DECOMPOSITION

Domain decomposition techniques are mostly used in computational analysis, when the mathematical model describing the physical phenomena cannot be solved in closed form. The idea is to decompose the 2 or 3-dimensional domain into regions of simpler geometry (usually polygons in 2D and polyhedra in 3D) and to discretize the equations on the obtained grid, in order to generate an approximate solution. This approach, which had its real boost with the advent of computers, has requested the development of more refined and accurate mesh generator algorithms, especially for unstructured grids.

In Rapid Prototyping, the physical domain can be assimilated to the part to be built in the 3D representation, where the computational domain is the solid model (STL file). However, most RP/SFF techniques are based on a layered manufacturing paradigm and the eventual domain decomposition of the STL model cannot be reproduced in the physical part. Instead of considering the entire solid model, the domains to be decomposed are the single layers and the final mesh is a new layer, with the same external contour but subdivided in a variable size and shape mesh.

With this approach, it is possible to increase the number and manipulate the characteristics of the domains, which at this level represent the building units. This results in a more flexible and customizable building process.

## DELAUNAY TRIANGULATION

In two dimensions, a triangulation of a set  $V$  of vertices is a set  $T$  of triangles whose vertices collectively form  $V$ , whose interiors do not intersect each other, and whose union completely fills the convex hull of  $V$ .

One of the most common techniques for generating triangular grids is based on Delaunay triangulation. The Delaunay triangulation  $D$  of  $V$ , introduced by its author in 1934, is the graph defined as follows. Any circle in the plane is said to be empty if it contains no vertex of  $V$  in its interior (Vertices are permitted on the circle). Let  $u$  and  $v$  be any two vertices of  $V$ . The edge  $UV$  is in  $D$  if and only if there exists an empty circle that passes through  $U$  and  $V$ . An edge satisfying this property is said to be Delaunay.

Although initial Delaunay triangulation algorithms have been developed for simply connected convex polygons [1], [2], current algorithms [3], [4], are able to generate variable density Delaunay triangulations within multiply connected arbitrary geometry polygons; some of them find applications in numerical modeling problems [5]. Delaunay triangulation is perfectly suited for a domain described with a set of segments; in our case, the program *trian.exe* developed in 1996 by Shewchuk [6] is able to generate triangles at a rate of  $10^5$  points in 30 seconds. The structure of the algorithm is presented here in pseudo-code:

```
· ssl_head()

  for i=1:number_of_layers
    for j=1:number_of_slices
```

```

        read slice file
        translate current_slice -> input_domain
        call trian.exe
        read output file
        write new_slice
    end
end

```

The function *ssl.m* has been implemented in MATLAB. The old set properties from the input SSL file generated with QuickSlice are read, and the file is scanned for number of layers and number of distinct domains within each of them. The structure of the layer is then read, translated and written into a file understandable by *trian.exe*. Once the domain decomposition has been performed, the generated triangular mesh is read, and each triangle is assigned to one of the previously set group (each of them can have different properties, as described above). Finally, the new data structure is written in SSL format and can be reentered in the standard software for toolpath generation.

In the tested cases, two different command-line options were used with *trian.exe*:

- *-p*, which causes the program to generate a Planar Straight Line Graph (PSLG), which is a collection of points and segments. Segments are edges whose endpoints are points in the PSLG, and whose presence in any mesh generated from the PSLG is enforced.
- *-a x*, which constrains the maximum area of a single triangle to *x*.

Each layer of the tensile test bars depicted in Figure 1 have been decomposed with a different maximum area constraint; the resulting triangles have been randomly assigned to a group with variable road orientation [ $0 \pm 30 \pm 45 \pm 60 \pm 90$ ].

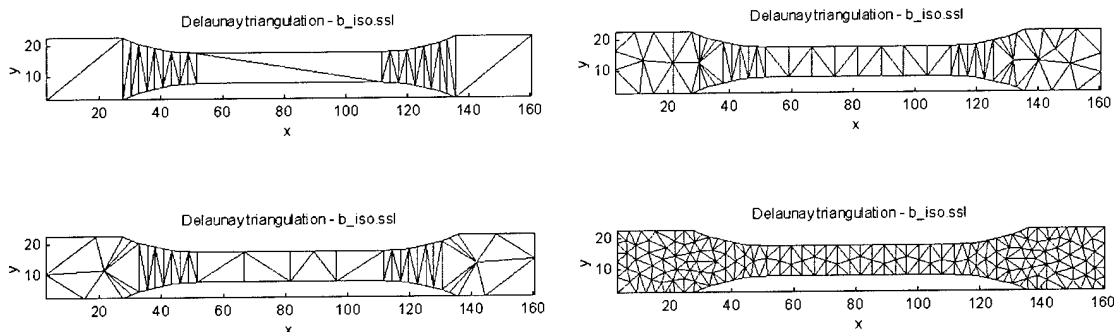


**Figure 1.** Domain decomposition of a tensile test bar

Another example is depicted in Figure 2. The interior of the octagon was tessellated with a constrained Delaunay triangulation, and constructed triangles were defined as individual contours within the SSL file. Road width was fixed to 0.5 mm; individual triangles were then randomly assigned to a set of group with variable raster angles and air-gaps (0.3 to 0.7 mm)

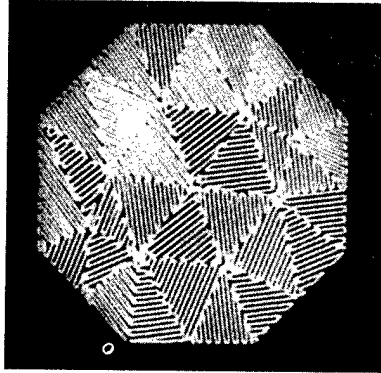


**Figure 2.** Domain decomposition structure

### *MACHINE FILE GENERATION*

The only way to fully explore the possibilities of the FDM process is to directly generate the machine level language, in order to avoid all the constraints of the standard toolpath processing software. It is in fact possible to skip the solid model generation and slicing steps (STL – SSL files) and directly output the final machine file (SML).

The Stratasys FDM 1650 machine used for the experimental tests is driven by an Asymtek A-201 digital motion controller. The A-201 controls the  $x$ - $y$  movement of the depositing head, the  $z$  movement of the stage, and the rotation of the two electrical servo-motors mounted on the head that feed the thermoplastic wire into the two liquefiers. The controller uses Automove Control Language (ACL) for programming [7]; Stratasys has implemented a slightly modified version of this language, called Stratasys Machine Language (SML). It is similar to Hewlett Packard's PCL used to control plotters and all commands are strings of ASCII text.

The structure of the SML file has been reverse-engineered in order to separate the common control sequences from the real flow and motion control commands. A set of routines has been developed in FORTRAN and then ported to MATLAB; the structure of the basic algorithm with a detailed description of each function is shown here in pseudo-code:

```

smlhead ()
purge ()

for i=1:number_of_layers_base
    base ()
    (curvebrk)
end

for i=1:number_of_layers
    level ()
    purge ()
    curve ()
    toolpath ()
    (curvebrk)
    endcurve ()
end
smltail ()

```

where:

smlhead	Establishes communication parameters, initializes the motion controllers and prepares the FD machine for the build.
purge	Performs on-the-fly cleaning operations (tip-wipe).
level	Switches materials if necessary and positions the z-stage for the current layer.
curve	Sets the flow-control parameters for the current road
toolpath	Generates motion control commands for the deposition of the road
curvebrk	Writes a pausing sequence. The motion controller has a very limited on-board memory that can store only 256 consecutive commands. When the buffer is full, the transmission is interrupted and the stored commands executed. Communication link is reactivated near the end of 256-command set and the next batch is loaded to the memory.
smltail	Performs final cleaning operations, clears the memory and puts the machine in stand-by mode for part removal.

It should be noticed that the 3D topology of the final structure can still be maintained; in fact, each layer can be generated with a different toolpath.

### *FRACTAL SPACE FILLING CURVES*

A space-filling curve (SFC) is a continuous line that can cover a region of space without intersecting itself. Applications of space filling curves can be found in digital images processing, ray tracing optimization and fluid dynamics. The idea of using fractals in RP is due to the intrinsic nature of the curve: it can cover each layer without starting-stopping sequences. The length of the unit steps within SFC's can be set to a value equal to the width of the roads, in order to completely fill each layer.

The Hilbert space-filling curve (Figure 3) has been found particularly useful and consequently applied to the toolpath planning issue. The developed MATLAB program, shown in pseudo-code, generates the Hilbert curve, which is stored in a vector (toolpath), translated into SML language and written to file. The function `main()` contains the connectivity matrix (a [4x4x3] array) that defines the topology of the curve and recursively calls the `hilbc()` function:

```
main ()
    conn_matrix = [...]
    hilbc (order);
end (main)

function hilbc (order)

if (order>0)
    for n=1:order
        hilbc (order-1);
        generate_toolpath ();
    end
end
```

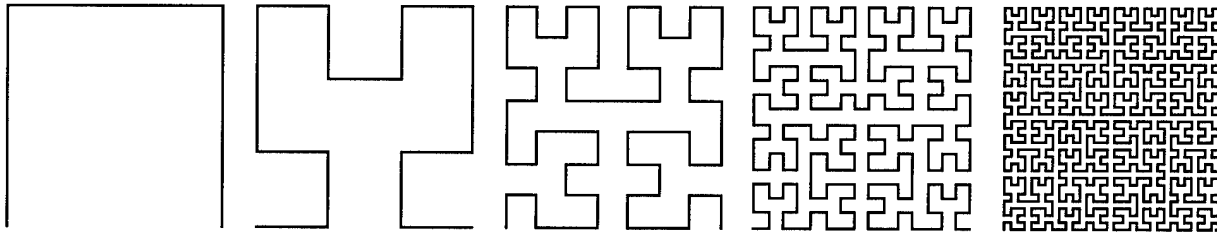


**Figure 3.** Hilbert curve generation

One of the main advantages of this approach is related to the thermal history of the part produced; from microscopy images, it has been observed that whenever the head deposits long straight lines, the bonding quality between two contiguous roads can be poor or non-existent. This is due to the thermal expansion and subsequent cooling and shrinking of the single road. With the fractal approach, it is possible to deposit one layer reducing significantly the length of the movements of the head. In this way, the void contents can be lowered and the bonding quality can be improved. The main disadvantage is the build time, which is 2-4 times longer compared to the standard toolpath, due to the exponentially increased number of motion commands.

The microstructure generated by 0/-90° stacking of a 4<sup>th</sup> order Hilbert curve is shown in Figure 4-a; Figure 4-b shows the part produced using this approach (ABS material).

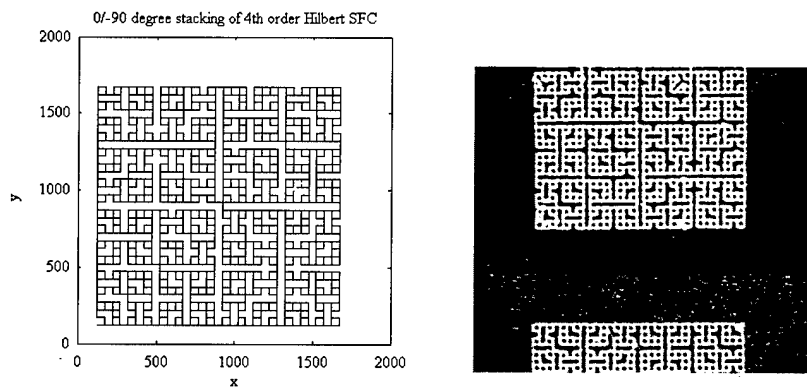


**Figure 4.** Microstructure toolpath (a) and real part (b)

## APPLICATIONS

Possible applications of the proposed techniques cover all the Fused Deposition uses, where custom physical and mechanical properties of the parts must be achieved. The software routines developed can be adapted to different needs and are easily configurable and customizable.

In particular, one interesting application concerns the mechanical behavior of the FDM parts. The standard raster settings cover every slice with a set of parallel roads, causing a strongly orthotropic behavior of the obtained part. Decomposing the domain and assigning the properties to each new contour independently allows more control on the internal microstructure. Specimens built with fractal space filling curves were tested, showing better mechanical properties compared to the standard parts.

Another interesting application taking direct advantage of the proposed techniques is in porous structure generation algorithms; see [8] for more details.

## CONCLUSIONS

With the new programming tools available, it is possible to generate different routines for developing new toolpath planning techniques. Some of them have been presented, discussed and deemed effective in the toolpath planning issue, either as a stand-alone product or interfaced with the standard processing software. Future work will include integration with other domain decomposition algorithms and STL three-dimensional domain decomposition.

## REFERENCES

1. Bowyer A., "Computing Dirichlet tessellations," *The Computer Journal*, vol. 24 no. 2, pp. 162-166, 1981.
2. Watson D. F., "Computing the n-dimensional Delaunay tessellation with application to Voronoi polytopes," *The Computer Journal*, vol. 24, no. 2, pp. 167-171, 1981.
3. Guibas L. J., Knuth D. E., Sharir M., "Randomized incremental construction of Delaunay and Voronoi diagrams," *Algorithmica*, vol. 7, no. 4, pp. 381-413, 1992.
4. Shimada K., *Physically-Based Mesh Generation: Automated Triangulation of Surfaces and Volumes via Bubble Packing*, Ph.D. thesis, Massachusetts Institute of Technology, 1993
5. M. A. K. Posenau, D. M. Moun t., "Delaunay triangulation and computational fluid dynamics meshes", National Aeronautics and Space Administration, Langley Research Center Hampton, V 1992.
6. Jonathan Richard Shewcuk , "Delaunay Refinement Mesh Generator" Computer Science Department, PhD Thesis, Carnegie Mellon University 1997.
7. Automotive Control Language (ACL) Programming Reference Manual - Version 3.61 Asymtek 1996.
8. M. Bertoldi, M. A. Yardimci, C. Pistor, S. I. Güçeri, S. C. Danforth, "Porous Structure Generation with Fused Deposition", Proceedings of the 1998 Solid Freeform Fabrication Symposium, The University of Texas at Austin, Austin, Texas 1998.





# **Reverse Engineering Trimmed NURB Surfaces From Laser Scanned Data**

Authors: Ben Steinberg<sup>1</sup>, Anshuman Razdan<sup>2</sup>, and Gerald Farin<sup>3</sup>

## **Abstract**

A common reverse engineering problem is to convert several hundred thousand points collected from the surface of an object via a digitizing process, into a coherent geometric model that is easily transferred to a CAD software such as a solid modeler for either design improvement or manufacturing and analysis. These data are very dense and make data-set manipulation difficult and tedious. Many commercial solutions exist but involve time consuming interaction to go from points to surface meshes such as BSplines or NURBS (Non Uniform Rational BSplines). Our approach differs from current industry practice in that we produce a mesh with little or no interaction from the user. The user can produce degree 2 and higher BSpline surfaces and can choose the degree and number of segments as parameters to the system. The BSpline surface is both compact and curvature continuous. The former property reduces the large storage overhead, and the later implies a smooth can be created from noisy data. In addition, the nature of the BSpline allows one to easily and smoothly alter the surface, making re-engineering extremely feasible. The BSpline surface is created using the principle of higher orders least squares with smoothing functions at the edges. Both linear and cylindrical data sets are handled using an automated parameterization method. Also, because of the BSpline's continuous nature, a multiresolutional-triangulated mesh can quickly be produced. This last fact means that an STL file is simple to generate. STL files can also be easily used as input to the system.

## **Introduction**

Reverse engineering, i.e. creating a digital representation of a physical object, is a powerful technique. As more of the engineering world goes digital i.e. vendors, suppliers and manufactures work from the same CAD model, it becomes even more important to convert the paper drawings into actual CAD model. Many times a part undergoes several design changes and after a few iterations it is difficult to predict how much the actual part has veered off from the original design intent. Also, many parts and objects which are still in high demand today, were created before CAD had become so mainstream. Having a digital representation of these objects makes upgrades and future analysis more efficient. Another reason is that for certain disciplines such as toy manufacturing the original character or model is created in clay by the artist. Its easier (more so because of the tradition) to sculpt the original rather than create in a CAD modeling software. In other cases even if the original part (such as a consumer part) is created in CAD, it may get modified (sanding etc.) as it undergoes

---

<sup>1</sup> Graduate Research Associate, PRISM, Arizona State University, Tempe AZ 85287-5106, USA.

<sup>2</sup> Technical Director PRISM, Arizona State University, Tempe AZ 85287-5106, USA. Email: razdan@asu.edu

<sup>3</sup> Professor, Dept. of Computer Science and Engineering, Arizona State University, Tempe AZ 85287-5106, USA

prototype feedback process. The only way to get the changes into the CAD model is to reverse engineer them. In addition, the need for automated inspection and verification of rapid prototyped and manufactured parts is also driving the field.

### **Part Digitizing and Reverse Engineering**

Recently many accurate data acquisition systems have come to market. There are three main types of systems, the touch probes and Coordinate Measuring Machines (CMM), optic or laser based systems and volumetric or CAT and MRI systems. At present the PRISM lab has two Cyberware laser digitizers. In this paper we will focus on data collected via laser scanning techniques only, although the same process could be applied to data collected from other systems as well such as an STL file. Each system has different resolution and accuracy of measurement. The Cyberware scanner that was used has an accuracy of  $\pm 0.035\text{mm}$ . The problem of reverse engineering (from laser scanned data) is described as follows.

The part to be reverse-engineered is scanned with the laser digitizer. Based on the complexity of the part, it may take several scans to get all the geometry. The main reason for this is optical occlusion. If the laser or light cannot reach a portion of the object being scanned then no data is collected. Therefore, it requires more than one scan to capture the geometry. The multiple scans after cleaning (removal of supports and other artifacts) is transformed to a single coordinate system. Cyberware provides software to achieve the *zipping* process. Most systems provide one form or another to accomplish this task. Different digitizing systems do it differently but the end result is the same. The scanned data is a point cloud data with a triangulation. We use the triangulation to detect bounding and dangling edges only. The captured data can be taken directly into the CAD software, but it is just points and the triangulation. It is tedious to work with such a large number of points and requires tremendous amount of memory (RAM) on the computer. None of the commercial software we tried was up to the task. Mathematical representation of the same data with NURB (Non Uniform Rational BSpline) or BSpline surfaces (see Section III for a brief explanation of NURB Surfaces) is much more efficient both in memory requirement and ease of editing. This process is also called surface fitting. Once the equivalent surface is successfully created, it can then be imported into the CAD software. If the CAD modeling software has solid modeling capabilities, the surfaces can be joined together to get a single coherent solid model. Two issues dictate the way the surfaces are created. These are accuracy and ease of surface creation.

### **Previous Work**

Many commercial software are now available that provide the user to interactively create surfaces from the digitized data. Of note are Imageware's Surfacar, Maya (Alias), Geomagic's Wrap, Nvision, etc. See [2] for a discussion of the hardware and software vendors. Hoppe et al.[6,7,8] and Lounsbery [10] also give methods to reduce the point cloud data and provide triangulation algorithms. Their work is motivated simply by the need for data reduction for faster display rather than geometric modeling requirements. The multiresolution wavelet modeling is excellent for reducing the data to be displayed quickly,

however, it does not serve well in a CAD setting since currently no solid modeler supports wavelet based models.

Current solutions (at the time of writing this paper) involve time consuming interaction to go from points to surface meshes. Typically the user is required to interactively select a region from the set of digitized points, or select a small region to create a network of curves. The curves then are used as the basis for skinning or lofting operation. Even for simple regions it requires a great deal of interactive input and several hours of work to create the network of curves. The quality of the surface is also dependent on the skill level of the user or the operator since the key points, such as regions of high curvature need to be captured in the network of curve for the resulting surface to be accurate.

Our approach differs from current industry practice in that we produce a mesh with little interaction from the user. The user can produce any degree BSpline surfaces and can choose the number of segments, tolerance etc. as parameters to the system. The BSpline surface is both compact and continuous. The result is an increase in automation and a decrease in needed user input. The combination of the least squares method, smoothing functions and automated data parameterization conversion, produces extremely accurate BSpline surface approximation. These surfaces are smooth, continuous and have well behaved boundaries. In addition we use trimming curves to preserve holes that part of the scanned object as well as define non-rectangular boundaries.

## **Methods**

### **Brief definition of NURB Surfaces**

A point on a NURB surface can be mathematically represented as:

$$X_{ij}(u, v) = \frac{\sum \sum w_{ij} d_{ij} N_i^m(u) N_j^n(v)}{\sum \sum w_{ij} N_i^m(u) N_j^n(v)} \quad (1)$$

Where  $m$  and  $n$  are the degrees of the surface,  $d_{ij}$  are the control points of the surface,  $w_{ij}$  are the weights attached to control points.  $N_i^m$  and  $N_j^n$  are the BSpline basis function, which depend on the degree and parameterization of the surface. For more detail on basis functions and NURB Surfaces the reader is referred to [3,4,9]. There is also an important component called the knot sequence that influences the shape of the NURB. In the case of a surface, there is a knot sequence for both the  $u$  and  $v$  directions. The basis function evaluation depends on how the surface is parameterized, and the surface parameterization is based on the knot sequences.

### **Brief description of the Least Squares Method (LSM)**

Given a set of points  $P$  in  $\mathcal{R}^3$ , the goal is to find a surface  $X(u,v)$  such that the sum of Euclidean distances from all points in  $P$  to their corresponding locations on  $X(u,v)$ , are minimized:

$$\text{Min } \sum \|P_i - X(u_i, v_i)\|^2 \quad i=1..K \quad (2)$$

where  $K$  is the number of points in the point cloud data. This guarantees the best-fit surface with minimum error for the given input parameters. The least squares method involves creating a standard equation:

$$A_{K \times R} x_{R \times 1} = b_{K \times 1} \quad (3)$$

Where  $R$  is the number of control points  $d_{ij}$ ,  $x$  represents the unknown  $d_{ij}$ , and  $b$  represents the set of data points  $P$ .  $A$  is the matrix of basis function contributions for the data set  $P$ . Applying  $A^T$  to both sides of Equation (3) results in:

$$A^T A x = A^T b \quad (4)$$

Equation (4) gives us the normal equations, a common form for the least squares method [1,9].

## Our Approach

### Scanning and Preprocessing

The object of interest is placed on the scanner. The scanning process, even at maximum resolution takes about 17 seconds per single pass. Depending on the complexity of the object's geometry, more than one scan may be necessary. Once the part is scanned, a pre-processing step is performed before surface fitting. The pre-processing identifies any boundary edges of the surface and any holes. At this time the user has a choice to fill the holes or keep them as trimmed holes. Since the boundary of the surface is rectangular i.e. we fit a surface that is larger than the data. Therefore, we have to identify the boundary trimming curve. The next step is to collect the necessary user input.

### User Input

The user selects the resolution (degree, and number of BSpline segments) of the surface in the  $u$  and  $v$  directions. Objects which have a large number of convolutions generally need to have large amount of *segments* in both the  $u$  and  $v$  directions. Each *segment* represents a low degree polynomial surface, which is guaranteed to be at least  $C^r$  ( $r = \text{degree} - 1$ ) continuity with its neighboring segments. The more segments that a NURB surface has, the more *flexible* it is for fitting to a data set. The higher the degree of the NURB the greater the continuity between segments. Finally the user selects a parameterization scheme based on the topological nature of the scanned data. The two schemes that are currently implemented are functional and cylindrical.

### Parameterization

Once the user has chosen the number of segments in the  $u$  and  $v$  directions, each data point in  $\mathcal{R}^3$  is mapped to a  $u, v$  parameter pair in the  $\mathcal{R}^2$  domain. This mapping is based on the

user's choice of parameterization scheme. The functional scheme maps the points onto the XY plane, and then finds their distribution in the plane. Cylindrical mapping uses a calculated centroid for the object and maps the points around a cylinder and is used for objects that closed in one direction. Currently, the cylindrical mapping assumes the object revolves around the vertical-axis as it passes through the centroid, however it would be possible to calculate the parameters around an arbitrary axis. The user would specify this axis if a best guess of the long axis of the object were not satisfactory.

### **Smoothing Functions**

At this point, the linear system is setup and the  $A$  matrix is complete. However, one of the problems with the least squares method is that *holes* or missing data can potentially cause the matrix to become singular. Each segment has a set of associated parameter values in  $u$  and  $v$ . If none of the data mapped into the domain fall within a given segment, the matrix becomes singular. If a segment is sparsely populated, it will behave poorly. We use smoothing functions to prevent poorly behaved regions from being generated. The smoothing functions add non-zero rows to the  $A$  matrix preventing the matrix from becoming singular [5]. The twist of a NURB segment is measure of how non-planar that quadrilateral segment is. Setting the twist to zero guarantees that the behavior of a segment in a region of little to no data is stable by forcing the segment to conform to the shape of neighboring segments. Since the splines are defined over a rectangular domain, any *rounded* shape data leaves segments unsupported around the border of the spline. The smoothing functions also help to force these border segments to continue in the direction of segments that do have data. The surface therefore continues smoothly past the areas of no data.

### **Trimming the Surface**

While the outer region of the surface, which has no data associated with it, remains smooth, this region is still extraneous. This extra region is therefore trimmed away using a boundary-trimming curve. The trimming curve is automatically fit from the border points of the data set. While this is an automated process, we are still refining it. Currently, a very high number of curve segments are used to ensure a close fit around boundaries which oscillate. This may result in a trimming curve that undulates because of noisy boundary data. However, we are in the process of implementing alternative methods (See Conclusion). The removal of the extra surface leaves a relatively smooth edge which follows the shape of the actual object (see section Results). The surfaces are output as IGES trimmed NURB surfaces. These can then be read into any CAD solid modeling software which can read IGES surfaces. STL output can either be generated from the surfaces or from the resulting solid or surface model in the CAD software.

### **Results**

We present some examples to show our results. The first example is of the trimmed hood and side fender of a toy car. The two pieces were individually scanned. Figure 1(a) and 2(a) show the raw digitized points. Figures 1 (b) and 2(b) shows the BSpline network with trimming curve. Figures 3 shows the trimmed surfaces in Maya (Alias) with a blend. The

hood surface was a 30 x 30 segment bi-quadratic BSpline with a 71 segment cubic trimming curve. The side fender was modeled with a 30 x 20 bi-quadratic BSpline and a 71 segment cubic trimming curve. They were merged using a fillet blend function in Maya (Alias). Each model was fit to the original data with an average error of less than 0.09mm.

The second example is of a flashlight. The flashlight was scanned in two stages, the top and the side. Figures 4 (a) and 4 (c) show the raw digitized points. For this example, we used a periodic BSpline solution since no seam was desired in the final surface. The periodic BSpline was 50 x 20 segments of degree two. The BSpline for the top portion was a 5 x 5 bi-quadratic with a 15 segment cubic trimming curve. Figures 4 (b) and 4 (d) show the BSpline control networks and trim boundary curve. There is no boundary curve in Figure 4 (b) since it is a periodic surface. The two surfaces were again imported into Maya, stitched and converted into one coherent geometric surface model, Figure 5, using the same fillet blend function as in the previous example.

### Conclusion

With very little interaction from the user our process can convert point cloud data from digitizers into IGES NURB surfaces, which can then be imported into a CAD solid modeler. Future work will focus on experiments with automated parameterization including non-uniform varieties. One reason that NURB surfaces provide powerful geometric models is due to the fact that the extra degrees of freedom the weight provides. Currently we set all the weights to one. Tighter fit or minimization of error can be achieved by manipulating the weights. The trimming curve has a tendency to undulate as the number of segments increase to ensure a tight fit around the boarder. We are planning to create the trimming curve in sections, joining the different pieces at junctures where the boundary data is naturally  $C^0$ . The trimming curves will be fit to small segment of data, and should be smoother than a single curve with a large number of segments.

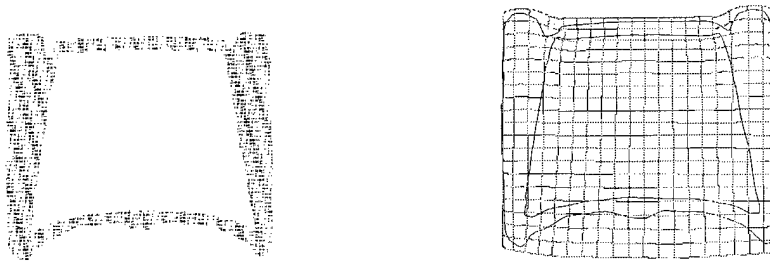


Figure 1: (a) Car top, raw points, (b) BSpline

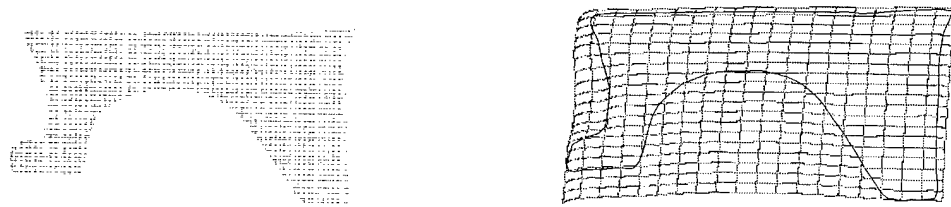


Figure 2: (a) Car side, raw points, (b) BSpline



Figure 3: Finished product. (a) Front view and (b) Side view

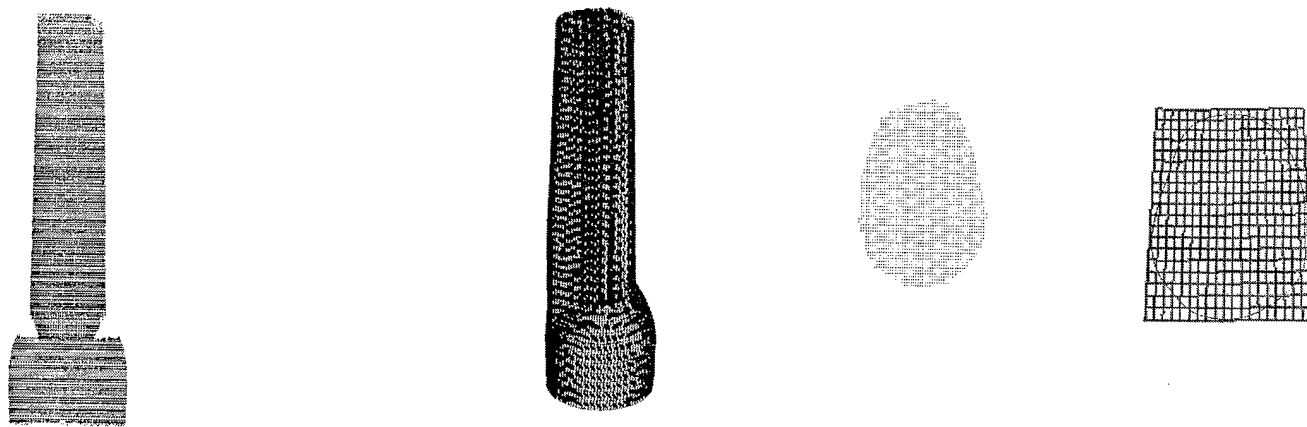


Figure 4: (a) Flashlight body, raw points; (b) Flashlight body, spline;  
(c) Flashlight top, raw points; (d) Flashlight top, spline



Figure 5: Finished product, two views

### Acknowledgements

The authors would like to acknowledge D. Hansford for her invaluable ideas and suggestions. We would also like thank C. Gosser and G. Kattethota.

### References

1. Å. Björk. Numerical Methods for Least Squares Problems. SIAM. Philadelphia, PA. 1996.
2. R. Broacha and M. Young. Getting from points to products. *Computer-Aided Engineering*, 1995.
3. G. Farin. Computer Aided Geometric Design. Academic Press. New York, NY. 1997.
4. G. Farin. NURB Curves and Surfaces, from Projective Geometry to Practical Use. AK Peters. Wellesley, MA 1996.
5. G. Farin and D. Hansford. Shape from permanence. Submitted, CAGD.
6. H. Hoppe, T. DeRose, T. Duchamp, J. McDonald and W. Stuetzle. Surface reconstruction from unorganized points. In *Computer Graphics, SIGGRAPH '92*, volume 26, 1992.
7. H. Hoppe, T. DeRose, T. Duchamp, J. McDonald and W. Stuetzle. Mesh optimization. In *Computer Graphics, SIGGRAPH '93*, volume 27, 1993.
8. H. Hoppe, T. DeRose, T. Duchamp, J. McDonald and W. Stuetzle. Piecewise smpth surface reconstruction. In *Computer Graphics, SIGGRAPH '94*, volume 28, 1994.
9. J. Hoschek and D. Lasser. Fundamentals of Computer Aided Geometric Design. AK Peters, Wellesley, MA. 1989.
10. M. Lounsberry, S. Mann and T. DeRose. Parametric surface interpolation. *IEEE Computer Graphics and Applications*, 1992.

## Stereometric Design for Desk - Top SFF Fabrication

Zbigniew M. Bzymek\*), Scott Theis \*), Tariq Manzur\*\*), Chandra Roychaudhuri \*\*\*),  
Lianchao Sun\*\*\*\*) and Leon L. Shaw\*\*\*\*)

\*) Department of Mechanical Engineering, University of Connecticut, Storrs CT

\*\*) Until 12/31/97 - Photonics Research Center, University of Connecticut, Storrs CT

\*\*\*) Photonics Research Center, University of Connecticut, Storrs CT

\*\*\*\*) Department of Metallurgy and Materials Engineering, University of Connecticut, Storrs C

### Abstract

Solid Freeform Fabrication (SFF) technologies refer to the fabrication of physical parts directly from computer based solid models described by STL (Stereo Lithography) or VRML (Virtual Reality Modeling Language) files generated by Computer-Aided Design (CAD) systems. Most of the SFF processes produce parts by building them layer by layer using a row by row pattern, though it is possible to build the part using other patterns. The SFF technology represents a challenge to designers who, in addition to making decisions concerning optimum shape and functionality of the entire part, have to take under consideration several other manufacturing factors. These factors cover a wide range of technical issues such as Computer-Aided Design model generation, part description and model slicing files, laser path files, precision of part design, rendering patterns, manufacturing tolerances, thermal expansion and residual stress phenomena.

This paper investigates the effect of rendering patterns on the integrity, material characteristics and mechanical properties of the parts prepared by a desk-top SFF device using diode lasers. Fe - Bronze (Cu - Sn) premixed metal powders were used as the starting material. The particle size was about 100  $\mu\text{m}$  to 200  $\mu\text{m}$ . Density, tensile strength and microstructure of the parts prepared using different rendering patterns were characterized. The results were analyzed to seek optimal rendering patterns. It was noticed that the samples were strong along the laser scanning direction, while they were weak perpendicular to the scanning direction. These results suggest that the laser scanning patterns should be designed to minimize the warping and maximize the strength of the part in the direction depending on the part's function.

### 1. Introduction

Solid Freeform Fabrication (SFF) is a Rapid Prototyping (RP) technology that makes it possible to build a part from metal or ceramic powders instead of cutting it out of blocks larger than the part dimension. The SFF process consists of two steps [1,2]:

- a) design parts using CAD methods to form a STL, VRML, or other file that, in turn, will be sliced and inputted into algorithms for generation of the paths for fabricating the SFF product; and
- b) manufacture the physical component by layering 2D sections with a small third dimension measurement.

A wide variety of RP technologies have been proposed during the last decade; these technologies can be used for the purpose of rendering 3D objects out of resin, plastic, ceramic, or metal powder[3]; but only a few were successfully applied to building structurally strong parts. One of them is SFF technology which allows for building objects from powders by thermal fabrication. The heat source in the SFF process is normally a laser impulse in the infrared region of the electromagnetic spectrum. This technology presents a real opportunity for

designers. They would have a chance to design and produce a part that would fit directly to the design or reconstructed system.

In spite of the fact that Selective Laser Sintering (SLS), Selected Area Laser Deposition (SALD) and Selected Area Laser Deposition Viper Infiltration (SALDVI) [1,5,9,10] are successfully used to prepare some parts in laboratories, there is an entire group of questions awaiting answers before a widespread industrial application of SFF can take place. These questions address the use of CAD systems, representation of the part model communication between CAD systems and the sintering setup, and effectiveness of the sintering process. Some of these questions can be readily solved, as for example the statement that the dimensional tolerance of a part cannot be smaller than the diameter of the laser beam, but other questions require further studies. The aspects that require studies are: orientation of the part, optimal shapes of the part for SFF processes, configuration of the part, and the relation between the part mechanical properties and the rendering patterns. In this paper, the effect of rendering patterns on the integrity, microstructure and mechanical properties of the part is investigated.

## 2. Desk-Top SFF System and Design and Rendering of Samples

The apparatus used in this research is a desktop SFF apparatus built in our laboratory. The apparatus is equipped with four kinds of software: the CAD software, slicing software, the laser path design software and the laser path control software. The primary functions and components of the apparatus are shown in Fig. 1. The apparatus includes a diode laser power system [4,5], powder feeding system, oxidation prevention system, and laser scan control system.

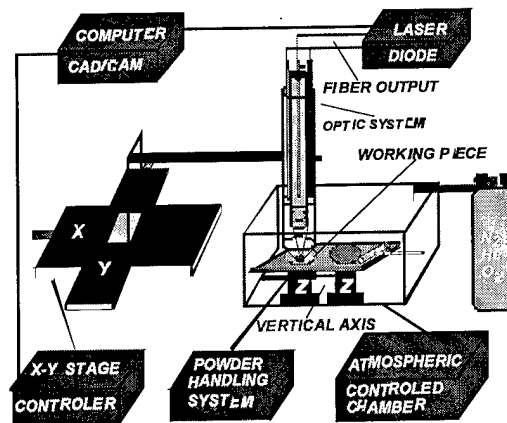


Fig. 1. Schematic diagram of the desk-top SFF system.

The solid models were designed using Cadkey software [6]. The Cadkey data were exported into STL file format [7,8]. The STL data are then converted into a Direct Motion Control (DMC) machine language tool path description in the desired pattern [11]. The application for the conversion was created especially for the project. The DMC format was compiled using Galil software [11]. The Galil software utility downloads the compiled data to a controller card attached to the computer. The controller card controls the separate X and Y servo step motors through a closed loop data feedback.

A total of six different scanning patterns, as shown in Fig. 2, were generated. The first scanning pattern was a horizontal scan, the second was a vertical scan, the third was a horizontal scan with skips, the fourth was a vertical scan with skips, the fifth was a random grid scan, and the sixth was a mix of horizontal and vertical scans. Every sample had three layers. This was done by sintering a powder layer with a diode laser, followed by laying down a new powder layer on top of the sintered one, layer-by-layer, to form a 3-D structure.

The material was a composition of pre-mixed powder (Fe 34-36, Cu 58-60, Sn6-7) with particle sizes of 100 - 200  $\mu\text{m}$ . The thickness of each powder layer was either 1 mm or 0.5 mm. However, it was found that the 1 mm layers did not bond well to each other, suggesting that sintering was not sufficient with 1 mm layers. As such, most of the samples fabricated had a powder layer thickness of 0.5 mm. Further, the results presented in this paper were obtained from samples made with layers of 0.5 mm thick, unless otherwise stated.

The laser spot diameter was 0.8 mm. The scan speed was 0.8 mm/sec with path axes speed 0.5 mm apart apart 0.5 mm (0.3 mm overlay). The spot temperature was in the range of 800 - 900 degrees C and the powder bed temperature was 80 - 200 degrees C. The experiment was done in flowing argon gas with a diode laser of 810 nm and a laser power of 15 watts.

Sample #	A	B	Laser Pattern
1 Top view Bottom view			
2 Top view Bottom view			
3 Top view Bottom view			
4 Top view Bottom view			
5 Top view Bottom view			
6 Top view Bottom view			

Fig. 2. The set of six test samples with different scanning patterns.

### 3. Sintered Parts and Their Properties

The physical images of six test samples are shown in Figure 2. Note that samples #1, #2, and #3 had small "tails". This was due to the fact that in those samples the origin of rendering was set up beyond the boundaries of the sample. This was slightly corrected in the sample #2 and an even bigger correction was done when generating sample #3. The tail was clipped completely when samples #4, #5 and #6 were generated. To clip the tail completely the origin of the laser path pattern was moved into the middle of those samples.

The surface roughness, density, tensile strength and microstructure of all the samples were characterized. The results are summarized in Table 1 (density and tensile strength), Fig. 3 ( the load vs. displacement curve), Fig. 4 (surface roughness), and Fig. 5 (microstructure). It was found that the densities of samples made through six different scanning patterns were similar and all of them were about 40% of the theoretical (Table 1). The low density of the sintered material was apparently due to the low density of loose powder used. A powder slurry has been considered to improve density in the future. The microstructure examined, as shown in Fig. 5, was consistent with the density measurement, i.e., there were many pores in the sample. Samples #1, 2,4, 5 and 6 (not shown in Fig. 5) also had microstructure similar to #3. The tensile test indicated that the strength of the samples was stronger along the laser scanning direction than perpendicular to the scanning direction. However, the strength obtained was far below the tensile strength of Fe or Cu metals. This was not a surprise since there was a substantial amount of pores in the samples. It was also noted that different scanning patterns (e.g., samples #1, 3, 5 and 6) did not seem to offer substantially different strengths. However, more work is needed to further elucidate this.

Sample #	Relative Density (%)	Tensile Strength (MPa)
1	36.2	7.6
2	36.7	4.4
3	40.8	5.9
4	37.5	3.5
5	36.8	6.9
6	37.3	7.1

Table 1. Density and tensile strength of samples with different scanning patterns

The tensile test results, recording load vs. displacement, are shown in Fig. 3. The surface roughness of sample # 3 is shown in Fig. 4. One can notice that the width of the laser path scans was about 0.5 mm with an overlap of about 0.3 mm. This agrees with the actual scan settings.

**4. Warping and Distortion During Sintering**

The sintering process resulted in warping and distortion of layers. This was expected. The degree of warping and distortion depended on the laser scanning pattern. With all patterns the warping was severe enough that part of each layer protruded above its intended plane a distance greater than the layer thickness. During the sintering process, powder added for a subsequent layer could not be plowed and smoothed to the proper height because of the protrusion. Instead the powder was smoothed using the peaks of the underlying layer as a guide. The depth of the powder for subsequent layers became variable. As a result, the powder thickness away from the peak could exceed the desired thickness, while near the peaks the thickness tapers to zero. With a given pattern of peaks the depth of subsequent layers also varies depending on the direction the powder is plowed in. When the powder was plowed so that the peaks occur in parallel then the powder would fill the depression between the peaks. When the powder was plowed so that the peaks occurred in series, there would be less powder overall and some areas wouldn't have any powder at all. The protrusion of the peaks also made it difficult to plow the powder without shifting the underlying pieces of sintering material. Samples which were accidentally shifted had to be discarded.

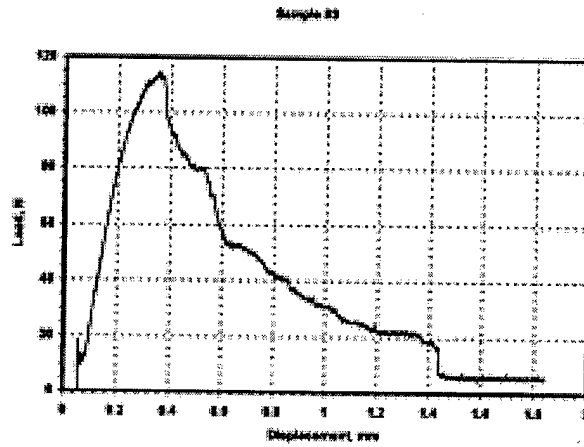


Fig. 3. The tensile test results of sample #3.

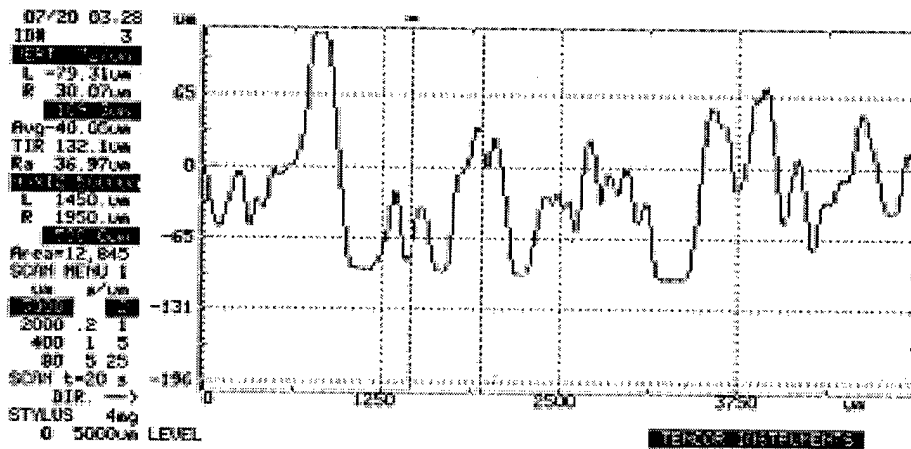


Fig. 4. The surface roughness of sample #3.

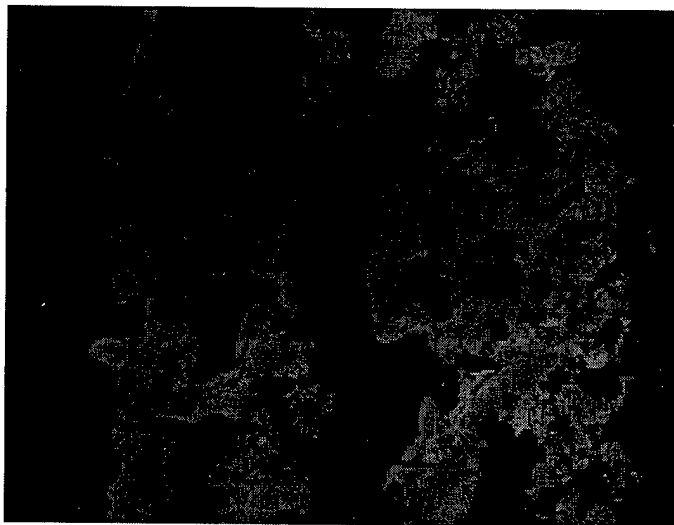


Fig. 5. The optical image of the cross section of sample #3. The bright area shows metals, while the dark area is porosity.

## 5. Conclusions

This paper concentrated on the laser pattern design to minimize the warping and distortion of layers during rendering and to maximize the density and mechanical properties. Certain laser scanning patterns help to release heat so that warping and distortion can be minimized; but these patterns may not be advantageous from the viewpoint of the density and strength of the material. It was found that the densities of samples made using different scanning patterns were similar. However, the tensile strength of the samples exhibited substantial dependence on the scan direction. In general it was noticed that the samples were strong along the laser scanning direction, and weak perpendicular to the scanning direction. These results suggest that laser scanning patterns should be designed to minimize the warping and maximize the tensile strength of a part in the direction according in which the tensile strength is the critical.

## 6. Acknowledgments

The desk-top sintering device was developed at the Photonics Research Center, where the described samples were fabricated. The samples were tested in the Institute of Material Sciences Laboratories. The research on design methods was conducted at the following University of Connecticut institutions: Mechanical Engineering CAD&CAM and Expert Systems Laboratory, Photonics Research Center, Institute of Material Science and the departments of Mechanical Engineering and Metallurgy. The authors appreciate all the support provided by the leadership of these institutions and help of colleagues, especially Prof. Harris Marcus, Jim Crocker and the other members of the IMS SFF group.

## 7. References

- [1] Manzur T., Roychoudhure C.S., and Marcus, H.L., 1996, "SFF Using Diode Lasers", *Proceedings of the Solid Freeform Fabrication Symposium*, University of Texas at Austin, Austin, TX, August 1996; SFF Symposium Proceedings, pp. 363 - 368.
- [2] Wang, Y., Dong, J. And Marcus, H.L., 1997, "The Use of VRML to Integrate Design and Solid Freeform Fabrication", *Proceedings of the Solid Freeform Fabrication Symposium*, University of Texas at Austin, TX, August, 1997, pp. 669 - 676.
- [3] Bzymek, Z.M., Benson, S., Garrett, R.E. and Ramakrishnan, B.T., 1996, "Thermo-Printing and Laser Sintering Slicing Simulation for Rapid Prototyping of Engine Parts", 29th ISATA International Symposium on Automotive Technology and Automation, June 6 - 9, 1996, Florence, Italy; *29th ISATA Conference Proceedings: "Simulation, Diagnosis and Virtual Reality Applications in the Automotive Industry"*, pp. 291-298.
- [4] Chen, W., Roychoudhuri C.S., and Bana S.C., "Design Approaches for Diode Laser Material Processing System", *Optical Engineering*, Vol. 33, pp. 3662-3669.
- [5] Manzur T., Roychoudhure C.S., Dua P., Hossain F. and Marcus H.L., 1997, "Net shape Functional Parts Diode Laser", *Solid Freeform Fabrication Symposium 1997*, University of Texas at Austin, Austin, TX, August 11 - 13, 1997; *SFF Symposium Proceedings*, pp. 99 - 114.
- [6] Cadkey 97, 1997, *www.cadkey.com.*, Baystate Technologies Publications, Baystate Technologies, 33 Boston Post Road West , Marlborough, MA 01752, USA.
- [7] Yanshuo Wang, "Computer Interfacing and Virtual Prototyping for SFF", *MS Thesis*, University of Connecticut, 1997, J. Dong, H. Marcus, Z.M. Bzymek - advisors.
- [8] Dong, J., 1996, "Issues in Computer Modeling and Interfaces to Solid Freeform Fabrication", 1996, *Proceedings of the ASME Winter Congress and Exposition*, Atlanta, GA, pp. 34 - 43.
- [9] L. Sun, K.J. Jakubenas, J.E. Crocker, S. Harrison, L. Shaw and H.L. Marcus, "Thermocouples in Macro-Components Fabricated Using SALD and SALDVI Techniques: Part II - Evaluation of Processing Parameters", *Materials and Manufacturing Processes*, in press (1998).

[10] J.E. Crocker, K.J. Jakubenas, S. Harrison, L. Shaw and H. Marcus, 1997, "SALDVI Optimization for the Tetramethylsilano - Silicon Carbide Systems", *Proceedings of the 8th Annual Solid Freeform Fabrication Symposium*, The University of Texas at Austin, pp. 489-496.

[11] *DMC - 1000 Technical Reference Guide*, Version 1.3, rev. 1.3, 1994, Galil Motion Control, Inc., 575 Mande Court, Sunnyvale, CA 94086 - 2803.



# A Process Planning Method and Data Format for Achieving Tolerances in Stereolithography

Charity M. Lynn, Aaron West, and David W. Rosen  
Rapid Prototyping and Manufacturing Institute  
Georgia Institute of Technology  
Atlanta, GA 30332-0405

(404) 894-9668

<http://rpm.marc.gatech.edu>

## ABSTRACT

When building parts in a stereolithography apparatus (SLA), the user is faced with many decisions regarding the setting of process variables. To achieve a set of tolerances as closely as possible, relationships between part geometry, tolerances, and process variables must be understood quantitatively. This paper presents a method for SLA process planning that is based on response surface methodology and multi-objective optimization, where the response surfaces capture these relationships. These response surfaces were generated by extensive design-of-experiment studies for a variety of geometries. An annotated STL data format is also presented that enables the inclusion of tolerance and surface information in faceted representations. Application of the data format and process planning method is illustrated on one part.

## 1. INTRODUCTION

Build performance is measured by how well the goals set forth by the operator for the build are met. For solid freeform fabrication systems, such as Stereolithography (SLA), the goals are often based on how quickly and accurately the CAD model is reproduced in a solid form. SLAs have dozens of processing variables that can be controlled by experienced operators to meet exacting build requirements of accuracy, surface finish, build time, and others. Experienced operators know qualitatively how process variables are related to build goals and can quantify some of their knowledge. Although SLA machine operation is predictable, the build quality is not always obvious, particularly when trade-offs must be made among goals to achieve specified tolerances.

A process planning method is presented in this paper to aid SLA operators in selecting appropriate values of build process variables in order to achieve a set of tolerances as closely as possible. The tolerances can be specified in order to reflect preferences of the operator or designer. Response surface models were experimentally constructed for evaluating accuracy, which enables the quantitative relationships between desired tolerances and the SLA process variable values that best achieve those tolerances. The process planning method is adapted from multiobjective optimization and utilizes response surface modeling to quantitatively relate variables to goals. Our objective is to render decision support by handling trade-offs among conflicting goals quantitatively. Our method is demonstrated on a part with non-trivial geometries.

## 2. BACKGROUND

### 2.1 Related Research

There is already a great deal of research available that is directly or indirectly related to the accuracy of a layer based manufacturing technology such as SLA. This research spans from build process optimization, inaccuracy prediction and correction, to support structure generation, alternative data structures and file formats for communicating between the manufacturing systems and CAD environments. The work presented in this paper relates to the process planning issues that arise when building prototypes. In the following paragraph a brief overview of some of this process planning research is provided.

Tata and Flynn have completed extensive studies in an attempt to quantify and correct down facing z-errors<sup>1</sup>. A down facing z-error is partially caused by the time difference as the laser scans the cross section of the first part and the last part in a multiple part build. This is due to the cure time of the liquid resin after it is exposed to the laser. Down facing z-errors can be reduced by using the correct time between layer scans. Gervasi has investigated the use of statistical process control in the SLA build process<sup>2</sup>. In this investigation statistical process control is applied to the X & Y shrinkage, and line width compensation factors for the SLA over a period of time. If effectively applied this could provide an indication of undesirable system changes during the build process. Onuh and Hon have addressed a research issue that is similar to the issue addressed in this paper<sup>3</sup>. They have applied the Taguchi Method to study and quantify the effects of layer thickness, hatch spacing, hatch overcure depth, and hatch fill cure depth on the quality of SLA prototypes.

Additional research on SLA accuracy is being performed by the Rapid Prototyping and Manufacturing Institute (RPMI) at Georgia Tech. This research is geared toward measuring, predicting, and correcting inaccuracies in parts and injection molding tools made either directly or indirectly from the SLA. One research topic involves measuring the inaccuracies of thin walled SLA parts. Research is also currently underway on an adaptive slicing methodology that takes into consideration build time and accuracy, as well as surface finish. One particular project was the predecessor of the present work. Computer Aided Build Style Selection (CABSS) is a method that renders decision support for building a part on a SLA based on response surface methodology and multi-objective optimization.<sup>4 5</sup> CABSS suggests appropriate values of process variables (limited to only three: part orientation, layer thickness, and hatch spacing) in order to achieve build goals of build time, surface finish, and accuracy as closely as possible. The main objective was to handle trade-off among these conflicting build goal objectives quantitatively. The method of providing the build style decision support described was based on solving a compromise decision support problem. Input to CABSS was an .STL file and user-specified goal weights. Exhaustive search was used to find a solution to the 3-variable, 3-goal problem.

## 2.2 Compromise DSP Construct

The Compromise DSP deals with only one alternative that is to be improved through modification<sup>6</sup>. This alternative can be improved by solving a CDSP where the values of all the system variables are found simultaneously, the requirements are met, and a set of objectives are achieved as well as possible. The CDSP is used to model decisions that consist of constraints, and linear and non-linear goals. The CDSP incorporates concepts from Goal Programming in that multiple objectives are represented as system goals. When there is more than one system goal, they are often in conflict with one another. In the case of the SLA build, a part is presented in a "default" build style to serve the purpose of the existing alternative to be improved. This build style is then improved by changing the build process variables. The conflicting goals are commonly build speed, accuracy, and surface finish. The structure of the CDSP is shown below.

- Given:* A feasible alternative, assumptions, parameter values, and goals.
- Find:* Values of design and deviation variables.
- Satisfy:* System Constraints, System Goals, and Bounds on variables.
- Minimize:* Deviation Function that measures distance between goal targets and design point.

Parameters are necessary to complete the modeling of the CDSP, but are not affected by the solution itself. Variables are classified as either of two types: system variables or deviation variables. System variables include design parameters the user can alter. A CDSP must have a minimum of two system variables. A system constraint must be met for the design to be feasible. System constraints are functions of the system variables. System goals model the design aspirations of the designer. For the SLA these goals are: low build time, high accuracy, and smooth surfaces. The deviation variables measure how far away the actual achievement levels are from the target levels and are often weighted when used to formulate the deviation functions. The

alternative (in this case a build process style) is improved by finding a combination of system variables, or build process variables, such that all the system constraints are satisfied while the deviation function is minimized.

### 3. PROCESS PLANNING METHOD

#### 3.1 Response Surface Methodology

In order to formulate a decision support problem that is based on concrete data, the interactions of the system variables and goals need to be known. Response Surface Methodology comprises mathematical and statistical techniques to enable the construction of approximation models<sup>7</sup>. RSM allows for a better understanding of the relationships between the inputs and the response, in this case between the build process variables and build goals, that can be written in the form of a polynomial function describing a surface, such as the one shown in the equation below. We use second order response surfaces in this work;  $k = 2$ .

$$y = b_0 + \sum_{i=1}^k b_i x_i + \sum_{i=1}^k b_{ii} x_i^2 + \sum_{i=1}^k \sum_{j=1, i \neq j}^k b_{ij} x_i x_j$$

Response surfaces are useful when detailed theoretical knowledge of the model does not exist, and all that is known is that the relationship between the input variables and the output variable is likely to be smooth. This is the case for the SLA. For instance, theoretical equations that give accuracy as a function of layer thickness and hatch spacing do not exist.

In order to create the response surfaces for the system goals, a number of experiments must be run to gather data for an empirical model. When the system goals are dependent on two or more factors (system variables), Design of Experiments (DOE) techniques can be practiced to determine the experiment sequence for the empirical model. Factorial experiment designs involve testing a number of variables, or factors, at different values, or levels. The experiments run in this research will be fractional factorial experiment designs with a face centered central composite design.

In a face centered central composite design, three levels of each factor are considered. The middle level is called the zero level. For example, in the case of the fill overcure variable, 0.009" is the zero level. At equal spacing from the zero level are the  $\alpha$  levels at +/- 1 from the zero level. This moves the axial points in a central composite design to the faces of the cube and reduces the required number of levels from five to three levels.

#### 3.2 Variable Selection for Accuracy Models

Two sets of experiments were run in this research, a screening experiment and a model building experiment. Screening experiments identify the most significant variables, reducing the size of the subsequent model building experiment. The design chosen for the accuracy screening experiment is the Plackett-Burman design, often utilized for a large number of variables and a small number of physical experiments. This is a 2-level design, using values that are the minimum and maximum range of each variable. The variables selected and their corresponding ranges are shown in Table 1. We used a SLA-250 and Dupont SOMOS 7110 resin for our experiments.

Variables	Layer thickness	Blade gap percentage	Pre-dip delay	Z-level wait time	Hatch overcure	Hatch spacing	Fill overcure	Sweep period
Max	0.008	200	20	20	0.001	0.012	0.012	15
Min	0.004	150	5	5	-0.003	0.006	0.006	5

Table 1 Plackett-Burman Variables and Ranges.

Three different shapes were built in the experiments, cubes, cones, and cylinders. The shapes were built at several orientations, 0, 30, 45, and 90 degrees. The surfaces were measured utilizing a Coordinate Measuring Machine, a Brown and Sharpe MicroVal PFX equipped with a Renishaw TP-IS touch probe (linear accuracy of +/- 0.0002" and repeatable within +/- 0.002").

The conclusion drawn from the Plackett-Burman experiment was that four variables would be carried out in the subsequent model building experiments: z level wait time, hatch overcure, fill overcure, and sweep period. The definitions of these factors are as follows:

1. Z-level wait time: Time between recoating and building the current layer.
2. Hatch overcure: Depth beyond the slice layer thickness to be cured with hatch vectors.
3. Fill overcure: Depth beyond the slice layer thickness to be cured with fill vectors.
4. Sweep period: Time required for one sweep across the length of the vat.

### 3.3 Response Surface Models

In order to build response surface models, a Face Centered Composite design of experiment was applied. The FCC experiment utilized the same maximum and minimum values as the screening experiment, however added a center value in order to compose the design, see Table 2. Utilizing the same range allowed for 10 of the previous screening runs' data to be utilized in this design. This resulted in 15 new runs to be completed.

Variables	Z-level wait time	Hatch overcure	Fill overcure	Sweep period
Max	20	0.001	0.012	15
Center	15	-0.001	0.009	10
Min	5	-0.003	0.006	5

Table 2 Model Building Experimental Variables and Points

After completing the builds and measuring the parts, response surfaces were constructed by computing an analysis of variations on the surface measurements. In this manner a set of response surface models were developed that relate the four build process variables with a specific type of geometric tolerance and surface type. As an example, a primitive cube could be used to measure parallelism for planar surfaces. The

resulting response surface equation could then be used to predict how well two parallel planar surfaces could meet a specified parallelism tolerance with a given set of build process variables. Six types of geometrical tolerances were considered: positional, flatness, parallelism, perpendicularity, concentricity, and circularity. Only parallelism, concentricity, and circularity will be applied in the example used in this paper.

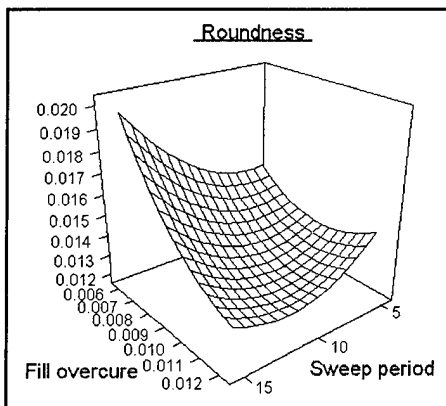


Figure 1 Example Response Surface.

A total of twenty-five different response surfaces were developed based on the type of geometric surface, the orientation of that surface, and the geometric tolerance annotation. Figure 1 provides a graph of roundness (circularity) response surface for a conical surface built vertically. This graph shows that the two concentric circles that make up the tolerance zone, which bounds the conical surface, obtain a more accurate part when the sweep period is long and the fill overcure vector is being drawn deeply.

Utilization of these accuracy models requires a mapping of the response surface equations to the actual CAD model that is to be built. Therefore, each of these accuracy models is associated with a specific type of geometric tolerance annotation that may be placed on the .STA file format. Figure 2 provides an overview of the different types of geometrical tolerances and their mapping to the response surfaces.

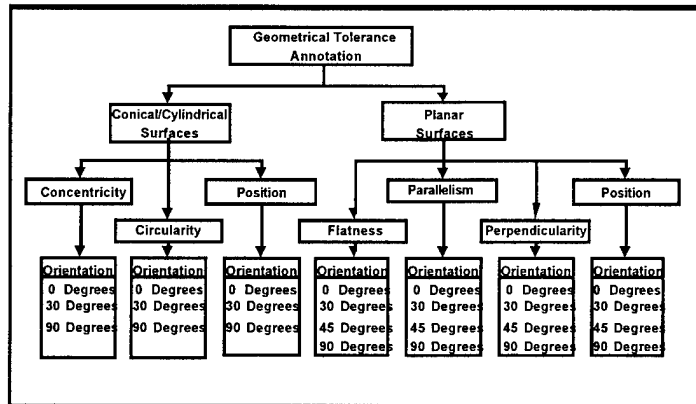


Figure 2 Accuracy Model Mapping.

The goals consist of surface finish, accuracy, and build time. The accuracy models discussed in the previous section constitute the primary method of measuring the achievable accuracy of a build. Similar models for the surface finish and build time have been developed in related research and are used in this problem formulation<sup>8</sup>.

**Given**

- part geometry in .STA file
- set of operator defined geometric tolerances
- set of operator specified surface finishes

**Find**

*System Variables*

- layer thickness
- hatch spacing
- part orientation (build height)
- z-level wait time
- hatch overcure
- fill overcure
- sweep period

*Deviation Variables*

- deviation from desired surface finish
- deviation from desired accuracy
- deviation from desired build time

**Satisfy**

*Goals*

- obtain the specified surface finishes for each surface
- obtain the specified geometric tolerances for each surface
- minimize the build time

*Bounds*

- set of discrete layer thicknesses
- set of discrete orientations
- upper and lower bounds on the other system variables

**Minimize**

*Deviation Function*

aggregate of surface finish, accuracy, and build time deviations

Figure 3 Compromise DSP Word Formulation.

manner a single measure for the overall surface finish and accuracy is obtained, where it is always desirable to minimize  $d_i^-$ , the underachievement of the goal.

$$GOAL = \sum_{n=0}^{n=} \begin{cases} \frac{SpecifiedTol_n}{AchievableTol_n} \geq 1 \Rightarrow & weight_n * 1 \\ \frac{SpecifiedTol_n}{AchievableTol_n} \leq 1 \Rightarrow & weight_n * \frac{SpecifiedTol_n}{AchievableTol_n} \end{cases}$$

$$GOAL + d_i^- - d_i^+ = 1$$

### 3.4 The Compromise DSP Formulation

Often, the goals for the build will lead to conflicting methods of selecting the build process parameters. However, by quantifying attributes such as the accuracy or surface finish, these build process variables can be selected quantitatively based on the relative importance of these goals. The word formulation of the Compromise DSP (see Section 2.2) for the selection of the build process variables is provided in Figure 3.

#### The Surface Finish and Accuracy Goals

The accuracy goal (and surface finish goal) is modeled using a weighted composite measure of the achievement of all specified tolerances, where achievement is the deviation between what is desired and what is achievable. To develop the composite evaluation, the specified tolerance is divided by the achievable tolerance and then multiplied by a weighting factor for that specific tolerance. The general form for these goal is presented below. In this development  $T$  represents the number of specified surface finish or accuracy tolerances and  $d_i^+$  and  $d_i^-$  represent the deviation (overachievement and underachievement) from the desired overall surface finish or accuracy. If the specified tolerance is found to be greater than the achievable tolerance, then the current feature is surpassing the specified tolerance and is not counted against the composite measurement. Otherwise, the current feature is not meeting the specified tolerance and is penalized. In this formulation,  $d_i^+$  will always be 0, and  $d_i^-$  will always lie in the interval [0,1]. In this

Based on the tolerance's type, the surface it tolerances, and that surface's orientation, a specific response surface equation is used to predict the achievable tolerance value for that surface. The specified and achievable surface finishes are also handled in a similar manner. Weights for tolerances and surface finish specifications are computed based on the tightness of the tolerance.

#### *The Build Time Goal*

The quantification of the build time is also based upon a response surface, very similar to that used to quantify the accuracy. The build time goal is based on the prediction of the build time using the current build process variables and the maximum and minimum build times as dictated by the upper and lower bounds of the build process variables. The build time goal is presented below.

$$\frac{BT(X) - BT_{\min}(X)}{BT_{\max}(X) - BT_{\min}(X)} + d_{BT}^- - d_{BT}^+ = 0$$

In this equation  $d_{BT}^-$  is always 0 and  $d_{BT}^+$  will lie on the interval [0,1]. In this manner a single measure of the build time is obtained where it is always desirable to minimize  $d_{BT}^+$ .

#### *The Deviation Function*

Using the three goals outlined above, the deviation function is simply a measure of the deviations of each of the goals. The user specifies the importance of each of these goals and the targets to be met. In the case of surface finish and accuracy, these targets are the tolerances annotated to the .STA file format, while the target for build time is a reasonable minimum time, which can be determined from the STL file. To measure the degree to which these targets are met the deviation function is evaluated for different combinations of the build process variables. The general form is presented below.

$$Z = SFweight * (d_{SF}^- + d_{SF}^+) + ACweight * (d_{AC}^- + d_{AC}^+) + BTweight * (d_{BT}^- + d_{BT}^+)$$

The build process variables that minimize the deviation function represent a solution that satisfies the operator preferences. This solution may be found through a variety of methods that search the feasible design space. Currently since this space is small an exhaustive search is used.

## 4. ANNOTATED STEREOLITHOGRAPHY FILE

The current *de facto* file format for rapid prototyping technologies is the .STL file format. The .STL file format merely lists the triangular facets of the tessellated part surface. The goal of .STL file *annotation* is to add important information to the .STL file format to create a more useful format, which is called the .STA (for **.STL Annotated**) format.<sup>9</sup> This important information includes topological information such as triangle connectivity and the presence of different types of surfaces which is derived from the existing .STL file. Additional annotations are supplied by the user, including tolerances and surface finish requirements for the part.

The .STA file format classifies surfaces as *planar, cylindrical, conical, spherical, or other*. After classifying surfaces, information pertaining to those surfaces is computed, including orientation, curvature, and surface area. Each of these properties is calculated using computational geometry algorithms implemented in a computer program. The next step is for the user to add information pertinent to the building of the part, such as required surface finish and accuracies. When this information is complete, everything is written to a new annotated .STA file. The information in this file will progress from high level to low level as shown in Figure 4.

The highest level of information pertains to the entire part. This includes how many surfaces, facets, and unique vertices comprise the part, as well as total part volume and surface area. The next level of information describes the surfaces of the part. Each surface is listed along with its

surface area, orientation, and any other annotations. The list of facets that make up the surface along with their connectivity information is also given for each surface. Facets comprise the highest level of information that the current .STL format exhibits. The facet level of the .STA format lists each facet along with the vertices that make up that facet. This alleviates the problem with .STL files of repeated vertices, and corresponding round-off and size problems. Numbers in the facet list then refer to these vertices. The final, lowest level of information is the vertex list. The vertex list lists each unique vertex in the .STL file and describes it using the 3D floating point Cartesian coordinates used in the original .STL file.

Information Location in the file	Information Level	Information Regarding...	Information
Beginning	High	...the entire part	<ul style="list-style-type: none"> <li>• # of surfaces</li> <li>• # of facets</li> <li>• # of vertices</li> <li>• Volume</li> <li>• Surface Area</li> <li>• Theoretical surface finish</li> <li>• Dimensional extents</li> <li>• The surface list</li> </ul>
		... each surface	<ul style="list-style-type: none"> <li>• Type of surface</li> <li>• # of facets</li> <li>• Area</li> <li>• Orientation</li> <li>• Curvature</li> <li>• Derived surface finish</li> <li>• User annotations</li> <li>• Surface topology (facet list)</li> </ul>
		... each facet	<ul style="list-style-type: none"> <li>• The vertex number of each of the 3 vertices that comprise the facet</li> </ul>
End	Low	...each vertex	<ul style="list-style-type: none"> <li>• The x, y, and z coordinates for each vertex expressed as a floating point number.</li> </ul>

Figure 4 General Information Structure of the .STA File.

accordingly. The CAD model shown in Figure 5 is a simple model with a geometry that will require a compromise to be made between the three goals: surface finish, accuracy, and build time. Several different trials (scenarios) are run in which the relative importances of the goals are altered to investigate the behavior of each of the individual goals. In addition, the model is simple enough that the results in most cases should be fairly intuitive.

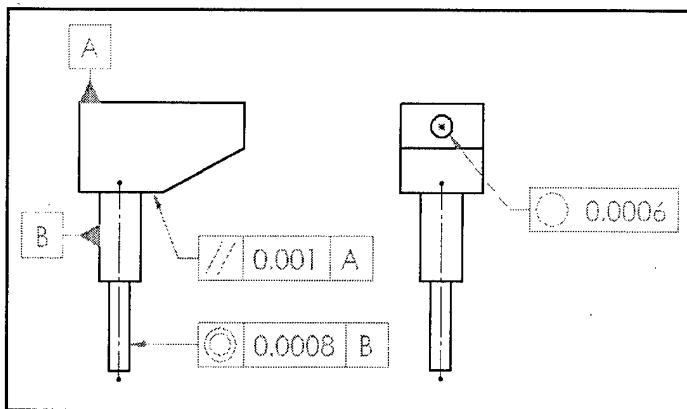


Figure 5 CAD Model with Geometric Tolerances.

## 5. RESULTS

To demonstrate the accuracy models and .STA file format developed in this research the following example problem is presented. This example is used to step through the process of annotating the model and selecting the build process variables that will best meet the preferences of the operator and the specified tolerances. The selection process was accomplished by refining the previous problem formulation of CABSS. In this formulation, the optimization program reads a .STA file directly, including the annotations. Then, the user is prompted for priorities for each of the build goals. The optimization program steps through the CDSP previously described and selects the best values for the variables

### 5.1 Annotating the Model

The first step involves annotating the .STA file format with the desired geometric tolerances and surface finishes. Figure 5 shows a drawing of the CAD model with three geometric tolerances. The first geometrical tolerance is a parallelism tolerance controlling the planar surface from which the cylindrical shaft extrudes. The second geometric tolerance is a circularity tolerance annotated to the hole in the part, due to this being a mating feature. The final geometric tolerance is a concentricity tolerance, which ensures that the

cylindrical shaft and shank lie on the same axis. The desired surface finish of the cylindrical shaft

and cylindrical hole are specified as 300µin. All other surfaces are assigned a default surface finish of 400µin. Shown in Figure 6 is a sample of how this type of information is stored in the .STA file format. After listing all the surfaces and their corresponding information, there is a list of the datum and tolerances.

```

solid SFF_example
Surfaces:      13
Facets:       468
Vertices:     236
Z-Height:    2.00
Area:        49.02
Volume:      15.56
Surface Finish: 383.61

Surface_List
Surface 0
  Type:                planar
  Number of facets:    2
  Surface area:        4.000000
  Orientation:         90.000000 x -180.000000
  Curvature:          0.000000
  Theoretical Finish: 363.000000

Facet_Connectivity and Angle List-
Fct Nbr1 - WVN - Angl  Nbr2 - WVN - Angl  Nbr3 - WVN - Angl
42  88  0 90.000000    43  2  0.000000    91  0 90.000000
43  42  0 0.000000    92  2 90.000000    39  0 90.000000
...
Surface 7
  Type:                cylindrical
  Number of facets:    76
  Surface area:        6.275793
  Orientation:         90.000000 x 90.000000
  Curvature:          0.5
  Theoretical Finish: 868.643494

Facet_Connectivity and Angle List-
Fct Nbr1 - WVN - Angl  Nbr2 - WVN - Angl  Nbr3 - WVN - Angl
169 168 1 9.729700    170 2 0.000000    1  0 90.000000
95  170 1 9.729801    96  2 0.000000    2  0 90.000000
...
Datum_list
datum primary 2
datum secondary 6
datum tertiary 0
end_datums

Tolerance_List
Parallelism 3 value 0.001 datums 1
Roundness 5 value 0.0006 datums 2
Concentricity 7 value 0.0008 datums 3
end_list

```

Figure 6 Sample of the .STA File Format.

### 5.2 Developing the Solutions

The results of each run are shown in Table 3. The weighting and deviation for each of the goals are provided in the table as well as the build process variable values. The three goals are accuracy (AC), surface finish (SF) and build time (BT). The seven build process variables are layer thickness (LT), hatch spacing (HS), build height (BH), z-level wait (ZW), hatch overcure (HO), fill overcure (FO), and sweep period (SP). Each of the trial runs is intended to demonstrate different aspects of the problem formulation. The first three trial runs basically represent a search for a single goal. One might expect the deviations for each of the three goals to be quite different across each of the three runs. The fourth trial run, in which all goals are assigned equal weighting, demonstrates the compromises that can be made between the three goals. Trial 5 provides a demonstration of the ability of compromises to be made in a more realistic scenario. The sixth trial was added after the surprising results for trial 2.

Trial 1, 3, and 6 all indicate that the problem behaves in a predictable manner. In each of these trials one of the three goals was given the highest priority and the resulting deviation for that goal was found to be the smallest. The results from trials 2 and 6 provide an excellent demonstration

of a compromise in progress. The original intent for these trials was to minimize the surface finish. However, Trial 2 produced a surface deviation that was a little higher than that found in Trial 6, but had a significantly lower build time deviation. This indicates that a slight improvement might be obtained in the overall surface finish if a large build time deviation is acceptable. The results of these trials also indicate that the settings for Trials 2, 3, 4, and 5 are the most robust.

Trial	Weighting of Goals (AC, SF, BT)	AC Dev.	SF Dev.	BT Dev.	Build Process Variables (LT, HS, BH, ZW, HO, FO, SP)
1	(0.90, 0.05, 0.05)	0.181282	0.141986	0.374125	0.007, 0.02, 4, 5, -0.003, 0.008, 5
2	(0.05, 0.90, 0.05)	0.383276	0.129583	0.001495	0.007, 0.02, 2, 5, 0, 0.009, 10
3	(0.05, 0.05, 0.90)	0.383276	0.129583	0.001495	0.007, 0.02, 2, 5, 0, 0.009, 10
4	(0.33, 0.33, 0.33)	0.383276	0.129583	0.001495	0.007, 0.02, 2, 5, 0, 0.009, 10
5	(0.60, 0.05, 0.35)	0.383276	0.129583	0.001495	0.007, 0.02, 2, 5, 0, 0.009, 10
6	(0.01, 0.98, 0.01)	0.181282	0.101584	0.811627	0.007, 0.02, 6, 5, -0.003, 0.008, 5

Table 3 Results of Six Trial Runs with Various Operator Defined Preferences.

## 6. CONCLUSIONS

This research identified four of the build process variables that have a quantifiable effect on the accuracy of a prototype built on a SLA machine. The responses of these variables for different geometrical tolerances are developed and fitted to a set of response surfaces. The trends that may be drawn from these accuracy models are used as a means of selecting the build process variable values to achieve a specified level of accuracy. The validity of these accuracy models is subject to the accumulated errors of the empirical measurements and approximations necessary to the development of the response surface equations. A file format was also introduced that aids in the selection of these process variables by allowing an operator or designer to indicate the preferences for the prototype in terms of accuracy and surface finish tolerances on specific part features. Finally a method of evaluating conflicting trade-offs between the multiple goals was developed to provide process planning for SLA using the accuracy models developed. Continuing efforts are underway to increase the validity of the accuracy models and expand the types of geometrical tolerances that have been developed in this research.

## ACKNOWLEDGEMENTS

We gratefully acknowledge the support from NSF grant DMI-9618039 and from the RPMI member companies.

## REFERENCES

- <sup>1</sup> Tata K., Flynn D., "Quantification of Down Facing Z-Error and Associated Problems," *Proceedings from the 1996 North American Stereolithography Users Group Conference*, San Diego, CA, March 11-13, 1996.
- <sup>2</sup> Gervasi V.R., "Statistical Process Control for Solid Freeform Fabrication Processes", *Proceedings from the 1997 Solid Freeform Fabrication Symposium*, University of Texas, Austin, Texas, August 11-13, 1997, pp. 141 - 148.
- <sup>3</sup> Onuh S.O., Hon K.K.B, "Optimising Build Parameters and Hatch Style for Part Accuracy in Stereolithography", *Proceedings from the 1997 Solid Freeform Fabrication Symposium*, University of Texas, Austin, Texas, August 11-13, 1997, pp. 653 - 660.
- <sup>4</sup> McClurkin, J. E. and Rosen, D. W., "Computer-Aided Build Style Decision Support for Stereolithography," *Solid Freeform Fabrication Symposium*, University of Texas, Austin, Texas, pp. 627-634, August 11-13, 1997.
- <sup>5</sup> McClurkin, J. E. and Rosen, D. W., "Computer-Aided Build Style Decision Support for Stereolithography," *Rapid Prototyping Journal*, Vol. 4, No. 1, pp. 4-13, 1998.
- <sup>6</sup> Mistree, F, Hughes, O F, Bras, B A, "The Compromise Decision Support Problem and Adaptive Linear Programming Algorithm," *Structural Optimization: Status and Promise*, AIAA, Washington, DC, pp. 247-289, 1993.
- <sup>7</sup> Myers, R. H. and Montgomery, D. C., 1995, *Response Surface Methodology: Process and Product Optimization using Designed Experiments*, John Wiley & Sons, New York.
- <sup>8</sup> McClurkin, Joel, "Development of a Decision Based Support Tool for Optimizing Rapid Prototyping Build Layout," Master Thesis, Georgia Institute of Technology, Atlanta, GA, 1997
- <sup>9</sup> Ibid.



# Dimensional Issues in Stereolithography

David L. Winmill, Daniel M. Hoopes and Suresh S. Jayanthi  
DuPont Somos<sup>®</sup>, Two Penn's Way, New Castle, DE 19720-2407

## Abstract

New stereolithography photopolymers have recently been introduced that provide a wider range of functional properties similar to those of high-density polyethylene. One of the important criteria for these materials is the dimensional accuracy and stability in end-use applications as mold masters or the actual functional parts. This work investigates the dimensional stability of one of these new materials with varying amounts of exposure during build. The effect of aging on the part dimensions is reported. The result of environmental humidity extremes at ambient temperature on part dimensions is investigated and compared for parts made from two different families of stereolithography resins, namely DuPont Somos<sup>®</sup> 7100 and Somos<sup>®</sup> 8100.

## Introduction

Rapid prototyping technologies have gone through several advances in the last few years. Stereolithography in particular has seen some dramatic improvements due to equipment changes and innovations in photopolymers. The primary driving forces for new photopolymers are the quest for improved mechanical properties and dimensional stability.

Prototypes made by stereolithography now offer high resistance to harsh environmental conditions. For example, some of the new materials now provide heat deflection temperatures over 100°C and can also be used in water applications without an appreciable drop in physical properties. More recent stereolithography materials are providing properties similar to commonly used plastics like high-density polyethylene and ABS. All of this has significantly increased the range of applications in which stereolithography can now be used.

To achieve a more enduring growth of these applications, a better appreciation of the changes that can occur in the properties of these materials is needed. The variations in the physical properties with different fabrication strategies, aging under different environmental conditions and endurance testing are becoming more important as these materials are being used to validate not only the design but also the functional intent of the prototypes.

This paper focuses primarily on aspects of the dimensional behavior of these new classes of materials and also highlights some of the technological limitations that we have to live with. In trying to build dimensionally accurate and stable prototypes many issues have to be monitored. These include the nature of the geometry and the subsequent slice files as well as the orientation of the part on the build platform. The aspects that are given more attention here are the stereolithography machine calibration, the photopolymer resin being used, the fabrication

style used to build parts, their subsequent post-curing and eventually the environmental conditions that they experience.

The experimental studies reported in this paper are based on two high performance materials for stereolithography. One of these is a high strength, high heat deflection temperature and humidity tolerant material called Somos<sup>®</sup> 7110. The other is a high flexibility and high impact strength material called Somos<sup>®</sup> 8100 or 8110 that will be commercialized in the third quarter of this year. This work will first highlight the contribution of machine calibration as a source of error in the production of stereolithography parts. Secondly, it characterizes the influence of laser exposure and post-exposure on dimensional stability. Thirdly, it shows the influence of environmental conditions on the dimensional stability of finished parts. Finally, the findings are summarized and observations are made with the view to improving the dimensional behavior.

## Recent Work

In 1997, Paul Jacobs (1) first showed that processes such as stereolithography exhibit non-uniform shrinkage behavior and contain a random noise shrinkage component. Following up on Jacobs' work, Tom Mueller (2) expanded the concepts into a more general model that would include the effects of pattern accuracy as well as the shrinkage of injection-molded plastic. This would allow tolerances to be predicted for the molded parts rather than the tool.

Prior to these two works, significant effort was focused on quantifying the achievable accuracy levels using an industry recognized "User-Part" (3). This particular diagnostic has been used to optimize the compensation factors necessary to improve achievable accuracy. It is also used as a confirmation diagnostic to assess the realistic tolerances achievable in a typical stereolithography machine after all compensation factors have been applied. Figure 1 illustrates the distribution of error across the part for a compensated diagnostic part. As the figure shows there is a high degree ( $\pm 6$  mil) of random noise. Contributing to the noise are the machine calibration status, process characteristics, possible non-uniform shrinkage behavior of the stereolithography material and the measurement techniques.

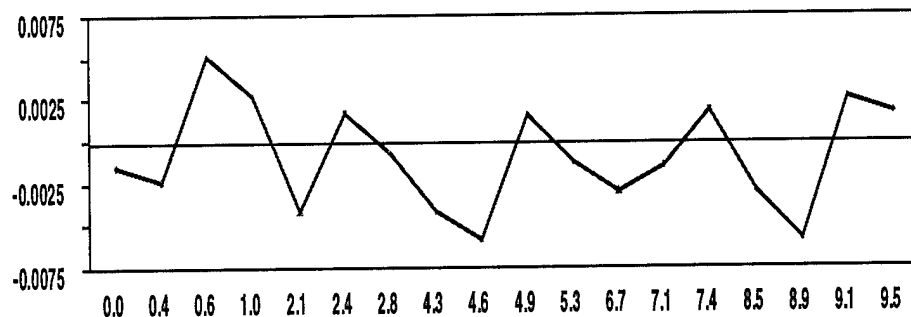


**Figure 1: Distribution of Random Noise in a Compensated SL Diagnostic Part**  
(Measured Error on Y axis; CAD Dimensions on X axis)

## System Status and Dimensional Accuracy

In order to investigate the system calibration status and the effect of different exposures on part dimensions, Somos 8100<sup>®</sup> was used in a 3D System's SLA<sup>™</sup> - 500 stereolithography machine. Sixteen square boxes (2 inch by 2 inch) were designed and spaced evenly on the platform in a four by four array. The CAD for the boxes featured sidewalls as well as an internal circular boss and flat panel. Each of the four columns of boxes received a different hatch over-cure of -2, 0, 2, or 4 mils whereas all the other build conditions stayed the same. All of these were quite normal, such as 6 mil layers, ACES build style (4 mil hatch spacing), and a box hatch. The boxes were built without any material shrinkage compensation. A beam width compensation of 6 mils was used. Just after the parts were imaged the X and Y dimensions of the boxes were measured and found to be substantially different from the chosen CAD values.

Initial Part Size Variation over the SLA - 500 Platform (Part minus CAD Dimension in mils)				
Row Number	Column Number			
	1	2	3	4
1	7	10	5	2
2	6	9	3	3
3	6	5	5	3
4	7	8	4	2

**Table 1: Dimensional differences for the X dimensions of the two-inch square boxes**

As shown above in Table 1, the measured X dimensions were all larger than the desired CAD dimension, and the largest errors tended to occur on the left-hand side of the platform. In the case of the Y dimensions (see Table 2 below), all the dimensions were smaller than intended and the greatest errors occurred on the right hand side of the platform. Clearly then, this machine has a poorly calibrated platform. Therefore the initial green state dimensions were taken as the starting point from which to measure any changes that might occur due to aging or post-cure procedure.

**Initial Part Size Variation over the SLA - 500 Platform  
(Part minus CAD Dimension in mils)**

Row Number	Column Number			
	1	2	3	4
1	-12	-10	-14	-14
2	-12	-11	-15	-15
3	-12	-12	-13	-16
4	-11	-8	-13	-15

**Table 2: Dimensional differences for the Y dimensions of the two-inch square boxes**

In the future it would seem to be a good idea if the platform calibration was measured with a photo responsive film such as Dylux™ before imaging the parts. The values obtained from this could then be used as the initial values and would be completely free of any effects (expected to be small directly after a build) of the photopolymer resin.

## Dimensional Accuracy after Imaging

After measuring the initial dimensions as described above, two boxes from each hatch over-cure exposure were post-cured with UV light for one hour in a 3D Systems' Post Cure Apparatus. A little later the extents, the circular boss and the panel thickness were measured. The results for the extents (see Figure 2) show that the lowest exposures (-2.0 mils hatch over-cure) actually produce an expansion of the parts.

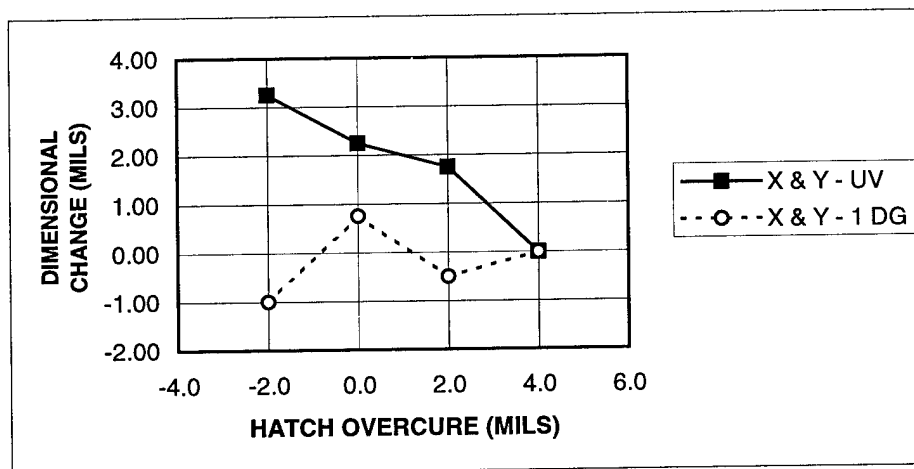


**Figure 2: Dimensional Behavior with Different Hatch Over-cures for Somos® 8100**

The amount of expansion falls with increasing exposure and reaches zero with 4.0 mils hatch over-cure. The boxes from each hatch over-cure that were not post-cured were left for a day at ambient conditions (labeled 1 DG) and again measured. These data are rather scattered

but show a general trend of the lower exposure to cause shrinkage as the parts age in their green state. The circular boss showed similar effects, but the data was noisier due to the smaller dimension. The panel was too thin (80 mils) to determine any dimensional changes in the Y direction.

In order to further investigate the effect of hatch over-cure on dimensional stability in the green state, tensile bars (150 mm long) were measured for four different exposure conditions over a prolonged period of time after imaging (Figure 3). These parts were made on a DuPont Somos<sup>®</sup> stereolithography machine with 2-mil scan spacing and a raster scan with a spot diameter of about 6 mil. Again the lowest exposures gave the most change, and in the case of parts made with 1 mil over-cure the dimensional change was + 0.8% after 30 days which equates to 8 mil per inch. However, in the case of higher hatch over-cure exposures of 8 and 9 mil, there was almost no dimensional change with time.

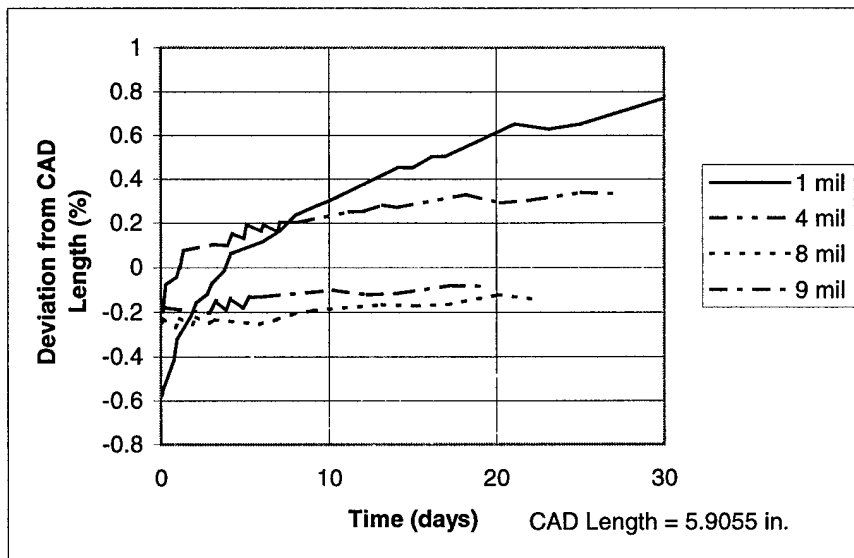


**Figure 3: Dimensional Behavior with Different Hatch Over-cures for Somos<sup>®</sup> 8100 Green Tensile Bars at Ambient Conditions**

## Environmental Effects and Dimensional Stability

The effect of the environment after the parts were imaged, cleaned and post-cured was determined on a set of 6 inch tensile bars that had been kept at ambient conditions for about a month. Three sets of six bars made from either Somos<sup>®</sup> 7110 or Somos<sup>®</sup> 8110 were sanded lightly, especially on the down-facing surfaces, to remove any remaining supports so that they would be suitable for repetitive weighing. Each set of bars was then left in a large glass jar either at ambient lab temperature (21°C) and humidity, immersed in distilled water, or at 0 % relative humidity (RH). At the start and approximately every five days after that each bar was weighed and the length measured.

The bars made from Somos<sup>®</sup> 7110 and held at 0 % RH lost an average of 0.003 % weight per day, but their weight was stabilizing. The bars at ambient conditions (Air) actually gained weight slightly presumably due to a slightly increasing humidity in the laboratory with the onset

of summer. The bars in water gained a total of 1.2 % weight over 47 days (an average of 0.03 % Wt per day) and had not yet reached equilibrium (Figure 4).

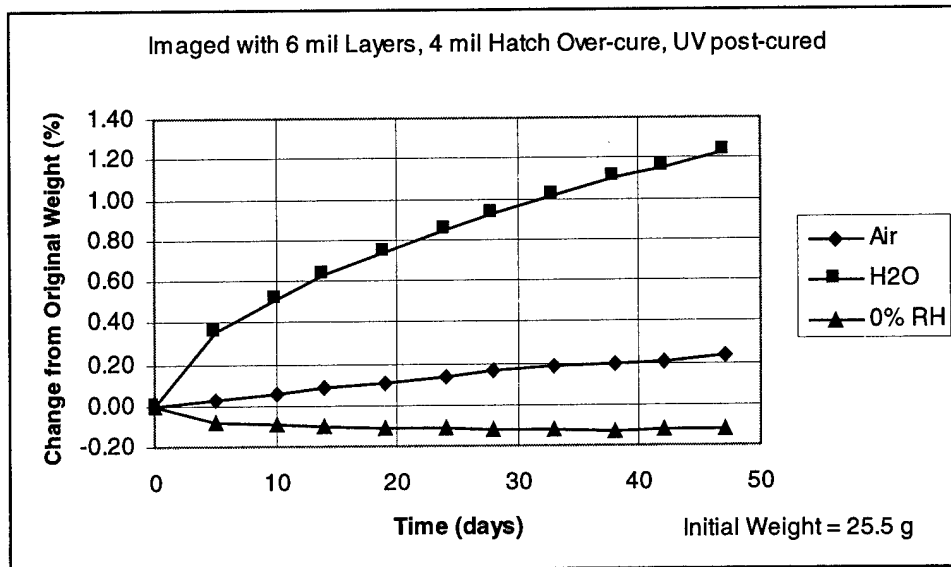


Figure 4: Weight change with Time for Somos<sup>®</sup> 7110 Tensile Bars at 21°C

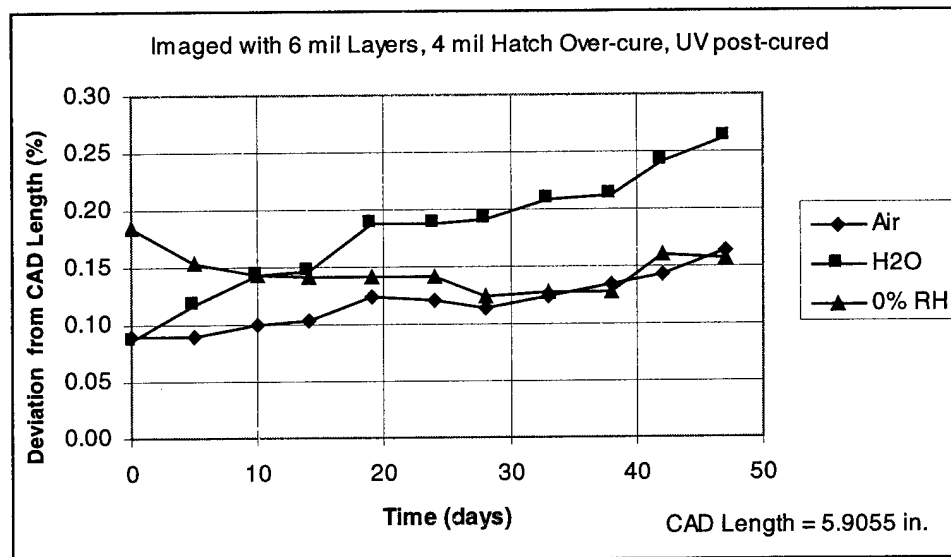


Figure 5: Change in Length with Time for Somos<sup>®</sup> 7110 Tensile Bars at 21°C

The overall effect on the length of the Somos<sup>®</sup> 7110 bars was very similar to the weight change (Figure 5). The bars at 0 % RH lost length throughout the study, but then seemed to gain some at the end. The length of the bars at ambient conditions (Air) varied slightly presumably due to varying humidity in the laboratory. The bars in water gained a total of 0.2 % length over 47 days (an average of 0.004 % per day) but had not yet reached equilibrium.

The bars made from Somos<sup>®</sup> 8110 and held at 0 % RH lost an average of 0.006 % weight per day, but their weight was stabilizing. The bars at ambient conditions (Air) actually gained weight slightly presumably due to a slightly increasing humidity in the laboratory with the onset of summer. The bars in water gained a total of 2.4 % weight over 48 days (an average of 0.05 Wt % per day) but had not yet reached equilibrium (Figure 6).

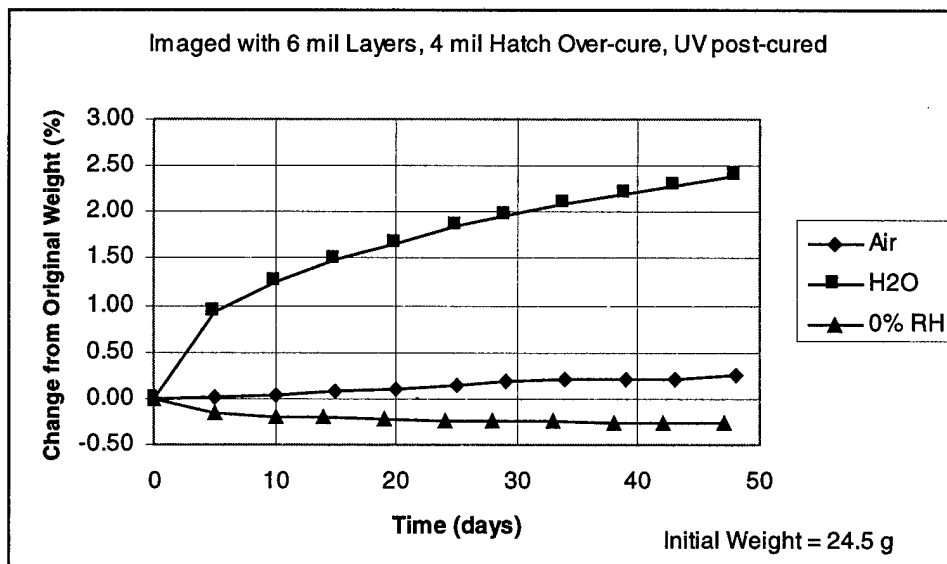


Figure 6: Weight change with Time for Somos<sup>®</sup> 8110 Tensile Bars at 21°C

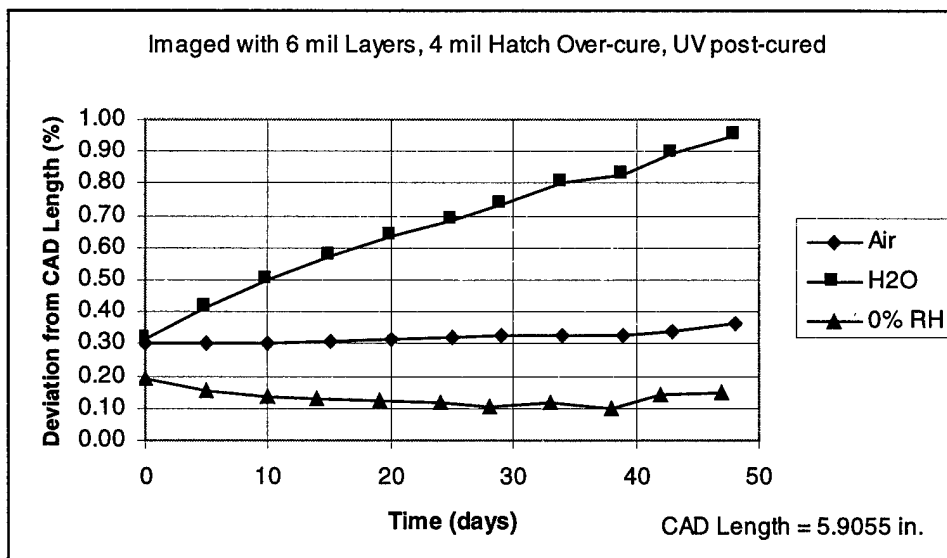


Figure 7: Change in Length with Time for Somos<sup>®</sup> 8110 Tensile Bars at 21°C

The overall effect on the length of the bars was very similar to the weight change (Figure 7). The bars at 0 % RH lost length throughout the study, but then gained some at the end. The length of the bars at ambient conditions (Air) varied slightly presumably due to varying humidity in the laboratory. The bars in water gained a total of 0.6 % length over 48 days (an average of 0.013 Wt % per day) but had not yet reached equilibrium even after that length of time.

## Conclusions

To build dimensionally accurate parts by stereolithography, machine calibration is a very important consideration that should not be overlooked. A way of measuring the imaging accuracy before building parts has been proposed.

It has been shown that the random noise component of the stereolithography process can be a significant contributor to the overall part accuracy. As more attention is given to the individual components that affect dimensional change and therefore random noise, the achievable accuracy levels will improve.

The amount of exposure used during the part build affects the dimensional stability of the part after building. In general, higher exposure provides more stable parts, whether they remain in the green state or if they are post-cured with UV radiation in the conventional way. This has been shown to be the case with Somos<sup>®</sup> 8100, one member of a family of stereolithography resins that produce flexible, high impact strength parts. The effect of exposure on other stereolithography resins will be the subject of future studies.

After parts have been built and post-cured it has been shown that environmental conditions, in particular humidity, have a pronounced effect on the dimensional stability. This occurred for parts made from both of the stereolithography resins tested, namely Somos<sup>®</sup> 7110 (a general purpose, high strength, high heat deflection temperature resin) and Somos<sup>®</sup> 8110, although the later resin changed the most. For six-inch tensile bars in some environments, equilibration had not occurred over a 47-day period. It was shown that parts left at ambient room conditions are susceptible to dimensional changes due to humidity changes. Further studies are underway to look into these issues at a greater depth and will be reported in the future.

## References

1. Paul F. Jacobs, "The Effect of Shrinkage Variations on Rapid Tooling Accuracy" presented at the 4<sup>th</sup> Annual Eugene C. Gwaltney Manufacturing Symposium, RPMI, Georgia Institute of Technology, October 1-2, 1997.
2. Tom Mueller, "A Model to Predict Tolerances in Parts Molded in Pattern Based Alternative Tooling" presented at the Rapid Prototyping and Manufacturing Conference, May 19-21, 1998.
3. Edward G. Gargiulo and Suresh S. Jayanthi, "Current State of Accuracy in Stereolithography" presented at the Measurements and Standards Issues in Rapid Prototyping Symposium organized by NIST, October 16-17, 1997.

## Acknowledgements

This work has been made possible by the active participation of some of our valued customers in our technical studies. We would also like to acknowledge the help we obtained from our colleagues within the Somos<sup>®</sup> Group and from other divisions within DuPont.

# Variable thickness ruled edge slice generation and three-dimensional graphical error visualization

Peter B. Chamberlain, Mark D. Van Roosendaal, Charles L. Thomas  
University of Utah

## Abstract

This paper describes a simple variable thickness ruled edged slicing algorithm that produces slices with zero integrated error. In its present state, the algorithm requires pre-sampled data to be taken from the STL file. Data points are extracted in a cylindrical coordinate system giving values of radius at regular intervals  $\Delta\theta$  and  $\Delta z$ . Using this data, the algorithm creates slices based on averaging of the data points and the slope of line segments connecting them. Error based constraints are used to determine slice thickness. A three-dimensional visualization technique using color contour plots (representing error) on the surface of the prototyped model provides a means of evaluating the accuracy of the prototyped part.

## Introduction

Most of the rapid prototyping systems currently available use vertical (zero order) edge layers to build parts (de Jager, 1997). Vertical edged layers result in parts with stair-stepping surfaces, see Figure 1. Vertical edge rapid prototyping systems use relatively thin layers to improve surface accuracy. Very large parts, on the order of feet or meters, become difficult and expensive to build from thin layers. Thick layers enable the building of very large parts without expensive increases in time. Higher order edge types should be used for thick layers to maintain as much accuracy as possible. Figure 2 shows a ruled (first order) edge, which is the simplest of the higher order edge types. Note that the surface quality of the ruled layer is much better than the quality of the vertical layer.

Several research groups from around the world are working on large-scale rapid prototyping with ruled edges. The groups have developed several different types of ruled edge definitions. Three basic types of edges will be discussed in this paper. Hope discussed two of the basic types (Hope, 1997b), which are derived from the vertical edge types discussed by Dutta (Dutta, 1996). He labels the two types tolerance all outside and tolerance all inside. The two edge types will be referred to as outside and inside ruled edges respectively. Outside ruled edges, lines 3 and 6 in Figure 3, completely contain the original volume of the model and can be sanded down to get a better approximation. Inside ruled edges, lines 1 and 4 in Figure 3, fit entirely within the original surface so that a prototyped part could physically fit inside the original part. Material could be added to the prototyped part to

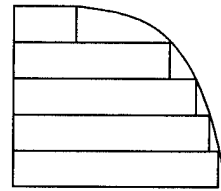


Figure 1  
Stair-stepping effect of vertical edges

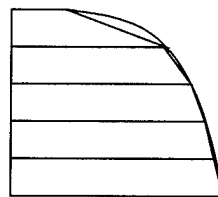


Figure 2  
Improved surface quality of ruled edges

make it identical to the original part. A third type of ruled edge definition is the zero integrated error ruled edge slice (ZIGER slice) definition, lines 2 and 5 in Figure 3. A ZIGER surface represents the surface where positive and negative surface deviations sum to zero producing a surface that is both inside and outside the original part.

Shape Maker II, an RP system developed by Lee and Thomas at the University of Utah, uses a very simple algorithm to create ruled edge slices (Lee, 1997). Surface contours are extracted from an STL model at regular intervals of height. Layers are then defined by connecting successive contours with ruled edges. This method creates both outside and inside edges represented by lines 1 and 6 in Figure 3. TrueSurf, an RP system developed by Hope at the University of Queensland (Hope, 1997a), uses a different slice generation algorithm. Slices of regular thickness are defined by a line tangent to the slice cross section at the slice center, represented by lines 3 and 4. As with Shape Maker II, TruSurf creates outside and insided ruled edges. Some preliminary work on ZIGER edges has been conducted at the University of Utah using wavelets and quasi-wavelets (Lee, 1997). An important characteristic of the different slice types is edge matching. Connecting interpolated loops (Lee and Thomas) leads to layer edges that match from layer to layer. Slices defined by tangents and ZIGER edges will not meet unless slice boundaries are chosen so that the edges line up. That requires an adaptive thickness algorithm.

Adaptive slicing provides a means of improving the surface quality of large-scale rapid prototyping. With adaptive layer thickness it is possible to have thin layers where surface complexity is high and thick layers where there is little surface complexity. Most of the current adaptive thickness ruled edge algorithms are error based. Work by Dutta (REFERENCE) with vertical edges uses the concept of cusp height, shown as  $\delta_D$  in Figure 4a. de Jager (de Jager, 1997) extended the concept of cusp height to ruled edges, shown as  $\delta_J$  in Figure 4b. Hope created a dual cusp height, shown as  $\epsilon$  and  $\delta_H$  in Figure 4c (Hope, 1997b). In all cases the variable thickness algorithm works by performing a systematic search to maximize the thickness of each layer without exceeding a threshold cusp height value.

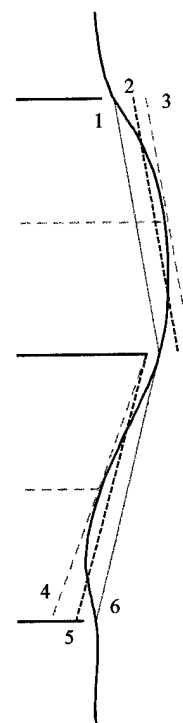


Figure 3  
Ruled edge types

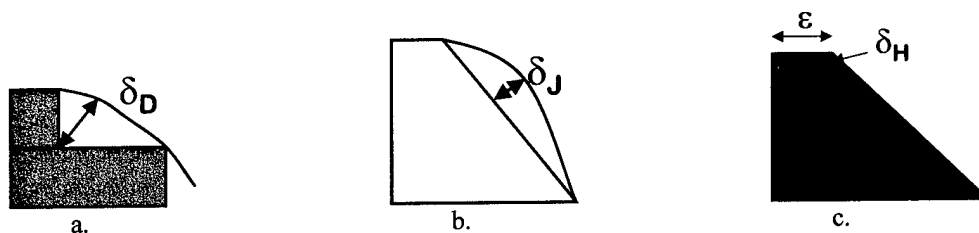


Figure 4  
Variable thickness algorithm error measures

## ZIGER Averaging Slicer

The focus of this paper is a slicing algorithm for the creation of ZIGER slices. The basic concepts and mathematics behind the slicer will be introduced here. For the initial discussion, assume that the geometry to be constructed is defined by a surface of revolution. Figure 5 shows a schematic diagram of how the slicer would work with such a surface. A ZIGER slice surface can be defined as a slice slope passing through a slice radius at the slice midline. The slice radius is simply the average value radius between the slice boundaries. The slice slope is the average value of slope between the slice boundaries. This procedure creates a ZIGER surface because the integral of the radial errors (using both positive and negative error) along the surface is zero. General equations for the ZIGER ruled slice are as follows:

$$r = \frac{\int_{z_0}^{z_1} r(z) dz}{z_1 - z_0} \quad \text{Equation 1}$$

$$s = \frac{\int_{z_0}^{z_1} \frac{dr(z)}{dz} dz}{z_1 - z_2} \quad \text{Equation 2}$$

where  $r$  is the slice radius,  $r(z)$  is the radius at a given height  $z$ , and  $s$  is the slice slope. It is possible to generalize the method beyond the surface of revolution. Later in this paper one such method is tested as a first step toward developing a truly useful ZIGER slicing algorithm.

### Adaptive Thickness Error Definition

The ZIGER averaging slicer lends itself to a new and sophisticated definition of slice error. The error definitions described in the introduction considered only one or two measures of error at points on the slice surface. It would be more desirable to have some measure of error representing the entire surface. One such measure will be proposed here. Once again, consider the special case of a surface of revolution. Figure 6 shows how the concept of error can be defined using the ZIGER slice. In the figure the original surface is shown as a gray line and the reconstructed surface is shown as a black line. Error is defined as the radius of the original surface subtracted from the radius of the original surface. Note that if the errors are integrated along the height of the slice, the result

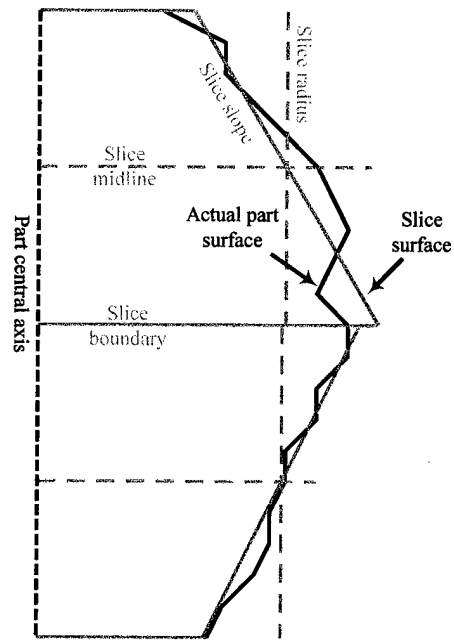


Figure 5  
Concept of radial slicer applied to a surface of revolution

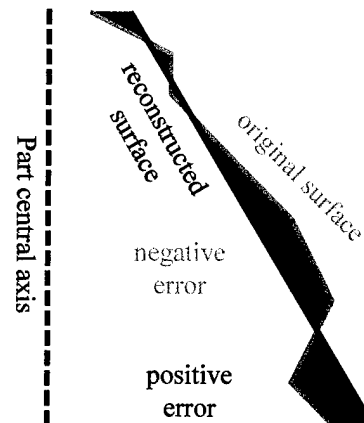


Figure 6  
Error of ZIGER ruled surface

is zero(positive and negative error cancel), see Eq. 3. A useful definition of error is the average absolute error,  $\bar{E}_{abs}$ , which provides a meaningful measure of error over the entire surface of the slice, see Eq. 4. Another useful indication of error is the maximum absolute error,  $E_{abs}^{max}$ , that occurs anywhere within the slice, see Eq. 5.

$$ZIGE = \int_{z_0}^{z_1} (r_{re}(z) - r_o(z)) dz = 0 \quad \text{Equation 3}$$

$$\bar{E}_{abs} = \frac{\int_{z_0}^{z_1} |r_{re}(z) - r_o(z)| dz}{z_1 - z_0} \quad \text{Equation 4}$$

$$E_{abs}^{max} = \max(|r_{re}(z) - r_o(z)|) \quad \text{Equation 5}$$

The adaptive ZIGER edge slicer works like any other adaptive slicer. In this case the slicer will attempt to maximize the thickness of each layer without exceeding the specified average absolute error and maximum absolute error thresholds.

### An Adaptive ZIGER Slicer

It is always useful to begin with a simplified model to test a new algorithm. For this paper a simple algorithm for adaptive slicing of any general single valued surface will be described. The algorithm contains three distinct components, a pre-sampler, a ZIGER slicer, and an adaptive thickness algorithm.

#### Pre-sampling

A surface of revolution provides a simple implementation of the algorithm, but a surface of revolution is not very interesting. A slightly more interesting model can be defined as a single valued surface in a cylindrical coordinate system. It is possible to use a coordinate transform to convert the triangle data of a single surface STL file from Cartesian to cylindrical coordinates. A further useful simplification is supply the algorithm with values of radius sampled at regular

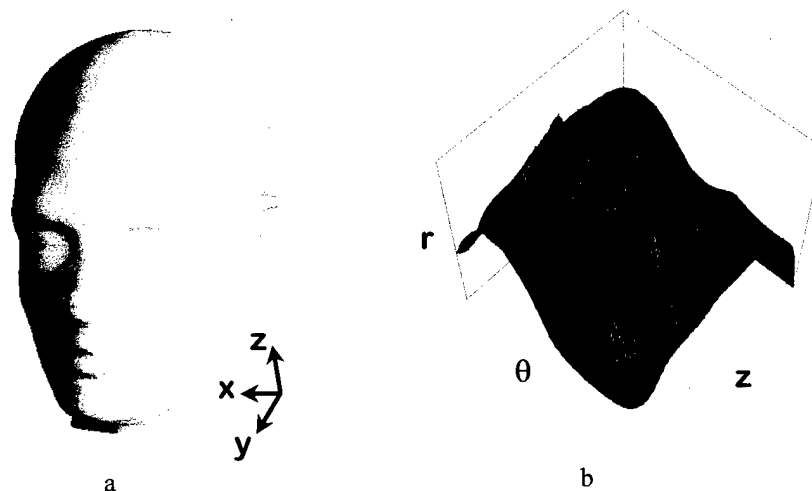


Figure 7  
Head in STL form and as regularly sampled points

intervals  $\Delta\theta$  and  $\Delta z$  from the STL model in cylindrical coordinates. Figure 7a shows a single valued STL model of a human head. Figure 7b shows a single valued set of points representing the surface of the STL model which were sampled at regular intervals in a cylindrical coordinate system.

There are several issues involved in sampling points from triangles. The most important issue is the loss of surface detail. It is difficult to precisely locate a specific feature with a regular grid, but it is possible to sample data points so that the details are partially represented. A good STL sampling algorithm has two parts, a triangle interpolator and a point averager.

Figure 8a shows how the process of triangle interpolation works. Figure 8b shows how point averaging works.

When the density of triangles in the STL file is higher than the density of points to be sampled, it is best to use some kind of averaging sampler. An averaging sampler works by averaging the values of points within the neighborhood of the point to be sampled.

Weightings based on the distance of a point from the point to be sampled can be easily applied. If there are fewer than four points in the neighborhood of the point to be sampled, triangle interpolation should be used. It is always desirable to over-sample data points. The averaging sampler is just a fallback for situations where over-sampling is not practical for computational reasons.

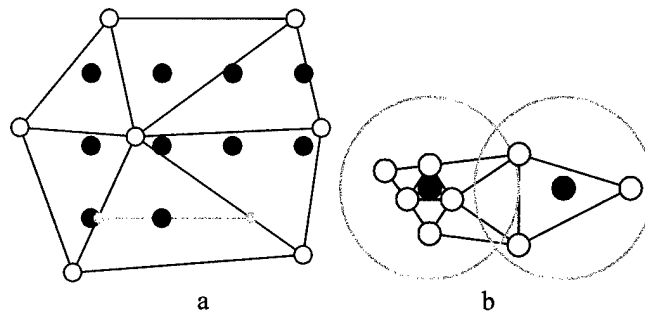


Figure 8  
Data sampling

### Slicer

Using a simplified set of regularly sampled data makes implementation of the ZIGER slicing algorithm trivial. Figure 9 shows a schematic of data points along a column of data representing the cross section of a surface at a particular angle theta. The gray points and their connecting lines represent the surface of the original part. The black points and their connecting lines represent the surface of a reconstructed slice at the particular angle. It is possible to create the entire slice by individual calculation and slope and radius for each cross sectional angle. For example, if a model were sampled with an incremental angle of one degree, 359 cross sections would have to be processed for each slice. Then each of the cross sections would be laced together to form the actual slice geometry. Calculation of a single slice cross section at a particular angle is carried out with the following formulas:

$$\bar{r} = \frac{\sum_{i=1}^N r_i}{N} \quad \text{Equation 10}$$

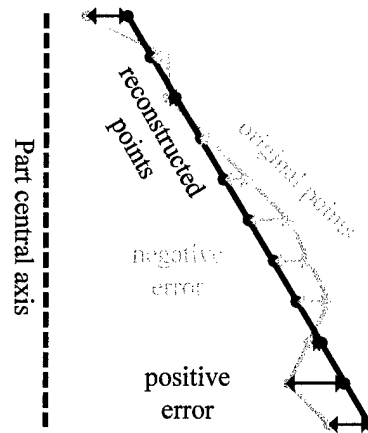


Figure 9  
Regularly sampled surface points representing slice cross section a particular angle theta

$$\bar{s} = \frac{\sum_{i=2}^N \frac{r_i - r_{i-1}}{\Delta z}}{N-1} \quad \text{Equation 11}$$

where  $\bar{r}$  is the sectional slice radius,  $\bar{s}$  is the sectional slice slope,  $\Delta z$  is the slice thickness, and  $N$  is the number of points in the slice. One  $\bar{r}$  and one  $\bar{s}$  would be calculated for each angle of each slice.

### Adaptive Slicing

Error computation for adaptive slicing is also easy because of the regularly sampled input data points. A look at Figure 9 shows that there are discrete points in the original and reconstructed surfaces, each having a discrete error. The slice errors are calculated using every point in the slice at all heights  $z$  and all angles  $\theta$ .

$$ZIGE = \sum_{i=1}^{N_\theta} \left( \sum_{j=1}^{N_z} r_{re_{i,j}} - r_{O_{i,j}} \right) = 0 \quad \text{Equation 12}$$

$$\bar{E}_{abs} = \frac{\sum_{i=1}^{N_\theta} \left( \sum_{j=1}^{N_z} |r_{re_{i,j}} - r_{O_{i,j}}| \right)}{N_\theta N_z} \quad \text{Equation 13}$$

$$E_{abs}^{\max} = \max_{i=1}^{N_\theta} \left( \max_{j=1}^{N_z} |r_{re_{i,j}} - r_{O_{i,j}}| \right) \quad \text{Equation 14}$$

where the error variables are the same as those defined in Eqs. 3-5.  $N_\theta$  represents the number of angular cross sections, and  $N_z$  represents the number of vertical points inside the slice for a given angular cross section. Slice thickness is determined by increasing the number of vertical points used to define a layer without exceeding the dual error criteria,  $\bar{E}_{abs}$  and  $E_{abs}^{\max}$ . A sample of the slices generated at one radial cross section is shown in Figure 10.

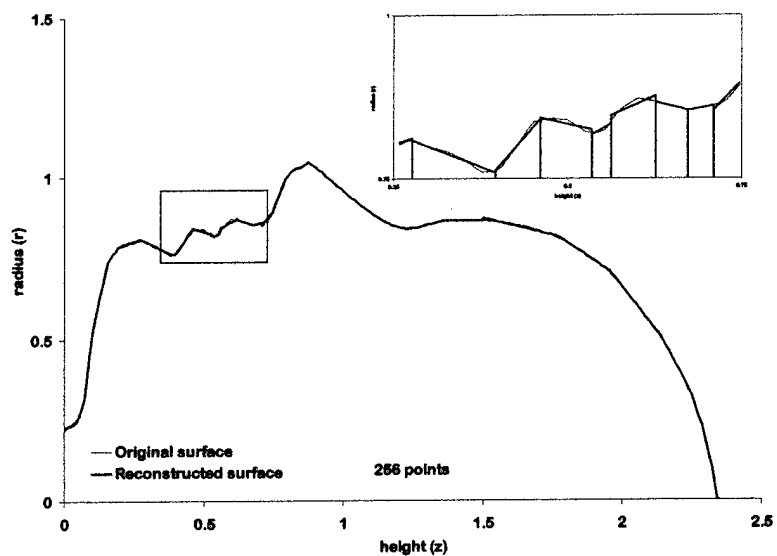


Figure 10  
Plot of slices on a single radial cross section through head

## Error Visualization

For further evaluation of the algorithm an error visualization system using color contour plots representing radial error on the surface of the reconstructed part were created. In its true form, the algorithm uses a color map. Areas that protrude from the actual surface are shaded blue, areas that are inside the actual surface are red, and areas that are close to the original are green. For this paper a grayscale colormap was used. Areas that are black represent reconstructed surfaces that extend radially beyond the original surface. Areas that are white represent reconstructed surfaces that are inside the original surface. Figures 11 and 12 show two of those plots using a grayscale colormap. Lighting of the surface caused problems with this particular visualization. Places where the light shines directly, the forehead and chin, have been whitened producing a misrepresentation of the actual error. A look at the head shows a banding effect where dark bands indicate boundary edges along the forehead. A look at Figure 12 shows a close up view of the head. It should be possible to pick out the slice boundaries from the plot, even in areas where banding is not pronounced.

## Conclusions

The zero integrated error ruled edge slice definition provides an alternative to other slicing definitions. The advantages of the slice definition include the fact that it produces a slice with zero integrated error, it provides a sophisticated measure of error across the entire slice instead of at one point, and it can be used as an adaptive thickness slicing algorithm. As presented here, the slicer is only useful for single valued surfaces. It is a simple first step that proves that the method can work for adaptive thickness ruled edge slicing.

The sophisticated error measures afforded by the algorithm allow slicing with higher accuracy. The important measures of error are the average absolute error, and the maximum absolute error. As stated, these measures are easily adapted to adaptive thickness slicing by using a dual error threshold criteria to determine the thickness of each slice. These errors are representative of the entire slice, not just a point on the slice.

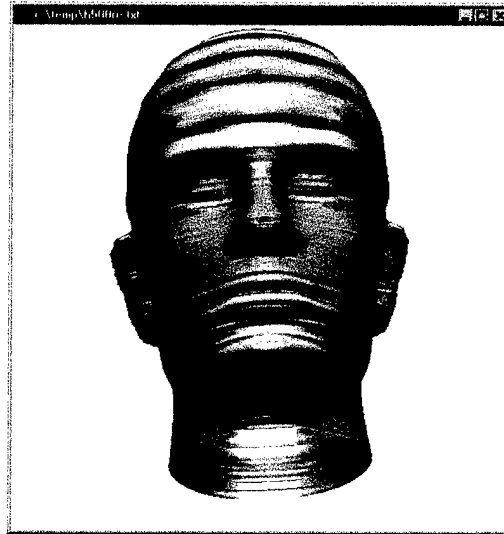


Figure 11  
Gray mapped contour plot of error on head  
reconstructed from slices  
Black represents surfaces that protrude  
outward, white represents recessed surfaces

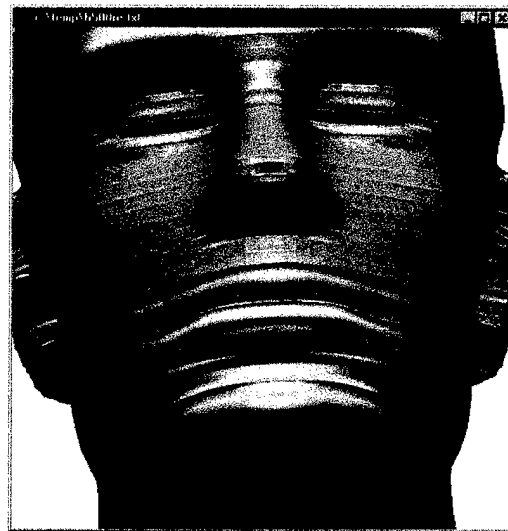


Figure 12  
Close up of error plot of reconstructed head

With more work the slicer can be modified to work with generalized geometry including multiple contour parts and sectional transition parts.

### References

- Dutta, D. and Kulkarni, P. An accurate slicing procedure for layered manufacturing. *Computer Aided Design*. Vol 28 No. 9. 1996. pp. 683-97.
- de Jager, P.J., Broek, J.J, and Vergeest, J.S.M. A comparison between zero and first order approximation algorithms for layered manufacturing. *Rapid Prototyping Journal*. Vol. 3 No. 4. 1997. pp. 144-149.
- Hope, R.L., Roth, R.N., and Jacobs, P.A. Rapid prototyping with sloping surfaces. *Rapid Prototyping Journal*. Vol. 3 No. 1. 1997. pp. 12-19.
- Hope, R.L., Roth, R.N., and Jacobs, P.A. Adaptive slicing with sloping layer surfaces. *Rapid Prototyping Journal*. Vol. 3 No. 3. 1997. pp. 89-98.
- Lee, Cheol H. and Thomas, Charles L. An analysis technique for layered manufacturing basee on quasi-wavelet transforms. *Proceedings of the Solid Freeform Fabrication Symposium*. 1997. pp. 577-584.
- Lee, Cheol H. New Analysis Methods for Three-Dimensional Objects in Solid Freeform Manufacturing. Ph.D. Thesis. University of Utah. 1997.

# TOPOLOGY DRIVEN IMPROVEMENT OF FDC BUILD PARAMETERS

Vikram R. Jamalabad, Jeffrey A. Chard<sup>α</sup>, Charles J. Gasdaska, Richard B. Clancy

*AlliedSignal Inc. Research & Technology  
101 Columbia Road, Morristown, NJ*

---

## ABSTRACT

*The likeliest failure origin for advanced ceramics parts, prepared by fused deposition, is a void from improper fill. Adequate filling of each cross-section is dependent upon the deposition toolpath. Cross-sectional spaces are conventionally filled with pre-defined parameters. We propose that adaptive build parameters will control variations in geometry and property of a part. Voids, overfilling, incomplete bonding and excess traversing can be suppressed by adjusting the fill parameters for cross-sectional areas. Improved build parameters and toolpath allows for faster build time and components of full density. Some implementations are discussed and presented.*

## INTRODUCTION

Fused Deposition of Ceramics (FDC) as a process has been shown to be a feasible and competitive technique for ceramic component manufacture. Descriptions of the FDC process, its advantages, limitations and achievements are documented in numerous articles [1, 2 & 3]. To briefly describe the process, the relevant zone (Figure 1) involves the deposition of a thermoplastic material, loaded with ceramic powder, in the form of a bead or "road". Roads are deposited exclusively in the areas that the part "exists", effectively building up the part. The part thus deposited is called a "green" part and this completes the FDC stage of the process.

The thermoplastic is then removed from the green artifact by a binder burnout (BBO) process. The residual powder is packed closely enough to retain the shape of the initial part but has no strength and has a volume density of ~55%. The part, in the "brown" stage, is then consolidated by sintering to full density (~99.9%). The last stage of sintering results in shrinkage of about 17% in X and Y and about 19% in Z [4].

The entire process is driven automatically by computer-generated code and firmware. From the initial CAD part, its conversion to an augmented shape (to take into account the post-processing shrinkage) and the generation of the toolpath control code, FDC is, as is all of SFF, enabled by computational algorithms. In this article, we will discuss some work done at AlliedSignal over the past few months relating to software for toolpath generation.

---

<sup>α</sup> Graduate Student at Department of Mechanical Engineering, University of Wisconsin, Madison

Commercial software for toolpath generation reflects the absence of a large family of SFF users interested in fully dense parts. We are currently using QuickSlice™, the software provided by Stratasys Inc., for the generation of toolpath codes to drive the FDM1650™ at our location. While this is an excellent package for most purposes it lacks the ability to generate toolpath codes to fully densify parts. Painstaking development of toolpaths comes to naught when a minor parameter is changed. We are in the process of developing technology that will remove the intensive and iterative nature of toolpath design that is currently required of FDC. Work at the University of Illinois [5] and to some extent Case Western Reserve [6] is beginning to look at aspects of toolpath layout that is relevant to SFF.

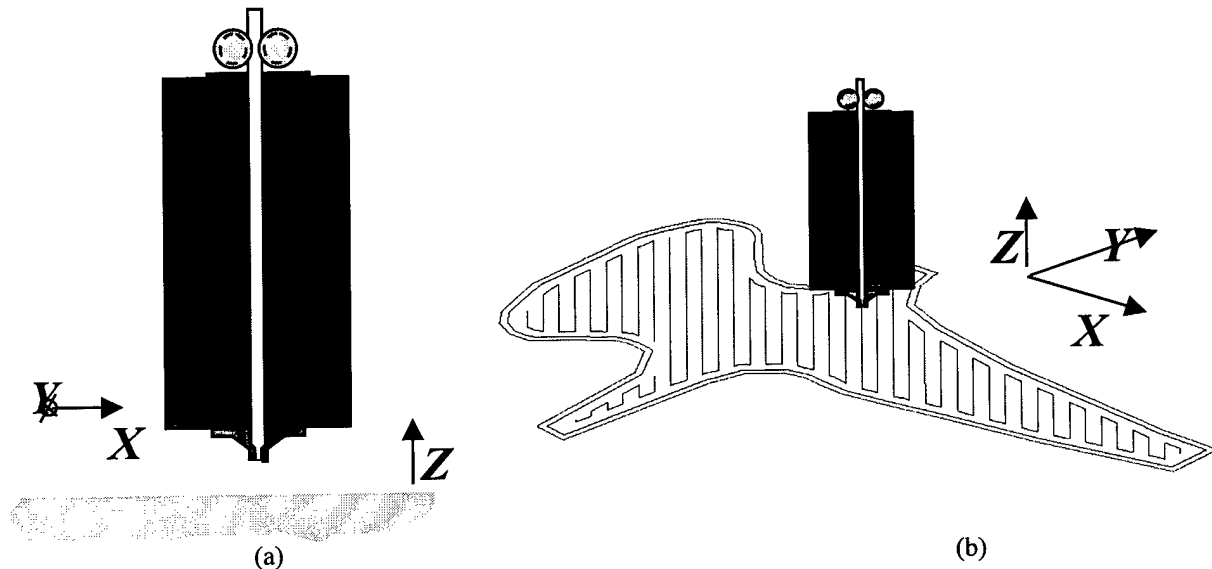


**Figure 1: Schematic of the Fused Deposition (FD) process.** To the left (a) is a close up of a straightened liquefier, showing the material being deposited on a flat platen to form the part. At right (b), the tool is shown traversing a path that describes the cross section of the part.

True three-dimensional parts are reduced to a single-dimensional road representation that cumulatively draws, or describes, the original part. The 3-d object (contemporarily in “StL” form) is partitioned into two-dimensional “slice” representations. Each slice is then used to generate the single dimensional road that will describe the slice. The conversion from 3-d to 1-d results in a loss of information at each step of the process. For instance, the fin of a blade in 3-d is not a “fin” feature in 1-d, but a series of locations for the tool to visit. While there may be no way to retain the required information at the road build level, determining the toolpath in accordance with the features that are to be built would lead to a better build process. These *procedural losses* are compounded with *systemic losses* that occur during the build itself. Systemic losses include voids and improper filling, incomplete bonding, etc [7] that need to be accounted for prior to generating the toolpath.

In the current work, we attempt to treat these problems at the slice level. Since most current SFF techniques, not just FDC, rely on 2-d slices (albeit of varying thickness or shape), this is a fair assumption. Considering each slice to be the elemental structure, four issues are crucial to the effort:

- Adequate filling of the particular slice with no unintended voids (systemic).
- Adequate bonding of all the deposited roads (systemic)

- Retention of 2-d features to the best ability of machine control (procedural).
- Incorporation of multi-material deposition to leverage 2-head machine (procedural).

Given a particular material and shape to be built, the only parameters at our disposal are the road deposition path and the flow-control of the material. While the two parameters are linked, there is an inherent independence in the deposition path from the process (it is applicable to any SFF technique using 1-d fabrication procedures). The flow control aspect is tied in with the material being deposited or the SFF process that is being used. In this paper we will concentrate on our efforts of the road path.

## FEATURE DEFINITION AND VOID REMOVAL

One of the limiting features of Fused Deposition of Ceramics is the formation of voids during slice filling. These voids can be caused by both procedural and systemic causes. Systemic loss of fill information was dealt with to a larger degree in earlier work [7]. In the current work, procedural causes are addressed. The solutions to these problems include systemic errors as well. It should be noted that surface finish of parts (primarily the stair-casing effect) is not considered here. We believe that the limits of surface improvement have almost been reached in our process and physical machining is the only alternative for further improvement.

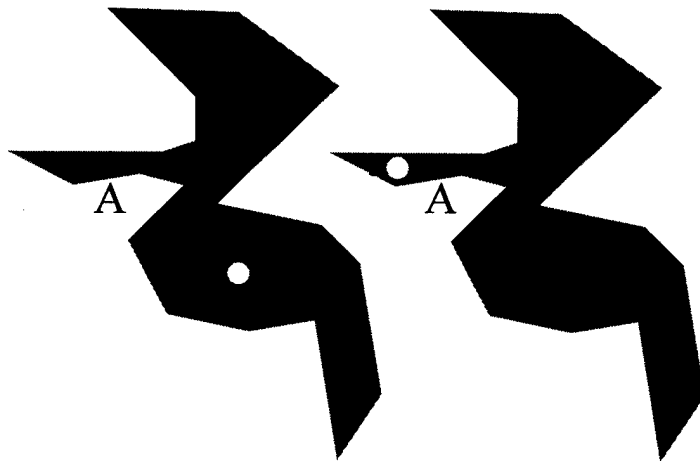


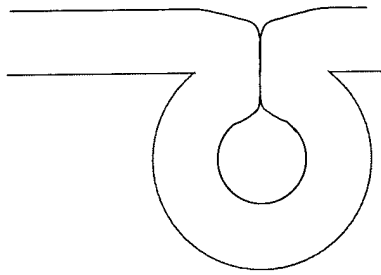
Figure 2: Two features, the fin “A” and the hole “b”, can be built independently but not necessarily together.

the lack of a better term, the meso- levels. Artifacts such as “thin fins” and “small holes” are defined as macro level features. We will address problems associated with interactions of macro-level features. Meso level features would include sharp edges and fillets. While this definition is rather arbitrary, it can be considered to be a separation between preservation of topology and the exact recreation of features.

**“Macro” Features:** Consider the construction of two features in a particular cross-section (Figure 2). The features that the designer wants to create are the fin “A” and the hole “b”. While these features can be built in the first configuration, the process may not be able to build the second configuration due to the road width being too wide. Moreover, even if the feature were possible with a fine road deposition, the time to build the entire part with those settings would increase significantly.

To keep the surface finish of the generated path as smooth as possible, the build procedure utilizes a perimeter deposition followed by an optional contour deposition and subsequent rastering of the internal areas of the slice. Features that are smaller than the road width cannot be defined. The focus here is to define these features better with improved deposition procedures.

We can look at features on two scales – the macro- and, for



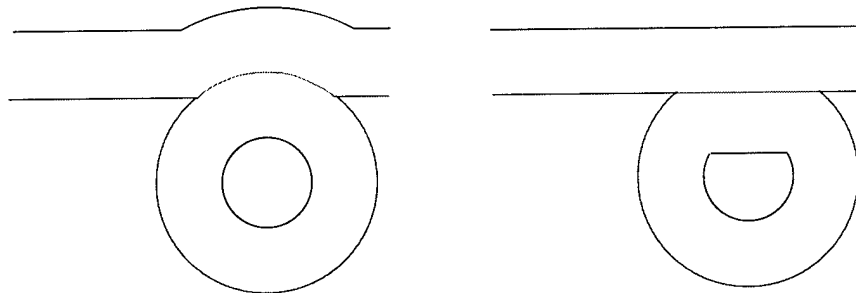
**Figure 3: Toolpath generated by QuickSlice™ for the interacting features of Figure 2 and the resulting part.**

Figure 3 describes the phenomenon in a toolpath generated by QuickSlice™. An expected hole is not completed in the fin structure. Unless thickness of the road is larger than designed, the gap may not fill. Moreover, a seam will be present at the juncture of the two sharply turning roads.

Figure 4 shows an alternate approach that allows the designer to choose the level of feature definition. Feature loss occurred here when two offset contours intersected, as shown in Figure 3. During toolpath generation, the designer is queried at such locations and given the option of continuing with the conservative procedure of Figure 3 or the overfills of Figure 4.

Figure 4 shows an alternate approach that allows the designer to choose the level of feature definition. Feature loss occurred here when two offset contours intersected, as shown in Figure 3. During toolpath generation, the designer is queried at such locations and given the option of continuing with the conservative procedure of Figure 3 or the overfills of Figure 4.

The advantage of this procedure is that design intent can be maintained while the part is being manufactured. Assuming that the hole is a locating pin with the outer surface unimportant, the toolpath of Figure 4(a) would be appropriate. For the case where the smoothness of the outer surface is more important, the hole can be deformed as long as it is retained (in this case the feature is a hole of some shape).



**Figure 4: Two options of the new toolpath giving the designer control over feature retention. On the left the circularity of the hole is preserved, while on the right the fin surface is preserved.**

**Meso-level Features:** Another drawback of the FD procedure for making parts is the rounding of corners that occurs during material deposition. This may not be such a bad thing for engineering applications, especially ceramics, as sharp corners are sites for stress concentration. However, the rounding of the internal roads leads to sub-perimeter voids\* and other incomplete filling. “Dog-earing” and offsetting of the rasters has been used successfully in suppressing these problems [7]. Apart from offsetting, a preliminary form of the dog-earing is available in QuickSlice™ to users through an escape sequence. However, the effects of both dog-earing and offsetting depend upon the angle of incidence of the raster & perimeter and the width of the road. The algorithms being currently developed and implemented take these empirically observed parameters into account.

\* Sub-perimeter voids are persistent errors occurring below the perimetric road due to incomplete filling – the cause of these voids is uncertain, but some of the parameters that treat them have been identified and implemented [7].

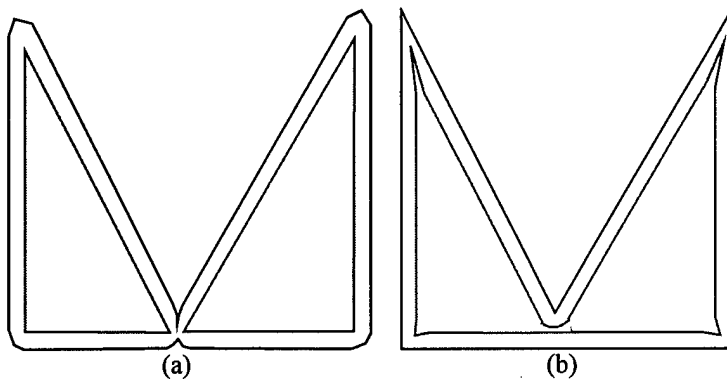


Figure 5: Improvement in perimeter feature definition.

specified distance from the original shape. Definition of features such as sharp corners or rounded fillets is thereby achieved. We assume that material and deposition properties are constraints, established for proper build<sup>†</sup>. These properties are used to establish flow criteria required in the FD machine. Specifically, we will look at sharp corners (outer and inner perimeter).

Using standard procedures, the perimeter for a double wedge shape generated by QuickSlice™ is shown in Figure 5(a). The part obtained is made constructed as two separate pieces welded together at the bottom. The top corners are defined as rounds. Apart from the inaccurate part, the weld area has notches on both surfaces. Utilizing the dog-earing procedure and rounding, the perimeter defined by the altered algorithm is shown in Figure 5(b). The part is now built as a single piece, which ensures that knit-lines or notches will not be created.

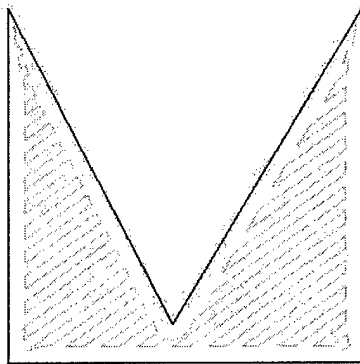


Figure 6: Raster toolpath for a double-wedge with no external perimeter.

The effect of these alterations has ramifications that extend to internal road patterns. Assuming that the same part is created strictly by rastering, Figure 6 describes the toolpath as generated by our algorithms. The rastering road deposits material in the areas that regular rastering (as done by QuickSlice™) would not. Overfilling does occur, especially in the areas such as the lower right corner and in the notch area (as with the contouring build pattern of Figure 5(b)). However, overfilling can be contained while under-filling is intolerable.

### INTERNAL PATH DETERMINATION – OPTIMIZATION OF TOOLPATHS

Deposition of the material in the internal sections of the slice requires adjustments that extend beyond the geometry of the cross-section. For the shape defined in Figure 7, the fill defined by QuickSlice™ is optimized for ensuring minimal fill. With the techniques used in

<sup>†</sup> These properties include the material composition, temperature of deposition, environmental temperature, etc.

the last section, the fill for the slice improves to the extent that voids from incomplete paths, inter-lamellar and sub-perimeter voids<sup>‡</sup> are filled in.

We are currently implementing a procedure by which the contour of the slice perimeter will direct the internal raster pattern. As the raster intersects an offset of the contour, a decision of breaking the raster or including the contour path is made. Comparing Figure 7(a) with 7(b), the effects of this method can be seen. Around the hole, the standard rastering technique terminates. This causes voids in the part, especially in the region just above the hole (Figure 7(a)). In Figure 7(b), the area above the hole is filled in with the contour following raster. Moreover, the hole is also adequately defined. A negative aspect of this method is the overfilling that occurs at the lower end of the curve where the offset road will interfere with the straight raster. Figure 7(c) shows the internal raster laid down taking into account the geometric features of the slice. Note the dog-earing of individual corners of the internal rastering. This ensures that the part is completely filled in.

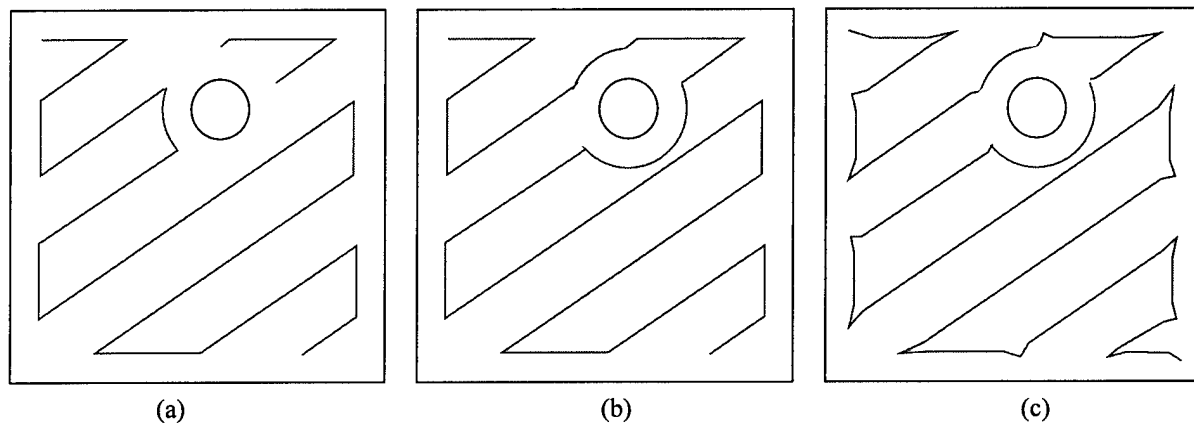


Figure 7: Internal raster filling with progressively increasing quality of fill.

Another advantage of the procedure is the reduction in the number of separate roads. From the analogy of a welding procedure, it is important to keep the material flowing continuously. Stopping and starting leads to higher chances of errors and under-fills. In Figures 7(b) and (c), there is a single toolpath that rasters the entire area. Tests have shown that this comparison is valid for more complex shapes.

## CONCLUSIONS

We have shown that utilizing the artifacts of geometry from the original shape of the slice help in ensuring that certain levels of feature are maintained in parts built by Fused Deposition. Dog-earing and rounding perimeter curves enables adequate filling of slice-sections. We have also demonstrated that using curves conformal to the perimeter as part of the internal raster improves the surface definition and the internal fill. A reduction in the number of stops and starts in the interior is also observed, thereby reducing the problems associated with startup.

<sup>‡</sup> Sub-perimeter voids are removed in response to the angle of incidence and road width.

Further work is being conducted in determining the flow parameters of the roads based upon the geometric aspects of the slice. The order of road deposition and multiple materials are areas that are to be developed.

### ACKNOWLEDGEMENTS

This work has been performed as part of the "Solid Freeform Fabrication of Advanced Ceramics Phase II" project, funded by the Office of Naval Research and The Defense Advanced Research Projects Agency under Contract #N00014-97-C-0154. We appreciate the support and advice of Dr. Stephen Fishman, program monitor and Dr. William Coblenz and Mr. Kevin Lyons, program managers for the project. We would also like to thank the input of Mr. Milt Ortiz, AlliedSignal Engines, Dr. Philip J. Whalen, AlliedSignal Inc., and Professor Vadim Shapiro, University of Wisconsin.

### REFERENCES

- [1] Comb, J. W., Priedeman, W. R. and Turley, P. W., "FDM technology process improvements", *Proceedings of the Solid Freeform Fabrication Symposium*, Austin, TX, August 1994, pp. 42-9.
- [2] Agarwala, M. K., *et al.*, "Structural quality of parts processed by Fused Deposition", *Rapid Prototyping Journal*, Vol. 2, No. 4, 1996, pp. 4-19.
- [3] Agarwala, M. K., *et al.*, "FDC, Rapid fabrication of structural components", *The American Ceramic Society Bulletin*, Vol. 75, No. 11, November 1996, pp. 60-5.
- [4] Clancy, R. B., *et al.*, "Fused Deposition of Ceramics: Progress towards a robust and controlled process for commercialization", *Proceedings of the Solid Freeform Fabrication Symposium*, Austin, TX, August 1997, pp. 185-94.
- [5] Yardimci, M. A., Personal communication, Morristown, NJ, July 1997.
- [6] Choi S. *et al.*, "CAD and control technologies for computer-aided manufacturing of laminated engineering materials", *Proceedings of the Solid Freeform Symposium*, Austin, TX, August 1997, pp. 643-52.
- [7] Jamalabad, V. R. *et al.*, "Process improvements in Fused Deposition of Ceramics (FDC): Progress towards structurally sound components", *Proceedings of the 1996 ASME Design for Manufacture Conference*, Irvine, CA, August 1996, pp. 18-22.
- [8] Tiller, W. and Hanson, E. G., "Offsets of two-dimensional profiles", *IEEE Computer Graphics and Applications*, Vol. 4, No. 9, September 1984, pp. 36-47.
- [9] Held, M., "A geometry-based investigation of the tool path generation for zigzag pocket machining", *The Visual Computer*, Vol. 17, No. 5/6, 1991, pp. 296-308.



# A Visual Tool to Improve Layered Manufacturing Part Quality

Gautham Kattethota, Mark Henderson, Ph.D.<sup>1</sup>  
Partnership for Research in Stereo Modeling (PRISM) and  
Department of Industrial and Management Systems Engineering  
Arizona State University, Tempe, AZ 85287-5906

## Abstract

A software tool is described that will aid the user in choosing the optimum build orientation to obtain the best composite set of surface finishes on a part built on a Fused Deposition Modeling (FDM) rapid prototyping machine. Experiments were conducted to obtain statistical surface roughness values as a function of orientation and layer thickness. Three types of surfaces (features) have been considered: planar (both upward facing and downward facing (overhang surfaces)), quadric and freeform surfaces. Data analysis of surface roughness of planar surfaces at various orientations and their mapping to quadric and freeform surfaces are presented. The decision support software tool allows dynamic color-coded visualization of the surface quality simultaneous with build parameters including orientation and layer thickness.

## Introduction

The Rapid Prototyping (RP) or Layered Manufacturing (LM) industry has grown by leaps and bounds since it started off a little over a decade ago. Among its numerous applications, increased stress is now being laid on rapid fabrication and form and fit applications. This in turn lays increased importance on the confirmation of the part quality of a part built on a RP process with the CAD model or the scanned model, or MRI/CAT scan of the part. The term *part quality* encompasses surface quality, dimensional accuracy, part strength and build time among others. Surface quality is decided by certain factors including surface deviation (surface roughness), surface flatness and amount of support structures. Since the build process is layered manufacturing, there are certain factors specific to this process that decide the eventual part quality. Chief among these are part orientation, layer thickness, material characteristics and certain process parameters. In this paper, we deal with the influence of part orientation and layer thickness on surface roughness or surface deviation specific to Fused Deposition Modeling (FDM). Surface deviation on a part built on a RP machine influences the amount of time that needs to be spent on subsequent post-processing (finishing) and may, in the process, distort dimensional accuracy. Therefore, it is important to select a good orientation and a suitable layer thickness before starting a build. An interactive software tool has been developed and described in this paper which can be used by a RP user as a confirmation tool in deciding a set of *good* orientation before building the part. The main visual in the software is the display of a color-coded part (read from a file in Stereolithography Tessellation Language (STL) format) which indicates to the user by the way of colors, the expected surface roughness on different surfaces comprising the part.

---

<sup>1</sup> [Gautham@asu.edu](mailto:Gautham@asu.edu) and [mark.henderson@asu.edu](mailto:mark.henderson@asu.edu)

## Previous Work

There has been some work carried out on the importance of factors like orientation and layer thickness for improved part quality, although none of them dealt with FDM. In fact, all of them have been carried out on RP processes such as Stereolithography (SLA) and Selective Laser Sintering (SLS). Thompson [1] conducted an experiment on a SLS machine using a factorial design of experiments method whose results validate the assumption that part orientation is *as* important as certain controllable process parameters such as laser power and layer thickness in deciding surface finish among other measures of quality. Since this surface finish effect due to the factor part orientation is a direct result of layered manufacturing technique, this particular result will hold true for other LM processes such as FDM. Frank and Fadel [2] have developed an expert system, which, with some user interaction, decides the best build direction with the best direction quantified by surface finish, build time and amount of support structures. In this case, the user can select two feature entities of a part that are important to him. Specifying more than two may lead to problems. Lan et al. [4] have developed a program that searches for fabrication orientations for a part with various build objectives like surface finish, build time and support structures on a SLA machine. Our system described in this paper, nicknamed the 'Orient Express', considers all surfaces simultaneously, gives a visual display for immediate feedback of both required and expected surface finish for FDM.

## Approach

Surface quality becomes a key issue in Rapid Prototyping because of the manner in which 3-dimensional parts are built in the layered manufacturing processes. The layer by layer additive build process creates an imperfect texture on the surfaces of a part especially on sloped surfaces (stair-stepping phenomenon), intricate features (thin walls, etc.) and certain curved surfaces (small radius cylinders, etc.). So, in view of the importance of surface quality in the rapid prototyped parts, these imperfect textures, which cannot be eliminated as such in many cases should be contained as much as possible. We have considered the effect of sloped surfaces on part surface finish. On the FDM, sloped surfaces affect the surface roughness through a combination of four effects - layer thickness, layer (edge) profile, layer composition [3] and sub-perimeter composition. The layer profile is the cross-sectional profile of the perimeter bead of material and is normally produced to smooth surface deviation at the edge of a step. "Layer composition is described as the method by which a layer is generated from its raw material, such as molten plastic, sintered powder or cured resin" [3]. Sub-perimeter composition is the composition of that region of a layer just inside the perimeter bead. The roughness value is largely dependent on the amount of this sub-perimeter region that is visible on the exposed part of a layer on an inclined surface. At surface inclinations (say  $15^\circ - 35^\circ$ ) where the sub-perimeter region and the corresponding perimeter bead are the only exposed part of the layers, the roughness is high.

Any 3-dimensional part is made up of planar and/or non-planar surfaces. Planar surfaces can be horizontal, vertical or at any inclination with a reference plane (throughout this paper we use a horizontal plane representing the build base as the reference plane). Non-planar surfaces usually consist of the set of quadrics (cylindrical, conical, spherical, etc.) or higher degree freeform surfaces. In a particular orientation, each of a part's surfaces can be either upward or

downward-facing (overhang surfaces) with respect to the base plane and a surface, depending on this will have different surface roughness. One fact to be kept in mind is that not all downward-facing surfaces require support structures. In QuickSlice® which is a software tool that works on STL files before building parts on the FDM machine, the user can control which overhang surfaces get supports under them based on their inclination with the base plane [5]. Among the support options available, at medium supports (where an inclined surface is supported if 50% or more of its perimeter roads are unsupported by the roads of the previous layer), surfaces at inclinations below the critical angle of 43° with the base plane are supported by support structures while at high supports (for inclined surfaces with 25% or more of its perimeter roads unsupported by roads of the previous layer), the critical angle is 26°. Normally downward-facing surfaces are smoother (lower surface roughness value) than upward-facing surface at the same absolute angle with the base plane and in general, horizontal and vertical surfaces of a part get the best surface finish though it has been found out through experiments that vertical surfaces on FDM parts are smoother compared to horizontal surfaces. This is because there are a lot of defects on the horizontal surface of a layer like sub-perimeter voids, inter-road defects, etc., which do not occur on vertical surfaces [6]. For all surface inclinations between the absolute values of 0° and 90°, the angle of inclination of the surface with the build plane decides the roughness on that surface. Typically, surfaces at shallow inclinations with the base plane are rougher than surfaces at higher inclinations. This behavior is not linear - roughness value does not increase linearly with inclination angle. At first we had perceived that a quadratic curve would fit this behavior as shown in Figure 1.

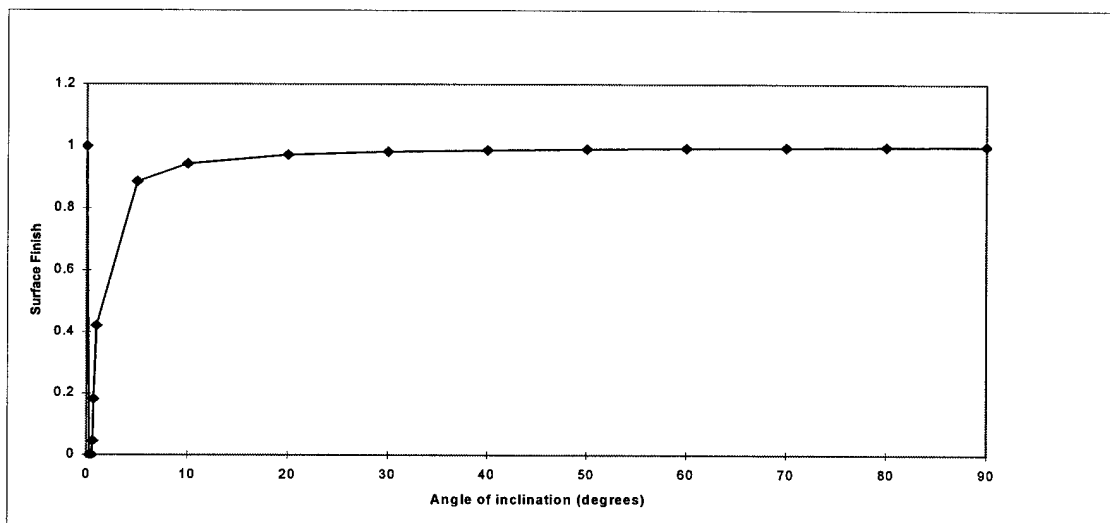


Figure 1 Chart showing surface finish (smoothness) vs. surface plane orientation

This curve characterizes surface roughness by the length of the exposed part of a step on a sloped surface at an inclination between 0° and 90° as shown in Figure 2. The length of the exposed part of a step (Y) is calculated by the equation:

$$Y = \text{layer thickness } (X) / \tan\theta$$

The concept behind using this equation is, the lower the inclination  $\theta$ , the greater is the length Y and for a constant layer thickness along the height of a sloped surface of a part, the

greater the difference in area between the actual surface and the desired surface which implies a greater surface deviation. This model is the initially forecasted mathematical model.

To validate this theoretical model, we built parts with planar surfaces at various inclinations and took roughness measurements on it using a surface profile scanner having a LVDT diamond stylus with a

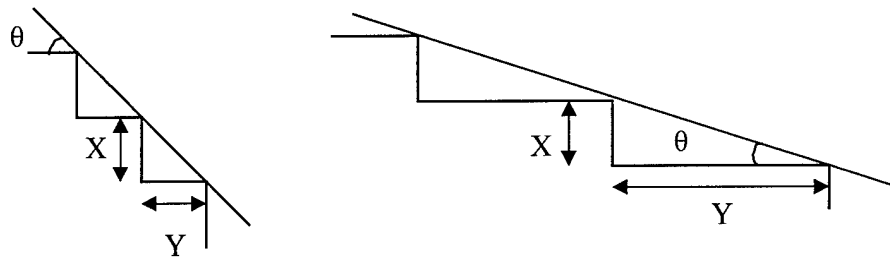


Figure 2 Figures showing the horizontal part of a step on a steep and shallow angled inclined surface

radius of 5  $\mu\text{m}$ . At the end of this data acquisition phase, we realized that we would need a cubic B-Spline curve to fit the data points representing surface roughness (Roughness Average number  $R_a$  in micro inch) at inclinations between  $0^\circ$  and  $90^\circ$ .

The part build process on a RP machine starts with the generation of a .stl file of the part. This .stl file is a surface (boundary) representation of a part in terms of a mesh of planar facets or triangles. In other words, all bounding surfaces or features of a part whether planar or non-planar and whether internal or external are represented by a mesh of planar triangles. Of course, surface representation by planar triangles is not what one would prefer during the data translation from a CAD file to a .stl file as it introduces some dimensional errors on curvilinear surfaces. Since the triangles literally ‘stick’ to the part surfaces and are planar, roughness values obtained on planar surfaces of parts during our data acquisition phase can be directly quoted as the roughness of a triangle at a particular inclination which decides the roughness on the area of the surface of the part it covers. Thus surface roughness values obtained on planar surfaces can be assigned to non-planar surfaces too.

In the software tool described later in this paper, part orientation (which decides the inclination of the part’s constituent surfaces with the base plane) and layer thickness are the two parameters that can be manipulated to change surface finish on the surfaces of a part built on a FDM machine. The part ‘read’ from its .stl file is displayed with all its surfaces color-coded, which is the net effect of coloring individual triangles based on their inclination with the base plane.

## Procedure

The process of obtaining roughness values on both upward and downward-facing planar surfaces at various inclinations started with the building of parts with such surfaces separately at 0.010” and 0.007” layer thickness on a FDM1650. Figure 3 shows one such part.

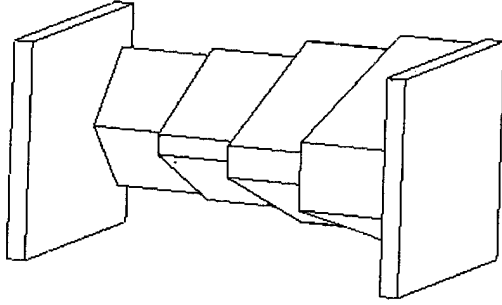


**Figure 3 A typical part used to obtain surface roughness values on its constituent planar surfaces**

Each of these parts has a set of upward-facing planar surfaces at certain inclinations between  $0^\circ$  and  $90^\circ$  and their corresponding downward-facing surfaces. The statistical roughness values on these surfaces were obtained by using a Sheffield Profile Measurement System which is a contact type surface roughness measurement system. Each measurement was taken over a traversal length which was ten times the sampling length or cutoff length of  $0.030''$ . So the roughness of a surface characterized by a Ra value (reported in micro inches) is a value

averaged over ten cutoff lengths. All measurements were taken at  $45^\circ$  to the direction of the lay since positioning the stylus so as to take measurements perpendicular to the lay is a cumbersome task. A check was made by taking a measurement perpendicular to and at  $45^\circ$  to the lay and the roughness data obtained showed that the difference was quite small. More surfaces were built and measured in the shallow inclination ( $0^\circ - 45^\circ$ ) region because of the greater variation of roughness in this region. The data obtained from the measurements and shown as a plot of surface roughness plotted against surface inclination in Figure 4 and Figure 5 proved this point.

The statistical data so obtained was compiled and used as a basis for assigning a roughness value to a triangle representing an area of a surface of a part from a stl file. Some interesting observations from the roughness data have been listed below:

1. The surface roughness (Ra) values reported in micro inch followed a more or less similar pattern for upward and downward facing surfaces on parts with slices  $0.010''$  and  $0.007''$  thick. A 'bell-shaped' pattern is seen in the  $10^\circ - 40^\circ$  region with the peak appearing between  $15^\circ - 25^\circ$ . The roughness decreases after the  $40^\circ$  inclination and decreases without much significant change to the lowest roughness value at  $90^\circ$  (a vertical surface).
2. At a particular angle, the roughness values on overhang surfaces are normally lower than on up-facing surfaces. This is logical since on an overhang surface filaments on the surface get deposited on an underlying layer of supports which introduces a smoothing effect on the modeling filaments. This effect is very much visible on parts made of  $0.010''$  thick slices.
3. The effect stated above is reversed in the  $10^\circ - 40^\circ$  region for parts made up of  $0.007''$  thick slices

## Software

A software tool has been developed as part of this project. It basically serves as a visual verification and informative tool that helps the user decide a /set of good orientation to build a part on a FDM machine and also provides him with an array of useful information and statistics.

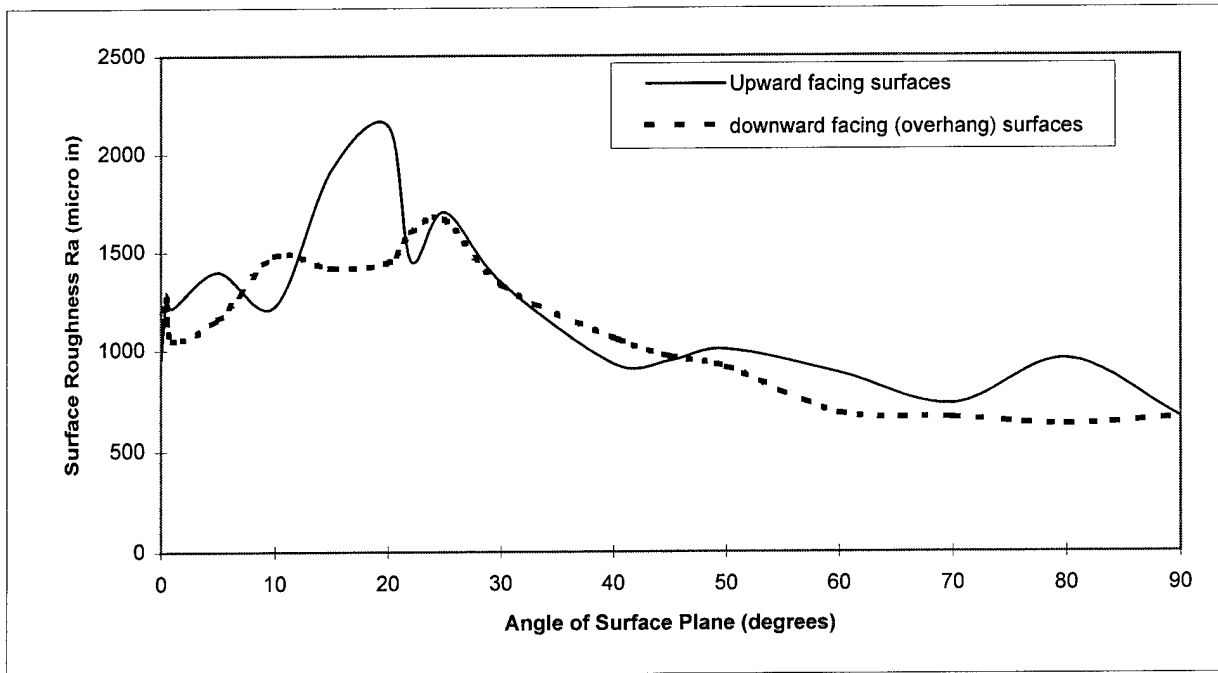


Figure 4 Surface roughness Ra (micro inches) for upward and downward-facing surfaces at various inclinations at 0.010" layer thickness

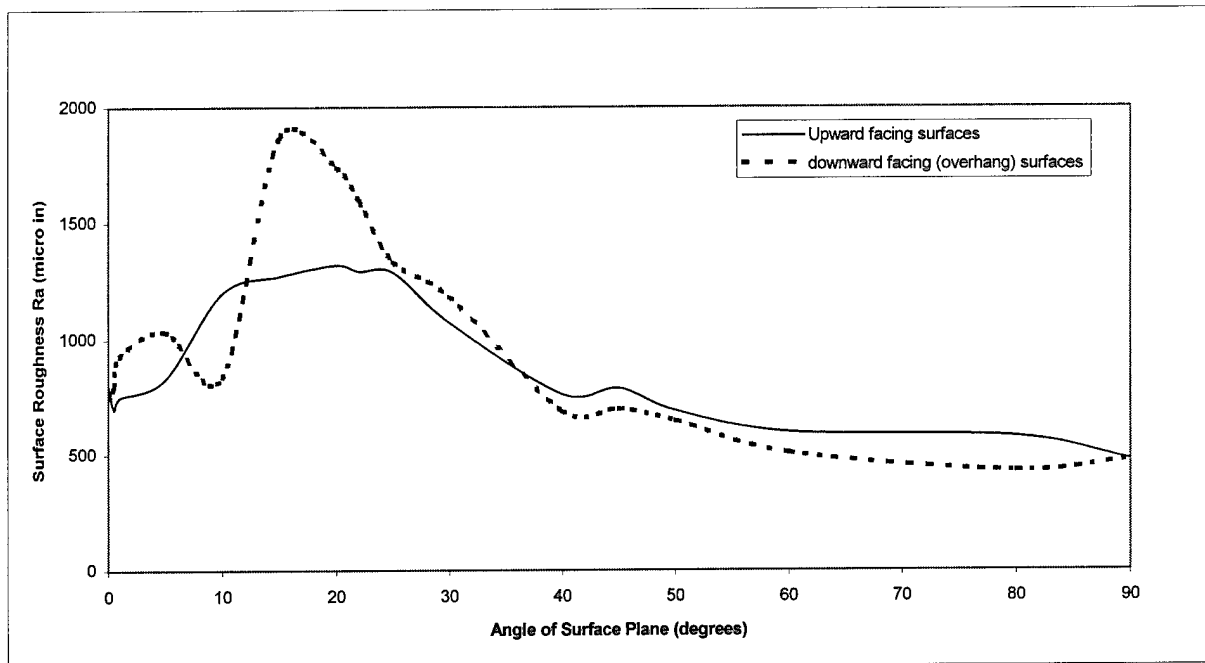


Figure 5 Surface roughness Ra (micro inches) for upward and downward-facing surfaces at various inclinations at 0.007" layer thickness

The main visual shown by the software when a user opens a .stl file is the part in the default orientation i.e., the orientation of the part when saving it in .stl file format. With the click of a button, the whole part is displayed as a color-coded entity with all its surfaces displayed with a hue of colors. The colors on the surfaces of the part is the net result of shading each component triangle with the color obtained by mapping its surface roughness value due to its inclination to a RGB color. Figure 6 depicts the steps that the software goes through before coming up with the color mapping on the part's surfaces.

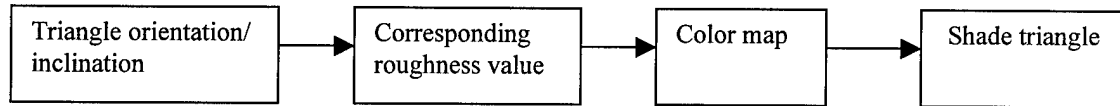


Figure 6 Sequence of steps followed in obtaining the color-coded part

The user can choose to reorient the part in either of two ways: specify values of rotation about the x, y or z-axis or use the mouse interactively. Irrespective of the mode the user may choose to operate in, any reorientation of the part will change the color-coding pattern on the surfaces of the part since all the surfaces and hence the triangles describing them are at new inclinations with respect to the base plane.

Another feature that will be incorporated is to give the user an option to view both the predicted and desired surface finishes simultaneously on a surface. The *predicted* finish is the estimated finish when produced that is calculated according to the orientation of the face. The *desired* finish is that specified in the CAD model as a tolerance. Such a surface will be displayed with two colors matching both the predicted roughness values in the present orientation superimposed by the stripes of the color corresponding to the predicted roughness. As the user reorients the part, the predicted color changes and the goal will be to orient the object such that the predicted and desired finishes are the same, that is, the stripes disappear and the surface is one color.

The volume of support structures required in a particular orientation is reported. Provision has been made for the user to view the part from various angles while the part remains fixed in a particular orientation. Several intermediate orientations can be saved for future review and any of these can be saved as a stl file of the part in the new orientation. The user also gets information regarding the percentage of triangles that are horizontal, vertical and in the critical range (between 10° - 40°).

## Results And Conclusions

From the data collected, it is obvious that the surface roughness deteriorates between 10°-40° with the worst occurring in the 15° - 25° for both upfacing and downfacing surfaces at 0.010" and 0.007" layer thickness. So whenever possible, it is better to avoid having surfaces oriented at angles in this range. The layer composition on the FDM is uneven especially near the edges.

The software can be used as a useful educational tool to improve the user's knowledge of the dependency of surface finish on layer thickness and orientation. It will be handy to RP users in reducing the time and costs during the part building phase since the possibility of making a wrong decision about the orientation and layer thickness is reduced. Portability is an important end-result of this research. The software in its current state can be used to evaluate the effect of two build parameters- orientation and layer thickness on surface finish *before* starting the build on a FDM1650 at the default process parameters at 0.010" and 0.007" layer thickness. But the same software can be used on an RP machine based on any layered manufacturing process. For this, the software can be made to read the set of surface roughness data from surfaces on parts built on that machine. Adding more parameters that affect surface quality including material properties and process parameters such as air gaps, widths of roads, etc., can increase the usefulness of the software. Also, it can be made more general by making it a tool to *predict* part quality.

## Acknowledgements

We would like to thank Don Benjamin of Allied Signal Aerospace, Tempe, AZ, for providing us the opportunity to use his surface profile scanner without which this work could not have been done. Our special thanks to Dr. Anshuman Razdan and Ben Steinberg for their invaluable help in developing the software.

## References

- [1] Thompson, D.C. **The Optimization of Part Orientation for Solid Freeform Manufacture**, Masters Thesis, University of Texas, Austin, December 1995
- [2] Frank, D. Fadel, G. **Expert System Based Selection of the Preferred Direction of Build for Rapid Prototyping Processes**, Proceedings of the Fifth International Conference on Rapid Prototyping, Dayton, June 1994
- [3] Reeves, P.E. Cobb, R.C. **Surface Deviation Modelling of LMT Process- A Comparative Analysis**, 5<sup>th</sup> European Conference on Rapid Prototyping and Manufacturing, pp59 - 75
- [4] Lan, P.T. Chou, S.Y. Chen, L.L. Gemmill, D. **Determining Fabrication Orientations for Rapid Prototyping with Stereolithography Apparatus**, Computer Aided Design, volume 29, number 1, January 1997, pp53-61
- [5] Chalasani, K. Jones, L. Roscoe, L. **Support Generation for Fused Deposition Modeling**, 6<sup>th</sup> Solid Freeform Fabrication Symposium 1995, pp229 - 241
- [6] Agarwala, M.K. Jamalabad, V.R. Langrana, N.A. Safari, A. Whalen, P.J. Danforth, S.C. **Structural Quality of Parts Processed by Fused Deposition**, Rapid Prototyping Journal, volume 2, number 4, 1996, ISSN 1355-2546

---

<sup>i</sup> Strataysys, Incorporated, Minneapolis, MN, USA

# Machine Design, Control and Performance of Automated Computer-Aided Manufacturing of Laminated Engineering Materials

Brian B. Mathewson\*, Ravi Hebbart, Sangeun Choitt,  
Wyatt S. Newmant, James D. Cawley††† and Arthur H. Heuer†††

\*CAM-LEM Inc., Cleveland, OH 44108.

†Dept. of Electrical, Systems, Computer Engineering and Science; ††Dept. of Mechanical and Aerospace Engineering; †††Dept. of Material Science and Engineering;  
Case Western Reserve University, Cleveland, OH 44106.

## Abstract

This paper describes machine design and control aspects of automating a viable CAM-LEM layered manufacturing process. The cut-then-stack sheet-based approach permits using sheet materials of different thicknesses, enabling optimization of build speed. Further, this cut-then-stack approach offers the possibility of assembling parts with multiple materials interleaved both layer-to-layer as well as within each layer. The key to realizing these prospective advantages is precise and reliable extraction and assembly of laser-cut regions from sheet feedstock. This paper presents our design approach and examples created on an automated CAM-LEM machine. It will be shown that the use of fugitive materials, automatically assembled interleaved with engineering materials, is feasible, allowing fabrication of laminated components with internal cusps and voids and improving the dimensional stability of components during post-processing. Results of this work are presented and applications of the technology are reviewed. Extensions to tangent-cut thick-sheet interleaved assemblies are described.

## I. Introduction

The CAM-LEM (Computer-Aided Manufacturing of Laminated Engineering Materials) process fabricates components using layers of sheet material via a cut-then-stack approach. The CAM-LEM process was introduced in [3,12], and further developments have been presented in [1,2,4,5]. While the cut-then-stack approach involves significant material-handling challenges, a prospective advantage is that different types of materials may be interleaved both layer-to-layer as well as within each layer. Benefits of mixing multiple materials include: enabling support for overhanging structures during the build; providing support to prevent slumping of thin unsupported areas during fabrication and/or post-processing; and achieving even distribution of pressure throughout the component if pressure-aided lamination is used.

This paper describes a machine that has been optimized for fabrication of laminated components using multiple materials, including use of fugitive materials assembled among persistent materials within each build layer. It also describes how the CAM-LEM machine can take advantage of thick and thin feedstock options. Finally, we demonstrate a method for extending our cut-then-stack technique to handling thick, tangent-cut slabs.

## II. The CAM-LEM Machine

CAM-LEM, Inc. has been developing a machine optimized for fabrication with multiple materials per layer. The current design supports up to five different in-feed options during automated fabrication. A picture of the machine is shown in Figure 1. At left is the feedstock carousel, which rotates one of six stacks of material into position for use in the machine. At the top center is a two-axis gripper, which performs most of the material handling in the system. The two-axis X-Y cutting table is just left of center, with the laser optics above. To the right is a waste chute, which collects waste materials cleared from the cutting table and directs them into a waste bin.

The gripper incorporates three independently controlled partitions: at left is a 100x100mm gripper for feeding sheet material from the carousel onto the cutting table. The center and right grippers are each capable of handling regions up to 150x150mm in size.

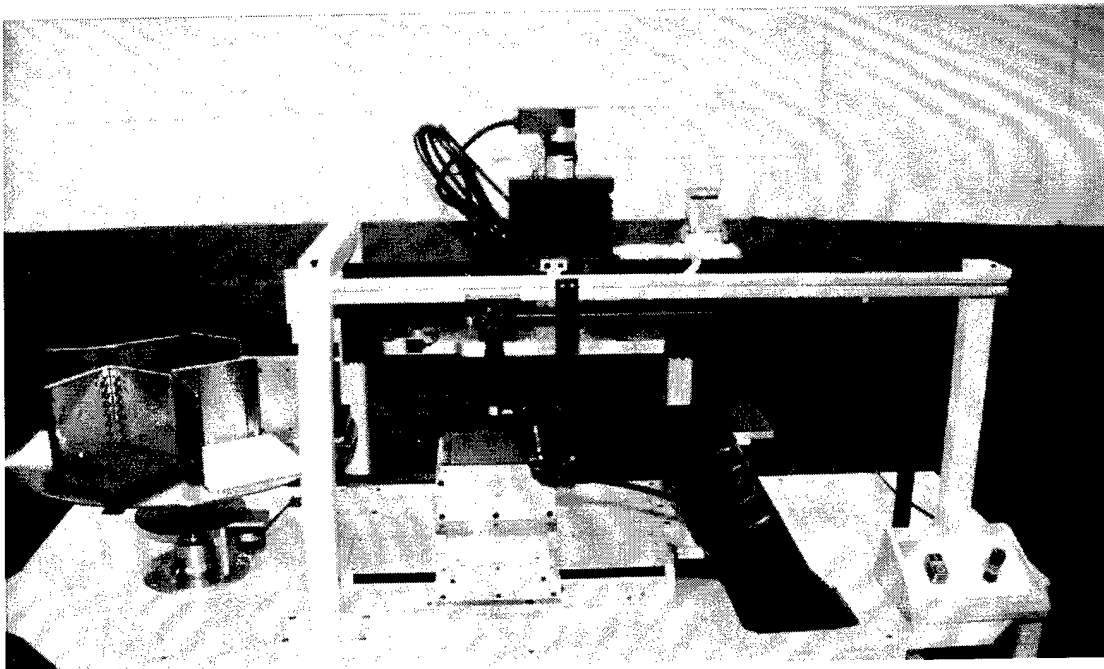


Fig 1: CAM-LEM machine

They are used to pick up and stack laser-cut materials, leaving the waste behind. This technique, described in [2], involves the use of a perforated mask through which vacuum pressure is drawn in selected areas. These areas are defined by the regions to be picked up, but may also be optimized to pick up multiple consecutive layers, depending upon the geometry of the layers.

Typically the left gripper handles the fugitive support material, and the right gripper handles the persistent component material. Because the masks required for the fugitive and persistent materials are complementary, a fugitive mask cannot be used for handling persistent material, and vice versa. The multiple-gripper design enables exploitation of multiple-use masks without the material-handling and space penalties associated with storing and retrieving masks.

The cutting table is mounted to a 200mm by 300mm X-Y positioning device. The active area of the cutting table is 150x150mm. The surface of the table has been designed to provide a high density of support, minimize reflection of the laser, collect fumes and debris due to laser-cutting, and provide vacuum to hold materials securely to the cutting table.

During multi-layer fabrication, the process must prevent any single error from compromising the entire build. One solution to this is to visually check each set of materials after it has been selectively removed from the laser-cut sheet, but before it is assembled onto the stack. We have incorporated a small CCD camera that can image either of the stacking grippers prior to assembly. At present, an operator views these images at run time to assure error-free handling prior to assembly. In the future, automated scene analysis will be performed, eliminating the need for human monitoring.

The most common errors encountered to date occur during cutting, gripping or waste clearing. During cutting, the material must be cut completely and cleanly, the material must not adhere to the cutting table (e.g., due to melting and resolidification of binder materials), and the material must be clamped to the table with sufficient vacuum suction to prevent displacement of cut regions by the laser-cutting air-jet assist. The first two issues are directly related to optimizing the cut quality by tuning laser power, cut speed, air-jet nozzle air pressure, and nozzle standoff. The last is simply a matter of replacing the cutting-table vacuum filter (which collects debris from the cutting operation) when the flow resistance becomes excessive.

During gripping, the most common errors are picking up excess material (the inclusion of waste material when picking up desired material), and leaving desired material on the cut table. The former is due to two factors: the geometry of the mask hole pattern and the porosity and mass density of the material. If mask holes are situated too close to the boundary of a part to be lifted, leakage may occur, resulting in undesired suction exerted on neighboring waste material. The second type of error, leaving behind materials meant to be picked up, is less common, and generally attributed to variations in the thickness of the mask and/or the flatness of the gripper and cutting table. The mask must make intimate contact with the desired material, or else sufficient vacuum force will not develop in order to lift and hold the piece. If the gripper and cut table surfaces are not flat or the mask material is thinner in some area, the material may not be picked up. Both these effects can vary based on the amount of vacuum and flow provided to the gripper plenums.

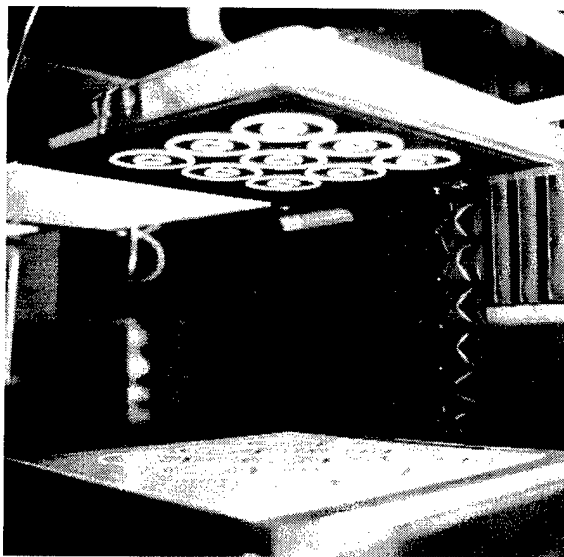


Fig 2. Fabrication of 9 parts in parallel.

Fig 2 illustrates correct operation of the gripper. In this photo, the gripper (above) has extracted a set of complex regions from the cutting table (below). The grasped parts are precisely located and ready for assembly onto the build stack.

Waste clearing from the cutting table is achieved by aiming a thin, 150mm wide region of compressed air generated using an air knife at the edge of the cutting table, then moving the table past the knife. The air lifts waste material up and into the waste chute, where it is directed down into a waste receptacle.

### III. Automation of Fugitive Supports

Some means of fugitive support is present in all commercial SFF machines. The technique closest to our approach is that used in SDM [10,13], where fugitive materials are built up alternately with persistent material, producing flat surfaces at each build layer.

While there are similarities, the approach to utilizing temporary support structures in CAM-LEM is unique among SFF processes. In the CAM-LEM process, temporary supports are created from fugitive materials, laser-cut from sheet feedstock and assembled onto the build stack alternating with assembly of the desired (persistent) material. The fugitive material is later removed in a bulk post-processing operation (see [12]). Within each layer, persistent and fugitive materials are assembled interlocking, in the style of a jigsaw puzzle, resulting in a smooth, horizontal surface at each layer of the build. Based on a model's STL description, the shapes of fugitive materials are computed automatically, layer by layer, as the exclusive OR of a (default) square, continuous fugitive sheet and the computed regions of desired persistent material. Fugitive shapes thus computed are automatically cut and assembled. This operation eliminates the need for manual "weeding", employed in semi-automatic extensions of Laminated Object Manufacturing (LOM) to engineering materials [14].

An example of the fugitive build process is shown in Figures 3 through 5. In this example, 1.2mm thick paperboard was used to illustrate the process and to provide good contrast. Gray paperboard represents desired persistent material, and white paperboard emulates fugitive material.

Figure 3 shows the cut and stacked persistent material for the first build layer. Figure 4 shows the assembly after cutting and stacking the fugitive material for this layer.



Fig 3. Persistent material.



Fig 4. Fugitive material integrated with persistent.

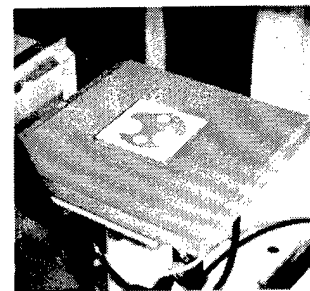


Fig 5. Stack after completion of fourth layer.

stack several layers later, with each completed layer constituting a horizontal surface of interlocking persistent and fugitive materials on which to build.

The sequence of operations to create such a stack is: 1) acquire a sheet of persistent material from the carousel and deposit it on the cutting table; 2) cut the contours of the desired persistent regions; 3) extract the desired persistent regions with the "part" gripper; 4) prepare the surface of the sub-assembly for lamination; 5) stack and laminate the persistent regions onto the build stack; 6) clear the waste material from the cutting table; 7) acquire a sheet of fugitive material from the carousel and deposit it on the cutting table; 8) cut the contours of the desired fugitive regions; 9) extract the desired fugitive regions from the cutting table using the "fugitive" gripper; 10) prepare the subassembly for bonding the next layer of fugitive to the build stack; 11) assemble and bond the fugitive regions (interlocked with the persistent regions for this layer) onto the build stack; 12) clear the waste material from the cutting table; 13) increment the z-height under consideration and repeat from step 1.

In the above sequence of operations, many of the steps can be executed in parallel. For example, assembly can be performed while waste is being cleared from the cutting table. Further, if new feedstock is provided to the cutting table before a grasped set of regions is assembled, then laser cutting can occur in parallel with preparation of the build stack for lamination to the next layer. By parallelizing operations, the build speed of the process is limited primarily by the laser cutting speed and not by the material handling requirements.

Steps 4 and 10 in the sequence above are required to provide at least temporary structure to the assembly. In previous work, we have described the importance of defect-free consolidation between layers. Our approach has been to dispense a fluid which acts as both a solvent (of the binder material) and an adhesive, then to stack the next layer and apply pressure rolling to assure intimate contact and express any surplus fluid or entrapped air. In our latest variation, we are exploring use of a heat-activated adhesive film pre-applied to the uncut feedstock. The top surface of the build stack is heated via a lamp, activating the adhesive just prior to assembly of the next layer. Early results are encouraging, indicating that this simpler lamination technique is also more robust than our previous fluid-based approach.

#### IV. Use of Multiple Materials

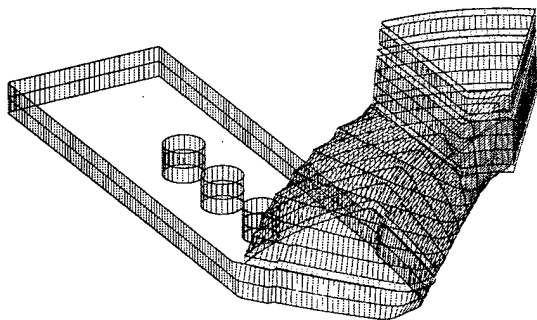


Fig 6. Model reconstructed with thick and thin layers

As shown in Fig 1, our CAM-LEM machine design is currently capable of drawing from 6 different stacks of sheet materials. As described, we allocate one stack each to gripper masks, fugitive materials, and persistent materials. The additional sites can be used for introducing additional materials. With the cut-then-stack process, CAM-LEM can vary the material constituency of an assembly layer-by-layer in the vertical direction, as well as within each layer, as we have demonstrated with fugitive materials. In addition, material variations can be

more numerous if feed stacks are loaded pre-sorted, with the planned required sequence of materials made available in the order of the stack.

Another valuable option for the multiple feedstock sites is to make available multiple thicknesses of sheets. For fast build rates, it is desirable to use the maximum feasible thickness material. However, the maximum acceptable layer thickness typically varies as a function of build height. An example is shown in Fig 6. The model shown in this figure is adequately approximated with relatively thick, tangent-cut layers. However, there are crucial features, e.g. steps and flats, that must occur at specified elevations to within a tolerance smaller than the thickness of our default sheet material. By having thin sheets also available on demand, the system can build with thick layers when acceptable, yielding faster build rates, and can insert thin layers, as required, to satisfy tolerance demands. Use of thick and thin layers has been treated theoretically (see, e.g. [6,7,8,9]), but SFF processes have not been able to exploit this option to the degree achievable by the CAM-LEM system introduced here.

### V. Extensions to Tangent-Cut Layers

In parallel with the CAM-LEM, Inc. machine design, researchers at Case Western Reserve University have been pursuing a CAM-LEM machine capable of building with tangent-cut thick slabs. A challenge of this extension is material handling after laser cutting. If a slab is cut with upward-facing surface normals about its edge, then the waste material can be extracted vertically without interfering with the cut part, whereas the cut part cannot be lifted without interfering with the waste. Conversely, if the cut part has all downward-facing edge normals, then it can be lifted without interfering with the waste. If, however, the part has both upward and downward-facing edge normals, then neither the waste nor the part can be extracted without interference. (A mathematically related problem is confronted by Shape Deposition Modelling in the process of depositing and machining persistent and fugitive materials to conform to the desired surface normals [13]).

To resolve this problem, we have proposed utilizing a second-pass, vertical cut through the waste material to enable extraction of part of the waste, followed by extraction of the desired cut piece. The process is illustrated in Fig 7. Figure 7a shows the top and bottom contours of a desired tangent-cut thick layer, where the bold line represents the bottom contour and the faint line represents the top contour. Figure 7b shows the result of subtracting the region enclosed by the top contour from the region enclosed by the bottom contour. The result represents the extent of the part's edge which has an upward-facing

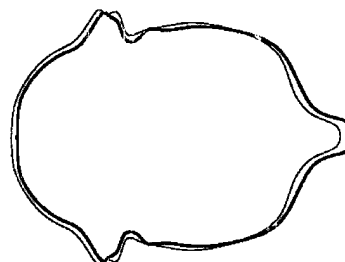


Figure 7a.



Figure 7b.

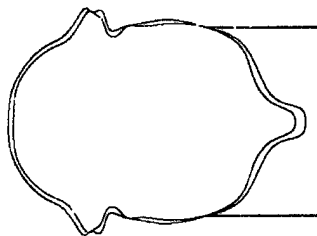


Figure 7c.

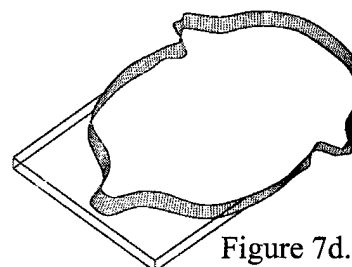


Figure 7d.

extractable by performing a second-pass cut with vertical orientation along the bold contour remaining in Fig 7b. However, in practice it was found that such a second-pass cut resulted in a chisel-point at the bottom of the waste material. For a finite-thickness kerf, this operation cut out the foundation of the waste “sliver”, upon which the waste sliver would drop into the wedge-shaped kerf. Upon dropping into the kerf, the top surface of the waste was below the top surface of the rest of the sheet, and it was thus ungraspable by the vacuum gripper.

To keep the waste graspable, we have left more waste material connected to the region we wish to extract, as illustrated in Fig 7c. This additional waste material provides z-support to maintain correct elevation of the upper surface of the part, thereby enabling manipulation via our vacuum grippers.

Having segregated a part layer’s edge into regions of upward and downward normals, manipulation without interference is possible, as illustrated in figures 8a through 8c. In Fig 8a, cutting a fugitive layer is illustrated. The desired part outline was laser cut, then the waste region (augmented with additional, connected waste material) was removed, the waste imitation of the desired part shape was removed, and the remaining waste material was transferred from the cutting table to the build platform. Figure 8b shows the result of operating on a sheet of the persistent material. The desired edge was cut, extra vertical cuts were added to the waste material occluding vertical extraction of the desired part, the resulting island of waste material was vertically extracted and discarded, and finally the desired tangent-cut part layer was vertically extracted and stacked within the “frame” of fugitive material originally positioned per Fig 8a.

In Fig 8c, a sheet of fugitive material was cut, again conforming to the desired contour, augmented with the second-pass vertical cut in the waste material. The waste material lying above the upward-facing edge normal regions (and the connected additional mass of waste) was removed. This contribution to the fugitive was stacked on the assembly table by the robot, completing the construction of a fully-dense layer with embedded fugitive materials.

## VI. Conclusions:

In this paper, we introduced the design of an automated process for CAM-LEM fabrication. Notable in the design is the availability of 6 feedstock options from an automatic carousel and the use of multiple grippers on a common gantry to improve material-handling efficiency. Exploitation of feedstock options enables the use of multiple sheet thickness alternatives, as well as use of fugitive support materials. The use of interleaved fugitive materials—introduced conceptually in the past—is reported here for the

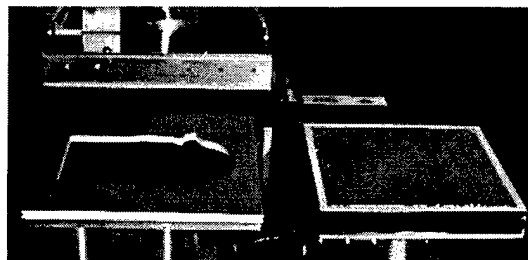


Fig 8a. Fugitive section transferred.



Fig 8b. Persistent material transferred.

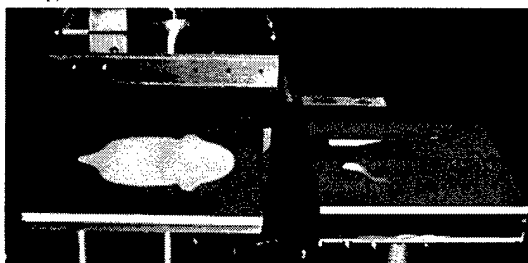


Fig 8c. Completed layer.

first time as being accomplished successfully in practice. Finally, an algorithm for extending the fugitive filler technique has been successfully demonstrated for tangent-cut part layers.

### Acknowledgements:

This work was supported at CWRU in part by the National Science Foundation under grant number DMI94-20373 and in part by Sandia Laboratories, DOE, under contract AU4857. Work at CAM-LEM, Inc. was supported by an SBIR award from the Army Research Office, contract DAAL01-96-C-0061. This support is gratefully acknowledged.

### References

1. Zheng, Y., and Newman, W.S., "Software Design Challenges for Computer-Aided Manufacturing of Laminated Engineering Materials", *The Sixth European Conference on Rapid Prototyping and Manufacturing*, Nottingham, UK, July 1997.
2. Newman, W.S., Mathewson, B.B., Zheng, Y., and Choi, S., "A Novel Selective-Area Gripper for Layered Assembly of Laminated Objects", *Robotics and Computer-Integrated Manufacturing*, Vol. 12, No. 4, pp. 293-302, 1996.
3. Newman, W.S., Zheng, Y., and Fong, C.C., "Trajectory Generation from CAD Models for Computer-Aided Manufacturing of Laminated Engineering Materials", *Proceedings of the 26<sup>th</sup> International Symposium on Industrial Robots*, Singapore, pp. 153-158, Oct 1995.
4. Choi, S., Hebbbar, R., Zheng, Y., Newman, W.S., "CAD and Control Technologies for Computer-Aided Manufacturing of Laminated Engineering Materials", *Proceedings of the Solid Freeform Fabrication Symposium*, University of Texas at Austin, Austin, Texas, pp. 643-651, Aug 1997.
5. Zheng, Y., "Enabling Computational Techniques for Tangential-Building Solid Freeform Fabrication", Ph.D. Thesis, Aug 1997, Department of Electrical Engineering and Applied Physics, Case Western Reserve University.
6. Jager, P.J. de, Broek, J.J., and Vergeest, J.S.M., "Using Adaptive Ruled Layers for Rapid Prototyping: Principles and First Results", *Proceedings of the Solid Freeform Fabrication Symposium*, University of Texas at Austin, Austin, Texas, pp. 585-592, Aug 1997.
7. Kulkarni, P., and Dutta, D., "Adaptive Slicing of Parametrizable Algebraic Surfaces for Layered Manufacturing", *Proceedings DE-Vol. 82, Design Engineering Technical Conferences*, Volume 1, ASME, pp. 211-217, 1995.
8. Kulkarni, P., and Dutta, D., "An Accurate Slicing Procedure for Layered Manufacturing", *Computer Aided Design*, Vol. 28(9), pp. 683-697, 1996.
9. Suh, Y., and Wozny, M.J., "Adaptive Slicing of Solid Freeform Fabrication Processes", *Proceedings of the Solid Freeform Fabrication Symposium*, University of Texas at Austin, Austin, Texas, pp.404-411, 1994.
10. Merz, R., Prinz, F.B., Ramaswami, K., Terk, M., and Weiss, L.E., "Shape Deposition Manufacturing", *Proceedings of the Solid Freeform Fabrication Symposium*, University of Texas at Austin, Austin, Texas, pp. 1-8, Aug 1994.
11. Kumar, C., Jones, L., and Roscoe, L., "Support Generation for Fused Deposition Modeling", *Proceedings of the Solid Freeform Fabrication Symposium*, University of Texas at Austin, Austin, Texas, pp. 229-241, Aug. 1995.
12. Mathewson, B.B., Newman, W.S., Heuer, A.H., and Cawley, J.D., "Automated Fabrication of Ceramic Components from Tape-Cast Ceramic", *Proceedings of the Solid Freeform Fabrication Symposium*, University of Texas at Austin, Austin, Texas, pp.253-260, Aug. 1995.
13. Weiss, L., Prinz, F., Neplotnik, G., Padmanabhan, P., Schultz, L., and Merz, R., "Shape Deposition Manufacturing of Wearable Computers", *Proceedings of the Solid Freeform Fabrication Symposium*, University of Texas at Austin, Austin, Texas, pp. 31-38, Aug. 1996.
14. Griffin, C., Daufenbach, J., and McMillin, S., "Solid Freeform Fabrication of Functional Ceramic Components Using a Laminated Object Manufacturing Technique", *Proceedings of the Solid Freeform Fabrication Symposium*, University of Texas at Austin, Austin, Texas, pp. 17-24, Aug. 1994.

## **Build Time Estimations for Large Scale Modelling**

G. Mensing and I. Gibson  
University of Hong Kong

### **Abstract**

Achieving speedy results in model making is very much desired if not a necessity in almost any manufacturing industry. There is no doubt that rapid prototyping contributes to this process. It is generally considered that when compared to conventional machining techniques like milling, the current rapid prototyping systems appear to be much faster. This is certainly true for complex, small objects. However, this is not always applicable to simple, large and bulky parts.

There are a number of projects and systems concentrating on the fabrication of large models. Work is being carried out at the University of Hong Kong, using milling along with slicing technology. This report compares some of the rapid prototyping systems with milling. Milling is an established technology and recent developments in materials and machines used in milling make it a good alternative to rapid prototyping when it comes to large scale modelling.

### **Introduction**

Industry has often expressed the need for prototypes larger than current rapid prototyping technology is capable of. A number of approaches [1][2] have been developed to address this. The system at the University of Hong Kong is similar to those developed at Ford Research [3]. This report follows as a result of the proposed system for large scale rapid prototyping [4]. Milling, combined with layer based technology results in faster prototyping for large, bulky objects. Milling is also more appropriate for tooling applications because of the variety of materials that can be used. Some simple objects of variable sizes are discussed with the view to understanding how rapid prototyping systems would deal with making models that are larger than they are currently capable of. Extrapolation is used to calculate the times needed for the largest models since these are too big for the current systems.

The systems are compared using build time. Companies are willing to pay more in the short term as long as there is a considerable saving in time. This makes the company more competitive and can save money in the long run. However rapid prototyping may not save time when building large models compared with conventional technology.

## **1. The rapid prototyping systems**

First some rapid prototyping systems are discussed. These are the systems that were used in the test. Each system displays characteristics that may make it difficult to construct them so they are capable of making larger models.

### **1.1.1. StereoLithography – 3D-Systems**

StereoLithography [5][6] uses photo-reactive polymers, which react to ultraviolet (UV) light. For this, the system utilises a precisely directed laser beam. When resin is struck by sufficient UV light,

it solidifies (polymerises). By scanning UV light onto the surface of the polymer according to the design, a layer (slice) of a model is created.

To make the next and subsequent layers, the object is lowered into the vat filled with resin. This way new resin flows over the object. Next, this new layer of resin is solidified. The process continues until the object is finished.

This process is accurate, but very limited in the variety of materials. It is possible though to use the models to manufacture moulds for casting.

### **1.1.2. Model Maker – Sanders Prototype**

Sanders [7] developed the Model Maker, a plotting system where a liquid-to-solid inkjet plotter with a separate Z-axis input is used. An inkjet subsystem rides on a precision X/Y drive carriage and deposits both thermoplastic and wax materials on the build substrate. The X/Y drive carriage also energises a flatbed milling subsystem for maintaining precise Z-axis dimensioning of the model by milling off the excess vertical height of the current build layer. A support material is used to support overhangs and cavities in the model during the build. Droplets are placed upon the build substrate to within 0.00025 inches (0.007 mm) in the X and Y directions. The droplets stick to each other during the liquid-to-solid phase transition to form a uniform mass. After solidification the milling of the layers immediately follows the deposition cycle. It is a slow but accurate process and only thermoplastic materials can be used.

### **1.1.3. Fused Deposition Modelling - Stratasys**

With Fused Deposition Modelling or FDM [8], a temperature-controlled head extrudes thermoplastic material layer by layer and thus creating a model. The CAD-model is sliced and, if necessary, supports are created similar to the StereoLithography process. Path data is then downloaded to the FDM system. The system operates in the X, Y and Z-axes. In effect, it draws the model one layer at a time.

Thermoplastic modelling material, a wire of 0.070 inches (.178cm) in diameter feeds into the temperature-controlled FDM extrusion head, where it is heated to a semi-liquid state. The head extrudes and deposits the material in ultra-thin layers (0.05 to 0.762 mm) onto a fixtureless base. The head directs the material into place with precision. The material solidifies, laminating to the preceding layer.

### **1.1.4. Selective Laser Sintering - DTM**

The Sinterstation, from DTM [9] works with powder, which is selectively sintered by means of a CO<sub>2</sub> laser. A roller spreads powder on a bed. A laser selectively sinters this layer. The model is indexed down. This process continues until the model is completed. An advantage of this process is that it does not need supports. DTM is in the process of developing a wider variety of materials, and although metal powder can be used it is not quite good enough for long term tooling.

### **1.1.5. Laminated Object Manufacturing - Kira**

The machine from Kira [10], Japan, is a Rapid Prototyping Machine suitable for installation in an office environment. The machine uses paper (wood) as material and the cutting process is not carried out with a laser as used by Helisys [11], but is realised mechanically by means of a cutting plotter. A laser printer is used to print the outline of the model onto a sheet of paper. This paper is

then bonded to any previous layers. The Kira then cuts the outline of the shape of this layer. Next a new sheet of paper is added on top of the former, bonded and then cut. This continues until the model is finished.

### 1.1.6. DeskProto [milling] - Delft Spline Systems

DeskProto [12], a software package, reads the STL-file and displays its contents. Next some milling parameters such as the type of cutting tool, required accuracy, etc. are entered. DeskProto then automatically calculates the milling paths. These milling paths are sent to the desktop NC milling machine, which produces the object. This process can be done with a wide variety of materials.

## 1.2. Current Rapid Prototyping Systems on a large scale

An obvious technique for producing large scale prototypes would be to increase the size of the current systems. This might not be a trivial process.

Increasing the size of all the systems would be costly, requiring much more attention to system stability and structure. With StereoLithography, for instance, system designers would have to consider the problem of maintaining the stability of the resin over a large surface area.

Laser based systems would require much more powerful lasers and larger surface areas would also result in significant problems with the optics.

A number of the systems use plotting mechanisms (e.g. Sanders, FDM). Large prototypes would require a significant amount of travel for these mechanisms which would result in long build times.

Kira, Helisys and milling rely more on the surface area than the volume of a part. This implies that fabrication of large bulky objects using these techniques would require less energy than purely additive processes.

## 2. The test objects

For this experiment only simple objects are chosen. With basic forms, it is possible to get an idea on how much time a more complex form would need, since most shapes are combinations of the basic forms. The data obtained was primarily from build time estimators, simple geometry therefore makes it easier to produce an estimation without significant amounts of processor, user or actual build time. Users of the different technologies were asked to provide estimations for building the defined geometries, figure 1.

Every object is available in four different sizes, this is to find the relationship between size and speed for the current layer based systems and milling and also to provide a means for extrapolation.

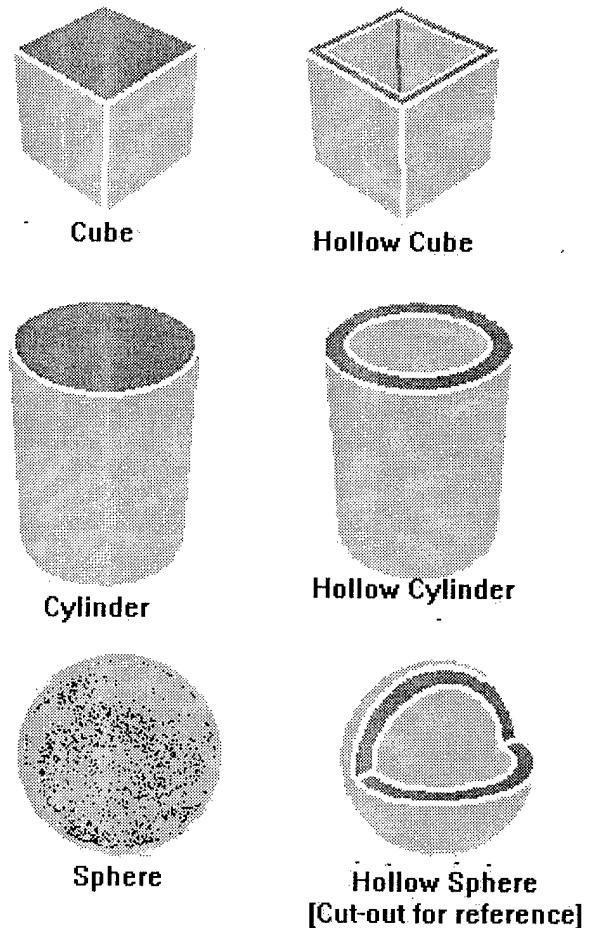


Figure 1

The objects were made in a vertical plane. This set-up is not necessarily the best for optimising the rapid prototyping system parameters.

Some rapid prototyping systems have the option to change solid structures into hollow or honeycomb structures. This has not been done with the models for this report. There is a solid and a hollow version of each model in this report, which may indicate the potential timesaving when using hollow build styles.

### **3. The experimental build data**

#### **3.1.1. 3D-Systems - SLA-500, SLA-250**

The build times were calculated with estimation software. While laser scan time depends mostly on the laser power, recoating time goes down significantly with thicker slices and smaller parts. The layer thickness that was used is 0.25 mm and STAR-Weave was used.

#### **3.1.2. Sanders - Model Maker II**

In the Model Maker II a 0.052 mm slice thickness was used for all but the largest models used in the experiment, where a 0.13 mm slice thickness was used. The build parameters are set by using what is called a 'Configuration'. This includes not only the slice thickness, but also the thickness of the line, velocities, line spacing, etc. 'Configuration' #470 ("Fast Regular") and #395 ("Concept Model") were used for all the builds. For the cubes and cylinders, an option to generate no support structures was also used, since none is needed. For the other parameters the system defaults were used.

#### **3.1.3. Stratasys - FDM-2000**

The FDM-2000 worked with a layer thickness of 0.25 mm. The object was not actually built. The build times were calculated with the build time estimator software that comes with the system, using the default settings.

#### **3.1.4 DTM - Sinterstation 2000**

The layer thickness used for the sinterstation was 0.25 mm. For the cubes and the cylinders only a 1 mm layer was made in Trueform and from this the total build time was calculated. Only half of the spheres were built because of symmetry. From this the build times were calculated.

#### **3.1.5. Kira - Laminated Object Manufacturing**

The objects were only partly built, for the cylinder and cube only 1mm layers were fabricated. The paper is 0.085 mm. From these times the total build times were calculated. The build times for the hollow objects is on the low side since minimal cross-hatching was used for the calculation. This may result in difficulties during the decubing process.

#### **3.1.6. Delft Spline Systems - DeskProto**

The milling estimates are very rough estimates, as the actual build times are very much dependant on the capabilities of the CNC milling machine and material used. For the larger models a lot of practical problems can be expected. For instance the steep vertical walls will need a very long cutter or a five-axis machine. These problems are not taken into account: assuming them to be solved.

The time mentioned in table 1 is for an accurate model in tooling board (a wood-like material). The build times for a cube (solid and hollow) and a cylinder (solid and hollow) are considered the same. This is done because the travelling time of the mill head is about the same for soft materials. Build times are also very dependent on the level of details: The more complex the model, the smaller the tool required, therefore the longer the build time. For the basic models in this test a large tool is considered: the larger the model, the larger the tool. The hollow sphere is made in two parts and later joined together.

### 3.2. The Results

STL-MODEL	Dimensions (mm)	SLA 250	SLA 500	SS 2000	Sanders MMII	FDM 2000	Kira	Milling
Cube1.stl	100x100x100	5.54	6.42	13.58	119.96	87	12.56	2
Cube2.stl	200x200x200	19.91	14.43	96.67	285.99	691	21.78	3
Cube3.stl	300x300x300	68.11	29.34	293.66	531.13	2329.5	39.52	5
Cube4.stl	1000x1000x1000	4432.76	951.68	10767.57	10427.83	86277.78	417.29	10
Hcube1.stl	Hollow 100x100x100x10	5.34	6.38	8.2	64.97	38	12.58	2
Hcube2.stl		15.6	13.56	50	152.46	296.4	31.67	3
Hcube3.stl		46.29	24.91	151.95	276.77	994.9	67.32	5
Hcube4.stl		3287.29	719.06	5065.77	2814.07	36848.15	713.00	10
Cylinder1.stl	80x100	5.34	6.38	7.61	63.45	43.5	10.75	2
Cylinder2.stl	160x200	15.35	13.5	50.44	135.3	343.4	18.33	3
Cylinder3.stl	240x300	44.93	24.51	163.33	240.27	1155.9	33.02	5
Cylinder4.stl	800x1000	2683.18	596.26	5444.25	2960.22	42811.11	347.98	10
Hcylinder1.stl	Hollow 80x100x10	5.13	6.33	5.44	41.41	22.4	n/a	2
Hcylinder2.stl		10.52	12.52	31.44	91.87	172	n/a	3
Hcylinder3.stl		18.77	19.31	98.33	156.04	575.7	n/a	5
Hcylinder4.stl		742.13	202.08	3277.85	1135.62	21322.22	n/a	10
Sphere1.stl	100	5.27	6.36	8.85	91.64	46.1	n/a	4
Sphere2.stl	200	13.45	13.12	52.21	203.49	361.5	n/a	6
Sphere3.stl	300	37.19	23.06	159.24	340.62	1215.1	n/a	10
Sphere4.stl	1000	3085.15	678.01	5430.10	3087.46	45003.7	n/a	20
Hsphere1.stl	Hollow 100x10	5.14	6.34	5.49	102.41	32.3	n/a	8
Hsphere2.stl		10.22	12.47	32.00	231.77	241.8	n/a	12
Hsphere3.stl		15.37	16.83	100.80	387.18	803.1	n/a	20
Hsphere4.stl		457.32	144.36	3386.88	3066.61	29744.44	n/a	40

### 3.3.Discussion

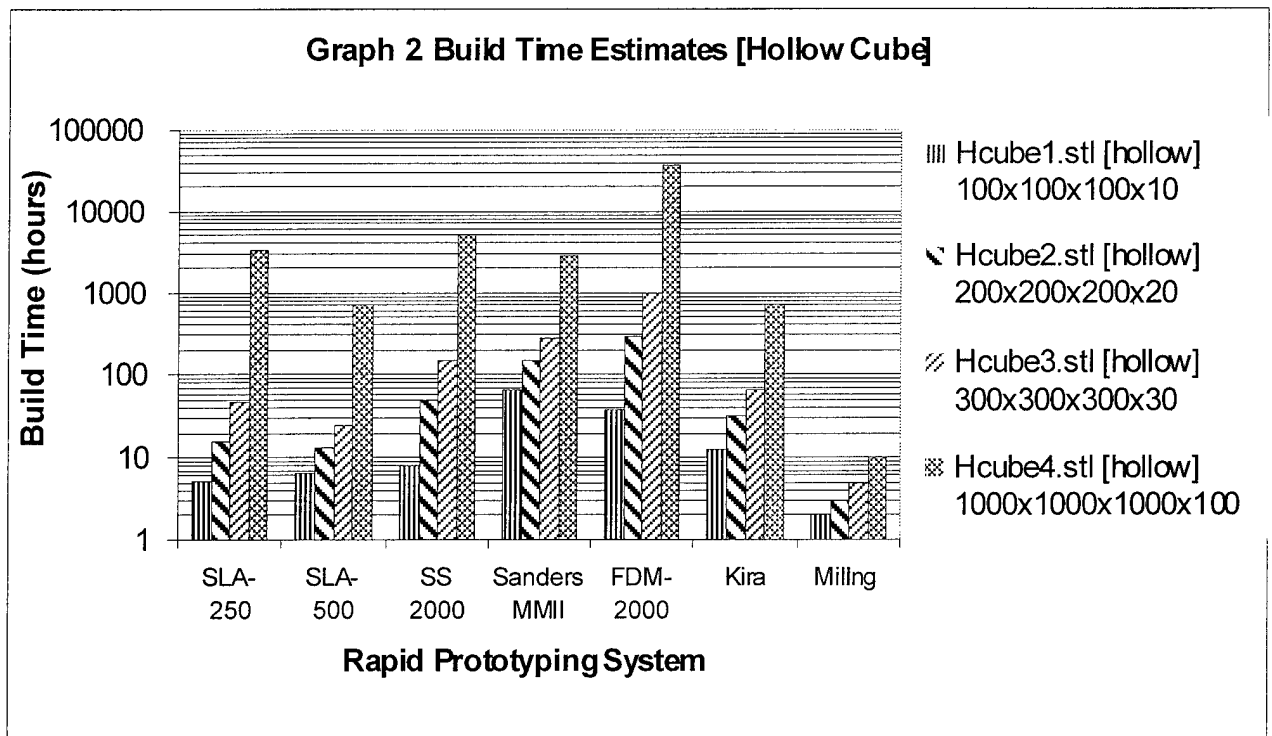
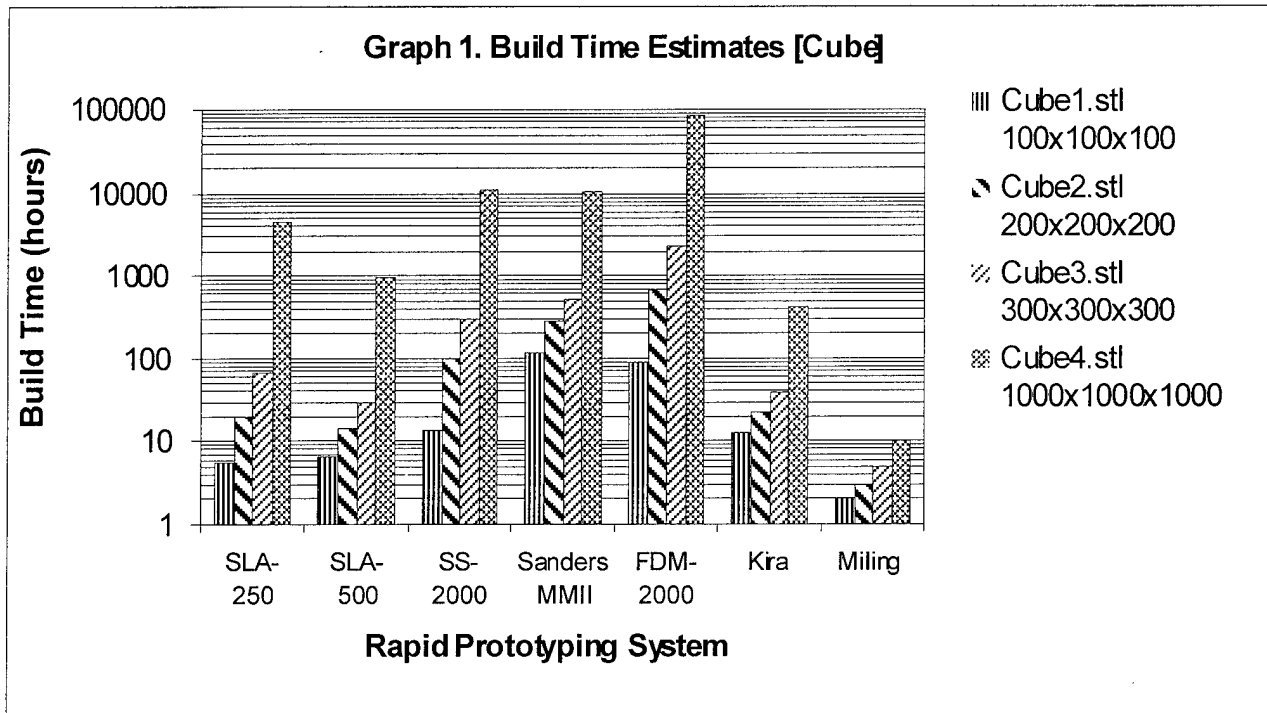


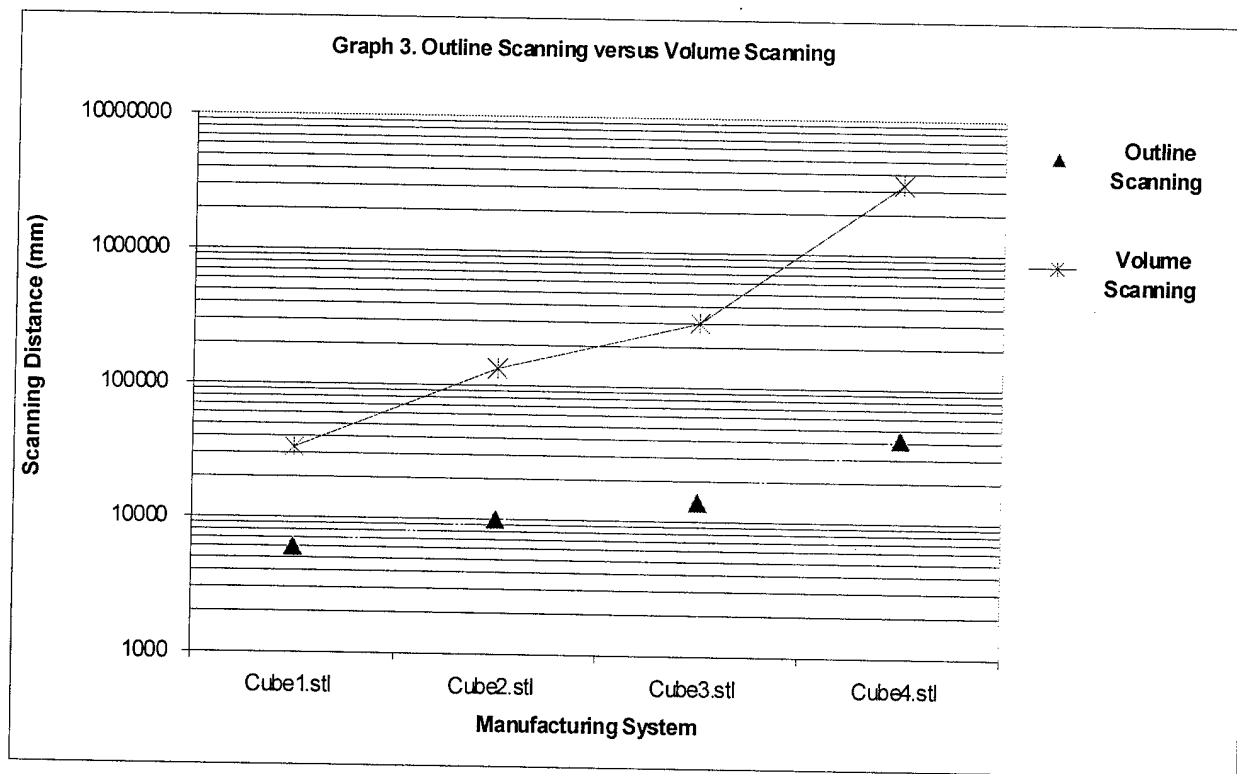
Table 1, graph 1 and graph 2 show that the current rapid prototyping systems do not compare favourably to milling. With the objects being basic shapes, the data for the cube, cylinder and the sphere are relatively the same, which therefore give comparable graphs. That is why only the graphs for the cube and the hollow cube are shown.

Graph 3 shows a comparison between outline scanning (milling, Kira, etc.) and volume scanning (StereoLithography, FDM, SLS. etc.). Volume scanning systems represented in the graph employ a scanning width of 0.3 mm. This figure is quite high for StereoLithography and selective laser sintering. These systems normally use a scanning width of about 0.2 mm. The FDM-2000 uses a scanning width of about 0.3 mm. but can use wider scanning widths.

These results are likely to be prone to error but even considering an error of 20% it is still clear that outline scanning systems are more competitive. A 20% error is acceptable based on the generally considered performance of the build time estimators and the true build time of the Sinterstation and the Kira.

For the smaller objects the time difference between volume scanning systems and outline scanning systems is not that different, however for the larger parts the difference is significant.

Rapid prototyping systems like ZCorp and Stratoconception are not mentioned. This is because data was not available. It is understood that the ZCorp machine in particular would provide a significant reduction in build time and should be the subject of further studies.



#### 4. Conclusion

A number of rapid prototyping systems have been compared with conventional milling for the fabrication of large models. Build time estimations have been made for a range of simple geometry models and sizes.

It can be deduced that for fabrication of large scale models, milling is still a very good option. Its advantage includes speed as well as the variety of materials that can be used. While rapid prototyping remains a very important technology in today's manufacturing industry, milling is no less valuable. A hybrid system combining milling and the layer based technology can produce large models with complex detail and internal structure.

#### References:

- [1] Rapid prototyping with sloping surfaces, Hope, R.L., Jacobs, P.A, Roth, R.N. (1997), Rapid Prototyping Journal, vol. 3, no.1. pp 12-19. (Waterjet cutting of thick layers)
- [2] Topographic Shell Fabrication, <http://www.formus.com/index.htm>
- [3] Precision Stratiform Machining (Brazing Concept), F. Zafar Shaikh, Bob Novak, Joseph Schim, and Bryan Stoll, internal document-Ford Research Laboratory
- [4] ICMA'97, April 28-30, 1997, Hong Kong, Rapid Prototyping on a large scale, I. Gibson and G. Mensing, ISBN 962-85138-1-8.
- [5] Rapid Automated Prototyping: An Introduction. Lamont Wood, ISBN 0-8311-3047-4.
- [6] <http://www.3dsystems.com/>
- [7] <http://www.sanders-prototype.com/>
- [8] <http://www.stratasys.com/>
- [9] <http://www.dtm-corp.com/home.htm>
- [10] <http://hkumea.hku.hk/~CRPDT/rpt/Japan/lnui1.html>
- [11] <http://helisys.com/>
- [12] <http://www.spline.nl>

# REVERSE ENGINEERING OF POLYMERIC SOLID MODELS USING REFRACTIVE INDEX MATCHING (RIM)

**Jon Christensen and Amit Bandyopadhyay**

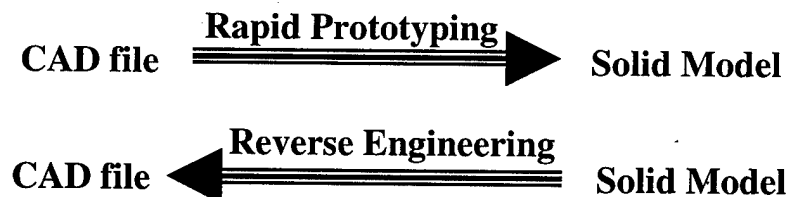
School of Mechanical and Materials Engineering  
Washington State University  
Pullman, WA 99164-2920

## Abstract

Reverse engineering (RE) techniques allows the creation of 3-D CAD files from a solid model. The benefits of reverse engineering are not new to the industrial design and manufacturing arena though wide spread applications are yet to be seen. A novel approach is used to reverse engineer polymeric parts with its internal features in a low cost, non-destructive manner. Solids created from polymers with an index of refraction matching that of an immersion liquid are reverse engineered using a CCD camera. The images are then used to create digital solid models from a physical model. Design and development of this novel low cost tool for reverse engineering of polymeric solid models is described in this paper.

## Introduction

The concept and the advantages of reverse engineering (RE) are not new to the industrial design and manufacturing arena [1-3]. But still the wide spread application of reverse engineering is yet to be seen. The simplest definition of reverse engineering is probably designing a product from its physical model, where as RP does reverse of reverse engineering as it builds solid models directly from CAD files.



Though the first impression of RE could be copying an existing product, which could be illegal in nature, but in reality, effective utilization of RE could save a significant amount of time and money in manufacturing. At present, some of the applications of RE are limited to redesign old products by the same company, or for products that are in use but whose vendor is no longer in business. Moreover, as rapid prototyping techniques are becoming more and more popular [4-5], the demand for better surface finish, better accuracy and tolerances are clear. Common customer complaints are dimensional accuracy, warpage, and surface finish of the parts. If the customer can receive a CAD file of the actual solid model built using RP along with its physical model, then they can compare their CAD model with the original CAD model.

Among the various systems that are available today for RE, probably coordinate measuring systems and laser scanning systems are the most popular ones. In the case of coordinate measuring system (CMM), a coordinate measuring arm with a probe at the end scans the part surface point by point and measure the X, Y and Z coordinates. These machines are relatively low cost and scan almost any parts irrespective of its materials. But these machines can not measure internal features, and for parts with a lot of critical features, this is an extremely laborious process. Moreover, the process generates a huge file of "point cloud" data that then needs to be converted to a solid or surface(s).

For laser scanner systems, the process certainly has some advantages over CMM but is more expensive. Some scanning systems, first machines a thin layer out and then scans the part and repeats this process for the complete part. For computed topography (CT) scanning system, the scanning process continues in a non-destructive manner. These scanning processes are fast and are capable of scanning large objects. The accuracy of these processes is also very good. But the equipment is expensive. Moreover, the resulting file that is generated is a large "point cloud" data set, similar to CMM.

The novel reverse engineering technique that is being described in this paper is primarily designed for application to polymeric solid models using the concept of refractive index matching (RIM). It is believed that simple RE equipment like this one will help significantly in designing and manufacturing of numerous engineering components.

### Concept of Refractive Index Matching

When a clear solid with a different index of refraction is placed into a clear liquid, the solid is usually easily seen because light passing through the two mediums changes its direction (Figure 1b). However, if the solid's index of refraction matches that of the liquid, the direction of the light passing through the two mediums will not change and the immersed solid can not be

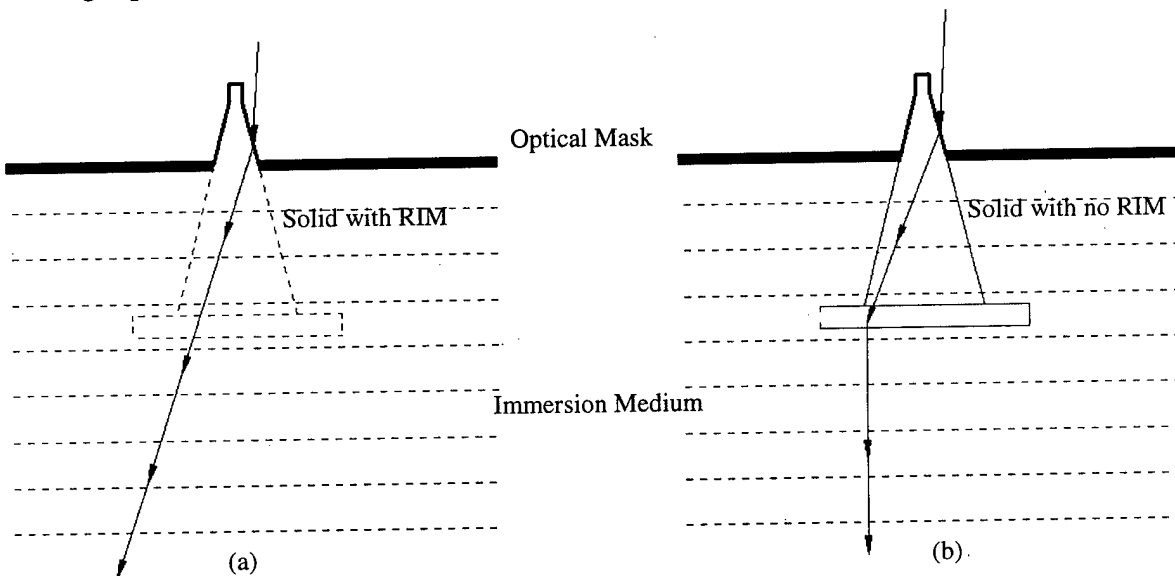


**Figure 1** Concept of refractive index matching

seen easily (Figure 1a). This disappearing effect of polymeric solids in a RIM liquid can be used to reverse engineer the part geometry. Using an optical mask, which floats on top of the immersion liquid (Figure 1), only the cross section of the part at a specific height/depth can be seen. The use of closely matched RIM liquid is needed in order to avoid inaccurate cross-sectional data due to possible distortion that can be seen in Figure 1b, where the light changes its direction due to a mismatch in refractive index.

### System Design

#### System Description

There are two main components in this reverse engineering (RE) system: hardware and software. Figure 2 shows a series of schematic illustrations of the process flow describing how both hardware and software work together to reconstruct a digital image from its polymeric physical solid model. First the object to be reverse engineered is made from a clear polymer. In our case, we used General Electric RTV615 silicone. The silicone part is then placed in the RIM immersion liquid making it virtually invisible to the CCD camera placed at the bottom of the tank. In Figure 2a, the picture on the screen shows only the color of the optical mask. The optical mask is a dyed liquid with an opposite polarity and a density less than that of the RIM immersion liquid. Because of these properties the mask floats on top of the immersion liquid. As the part is raised up through the mask (Figure 2 b, c, and d), cross-sectional images can be seen, by the CCD camera, where the part penetrates the mask or the dyed liquid. By maintaining

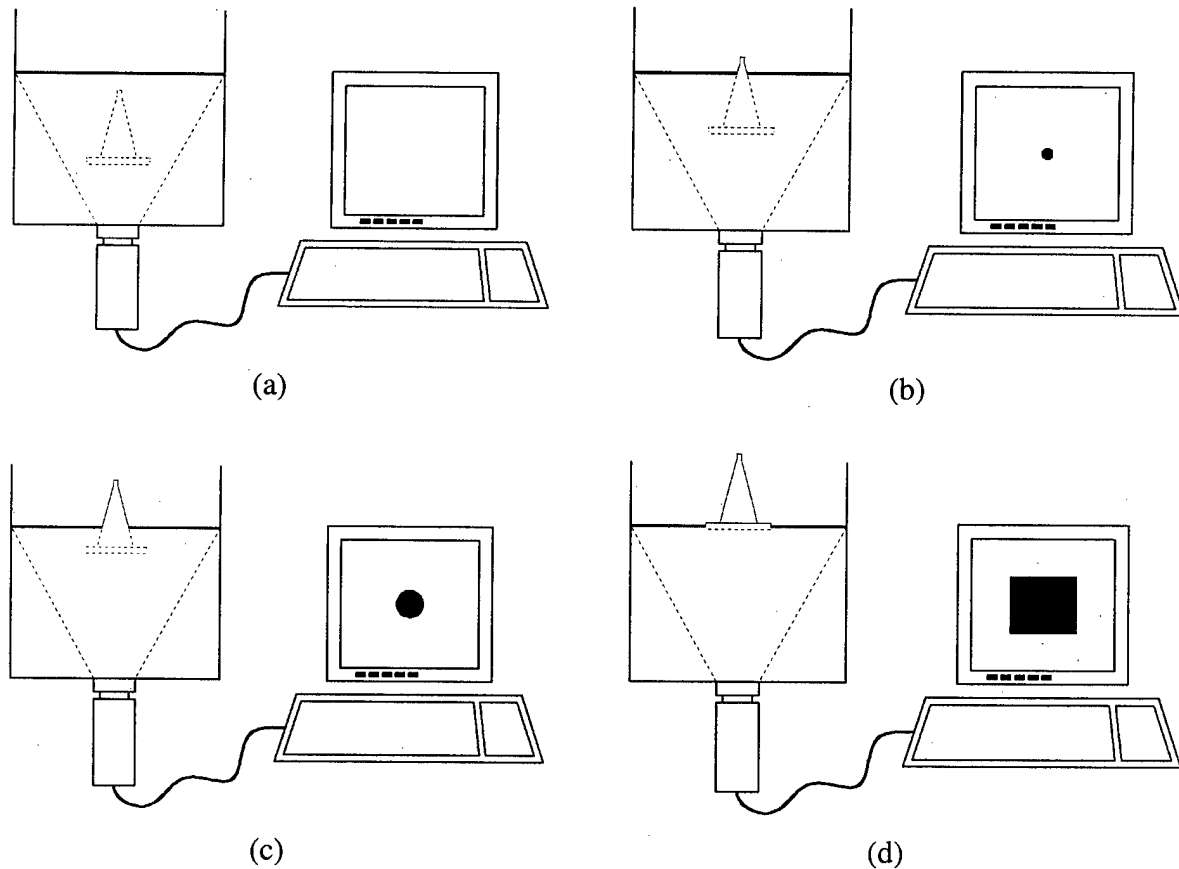


**Figure 2** Schematic representation of the RIM RE process of a polymeric solid

the Z level of the mask, a series of cross-sectional pictures of the part is taken as it is raised up through the mask. These pictures can then be used to create a 3-D model of the part by following this order:

**Polymer tool → Serial images → Raster to vector conversion → CAD file**

System hardware

There are four primary hardware components in this RE system and they are:

- Containment tank for the immersion liquid and the mask
- Z axis linear slide/stepper motor and its controller
- Liquid solutions (immersion and mask)
- Imaging system (CCD camera and computer)

The containment tank is a simple glass tank with a Z-axis linear slide mounted on the back to raise the solid model up through the mask. A CCD camera is mounted on the bottom of the tank, below the glass wall. The RIM liquid is placed inside the tank and the mask or the dyed liquid is placed on top of that. In order to remain environmentally safe, a simple sugar water solution is used as a RIM liquid. The concentration of sugar in water determines the index of refraction and can be matched with many clear polymers with refractive indexes varying from 1.33 to 1.45 with up to 2 g/ml sugar concentration. For RTV615, a sugar solution of concentration 0.79 g/ml is used whose refractive index is 1.406. Figure 3 shows the refractive index of sugar-water solutions experimented with thus far along with corresponding sugar concentrations. The refractive indices of these solutions were measured using a Bausch and Lomb refractometer.

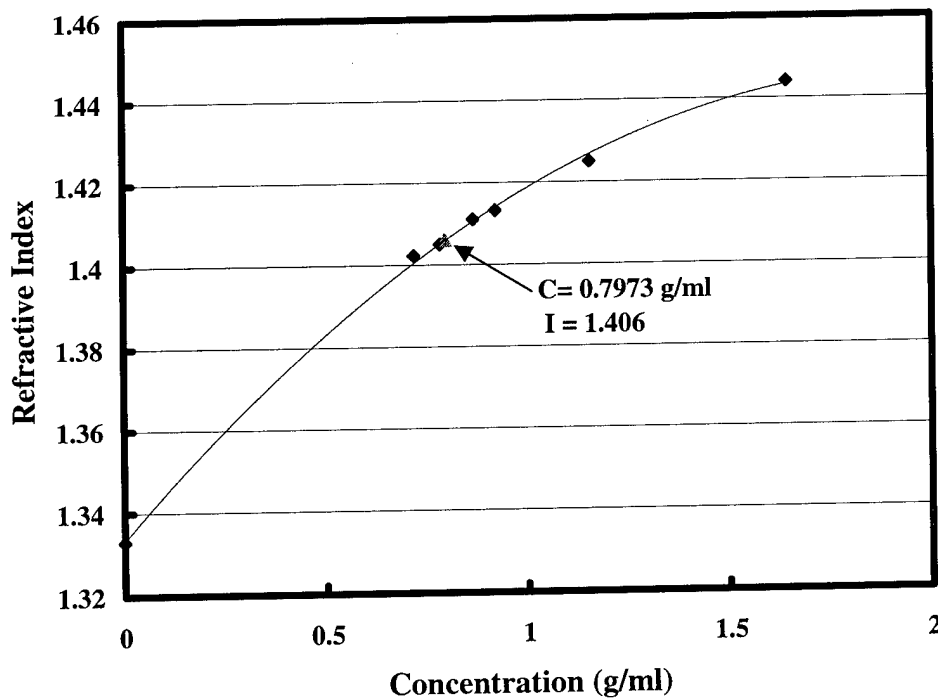


**Figure 3** Refractive indices of solution made from sugar and water.

Imaging in the test system is done with a 640x480 pixel, ViCAM digital camera. The camera is attached to a Pentium II-266 computer for data acquisition.

### Software

Software development is required for four different tasks in this RE system. First, cross section images must be saved serially according to its Z-axis position. Second, simple positioning of software is required to drive a stepper motor that is triggered after each picture is taken. In order to use the pictures for RE, the cross section edges must be detected with edge detection algorithms and then converted to a vector format. Currently the DXF file format is being used. Once created, each cross section is then imported into a CAD program with its corresponding Z level. This whole process will be automated so that no user intervention is needed unless part feature editing is necessary. Processing time takes about 7 seconds for each cross section.

### Accuracy

Model accuracy is probably the most important parameter during reverse engineering. With the optical RIM technique of reverse engineering a complete analysis of achievable accuracy has not been performed so far. Several test parts have been used to test the system and these parts show that a high degree of accuracy can be achieved. Various factors that can affect accuracy have been discussed in the order that it is believed they affect the accuracy most.

RIM and mask liquid surface tension plays a significant role in model accuracy. If the surface tension is high, the liquid will not easily flow around the part to the correct Z level because it may cling to the part as it is being drawn up out of the tank. In parts that have horizontal surfaces, parallel to the surface of the liquid, surface tension may cause considerable inaccuracies. Low surface tension fluids can greatly reduce this source of error.

The part geometry has also been found to affect accuracy. Parts having many internal features that are not open to the free flow of liquid will not have those features reverse engineered. It has yet to be determined how complex of a part can be reverse engineered before the accuracy drops off significantly.

Lighting for the camera has been found to be another important factor in accuracy. If the picture is over-exposed, the cross sectional edges can be distorted. In experiments with monochromatic light, it has been found that light in the same frequency range as that of red (visible) LASERS would not penetrate the mask. The monochromatic light source provided an excellent contrast with very sharp edges. In the example part, normal room lighting was used which gives a lower accuracy.

Edge detection software is a critical factor in this method of reverse engineering. While the human eye does an excellent job, it is not very efficient for this task! A good quality, edge detection algorithm is an essential tool to get accurate cross sectional information to reconstruct an accurate 3-D image. However, if lighting is good then this is not a very difficult task.

### Example

In order to see how sample parts can be reverse engineered, a simple cone with a rough-cut rectangular base was created from silicone. It was then placed in the RE system. Cross sections on this example were taken every 0.050 of an inch in the Z direction. Because custom software has not yet been created to automate the entire procedure slice intervals have been kept at or above 0.025 inches. Figure 4 shows the results of the raw data after it was imported into CADKEY 97. In this example, the accuracy ranged from 0.004 inches to about 0.029 inches across the X-Y plane. In the top view, the small deformations on the left side of the rectangle that showed up in the RE model was actually a small tear in the silicone part. In Figure 4a, the cone looks slightly elliptical which is the true representation of the part, because the mold for the original part was deformed during its cure cycle.

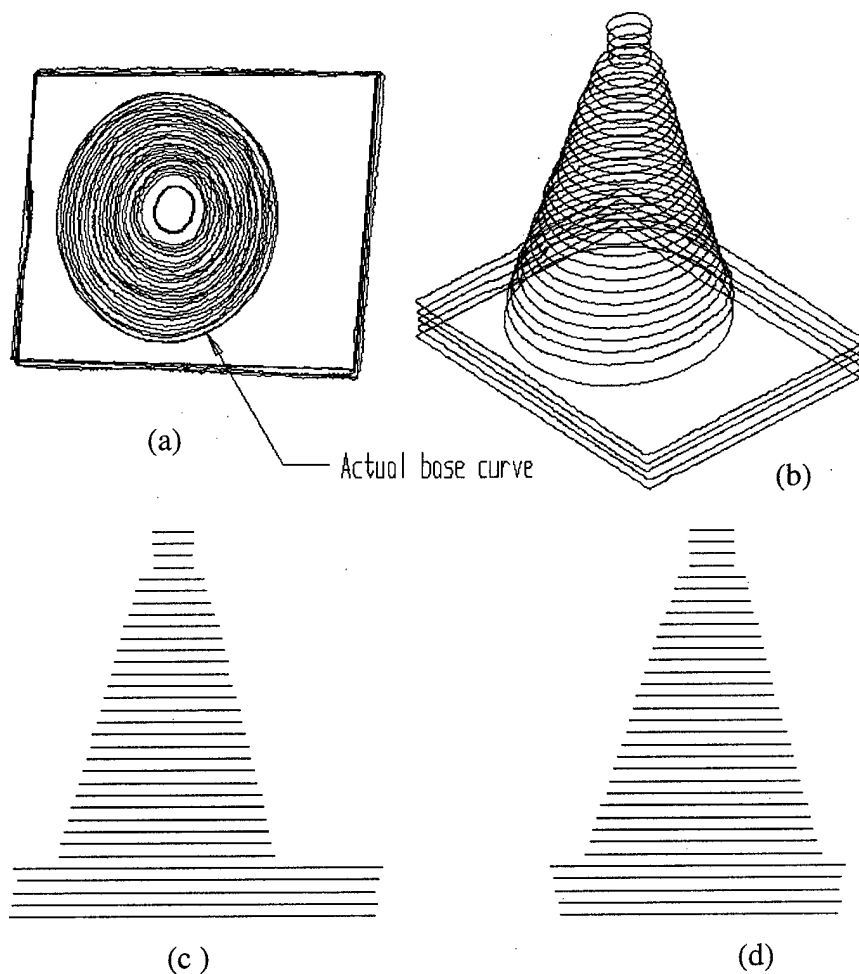


**Figure 4** CAD pictures of imported DXF cross sections. (a) Top view, (b) Isometric view, (c) side view and (d) front view.

From the above CAD file a *.stl* file was generated. This file was then used to create an ABS solid model using an FDM 1650. Figure 5 shows the original silicone part beside the ABS RP model for comparison.

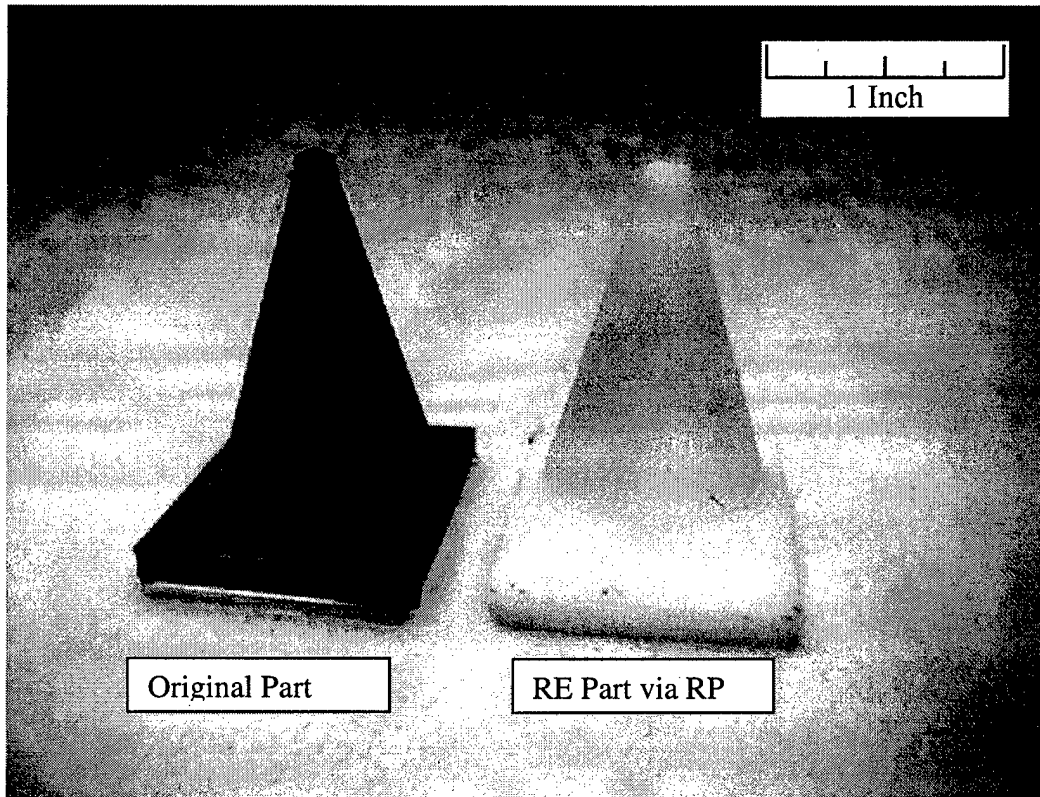


**Figure 5** Original polymeric part next to the reverse engineered ABS RP model

### Conclusions

Refractive index matching (RIM) concept is used to build novel reverse engineering equipment that can be used for polymeric materials. The equipment has been successfully used to reverse engineer both simple and complex shaped silicone parts. From different geometries, which have been tested so far, accuracy of better than 0.010 inches have been achieved. Further developmental work is currently in progress to understand the effects of various parameters on the accuracy of this process.

### Acknowledgment

The authors would like to acknowledge Prof. Leonard Henscheid of Department of Chemistry at WSU for lending refractive index measurement equipment and providing advice on chemical solutions. Karl-Heinz Kuhl's *Kvec* raster-to-vector software was greatly appreciated.

## References

1. T. Varady, R. R. Martin and J. Cox, "Reverse Engineering of Geometric Models," *Computer Aided Design*, **29** [4], pp 255-68 (1997).
2. B Guo, "Surface Reconstruction: from points to splines," *Computer Aided Design*, **29** [4], pp 269-78 (1997).
3. A. P. Rockwood and J. Winjet, "Three-dimensional Object Reconstruction from Two Dimensional Images," *Computer Aided Design*, **29** [4], pp 279-86 (1997).
4. Solid Freeform Fabrication Symposium Proceedings, Vol. 1-7, Edited by H.L.Marcus, J.J. Beaman, J. W. Barlow, D. L. Bourell and R. H Crawford, The University of Texas at Austin, Austin, Texas
5. International Conference on Rapid Prototyping, Vol. 1-7, Edited by R. P. Chartoff, A. J. Lightman, University of Dayton, Dayton, OH.

# Software Development for Laser Engineered Net Shaping

M. T. Ensz, M. L. Griffith, L. D. Harwell

Sandia National Laboratories  
Albuquerque, NM 87185

## Abstract

Laser Engineered Net Shaping, also known as LENS™, is an advanced manufacturing technique used to fabricate near-net shaped, fully dense metal components directly from computer solid models without the use of traditional machining processes. The LENS™ process uses a high powered laser to create a molten pool into which powdered metal is injected and solidified. Like many SFF techniques, LENS™ parts are made through a layer additive process. In the current system, for any given layer, the laser is held stationary, while the part and its associated substrate is moved, allowing for the each layer's geometry to be formed. Individual layers are generated by tracing out the desired border, followed by filling in the remaining volume. Recent research into LENS™ has highlighted the sensitivity of the processes to multiple software controllable parameters such as substrate travel velocity, border representation, and fill patterns. This research is aimed at determining optimal border outlines and fill patterns for LENS™ and at developing the associated software necessary for automating the creation of the desired motion control.

## Introduction

During the past few years, the capabilities of solid freeform fabrication have progressed enough to allow for the direct fabrication of fully dense metallic components using computer aided design (CAD) models [1-4]. One such technique, being developed at Sandia National Laboratories to fabricate high strength, near net shape metallic components, is Laser Engineered Net Shaping (LENS™). In the past several years, a variety of components have been fabricated using LENS™ for applications ranging from part prototypes to tooling for injection molding [5-6].

The basic LENS™ system consists of a high power Nd:YAG laser, a 3-axis computer controlled positioning system, and multiple powder feed units. The positioning stages are mounted inside an argon-filled glove box (nominal oxygen level of 2-3 ppm), while the laser beam enters the glove box through a top mounted window. A powder delivery nozzle is used to inject a metal powder stream directly into the focused laser beam. The lens and powder delivery nozzle move as an integral unit in the  $z$ -axis, while the part, positioned under the laser beam, is transitioned in  $x$  and  $y$ .

To create a part, a CAD solid model is sliced into a sequence of cross-sections that are then translated into a series of tool path patterns to build each layer. The laser beam is focused onto a substrate (or previous layer of the part) to create a weld pool into which powder is simultaneously injected to buildup each layer. The substrate is translated beneath the laser beam to deposit the desired geometry for the current layer. After completing a layer, the powder delivery nozzle and focusing lens assembly is incremented in the  $z$ -direction, and the process begins again.

After determining the basic LENS™ parameters (i.e. laser power, powder feed rate, traverse velocities, layer thicknesses and hatch spacings) for a chosen material or materials, extrusion or solid geometries may be fabricated. With a full understanding of the LENS™ parameters and with proper computer

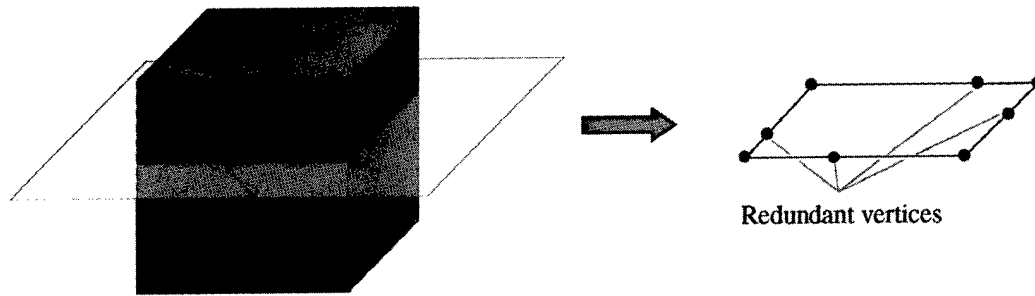


Figure 1. Intersection of a triangular mesh with a plane typically results in a 2D contour with redundant vertices.

control of the LENS™ process, fully dense parts may be repeatedly built with errors less than +0.005” in the x and y-axes, and less than 0.015” in the z-axis.

Recent research into LENS™ has highlighted the sensitivity of the processes to multiple software controllable parameters such as substrate travel velocity, border representation, and fill patterns. This research is aimed at determining optimal border outlines and fill patterns for LENS™ and at developing the associated software necessary for automating the creation of the desired motion control.

## Overall Software Flow

For any layered manufacturing technology, the overall goal of the control software is to take a CAD representation of the part, slice the model into appropriate thickness layers, and create path instructions for the manufacturing equipment. For LENS™, the path planning process begins with an object defined using the STL format. This triangular mesh is intersected with appropriately defined planes in order to create 2D contours for each layer to be formed. These contours are then refined to remove any vertex redundancies and to improve part quality. After cleanup, if creating a solid part, the contours are used as a basis for creating the necessary fill pattern. The final result of the path planning process is a tool path program (G-code) that is used to drive the three axes of the LENS™ machine.

## File Format Used by LENS

As previously stated, the LENS™ process starts with an object defined through the RP industry standard STL format. While the deficiencies of this format are well understood, the use of STL meshes for object definition does allow a large variety of CAD packages to be used to develop parts for use with LENS™. Further, the simple triangular format used by STL allows for relatively easy manipulation of the part files. While the STL format is typically not a precise representation of the original CAD model (curved surfaces are faceted), meshes can be readily cut which are well within the tolerances of the LENS™ process. The only true difficulty posed by the use of the STL format is that the triangular representation, when sliced, often results in vertex redundancies (straight edges defined by more than two vertices, arcs being “over defined”, etc.). As will be discussed, these redundancies will often have adverse affects on the build process. To minimize these affects, the contours require significant refinement.

## Contour Refinement

Due to the nature of triangular meshes, when intersecting a mesh with a plane to create a 2D contour, the vertices formed from the intersection process will inevitably contain numerous “redundant” vertices – vertices that do not add information about the contour’s geometry or topology. Even for a simple cube, as

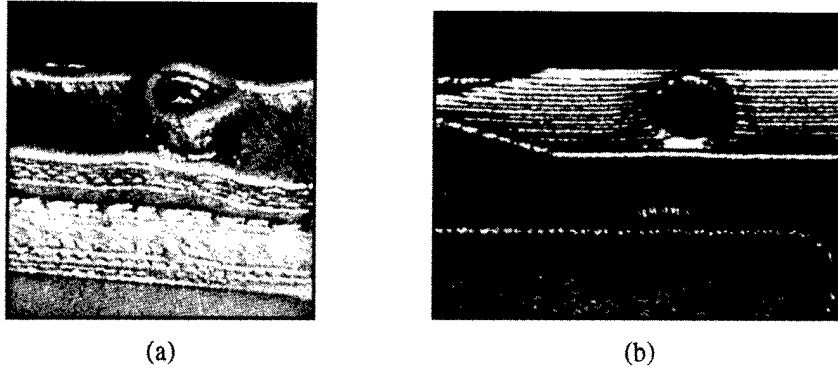


Figure 2. (a) Using too many edges to define contours results in excessive buildup. (b) Reducing the number of edges used to define the contour produces a more desirable part.

shown in Figure 1, a straightforward intersection of any plane with the triangular mesh will create line segments which contain more than the minimum two vertices. While these redundancies may not pose problems for other layered manufacturing processes, they may significantly affect the quality of parts produced through the LENS™ process. Primarily, each line segment start/stop reduces the physical machine speed as the stages are forced to decelerate and accelerate through each vertex. Since the LENS™ build rate is related to laser energy per unit time, decreasing the stages' velocities results in a significant alteration of the metal deposition. Another obstacle, resulting from the use of a triangulated mesh to define the object, is a possible "over refinement" of arcs and circles. As with over-defined straight segments, the accelerations and decelerations through each vertex of an over defined arc results in a decrease in the travel speed and a corresponding increase in the metal deposition rate (Figure 2(a)).

The contour refinement process is relatively straightforward. First, any duplicate vertices are removed from the contour. (Duplicate vertices are considered as those that are coincident to each other within some epsilon.) Next, any redundant vertices are located and removed from line segments. To locate the redundant vertices, the included angle of the two line segments that share each vertex is computed. Any vertex whose included angle is greater than a user defined value (typically around  $179^\circ$ ) is removed. It should be noted that this process also eliminates excessive vertices in arcs or other curve segments. It is also possible at this stage to locate any arcs or circles in the contour representation and replace the segmented representation with appropriate second order formulations. As shown in Figure 2(b), dramatic improvements in part quality may be obtained through proper contour refinement.

Finally, any desired beam offset calculations are applied to the contour. It should be noted that for LENS™, the beam offset serves several purposes. First, beam offset may be utilized in its traditional fashion, correcting for the fact that the weld pool created by the laser has a finite width by providing an

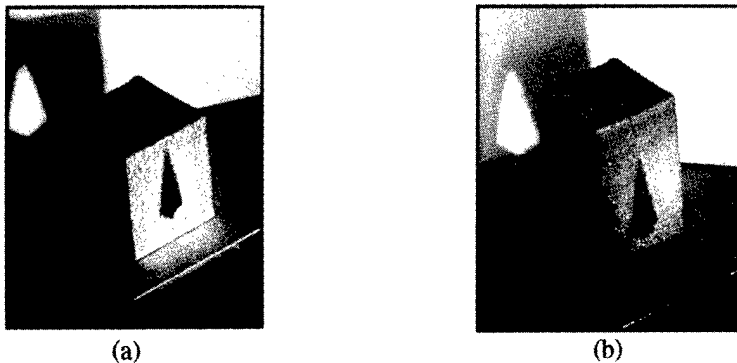


Figure 3. (a) With no beam offset applied, the weld beads drawn for the borders at the tip of the channel overlap, resulting in an uneven surface. (b) Applying beam offset eliminates the overlap, resulting in a flatter top face.

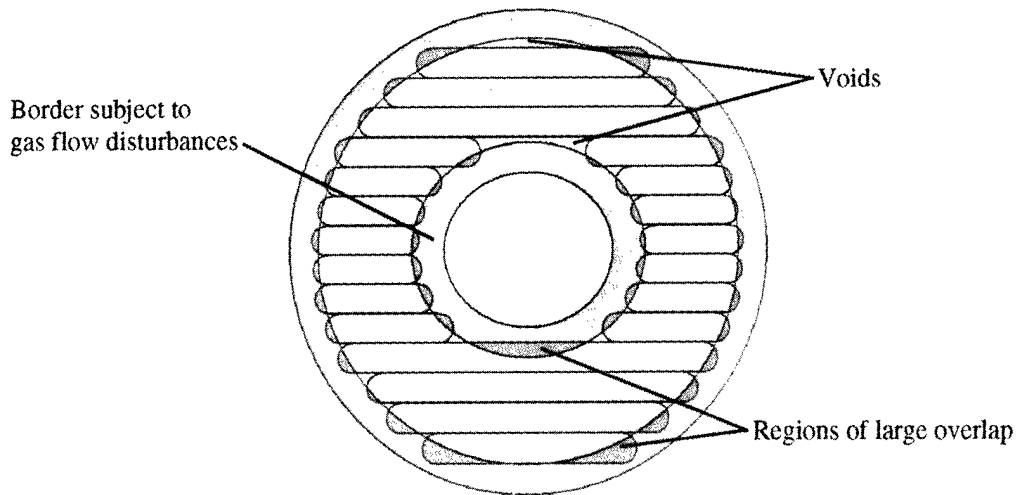


Figure 4. For even basic geometry, many problems may be encountered during a fill pass. Since the width of the weld pool will not always produce weld bead edges aligned with the border geometry, regions of large overlap, and regions with voids may be formed. Further, gas currents blowing back from the part may affect the powder stream, especially in tight areas. If the same fill pattern is repeated, the small disturbances produced by these flaws will build upon themselves, resulting in a poor final product.

offset compensation to account for this width. This compensation not only provides for improved dimensional accuracy in the  $xy$ -plane, but also assists in creating flat, even layers by preventing weld beads from overlapping each other (Figure 3). Since LENS™ is focusing on creating near-net shapes, rather than net shapes, beam offset may also be used to control the amount of excessive material left on a part, providing for the proper amount of stock required for the final finishing process.

## Fill Pattern

For solid parts, an appropriate technique must be utilized to create the necessary fill pattern. The choices for this fill technique may be broken down into one of two primary methods: rasters and “conformal” contours. Regardless of method, the fill technique must meet one primary requirement. Since the metal for material buildup is injected into the LENS™ part as a powder stream, effects of the localized geometry on the powder stream must be controlled. Further, it must be recognized that the weld beads have finite width; widths that may not always “fit” evenly into a layer’s border geometry, causing both regions of excessive overlap and possible voids (Figure 4). While neither overlaps nor voids are in and of

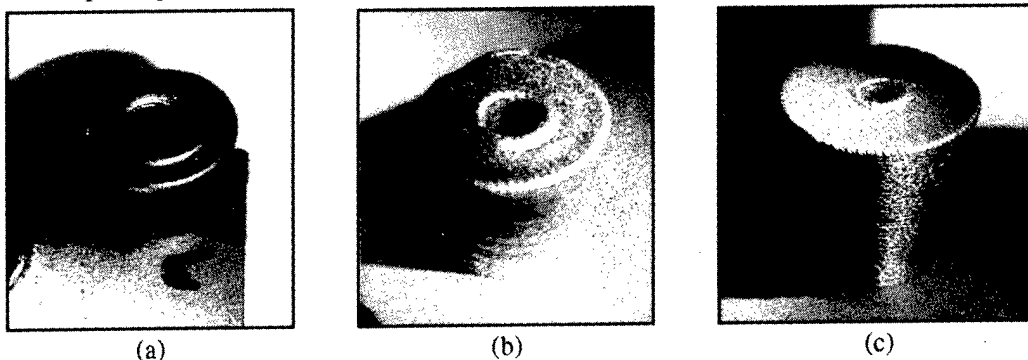


Figure 5. (a) Created using conformal contours. (b) Created using a  $0^\circ$ ,  $90^\circ$  raster hatch pattern. (c) Created using a  $0^\circ$ ,  $105^\circ$ ,  $220^\circ$ , ... hatch pattern.

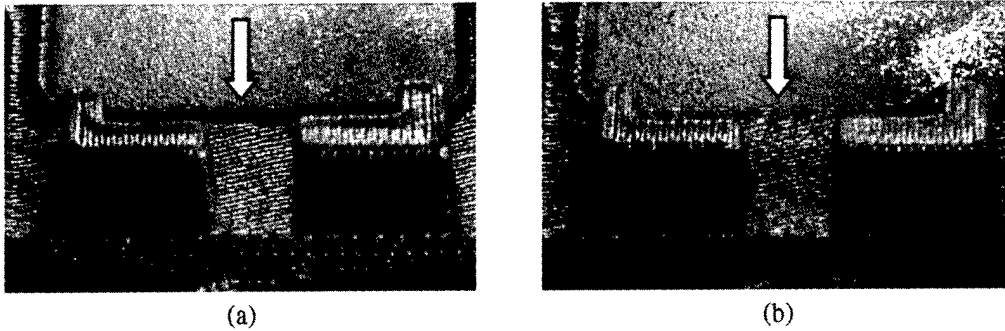


Figure 6. (a) Shallow angles of attack between border vectors and the fill rasters produce buildup along borders. (b) Eliminating these shallow attack angles produces improved characteristics.

themselves detrimental to the build process (overlaps will produce a slight increase in thickness, while voids will result in a slight decrease), the errors caused by these localized flaws can, if compounded across enough layers, will result in a poor part. Attacking the geometry from different directions during the fill process can alleviate the localized affects. To accomplish the different angles of attack, the fill pattern must be designed such that a “randomness” is introduced into the build process.

Conformal contours, which follow the outline of the part in decreasing size, were studied as one possible fill technique. However, basic experiments with conformal contours revealed that even for simple cylindrical parts, the required randomness is not introduced, resulting in extremely poor builds (Figure 5(a)).

The use of raster fills has proven an effective method of introducing the necessary variations between the fill vectors on each layer. However, even here, care must be exercised when determining the raster angles on a per layer basis. Early work on LENS™ utilized rasters that were always oriented at either  $0^\circ$  or  $90^\circ$ . While a vast improvement over the use of conformal contours, these static angles were still the source of localized build errors, due to the repetition of the fill angles. As a result, regions aligned with the  $x$  and  $y$ -axes would often experience unevenness in the build (Figure 5(b)).

The first attempt at introducing more variation into the hatch angles was to use randomly generated values for the hatch orientations. However, this allowed for angles that are just a few degrees off of the “standard” angles of  $0^\circ$ ,  $30^\circ$ ,  $45^\circ$ ,  $60^\circ$ , and  $90^\circ$ . When filling near these standard angles with a shallow angle of attack (e.g. filling along a  $30^\circ$  border with a  $31^\circ$  hatch angle), the width of the weld bead repeatedly overlaps the border, producing a significant buildup, again resulting in an uneven build, as demonstrated in Figure 6. Furthermore, retracting the hatch to prevent the overlap was undesirable due to the likelihood of forming voids in the part.

After several iterations, the angle pattern converged on using a value of  $105^\circ$  between successive layers. This value provided several key benefits. First, the fill angles across two layers are nearly orthogonal, allowing for a large differentiation of attack angle to minimize the localized geometry effects. Also, at  $105^\circ$ , it takes 12 layers before any raster angle is repeated in a part, which further introduces pseudo-randomness into the process. Finally,  $105^\circ$  causes the standard angles to be either hit exactly, or at an angle greater than or equal to  $15^\circ$ , preventing the shallow angle of attack problems previously discussed. As shown in Figure 5(c), the results obtained through the  $105^\circ$  hatch algorithm are significantly improved over both  $0^\circ$ ,  $90^\circ$  hatching and conformal contours.

## Future Work

Even though the current three-axis LENS™ system is “officially” a two-1/2D process, the weld pool characteristics, combined with the high weld pool freezing rates do allow for the creation of slight overhung surfaces. To date, parts with overhangs up to 15° (for 0.015” thick layers) have been created. However, the creations of overhangs is still not fully understood in terms of the best speeds and feeds required to consistently create even, non-distorted layers. Future work will study what software alterations can be used to aid in the process of creating overhung surfaces.

Another near-term task being studied is what software controls will be required for creating complex, multi-material geometries. While previous work has looked at creating layered objects (where the material choice for each layer is user defined on a layer-by-layer basis), future work will look at the software controls needed to identify and control material composition throughout any given layer. Recent experiments with using implicit blending functions, combined with surface-distance functions, have proved promising [7].

## Conclusions

Recent experience in LENS™ has demonstrated the strong reliance that the metal deposition process has to parameters such as border representations and fill patterns. This research was aimed at understanding and developing optimized software solutions for the generation of LENS™ parts. Specifically, this work studied the affects of the border representation schemes, identified difficulties associated with over-defined representations, and developed methods of refining the contour data to improve the build process. Further, this research was directed at identifying an “ideal” fill pattern for creating solid parts. The final result of the fill pattern studies produced pseudo-random raster fill technique which introduces the necessary randomness into the build process to minimize localized geometry affects, while preventing problems with shallow angles of attack along standard design surfaces.

## Acknowledgements

This work is supported by the U.S. Department of Energy under contract DE-AC04-94AL850000. Sandia is a multiprogram laboratory operated by Sandia Corporation, a Lockheed Martin Company, for the United States Department of Energy.

## References

- [1] M.L. Griffith, D.M. Keicher, C.L. Atwood, J.A. Romero, J.E. Smugeresky, L.D. Harwell, D.L. Greene, *Free Form Fabrication of Metallic Components using Laser Engineered Net Shaping (LENS™)*, Proceedings of the Solid Freeform Fabrication Symposium, August 12-14, 1996, Austin, TX, p. 125.
- [2] J.R. Fessler, R. Merz, A.H. Nickel, F.B. Prinz, L.E. Weiss, *Laser Deposition of Metals for Shape Deposition Manufacturing*, Proceedings of the Solid Freeform Fabrication Symposium, August 12-14, 1996, Austin, TX, p. 117.
- [3] F. Klocke, H. Wirtz, W. Meiners, *Direct Manufacturing of Metal Prototypes and Prototype Tools*, Proceedings of the Solid Freeform Fabrication Symposium, August 12-14, 1996, Austin, TX, p. 141.
- [4] J. Mazumder, K. Nagarathnam, J. Choi, J. Koch, D. Hetzner, *The Direct Metal Deposition of H13 Tool Steel for 3-D Components*, Journal of Materials, Vol. 49, Number 5, May 1997, p. 55.

[5] D.M. Keicher, J.L. Jellison, L.P. Schanwald, J.A. Romero, D.H. Abbott, *Towards a Reliable Laser Powder Deposition System through Process Characterization*, 27<sup>th</sup> International SAMPE Technical Conference, Vol. 27, Diversity into the Next Century, proceedings of SAMPE '95, Albuquerque, NM, Oct. 12-14, 1995, p. 1029.

[6] M. L. Griffith, C.L. Atwood, J.E. Smugeresky, L.D. Harwell, D.L. Greene, E. Schlienger, *Using Laser Engineered Net Shaping (LENS™) to Fabricate Metal Components*, proceedings of the Rapid Prototyping and Manufacturing Conference, April 22-24, 1997, Dearborn, MI.

[7] C.T. Lim, M.T. Ensz, M.A. Ganter, D.W. Storti, *Object Reconstruction from Layered Data using Implicit Solid Modeling*, Journal of Manufacturing Systems, Vol. 16, Number 4, 1997, p. 260.



## Measurement and Modeling of Residual Stress-Induced Warping in Direct Metal Deposition Processes

N.W. Klingbeil, J.L. Beuth, R.K. Chin and C.H. Amon  
Department of Mechanical Engineering  
Carnegie Mellon University  
Pittsburgh, PA 15213

### Abstract

Tolerance loss due to residual stress-induced warping is a major concern in solid freeform fabrication (SFF) processes. An understanding of how residual stresses develop and how they lead to tolerance loss is a key issue in advancing these processes. In this paper, results are presented from warping experiments on plate-shaped specimens created by microcasting and welding processes used in Shape Deposition Manufacturing (SDM). Results from these experiments give insight into differences between the two processes, the role of preheating and insulating conditions during manufacture and the influence of deposition path on magnitudes and distributions of warping displacements. Results are then compared to predictions from two types of residual stress models. While the models effectively predict warping magnitudes and the effects of various thermal conditions, they are unable to capture some of the more subtle trends in the experiments. Results from the experiments and numerical models suggest that a combination of initial substrate preheating and part insulation can be applied to SDM and similar SFF processes to limit warping deflections, which is substantially simpler than active control of part temperatures during manufacture. Results also suggest that 3-D mechanical constraints are important in achieving precise control of warping behavior in SFF processes.

### Introduction

Residual stress-induced warping is a concern in a variety of solid freeform fabrication (SFF) processes, particularly those seeking to build parts directly, without post-processing steps such as sintering or infiltration by a low-melt alloy. One such process is Shape Deposition Manufacturing (SDM), currently under development at Carnegie Mellon University (Merz *et al.*, 1994) and Stanford University (Fessler *et al.*, 1996). Several methods have been investigated for the deposition of fully-dense metals within the SDM process, including microcasting, conventional welding and laser deposition. This paper directly considers the microcasting and welding techniques under development at Carnegie Mellon University. The microcasting deposition process involves the deposition of discrete macroscopic droplets (1/8"-1/4" in diameter) of molten metal, and has been the primary method of material deposition used in SDM. The desire for increased speed and accuracy of material deposition has recently motivated research into welding deposition, where material is deposited in continuous beads using a standard MIG welder. As summarized by Prinz *et al.* (1997), other SFF techniques under development for direct layered manufacturing of fully-dense metals include Direct Selective Laser Sintering (University of Texas), Laser Engineered Net Shaping (Sandia National Labs) and Directed Light Fabrication (Los Alamos National Labs).

One of the most critical issues in direct deposition of fully-dense metals is residual stress-induced warping, which can lead to unacceptable losses in dimensional tolerance (Prinz *et al.* (1995), Amon *et al.* (1998)). Thus, methods are required for measuring and modeling warping, with the goal of understanding the effects on warping of deposition process parameters. Measurement of warping in laser deposition has been considered for beam-shaped deposits by Fessler *et al.* (1996). The present paper outlines an experimental technique for the systematic measurement of warping in plate-shaped deposits, which allows quantification of warping parallel and transverse to the material deposition direction (Klingbeil *et al.*, 1997 and Klingbeil, 1998). Experimental results are presented for both microcast and welded stainless steel specimens, and the effects on warping of substrate pre-heating and material deposition path are outlined. The experimental results are next compared to numerical model predictions, which are obtained using

the one-dimensional (1-D) axisymmetric and two dimensional (2-D) generalized plane strain (GPS) thermomechanical finite element models of Chin (1998). The thermomechanical models used in this study specifically model the microcasting process and follow those of Chin *et al.* (1995, 1996a, 1996b).

While the experimental and numerical results presented herein relate quantitatively to two metal deposition processes used in SDM, the results offer qualitative insight applicable to other direct layered manufacturing applications. The experimental and numerical results suggest that the effects on warping deformation of substrate pre-heating/insulating conditions and material deposition path can be substantial. Furthermore, results suggest that somewhat subtle differences in mechanical constraints during material deposition can result in significant differences in residual stress generation and subsequent part warping.

### Measurement of Warping

The warping measurements discussed herein involve high-precision deflection measurements in conjunction with 2-D polynomial least square fits of the displacement data, which are subsequently used to obtain curvatures. The experimental procedure for obtaining warping deflections follows that of Klingbeil *et al.* (1997), with further details provided in Klingbeil (1998). In brief, molten stainless steel is deposited over a square region onto the surface of a 6" x 6" x 0.47" fully-annealed carbon steel substrate, which is bolted along its edges to prevent warping during manufacture. Following material deposition the specimen is allowed to cool to room temperature, after which the deposit is machined flat to a final thickness of 0.055". The specimen is then unbolted, which results in residual stress-induced warping. The warping deflections are measured using the coordinate measuring capabilities of the CNC milling machine (precise to within  $\pm 0.0001$ "). Deflection measurements are taken at 81 equally-spaced points forming a 4.0" x 4.0" grid centered on the surface of the deposit. Once the deflections are measured, a 2-D polynomial surface  $w(x,y)$  is determined from a 2-D least square curve fit (order  $n$ ) of the measured deflections, after which the curvatures  $w_{,xx}(x,y)$  and  $w_{,yy}(x,y)$  in the  $x$  and  $y$  directions are obtained by analytical differentiation of the function  $w(x,y)$ . Details of the curve fitting procedures are outlined by Klingbeil (1998). In the upcoming paragraphs, results are presented for both  $n = 2$  and  $n = 3$  least square fits. The  $n = 2$  fits result in uniform curvatures  $w_{,xx}$  and  $w_{,yy}$ , which can be interpreted as average curvatures in the  $x$  and  $y$  directions. The  $n = 3$  fits allow a bilinear variation in  $w_{,xx}$  and  $w_{,yy}$ , and are highly useful in illustrating deposition path effects. All curvature results are normalized by  $\kappa_{max} = 0.00834 \text{ in}^{-1}$ , the maximum theoretical curvature corresponding to release of a fully-plastic biaxial moment with an assumed room temperature yield stress of 60 ksi (Klingbeil, 1998). Measured deflections are normalized by  $L = 4.0$ ".

### Representative Microcast Specimen Results

Average ( $n = 2$ ) curvature results are summarized for five microcast specimens in Table 1. Results are presented for three initially room temperature specimens, as well as for two specimens subjected to a uniform 200°C substrate pre-heat prior to material deposition. All microcast specimens are manufactured using a raster deposition path, where material deposition begins in the positive  $x$ - $y$  corner and continues back and forth parallel to the  $x$  direction. The results of Table 1 indicate that for all specimens, warping is more severe in the  $x$  direction (parallel to the deposition direction). On average, uniform substrate pre-heating is seen to decrease warping magnitudes transverse to the deposition direction, however no measurable effect is observed parallel to the deposition direction. The actual measured deflections and corresponding  $n = 3$  least square deflections and curvatures for specimen #1 (no pre-heat) are depicted in Fig. 1. Note that both  $w_{,xx}$  and  $w_{,yy}$  are greatest at the start of material deposition, and decrease with decreasing values of  $y$  (i.e., as the total amount of deposited material increases). This suggests that inherent

substrate pre-heating during material deposition acts to reduce the thermal mismatch, which ultimately results in less warping. Furthermore,  $n = 3$  results for pre-heated specimens (not shown here) indicate that the payoff in decreased values of  $w_{,yy}$  is greatest at the start of material deposition, where the substrate would otherwise be comparatively cold. Thus, an initial pre-heat is of greatest advantage for the first few deposited rows, after which the deposition process inherently provides substantial substrate pre-heating.

Table 1. Microcast Specimen Average ( $n = 2$ ) Curvature Results

Specimen #	No Pre-Heat			200°C Pre-Heat	
	1	2	3	4	5
$w_{,xx} / \kappa_{max}$	0.434	0.478	0.481	0.457	0.483
$w_{,yy} / \kappa_{max}$	0.376	0.355	0.397	0.331	0.307

(Note:  $\kappa_{max} = 0.00834 \text{ in}^{-1}$ )

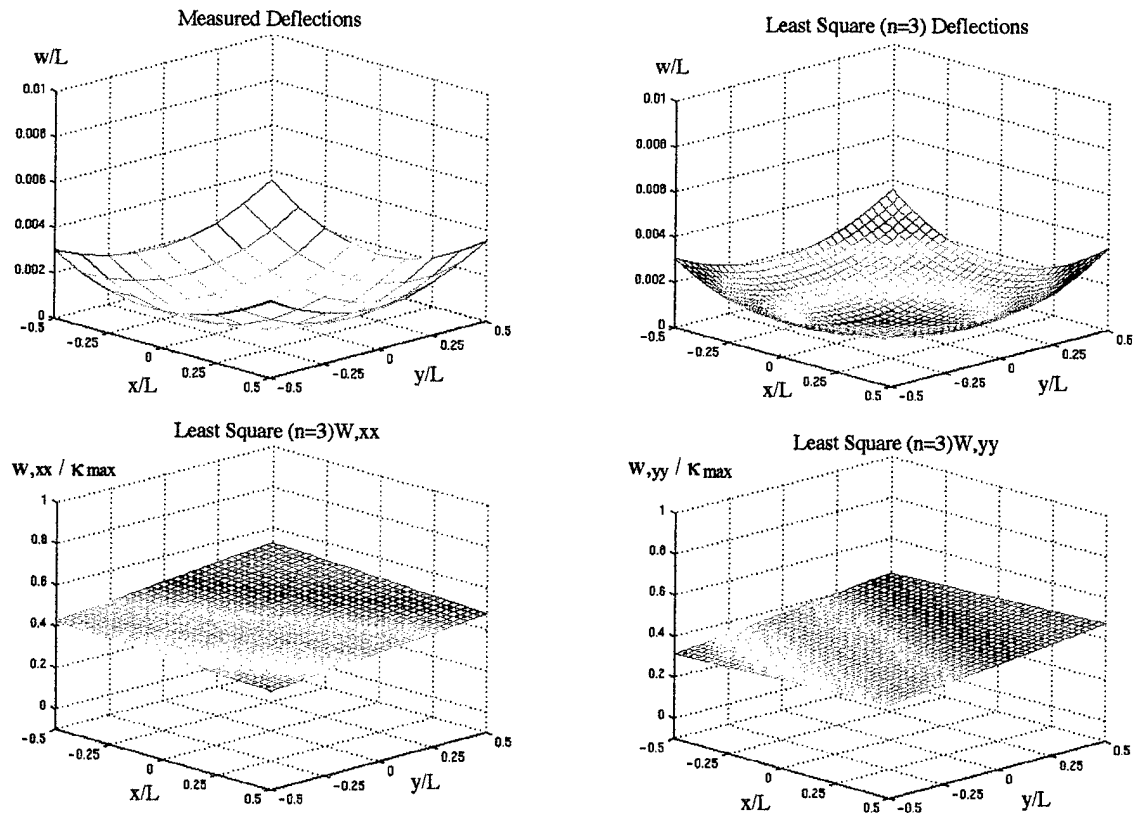


Figure 1. Representative Measured and Least Square ( $n = 3$ ) Microcast Results

### Representative Welded Specimen Results

Average ( $n = 2$ ) curvatures are presented for five welded specimens in Table 2. Results are presented for three deposition paths: the raster path used for microcast specimens, an outside-in spiral path and an inside-out spiral path. The outside-in path begins in the positive  $x$ - $y$  corner and continues in a spiral fashion until ending in the center, while the inside-out path begins in the center and ends in the positive  $x$ - $y$  corner. The measured deflections and  $n = 3$  results are depicted for a raster path specimen (specimen #1) in Fig. 2. Note the strong decrease in  $w_{,xx}$  and  $w_{,yy}$  during material deposition. While  $n = 3$  results for the spiral deposition paths (not shown here) indicate

much more uniform warping, the resulting average ( $n = 2$ ) curvatures in Table 2 are substantially larger than those obtained with the raster path. This is because the spiral paths fail to take full advantage of inherent substrate pre-heating, which for the raster path significantly reduces the average warping. A comparison of Figs. 1 and 2 indicates more strongly decreasing curvatures (i.e., more inherent substrate pre-heating) in welding than in microcasting. As a result, the average ( $n = 2$ ) curvatures for the raster path specimens of Table 2 are much lower than the microcast results of Table 1. It should finally be noted that as observed for microcasting, results for the welded raster path specimens indicate greater warping parallel to the deposition direction.

Table 2. Welded Specimen Average ( $n = 2$ ) Curvature Results

Specimen # (Path)	1 (Raster)	2 (Raster)	3 (Outside-In)	4 (Inside-Out)	5 (Inside-Out)
$w_{,xx} / \kappa_{max}$	0.0933	0.0948	0.151	0.302	0.300
$w_{,yy} / \kappa_{max}$	0.0784	0.0734	0.197	0.270	0.283

(Note:  $\kappa_{max} = 0.00834 \text{ in}^{-1}$ )

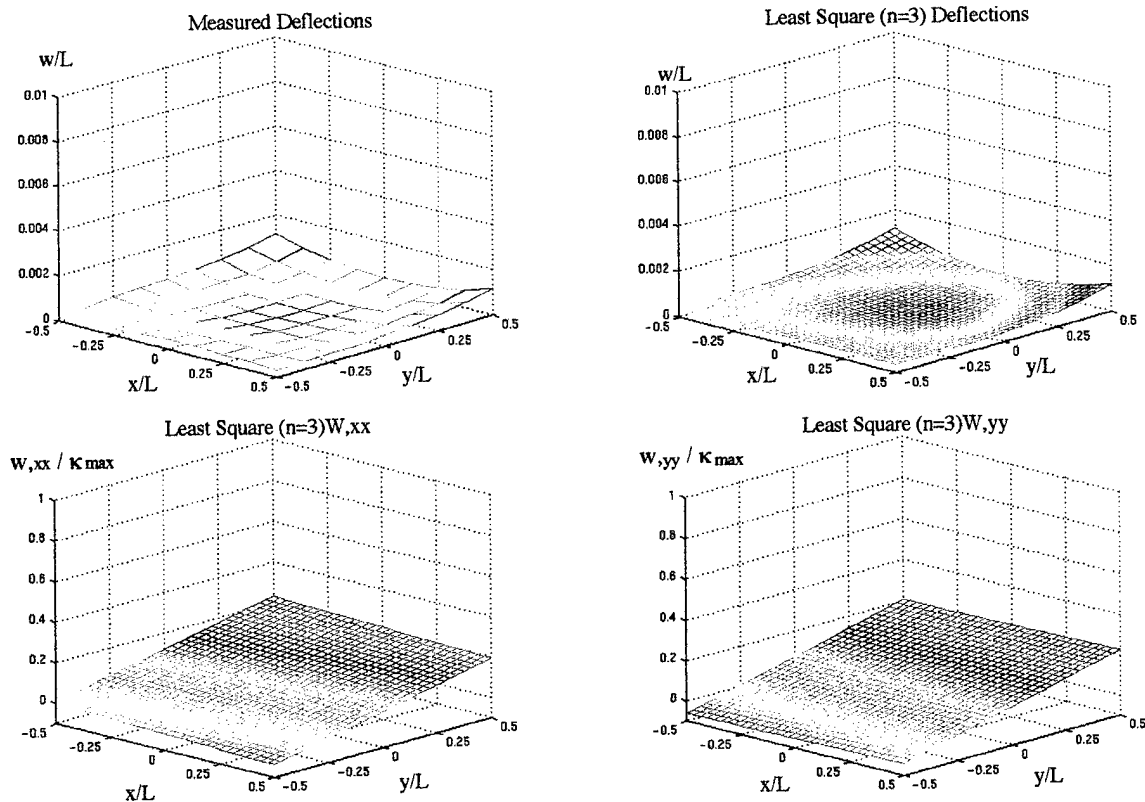


Figure 2. Representative Measured and Least Square ( $n = 3$ ) Welded Raster Path Results

### Implications of the Measured Results

Several practical implications for direct metal deposition processes are evident from the experimental results. First of all, results suggest that when depositing in a raster path, material should not be deposited parallel to the longest part dimension. Because the curvature is greatest parallel to the deposition direction, depositing parallel to the longest part dimension would result in greater warping deflections and loss of tolerance. Secondly, it is advisable to use a deposition path which takes full advantage of inherent substrate preheating. While spiral paths result in more uniform warping, raster paths are more effective for pre-heating the substrate. Finally, the

experimental results suggest that a uniform substrate pre-heating prior to material deposition can be used to gain an initial advantage, after which the process provides substantial substrate heating.

### Modeling of Warping

Modeling warping in deposited metals is facilitated by the following key ideas. During material deposition, the deposit and substrate are constrained from warping and the resulting residual stress state is determined by high-temperature nonlinear material response. Following manufacture, the plate is released from its constraints, which results in primarily elastic unloading. Thus, given the constrained residual stress state, subsequent warping can be predicted by an elastic analysis. In this study, the 1-D axisymmetric and 2-D generalized plane strain (GPS) thermomechanical finite element models of Chin (1998) are used to model the constrained residual stress state for a thin layer of stainless steel deposited onto a carbon steel substrate. As previously mentioned, the numerical models are designed to approximate residual stresses in microcasting. The 1-D models effectively represent an entire layer deposited at once (Fig. 3a), and predict upper bounds on warping in microcast deposits (Chin *et al.* 1996a). The GPS models are used in this study to model a single deposited layer composed of five successively deposited rows (Fig. 3b). As opposed to the 1-D models, the GPS models can account for deposited row free-edge effects as well as substrate pre-heating occurring during material deposition. In addition, they enable a comparison of the warping curvatures parallel and transverse to the deposition direction.

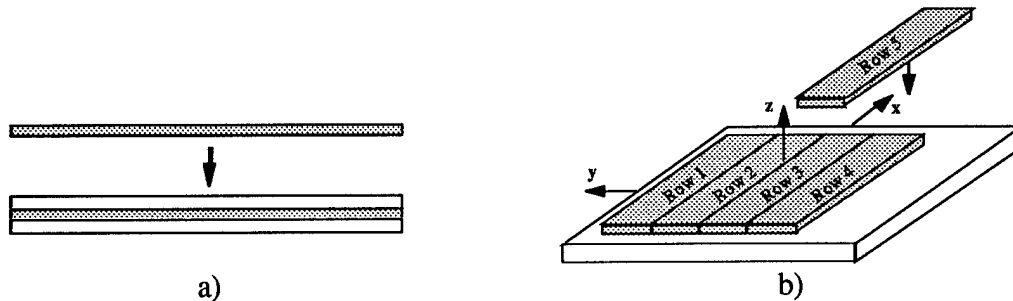


Figure 3. Physical Interpretation of a) 1-D Axisymmetric and b) GPS Models

#### 1-D Axisymmetric Models

The 1-D numerical modeling procedures used here follow those described in detail by Chin *et al.* (1996a). A schematic of the 1-D axisymmetric model geometry and boundary conditions is depicted in Fig. 4.

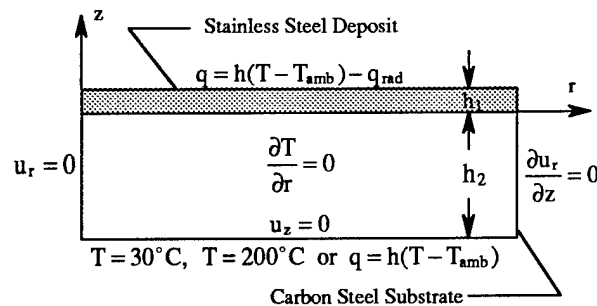


Figure 4. 1-D Axisymmetric Model Geometry and Boundary Conditions

In brief, an initially molten stainless steel deposit is bonded to an initially room temperature carbon steel substrate, after which the deposit and substrate are allowed to cool to room temperature. Both the deposit and substrate are assumed to have elastic-perfectly plastic constitutive behavior, with temperature-dependent elastic properties and yield strengths (Chin *et al.* 1996a). The thicknesses of the stainless steel deposit and carbon steel substrate are  $h_1 = 0.055''$  and  $h_2 = 0.470''$ ,

respectively, which are in keeping with the final dimensions of the warping specimens previously discussed. The mechanical constraints are meant to approximate the bolted constraints in the experiments (i.e., no warping). The thermal model used is one-dimensional, with appropriate boundary conditions applied to the top and bottom surfaces. As seen in Fig. 4, three separate thermal boundary conditions on the bottom surface of the substrate are considered: a fixed temperature of  $T = 30^\circ\text{C}$ , a fixed temperature of  $T = 200^\circ\text{C}$ , and a convection condition. Compared to the fixed temperature conditions, the convection condition is nearly equivalent to thermal insulation. The 1-D axisymmetric models predict an equal biaxial constrained residual stress distribution  $\sigma_r(z)$ , which can be readily used in obtaining curvatures. As outlined in Klingbeil (1998), the elastic release of constraints is equivalent to application of the biaxial bending moment  $M = \int -\sigma_r(z) z dz$ , which is related to the warping curvatures  $w_{,xx} = w_{,yy} = \kappa$  through the elastic plate theory relation  $\kappa = (1 - \nu)M/EI$ . Note that the 1-D models can only predict equal and uniform curvatures in the x and y directions.

### 2-D Generalized Plane Strain (GPS) Models

The thermomechanical modeling procedures used for the GPS models are described in detail by Chin (1998), and are only briefly summarized here. The GPS model geometry and boundary conditions are depicted in Fig. 5. In short, each initially molten "row" of stainless steel (which corresponds to four deposited rows in the actual microcasting process) is successively bonded to the carbon steel substrate, with a 160 second delay between rows to approximate the real-time experiments. The generalized plane strain theory applied here assumes that the 2-D model lies between two rigid bounding planes which are orthogonal to the axial direction of the model (the x direction in Fig. 5). As opposed to plane strain, where the bounding planes are fixed, generalized plane strain allows relative rigid body movement between the two planes. Thus, the planes may undergo a relative uniform axial displacement  $u_x$ , as well as relative rotations per unit length  $\phi_y$  and  $\phi_z$  about the y and z axes, respectively. As for the 1-D models, the mechanical constraints of Fig. 5 are chosen to approximate the bolted constraints in the experiments (i.e., no warping). Thus, the right and left edges are constrained to be vertical, while the out-of-plane rotation  $\phi_y$  is constrained to be zero. As for the 1-D models, three separate thermal boundary conditions on the bottom of the substrate are considered ( $T = 30^\circ\text{C}$ ,  $T = 200^\circ\text{C}$ , and convection). Following deposition of the final row and cooling to room temperature, warping deformation is obtained in a separate solution step by releasing both the in-plane constraints and the out-of-plane constraint  $\phi_y$ . As discussed by Klingbeil (1998), it is possible to obtain 3-D numerical plate deflections from the 2-D GPS in-plane deflections and out-of-plane rotation  $\phi_y$ . Predicted  $n = 2$  and  $n = 3$  curvatures  $w_{,xx}$  and  $w_{,yy}$  are then obtained using the same 2-D polynomial least square fits applied to experimental displacement data.

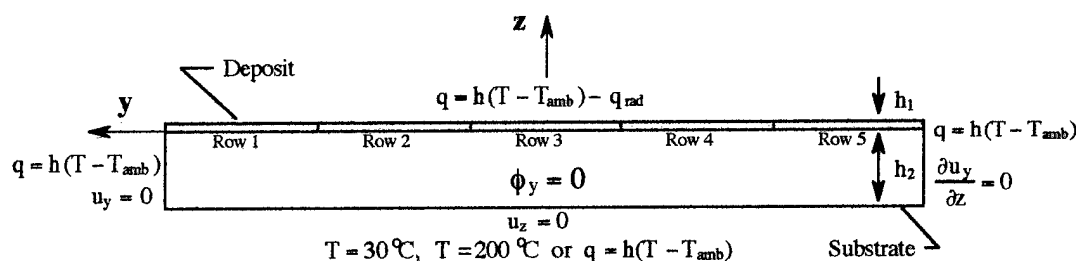


Figure 5. Generalized Plane Strain Geometry and Boundary Conditions

### Representative Numerical Results

The 1-D axisymmetric and average ( $n = 2$ ) GPS curvature results for each of the three thermal boundary conditions are given in Table 3. As seen in Table 3, the GPS curvatures in each

direction are for all cases substantially less than the 1-D model predictions. This result is consistent with the deposited row free-edge effects and inherent substrate heating accounted for in the generalized plane strain modeling, which suggests that the GPS models are closer to capturing the physical conditions present during actual material deposition. In addition, the trends in both sets of results with respect to the thermal boundary condition on the bottom are as expected. Namely, the  $T = 30^{\circ}\text{C}$  condition results in the most warping, while the convection condition results in the least warping.

Table 3. Numerical Model Curvature Predictions

Thermal B.C. on Bottom	1-D Model $\kappa / \kappa_{\max}$	GPS Average (n = 2) Curvatures	
		$w_{,xx} / \kappa_{\max}$	$w_{,yy} / \kappa_{\max}$
$T = 30^{\circ}\text{C}$	0.819	0.661	0.689
$T = 200^{\circ}\text{C}$	0.515	0.371	0.472
Convection	0.257	0.134	0.186

(Note:  $\kappa_{\max} = 0.00834 \text{ in}^{-1}$  )

As previously mentioned, the thermomechanical models are designed to capture residual stresses in microcasting. A comparison of Tables 1 and 3 indicates that for both the 1-D and GPS models, the  $T = 30^{\circ}\text{C}$  and convection conditions respectively serve as upper and lower bounds on the measured microcast results. In addition, both the 1-D and GPS numerical models indicate that the  $T = 200^{\circ}\text{C}$  condition offers substantially less warping than the  $T = 30^{\circ}\text{C}$  condition, which supports the observation that substrate preheating results in less warping. With respect to a difference in warping in the two directions, however, the GPS results do not agree with the measured observations. Furthermore,  $n = 3$  GPS curvature results (not shown here) were unable to capture the variation in  $w_{,yy}$  observed in the raster path experiments. As discussed by Klingbeil (1998), the discrepancies between trends in the GPS and measured results can be attributed to the out-of-plane constraints of the GPS models coupled with large-scale elastic-plastic deformation during manufacture. In brief, the GPS constraints result in severe interactions between rows, which when accompanied by large-scale nonlinear behavior can substantially affect the gradients in the out-of-plane stress distributions responsible for subsequent warping in the x direction. Such interactions could physically exist for rectangular plates which are long in the x direction, however such interactions are unlikely for square plates such as those used in the experiments.

#### Implications of the Numerical Results

The numerical results suggest that substrate pre-heating/insulating conditions can play an important role in direct metal deposition processes. Both the 1-D and GPS numerical models indicate that the  $T = 200^{\circ}\text{C}$  condition offers substantially less warping compared to the  $T = 30^{\circ}\text{C}$  condition, while the convection condition gives the least warping of all. Thus, the results suggest that a combination of uniform substrate pre-heating and thermal insulation beneath the substrate could be an effective means for reducing warping. Another important implication of the numerical results is evident from the discrepancies between the GPS models and the measured observations. Namely, the generalized plane strain models indicate that when modeling high-temperature nonlinear material response, the role of constraints is vitally important. This suggests that constraints used during actual material deposition (i.e., exactly how the part is secured during manufacture) may have a measurable effect on subsequent warping.

#### Conclusions

Residual stress-induced warping is perhaps the most fundamental obstacle to overcome in direct layered manufacturing of fully-dense metal parts. From this work two major conclusions can be made, which are relevant to SDM and other SFF processes. First, it appears that a

combination of substrate preheating (to reduce initial thermal mismatches) and substrate insulation (to exploit preheating by the process itself) could give substantial payoffs in limiting residual stress-induced warping. This is in contrast to active, controlled part heating throughout the deposition process, which would be cumbersome and costly to implement. Previous work by the authors has demonstrated the importance of constraining parts from warping during manufacture to limit warping deflections in finished parts. The results of this study further suggest that maintaining 3-D mechanical constraints that are consistent from part to part is also important. Because of large-scale thermoplastic deformation during manufacture, small changes in part constraints can result in unacceptable changes in warping deformations. Specifically, results in this study suggest that subtle changes in 3-D part constraints can reverse directional differences in warping seen as a result of deposition path.

### Acknowledgments

This work has been supported by the National Science Foundation under grants EID-9256665, DMI-9700320 and DMI 9415001.

### References

- Amon, C.H., Beuth, J.L., Merz, R., Prinz, F.B. and Weiss, L.E., 1998, "Shape Deposition Manufacturing with Microcasting: Processing, Thermal and Mechanical Issues," *Journal of Manufacturing Science and Engineering*, in print.
- Chin, R.K., 1998, "Thermomechanical Modeling of Residual Stresses in Layered Manufacturing with Metals," Ph.D. Thesis Dissertation, Carnegie Mellon University.
- Chin, R.K., Beuth, J.L. and Amon, C.H., 1996a, "Thermomechanical Modeling of Molten Metal Droplet Solidification Applied to Layered Manufacturing," *Mechanics of Materials*, Vol. 24, 257-271.
- Chin, R.K., Beuth, J.L. and Amon, C.H., 1996b, "Thermomechanical Modeling of Successive Material Deposition in Layered Manufacturing," *Proc. 1996 Solid Freeform Fabrication Symposium* (D.L. Bourell, J.J. Beaman, H.L. Marcus, R.H. Crawford, and J.W. Barlow, eds.), Austin, August 1996, 507-515.
- Chin, R.K., Beuth, J.L. and Amon, C.H., 1995, "Control of Residual Thermal Stresses in Shape Deposition Manufacturing," *Proc. 1995 Solid Freeform Fabrication Symposium* (H.L. Marcus, J.J. Beaman, D.L. Bourell, J.W. Barlow and R.H. Crawford, eds.), Austin, August 1995, 221-228.
- Fessler, J.R., Merz, R., Nickel, A.H. and Prinz, F.B., 1996, "Laser Deposition of Metals for Shape Deposition Manufacturing," *Proc. 1996 Solid Freeform Fabrication Symposium* (D.L. Bourell, J.J. Beaman, H.L. Marcus, R.H. Crawford, and J.W. Barlow, eds.), Austin, August 1996, 117-124.
- Klingbeil, N.W., 1998, "Residual Stress-Induced Warping and Interlayer Debonding in Layered Manufacturing," Ph.D. Thesis Dissertation, Carnegie Mellon University.
- Klingbeil, N.W., Zinn, J.W. and Beuth, J.L., 1997, "Measurement of Residual Stresses in Parts Created by Shape Deposition Manufacturing," *Proc. 1997 Solid Freeform Fabrication Symposium* (D.L. Bourell, J.J. Beaman, R.H. Crawford, H.L. Marcus, J.W. Barlow, eds.), Austin, August 1997, 125-132.
- Merz, R., Prinz, F.B., Ramaswami, K., Terk, M. and Weiss, L.E., 1994, "Shape Deposition Manufacturing," *Proc. 1994 Solid Freeform Fabrication Symposium* (H.L. Marcus, J.J. Beaman, J.W. Barlow, K.L. Bourell and R.H. Crawford eds.), Austin, August 1994, 1-8.
- Prinz, F.B., *et al.*, 1997, *JTEC/WTEC Panel Report on Rapid Prototyping in Europe and Japan, Vol. 1*, Rapid Prototyping Association of the Society of Manufacturing Engineers, 1997.
- Prinz, F.B., Weiss, L.E., Amon, C.H. and Beuth, J.L., 1995, "Processing, Thermal and Mechanical Issues in Shape Deposition Manufacturing," *Proc. 1995 Solid Freeform Fabrication Symposium* (H.L. Marcus, J.J. Beaman, D.L. Bourell, J.W. Barlow and R.H. Crawford, eds.), Austin, August 1995, 118-129.

# FDM Systems and Local Adaptive Slicing

Justin Tyberg and Jan Helge Bøhn

Mechanical Engineering, Virginia Tech  
Blacksburg, VA 24061-0238, U.S.A.  
tel.: 540-231-3276, fax.: 540-231-9100, e-mail: bohn@vt.edu

Fabrication times for layered manufacturing systems can be significantly reduced by continuously maximizing the build layer thickness, within the bounds of the system's fabrication capabilities and the surface deviation tolerance derived from the part surface geometry. This paper describes how parts and features within a build volume can be adaptively sliced independently of each other such that each is fabricated with distinct build layer thicknesses. This enables significant reduction in fabrication times relative to conventional adaptive build layer thickness techniques. The new approach has been implemented on a FDM 1600 rapid prototyping system, together with a revised system calibration to ensure smooth surface transitions between dissimilar build layer thicknesses.

## 1 Introduction

Fused Deposition Modeling (FDM) is today the second most common commercial layered manufacturing system. It fabricates parts by extruding molten wax or thermoplastic material through a small nozzle to form a thin bead or "road" that is deposited in a predetermined pattern to complete each build layer, bonding the extrudate to adjacent and previously deposited roads. The motion of the extrusion system operates under three-dimensional computer numerical control (CNC). The extrusion system consists of a small ram extruder in which the spooled filament feedstock pushes molten material through the liquefier with low shear. The feedstock is driven into the extruder by counter rotating rollers as needed under CNC, where it is heated to a manually set temperature,  $T_L$ . The extrudate is deposited within a build chamber holding a manually set temperature,  $T_C$ . In the FDM 1600 rapid prototyping system,  $T_L$  and  $T_C$  can be up to 300°C and 70°C, respectively.

The most common build material used with FDM systems is P400 ABS plastic (Stratasys, Inc.), and it is available in several stock colors, including white, red, blue, green, yellow and black. This material is, in the FDM 1600 rapid prototyping system, typically extruded with  $T_L$  and  $T_C$  set at 270°C and 70°C, respectively, through a 0.012" (0.30 mm) nozzle orifice to form roads that are 0.010" (0.25 mm) thick and 0.020" (0.51 mm) wide, while being deposited at a rate of 0.8 in/s (2 cm/s). This corresponds to a maximum standard deposition rate of 0.6 in<sup>3</sup>/hr (9.4 cm<sup>3</sup>/hr), that is reduced by delays in starting and stopping of deposition, motion from one build layer to the next, and the fabrication of support structures as needed. This particular combination of hardware, materials and processing parameters has been precisely calibrated by Stratasys, Inc. to enable FDM users to produce some of the most dimensionally accurate parts in the layered manufacturing industry; and it has proven itself particularly useful in the prototype production of functional and semi-functional to-be-injection-molded plastic parts.

As with most layered manufacturing systems, there are two areas in which FDM systems could benefit from further improvements. These are (1) reduction of build times, and (2) improvement of part surface smoothnesses. These needs for improvement are driven by design

and marketing personnel's desire to access smooth functional prototype parts within minutes of a design change. This, however, is still beyond the capabilities of current layered manufacturing technologies: Today a prototype part takes hours or days to build—and hours of manual labor to finish—only for it to often be disposed of within minutes of its completion once the quick inspection or test it was intended for has been performed. It is therefore desirable to (a) increase the average material deposition rate to reduce the build time, and (b) reduce the build layer thicknesses to produce smoother parts that require less finishing.

These two objectives can be approached by applying the basic principle of continuously varying the material deposition rate such that, at all times, the maximum material deposition rate is used that satisfies the local surface deviation tolerance across the part being fabricated. This principle has been demonstrated by adaptively adjusting the build layer thicknesses such that they are maximized subject to meeting surface deviation tolerances [1-5], and by increasing build layer thicknesses in the interior of the part [4,6]. As these two approaches are combined, significant improvements in material deposition rates can be realized; limited primarily by the capabilities of the hardware. For instance, in the case of the FDM 1600 rapid prototyping systems building with P400 ABS plastic and using the standard 0.012" (0.30 mm) nozzle orifice, the maximum physical material deposition rate achievable is 4.3 in<sup>3</sup>/hr (70.8 cm<sup>3</sup>/hr). This corresponds to a 0.030" (0.76 mm) thick by 0.050" (1.27 mm) wide road being deposited at 0.8 in/s (2 cm/s), which is 7.5 times the standard rate. If, in addition, a 0.100" (2.54 mm) air spacing is inserted between the roads interior to the part, then the maximum virtual material deposition rate increases to 13 in<sup>3</sup>/hr (212 cm<sup>3</sup>/hr), or 22.5 times the standard rate. We therefore see the potential of fabricating parts by FDM in hours instead of days while achieving a surface smoothness equivalent to that of 0.003 - 0.005" (0.07 - 0.13 mm) uniform thickness build layers.

This paper reviews recent efforts towards achieving these objectives, and, in particular, that of fabricating smooth-surface parts by FDM in the minimum amount of time. The following sections describe a significant improvement to previous adaptive slicing techniques [7,8], issues that surfaced when migrating this work from computer simulations to actual fabrication, and how these issues were resolved to produce the desired outcome; namely, fast, smooth-surface parts by FDM.

## 2 Local Adaptive Slicing

Conventional adaptive slicing techniques [1-5] have demonstrated the potential benefit of adaptive slicing, but have not made it out of the laboratory setting. In particular, adaptive slicing has only been applied to simple geometries, one part at a time; a situation that differs substantially from most industry settings where part geometries are often complex and where multiple parts are often fabricated concurrently within the build envelope. Figure 1 illustrates the consequence of applying conventional adaptive slicing techniques to a more complex scenario. It shows how decisions made to satisfy the surface deviation tolerance of one part or part-feature, in this case the sphere, overrule the lesser needs of the more simplistic block. As a result, the block is fabricated with layers that are needlessly thin and valuable fabrication time is wasted.

Figure 2 illustrates a more desirable situation that results from fabricating the same parts independently of one another. A method to achieve this independence has been developed and is described in detail elsewhere [7,8]. Briefly, this new approach, which has been termed local adaptive slicing, consists of a three-step process that is based on stepwise uniform refinement [4,5]. First, all the parts in the build volume are sliced into thick uniform-thickness slabs. Then the contours on the top and the bottom of each slab at a given height are grouped into sub-slabs that

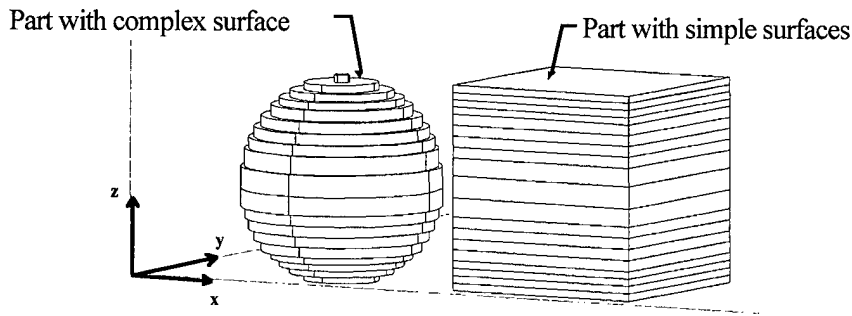


**Figure 1** The potential savings of adaptive slicing is lost by conventional slicing methods that slice all parts of a given build volume with the same resolution, regardless of their dissimilar surface characteristics. In this figure, the thin layers necessary for the sphere are imposed unnecessarily on the block.

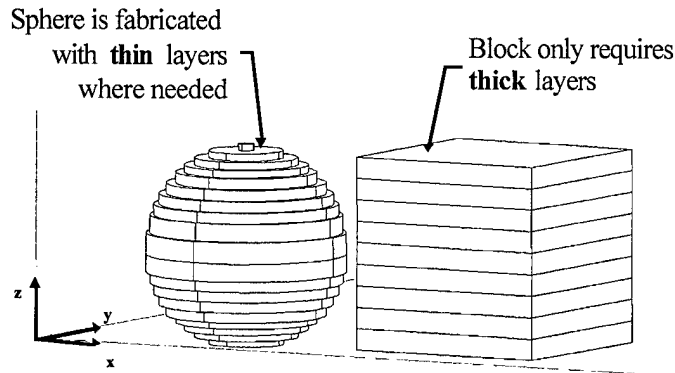


**Figure 2** The new approach fabricates individual parts and part-features independently with distinct layer resolutions applied locally as necessary.

reflect that these contours would be physically connected by a surface even if only the sub-slabs at that particular height were fabricated. Finally, each sub-slab is sliced independently into some integral number of uniform-thickness slices to satisfy the surface deviation tolerance of that particular sub-slab. Hence, all sub-slabs are of equal thickness, regardless of how each one is subdivided into thinner build layers, and can therefore easily be processed and fabricated independently of one another.

In the FDM 1600 rapid prototyping system, the build volume is subdivided into 0.030" (0.76 mm) thick slabs, that correspond to the thickness of the maximum flow rate roads described in Section 1. This facilitates the fabrication of the interior of each sub-slab using these roads and the exterior using thinner roads that satisfy local surface deviation tolerance requirements [4,6]. Each sub-slabs' exterior regions are subdivided into an integral number of uniform thickness build layers,  $\alpha_{slab}$ , using the criteria developed by Dolenc and Mäkelä [1] and refined by Sabourin *et al.* [4,5], but limiting the points of consideration to only those that are associated with a particular sub-slab when determining the optimal subdivision for that sub-slab:

$$\alpha_{sub-slab} = \text{int} \left( \frac{L_{max}}{C_{max}} \max\{n_z\} \right), \quad \alpha_{sub-slab} \in [1, \alpha_{max}], \quad \alpha_{max} = \text{int} \left( \frac{L_{max}}{L_{min}} \right) \quad (1)$$

where  $L_{min}$  and  $L_{max}$  are the minimum and maximum build layer thicknesses available, respectively;  $C_{max} \geq L_{min}$  is the maximum permissible surface deviation error; and  $\{n_z\}$  is the set of unit normal z-components for all the points along all the contours of the sub-slab. The build layer thickness used to fabricate this particular sub-slab therefore becomes

$$l_{sub-slab} = \frac{L_{max}}{\alpha_{sub-slab}} \quad (2)$$

The FDM 1600 has a Z-stage resolution of 0.0005" (0.013 mm) and a proven quality fabrication capability with P400 ABS plastic for build layers with thicknesses in the range of 0.005" to 0.015" (0.13 - 0.38 mm); the 0.030" (0.76 mm) layers produce overly rough part surfaces. Therefore, it is reasonable to limit  $\alpha_{slab}$  to integers between 6 and 2, inclusive, which corresponds to fabricating with 0.0050", 0.0060", 0.0075", 0.0100", and 0.0150" (0.13, 0.15, 0.19, 0.25, and 0.38 mm) build layers. Hence, these are the only layer thicknesses for which we need to determine and manage flow rates.

### 3 Implementation Issues

The above fabrication procedure was implemented using an FDM 1600 with a 0.012" (0.30 mm) nozzle orifice and P400 ABS plastic. The software developed reads any CAD model described in the .STL file format, generates the contours on each build layer, and exports them as an .SSL file complete with layer thickness and flow rate information. QuickSlice 5.0, the FDM post-processor by Stratasys, Inc., can then use this information generate the actual roads that are described in the .SML file format for control of the FDM 1600.

The software appears to be robust and it generates .SML files with values that are identical to what would be generated if this process had been executed manually. Unfortunately, the initial fabricated parts were not satisfactory. While the part surfaces where the build layers were constant were smooth, including across sub-slabs, there was a small but noticeable discontinuity wherever there was a change in build layer thickness, and particularly when there was a change between the 0.005" (0.13 mm) and 0.015" (0.38 mm) build layers. In addition, the thinner layers tended to delaminate and thus further reduced the resulting surface quality.

The smooth part surfaces where the layer thickness was constant indicated that it is within the capability of the hardware and material to consistently produce high-quality part surfaces. This led us to suspect that the discontinuity problem was a function of poor calibration. A closer examination of the calibration tables used by QuickSlice 5.0 strengthened this hypothesis. As shown in Figure 3, the calibration curves for several of the layer thicknesses used, are composed of several  $C^0$  discontinuous, piecewise logarithmic curve segments. This is contrary to what one would expect since there is no discontinuity or sharp change in the flow characteristics of ABS plastic at these flow, pressure, and temperature levels. Therefore, if the transitions along a constant layer-thickness curve are imprecise, the transitions from one build-layer-thickness curve to the next would also have to be imprecise, and this latter imprecision would explain the discontinuities that were experienced on the part surfaces when changing from one build layer thickness to another. The standard FDM calibration tables for P400 ABS plastic should therefore be revised to accurately reflect actual material behavior so smooth, adaptively sliced part surfaces can be fabricated.

The delamination problem, on the other hand, was not due to inaccurate calibration, but to insufficient material weld time. The low material volumes and flow rates associated with thin

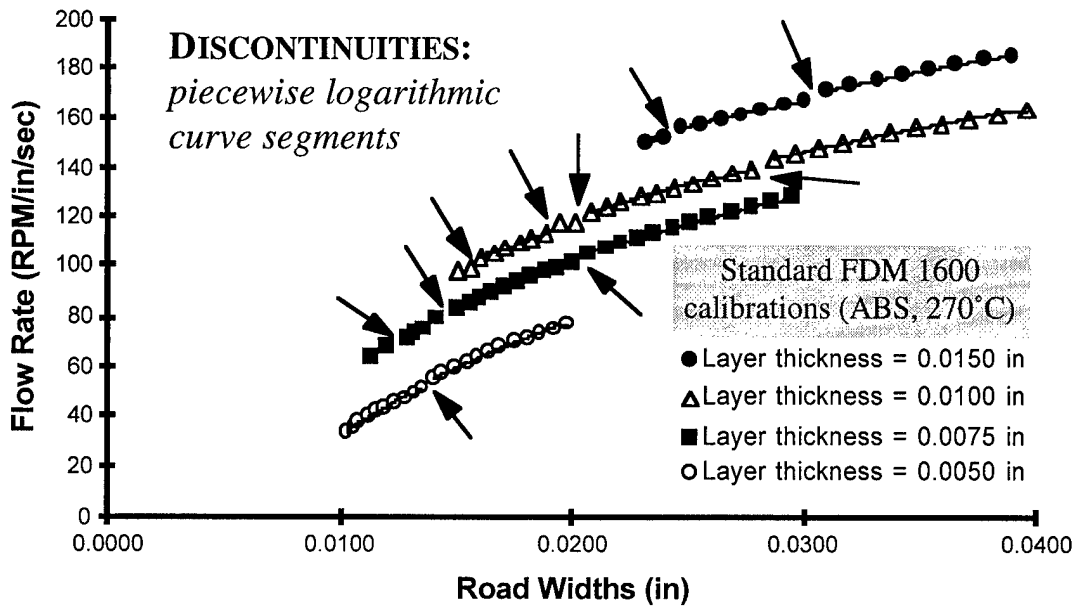


**Figure 3** Standard FDM 1600 calibration values for P400 ABS plastic extruded at  $T_L = 270^\circ\text{C}$  through a 0.012" (0.30 mm) nozzle orifice into a  $T_C = 70^\circ\text{C}$  build envelope.

roads cause the extrudate to cool down too fast for it to weld sufficiently to the previously deposited material. This weakened weld often breaks under the pulling force exerted by the liquefier as it traces across the build plane. When this occurs, the newly deposited road will be free to lean in the direction of the motion of the liquefier, which will change the road's location and disrupt the steady-state material flow rate, and, ultimately, distort the part geometry.

The effective weld time can be extended, to increase the strength of the weld, by increasing the extrusion temperature,  $T_L$ . Stratasys, Inc. recommends increasing  $T_L$  to  $290^\circ\text{C}$  and lowering  $T_C$  to  $50^\circ\text{C}$  when fabricating with 0.007" (0.18 mm) build layers in the FDM 2000 [9]. We therefore duplicated these temperature changes in the FDM 1600, and we found that it effectively eliminated the delamination problem while still allowing fabrication with the thicker build layers. This observation is important because the temperature settings are set manually, and, therefore, all build layer thicknesses must be fabricated at the same temperature configuration. However, since the material flow rate is affected by changes in temperature, and the standard calibration tables are based on a different  $T_L / T_C$  combination, a change in processing temperatures called for a revision of the calibration tables, at the new  $T_L / T_C$  combination, to enable accurate and smooth part-surface fabrication.

#### 4 Calibrations

Both the apparent inaccuracies of the standard FDM 1600 calibration tables and the change in processing temperatures made revising the calibration tables necessary to facilitate accurate and smooth part-surface fabrication using adaptive slicing techniques. The actual road widths that result from various constant build layer thickness / material feed rate /  $T_L / T_C$  combinations had to be measured. These measurements were obtained by building several series of vertical walls. Each wall was 2.0" (50 mm) long, 0.25" (6.4 mm) tall, had the width of a single bead, and was assigned a flow rate value of even number between 2 and 254 (RPM/inch/sec) [10]. Each series

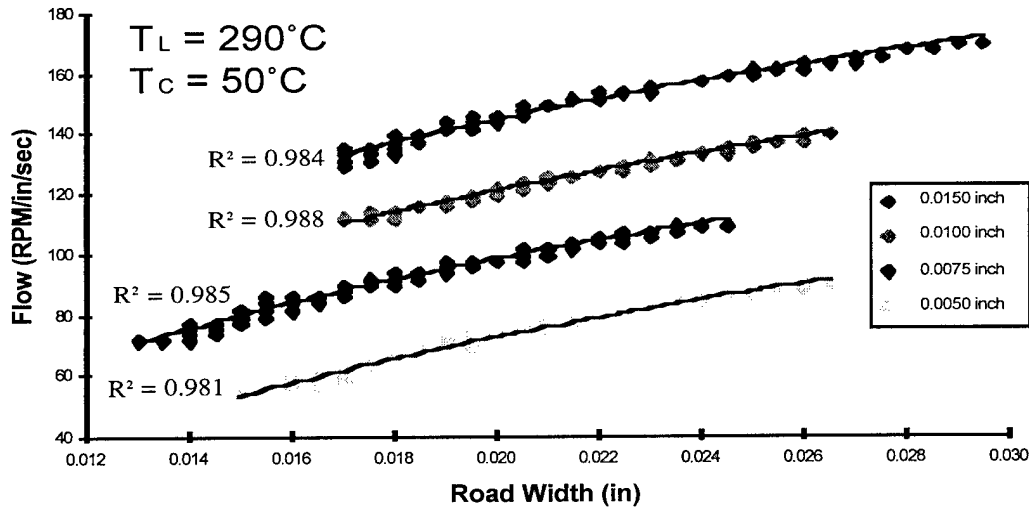


**Figure 4** Revised FDM 1600 calibration values for P400 ABS plastic extruded at  $T_L = 290^\circ\text{C}$  through a 0.012" (0.30 mm) nozzle orifice into a  $T_C = 50^\circ\text{C}$  build envelope. Continuous logarithmic curves are fitted to data points that represent measured road widths for given flow rates at fixed build layer thicknesses.

contained up to 21 parallel walls that were given sequentially increasing flow rates and were located about 0.4" (10 mm) apart on a single support material base. This base was placed in the center of the build chamber, and its walls were oriented in the direction of the heated air flow in the build chamber, to provide near uniform material cooling.

12 series of walls were fabricated using a nozzle orifice diameter of 0.012" (0.30 mm);  $T_L / T_C$  settings of  $270^\circ\text{C} / 70^\circ\text{C}$ ,  $290^\circ\text{C} / 70^\circ\text{C}$ , and  $290^\circ\text{C} / 50^\circ\text{C}$ ; and build layer thicknesses of 0.0050", 0.0075", 0.0100", and 0.0150" (0.13, 0.19, 0.25, and 0.38 mm). The flow rates comprised all even numbers between 50 and 90, 70 and 110, 112 and 140, and 130 and 170, for the 0.0050", 0.0075", 0.0100", and 0.0150" (0.13, 0.19, 0.25, and 0.38 mm) build layer thickness, respectively. The head speed was kept constant at 0.8 in/s (20.3 mm/s). The external ambient conditions were measured with a thermometer and hydrometer on top of the FDM 1600. The temperature measured between  $78^\circ\text{F}$  and  $80^\circ\text{F}$  ( $25^\circ\text{C}$  and  $27^\circ\text{C}$ ), and the relative humidity measured between 25% and 32%.

Five measurements were taken from each wall using a caliper with a 0.0005" (0.01 mm) resolution. All measurements were obtained from the central regions of the lines to ensure that only steady-state deposition was being measured. These measurements were graphed using Microsoft Excel 7.0 and fitted with a single continuous logarithmic curve for each build layer thickness /  $T_L / T_C$  combination (Figure 4). The functions described by these curves were then used to revise the calibration tables used by QuickSlice 5.0.

## 5 Results

With the revised calibration tables installed, the part surface quality produced by the FDM 1600 rapid prototyping system noticeably improved. The former discontinuities that occurred at transitions between dissimilar build layer thicknesses can no longer be observed visually or by human touch (ref. arrow in Figure 5). The only remaining sign of these transitions are the line density changes reflecting off the part surfaces.

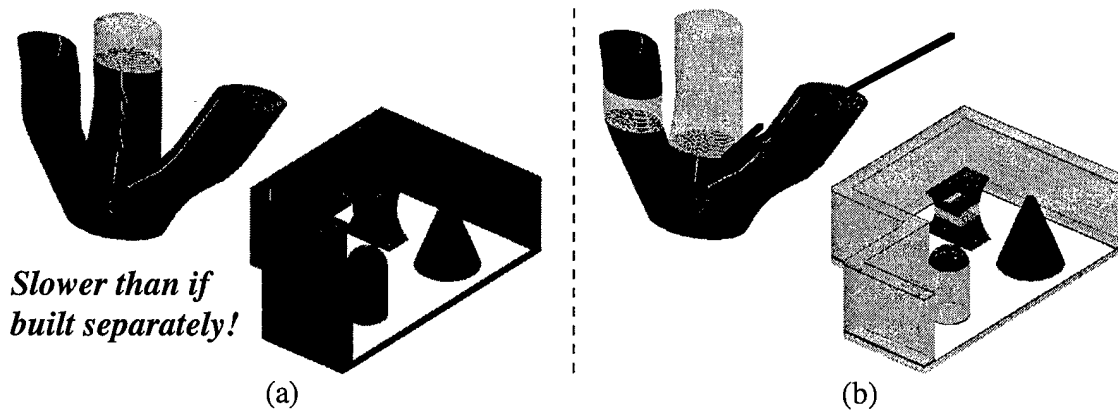


**Figure 5** Two parts with a number of individual features were fabricated concurrently in a single build volume using (a) conventional adaptive slicing and (b) local adaptive slicing. Both sets hold the same overall surface tolerance, but set (b) requires 37% less fabrication time. The medium, dark, and light gray areas are 0.0050", 0.0075", and 0.0150" (0.13, 0.19, and 0.38 mm) build layers, respectively. The arrow shows the location of the approximate 0.005" (0.13 mm) discontinuity before revising the calibration tables.

The potential time savings from adaptively slicing each part-feature independently are substantial. In Figure 5, the two parts were adaptively sliced with  $C_{max}$  set to 0.0035" (0.09 mm) and fabricated with 0.0050", 0.0075", and 0.0150" (0.13, 0.19, and 0.38 mm) build layer thicknesses. With this configuration, local adaptive slicing reduced the fabrication time by 37% compared to conventional adaptive slicing. This case illustrates how the performance of conventional adaptive slicing degrades as the number of parts and part-features increase: In Figure 5(a), the right-most "finger" of the left part requires thin build layers, and these thin layers are imposed onto the two other fingers and the vertical walls on the part to the right. Hence, when using conventional adaptive slicing, it takes 12% longer to fabricate the two parts concurrently than sequentially. Local adaptive slicing, on the other hand, does not carry a penalty for concurrent fabrication; instead, in the case shown here, there is a 4% reduction because fewer vertical layer-to-layer movements are needed during concurrent fabrication.

## 6 Conclusions

A new effective approach to adaptive slicing has been developed. It fabricates all parts and part-features independently of one another. Therefore, its effectiveness does not deteriorate as part complexities and build volumes increase. Conventional adaptive slicing techniques, on the other hand, do deteriorate under such conditions, and are therefore impractical in an industrial setting.

To implement local adaptive slicing on FDM 1600 rapid prototyping system, it was necessary to (1) increase the extrusion temperature to prevent delamination when fabricating with thin build layers, and (2) revise the calibration tables to enable accurate and smooth part-surfaces.

## Acknowledgement

FDM® is a registered trademark of Stratasys, Inc. of Minneapolis, Minnesota, U.S.A., Reg. No. 1,663,961.

## References

- [1] A. Dolenc and I. Mäkelä, "Slicing Procedures for Layered Manufacturing Techniques," *Computer-Aided Design*, vol. 26, no. 2, February 1994, pp. 119-126.
- [2] Y. S. Suh and M. J. Wozny, "Adaptive Slicing of Solid Freeform Fabrication Processes," *Proc., Solid Freeform Fabrication Symposium*, H. L. Marcus, *et al.*, eds., University of Texas at Austin, Austin, Texas, U.S.A., August 8-10, 1994, pp. 404-411.
- [3] P. Kulkarni and D. Dutta, "An Accurate Slicing Procedure For Layered Manufacturing," *Computer-Aided Design*, vol. 28, no. 9, September 1996, pp. 683-697.
- [4] E. Sabourin, "Adaptive High-Precision Exterior, High-Speed Interior, Layered Manufacturing," M.S. thesis, Mechanical Engineering, Virginia Tech, Blacksburg, Virginia, U.S.A., February 1996.  
URL: <http://cadserv.cadlab.vt.edu/bohn/projects/sabourin/>
- [5] E. Sabourin, S. A. Houser, and J. H. Bøhn, "Adaptive Slicing Using Stepwise Uniform Refinement," *Rapid Prototyping Journal*, vol. 2, no. 4, 1996, pp. 20-26.
- [6] E. Sabourin, S. A. Houser, and J. H. Bøhn, "Accurate Exterior, Fast Interior Layered Manufacturing," *Rapid Prototyping Journal*, vol. 3, no. 2, 1997, pp. 44-52.
- [7] J. Tyberg, "Local Adaptive Slicing for Layered Manufacturing," M.S. thesis, Mechanical Engineering, Virginia Tech, Blacksburg, Virginia, U.S.A., February 1998.  
URL: <http://cadserv.cadlab.vt.edu/bohn/projects/tyberg/>
- [8] J. Tyberg and J. H. Bøhn, "Local Adaptive Slicing," *Rapid Prototyping Journal*, vol. 4, no. 3, 1998, in print.
- [9] Stratasys, Inc., *QuickSlice Training Manual*, Release 5.0, October 1997.
- [10] Stratasys, Inc., *Utilities Manual*, Release 5.0, October 1997.

# Virtual Design and Fabrication in Layered Manufacturing

Kathryn B. Higgins, Noshir A. Langrana, Mechanical and Aerospace Engineering  
Rutgers, The State University of New Jersey, Piscataway, New Jersey 08855  
<http://www.caip.rutgers.edu/~kbhiggin/VDF/VDF.html>

## ABSTRACT

A web-based, user friendly virtual design and fabrication system has been developed. It informs new users of basic rapid prototyping concepts and techniques, and provides a linked dictionary for unfamiliar terminology. Important details are given on the quickly emerging field of rapid tooling. Beyond this preliminary information, Java applets provide an interactive element to allow the user to make informed decisions regarding machines and materials. Several tutorials guide the user through the process, from initial design through selection of build parameters. In many cases, there exists a need for a smooth transition from CAD design to complex rapid prototyping techniques. This knowledge base should reduce the iterations required to successfully build parts via stereolithography or fused deposition modeling.

## INTRODUCTION

Rapid Prototyping is a valuable tool for efficient and concurrent engineering. This technology allows engineers and designers to move from concept modeling through part testing in a matter of weeks or months, when previously the turnaround period was much longer. The basic concept underlying all rapid prototyping processes, also known as layered manufacturing or solid freeform fabrication, is the same. A computer model of the desired object is first developed with a three dimensional modeling software. I-DEAS from SDRC, Pro-E from Parametric Technology, or 3D AutoCAD can all be used to draw the model. The volume of this part is meshed, or broken down into small elements. The volume of the original object is now described by the x, y, z coordinates of each endpoint of the mesh as well as the outward normal of each mesh element. This file is known as an .stl file. [Jacobs, 1996] Most prototyping machines can read this format. [Aubin, 1994]

After the .stl file is prepared, the various techniques begin to diverge. At this stage the user needs to orient the part for the best build, edit the support structure, determine material selection and other build parameters that are specific to the selected method. The build process typically begins with several layers of lattice-like support, then the machine builds the object by depositing thin layers of material on an xy plane. Supports are also needed for walls and overhangs to prevent the part from collapsing during build. When one layer is finished, the platform drops in the z direction and another layer is deposited on top of the existing structure. The various prototyping techniques are dissimilar in their build preparation and deposition methods.

## **MOTIVATION**

The two solid freeform fabrication methods used at Rutgers are stereolithography and fused deposition modeling. Both utilize their hardware specific user interface to manipulate the .stl file. Maestro™ is used for stereolithography apparatus (SLA) from 3D Systems, Inc. After the user selects the appropriate machine and material, this software recommends an orientation and position for the part, as well as supports. For fused deposition modeling, FDM from Stratasys Inc., a package called QuickSlice™ is used to prepare the build file. Orientation, position, and support structures are all recommended by the software but the user can edit as desired. With this technology, the user must also advise build parameters such as layer thickness, nozzle diameter and toolpath, offset, roadwidth, etc. These parameters are critical when building functional parts.

Although both technologies make recommendations for part building, the recommendations may not be exactly what is required by the user. Furthermore, these interface programs require some amount of input from the user. Such a wide range of parameters could be very confusing for an inexperienced user, resulting in costly and time-consuming mistakes. A knowledge base offering a broad range of general rapid prototyping information, as well as part-specific advice would be very useful prior to the first build. This knowledge base would serve to further eliminate common mistakes thus making rapid prototyping an even more effective engineering tool.

## **OBJECTIVES**

Looking at rapid prototyping through the eyes of a novice, several needs were identified. These needs later defined the primary objectives for the knowledge base:

- General introduction to rapid prototyping concepts and terminology
- Targeted description of available techniques at Rutgers University
- Capabilities and limitations of rapid prototyping, including information on accuracy and surface finish.
- Advice on material properties and selection, information on fabrication speed
- Step-by-step guide through part preparation, build process, and post process

Due to the amount of material available on rapid prototyping, it was easy to get too detailed and in-depth when presenting the information. From this came a few rules:

- Present reader with a solid general introduction
- Use Java™ applets to provide part-specific information
- Provide appendices and links to manufacturers for machine and material specifications
- Advanced information should come in the form of “tips” and “tutorials”

## METHODS

An introductory page was used to describe the purpose of rapid prototyping. From here, the reader could follow links to either stereolithography or fused deposition, which are the two technologies used at Rutgers University. Rapid tooling was included as a third link because it is a very broad field that must be given special considerations. Furthermore, the reader is notified of the existence of a "dictionary" for unfamiliar terms.

### *Stereolithography*

In stereolithography, Maestro™ accepts the .stl format and requests input, such as type of material, part orientation, and more from the user. The many available materials and machines for stereolithography can be overwhelming for a new user. The stereolithography web pages that help make up this knowledge base offer some guidance. Appendices provide details on SLA size, laser power, available materials, and material properties. The applet shown in Fig.1 helps a user choose an SLA machine based on part size, since the build envelopes for the SLA machine are limited:

#### **Allowable Part Sizes**

The size of the part you intend to build may dictate what machine you will use. Check your dimensions here:

Length x Width x Height:

↕ Inches   ↕ Millimeters

The Part Volume (cubic inches):

Recommended Machine:

**Figure 1. Machine Selection Applet**

The applet shown in Fig.2 assists the user in selecting the best material for their purpose. The user is asked to choose their primary concern, strength, speed, or appearance. In the event that more than one material meets all the user's criteria, the applet considers a secondary concern before making a recommendation. A build style is also recommended:

#### **Materials used in SL Processes**

SLA must use a photocurable resin which can be classified as an epoxy, vinyl ether, or acrylate. See the available machines above, and note the recommended materials for each. If several options are available, it is important to consider your particular requirements such as desired mechanical properties before selecting the material. The information provided below will help you determine the best material based on your requirements:

The recommendations offered below are based on manufacturer's available information. [2] [3] [4] [5] [6] [7]

What machine will be used?

What is the primary important property?

What is the secondary important property?

The Recommended Material Is:

Important Notes:

**Figure 2. Material Selection Applet**

A final applet helps a user estimate the time to build their part, based on the scan velocity of the laser and xy dimensions of the part, approximate number of layers to build the part, and the z wait between layers:

**Time To Build**

The time it takes for the machine to build your part depends on the speed of the machine selected, or more precisely, on the power of the laser employed by the machine as well as the "photospeed" of the selected material. Of course, the build time also depends on the part's height and on the layer thicknesses selected. The approximate time to build your part can be calculated below (Only SLA 190 and 250 series are included at this time) [R]

Dimensions Of Your Part(x,y,z)

Inches  Millimeters

What Is The Machine?

What Is The Material?

What Is The Build Style?

The Scan Velocity Is: (in/sec)

The Time To Build Is: (hours)

Additional Notes:

 Are you getting "ft" for your scan velocity or "in" for your build time?  
Check to make sure the material you specified is recommended for your machine!

Figure 3. Time Applet

The time approximations come from the following equations:

$$\text{Scan Velocity} = V_s = (2/\pi)^{1/2} * P_l / (W_o * E_c) \exp(-C_d/D_p) \quad (1)$$

$P_l$  is laser power,  $W_o$  is beam radius, typically 0.0045",  $E_c$  is the critical exposure and  $D_p$  is the penetration depth of the material, and  $C_d$  is the desired cure depth, an average of 2 mils is assumed for this applet. [Jacobs, 1996] In the event that the scan velocity exceeds the maximum scan velocity for the selected machine, the default scan velocity is used. [3D Systems, 1998] In Eqtn. 2 X, Y, Z are x, y, z dimensions respectively and T is the expected z wait used to calculate an approximate time to build:

$$\text{Build Time} = [(X * (Y/2W_o))/V_s + T] * [Z/C_d] / 3600 \quad (2)$$

Spread among these applications is additional information to help a user optimize their build. All machine and material information is taken directly from the manufacturer's web pages, technical journals, or material data sheets.

Links from these pages jump to a tips page and a step-by-step tutorial. This tutorial uses pictures and command names to lead a user through a simulated build process, from I-DEAS (the 3D modeling software at Rutgers) to post curing. This tutorial is intended to give users exposure to the process before their first build.

## Fused Deposition Modeling

In FDM, filament is extruded through a heated nozzle onto a platform. The xy path the nozzle follows in building the part is called a toolpath. The user is responsible for determining this toolpath along with many other parameters. Web pages offer help on selecting these parameters. These pages were approached in the same way as above. Appendices provide details on size, available materials and properties. An applet helps a user choose a machine based on part size. The screen is similar to that shown in Fig. 1.

There are four major steps in solid free form fabrication process using ceramics. They include filament development, fused deposition of part build (green part), and binder removal and sintering. Since these are the sequential steps, any problems or defects get propagated in the subsequent steps. Quality and consistency of filament fabrication and preservation are critical for the success of green part fabrication. By the same token, defect free green part fabrication is critical for the binder burn out and sintering. These issues have been investigated in our group at Rutgers University. [Argawala, 1996][Dai, 1997] [McIntosh]. The current knowledge base utilizes the relevant information related to fabrication of defect and void free build parts. There is also a tutorial for building parts via FDM.

## Rapid Tooling

The rapid tooling information page provides background information on the various types of tooling that can be accomplished by rapid prototyping techniques, including making a metal part with RTV molding [Langrana et al., 1998], Direct AIM™, Keltool™, [Jacobs, 1997] [3D Systems, 1996] and various research at Rutgers and other research facilities around the country. [Whalen et al., 1998] [Aubin, 1994] The information contained in these pages reflect the increasing interest in applying rapid prototyping technology to tooling and manufacturing.

Also included is a page detailing injection mold making techniques. This page is very valuable since traditional mold making concerns cannot be ignored when applying rapid prototyping technologies. Part to mold conversion is first discussed, followed by runners and gates, cooling lines, ejection systems, and venting systems [DuBois et al., 1965] [Menges et al., 1986]. Examples are shown in Fig. 4:

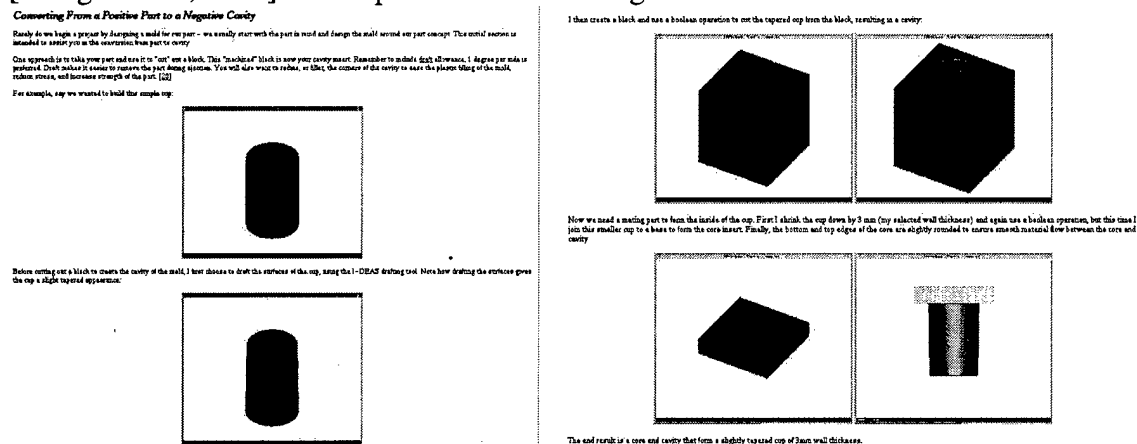
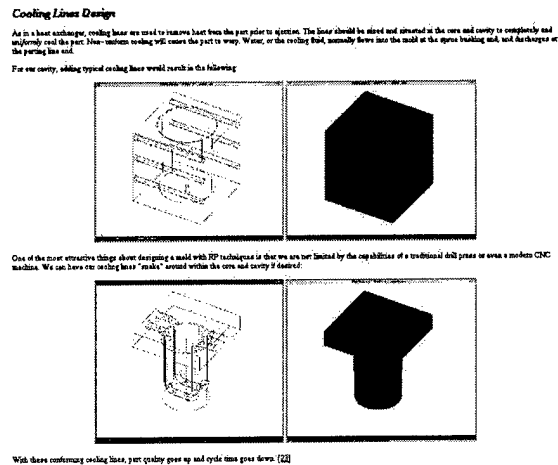


Figure 4a,b. Rapid Tooling Information Page Examples



**Figure 4c. Rapid Tooling Information Page Examples**

## CASE STUDY

The knowledge base when properly utilized should reduce build iterations. Two cases in particular can be used as examples. In the first case, experimenters needed to build several variations on an injector disk for a supersonic wind tunnel. [Price, 1998] The same disk shape was to be used but the location, diameter, and inclination of through holes needed to be altered for the purpose of optimizing transverse injection of gas into a crossflow. Rapid prototyping was selected as an efficient and inexpensive method to build the parts. The SLA 190 series and FDM 3D Modeler were the available machines. Several parameters were very important to the experimenters. The surfaces parallel to the tunnel walls had to be very flat and smooth to prevent disturbances to the flow. Also, surfaces should be flush with the wind tunnel wall. It was preferred to build several parts at one time so more time could be spent testing rather than building the parts. SLA was selected as the more accurate RP machine. The knowledge base would have helped the experimenters select the best build orientation for the part. For example, the interface software may recommend building a part so the longest dimension is along the z axis, which is a good way to achieve the fastest build. However, if there is very fine detail on one side of the part, that side should face up to achieve the best finish. Here, at least one surface had to be as smooth as possible, so this critical injector face should be built last. The experimenters discovered after building that the disk warped slightly due to two factors, shrinkage of the material and the laser power was too low to build successfully. The material property tables contained in the knowledge base would have recommended a more accurate material for their purposes, and warned them not to continue with their build unless the laser power was acceptable. These recommendations may have saved the experimenters time by improving their first round of test results.

In the second case, students designed a high speed inlet nozzle, also for a wind tunnel application. As one of the final steps, the nozzle was to be built on a stereolithography machine and used in tests. The nozzle is approximately 3" x 3" x 10", and unfortunately, the students were surprised to learn from this knowledge base that they could not build the inlet nozzle as one part on the SLA 190, as that build envelope is only 7" x 7" x 7". The students also learned from the knowledge base that the FDM wax material would not be strong enough to withstand the tunnel testing. The students did however learn of several rapid tooling alternatives, and introduced this as possible future work. Ultimately, the SLA was selected as the more accurate machine with stronger material, and the students built the nozzle in two parts to be joined in a post-processing task.

## **SUMMARY**

A first version of a web-based, user friendly virtual design and fabrication environment has been created. Java applets provide an interactive element in a user's decision making process with respect to machines and materials. Two case studies are shown. In these case studies, information contained in this knowledge base would have been valuable to both parties. It is hoped that even more part specific applications can be developed and added to the already comprehensive knowledge base. Due to the quickly developing nature of this industry, facts should be checked periodically. As new machines and materials emerge, their information should be added to the pages.

On a larger scale, more research should be done on rapid tooling. The pages introduce interesting alternatives to traditional rapid prototyping, but no final recommendation can be made since many of the technologies are untested. For example, trials need to be run on making injection-type molds with stereolithography or fused deposition modeling. Comparisons should be provided for the different techniques, i.e. how many parts can be produced from each method, what are the materials that can be molded, what is the cycle time, etc. In short, the knowledge base needs to continue to research new rapid prototyping developments.

## **ACKNOWLEDGEMENTS**

Thanks to CAIP, Computer Aids for Industrial Productivity, at Rutgers University for the funding for this research. Also, special thanks to the students and staff of the Mechanical and Aerospace Engineering Department for their assistance.

## REFERENCES

- Agarwala, A. Bandyopadhyay, R. van Weeren, V. Jamalabad, P. Whalen, N. Langrana, A. Safari and S. Danforth, "Fused Deposition of Ceramics", *J. Rapid Prototyping*, Vol. 2, 4, 4-19, 1996
- R. Aubin, "Worldwide Assessment of Rapid Prototyping Technologies" January 1994
- C. Dai, G. Qi, S. Rangarajan, N. Langrana, A. Safari and S. Danforth, "High Quality, Fully Dense Ceramic Components Manufactured Using Fused Deposition of Ceramics", Proceedings of the Solid Freeform Fabrication Symposium, The University of Texas at Austin, Austin, TX, August 1997
- J. DuBois and W. Pribble, ed. Plastic Mold Engineering Reinhold Publishing Corporation, New York 1965
- P. Jacobs, "Recent Advances in Rapid Tooling From Stereolithography" 3D Systems Inc., 26081 Avenue Hall Valencia, CA 91355, 1997
- P. Jacobs, ed. and T. Pang, "Advances in Stereolithography Photopolymer Systems" from Stereolithography and Other RP&M Technologies Society of Manufacturing Engineers, One SME Drive Dearborn, MI 48121 1996
- N. Langrana, S. Danforth and A. Safari "Solid Freeform Manufacturing of Hard Tooling" Multi-lifecycle Engineering and Manufacturing Program Final Report: Year One, #97-2890-051-14, New Jersey Commission on Science and Technology, February 1998
- McIntosh, V. Jamalabad, and S. Danforth, "Shrinkage and Deformation in Components Manufactured by Fused Deposition of Ceramics", Proceedings of the Solid Freeform Fabrication Symposium, The University Of Texas at Austin, Austin, TX, August 1997
- G. Menges, and P. Mohren, How To Make Injection Molds Hanser Publishers, New York, 1986
- B. Price, G. Elliot, and M.Ogot "Experimental Optimization of Transverse Jet Injector Geometries for Mixing into a Supersonic Flow" presented at 29<sup>th</sup> AIAA Fluid Dynamics Conference, June 1998
- P. Whalen, "Solid Freeform Fabrication of Advanced Ceramics - Phase I Final Report" Office of Naval Research, Allied Signal Inc. 101 Columbia Turnpike, Morristown, NJ 07962-1021, February 1998
- 3D Systems Inc. "3D Keltool™ for Sintered Metal Tools" 26081 Avenue Hall Valencia, CA 91355, 1996
- 3D Systems Inc. web pages, "www.3dsystems.com" Information taken in February 1998.

## INFLUENCE OF RHEOLOGY ON DEPOSITION BEHAVIOR OF CERAMIC PASTES IN DIRECT FABRICATION SYSTEMS

Bruce H. King, Sherry L. Morissette, Hugh Denham, Joseph Cesarano, III and Duane Dimos  
Sandia National Laboratories  
Albuquerque, NM 87185

### ABSTRACT

Rheology and deposition behavior of four commercially available thick-film inks and an aqueous alumina slurry were investigated using two different slurry-based deposition systems. The first of these deposition systems, a Micropen, is a commercially available system designed for the deposition of electronic thick film circuits. The second system, referred to as a Robocaster, is a developmental system designed to build thick or structural parts. Slurry rheology was seen to have a minor effect on deposition behavior and the bead shape when deposited using the Micropen. The deposition behavior was instead dominated by drying rate; too rapid of a drying rate led to excessive clogging of the tip. Slurry rheology had a greater impact on the shape of beads deposited using the Robocaster. Highly viscous slurries yielded initially well-defined beads, whereas beads deposited using fluid slurries spread quickly. In both cases, significant spreading occurred with time. These observations only held for slurries with slow drying rates. It was observed that very fluid slurries produced well-defined beads when the drying rate was suitably high.

### INTRODUCTION

Slurry-based direct fabrication systems offer a number of advantages over conventional fabrication techniques and have capabilities not found on other direct fabrication systems. The material systems are relatively simple and a wide range of materials can be used, including pastes of metals, polymers or ceramics. Additionally, there are a number of commercially available pastes available from the screen-printing industry. Unique capabilities include multi-materials/graded parts, incorporation of tailored porosity via fugitive materials and rapid turnaround of finished pieces. It is also possible to fabricate multilayer thick film circuits directly on a substrate, a difficult task using conventional screen printing techniques.

We are working with two slurry-based deposition systems at Sandia. The first is a commercially available system called Micropen.\* The second is a system under development at Sandia called Robocasting. The Micropen is designed for use in the electronics industry for the deposition of thick film circuits and typically uses commercially available thick film inks.<sup>1</sup> The design focus of the Robocaster is for thick or structural parts and typically uses aqueous slurries.<sup>2</sup>

A schematic of the Micropen system is shown in Figure 1, along with a circuit printed onto a curved surface. The system consists of a cantilevered tube to the end of which a pen tip and permanent magnet are attached. An electromagnetic actuator positioned above the permanent magnet controls the height of the pen tip by varying the strength of the magnetic field. A height detector consisting of a flag attached to the tube, an LED and photodiode provides

---

\* Ohmcraft, Inc. Honeoye Falls, NY 14472

height feedback to the processor controlling the electromagnetic actuator. This system employs a stationary Z-axis; a pattern is written by pumping the slurry through the tube and moving an X-Y table beneath the tip. A circuit is deposited as follows; the pen tip is brought into contact with the substrate and ink is pumped through the pen tube into the pen tip. As ink begins to build up under the pen tip, the pen tip rises until it reaches a predetermined trigger height. At this point, the X-Y table begins to move and the pattern is deposited. A small downward force is applied during writing via the electromagnetic actuator. This helps to ensure that a uniform line of material is deposited. An advantage of this type of system is that in addition to the feedback provided by the height sensor, there is a force feedback provided by the electromagnetic actuator. Thus, the system can vary the pen height based on the force feedback to account for topography on the substrate. This enables a uniformly thick circuit to be deposited onto a curved surface or over existing features on a flat substrate. The Micropen typically uses pen tips in the size range of 25-250  $\mu\text{m}$ . A typical slurry composition is 25-30vol% solids, 40-50vol% resin and 25-30vol% solvent.

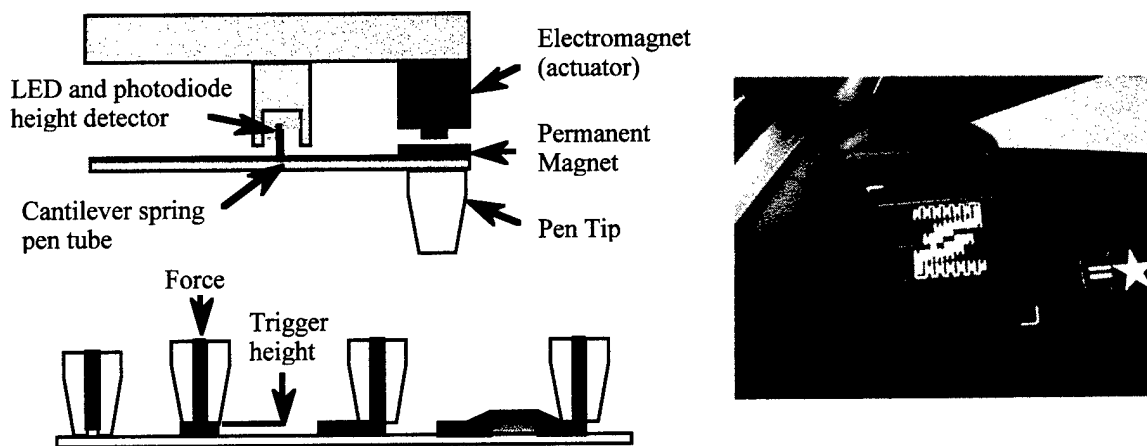


**Figure 1:** Schematic of the Micropen system and a circuit printed on a curved surface.

In contrast, the Robocaster, shown in Figure 2, is a more straightforward design. The slurry is extruded from a syringe mounted on a Z-axis above a moving X-Y table. Once a layer is completed, the Z-axis is incremented by a predetermined layer height and the next layer is deposited. Currently, this system provides no feedback about the actual distance between the build surface and the pen tip. However, a laser height system is under development at Sandia that will provide this information. This system should allow for feedback to the pumping system to account for imperfections in the build of previous layers. The Robocaster typically uses pen tips in the size range of 250-1500  $\mu\text{m}$ . A typical slurry composition is very highly loaded with 58-61vol% solids, 40vol% water and a very small amount of processing aids such as Darvan and citric acid. Typical parts are also shown in Figure 2.

Both systems rely on good bead definition to build accurate parts. The electrical properties of electronic components deposited with the Micropen often depend on the accuracy of the line width which is in turn influenced by the degree of bead spreading after the line has been printed. Minimum feature sizes and the minimum spacing between components are also

influenced by bead spreading. These aspects are important for both systems. Electronic components that are too close together may be subject to shorting or electromigration. The dimensional accuracy of 3-D parts fabricated with the Robocaster is highly dependent on bead spreading. Additionally, significant bead spreading of one layer leads to problems during the deposition of subsequent layers, resulting in gross defects within the finished piece. The rheology of the slurries used in these systems was investigated to gain an understanding of its influence on bead shape. This information will drive both system development and materials processing as new slurries are developed for each system.

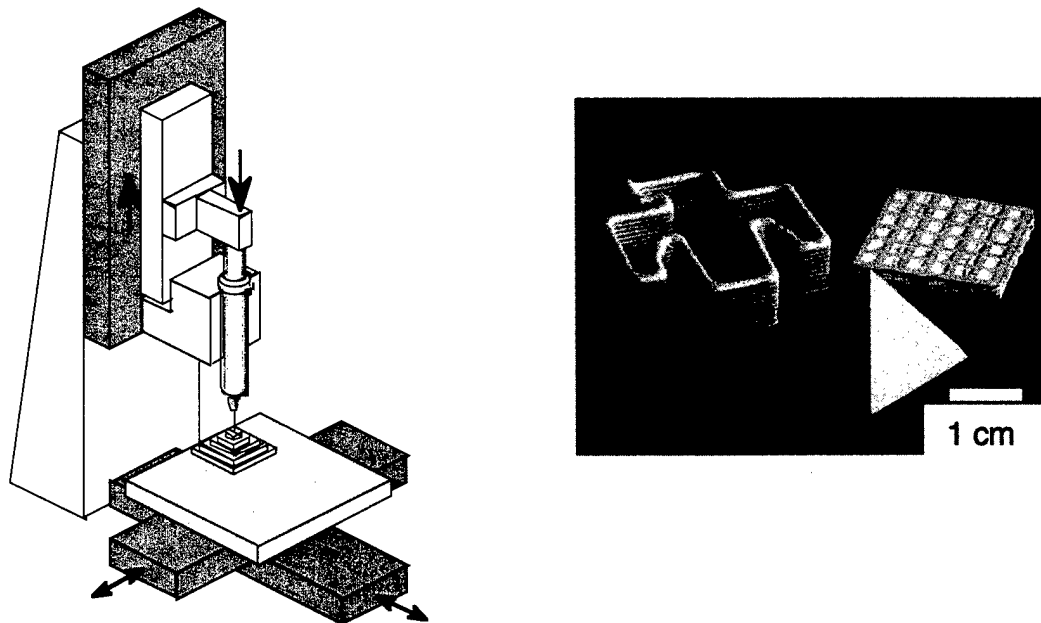


**Figure 2:** Schematic of the Robocaster and examples of complex shapes fabricated with it.

## EXPERIMENTAL

A number of slurries were investigated, four commercial thick film pastes and an aqueous alumina slurry prepared at Sandia. Two of the commercial inks were DuPont<sup>\*</sup> post-fire inks; 5715, a gold conductor paste, and 1731, a ruthenium oxide-based resistor paste. Both of these pastes are designed to be printed on dense alumina substrates and fired at high temperatures (> 1200°C). The other two commercial pastes were polymer thick film (PTF) pastes, Minico<sup>†</sup> M-4100 silver conductor paste and Asahi<sup>‡</sup> TU-1k carbon resistor paste. Both of these pastes consist of solids (either silver or carbon) loaded in an epoxy carrier and are designed to be printed on FR4 epoxy board. The epoxy carrier is cured at low temperature ( $\approx 200^\circ\text{C}$ ). The aqueous alumina slurry was prepared at Sandia by ball milling 60vol% Alcoa A-15 alumina for 2 weeks in deionized water with Darvan 821A dispersant and citric acid.

<sup>\*</sup> DuPont Electronic Materials, Research Triangle Park, NC 27709

<sup>†</sup> Emerson and Cuming, Lexington, MA 02173

<sup>‡</sup> Multicore Solders, Inc., Richardson, TX 75081

The rheology of the five pastes was characterized using a controlled stress rheometer\*. The commercial pastes were characterized with a 1° cone and plate geometry, while the aqueous alumina slurry was characterized using a cup and bob geometry. All rheology data was plotted as viscosity (cP) vs. shear rate (1/s) on a semi-log plot.

In addition to rheology, the slumping behavior of beads printed from each paste was investigated when deposited from each of the two systems. In all cases, a single bead of material was deposited onto the substrate and the shape of the bead was characterized via laser profilometry.† The post-fire inks were deposited onto alumina substrates, while the PTF inks were deposited onto FR-4 epoxy board. The aqueous alumina slurry was deposited onto dense alumina substrates. Pastes deposited with the Micropen were deposited using a 250 μm (10 mil) tip and bead profiles were obtained at times ranging from 1 minute to 1 hour after printing. Pastes deposited with the Robocaster were deposited with an 890 μm (35 mil) tip. In this case, the profilometer was mounted on the equipment and profiles were obtained within ≈ 10 seconds of printing. Profiling of each bead was performed for up to 30 minutes after printing. To investigate the effect that the substrate has on the profile, these experiments were repeated for the silver PTF paste deposited on a dense alumina substrate. From these profiles, the bead width and area as a function of time after printing were obtained.

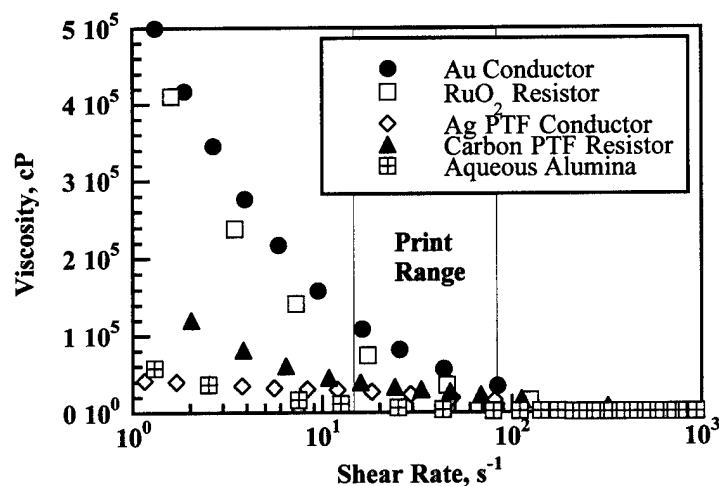


**Figure 3:** Viscosity as a function of shear rate for commercial screen printing inks and aqueous alumina slurry.

## RESULTS

Viscosity as a function of shear rate for each of the pastes is shown in Figure 3. Included on the plot is the calculated range of shear rates experienced during printing.<sup>3</sup> Of the slurries investigated, the post-firing inks were by far the most viscous. At low shear rates, the PTF inks were significantly lower. The carbon resistor ink was the more viscous of the two, but they converged in the print range. At low shear rates, the aqueous alumina slurry exhibited a higher

\* Bohlin CS-10, Bohlin Instruments, Cranbury, NJ 08572

† CyberScan Cobra, CyberOptics, Minneapolis, MN 55416

viscosity than the silver PTF conductor, but at high shear rates its viscosity was the lowest of the five pastes. All pastes were observed to converge to the same viscosity at very high shear rates, however this is above the print range.

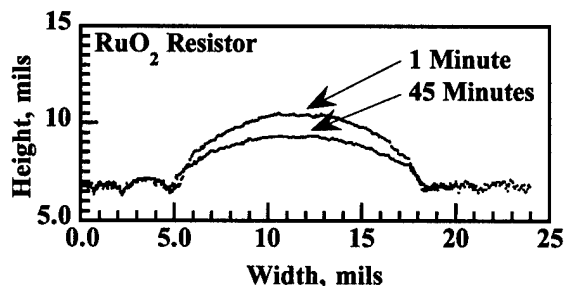


Figure 4: Profile of a resistor paste bead printed with the Micropen at times of 1 minute and 45 minutes after printing.

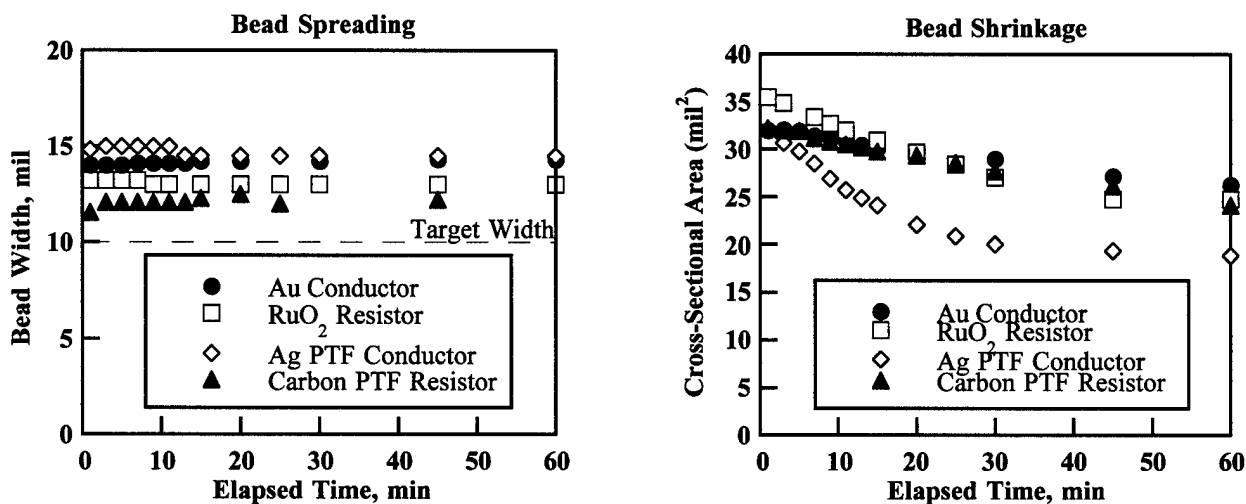


Figure 5: Spreading and Shrinkage as a function of time after printing of thick film inks printed with the Micropen.

Profiles similar to the profile shown for the ruthenium oxide resistor paste in Figure 4 were obtained for all of the pastes printed in the Micropen, with the exception of the alumina slurry. This slurry proved to be impossible to deposit with the Micropen due to excessive drying. Figure 5 plots width and cross-sectional area as a function of time after printing. Of the remaining four slurries, minimal spreading was observed after the first minute after printing. However, a significant change in the cross-sectional area of each bead was noted over the course of an hour. This change in area may be attributed to drying shrinkage.

Figure 6 compares the profiles of pastes printed with the Robocaster. In this case, only three pastes were printed for comparison; the highly viscous ruthenium oxide resistor paste, the relatively fluid silver PTF conductor paste and the aqueous alumina slurry. Initially, the ruthenium oxide resistor paste had a well-defined profile. However, the bead spread quite

rapidly and continued to spread for up to 20 minutes. This is shown clearly in Figure 7, which plots bead width as a function of time after printing. The fluid silver PTF paste, on the other hand, spread significantly before the first profile was taken. After this, spreading continued but at a much slower rate. In contrast, the alumina slurry exhibited a well-defined bead initially. Unlike either of the thick film pastes, it exhibited no spreading with time. This is contrary to what would be expected based on the rheology measurements; the viscosity of the aqueous system indicated that it should have an initial profile similar to the silver PTF conductor paste and should probably have spread in a similar manner. However, as is shown in Figure 7, there was no change in width with time. The reason for this behavior is also shown in Figure 7; the alumina slurry was seen to shrink rapidly during the first two minutes after printing. Beyond that, there was no shrinkage. It can be concluded that the aqueous alumina slurry dries rapidly enough to form a hard shell that prevents spreading.

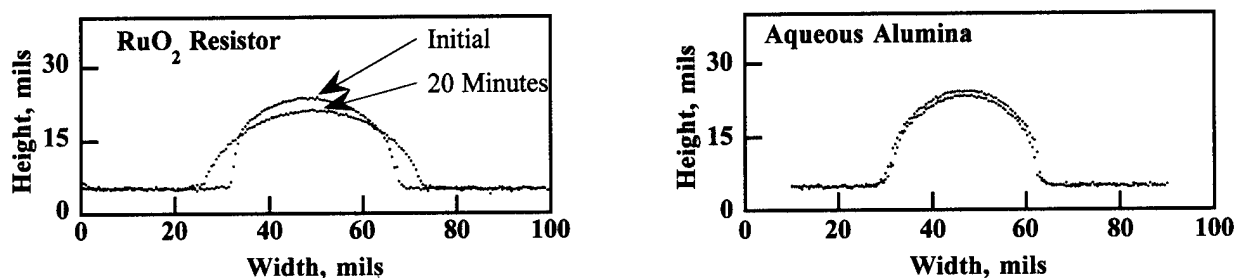


Figure 6: Profiles of ruthenium oxide resistor paste and aqueous alumina slurry deposited by the Robocaster

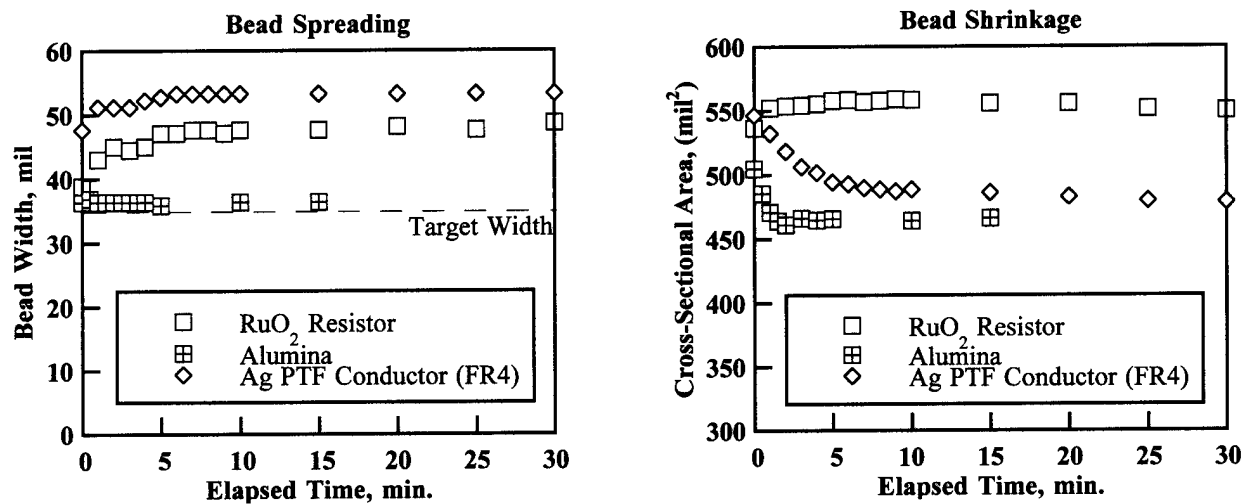


Figure 7: Spreading and Shrinkage as a function of time after printing of thick film inks and aqueous alumina slurry deposited with the Robocaster.

A series of experiments were performed to investigate the effect that the substrate has on spreading. These experiments were performed using silver PTF beads printed on FR4 and on alumina. The results are shown in Figure 8. It was seen that when printed on the alumina substrate, the silver paste spread to a greater extent initially and also continued to spread for a longer period of time than when printed on the FR4. At first, it appeared that this was a matter of

wetting. However, when the plot of bead shrinkage vs. time was examined for the two different substrates, it was seen that shrinkage occurred much more rapidly when the bead was printed on FR4 than when printed on alumina. Shrinkage on the FR4 was rapid during the first 5-7 minutes after printing, at which time the shrinkage rate changed to a much slower rate. Since the ink and printing conditions were identical in both cases, this shrinkage can be attributed to solvent loss into the FR4 substrate. There are at least two possible explanations for this behavior. One explanation is that the substrate was porous, extracting the solvent from the ink through capillarity. Another possible explanation is that the solvent dissolved into the epoxy matrix of the substrate. At this time, not enough is known about the substrate/solvent system to distinguish between the two mechanisms for solvent removal. Regardless of the mechanism for solvent removal, it is evident that the extra drying provided by the FR4 substrate slowed the rate of bead spreading and resulted in less spreading overall.

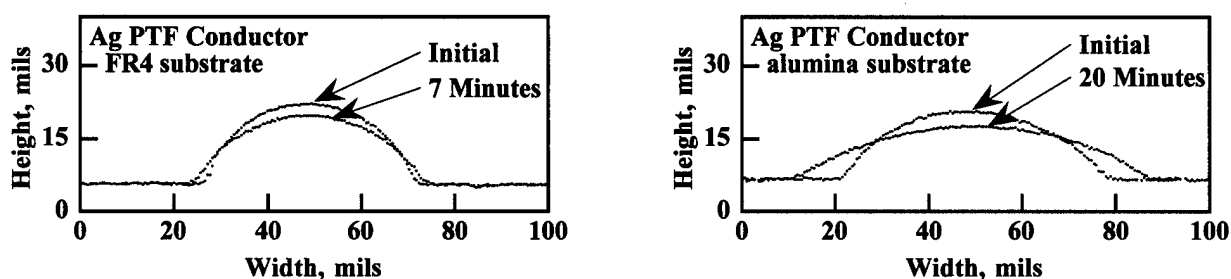


Figure 8: Profiles of silver PTF conductor paste deposited with the Robocaster onto FR4 substrate and alumina substrates.

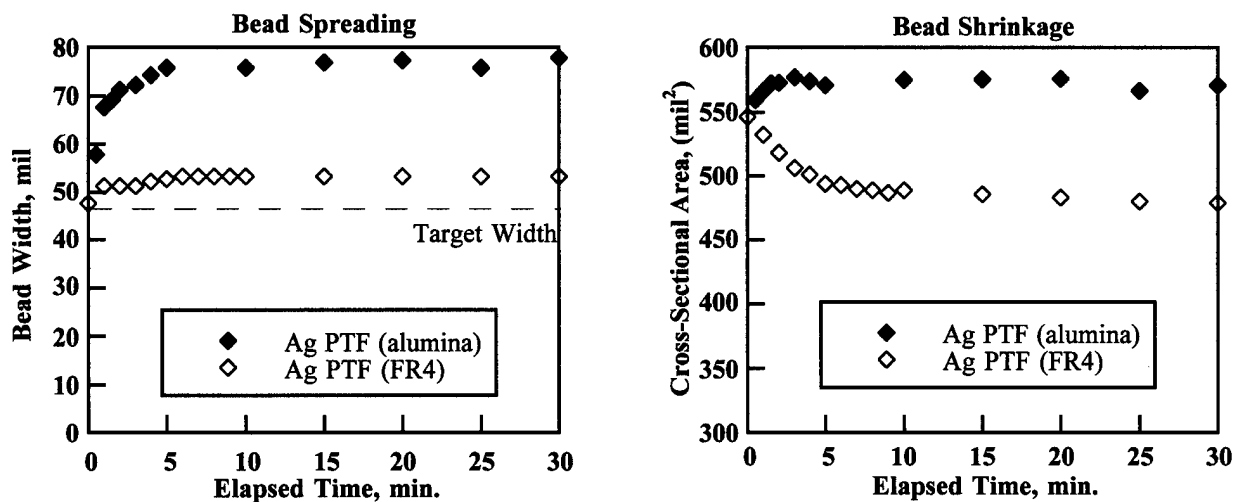


Figure 9: Spreading and Shrinkage as a function of time after printing of silver PTF paste deposited with the Robocaster onto FR4 substrate and alumina substrates.

## SUMMARY

Five different pastes were investigated; two commercial post-fire inks, two commercial polymer thick film inks and an aqueous alumina slurry produced at Sandia. The post-fire inks were observed to be the most viscous of the five, while the polymer thick film inks and aqueous

slurry were similar to each other and significantly more fluid than the post-fire inks. When printed with the Micropen, an insignificant amount of spreading occurred after the first minute with commercial screen printing inks. The aqueous alumina slurry dried too rapidly to be printed with the Micropen. In contrast, a significant amount of spreading occurred when the commercial screen printing inks were printed with the Robocaster. There was an insignificant amount of spreading when the aqueous alumina was deposited using the Robocaster. This was contrary to expectations based on the rheological examination. Examination of the cross-section of the aqueous alumina bead deposited with the Robocaster indicated that it dried very rapidly, allowing the bead to hold its shape. Drying was also seen to be a significant factor in the case of the silver PTF ink printed on the FR4 substrate. Significantly less bead spreading was noted when compared to a bead of the same ink printed onto a dense alumina substrate. This behavior was attributed to solvent wicking into the FR4 substrate.

Several conclusions can be drawn from the experimental results. In general, the Micropen requires slurries with low vapor pressure solvents to slow drying times and prevent clogging. In contrast, the Robocaster requires slurries with high vapor pressure solvents to speed drying times. This reduces the amount of bead spreading and leads to an ideal bead shape. Finally, it can be concluded that the influence of viscosity on the bead shape is not as important as the effect of solvent removal through drying and wicking.

#### ACKNOWLEDGEMENTS

This work was supported by the United States Department of Energy under Contract DE-AC04-94AL85000. Sandia is a multiprogram laboratory operated by Sandia Corporation, a Lockheed Martin Company, for the United States Department of Energy.

#### REFERENCES

- <sup>1</sup> C. E. Drumheller, ISHM '82 Proceedings (1982).
- <sup>2</sup> Joseph Cesarano III, Thomas Baer and Paul Calvert, "Recent Developments in Freeform Fabrication of Dense Ceramics From Slurry Deposition," p. 25-32 in *Solid Freeform Fabrication Symposium Proceedings*. Austin, TX: University of Texas at Austin (1997).
- <sup>3</sup> D. Dimos, P. Yang, T. J. Garino, M. V. Raymond and M. A. Rodriguez, "Direct-Write Fabrication of Integrated, Multilayer Ceramic Components," p. 33-40 in *Solid Freeform Fabrication Symposium Proceedings*. Austin, TX: University of Texas at Austin (1997).

# A Theoretical Model for Optimization of SALD Parameters

Zbigniew M. Bzymek\*), Leon L. Shaw\*\*) and Wojciech Marks\*\*\*)

\*) Department of Mechanical Engineering, University of Connecticut, Storrs CT

\*\*) Department of Metallurgy and Materials Engineering, University of Connecticut, Storrs CT

\*\*\*) Institute of Fundamental Technical Problems of the Polish Academy of Science, Warsaw, Poland

## Abstract

This paper addresses the need to conduct theoretical work concerning an economical way of Solid Freeform Fabrication rendering by using selective Area Laser Deposition (SALD). The part in SALD rendering process is formed layer by layer that, in turn, is composed of stripes of material produced in the path of a laser. There are three situations in which such a stripe can be rendered: a) alone, b) with one neighbor on one side, and c) with neighbors on both sides. Residual thermal stresses in the part are expected to be affected by how a stripe is rendered. Furthermore, the residual thermal stress and the mechanical property of the part are also dictated by other processing variables such as laser scanning patterns, laser input power, scanning speed, scanning spacing, deposition temperature, gas precursor pressure, intrinsic thermal conductivity and mechanical properties of the rendered material. A theoretical approach is proposed to address the minimization of residual thermal stresses and rendering times and the maximization of the strength of the part. It is proposed that such multiple optimizations that are dictated by many decision variables can be solved by minimizing and/or maximizing object functions depending on the design criteria for each attribute of the rendered part.

## 1. Introduction

Solid Freeform Fabrication (SFF) is advancing very rapidly. Although there still are problems to be solved from the viewpoint of materials science, problems of the design of parts rendered by SFF are more and more in the interest of designers, who have to answer questions of design of machine parts and other shapes to fulfill their functions in optimal ways, maintain required tolerances and desired properties. It is apparent that design for SFF starts at technology level. It is not irrelevant how the part will be rendered [1]. Specifically, for the process of Selective Area Laser Deposition (SALD) [2,3], a designer has to consider a variety of processing variables that could affect the residual stress and properties of the resulting part. These processing variables include at least laser scanning patterns, laser input power, scanning speed, scanning spacing, deposition temperature, gas precursor pressure, intrinsic thermal conductivity and mechanical properties of the rendered material [4].

What values of the processing variables should be selected to achieve the optimization of the rendering process? What would be the proper criteria for the optimization of the rendering process? These questions now stand before designers who are trying to establish some rules and recommendations for SFF fabrication and design that can make the work of designers easier and faster and establish closer cooperation between material and design specialists to solve problems of optimal design of the part not only from functional, but also technological points of view. These issues are addressed in this paper. The model presented proposes optimization of rendering of small plates in an optimal way, according to assumed criteria.

## 2. Assumptions

The part in the SALD rendering process is formed layer by layer that, in turn, is composed of stripes of material produced in the path of the laser [2]. There are three situations in which such stripes can be rendered. It can be alone, with a neighboring stripe on the one side, or with the neighbors on both sides. If it is rendered alone, the stresses induced by the thermal deformation are small and due only to the different thermal shrinkage between the rendered stripe and the layer underneath the stripe. However, if it is rendered with neighbors on both sides, the stresses will be maximum due to the constraints from both sides as well as underneath. If we imagine cutting a small piece of a stripe in such a worst case, the stress within the stripe due to the constraints can be described by Fig. 1. For the illustration purpose, a simplest possible case is assumed in Fig. 1, that is, the layer deposited is a flat and thin layer. As such, the problem can be treated as two dimensional [1].

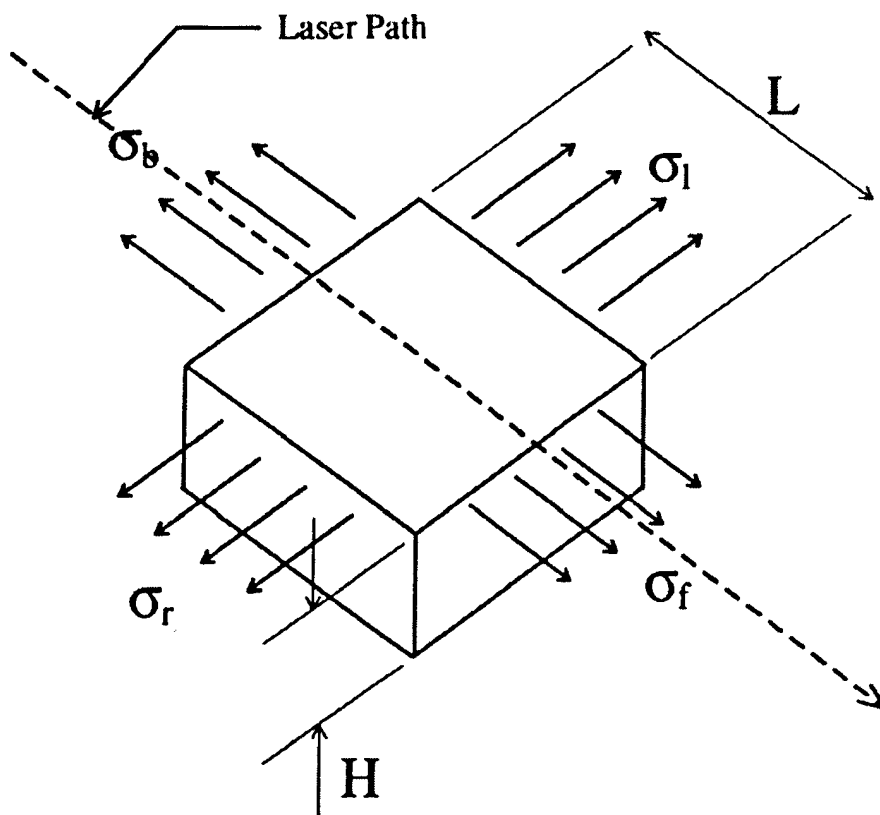


Fig. 1 An idealized elementary block of rendered slice of a part.

## 3. Thermal Stresses and Deformations

In the dynamic problem of thermoelasticity the heat conduction equation is completed by

the equation of motion in displacements [5] in the following way:

$$\sigma_{ji,j} + X_i = \rho u_i^{**} \quad (1)$$

The equation (1) expresses a set of partial differential equations,

where :  $\sigma_{ij} = 2\mu \varepsilon_{ij} + (\lambda \varepsilon_{kk} - \gamma T) \delta_{ij}$ . (2)

Expressing the strains in terms of displacements

$$\varepsilon_{ij} = 1/2(u_{i,j} + u_{j,i}) \quad (3)$$

and substituting (2) and (3) into (1) one can obtain the following form of equation (1)

$$\mu u_{i,jj} + (\lambda + \mu) u_{j,ji} + X_i = \gamma T_{,i} + \rho u_i^{**} \quad (4)$$

where:

$u_i^{**}$  - second derivative of displacement with respect to time,

$\rho$  - a constant in the following kinetic energy expression  $K = \frac{\rho}{2} \int_V v_i v_i dV$ ,

$\gamma$  - the quantity appearing in the Duhamel - Neuman relation such that :  $\gamma = (3\lambda + 2\mu)\alpha_t$ ,

$X_i$  - represent the mass forces,

$$T_{,i} = \delta T / \delta x_i, \quad (5)$$

$$G = E/2(1+\nu) \text{ and } G = \mu \quad (6)$$

$$\mu, \lambda - \text{Lame constants} \quad (7)$$

Equations (1) to (7) express the dynamic problem of thermoelasticity [5] represented in summation notation [6]. If the thickness of the layer is such that the problem should be considered as three dimensional, the equations should be modified by adding components in the direction of Z axis.

Since the conditions will be the most advantageous when the thermal stresses and deformations are minimum, the following object function F expressing thermal stresses and deformations due to the temperature changes can be derived:

$$F(\varphi, k, \omega, v, \delta, p, T) \quad (8)$$

Where:  $\varphi(x, y, t)$  - laser pattern function (Fig. 2)

$k$  - thermal conductivity of the rendered layer

$\omega$  - laser power

$v$  - scanning speed

$\delta$  - scan spacing

$p$  - gas pressure

$T$  - temperature

The equation (8) is written in a general form and can be presented in different ways depending on the specific formulation of the optimization problem as indicated in Section 4.

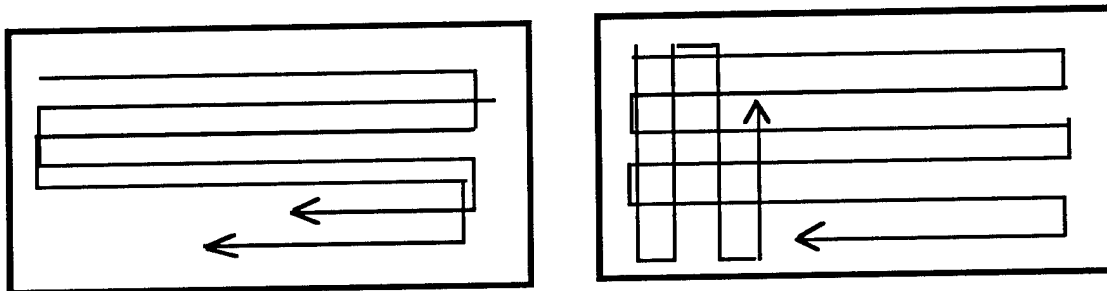


Fig. 2 Examples of the laser pattern working path: (a) parallel scans, and (b) cross scans.

#### 4. Optimization problem in SALD

In this study, it is assumed that rendered elements should be characterized by the following attributes:

- deformation of every layer should be as small as possible,
- the sintered part should have mechanical properties close to the isotropic material,
- the ultimate strength for tension should be as large as possible,
- the time necessary to render every layer should be as large as possible.

To satisfy these requirements, the following criteria for the four -criterion (A, B, C, and D) optimization are assumed:

A -the vertical deformations of any layer of the material and deformations resulting from fabrication of that layer should be minimal

$$F_A = \int_S w^2 = F_A^{\min} \quad (9)$$

where  $w$  is the vertical deformation and  $S$  the area of the rendered plate.

B -the difference of the constants  $\mu$  (or  $E$  - Young Modulus) in the two orthogonal directions should be minimal:

$$F_B = \mu_x - \mu_y = F_B^{\min} \quad (10)$$

C -the ultimate strength  $\sigma_u$  for tension

$$F_C = \sigma_u = F_C^{\max} \quad (11)$$

D -minimum time needed to render the layer  $i$  of the part:

$$F_D = \frac{S_i}{\delta \tilde{v}} = F_D^{\min} \quad (12)$$

where:

$S_i$  - the area of the layer  $i$ ,

$\tilde{v}$  - the average velocity of the laser,

$\delta$  - the width of the material strip rendered with single pass of laser.

The decision variables are:  $\varphi(x,y,t)$ ,  $\omega$ ,  $v$ ,  $T$ ,  $k$ ,  $\delta$  and  $p$ , as defined in equation (8). Note that the decision variables are functions or parameters of the material used to render the element and characteristics of the laser. Further, the decision variables have to comply with the following constraints:

$$\delta \int_s \varphi(x,y,t) dS = S \quad (13)$$

$$\underline{\omega} \leq \omega \leq \overline{\omega} \quad (14)$$

$$v \leq \overline{v} \quad (15)$$

$$\tilde{v} = \frac{v_1 L_1 + v_2 L_2}{L_1 + L_2} \quad (16)$$

where:

$L_1$  - the length of the longer laser path (Fig. 3),

$L_2$  - the length of the shorter laser path ( Fig. 3),

$\underline{\omega}$  and  $\overline{\omega}$  - the maximum and minimum laser powers,

$\overline{v}$  - the maximum laser scanning speed,

$v_1$  and  $v_2$  - the laser scanning speed along  $L_1$  and  $L_2$ , respectively.

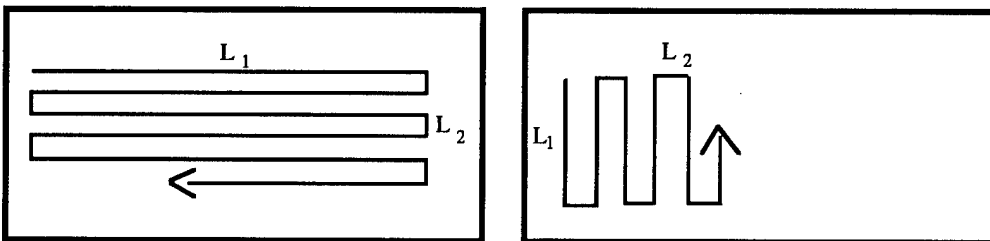


Fig. 3 Horizontal and vertical laser patterns

Physically, the constraint (13) means that the length of the laser path times the width of the rendered strip should cover the entire area of the layer and cannot pass through the path vector more than once. The constraint (14) means that the working laser power has to be included between the maximum and minimum possible powers. The constraint expressed by equations (15) and (16) means that the working velocity of the laser has to be smaller than the maximum possible velocity and that the average velocity of the laser is composed of the velocity on the longer and shorter part of the laser path (Fig. 3).

## 5. Proposed Optimization Problem Solution

The solution to the problem formulated above is a multicriteria optimization task [7]. It can be achieved in the following steps:

- 1) The ideal point should be found. To find such a point, the extreme of all object functions  $F_A$  to  $F_D$  should be satisfied.
- 2) Such set of compromises should be found. This means such a domain in which no one of the object functions can be improved without spoiling the other must be found.
- 3) The solution could be found using one of the methods proposed by C.L. Hwang [8].

In order to find the preferred solution of the problem, we will introduce dimensionless object functions,  $\Phi_i$ , such that:

$$\Phi_i = \frac{F_i}{F_i^-} \quad (17)$$

where:  $i = A, B, C, D$  and  $\Phi_i \leq 1$  and  $F_i^-$  is the maximum value of the function  $F_i$  which belongs to the set of compromises. The introduction of the dimensionless object function is to facilitate the finding of the preferable solution.

The preferable solution can be found using one of the two approaches:

- (a) by method of utility function, (b) by method of matrix function.

Looking for the preferable solution by method of utility function, one has to assign to every dimensionless object function  $\Phi_A, \Phi_B, \Phi_C$  and  $\Phi_D$  a coefficient of importance  $\alpha$ , such that

$$\alpha_A + \alpha_B + \alpha_C + \alpha_D = 1 \quad (18)$$

and create a substitution object function such that

$$\Phi = \alpha_A \Phi_A + \alpha_B \Phi_B - \alpha_C \Phi_C + \alpha_D \Phi_D \quad (19)$$

and find the minimum value of that function. The minus sign in front of  $\alpha_C$  indicates that we are looking for the maximum but not minimum of the function  $\Phi_C$ .

If we are looking for preferred solution by matrix function method, we have to find the point that belongs to the compromise domain and is located as close as possible to the ideal point. In order to

do this, we have to define a function

$$\Phi = (\Phi_A - \Phi_A^{id}) + (\Phi_B - \Phi_B^{id}) + (\Phi_C + \Phi_C^{id}) + (\Phi_D - \Phi_D^{id}) \quad (20)$$

and find its minimum.

In the cases of only two object functions the solution can be found in the way shown on Fig. 4. As the Fig. 4 shows the preferable point is found as a result of a compromise between  $F_A^{min}$  and  $F_B^{min}$ .

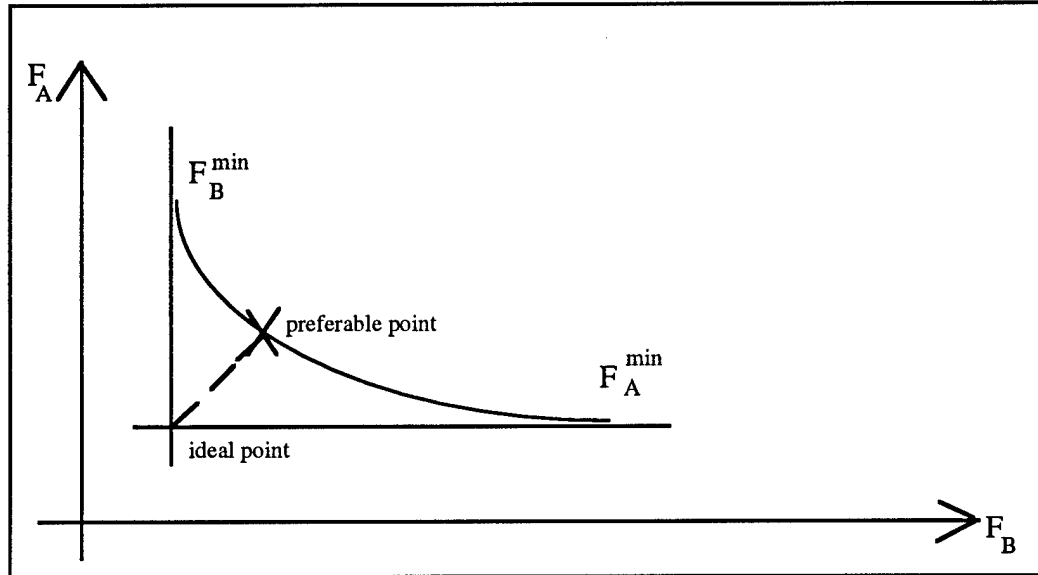


Fig. 4 Solution of the multicriteria optimization problem in the case of two object functions

## 6. Concluding remarks:

In order to make it possible to find the solution in the way proposed above, it is necessary to know how the object functions depend on the decision variables. The expressions of  $\Phi_A$ ,  $\Phi_B$ ,  $\Phi_C$  and  $\Phi_D$  as functions of the decision variables can be developed on the basis of theoretical or empirical findings. In the case described above, it will be necessary to continue the theoretical derivations and empirical tests and describe the object functions as an exact expression, and approximations of the empirical results by polynomials of approved order.

## 7. Acknowledgments:

The authors would like to acknowledge the help of the Institute of Material Science, the Institute of Fundamental Research of the Polish Academy of Science, Mechanical Engineering Department and Research Foundation of the University of Connecticut as well as Professors: Harris Marcus, Stefan Owczarek and Jan Holnicki for their help and support.

## 8. References:

- [1] Bzymek Z.M., Benson S., Garrett R.E. and Ramakrishnan B.T., "Thermo-Printing and Laser Sintering Slicing Simulation for Rapid Prototyping of Engine Parts", 29th ISATA International Symposium on Automotive Technology and Automation, June 6-9, 1996, Florence, Italy; *29th ISATA Conference Proceedings: Simulation, Diagnosis and Virtual Reality Applications in the Automotive Industry*, 1996, pp. 291-298.
- [2] G. Zong, R. Carnes, H.G. Wheat and H.L. Marcus, "Solid Freeform Fabrication by Selective Area Laser Deposition", *Solid Freeform Fabrication Proceedings*, The University of Texas at Austin, 1990, pp. 83-90.
- [3] J.E. Crocker, K.J. Jakubenas, S. Harrison, L. Shaw and H. Marcus, "SALDVI Optimization for the Tetramethylsilano - Silicon Carbide Systems", *Proceedings of the 8th Annual Solid Freeform Fabrication Symposium*, The University of Texas at Austin, pp. 489-496, 1997.
- [4] L. Sun, K.J. Jakubenas, J.E. Crocker, S. Harrison, L. Shaw and H.L. Marcus, "Thermocouples in Macro-Components Fabricated Using SALD and SALDVI Techniques: Part II - Evaluation of Processing Parameters", *Materials and Manufacturing Processes*, in press (1998).
- [5] Nowacki W., *Thermoelasticity*, 1986, PWN- Polish Scientific Publishers, Warszawa, Pergamon Press, Oxford, New York, Toronto, Sidney, Paris, Frankfurt.
- [6] Fung Y.C., *Foundations of Solid Mechanics*, Prentice-Hall Inc., Englewood Cliffs, New Jersey, 1965.
- [7] Marks W., 1997, "Multicriteria Optimization of Shape of Energy-Saving Buildings", *Building and Engineering*, Elsevier Science Ltd., Printed in Great Britain, Vol. 32, No. 4, p. 331 - 339.
- [8] Hwan C.L. and Masus A.S.M., "Multiple objective decision making - methods and applications - a state-of-the-art survey", *Lecture Notes in Economics and Mathematical Systems*, Springer-Verlag, Berlin, 1979.

# SIMULATION OF LAMINATED OBJECT MANUFACTURING (LOM) WITH VARIATION OF PROCESS PARAMETERS

Lawrance Flach, Michelle A. Jacobs  
Department of Chemical and Materials Engineering

Donald A. Klosterman, Richard P. Chartoff  
Rapid Prototype Development Laboratory  
and  
Ohio Rapid Prototype Process Development Consortium

University of Dayton  
300 College Park  
Dayton, OH 45469  
U.S.A.

## ABSTRACT

A previously developed and verified thermal model for Laminated Object Manufacturing (LOM) was used to investigate the effects of various processing parameters on the temperature profile in a LOM part during the build cycle. The mathematical model, based on 3-dimensional transient heat conduction in a rectangular geometry LOM part, allows calculation of the transient temperature distribution within the part during the application of a new layer as well as during other periods of the LOM build cycle. The parameters roller temperature, roller speed, chamber air temperature, base plate temperature, and laser cutting time were independently varied, and the LOM process response simulated. The results were analyzed in order to gain insight into potential strategies for intelligent process control.

## INTRODUCTION

LOM users are fast becoming aware that an understanding of the thermal behavior of a LOM part during the build process is crucial for the fabrication of parts with good lamination characteristics. Low temperatures in the upper layers may result in poor adhesion of the individual layers causing delamination of the completed part. On the other hand, excessive build-up of heat in the body of the part may result in a general loss of structural rigidity during the build leading to excessive compression or shearing during application of pressure by the roller. While this is important for prototype parts made from standard LOM paper and plastic materials, it has become extremely significant now that the fabrication of high performance, functional ceramic and composite parts is being considered [1-8].

In order to obtain a better understanding of the transient thermal behavior of the part body during the LOM build cycle, a mathematical model was developed and its performance

verified [9]. As part of a continuation of this work, it was decided to use this process model to investigate the effects of varying certain parameters during a number of simulated LOM builds. Use of this model allows a number of experiments to be conducted in a relatively short time, and also does not require use of the actual LOM apparatus with associated relatively high cost. In addition, this approach allows for variation of process parameters that are not currently implemented on the LOM machine, such as base plate and chamber air temperatures.

A series of simulation experiments was thus planned to see which of the process variables had significant effects on the transient thermal behavior and which variables could potentially be used for process control purposes. The results of these experiments are presented here together with a brief discussion of their significance.

## BACKGROUND

Full details of the mathematical model have been previously documented [9] so only a brief description of the model and its capabilities as is pertinent to this discussion will be presented here.

The thermal behavior of a part during a LOM build is determined by heat transfer to the part from the roller, heat conduction within the part itself, heat loss from the part to the metal base plate, and heat loss to the surroundings. The appropriate differential equation and boundary conditions were set up for a rectangular geometry part (because all LOM parts are built as rectangular blocks) and then together with appropriate initial conditions, material properties and heat transfer coefficients numerically solved to reveal the temperature distribution within the part. The model is capable of handling the addition of new layers of build material as well as all other phases of the build cycle and generates the full 3-dimensional transient temperature profiles within the part. The model does not include a mechanical submodel, and therefore, the coupling of thermal and mechanical behavior cannot be fully simulated. However, by tuning one of the model parameters (roller to part heat transfer coefficient), excellent agreement was obtained between predicted temperatures within a part and the actual temperature as measured by embedded thermocouples [9], see Figure 1. Thus, the model is fully capable of measuring the thermal behavior of the LOM process.

## MODELING EXPERIMENTS

A series of simulation experiments was designed around a base simulation taken from the previous work [9]. This work involved layup of 250 $\mu$ m-thick SiC ceramic tapes on a LOM2030 machine. A twenty-layer, 12.19 cm x 5.33 cm block of "green" ceramic material was produced. Material property data and simulation parameters for this base case are summarized in Table 1. All parameters were experimentally measured, except the roller to part heat transfer coefficient which was used as a tuning parameter.

**Table 1:** Material properties and machine parameters for base simulation [9].

Material	Silicon carbide ceramic tapes
Thermal Conductivity	$1.25 \text{ Wm}^{-1}\text{K}^{-1}$
Density	$1.98 \text{ g cm}^{-3}$
Heat Capacity	$1.05 \text{ Jg}^{-1}\text{K}^{-1}$
Part dimensions	121.9 mm x 53.3 mm
Layer thickness	0.25 mm
Number of layers	20
Heat transfer coefficient (part to air)	$18 \text{ Wm}^{-2}\text{K}^{-1}$
Heat transfer coefficient (part to base)	$14 \text{ Wm}^{-2}\text{K}^{-1}$
Air temperature	22°C
Base plate temperature	22°C
Initial temperature of material	22°C
Roller velocity	$25.4 \text{ mm sec}^{-1}$
Roller contact strip width	9 mm
Roller temperature	91°C
Heat transfer coefficient (roller to part)	$3300 \text{ Wm}^{-2}\text{K}^{-1}$
Build cycle time	120 seconds

Parameters selected for investigation included the following: roller temperature, base plate temperature, chamber air temperature (surrounding air temperature), roller speed, laser cutting time. The roller temperature and speed influence the amount of heat transfer from roller to part. Base plate and chamber air temperatures influence the rate of heat loss of the part block. The entire part block as a whole gains negligible heat from the laser cutting (although this may not be true for the top layer or two), so the laser cutting time affects the amount of cooling between application of successive layers. All of these parameters directly influence the transient as well as long term thermal behavior of the part. Table 2 summarizes the parameter values used and the changes made to these parameters. In some cases (Trials 15-18) the parameter value was changed halfway through the simulation in order to observe the dynamic response of the process to that variable change. This information is important for process control purposes. The full experiment and results are documented elsewhere [10].

## RESULTS AND DISCUSSION

During model verification [9] it was observed that the temperature below the 1<sup>st</sup> layer (bottom most) of build material was representative of the part body temperature, i.e. apart from surface transient behavior near the part block surface during roller activity, the temperature through the depth of the part was fairly uniform. Thus, in order to compare the behavior of the part when subjected to the different sets of parameters, it was decided to observe the first layer temperature only. Thus, the results shown in the various figures herein represent how the temperature below the bottom most layer varies with time during the build, and this can be interpreted as how the part body temperature as a whole varies with time (referred to as the "representative part body temperature"). In all cases, fluctuation of the representative part body

**Table 2:** schedule of investigated LOM parameters.

Trial #	Roller Temperature (°C)	Base Plate Temperature (°C)	Chamber Air Temperature (°C)	Roller Speed (cm/sec)	Laser Cutting Time (sec)
1	91	22	22	2.54	77
2	150	22	22	2.54	77
3	200	22	22	2.54	77
4	250	22	22	2.54	77
3	200	22	22	2.54	77
5	200	50	22	2.54	77
6	200	75	22	2.54	77
7	200	100	22	2.54	77
3	200	22	22	2.54	77
8	200	50	50	2.54	77
9	200	75	75	2.54	77
3	200	22	22	2.54	77
10	200	22	22	3.81	77
11	200	22	22	5.08	77
12	200	22	22	2.54	57
3	200	22	22	2.54	77
13	200	22	22	2.54	97
14	200	22	22	2.54	117
15	91	22 / 50*	22	2.54	77
16	91	22 / 100*	22	2.54	77
17	91 / 150*	22	22	2.54	77
18	91 / 200*	22	22	2.54	77

\*Parameter changed halfway through the run from the first value to the second.

temperature tends to dampen as more layers are added, and an "average part body temperature" is also referred to throughout the discussion.

The first parameter investigated was roller temperature. The roller temperature was varied in the range 91°C to 250°C, and all other parameters were kept the same as the base case simulation (trial #1 is the base case simulation). Figure 2 reveals that peak temperatures are dramatically increased and the long-term part body temperature is only minimally affected. The average part body temperature increased about 10°C for every 50°C increase in roller temperature. Although not shown in Figure 2, the temperature of the surface layer (in direct contact with the roller) is most dramatically affected.

The next test involved variation of the base plate temperature only. At this point in the study, it was decided to deviate from the base case parameters by using a roller temperature of 200°C for many of the remaining trials. The reason for doing this was to amplify the effects of changes in the other parameters such as base plate temperature, chamber air temperature, etc. The results for parametric variations in the base plate temperature are given in Figure 3. As can

be seen, higher base plate temperature resulted in higher temperatures of the part being built. The average part body temperature for this simulation seems to increase approximately 9°C for each 25°C rise in base plate temperature. This effect was considered to be more "efficient" or "sensitive" than the roller temperature effect.

The next test involved parametric variations in the chamber air temperature. It should be noted that in all cases the base plate temperature was assumed to vary with the chamber air temperature. This would seem to be reasonable considering the geometry and layout of the LOM apparatus. Figure 4 shows how the part body temperature varies with time for different LOM chamber air and base plate temperatures. The response of the part is similar to that of the previous test, with the exception that the magnitude of the part temperature change was more. The average part body temperature for this simulation increases approximately 20°C for each 25°C rise in air and base plate temperature. Thus, this effect was viewed as the most "efficient" or "sensitive" so far. With the previous test in mind, this result was qualitatively expected, i.e. the block loses less heat because all surfaces are maintained at elevated temperature, not just the base plate as before. From a process control viewpoint, however, it may be a lot easier and more practical to manipulate the base plate temperature only and not the combination of base plate and chamber air temperature.

The roller speed was also investigated since time of roller contact will also influence the amount of heat transferred to the part. Changing the roller speed also has the effect of changing the overall build time of the part, so these results are not so easily compared graphically. It was discovered that for a 50% increase in roller speed, the average part body temperature decreased by about 7°C, and for a 100% increase by about 23°C [10]. Again, the surface layer in direct contact with the roller was the most affected.

A laser cutting time of 77 seconds was used in the base simulation. Changing the laser cutting time between the application of successive layers of build material should affect the part temperature due to the fact that increasing this delay time allows additional time for the part to cool by heat loss to the surroundings and base plate. The reason for investigating this effect is because the cycle time usually varies throughout a build due to changes in the laser cutting from layer to layer. It was discovered that this effect was fairly small, in most cases resulting in only about a 3°C drop in part body temperature for every 20-second increase in delay time. [10]

Some dynamic tests were also conducted where the base plate and roller temperatures were changed halfway through the build process. This was done to estimate how many cycles (or layers) were required for the part to respond to the change in the parameter value. The effect of changing the base plate temperature halfway through the build is shown in Figure 5. It can be seen that the part body temperature typically reaches its new average temperature within 3 to 4 cycles. A similar result was observed for the change in roller temperature (Figure 6). These results are significant when considering on-line control of the process and gives one some idea of the overall speed of response.

## CONCLUSIONS

Use of the LOM process for the fabrication of functional ceramic and composite parts has resulted in additional requirements being placed on the LOM build environment to ensure the integrity and functionality of the produced parts. One of these requirements concerns the thermal environment of the part. Control of this environment thus has become an important consideration for the development of LOM using ceramic and composite materials.

The simulation and modeling work done has revealed that a number of parameters have influence over the thermal environment of the part and that some of these show promise as being suitable for manipulation of the process during online control. In particular, the chamber air temperature and base plate temperature combination would seem to be the most effective for control of the overall part temperature. From an overall practicality viewpoint, limited control could also be achieved using the base plate temperature only. The roller temperature proved to be the most effective in affecting the temperature of the surface layers of the part, i.e. those close to the roller during lamination. Thus, if high temperatures are required in the surface layers and somewhat lower temperatures throughout the remainder of the part, then control of the roller temperature would provide a means to accomplish this. However, large fluctuations in the temperatures near the surface would have to be tolerated.

The simulations also revealed some useful information with regard to the dynamic response of the temperature of the part. While this is known to be a function of the overall part dimensions and thermal properties of the build material, the response times obtained indicated that online control of the process is feasible and that reasonable dynamic responses should be obtained.

## REFERENCES

1. Klosterman, D., R. Chartoff, N. Osborne, G. Graves, A. Lightman, G. Han, A. Bezeredi, S. Rodrigues, S. Pak, G. Kalmanovich, L. Dodin, S. Tu, "Curved Layer LOM of Ceramics and Composites," *Prototyping Technology International '98*, (Annual Review Book), ed. Jonathan Lawson, UK & International Press, Surrey, UK, April, 1998, pp.145-149.
2. Klosterman, D., R. Chartoff, et al., "Automated Fabrication of Monolithic and Ceramic Matrix Composites via Laminated Object Manufacturing (LOM)," *Proceedings of the Solid Freeform Fabrication Symposium*, Austin, TX, August, 1997, pp. 537-549.
3. Klosterman, D.A., B.E. Priore and R.P. Chartoff, "Laminated Object Manufacturing of Polymer Matrix Composites", *Proc. 7<sup>th</sup> Int. Conf. Rapid Prototyping*, University of Dayton and Stanford University, San Francisco, CA, March 1997.
4. Steidle, C.C., *Automated Fabrication of Bioceramic Bone Implants Using Laminated Object Manufacturing*, M.S. Thesis, Chemical Engineering, University of Dayton, May, 1998.
5. Chi, C., L. Dodin, and S. Pak, "Development and Fabrication of Metallic LOM Objects", *Proc. 7<sup>th</sup> Int. Conf. Rapid Prototyping*, University of Dayton and Stanford University, San Francisco, CA, March 1997.
6. Griffin, A., et al., "Bioceramic RP Materials for Medical Models", *Proc. 7<sup>th</sup> Int. Conf. Rapid Prototyping*, University of Dayton and Stanford University, San Francisco, CA, March 1997.

7. Griffin, E.A., D.R. Mumm, D.B. Marshall, "Rapid Prototyping of Functional Ceramic Composites," *The American Ceramic Society Bulletin*, Vol. 75, No.7, July 1996.
8. Pope, M., M. Patterson, W. Zimbeck, M. Fehrenbacher, "Laminated Object Manufacturing of Si<sub>3</sub>N<sub>4</sub> with Enhanced Properties," *Proceedings of the Solid Freeform Fabrication Symposium*, Austin, TX, August, 1997, pp. 529-536.
9. Flach, L., D. Klosterman, R. Chertoff, "A Thermal Model for Laminated Object Manufacturing Process," *Proceedings of the Solid Freeform Fabrication Symposium*, Austin, TX, August, 1997, pp. 677-688.
10. Jacobs, M.A., *Thermal Modeling and Control of the LOM Process*, Undergraduate Honors Thesis, Chemical Engineering, University of Dayton, April, 1998. (note, trial numbers in this paper and Jacob's thesis do not correspond).

## ACKNOWLEDGEMENTS

This work was made possible by a grant from the Ohio Board of Regents, Research Challenge Program at the University of Dayton. The LOM equipment was available through a grant from DARPA/ONR, N00014-95-1-0059. Student participation was through the University of Dayton Honors Program.

## ILLUSTRATIONS

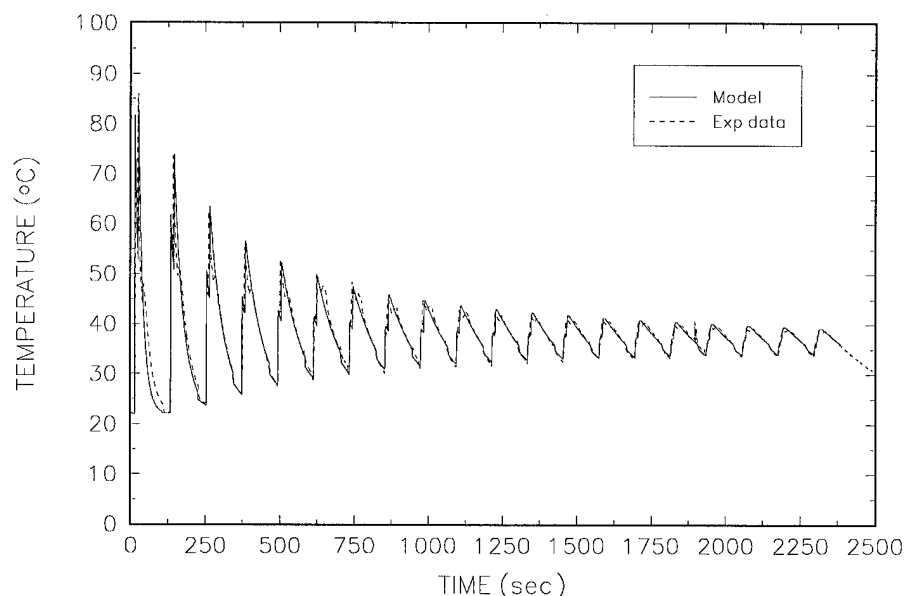


**Figure 1:** Base simulation and experimentally measured temperature profile for a 20-layer, SiC LOM part, as measured by a thermocouple just above the 0<sup>th</sup> layer (foam tape base) during the build process [9]. The cycle time is 120 seconds per layer. The experimental conditions are given in Table 1 and Table 2 (trial #1).

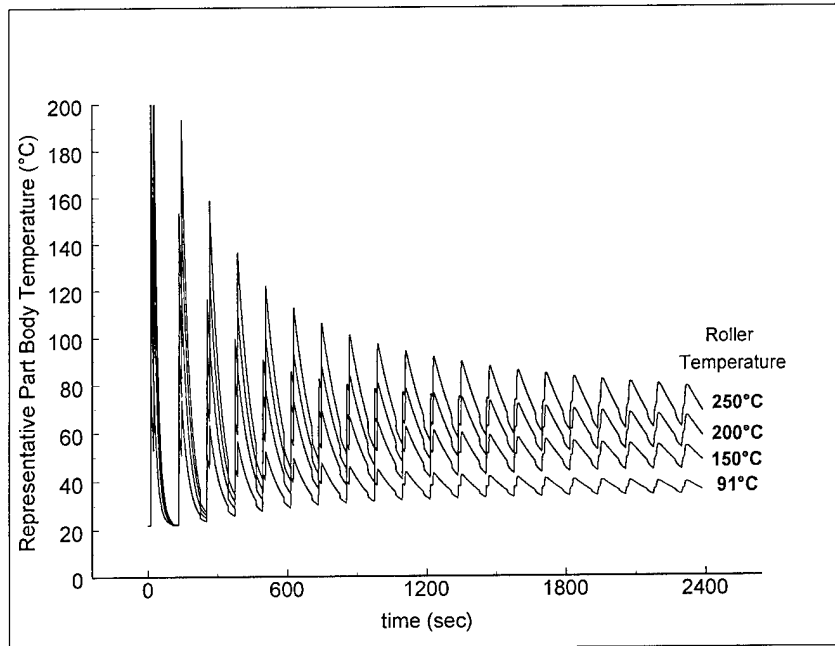


**Figure 2:** Parametric variation of roller temperature: simulated, dynamic temperature profiles inside a 20-layer SiC LOM part during the building process (120 seconds per layer) using the parameters given in Table 2 (trials 1-4).

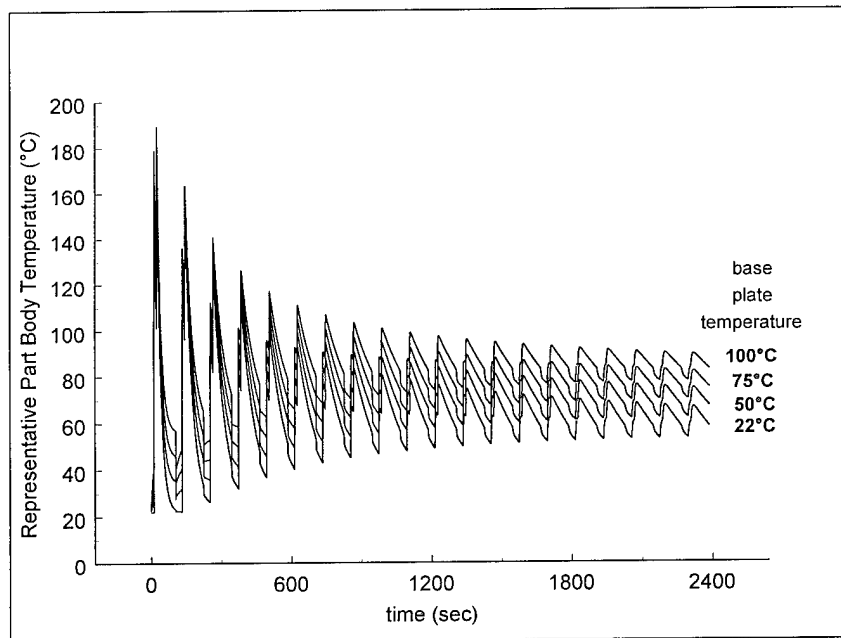


**Figure 3:** Parametric variation of base plate temperature: simulated, dynamic temperature profiles inside a 20-layer SiC LOM part during the building process (120 seconds per layer) using the parameters given in Table 2 (trial 3, 5, 6, 7).

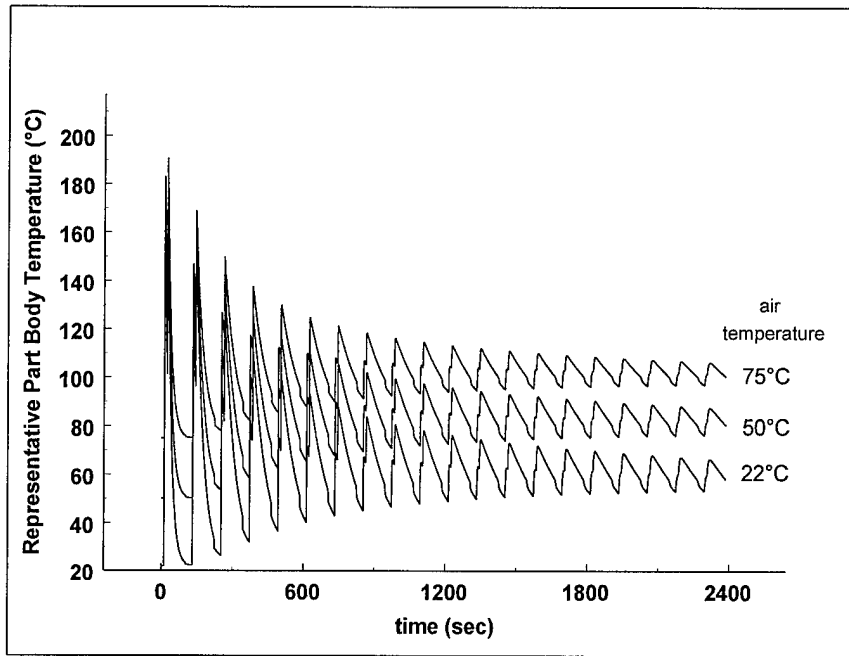


**Figure 4:** Parametric variation of chamber air temperature: simulated, dynamic temperature profiles inside a 20-layer SiC LOM part during the building process (120 seconds per layer) using the parameters given in Table 2 (trials 3, 8, 9).

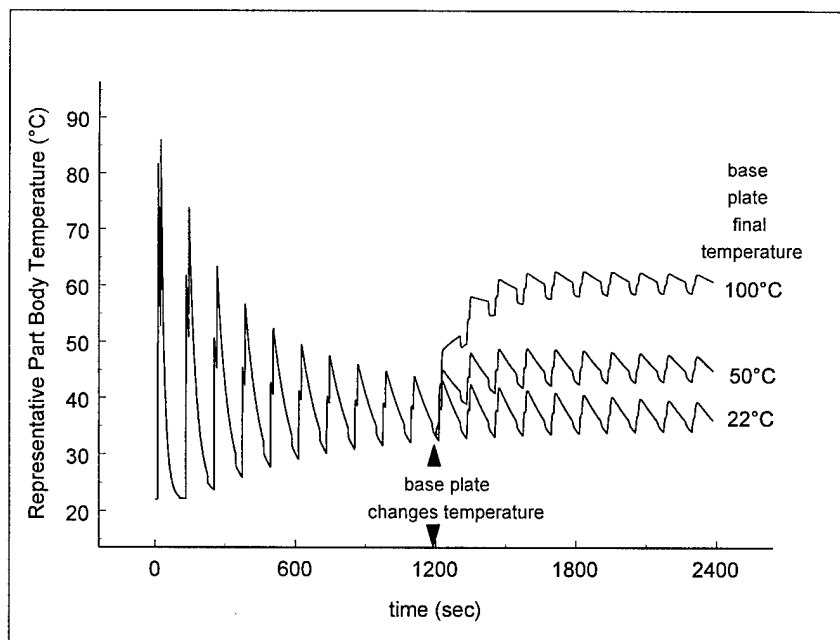


**Figure 5:** Effect of changing base plate temperature halfway through a run: simulated, dynamic temperature profiles inside a 20-layer SiC LOM part during the building process (120 seconds per layer) using the parameters given in Table 2 (trials 15, 16).

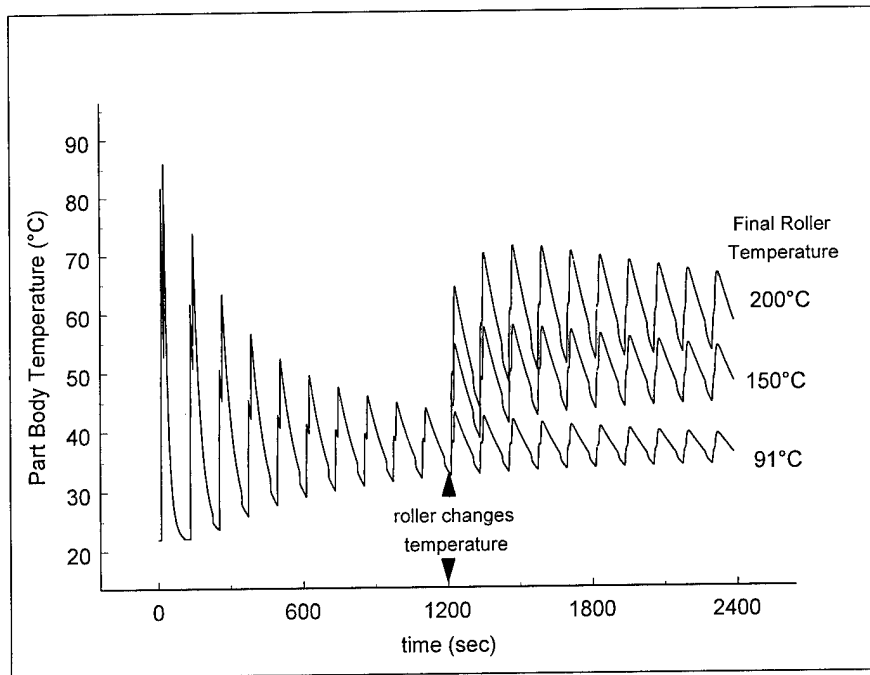


**Figure 6:** Effect of changing the roller temperature (from 91°C) halfway through a run: simulated, dynamic temperature profiles inside a 20-layer SiC LOM part during the building process (120 seconds per layer) using the parameters given in Table 2 (trials 17, 18).

# **Dimensional Variability Analysis In Post-Processing Of Rapid Tooling**

Wanlong Wang, James G Conley and Henry W Stoll  
Department of Mechanical Engineering  
Northwestern University  
Evanston, IL 60208

## **Abstract**

Rapid tooling for sand casting can be made by creating pattern with elements made by solid freeform fabrication (SFF) devices. Using this approach, post-processing and hand finishing remain as necessary steps to improve the surface finish quality of the pattern. For rapid tooling using laminated object manufacturing (LOM) models, post-processing includes decubing, sanding and sealing followed by integration with a match plate and/or conventional cope & drag pattern elements. Since the critical finishing operations are intensively manual, it is difficult to estimate the dimensional capability of rapid tooling by LOM process. The objective of this paper is to use statistics to evaluate dimensional variability associated with post processing using the accepted industry best practice.

## **1.0 INTRODUCTION**

Solid freeform fabrication (SFF) refers to the physical modeling of component or tooling geometry using layered manufacturing technologies. These technologies make it possible to quickly generate polymer, wax, or paper-based prototype parts from solid model computer-aided design (CAD) representations. Parts are typically generated by building up one layer at a time with the thickness of each layer determining the accuracy of the part and the time required to build it. Initially used for the production of parts for design validation, the use of SFF technologies logically extends to rapid fabrication of tooling for casting processes such as investment casting, die casting, and sand casting.

Over the past decade, rapid tooling (RT) based on SFF models has found an increased number of industrial applications. For example, the QuickCast system, developed by 3D Systems Inc. [1], is already used in the automobile product development in Ford Motor Company. Gustafson [2] uses laminated object manufacturing (LOM) models as elements of patterns for sand casting.

For rapid tooling with LOM, the dimensional capability of the tool making process is a key factor influencing industrial applications. While rapid tooling with SFF can help to realize significant time and cost savings, the dimensional capability and stability is not as competitive as that achieved with computer numerical control (CNC) machined pattern production. To understand the dimensional accuracy and consistency of rapid tooling using SFF methods, some research

work has been done in this area. For example, Wang, *et al*, [3] studied the error sources in the rapid tooling process using the LOM models. Hopkinson, *et al*, [4] investigated the thermal effects on accuracy in the 3D Keltool™ process.

In this paper, we briefly introduce the sand casting process and its established error sources. We then consider the sources of error in rapid tooling production using the LOM process. The dimensional variability associated with post processing is then addressed. Since the operations are manual, it is difficult to give an accurate estimation of the dimensional loss or increment in post-processing. Thus it is reasonable to employ the statistics to analyze the dimensional consistency and variability. While the focus of this paper is on rapid tooling using the LOM process, the results are also applicable to other rapid tooling processes.

## **2.0 SAND CASTING AND ITS ERROR RESOURCES**

Sand casting is an old and widely used metal forming process in which parts are produced by casting molten metal into sand molds. It is estimated that more than 90% metal parts are produced by this process [5]. To improve the dimensional accuracy, the error sources must be identified. The error sources in the sand casting are illustrated in Figure 1 [6].

Traditionally, the pattern for sand casting is made by manual or computer numeric control (CNC) machining. Manual machining is a time-consuming and high cost method and needs experience, knowledge and skills. With this experience-dependent method, it is difficult to guarantee the dimensional accuracy and improve productivity. CNC machining is a good candidate to improve the efficiency and processing accuracy. It is being widely used in today's pattern making industry. Figure 2 gives a flowchart of product development steps for a sand casting process using laminated object manufacturing (LOM) pattern elements.

## **3.0 POST-PROCESSING ERROR SOURCES IN LOM RAPID TOOLING**

The LOM process starts with a 3D computer-aided design (CAD) model of the desired tool or pattern. The model is then tessellated into triangular facets and sliced into layers each having the thickness of a sheet of paper. The LOM model is then constructed by laser cutting and gluing sheets of paper together. Surround material and material in regions of the part that are hollow must be removed in a subsequent "decubing" process. The surface of the resulting LOM model must then be sanded to smooth the "stair step" texture created by the layers of paper. Finally, the surface must be sealed with lacquer or an equivalent sealant to keep moisture from being absorbed into the model. Each step in this process introduces error as shown in Figure 3.

Of the sources identified in the figure 1, decubing error and post-finishing error are those associated with post-processing that can cause delamination or dimensional swelling. Since this operation is typically conducted manually, it is difficult to make an accurate quantitative analysis for the dimensional change before and after this process, since each would be subjective.

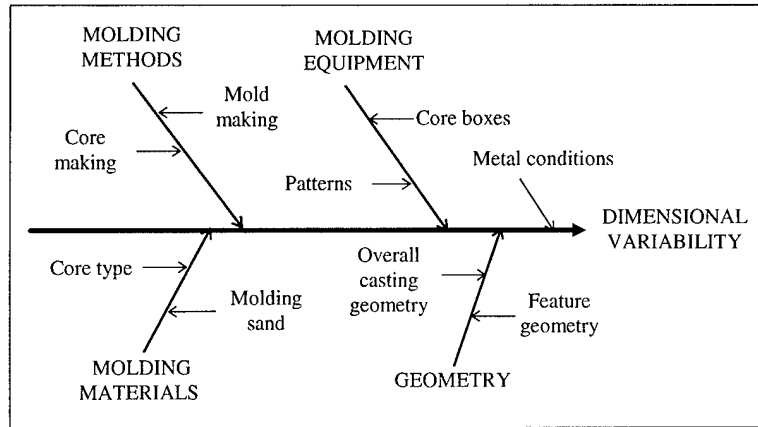


**Fig 1** Fishbone diagram of major factors affecting dimensional variability of casting

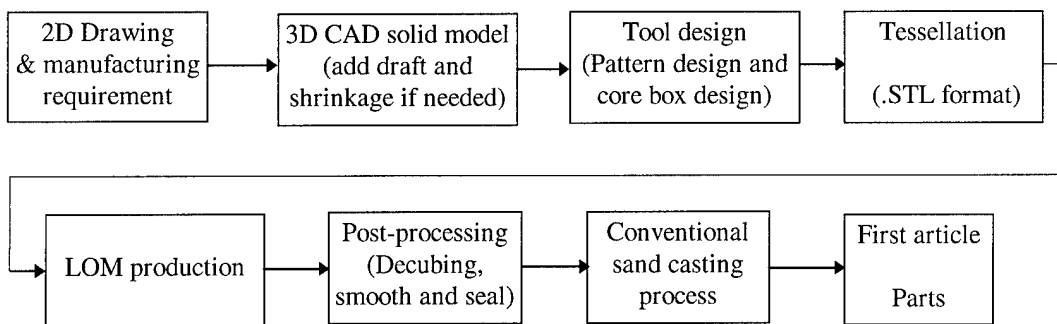


**Fig 2** The sand casting process using rapid tooling (LOM)

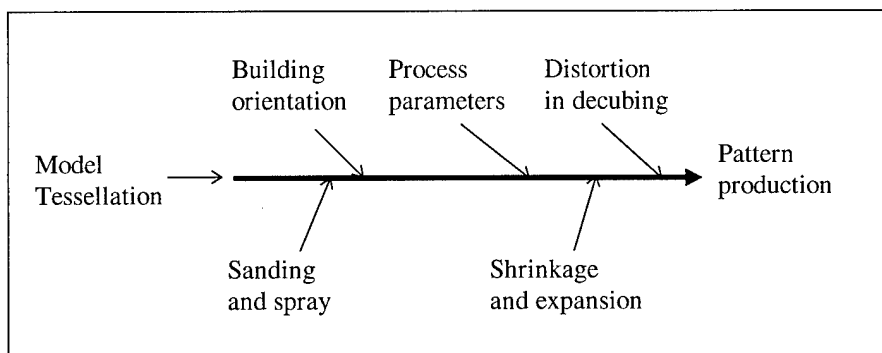


**Fig 3** Fishbone diagram of error sources associated with the LOM process

### 3.1 Decubing Error

Residual stress can develop in the LOM build as the result of the temperature change. During the building process, the temperature of the workpiece will rise because of heat used to improve the adhesive bonding between paper layers. After the building process is finished, residual stress due

to volume shrinkage develop within the model as it cools to room temperature. When the model is “decubed”, constraints are released and the residual stresses are redistributed. This can result in shape distortion of the model and in some cases, delamination of layers. As with other sources of error in the LOM process, the dimensional error that may occur depends on the detailed geometry of the part, the part orientation with respect to build direction, paper thickness and other process factors. In general, distortion is greatest in thin wall parts [3].

### **3.2 Post-Finishing Error**

After decubing, the model is usually sanded and sealed. Sanding is necessary to remove “stair step” irregularities and to smooth part features. The sealed lacquer coating seals the surface and strengthens the model. The lacquer coating is also sanded to smooth the surface finish of the model. These operations are usually performed manually by experienced operators. Error introduced during these manual procedures depends on operator skill and specific part geometry. Because of the number of hard to control factors involved, post finishing error is likely vary significantly with tool geometry.

## **4.0 EXPERIMENTAL INVESTIGATION**

### **4.1 Test part**

An experimental investigation was conducted to statistically analyze the errors discussed above. The test part selected is a thin wall aluminum sand casting used in an aerospace application. A 3D CAD representation of the part is shown in Figure 4. This part has many typical features including cylindrical surfaces and transitions, planes, and small through holes. Because of its thin walls, the part is sensitive to decubing and post finishing. Although this is a tooling master, not a casting model, it suits the purpose of our study. Our purpose is to determine the influence of post-processing on part dimensions. Generally the part is supplemented and extended in some dimensions to add the machining stock).

The models was built with the chord height of 0.001 inch. The LOM models were built using a LOM 1015 *Plus* machine. Tessellation and process parameters and resulting build time are given as follows:

- Laser power: 43 W
- Laser beam radius: 0.0050 in
- Plotter speed: 10.0 in/s
- Heater-slow-speed: 3.00 in/s
- Heater-fast-speed: 5.00 in/s
- Platform-slow-speed: 0.50 in/s
- Paper thickness: 0.0044 in
- Chord length: 0.001 in
- Build height: 4.68194 in
- Total layers: 1089
- Elapsed time: 12 hrs 50'

## **4.2 Dimensional Measurement**

To assess the effect of tessellation, the dimensions of a variety of features were measured before and after post-finishing using a Brown & Sharpe coordinate-measuring machine (CMM) [7] and compared with the CAD model nominal dimensions. Best metrology practices were used throughout the investigation to ensure that measurement system error did not influence results. Each measurement was repeated five times using the CMM machine. For each trial, the touch points were randomly chosen and distributed around the surface or plane to insure that all variation was included. Figure 5 identifies the location of each dimension.

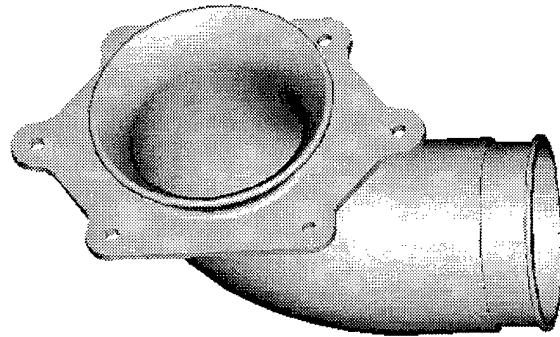


**Fig 4** The solid model of the test part

To assess the measurement validity and reduce any influence from the measurement error, gage repeatability and reproducibility (Gage R&R) [6, 8, 9] has been implemented on the CMM machine.

## **4.3 Decubing Error Measurement**

As discussed above, decubing error may occur due to residual stresses and delamination. To measure the distortion caused by the decubing operation, the concepts of flatness and roundness are introduced. Flatness is the condition of a surface having all points in one plane (generally measuring 4 points). Roundness is the condition where all points are in a circle (generally measuring 4 points). It is computed by subtracting the maximum point from the minimum point about the best fit circle [7, 10]. The flatness and roundness measured here are the flange plane and the right side of the elbow part (dimensions 13~16, see Figure 5). Each measurement has been repeated five times and the average value and standard deviation calculated.

## **4.4 Post-Finishing Error Measurement**

The prototype is sanded and sealed to achieve a final finish according to the conventional post-finishing process. This is done by sanding-sealing-sanding-sealing iterations. Sanding and sealing are generally done manually. As such, it is difficult to consistently control dimensions of the part. In this study, the sand paper and lacquer are used to sand and seal. After post-finishing, the prototype can be used as the pattern in sand casting process. Then the same measurement can be performed on the pattern.

### 4.5 Analysis of Results

The dimensions measured can be categorized as five types: distance or thickness (1, 2, 4, 6, 7 and 12), internal cylindrical surface (8 and 10), external cylindrical surface (3, 5, 9 and 11), flatness (13 and 14) and roundness (15 and 16). The statistical analysis is performed by StatView [11] software. The results are shown in Table 1 and 2. Some typical dimensional distribution diagrams are shown from Figure 6~10.

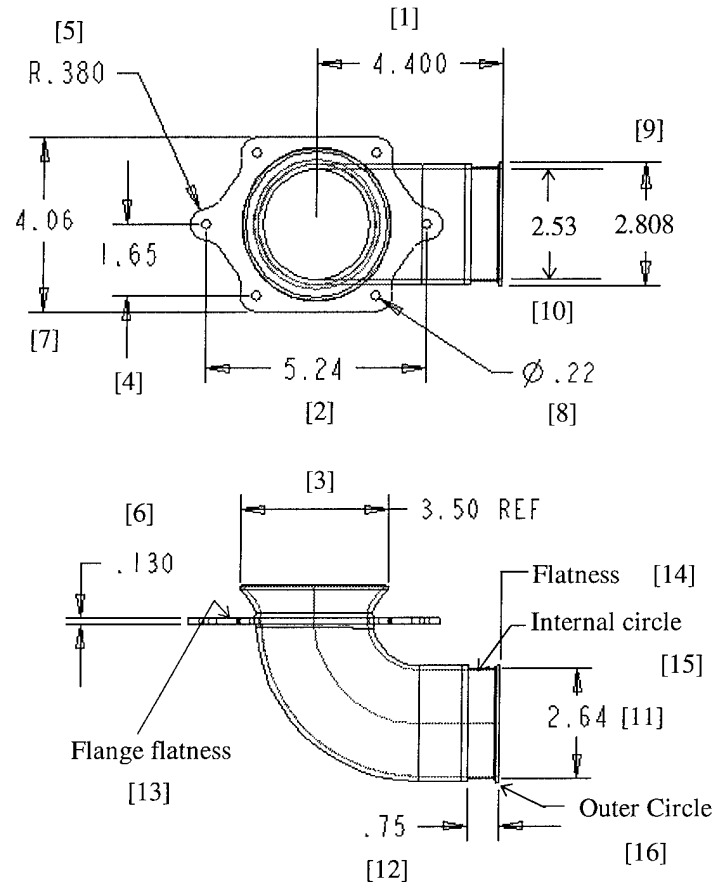


**Fig 5** Test part dimensions measured by CMM

Comparing the items and values in Table 1 and 2 and refer to Figure 6~10, we can make the following observations:

Generally speaking, the variability of dimensions is the same before post-finishing as it is after post-processing. Of 16 dimensions, there are 6 dimensions greater in standard deviation before than after post-processing, 7 less and 3 equal. As such, there are no obvious trends demonstrating that the standard deviation increased or decreased with geometry.

Considering the standard error, there are 4 dimensions greater before than after, 8 less and 4 equal. This suggests that the standard error worsens as a result of post-processing.

For the range, there are 8 dimensions greater before than after, 6 dimensions less and 2 dimensions equal. This indicates that the total dimensional consistency is improved as a result of post finishing.

**TABLE 1** Test Part Dimensional Variability (before sanding and sealing)  
(The location of each measurement is indicated by number on Figure 3)

	Mean	Std. Dev.	Std. Error	Count	Minimum	Maximum	Range
dim1	4.395	.006	.003	5	4.387	4.404	0.016
dim2	5.250	.003	.001	5	5.246	5.253	0.007
dim3	3.524	.016	.007	5	3.503	3.546	0.043
dim4	1.650	.002	.001	5	1.649	1.654	0.005
dim5	.766	.003	.001	5	.761	.769	0.008
dim6	.136	.006	.003	5	.131	.146	0.015
dim7	4.065	4.479E-4	2.003E-4	5	4.064	4.065	0.001
dim8	.221	.002	.001	5	.219	.223	0.004
dim9	2.817	.002	.001	5	2.815	2.819	0.004
dim10	2.538	.005	.002	5	2.531	2.543	0.012
dim11	2.636	.003	.001	5	2.632	2.640	0.007
dim12	.749	.002	.001	5	.747	.751	0.005
dim13	.013	.001	.001	5	.012	.015	0.004
dim14	.003	.001	2.260E-4	5	.002	.004	0.001
dim15	.014	.001	3.720E-4	5	.013	.015	0.002
dim16	.006	.003	.001	5	.001	.009	0.008

**TABLE 2** Test Part Dimensional Variability (after sanding and sealing)  
(The location of each measurement is indicated by number on Figure 3)

	Mean	Std. Dev.	Std. Error	Count	Minimum	Maximum	Range
dim1	4.382	.006	.003	5	4.376	4.388	0.013
dim2	5.247	3.946E-4	1.765E-4	5	5.247	5.248	0.001
dim3	3.548	.002	.001	5	3.546	3.550	0.004
dim4	1.651	.001	.001	4	1.650	1.652	0.003
dim5	.763	.009	.004	5	.751	.772	0.022
dim6	.140	.003	.001	5	.137	.143	0.007
dim7	4.066	.001	3.710E-4	5	4.065	4.067	0.002
dim8	.217	.002	.001	5	.215	.219	0.004
dim9	2.819	.006	.003	5	2.810	2.827	0.017
dim10	2.542	.001	.001	5	2.541	2.544	0.003
dim11	2.660	.017	.008	5	2.633	2.673	0.040
dim12	.747	.004	.002	5	.743	.751	0.008
dim13	.008	.005	.002	5	.003	.014	0.012
dim14	.003	.001	3.274E-4	5	.002	.004	0.002
dim15	.005	.002	.001	5	.003	.007	0.004
dim16	.007	.001	.001	5	.005	.009	0.004

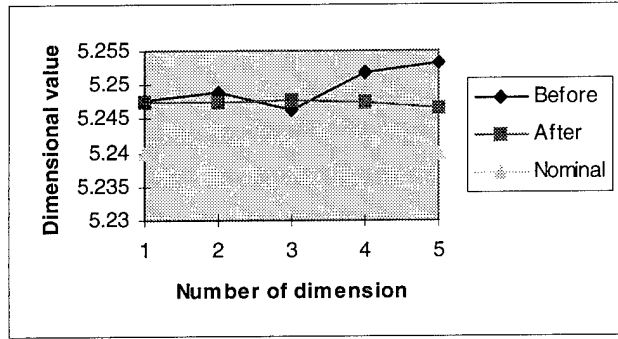


Fig 6 Diagram of dimensional distribution of Dim2

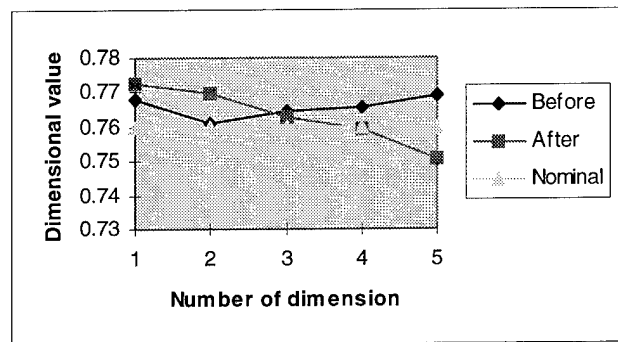


Fig 7 Diagram of dimensional distribution of Dim5

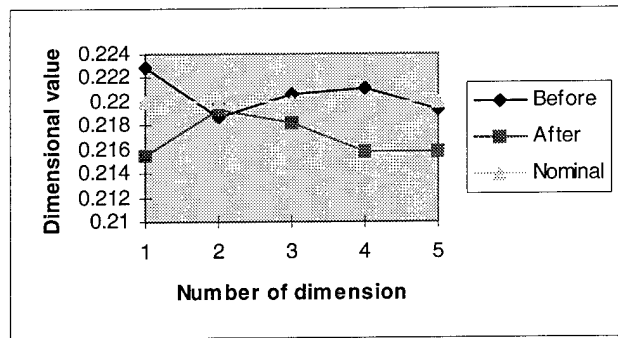


Fig 8 Diagram of dimensional distribution of Dim8

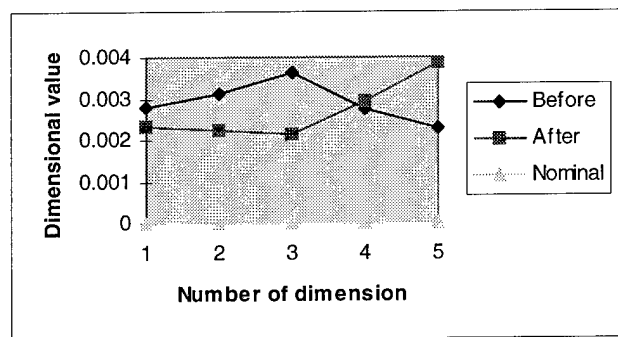
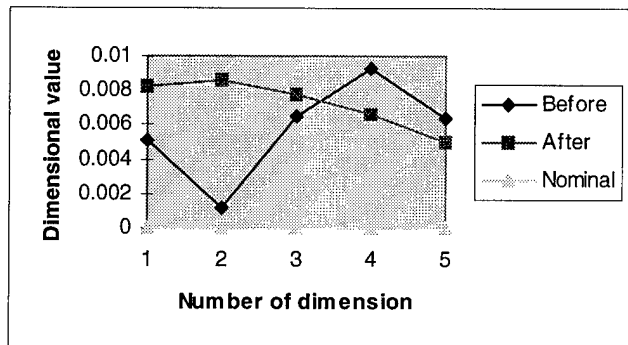


Fig 9 Diagram of dimensional distribution of Dim14



**Fig 10** Diagram of dimensional distribution of Dim16

For the specific type of dimension, the difference is not outstanding either. For example, for distance and thickness dimensions, there are 3 dimensions greater before than after, 2 less and 1 equal in standard deviation. For the outer cylindrical surface dimensions, 1 greater and 3 less. For the inner cylindrical surface, 1 equal and 1 greater. For flatness, 1 less and 1 equal. For roundness, 1 greater and 1 less.

#### 4.6 Discussion

From the above results, we present the following discussions to further clarify our findings:

- Post-processing can be useful and flexible to guarantee the dimensional accuracy. In comparison with CNC finish machining, post-processing can complement dimensional capability with its sanding-sealing-sanding-sealing process (e.g. overcut area). CNC finish machining is less forgiving if an overcut occurs. While comparing with manual making, the overall dimensional accuracy can be achieved and the productivity is relatively better.
- Post-processing can repair or reduce some systematic error sources inherited from previous process stages, i.e. paper thickness, tessellation, build direction, etc. As indicated by Wang, *et al* [3], systematic errors are not avoidable because of the nature of layered manufacturing. But post-processing can help to repair or reduce these errors by its sanding and sealing iterations, if the operator has a better understanding of the process and is experienced with mold making.
- Different rapid tooling processes may be more suitable to different geometry. According to our experience, the LOM process is good for block, thick wall and very complicated surfaces geometry, but not for small holes or bars, thin walls, shallow surfaces and difficult undercuts. Dimension 8 (diameter is 0.22 inch) has verified this. The error is evident even though the chord height is already the minimum. Other SFF processes (e.g. SLA, FDM) may be better suited to handle the geometry features that challenge LOM.

## 5.0 CONCLUSION

From the above analyses, we may find that there are no obvious relations of dimensions existing before and after post-processing. So it is hard to give the numerical equations of the dimensional consistency or the accurate relationship. But if we can understand this and make full use of the advantages of post-processing, the systematic errors maybe repaired or reduced and thus the dimensional capability may be improved. Geometry drivers for LOM process are also discussed. The flexibility in post-processing can be helpful for rapid tooling in processing accuracy and thus strengthen the pattern matches competitive position in the sand cast tool making market.

## Acknowledgment

This on-going research is supported by the American Metalcasting Consortium/Defense Logistic Agency (AMC/DLA) Lead Time and Cost Reduction Program. We are indebted to Milos Coric who made and decubed the LOM models, and performed the post-finishing.

## References

1. K. Denton, P. Jacobs, "Quickcast & Rapid Prototyping: a case history in Ford Motor Company", The 5<sup>th</sup> International Conference on Rapid Prototyping, Dayton, Ohio, June 12-15, 1994, p301-320.
2. R. Gustafson, Guinn, E. Tait, David. "Rapid prototyping for pattern and foundry tooling", Modern Casting. v 85 n 2 Feb 1995. p 48-50.
3. W. L. Wang, J. G. Conley and H. W. Stoll, "Rapid Tooling Error Analysis for Sand Casting", Transactions of the AFS 102nd Casting Congress, Atlanta, GA, May 10-13, 1998.
4. N. Hopkinson and P. Dickens, "Thermal effects on accuracy in the 3D Keltool process", Proceedings of Solid Freeform Symposium, The University of Texas at Austin, Texas, August 11-13, 1997. p 267-274.
5. S. S. Pak, D. A. Klosterman, et al, "Prototype tooling and low volume manufacturing through laminated object manufacturing (LOM), The 7<sup>th</sup> International Conference on Rapid Prototyping, San Francisco, CA, March 31-April 4, 1997, p325-331
6. F. E. Peters, R.C. Voigt, "Assessing the capabilities of patternshop measurement systems", AFS transactions, 1996, p207-213
7. Brown & Sharpe, CMM software user guide, Brown & Sharpe Company, 1995
8. AIAG, Measurement system analysis – reference manual, Automotive Industry Action Group, Southfield, MI, 1995
9. Eric Coblin, Repeatability of the Brown and Sharpe CMM, Mechanical Engineering Internal Report, Northwestern University, Evanston, IL. June 1997
10. L. W. Foster, Geo-Metrics II – The application of geometric tolerancing techniques, Addison-Wesley Publishing Company, Reading, Massachusetts. Revised 1986 Edition
11. Abacus Concepts, Inc. StatView Reference. Berkeley, CA. 1996

# SHELL CRACKING IN INVESTMENT CASTING WITH LASER STEREOLITHOGRAPHY PATTERNS

W. L. Yao

Department of Mechanical and Production  
Engineering  
National Kaohsiung First University of Science  
and Technology  
Kaohsiung, Taiwan, R.O.C.

Ming C. Leu<sup>1</sup>

Department of Mechanical Engineering  
Multi-lifecycle Engineering Research Center  
New Jersey Institute of Technology  
Newark, New Jersey 07102

## ABSTRACT

This paper presents an investigation of ceramic shell cracking during the burnout process in investment casting with internally webbed laser stereolithography patterns. We hypothesize that shell cracking will occur when the rupture temperature of the ceramic shell is lower than both the glass transition temperature of the pattern material and the web link buckling temperature. The hypothesis is validated by our experimental observations which confirm the numerical predictions from our finite element analysis. This provides a basis for design of the internal web geometry of a lithography pattern and evaluation of the burnout process with such a pattern. We show the shell cracking and web link buckling temperatures to be functions of the pattern geometry (including the cross-sectional dimensions and span length of the web link) and the shell thickness.

*Keywords:* Rapid Prototyping; Investment Casting; Solid Freeform Fabrication; Rapid Tooling;

## 1. INTRODUCTION

Investment casting is a precision casting process. It begins with the making of an expendable pattern — usually produced by injection of liquid wax into a precision mold. The wax pattern is assembled with gating and feeding subsystems and cleaned prior to the ceramic coating. The coating is built through successive stages of dipping and stuccoing. This procedure is repeated until the required shell thickness is obtained. On completion of the coating the expendable wax pattern is removed by melting in a steam autoclave or flash furnace, and the ceramic shell is fired prior to casting. After the molten metal is poured and solidified, the shell is broken away and the castings removed [1].

Solid freeform fabrication (SFF) is increasingly being used for tooling and manufacturing applications, besides making design prototypes from CAD models. The use of Stereolithography Apparatus (SLA) is the most popular among the various SFF technologies existing today. SLA builds a part by controlling a laser beam to selectively cure photocurable liquid resin layer by layer [2] [3] [4] [6]. The SLA built epoxy pattern can be used as a thermally expendable pattern

---

<sup>1</sup> Dr. Ming C. Leu is on leave at the National Science Foundation as the Program Director for Manufacturing Machines and Equipment.

in investment casting. Compared with the conventional wax pattern, this enables prototyping new physical products more quickly and cost effectively. However, because the coefficient of thermal expansion of the epoxy resin is one order of magnitude larger than that of investment ceramic material, the ceramic shell may crack during the pattern burnout process. Cracking occurs when the stress induced in the ceramic shell is greater than the Modulus Of Rupture (MOR) of the shell material.

There have been some studies about thermal effects on the webbed pattern and ceramic shell in investment casting, but the generated knowledge is still very limited [5] [7] [8] [9] [10]. A research team at 3D Systems, the SLA manufacturer, developed quasi-hollow webbed patterns in investment casting (see Figure 1) Jacobs [7] observed the yield of castings as a function of the pattern void ratio, defined as the fraction of air space in a pattern. He stated that under such a situation the SL webbed pattern will collapse inwards under the influence of heat, rather than cracking the ceramic shell by expanding outwards. Hague and Dickens [8][9] observed shell cracking at temperatures below the glass transition temperature of the epoxy material, but did not observe buckling of hollow SL patterns in their burnout experiments.

The objective of this study is to provide a better understanding about why quasi-hollowed SL models cause cracking in the ceramic shells and what causes the webbed pattern to collapse. Our hypothesis is that shell cracking will occur when the temperature of shell rupture is lower than the glass transition temperature of epoxy resin and the temperature of web buckling. This hypothesis is verified by our experimental observations which confirm that the cracking of the shell can be prevented if either the material softens or the web links buckle during the burnout process. An analytical model with finite element analysis is used to determine the stresses in the webbed pattern and the ceramic shell during the burnout process.

## 2. HYPOTHESIS DESCRIPTION

When an investment casting shell with an SL epoxy pattern inside is placed in an autoclave or flash-fire oven during the burnout process, it is subjected to high temperature rise, thermal expansion, and large strains. Since the difference between the coefficient of thermal expansion of pattern material (epoxy) and that of investment material (ceramic) is more than one order of magnitude, the epoxy pattern exerts considerable stresses on the ceramic shell. Under the influence of heat, whether an investment shell will break or not depends upon factors governed by the epoxy web structure and the investment shell. The primary hypothesis of this work is the follows: whether the shell cracking, pattern buckling, and epoxy softening occurs first depends on which of the pattern buckling temperature ( $T_b$ ), the resin glass transition temperature ( $T_g$ ), and the shell rupture temperature ( $T_u$ ) is the lowest. If the epoxy resin softens or the internal epoxy web structure buckles first, the exerted stress upon the shell wall will drop dramatically, thus keeping the shell intact. On the other hand, the cracking of the ceramic shell will occur if the shell rupture temperature is lower than both the pattern buckling temperature and the resin glass transition temperature.  $T_u$  is the temperature at which the induced stress is greater than the MOR of the shell ceramic material;  $MOR = S_u = 3.0\text{MPa}$  in this study [13].  $T_g$  is the glass transition temperature of the epoxy resin,  $T_g = 60 - 70^\circ\text{C}$  for SL5170 epoxy from Ciba-Geigy [8] [9].  $T_b$  is the temperature at which the compressive pressure causes the web link to

buckle. The temperatures of shell cracking and web link buckling are related to the dimensions of the web structure and the thickness of the investment ceramic shell.

### 3. FINITE ELEMENT ANALYSIS

Since the skin of SL pattern is very thin, the effect of the outer skin can be negligible in the analysis. The internal square web structure pattern can be treated as a girder-type planar frame with fixed ends (see Figure 2). Due to the complexity of the internal web structure, it is necessary to perform numerical simulations to determine stresses induced in the burnout process. In this analysis, a two-dimensional model of a ceramic shell with the internal web structure, under a heating process to stepwise isothermal temperatures, is assumed. The buckling of a square frame is adopted to determine the temperature of web structure buckling. To simplify the analysis, we do not consider transient heat transfer during the thermal expansion of the pattern and shell. The basis of the two-dimensional model is the "simple, topologically connected" internal web structure, i.e. two consecutive layers of the internal web structure are simply stacked without any interaction in the z-direction (see Figure 1). Additionally, the temperature uniformity within the webbed pattern and the ceramic shell is assumed throughout this study. Practically it is difficult to keep the temperature uniform during the burnout process of the specimens. For each step temperature increase, the oven temperature is increased and kept long enough to reach the desired temperature. The assumption on the buckling of the internal web structure is based on the confluence of a number of small square grids in the webbed pattern and the rigidity of the joints of the internal web structure to preserve the angles between the various link members [11]. Due to the thermal expansion, the resultant forces are likely to cause the individual square grids to buckle (see Figure 3). Our experimental observations (to be discussed) show a good agreement with the FEA results with the model of square frame buckling. The previous use of the buckling of a beam with two fixed ends was less accurate [12]. The square frame buckling model enables determining the buckling temperature of the web link structure.

The numerical result of a part ( $L=6.35\text{mm}$ ,  $b=0.3048\text{mm}$ , and  $h=1.4372\text{mm}$ ) with 1mm thickness ceramic shell is depicted in Figure 4. The FEA models used in this study are quarter models and they are automatically meshed in level #2 using the PLANE82 element and axisymmetric boundary condition. The  $\sigma_c$  and  $\sigma_x$  (or  $\sigma_y$ ) represent the principal (hoop) stress in the ceramic shell and the compressive stress in the epoxy webbed pattern, respectively. The  $\sigma_c$  value is compared with MOR to define the rupture temperature of the ceramic shell.  $P_{cr}$  is the critical pressure that causes the web link to buckle. The critical unit pressure of the buckling of square frame,  $P_{cr}$  is  $16.47EI/AL^2$  [11], where  $A$  is the cross-sectional area of web link,  $E$  is Young's modulus of the epoxy material,  $I$  is the moment of inertia of web link cross-section, and  $L$  is the web link space length.  $A = b \times h$  and  $I = hb^3/12$ , where  $b$  is the width of web structure, and  $h$  is the depth of web structure. This  $\sigma_x$  value is compared with  $P_{cr}$  to determine the buckling temperature of the web link. For this part the obtained results are  $T_u = 35^\circ\text{C}$ , and  $T_b = 52^\circ\text{C}$  (refer to Table 1). Note that Young's modulus of the epoxy resin is a function of temperature. Figure 5 shows the effects of the ceramic shell thickness on the generated stresses in the ceramic shell and webbed pattern. It is seen from Figure 5a that the maximum hoop stress decreases as the shell thickness is increased. That is, a thicker ceramic shell can better resist the thermal expansion of the SL epoxy pattern. Figure 5b shows that the shell thickness effect on the maximum

compressive stress in the internal web structure is quite small. In fact, the stress curves for 6mm and 9mm thickness are indiscernible.

#### 4. EXPERIMENTAL STUDY

The experimental study consists of two parts. First, experiments are conducted to observe the pattern burnout process. Figure 6 shows an SL pattern without and with the ceramic shell. Second, the induced stresses on the shell are measured by strain gauges. Figure 7 shows strain gauged samples. Both the qualitative observations and the strain gauge measurements validate the prediction of FEA.

The test samples are geometrically designed with the Pro/ENGINEER package and built using SLA250 with the SL5170 epoxy resin from Ciba-Geigy. The internally webbed SL samples have a simple cylindrical geometry of 25.4mm (1inch) diameter and 76.2mm (3inch) long. The built parts are coated with ceramic using a Sandia National Laboratories facility.

A number of experiments have been carried out to observe the pattern burnout process. The oven used for the experiments has its temperature controlled electrically. The test samples are examined and recorded at the interval of ten degrees, up to 100°C. The observations of test samples are made with a magnifier and an imaging camera. The observations recorded include shell cracking, epoxy softening, and web link buckling. For the test samples with strain gauges, the pattern is coated with ceramic slurry after mounting the strain gauges on the surface of each pattern. If the webbed SLA pattern collapses because of the buckling of the web structure, the web link will look wavy. If the pattern collapses because of epoxy resin softening, then the pattern will look "leathery".

#### 5. RESULTS AND DISCUSSION

Several phenomena of the pattern burnout process have been observed. These observed phenomena include 1)shell cracked, 2)web link slightly buckled, 3)web link severely bucked, 4)no buckling in the web link, and 5)web link buckled and shell cracked. The basic test sample has the typical dimensions of web structure ( $L=6.35\text{mm}$ ,  $b=0.3048\text{mm}$ , and  $h=1.4732\text{mm}$ ) used in the QuickCast build process. The samples of this part that are invested with 1mm shell thickness show shell cracking when the temperature reaches 40°C. This is shown in Figure 8a. The web links remain straight because the shell has cracked already. This observation indicates that the shell cracking occurs at early stages of the burnout process in investment casting, when the invested shell is not strong enough to resist the exerted forces from the thermal expansion of the internal web structure. From FEA, the predicted rupture temperature is about 35°C (see Figure 5), at which the induced stress exceeds the MOR of the ceramic material and thus fractural cracking occurs.

The observations show that the web links of the basic test samples (with the typical web structure) and 3, 6, 9mm in shell thickness are slightly buckled when the temperature reaches 50°C. There is no occurrence of shell cracking at all, whereas the web link becomes brittle and collapsed after the glass transient temperature. Likewise, the web links of the test samples with a

smaller web link height and coated with 6 and 9mm thickness appears slightly buckled. Again, the results of FEA are confirmed by the experimental observations.

The experimental results of the test samples which have 50% longer web link span than the basic test samples and coated with 6mm and 9mm ceramic, show that the web link becomes very wavy when the temperature reaches around 40°C (see Figure 8b). The temperature (37°C) at which the web link starts to bend is significantly lower than the glass transition temperature (60 - 70°C) of the epoxy material. The test samples which have a web span length smaller than the typical web structure by 50% and coated with 6mm and 9mm ceramic show that the web structure becomes brittle and breaks down at high temperatures (> 100°C) with no sign of web link bending (see Figure 8c). The buckling temperature of this part is infinity, which means that buckling will never occur. The experimental observations of test samples which have 50% longer web link span than the basic test samples and coated with 1mm ceramic show that the web links buckle but the ceramic shell still cracks. The FEA results predict that for this part, the web link buckles and the shell cracks at about the same low temperatures. The experimental observations confirm the FEA predictions for the relationships among  $T_b$ ,  $T_g$ , and  $T_u$  for all these test parts.

An example of experimentally measured stresses on the strain gauged test samples is shown in Figure 9. The experimental data exhibit the same trend as the predictions from the finite element analysis. The discrepancy between the predicted and measured results is due primarily to the following: 1) The material property of the thermoset epoxy resin is uncertain after the glass transition temperature (60 - 70°C), which makes numerical predictions difficult at temperatures near and above 60°C. 2) Our FEA assumes constant temperature of the shell-pattern construction during the burnout process and does not take transient heat transfer into consideration. Although the oven temperature is kept constant for a period of six minutes after heating up for each interval of ten degrees, the temperature of the shell-pattern construction is still not uniform and cannot be simply represented by the measured temperature at the center of the webbed structure. A longer duration will be needed in future experiments, or a transient heat transfer model needs to be developed.

## 6. CONCLUSION

The mechanisms of shell cracking and internal web structure collapse are clarified by the described numerical and experimental study of investment casting with internally webbed stereolithography pattern. Finite element analysis shows that the shell cracking and web link buckling temperatures are functions of the pattern geometry (including the cross-sectional dimensions and the span length of the web link) and the shell thickness. The pattern with a longer web span and a smaller moment of inertia buckles more readily under the influence of heat. The experimental observations agree fairly well with the numerical predictions both qualitatively and quantitatively. Thus the shell cracking can be prevented by the buckling of epoxy webbed pattern in early stages of the burnout process. Simulation of the burnout process and evaluation of a new internal web structure design can be made by the described approach.

## ACKNOWLEDGMENT

This work was partially supported by the Multi-lifecycle Engineering Research Center at New Jersey Institute of Technology and by the National Science Foundation. The coating of ceramic on the test parts was done with the help of Michael Maguire at Sandia National Laboratories. We are also thankful to the Center for Manufacturing Systems and Center for Environmental Engineering and Science at New Jersey Institute of Technology for their help and cooperation.

## REFERENCES

1. Kalpakjian, S. *Manufacturing Processes for Engineering Materials*, Chapter 5, 1991.
2. Conley, J. G., and Marcus, H. L., "Rapid Prototyping and Solid Free Form Fabrication," *Journal of Manufacturing Science and Engineering, ASME*, 1997, Vol. 119, pp 811 - 816.
3. Koch, M., "Rapid Prototyping & Casting," *3rd European Conference on Rapid Prototyping & Manufacturing*, 1994.
4. Sachs, E., et al., "Micro-Constructive Manufacturing by 3D Printing," *Proc. Of the 1994 NSF Design and Manufacturing Grantees Conference*, Cambridge, MA, 1994.
5. Blake, P., Baumgardner, O., Haburay, L., and Jacobs, P., "Creating Complex Precision Metal Parts Using QuickCast," *Proceedings of SME Conference on Rapid Prototyping & Manufacturing*, April, 1994.
6. Jacobs, P., *Rapid Prototyping and Manufacturing Fundamentals of Stereolithography*, SME, Dearborn, MI, 1992.
7. Jacobs, P., "QuickCast 1.1 & Rapid Tooling," *NASUG 1995 Annual Meeting and Conference*, Tampa, FL, 1995.
8. Hague, R., and Dickens, P. M., "Stresses created in ceramic shells using QuickCast models," *First National Conference on Rapid Prototyping and Tooling Research*, Buckinghamshire College, UK, 1995, pp. 89-100.
9. Hague, R., and Dickens, P. M., "Requirements for the successful autoclaving of stereolithography models in the investment casting process," *Second National Conference on Rapid Prototyping and Tooling Research*, Buckinghamshire College, UK, 1996, pp. 77-92.
10. Pang, T. H., "Advances in Stereolithography Photopolymer Systems," *Stereolithography and other RP&M Technologies*, SME Dearborn, MI, July 1996, Chapter 2.
11. Wang, C. T., *Applied Elasticity*, McGraw-Hill, New York, 1953, Chapter 9, pp. 209-239.
12. Yao, W. L., Wong, H., Leu, M. C., and Sebastian, D. H., "An Analytic Study of Investment Casting with Webbed Epoxy Patterns," *Proceedings of ASME 1996 Winter Annual Conference and Rapid Response Manufacturing (RRM) Symposium*, Atlanta, GA, 1996, MED-Vol. 4, pp. 11-15.
13. Sandia National Laboratories, *Properties of Investment Ceramic*, 1995.

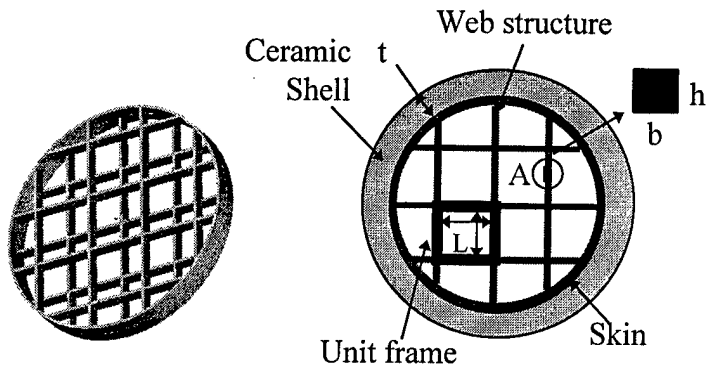


**Figure 1** Typical offset layers of web structure in SL quasi-hollow pattern.

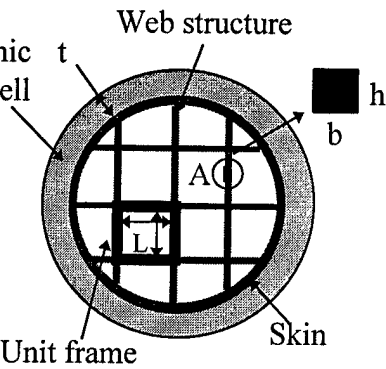


**Figure 2** Internally webbed SL pattern with ceramic shell.

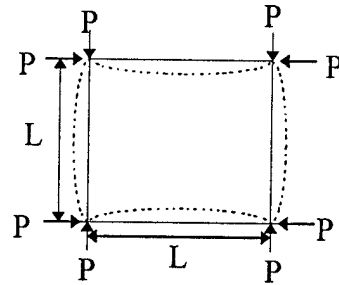


**Figure 3** The buckling of square frame under compressive loads.

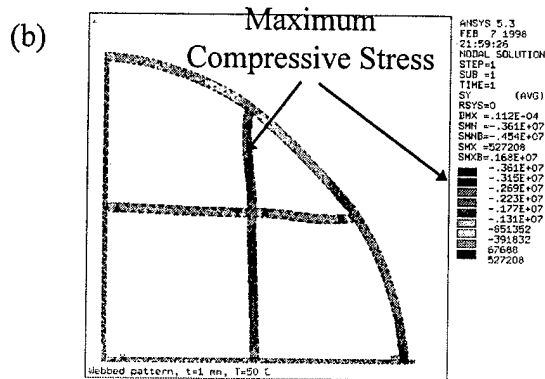
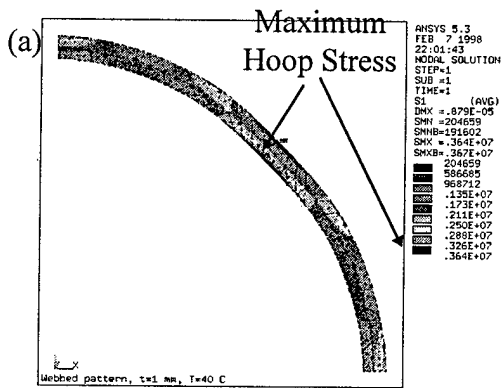


**Figure 4** The stress profile from the FEA result for Part1 with 1mm ceramic shell: (a) hoop stress in ceramic shell and (b) compressive stress in webbed pattern.

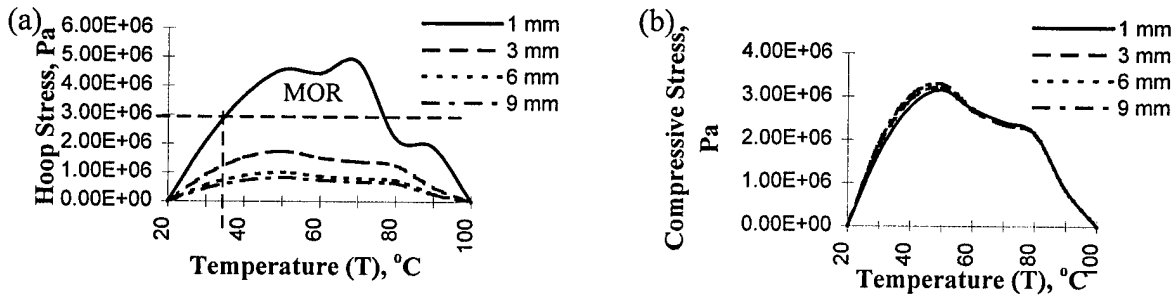


**Figure 5** Stresses varied with temperature for different shell thickness: (a) maximum hoop stress in the ceramic shell and (b) maximum compressive stress in the webbed pattern.

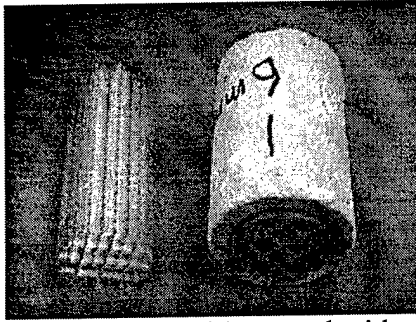


Figure 6 SL pattern without and with ceramic shell.

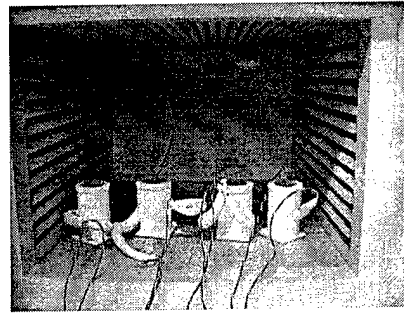
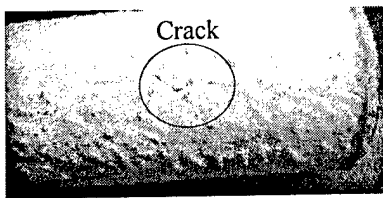
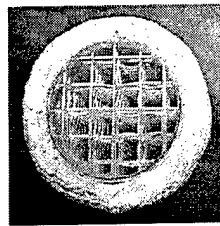


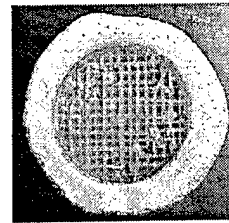
Figure 7 Samples mounted with strain gauges in a temperature controlled oven.



(a)



(b)



(c)

Figure 8 Several observed phenomena of the pattern burnout process: (a) shell cracked, (b) web links bend severely, and (c) web link do not bend.

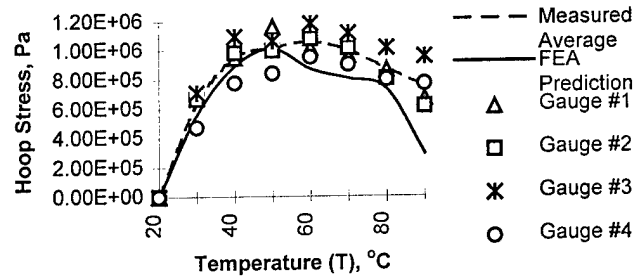


Figure 9 Comparison of measured and prediction hoop stress at the shell-pattern interface.

Table 1 Comparison of analytical values of  $\sigma_c$  and  $\sigma_x$  with MOR and  $P_{cr}$ , respectively, to determine  $T_u \approx 40^\circ\text{C}$  and  $T_b \approx 50^\circ\text{C}$ .

T (°C)	$\sigma_c$ (Pa)	$\sigma_x$ (Pa)	$P_{cr}$ (Pa)
30	$2.07 \times 10^6$	$1.69 \times 10^6$	$6.30 \times 10^6$
40	$3.64 \times 10^6$	$2.76 \times 10^6$	$5.20 \times 10^6$
50	$4.55 \times 10^6$	$3.15 \times 10^6$	$3.24 \times 10^6$
60	$4.43 \times 10^6$	$2.71 \times 10^6$	$0.28 \times 10^6$

# 2-D Wavelet Analysis of Solid Objects: Applications in Layered Manufacturing

Mark D. Van Rosendaal, Peter Chamberlain, Charles L. Thomas  
University of Utah

## ABSTRACT

In this paper, we introduce two-dimensional discrete wavelet basis functions and their application in the analysis and modeling of surface topography in layered manufacturing objects. In previous work, a one dimensional wavelet transform technique was developed to generate variable thickness layers. [1] For vertical edge layers Haar wavelet decomposition is used in the slicing direction but is not useful in the slicing plane. For frequency analysis within the slicing plane, biorthogonal wavelets provide the desired analysis ability. When analyzing layered manufacturing with ruled edges a true 2-D transform is appropriate. Two-dimensional wavelet analysis simultaneously controls the layer thickness as well as the density of control points required in the surface definition of each layer edge.

## INTRODUCTION

### 1) What is frequency analysis in layered manufacturing?

It is possible to analyze a 3-D solid object in terms of its spatial frequency content. Using spatial frequency analysis, regions of high complexity appear as high frequencies and flat or gently curved regions appear as low frequencies. Wavelet analysis allows spatially resolved frequency analysis, where the location of the high or low frequencies is identified. By operating on the wavelet representation of an object with custom frequency filters, it is possible to simulate the results of various layered manufacturing processes. [2]

### 2) Why do we want a frequency analysis technique?

- Simulate the results of layered manufacturing
  - Haar wavelet for vertical edges
  - biorthogonal wavelet for ruled edges
- Control variable layer thickness generation
- Identify appropriate slice direction
- Potential file size reduction

## WAVELETS

A wavelet transform (WT) decomposes a function into a summation of scaled and translated basis functions called wavelets. [3] An inverse wavelet transform (IWT) sums the basis functions

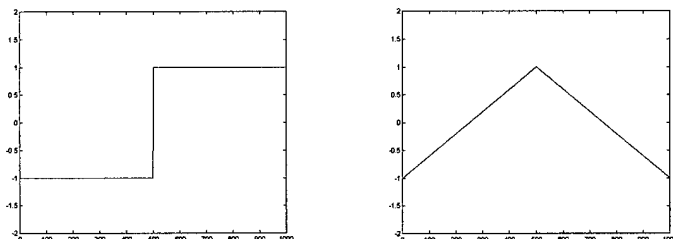


Figure 1. a) Haar wavelet b) biorthogonal wavelet

back together to form the original signal. The wavelets must satisfy certain criteria in order to be valid basis functions. Among these criteria, wavelets must be oscillatory and decay quickly to zero. [4] Two wavelets that have been found useful in layered manufacturing are the Haar wavelet [5] and the biorthogonal wavelet shown in Fig. 1.

Discrete wavelet analysis (DWT, IDWT) assumes that a signal  $f(x)$  has been sampled at equally spaced intervals. The sequence length  $N$  of the signal being analyzed determines how many wavelet levels can be represented. [6] When  $N=2^n$  there are  $n + 1$  wavelet levels. The levels represent different frequencies in the signal. Fig. 2 demonstrates frequency decomposition of a signal into wavelet levels. Level  $a_{10}$  is the lowest frequency level and  $a_1$  is the highest frequency level.

### PROPOSED PROCESS OVERVIEW

The proposed process of analyzing solid objects for frequency content is outlined in Fig. 4. From an STL file, in the cartesian coordinate

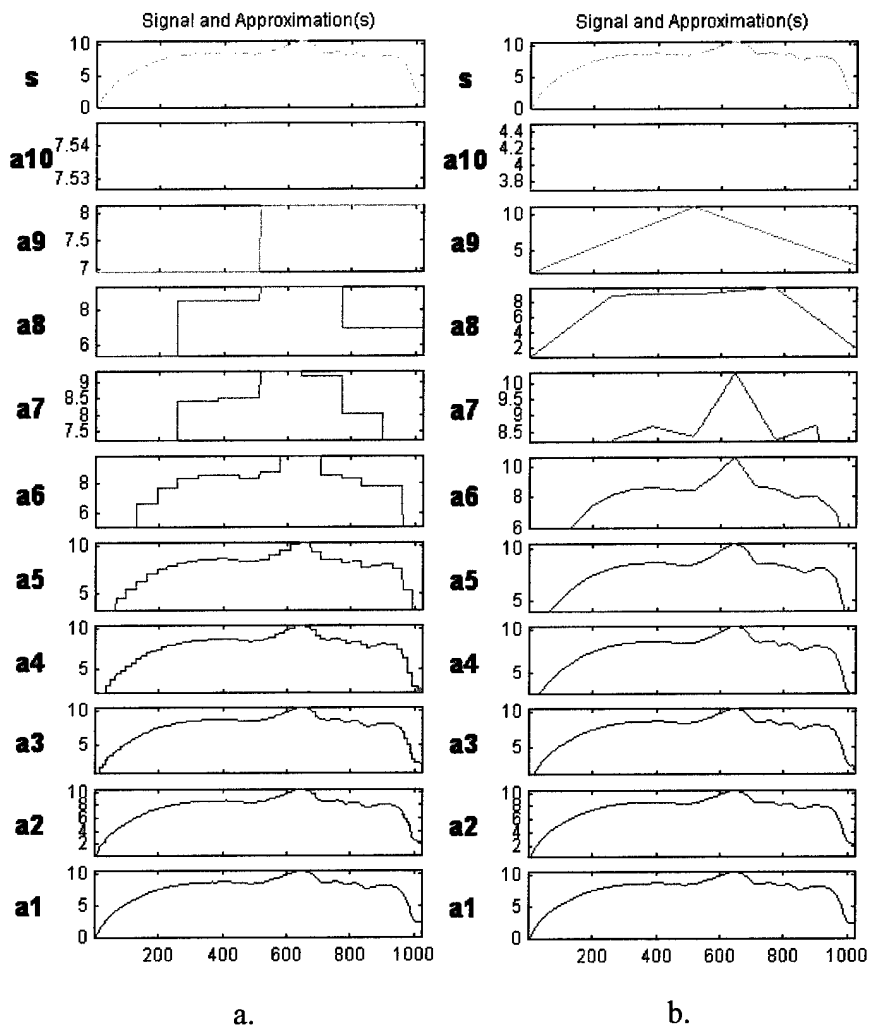


Figure 2. Frequency decomposition of the object. a) Using Haar, b) using biorthogonal wavelets.

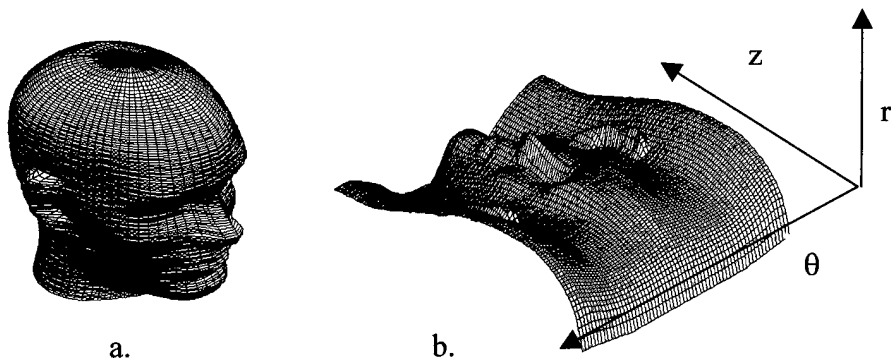


Figure 3. Unwrapping of the object. a) cartesian representation, b) cylindrical presentation.

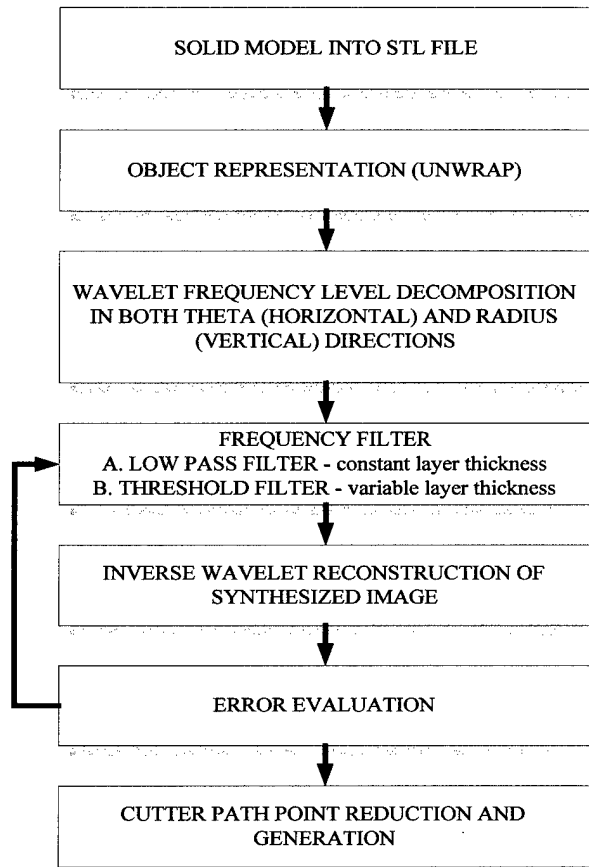


Figure 4. An overview of the 2-D wavelet analysis procedure.

## FILTERING

Two types of filters, low pass and threshold, have been examined for application in layered manufacturing.

### Low Pass Filter

Here, all wavelet coefficients above a specified frequency level are removed. After inverse transforming, the model contains no frequency components above the cutoff. The resulting model looks as if it were produced by a constant layer thickness LM technique. Fig. 5b. shows these results.

### Threshold Filter

Here, all wavelet coefficients below a specified threshold value are removed. The resulting model looks as if it were constructed from variable thickness layers. Fig. 5c. shows this result. Because of the ability to independently vary the filtering of each frequency level, remove wavelet coefficients above a specified frequency level, or perform global filtering of all frequency levels, thousands of possible filter combinations can be constructed.

system, 3-D solid objects are sampled at equally spaced intervals in determined sequence lengths  $N$ . The object is unwrapped by converting sampled data into cylindrical coordinate representations. Changes in the part radius ( $r$ ) can therefore be analyzed in two dimensions: vertical ( $z$ ) and horizontal ( $\theta$ ). Fig. 3 shows how the part is unwrapped. [1] The discrete wavelet transform is extended to two dimensions, which are decomposed and filtered simultaneously. Decisions regarding the type of wavelet basis function and the type of filter are made. After filtering, an inverse discrete wavelet transform is then used to reconstruct the object. From the resulting reconstruction, error is evaluated.

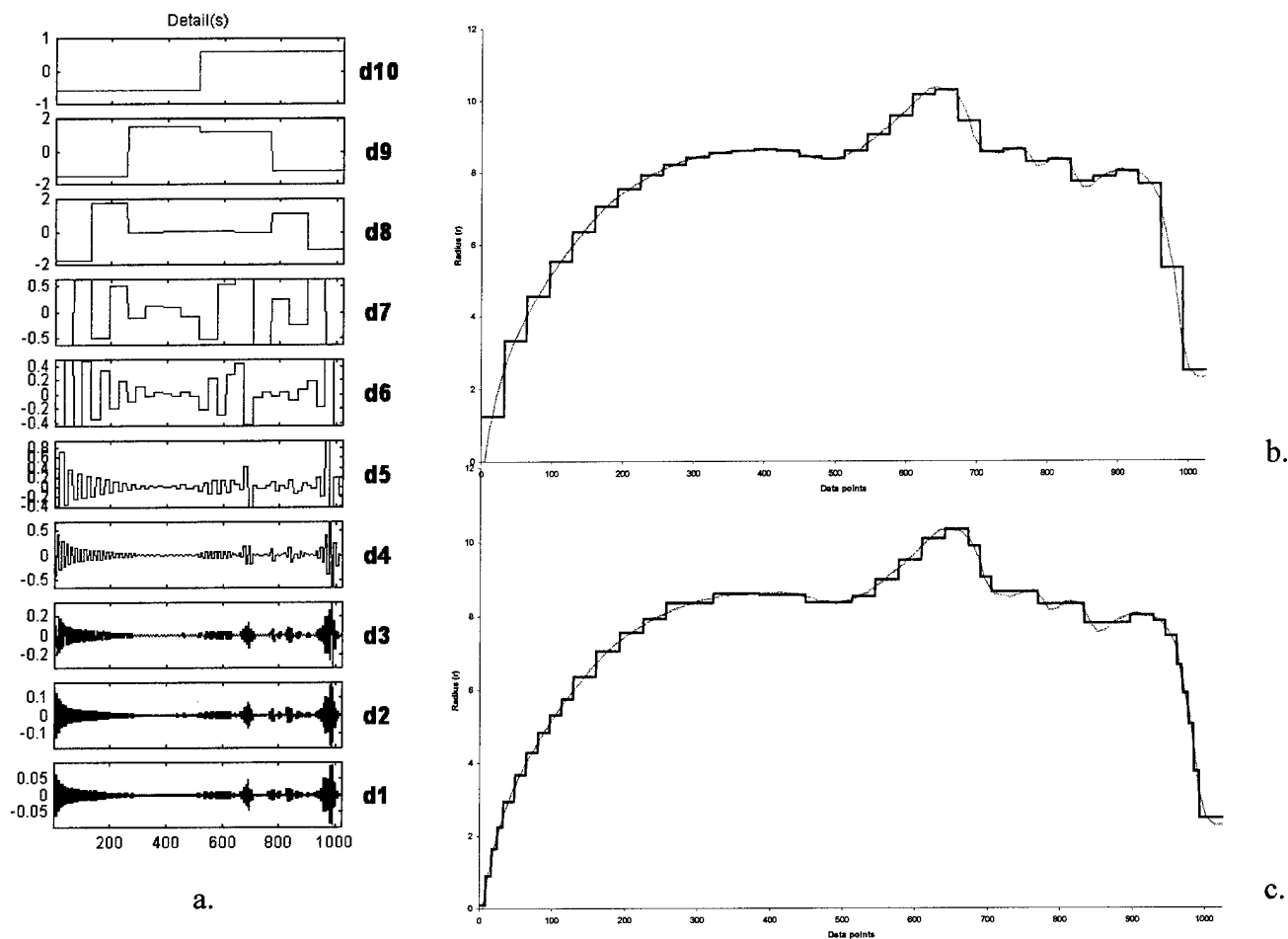


Figure 5. a) This figure shows the Haar wavelet frequency coefficients for a single slice of the head. All ten wavelet levels are shown. Level d1 is the highest frequency. b) Results from low pass filtering, yielding uniform slice thickness. c) Results from threshold filtering, yielding adaptive slice thickness. Filtering was intentionally set high to better illustrate the results.

### POINT REDUCTION

When the original model is put into cylindrical format, the file consists of regularly spaced points as shown in Fig. 6a. Threshold filtering forces the points into straight lines, but the total number of points in the file remains constant. Deleting redundant points along each line segment reduces both point density and file size.

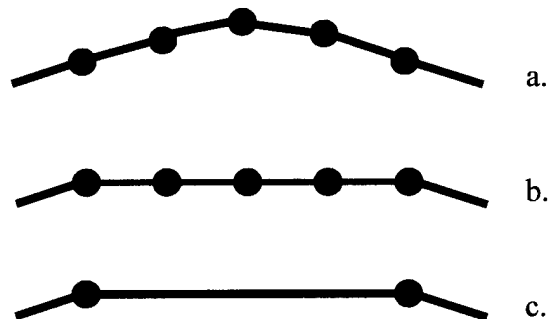


Figure 6. a) Point density prior to wavelet filtering. b) After wavelet filtering. c) After point reduction.

## VERTICAL DIRECTION (z) RESULTS

The ability to analyze the object in the vertical direction enables the operator to generate variable thickness layers. In Figures 7 and 8, below, a single contour in the slicing direction was analyzed.

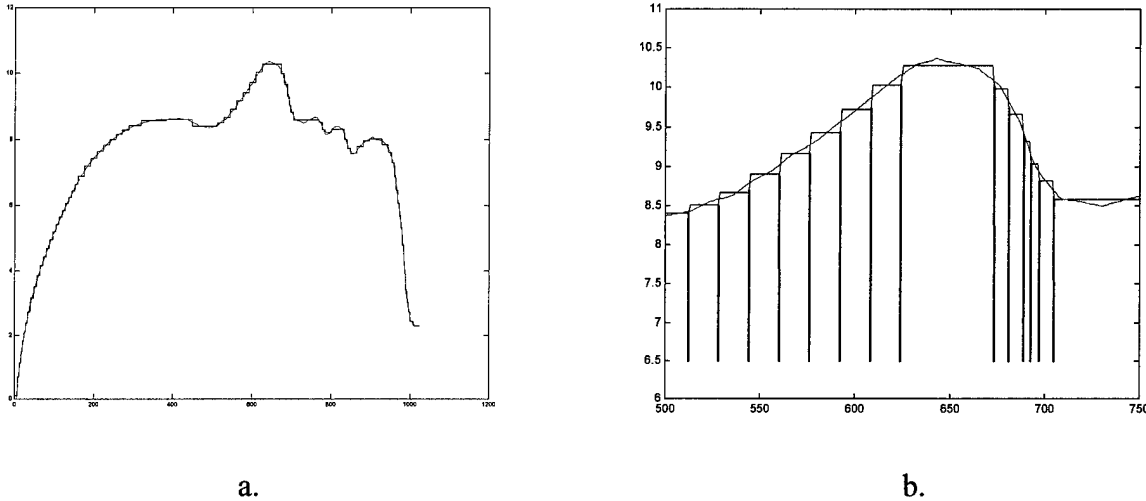


Figure 7. a) Vertical slice (side view of front portion of the head) after wavelet filtering. Filtering was intentionally set high to better illustrate the results. b) Close up view of the nose. Notice the variable layer thickness. Gray represents the original contour; black represents the contour after processing. The Haar WT is ideal for vertical edge layered manufacturing. In this example the head was reconstructed from 76 variable thickness layers.

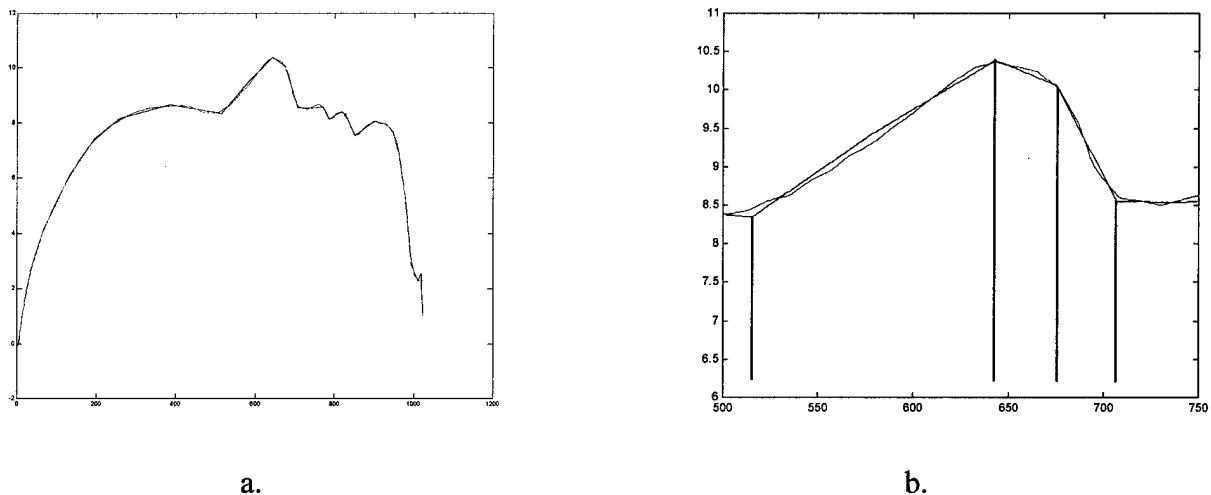


Figure 8. a) Vertical slice (side view of front portion of the head) after wavelet filtering. Filtering was intentionally set high to better illustrate the results. b) Close up view of the nose. Notice the variable layer thickness. Gray represents the original contour; black represents the contour after processing. The biorthogonal WT is ideal for ruled edge layered manufacturing. In this example the head was reconstructed from 40 variable thickness layers.

## HORIZONTAL ( $\theta$ ) DIRECTION RESULTS

The ability to analyze the object in the  $\theta$  direction enables the operator to filter unwanted information (high frequency steps) in the cutter path.

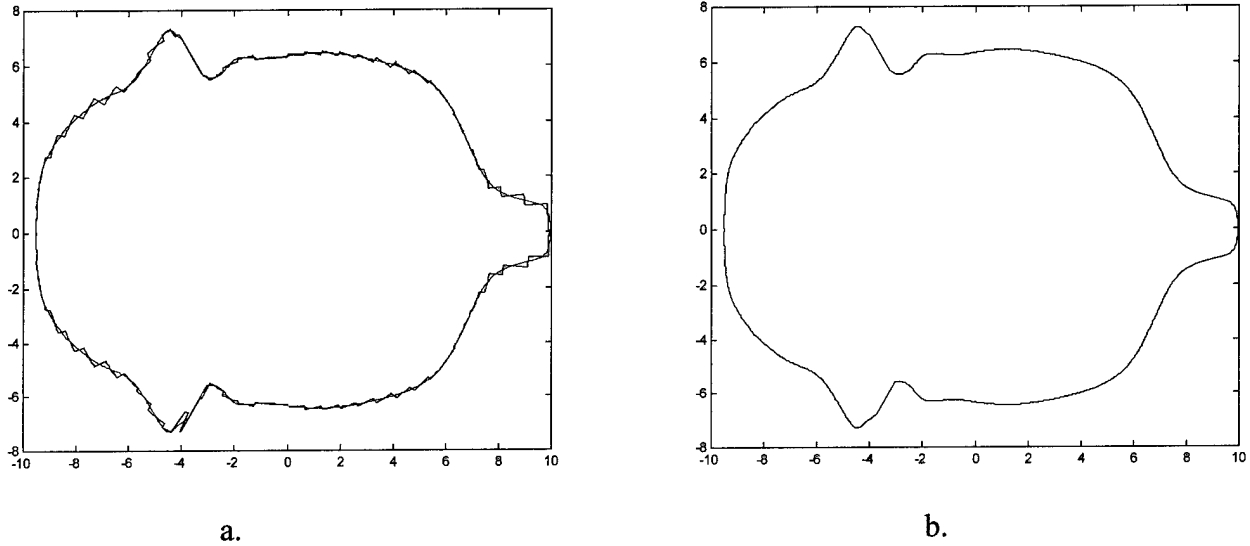


Figure 9. Original slice, gray (1024 points), slice after processing using filtered Haar wavelets and point reduction scheme, black. a) 784 points. b) 1020 points.

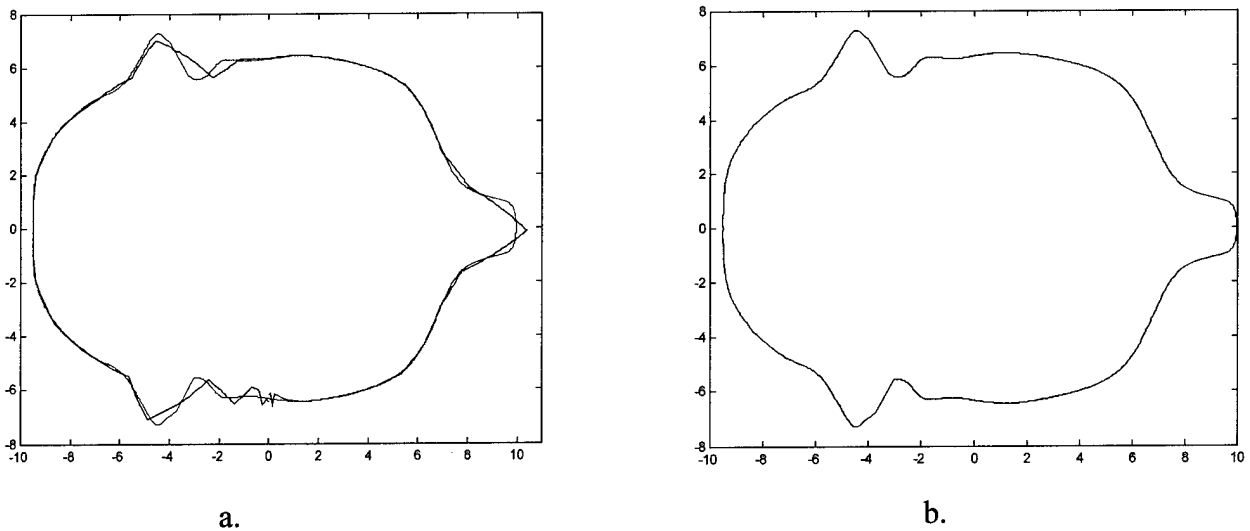


Figure 10. Original slice, gray (1024 points), slice after processing using threshold biorthogonal wavelets and point reduction scheme, black. a) 560 points. b) 630 points.

The above figures (Fig. 9,10) show how wavelet filtering provides a reduction in the number of control points defining the layer edge while preserving an accurate edge

representation. Figures 9 and 10 demonstrate the advantage of using the biorthogonal wavelet over the Haar in the theta direction. Using Haar, 1020 points were required to reproduce the original slice geometry while only 630 points were required using the biorthogonal wavelet. Based on the results shown, we anticipate this analysis will simplify and smooth the cutter path definition file.

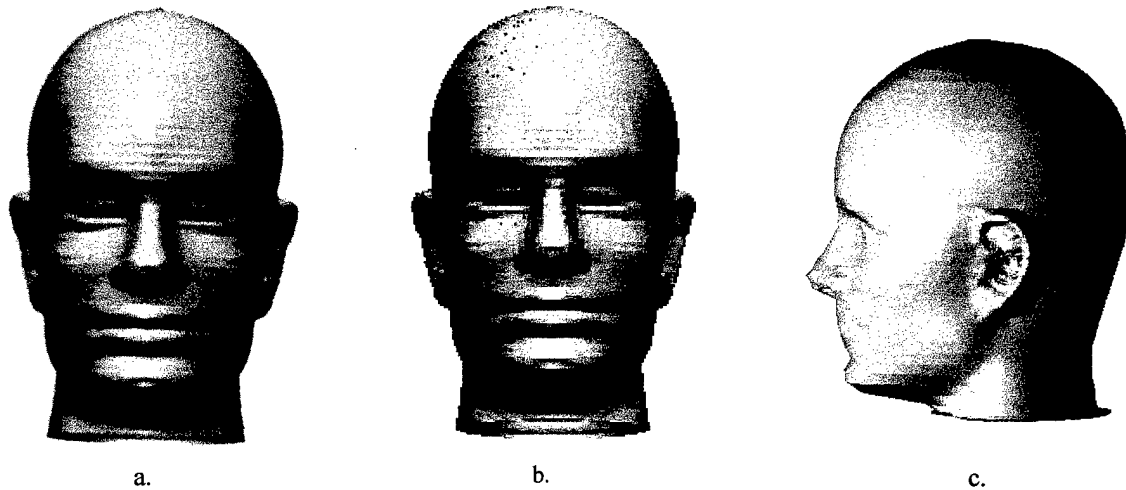


Figure 11. a) Original 3-D object. b) Predicted head after 2-D WT filtering and IDWT (low resolution in theta direction). c) Predicted head after 2-D WT filtering and IDWT (low resolution in the stacking direction).

Fig. 11 shows the original head and the reconstructed head after unwrapping, biorthogonal wavelet transform decomposition, threshold filtering, inverse transforming, and re-wrapping. Fig. 11 (a) is the original STL file. It is assumed that the apparent layering effect is an artifact produced when the head was scanned. In Fig. 11 (b) the filters were set for fine resolution in the layering direction ( $z$ ) and low resolution around the circumference direction ( $\theta$ ). Note that there is no apparent change in resolution in the  $z$  direction. The nose is broadened and the definition around the ears is poor due to the more aggressive filter in the  $\theta$  direction. In Fig. 11 (c) the filters were set for low resolution in the layering direction ( $z$ ) and fine resolution around the circumference direction ( $\theta$ ). Now thicker layers are apparent in the  $z$  direction. As expected, the low resolution filtering greatly affected the accuracy of the part causing the lips to be completely removed.

## LIMITATIONS

There are two primary limitations for the process outlined in this paper. 1) Currently, this technique works only for single-value functions. Decomposing complex geometry into simple sub-parts prior to processing can eliminate this limitation. 2) The sequence length  $N$  is chosen so that  $f(x)$  is a desirable representation of the original data. For simple, low-resolution parts, a lower value of  $N$  (say, 128) is adequate. For higher resolution parts, a larger  $N$  (say, 1024) is recommended. Although a larger value of  $N$  gives a better approximation, the value of this integer is limited by the physical constraints of the decomposition software or by the desire to perform computations effectively and efficiently. [5]

## CONCLUSIONS

The 2-D wavelet transform is a useful tool for mathematical analysis of the spatial frequency content of three-dimensional objects. This analysis enables the prediction of appropriate layer thickness as well as reducing the cutter path point load for layered manufacturing processes. In order to perform wavelet analysis, 3-D objects are decomposed (unwrapped) into a cylindrical coordinate representation. This single valued representation is then wavelet transformed, filtered, and inverse transformed. The choice of filter (low-pass or threshold) is motivated by the application. Uniform layer thickness part decomposition is created using low-pass filtering. Threshold filtering produces adaptively sliced representations.

As expected, there is a direct relationship between filtering and error. Under-sampling and over-filtering were the most common sources of error. The Haar wavelet is useful for analyzing vertical edge layered manufacturing while the biorthogonal wavelet proved useful for ruled edges. In addition, the 2-D wavelet representation of the part is quite compact and may be useful for file compression.

## FUTURE WORK

Several areas have been identified for further work. These areas include techniques for error quantification and filter optimization. These techniques will allow user input of maximum error desired in both directions and will adjust the frequency filtering accordingly. Future work includes the development of more sophisticated software tools for analyzing, decomposing, and filtering stereolithography files and the creation of cutter paths. Future software will automate the process outlined in this paper.

## REFERENCES

1. Lee, C. H., "New Analysis methods for Three-Dimensional Objects in Solid Freeform Manufacturing." Ph.D. dissertation, University of Utah Dept. of Mechanical Engineering, 1997.
2. Lee, C. H., Thomas, C.L., "Wavelet transform based analysis for layered manufacturing", *Proceedings of the Seventh international Conference on Rapid Prototyping*, 3/31-4/3, 1997.
3. Akansu, A. N., Smith, M.J.T, *Subband and Wavelet Transforms, Design and Applications*. Kluwer Academic Publishers, 1996, 55-82.
4. Young, R. K., *Wavelet Theory and its Applications*. Kluwer Academic Publishers, 1993, 1-15.
5. Chui, C.K, *Wavelets: A Mathematical Tool for Signal Analysis*, Society for Industrial and Applied Mathematics, 1997, 1-17.
6. Newland, D. E., *Introduction to Random Vibrations, Spectral and Wavelet Analysis*. Longman Scientific & technical, England, 1993.

## STRENGTH OF THE DTM RAPIDSTEEL 1.0 MATERIAL

T D STEWART, K W DALGARNO, T H C CHILDS, J PERKINS

*The School of Mechanical Engineering, The University of Leeds, Leeds LS2 9JT UK*

### ABSTRACT

This paper reports the results of a study into the strength of the DTM RapidSteel 1.0 material. Elastic modulus and strength of the metal/copper composite material was investigated as a function of the distance from the point of copper infiltration, the furnace cycle duration, and the furnace type. The microstructure of the RapidSteel material was also examined in an attempt to understand the science behind the infiltration process. The results have implications for the design of tools to be made using the RapidTool process in situations where the tool will be used as a production tool, rather than a prototype tool.

### INTRODUCTION

Rapid prototyping has evolved over the past five years from the ability to produce polymer models for visualisation of a single prototype part to the ability to manufacture Rapidtooling from metals or ceramics for the manufacture of hundreds or thousands of parts. There are several different processes available for Rapidtooling each with it's own specialised materials which are a complex mixture of polymer binders, structural metal powder and some form of infiltrant. This paper considers one type of Rapidtooling produced by the DTM Corporation in Austin comprised of a steel/copper composite called RapidSteel 1.0.

RapidSteel is produced in a three stage process. Initially a green part is sintered from polymer coated steel powder using conventional selective laser sintering technology. The fragile green part is then placed in a bath of polymer resin and then dried providing additional support for handling and binding for the steel powder. Finally the part is placed in a furnace where the polymer is burned away leaving the steel powder which is lightly sintered into a weak porous skeleton defining the shape of the part. This structure is then infiltrated with molten copper which is absorbed from the base of the part by a wicking action which draws the copper through the porous matrix resulting ideally in a fully dense composite. The process of the copper infiltration into the steel matrix is referred to as Liquid Phase Sintering, and is most commonly experienced in powder metallurgy. German (1) described the time dependant nature of the infiltration process in which in powder metallurgy of steel/copper composites can require in excess of 10 hours at 1150 °C for fully dense parts to be produced.

Many studies have been completed on the variation in properties of materials produced by selective laser sintering (2,3,4) considering the effects of parameters such as energy density and laser orientation. The additional furnace infiltration required for the manufacture of RapidSteel adds a further source of this variation. Two furnace types are recommended by DTM for the processing of RapidSteel. The Carbolite furnace (Carbolite Furnaces Limited, Aston Lane, Hope, Sheffield S30 2RR) is a bottom loading hearth furnace with a sand seal, while the Lindberg furnace (304 Hart Street, Watertown, WI 53094) is a front loading furnace with a liquid

cooled seal. The possibility of variable environments and temperature profiles produced from each furnace combined with the pressures to decrease cycle times was proposed as a possible source of anisotropy in material properties, hence this study was undertaken.

### EXPERIMENTAL PROTOCOL

Cubic test blocks 80 millimetres in size were manufactured from RapidSteel 1.0 both at Leeds University and at DTM Germany (DTM GmbH, Otto-Hahn-Straße 6 40721 Hilden, Germany), the size chosen to represent the thickest cross section expected in a tool. Green parts were manufactured using the DTM default settings which include a laser power of 30 watts, a scan speed of 1550 mm/s and a layer thickness of 0.1 mm. The infiltration process was completed using a Carbolite furnace at Leeds and a Lindberg furnace at DTM Germany. The different furnace cycles investigated are shown in Figure 1. The part temperature generally followed quite closely to the specified temperature as shown for the 24 hour cycle by “Part @24 hour” and “24 hour” curves respectively.

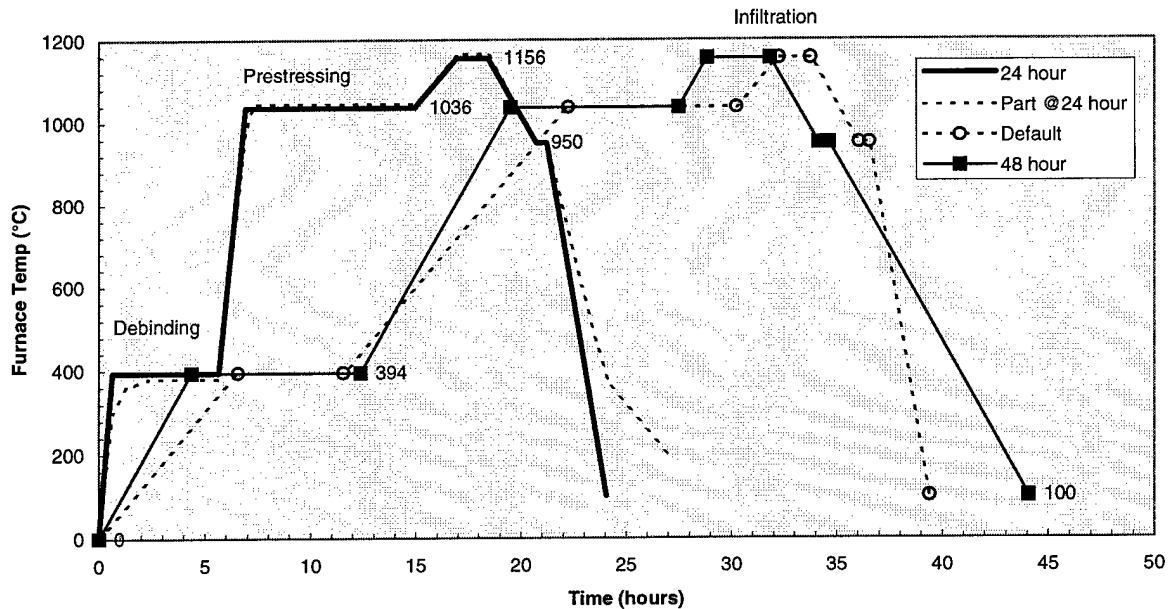


Figure 1. Variable Furnace Cycles

Each block was cut into sixteen 20 x 20 x 80 millimetre slices cut either horizontally or vertically which were then machined into tensile specimens. Strain gages were also mounted onto various specimens to obtain an accurate representation of the Young's Modulus. Tensile testing was conducted using a Dartec Universal Testing Machine (Dartec, Stourbridge, West Midlands, DY9 8SH, UK) at a fixed crosshead speed of 0.05 mm/sec. Crosshead position, load, and strain were recorded. Material samples from the fractured specimens were further evaluated under a microscope. Copper nitrate was used to etch samples for further analysis of grain boundaries. A typical test block for horizontal samples is shown in Figure 2 before machining. The copper was infiltrated at the base of the block along the length of sample A1. For vertical specimens the copper was infiltrated from the base of samples A1, B1, C1 and D1.

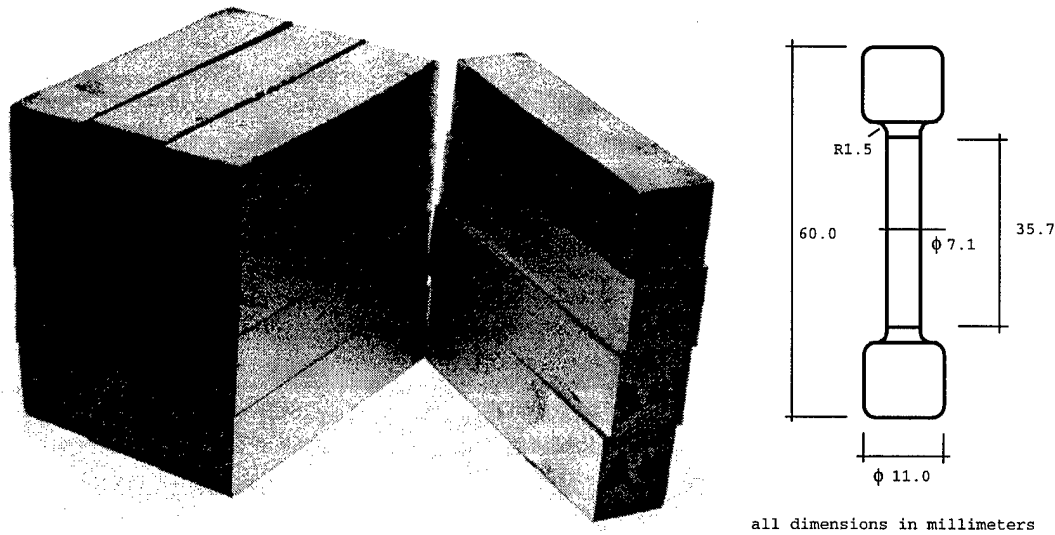


Figure 2. 80mm cubic RapidSteel block cut into horizontal sections for machining into tensile specimens.

### RESULTS AND DISCUSSION

Typical stress Vs strain variations within a single block manufactured at Leeds using the DTM default furnace cycle are shown in Figure 3. Samples were cut horizontally, A1 is closest to the copper infiltration point while sample D4 is the farthest away. The Figure shows the fracture load for all of the samples as a function of the horizontal and vertical distance the sample was taken from the point of copper infiltration (A1).

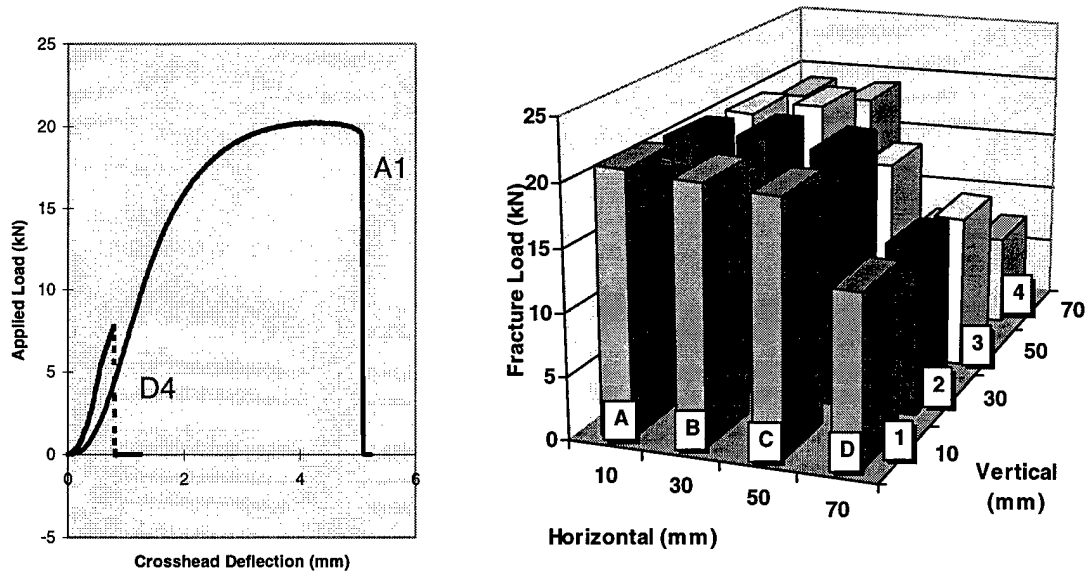


Figure 3. Variation in material properties of a Leeds sample cut horizontally.

A pattern of degradation appears to be present with strength decreasing with distance from the point of copper infiltration in both the vertical and horizontal directions. The yield strength of

the RapidSteel material varied from 100 to 500 Mpa, with the elastic modulus remaining relatively constant at 210 GPa.

When comparing the Leeds results to those taken from identical samples manufactured in Germany with the default furnace cycle a similar pattern is observed as shown in Figure 4. In this case samples were cut vertically and the Figure shows the fracture load as a function of horizontal distance from the copper infiltration which is essentially the same for all samples A to D.

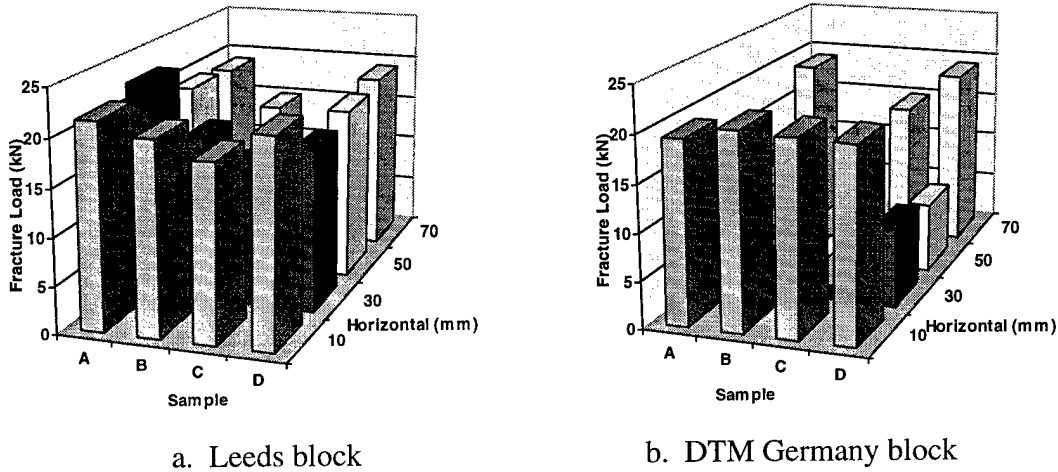


Figure 4. Variation in Material Properties from Leeds and DTM Germany both cut vertically.

The majority of specimens which were taken vertically generally fractured at the top of the block and a similar trend of decreasing fracture load was observed with distance from the point of copper infiltration. Internal horizontal cracking was observed within the block manufactured by DTM Germany which limited the number of samples tested.

The variation in fracture load with furnace cycle duration is shown in Figure 5. Both blocks were manufactured at Leeds and cut horizontally.

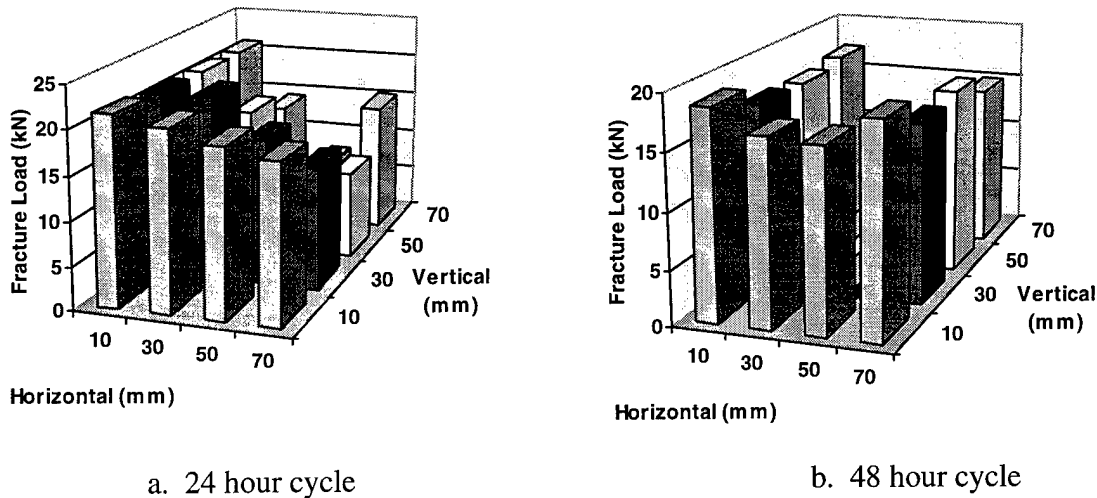


Figure 5. Variation in Material Properties as a function of cycle time.

The observed degradation in strength appears to be more prevalent with the shorter 24 hour furnace cycle than the 48 hour furnace cycle. Internal horizontal cracking was also observed, in this case in the block manufactured at Leeds with the 48 hour furnace cycle, limiting the number of samples tested. Cracking has only been observed in parts with thicknesses in excess of 60mm, and is, therefore, believed to be the result of incomplete drying or internal stresses developed during processing. As yet a systematic method has not been developed to avoid this effect .

A further visual inspection of the fracture surfaces was also completed. Figure 6 shows the side view of the block previously shown in Figure 2 and 3 manufactured at Leeds with the default furnace cycle.

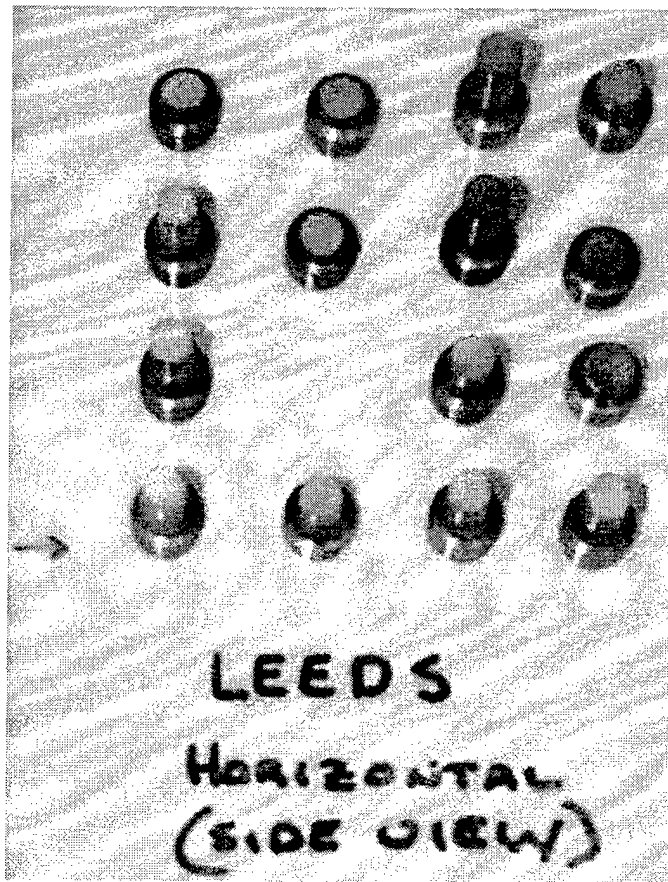


Figure 6. Visual inspection of fracture surfaces.

It can be clearly seen by visual inspection alone that with the default furnace cycle samples further away from the point of copper infiltration (marked as an arrow) are darker and have more porosity. The amount of porosity seen is also directly related to cycle time as the longer 48 hour cycle is noticeably less porous, and the shorter 24 hour cycle is more porous.

Analysis of the RapidSteel material under a microscope reveals spherical metal particles ranging from 10 to 60  $\mu\text{m}$  in diameter located within the copper. Further detailed etching with Ferric Chloride will reveal the large copper grains approximately 200  $\mu\text{m}$  in size. Other analysis

techniques such as scanning electron microscopy (SEM) shown in Figure 7 will continue to be used in attempts to better understand the science behind the infiltration process.

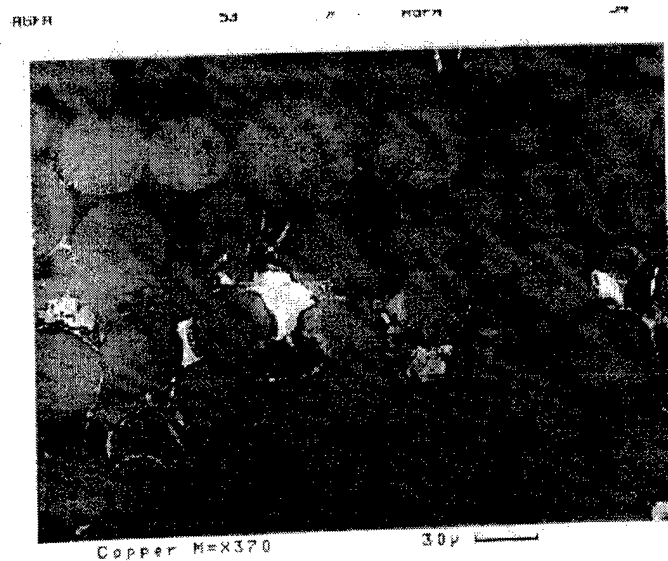


Figure 7. SEM of sample showing porosity.

#### CONCLUSIONS

The infiltration of copper into the DTM RapidSteel 1.0 material appears to have a time dependant nature to the process. The DTM default sintering time of 1.5 hours at 1156° C is for a typical 6 inch square block with a 2 inch thickness (5). Parts in excess of 2 inches thick may, therefore, need special attention with increased infiltration times to allow the wicking of the copper into the porous metal skeleton to complete naturally.

No significant variation in material properties was observed between samples manufactured in Leeds with the Carbolite furnace and those manufactured in Germany with the Lindberg furnace, as the fully infiltrated material was equally as strong and both displayed general decreases in strength with distance from copper infiltration. The fully infiltrated RapidSteel material was found to have a yield strength of 500 MPa and an Elastic Modulus of 210 GPa.

The nature of a rapid process for the manufacture of tooling may introduce pressures to increase the speed of the processing cycle. The furnace cycle which takes up a significant portion of the manufacturing time is, therefore, likely to be optimised by companies to the shortest possible time. Tooling may appear identical with faster cycle times as low as 12 hours, however, the resultant porosity within the material can significantly weaken the structure below 25% of its original strength. For prototype tooling this may be an acceptable risk, however, for long term success in a production environment the time dependent nature of the copper infiltration process should be considered.

#### ACKNOWLEDGEMENTS

This work was supported by the UK Engineering and Physical Sciences Research Council in conjunction with Hasbro Europe, McKechnie Plastic Components and Simpson Industries. The authors would like to thank DTM GmbH for their assistance in supplying samples, and the School of Material Science at the University of Leeds for assisting in the analysis.

#### REFERENCES

1. German R M (1985). *Liquid Phase Sintering*. Plenum Press, New York, pp102.
2. Childs T H C, Ryder G R, Berzins M (1997). Experimental and theoretical studies of selective laser sintering. *Proceedings of the 8th International Conference on Production Engineering*, Saporro, Japan, pp 132-141. Chapman and Hall, London.
3. Badrinarayan B, Barlow J W (1995). Effect of processing parameters in SLS of metal-polymer powders. *Proceedings of the Solid Freeform Fabrication Symposium*. The University of Texas at Austin, pp 55-63.
4. Subramanian P K, Vail N K, Barlow J W, Marcus H L (1996). Anisotropy in Alumina produced by SLS. *Proceedings of the Solid Freeform Fabrication Symposium*. The University of Texas at Austin, pp 330-338.
5. DTM Corporation (1996). *The RapidTool LR Process Using RapidSteel (LM-6000)*. DCN: 8001-10004, September.



## **Direct Injection Molding Tooling Inserts from the SLS Process with Copper Polyamide**

Christian Nelson, Jason Kepler, Rick Booth, Phillip Conner  
DTM Corporation, Austin, TX

The "RapidTool" Short Run (SR) Tooling Process using the Copper Polyamide material provides a route to mold inserts for injection molding made directly in the Selective Laser Sintering machine. The STL files for the mold inserts are shelled and conformal cooling lines and ejector pin guides are added before SLS processing. Sintering of the material in the SLS machine provides quick metal/plastic tooling with good thermal conductivity. Final preparation of the tooling inserts includes sealing the surface with epoxy, final finishing using sandpaper, and backing up the shells with a metal alloy. The Copper Polyamide SR Tooling inserts are used to mold several hundred parts with common plastics with injection cycle times similar to conventional molding cycle times.

Rapid Prototyping and Rapid Tooling continue to change how products are designed and tested. Prototyping equipment used to make plastic models for visualization ten years ago is now used to make investment casting patterns, sand casting cores and molds, patterns for secondary processes, functional prototypes, and mold inserts for injection molding.

Market acceptance of Rapid Tooling continues to grow as designers realize the benefits of molding prototype parts with the actual production material. DTM introduced RapidSteel 1.0 in 1996 for the creation of steel/copper mold inserts [1]. DTM introduced the next generation of metal material in 1998. The RapidSteel 2.0 material provides improvements in processing time, finishing time, and accuracy compared to the original RapidSteel material. 3D Keltool was introduced by 3D Systems as a secondary process to produce steel/copper inserts from a RP pattern [2]. Extrude Hone announced the ProMetal RTS-300 system for creating porous steel inserts using the three-dimensional printing (3DP) technology licensed from MIT [3]. These processes require a furnace to sinter the steel and infiltrate the porous steel part with a copper alloy. The resulting parts are fully dense and can be used to mold over 100,000 plastic parts with most plastics.

Recently, a new breed of Rapid Tooling solutions has emerged to provide short runs of production equivalent plastic parts. These limited runs of molded plastic parts are often used in the product development stage where several hundred parts in the final material are needed. The faster and more economically a manufacturer can get a supply of parts produced in actual production materials, the faster he can perform life testing, make adjustments to the design if necessary, and get the new product on the market.

Methods of creating short run mold inserts available in today's market include direct manufacture using RP, cast metal/epoxy tooling, and CNC machining. Mold inserts made directly in rapid prototyping devices include SLA epoxy, SLS metal/plastic, and SLS direct metals [4]. The metal/plastic material available for processing in the Selective Laser Sintering process is Copper Polyamide introduced in mid-1998.

The Copper Polyamide material is a heat resistant, thermally conductive composite of copper and plastic that was introduced for use with DTM's Sinterstation System. The Copper PA material processes in the Sinterstation at conditions similar to the DuraForm Polyamide material. The Sinterstation builds the mold inserts directly from the geometry described in the STL file. Features like runners, gates, conformal cooling lines, and ejector pin guides are included in the STL file and built directly into the part. Turnaround times for the production of a mold insert are as short as a day. The key is that no furnace process is involved.

The Copper PA composite makes parts that are machinable and easily finished with wet sanding. Heat resistance and thermal conductivity are better than most plastic tooling materials, and it is possible to mold parts with cycle times that approach production rates. Injection mold inserts made with this material are used to mold 100 to 400 parts in polystyrene (PS), polyethylene (PE), polypropylene (PP), glass filled polypropylene (GF PP), ABS, PC/ABS, and other common plastics.

### Mold Preparation

Injection molding incorporates a cavity into which hot plasticized material is injected under pressure. Heat is removed from the material in the mold until it is rigid enough to be ejected so that the final part will conform to all of its specifications. Both the design of the part and the design of the mold are critical in insuring the right mold. While the design of the part is not within the scope of this paper, it should nevertheless be thoroughly reviewed by those people directly involved in the design of the mold and in the molding operation [5].

Before an injection mold is built the mold design must be established. Some basic considerations for the mold include the type of gating, the thermal control system, the type of ejection, the type of venting, and anticipated shrinkage. With these items in mind, the designer defines a parting line and adds the necessary features to the mold halves.

When designing a mold for direct manufacture using SLS in the Sinterstation the cooling lines, ejector pin guides, gates, and runners can be included in the CAD design and built directly in the Sinterstation, see Figures 1 and 2. Building these features directly into the mold saves time by reducing the man-hours spent preparing the mold for injection molding.

Adding the cooling lines to the CAD file is an advantage because they can be placed near crucial mold features. The alternative to adding cooling lines to the CAD model is placing copper tubing in the back of the mold-half prior to backfilling. The copper tubing can also be placed near critical mold features. However, placing copper tubing is more difficult and time consuming than the placement of virtual cooling lines in the CAD model.

Ejector pin location plays a critical role in the success of the mold. A Copper Polyamide mold requires 30 to 40 percent more ejector pins than a standard aluminum tool. Adding more ejector pins makes part ejection easier which extends the life of the mold. When applying ejector pin holes in the CAD file, the holes should be made the size of the ejector pin. These holes are reamed

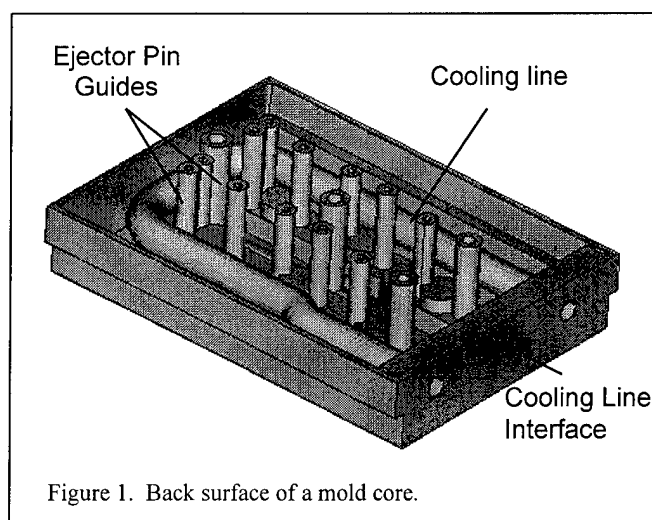


Figure 1. Back surface of a mold core.

out during the mold-finishing phase. After the shelling operation, extend the ejector pin guides beyond the back surface of the mold to prevent the holes from becoming clogged when the backfill material is added.

Runner and gate designs are important to mold life and part quality. Gates for the Copper Polyamide molds should be larger than gates on an aluminum tool. The larger gate will keep the cavity pressure down. On large molds, fan gates are recommended. On smaller molds, edge gates are used.

When the CAD design of the mold is complete, the mold half is shelled so that a backfill material can be added to aid in the conduction of heat away from the mold surface. The shelling operation is performed either in the CAD package by operating on the solid model, or in a specialized application like Materialise's Magics RP [6] which operates on the STL file. In this step, the mold is hollowed out such that the external surfaces have a wall thickness of 3.8 mm. The bottom surface is then removed to provide access to the back surface of the mold face.

If the cooling lines are added to the CAD file, the wall where the cooling lines enter/exit should be 12.5 mm thick. Since the Copper Polyamide is machinable the cooling line interface can be reamed and tapped for connecting the water source.

When using a low melting metal alloy as a backfill material, include a rib grid in the back of the mold to lock the alloy into the mold, see Figure 3. This rib grid is not necessary if a metal filled epoxy is used as the backfill material, see Figure 5.

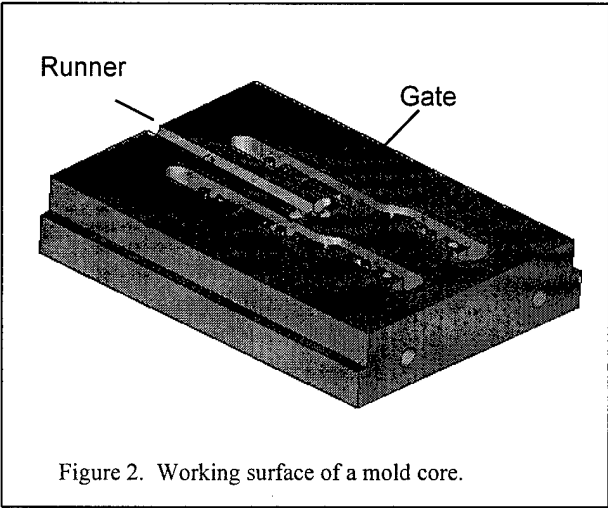


Figure 2. Working surface of a mold core.

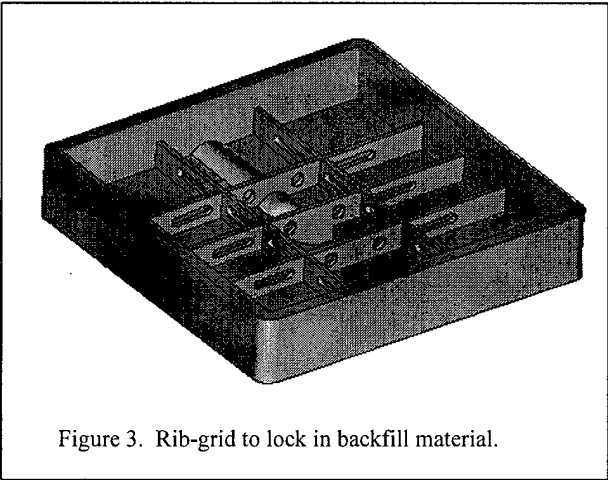


Figure 3. Rib-grid to lock in backfill material.

### SLS Processing

After the mold design is complete and a STL file is created, the part is built using the Selective Laser Sintering Process [7]. The Copper Polyamide material is processed with temperatures set points and scan parameters similar to those used to process DTM's other polyamide materials.

The STL file is oriented so that the parting line is facing up with the longest dimension parallel to the x-axis, then rotated 15 degrees around the x-axis. The purpose of angling the part is to add strength to small post features.

Sacrifice geometry is added at the top and bottom of the build to control the cooling rate. The additional layer of scanned material acts as a heat fence reducing the thermal gradient within the part cake. Without this barrier, the mold inserts would cool too quickly because of the good thermal conductivity of the Copper Polyamide material, resulting in curled or warped mold inserts. The sacrifice geometry can be any geometry that covers a majority of the build area and is at least 2 millimeters thick.

## Mold finishing

After the mold insert is built in the Sinterstation, it is finished and prepared for molding. The finishing steps include sealing the surface, finishing the surface, casting backfill material, machining ejector pins and cooling line connections, and aligning the insert in the mold base.

The Copper Polyamide parts as built in the Sinterstation are porous. The inserts must be sealed to prevent the molded plastic from adhering to the surface and to prevent the conformal cooling lines from leaking. A low viscosity epoxy or acrylate works well to seal the surface. It is important to select a sealant that can withstand high temperatures during molding. DTM recommends Imprex Superseal 95-1000A, which is a heat cure acrylate.

After sealing the part, the mold surface is finished with a flexible sanding cloth, see Figure 4. Start with 220 grit, then 320 grit, and finally a 400 grit. Either wet or dry sanding techniques can be used. Apply another coat of sealer to the mold surface after sanding.

The backfill material recommended by DTM is Metspec 217. This material is a metal alloy with a melting temperature of 103°C. The Metspec is poured in layers to avoid softening and deforming the mold insert. When these steps are complete, the mold insert is inserted into the mold base. Different types of mold bases have been used successfully. If using a two-plate type mold base, dowel holes can be added to the CAD model in the corners of the mold insert to aid in alignment. If using a one-plate pocketed base, conventional methods are used to square up the insert before placing the mold insert into the pocketed base.

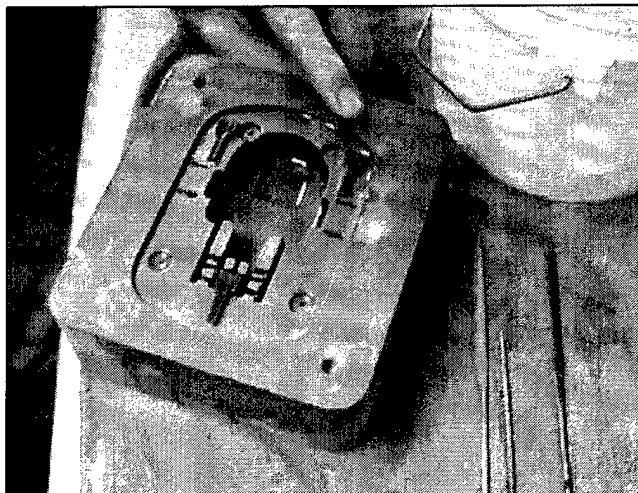


Figure 4. Finishing of the mold surface with sanding cloth.

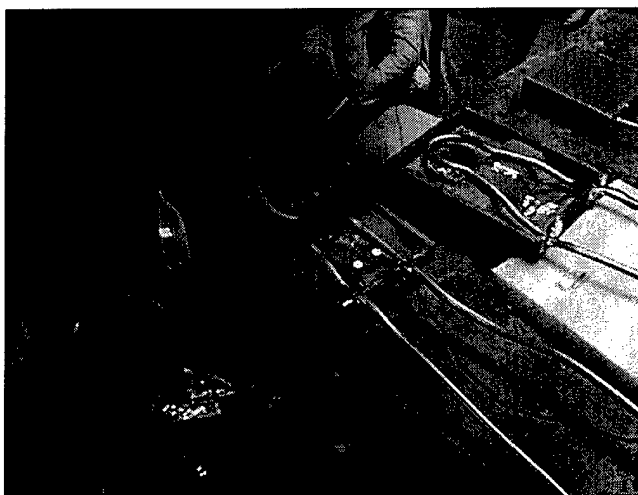


Figure 5. Backfilling mold inserts with a metal filled epoxy.

## Molding Trials

The mold inserts are fairly durable allowing a molding house to run the mold without special instructions. The durability of the Copper Polyamide mold inserts is similar to that of cast metal/epoxy tooling. The thermal conductivity of the material is good, 1.28 W/m-K at 40°C, and is also similar to that of cast metal/epoxy tooling. The good thermal conductivity, in combination with the conformal cooling lines and a metal backfill material, allows the mold to be run with normal cycle times, typically 25 to 40 seconds. The mechanical and thermal properties of SLS objects made with the Copper Polyamide are reported in Table 2.

When molding, the mold should be at a consistent molding temperature before injection of the plastic. Try to get a full shot the first time. If there is a short shot, it is more likely to stick in the mold and cause damage. Mold release can be used at the beginning of the molding run. It is not necessary to apply mold release after every shot or late in the molding run. Several different release agents have been used with no problems.

A number of common plastics have been successfully molded in the Copper Polyamide mold inserts. The melting temperatures and processing temperatures for the plastics used in the mold inserts are listed below. In most cases, the mold inserts showed little or no wear and can be used to mold additional parts.

**Table 1. Examples of plastics successfully molded in Copper Polyamide mold inserts.**

Material	Melting Temperature, °C	Processing Temperature Range, °C (°F)	Parts molded
Polyethylene	T <sub>m</sub> 122 – 137	175 – 260 (350 – 500)	50 – 350
Polypropylene (PP)	T <sub>m</sub> 160 – 175	190 – 285 (375 – 550)	50 – 200
10-40% talc filled PP	T <sub>m</sub> 158 – 168	175 – 285 (350 – 550)	50 – 350
40%GF Polypropylene	T <sub>m</sub> 168	230 – 285 (450 – 550)	30 – 150
ABS (medium impact)	T <sub>g</sub> 102 – 115	200 – 275 (390 – 525)	40 – 150
ABS/PVC	T <sub>g</sub> 175 - 205	185 – 210 (370 – 410)	100 – 200

**Case Study #1: Brake fluid reservoir molded in polypropylene [8]**

Last spring at BASTECH, Inc [9], an automotive OEM client offered a challenging assignment. It needed 20 to 50 sets of brake reservoir parts produced in the intended production material, polypropylene. The parts had to withstand prolonged contact with brake fluid. Moreover, they had to perform like production parts during functional testing on a prototype vehicle.

BASTECH had faced a similar situation a year ago. Back then, the company had used 3D Systems’ AIM Tool process to create prototype tooling. The results were only marginally successful. After 10 shots with the AIM Tool they began to see deformation of the parting line and the mold itself. The run produced only 40 polypropylene parts, with each set becoming slightly more deformed.

Wanting something better for this molding run, BASTECH used the Copper Polyamide material. The brake reservoir consisted of two pieces, which eventually would be welded together. Two tools were required to make these parts. One tool was made up of 13 pieces; the other was made up of 6 pieces. Eight pieces of the thirteen-piece tool were made using the Copper Polyamide (Figure 6), as were five pieces of the six-piece tool. The remaining pieces, very simple inserts or sleeves, were machined out of metal. The final part, after welding, measured approximately 110 mm by 154 mm by 41 mm.

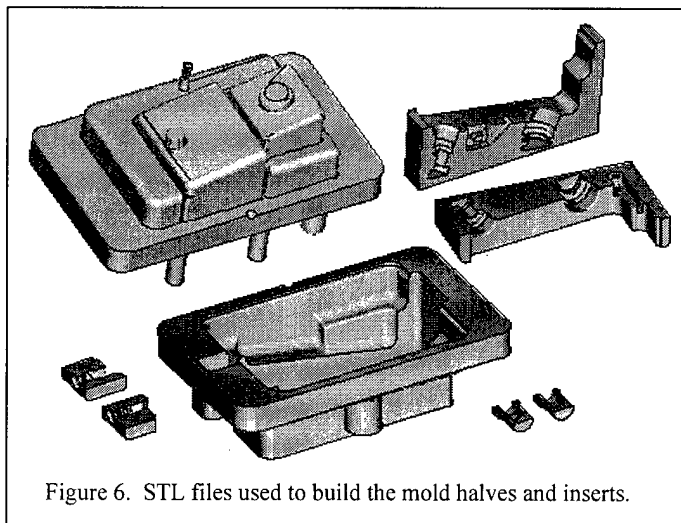


Figure 6. STL files used to build the mold halves and inserts.

BASTECH ran 75 sets of parts on the Copper Polyamide tools and noticed very little wear. They started to see a little degradation in a few areas, but could easily have gotten 100 to 150 sets of parts from the molds. The SLS Copper Polyamide tooling withstood an injection molding pressure of 400 psi and injection molding temperatures of 230°C. They stated that the molds were very sturdy which impressed them the most. Overall, both BASTECH and their customer were very pleased. The molded parts are pictured in Figure 7 next to one of the mold halves.

The SLS Copper Polyamide tooling well outlasted the AIM tooling. It took an extra day to fit, finish, and polish the SLS tooling; but the resulting tools were more stable, not deforming during molding, and the parts produced looked much better. The time and costs for producing tools using Copper Polyamide in the SLS process or Epoxy in the SLA process are roughly the same.

Comparing the timing and costs of an SLS Copper Polyamide tool to that of a conventional steel or machined production tool offers more compelling numbers. The SLS molds can be produced at roughly one fourth the cost in only one half the time when compared to steel tooling. These savings are important when only 50 to 500 molded parts are needed.

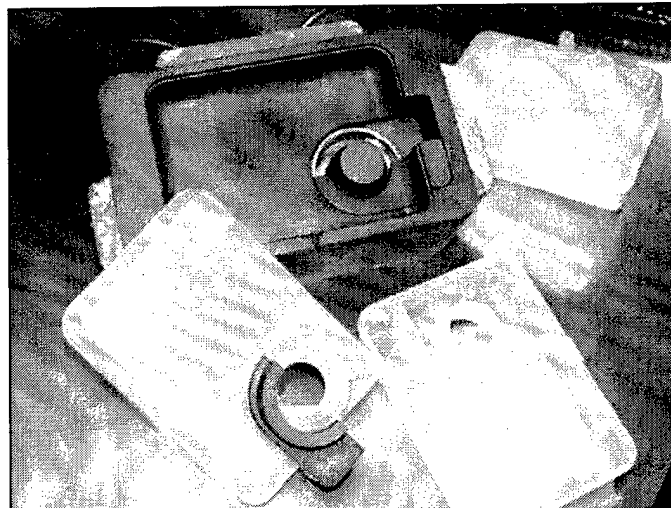


Figure 7. Parts molded by BASTECH in the Copper Polyamide molds pictured next to one of the mold inserts.

### Case Study #2: Glass guide molded in nylon 6,6 [8]

The Rover Group [10], at their Rapid Prototyping and Tooling Department situated on the campus of the University of Warwick, has participated as a beta test site for the Copper Polyamide material. Rover has studied, among other things, how tooling made via the SLS process with the new Copper Polyamide material compares to alternative low cost tooling routes.

One of the parts selected for Rover's comparison was a glass guide (approximately 90 mm x 60 mm x 25 mm). This part is used to ensure the automobile door window locates in the rubber seal when closing. The intended production material was nylon 6,6. They had already created the tool geometry in cast resin, so when they created a Copper Polyamide tool with the SLS process it was purely for the sake of comparison.

Rover designed the single cavity mold inserts as solid objects on a CATIA workstation. The STL files were then shelled to a wall thickness of 2.5-mm using Materialise Magic RP software. The inserts were produced in one of Rover's two in-house Sinterstation 2500 systems. Once removed from the Sinterstation, the hollow tool inserts were backed with an epoxy resin loaded with aluminum powder and granules. The tool was subsequently machined to fit one of Rover's standard injection molding bolster sets.

To trial the Copper Polyamide mold inserts and to ensure the tool was working properly, Rover shot an initial run of 33 polypropylene parts. Once confident that the tool was working properly, they shot another

117 nylon 6,6 parts into the Copper Polyamide tool. Nylon 6,6 parts molded in the Copper Polyamide tool are pictured in Figure 8.

Rover was pleasantly surprised with the results. They had not expected the Copper Polyamide tooling to withstand the high injection temperature of nylon 6,6 which is 285°C. Some minor degradation of the Copper Polyamide tool began to occur after 20 shots. The degradation was most noticeable around the sprue puller where the sharp edges began to erode. This area was directly across from the injection sprue where the mold reaches the highest temperatures. Dr. Illston at Rover stated that the degradation of the tool was also exaggerated because the part geometry was an early prototype design. The glass guide part featured a section of approximately 1 cm<sup>3</sup> that retained considerable heat during injection molding. Increased localized heat build up resulted in additional erosion of the male part geometry where the small radii were intended.

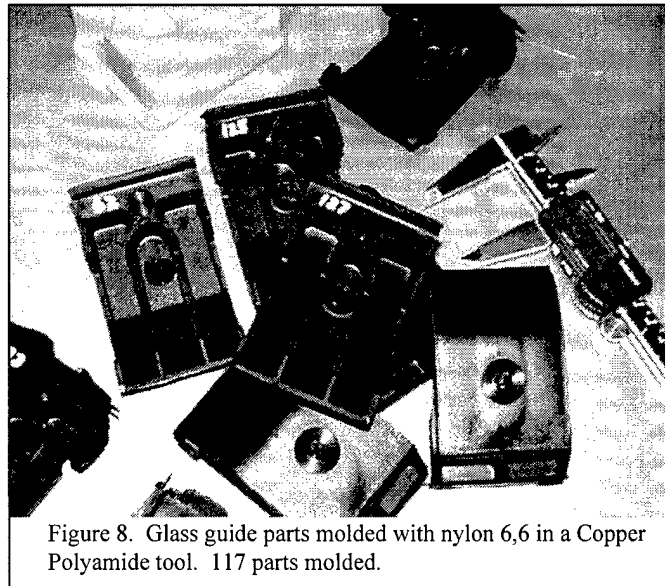


Figure 8. Glass guide parts molded with nylon 6,6 in a Copper Polyamide tool. 117 parts molded.

The final result of this project was that 60 nylon glass guides made from the Copper Polyamide tools have been installed on Rover Group's prototype vehicles. Under the circumstances, the performance of the tool was far better than expected.

Rover has continued to explore the advantages of the SLS-generated Copper Polyamide tooling. Another project resulted in 300 parts molded with 30% talc filled polypropylene. The part is a speaker fret (or speaker cover) which measures 38 mm in diameter and features a complex geometry, see Figure 9. During the production of these parts, the tool showed no wear or part flashing. The injection temperature of the polypropylene material was 240°C.

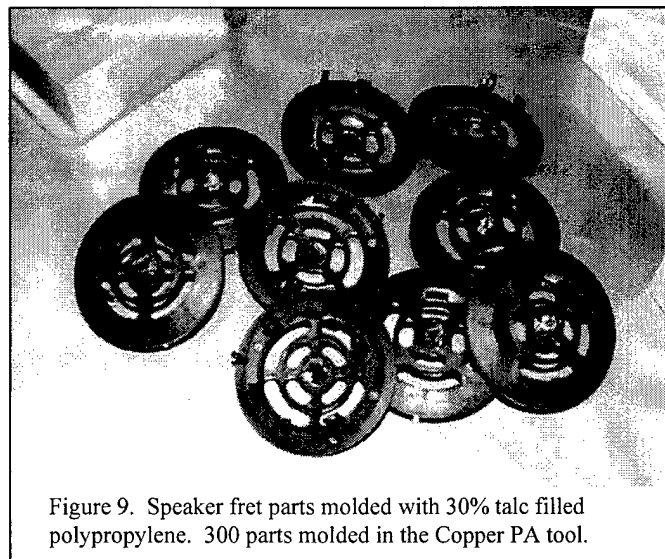


Figure 9. Speaker fret parts molded with 30% talc filled polypropylene. 300 parts molded in the Copper PA tool.

Rover has worked with a number of rapid tooling methods. Their view is that the Copper Polyamide mold inserts compare more favorably to cast resin tools. Although the performance of the Copper Polyamide tools is comparable to cast tools because the thermal conductivity of the two material systems are similar, there are advantages to building the mold inserts directly in the Sinterstation from the CAD data. When asked which method is faster, Dr. Illston says it all depends on the data available. If the CAD data is available for the mold inserts then the Copper Polyamide route is quicker. If the CAD data is only available for the part, then it is quicker to create a RP master pattern and cast the resin tool. Rover is currently evaluating the cost and time comparisons between the two processes.

## Conclusion

The Copper Polyamide material and the Sinterstation system can rapidly produce limited life prototype mold inserts. Prototype quantities of production-quality molded plastic parts can be manufactured with these metal-based mold inserts.

The important attributes of a short run tool are durability, molding cycle times, and speed. The durability of the Copper Polyamide tools is comparable to epoxy/metal tooling and is much better than Direct AIM tools. The molding cycle times for Copper PA are similar to metal tooling. This is important because cycle times can affect the mechanical properties of the molded parts. Mold inserts are created relatively quickly with the Copper Polyamide material. Molds can be ready for molding in 5 workdays; this includes all processing steps required to move from a STL file to molded parts.

**Table 2. Copper Polyamide product specification**

	UNITS	ASTM TEST METHOD	BUILT in Sinterstation	
			@15° angle	FLAT
<b>PHYSICAL PROPERTIES</b>				
Density	23°C	g/cm <sup>3</sup>	D-792	3.45
<b>THERMAL PROPERTIES</b>				
DTUL, 0.45 MPa (66 psi)		°C	D-648	174   176
DTUL, 1.82 MPa (264 psi)		°C	D-648	122   123
Thermal Conductivity	40° to 150°C	W/m·°C	E-1530	1.28 – 0.92
Specific Heat	40° to 150°C	J/g·°C	DSC	0.66 – 0.87
Coefficient Thermal Expansion	30° to 150°C	m/m/°C	E-831	92.6 x 10 <sup>-6</sup>
<b>MECHANICAL PROPERTIES</b>				
Tensile Strength, ultimate		MPa (lb/in <sup>2</sup> )	D-638	33.6   35.9 (4,870)   (5,208)
Flexural Strength, 5% strain		MPa (lb/in <sup>2</sup> )	D-790	53.5   58.3 (7,760)   (8,460)
Flexural Modulus		MPa (lb/in <sup>2</sup> )	D-790	3,068   3,223 (445,000)   (468,000)
Compressive Strength, 0.2% offset		MPa (lb/in <sup>2</sup> )	D-695	88   99 (12,800)   (14,400)
Hardness-Shore "D"			D-2240	75   75
<b>SURFACE FINISH</b>				
As SLS Processed, Ra		µm (µ in.)	-	27.7 (1108)   12.5 (500)
After Finishing, Ra		µm (µ in.)	-	5.2 (208)   2.5 (88)

Data was generated from the testing of SLS™ parts produced with the Copper PA material under typical processing conditions. (New material processed with a laser power of 15 watts, scan speed of 5000 mm/sec, scan spacing of 0.1 mm, and a layer thickness of 0.1 mm in the Sinterstation 2500. Samples infiltrated with Imprex Superseal)

## References

1. U. Hejmadi and K. McAlea, "Selective Laser Sintering of Metal Molds: The RapidTool Process", *Solid Freeform Fabrication Symposium Proceedings*, The University of Texas, Texas, pp. 97-104, 1996.
2. R. Connelly, "Rapid Tooling for Medical Products Using 3D Keltool", *Rapid Prototyping and Manufacturing Conference*, Dearborn, Michigan, pp. 89-99, 1997.
3. S. Ashley, "Progress Toward Rapid Tooling; Extrude Hone", *Mechanical Engineering*, **120**, [7], pp. 65-67, 1998.
4. T. Wohlers, *Rapid Prototyping & Tooling, State of the Industry*, Wohlers Associates, Inc.: Fort Collins, Colorado, pp. 71-72, 1997.
5. J. Frados, *Plastics Engineering Handbook of the Society of the Plastics Industry, Inc.*, 4<sup>th</sup> edition, Van Nostrand Reinhold: New York, pp.131-155, 1976.
6. Materialise, 6111 Jackson Road, Ann Arbor, Michigan, 48103, [www.materialise.com](http://www.materialise.com).
7. C. Nelson, "Improvements in SLS Part Accuracy", *Solid Freeform Fabrication Symposium Proceedings*, The University of Texas, Texas, pp. 159-169, 1995.
8. "BASTECH and Rover Share Experiences With New Copper Polyamide", *Horizons*, A Publication of DTM Corporation, Austin, Texas, Q3 1998.
9. B. Staub, BASTECH Inc., 3541 Stop Eight Road, Dayton, Ohio, 45414, [www.bastech.com](http://www.bastech.com).
10. T. Illston, Rover Group, ATC, 3<sup>rd</sup> Floor, The University of Warwick, Coventry, CV4 7AL.



## Rapid Steel Tooling Via Solid Freeform Fabrication

Timothy J. Weaver, Julian A. Thomas, Sundar V. Atre,  
and Randall M. German

P/M Lab, 118 Research West  
The Pennsylvania State University  
University Park, PA 16802-6809

### ABSTRACT

With increasing part complexity and requirements for long production runs, tooling has become an expensive process that requires long lead times to manufacture. This lengthens the amount of time from "art to part". Rapid tooling via stereolithography (SLA), filled epoxies, etc. have been stopgap measures to produce limited prototyping runs from (10 to 500 parts). This gives poor dimensional analysis and does not allow for limited production runs of 1000+ parts. The method of producing prototype tooling with a powdered metal process has been developed that produces tooling with a hardness greater than 35 HRC and total shrinkage less than 0.5%. This tooling process manufactures production ready tooling that will perform extended cycle runs (100,000+). Manufacturing of this tooling takes 1 to 2 weeks and will compare favorably with production grade steel tooling. Originals drawn in 3D CAD can be used to prototype the master that will allow for the production of the rapid metal tool set.

This process starts with a rapid prototyped model made by whatever process is desired or a machined master. For this paper a Sander's Model Maker II® rapid prototyping machine was used to fabricate the model. After the model of the tool set is made, a silicone rubber negative is cast around that model. After the silicone rubber model is made, a heated slurry of metal powders and polymers is poured into the mold to create the green tool set. The tool set is left to cool, and then removed from the silicone rubber mold. The tool set is then debound and sintered to produce a final tool set with properties approaching hardened tool steel.

### INTRODUCTION

Rapid tooling has many different forms for various applications. Tooling from silicone rubber, epoxies, aluminum, powder metal, and prehardened tool steel could all fall under the category of rapid tooling. Each method of rapid tooling has its applications and shortcomings. Therefore the defined application of the tooling is required to determine the properties that the tooling needs to exhibit.

As the race to get a product to market increases in speed, the drive for tooling lead times to decrease will become higher. This drive in time compression in the manufacturing sector leads to unique opportunities to create tooling via non traditional methods that dramatically reduce lead times while not sacrificing mechanical properties. Therefore the goal of this paper was to develop tooling quickly (< 2 weeks) with mechanical properties comparable to hardened tool steel. This tooling was fabricated using a powder metallurgy process combining the

processing of various metals and or ceramic powders to form a tool set with tailored mechanical properties. This in turn leads to a decrease in lead-time with no sacrifice in properties.

## BACKGROUND

Rapid tooling is a growing technology that is currently moving from temporary tooling silicone rubber, epoxies, etc. to a more robust tooling that can still be made in a rapid fashion. DTM® selective laser sintering has been making tooling inserts for injection molding for a number of years. [1] Keltool has been using a casting process to make inserts since patenting the technology in 1980. [2] Most current techniques that produce metal tooling fail in one of the following ways:

1. Rough Surface
2. Low mechanical properties
3. Poor wear resistance
4. Poor thermal conductivity
5. Difficult or complex process
6. Needs excessive finishing or post processing

These reasons have allowed traditional tooling to continue to have an advantage over the current rapid tooling processes. In order for rapid tooling to have a significant impact on the industry these problems need to be overcome and the final product must not only be delivered quicker, but with either a cheaper price or better mechanical responses. The process that is described in this paper provides a potential processing route to overcome these issues, except low impact strength.

## PROCESS DESCRIPTION

To make a rapid tool mold or part you must first design the part in a 3 dimension (3D) computer aided design (CAD) software package or fabricate a model of the part by hand. There are many software programs available to design the part or tool mold. [3] The particular program used for this paper was Solidworks 97 Plus. The part or tool mold is designed in the software program in 3D, to the dimensions or size required for that part or tool mold. The software in the (stereolithography) .STL format saves the design.

The next step is to actually build a model of the part or tool mold using the computer design. Once again this can be accomplished on a variety of machines, but care must be given to obtain a good surface finish and closed surface model. For this processing step a Sanders Model Maker II prototyping machine was used. [4] Before actually building the model of the part or tool mold, the .STL file is loaded into the software program provided by the manufacturer of the prototyping machine to generate sections or slices of the 3D designed part into very thin layers on the computer. The Model Works software, provided by Sanders, allows the user to take the 3D .STL file and divide it into very thin layers with thicknesses ranging from 0.0005 to 0.005 inches. For reference, the thickness of a sheet of paper is 0.0015 inches. The user chooses the layer thickness, and how the modeling material is to be deposited to form the model of the part. The Model Works software program incorporates the user's choices and slices or sections the

computer design into the appropriate layer thickness and determines the way the modeling material will be deposited to form the model of the part. This slicing data of the 3D.STL file is saved in a separate file that will be downloaded by the machine to fabricate or build the model of the part.

The next step is building the model of the part or tool mold. The file with the layer or slice data is fed into the machine and the machine begins to build the model, layer by layer, until the entire model has been finished. This process can take from hours to days depending on the size, complexity, and layer thickness that was chosen by the user. Figure 1 shows the final model.

After the model has been fabricated, the next step is to make a silicone rubber negative of the model. A frame is built around the model to contain the resin mixture. This resin is poured over the model contained inside the walls to create a negative or reverse impression of the final part or tool mold, as shown in Figure 2. The rubber is then left to cure until solid. After the rubber has cured, the model that was built on the rapid prototyping machine is removed from the silicone rubber. The silicone rubber mold is now ready to create the final tool mold or part. The silicone rubber was selected due to its ability to hold tolerances, pick up fine surface detail, and its elasticity to facilitate part release.

The next step is to prepare molten slurry of molten polymers and a blend of powdered metal or ceramic materials. The molten polymers are used as a carrier to allow the powdered material to flow and conform to the details of the silicone rubber mold. The slurry is poured into the silicone rubber mold, and is allowed to cool to room temperature as shown in Figure 3. Once the slurry has solidified, it is removed from the silicone rubber mold by flexing the rubber and releasing the part of polymer-metal and or ceramic powder. The part should now be the exact replica of the 3D-computer design and the model that was built on the Sanders rapid prototyping machine, as shown in Figure 4. The final part is now ready to be processed to form a finished product.

To process the cast part the next step is to remove the remaining polymers from the final part. Once the binder is removed, the tool set is sintered to fuse the metal or ceramic powders together and eliminate porosity that is developed during the debinding process. For the tooling material the process has been developed such that shrinkage is limited to approximately 0.4%. For other materials like stainless steels, ceramics, etc. typical powder injection molding linear shrinkage values of 15 to 18%, would be expected. Final finishing and polishing is performed on the final part as shown in Figure 5. Once the finishing process is done, the final part is complete and ready for use as a part or tool mold to make the desired geometry, as shown in Figure 6.

## MECHANICAL PROPERTIES

The mechanical properties of the tool sets made are listed in Table 1 below. As can be seen from Table 1 some of the mechanical properties are comparable to hardened tool steel, and the tooling material has a very good wear resistance. The impact properties of the material are particularly low, and improvements will need to be made to produce a satisfactory final material. The surface roughness is also a little high, but with polishing a surface finish of 0.25-0.3 $\mu$ m

average roughness can be achieved. This is comparable to polished tool steel with a surface finish of 0.2 $\mu$ m average roughness. The hardness of the tooling material is dependent on powder loading and the actual blend of powders used. It is envisioned that optimizing the blend of powders the hardness of the material will increase to 50+HRC.

**Table 1. Mechanical Properties of Tool Sets**

Mechanical Property	Recorded Value
Strength	950 MPa – transverse rupture strength (TRS)
Hardness	30 to 35 HRC
Impact Strength	5 J/cm <sup>2</sup>
Wear Resistance – ASTM G65 Procedure A	0.052cm <sup>3</sup> (hardened tool steel 0.059cm <sup>3</sup> )
Surface Roughness	1.75 to 2.25 $\mu$ m average roughness
Surface Roughness (after polishing)	0.3 $\mu$ m (polished tool steel ~0.2 $\mu$ m)
Shrinkage	~ 0.4%

A comparison of different types of tooling is shown in Table 2 below. This tooling material has some properties higher than prehard steel like P20, and some of the properties are similar to hardened tool steel. It is envisioned that the life of the tool set would be similar to tool steel. Further life cycle testing will be done to evaluate this claim.

**Table 2. Comparison of Various Types of Tooling for Powder Injection Molding**

Type of Tooling	Hardness	Cycle Time	Life Cycle
Rubber Mold	15-65 Shore “A”	5-30 minutes	1-100
Epoxy	80-110 RM	3-5 minutes	100-1,000
Filled Epoxy	85 RM	3-5 minutes	250-2,500
Aluminum	60-95 BHN	10 to 60s	2,500-10,000
Prehard Steel	28-32 HRC	10 to 60s	10,000-100,000
Hard Tooling	60’s HRC	10 to 60s	100,000+

## CONCLUSIONS

The goal of this research was to develop a tool set or specific geometry rapidly from a machined master or prototyped component. This goal has been realized by fabrication techniques that allow for the production of a tool set or geometry in less than two weeks. Another goal was to make it a simplistic technology that could be practiced by anyone (with limited capital investment) that is currently practicing powder injection molding. [5] The processing steps are very simple with less than a \$5,000 investment needed if currently practicing powder injection molding. Finally the ability with the same process to make limited components is possible. This allows the first real components to be placed in the customer’s hand or used for marketing studies without the expenses and time associated with conventional tooling.

## FUTURE WORK

The need to replicate the process to determine the absolute dimensional shrinkage and reproducibility is still required. The ability to reproduce dimensions accurately will be one of the main focuses of future research. The size envelope that this technology will allow is still under evaluation, but is probably limited to the debinding technology developed and thermal conductivity of the metal powder system over large cross-sections. Experimental work to reduce the shrinkage of the tooling material to net zero shrinkage is underway. This is needed for exact reproduction of a master that cannot be oversized for shrinkage. Also, further focus on the binder rheology and its ability to form the tool set or part at low viscosities while retaining good green strength is being investigated. Finally, optimizing the debinding conditions to allow the processing of thicker parts is necessary.

## ACKNOWLEDGEMENTS

We would like to thank Arthur Holloway and Amy Bailey for performing some of the experiments to acquire the data in this paper. We would also like to thank Eastman Kodak for supplying some of the polymers used in the formulation of the rapid tooling material system.

## REFERENCES

1. Harris L. Marcus, Joseph J. Beaman, Joel W. Barlow, and David L. Bourell, "From Computer to Component in 15 Minutes: The Integrated Manufacture of Three-Dimensional Objects", *Journal of Materials*, April 1990, pp. 8-10.
2. Minnesota Mining and Manufacturing Company, "Infiltrated Powder Metal Composite", U.S. Patent No. 4327156.
3. Julian Brailsford, "Time-Compression Software Review", *Rapid News*, Vol. 2, No. 4, 1997 pp. 30-35.
4. Joseph J. Beaman, Joel W. Barlow, David L. Bourell, Richard H. Crawford, Harris L. Marcus, and Kevin P. McAlea, *Solid Freeform Fabrication: A New Direction in Manufacturing*, Kluwer Academic Publishers, Norwell, MA, p. 40.
5. Randall M. German, and Animesh Bose, *Injection Molding of Metals and Ceramics*, Metal Powder Industries Federation, Princeton, NJ, 1997, pp. 14-17.



Figure 1. Picture of the Final Green Model in Mold Frame.

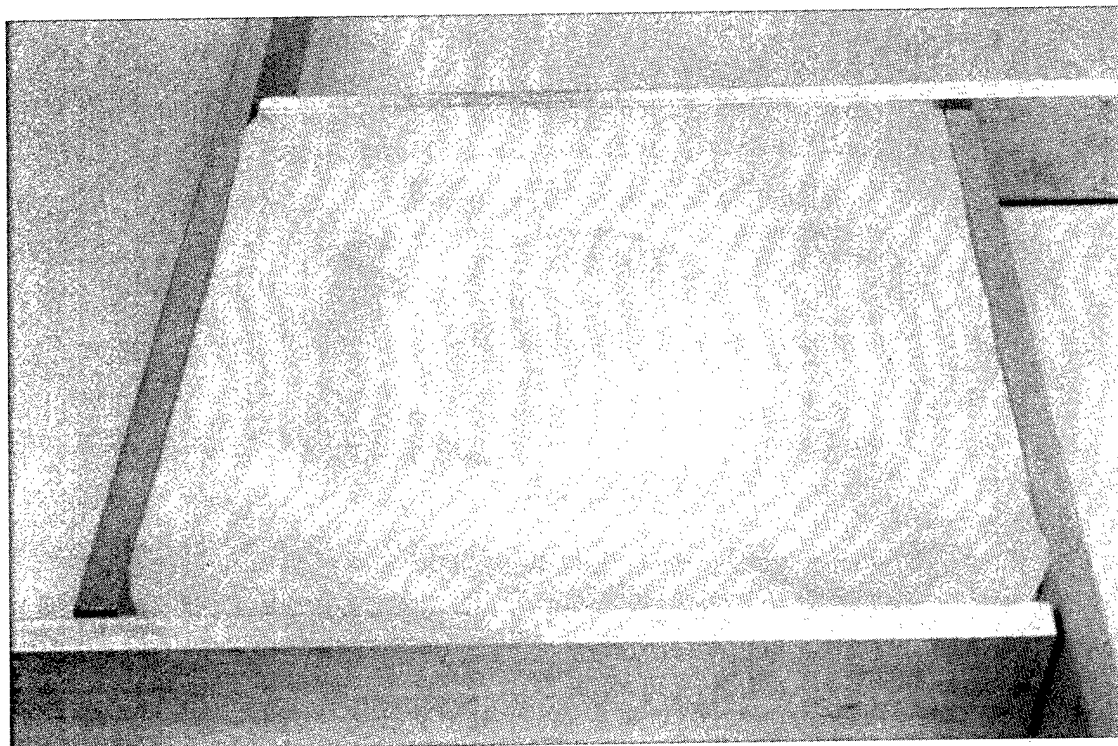


Figure 2. Picture of Silicone Rubber Negative Mold Setup.

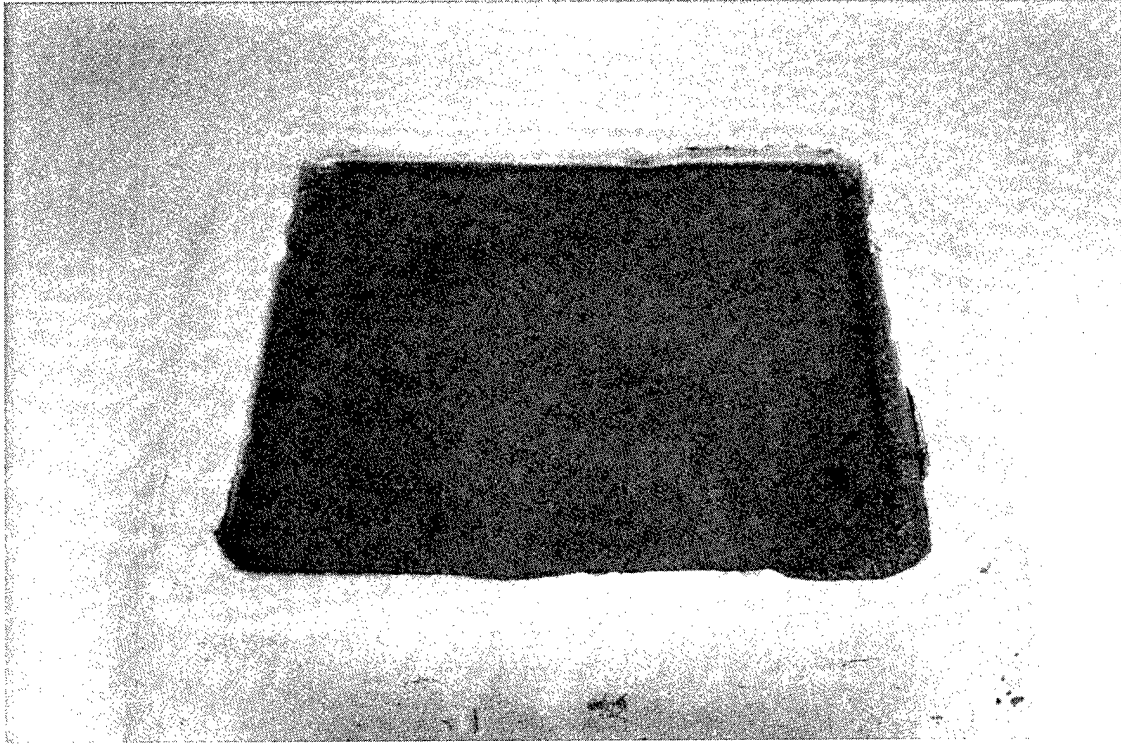


Figure 3. Picture of Metal Slurry in the Silicone Rubber Mold.

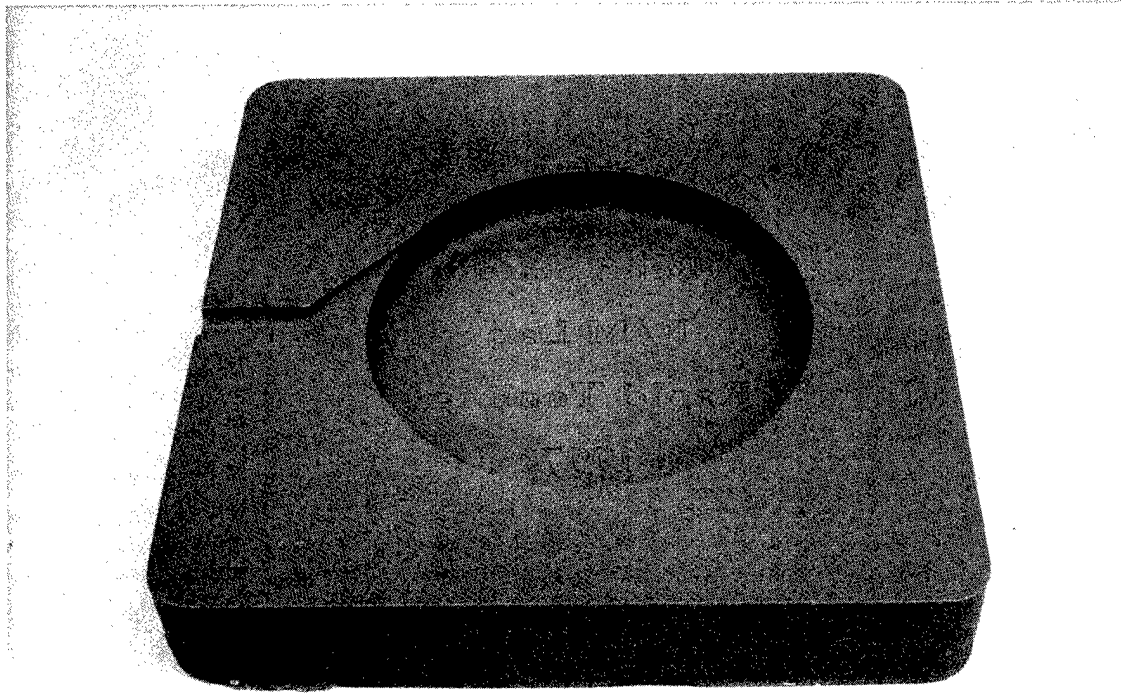


Figure 4. Picture of the Green Part Removed From the Silicone Rubber Mold.

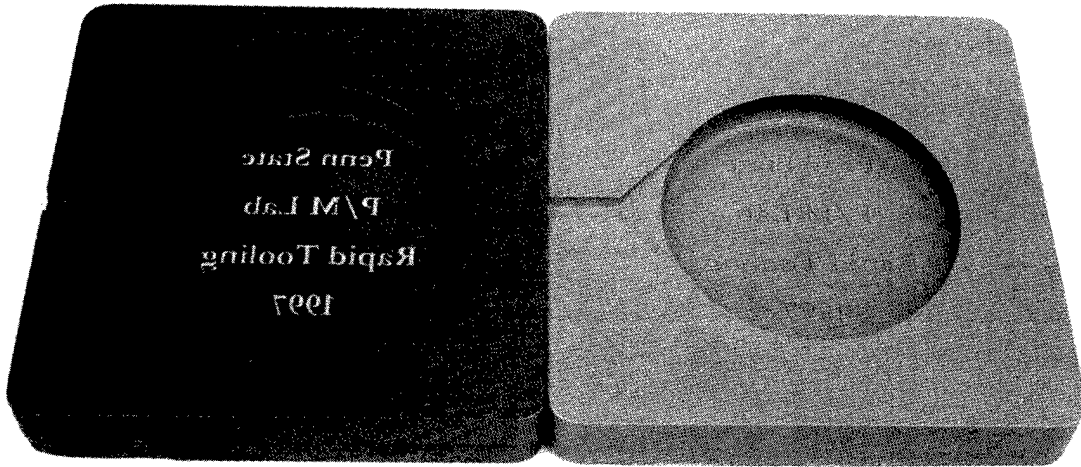


Figure 5. Picture of the Green Part Compared to Original Model.

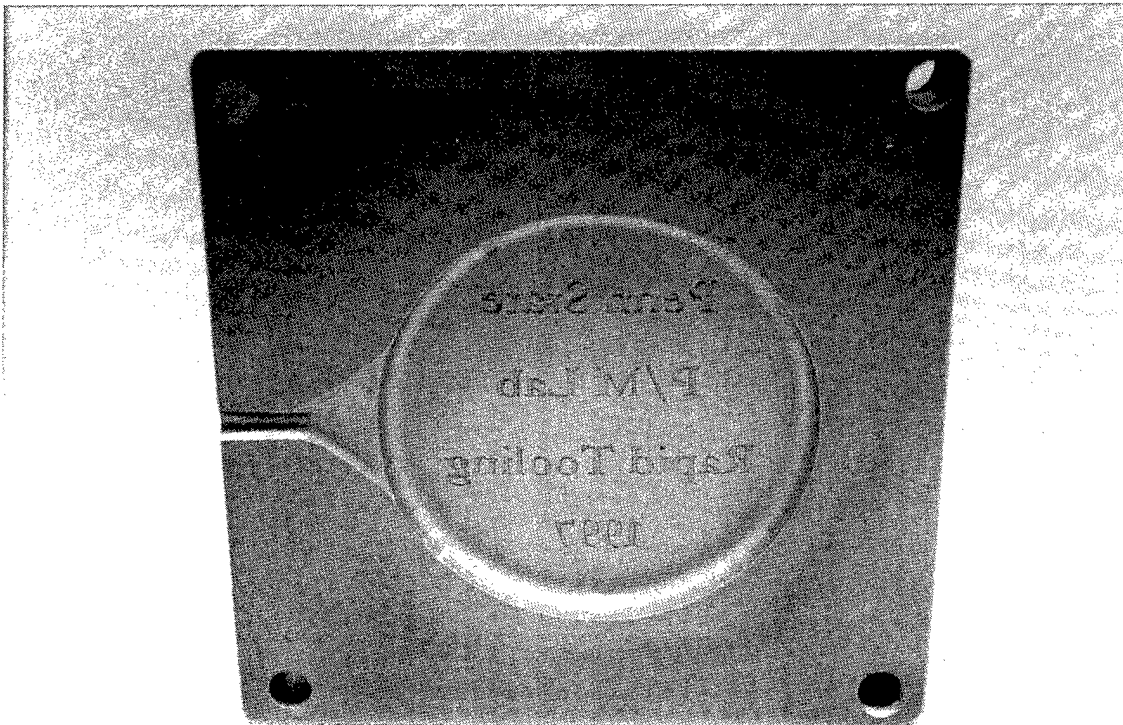


Figure 6. Picture of Final Tool Set Ready for Injection Molding.

## Processing of Titanium Net Shapes by SLS/HIP

Suman Das, Martin Wohlerl, Joseph J. Beaman and David L. Bourell

Laboratory for Freeform Fabrication  
The University of Texas at Austin  
Austin, Texas 78712-1063

### Abstract

SLS/HIP is a hybrid direct laser fabrication method that combines the strengths of selective laser sintering (SLS) and hot isostatic pressing (HIP). SLS can produce complex shaped metal components with an integral, gas impermeable skin. These components can then be directly post-processed to full density by containerless HIP. SLS/HIP is envisioned as a rapid, low cost replacement for conventional metal can HIP processing. The advantages of freeform fabrication combined with *in-situ* HIP encapsulation include the ability to perform containerless HIP, no adverse container-powder interactions, reduced pre-processing time, and fewer post-processing steps compared to conventional HIP of canned parts. SLS/HIP is currently being developed for Inconel<sup>®</sup> 625 superalloy and Ti-6Al-4V. This paper focuses on microstructure and mechanical properties of SLS processed and HIP post-processed Ti-6Al-4V. SLS/HIP technology for Ti-6Al-4V was demonstrated by fabricating a subscale AIM-9 missile guidance section housing to specification. This work is funded jointly by DARPA and ONR under contract N00014-95-C-0139 titled "Low Cost Metal Processing Using SLS/HIP".

### INTRODUCTION

Over the last ten years, SFF technologies worldwide have attained a state of maturity. A variety of SFF technologies are commercially available to produce complex shaped three-dimensional parts and tooling in a variety of materials including plastics, paper, polymers, wax, sand, ceramics and metals. The next major advance in SFF research and development is taking place in the area of direct fabrication processes, especially for low volume production of functional metal, cermet and ceramic components or tooling. Direct fabrication implies layerwise shaping and consolidation of feedstock (e.g. powder, wire, ingot, paste or melt) to complex shapes having full or near full density without the use of intermediate binders, furnace densification cycles, or secondary infiltration steps. These methods typically require minimal thermomechanical post-processing or machining to obtain desired geometry, structure and properties. There is a growing demand amongst industrial and government users for direct SFF processes that enable production of small lot or "one of a kind" functional metal, cermet and ceramic components. A number of direct fabrication methods are under development<sup>1,2,3,4,5,6,7</sup>. The materials systems investigated by these methods include steels, nickel base superalloys, titanium and its alloys, refractory metals, bronze-nickel and cermets.

Selective laser sintering (SLS) is a SFF technique that creates three-dimensional freeform objects directly from their CAD models. An object is created by sequentially fusing thin layers of a powder with a scanning laser beam. Each scanned layer represents a cross section of the object's mathematically sliced CAD model. In direct SLS, a high energy laser beam directly

fuses a metal or cermet powder to high density (> 90%), preferably with minimal or no post-processing requirements.

As part of ongoing direct SLS research efforts at the University of Texas, a hybrid net shape manufacturing technique called SLS/HIP is being developed for high performance metal components<sup>8,9</sup>. SLS/HIP combines the freeform shaping capability of SLS with the full densification capability of HIP to produce net shape, high value metal components at significantly reduced costs and shorter lead times. Such components include fighter aircraft turbine engine hardware, naval and submarine components. Since direct SLS had previously demonstrated the potential to consolidate metal powders to net shapes with densities in excess of 80% theoretical density<sup>10</sup>, SLS/HIP is envisioned as a natural combination of SLS and containerless HIP to obtain full density metal parts.

The working principle of SLS/HIP is to consolidate the interior of a component to 65% or higher density and to fabricate an integral, fully dense, gas impermeable skin or "can" at the part boundaries *in-situ*<sup>11</sup>. A component is produced by selectively consolidating a metal powder with a laser beam layer by layer. Unlike other direct laser fabrication processes that strive to fuse powder to full density across each layer, in SLS/HIP the laser beam fuses the metal powder only at the part boundaries to form an integral, gas impermeable skin or "can" to a density exceeding 92% theoretical density. This is the fractional density at which the porosity typically changes from interconnected or surface connected to closed<sup>12</sup>. The powder in the interior of each layer cross-section can either be left unsintered so as to provide 65% packing density or be optionally laser sintered to an intermediate density typically exceeding 80% of theoretical density. Thus, the net shape P/M part is shaped, canned, evacuated and sealed *in-situ*. The encapsulated part is then post-processed by containerless HIP to full density. A final machining step may be applied if necessary.

SLS/HIP has several advantages over conventional HIP methods. Since an integral skin or "can" is formed of the same material as the part, a secondary canning step is not necessary. The integrally canned, net shape component produced by SLS is directly post-processed by containerless HIP to full density. Adverse container-powder interactions are eliminated and post-HIP container removal is not required. Tooling and pre-processing steps associated with container fabrication and filling are also eliminated. SLS/HIP enables production of complex shapes at reduced cost and shorter lead-times.

Under the ongoing research program, SLS/HIP process development is being undertaken for two materials. Based on a survey<sup>8</sup> of several naval installations, the materials selected for technology development and demonstration are the alloys Inconel<sup>®</sup> 625 and Ti-6Al-4V. The component selected for SLS/HIP technology demonstration of Ti-6Al-4V is the AIM-9 Sidewinder missile guidance section housing, shown in Figure 1.

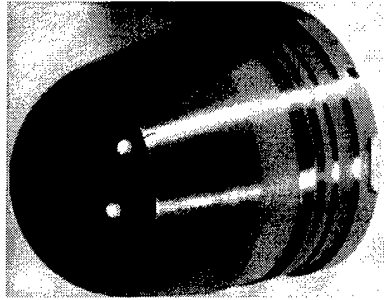


Figure 1. Guidance section housing base for the Sidewinder missile, baseline component for Ti-6Al-4V SLS/HIP technology demonstration.

### SLS/HIP PROCESSING

To demonstrate the feasibility of constructing integrally canned shapes by SLS suitable for HIP post-processing, a number of cylindrical specimens, 0.5 inches diameter, 2 inches long with 0.100 inches skin wall thickness were produced by SLS. A typical integrally canned cylindrical specimen is shown in Figure 2. These specimens were post-processed to full density by a HIP cycle consisting of 4 hours at 925° C and 93 MPa (15000 psi).

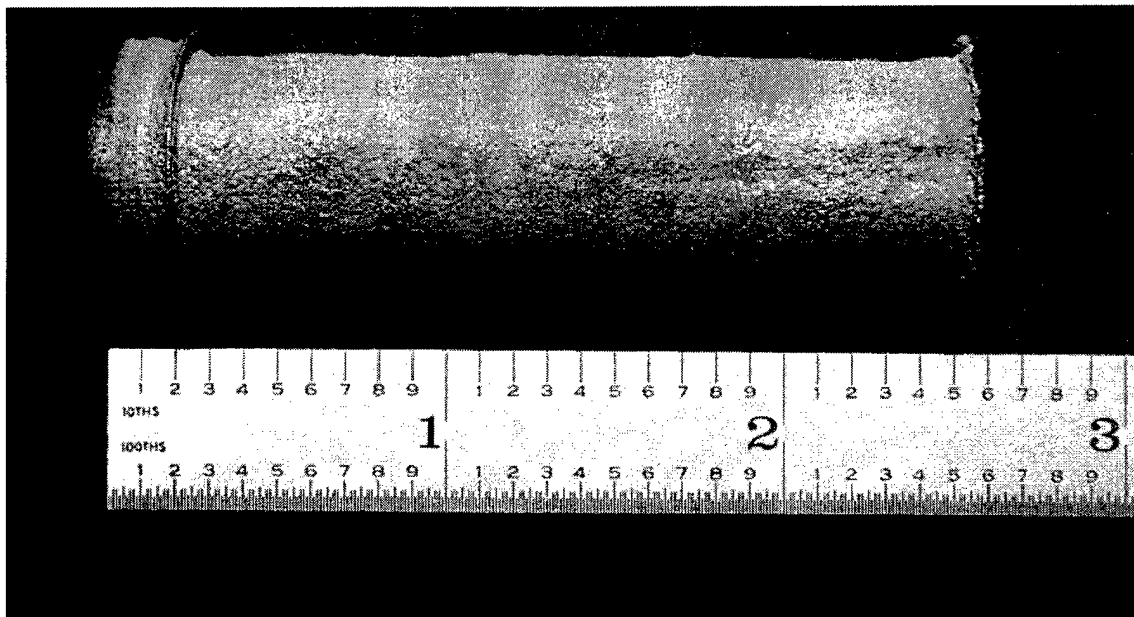


Figure 2. Typical SLS processed, Ti-6Al-4V integrally canned cylindrical specimen.

### MICROSTRUCTURE AND MECHANICAL PROPERTIES

To compare the microstructure of SLS/HIP processed Ti-6Al-4V against conventionally canned and HIPed Ti-6Al-4V, a reference specimen from the same lot of powder as that used to fabricate cylindrical specimens was encapsulated in glass and post-processed using the same HIP cycle. The results, shown in Figure 3, indicated that the microstructure of SLS/HIP processed Ti-6Al-4V in the bulk is the same as that of conventionally canned and HIPed Ti-6Al-4V. The

skin region of a SLS/HIP processed Ti-6Al-4V part exhibits a microstructure different from that seen in the bulk. This is expected because during SLS, the skin region is completely melted by the laser and undergoes rapid solidification, whereas the interior of the part is left unprocessed, and undergoes densification during HIP post-processing. The micrograph in Figure 4 shows the interface between the skin and the core. The difference in microstructures is clearly evident with the skin region exhibiting a high aspect ratio Widmanstätten type microstructure while the core exhibits a coarser microstructure that results from the coalescence of prior particle grain boundaries.

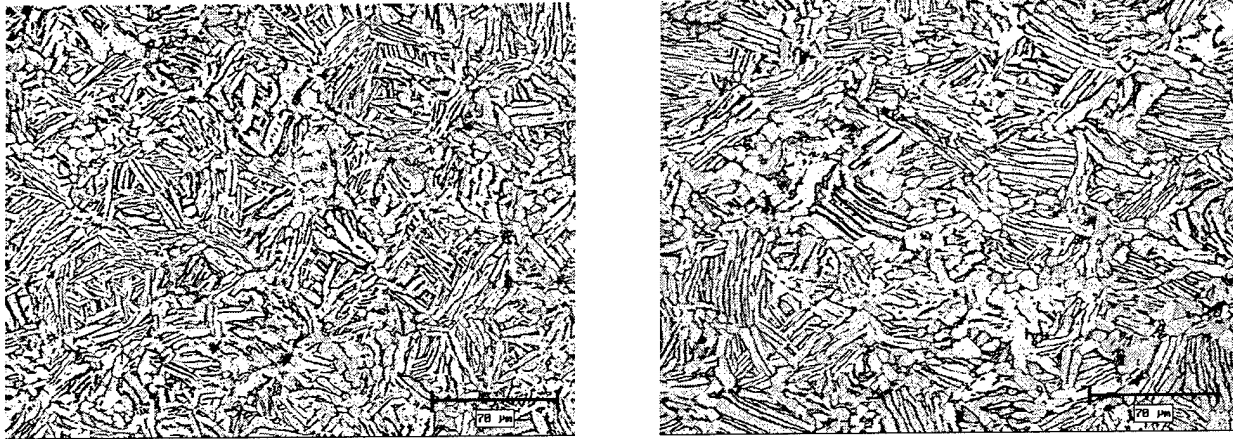


Figure 3. Etched microstructure of glass encapsulation HIP Ti-6Al-4V (left) and SLS/HIP processed Ti-6Al-4V (right)

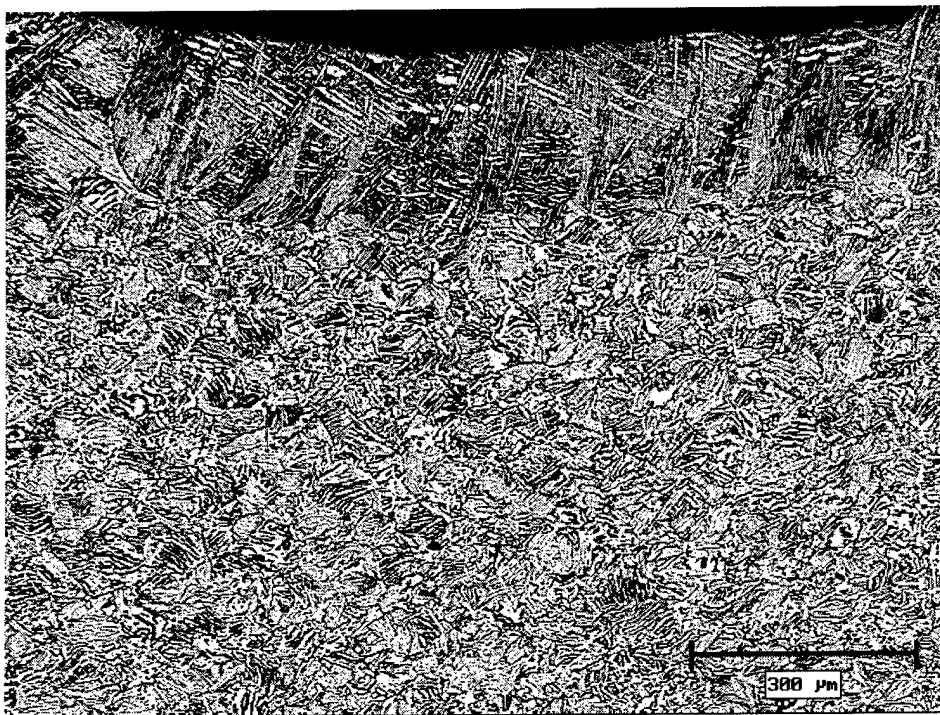


Figure 4. Can-core interface

Hardness was evaluated and compared against conventionally processed material. SLS processing of the skin to full density resulted in material having hardness values comparable to cast material. Hardness values for the SLS/HIP processed core agreed well with values for conventionally canned and HIPed material and did not differ much from the hardness values for the SLS processed skin region.

Material	Processing	Hardness
Ti-6Al-4V	SLS processed skin	36 HRC
Ti-6Al-4V	Cast (grade C-6) <sup>13</sup>	36 HRC
Ti-6Al-4V	Cast (grade C-5) <sup>13</sup>	39 HRC
Ti-6Al-4V	SLS/HIP processed core	35-37 HRC
Ti-6Al-4V	Glass encapsulated HIP	34-36.5 HRC

Table 1. Ti-6Al-4V hardness values.

Tensile specimens conforming to ASTM E 8, round tension test specimen (small-size specimens, 0.25 in. nominal diameter) were machined from integrally canned Ti-6Al-4V cylinders fabricated by SLS and post-processed to full density by HIP. The results indicated that the tensile strength specification for the Sidewinder housing demonstration component was exceeded while the minimum elongation was barely met. Future testing will establish correlations between tensile properties and oxygen levels in SLS/HIP processed parts.

Processing	Tensile Strength (ksi)	Elongation (%)
SLS/HIP	162	5
Sidewinder specification	111	5
Annealed <sup>14</sup>	130	10
Solution treated <sup>15</sup>	150	8
Cast (grade C-5) <sup>13</sup>	130	6
Cast (grade C-6) <sup>13</sup>	115	8

Table 2. Ti-6Al-4V tensile properties.

## CHEMICAL ANALYSIS

Oxygen levels in commercially available titanium feedstock and finished product are critical from performance considerations. The oxygen levels can vary from 0.08% to 0.40% by weight depending on the particular application. The strength typically increases with increasing oxygen content at the expense of ductility. Lower oxygen levels improve ductility, fracture toughness, stress-corrosion resistance and resistance to crack growth.

Oxygen and nitrogen levels in SLS/HIP processed Ti-6Al-4V specimens were determined by ASTM E 1409-97 inert gas fusion technique<sup>16</sup>. The levels were compared against levels in the starting powder as well as against specifications for the Sidewinder housing component. The results of analyses conducted by two analytical labs are shown in Table 3. All three SLS/HIP specimens were taken from the core region of each part. The results indicated that the oxygen specification on the Sidewinder housing was barely met. However, it is to be noted that both

starting powders (PREP™ and Argon atomized) have 0.19% by weight oxygen and the powder used to fabricate each of the three SLS/HIP specimens had been recycled at least 6 times. This indicates that on average 100 ppm oxygen pickup occurred during each SLS run. This is an extremely encouraging result since it corresponds to the typical oxygen pickup observed by Crucible Research in conventional metal can Ti-6Al-4V HIP processing<sup>17</sup>.

To lower oxygen levels in SLS/HIP processed Ti-6Al-4V as well as to increase powder recyclability, ELI (Extra Low Interstitials) grade Ti-6Al-4V powder with 0.099% by weight or lower oxygen may have to be used. In addition, protocols will be established for mixing recycled powder with virgin powder so as to maintain oxygen levels well within specification. During the establishment of such protocols, tracking chronological changes in oxygen levels of parts produced sequentially from the same lot of powder will be an important criterion. ELI grade Ti-6Al-4V powder will be tested in future SLS trials.

Specimen	Oxygen (wt. %)	Nitrogen (wt. %)
Sidewinder specification	0.25 max	-
PREP™ Ti-6Al-4V	0.19	0.01
Ar atomized Ti-6Al-4V	0.196	0.02
SLS/HIP 040898 (Lab A)	0.250	0.019
SLS/HIP 040898 (Lab B)	0.255	0.037
SLS/HIP 042998 (Lab A)	0.2485	0.073
SLS/HIP 042998 (Lab B)	0.200	0.016
SLS/HIP 050198 (Lab A)	0.251	0.038
SLS/HIP 050198 (Lab B)	0.167	0.040

Table 3. Oxygen and Nitrogen levels in Ti-6Al-4V.

## TECHNOLOGY DEMONSTRATION

A subscale version of the guidance section housing for the AIM-9 Sidewinder missile was processed by SLS. This demonstration component, shown in Figure 5 was built at 90% scale. The typical length scale on the component shown is 3 inches. Although this component was selected for SLS/HIP technology demonstration, metallographic evaluation of the “as SLS processed” component revealed full density, as shown in the micrographs of Figure 6. This microstructure is consistent with cast Ti-6Al-4V.

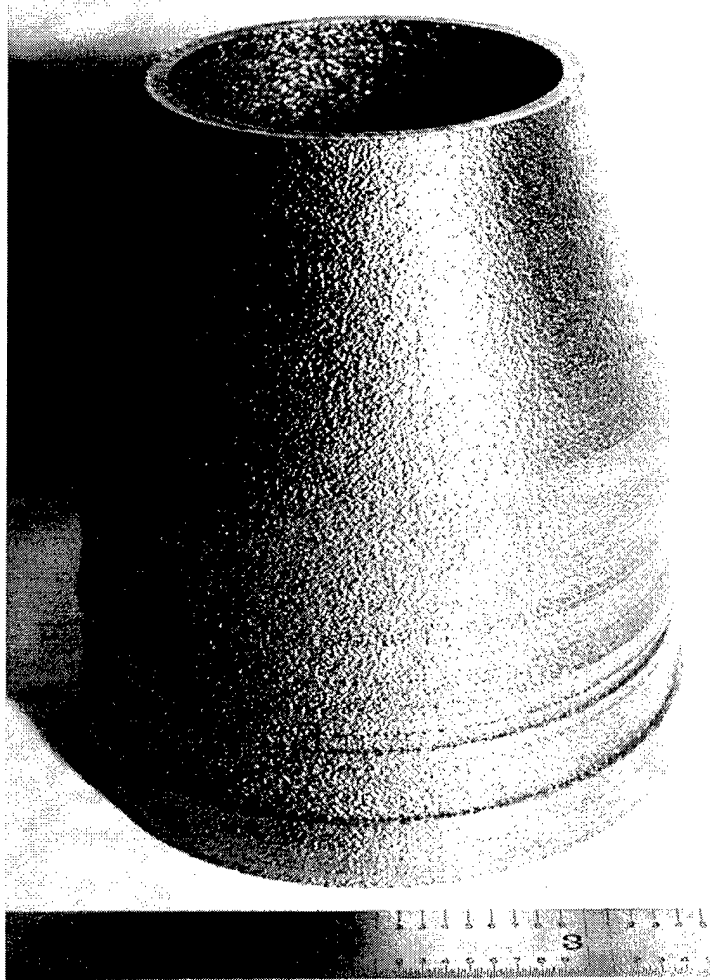


Figure 5. SLS processed Ti-6Al-4V demonstration component.

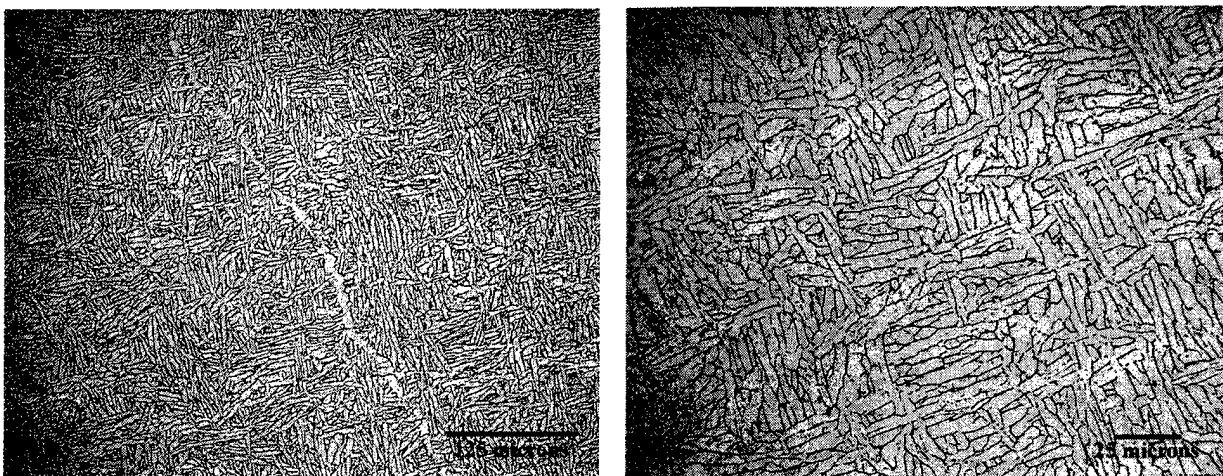


Figure 6. Microstructure of fully dense, SLS processed Ti-6Al-4V demonstration component.

## CONCLUSIONS

Feasibility of fabricating integrally canned complex shapes by SLS for containerless HIP post-processing has been demonstrated for Ti-6Al-4V. Simple cylindrical shapes were fabricated and consolidated to full density by HIP. Microstructure and mechanical properties (hardness and tensile) reveal that material processed by the SLS/HIP technique is equivalent to conventionally processed material. Oxygen levels in SLS/HIP processed Ti-6Al-4V meet specification on the component chosen for technology demonstration. A simplified version of a Ti-6Al-4V demonstration component was successfully fabricated.

Future work will focus on demonstrating SLS/HIP technology for Inconel 625, further characterization of structure/property relationships as well as optimization of processing parameters for build speed, skin thickness, oxygen content and HIP cycle time.

## ACKNOWLEDGEMENTS

The authors wish to acknowledge research funding provided by DARPA/ONR under contract N00014-95-C-0139 titled "Low Cost Metal Processing Using SLS/HIP".

## REFERENCES

- <sup>1</sup> S. Das et al., "Direct SLS Processing for Production of Cermet Composite Turbine Sealing Components", *Materials and Manufacturing Processes*, 13(3), 1998.
- <sup>2</sup> M. L. Griffith et al., "Freeform Fabrication of Metallic Components Using Laser Engineered Net Shaping (LENS<sup>TM</sup>)", *Solid Freeform Fabrication Symposium Proceedings*, 1996.
- <sup>3</sup> J. Mazumder et al., "The Direct Metal Deposition of H13 Tool Steel for 3-D Components", *JOM*, May 1997.
- <sup>4</sup> G. K. Lewis et al., "Properties of Near-Net Shape Metallic Components Produced by the Directed Light Fabrication Process", *Solid Freeform Fabrication Symposium Proceedings*, 1997.
- <sup>5</sup> J. R. Fessler et al., "Laser Deposition of Metals for Shape Deposition Manufacturing", *Proc. Solid Freeform Fabrication Symposium Proceedings*, 1996.
- <sup>6</sup> F.G. Arcella et al., "Materials Characterization of LaserCast<sup>TM</sup> Titanium", *Advances in Powder Metallurgy and Particulate Materials 1996*.
- <sup>7</sup> S. Das et al., "Direct Selective Laser Sintering of High Performance Metals for Containerless HIP", *Advances in Powder Metallurgy and Particulate Materials 1997*.
- <sup>8</sup> S. Das et al., "Direct Selective Laser Sintering and Containerless Hot Isostatic Pressing for High Performance Metal Components", *Solid Freeform Fabrication Symposium Proceedings*, 1997.
- <sup>9</sup> R. Knight et al., "Metal Processing Using Selective Laser Sintering and Hot Isostatic Pressing", *Solid Freeform Fabrication Symposium Proceedings*, 1996.
- <sup>10</sup> G. Zong et al., "Direct Selective Laser Sintering of High Temperature Materials", *Solid Freeform Fabrication Symposium Proceedings*, 1992.
- <sup>11</sup> D. W. Freitag et al., "Laser directed fabrication of full density metal articles using hot isostatic pressing", U.S. Patent 5,640,667, 1997.
- <sup>12</sup> R. M. German, *Powder Metallurgy Science*, Chapter 7, pp. 57, MPIF, 1994.
- <sup>13</sup> American Society for Testing and Materials, ASTM B 367-93 Standard Specification for Titanium and Titanium Castings, 1993.

<sup>14</sup> American Society for Testing and Materials, ASTM B 348-95a Standard Specification for Titanium and Titanium Alloy Bars and Billets, 1995.

<sup>15</sup> ASM, Metals Handbook Ninth Edition, Volume 3 Properties and Selection, ASM International, 1993. pg. 388.

<sup>16</sup> American Society for Testing and Materials, ASTM E 1409-97 Standard Test Method for Determination of Oxygen in Titanium and Titanium Alloys by the Inert Gas Fusion Technique, 1997.

<sup>17</sup> C.F. Yolton, Crucible Research, Personal Communication, 1998.



# Feasibility of Fabricating Metal Parts from 17-4PH Stainless Steel Powder

Guohua Wu\*, Noshir Langrana\*, Sriram Rangarajan\*\*,  
Rajendra Sadangi \*\*, Amhad Safari\*\* Stephen C. Danforth\*\*

\* Department of Mechanical and Aerospace Engineering, Rutgers,  
The State University of New Jersey, 98 Brett Road, Piscataway, NJ 08854.

\*\* Department of Ceramic and Materials Engineering, Rutgers,  
The State University of New Jersey, Piscataway, NJ 08854.

## Abstract

17-4 PH stainless steel is known to provide an attractive combination of high strength and corrosion resistance. In this research, the feasibility of SFF fabrication of high density parts using 17-4 PH powder is examined. A part can be fabricated using both indirect and direct methods. The indirect method includes making a negative RTV mold, making compounded material using ECG binder and stearic acid with the metal powder, and pouring the compounded material to get a green part. This is followed by binder burn out(BBO) and sintering cycles. The direct method uses Fused Deposition of Metals(FDMet). In FDMet, the 17-4PH powder is compounded with a FD binder and extruded into filaments, followed by part building, BBO and sintering. The initial results of the indirect method of fabrication produced 91% theoretical density of 17-4 PH parts with Vickers hardness of 223.

**Keywords:** Rapid Prototyping RTV mold 17-4PH FDMet Binder Burning Out(BBO) Sintering

## Introduction

Solid Freeform Fabrication emerged about ten years ago, due to the advantage of making complex parts with low cost and high speed. It is becoming one of the most important new techniques in the manufacturing area. Although there are many advantages, there exists some drawbacks. For example, in many cases, a part can be used as a physical prototype, but can not withstand high service stresses and temperature. Various efforts have been focused on developing new process to make high strength, low cost parts with SFF, such as DTM Rapid Tooling[1], MIT 3DP[2], and Fused Deposition of Ceramic[3].

The objective of this study is to develop an efficient method to fabricate metal parts quickly with low cost. Two methods are adopted in the research, one is the direct method or Fused Deposition of Metal(FDMet), and the other is RTV Molding method. Building a metal part by FDMet is our final goal, the indirect method is used as an initial step to determine the right material composition. In this paper, full details of this RTV Molding technique are reported.

## Experiment Procedure

Two different approaches are under investigation for manufacturing functional metal components referred to as the "direct" and the "indirect" techniques as Fig.1. The direct method ( Fused deposition of metals, FDMet) uses metal particle loaded thermoplastic filament as the material feedstock, fed via counter rotating rollers into a heated extruder, referred to as a liquefier. The filament acts as the piston to extrude the molten metal loaded polymer material out of a 250 micron to 635 micron diameter nozzle onto a z-stage platform, where the material cools rapidly and bonds to adjacent layers. The material deposition rate and liquefier x-y position, etc., are controlled by the computer. For powder metal parts, the binder is subsequently removed in a thermally driven process called binder burn out (BBO), then sintered to full density. In the indirect method or RTV Molding method, a STL file is generated from the desired part, the file is delivered to the SLA or FDM machine which builds a positive prototype. The RTV mold is made by pouring a molding material around the prototype. This is done by mixing the metal powder with the ECG2 and stearic acid, pushing the mixture into the RTV mold. The binder removal and sintering process of the indirect method are the same as those of the FDMet.

The development of the direct and indirect SFM processes for hard tooling are going on simultaneously. Several steps in each of these processes have been accomplished. The processing details and the preliminary results are described below.

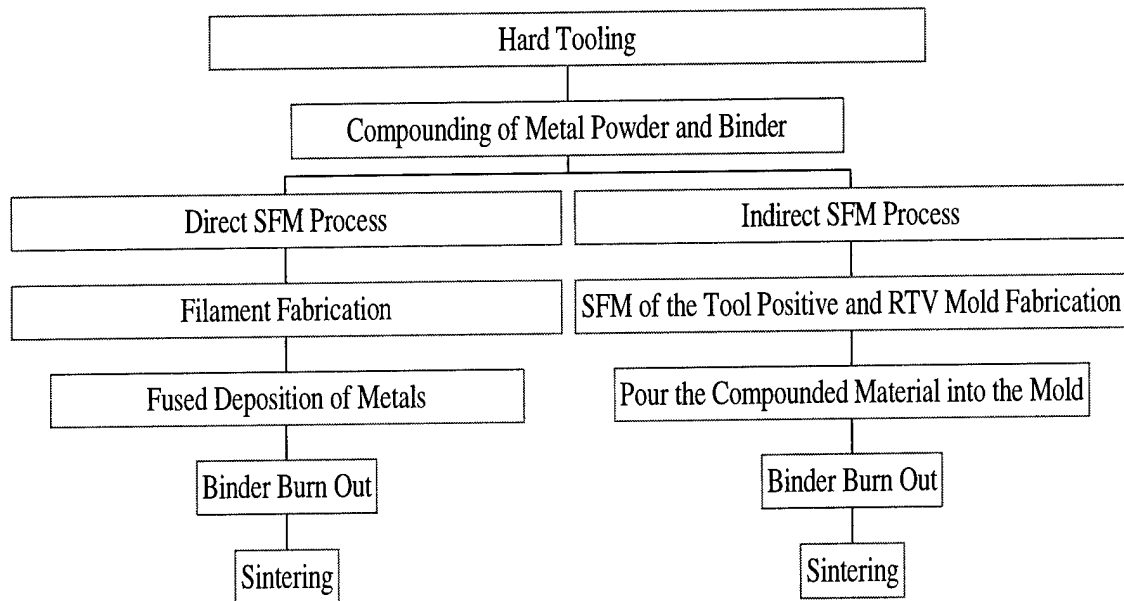


Fig1. Flow chat of FDMet and RTV mold methods

## Materials

The material used in this research was 60% volume 17-4 PH stainless steel(-10 microns water atomized), provided by Ametek company in PA of U.S.A. The powder particles were irregular in shape, the chemical composition is Fe-0.031C-4.39Ni-15.82Cr-0.12Si-0.21Mn-

3.78Cu-0.014S-0.22Cb-0.61O-0.02P-0.09N, and its particle size distribution (as provided by the manufacturer) is given in the Table 1.

Table 1. The size distribution of the -10 microns 17-4PH SS powder

Microns	Percent(less than)
62	100.0
44	100.0
31	96.2
22	81.7
16	59.6
11	37.9
5.5	10.3
3.9	3.0

The binder used in this research was ECG2(Electro Ceramics Group binder #2), which was developed by the Ceramic and Materials Engineering Department of Rutgers University[4].

Stearic acid is a common surfactant for metal powder, although there are some other surfactants that could be used such as zinc stearate or magnesium stearate.

### **Feedstock preparation**

In order to get full dispersion of the stearic acid, ball milling was used. First some grinding media and a certain volume percent of metal powder were added into a bottle, with some stearic acid added to acetone. The mixture was full dissolved and then added to the bottle, after the mixture was ball milled about 20 hrs, it was then passed through two sieves, one to remove the grinding media and one to sieve the powder, followed by drying.

The binder and coated powder are mixed using a HAAKE torque rheometer at a temperature of 165°C. First, all of the ECG binder is added to the hot mixer and melted. Next, the stearic acid coated metal powder is added into the mixer in four sub-steps (40%, 30%, 20% and 10% of the total amount of metal powder) at 15 minute intervals. After all of the metal powder is added, and when the torque in the mixer is constant, i.e. reaches a steady state value, the temperature was lowered to 130°C, after another hour a uniform compound is achieved. The whole process usually takes three to four hours. After the compounding is completed, the compounded material is removed from the mixer, and grounded into small pieces.

This granulated, compounded material is now ready either for RTV molding of the part in the indirect method, or for fabrication of filament (by extrusion) for direct part fabrication by FDMet.

### **RTV mold making**

RTV tooling is a process which creates a soft rubber mold from an original positive prototype structure. In this work, the desired positive tool is made by stereolithography. The

silicon material of the soft mold can withstand the 100-200°C temperature of the metal filled binder formulation that will be cast into the mold. In addition, the fabrication process is fast, accurate and inexpensive. The RTV mold process used in this project is as follows:

- (1) Prepare the base, curing agent and a container.
- (2) Stick wax on the bottom of the original positive part so that the part can be attached to the box, and prevent creation of air bubbles.
- (3) Record the weight of the base mold material (approximately 40 g), use the curing agent (10% by weight of the base), stir the base and agent, and then put them into the vacuum oven to remove any air, pour the material around the part, making sure that the part is completely covered.
- (4) Put the container (which now holds the uncured mold material and part) into the vacuum oven again. This is performed to remove any air trapped in the mold material. Continue this process until all of the air bubbles are removed.
- (5) The mold material is fully cured by keeping it at room temperature and 1 atm pressure for 24 hrs, then the positive part is removed from the cured mold material.

After the RTV mold is ready, the compounded material is poured into the mold to form a green part.

## De-binding and Sintering

Before sintering, the green part must be processed through a treatment to extract the organic binder. Based on earlier work, a heat treatment approach was developed which has successfully removed the binder from the green 17-4PH metal part. The development of an appropriate heat treatment to burn out the binder requires that we have a good understanding of weight loss and shrinkage characteristics of the material system during heating. Stresses can develop in the parts during heating if the binder decomposition gases evolve in the interior of the component without a sufficiently easy diffusion path to the surface. During the burn out process, the green part was buried in a very high surface area carbon powder to aid in the removal of the binder through wicking (via capillary suction) at low temperature. An optimized binder burnout schedule will be determined by measuring the shrinkage and weight loss after a finite hold at various temperatures, followed by furnace cool to room temperature.

The BBO schedule for hard tooling was derived from the current PZT project [4]. It is a slow process. Following the BBO process, the part is sintered in hydrogen. The sintering can be performed at temperatures as low as 1121°C, but higher temperatures will yield better mechanical properties. The cooling process can not be slower than what it would be in still air, and the part must be cooled to below 32°C prior to precipitation hardening heat treatment process[5].

Table 3. Sintering schedule for 17-4 PH metal parts

Temp(°C)	Rate	Time (Hrs)
20-1260	5°C/min.	4.1333
1260	hold 30min.	0.5
1260-20	Natural cooling	~ 5

## Results

Two applications were investigated in this research, a wrench part and a lug fit part. The wrench part was first made, then the process was improved and a more complex lug fit part was made successfully.

### Fabrication of the wrench part

The wrench part was used to demonstrate the process. A CAD file was generated in IDEAS-5 software. .STL file was exported to the Maestro software of Stereolithography machine(SLA-190). The generated data files were transferred to the control computer to run the machine and build the SLA wrench part.

The RTV wrench shown in Fig.2 mold was made after applying RTV molding process on the SLA wrench part as in Fig.3. The green wrench as Fig.4 was made by pouring the compounded material into the RTV wrench mold. The de-binding process took a long time and very fragile mechanical properties the BBO wrench part were found. The sintering process was done by putting BBO part into a Alumina tube at high temperature as Table 3. The reason the sintered wrench part in Fig.5 was broken is that the BBO part was so fragile as to be easily broken.

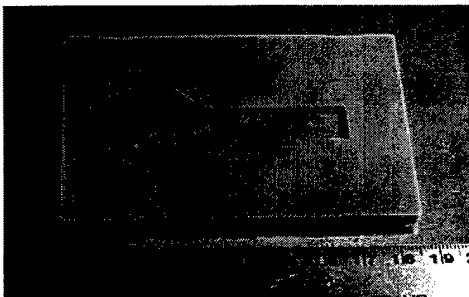


Fig.2 RTV wrench mold

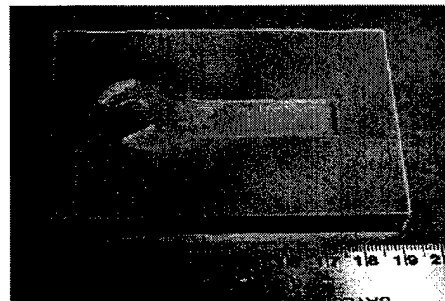


Fig.3 Demonstration of the RTV mold process

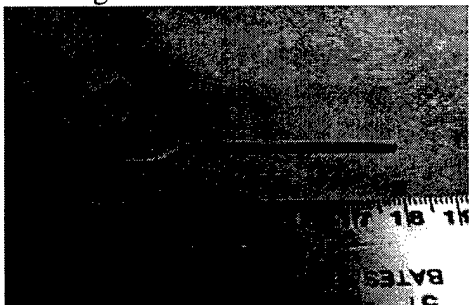


Fig.4 Green wrench part



Fig.5 Sintered Wrench part, broken during the BBO

Analyses of the sintered part were performed. The hardness of the sintered metal is B97 or Vickers hardness of 223. The microstructure consists of ferrite grains with ASTM grain size of 10-11 as Fig.6. It was also found that the sintered part was not full dense as Fig.7. The porosity is

approximately 8%-9%. The distribution of the Pore Size is as Table 4. The Pore Size Range is 0.5-5.5 microns.

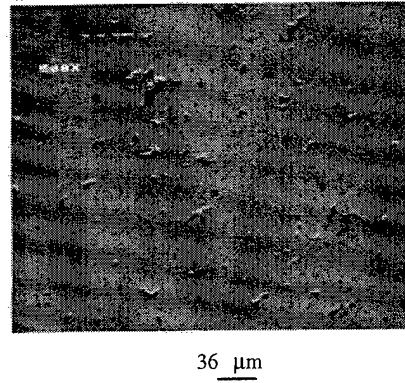
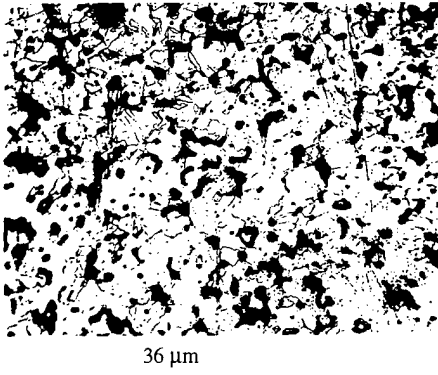


Fig.6 Microstructure of sintered part. Fig.7 Pore size graph of the sintered part.

Size, Microns	Distribution -#/Inch <sup>2</sup>
Less than 1.0	3270
1.0-5.0	1048
More than 5.0	635

### Fabrication of the lug fit part

Since the wrench was not a complex geometry, further efforts were made to fabricate a more complex part, the lug fit part which was required by the research program.

Since the lug fit part is hollow inside, care must be taken during the RTV mold making process. Since the process was done in a vacuum, if the SLA part was not attached to the bottom of the container firmly, the SLA part would rise in the RTV material, and RTV material would fill inside the lug fit part. A de-molding agent was also preferred because it was very hard to remove the SLA lug fit part from the mold. The mold was cut in half, and the SLA lug fit was removed. A piston RTV positive mold was also made to push the compounded material into the mold. The SLA lug fit, Green part, BBO part and sintered part can be seen in Figures 8 to 11. The dimension of the part in various stages are shown in Table 5.

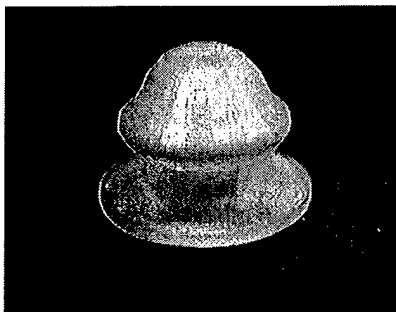


Fig.8 SLA lug fit part

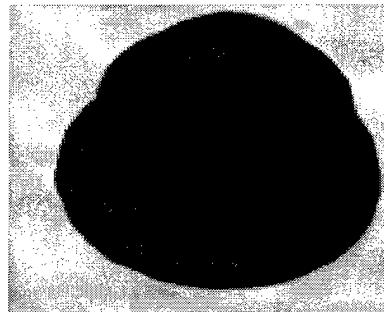


Fig.9 Green lug fit part

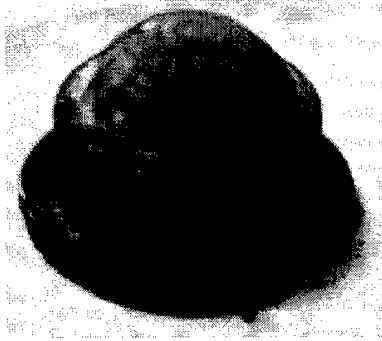


Fig.10 BBO lug fit part

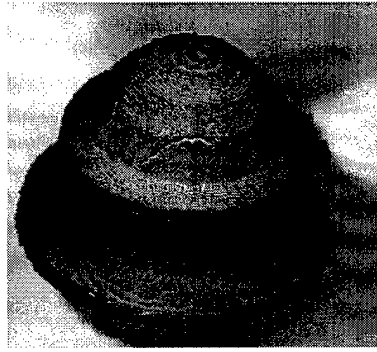


Fig.11 Sintered lug fit part

Since the lug fit part was hollow inside, additional supports were added when it was put into the sintering oven. Initially, no additional support was used and the part collapsed during the sintering, after correcting the problem, a successful Lug fit part was fabricated as shown in Fig.11 .

Shrinkage of the green to sintered part was measured. The results are shown in Table 5. The maximum shrinkage of 8.64% in diameter in the sintered part was found. The shrinkages in all three dimension were similar. The shrinkage effect on the final dimension of the part can now readily be incorporated into the whole design process to gain higher accuracy.

Table 5 Shrinkage Measurement Results

	SLA	GREEN PART *	SINTERED PART*
Inner Diameter(in)	0.466	0.471(+1.07%)	0.430(-7.7%)
Middle Outside Diameter(in.)	1.053	1.059(+0.57%)	0.962(-8.64%)
Bottom Outside Diameter(in.)	1.353	1.368(+1.1%)	1.245(-7.98)
Height(in.)	0.935	0.974(+4.17%)	0.880(-5.8%)

\* The data in the ‘()’ is the increase/decrease percent with respect to the SLA PART.

## Conclusions

The present experiment work showed that using 17-4PH metal powder to fabricate a part directly and indirectly is very promising. From the results, the following conclusions can be drawn as follows:

- (1) Materials for the hard tooling formulation were investigated, SS 17-4PH with ECG2 binder and stearic acid as a surfactant.
- (2) RTV mold development for 17-4PH SS powder has been demonstrated. Several prototype hard tool structures have been fabricated and are being evaluated.
- (3) Compounding of SS 17-4PH with ECG2 has been performed and the investigation on the filament fabrication is underway.

## Acknowledgments

This research reported here has been performed towards the partial fulfillment of the requirements for a thesis of the first author. The authors would like to thank the New Jersey

Commission of Science and Technology for the financial support under Grant #97-2890-14 through the NJIT Multi-Lifecycle Engineering Research Center Program. Also the authors would like to thank Drs. Reggie J. Caudill and Sanchoy Das, NJIT for their cooperation.

## Reference

- [1] Emanuel Sachs, Samuel Allen, Honglin Guo, "Progress on Tooling by 3D Printing: Conformal Cooling, Dimension Control, Surface Finish and Hardness", Proceedings of the solid freeform fabrication symposium, The University of Texas at Austin, Texas, Aug. 11-13,1997.
- [2] R. Clancy, V.Jamalabad "Fused Deposition of Ceramics: Progress Towards a Robust and Controlled Process for Commercialization" Proceedings of the solid freeform fabrication symposium, The University of Texas at Austin, Texas, Aug. 11-13,1997.
- [3] Suman Das, Martin Wohler, Joseph J. Beaman, "Direct Selective Laser Sintering and Containerless Hot Isotatic Pressing for High Performance Metal Components", Proceedings of the solid freeform fabrication symposium, The University of Texas at Austin, Texas, Aug. 11-13,1997.
- [4] Thomas McNulty, Farhad Mohammadi, "Development of a Binder Formulation for Fused Deposition of Ceramics(FDC)", Proceedings of the solid freeform fabrication symposium, The University of Texas at Austin, Texas, Aug. 10-12,1998.
- [5] John H. Reinshagen, John C. Witsberger," Properties of Precipitation Hardening Stainless Steel Processed by Conventional Powder Metallurgy techniques", International Conference and Exhibition on Powder Metallurgy and Particulate Materials, May 8-11, 1994, Toronto, Canada.

# INDUSTRIAL USE OF DIRECT METAL LASER SINTERING

Olli Nyrhilä, Juha Kotila, Jan-Erik Lind, Tatu Syvänen

Electrolux Rapid Development

Aholantie 17

FIN-21290 Rusko

Finland

Tel. +358-2-4365611

Fax. +358-2-4399620

Email: [olli.nyrhila@notes.electrolux.fi](mailto:olli.nyrhila@notes.electrolux.fi)

## Abstract

The Direct Metal Laser Sintering (DMLS) process was developed a few years ago by Electrolux Rapid Development (ERD) and EOS. DMLS has now been in commercial use for more than two years at Electrolux and also at other European prototype manufacturers, and the machine itself is also available for purchase.

This paper describes the development of the process in particular the industrialization of DMLS and how it has changed the prototype mould manufacturing process at Electrolux. Issues concerning the materials used are also described, as well as the necessary post-treatment methods in prototype mould manufacturing. Several case studies, from various injection mouldings to pressure die-casting, are presented.

## 1. Background

Direct Metal Laser Sintering was commercially introduced in 1996. ERD received the first laboratory machine at the beginning of 1995. ERD had conducted the first laboratory tests even earlier than this, but a more professional development of DMLS as an industrial manufacturing method started when the first laboratory machine was received.

Some of the earlier research work on materials for DMLS has been reported previously in (1), however the history of the powder concept dates back to the end of the 1980's. This basic idea has been briefly described in (2), and more thoroughly in (3). Direct laser sintering of the proprietary bronze powder has been studied in one M. Sc. work (4). A more general survey of the laser sintering of steel powders is studied in one additional M. Sc. work (5).

Apart from research and development work on materials used in direct laser sintering, the major task of the research team at ERD has been to develop new applications for laser sintered inserts. This work includes everything from surface finishing to mould concepts in the manufacture of injection moulds. The research group has been particularly successful in

being able to apply research and development results to in-house prototype production – one of the tasks set out for the group.

## **2. DMLS Characteristics**

### **2.1. Net-Shape Operation**

The main goal of DMLS is net-shape operation. This aim was set, in fact, before rapid prototyping, because the sintering method which DMLS is based on is a net-shape furnace sintering process. There are several reasons why the net-shape process is beneficial and in some cases essential:

- It is a simple operation: no shrink factors or compensations are needed
- Accuracy
- The potential to build large parts

The first argument is perhaps somewhat outdated, because of the ease in manipulating solids in computer models, but it is still an additional operation to take shrinkage into account in mould manufacturing. In layer manufacturing processes shrinkage is often different in the x, y and z –directions and with free-formed surfaces this can create problems.

Accuracy is probably the most important reason why net-shape operation is recommended. Shrinkage almost never occurs uniformly and this is why all rapid prototyping methods that include shrinkage can meet the given tolerances only up to a certain length or thickness (6). Size limits in some rapid prototyping methods are due to this fact.

The third argument can actually be derived from the second point. If no shrinkage is associated with the process, the only limitation for the part or mould size is the size of the manufacturing machine itself. In mould manufacturing with shrinking processes, apart from meeting the tolerances it is in many cases impossible to fit the mould halves together because distortions in different regions in the parting plane are not equal. If you cannot fit the mould halves together, the mould is useless.

Accuracy of the parting plane is naturally essential in mould making. In a shrinking process it is often suggested that extra material be added to the parting planes, and then milled away so that the mould halves can be accurately fitted together. What is often forgotten, however, is that the same unpredictable amount of distortion is also taking place in the cavity of the mould, and if this is also not corrected the part is simply not usable. If both parting planes and cavities are machined, why use the free-forming method in the first place.

### **2.2. Material Properties**

The properties of DMLS materials have been discussed in (2). One of the problems in dealing with porous materials is mechanical strength. Because DMLS is a net-shape sintering process, it inevitably produces porous material, which is naturally not as strong as fully dense material. Development of materials has been done after reporting in (2). Normal tensile strength of the material near mould surfaces is about 200 MPa. The properties of the material depend

strongly on the equipment used. The main factors are laser power and the quality of the laser beam.

In practice, weaker material has to be taken into account in the mould insert design. If a designer thinks that a certain detail in a mould needs stronger material, the detail in question simply has to be taken from a CAD file and made by other means. The detail is later added in the mould as a separate insert. This kind of hybrid construction is very common in prototype mould manufacturing, and normally does not cause serious problems. It is also becoming more and more common in series mould manufacturing.

Another possibility is to treat the critical regions as separate files. The detail files are then laser sintered together with the main part of the mould, but with extremely hard sintering parameters - essentially melting. As mechanical properties of the detail are then much greater than in the mould insert generally, dimensional variations in the hard sintered detail are greater and thus this approach can not be applied in cases of high volume. Combining normal direct laser sintering and melting in the detail dimension can also be preserved.

Mechanical properties can also be enhanced by infiltration. Metal infiltration is normally applied in increasing the density of sintered inserts. Unfortunately, this technique can only be used when dealing with materials that have a higher melting point, such as steel, because there are no suitable infiltrants available for bronze-based materials. There is also a risk of losing dimensional accuracy through the interactions between solid particles and the infiltrant. Mechanical properties gained after metal infiltration are comparable with the ones of the infiltrant metal itself. Normally in case of DMLS, only polymer infiltration is used, more precisely, surface infiltration because the whole volume of the insert is not filled. The purpose of surface infiltration is to enhance surface properties, not to fill all pores of the insert.

One problem associated with layer manufacturing is determining material properties. Before layer manufacturing the task was easier because everything was machined in standardized materials. In most layer technologies, the properties are different in the x, y and z -directions. In DMLS the possibility of using different parameters in predetermined three-dimensional sections of the body makes it even more difficult to characterize the properties in the conventional way.

### **2.3. Surface Properties**

One of the biggest problems in direct laser sintering methods, and also in DMLS, is the insert surface quality of the after sintering. Direct laser sintering is quite an aggressive method, a combination of sintering and melting. The sintered material, which is partly agglomerated particles, partly solidified melt pools, cannot form a very good surface directly from laser sintering. Therefore all critical surfaces have to be finished.

A special polymer infiltration can be used to enhance surface finish. This infiltration differs from conventional methods, because only pores on and just beneath the surface are filled. The method is called surface infiltration, and it uses a mixture of suitable metal particles and liquid polymer. Because the insert is porous, capillary forces drag the liquid inside the body. Particles move with the liquid deeper inside the pores and gradually close most of the pores on the surface.

After surface infiltration there are several possibilities for finishing the surface. Some prefer hand finishing, some try to apply automated NC-based methods. The quality of finish depends on the method chosen. If the quality is expressed in R scale, values of about  $0.5 R_a$  and about  $2 R_{max}$  can be reached by applying present methods. These values are subject to change because surface finishing is always undergoing intensive development.

### **3. Industrial Use**

The use of DMLS inserts, as well all other mould inserts, differs considerably from the use of the other 'conventional' rapid prototyping parts. Service bureaus dealing with rapid prototyping machines normally just deliver rp parts. As input data they get STL files. In this kind of business the value added remains low. This can also be seen in the performance of many service bureaus – they are quite vulnerable to fluctuations in demand.

#### **3.1. Traditional Mould Industry**

The plastic component industry has been strictly divided into separate fields. Some companies manufacture tools, and some mould the plastic parts. This means that the most of the industry is quite specialized, and knowledge of the entire development process is very rare.

The development of the injection mould chain can be troublesome, because the process has to be done simultaneously in several different places. If a mould maker develops a new design concept, good results cannot be achieved unless the injection moulder is deeply involved in the development. All the problems are emphasized in the production of prototype molds, because of all additional trouble associated with product development. This difficulty has been seen many times in the history of laser sintered mould inserts.

#### **3.2. Industrial Use at ERD**

At ERD the traditional way of making injection mold business was almost totally rejected years ago. This was done even before the era of rapid prototyping. ERD realized that to be effective in product development, one must be able to control the whole development chain, from component design to the manufacturing process, including all prototype-manufacturing processes.

In prototype services, all rapid prototyping and rapid tooling methods are but a small part of the prototype production process. Services provided by an rp machine should fulfill their tasks in the development process. The tasks are many and they depend naturally on the project. This inevitably leads to the fact that there is not just one right method, not even for rapid tooling.

Because ERD specializes in product development, DMLS is only one of many tools used handle a large variety of product development projects. The reason why ERD developed the DMLS was to satisfy the internal need for such a machine. The same motivation led to the development of the furnace sintering process, which DMLS is based on.

Normal DMLS project starts when a plastic component CAD-data is received. If the part is suitable for DMLS, a CAD-designer specialized in DMLS starts to design the mould. The

mould design covers both the insert and the mold itself. ERD's knowledge of the strengths and weaknesses of the DMLS process is especially important when it comes to the design of the insert.

The project manager makes the choice between different manufacturing methods. DMLS is suitable for moulds with extremely complex surfaces. It measures up very well with milling if large amounts of material have to be removed by this process. In cases where milling is impossible, DMLS is the best choice. If spark erosion is going to be the manufacturing method for the production mould, DMLS is an extremely competitive alternative.

The CAD designer provides the DMLS operator with a net-shape STL model. At this stage, the DMLS operator has numerous possibilities to alter the material properties at different regions of the insert. The parameters are adjusted so that strong material is produced at regions where maximum stress is expected. It is advantageous if the DMLS operator has knowledge of laser sintering materials. At ERD this is the case, because the laser sintering machines are operated by the DMLS materials development team.

The goal in the production of DMLS inserts is to be able to do it then net-shape. At present, it can be done with an overall accuracy of  $\pm 0.05$  mm. This accuracy is good enough in most of the injection moulding cases. The accuracy depends both on the material and also on the machine condition - particularly on the laser power. The interaction between the laser and the material varies with the power of the laser and this variation cannot be entirely compensated for by adjusting the scan speed.

After laser sintering the insert undergoes surface infiltration, as described in chapter 2.3. The aim of surface infiltration is to make polishing easier by filling surface pores. Polishing is at the moment the most human labour-intensive process in the chain, and a lot of effort is being put into improving post-treatment methods. It seems, though, that it is extremely difficult to combine good surface quality and direct laser sintering. Some surface treatment is always needed. A completely different question is whether this task can be automated or not.

The typical turnaround time of a DMLS project from receiving the component's CAD-data to the delivery of the plastic parts is two weeks. If everything goes well, smaller components can be delivered in one week. Parts that are complicated and/or large can sometimes require three or four weeks. Figure 1 shows a typical injection mould and plastic parts, suitable for DMLS. The parting planes are complicated, and an alternative manufacturing method would probably be spark erosion, which is very time consuming. This mould was used as a small series manufacturing tool, and the number of plastic parts was in the thousands.

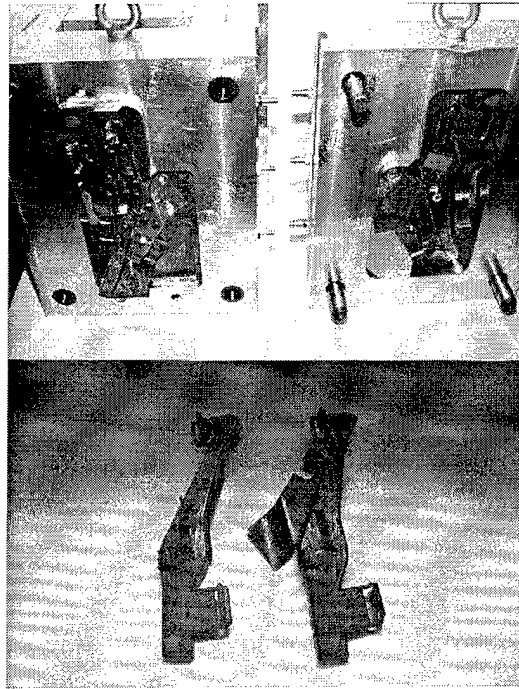


Figure 1 A Typical DMLS Mould and Plastic Parts

The maximum mould size a DMLS machine can manufacture at present is 250 x 250 x 150 mm. Larger moulds can be manufactured if the insert is divided into smaller sections the machine can handle. The injection mould is then assembled from these sections. The assembly is not very easy and it requires accurate manufacturing of the inserts. Figure 2 shows a large double injection mould. The maximum size is about one meter.

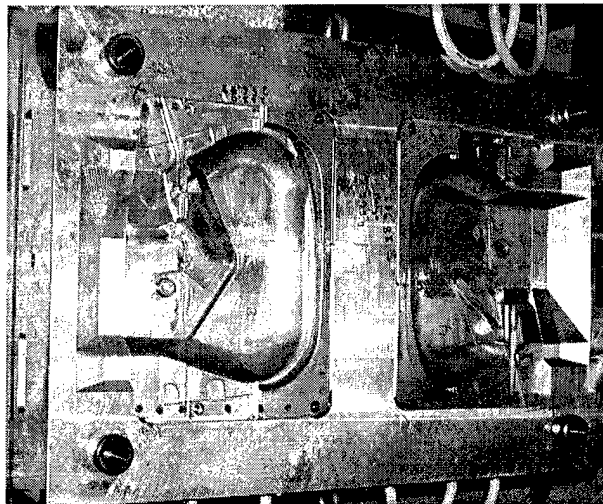


Figure 2 Large Double Injection Mould Assembled from Several Inserts

#### 4. The Future of DMLS

The suitability of DMLS in various plastic and rubber moulding processes has been proven in many projects. The next major application field will be die-casting. First testing has been done and the results hold promise.

In materials development, the next step is stronger powder material. The goal, however, is to consistently make net-shape inserts. Good results have been achieved with steel powders. Figure 3 shows a die-casting insert made from proprietary steel powder.

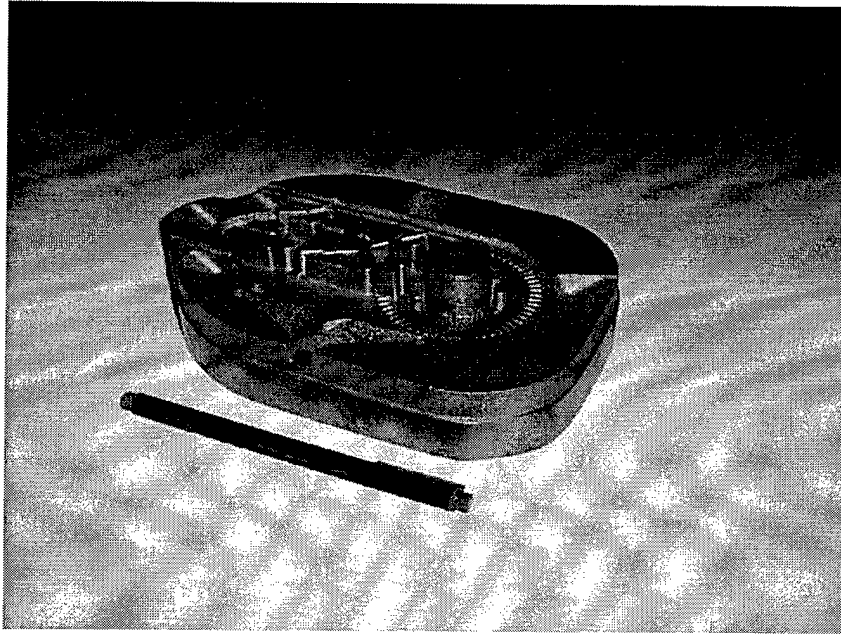


Figure 3 Die-casting Insert Made In Steel

## References

1. M. Sindel, T. Pintat, M. Greul, O. Nyrhilä, C. Wilkening, "Direct Laser Sintering of Metals and Metal Melt Infiltration for Near Net Shape Fabrication of Components", Proceedings of the Solid Freeform Fabrication Symposium, The University of Texas at Austin, 1994.
2. O. Nyrhilä, "Direct Laser Sintering of Injection Moulds". Proceedings of the 5<sup>th</sup> European Conference on Rapid Prototyping and Manufacturing, University of Nottingham, June 1996.
3. O. Nyrhilä, "Pressureless Sintering of Metal Powders", M. Sc. Thesis, University of Turku, 1993.
4. T. Syvänen, "Direct Laser Sintering of Metals – Material and Process Development", M. Sc. Thesis, Tampere University of Technology, 1996.
5. J. Kotila, "Development of Steel Based Metal Powder for DMLS-Process", M. Sc. Thesis, Tampere University of Technology, 1998.
6. P. Jacobs, "The Effects of Shrinkage Variation on Rapid Tooling Accuracy". Proceedings of the Autofact '97, Detroit, Michigan 1997.



# 3D Welding and Milling for Direct Prototyping of Metallic Parts

Yong-Ak Song\*, Sehyung Park\*, Kyunghyun Hwang\*\*, Doosun Choi\*\*, Haeseong Jee\*\*\*

\* *Korea Institute of Science and Technology KIST, CAD/CAM Research Center*

\*\* *Korea Institute of Machinery and Metals KIMM*

\*\*\* *Hongik University, Dept. of Mechanical Engineering*

## Abstract:

Welding has been used for the direct fabrication of metallic prototypes and prototype tools by several research institutes. Since welding alone is not able to deliver the accuracy and the surface quality needed for prototype tools, especially for injection molds, a combination with conventional machining is necessary. In this paper, welding and 5-axis milling are combined together for the direct fabrication of metallic parts. For welding, conventional CO<sub>2</sub> arc welding is used. Test parts with conformal cooling channels and undercuts demonstrate the technological potential of this process combination for rapid tooling applications.

## 1. Introduction

With an increasing demand to the prototype tools in regard to dimensional accuracy as well as to mechanical strength, several rapid tooling techniques have been developed and applied in industrial application [1, 2]. Although they seem quite promising, the critical issue of dimensional accuracy remains for the currently used rapid tooling techniques. Usually, each extra step required for the conversion process towards the final part implies a deterioration of its dimensional accuracy. As matter of fact, it would be best if the prototype tool can be manufactured directly without any secondary process.

For this purpose, several approaches for the direct prototyping of metallic tools are being developed. The common feature of the processes consists in direct melting of metal with a focussed laser beam, an arc or a plasma. The material used is normally supplied either in form of powder or wire. Because of the complete melting, however, the obtained accuracy as well as the surface quality of parts are generally lower than that of machined parts.

To overcome this difficulty, the process combination with a subtractive technique such as conventional milling can be an appropriate solution. This kind of process combination has been already successfully implemented in shape deposition manufacturing [3,4] and laser generating [5]. In this investigation, it is aimed to discuss some fundamental technological aspects of the process combination for its further development.

## 2. Experimental Procedure

The test facility consists of a 5-axis vertical milling machine and an arc welding equipment, **Fig. 1**. The welding gun attached to the spindle can be moved in z direction. The substrate plate is fixed on a rotary table mounted on the linear x-y table of the machine tool.

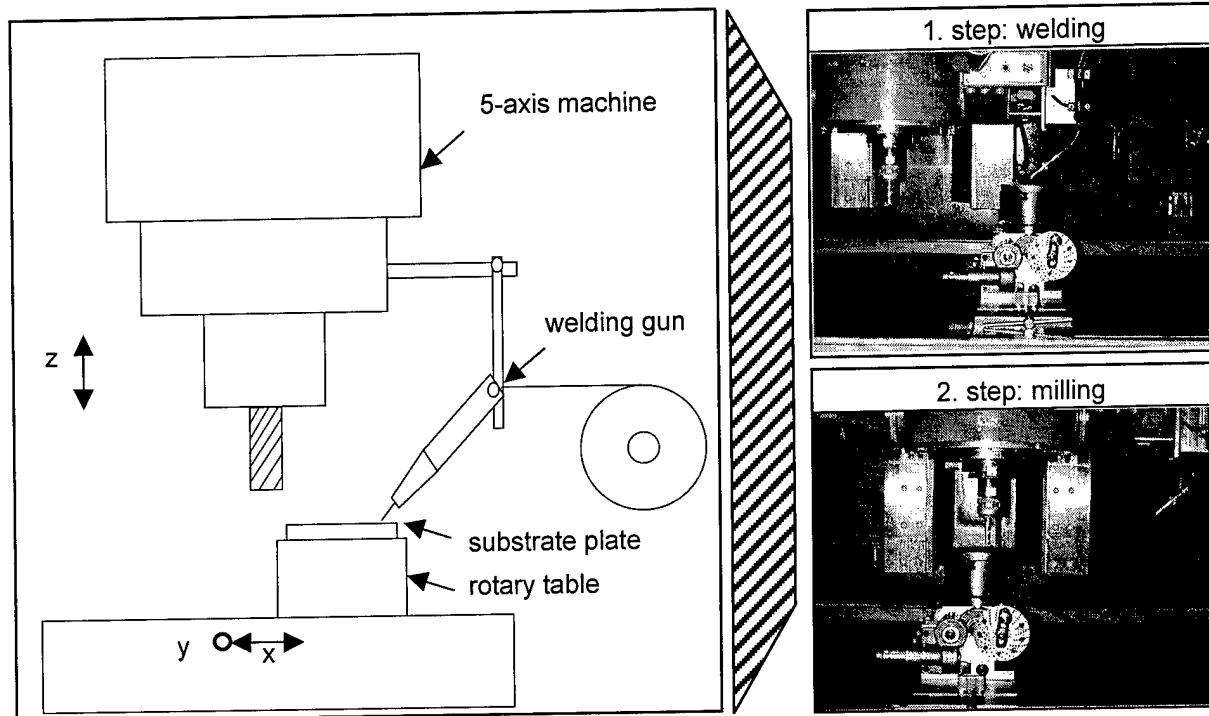


**Fig. 1:** View of the test facility

As shown on the right side of Fig. 1, the substrate plate is placed directly beneath the welding gun at first, and then moved to the milling tool after welding operation is completed. In milling operation, the top as well as the sides of the bead are machined to a specified height and width before depositing a new layer upon the previous one. This procedure repeats until part is completed.

Among the significant process parameters of 3D welding and milling are voltage and current as well as travelling speed of the substrate plate. Prior to the experiment, the relative position between the welding gun and the substrate plate and the flow rate of shielding gas were set according to the result of the previous investigation and kept constant during the experiment. For welding operation, a carbon steel wire (AWS A5.18) with a diameter of 0.9 mm was used. The substrate plate was also made of a carbon steel.

As an alternative to arc welding, laser beam welding can be used in the experiment. Since laser beam can be more precisely focussed than welding arc, more accurate parts can be built. In addition, focussed laser beam allows a less heat input into the part, thus making the part less susceptible to distortion. However, the deposition rate of laser beam welding is generally lower than that of arc welding. Besides, the utilization of laser requires a more complicated beam delivery mechanism and a more precise wire feeding system. Considering these features, laser beam welding is more suitable for manufacturing small and precise parts rather than large and bulky parts. A selection between arc and laser beam welding should be made depending on the geometrical complexity and the size of part.

### 3. Results and Discussion

#### 3.1 Single layer experiment

Starting from the single bead experiment, the influence of voltage, current and travelling speed on the formation of welding beads was investigated. Voltage and current were varied in ranges of 16V-36V and 60A-140A, respectively. Optimizing the parameters in the ranges above at a constant travelling speed allowed to deposit single connected beads instead of loose spheres. It was shown that the bead size heavily depends on the travelling speed of the substrate plate, **Fig. 2**. When the travelling speed exceeds  $v_s = 600$  mm/s, however, the height decreases only slightly down to 0.5 mm, whereas the width linearly decreases to 1.8 mm.

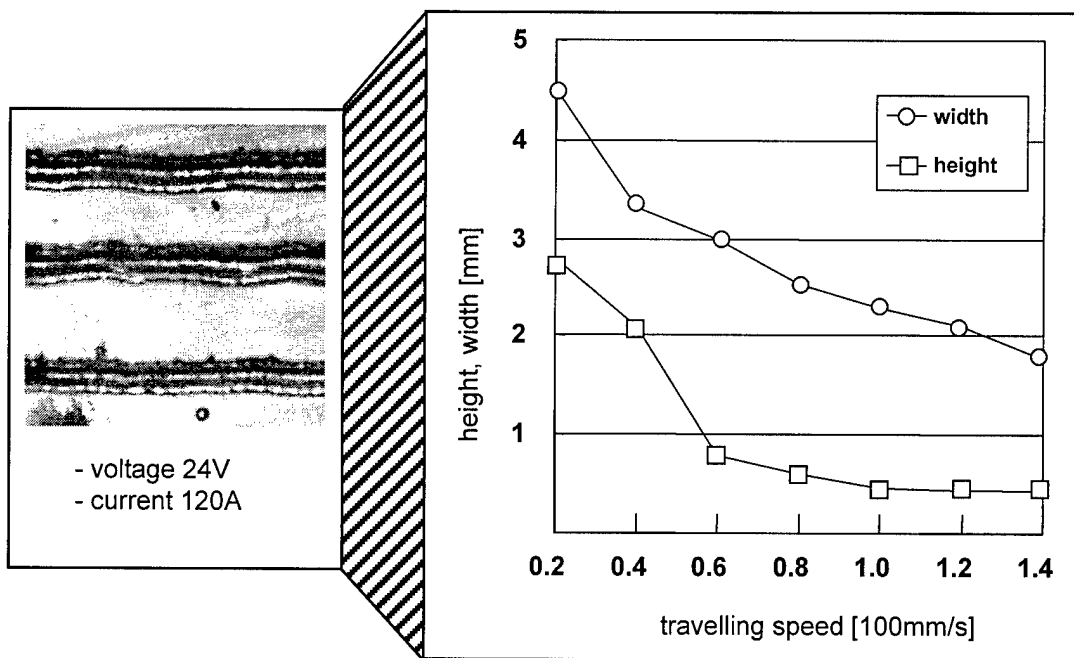


**Fig. 2:** Height and width of single beads at different travelling speeds

The result in Fig. 2 also shows that varying the travelling speed between  $v_s = 200$  mm/s and 1200 mm/s constitutes an effective method to control the size of beads. Compared to the other process parameters such as voltage and current, the travelling speed is relatively easy to change during the process. For this reason, if the bead size is required to be changed during the process, the travelling speed should be varied.

### 3.2 Multiple layer experiment

The fundamental difference between a single layer and a multiple layer is the condition of heat conduction from the processing area. In case of the single layer, the heat can dissipate relatively fast to the substrate plate, whereas in case of the multiple layer, the heat is only slowly conducted to the substrate plate. This is partly due to the reduced cross-sectional area and partly due to the dissipated heat from the previous layers. Consequently, the heat is constantly accumulated in the part until an equilibrium between heat input and dissipation is achieved. Since this accumulation of heat influences the welding result, variation of the process parameters is necessary depending on the height. An effective method to obtain a constant result would be adapting the travelling speed according to the actual height of building part.

In Fig. 3, thin walls made of 8 layers are shown without and with machining. In case of the part without machining between depositing layers, the instability of arc welding process caused a defect in the middle of the beads. Initially small in size, the defect in the second layer influenced the height of the next deposited bead and, thereby, amplified itself until a further deposition was no longer possible. Therefore, machining the bead perpendicular to z direction is not only necessary to increase the part accuracy, but also to make the process more stable for the further deposition. When milling the deposited beads perpendicular to z direction, a change of the height was observed. The first four layers had a height of around 2.8mm, while the succeeding layers showed a decreased height of around 1mm. This result is to explain with the changing cooling rate in the part, as mentioned in the previous paragraph.

The analysis of the cross-section in the wall reveals a different microstructure depending on the height. The microstructure taken from the upper area of the wall shows enlarged grains with a spherical shape (see a in Fig. 3). In each grains, a second phase can be observed which is only viable when the cooling rate is relatively low. Compared to that, the microstructure of the lower area contains relatively small grains as well as some dendrites (see b in Fig. 3). Such a microstructure results from rapid cooling due to the large amount of heat conduction to the substrate plate. In conclusion, the formation of microstructure also proves the changing cooling rate with increasing height. Therefore, an adjustment of the process parameters according to the height is necessary to maintain a homogeneous microstructure in the part. Otherwise, the part has to be heat-treated.

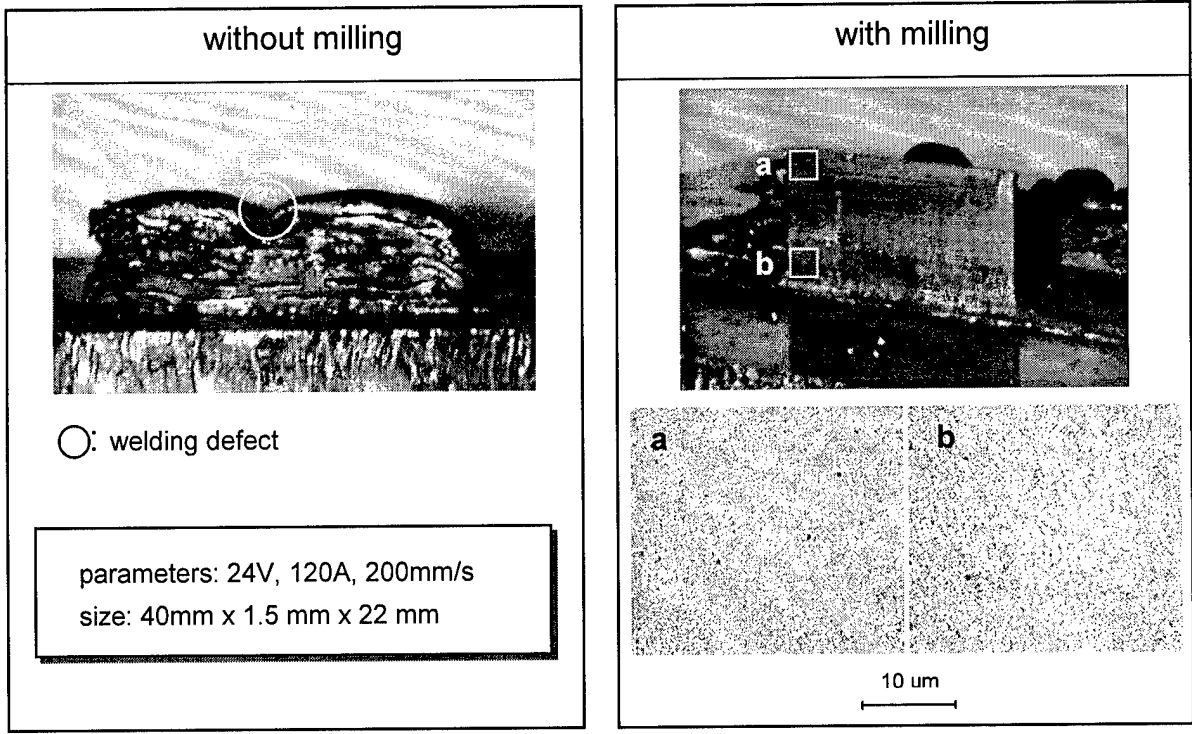


**Fig. 3:** Thin-walled parts without milling and with milling

In Fig. 4, two inclined walls built with an offset value of 0.5 mm and 1 mm, respectively, are shown. After depositing 15 layers, the walls were machined with a tilted milling tool in one operation.

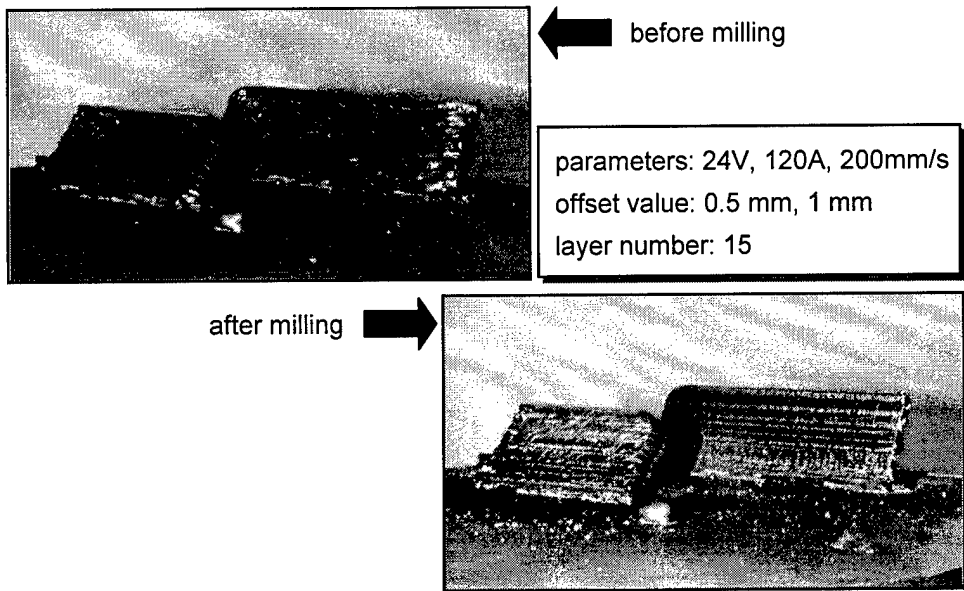


**Fig. 4:** Inclined walls with angles of 24° and 44°

Besides thin walled parts, 3D welding and milling also enables manufacturing solid parts with good surface and dimensional accuracy. In Fig. 5, a solid part fabricated with 3D welding and milling is shown. The shifting distance between each beads was 3.7mm. The test part contains an internal channel around the rectangular cavity. Theoretically, it would also have been possible to machine the internal channel of the part from a block and close the channel with welding afterwards. The cavity in the middle of the part could also have been completely machined after finishing deposition. However, it would have taken much more time because of the large volume to be removed. If the volume to remove were less than the deposited one (e.g., the walls of the internal channel were thicker than the channel itself), then machining would have been preferable to welding.

This example implies how flexible the combination of welding as additive and milling as subtractive technique can be applied for prototyping. To use the process effectively, however, an intelligent process planning is necessary taking the complexity and the size of features into consideration as well as the required mechanical properties. Based on this consideration, it has to be decided which features of the part to build with additive or subtractive method.

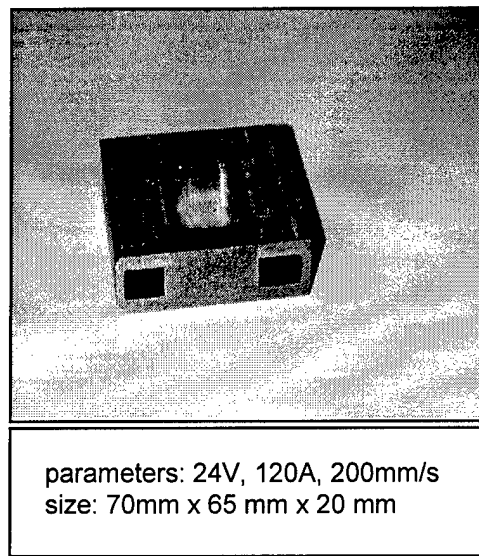


**Fig. 5:** Solid test part

#### 4. Conclusions

According to the current state of the art, dimensional accuracy as well as surface quality of rapid prototyped metallic tools are still far behind that of conventionally machined tools. To increase the quality of rapid prototyped tools, a hybrid approach comprised of an additive and a subtractive technique called 3D welding and milling is being developed.

The combination with milling operation not only increases both the surface quality and the dimensional accuracy, but it also gives a great manufacturing flexibility. To use the process combination effectively, however, an intelligent process planning depending on the part geometry and its size is a prerequisite. In addition, a process control is required as the heat dissipation changes with increasing part height.

#### 5. References

- [1] S. Ashley, "From CAD art to rapid metal tools", Mechanical Engineering, ASME, March 1997, pp.82-87
- [2] Rapid Prototyping Report, CAD/CAM Publishing, June 1998
- [3] R. Merz, F.B. Prinz, K. Ramaswami, M. Terk, L. Weiss, "Shape Deposition Manufacturing", Proceedings of the Solid Freeform Fabrication Symposium, University of Texas at Austin, August 8-10, 1994
- [4] J. R. Fessler, R. Merz, A. H Nickel, F.B. Prinz, "Laser Deposition of Metals for Shape Deposition Manufacturing", Proceedings of the Solid Freeform Fabrication Symposium, University of Texas at Austin, August 1996
- [5] F. Klocke, T. Celiker, Y.-A. Song, "Rapid Metal Tooling", Proceedings of the 4<sup>th</sup> European Conference on Rapid Prototyping and Manufacturing, Belgirate, Italy, June 13-15, 1995



## **Materials Issues in Laminated Object Manufacturing of Powder-Based Systems**

J. D. Cawley, Z. Liu, J. Mou and A. H. Heuer  
Department of Materials Science and Engineering  
Case Western Reserve University  
10900 Euclid Avenue  
Cleveland Ohio 44106-7204

### **Abstract**

Laminated object manufacturing of fine ceramic and powder metallurgy components can be carried out using either the cut-then-stack or stack-then-cut motif. With either approach, it is necessary to effect laser cutting to define layer geometry and lamination to fuse the stack into a seamless monolith. The relationship between the microstructure of the green tape used as feedstock on the relative ease of each process is reviewed.

### **Introduction**

In general, the production of components from either ceramic or metal powders requires shaping and densification to be carried out in separate unit operations. That is, first a green powder compact is formed that has the desired shape; subsequently, the compact is fired to cause densification. This is no less true when freeform fabrication is used. The shrinkage that occurs during densification is anticipated and designed into the green shaping process so that the final fired part is true to the desired dimensions. Difficulty in meeting dimensional specifications is the result of part shrinkage that deviates from expectation. Such deviations can be either systematic or random. In both cases, the source of nonuniform shrinkage is ultimately inhomogeneous packing of particles; areas of local low-density particle packing tend to shrink more than regions associated with high packing.

### **Laminated Object Manufacturing**

There are two motifs for producing green powder compacts via laminated object manufacturing; the Helisys process, which is a stack-then-cut process, and the CAM-LEM process, which employs the cut-then-stack approach. Regardless of which is employed, the two key unit operations are: laser cutting to define the geometry of the outline corresponding to each layer and lamination to produce a powder compact that is compatible with subsequent binder burnout and sintering without delamination.

### **Material Systems**

The material systems are summarized in Table 1. For CAM-LEM, tape has been produced two ways; tape casting and compression molding. Tape-cast materials are characterized by a relatively high volume fraction of porosity (as high as 20 vol. %) whereas compression molded sheets are essentially pore-free. Another important

distinction is that the polymers used in tape-casting (polyvinyl butyral-based) are precipitated from solution during casting and are amorphous, whereas the compression molded sheets used in this work are based on the BASF commercial injection molding feedstock that employ a highly crystalline polyacetal-based binder, which is melted and resolidified during forming.

These two systems have proven very flexible as carriers for a variety of inorganic powders. Tapes have been produced that yield: alumina, zirconia-toughened alumina, partially stabilized zirconia, silicon nitride, stainless steel, and iron-nickel alloys.

### **Laser Cutting**

Laser cutting in LOM processes typically employs a low-power carbon dioxide laser that couples strongly to the polymeric binder, which is melted and removed from the kerf through the action of a gas jet that is coaxial to laser. In the cutting of arbitrary outlines, it is necessary for the average cutting speed to be low (to avoid inertial effects on the cutting trajectory) and to have the speed vary, for example, to slow down when going around corners. Even if the same amount of energy is deposited per unit line length, low-speed/low-power cutting differs from the standard industrial process of high-power/high-speed because lateral heat conduction plays a larger role. In fact, experience has shown that controlling heat conduction away from the kerf region is the key to producing cuts that have the desired narrow and smooth kerfs. Machine variables are important, but it appears that a great deal of control can be effected by tailoring tape composition and microstructure.

An example of a deleterious effect of heat conduction is shown in Fig. 1a & b. This is a kerf cut in a commercial green tape that is produced using a combination of a polyvinyl chloride binder and highly volatile plasticizer. The presence of the chlorine ion, with its large radius, causes the structure to be open and mass transport is relatively easy. Therefore the plasticizer is "boiled out" of the tape on a time scale that is rapid compared to the cutting. The result is that the material immediately adjacent to the kerf is embrittled and it breaks away under the gas jet. This gives the very wide kerf and ragged edge seen in Fig. 1b. Tapes that employ polyvinyl butyral and low volatility plasticizers do not show this effect.

Given that a binder system with favorable properties is chosen, cutting characteristics can be further improved by controlling the amount of binder in the tape. Shown in Fig. 2 are scanning electron microscopy images of top and bottom of cut tapes that are similar in all respects except in the relative amounts of binder. The lower binder content corresponds to a matching increase in porosity. In both cases, the kerf is narrow and straight, but the lower binder content gives a distinctly smoother cut. Using optimized binder content also can minimize the amount of kerf taper, see Fig. 3. In general, increasing porosity of green tape can be advantageous with respect to laser cutting. This is attributed, at least in part, to the decrease in thermal conductivity of the tape.

Further evidence of the importance of binder can be seen by comparing the results of laser cutting of sheet stock based on the BASF binder to those observed with the green alumina tape. For comparable cutting conditions, e.g., velocity of 19.1 mm/s (0.75 in/s) and laser power of 10 W, the kerf width measured on the top surface is 160  $\mu\text{m}$  for the alumina feedstock versus 350  $\mu\text{m}$  for the steel feedstock. Furthermore, the taper angle of the kerf is roughly 7-8° for the alumina, but nearly 21° for the steel. Clearly, the high thermal conductivity of the dense crystalline polymer matrix creates a less favorable set of conditions for cutting.

Machine variables also play an important role. The key dimension group for lateral heat conduction away from a moving line source is the Peclet number,  $Pe = Vx/2\alpha$ , where  $V$  is the cutting velocity,  $x$  is some reference position (in our case, a position near to the kerf where temperature rise is important) and  $\alpha$  is the thermal diffusivity. Conduction effects get small when the value of  $Pe$  gets large. Given that  $\alpha$  is fixed for a given feedstock, the question becomes how large does  $V$  need to be for conduction effects to be modest enough to be neglected. One method to assess the relative role of heat conduction is to experimentally determine to minimum laser power,  $P^*$ , necessary to produce a through-cut as a function of table velocity. When conduction effects are negligible, the ratio of  $P^*/V$ , which has units of joules deposited per unit line length, should be constant. This is because it corresponds to the amount of energy necessary to remove equivalent volumes of material. Figure 4 shows such a plot for the case of an alumina-based tape. It can be seen that at high values of  $V$ , and thus  $Pe$ , the ratio does approach a constant value, whereas at low values very high relative power is required because conduction bleeds heat away from the illuminated region on a time scale that is competitive with the cutting speed. For practical cases, heat conduction effects were noted at speeds below 6.35 mm/s (0.25 in/s), but were never observed at cutting speeds above 10 mm/s.

## Lamination

The second key issue is lamination, which must serve two independent roles. Firstly, it must provide "tacking" to preserve registration during stacking that is sufficiently strong to allow subsequent handling. Secondly, the process must eventually lead to complete fusion of the stack, that is, the final part must not have any memory of the original stacked motif. It is important to note that preservation of geometry only requires the former, and therefore the latter may be achieved with supplementary processing after assembly is complete.

In prior work, an adhesive joining process was described that has proven very successful in terms of laminating a wide variety of green tapes. A variety of adhesive formulations have been developed for different feedstocks, but all involve volatile solvents. Although eminently workable on the lab scale, this can cause a problem due to potentially harmful or flammable vapors collecting in high concentration when production quantities of parts are being produced. Thus, it would be a great advantage to design a feedstock that could be thermally laminated. Recently, such a system has been developed. A technique has been developed to apply a thin coating of a heat sensitive adhesive to the surface of green tape. Tacking is then achieved by either serial application of heat and pressure (e.g., a

heat lamp followed by cold rolling) or simultaneous application of heat and pressure (e.g., a heated roller). The latter is of particular interest since it means that the tape can be directly laminated by a technology that has already been proven by the Helisys system.

The results of laboratory experiments are shown in Figs. 5a-d. These figures present scanning electron microscopy images of the cross sections of samples that each had a one-mil adhesive film and were laminated using a very small applied load at different temperatures. It can be seen that as higher temperatures are used, the film diffuses away leaving the continuous particle network necessary for good sintering behavior.

More importantly, it has been shown that if tacking is completed at a low temperature, e.g., 125°C, then subsequent annealing more elevated temperatures will cause complete fusion of the tapes, see Figs 6 a & b. This means a heated roller need only induce tacking, it need not dwell for a long time to allow complete migration of the adhesive.

To determine the feasibility of using a heated roller for laminating this type of feedstock, a set of two 3"x2" rectangular blocks was produced using a Helisys LOM2030. The following conditions were used for the roller: temperature = 140°C; speed = 1 in/s; compression = 0.015; and number of passes = 2. The feedstock laminated without difficulty and was later observed to fire to full density without delamination.

Equal success, though with a different method, has been demonstrated for steel feedstock.

### Summary

The key technical challenges of laminated object manufacturing, laser cutting and defect-free lamination, can both be engineered through design of the feedstock on the microstructural level.

**Acknowledgements:** The test of the suitability of the coated feedstock for use in a system with a heated roller was carried out by D. Klosterman in the Ohio Rapid Prototyping Process Consortium at the University of Dayton, his help (on very short notice) is gratefully acknowledged. Support for this work includes a Phase II STTR grant from the Army Research Office to CAM-LEM, Inc. and an ONR grant to CWRU (N00014-95-10107).

Table 1. Green Tape Characteristics

<u>Tape</u>	<u>Thickness</u>	<u>Solids Loading</u>	<u>Binder Content</u>	<u>Binder Type</u>	<u>Porosity</u>
Alumina	600 µm	56.6 vol.%	20.5 vol.%	PVB*	22.9 vol.%
Silicon nitride	300	51.6	29.9	PVB	18.5
Stainless steel	600	64.0	36.0	Polyacetal	none
Graphite	300/600**	42.8	21.9	PVB	35.3

\*Plasticized polyvinyl butyral

\*\*Fugitive tape for temporary support, thickness varies to match persistent material

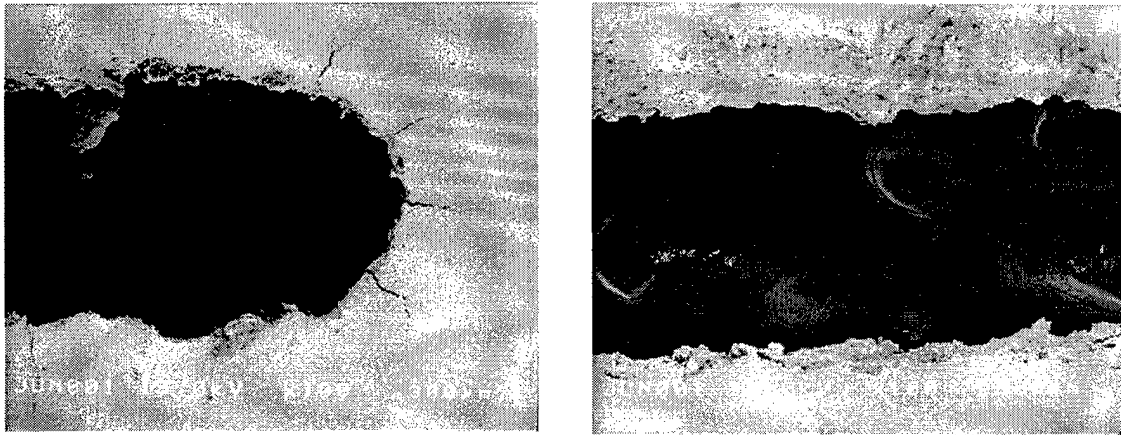
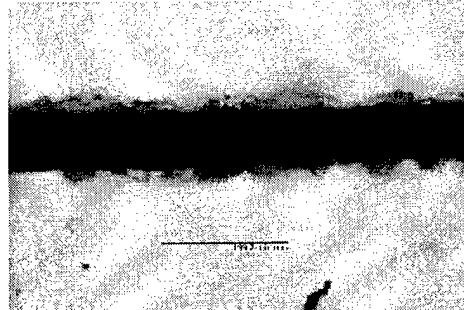
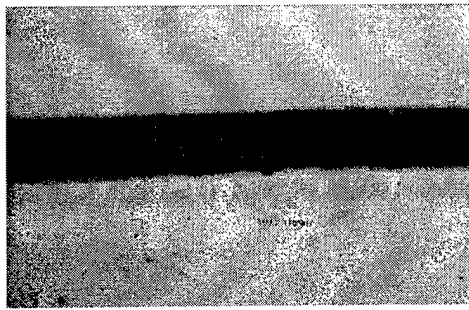
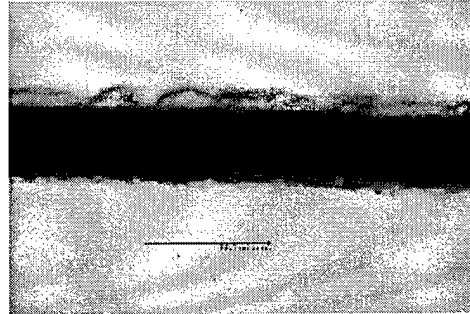
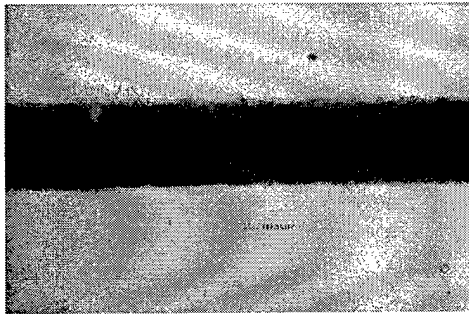


Fig. 1a & b. Scanning electron micrographs of laser-cut commercial PZT tape that contains a polyvinylchloride-based binder. The kerf width is nearly twice the diameter of the beam, it has a ragged edge, and there is cracking both ahead of the moving laser (see Fig. on right) and along the edges of the cut part.

21 vol. % Binder / 29 vol % Porosity

37 vol. % Binder / 13 vol % Porosity



200  $\mu\text{m}$

Fig. 2. Scanning electron micrographs of the top (upper row) and bottom (lower row) faces of a laser cut silicon nitride tape that were identical except for the relative concentrations of binder and porosity.

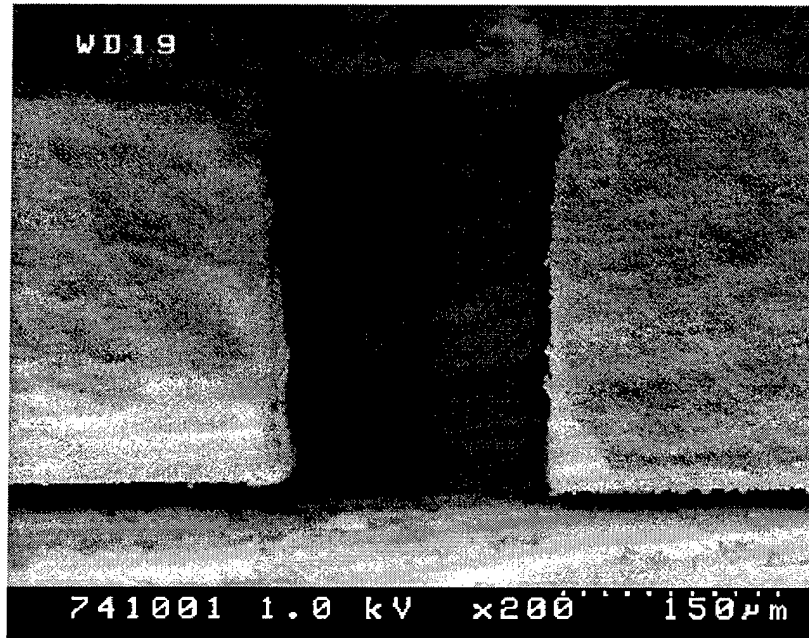
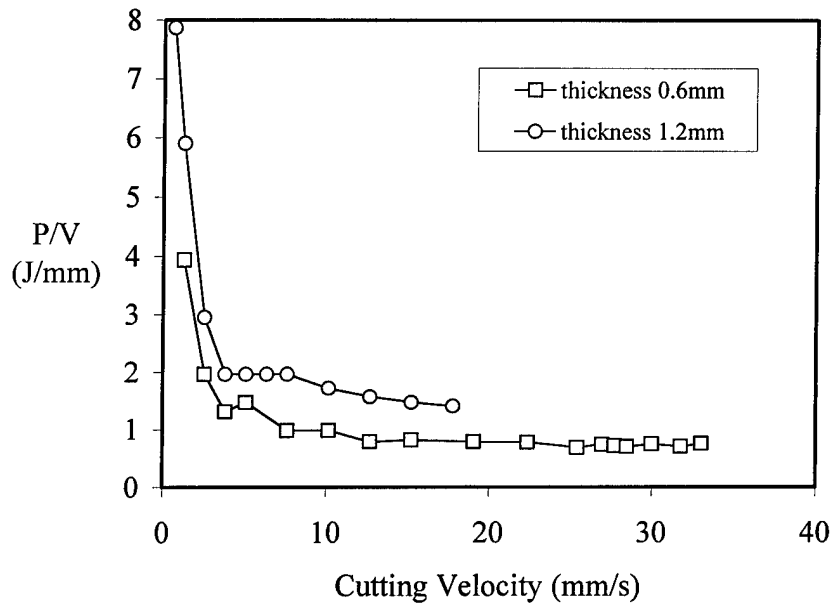
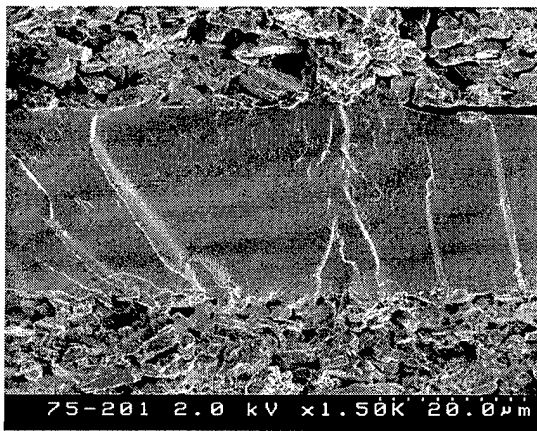


Fig. 3. Cross section of the laser cut silicon nitride tape (21% binder) shown in Fig. 2.

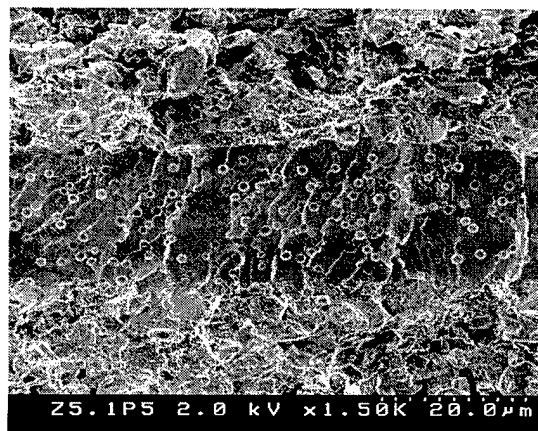


Minimum power-velocity ratio, commercial  $\text{Al}_2\text{O}_3$  tape, standing start  
 $(a=2540\text{mm/s}^2)$

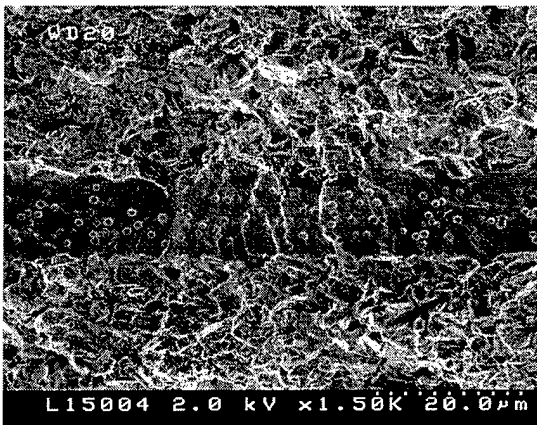
Fig. 4. Plot showing the minimum power necessary to cut through either a single or double layer of alumina-based tape. At high velocities, the power consumption reached a plateau that is directly related to the thickness being cut.



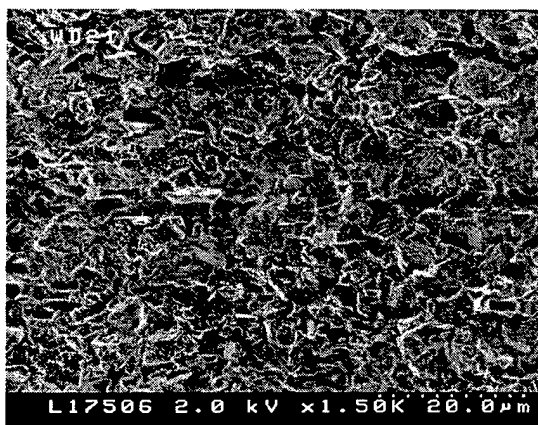
(a) 75°C



(b) 125°C

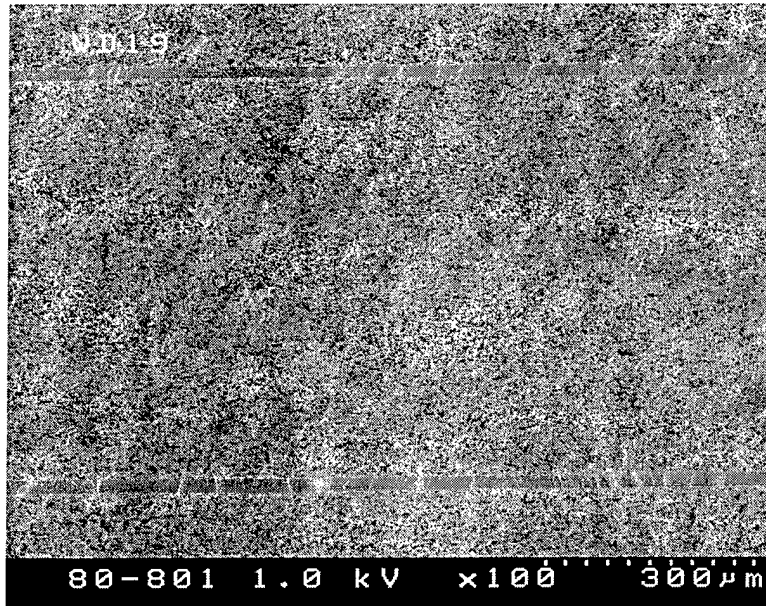


(c) 150°C

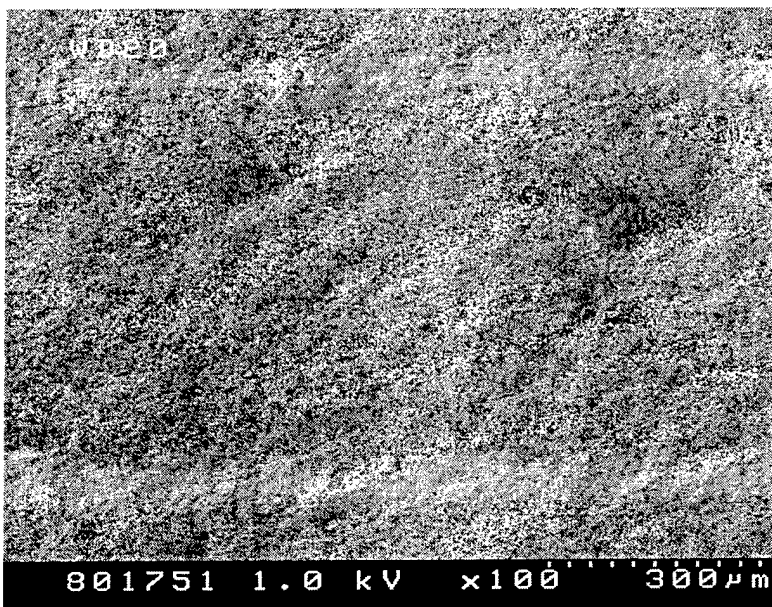


(d) 175°C

Fig. 5. Scanning electron micrographs of the cross section of alumina laminates made from polymer-coated green tape (2.5kPa for 2 hrs at specified temperatures). It can be seen that at higher laminating temperatures, the polymer layer dissolves into the base tapes giving rise to a uniform green microstructure.



(a) As-laminated sample at 125°C



(b) Heat as-laminated sample to 175°C for 10hrs

Fig. 6. Scanning electron micrographs showing the cross section of polymer-coated alumina tack laminated at 125°C, then annealed at 175°C for 10hrs. These micrographs indicate that, provided intimate contact is established during tacking, it is not necessary to apply pressure to induce the redistribution of the polymer coating.

## **Issues Associated with the Development of a Water Soluble Support Material for use in Extrusion Freeforming & Fused Deposition Modelling**

John L. Lombardi, Gregory J. Artz, Dragan Popovich, Ranji Vaidyanathan  
Advanced Ceramics Research, Inc. Tucson, AZ 85706

Sajiv Boggavarapu

University of Arizona, Arizona Materials Laboratories Tucson, AZ 85713

### **ABSTRACT**

Extrusion freeforming (EFF) and Fused Deposition Modelling (FDM) are promising techniques for fabricating complex shaped prototypes from a variety of engineering materials. Both techniques build prototypes by depositing and solidifying free standing layers of molten thermoplastic material upon one another until the final part results. Unfortunately many prototypes have complicated geometries (i.e. numerous overhangs or internal features) such that they are not easily fabricated by these techniques without the assistance of a fugitive material to support the freeformed layers. This paper discusses the development and characterization of water soluble thermoplastic support materials for use in EFF & FDM fabrication processes.

### **INTRODUCTION**

Extrusion Freeforming (EFF) & Fused Deposition Modelling (FDM) processes are established freeforming techniques capable of fabricating complex shaped prototypes by the sequential deposition and solidification of molten thermoplastic layers upon one another until the final part results. Unfortunately it is often difficult to accurately fabricate complex geometry prototypes having numerous overhangs by these techniques without the assistance of a fugitive support material to prevent slumping of the freeformed layers prior to their solidification. Current freeforming technology utilizes a support material that is initially deposited and later mechanically removed from the completed prototype. This type of fugitive support has limited utility, however, when fabricating fine featured, intricate prototypes due to its labor intensive removal process. Consequently, it is advantageous to develop fugitive support materials which are removable by solvent means. It was therefore decided that water soluble support materials would be developed since water is a non solvent for most freeformable thermoplastics coupled with its ready availability and minimal environmental concerns.

A review of the polymer literature reveals that most common commercial water soluble polymers have the drawback of either exhibiting inferior melt stability (i.e. polyvinyl alcohol & polyvinylpyrrolidone) or rapid crystallization and low cohesion (i.e. polyethyleneoxide) (1). For these reasons, most commercial water soluble polymers are not easily freeformable. Poly 2-ethyl-2-oxazoline (PEOx), however, is a lesser known commercial water soluble thermoplastic which does not suffer from the above drawbacks. PEOx is also an amorphous homopolymer ( $T_g = \text{approx. } 70^\circ\text{C}$ ) that has been shown to possess high cohesion as well as adhesion to a wide variety of substrates (2). Furthermore, light scattering studies conducted by Chen et al. on solutions of the polymer

suggest that PEOx is less strongly solvated and therefore not as sensitive to water compared to common organic solvents (3). efforts were therefore focused upon developing PEOx based water soluble support filament feedstocks which could be processed using a conventional Stratasys 1600 FDM Modeller or high pressure EFF extruder apparatus. Since the processing criteria and materials property requirements for FDM compatible feedstocks are more stringent than EFF materials, greater discussion will be made of the former.

Besides exhibiting water solubility, several other considerations should be factored into account when developing FDM compatible filament feedstock. First, the filament should possess sufficient elastic modulus coupled with flexural strength such that the filament feeds uniformly through the FDM apparatus dispensing head without buckling or fracturing. Furthermore, the feedstock should not undergo significant changes in its rheological properties or swell when exposed to ambient relative humidities ranging from 30 to 70 percent.

## EXPERIMENTAL

All water soluble support raw material batches were formulated using a Brabender mixer operating at a 60 rpm mixing speed and 140 °C temperature. After formulation, the water solubility of the batches was evaluated by measuring the amount of time require to dissolve an 8g sample in 80 ml water. Filament specimens measuring 3 ft. in length by 0.070 inches in diameter were subsequently extruded from these batches using a Haake Rheomix Model 103 Microextruder. Following extrusion the filament lengths were fed into a Stratasys 1600 FDM modeller and simple test bars were subsequently freeformed from the material. The microstructure of several filaments was characterized using a Hitachi Model S-4500 Field Emission Scanning Electron Microscope. All SEM samples were prepared by first fracturing the filament followed by sputter coating a conductive Au-Pd coating on the fractured surface prior to their characterization. Energy Dispersive X-ray Spectra were obtained from the blend microstructures using a Noran Model 5500 Spectrometer having a light element detector. Comparison was made between the intensity of the individual sample spectral peaks with those of the sputtered Au-Pd coating standard. The thermal properties of select blend compositions were determined using a Perkin Elmer Model 7 Differential Scanning Calorimeter (DSC) apparatus operating at a 20 °C/minute heating rate while scanning through a 30 to 120 °C range. Finally optimized filament support material was used in the FDM fabrication of a prototype asthma inhaler diaphragm made on a Stratasys 1600 Modeller from polyacrylonitrile-butadiene-styrene (ABS) modelling material. (See Fig. 5.) The FDM modeller operating parameters were similar to those employed in the fabrication of conventional polymer prototypes with 0.010 in. slice interval, .070 in. road width, 70 °C modelling envelope, & 270° C ABS polymer extrusion temperature.

## RESULTS

Initial research efforts focused upon blending PEOx with sufficient plasticizer and talc filler using a Brabender mixer in an effort to decrease the polymer melt viscosity

while simultaneously increasing the compression strength and creep resistance of the material. Candidate formulations were then extruded into filament test specimens measuring  $0.070 \pm 0.002$  inches in diameter by 3 ft. in length using a Haake Rheomix Model 130 microextruder. Despite the fact that these filaments were initially successfully used as processible feedstock for a conventional Stratasys Modeller, the specimens swelled significantly and proved unusable upon prolonged exposure to a humid atmosphere ( $> 40\%$ ).

Consequently research efforts were then directed towards modifying the PEOx formulation such that its sensitivity towards humidity was decreased. This was accomplished by blending PEOx with water insoluble polymers. Several PEOx blends were then formulated using a Brabender containing between 1 and 15 vol. % of both polystyrene-co-acrylonitrile (SAN) and polyphenyleneoxide (PPO) resins. SAN and PPO were blended with PEOx due to their water insolubility coupled with their reported ability to form miscible blends with the polymer (4). Filament specimens of these polymers were also prepared and evaluated as feedstock in the Stratasys FDM Modeller. Even though these PEOx blend specimens were shown to be FDM compatible and less strongly effected by humidity (particularly at SAN & PPO concentrations exceeding 10 wt. percent), the blends were insoluble in water. The insolubility of these blends was pronounced even at low SAN & PPO concentration in the blend ( $< 1.5$  wt. %).

Blends were also formulated using PEOx and 5 to 30 volume percent of a water insoluble styrenic copolymer. These blends differed from the former in that the styrenic phase was believed to be immiscible in PEOx. A compatibilizer was added to the formulation to enable adhesion between the two phases in the blend. Since the styrenic copolymer had a reported glass transition temperature greater than the FDM apparatus modeller heated envelope but below the PEOx extrusion temperature, it was believed that the styrenic phase would increase the overall softening temperature of the blend while concurrently enhancing its creep resistance at the modeller envelope operating temperature. FDM filament specimens were fabricated and were found to be readily processible by a conventional Stratasys FDM Modeller. Table I below depicts a typical PEOx/Styrenic blend composition.

Table I Typical Freeformable PEOx/Styrenic Blend Composition

Component	Concentration (Vol. %)
Talc Filler (submicron sized)	15
Poly-2-ethyl-2-oxazoline	45
Polystyrene copolymer	30
Plasticizer	7.0
Compatibilizer	3.0

The above listed blend was characterized using both SEM and DSC. Figures 1 and 2 depict microstructures of blends containing 26 and 30 volume percent of styrenic

copolymer phase respectively. Both microstructures contain spheres having an average diameter of 2 microns uniformly dispersed throughout a continuous phase. Since there appears to be a higher concentration of spheres in Fig. 2 compared to Fig. 1, it is believed that these spheres are composed of the styrenic copolymer. SEM EDS microprobe analysis spectra of the continuous versus spherical phases depicted in Figure 3 present in the blend containing 26 volume percent styrenic phase suggest that the talc  $\{Mg_3Si_4O_{10}(OH)_2\}$  filler is segregated to the PEOx phase. This is expected since PEOx has been shown to have a high affinity for siliceous mineral surfaces (5). Further support suggesting the presence of a two phase polymer blend in these samples can be found in the DSC results obtained from the sample blend containing 26 volume percent styrenic copolymer whereby two glass transition temperatures were measured in the sample as seen in Figure 4. The onset of the first Tg was measured at 45.1° C while the latter was at 113° C . These compare favorably with the Tg data obtained for the pure styrenic copolymer, compatibilizer, and blend composed of all components minus the styrenic material listed in Table II below. From these results it can be seen that there is no significant difference in the Tg of the blend components compared to its individual components.

Table II DSC Results for PEOx Blend & Individual Components

	Glass Transition Temp. (°C)
PEOx/26 vol. % Styrenic Blend	45.1, 113
PEOx Blend without Styrenic	48.7
Styrenic Copolymer	116
Compatibilizer	52.2

## CONCLUSIONS

PEOx/Styrenic copolymer blend has been successfully developed as a fugitive FDM water soluble support material. The blend is composed of a continuous phase of PEOx containing talc along with a discrete styrenic copolymer phase uniformly dispersed throughout the major phase as spherical droplets measuring approximately 2 micrometers in diameter. The similarity in Tg values between the blend and its pure constituent components suggest that there is minimal intersolubility between each of the blend components. Future research will focus upon quantitatively determining the creep and stress relaxation properties of these blends.

## REFERENCES

- 1.S. Shalaby, C.L. McCormick, G.B. Butler, *Water Soluble Polymers: Synthesis, Solution Properties, & Applications*, American Chemical Society Symposium Proc. #467 (1989)
- 2 .K.S Lin, T. Mammen, *European Patent Appl.*, EP 385747 A2 (1990)
3. C.H. Chen, J. Wilson, W. Chen, R.M. Davis & J.S Riffle, *Polymer* **35**, 3587-92 (1994)
4. J.L Pfennig, H. Keskkula & D.R.Paul, *J. Applied Polymer Science* **32**, 3657-73 (1986)
5. C.H. Chen, J.E. Wilson, R.M. Davis, & J.S. Riffle, *Macromolecules* **27** 6376-82 (1994)

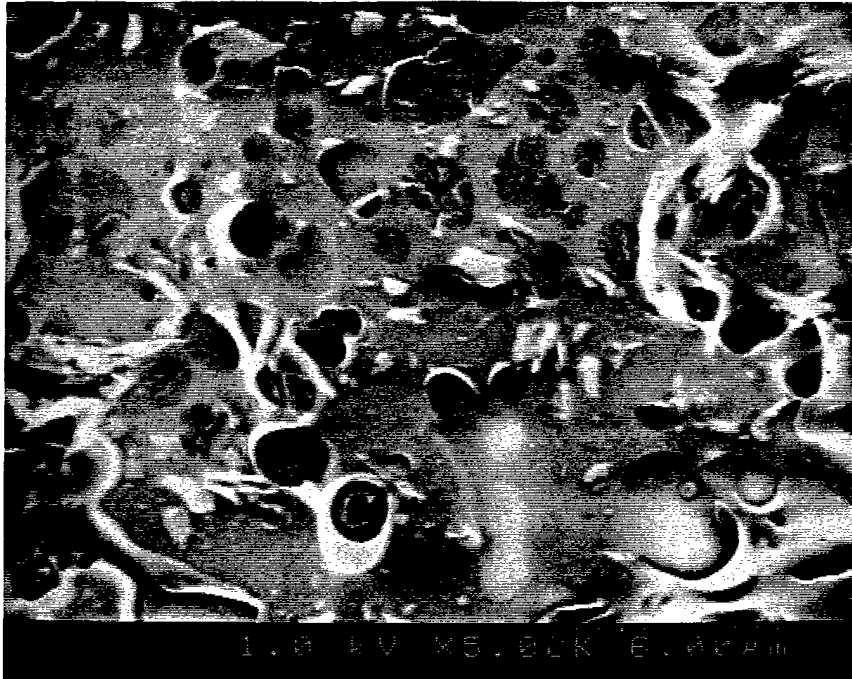


Figure 1. SEM micrograph of PEOx blend containing 26 vol. % styrenic copolymer

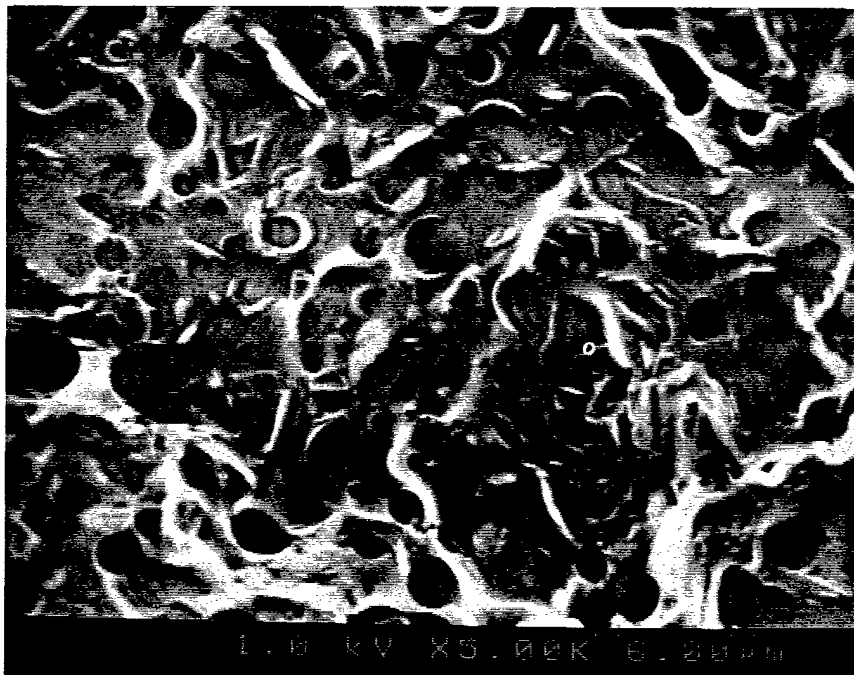


Figure 2. SEM micrograph of PEOx blend containing 30 vol. % styrenic copolymer

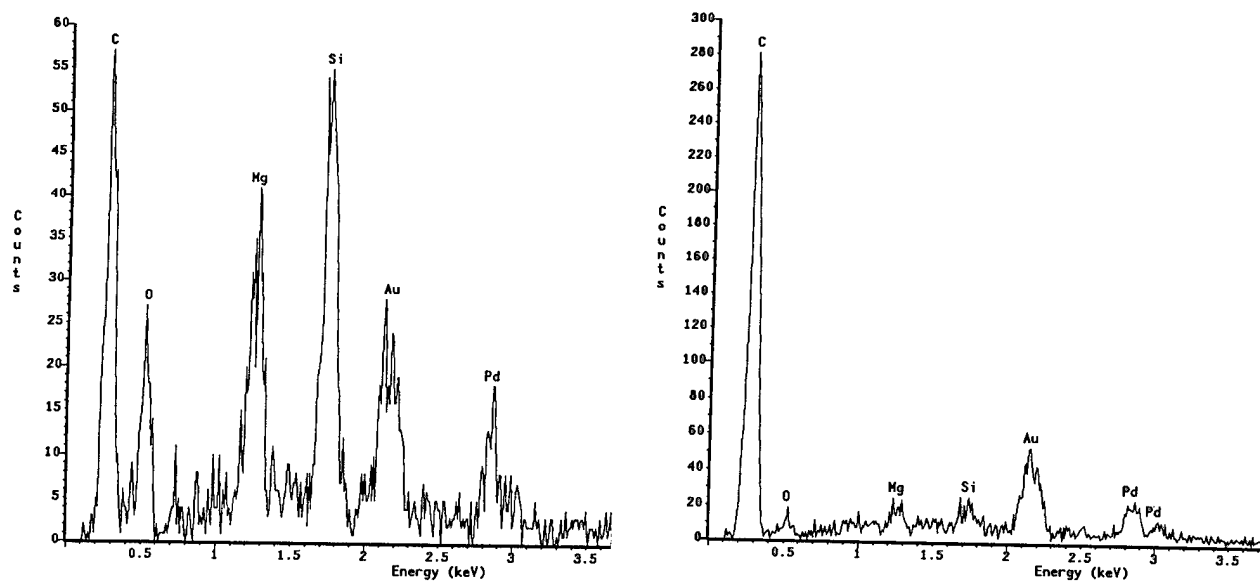


Figure 3. SEM EDS spectra of PEOx blend containing 26 vol. % styrenic copolymer microstructure matrix (left) & spherical phase (right)

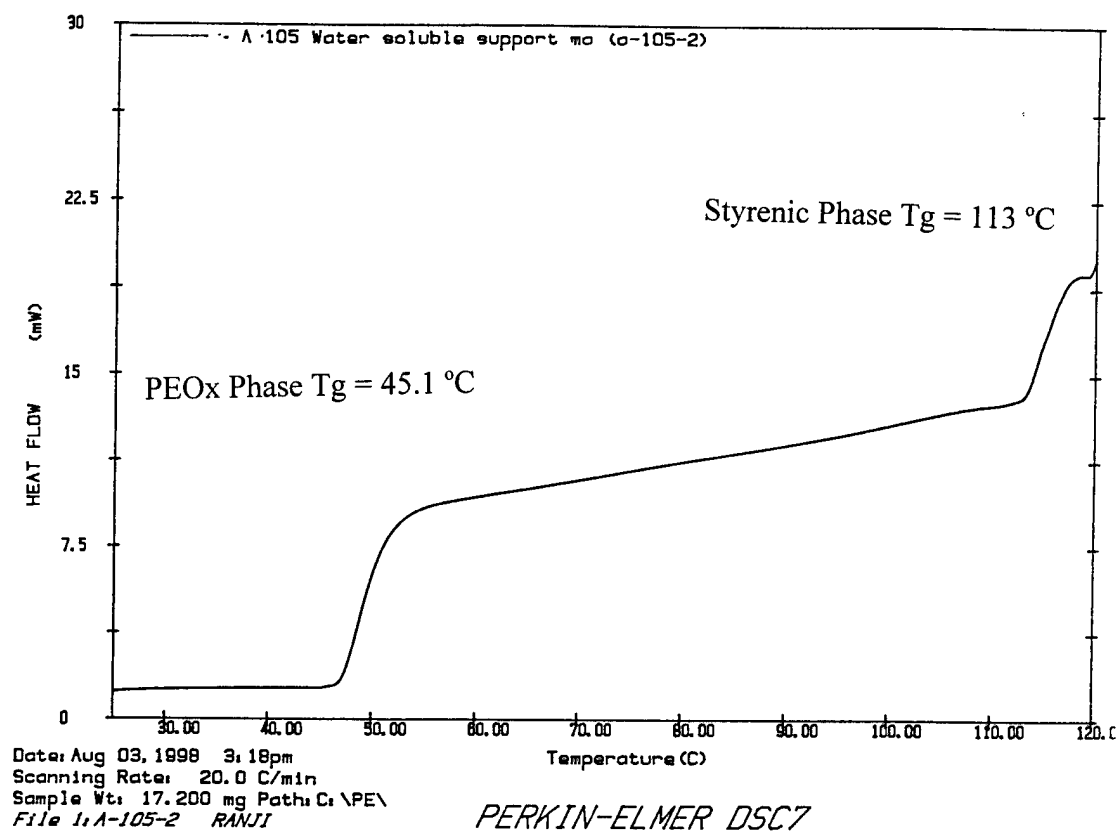


Figure 4. DSC plot obtained from PEOx/26 vol. % styrenic copolymer



Figure 5. Photograph of P400 ABS Inhaler Diaphragm Prototype freeformed using PEOx/Styrenic water soluble support by Stratasys 1600 Modeller

#### ACKNOWLEDGEMENTS

The authors would like to acknowledge ACR, Inc. and DARPA. for financial support and Mr. Gary Chandler at the University of Arizona for SEM micrographs. Messers. Brian Berkman and Brian Curley are also thanked for formulating PEOx blends. Mr. Blake R. Tennison is also acknowledged for his assistance in the FDM fabrication of the ABS prototype.



# Thermal-Expansion and Fracture Toughness Properties of Parts made from Liquid Crystal Stereolithography Resins

J. S. Ullett, T. Benson-Tolle\*, J. W. Schultz\*\* and R. P. Chartoff

The Rapid Prototype Development Laboratory and  
Ohio Rapid Prototype Process Development Consortium, Dayton, OH 45469-0130

\*The WL/MLBC, Wright-Patterson AFB 45433-7750

\*\*The Georgia Tech Research Institute, Atlanta, GA 30332-0824

## Introduction

Liquid crystal (LC) resins are a new kind of stereolithography material that can produce parts with structured or ordered morphologies instead of the amorphous morphologies that result from standard resins. The LC molecules can be aligned before cure resulting in an anisotropic crosslinked network when the laser induced polymerization "locks-in" the alignment. Previous papers have explored liquid crystal orientation dynamics [1], the effects of orientation on visco-elastic and mechanical properties [2,3], and the processing of LC resins by stereolithography [4]. This paper considers the effects of morphology on fracture toughness and thermal-expansion properties. Both toughness and thermal-stability continue to be important issues for stereolithography parts. The use of LC resins may provide a way to significantly improve performance in both of these areas, and in addition result in parts with high upper use temperatures.

## Background

### *The Role of Morphology in Fracture Toughness*

The importance of morphology and microstructure on material properties has been long recognized by materials scientists. In metals, goals of increased strength and toughness have been addressed through improving alloy chemistry or increasing purity; developing and optimizing microstructures and phase distributions; and manipulating microstructures. Manipulation of microstructures through processing often has the objective of obtaining microstructural anisotropy for some improved mechanical property.

Orientation of polymeric molecules to increase strength and stiffness has been practiced by the fiber industry and been achieved through techniques such as drawing, spinning or extruding. Pitch-based fibers employ orientation and anisotropy of morphology as well. Though pitch was used as a carbon fiber precursor and spun into filaments in 1965, the breakthrough which provided high properties came in 1973 when pitch was first transformed from an amorphous material into a liquid crystalline (mesophase) state prior to spinning into a filament. The LC pitch is then sent through a spinning and extruding operation which orders and aligns the polymer prior to it being stabilized, carbonized and graphitized. This alignment of the morphology and molecular bonds results in anisotropic properties with higher properties in the aligned direction.

Fracture toughness is a mechanical property of importance to many applications. Fracture toughness is defined as a material's resistance to brittle fracture. The fracture toughness of a material is very sensitive to morphology, anisotropy and planes of weakness [5]. A material's morphology can provide mechanisms that enhance energy absorption during fracture and hence enhance fracture toughness. Such mechanisms include those that shield the crack tip

from the full extent of the driving force, deflect the crack path, pin the crack front, shield the tip and creating a favorable residual stress pattern, or relax the crack tip stress. Microstructural alignment through processing or morphology can play a large role in such mechanisms.

Highly crosslinked thermosets typically fracture in a brittle manner at conventional test rates. The concepts of linear elastic fracture mechanics (LEFM) have been successfully applied to such materials as epoxies, acrylates, unsaturated polyesters, and vinyl ester resins. In this research, ordered (non-aligned) nematic and isotropic LC thermosets were fabricated by stereolithography and fracture toughness testing was performed with the objective of determining the effect of the liquid-crystal phase on fracture toughness.

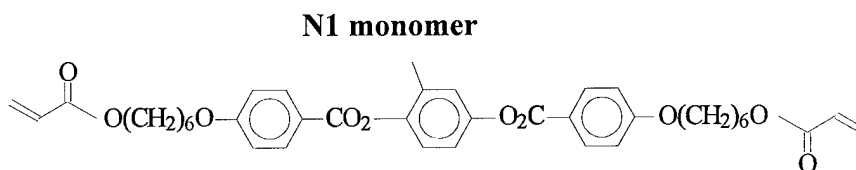
#### *The Effect of Alignment on Thermal-Expansion Properties*

The effect of molecular alignment on thermal expansion has been well studied in polymeric materials, in particular, fibers. The effects of alignment in liquid crystal thermosets has also been studied. Broer and Mol [6] studied the anisotropic thermal expansion of a series of LC thermosets. They found that as the order parameter increased with change in spacer length, the anisotropy in the linear thermal expansion increased as well. They observed a greater difference above the glass transition temperature than below it.

Thermal expansion measurements of aligned films provide benchmark values to which thermal expansion of multi-layered parts can be compared. The usual process by which films are made allows for more perfect alignment compared with the stereolithography process. The modified LC stereolithography process [7] provides the flexibility to change alignment directions from one layer to the next. This is akin to altering the fiber direction in continuous fiber reinforced composites (FRC). Properties of multi-layer LC structures that are unidirectionally aligned can be compared with the properties of aligned films to assess the overall alignment in the structures. When the layer-to-layer alignment is varied, as is done in FRCs, the in-plane thermal expansion coefficients can be minimized.

#### **Specimen Fabrication**

Multi-layer specimens for fracture toughness and thermal expansion measurements were made with the table-top stereolithography apparatus (TTSLA) using an Argon ion laser tuned to 364 nm. The laser power level was 35 mW and the beam spot size was about 200 microns. The N1 resin shown below was used for all specimens and was catalyzed with 0.5 % Irgacure 369 photo-initiator from Ciba. The N1 resin temperature was controlled at 85 °C during part build for liquid crystal parts, and 118°C for isotropic parts.



A magnet was used for alignment of the liquid crystal resin. It was mounted on a turntable so its position relative to the build platform could be manually adjusted. A T-square was used to adjust the magnet poles to be either parallel or perpendicular to the build platform. A

four minute wait period was allowed between the time the magnet was positioned and the next layer was drawn. All parts were made using an alternating draw style with a center-to-center spacing of 6 mils (0.152 mm). The layer thickness used was either 10 mils (0.254 mm) or 8 mils (0.203) depending on the part. All parts made were rectangular in shape with the short side measuring about 10 to 15 mm and the long side measuring about 25 to 30 mm.

When the magnetic field was aligned parallel to the long direction of the part the orientation was labeled 0 degrees. Likewise, when the magnetic field was aligned perpendicular to the long direction of the part, the orientation was labeled 90 degrees. Aligned parts were made for thermal expansion studies. Future work will involve fracture toughness analysis of aligned parts. The fracture toughness parts were made either in the un-aligned nematic state or in the isotropic state.

After building a part, it was removed from the platform. Any support structures attached to the part were removed before post-cure. The parts, heated to 150 °C, were post-cured using a broad-band Mercury vapor lamp. The parts were post-cured bottom-side up for two hours; and then top-side up for two hours. Thermal expansion measurements were done using a TA Instruments model 2940 TMA using a scan rate of 5°C/min.

Two draw patterns were tried for building parts in the unaligned nematic phase for fracture toughness testing: the original pattern, and the 3D Systems STARWEAVE [8] style was evaluated with a center-to-center spacing of 8 mils. Parts made from the STARWEAVE pattern were substantially flatter before postcure than parts made with the original style. However, after postcure the STARWEAVE parts were as warped as the original parts. The more open pattern of STARWEAVE leaves more material (particularly below the mid-plane of the part) to be fully cured during the postcure, which causes warpage during postcure. Parts made in the isotropic state were only made using the original draw style.

The parts for fracture toughness testing were cut into compact tension coupons on a diamond cutting wheel, then sanded to obtain plane surfaces and accurate outer dimensions. The dimensions were: length = 0.5 inch, and width = 0.48 inch. Coupon thicknesses varied between 0.10 and 0.15 inch. A drilling jig was utilized with a carbide bit to drill the holes for the compact tension specimen, and a diamond cutting wheel was used to cut the notch. The notch was cut perpendicular to the build layers. The coupons were then polished with a polishing wheel to provide enhanced surface smoothness to better view crack propagation. A starter crack was made by scratching the notch with a sharp razor blade just prior to testing. Specimens were tested using an MTS machine at a crosshead displacement rate of 0.02 inch/minute.

## Results and Discussion

### *Compact Tension Analysis*

Calculations for fracture toughness were made using ASTM Standard E399. This standard is developed for metallic materials and is based on linear elastic fracture mechanics (LEFM), defining the stress intensity factor by assuming a linear elastic material and a state of plane strain. The calculations provide a conditional result  $K_Q$ , the value of the stress intensity factor where a material begins to crack significantly, from the following equation:

$$K_Q = (P_Q/bW^{1/2})*(f(a/W)) \quad (1)$$

where  $P_Q$  = load, lbf, at crack propagation

$b$  = specimen thickness, inches

W = length from the center of the loading hole to the end of the specimen, inches  
a = crack length, inches

and where  $f(a/W)$  is determined from

$$f(a/W) = (2+a/W)\{0.866+4.64a/W- 13.32 (a/W)^2 + 14.72(a/W)^3 - 5.6(a/W)^4\}/(1-a/W)^{3/2} \quad (2)$$

$K_Q$  may equal the plane strain fracture toughness,  $K_{IC}$  (opening mode), if the plastic zone is small compared to the specimen thickness and dimensions, or in other words when a state of plane strain can be assumed. In plane strain, only limited slow-stable crack growth occurs.

Both nematic and isotropic specimens fractured in a stick-slip manner, which is common for thermosets. That is, multiple crack arrest and initiation events occurred before catastrophic failure. The  $a/W$  values closest to 0.5 (value recommended by ASTM E399) are reported for each specimen. Results for the first set of unaligned nematic specimens are given in Table 1. This set was made using the original draw style. The average  $K_Q$  value calculated for seven specimens was 566 psi $\sqrt{\text{in}}$  with a standard deviation of 4.6 % (25 psi $\sqrt{\text{in}}$ ). The results for the second set of unaligned nematic samples are given in Table 2. Recall, these specimens were made using the STARWEAVE drawstyle. The average  $K_Q$  for this specimen set was 639 psi $\sqrt{\text{in}}$  with a standard deviation of 12.7 % (81 psi $\sqrt{\text{in}}$ ). So there was a small (14 %) effect that may be attributable to drawstyle. The overall effect of drawstyle on nematic microstructure is unknown.

**Table 1 Fracture Toughness Results for Unaligned Nematic Samples**

Specimen #	a/W	b, thickness (inch)	$K_Q$ (psi $\sqrt{\text{in}}$ )
2	0.573	0.110	563
3	0.500	0.092	529
4	0.510	0.105	550
5	0.500	0.090	581
6	0.537	0.085	610
7	0.493	0.104	572
8	0.660	0.090	558
Avg. (std. dev.)			566 (4.6%)

**Table 2 Fracture Toughness Results for Unaligned Nematic Samples made Using STARWEAVE Drawstyle**

Specimen #	a/W	b, thickness (inch)	$K_Q$ (psi $\sqrt{\text{in}}$ )
a	0.533	0.100	760
b	0.572	0.106	552
c	0.531	0.104	623
d	0.51	0.085	586
e	0.56	0.103	672
Avg. (std. dev.)			639 (12.7%)

**Table 3 Fracture Toughness Results for Isotropic Samples**

Specimen #	a/W	b, thickness (inch)	K <sub>Q</sub> (psi√in)
1	0.522	0.148	429
2	0.514	0.151	373
3	0.601	0.145	270
4	0.477	0.146	228
5	0.554	0.156	200
6	0.587	0.158	241
Avg. (std. dev.)			290 (31%)

Results for specimens built in the isotropic state are given in Table 3. The average K<sub>Q</sub> for 6 specimens was 290 psi√in with a standard deviation of 31 % (90 psi√in). The reason for the larger deviation in K<sub>Q</sub> values has not been assigned to a single cause. The lower load values measured for these samples make errors in crack length measurement more of a factor .

Analysis by scanning electron microscopy (SEM) of the nematic and isotropic fracture surfaces suggests an explanation for the higher toughness measured for nematic samples. Figure 1a shows a photomicrograph of a nematic fracture surface. There is considerable surface roughness, which is a qualitative indicator of high toughness. Studies have suggested that the amount of strain energy involved in a fracture may be proportional to the areas of surface created and the amount of plastic deformation at the crack tip [9]. The large number of planes seen on the fracture surface of the nematic specimens indicate that a greater surface area had to be created to move the crack front forward. In contrast, the fracture surface of the isotropic specimens is almost featureless and typical of brittle, glassy materials. It shows only a few river mark patterns perpendicular to the crack front (Figure 1b).

#### *Thermal Expansion of Multi-layered Parts*

Concerning the thermal expansion behavior, the first question to be answered was how do the thermal expansion properties of thick parts manufactured via stereolithography compare with those of thin films made under ideal conditions? Figure 2 shows the thermal expansion of the 16 layer uni-directional N1 part compared with the thermal expansion of N1 films. Table 4 lists linear thermal expansion values above and below the glass transition temperature for these specimens. The transverse, or 90 degree, data matched with no significant difference for the 90 degree film and part. There was a greater difference between the 0 degree film and part. The differences may be due to procedural error in aligning the magnet poles before scanning the film or part, or errors in mounting the film for thermal expansion measurement.

Another possibility is that the differences in the slopes of the expansion curves indicate that the multi-layer part is not as perfectly aligned as the thin film. There are several possible sources of disorder inherent with the laser scanning process. Xu et al. [10] have shown that as a strand of polymer is formed by a scanning laser, considerable flow occurs in the resin surrounding the strand. They attribute the flow to gradients in temperature, and thus density, resulting from released heat of reaction

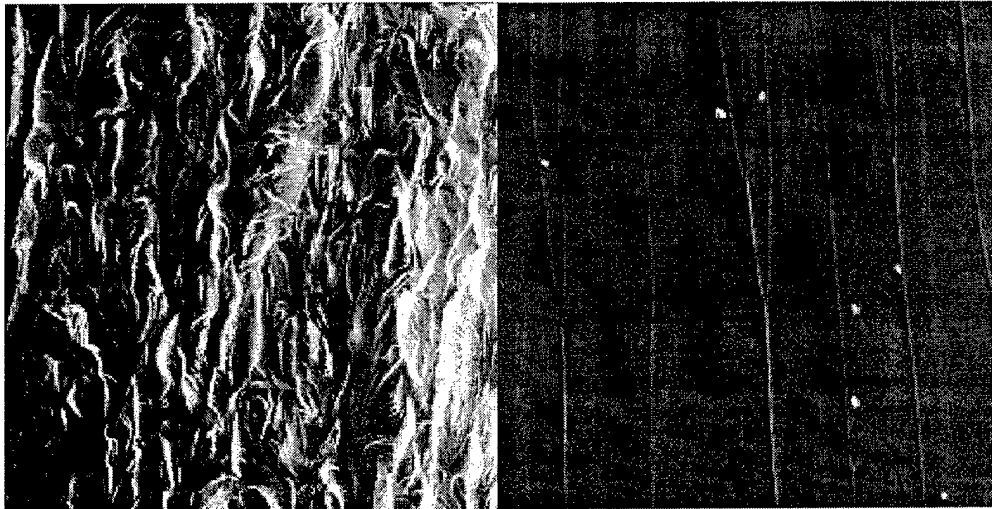
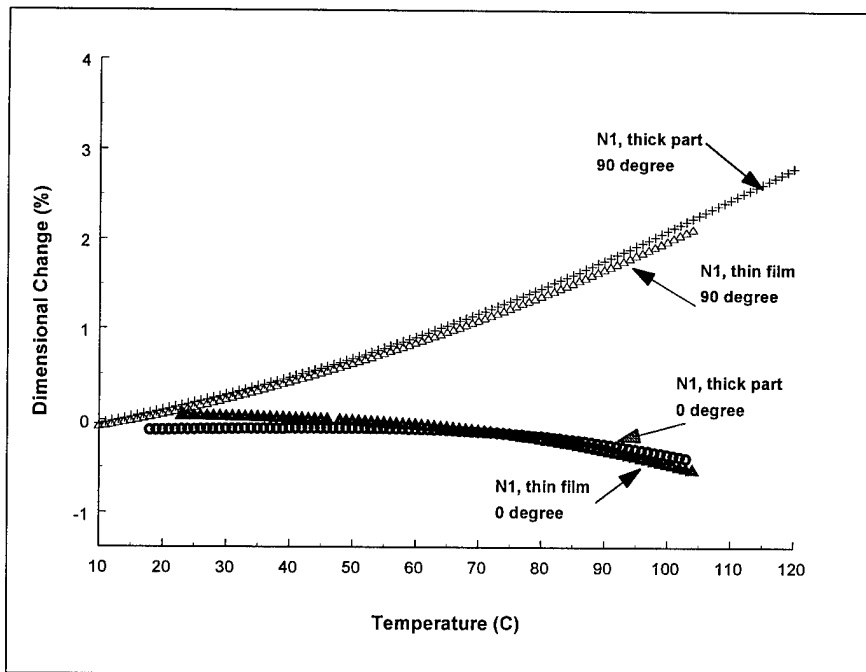


Figure 1: Photomicrographs (250 x) of fracture surfaces from compact tension specimens: a) fracture surface of nematic sample, b) fracture surface of isotropic sample.

The N1 data in Figure 2 indicate that thick parts can be made with a significant degree of alignment resulting in anisotropic thermal expansion properties. A similar anisotropy in thermal expansion properties is characteristic of continuous fiber-reinforced composite plies. In-plane thermal expansion is minimized in composite laminates by arranging the plies at different angles. This technique was evaluated with the aligned N1 resin. A 13 layer part was made having layers aligned alternating between 0 degrees (angle between magnetic field and long side of part) and 90 degrees. The variation in alignment was symmetric about the mid-plane of the part. The first attempt at building this part failed due to delamination at one corner of the part. The 0/90 configuration results in large normal forces at the edges of a part. In the N1 part the normal forces were large enough to cause delamination after about 6 layers were built.

**Table 4 Thermal Expansion Values for N1 Films and Parts**

N1 Specimen	$\alpha$ , from 25 to 40 °C	$\alpha$ , from 85 to 100°C
Film, 0 degree	-17.6 ppm/°C	-139 ppm/°C
Part, 0 degree	7.9 ppm/°C	-102 ppm/°C
Film, 90 degree	179 ppm/°C	315 ppm/°C
Part, 90 degree	180 ppm/°C	328 ppm/°C



Comparison of linear thermal expansion data for N1 thin film and thick part specimens.

To compensate for the normal forces, the layer thickness was decreased from 10 mil to 8 mil keeping the scan speed the same. The result of this change was to generate deeper overcure into the last-built layer. After the part was made, it was removed from the supports and examined. A small (2-3 mm) length of delamination was evident at one corner. This section was cut off using a diamond saw after the part was post-cured. The thermal expansion in the long direction was then measured and compared with the thermal expansion of the uni-directionally aligned 16 layer part as shown in Figure 3. As expected, the thermal expansion of the 0/90 part falls somewhere in between the expansion curves for the 0 degree and the 90 degree part. The in-plane expansion coefficient below the glass transition was about 54 ppm/°C and was about 33 ppm/°C above the glass transition. To eliminate delamination,  $\pm 45$  degree layers need to be used between the 0 degree and 90 degree layers. This type of "lay-up" is commonly used with continuous fiber reinforced composites to minimize normal stresses that can lead to delamination.

### Summary

It has been shown that significant improvements in fracture toughness can be made by processing liquid crystal resins in the un-aligned nematic phase versus the isotropic phase. SEM photomicrographs indicate that considerably greater surface area is formed during the crack propagation process for the unaligned nematic samples. Future work should consider the effects of: layer alignment, alternating alignments layer-to-layer, and alternating alignments strand-to-strand, on fracture toughness.

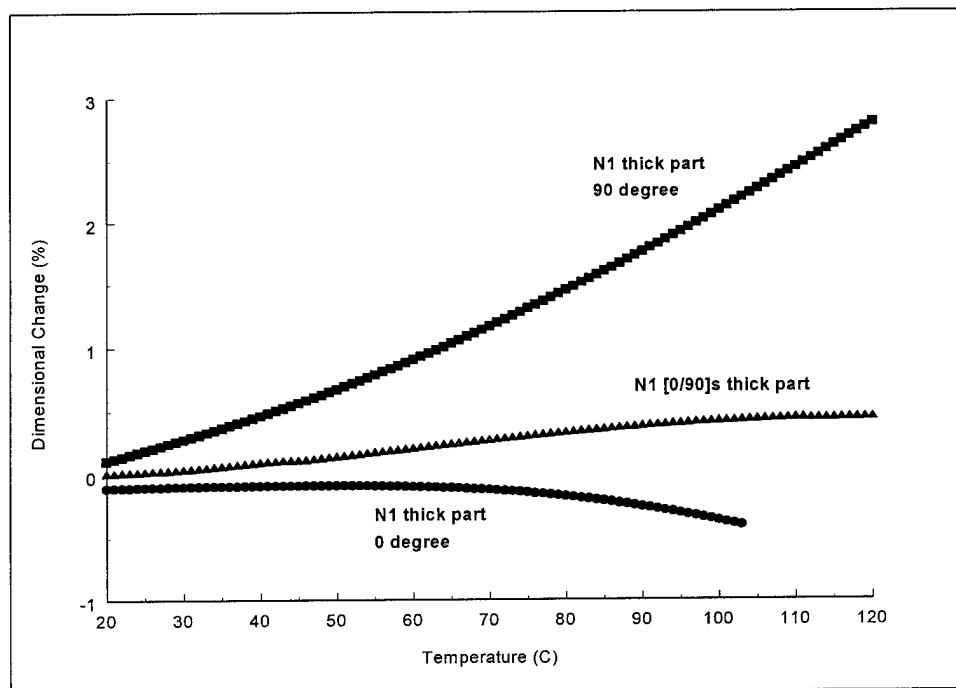


Figure 3. Comparison of N1 thermal expansion data for a 0/90 symmetric part with data for a uni-directionally aligned part.

Thermal expansion measurements of multi-layer parts indicate that considerable alignment of LC monomer can be achieved via a modified LC process. In the direction of alignment the thermal expansion is low below the glass transition temperature and negative above the glass transition temperature.

By alternating the alignment direction layer-to-layer, parts can be made that have low in-plane thermal expansion below and above the glass transition temperature. Consequently, LC resins may be useful in high-temperature applications where in-plane dimensional stability is critical.

### Acknowledgements

The authors are pleased to acknowledge that this research was supported by the U. S. National Science Foundation through NSF Grant # DMR-9420357, from the Polymer Program, Division of Materials Research. Dr. Andrew Lovinger was program manager. From the University of Dayton, we also thank John Murphy for assistance in setting up experiments.

### References

1. J.W. Schultz, R.P. Chartoff, "Photopolymerization of Nematic Liquid Crystal Monomers for Structural Applications: Molecular Order and Orientation Dynamics," (in press) *Polymer* (1998).
2. J.W. Schultz, R.P. Chartoff, J.S. Ullett, "Photopolymerization of Nematic Liquid Crystal Monomers for Structural Applications: Linear Viscoelastic Behavior and Cure Effects," (in press) *Journal of Polymer Science: Part B: Polymer Physics*, (1998).

3. J. W. Schultz, J. S. Ullett, and R. P. Chartoff, "Novel Liquid Crystal Resins for Stereolithography - Mechanical Properties," *Proceedings of the 8th Solid Freeform Fabrication Symposium*, August 11 - 13, 1997, Austin, Texas.
4. J. S. Ullett, J. W. Schultz, and R. P. Chartoff, "Novel Liquid Crystal Resins for Stereolithography - Processing Parameters," *Proceeding of the 6th European Conference on Rapid Prototyping and Manufacturing*, July 1- 3, 1997, Nottingham, England.
5. N. E. Dowling, *Mechanical Behavior of Materials*, Prentice Hall, New Jersey, 1993.
6. D. J. Broer and G. N. Mol, "Anisotropic Thermal Expansion of Densely Cross-Linked Oriented Polymer Networks," *Poly Eng. & Sci.*, 31, 625 (1991).
7. J.S. Ullett, J.W. Schultz, and R.P. Chartoff, "Advanced High Temperature Resins for Stereolithography," *Proceedings of the Seventh International Conference on Rapid Prototyping* March 31 - April 3, 1997, San Francisco, CA, p. 203.
8. P. F. Jacobs, *Rapid Prototyping & Manufacturing Fundamentals of Stereolithography*, McGraw Hill, New York, p. 211 (1992).
9. R. J. Kar, *Composite Failure Analysis Handbook Vol II: Technical Handbook, Part 2: Atlas of Fractographs*, Final Report, WL-TR-91-4021 (1991).
10. Xu, Y., Imamura, M., and Nakagawa, T., (1997) " Microscopic Flow Observation of Photopolymer by UV-Laser Exposure," *Proceedings from the 1997 Solid Freeform Fabrication Symposium*, Austin, TX, April 11 - 13, pp 177-184.  
Figure 2 :



# Rapid Prototyping of Functional Three-Dimensional Microsolenoids and Electromagnets by High-Pressure Laser Chemical Vapor Deposition

J. Maxwell,<sup>†</sup> K. Larsson, M. Boman

Dept. of Inorganic Chemistry, Ångström Laboratory, Uppsala Univ., Uppsala, Sweden

P. Hooge, Kirk Williams, P. Coane

Institute for Micromanufacturing, Louisiana Tech Univ., 911 Hergot Ave., Ruston, LA, USA

*High field-density microsolenoids from 100 to 500 microns in diameter were prototyped using both low and high pressure laser chemical vapor deposition. Tungsten lines were drawn about coated Co-Fe-Si-B magnetic cores from a mixture of WF<sub>6</sub> and hydrogen, yielding prototype microelectromagnets. Free-standing tungsten carbide coils and single crystal tungsten needles were deposited at high deposition rates from a variety of WF<sub>6</sub>-H<sub>2</sub>-He mixtures. The WF<sub>6</sub>-H<sub>2</sub>-He system was studied to obtain desired crystal morphologies. The convective cooling and diffusion of Xe vs. He was explored. Carbon fibers and helices were also grown at pressures up to 3000 mbar from ethylene. Peak temperatures during the growth process were monitored continuously with a simple apparatus which will be described. The future of high-pressure LCVD for micro-scale rapid prototyping of metals appears to be promising.*

**Keywords:** Laser Deposition, Tungsten, Carbon, Direct-writing, Freeform Growth, Microsolenoid, Microelectromagnet, Microcoils, Microsprings, Probes

## I. Introduction

Three-dimensional laser chemical vapor deposition (3D-LCVD) is an emerging process which bridges the gap between various macro-scale rapid prototyping (RP) systems and micro-fabrication technologies. With the ability to deposit both metals and dielectrics 3D-LCVD may be used to prototype integrated electromechanical components from sub-micron to centimeter scales. This technological niche is increasingly important with the ever-decreasing size and sophistication of consumer and industrial products.

The objective of this work was the development of functional microsolenoids and electromagnets, using 3D-LCVD as the primary fabrication tool. High-aspect-ratio microsolenoids have the potential to generate much greater magnetic-field densities than their thin-film counterparts,<sup>1</sup> and have many advantages when used as actuators in microelectromechanical systems (MEMS).<sup>2</sup> 3D-LCVD provides a means of fabricating such helical structures, with an ease unparalleled by any lithographic or rapid prototyping process.

## II. Method

There are several ways in which 3D-LCVD can be used to generate a microcoil. The first and simplest method is the direct-writing of a conductive line on an insulated fiber. In this case, the laser beam is focused onto the fiber, normal to the axis of rotation, while the fiber rotates about its axis and is pulled at constant velocity along the axis. This is illustrated in Fig. 1A. The method was first demonstrated with the growth of a tungsten line about a silicon fiber.<sup>3</sup> Note that the fiber itself may also have been previously grown using 3D-LCVD, allowing a complete microsolenoid to be fabricated with one production tool. If the fiber is grown from the gas phase, it can be made to differ in composition from that of the conductive line, merely

<sup>†</sup> Visiting Fellow at Ångström Laboratory

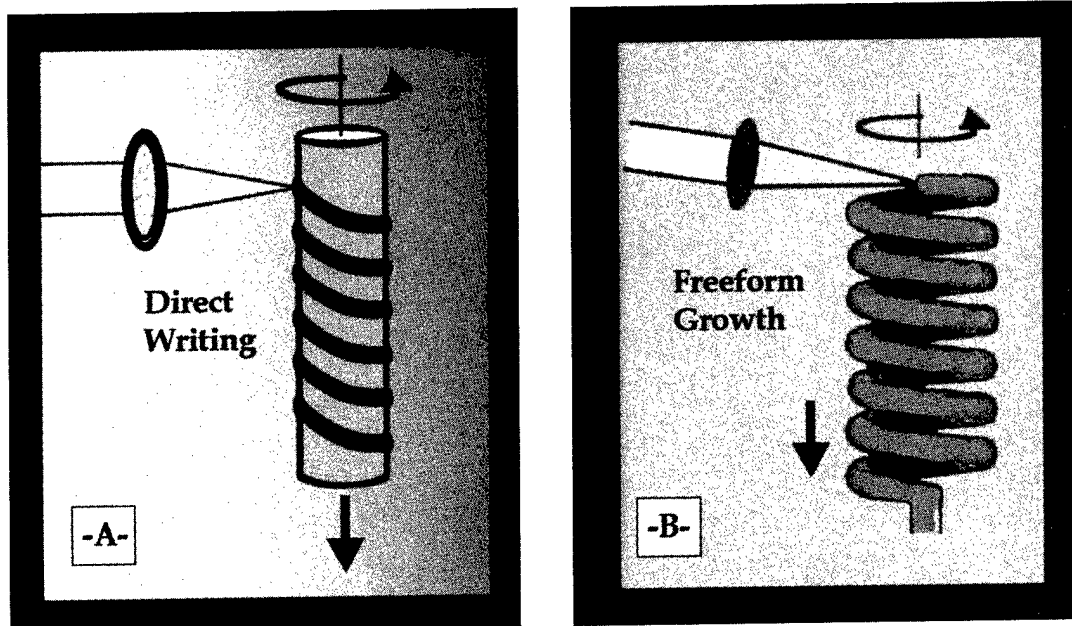


**Fig. 1: Techniques for Growing Coils Using 3D-LCVD**

by changing the precursor gases.<sup>4</sup> The fiber may also be coated with an insulator from the vapor phase, either by localized direct-writing or large-area heating, so that the conductive line is isolated from the core fiber. In this way, a ferromagnetic material such as iron, nickel, or cobalt (or an alloy of the same) can form the core of an electromagnet, while this core is electrically-insulated from one or more conductive lines by intermediate coatings. Clearly the writing process may be repeated, allowing multiple coils about a single core—with the associated increase in magnetic field strength.

*Freeform* coils may be grown via 3D-LCVD, as illustrated in Fig. 1B. The laser beam is initially focused on the end of a fiber which is offset from an axis of rotation by the intended helix radius. Once three-dimensional growth initiates, rotation commences about the axis, and the structure is drawn downwards. The tangential velocity of the helix at the focal point, must match (or be slightly less than) the deposition rate, so that the growth front on the tip of the evolving helix appears stationary at the laser focus.

Comparing the convective heat transfer from such a freeform coil to that of a direct-write solenoid, one can see that the freeform coil is more efficient due to the attendant increase in surface area for heat losses. For two coils of identical coil diameter, the freeform coil will have a larger effective surface area by a factor of  $\pi\omega N$ , where  $\omega$  is the width of the freeform metal fiber and  $N$  is the number of loops per unit length. For a coil diameter of  $100\ \mu\text{m}$ , and fiber width of  $15\ \mu\text{m}$ , the freeform coil is 5 times more efficient at dissipating heat. In addition, greater currents may be passed through the solid metal fiber than through the thin-film direct-write coil, so much greater magnetic flux densities may be obtained with freeform coils.

The potential to fabricate free-standing microsolenoids using 3D-LCVD was first demonstrated successfully at Uppsala University,<sup>5</sup> with the growth of a free-standing, polycrystalline boron coil. However, a conductive coil which could be used to generate a magnetic field or a flexible coil with adequate mechanical properties had not been realized. The following work describes efforts using both fabrication techniques: direct-writing and freeform growth of metal helices.

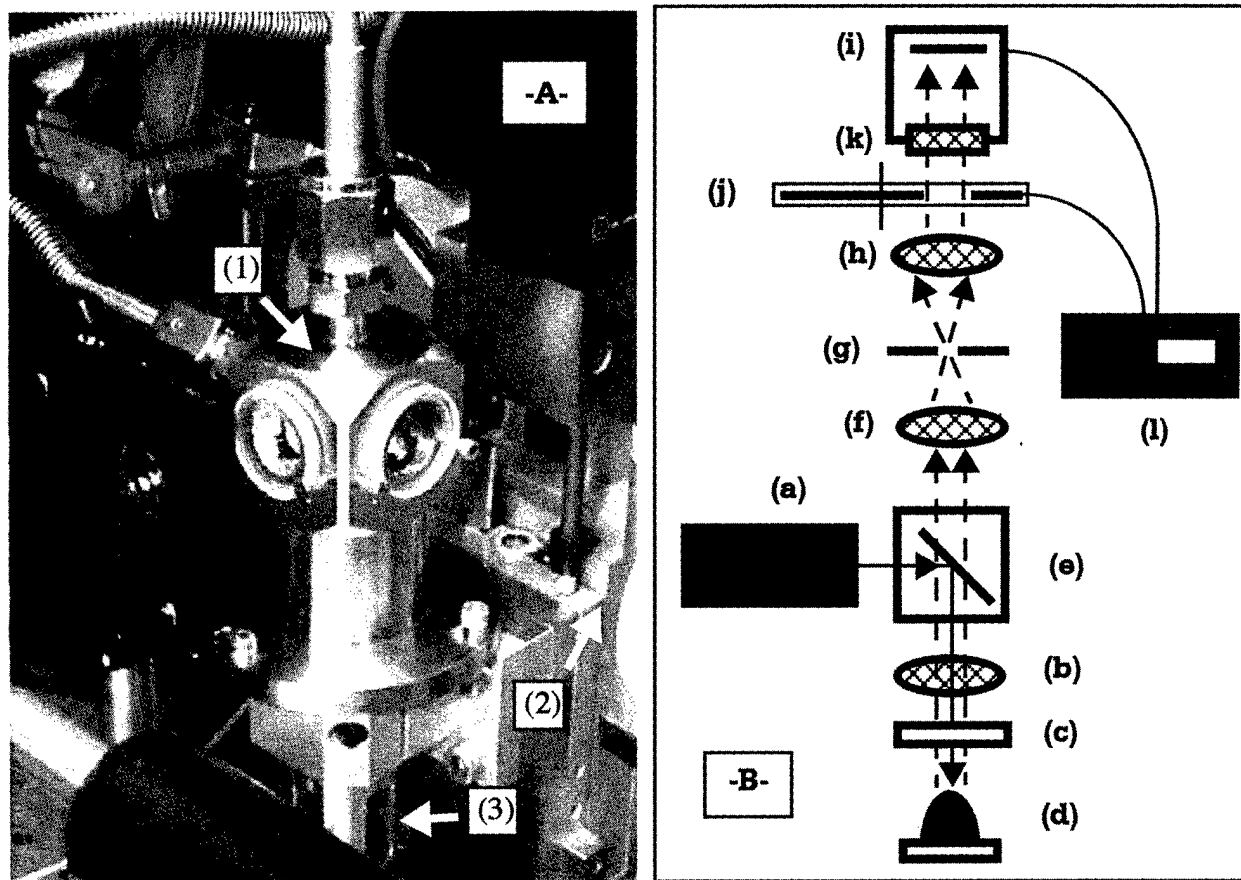


**Fig. 2: (A) Pressure Chamber/Stages, (B) Temperature Measurement System**

### III. Experimental

The 3D-LCVD apparatus shown in Fig. 2A was used for the growth experiments. It consists of a small pressure chamber (1) with two windows, mass flow control system, and vacuum pump with a cold trap. The chamber travels on a Burleigh X-Y-Z stage (2) with piezoelectric actuators, and it is connected to the mass flow control system and vacuum pump with flexible bellows. Repeatability of the stages is greater than  $0.1 \mu\text{m}$ . Rotary motion of the sample is provided by a motion feedthrough (3), driven by a precision DC motor and 1:132,000 planetary gearbox, giving a minimum rotational velocity of 3.0 rph. The sample holder inside the chamber rides on a manual 4-axis goniometer which allows precise alignment of the sample to the feedthrough rotary axis.

The optical system and temperature measurement apparatus is shown in Fig. 2B. A single-mode cw Ar<sup>+</sup> laser (a) at 488/514 nm was employed at average powers up to 12 watts, while a 60 mm focal length gradient-index lens (b) was used to focus the beam through a fused-silica window (c) on the chamber, yielding a  $1/e^2$  spot waist of approximately  $10 \mu\text{m}$  at the sample (d). Between the laser and focusing lens, a dielectric plate beamsplitter (e) was used to turn the beam by  $90^\circ$ , while passing near infrared wavelengths from 900 to 1500 nm. In this way, it was possible to monitor the emissions and radiation emanating from the center of the growth front.

To measure the peak growth temperature, light passing through the beamsplitter (e) was imaged by an achromat (f) onto a  $10 \mu\text{m}$  or  $22 \mu\text{m}$  diameter pinhole (g), which was carefully centered to obtain maximum throughput. In this way, only light from the center of the growth

zone was allowed to pass—where the peak temperature (and brightest signal) would be observed. This also simplified the temperature measurement, so that a local micro-scale temperature could be inferred, rather than an average temperature over the growth front. A relay lens (h) was then used to concentrate the light onto a photodiode (i), through a chopper (j) and narrow band filter (k) with center wavelength at 1100 nm. The chopper frequency selected for all experiments was 142 Hz. The signal from the photodiode was passed into a current preamp, then into a lock-in amplifier (l) to eliminate noise. This simple temperature measurement system works with a signal-to-noise ratio of over 25 dB, and is able to accurately detect temperatures to within  $\pm 10^\circ\text{C}$ , which is sufficient to avoid melting of the deposit during transient growth and adequate for rudimentary growth rate control in the kinetically-limited regime.

For the deposition of tungsten, the precursor tungsten hexafluoride,  $\text{WF}_6$ , was employed in various ratios to hydrogen, which acts as a reducer. The overall deposition reaction was:



Tungsten hexafluoride is a liquid at room temperature, with a vapor pressure of approximately 800 mbar. Hot air guns were directed at the chamber windows, and run continuously, to eliminate condensation (and deposition) on the windows. It was found that pre-heating the windows under vacuum to  $100^\circ\text{C}$  for 15-20 minutes prior to the introduction of  $\text{WF}_6$  greatly reduced the probability of adsorption and condensation on the windows, presumably due to desorption of all water on the window surfaces.

Competition between deposition and etching was also observed on the boron substrates. Boron may be etched by both hydrogen and fluorine; the reaction:

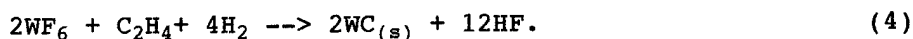


dominates if the relative hydrogen concentration is high, while:



is dominant if the relative concentration of  $\text{WF}_6$  is high. Thus, it was necessary to balance the molar ratio of  $\text{H}_2/\text{WF}_6$  to eliminate etching. A variety of hydrogen to  $\text{WF}_6$  ratios were attempted from 1:5 to 10:1.

Tungsten carbide was also grown using a mixture of  $\text{WF}_6$ ,  $\text{H}_2$ , and ethylene,  $\text{C}_2\text{H}_4$ . A stoichiometric mix was employed to obtain the intermetallic WC:



As the tungsten hexafluoride threshold temperature for decomposition is approximately  $300^\circ\text{C}$  in the presence of  $\text{H}_2$ , while that for ethylene is over  $800^\circ\text{C}$ , ethylene is not necessarily an ideal precursor. To compensate for the tendency to grow tungsten-rich deposits, greater ethylene concentrations were also investigated, as well as deposition temperatures over  $1000^\circ\text{C}$ .

## IV. Results

### A) Direct-write Microsolenoids

To fabricate microsolenoids using the direct-write technique,  $100\ \mu\text{m}$  boron fibers were carefully aligned with the axis of rotation of the motion feedthrough described above, and the laser focus was aligned to the center of the fiber. Tungsten was successfully deposited on these boron fibers at a variety of scan rates and precursor partial pressures. The best results to date were obtained with a 1:4 mixture of  $\text{WF}_6$  to  $\text{H}_2$  at 100 mbar. The laser power employed was 180 mW. Fig. 3 shows an example of a microsolenoid grown under these conditions. Note that the lines are well-defined and nearly flat, the tungsten grain sizes are less than 1-2 microns,

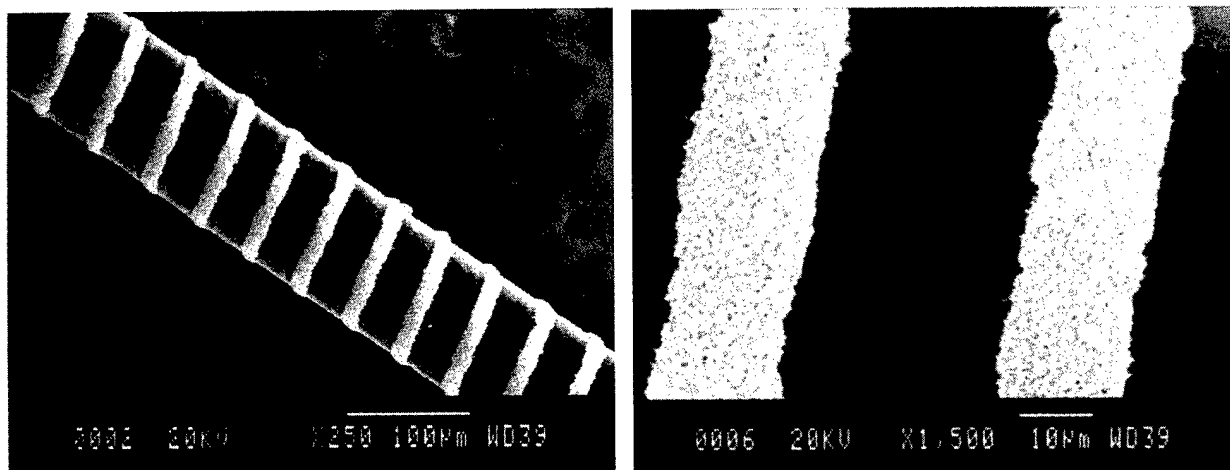


**Fig. 3: Tungsten on Boron Microsolonoid by Laser Direct-writing**

and there is little deposition of tungsten or etching of boron between the lines. Average central line thickness was  $3 \mu\text{m}$ .

The thickness of the tungsten lines was found to be inversely proportional to the scan rate, while the width of the lines was approximately the same as the spot size ( $10\text{-}15 \mu\text{m}$ ) over a wide range of scan rates, but broadened as the scan rate approached zero velocity, reducing the resolution of the helix and number of possible turns per unit length. In addition, it was noted that increasing overall pressure tended to increase the deposition rate and reduce the grain size of the tungsten deposit. So, to maintain consistent results and high definition lines, the scan rate had to be raised as the pressure was increased.

In addition to the boron-core microsolonoids, tungsten was also deposited on  $100 \mu\text{m}$  diameter Co-Fe-Si-B alloy fibers. To insulate the core from the tungsten coil, the fibers were CVD-coated with a  $1\text{-}2 \mu\text{m}$  thick silicon layer using a silane and hydrogen ambient and resistive heating of the Co-alloy fibers. The adhesion of the silicon coating to the Co-alloy fibers was adequate. Tungsten could be readily grown on these fibers, as in the case of the boron-core microsolonoids, although higher laser powers, on the order of  $500 \text{ mW}$ , were required to compensate for the thermal conductivity of the Co-alloy, and the Si coating was readily etched, leaving the metal lines uninsulated. Ongoing efforts are being made to substitute a boron coating for the silicon, so that these microelectromagnets may be fully tested.

### **B) Free-standing Microsolonoids**

As a basis for comparison and because of its outstanding mechanical properties and favorable microstructure, carbon was selected as the preliminary deposit material for growing free-standing microcoils, since the 3D-LCVD of amorphous carbon rods from ethylene has been previously characterized.<sup>6</sup> As described earlier, functional microsolonoids could also be fabricated using the carbon helices as cores, or the carbon could be used as a sacrificial layer in the production of microtubes.

Again, boron fibers were used as the substrates, aligned to the rotary feedthrough axis. Ethylene was introduced at pressures between  $400$  and  $3000 \text{ mbar}$ , and laser powers between  $150 \text{ mW}$  and  $1200 \text{ mW}$  provided a variety of carbon fiber diameters. At  $930 \text{ mbar}$  and  $150 \text{ mW}$ , smooth, amorphous carbon fibers could be grown with a diameter of only  $14 \mu\text{m}$ . Using these parameters as a basis, several dozen helices were grown, one of which is displayed in Fig. 4. Note that the individual coils could be spaced less than  $5 \mu\text{m}$  apart without affecting

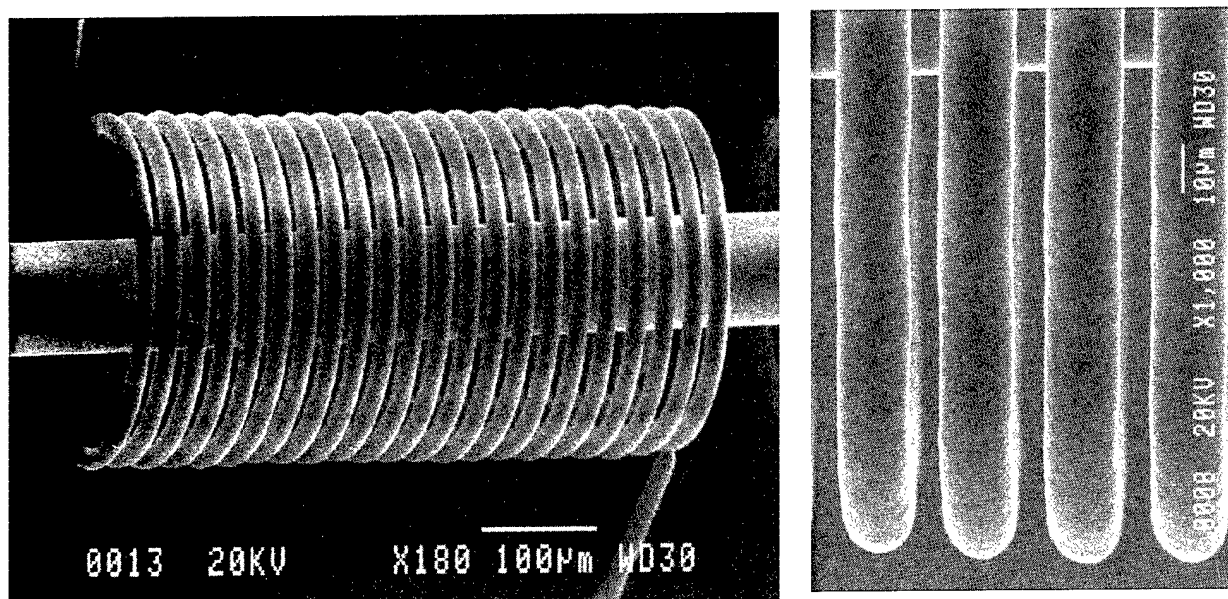


**Fig. 4: Amorphous Carbon Microcoils**

the shape of the deposit; in fact, it was possible to continuously grow the coils with zero spacing—so that they just barely touch. An attempt was made to grow a tube in this manner, with several microns overlap between coils; in this case, however, heat losses to the adjacent coil were excessive, and the growth became unsteady. Given a  $14\ \mu\text{m}$  loop width with  $2\ \mu\text{m}$  clear spacing, a metal-coated inductor with over 600 loops per centimeter can be fabricated, more than sufficient to saturate most ferromagnetic cores.<sup>7</sup>

It was also possible to grow very small diameter microcoils of carbon, the smallest to date having a clear internal diameter of only  $60\ \mu\text{m}$ . Even smaller diameter solenoids could be prototyped, down to at least  $20\ \mu\text{m}$  clear ID, provided the laser spot size is reduced, and a rotary drive and stages with improved resolution were employed. Note that alignment of the focus on the tip of the evolving helix is critical for continual growth. If the helix moves too quickly relative to the focus, either in rotary motion, or along the rotational axis (z-axis), so that the focus is more than a few microns out of place, growth will cease due to reflective losses on the narrow carbon fiber.

#### Freeform Growth of Tungsten

Using  $\text{WF}_6$  and  $\text{H}_2$ , very rapid growth of free-standing tungsten rods was obtained, up to  $160\ \mu\text{m/s}$  continuous rates, and a variety of morphologies were obtained, depending on the laser power and precursor pressure employed. Typical gas mixtures were 3:1  $\text{H}_2$  to  $\text{WF}_6$ , at chamber pressures from 750 to 3000 mbar. At these pressures, explosive crystal growth would occur using laser powers over 3 W, and rods composed of very large grains would result, or multiple large crystals would grow slowly away from the substrate at various angles to the beam. At lower powers, between 1.5 W and 3.0 W, rods with a single-crystal cores and polycrystalline coatings would form. Within a narrow power range, around 800-900 mW, clean single-crystal, cubic tungsten rods, over 2 mm in length could be grown continuously using focal tracking at rates of over  $2\ \mu\text{m/s}$ . These rods were of square cross-section, as shown in Fig. 5A, and could potentially be used as rectangular building blocks in microelectromechanical systems or as wear-resistant probes. At higher pressures, over 1100 mbar chamber pressure, rapid

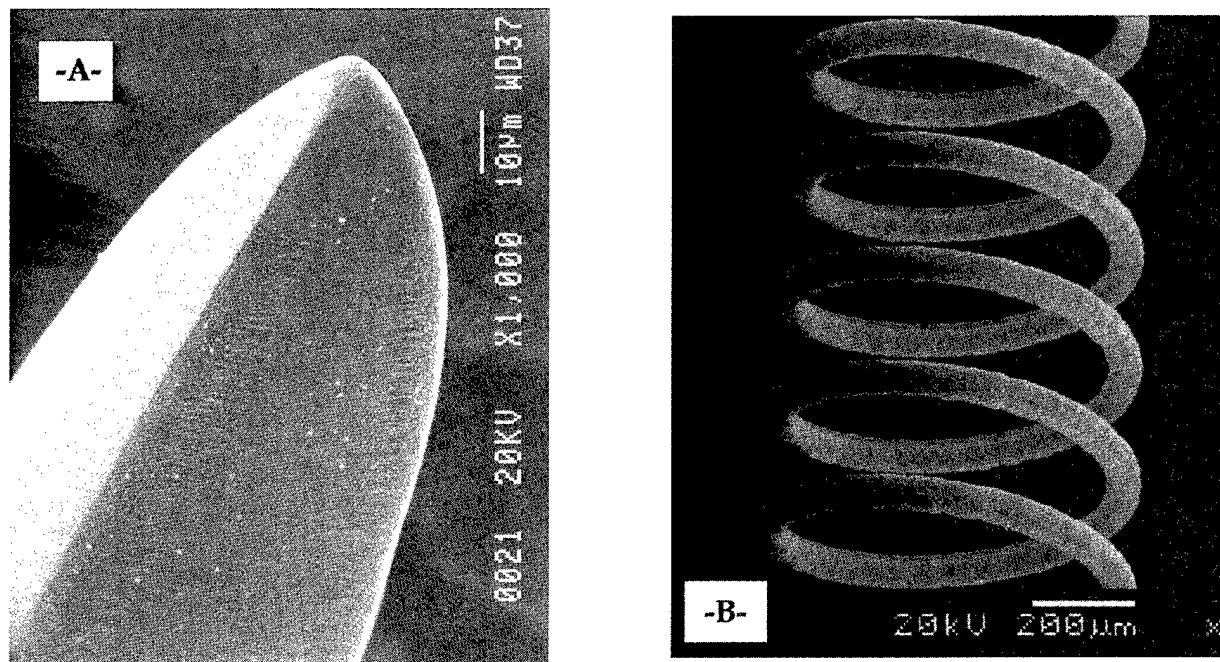


**Fig. 5: (A) Tungsten Crystals, (B) Tungsten Carbide Microsolenoid**

polycrystalline growth of 10-20  $\mu\text{m/s}$  was obtained, and very narrow rods could be grown, down to about 30  $\mu\text{m}$  in diameter.

It was difficult to obtain circular helices of pure tungsten. Invariably, the growth tended to orient in one direction, and deposition would cease as the angle of incidence to the growth front changed. Precursor pressures greater than 1100 mbar were necessary to produce fine-grained tungsten deposits. Several partial helices were possible, using a chopped beam to induce polycrystalline growth.

Previous papers have studied the influence of convective losses on the ability to grow steady-state metal deposits without self-limiting effects.<sup>8</sup> To compare the losses due to natural convection versus those due to diffusion during steady-state growth, noble gases were also added to the  $\text{WF}_6/\text{H}_2$  mixture in 50 mbar increments. The temperature was measured using the apparatus described in Fig. 2B. In this case, the base partial pressures of  $\text{WF}_6$  and  $\text{H}_2$  were 400 mbar and 600 mbar, respectively, and the chamber pressure varied depending on the addition of helium or xenon. A marked cooling effect was noted with the helium mixtures; in one case it was estimated that a 100 mbar increase in helium partial pressure corresponded to additional heat losses of over 100 mW. In addition, heat transport by the helium broadened the transient diameter of the rods, and when over 200 mbar of helium was introduced, homogeneous nucleation in the gas phase commenced near the deposit. As helium has a very high diffusivity, it tends to transport heat rapidly away from the growth front, into the surrounding gas mixture. This, in turn, heats any nearby solid surfaces, and the growth region broadens noticeably. The instantaneous helium concentration in a reactor can thus tailor the growth diameter to follow a specific profile. Experiments were also performed with xenon, which has a gas diffusivity typically 1/6th that of Helium. The deposits grown with Xe were noticeably more well-defined, and homogeneous nucleation was not present even at partial pressures up to 300 mbar.

Purity of the tungsten deposits was examined using energy dispersive x-ray spectroscopy (EDS). No trace of oxygen or fluorine was detected in the deposits, even with  $\text{H}_2:\text{WF}_6$  flow ratios as low as 1:3.

### Freeform Growth of WC Helices

To obtain conductive, freestanding helices, experiments were also performed in the growth of tungsten carbide from a stoichiometric mix of  $WF_6$ ,  $C_2H_4$ , and  $H_2$ . Again, very rapid continuous growth was obtained, up to  $175 \mu\text{m/s}$ , while the diameter of the fibers was much smaller than that of the pure tungsten samples—as narrow as  $20 \mu\text{m}$  across. Focal tracking was employed to grow fibers as long as 4 mm, with height-to-width aspect ratios of 200:1. The fibers tended to grow in spurts, as hexagonal single-crystals with peak growth rates exceeding  $200 \mu\text{m/s}$  in many instances. Single-crystal deposition rates were so rapid that they were difficult to measure. To obtain polycrystalline deposits, a chopper at 72 Hz was introduced, and smooth, continuous growth at  $10\text{-}20 \mu\text{m/s}$  was obtained. In this way, it was possible to change the axial direction of the growth, allowing helices of WC to be prototyped, such as that shown in Fig. 5B. This helix was grown with a 1:2:2 ratio of  $WF_6:C_2H_4:H_2$  at 765 mbar.

Morphology of the tungsten carbide deposits depended strongly on the laser power employed. At the highest powers, several different phases of the W-C system were present, while at low powers, bare hexagonal crystals of WC were obtained. X-ray diffraction studies are currently underway to identify all of the phases. A thin, pure tungsten coating was present on the exterior of many WC structures, due to the differential in threshold decomposition temperatures between  $WF_6$  and  $C_2H_4$ . This coating may be readily delaminated, and can be eliminated through the use of low powers, pulsed lasers, or alternate precursors for carbon.

## V. Conclusions

Both direct-write and free-standing microsolenoids and electromagnets may be fabricated using 3D-LCVD. Future work will include the incorporation of ferromagnetic materials, the testing and characterization of the resulting microelectromagnets, and their application in microelectromechanical systems (MEMS). Additional studies will be carried out on the effects of noble gases on heat losses during 3D-LCVD, and the deposition of tungsten and tungsten carbide systems will be fully characterized.

## VI. Bibliography

1. J.A. Rodgers, R. J. Jackman, G. M. Whitesides, "Constructing Single- and Multiple- Helical Microcoils and Characterizing Their Performance as Components of Microinductors and Microelectromagnets," *Journal of Microelectromechanical Systems*, Vol. 6, No. 3, Sept. 1997, pp. 184-191.
2. J. Klein, H. Guckel, "High Winding Density Micro Coils for Magnetic Actuators," *HARMST '97*, Madison, WI, Jun. 1997.
3. H. Westberg, M. Boman, "Free-standing Silicon Microstructures Fabricated by Laser Chemical Processing," *J. Appl. Physics*, Vol. 73, No. 11, 1 Jun. 1993, pp. 7864-7871.
4. Maxwell, J., Pegna, J., DeAngelis, D., Messia, D., "Three-dimensional Laser Chemical Vapor Deposition of Nickel-Iron Alloys," *Material Research Society Symposium Proceedings*, v. 397 (B3.30): Advanced Laser Processing, MRS Fall 1995 Meeting, Boston, MA (Nov. 27--Dec.1, 1995).
5. S. Johansson, J. Schweitz, H. Westberg, M. Boman, "Microfabrication of Three-Dimensional Boron Structures by Laser Chemical Processing," *J. Appl. Phys.*, Vol. 72, No. 12, 15 Dec. 1992, pp. 5956-5963.
6. J. Maxwell, "Three-Dimensional Laser-Induced Pyrolysis: Modelling, Growth Rate Control, and Application to Micro-Scale Prototyping," *PhD Thesis*, Rensselaer Polytechnic Institute, 1996.
7. P. Lorrain, D. Corson, *Electromagnetic Fields and Waves*, 2nd Edition, Freeman Publ. San Francisco, CA, 1970, pp. 398.
8. Maxwell J., Krishnan, K., "High-Pressure, Convectively-Enhanced, Laser Chemical Vapor Deposition of Titanium," *Proc. Solid Freeform Fabrication Symposium*, Austin, Texas, Aug. 1997.

**Gas-Phase Selective Area Laser Deposition(SALD)  
Joining of SiC Tubes with SiC Filler Material**

by S. Harrison and H.L. Marcus

Institute of Materials Science

University of Connecticut

97 North Eagleville Road

Storrs, CT 06269-3136

Phone: 860-486-4410 Fax: 860-486-4745

**Abstract**

The laser-driven, gas-phase based SFF technique for joining together ceramic components with ceramic filler material, known as Selective Area Laser Deposition(SALD) Joining, was utilized in fabricating joined silicon carbide structures. Specifically, silicon carbide tubes were 'welded' together by depositing silicon carbide from a gas phase reaction. Two different precursor environments were examined, one a tetramethylsilane/hydrogen mixture and the other composed of methyltrichlorosilane. The quality of the joints were examined by bend tests and hermeticity measurements. In addition, the composition and morphology of the silicon carbide deposit was studied and is discussed here.

**Introduction**

The technology for fabrication of robust ceramic parts lacks a proven and reliable method for assembling together complex designs from simple shapes. The challenges presented in joining together ceramic shapes arise from the very properties that make ceramics attractive. Their high melting temperatures preclude traditional welding techniques that utilize base material melting. In fact, silicon carbide and silicon nitride sublime from the solid phase to their constituent gases and therefore display no melting characteristics. The poor wettability of ceramic surfaces with most metals presents many difficulties in brazing efforts. In attacking these challenges, a variety of novel ceramic joining procedures have been devised and examined. Diffusion bonding forms ceramic joints by diffusion of atoms across the joint seam at very high processing temperatures. Analogous to solid-state sintering, diffusion bonding suffers from the characteristic low diffusivity of ceramic chemical species and low ductility. Efforts to avoid these shortcomings have utilized metal foils, such as nickel, nickel-chromium and aluminum boride, as interlayers at the joint seam to enhance the diffusion and ductility<sup>1,2,3</sup>. Reactive metal brazing operates by using a metal filler in a traditional braze mixture to react with the ceramic surface and produce a more stable, wettable surface material<sup>4</sup>. The most promising brazes are silver-copper alloys with titanium or zirconium mixed in as the reactive agents<sup>5,6</sup>.

This research program applied the gas-phase, laser-driven Solid Freeform Fabrication technique of Selective Area Laser Deposition(SALD) to the ceramic joining problem, in a process called SALD Joining. The initial, proof-of-concept investigation of this process at the University of Texas showed its feasibility by linking together alumina tubes, silicon carbide tubes, and silicon nitride tubes<sup>7,8</sup>. The UCONN research efforts studied in-depth the attachment of silicon carbide tubes together using silicon carbide filler material deposited in the SALD Joining process. The ultimate goal is to show the ability of gas-phase SFF techniques to fabricate separate ceramic parts and then *in-situ* 'weld' them together to form a complex ceramic structure. The tube geometry utilized in this program was chosen for convenience with the expectation that the SALD Joining procedure will work for other geometries and types of ceramic material, including those fabricated by SFF.

### Experimental Approach

SALD employs a high-powered laser beam to induce a thermal decomposition reaction of specific gases inside a vacuum chamber. The decomposition reaction leads to a desired solid product deposited inside the laser spot heated zone. The laser beam can be scanned by a motion control computer system to selectively deposit material in a desired pattern. SALD Joining utilizes the SALD technique to deposit solid product and use it as a filler material to join together ceramic parts. The UCONN joining chamber contains a rotational device to which the experimental tubes were attached. The joint seam could be scanned relative to the laser in several patterns, from a wiggle pattern back and forth across the seam to a simple stationary beam centered on the joint. A schematic of the tube rotation device is found in Figure 1. This scanning, as well as the tube rotation speed, was computer controlled by the Microsoft Visual Basic-based SFF Control System software. A stabilized, continuous wave(cw) 50 watt Nd:YAG laser from Excel/Quantronix served as the primary laser, operating at a 1.06 micron wavelength. The primary gas precursors used were a mixture of tetramethylsilane(TMS,  $\text{Si}(\text{CH}_3)_4$ ) and hydrogen. Alternative gas precursors for silicon carbide deposition include methyltrichlorosilane(MTS,  $\text{SiCH}_3\text{Cl}_3$ ) and a combination of silane( $\text{SiH}_4$ ) and methane( $\text{CH}_4$ ).

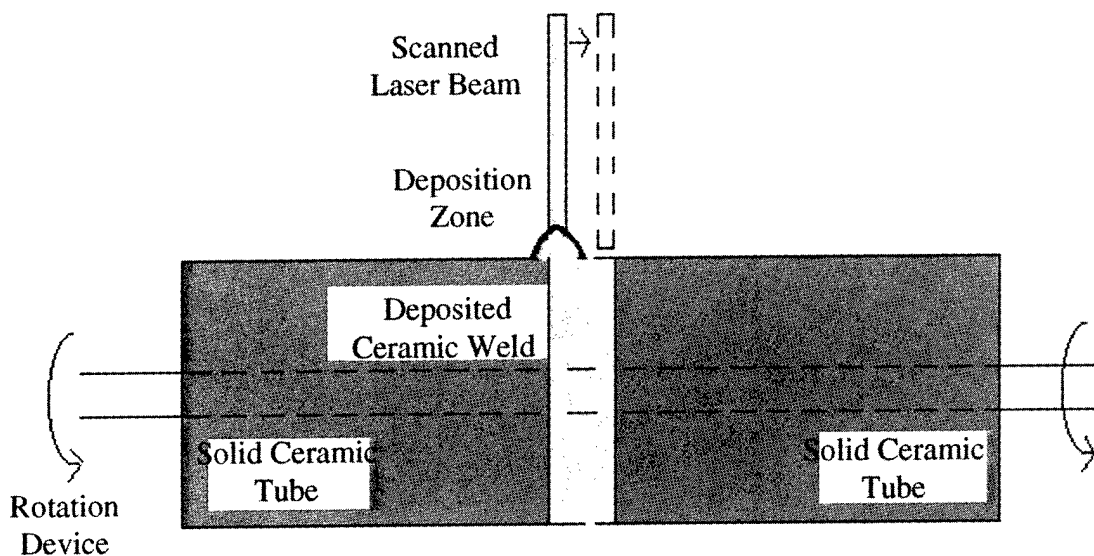


**Figure 1:** Schematic of Tube Rotation Joining Geometry

Two different types of silicon carbide tubes were used, a clay-bonded tube from Bolt Technical Ceramic of approximately 85 to 90% density and a DuPont Lanxide Composite tube of HiNicalon fiber in a silicon carbide matrix, referred to hereafter as fiber tube. The clay-bonded tubing came in 1/2 inch and 1 inch outer diameter sizes, while the fiber tube's outer diameter measured 3/8 of an inch. Experiments were run in two different manners, one with deposition temperature monitoring using an infrared pyrometer and one without the pyrometer. When utilizing the pyrometer, tube samples were weighed before and after deposition in order to calculate a mass deposition rate in correlation with the approximate temperature range. Otherwise, the samples were directly placed in the chamber. After a completed experiment, the sample underwent sonication for approximately 20 minutes to remove as much polymer reaction by-product as possible and then photographed using a Snappy frame-grabber video card and a color CCD camera. Further analysis was performed after the samples were catalogued.

## Experimental Results

Figures 2 and 3 display two successful tube joints. Both joints were fabricated using a 1 to 2 gas pressure ratio of TMS to hydrogen. Each tube section end was perpendicular to the tube wall, making a simple butt joint geometry. The 1/2" OD clay-bonded joint was deposited from a 1.5 millimeter wide wobble scan program (i.e. relative to the joint seam), while the fiber joint originated from a stationary beam scan.

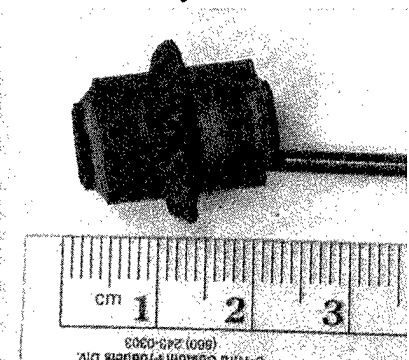


**Figure 2:** Clay-bonded SiC Tube Joint

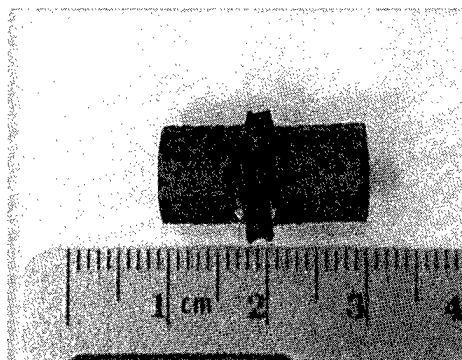


**Figure 3:** Fiber SiC Tube Joint

Cross-sectional micrographs of selected joints are found in figures 4, 5, 6 and 7, the first two from a clay-bonded tube joint sample and the last two from a fiber tube joint sample.

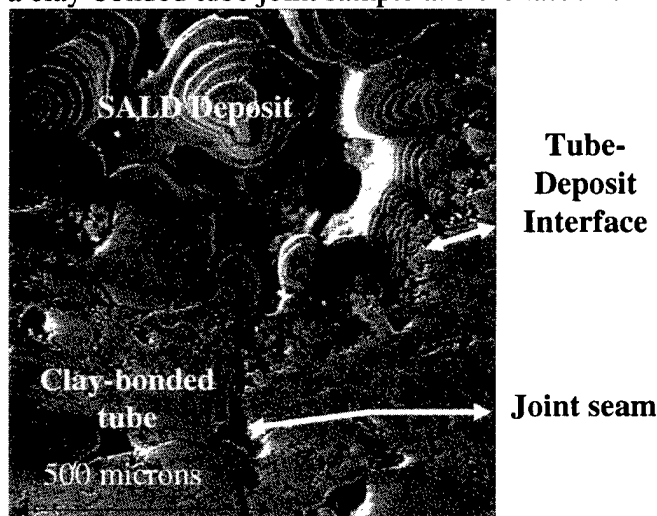


**Figure 4:** ESEM Image of Clay-bonded Tube Joint

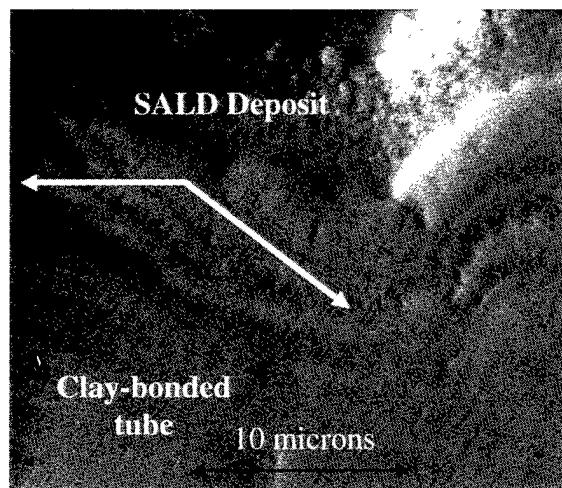


**Figure 5:** ESEM Image Close-up of Tube-Deposit Interface

Mechanical testing of the joints was accomplished using a cantilever-type bend test. One end of the joint remained stationary in a fixture while the other end was forcibly bent by the upward motion of a crosshead on an Instron tensile testing machine. The strength of the several joints tested showed low strength compared to that of the monolithic tube standards.

The hermetic quality of several joints was determined by connecting the samples to the deposition chamber and its mechanical vacuum pump by means of a Swagelok fitting and Tygon tubing. The joined structures were exposed to the running vacuum pump and the vacuum pressure in the chamber allowed to equilibrate, thus giving a measure of the lowest possible vacuum level possible for the joints. The results appear in Table 1, along with the vacuum level achieved with a monolithic tube standard.

Microhardness evaluation of the SALD material was performed with a Vickers indenter at a 500 gram load and 15 seconds indenter dwell time. The results are displayed in bar graph form in Figure 8. A total of 20 indentations were taken, and the average Vickers hardness number was 1446 kg/mm<sup>2</sup>. The pure silicon carbide Vickers number has been reported as 3300<sup>9</sup>.

Various samples of the silicon carbide SALD material underwent x-ray diffraction spectroscopy(XRDS). All showed the three peak configuration, at d-spacings of 2.52, 1.54 and 1.31 Angstroms, characteristic of beta silicon carbide, as has consistently been reported in silicon carbide CVD literature<sup>10,11,12</sup>. Higher temperature deposition material, in the 1300 to 1500 degrees Celsius range as measured by the pyrometer, displayed an additional peak at d = 3.35 Angstroms corresponding to the main carbon/graphite line

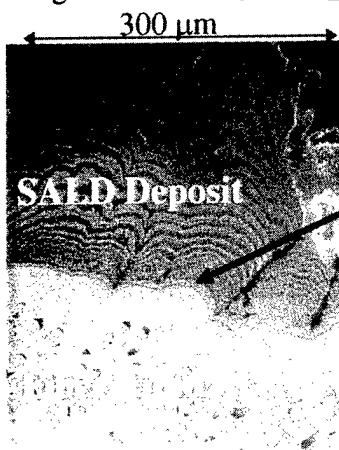


Figure 6: ESEM Image of Fiber Tube Joint

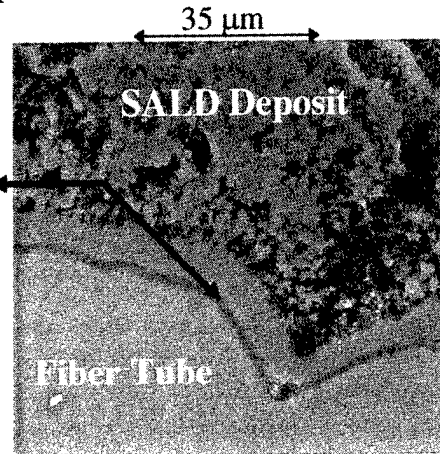


Figure 7: ESEM Image Close-up of Tube-Deposit Interface

Sample	Steady-State Vacuum Level(in Torr)
1/2" OD Clay-bonded tube standard	9
1/2" OD Clay-bonded tube sample SJ#18	74
1/2" OD Clay-bonded tube sample SJ# 32	116

Table 1: Hermetic Quality of Tubes

### Vickers Microhardness Measurements for SALD Deposited Material

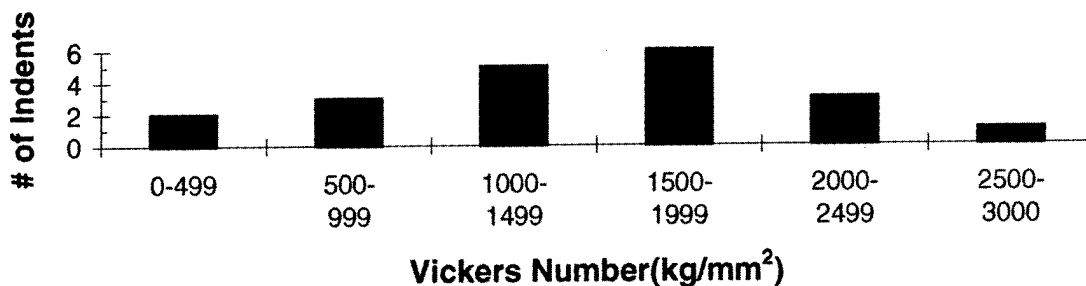


Figure 8: Vickers Hardness Determination of SALD Material

## Discussion

In this investigation, the SALD Joining process produced successful joints with two different types of silicon carbide tubing. The morphology of the deposit on each tube surface, in the Environmental SEM images above, shows excellent adherence with well integrated interfaces. The low mechanical response of the joined structures can likely be traced to the butt end joint configuration and not a function of the deposit bonding to the tube. This butt end alignment leaves a starting crack at the joint that is the length of the tube wall thickness. Future work will focus on minimizing this crack by beveling the tube ends with an expected improvement in the mechanical behavior. The hermetic seals of the tested joint structures were within an order of magnitude of the standard tube value. The better vacuum sealed joint, at 74 Torr equilibrium pressure, possessed a much smoother deposit morphology, while the other tested joint, at 116 Torr, deposited in a rougher columnar shape. We believe that a smoother deposit structure, i.e. more laminar than columnar, will produce better sealing by reducing the porosity and therefore the leak path. The microhardness values show regions of high purity silicon carbide as well as regions of very soft deposited material. The porosity inherent in the growth columns likely contributes to the response of these soft regions as does co-deposition of carbon in areas where the deposition temperature shot above approximately 1300 degrees Celsius. The hermetic sealing, microhardness uniformity and compositional uniformity will improve with the full implementation of the temperature control system. The deposition temperature can then be maintained in temperature regions where higher purity silicon carbide forms in a more even, layered manner.

The x-ray diffraction spectra obtained from the SALD silicon carbide material contained two interesting features. The first was broadening of the main peak at  $d = 2.52$  Angstroms, leading to a grain size analysis. Over several samples, the average grain size was determined to be in the range from 5 to 40 nanometers. Further grain size analysis with dark field TEM was performed and yielded an average size of approximately 30 nanometers. The second interesting feature was examined only after Nuclear Magnetic Resonance(NMR) magic angle spinning characterization of the SALD material. The NMR data showed unexpected profiles compared to a beta silicon carbide powder sample. Closer analysis of the TEM imaging and of the fine structure of the x-ray patterns around the main peak, in conjunction with computer simulations of silicon carbide x-ray spectra<sup>13,14</sup>, lead to the conclusion the SALD material is highly faulted. A publication concerning this examination of the SALD silicon carbide material is expected in the near future.

## Conclusions

The SALD Joining process offers great potential to solve the problems involved in ceramic joining. Monolithic joints, composed of the same material as the base material being 'welded' together, are possible. A dependable ceramic joining procedure could be integrated into a SFF fabrication system to build up large, complex parts from small, simple shapes in one step. This research shows that silicon carbide joints can be repeatedly fabricated with good mechanical, compositional and hermetic properties. Future work will focus on improving these properties and include tube end beveling, temperature closed-loop control and use of a second, higher power cw Nd:YAG laser. Higher purity silicon carbide tubes will also be joined together.

### Acknowledgments

The authors would like to recognize Drs. J.V. Tompkins and B.R. Birmingham for their initial SALD Joining work at UT-Austin, as well as Dr. K.J. Jakubenas for his work on the project as a postdoctoral fellow at the University of Connecticut. This research was funded in part by ONR Grant #N00014-95-1-0978.

### Footnotes

1. "Feasibility Study of the Welding of SiC" by T.J. Moore, *Journal of the American Ceramic Society*, Vol. 68, 1985, pgs. C151-C153
2. "Joining Silicon Nitride to Itself and to Metals" by S.D. Peteves, G. Ceccone, M. Paulasto, V. Stamos and P. Yvon, *Journal of Materials*, Vol. 48, January, 1996, pgs. 48-52 & 74-77(52)
3. "Solid-State Bonding of Silicon Nitride Ceramics with Nickel-Chromium Alloy Interlayers" by M. Nakamura and S.D. Peteves, *Journal of the American Ceramic Society*, Vol. 73(#5), 1990, pgs. 1221-1227
4. "Joining of Ceramics" by R.E. Loehman and A.P. Tomsia, *American Ceramic Society Bulletin*, Vol. 67(#2), 1988, pgs. 375-380(377)
5. "The Influence of Brazing Conditions on Joint Strength in  $Al_2O_3/Al_2O_3$  Bonding" by H. Hongqi, J. Zhihao and W. Xiaotian, *Journal of Materials Science*, Vol. 29, October 1<sup>st</sup>, 1994, pgs. 5041-5046
6. "Ag Effect on Microstructures and Strength of SiC/SiC Joint Brazed with Cu-Ag-Ti Filler Metals" by T. Tamia and M. Naka, *Journal of Materials Science Letters*, Vol. 15(#12), June, 1996, pgs. 1028-1029
7. "Ceramic Joining by Selective Beam Deposition" by J.V. Tompkins, B.R. Birmingham and H.L. Marcus, 1995 Solid Freeform Fabrication Symposium, Austin, Texas, August, 1995, pgs. 409-416
8. Joining Ceramics by Selective Beam Deposition by J.V. Tompkins, PhD Dissertation, University of Texas at Austin, May, 1998, pgs. 103-122
9. Modern Ceramic Engineering, 2<sup>nd</sup> Edition by D.W. Richerson, Marcel Dekker Publishing, New York, 1992, pg. 179
10. "The Structure of Chemical Vapor Deposition Silicon Carbide" by J. Chin, P.K. Gantzel and R.G. Hudson, *Thin Solid Films*, Vol. 40, 1977, pgs. 57-72
11. "Growth Characteristics of Beta-Silicon Carbide by Chemical Vapor Deposition" by C-H. Chu, Y-M Lu and M-H Hon, *Journal of Materials Science*, Vol. 27, July 15<sup>th</sup>, 1992, pgs. 3883-3888
12. "A Morphological and Structural Study of SiC Layers Obtained by LPCVD Using Tetramethylsilane" by A. Figueras, S. Garelik, R. Rodriguez-Clemente, B. Armas, C. Combescure and C Dupuy, *Journal of Crystal Growth*, Vol. 110, 1991, pgs. 528-542
13. "Effect of Stacking Faults on the X-ray Diffraction Profiles of Beta-SiC Powders" by V.V. Pujar and J.D. Cawley, *Journal of the American Ceramic Society*, Vol. 78(#3), March, 1995, pgs. 774-782
14. "Computer Simulations of Diffraction Effects due to Stacking Faults in Beta-SiC: I Simulation Results" by V.V. Pujar and J.D. Cawley, *Journal of the American Ceramic Society*, Vol. 80(#7), July, 1997, pgs. 1653-1662

## Preparation and Properties of In-Situ Devices Using the SALD and SALDVI Techniques

James E. Crocker, Lianchao Sun, Leon L. Shaw, and Harris L. Marcus  
Institute of Materials Science  
University of Connecticut  
Storrs, CT

One of the many advantages of Selective Area Laser Deposition (SALD) and Selective Area Laser Deposition Vapor Infiltration (SALDVI) is that they can be used to embed in-situ micro-sensors within macro-components. A single-point SiC/C thermocouple sensor embedded within a SiC macro-component and electrically insulated with silicon nitride layers has been demonstrated<sup>1</sup>. In many applications, multi-point sensors within a single component are needed, e.g., in monitoring the temperature gradient and distribution at different positions. In this paper, multi-point thermocouple devices are demonstrated. The macro-component is a SiC bulk shape made by infiltrating vapor deposited silicon carbide into a silicon carbide powder bed using the SALDVI technique. Multiple SiC/C thermocouples are embedded in-situ in the SiC bulk shape using the SALD technique. The transient and steady state responses of the embedded thermocouples are compared to reference thermocouples probing the surfaces of the bulk shape.

### Introduction

Selective Area Laser Deposition (SALD)<sup>2</sup> and Selective Area Laser Deposition Vapor Infiltration (SALDVI)<sup>3,4</sup> are two Solid Freeform Fabrication (SFF) techniques utilizing gas precursors. Gas phase approaches to SFF are based on the concept of building structures by depositing solid material from reactive gases<sup>5-7</sup>. The chemical vapor deposition reaction in these processes is localized using a laser beam, and the gas composition and processing conditions can be selected to achieve a desired chemistry in the vapor deposited material. SALD deposits material directly from the gas phase to create overall structures. In SALDVI, the vapor deposited material infiltrates a layer of powder, forming a continuous matrix between the powder particles to build shapes.

The ability to deposit combinations of vapor deposited material from different gas precursors and in arbitrary patterns by a scanning laser beam is a key feature of SALD and SALDVI in fabricating multiple material devices such as thermocouples which can be embedded into a bulk shape. The fabrication of functional SiC/C thermocouples deposited by SALD on several substrates have been described and demonstrated<sup>8</sup>. SALDVI fabricates multiple layer shapes of SiC particles in a matrix of vapor deposited SiC<sup>4</sup>. This paper describes how the two techniques are used to embed multiple SiC/C thermocouples into a bulk SiC shape and reports its performance in response to an applied temperature gradient.

### SALD of SiC/C Thermocouples

A detailed account of precursor selection and processing conditions related to the fabrication of SiC/C thermocouples using SALD is presented elsewhere<sup>1</sup>. Here a general overview of the procedure is presented. The SiC/C thermocouple package consists of three materials all of which are deposited from gas precursors using the SALD technique: silicon

carbide, carbon, and silicon nitride. Figure 1 shows a schematic of the thermocouple, both in an exploded view and as fabricated, showing the location of the three SALD materials. First, a

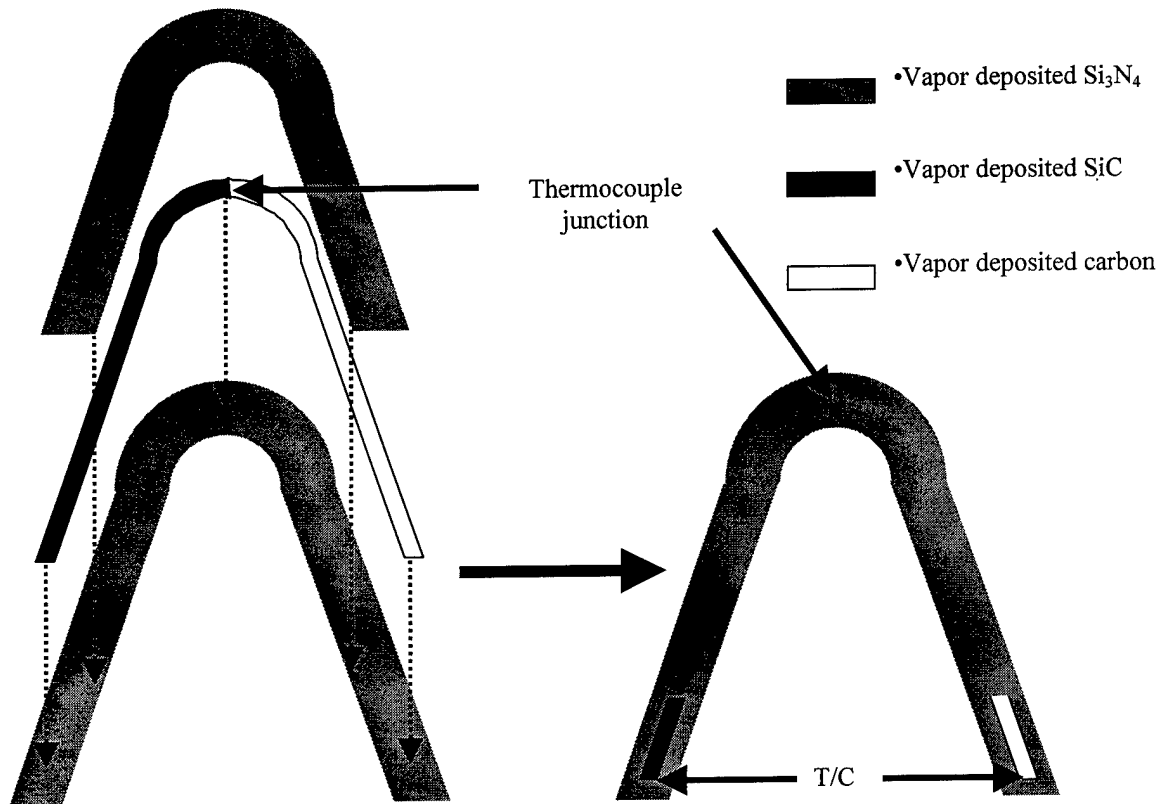


Figure 1. Fabrication of the SiC/C thermocouple device using the SALD technique.

layer of  $\text{Si}_3\text{N}_4$  is deposited from a gas mixture of tetramethylsilane and ammonia. Next a line of SiC is deposited from tetramethylsilane and a line of carbon is deposited from acetylene. The point where the two lines meet defines the temperature sensing junction of the SiC/C thermocouple. Finally a second layer of  $\text{Si}_3\text{N}_4$  is deposited over the SiC/C thermocouple, leaving a portion of each leg exposed for attaching probes to measure the emf. The  $\text{Si}_3\text{N}_4$  layers are necessary to electrically insulate the thermocouple legs from the bulk shape into which the device will be embedded.

### Embedding Thermocouples into a Bulk Shape

Figure 2 shows a schematic and actual view of a multiple layer bulk shape containing two thermocouples embedded at different locations through the thickness. SALDVI is used to fabricate a bulk shape by infiltrating layers of SiC powder with vapor deposited SiC. At an appropriate intermediate layer in the bulk shape, a thermocouple device as described in Figure 1 is deposited directly onto the SALDVI layer using SALD. Additional SALDVI layers are added on top of the SALD thermocouple device, embedding it into the bulk shape. The process is repeated in this fashion to achieve the desired number of layers.

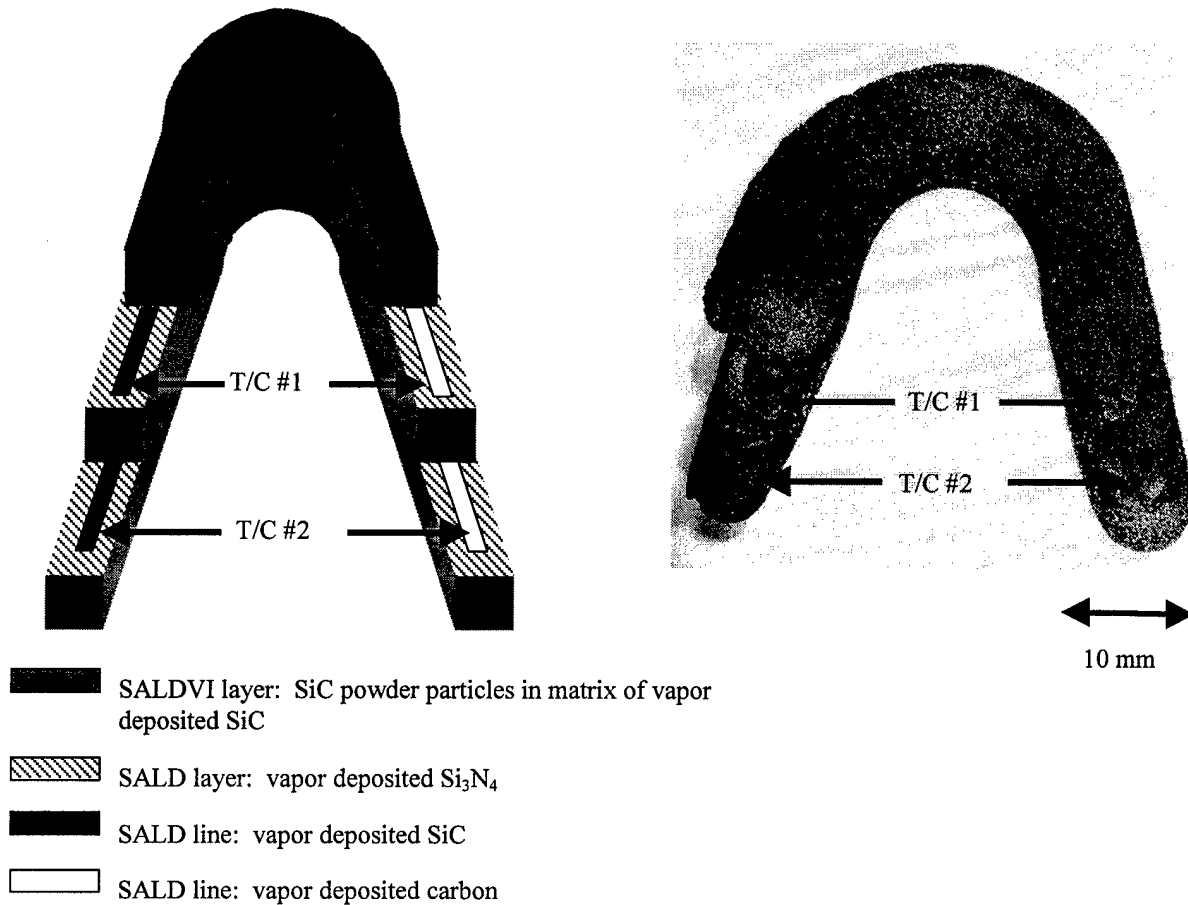


Figure 2. Bulk SiC shape containing two embedded SiC/C thermocouples

### Performance of Embedded Thermocouples

A temperature gradient was applied through the thickness of the bulk shape from Figure 2 to test the response of the two embedded thermocouples. The top surface of the shape directly above the thermocouple junctions was locally heated with a laser. K-type reference thermocouples were attached to the top and bottom surfaces of the bulk shape, also directly above and below the locations of the embedded thermocouple junctions. The laser power was systematically varied to check the transient and steady state emf signals from the two SALD SiC/C thermocouples. The response of the embedded thermocouples is plotted in Figure 8 against the two reference K-type thermocouples.

The top K-type reference thermocouple measures the thermal history applied by surface heating with the laser. The K-type thermocouple on the bottom of the bulk shape measures the temperature resulting from heat conduction through the thickness of the shape. Comparing these two curves in Figure 8, we see that for each perturbation in temperature at the top surface there is about a 100 second transient period at the bottom surface before steady state thermal conditions are reached. The corresponding emf histories from the two embedded thermocouples reflect these trends. There is a slightly longer transient period tending toward a plateau after about 200

seconds. Also, the emf from the embedded thermocouple closer to the heated surface is higher than the second embedded thermocouple as expected. This research demonstrates the viability of embedding thermocouples in bulk shapes and using the response of these devices to monitor thermal conduction through the part.

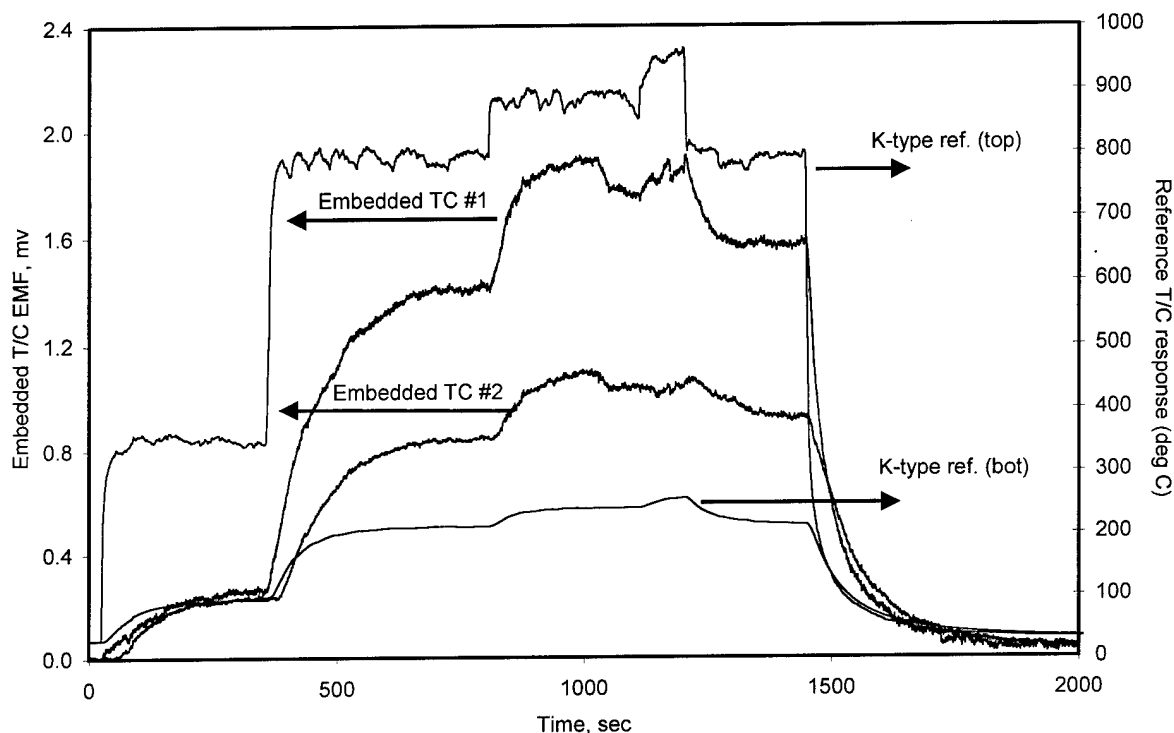


Figure 3. Response of embedded SiC/C thermocouples to an applied temperature history

### Conclusions

A multiple layer bulk shape containing two thermocouples embedded at different internal locations has been fabricated using SALD and SALDVI. The thermal response of the embedded thermocouples matches that expected when a temperature gradient is applied to the bulk shape by surface heating. The viability of the proposed process has been demonstrated.

### Acknowledgements

The authors gratefully acknowledge the generous support of the Office of Naval Research (grant #N00014-95-1-0978) and ARPA/ONR (#N00014-96-1-1299).

### References

1. L. Sun, K.J. Jakubenas, J.E. Crocker, S. Harrison, L. Shaw, and H.L. Marcus, "In-Situ Thermocouples in Macro-Components Fabricated Using SALD and SALDVI Techniques:

- III. Fabrication and Properties of the SiC/C Thermocouple Device," to be published in *Materials and Manufacturing Processes*, vol. 14, no. 1, 1999.
2. G.S. Zong, R. Carnes, H.G. Wheat, and H.L. Marcus, "Solid Freeform Fabrication by Selective Area Laser Deposition," Proceedings of the Solid Freeform Fabrication Symposium, The University of Texas at Austin, 1990, pp. 83-90.
  3. B.R. Birmingham and H.L. Marcus, "Silicon Carbide Shapes by Selective Area Laser Deposition Vapor Infiltration," Proceedings of the Solid Freeform Fabrication Symposium, The University of Texas at Austin, 1994, pp. 348-355.
  4. J.E. Crocker, K.J. Jakubenas, S. Harrison, L. Shaw, and H.L. Marcus, "SALDVI Optimization for the Tetramethylsilane - Silicon Carbide System," Proceedings of the Solid Freeform Fabrication Symposium, The University of Texas at Austin, 1997, pp. 489-496.
  5. J.L. Maxwell, J. Pegna, and D.V. Messia, and D. DeAngelis, "Direct Feedback Control of Gas Phase Laser-Induced Deposition," Proceedings of the Solid Freeform Fabrication Symposium, The University of Texas at Austin, 1996, pp. 227-237.
  6. M. Wanke, O. Lehmann, K. Muller, Q. Wen, and M. Stuke, "Laser Rapid Prototyping of Photonic Band-Gap Microstructures," *Science*, vol. 275, 28 February 1997.
  7. F.T. Wallenberger and P.C. Nordine, "Amorphous Silicon Nitride Fibers Grown From the Vapor Phase," *J. Mater. Res.*, vol. 9, No. 3, March 1994.
  8. L. Sun, K.J. Jakubenas, J.E. Crocker, S. Harrison, L. Shaw, and H.L. Marcus, "Fabrication of In-Situ Silicon Carbide/Carbon Thermocouples by SALD," Proceedings of the Solid Freeform Fabrication Symposium, The University of Texas at Austin, 1997, pp. 481-488.



# Temperature Dependent Optical Properties of Polymers as a Basis for Laser Process Modeling

*Bernd Keller, Rolf Pfeifer, Wei-Nien Su, Peter Eyerer*  
*Institute of Polymer Testing and Polymer Science, IKP - University of Stuttgart*

## Abstract

The knowledge of laser absorption is essential to describe the behavior of polymers in different laser processes, i.e. SLS, LOM, etc. By means of transmission IR-spectroscopy a method for measuring temperature dependent penetration depths (absorption length) of polymers, especially at a wavelength of 10.6 $\mu\text{m}$  (CO<sub>2</sub>-Laser), is developed. Results for the laser sintering materials polystyrene (PS), nylon 11 (PA 11), nylon copolymer (CoPA) and polyethylene terephthalate (PET) are presented. It is detected that the absorption length of polymers will increase or decrease significantly dependent on temperature. This paper will point out simplified methods based on the one dimensional heat transfer equation with volume heat source to set the processing parameters i.e. for the SLS process. The calculations correspond with the measured data.

## 1 Introduction

Optical and thermal properties are the most important parameters to characterize polymers for laser processing and even determine the applicability of some special applications, i.e. for selective laser sintering. In this work, a method for measuring temperature dependent absorption length of polymers, especially at a wavelength of 10.6 $\mu\text{m}$  (CO<sub>2</sub>-Laser), will be explored by means of transmission IR-spectroscopy. The temperature dependent absorption coefficient, which is in addition to the thermal properties the decisive material property, permits the prediction of the processability of the polymer in laser sintering. On the basis of the thermal conductivity equation, simplified work curves will be estimated to derive significant processing parameters which will be compared with experimental results. The obtained experimental results of the IR-spectroscopy will be used in the calculations.

## 2 IR-spectroscopy

Most of the relevant thermal properties (phase change- $T_g$ ,  $T_m$ ,  $T_z$ ; specific heat capacity- $c_p$ ; thermal conductivity- $\lambda$ ; thermal diffusivity- $\kappa$  and coefficient of thermal expansion) can be determined by standardized testing methods. Optical properties like absorption rate and penetration depths of electromagnetic waves depend on the structural constitution of aliphatic macromolecules. In this case, no direct reliable measurement system is known and the related issues has been less discussed. A device is required to determine the interaction between light, electrons, atoms and molecules. Transmission IR-spectroscopy is suitable to measure eigenfrequencies of atoms in the range of  $10^{12}$  to  $3 \cdot 10^{14}$  Hz (IR). With the knowledge of the position of the „absorption bands in the frequency spectrum“ one receives a so-called fingerprint of the polymer. The extinction which depends on the functional groups of the polymers and the amount of molecules (sample thickness) could be measured by transmission IR-spectroscopy. The quantitative absorption spectroscopy is defined by the Beer-Lambert law:

$$I = I_0 \cdot \exp(-\epsilon \cdot c \cdot d), \quad (1)$$

where  $I$  the transmitting intensity,  $I_0$  the entering intensity,  $d$  the sample thickness,  $c$  the coefficient of the relative density (for dense films  $c=1$ ) and  $\epsilon$  the extinction coefficient. The

exponent  $\epsilon d$  is the measured extinction  $E$ . The absorption coefficient  $a$  is given by  $a = \log e^{-1} \cdot \epsilon$ . The optical penetration depth, also called absorption length  $l_a$ , is defined as:

$$l_a = \frac{1}{a}, \quad (2)$$

and represents the penetration depth in a workpiece where the radiation intensity decreases at  $1/e$  of the entering intensity  $I_0$ . The absorption quotas  $A$  of the polymers were measured using a diffuse reflexion spectroscopy device. The absorption quota  $A$  was found to be above 95% of the entering intensity and varies only slightly for the different polymer powders.

### 3 Experiments of measuring temperature dependent absorption lengths

The results will help explain the different processability of polymer powders. In addition, the obtained absorption length is an important property to understand the absorption mechanism in polymers by irradiation of CO<sub>2</sub>-laser and will be used the later calculations.

#### 3.1 Preparation of polymer films and measuring device

To estimate the extinction- and absorption coefficients with IR-spectroscopy, the transmittance of irradiation on polymer films must be measured. Solid parts (50x30x5mm) are produced by injection molding of the polymer sintering powders and will be subsequently cut into polymer films of 40 $\mu$ m, 80 $\mu$ m and 160 $\mu$ m thickness using a microtome. The temperature history and the influence of moisture were eliminated by tempering the films for 10 min. (PA 11: 160°C, CoPA: 70°C, PET: 160°C) and cooling gradually down to the room temperature. The films were positioned in a temperature cell (max. T=600°C) and adjusted in the envelop between IR-detector and IR-bulb. During measurement the cell was floated with inert gas (Argon) and thermocouples were used to control the temperature.

#### 3.2 IR-Spectra of polymers

Fig. 1 points out an example of a PET-spectrum with characteristic bands of some vibrational forms. The wavenumber of the CO<sub>2</sub>-laser ( $\nu = 943.4\text{cm}^{-1}$ ) is marked with a line. The corresponding film thickness is  $d = 80\mu\text{m}$ . An exact determination of the vibrational systems responsible for the absorption of the CO<sub>2</sub>-irradiation is not possible as a result of superposition of bands.

In this case, the extinction for the wavenumber of the CO<sub>2</sub>-laser will be determined by the base-line method. The base-line will be constructed by tangentially connecting two minima of the extinction curve. These two minima have to be two sections of the extinction curve,

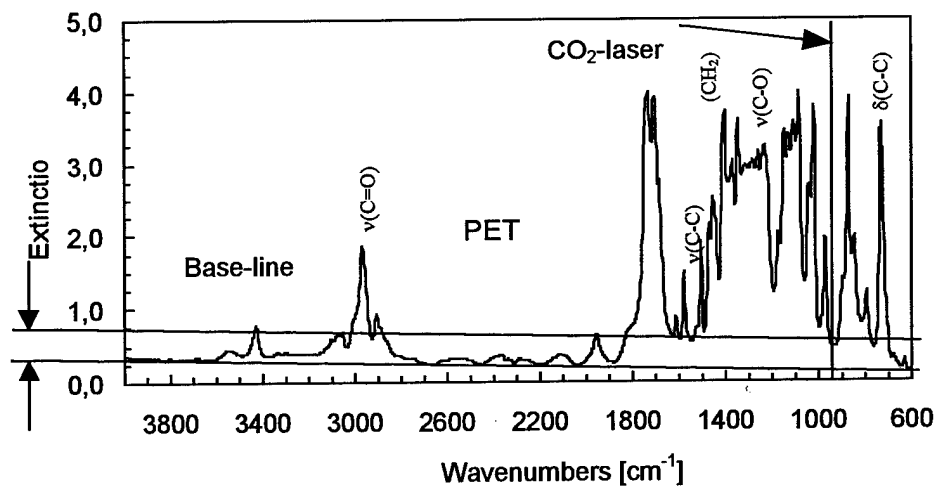


Fig. 1: IR-Spectrum of the sintering material PET at room temperature including the construction of the base-line to determine the extinction  $E$

where there are no intensive bands of vibration. This is a requirement to determine temperature dependent extinctions and as a result to calculate the temperature dependent optical penetration depth. Experiments show that every investigated sintering material has some wavenumber ranges, so-called windows, where the extinction is independent of the temperature and remains at a constant level. The distance between the intersection points of the base-line and the detected IR-extinction line with the plummet at  $\nu = 943.4\text{cm}^{-1}$  is the extinction  $E$ .

### 3.3 Determination of absorption length

According to the extinction  $E$  from the IR-spectrum, the extinction coefficient  $\epsilon$  can be obtained by division with the corresponding film thickness  $d$ . The absorption length are calculated according to equation (2).

Fig. 2 indicates the calculated absorption lengths of different sintering materials as a function of temperature. Deviations for other film thicknesses are in the range of 10% to 15%. For PA 11 and CoPA which have a similar IR-spectra, the temperature dependent absorption lengths show an analogous progression.

Whereas PS also has an increasing curve, the PET curve demonstrates a constant decrease.

This effect describes the experimental results that the thickness of PET sintering layers could not be increased by raising preheating temperature /1/. A quantitative determination above the melting point is not possible with the transmission method.

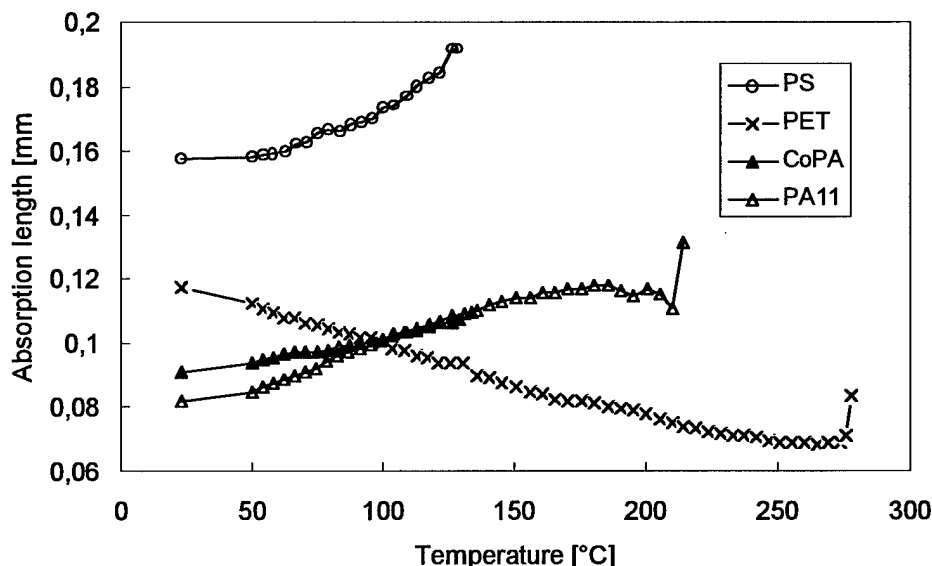


Fig. 2: Absorption length as function of temperature measured on  $80\mu\text{m}$  films of the sintering materials PET, PS, PA 11 and CoPA

### 4 Laser process characteristics (SLS)

The main processing variables in the SLS application are the laser power, beam radius, scan speed, scan spacing, layer thickness as well as the temperature in the powder bed and process chamber.

The laser sintering lab device installed at IKP has a focused beam radius  $w_0=0.225\text{mm}$ . According to the scan spacing  $h_s$ , usually smaller than the laser beam radius, each laser intensity distribution (approximately Gaussian distribution) will partially overlay with the next one. Additionally, the polymer has less thermal conductivity in comparison with other materials. It is thus assumed that at the moment at which the laser is scanning and immediately afterwards it is likely that a heat block will arise on the surface of polymer powder. Hence, an overlapping variable  $\gamma$  to account this effect could be defined as follows /2/,

$$\gamma = \frac{I}{I_0} = 1 + 2 \cdot \sum_{i=1}^N \exp\left(\frac{-2 \cdot (i \cdot h_s)^2}{w_0^2}\right) \quad (3)$$

where  $h_s$  and  $w_0$  are the scan spacing and the beam radius respectively.

The value for laser power, scan speed and scan spacing must be chosen appropriately, so as to best influence the properties of the sintered parts. For further investigation, the following assumptions are made :

1. The powder bed is treated as a homogenous and isotropic medium.
2. The heat transfer from the laser radiation to the material is a one dimensional case and the heat lost through the heat convection and radiation on the surface will be neglected.
3. The temperature dependent material properties will be approximated by an average value and the phase change and decomposition will be excluded.
4. The laser intensity and the scan speed are assumed constant, and also the average interaction time.
5. The cooling time between the superposition of the laser radiation with respect to a point on the plane can be neglected, since the thermal conductivity of polymer powder is relatively inferior (for  $v \geq 500$  mm/s and average sample length of 50mm)

The equation to describe the heat transfer in the material caused by a Gaussian radiation distribution is shown in [3]. With consideration of the overlapping variable  $\gamma$  and the preheating temperature  $T_0$ , the modified equation is expressed as:

$$T(z, t) = \frac{A I_0 \gamma}{\lambda} \left\{ \begin{aligned} &2\sqrt{kt} \cdot \operatorname{ierfc}\left(\frac{z}{2\sqrt{kt}}\right) - \frac{1}{a} \exp(-az) \\ &+ \frac{1}{2a} \exp(a^2 kt) \left[ \exp(-az) \cdot \operatorname{erfc}\left(a\sqrt{kt} - \frac{z}{2\sqrt{kt}}\right) + \exp(az) \cdot \operatorname{erfc}\left(a\sqrt{kt} + \frac{z}{2\sqrt{kt}}\right) \right] \end{aligned} \right\} + T_0 \quad (4)$$

where  $A$  and  $a$  are the absorption quota and absorption coefficient respectively, when the material is subjected to a laser radiation.

## 5 Simplified heat transfer equations

The working curves are derived and utilized so as to ensure that the surface temperature should not exceed the decomposition temperature (*see A*), and so that there should simultaneously be sufficient laser power available for melting or sintering powder at a specific depth in the powder bed (*see B*).

### A: Equation for $T \leq T_z$ on the surface of material, at $z=0$

The temperature on the surface is easily to obtain by inserting  $z=0$  into the equation (4) and it becomes

$$\frac{(T(0, t) - T_0) \cdot \lambda \cdot a}{A \cdot I_0} = \frac{2}{\sqrt{\pi}} a\sqrt{kt} - \left[ 1 - \exp(a^2 kt) \cdot \operatorname{erfc}(a\sqrt{kt}) \right] \quad (5)$$

The maximal temperature on the surface should not exceed the degradation temperature. The right side of the equation (5) could be further simplified, but the intermediate steps need not

be shown in this work /4/. The simplified result delivers a clear relationship between the material properties and the relevant processing parameters:

$$\frac{(T(0,t) - T_0) \cdot \lambda}{A \cdot l_0} \approx a \cdot \kappa \cdot t \quad (6)$$

where the temperature difference  $T(0,t) - T_0$  can be expressed as  $\Delta T_{z0}$  instead and  $l_0$  replaced by

$$l_0 = \frac{2 \cdot P}{\pi \cdot w_0^2} \quad (7)$$

Hence, the maximal suitable laser power  $P_z$  which could be used in the process so that the material will not decompose is expressed as follows:

$$P_z = \frac{\pi \cdot v \cdot w_0 \cdot \Delta T_{z0} \cdot c_p \cdot \rho}{4 \cdot A \cdot a \cdot \gamma} \quad (8)$$

In addition this equation indicates the proportionality between absorption coefficient  $a$  and density  $\rho$ .

**B: Equation for  $T \geq T_m$  at a specific depth  $z = z_m$**

To guarantee a sufficient layer cohesion in the sintering parts, the layer thickness must usually be greater than 0.1 mm. This means that the temperature is supposed to reach the melting point at a specific desirable sintering depth in the powder bed  $z = z_m$ . Under this assumption, the terms in equation (4) can be reduced and the equation becomes:

$$T(z_m, t) - T_0 = \frac{A l_0}{a \lambda} \cdot \exp(-a z_m) \cdot [\exp(a^2 \kappa t) - 1] \quad (9)$$

where  $T(z_m, t) - T_0$  can be replaced by the term  $\Delta T_{m0}$  and  $l_0$  likewise by equation (7). Thus, a minimal necessary laser power  $P_m$  to ensure a satisfactory sintering at the depth  $z_m$  is obtained.

$$P_m = \frac{\Delta T_{m0} \cdot \exp(a \cdot z_m) \cdot a \cdot \lambda \cdot \pi \cdot w_0^2}{2 \cdot A \cdot \gamma} \cdot \left[ \exp\left(a^2 \cdot \kappa \cdot \frac{2w_0}{v}\right) - 1 \right]^{-1} \quad (10)$$

The calculations will be performed with average values (in this work not explicit described) of thermal properties detected accordingly DIN 53765 (DSC) and the thermogravimetric analysis (TGA). The thermal conductivity was estimated using the Zehner, Bauer and Schlünder equation (secondary parameters were taken into account) /5/.

The validity of the two simplified equations (8) and (10) will be verified at  $z=0$  and  $z=0.15$  mm respectively and illustrated in Fig. 3. As this reveals, the original and simplified equations coincide well with each other over the usual scan speed range, especially at  $z=0.15$  mm. It is also useful to recognize that the interaction time has to lie in the range between 0.425 ms and 0.28 ms to fulfill the above mentioned requirements. A suitable working area related to the scan speed is then developed.

With CoPA, PA 11 and PS, it is quite easy to find an appropriate working area for a given layer thickness. In contrast to these three materials, PET seems less suitable for the laser sintering process because it is not possible to build a sufficient layer thickness without damaging the material on the surface. In addition to this, the absorption length decreases with the increasing

temperature, which restricts the laser radiation around the surface region and the laser is thus not able to “penetrate” material to the required depth.

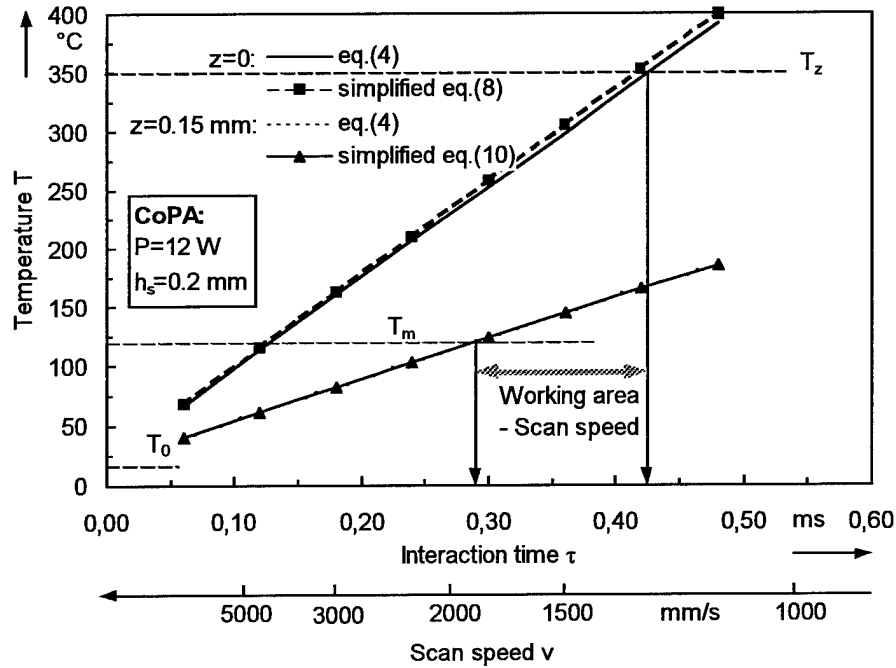


Fig.3: Comparison of the equation (4) and simplified ones

It is obvious that the  $P_z$ -line should lie above the  $P_m$ -line. The maximal possible sintering depth is to obtain through equating the equation (8) and (10) and it follows

$$z_m = \frac{1}{a} \cdot \ln \left[ \frac{\Delta T_{z0}}{\Delta T_{m0}} \cdot \left( \frac{\exp(x) - 1}{x} \right) \right] \quad \text{with } x = a^2 \cdot \kappa \cdot \frac{2w_0}{v} \ll 1 \quad (11)$$

Because  $x$  is much smaller than 1 for the common polymer materials and processing conditions, the above equation could be further simplified to

$$z_m(T_0) = \frac{1}{a(T_0)} \cdot \ln \left( \frac{T_z - T_0}{T_m - T_0} \right) \quad (12)$$

The progression of maximal achievable sintering depth with respect to the temperature dependent absorption length demonstrates consequently an asymptotic approach to the glass transition or melting temperature of the polymer respectively, see Fig. 4.

## 6 Comparison of calculated and measured sintering depths

To evaluate the validity of these equations, they could be directly compared with the experimental results. Through converting the equation (10), the achievable sintering depth could be expressed as a function of other material properties and processing parameters:

$$z_m = \frac{1}{a} \cdot \ln \left\{ \frac{2 \cdot A \cdot \gamma \cdot P_m}{\Delta T_{m0} \cdot a \cdot \lambda \cdot \pi \cdot w_0^2} \cdot \left[ \exp \left( a^2 \kappa \frac{2w_0}{v} \right) - 1 \right] \right\} \quad (13)$$

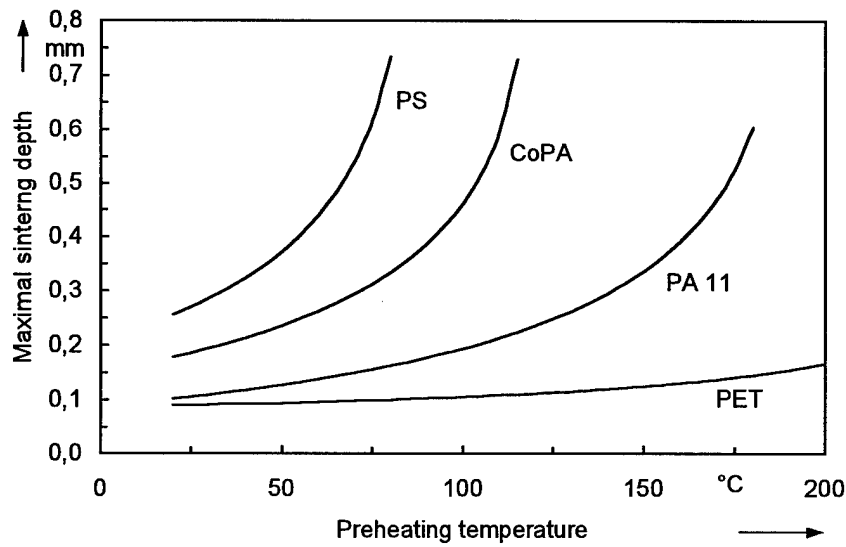
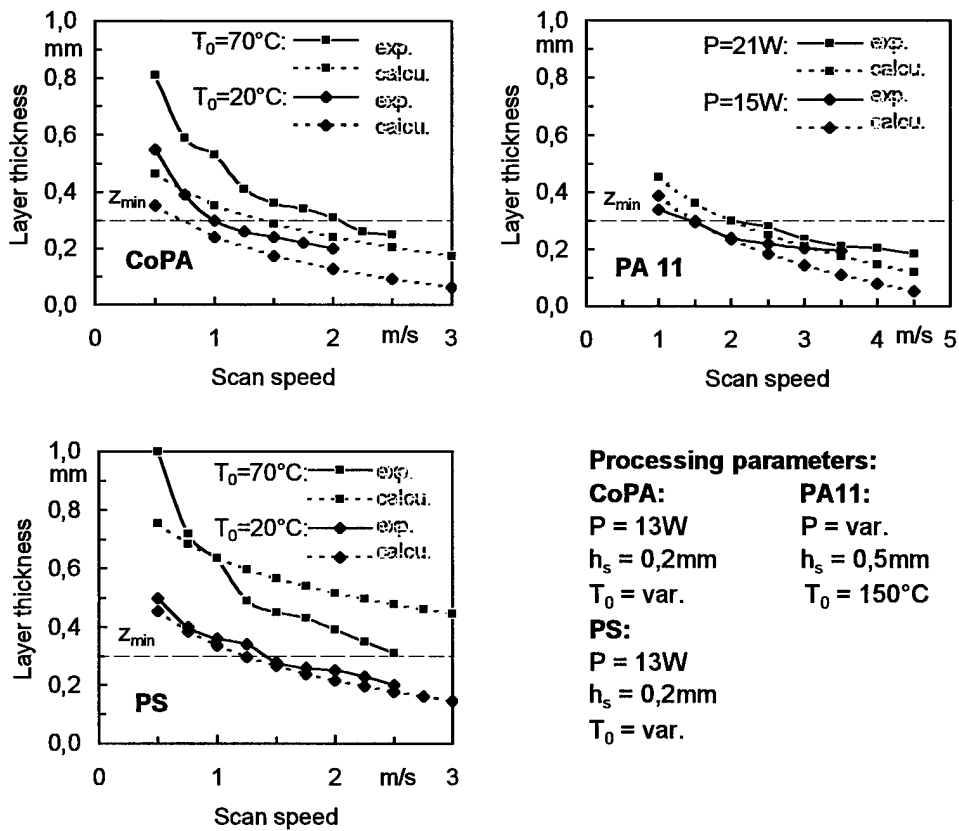


Fig. 4: Maximal reachable sintering depth for PS, CoPA, PA 11 and PET



**Processing parameters:**  
**CoPA:** P = 13W,  $h_s = 0,2\text{mm}$ ,  $T_0 = \text{var.}$   
**PA11:** P = var.,  $h_s = 0,5\text{mm}$ ,  $T_0 = 150^\circ\text{C}$   
**PS:** P = 13W,  $h_s = 0,2\text{mm}$ ,  $T_0 = \text{var.}$

Fig. 5: Comparison of measured and calculated results in respect of sintering depth

It has to be stressed that the layer thickness was measured in experimental parts and this could differ from the sintering depth  $Z_m$  in the theoretical view owing to the adhered particles on both sides of the sample. If the particle size is taken into consideration, through examination of

the comparisons in Fig. 5 it is clear that the experimental and calculated results show a very satisfactory agreement.

## 7 Conclusion and Outlook

By means of transmission IR-spectroscopy, a method for measuring temperature dependent absorption lengths of polymers, especially at a wavelength of 10.6 $\mu$ m (CO<sub>2</sub>-Laser), is developed. This paper also points out simplified equations based on the one dimensional heat transfer equation with a volume heat source to set the processing parameters i.e. for the SLS process. The calculations show a satisfactory agreement with the measured results. The equations can be used to determine the working curves in the laser sintering technology and are suitable to estimate the processing parameters in other laser material processing as well such as, surface treatment, welding, cutting or drilling. The methodology of measuring the optical absorption length for CO<sub>2</sub>-laser could be also extended to another wavelength range or laser types in the future.

## 8 Acknowledgement

The authors gratefully acknowledge the financial support of the German Research Foundation, DFG (Sfb 374), for this work. Thanks are due to Dr. Jialin Shen (Daimler-Benz AG) and Frieder Nagel (Fh-ICT), whose persistence and meticulousness contribute to the accomplishment of this work. The authors also appreciate the students for their considerable effort.

## Nomenclature

A	Absorption quota [-]	$T_m, T_z$	Melting point and decomposition temperature [K]
a	Absorption coefficient [1/mm]	t	Interaction time [ms]
c	Relative concentration [-]	v	Scan speed [mm/s]
$c_p$	Specific heat capacity [J/g K]	$w_0$	Laser radius [mm]
d	IR-sample thickness [mm]	z	Depth in powder bed [mm]
E	Extinction [-]	$\Delta T_{m0}$	Temperature difference of $T_m$ and $T_0$
$h_s$	Scan spacing [mm]	$\Delta T_{z0}$	Temperature difference of $T_z$ and $T_0$
$I_0, I$	Entering and transmitting laser intensity [W/m <sup>2</sup> ]	$\gamma$	Defined overlapping variable [-]
$l_a$	Absorption length [mm]	$\epsilon$	Extinction coefficient [mm]
$P_m$	Minimum necessary laser power [W]	$\kappa$	Thermal diffusivity [mm <sup>2</sup> /s]
$P_z$	Maximum allowed laser power [W]	$\lambda$	Thermal conductivity [W/m K]
$T_0$	Preheating temperature [K]	$\nu$	Frequency [cm <sup>-1</sup> ]
$T_g$	Glass temperature [K]		

## Reference

1. Pfeifer, Rolf: Untersuchung thermoplastischer Werkstoffe für die Lasersinter-Technologie. Diplomarbeit, IKP, Universität Stuttgart (1997).
2. Su, Wie-Nien: Untersuchung des thermischen Verhaltens von Kunststoffen beim selektiven Lasersintern und Analyse der Prozessparameter. Diplomarbeit, IKP, Universität Stuttgart (1997).
3. Carslaw, H. S.; Jaeger, J. C.: Conduction of Heat in Solids. Oxford University Press (1959).
4. Keller, B.: Rapid Prototyping: Grundlagen zum selektiven Lasersintern von Polymerpulvern, Dissertation, Universität Stuttgart - to be published 1998.
5. Tsotsas, E.; Martin, H.: Thermal Conductivity of Packed Beds: A Review. Chem. Eng. Proc., Vol. 22, 19-37 (1987).

# Mechanical Characterization of Parts Processed via Fused Deposition

Bertoldi M., Yardimci M. A., Pistor C. M., Güçeri S. I., Sala G.  
University of Illinois at Chicago

## ABSTRACT

The possibility of using materials with better physical and mechanical properties together with the quickly improving capabilities of various processes increasingly make Rapid Prototyping (RP) as a new manufacturing technology for specialty components.

In Fused Deposition Modeling (FDM), the build orientation and the toolpath used strongly affect the properties of the part. This study presents the results of experimental work based on mechanical characterization of parts fabricated with fused deposition to determine the stiffness matrix and the thermal expansion coefficients for an equivalent orthotropic material. The results can be directly adapted into computational analysis tools based on classical lamination theory, for part quality and performance prediction. Current investigation focuses on use of ABS material in Stratasys FDM 1650 rapid prototyping equipment.

## BACKGROUND

For conventional polymer-based material technologies the properties of the fabricated parts are well known and can be predicted and determined with different tools and characterization techniques. However, for parts fabricated using rapid prototyping, there are no standard methods available. In the current work, complete mechanical characterization for ABS parts with a pseudo-isotropic stacking sequence has been performed.

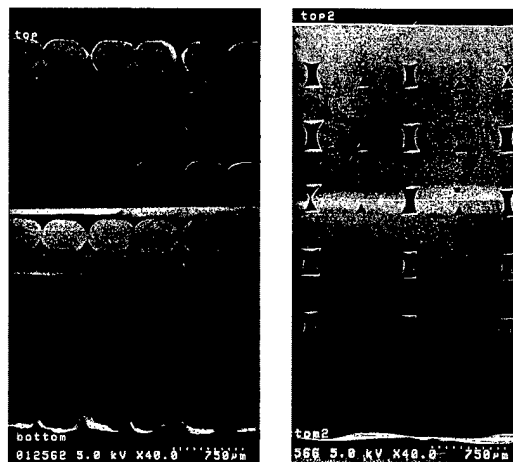


Figure 1 SEM pictures of a section of a standard lay-up part [0 90] [1]

Fused Deposition process produces a 3D part by superimposing a specified number of layers, where each of them is generated by parallel roads. The internal microstructure can be assimilated to a composite two-phase material, where the roads correspond to fibers (**Figure 1**). Weak bonding between the roads and voids, coupled with inherently anisotropic properties of extruded roads enhance this similarity and make the local orthotropic behavior more pronounced.

Similar to a standard polymeric matrix composite, the FDM parts can be assumed to be linear, elastic and orthotropic. The general strain-stress relation (see [1] for details) for an orthotropic material is:

$$\begin{bmatrix} \varepsilon_1 \\ \varepsilon_2 \\ \varepsilon_3 \\ \gamma_{23} \\ \gamma_{13} \\ \gamma_{12} \end{bmatrix} = \begin{bmatrix} S_{11} & S_{12} & S_{13} & 0 & 0 & 0 \\ & S_{22} & S_{23} & 0 & 0 & 0 \\ & & S_{33} & 0 & 0 & 0 \\ & sym. & & S_{44} & 0 & 0 \\ & & & & S_{55} & 0 \\ & & & & & S_{66} \end{bmatrix} \begin{bmatrix} \sigma_1 \\ \sigma_2 \\ \sigma_3 \\ \tau_{23} \\ \tau_{13} \\ \tau_{12} \end{bmatrix} \quad (1)$$

The [6x6] compliance matrix can be inverted to obtain the stiffness matrix:

$$\begin{bmatrix} \varepsilon_1 \\ \varepsilon_2 \\ \varepsilon_3 \\ \gamma_{23} \\ \gamma_{13} \\ \gamma_{12} \end{bmatrix} = \begin{bmatrix} \frac{1}{E_1} & -\frac{\nu_{21}}{E_2} & -\frac{\nu_{31}}{E_3} & 0 & 0 & 0 \\ & \frac{1}{E_2} & -\frac{\nu_{32}}{E_3} & 0 & 0 & 0 \\ & & \frac{1}{E_3} & 0 & 0 & 0 \\ & & & \frac{1}{G_{23}} & 0 & 0 \\ & sym. & & & \frac{1}{G_{13}} & 0 \\ & & & & & \frac{1}{G_{12}} \end{bmatrix} \begin{bmatrix} \sigma_1 \\ \sigma_2 \\ \sigma_3 \\ \tau_{23} \\ \tau_{13} \\ \tau_{12} \end{bmatrix} \quad (2)$$

In order to determine nine independent constants it is necessary to test six different specimens. The elastic modulus can be obtained from the stress-strain diagram:

$$E_x = \frac{\Delta \sigma_x}{\Delta \varepsilon_x} \quad (3)$$

Poisson ratio is defined as:

$$\nu_{xy} = \frac{-\varepsilon_y}{\varepsilon_x} \quad (4)$$

In-plane shear modulus G can be obtained from the test of a 45° oriented bar, as follows:

$$G_{ab} = \frac{E_x}{2(1 + \nu_{xy})} \quad (5)$$

where  $x$  and  $y$  are the direction of load application and the normal direction respectively. Also,  $a$  and  $b$  correspond to 1 and 2 for the specimen in the  $xy$  plane, 2 and 3 for the one in the  $xz$  plane and 3 and 1 for the one in the  $yz$  plane.

If we also consider an externally applied temperature variation, and assuming that the free thermal strain is linearly dependent on temperature, the stress-strain equations take the form:

$$\begin{bmatrix} \varepsilon_1 - \alpha_1 \Delta T \\ \varepsilon_2 - \alpha_2 \Delta T \\ \varepsilon_3 - \alpha_3 \Delta T \\ \gamma_{23} \\ \gamma_{13} \\ \gamma_{12} \end{bmatrix} = \begin{bmatrix} S_{11} & S_{12} & S_{13} & 0 & 0 & 0 \\ & S_{22} & S_{23} & 0 & 0 & 0 \\ & & S_{33} & 0 & 0 & 0 \\ & sym. & & S_{44} & 0 & 0 \\ & & & & S_{55} & 0 \\ & & & & & S_{66} \end{bmatrix} \begin{bmatrix} \sigma_1 \\ \sigma_2 \\ \sigma_3 \\ \tau_{23} \\ \tau_{13} \\ \tau_{12} \end{bmatrix} \quad (6)$$

and consequently the inverse relations (3) becomes:

$$\begin{bmatrix} \sigma_1 \\ \sigma_2 \\ \sigma_3 \\ \tau_{23} \\ \tau_{13} \\ \tau_{12} \end{bmatrix} = \begin{bmatrix} C_{11} & C_{12} & C_{13} & 0 & 0 & 0 \\ & C_{22} & C_{23} & 0 & 0 & 0 \\ & & C_{33} & 0 & 0 & 0 \\ & sym. & & C_{44} & 0 & 0 \\ & & & & C_{55} & 0 \\ & & & & & C_{66} \end{bmatrix} \begin{bmatrix} \varepsilon_1 - \alpha_1 \Delta T \\ \varepsilon_2 - \alpha_2 \Delta T \\ \varepsilon_3 - \alpha_3 \Delta T \\ \gamma_{23} \\ \gamma_{13} \\ \gamma_{12} \end{bmatrix} \quad (7)$$

Eq. (7) represents the complete constitutive relation for an orthotropic material.

### TEST SETUP

The experimental testing has been conducted using the procedure explained in [3] and [4], on a INSTRON 5569 machine, with the following equipment:

- a cross-head screw-driven by a DC servo motor, with a speed range of 0.001 to 500 mm/min.
- a load cell with a maximum load capacity of  $\pm 50$  KN.
- two wedge action grips
- one axial strain extensometer with a gauge length of 50 mm
- one transverse strain extensometer with a gauge length of 10 mm

### PREPERATION OF TENSILE TEST BARS

The specimens for the tensile tests were designed according to the specifications of the ASTM D 5937-96 standard for molded plastic parts [5], since no special standard exists for the

characterization of RP parts. The bar was designed using Pro/Engineer and exported in the STL format. Using QuickSlice 5.0, it was oriented in six different ways (**Figure 2**) and then sliced. The vertical and the 45° oriented bars in the  $xy$  and  $zy$  planes were built with the "contain support" option (the entire part is surrounded by support).

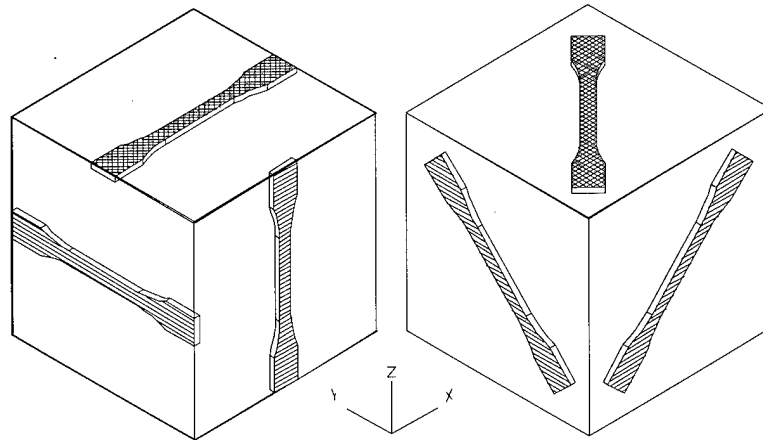


**Figure 2** Test specimen orientation

The properties of the layers have been set to obtain a road orientation variable in the  $z$  direction with the pseudo-isotropic stacking sequence:

$$[0\ 90\ +45\ -45]$$

## RESULTS

For every specimen the following data have been collected:

- Ultimate tensile strength
- Elastic (Young's) modulus
- Poisson ratio

The Young's modulus has been calculated from the stress-strain diagram (Eq. 3); a MATLAB function has been implemented to perform a least square interpolation of the linear portion of the curve. The same has been done to calculate the Poisson ratio (4), which is the ratio between the slopes of the two curves (stress-axial strain and stress-transverse strain). The data reduction of the results presented some difficulties due to the scattered values obtained; small variations of the processing parameters can strongly affect the measurements. Premature failure of the specimens was caused by different reasons:

- Intralaminar defects, due to presence of excess material stuck to the nozzle and then dropped onto the layer
- Interlaminar defects due to over or under fill between rasters or between rasters and contour
- Surface roughness (initiation of microcracks)

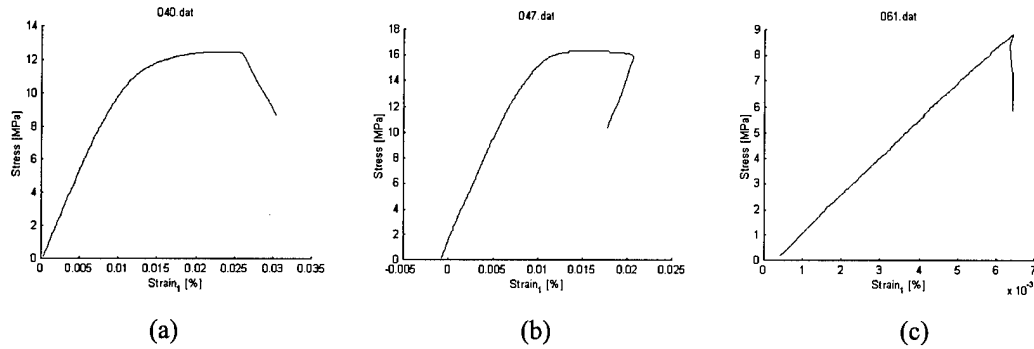


**Figure 3** Stress – strain curves for  $x$ - $y$  (a),  $y$ - $z$  (b) and  $x$ - $z$  (c) oriented specimens.

The first point has been particularly critical for the vertical ( $x$ - $z$ ) bar, because of the large number of layer ( $> 600$ ), causing in all the specimens a brittle failure (**Figure 3-c**). In some tests the failure occurred close to the grips, and the results had to be discarded. The parts in the  $x$ - $y$  and  $y$ - $z$  planes presented a common elasto-plastic behavior (**Figure 3-a** and **Figure 3-b**); however, it must be noticed as the  $y$ - $z$  part resulted in the highest value for both the elastic modulus and the tensile strength. The  $xz$  part has the lowest tensile strength (**Figure 4**). All the results are presented in **Table 1**.

Toolpath	Build plane	Orientation	Number of specimens tested	Number of specimens considered	Avg.tensile strength [MPa]	Avg. elastic modulus [MPa]
[0 90 +45 -45]	xy	X	4	4	11.700	1072.900
[0 90 +45 -45]	yz	Y	4	4	15.987	1652.523
[0 90 +45 -45]	xz	Z	11	6	7.608	1391.448
[0 90 +45 -45]	xy	x+45	5	5	10.808	970.944
[0 90 +45 -45]	yz	y+45	5	4	13.465	1519.115
[0 90 +45 -45]	xz	z+45	3	3	14.702	1527.600

**Table 1** Tensile test results

Finally, the stiffness matrix is obtained as:

$$C = 1.0e + 003 * \begin{bmatrix} 1.8530 & 1.4348 & 1.1810 & 0 & 0 & 0 \\ 1.4348 & 3.0843 & 1.6444 & 0 & 0 & 0 \\ 1.1810 & 1.6444 & 2.4141 & 0 & 0 & 0 \\ 0 & 0 & 0 & 0.5540 & 0 & 0 \\ 0 & 0 & 0 & 0 & 0.5405 & 0 \\ 0 & 0 & 0 & 0 & 0 & 0.3696 \end{bmatrix}$$

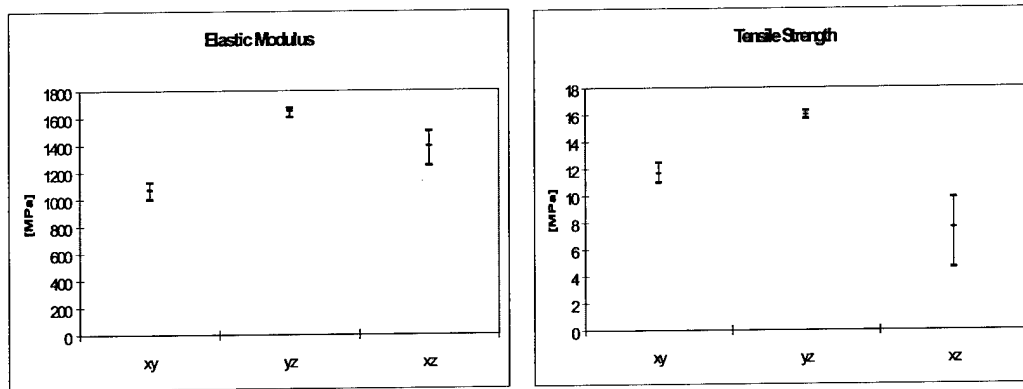


**Figure 4** Max, min and avg. values of elastic modulus (a) and tensile strength (b).

### *THERMAL EXPANSION*

To calculate the three thermal expansion coefficients, a series of tests has been conducted; three square specimens have been built with the same stacking sequence of the tensile test bars ([0 90 +45 -45]). **Figure 5** shows the specimens built, for which the dimensions can be found in **Table 2**. The test procedure is presented in [3].

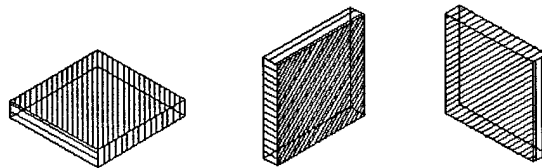


**Figure 5** Thermal expansion specimens

The test setup consists of:

- A Scientific Inc. VWR 1410 oven.
- A Power Macintosh equipped with a Lab NB Data Acquisition Board and LabVIEW Software for data acquisition and processing.
- Strain gages and thermocouples.

The technique employed [6] uses two well-matched strain gages, one bonded to a specimen of the reference material (glass, which was considered to have isotropic thermal expansion coefficient) and the other to the specimen of the test material. The temperature range is 0 to 150 °C. Under stress-free environment, the differential output between the two gages, at

any common temperature, is equal to the differential unit expansion. One of the many advantages of using strain gages for measuring thermal expansion coefficient is the possibility to determine expansion coefficients in one direction. The electrical circuit employed is depicted in **Figure 6**.

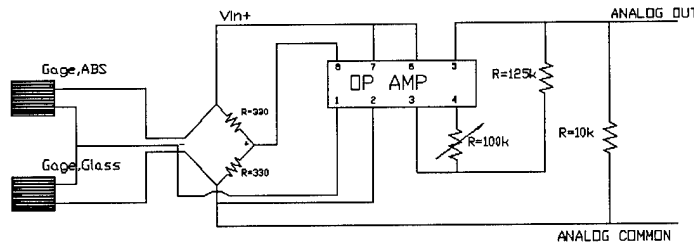


**Figure 6** Strain gages circuit

The electrical output of the circuit is due to the combined resistance changes from both sources (ABS and glass specimens). The net resistance change can be expressed as the sum of resistivity and differential expansion effects as follows:

$$\frac{\Delta R}{R} = [\beta_G + (\alpha_s - \alpha_G)F_G]\Delta T \quad (8)$$

where:

- $\frac{\Delta R}{R}$  = unit resistance change
- $\beta_G$  = thermal coefficient of resistivity of grid (strain gage) material
- $\alpha_s - \alpha_G$  = difference in thermal expansion coefficients between specimen and grid, respectively
- $F_G$  = gage factor of the strain gage
- $\Delta T$  = temperature change from arbitrary initial reference temperature

To calculate the strain due to a resistance change the following formula can be used:

$$\varepsilon = \frac{\Delta R / R}{F_G} \quad (9)$$

Therefore, substituting  $\frac{\Delta R}{R}$  into equation (8) we have:

$$\varepsilon_{G/s} = \left[ \frac{\beta_G}{F_G} + (\alpha_s - \alpha_G) \right] \Delta T \quad (10)$$

where  $\varepsilon_{G/s}$  is the thermal output for grid alloy G of the test specimen.

By introducing glass (reference material) and deriving the thermal output  $\varepsilon_{G/g}$  from a half Wheatstone bridge configuration, the effect of the grid material resistivity  $\frac{\beta_G \Delta T}{F_G}$  is eliminated. The thermal expansion coefficient can be finally obtained:

$$\alpha_s = \alpha_g + \frac{\varepsilon_{(s-g)}}{\Delta T} \quad (11)$$

where:

$$\varepsilon_{(s-g)} = \varepsilon_{G/s} - \varepsilon_{G/g} \quad (12)$$

To find an actual strain  $\varepsilon_{(s-g)}$  an expression for Wheatstone bridge was used as:

$$\frac{V_o}{V} = \frac{F_G \varepsilon_{(s-g)} * 10^{-6}}{4 + 2F(G) \varepsilon_{(s-g)} * 10^{-6}} \quad (10)$$

where  $V_o$  = Voltage output [V] and  $V$  = Voltage input [V].

## RESULTS

Different values for the thermal expansion coefficient of molded ABS can be found in literature: 80 and 130 \*10<sup>-5</sup> [m/m\*C<sup>-1</sup>] for Bayer's ABS (Novodur), 78 and 105 \*10<sup>-5</sup> [m/m\*C<sup>-1</sup>] [4], 62 and 130 \*10<sup>-5</sup> [m/m\*C<sup>-1</sup>] (standard molded, medium impact ABS).

All the values measured are at the lower boundary of the available data; this can be explained considering the voids existing between the roads, which allow expansion within the layers. It can also be observed how the vertical specimen presents the largest thermal expansion coefficient, due to the lower content of intralaminar voids. The results are presented in **Table 2**.

Build plane	Build direction	Number of specimens tested	Number of specimens considered	Width [mm]	Length [mm]	Thickness [mm]	Number of layers	Thermal expansion coefficient
xy	x	2	2	50	50	5.3	20	4.785E-05
yz	y	1	1	50	50	5.3	197	6.475E-05
xz	z	1	1	50	50	5.3	197	7.697E-05

**Table 2** Thermal expansion results

## *CONCLUSIONS*

The results of the experimental work conducted show the build orientation strongly affects the tensile strength, the elastic modulus and the thermal expansion coefficient of parts processed via Fused Deposition Modeling. The stiffness matrix obtained can be directly utilized for prediction and analysis purposes.

This work is of particular importance as Fused Deposition Modeling evolves from a Rapid Prototyping to a Rapid Manufacturing process. Future research will be focused on:

- Application of similar analysis to other materials and processes.
- Integration of part properties prediction model in the design phase.

## *REFERENCES*

1. Takeshi Hattori, private communications, Mitsubishi Chemicals, 1998
2. Stress analysis of fiber reinforced composite materials, Michael W. Hyer, WCB/McGraw-Hill 1997
3. Experimental Characterization of Advanced Composite Materials, Leif A. Carlsson - R. Byron Pipes, Prentice-hall,INC, Englewood Cliffs, New Jersey 07632 1987
4. Handbook of Plastics Testing Technology, Vishu Shah, John Wiley & Sons 1984
5. D5937-96 Standard Test Method for Determination of Tensile Properties of Moulding and Extrusion Plastics, American Society for Testing and Materials, Conshohocken, PA. 1997
6. Measurement of Thermal Expansion Coefficient, Measurements Group Tech Note TN-513-1 1994



# Material Strength in Polymer Shape Deposition Manufacturing

J. W. Kietzman and F. B. Prinz

Department of Mechanical Engineering  
Stanford University, Stanford, California

## Abstract

Shape Deposition Manufacturing (SDM) is a layered manufacturing process involving an iterative combination of material addition and material removal. Polymer SDM processes have used castable thermoset resins to build a variety of parts. The strength of such parts is determined by the bulk material properties of the part materials and by their interlayer adhesion. This paper describes tensile testing of three thermoset resins used for SDM - two polyurethane resins and one epoxy resin. Both monolithic specimens and specimens with two interlayer interfaces were tested. Interlayer tensile strengths were found to vary greatly among the three materials, from 5-40 MPa.

## Introduction

Shape Deposition Manufacturing (SDM) is a layered manufacturing process involving an iterative combination of material addition and material removal [1] [2]. Two materials are used: a part material and a sacrificial support material which surrounds it. Objects are built in layers by depositing and machining part material. Layers containing under-cut features are produced by replicating them from complementary features machined into surrounding support material. When objects are completely finished, they are freed by dissolving the support material. The current polymer part materials are thermoset resins, and the current support materials are machinable waxes although other combinations have been used in the past [3]. The part materials are two-part, castable resins which must be mixed together and immediately cast onto the growing part. Vacuum degassing is used to prevent voids caused by air bubbles. The mixing and casting process is currently performed manually, but its automation would be straightforward using equipment similar to that developed for the Mold SDM process [4]. Polymer SDM is especially suited for building parts which are relatively large but have few transitions between non-undercut and undercut features. Such parts can be made using a few thick layers at a reasonable process speed.

Since Shape Deposition Manufacturing is a layered manufacturing process, the mechanical properties of SDM parts are dependent both upon the bulk material properties and upon the quality of the resulting interlayer bonds. The successive deposition of cast layers also produces anisotropic mechanical properties in polymer SDM parts; these properties are investigated in the present study.

## Polymer SDM Materials

Several materials are currently used for the production of polymer parts via SDM. All of the part materials are castable thermoset polymers while the support material is a machinable wax. The first part material is LUC 4180 polyurethane from Adtech Plastic Systems Corp. of Charlotte, Michigan. This material is reasonably strong, has good impact properties, and can be machined about twelve hours after casting. It was initially chosen for its low water absorption for use in wearable computers for divers [5]. However, later experiments indicated that this material suffers from poor interlayer bonding. The second material is TDT 205-3 polyurethane from Ciba Specialty Chemicals Corp. in East Lansing, Michigan. This material was chosen for its rapid cure speed; successive layers can be machined two hours after casting. Finally, the third material is EE-501/530 epoxy, also from Adtech Plastic Systems Corp. This material is a highly filled encapsulation resin which was chosen for its good adhesion to other materials; it was hoped that it

would also adhere well to previous layers of the same material. This material requires a significantly longer cure time than either of the other materials; twenty-four hours' delay is required between casting and machining. Manufacturer's specifications for each of the materials are summarized in Table 1.

Material	Adtech LUC 4180 Polyurethane	Ciba TDT 205-3 Polyurethane	Adtech EE-501/530 Epoxy
Ultimate Tensile Strength (MPa)	55	23	42
Elongation to Failure	15%	9%	1%
Hardness (Shore D Scale)	78-80	70	86-89
Mixed Viscosity (cPs)	800-900	80	3500
Reference	[6]	[7]	[8]
Cure Time before Machining	12 hours	2 hours	24 hours

**Table 1.** Manufacturer's Specifications

### Tensile Strength Testing

The objective of these tests is to determine the tensile strengths of parts made via SDM with these three materials. Since SDM is a layered manufacturing process, test specimens constructed in different orientations may have different tensile strengths. This difference might be particularly pronounced when comparing test specimens built within a single layer to those which extend over multiple layers, since interlayer bonds may be weaker than the bulk material. ASTM D 638-96 specifies shapes and sizes for plastic tensile specimens, as well as conditioning and testing procedures [9]. This standard describes methods of measuring material properties, and was used as a baseline for the present study. The recommended dimensions for ASTM Type I dogbone tensile specimens were used: a 13.0 mm x 57.0 mm narrow section of 3.2 mm thickness, with 20mm-wide grip ends and a total length of 170 mm (as shown in Figure 1).

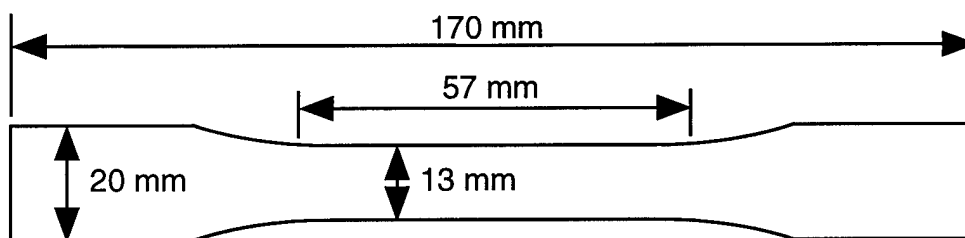


**Figure 1.** ASTM Type I Tensile Specimen

Ideally, bulk and interlayer tensile strengths would be compared by building standard ASTM tensile specimens both perpendicular and parallel to the build direction. The specimens built perpendicular to the build direction would be planar and monolithic, built horizontally within a single layer of material. The specimens built parallel to the build direction would be vertical, composed of many layers of material. Both ideal specimens are shown in Figure 2.

Building thin-layer vertical tensile specimens, however, would take a long time since single layers of one of these materials require 24-hour cure times. Therefore, a simplified dual-interface test specimen was developed which can be made in two cure cycles; this design is shown in Figure 3. These specimens are constructed by casting a complete layer of material, machining a transverse trench through the layer, casting material into that trench, and finally machining the outlines of individual tensile specimens. The resulting specimens have two interlayer interfaces, rather than the  $n-1$  interfaces present in an  $n$ -layer vertical tensile specimen. The tensile strengths of these dual-interface specimens will be expected to represent an upper bound on the tensile strength of an actual vertical  $n$ -layer tensile specimen made via SDM.

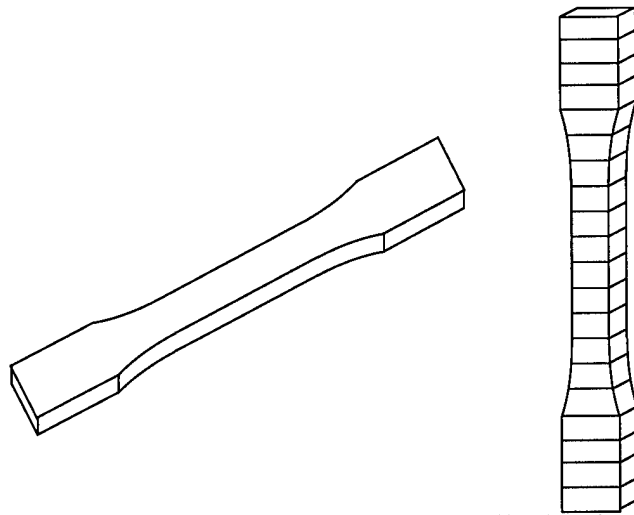


**Figure 2.** Ideal Planar and Vertical Tensile Specimens

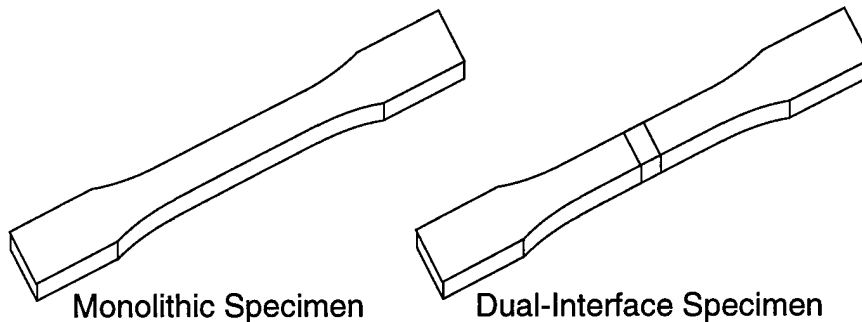


**Figure 3.** Monolithic and Simplified Dual-Interface Tensile Specimens

The tensile tests for LUC 4180 were conducted in four rounds, split between General Motors and Stanford University. Several different batches of LUC 4180 were used, including both material from newly opened containers and older material from containers which had been opened before. While this may result in variations in material properties, it is consistent with part production methods. The TDT 205-3 and 501/530 material used for tensile specimens came from newly opened containers.

After the initial casting, the monolithic tensile specimens were cut out, and trenches were cut into the dual-interface specimens. Additional polymer material was then cast into the trenches and allowed to cure. The dual-interface specimens were cut out, and all specimens were aged for two weeks to ensure complete curing. LUC 4180 specimens were machined 18-26 hours after casting, except for those of Series II (which were machined four days after casting). The TDT 205-3 polyurethane specimens were machined between 4-6 hours after casting, and the 501/530 epoxy specimens were machined between 24-46 hours after casting. As would be expected during part production, very little surface preparation was performed between the initial machining step and the second casting step. Chips and any residue from the machining process were cleared with compressed air, and the surfaces were wiped with Kimwipes; no cleaning solvents were used.

Since the objective was to determine the strengths of parts made through SDM, several specimen preparation steps normally recommended by the ASTM were skipped because they might overestimate actual strengths. The D 638 standard specifies smoothly polished surfaces, but the machined or replicated surfaces resulting from the SDM process were tested without any additional

polishing. On dual-interface tensile specimens, there were slight thickness variations between the initial casting and the second casting. These artifacts were left undisturbed rather than attempting to remove them.

Series I of the LUC 4180 tests was conducted at GM, while the remaining series were conducted at Stanford. All of the tests of TDT 205-3 and 501/530 were conducted at Stanford. The tests at GM were performed on an Instron machine with an extensometer, while the Stanford tests were performed on an Instron machine without an extensometer. The Series I LUC 4180 tests were conducted at a constant crosshead speed of 50 mm/min, while all other tests were conducted at 0.2"/min (5.1 mm/min). At Stanford, data from LUC 4180 Series II and III tests was collected using a chart recorder while Series IV, TDT 205-3, and 501/530 data was digitized and stored by a Labview program.

## Results

The tensile testing produced some interesting results for both monolithic and dual-interface specimens. The monolithic LUC 4180 polyurethane specimens failed very differently from monolithic specimens of the other materials. LUC 4180 specimens yielded and formed necks before finally breaking; both TDT 205-3 polyurethane and 501/530 epoxy failed in a more brittle fashion. A summary of the test data is presented in Table 2, and typical plots of applied stress versus crosshead position for monolithic specimens are shown in Figure 4. LUC 4180 failed at the highest stresses, followed by 501/530, while TDT 205-3 failed at much lower stresses.

Dual-interface specimens produced more surprising results. There were great difficulties manufacturing LUC 4180 specimens with dual interfaces; 8 out of 18 were destroyed during removal from their support material substrates. The LUC 4180 specimens always failed exactly at the interfaces, at very low stresses. The handling difficulties indicate that the average tensile strength would have been even lower if all LUC 4180 specimens had been successfully tested. The TDT 205-3 polyurethane specimens, on the other hand, always failed away from the dual interfaces, and failed at nearly the same stresses as the monolithic specimens had. The 501/530 epoxy specimens usually failed very close to or at the dual interfaces, and also failed at a large fraction of their monolithic failure stresses. Typical plots of applied stress versus crosshead position for the dual-interface specimens are shown in Figure 5. Overall, the 501/530 epoxy dual-interface specimens failed at the highest stresses, while the TDT 205-3 specimens failed at half those stresses, and LUC 4180 specimens failed below one eighth of the 501/530 values. A plot of all test data is shown in Figure 6.

	LUC 4180	TDT 205-3	501/530
Monolithic Specimens	58 MPa	22 MPa	49 MPa
Dual-Interface Specimens	4.6 MPa	20 MPa	40 MPa

Monolithic LUC 4180 specimens: engineering stress at yield  
 All other specimens: engineering stress at break

**Table 2.** Average Tensile Strengths

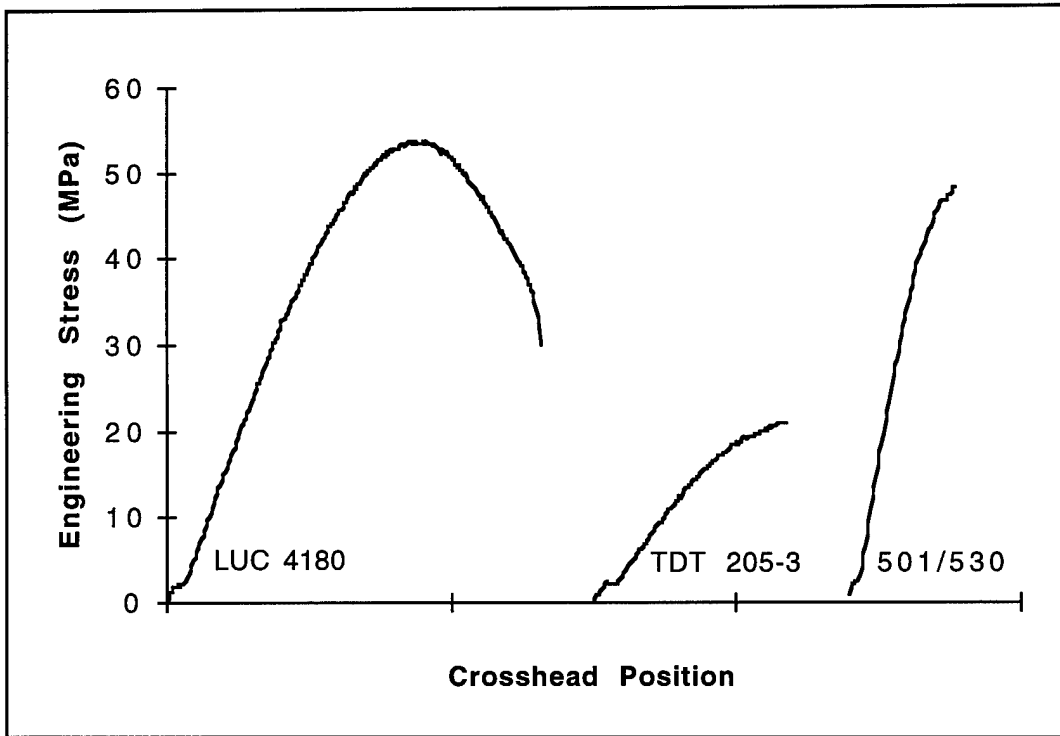


**Figure 4.** Typical Tensile Tests of Monolithic Specimens

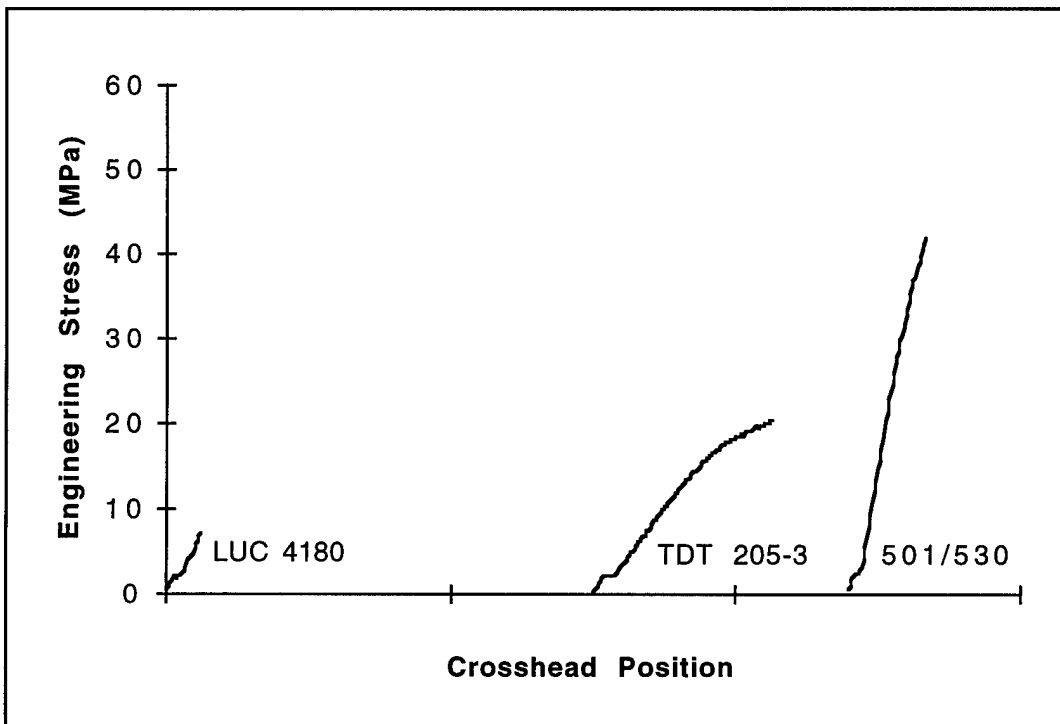


**Figure 5.** Typical Tensile Tests of Dual-Interface Specimens

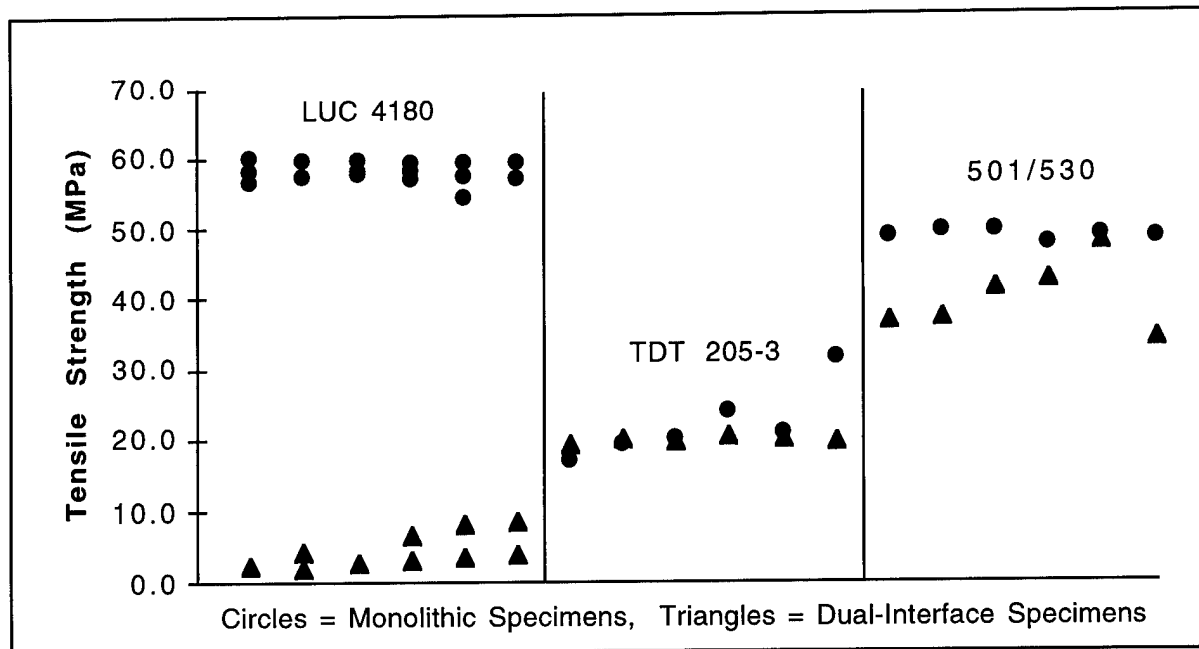


Figure 6. Tensile Strength Summary

## Discussion

While monolithic LUC 4180 polyurethane is reasonably strong, dual-interface specimens of this material failed at very low stresses during tensile testing. Some layered LUC 4180 parts have suffered from delamination during handling, indicating that this problem also arises during actual use of the material. These results indicate that LUC 4180 is only useful for monolithic parts, such as those produced in the Mold SDM process [4].

Dual-interface specimens of both TDT 205-3 polyurethane and 501/530 epoxy failed at much higher tensile stresses - these two materials are better suited for producing layered parts. While TDT 205-3 has a lower interlayer strength than 501/530, it does have some advantages over that material for use in the SDM process. It has very low viscosity and good air-release properties, both of which help prevent voids in interior corners of layers. More importantly, it can be machined almost ten times sooner than 501/530, in two hours rather than twenty-four. For these reasons, TDT 205-3 is currently the polymer material of choice except for situations where the strongest possible parts are needed.

These test results demonstrate that there can be a very substantial anisotropic variation of mechanical properties in polymer Shape Deposition Manufacturing. "Relative interface strength" can be defined as the ratio of interlayer tensile strength to intralayer tensile strength; the relative interface strengths of the materials tested are reported in Table 3. Relative interface strength is a measure of strength anisotropy since it should be proportional to the difference in strengths between tensile tests parallel to and perpendicular to the build direction. For LUC 4180, tensile strength in the build direction may be twelve times lower than tensile strength within a single layer.

Both bulk strength and relative interface strength must be considered when selecting polymer part materials for SDM. However, neither a relative interface strength nor an absolute interlayer strength is normally tabulated by manufacturers since few applications require materials to adhere well when cast over machined surfaces of the same material. Maximizing interlayer strength results in the strongest objects although it can produce parts with greater anisotropy. An

example is that 501/530 forms stronger interlayer interfaces than TDT 205-3, even though its tensile strength is more anisotropic.

	LUC 4180	TDT 205-3	501/530
Relative Interface Strength	8 %	90 %	82 %

**Table 3.** Relative Interface Strengths

As a comparison between LUC 4180 and TDT 205-3 indicates, relative interface strengths can vary significantly even within a class of materials. Both of these materials are two-part, castable, MDI-based polyurethane resins, but their relative interlayer strengths are 8% and 90%, respectively. The reasons for such differences are not well understood. The Adsorption model of adhesion is the most generally accepted theory of adhesion [10]; it suggests that complete wetting of a surface is required to form strong adhesive bonds [11]. Wetting of crosslinked surfaces by chemically similar liquids is a complex phenomena, and the degree of wetting can be affected by the degree of crosslinking of the solid surfaces [12]. Both LUC 4180 and TDT 205-3 have complex systems of chemical additives, including plasticizers, antifoam agents, and particulate fillers. All three of these components affect the wetting behavior of the materials: plasticizers directly improve wetting [13], antifoam agents reduce surface tension, and fillers raise viscosity (which can limit wetting [14]). Differences in the degree of crosslinking of the cured surfaces or wetting characteristics of the uncured liquid resins are thought to determine the relative interface strengths of these two materials by affecting their wetting behavior.

Future work will focus on the identification of stronger materials with good interlayer bonding for the production of functional parts via polymer Shape Deposition Manufacturing.

### Acknowledgments

This work was supported by the Defense Advanced Research Projects Agency under contracts N00014-96-1-0625 and DABT63-95-C-0026. Additional support was provided by a Department of Energy Integrated Manufacturing Pre-Doctoral Fellowship and a National Defense Science and Engineering Graduate Fellowship. We would also like to thank Mike Uchic, Professor W. D. Nix, and Gayle R. Link of Stanford University, and the Materials Testing Laboratory of General Motors North American Operations for their assistance with testing and equipment.

### References:

- [1] R. Merz, F. B. Prinz, K. Ramaswami, M. Terk, and L. E. Weiss, "Shape Deposition Manufacturing," *Proceedings of the 1994 Solid Freeform Fabrication Symposium*, The University of Texas at Austin, August 1994, pp. 1-8.
- [2] F. Prinz and L. Weiss, "Method for Fabrication of Three-Dimensional Articles," U. S. Pat. No. 5,301,415, April 12, 1994.
- [3] J. W. Kietzman, A. G. Cooper, L. E. Weiss, L. Schultz, J. L. Lombardi, and F. B. Prinz, "Layered Manufacturing Material Issues for SDM of Polymers and Ceramics", *Proceedings of the 1997 Solid Freeform Fabrication Symposium*, The University of Texas at Austin, Austin, Texas, August 1997, pp. 133-140.

- [4] A. G. Cooper, S. K. Kang, J. W. Kietzman, F. B. Prinz, J. L. Lombardi, and L. E. Weiss, "Automated Fabrication of Complex Molded Parts Using Mold SDM," *Proceedings of the 1998 Solid Freeform Fabrication Symposium*, The University of Texas at Austin, Austin, Texas, August 1998.
- [5] L. Weiss, F. Prinz, G. Neplotnik, K. Padmanabhan, L. Schultz, and R. Merz, "Shape Deposition Manufacturing of Wearable Computers," *Proceedings of the 1996 Solid Freeform Fabrication Symposium*, The University of Texas at Austin, Austin, Texas, August 1996, pp. 31-38.
- [6] "LUC-4180 Lowex Casting System," Adtech Plastic Systems Corp., Charlotte, Michigan.
- [7] "TDT 205-3 Resin and Hardener / DT 081 / DT 082 Three Component Rapid-Curing Polyurethane Casting System," Ciba Specialty Chemicals Corporation, East Lansing, Michigan, October 1996.
- [8] "System<sup>5</sup> Epoxy Encapsulation Systems," Adtech Plastic Systems Corp., Charlotte, Michigan.
- [9] "Standard Test Method for Tensile Properties of Plastics," ASTM D 638-96, *1997 Annual Book of ASTM Standards*, Vol. 08.01, West Conshohocken, Pennsylvania: ASTM, 1997, pp. 44-56.
- [10] A. J. Kinloch, "Review: The Science of Adhesion - Part 1. Surface and Interfacial Aspects," *Journal of Material Science*, Vol. 15, 1980, pp. 2141-2166. Page 2156 describes the adsorption theory.
- [11] Georges Fourche, "An Overview of the Basic Aspects of Polymer Adhesion. Part I: Fundamentals," *Polymer Engineering and Science*, Vol. 35, No. 12, June 1995, pp. 957-967. Pages 958ff describe the adsorption theory.
- [12] T. Kerle, R. Yerushalmi-Rozen, and J. Klein, "Cross-Link-Induced Autophobicity in Polymer Melts: A Re-Entrant Wetting Transition," *Europhysics Letters*, Vol. 38, No. 3, 1997, pp. 207-212. This article describes the transitions from complete wetting, to partial wetting, and back to complete wetting as a surface's degree of crosslinking was increased from none, to partial, to complete.
- [13] J. K. Sears and N. W. Touchette, "Plasticizers," in eds. Herman F. Mark, Norbert M. Bikales, Charles G. Overberger, and Georg Menges, *Encyclopedia of Polymer Science and Engineering*, Supplement Volume, New York: Wiley-Interscience, 1985, pp. 568-647. Page 614 describes the effects of plasticizers in thermoset materials.
- [14] A. J. Kinloch, "Review: The Science of Adhesion - Part 1. Surface and Interfacial Aspects," *Journal of Material Science*, Vol. 15, 1980, pp. 2141-2166. Page 2142 describes the qualities of an ideal adhesive, specifying a viscosity of a few centipoise.

# Rapid Prototyping of Titanium Nitride Using Three-Dimensional Laser Chemical Vapor Deposition

James Maxwell, Jubin Shah, Terry Webster, Jason Mock

Institute for Micromanufacturing, Louisiana Tech Univ., 911 Hergot Ave., Ruston, LA, USA

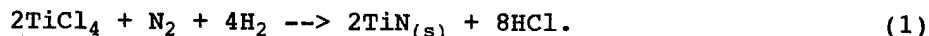
*Selective vapor deposition of titanium nitride was realized from titanium tetrakis-dimethylamide,  $Ti(N(CH_3)_2)_4$ , at pressures up to 138 mbar. High-aspect-ratio needles up to 12 mm long were grown at axial rates up to 10  $\mu\text{m/s}$ . The morphology and composition of the fibers will be described. The temperature rise during transient growth was apparent in the grain size of the resulting needles. Severe mass-transport limitations were also observed due to the multiplicity of precursor by-products. A primary application of this work will be the rapid prototyping of highly-elastic, lightweight structural elements and matrices.*

**Keywords:** Laser Deposition, Titanium Nitride, Fibers, Freeform Growth, Micro-electromechanical Systems.

## I. Introduction

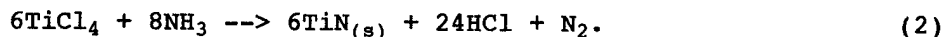
For the *micro-scale* rapid prototyping of metals and ceramics, interest is growing in three-dimensional laser chemical vapor deposition (3D-LCVD). This process employs a laser to deposit solids through the thermal decomposition of organometallic or metal halide vapors, termed *precursors*. A variety of materials may be deposited via 3D-LCVD, including most transition metals,<sup>1-8</sup> refractory metals,<sup>9-11</sup> and alloys of the same.<sup>12</sup> As demonstrated in a companion paper,<sup>13</sup> intermetallics may also be grown freely without self-limiting effects. This work represents a first-attempt at depositing another intermetallic, titanium nitride, from the vapor phase.

There have been many attempts to laser-deposit thin TiN films, due to its importance as a diffusion barrier material in microelectronics and as an excellent coating material for wear and abrasion resistance; a variety of precursors have been explored in these attempts. Hopfe et al. produced TiN films, using a mixture of  $TiCl_4$ ,  $N_2$ , and  $H_2$ .<sup>14</sup> The overall reaction was:



In this case, fine-grained TiN films were produced at axial deposition rates of up to 0.2  $\mu\text{m/s}$ . In another experiment, Conde et al. grew a 30  $\mu\text{m}$  thick TiN film on Incoloy, with an average axial deposition rate of over 3.7  $\mu\text{m/s}$ .<sup>15</sup> Here, the total chamber pressure was 275 mbar, with a  $TiCl_4$  partial pressure of 9.3 mbar, the balance of the gas mixture being a 1:1 ratio of  $N_2$  to  $H_2$ . Even more impressive results were obtained on mild steel using a similar gas mixture.<sup>16</sup> In this case, the laser beam was scanned at 4000  $\mu\text{m/s}$ , resulting in a 3  $\mu\text{m}$  thick film. The inferred axial deposition rate was 8.6  $\mu\text{m/s}$ . Other authors have reported similar axial rates of up to 3.5  $\mu\text{m/s}$ .<sup>17</sup>

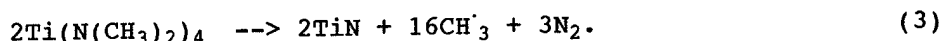
An alternate precursor set for TiN deposition is a mixture of titanium tetrachloride and ammonia, with the reaction:



When this precursor was attempted,<sup>17</sup> solid ammonia-titanium-chloride by-products formed on the substrate and laser windows, making it difficult to produce consistent films. To reduce

the formation of solid by-products, a high concentration of  $H_2$  may be added to the gas mixture, and the gas mixture and chamber should be preheated.

Finally, two additional titanium precursors have been suggested in the literature. The first is titanium tetrakis-dimethylamide,  $Ti(N(CH_3)_2)_4$ ,<sup>18</sup> which, at low temperatures, decomposes as follows:



At temperatures over approximately  $1000^\circ C$ , the  $CH_3$  ligands dissociate as well, leading to carbon contamination in the deposit.  $Ti(N(CH_3)_2)_4$  may also be mixed with ammonia gas, which tends to prevent the inclusion of carbon.<sup>17</sup>

The second precursor, titanium tetrakis-diethylamide,  $Ti(N(C_2H_5)_2)_4$ ,<sup>19</sup> is more volatile than its dimethyl- counterpart, but has yet to be used in a laser-induced deposition process. In this paper, preliminary results will be presented on the three-dimensional growth of TiN from pure titanium tetrakis-dimethylamide, leaving its mixture with ammonia, and the potential use of  $Ti(N(C_2H_5)_2)_4$  for future papers.

## II. Experimental

The apparatus which was used for the TiN experiments is illustrated in Fig. 1. The precursor gases were evaporated into the chamber (A) by heating a source cylinder (B), or by direct connection to a gas cylinder/regulator. The chamber was uniformly heated to a temperature  $10-15^\circ C$  higher than the source cylinder to prevent condensation of the gases within the chamber; in this way, the precursor partial pressure was always determined by the temperature of the source cylinder. Since titanium tetrakis-dimethylamide has a vapor pressure of only 1.3 mbar at  $55^\circ C$ , the precursor was heated in the source cylinder to temperatures over  $125^\circ C$ , yielding  $Ti(N(CH_3)_2)_4$  pressures to 138 mbar. Higher  $Ti(N(CH_3)_2)_4$  partial pressures were not possible, as the precursor decomposes above  $150^\circ C$ , so the chamber temperature had to be maintained at less than  $140^\circ C$ .

The titanium substrate (C) was rigidly affixed to the chamber, through a detachable sample holder (D) which could be placed directly into a scanning electron microscope. The reactor consisted of a spherical cube with six 1.33" CF ports; two ports served as windows for observation and illumination of the sample, while a third port acted as the laser window (E). Each window was heated with a hot air gun (F) to prevent fogging during growth. The fourth chamber port fed a heated nozzle (G) into the chamber from the source cylinder, while the fifth connected the chamber to a cold trap (H) and rotary pump (I), via a flexible bellows (J). The chamber and source cylinder rode on micrometer-driven X-Y-Z stages (K), allowing the sample to be positioned relative to the laser focus. Throughout the experiment, a Lee Laser Nd:YAG laser (10 W TEM<sub>00</sub>) was employed at 1064 nm. The cw beam was focused with a 90 mm gradient-index lens (L), yielding a  $1/e^2$  spot size of approximately 50 microns.

## III. Results

Rapid growth of grey-green fibers was possible using the  $Ti(N(CH_3)_2)_4$  precursor at a variety of precursor pressures and laser powers. The color of the deposit indicates that a  $TiN_xC_y$  phase, rather than pure TiN was obtained.  $TiN_xC_y$  fibers up to 12 mm in length were grown *without focal tracking*, yet with length-to-width aspect ratios as high as 24:1. Typical fiber diameters were on the order of 500-1,000  $\mu m$ , while in one case, the fiber diameter exceeded 1.3 mm. These diameters

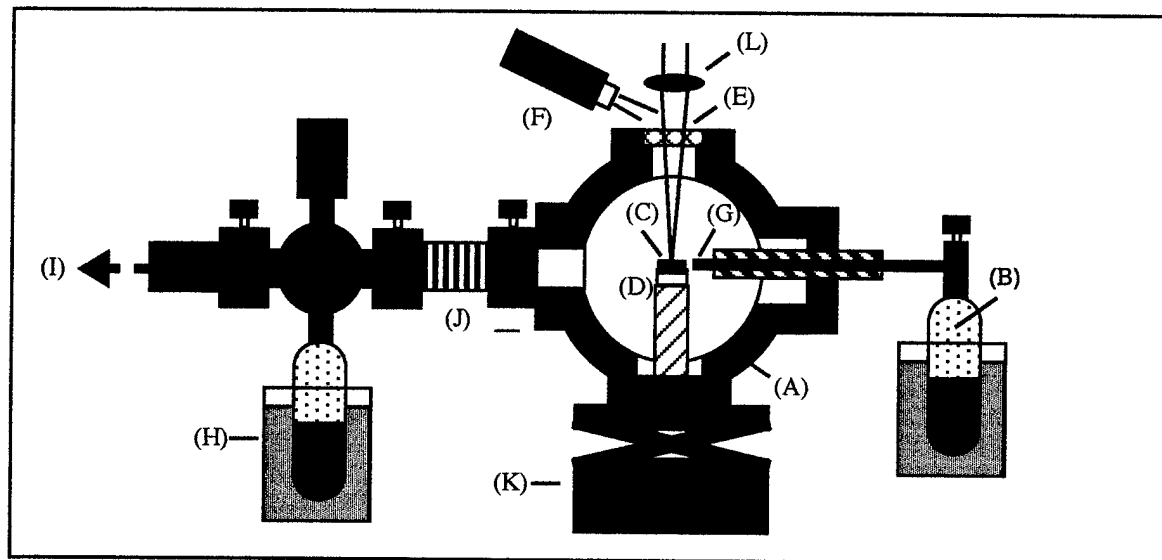


**Fig. 1: Experimental Apparatus for the TiN Experiments**

are large compared with most laser-deposited materials,<sup>20</sup> and are caused by the high thermal conductivity of  $TiN_xC_y$  (approx. 0.08 cal/s-cm-K), which tends to broaden the reaction zone—allowing conduction down the rod, so that continued growth occurs far from the rod tip. The initial (transient) diameter of the fibers was comparable to (or slightly less than) that of the steady-state fiber diameters, with a very short transient growth period. This is due to the low threshold decomposition temperature of the precursor, combined with the higher thermoconductivity of the TiN deposit (0.080 cal/s-cm-K) relative to that of the Ti substrate (0.05 cal/s-cm-K). Similar transient results were obtained in the growth of iron and nickel rods on alumina and graphite sheets.<sup>12</sup> Interestingly, the steady-state diameter of the  $TiN_xC_y$  rods narrowed with rising laser power, perhaps due to the decreasing thermoconductivity of  $TiN_xC_y$  with temperature.

A wide variety of laser powers were employed, from 0.60 W to 10 W. No significant growth was observed below 2.0 W, while at the threshold power of 2.1 W, rods could be readily grown at rates of 2-3  $\mu\text{m/s}$ , such as those shown in Fig. 2. The reaction rate was mass-transport limited, with increased natural convection observed at the highest laser powers (by monitoring particulate motions in the precursor gas). Growth rates rose slowly with laser power, reaching a maximum of 10  $\mu\text{m/s}$  at 7.9 W. This growth rate is excellent for such low precursor pressures. Clearly, the multiplicity of by-products, coupled with a  $Ti(N(CH_3)_2)_4$  mass-diffusivity approximately 1/15th that of hydrogen, gave rise to convection cells even at low pressures—enhancing the average fiber growth rate.

At the highest powers, the deposition rate became erratic, no growth being observed at powers between 9 - 10 W. This phenomenon has been previously observed in the growth of nickel rods,<sup>21</sup> and may be explained in two possible ways. If the reaction is endothermic, the rate may be thermodynamically-limited at excessive temperatures. Second, since there is a high Stefan flow, for every precursor molecule which decomposes, a plume of by-products builds up in the center of the rod where the temperature is the highest, and the reaction is starved at the center. This was clearly seen in SEM photos of the  $TiN_xC_y$  fibers, where all of the rods have a central depression. In several cases, the fibers were completely hollow!

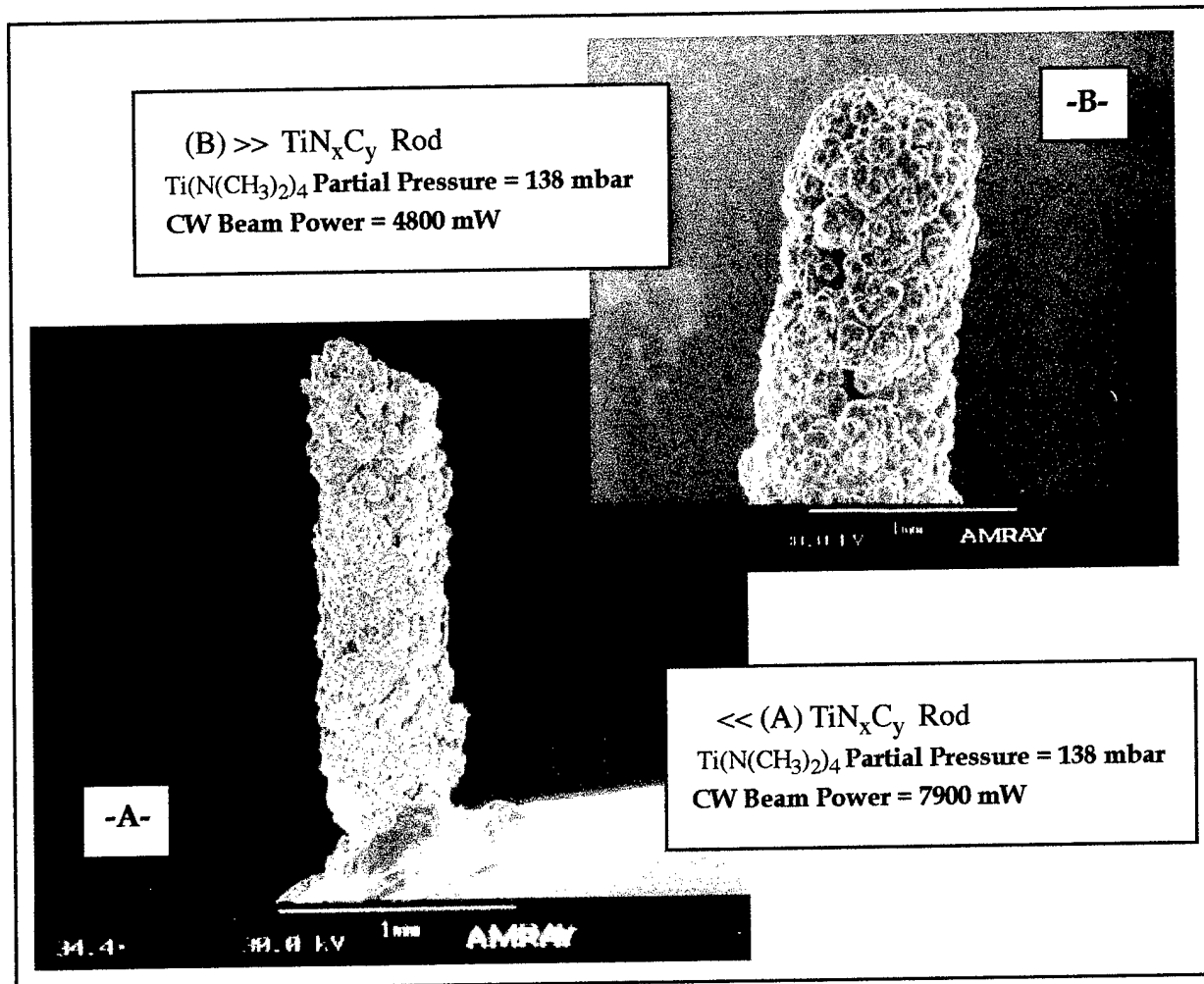


**Fig. 2: Three-dimensional Titanium Nitride Growth**

The steady-state grain size of the deposit varied markedly with laser power, in some cases reaching over  $100\ \mu\text{m}$ . Large grain sizes are to be expected for  $\text{TiN}_x\text{C}_y$  at low precursor pressures, because of the simple cubic structure of  $\text{TiN}$  and  $\text{TiC}$ . As can be seen in Fig. 2, the grain size also increased rapidly over the transient growth regime—indicating a rapid rise in temperature with distance from the Ti substrate. Yellow-white emissions were observed during all of the steady-state growth experiments, indicating a high deposition temperature, probably in excess of  $1000^\circ\text{C}$ .

Several methods are being investigated to measure and control the temperature during growth, so that high-strength fibers of fine grain structure may be grown. The addition of inert gases, such as xenon or krypton, is being investigated as a means to cool the fibers during the steady-state regime, and active feedback control of the peak reaction temperature will be possible through a simple temperature measurement apparatus.<sup>13</sup>

At most laser powers, solid by-products were generated readily in the gas-phase, and coated the laser window and chamber walls. This grey-green powder was also  $\text{TiN}_x\text{C}_y$ , but with high concentrations of carbon—again indicating that the reaction temperatures were greater than  $1000^\circ\text{C}$ . In addition, the powder formed freely away from the substrate or deposit, so some photolysis of the precursor was apparent. To avoid this phenomenon, efforts are underway to determine the absorption spectrum of  $\text{Ti}(\text{N}(\text{CH}_3)_2)_4$  and employ alternate laser wavelengths.

## IV. Conclusions

While  $\text{Ti}(\text{N}(\text{CH}_3)_2)_4$  holds promise as a precursor for micro-scale rapid prototyping of TiN, the deposition rate is limited by the maximum vapor pressure which can be attained before decomposition of the precursor occurs. The exact composition of the  $\text{TiN}_x\text{C}_y$  deposit is presently under investigation using glow discharge optical spectroscopy; however, the deposits appear to be contaminated with carbon, indicating decomposition of the  $\text{CH}_3$  groups. To eliminate this contamination, high pressures of ammonia and hydrogen will be attempted with this precursor, as well as the addition of noble gases to cool the reaction. Active control of the temperature may also be necessary to obtain fine-grained deposits. To achieve the rapid TiN growth rates which would be appropriate for large-scale prototyping ( $>100 \mu\text{m/s}$ ), however, an alternate precursor should be selected.

## V. Bibliography

1. Boughaba, S., Auvert, G., "Growth Kinetics of Micron-size Nickel Lines Produced by Laser-assisted Decomposition of Nickel Tetracarbonyl," J. Appl. Phys., Vol. 73, No. 12, (15 Jun. 1993), pp. 8590-8600. [384]
2. Rytz-Froidevaux, Y., Salathé, R. P., "Laser-Induced Deposition of Metals," Proceedings Of SPIE-The International Society for Optical Engineering, Laser Assisted Deposition, Etching, and Doping, Vol. 459, (1984), pp. 55-60. [163]
3. Braichotte, D., Van Den Bergh, H., "Structure of Platinum and Tin Films Formed by Laser-Induced Chemical Vapor Deposition," Springer Series in Chemical Physics 39, Laser Processing and Diagnostics, (1984), pp. 183-187. [207]
4. Natzle, W. C., "Distinguishing Laser Induced Thermal and Photochemical Surface Reactions by Photodeposit Morphology," Materials Research Society Symposium Proceedings, Vol. 101, Laser and Particle-Beam Chemical Processing for Microelectronics, (1988), pp. 213-220. [209]
5. Allen, S. D., Tringubo, A. B., "Laser Chemical Vapor Deposition of Selected Area Fe and W Films," J. Appl. Phys., Vol. 54, No. 3, (Mar. 1983), pp. 1641-1643. [348]
6. Willwohl, H., Wolfrum, J., "Excimer Laser Photolysis of Metalorganic Complexes of Platinum and Palladium in the Gas Phase," Applied Surface Science, Vol. 54, (1992), pp. 84-94.
7. Braichotte, D., Garrido, C., van den Bergh, H., "The Photolytic Laser Chemical Vapor Deposition Rate of Platinum, Its Dependence on Wavelength, Precursor Vapor Pressure, Light Intensity, and Laser Beam Diameter," Applied Surface Science, Vol. 46, (1990), pp. 9-18.
8. Kudas, T. T., Comita, P. B., "Mass Spectrometric Study of Laser-Induced Chemical Vapor Deposition of Gold," Materials Research Society Symposium Proceedings, Vol. 101, Laser and Particle-Beam Chemical Processing for Microelectronics, (1988), pp. 249-255.
9. Reisse, G., Gaensicke, F., Ebert, R., Illmann, U., Johansen, H., "Laser-induced Chemical Vapour Deposition of Conductive and Insulating Thin Films," Applied Surface Science, Vol. 54, (1992), pp. 84-88. [18]
10. Kullmer, R., Kargl, P., Bäuerle, D., "Laser-induced Deposition of Tungsten from Tungsten Hexachloride," Thin Solid Films, Vol. 218, (1992), pp. 122-136.
11. Maxwell J., Krishnan, K., "High-Pressure, Convectively-Enhanced, Laser Chemical Vapor Deposition of Titanium," Proc. Solid Freeform Fabrication Symposium, Austin, Texas, (Aug. 1997)
12. Maxwell, J., Pegna, J., DeAngelis, D., Messia, D., "Three-dimensional Laser Chemical Vapor Deposition of Nickel-Iron Alloys," Material Research Society Symposium Proceedings, v. 397 (B3.30): Advanced Laser Processing, MRS Fall 1995 Meeting, Boston, MA (Nov. 27--Dec.1, 1995).e

13. Maxwell, J., Larsson, K., Boman, M., Hooge, P., Williams, K., Coane, P., "Rapid Prototyping of Functional Three-Dimensional Microsolenoids and Electromagnets by High-Pressure Laser Chemical Vapor Deposition," Proc. Solid Freeform Fabrication Symposium, Austin, Texas, (Aug. 1998).
14. Hopfe, V., Tehel, A., Baier, A., Scharsig, J., "IR-laser CVD of TiB<sub>2</sub>, TiC<sub>x</sub> and TiC<sub>x</sub>N<sub>y</sub> Coatings on Carbon Fibres," Applied Surface Science, Vol. 54, (1992), pp. 78-83. [17]
15. Conde, O., Ferreira, M. L. G., Hochholdinger, P., Silvestre, A. J., Vilar, R., "CO<sub>2</sub> Laser Induced CVD of TiN," Applied Surface Science, Vol. 54, (1992), pp. 130-134. [23]
16. Silvestre, A. J., Paramês, M. L. G. F., Conde, O., "Investigation of the Microstructure, Chemical Composition and Lateral Growth Kinetics of TiN Films Deposited by Laser-induced Chemical Vapour Deposition," Thin Solid Films, Vol. 241, (1994), pp. 57-60. [360]
17. Illmann, U., Ebert, R., Reisse, G., Freller, H., Lorenz, P., "Laser Based Chemical Vapour Deposition of Titanium Nitride Coatings," Thin Solid Films, Vol. 241, (1994), pp. 71-75. [362]
18. Bradley, D. C., "New Metallo-organic Precursors for Surface Processing," Applied Surface Science, Vol. 46, (1990), pp. 1-4. [60]
19. Kudas, T., Hampden-Smith, M., The Chemistry of Metal CVD, VCH Publishers, Inc., 1994, p. 25.
20. J. Maxwell, Three-Dimensional Laser-Induced Pyrolysis: Modelling, Growth Rate Control, and Application to Micro-Scale Prototyping, PhD Thesis, Rensselaer Polytechnic Institute, 1996, Ch. 6.
21. Maxwell, J., Pegna, J., "Laser-induced Pyrolysis of Tapered Microstructures," Proc. Solid Freeform Fabrication Symposium, Austin, Texas, (Aug. 1995).

# Si/SiC-Ceramic low process shrinkage - high temperature material for the Laser Sinter process

Peter Stierlen\*, Peter Schanz\*\*, Peter Eyerer\*

\* Institute of Polymer Testing and Polymer Science (IKP), University Stuttgart

\*\* German Aerospace Center (DLR), Institute of Structures and Design, Stuttgart

## Abstract

Actual RP-systems are very limited in producing adequate ceramic prototypes. In the presented process, the SiC-green part manufacturing by the laser sintering process in combination with special postprocessing allows the fast production of Si/SiC prototypes. A mixture of SiC powder and a reactive polymer binder system is used in the Laser Sinter process. In the following postprocessing the porous green part has to be infiltrated with a precursor resin, carbonised and finally infiltrated with molten silicon. In contrast to cold isostatic moulding or slip casting the shrinkage is very low (2-4 %). Experiments with suitable materials and process conditions were successful. This paper will show the state of and the possible further investigation into process.

## Introduction

Up to now, there exists no commercialised Rapid Prototyping technique to directly generate ceramic parts without any post processing. All the known techniques require complex post processing such as debinding and sintering. Several investigations were carried out with ceramic filled SLA-resins, binder coated ceramic powders for SLS or 3D printing processing, ceramic filled sheets for LOM and other technologies like laser induced generating by vapour deposition [1,2,3,4,5,6]. Post processes such as debinding and sintering are necessary to obtain a high density ceramic structure. The theoretical maximum density of monomodal particles is 74 % with an increase in density during sintering to over 95 %, so, in existing processes, this leads to high shrinkage. The precise heating and cooling parameters used for debinding are very difficult to implement accurately.

The presented technology is also a combination of laser sintering and post processing techniques. But in opposite to the other techniques, the polymeric binder must not be burned out completely. The porous green part structure must be filled with special liquid phenol resin or any other infiltration materials with high carbon yield after pyrolysis [7,8]. After polymerisation of the infiltrated resin, the binder system and the infiltrated resin are transformed in an inert pyrolysis reaction process to carbon. During pyrolysis the polymeric systems utilised result in a stable carbon binding structure. Due to the shrinkage during pyrolysis the carbon regions show a fine structured crack system. In the final process the crack system has to be infiltrated with molten silicon. Because of the very low viscosity of the molten silicon and the capillary forces, the molten Si will fill the whole open porosity. The infiltrated silicon will finally react with the residual carbon to form  $\beta$ -SiC.

## Si/SiC Processing with laser sintered pre-forms

### Greenpart production by lasersinter process

The process technique for the green part production is similar to the well known direct croning process from EOS GmbH. The SiC powder has an average particle size of about 70  $\mu\text{m}$  and a powder density of 1.25-1.40  $\text{g}/\text{cm}^3$  (~39-44 % of full SiC density). The use of a dry powder resin as binder removes the need for the complex process of coating the SiC particles. Coating SiC particles requires a complex procedure because of the very high abrasiveness of the particles. The particles scrape the coating chamber as well as the coating on other particles. The powder resin shows a very low melt viscosity and a good wetting of the SiC particles. Higher contents of binder increase the green part stability, but the greater the percentage of the binder contents, the more polymer is present between the SiC particles and therefore the higher shrinkage during pyrolysis.

Tests performed show that a powder mixture with a binder content of 18 %wt performs very well. The average open porosity of 55 % is very high but the green part strength is still good. The measured SiC-content in the green parts is about 31 % vol.. Recoating tests with the pure unbonded SiC powder showed densities of about 35 % in the powder bed. The complete process chain is shown in figure 1.

### Post-infiltration with precursor resin

In the second step the open porosity of the laser sintered part is infiltrated with precursor resin. The resin must be pre-heated to get the lowest melt viscosity for the infiltration which takes place in a vacuum desiccator. Following the infiltration, the parts are put in an autoclave and the resin is cured under a pressure of 20 MPa and a temperature of approximately 170 °C. The weight increases by 50 % on average, and the open porosity is filled completely.

The following processing steps of pyrolysis and silicon infiltration are quite similar to the well known Liquid Silicon Infiltration Process (LSI) of the DLR for manufacturing fibre reinforced CMC materials /9/,/10/,/11/.

### Pyrolysis of the polymeric components

The infiltrated and cured parts are now ready for the carbonisation process. During pyrolysis at a temperature of up to 900 °C under a nitrogen environment the polymer shrinks in an almost unrestricted manner in all directions, due to cracking of the compounds driving out the volatile components of the polymer and resulting in amorphous carbon. In this process the shrinkage of the resin during the

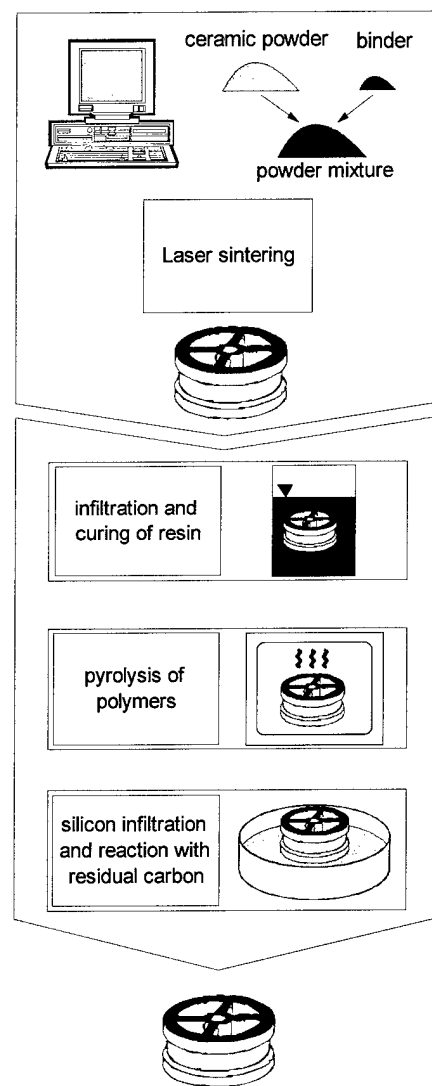


Figure 1: Process chain of the Si/SiC process

carbonisation is hindered by the SiC powder particles. Therefore a crack structure in the carbonised matrix is produced, which is necessary for the following silicon infiltration step. The crack structure is of interest for the infiltration and reaction dynamics during the silicon infiltration and therefore decisive for the resulting structure and the resulting material properties. The crack system can be influenced by different parameters such as SiC particle size, particle form, binder and infiltration resin, infiltration and carbonisation process parameters.

### Silicon infiltration

During the last manufacturing step at temperatures up to 1600 °C, and in vacuum, the liquid silicon infiltrates the porous specimens due to the capillary forces, and reacts with the carbon of the residual matrix and forms to silicon carbide. The degree of conversion can be controlled by the temperature profile.

Therefore it is one of the main aims to realise a stoichiometric formation of the components to get a high yield of  $\beta$ -SiC. The resulting surface of the parts primarily depends on the surface of the green part. The surface quality can be improved by the use of smaller powder particles with a more uniform particle geometry.

Additional finishing of the infiltrated greenparts also improves the surface quality.

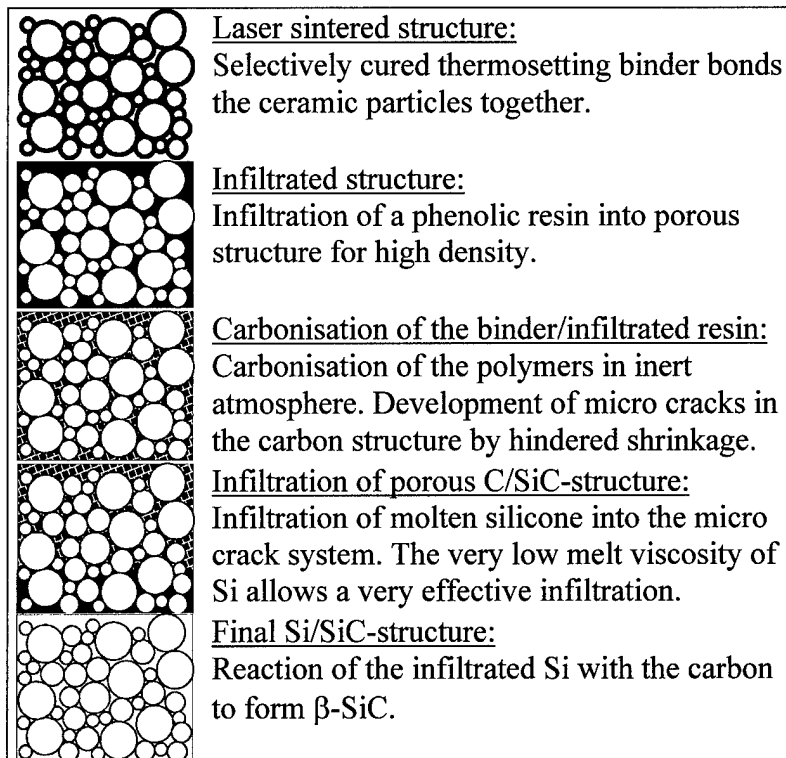


**Figure 2:** Modifications of the structure in each step of the process chain

### Results of previous investigations

The aim of the first investigations was to show the feasibility of the process. Therefore a SiC-powder with a particle size of about 70  $\mu\text{m}$  was chosen for easy powder recoating in the Laser Sinter machine. The mixture of the SiC-powder and the phenolic binder powder was varied in several steps. The phenolic powder resin melts between 70 and 110°C and is cured by condensation reaction. At temperatures higher than 150°C the included hexamethylene-tetramine degrades. A very high binder content of 18 %wt was applied because of the better stability for handling and the following post-infiltration process. The powder mixture can be processed with a laser energy density of about 50-90  $\text{mJ}/\text{mm}^2$ . The phenolic binder showed a loss of weight of

approximately 4 % during laser induced curing. The single layers showed a thickness of more than 0.6 mm. Therefore there are no problems to build parts with 0.2 mm slices. It could be expected that the layer thickness decreases by increasing SiC-powder content. The parts taken out of the Lasersinter machine have to be post-cured with a low heating rate up to 200°C. Deformations during the post-curing can be prevented by placing the complex parts in a box with supporting SiC-powder (without binder).

**Figure 3** shows a Si/SiC sample processed without infiltration of a precursor resin. The content of SiC (shown dark grey in figure 3) is low and the SiC phase is embedded into silicon with less connections between the SiC regions. The resulting porous structure has larger crack diameters and the conditions are therefore not optimal for capillary action induced infiltration.

Therefore the post-infiltration step is necessary to realise a higher content of carbon after the pyrolysis of the polymers. During the curing of the resin the specimen showed a shrinkage of 2% in thickness and about 1% in the other directions.

The infiltrated initial state for pyrolysis is shown in **Figure 4**. In this state, the material shows round about 5 % open porosity and a density of about 1.78 g/cm<sup>3</sup>. The content of SiC powder (bright areas) in this section amounts to only 28 %. The powder packing density is very low and the particles are sharp edged. This oblong geometry prevent higher particle packing densities. With a more cuboid geometry the SiC-powder density can be increased up to more than 45 %.

The structure of a carbonised sample is shown in **figure 5**. The mass loss during pyrolysis can be determined at about 18 % and the density at about 1.6 g/cm<sup>3</sup>. As a result of mass loss and decreasing density the open porosity increases up to about 35 %. The SiC powder (bright areas) is now embedded in a highly porous carbon matrix (dark areas). With an average particle size of 70 µm, the crack system is not as fine structured as necessary to form SiC well.

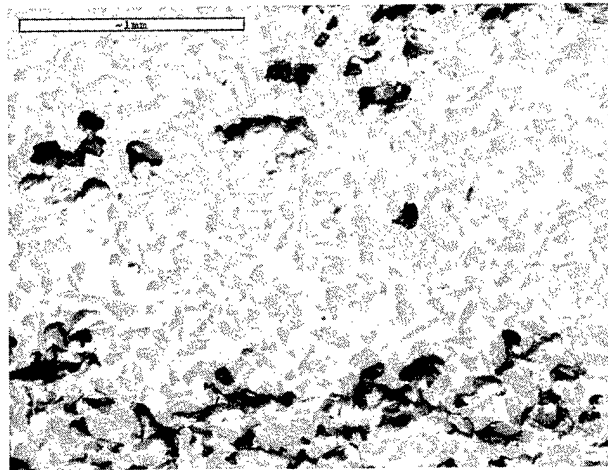


**Figure 3:** Si/SiC part processed without post-infiltration of precursor resin



**Figure 4:** Part infiltrated with precursor resin



**Figure 5:** Carbonised structure with crack system

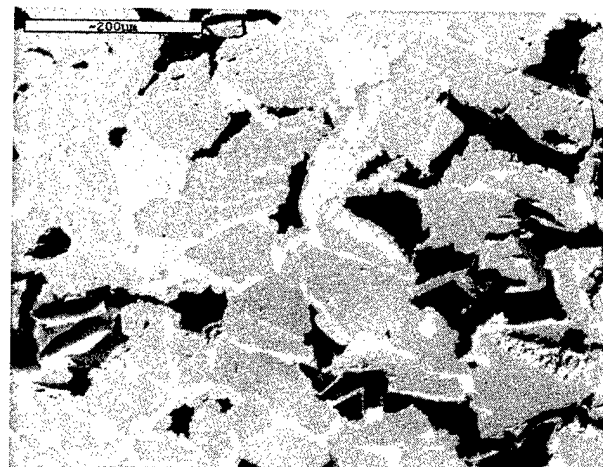


**Figure 6:** Final structure after Si infiltration

**Figure 6** shows the final structure after the Si infiltration. The content of SiC (shown light grey) reaches 69 %, residual carbon 14 % (dark grey) and the residual silicon 13 % (bright). After siliconization mass increases up to about 15 % and the open porosity of the specimens decreases to approximately 4-6 %. The density increases to about 2.5 g/cm<sup>3</sup>. The  $\beta$ -SiC content and structure must be optimised by a finer crack structure, a more regular dispersed carbon and a longer temperature dwell time during silicon infiltration. Therefore a smaller particle size and a higher particle packing density are the main keys for the further developments.

### Test shapes and Examples

**Figure 7** shows a selection of different precursor infiltrated test patterns. The flat plates on the left side were pyrolysed, siliconized and finally used for the 4 point bending test bars. The blades of the turbine wheel have a thickness of less than 1mm. The quality of the backside of the blades is also acceptable and shows no problematical overcure. The box on the right side of the picture has walls with different thicknesses to find the limitations in geometry. Also parts with 1mm walls have been built successfully. All greenparts were built up in the laboratory sinter station at IKP.

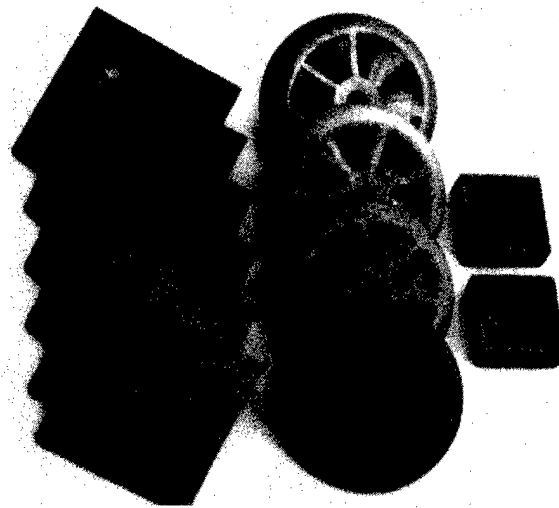


**Figure 7:** Selection of samples infiltrated with precursor

**Figure 8** shows the test box with different walls in the three post-processing stages. The present limit in wall thickness with the 70  $\mu\text{m}$  SiC powder is 1 mm. The shrinkage during the complete process is 2 %, measured along the walls of the box. The geometry also allows the estimation of the rounding of inner edges by the precursor resin and by the molten silicon by building a meniscus in the liquid phase. Whereas sharp edges normally must be avoided because of the high notch sensitivity of monolithic ceramics.

The Lasersinter process is quite fast with a scan speed of 1000 mm/sec., 0.2 mm hatch distance and up to 0.2 mm slices. The post-curing and the precursor infiltration is done in approximately one day. The rapid pyrolysis requires two further days and the final silicon infiltration is also done in 2 days. The whole post-processing can be executed in 5 days.

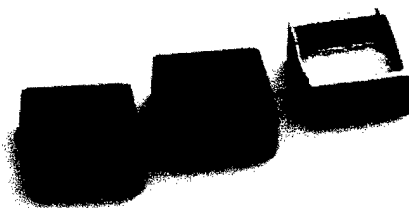


**Figure 8:** Sample box 25x25x10mm<sup>3</sup> (left: infiltrated with precursor resin; middle: pyrolysed; right: silicized).

### **Mechanical properties**

Several test bars were tested in a 4 point bending test according to the EN 843-1 standard. The bars with a dimension of 45 x 3 x 4 mm were cut out of a flat sintered plate and were used directly in the tests without any further surface finishing. Therefore the measured strength values are low. The average bending strength of the first tested samples was 70 MPa, with a maximum strength of 99 MPa. Parts with a lower resin absorption show lower strength. Test bars made out of a plate produced with a 9 % lower resin absorption showed on average an 18 % decrease in strength. The strength of the test bars (surface quality of saw cut) cannot be compared with the values for Si/SiC found in literature. The next test series with improved material structures will be carried out with polished test bars for comparable results.

### **Conclusion**

From these investigations we know that smaller particle sizes are of interest for structural  $\beta$ -SiC formation. Therefore further investigations must be focused on the reduction of the particle size in combination with a more regular particle shape for higher powder packing densities. The recoating system and especially the wiper blades of the sinter machine must also be adapted to the abrasive powder. The shrinkage during the precursor infiltration and curing must be reduced by a optimised binder content. The dimensions of the part are limited by the diffusion of water formed by the polycondensation of the phenolic precursor resin. Therefore the curing conditions of the precursor resin in the porous structure must be cleared. The parameters for the pyrolysis are of interest for an optimised porous crack structure. In conjunction with the parameters of the silicon infiltration, they specify the forming of the  $\beta$ -SiC and therefore the final structure.

Further investigations will also be made into the integration and combination of carbon fibre reinforced C/SiC strengthening elements into the RP-Si/SiC parts.

## Acknowledgement

Parts of the presented research were supported by the German Research Foundation (DFG/Sfb 374). The authors thank especially Bakelite AG, Iserlohn, Mineralien-Werke Kuppenheim GmbH, Kuppenheim, Institut für Nichtmetallische Anorganische Materialien (INAM), University of Stuttgart, Mr. Wolfgang Löschau, FhG/IWS Dresden, Fraunhofer-Institut für Chemische Technologie (FhG/ICT), Pfinztal for the help and encouragement as well as Retallick Systems and SCAPS GmbH for the new innovative process software for our laboratory sinter machine.

Further informations:

Dipl.-Ing. Peter Stierlen  
Institute for Polymer Science and Polymer Testing  
University Stuttgart  
phone: +49-711-641-2276  
stierlen@ikp2.uni-stuttgart.de

## Literature:

- /1/ Lakshminarayan, U.; et al. Selective Laser Sintering of Ceramic Materials. Proceedings of the Solid Freeform Fabrication Symposium 1990, University of Texas, Austin (TX), 1990
- /2/ Vail, N.K.; et al. Silicon Carbide Preforms for Metal Infiltration by Selective Laser Sintering of Polymer Encapsulated Powders. Proceedings of the Solid Freeform Fabrication Symposium 1993, University of Texas, Austin (TX), 1993
- /3/ Deckard, L.; Claar, T.D. Fabrication of Ceramic and Metal Matrix Composites from Selective Laser Sintered Ceramic Preforms. Proceedings of the Solid Freeform Fabrication Symposium 1993, University of Texas, Austin (TX), 1993
- /4/ Birmingham, B.R.; Marcus; H.L. Solid Freeform Fabrication of Silicon Carbide Shapes by Selective Laser Reaction Sintering (SLRS). Proceedings of the Solid Freeform Fabrication Symposium 1993, University of Texas, Austin (TX), 1993
- /5/ Birmingham, B.R.; et al. Silicon Carbide Shapes by Selected Area Laser Deposition Vapor Infiltration. Proceedings of the Solid Freeform Fabrication Symposium 1994, University of Texas, Austin (TX), 1994

- /6/ Jakubenas, H.; Marcus, H.L. Selective Laser Pyrolysis for Solid Free-Form Fabrication of Silicon Carbide. Proceedings of the Solid Freeform Fabrication Symposium 1994, University of Texas, Austin (TX), 1994
- /7/ Löschau, W. Selektives Lasersintern von Strukturkeramik. Jahresbericht FhG-IWS. Fraunhofer-Institut für Werkstoff und Strahltechnik (FhG-IWS), Dresden, 1997
- /8/ Löschau, W.; Lenk, R.; et al. Prototyping of complex shaped parts and tools of Si/SiC-ceramics by selective laser sintering. Proceedings of the 9<sup>th</sup> CIMTEC, Florence, Italy, June 14-19, 1998 (to be published)
- /9/ Schanz, P.; Krenkel, W. Description of the Mechanical and Thermal Behaviour of Liquid Siliconized C/C. Proceedings of the 6<sup>th</sup> ECCM, Bordeaux, France, Sept. 20-24, 1993
- /10/ Gern, F. Interaction between Capillary Flow and Macroscopic Silicon Concentration in Liquid Siliconized Carbon/Carbon. Proceedings of 2th HT-CMC, Santa Barbara, California, Aug. 21-24, 1995
- /11/ Fabig, J.; Krenkel, W. Principles and New Aspects in LSI-Processing. Proceedings of the 9<sup>th</sup> CIMTEC, Florence, Italy, June 14-19, 1998 (to be published)

# Mechanical Behavior of Robocast Alumina

Hugh B. Denham, Joseph Cesarano III, Bruce H. King  
Sandia National Laboratories

Paul Calvert  
University of Arizona

## Abstract

Direct fabrication of alumina parts by robocasting was completed. This method is based on three-dimensional deposition of binderless aqueous alumina slurries. Parts were made with different deposition paths and mechanical testing performed to determine the effects of bead alignment. Properties were also compared to alumina processed more traditionally.

## Introduction

Robocasting is a method of solid freeform fabrication of ceramic parts from aqueous slurries [1]. A computer controls the robotic deposition of highly concentrated colloidal slurries (Figure 1). The slurry is deposited from a syringe at a controlled rate in a layerwise process. Upon deposition, robocasting relies on a small amount of drying to induce a rheological transition of the slurry. The slurry changes from a flowable pseudo-plastic state to a solid-like dilatant mass. This transition gives each layer the strength necessary to support subsequent layers of freshly deposited slurry. Robocasting does not require polymerization reactions or wax crystallization. Only drying is necessary to build three-dimensional parts.

In order to make good parts via robocasting several issues must be balanced. High solids loadings are necessary, so powder surface chemistry and interparticle forces must be controlled. Pseudo-plastic rheology is needed to allow for flow through a small nozzle followed by enough strength to form a bead. The drying rate of the deposited beads is also critical to form ideal bead shapes. Bead knitting is also an issue; the beads must wet one another and flow enough so that there are no channels or voids between the beads. In addition to these materials issues are the parameters associated with the freeform process: table speeds, deposition rate, nozzle size and associated software.

The advantages of robocasting are many. The aqueous systems are binderless and have very low toxicity. A densified part can be made in less than 24 hours. The technique is amenable to multi-material fabrication. What is investigated here is the mechanical behavior of robocast parts with attention to the deposition paths used during fabrication.

## Experimental

Alumina bars were made for mechanical testing via four routes: uniaxial pressing, isostatic pressing, slip casting and robocasting. In addition, the robocast samples were made with different build patterns to investigate possible anisotropy due to bead alignment and inter-bead strength.

Alcoa A15 alumina powder was used in all samples. The surface area was  $4.3 \text{ m}^2/\text{g}$  with an average particle size of  $2.24 \text{ }\mu\text{m}$ . The entire particle size distribution ranged from  $10 \text{ }\mu\text{m}$  to  $0.2 \text{ }\mu\text{m}$ . Uniaxial pressed bars were made at 6 ksi (41 MPa) in a Carver press. Isostatic pressed samples were first pressed uniaxially to  $\sim 1.5$  ksi (10 MPa), followed by isostatic pressing to 25 ksi (172 MPa). No binders were used during pressing.

Slurry preparation for slip casting and robocasting was carried out using the alumina powder, water, and Darvan 821A as a dispersant. The slip casting slurry was 40 volume percent solids, and was cast in a plaster mold. A simple box shaped mold was used, with the walls being removed in the green state yielding a flat slab for cutting into test bars. Bars were only cut from regions near the center of the flat slab as to insure a sample set that was cast uniformly.

For the robocast samples, a 60-volume percent solids aqueous slurry was used. The slurry was ball milled slowly to allow mostly mixing and little milling. The slurry was mixed in this manner until the proper rheology was obtained (about 2 weeks). Extrusion was performed at a table speed of 8-10 mm/sec, with a 0.8347mm diameter nozzle, and table temperature of  $40^\circ\text{C}$  (typical laboratory humidity is 20-40%). Test bars were made with three different build patterns: a lengthwise writing pattern, a widthwise writing pattern, and a cross-hatch pattern alternating lengthwise and widthwise writing (Figure 2). These patterns were chosen to characterize the strength of the material when broken parallel to the bead direction (lengthwise build), perpendicular to the bead direction (widthwise build), and a combination of these (crosshatch build).

Densities were measured by Archimedes method, with green densities measured after bisque firing to  $1050^\circ\text{C}$ . All parts were fired to  $1650^\circ\text{C}$  for 2 hours. Four-point bend specimens were machined to specifications for MIL-STD-1942b, by Chand Associates. Mechanical testing was performed on an Instron machine, with a crosshead speed of 0.5mm/sec. There were 8 samples each from the pressing methods, 47 slip cast samples, and 10-12 samples from each of the different robocasting deposition patterns.

## Discussion

The densities for the four processes are shown in Table 1. While the isostatic pressed bars yielded the highest fired density; the others were comparable. This demonstrates that robocasting produces sintered parts of similar density to other processing routes. A sintered density on the order of 94% is all that can be reasonably expected from unmilled A-15 powder.

**Table 1:**  
**Percent of theoretical density for A15 alumina parts for various processing methods.**

	Green	Fired
Uniaxial Pressed	64.5	93.4
Isostatic Pressed	69.3	95.2
Robocast	68.4	93.7
Slip Cast	71.3	93.0

The flexural strengths from the 4-point bend tests are shown in Figure 3. It should be noted that these values are not as high as are often listed for high purity aluminas but the relative values are still useful for determining differences due to processing. These bars were made with Alcoa A15 alumina, which is not an optimal powder for making high strength parts. In addition, these parts were not sintered to theoretical density, and the surface finish on MIL-STD-1942b was a relatively rough 320-grit wheel. Regardless, as expected, the isostatic pressed bars performed better than the uniaxial pressed. The slurry based parts, slip cast and robocast, exhibited higher strengths than the pressed samples. The robocast parts varied in strength for different building paths, with the lengthwise fill having the same strength as the slip cast parts. Additionally, even the weakest robocast bars have strengths higher than isopressed bars. This shows that robocast parts can be made relatively strong when compared to parts fabricated more traditionally.

What is interesting is that the strength of the robocast parts is dependent on the build direction. The robocast lengthwise fill pattern shows strength 60 MPa higher than the widthwise or crosshatch fill. That is, the strength parallel to the build direction is approximately 20% higher than the strength perpendicular to the build direction. This behavior is analogous to a fiber reinforced material and may be due to two effects. Flaws may develop when two beads are deposited side by side and/or residual stresses may develop between beads due to small density variations induced during drying and sintering. The average strength of the crosshatch build pattern is nearly the same as the widthwise build. This is not entirely surprising since the ultimate strength is most likely controlled by the weaker widthwise layers and the inherent toughness of the alumina is low. However, upon further examination of the crosshatch strength data a small but significant alignment effect was discovered and is discussed below.

What is interesting is that the strength of the robocast parts is dependent on the build direction. The robocast lengthwise fill pattern shows strength 60 MPa higher than the widthwise or crosshatch fill. That is, the strength parallel to the build direction is approximately 20% higher than the strength perpendicular to the build direction. This behavior is analogous to a fiber reinforced material and may be due to two effects. Flaws may develop when two beads are deposited side by side and/or residual stresses may develop between beads due to small density variations induced during drying and sintering. The average strength of the crosshatch build pattern is nearly the same as the widthwise build. This is not entirely surprising since the ultimate strength is most likely controlled by the weaker widthwise layers and the inherent toughness of the alumina is low. However, upon further examination of the crosshatch strength data a small but significant alignment effect was discovered and is discussed below.

**Table 2:**  
**Flexural strength in MPa for different orientations of slip cast and robocast alumina.**

	Top in Tension	Base in Tension	Standard Deviation
Slip Cast	309.80	288.67	40.3
Robocast Lengthwise	301.89	310.21	27.6
Robocast Widthwise	242.07	234.01	33.4
	Lengthwise in Tension	Widthwise in Tension	Standard Deviation
Robocast Cross-Hatch	256.64	225.09	37.1

When fracture surfaces of the robocast bars are examined some interesting features are revealed. Figure 4 shows the fracture surfaces for three robocast bars. The widthwise samples and cross-hatch samples show artifacts of the layerwise building process, while the lengthwise samples shows no remnants of the build path or layers. These textured surfaces show that there are preferential fracture paths parallel to the build direction. Therefore, the first inclination is to believe that defects were formed between beads during robocasting because of a lack of ample bead meshing during deposition. However, the micrographs in Fig. 5 may suggest an alternative explanation.

The micrographs in Figure 5 are of a part that was sectioned parallel to the build direction. At low magnification, the build pattern can still be barely discerned. At high magnification, pores and defects on the order of 4 to 10  $\mu\text{m}$  can be observed. Voids of this size are reasonable for unmilled A-15 alumina and are probably not due to robocasting defects. Also, the porosity present appears to be uniform both in the interior of beads and in the regions between the beads. Regardless of where micrographs are taken the microstructure is very similar to Fig. 5b. Why the microstructure appears uniform throughout the section while a clear texture reminiscent of the build pattern can be seen optically, remains a curiosity. The presence of residual stresses may be a possible explanation. Since robocasting relies on the drying of the deposited beads, uneven drying could lead to small density differences within each bead. If we consider a single deposited bead, drying occurs from the outside in. If the exposed surface dries too fast it would form a hard shell and the inside material may not be able to achieve the same density. A density difference within the part could lead to some residual stresses being built up during sintering.

### Conclusions

We have shown that robocast alumina exhibits densities and strengths comparable to alumina processed more traditionally. However, the mechanical properties of robocast alumina are slightly anisotropic and dependent on the build path used. Strengths parallel to the build direction are nearly identical to slip cast parts. Strengths perpendicular to the build direction are slightly lower than the parallel strengths but higher than isostatically pressed parts. Also, when parts are broken in the proper orientation, preferential fracture paths may be observed that appear to mimic the layerwise build pattern. However, it is not yet clear if the preferential fracture paths

are due to inadequate bead meshing or residual stress induced by nonuniform drying and sintering.

### **Acknowledgment**

Sandia is a multiprogram laboratory operated by Sandia Corporation, a Lockheed Martin Company, for the United States Department of Energy under Contract DE-AC04-94AL85000.

### **Reference**

1. J. Cesarano III, R. Segalman, and P. Calvert, "Robocasting Provides Moldless Fabrication from Slurry Deposition," *Ceramic Industry*, pp 94-102, April 1998.

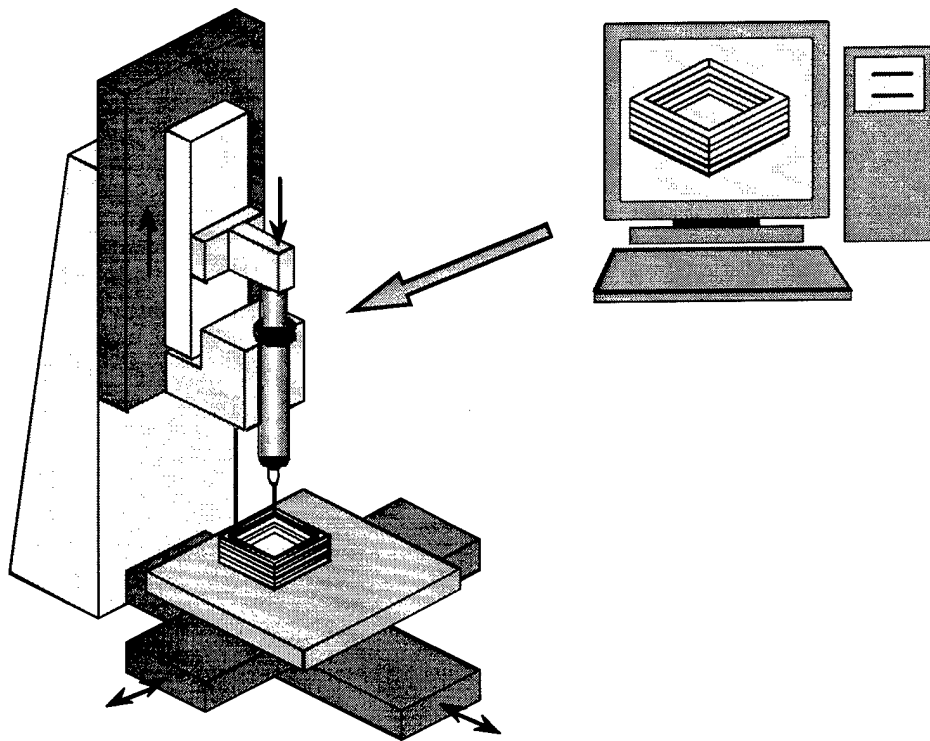


**Figure 1: Robocasting: Computer Controlled Extrusion of Aqueous Slurries**

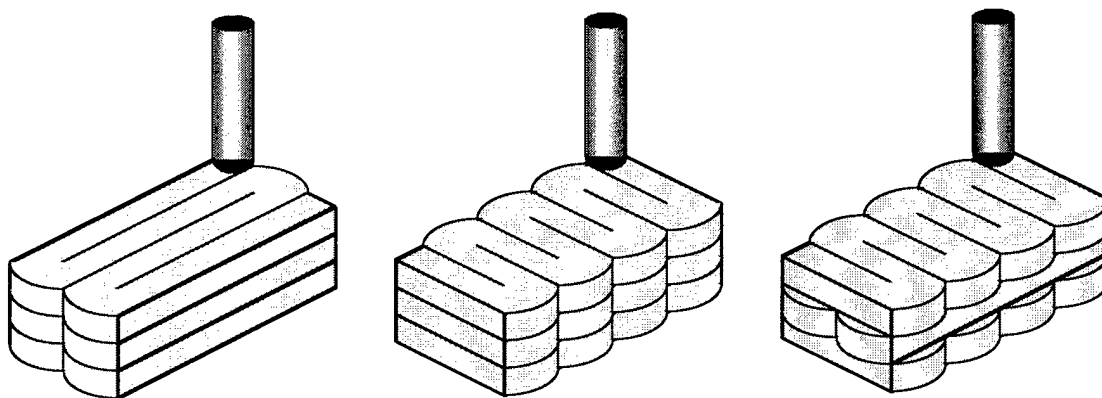


**Figure 2: Robocasting build patterns; lengthwise, widthwise, and crosshatch.**

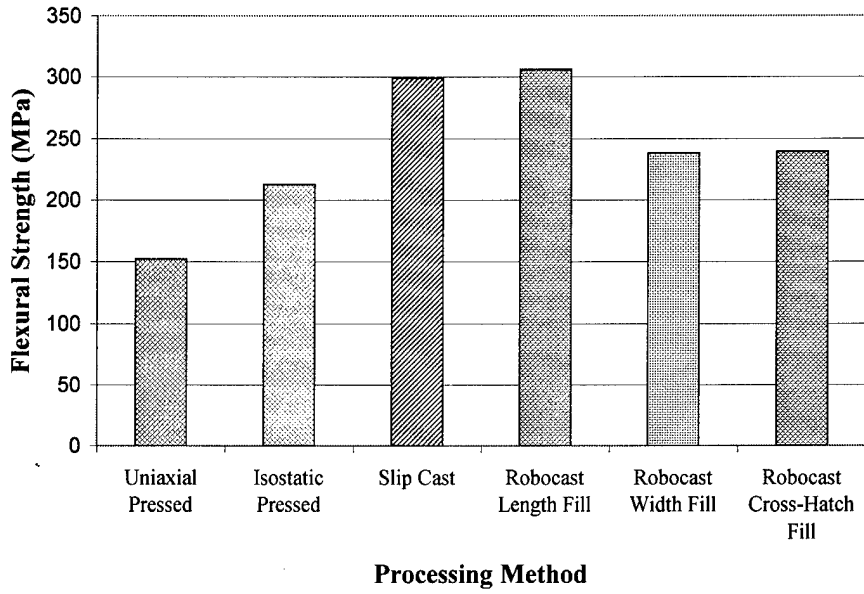


**Figure 3: Flexural strength of alumina for various processing methods (Mil-Std-1942b).**

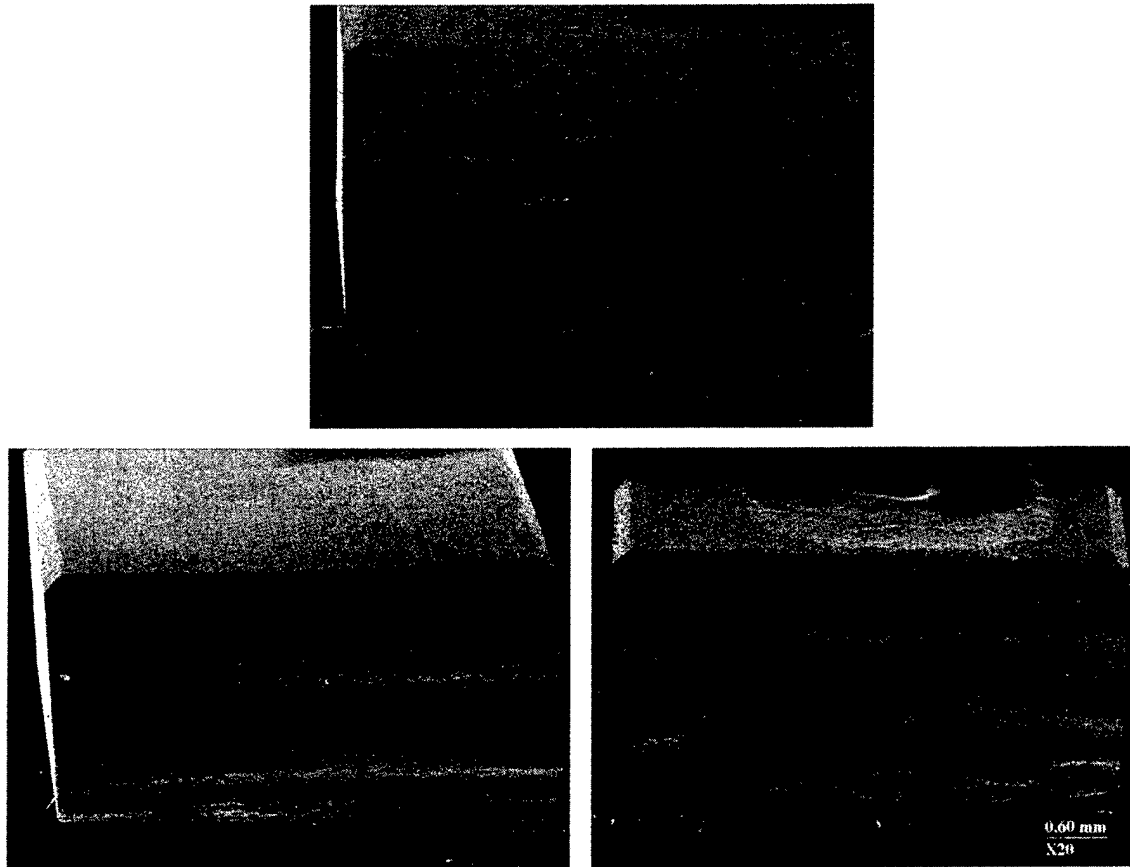


**Figure 4: Cross-Sections of the Different Build Patterns of Robocast Alumina Showing Texture.**

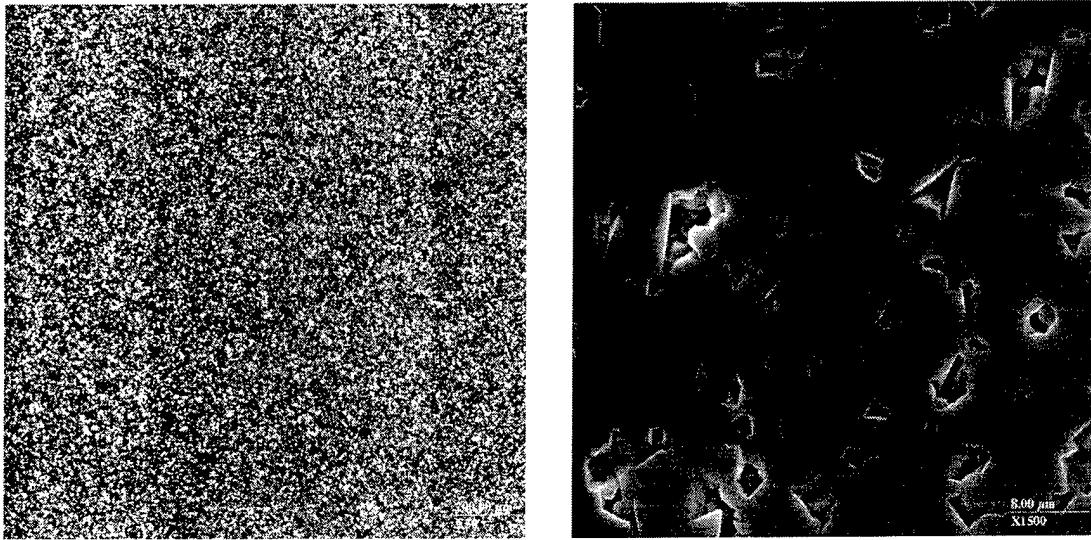


**Figure 5: SEM Micrographs of Cross-Sectioned Robocast Alumina Showing the Layered Pattern at (left to right) Low and High Magnifications.**

## **Titanium Casting Molds via Selective Laser Sintering**

Nicole Harlan, David Bourell, Joe Beaman  
The University of Texas at Austin

### **Abstract**

A mold material system has been developed that can be SLS processed and used to cast titanium alloys. Stabilized zirconia, chosen for its low reactivity with molten titanium, has been sintered into mold shapes. The molds have been infiltrated with a colloidal solution of unstabilized zirconia and fired to create a partially stabilized structure. SEM analysis shows that the unstabilized zirconia forms bridges between the larger stabilized zirconia particles that provide strength to the mold.

### **Introduction**

Titanium has interested designers for years because of its light weight, high strength, corrosion resistance and its abundance as a natural resource. Difficulties in room-temperature machining and forming have prevented wider spread use of titanium. Near-net-shape fabrication processes such as casting are the most commonly used methods to produce titanium parts since they require minimal post machining.

Investment casting is a conventional way to produce titanium parts. Because molten titanium reacts with most solids, liquids and gases, specific mold materials and casting environments are used to minimize contamination of the final part. Rammed graphite molds are widely used because of the low cost and availability of graphite. However, the carbon reacts with titanium and forms a hardened titanium shell on the cast part that must be machined off. When casting parts in small quantities, a less reactive, more expensive mold material can be cost efficient by reducing the post-machining costs.

Several studies show that zirconia is one of the least reactive materials with molten titanium [1,2]. However, zirconia undergoes a destructive phase transformation at 1100°C that can crack the mold during casting. It converts from a monoclinic to a tetragonal atomic structure, resulting in a 7 percent volume shrinkage. The addition of a small amount of yttria stabilizes the zirconia in a cubic structure that does not change phase at 1100°C [3]. If a cubic phase zirconia mold is fabricated and infiltrated with unstabilized monoclinic zirconia, a "partially stabilized" structure is created. The partially stabilized zirconia structure has better thermal shock resistance than either the unstabilized or fully stabilized structures [4].

Selective laser sintering (SLS) has been used to build partially stabilized zirconia molds for titanium casting. Prototype titanium parts have applications in the aerospace and automotive fields and as customer specific biomedical implants.

### Experimental Procedure

Granulated yttria-stabilized zirconia powder from TOSOH Ceramic Corporation was used as the base material for the casting mold. The average zirconia crystallite size was 24 nm; the average granulate size was approximately 50  $\mu\text{m}$ . To prevent post SLS shrinkage, the granulated particles were presintered for one hour at 500°C followed by two hours at 1250°C to burn off the binder and densify each particle. The sintering schedule was determined from a sintering map generated by Bourell, shown below [5].

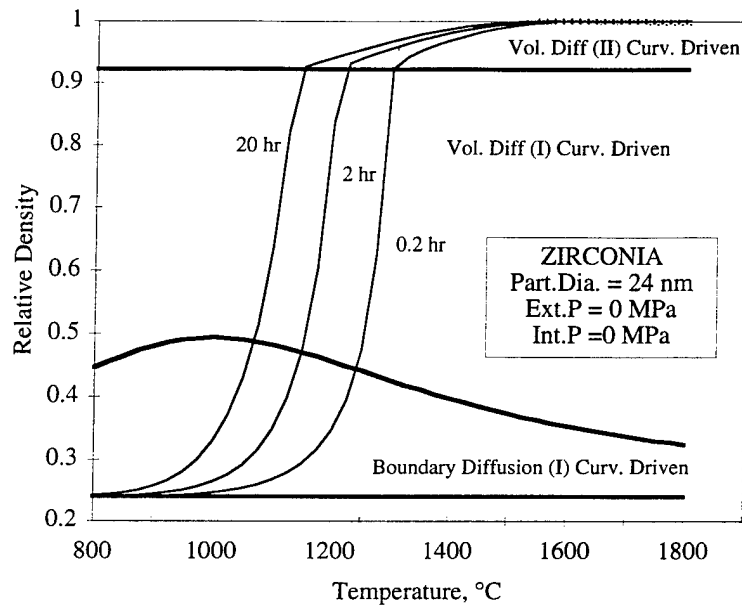


**Figure 1.** Zirconia sintering map

The pre-sintered powder density was measured using a Quantachrome Ultrapycnometer 1000.

The SLS binder, an 80:20 molar blend of methylmethacrylate and butylmethacrylate, respectively, was produced by methods discussed elsewhere [6]. This particular copolymer binder was chosen because it completely “unzips” during firing, leaving no contaminating residue [7]. The copolymer binder was spray dried into fine particles using an Anhydro Laboratory 1 Model Spray Drier. The resulting powder was on

the order of 5  $\mu\text{m}$ . Copolymer powder density was measured using the same Quantachrome gas pycnometer mentioned earlier. The melt flow index, ASTM D1238, of the copolymer was measured at 200°C using a Kayeness Galaxy I capillary rheometer. Copolymer flexural properties were tested per ASTM D790 using a three point bend apparatus. Ten samples were used for each measurement.

Preliminary blends of pre-sintered stabilized zirconia powder and 10 to 40 vol% copolymer powder, in increments of 5 vol%, were heated to 175°C in a furnace. Based on visual inspection, it was determined that at least 20 vol% copolymer was needed to bind the zirconia together in a solid mass, and blends containing 30 vol% copolymer possessed sufficient handling strength. Hence, 20 vol% and 30 vol% copolymer -zirconia blends were tested for SLS processing. The appropriate amounts of copolymer and zirconia were weighed out and mixed together in a rolling mill for 24 hours.

An SLS Model 125 Workstation was used to build bend test specimens. A layer thickness of 0.005 inches, scan spacing of 0.003 inches and CO<sub>2</sub> laser power of 5 watts were used. Laser scan speed was 16 in/s. The fabricated bend specimens, at least five in each set, were tested per ASTM D790 using a four point bend apparatus. Open porosity of the samples was measured using Archimedes density measurements.

A set of 20 vol% and 30 vol% copolymer SLS samples were infiltrated using Nyacol Zr100/20 colloidal zirconia. The Zr100/20 colloidal solution is 20 wt% unstabilized zirconia suspended in water by a nitrate counter ion. The zirconia crystallite size is 100 nm. The colloidal solution would not infiltrate the samples in its original concentration, so it was blended in 3:2 and 1:1 ratios with methanol to decrease viscosity and facilitate infiltration. The SLS samples were infiltrated with solution and dried until no further solution absorption was observed, typically after four infiltrations. Weight gain during infiltration was measured to determine a) whether the 20 or 30 vol% samples absorbed more infiltrant and b) which colloidal zirconia:methanol ratio resulted in more solid weight gain. At least five specimens were tested in each experiment. Sample weight was measured initially, after the specimens were dried 24 hours following the final infiltration, and after a 60 minute cure cycle at 100 and 150°C.

The following schedule was used to fire the infiltrated specimens. It was designed to burn off the copolymer binder and sinter the infiltrated zirconia to the base particle structure:

Heat Schedule	Desired Effect
Ramp 1°C/min to 500 °C	Slow ramp to prevent cracking
Dwell 60 minutes	Copolymer burn off
Ramp 20°C/min to 1000°C	
Ramp 10°C/min to 1400°C	
Dwell 480 minutes	Zirconia sintering and grain growth
Ramp 10°C/min to 25°C	

The change in the ramp rate from 20 to 10°C/min at 1000°C was due to furnace limitations. SEM micrographs were taken on the final specimens to determine the effectiveness of the zirconia infiltrant as a binder for the stabilized zirconia particles. No mechanical testing has been done.

### Results and Discussion

Specimen preparation and SEM analysis show the TOSOH granulated particles were sintered to full density during the 1250°C thermal cycle. This agrees with the sintering map prediction shown earlier.

Pycnometer Density	Theoretical Density
6.05 +/- 0.01 g/cc	5.9 g/cc

The 80:20 methylmethacrylate butylmethacrylate copolymer had comparable material properties to the same copolymer produced by Vail, shown in the following table [8]. Copolymer powder density was measured as 1.24 g/cc.

#### *Copolymer Material Testing*

	Melt Flow Index g/10 min	Flexural Strength [Pa] x 10 <sup>4</sup>	Flexural Modulus [Pa] x 10 <sup>6</sup>
80/20	17.9	2.6 +/- 0.2	2.20 +/- 0.04
80/20, Vail	15	2.6 +/- 0.1	2.37 +/- 0.08

Figure 2 shows a close up of the copolymer binder tacking the stabilized zirconia particles together after SLS processing.

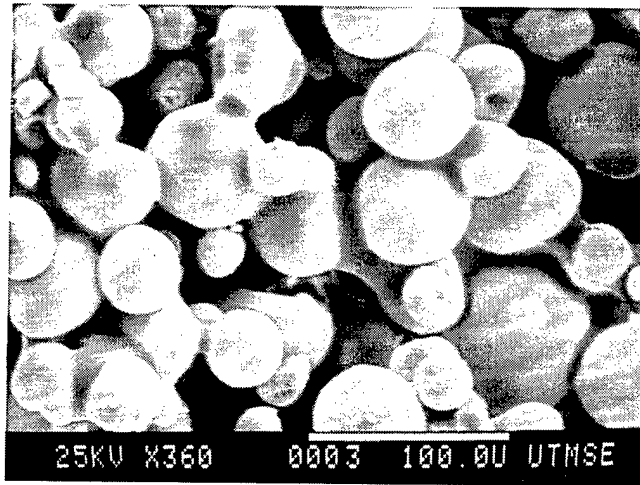


**Figure 2.** Zirconia + 30 vol% copolymer after SLS processing

The coupons produced with 30 vol% copolymer were easier to handle than those with 20 vol% copolymer. The latter chipped and broke during transport and handling.

The following two tables show open porosity and mechanical testing data for the 20 vol% and 30 vol% copolymer samples.

***Archimedes Density Measurements***

	Open Porosity vol%
zirconia + 20 vol% copolymer	35
zirconia + 30 vol% copolymer	23

***Four Point Bend Testing***

	Flexural Strength [Pa] x 10 <sup>2</sup>
zirconia + 20 vol% copolymer	8.0 +- 0.6
zirconia + 30 vol% copolymer	14.6 +- 0.6



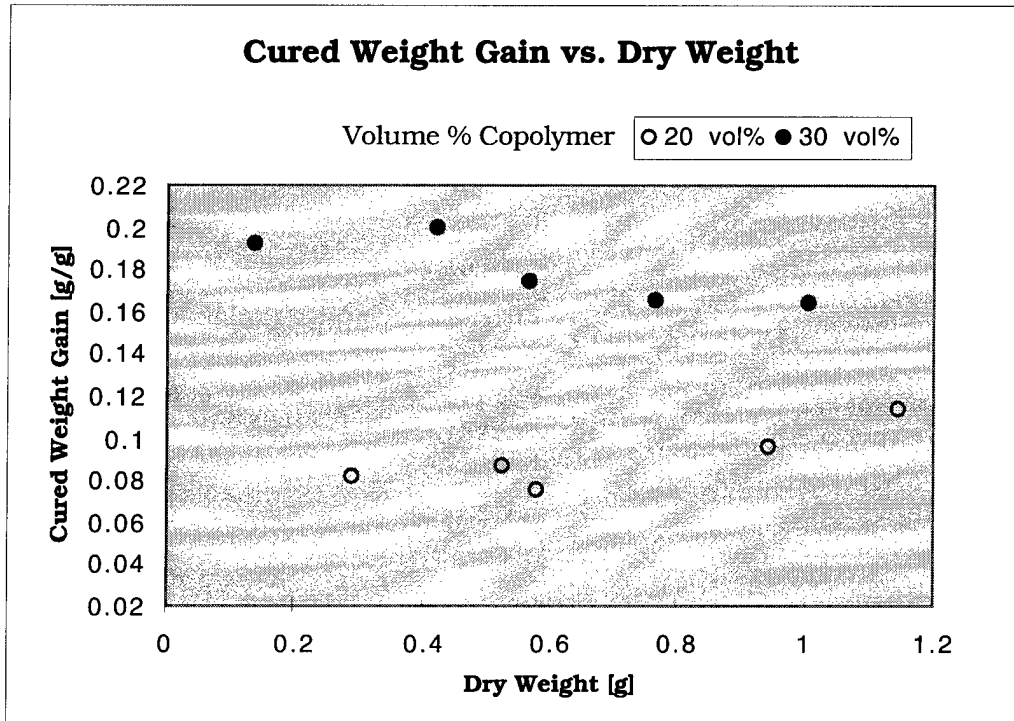


**Figure 4.** Weight Gain in 20 vol% and 30 vol% Copolymer Samples

An SEM micrograph of a specimen fired at 1400 °C for 8 hours, Figure 5, shows that the copolymer binder has burnt off and that the infiltrated zirconia, identified by its irregular shape, has formed bridges between the spherical zirconia particles

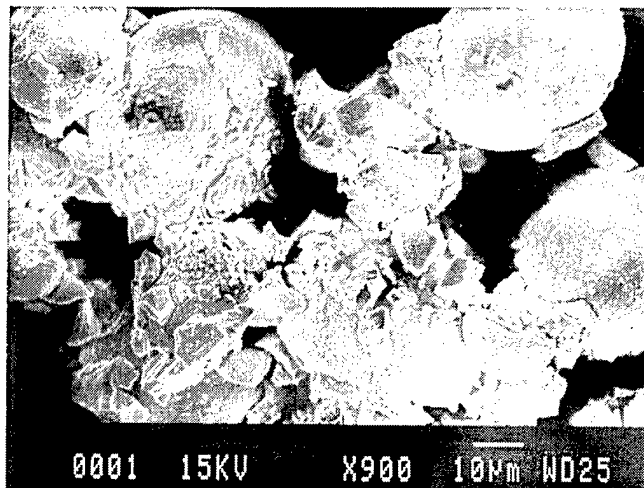


**Figure 5.** Zirconia + infiltrated zirconia

This result is promising because the infiltrated zirconia has replaced the copolymer bridges and can provide strength in the mold.

## Conclusion

Mixtures of stabilized zirconia powder and a 80:20 PMMA-BMA copolymer binder have been selective laser sintered to form casting mold green shapes. Parts made from a 30 vol% copolymer - zirconia powder blend were found to have higher green strength than those made from a 20 vol% copolymer - zirconia blend. A solution of colloidal zirconia (3 parts) and methanol (2 parts), infiltrates the porous green shapes at room temperature. The 30 vol% copolymer green parts experience a higher weight gain than 20 vol% copolymer green parts when infiltrated. After binder burn out and firing at 1400°C, bridges of unstabilized zirconia from the colloidal solution remain as structural bonds between the stabilized zirconia particles.

## Acknowledgments

I would like to acknowledge Dr. Neal Vail and Dr. Joel Barlow for their guidance in this project and for their assistance in preparing the copolymer.

## References

1. E.D. Calvert, *An Investment Mold for Titanium Casting*, U.S. Bureau of Mines Report of Investigations, n. 8541, 1981, pp. 6-7.
2. R.L. Saha and K.T. Jacob, Casting of Titanium and Its Alloys, *Defense Science Journal*, Vol. 36, No. 2, April 1986, p. 125.
3. David W. Richerson, *Modern Ceramic Engineering*, Marcel Dekker, Inc., 1992, p. 106.
4. Calvert, p. 20.
5. David L. Bourell, Parimal and Wolfgang Kaysser, *Sol-Gel Synthesis of Nanophase Ytria-Stabilized Tetragonal, Zirconia and Densification Behavior Below 1600K*, *Journal of the American Ceramic Society*, Vol. 76, No. 3, March 1993, p. 709.
6. Neal K. Vail, *Preparation and Characterization of Microencapsulated, Finely Divided Ceramic Materials for Selective Laser Sintering*, U.T. Austin, 1994, pp. 317-322.
7. Vail, pp. 35-39.
8. Vail, pp. 150-151.

# Selective Laser Sintering of Zirconium Silicate

F. Klocke, H. Wirtz  
Fraunhofer Institute of Production Technology IPT  
Steinbachstr. 17  
52074 Aachen  
Germany

## Abstract

The Fraunhofer Institute of Production Technology (IPT) and the Fraunhofer Institute of Laser Technology (ILT) have joined forces in a project dedicated to Selective Laser Sintering (SLS) of metals and ceramics, funded by the German Government and 6 industrial partners.

Selective Laser Sintering of zirconium silicate as a ceramic material used for investment casting shells and cores is an attractive alternative to the conventional, time-consuming way of producing these shells from a wax master. This paper will present current process results concerning laser sintering of shells made from zirconium silicate and explain the related potentials and benefits.

## Acknowledgements

The authors would like to gratefully acknowledge the financial support of the six industrial partners, Bremer Werkzeug- und Maschinenbau (BWM) GmbH, Bremen, Electro Optical Systems (EOS) GmbH, Planegg, Fockele & Schwarze (F&S) GmbH, Borchon-Alfen, Laser Bearbeitungs- und Beratungszentrum (LBBZ) NRW GmbH, Aachen, STEMO-TEC Design GmbH, Castrop-Rauxel, United Technologies Research Center (UTRC), Aachen as well as of the German Government.

The authors would also like to gratefully acknowledge the support of the foundry institute of the Rheinisch-Westfälische Technische Hochschule Aachen, the GI RWTH Aachen.

## 1 Investment Casting

Investment casting is an industrially well established casting process for the production of complex metal parts for small- to large-sized batches. A pattern, usually made from wax by injection molding, is used to create a coating by dipping the pattern in a ceramic slurry and drying the coating. This procedure is repeated up to nine times to create a shell, consisting of ten layers with an overall thickness of about 6 mm. The ceramic shell is then fired in an oven to burn out the pattern and sinter the material to gain additional strength. A metal is poured into the shell to cast the metal positive; the process ends with removal of the shell as well as the runner systems and additional cleaning. Both the pattern and the shell are destroyed during the casting procedure (lost pattern, lost form casting process). An advantage of investment casting is that practically all metals may be processed (König, 1990).

Investment casting is often used in conjunction with Rapid Prototyping (RP). Usually, RP is employed to create the master pattern; QuickCast from 3D Systems and Selective Laser Sintering of polystyrene or polycarbonate are good examples (Jacobs, 1995, Venus, 1995).

However, time is only saved during production of the pattern, yet the casting process itself takes about two weeks due to the necessary step of drying the ceramic slurry coatings that are repeatedly being applied. Thus, the direct production not of patterns but of ceramic shells by RP yields great benefits since creation of both a pattern and a shell is superfluous. The Direct Shell Production Casting process developed at MIT and in application at Soligen already follows this route utilizing 3D Printing (Cima, 1991).

## 2 Experimental Results

Selective Laser Sintering is a process also capable of generating parts from ceramic powder (Esser, 1996, Langer, 1996, Lakshminarayan, 1992, Griffin, 1995, Lee, 1995, Vail, 1993). The materials most often used in investment casting are aluminum silicates, zirconium silicates, alumina and silica. From initial tests, zirconium silicate was found suitable for use with Selective Laser Sintering.

Figure 1 shows first experimental results that were obtained by Selective Laser Sintering of a zirconium silicate (-125 mesh, particle size < 119  $\mu\text{m}$ , irregular particle shape) using a cubic test geometry ( $10 \times 10 \times 10 \text{ mm}^3$ ) and varying laser power from 14 to 88 W, scan speed from 100 to 800 mm/s and hatch spacing from 0.05 to 0.4 mm. Each layer was exposed to the laser light once and scanning was performed in just one direction. The slice thickness was set to 0.2 mm, the machine used was an EOSINT M 160 with a  $\text{CO}_2$  laser source. The substrate used was a granite plate which was found more suitable for this purpose than other materials, e.g. metals, due to the low thermal conductivity and the good adhesion characteristics.

- processing is possible with an energy density of  $E=2$  to  $6 \text{ J/mm}^2$
- agglomerated particles formed from molten material cause break-outs while wiping
- little curling

**material**  
zirconium silicate  
grain -125, particles < 119  $\mu\text{m}$   
**machine parameters**  
laser power  $P_L = 14$  to 88 W  $\text{CO}_2$   
scan speed  $v_s = 100$  to 800 mm/s  
hatch spacing  $h_s = 0.05$  to 0.4 mm  
exposure x-direction  
thickness of layer 0.2 mm  
**test part geometry**  
 $10 \times 10 \times 10 \text{ mm}^3$

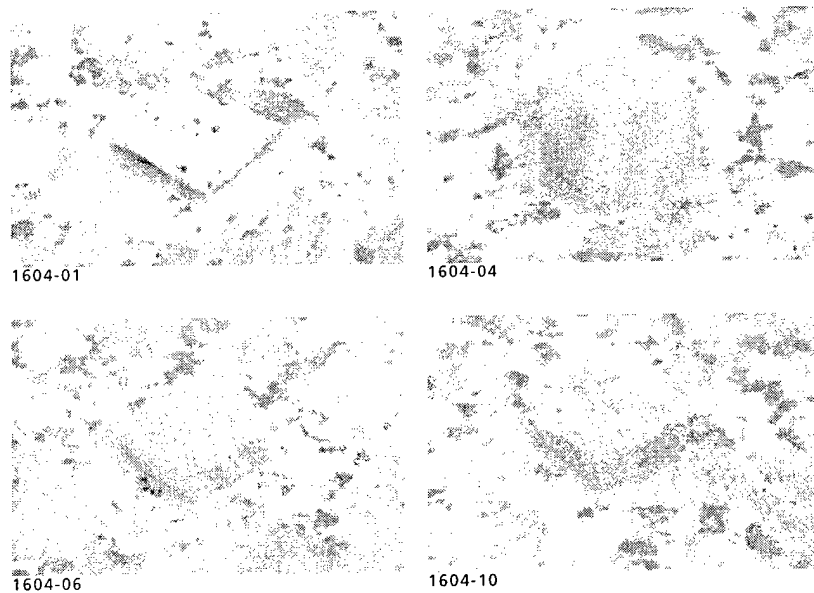


Figure 1 SLS of zirconium silicate – experimental results

The experiments were successful for some parameter combinations (see figure 1, upper right hand corner: laser power  $P_L=88 \text{ W}$ , scan speed  $v_s=100 \text{ mm/s}$ , hatch spacing  $h_s=0.4 \text{ mm}$ ) while others either led to irregular, totally molten shapes (see figure 1, upper left hand corner: laser power  $P_L=88 \text{ W}$ , scan speed  $v_s=100 \text{ mm/s}$ , hatch spacing  $h_s=0.05 \text{ mm}$ ) or to agglomerations

that were destroyed when a new layer of powder was applied by the wiper (see figure 1, lower left hand corner: laser power  $P_L=88$  W, scan speed  $v_s=200$  mm/s, hatch spacing  $h_s=0.1$  mm; see also figure 1, lower right hand corner: laser power  $P_L=88$  W, scan speed  $v_s=400$  mm/s, hatch spacing  $h_s=0.1$  mm).

After these initial tests to roughly find suitable parameter combinations for the successful SLS of the material, further experiments were conducted with a powder mix of DIN 70 (particle size  $< 90 \mu\text{m}$ ) and -125 mesh (particle size  $< 119 \mu\text{m}$ ), this time using a larger test geometry ( $20 \times 20 \times 8 \text{ mm}^3$ ) and scanning one layer in x- and y-direction. The purpose for using a powder mix was to increase the portion of smaller particles in the powder providing an increased amount of liquid phase during sintering, since smaller particles need less energy to melt than larger particles. A further decrease in grain size of the powder was not possible due to an increased amount of agglomerations, making an even spread of new powder layers with the wiper impossible.

Some basic mechanisms were found to prevail during SLS of zirconium silicate as illustrated in figure 2. An increase in laser power leads to an increase in the density of the specimen, since more energy is delivered into the powder and larger melt pools fill up the porous structures of previous layers (see figure 2, upper left hand corner). However, surface roughness also increases since the molten particles tend to form larger spherical structures due to their effort to reduce the free enthalpy by optimizing the ratio between the area of free surfaces and the related volume. Figure 3 is an illustration of this effect; a high speed camera was used to monitor SLS of zirconium silicate, this time on a test facility equipped with a Nd:YAG laser. Laser power was varied from 97 W to 120 W to 161 W, making the effect of formation of increasingly larger structures with increasing laser power visible.

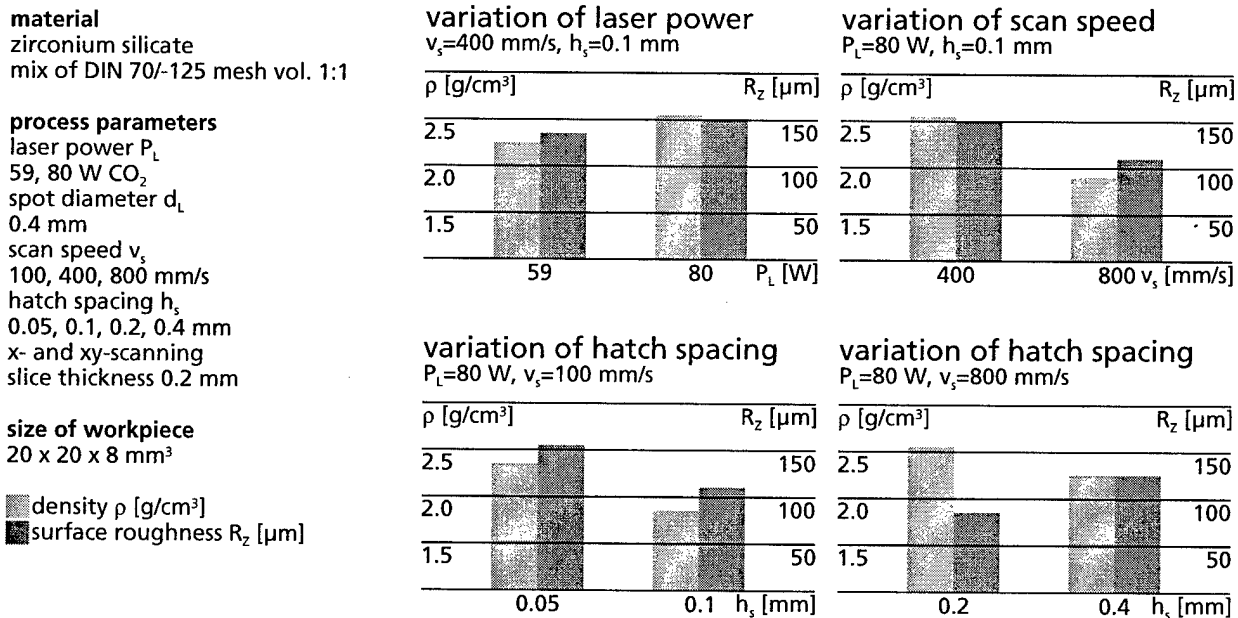


Figure 2 Basic mechanisms of SLS of zirconium silicate

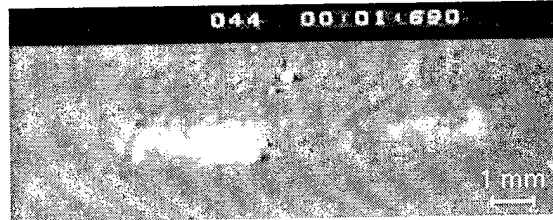
**material**  
zirconium silicate  
mix of DIN 70/-125 mesh  
vol. 1:1

**process parameters**  
laser power  $P_L$  varying  
from 97 to 161 W  
Nd:YAG laser  
scan speed  
 $v_s=100$  mm/s  
hatch spacing  
 $h_s=0.4$  mm  
exposure of a single  
layer in x-direction  
layer thickness is 2 mm  
on aluminum plate

**size of workpiece**  
 $10 \times 10$  mm<sup>2</sup>

**camera parameters**  
400 shots/s  
time notation  
mm:ss:1/1000sss

**analysis**  
the influence of laser  
power on melting  
characteristics of the  
powder is evident



laser power  $P_L=97$  W



laser power  $P_L=120$  W



laser power  $P_L=161$  W

Figure 3 SLS of zirconium silicate – high speed video pictures

Increasing scan speed has the opposite effect; because less energy is delivered into the powder bed and the velocity of the laser beam on the part surface is higher, less material is melted and less time is available for the formation of agglomerations, see figure 2. Thus, density decreases and surface finish improves.

A variation of hatch spacing leads to two different effects, see figure 2 and figure 4. For the case when hatch spacings are small compared to the laser diameter ( $h_s \ll d_L$ ), the molten powder particles form separate larger beads of high density leading to an overall high density of the part, yet the surface roughness also increases. An optimum combination of density and surface roughness is obtained for hatch spacings that are comparable to the size of the spot. For hatch spacings larger than the diameter of the laser, the molten beads of material are not connected to each other, but the gap is filled with unsintered powder, resulting in a rough surface and low density.

Of all the parameter combinations that led to a stable sintering process, the maximum density achieved was 55.3% of theoretical density ( $P_L=80$  W,  $v_s=400$  mm/s,  $h_s=0.1$  mm, xy-exposure). However, density is not an important quality criterion for investment casting shells. Actually, a certain porosity is desirable to allow gases to diffuse out of the shell when the hot metal is cast. Rather, process stability and repeatability becomes an important criterion. Parts

sintered from zirconium silicate are extremely brittle and a collision with the wiper blade during the process due to agglomerates will almost always lead to a destruction of the workpiece.

**bead forming, balling effect**

- the molten powder particles tend to form larger spherical structures to reduce their free enthalpy
- the wettability characteristics depend on (among other things) the material used and the process temperature
- small grain sizes usually lead to a reduction of this effect, however the powder material may not be processable, i.e. wipable

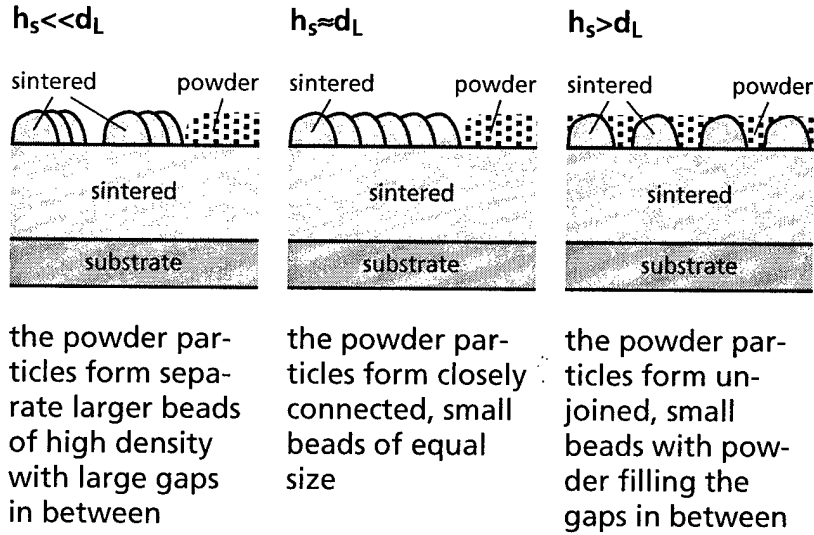


Figure 4 Basic mechanisms of SLS of zirconium silicate – effect of hatch spacing

**3 Practical Testing**

A stable parameter combination was found to be a laser power of 80 W, a scan speed of 400 mm/s, a hatch spacing of 0.1 mm using xy-exposure. Vat-like parts were built with these parameters for initial investment casting tests, see figure 5. To improve surface finish and test the effect of infiltration and pre-burning, parts were either left untreated, fired or coated with a  $ZrSiO_4$  or  $AlSiO_2$  slurry (particle size -325 mesh) and fired. In all cases, the material could successfully be cast into the shells. The infiltration led to an improvement of surface finish, however the small particles in the infiltration slurry do not penetrate the part but clog up the small pores, leading to a sieve-like effect, covering the surface of the workpiece and leading to undesirable dimensional inaccuracies. Firing the specimen before casting the metal does not lead to a measurable advantage in surface finish or density.

Finally, test parts (tensile test bars, articulated lever) were constructed and runner systems were added. The parts were triangulated and shells were created by offsetting the outer surfaces (6 mm) of the parts using STL file manipulation software. Several shells were built (build time: about 20 h each) on the EOSINT M 160 employing the parameters mentioned above. The internal structures were reproduced without affecting process stability. The shells were cleaned externally and internally from excess powder with compressed air and water and then preheated for 3 hours to 380° C. The metal cast was an AlSi 7 with a melt temperature of 750° C. The shells were fully filled and all features were reproduced, see figure 6 and figure 7. At this stage of development, the primary goal was to prove the suitability of the SLS process for the production of shells made from zirconium silicate, thus attainable accuracies were not measured. The surface of the cast part was an accurate reproduction of the surface of the ceramic negative, thus surface roughness was in the range of 100 to 150  $\mu m$ .

**material**

zirconium silicate  
mix of DIN 70/-125 mesh vol. 1:1

**process parameters**

layer thickness 0.2 mm  
exposure in xy-direction  
CO<sub>2</sub> laser  
spot diameter  $d_L=0.4$  mm

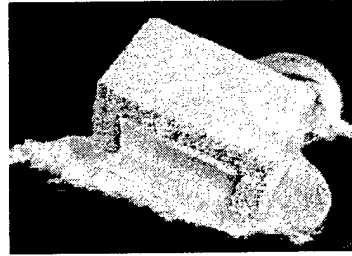
laser power  $P_L=80$  W  
scan speed  $v_s=400$  mm/s  
hatch spacing  $h_s=0.1$  mm  
energy density  $E=4$  J/mm<sup>2</sup>  
line energy  $E_L=0.5$  J/mm<sup>2</sup>

**test piece geometry**

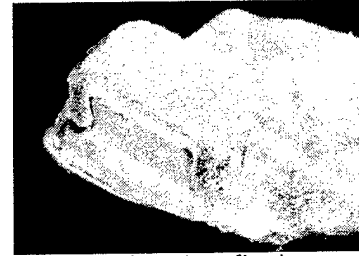
30 x 20 x 14 mm<sup>3</sup>  
wall thickness 6 mm

**temperature**

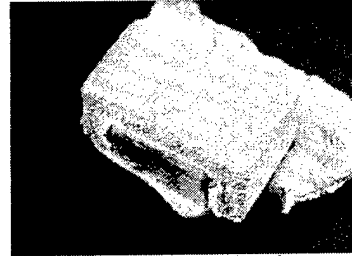
burning temperature 1000°C  
preheating temperature 380°C  
melt temperature 750°C



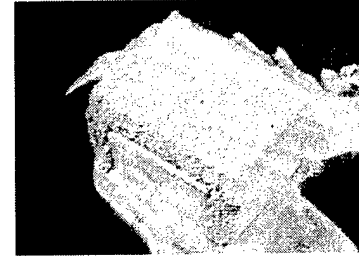
fired



coated with ZrSiO<sub>4</sub>, fired

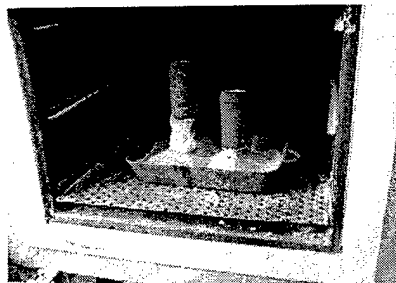


coated with AlSiO<sub>2</sub>, fired

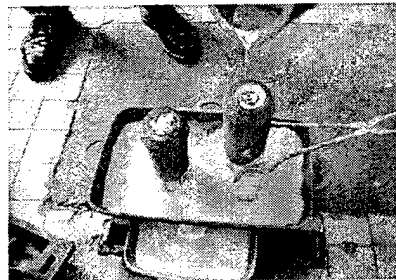


untreated

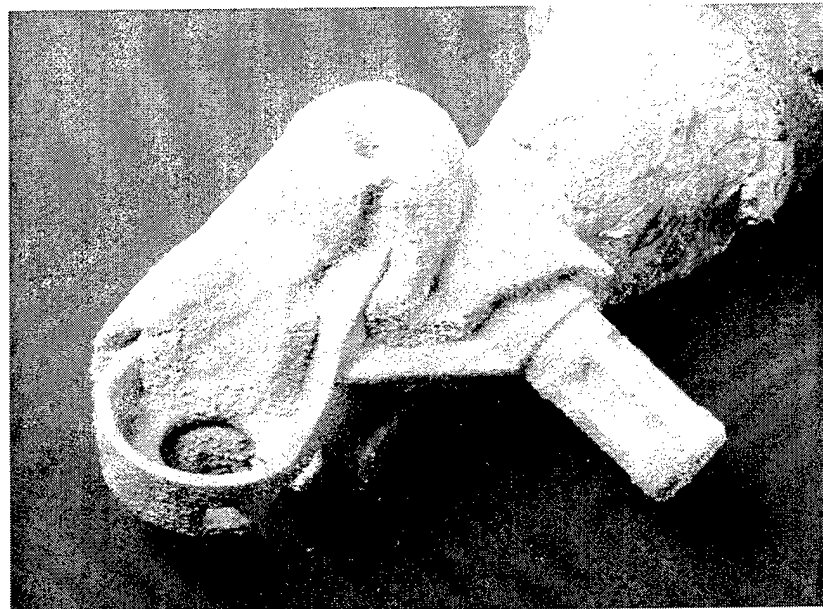
Figure 5 SLS of zirconium silicate – investment casting tests



preheating of the shells at 380° C



casting using an aluminum alloy at 750° C



removal of the shell; cleaning; part is an articulated lever for the aerospace industry

Figure 6 Casting of the SLS shells

#### 4 Summary and Outlook

Constructing the runner systems, combining the runner system with the parts, creating the shells and preparing the slice data for the SLS machine was done in two hours. Sintering the parts took about 20 h each, preparing the parts for investment casting (cleaning, preheating), casting the metal and removing the shells took additional 8 h. The overall lead time of two days compares favorably to a lead time of about two weeks required to produce the same parts using

the conventional investment casting process. Thus, Selective Laser Sintering of zirconium silicate to ceramic shells for investment casting is an attractive alternative for rapidly manufacturing metal parts.

However, surface finish needs to be improved to satisfy industrial demands which poses a problem with the currently employed zirconium silicate; smaller grain sizes lead to agglomerates which hinder an even spread of new powder layers. Future work will thus include the finding of suitable ways to apply new layers of powder to the powder bed or the use of powders with more regular particle shape.

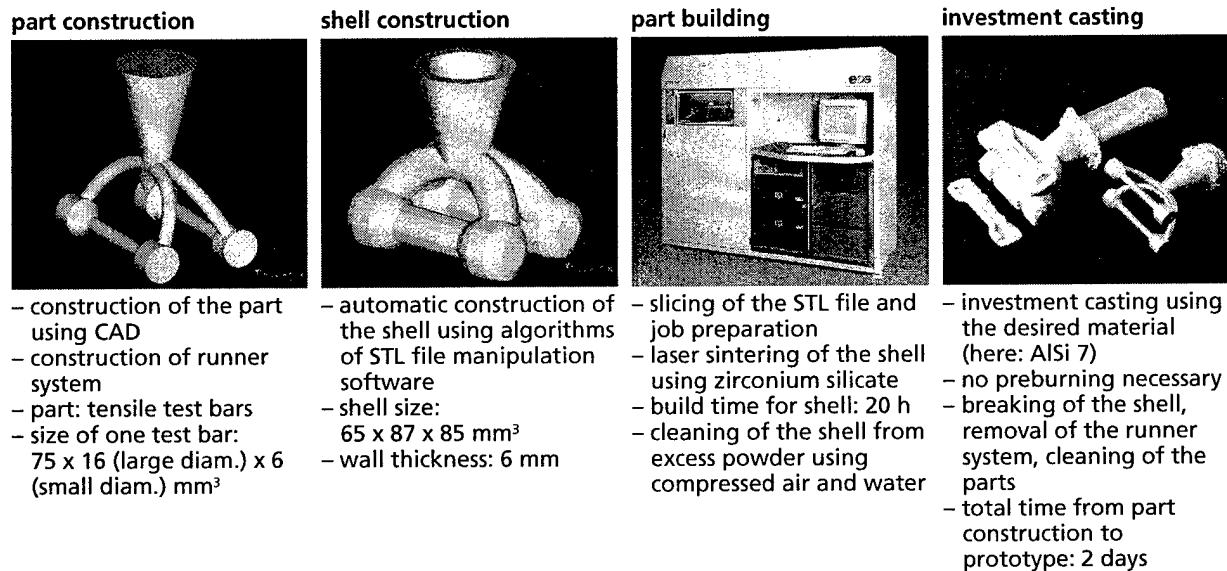


Figure 7 SLS of investment casting shells – rapidly to metal parts

## 5 References

König, W. (1990) *Fertigungsverfahren Band 4, Massivumformung*, VDI-Verlag, Düsseldorf

Jacobs, P.F. (1995) QuickCast 1.1 and Rapid Tooling. *Proceedings of the 4<sup>th</sup> European Conference on Rapid Prototyping and Manufacturing*, Belgirate

Venus, A.D. (1995) Opportunities for Selective Laser Sintering (SLS) in Integrated Rapid Product Development. *Proceedings of the 4<sup>th</sup> European Conference on Rapid Prototyping and Manufacturing*, Belgirate

Cima, M.J., Sachs, E.M. (1991) Three Dimensional Printing: Form, Materials, and Performance. *Solid Freeform Fabrication Symposium*, Austin

Esser, K. (1996) SLS – Selective Laser Sintering. *Intelligente Produktionssysteme – Solid Freeform Manufacturing*, 4. Anwendertagung, Dresden

Langer, H. J. (1996) The Status of Rapid Prototyping in Europe. *International conference on Rapid Product Development*, Stuttgart

Lakshminarayan, U. (1992) *Selective Laser Sintering of Ceramic Materials*, Dissertation, University of Texas at Austin, Austin

Griffin, E. A., McMillin, S. (1995) Selective Laser Sintering and Fused Deposition Modeling Processes for Functional Ceramic Parts. *Solid Freeform Fabrication Symposium*, Austin

Lee, I., Manthiram, A. et al. (1995) Selective Laser Sintering of Alumina-Zinc Borosilicate Glass Composites using Monoclinic  $\text{HfO}_2$  as a Binder. *Solid Freeform Fabrication Symposium*, Austin

Vail, N. K., Barlow, J. W. et al. (1993) Silicon Carbide Preforms for Metal Infiltration by Selective Laser Sintering of Polymer Encapsulated Powders. *Solid Freeform Fabrication Symposium*, Austin

# Development of a Binder Formulation for Fused Deposition of Ceramics

Thomas F. McNulty, Ivan Cornejo, Farhad Mohammadi, Stephen C. Danforth, and Ahmad Safari

Rutgers University  
Department of Ceramic and Materials Engineering  
Piscataway, NJ 08854

## Abstract

A new binder formulation has been developed for Fused Deposition of Ceramics (FDC) which consists of commercially-available polymer constituents. This formulation was used in conjunction with lead zirconate titanate (PZT) and hydroxyapatite (HAp) powders. Adsorption studies were performed to test the effectiveness of several carboxylic acids and alcohols on the dispersion of these powders in the binder system. In both cases, it was found that stearic acid was most effective as a dispersant for the ceramic powder / thermoplastic system. After a suitable dispersant was chosen, ceramic powders were compounded with the binder formulation to yield 55 vol.% ceramic-loaded materials. The resultant compound was used to make filament suitable for use in a modified Stratasys™ 3D-Modeler. The filament was well suited for FDC usage, and the parts made using FDC contained no detectable filament-related defects.

## Introduction

Among the various techniques that have been used for the fabrication of functional quality ceramic components, Fused Deposition of Ceramics (FDC) has shown great promise.<sup>1</sup> In this process, spooled filament with a diameter of 1.75 mm is fed into a heated liquefier via a set of computer-driven counter-rotating rollers. The liquefier motion is computer controlled in the X-Y plane, and material is extruded through a circular nozzle attached to the end of the liquefier. A foam platform moves in the Z direction, allowing material to be deposited layer by layer. The filament, comprised of ceramic particles in appropriate thermoplastic binders, is used for the fabrication of green ceramic components. When ceramic (or metal) powder-loaded filament is fed into the liquefier, the binder softens and melts inside the liquefier, and acts as a carrier for the particles. The cold filament at the top of the liquefier acts as a piston, creating a positive pressure to extrude the molten material out of the liquefier through the nozzle. Components are built layer by layer on the platform, and the bonding between neighboring "roads" or beads of material takes place due the "adhesiveness" of the molten binders, combined with the re-melting of previously deposited layers.

The motivation for this work was to develop a family of thermoplastic binders suitable for the Fused Deposition (FD) of various ceramics and metals using commercially available thermoplastic polymer constituents. Since the compositions of the various binder components are known, specific binder properties can be tailored based on the requirements of the filler phase and the FDC process. Therefore, a detailed understanding of the various polymer ingredients, and their role in the final formulation can be developed. Since the new binder will be a multi-component system, the compatibility of each constituent is critical. In addition to compatibility, it is important

that similar processing exists for each component. This includes factors such as melting temperature, decomposition temperature, and decomposition atmosphere. Finally, the binder must exhibit high strength, high stiffness, low residue after burnout, and a relatively low melt viscosity, particularly when mixed with high solids loadings of ceramic or metal powders (50-65 vol.%).<sup>1</sup>

The quality of the feed filament is one of the most important parameters for successful FDC. The critical properties for high quality filament include viscosity, strength, flexibility, and modulus. In addition to forming the part once deposited, the filament also acts as a piston at the entrance of the liquefier, forcing molten material out of the nozzle. If the filament exhibits a low stiffness or high viscosity, buckling will occur just before the entrance to the liquefier, thus making FDC impossible. Filaments with high melt viscosity require either a very high stiffness, or a relatively high operating temperature to lower the melt viscosity to a useable level. Finally, the temperature dependence of viscosity is also important. A high dependence of viscosity on temperature allows the filament to maintain consistent mechanical properties up to its entry into the liquefier. This combination of properties makes the design of a working filament a challenge, particularly for highly loaded systems.

Although a good binder alone is important, it is not the only requirement for high solids loading of ceramic powder. The degree of dispersion of the powder in the molten thermoplastic binder has a dramatic effect on the rheological properties of resultant FDC filament. In general, the better the powder is dispersed in the polymer medium, the lower the resultant viscosity; and by extension, the higher the usable solids loading for a given viscosity range.

Studies have been made on dispersing Si<sub>3</sub>N<sub>4</sub> in thermoplastic binders for FDC applications<sup>2</sup>. In this case, oleyl alcohol is coated on the powder surface by ball milling in ethanol to provide dispersion for this system. Oleyl alcohol is a C<sub>18</sub> hydrocarbon with an OH functional group. In this case, the OH functional group probably hydrogen bonds

**Table 1: Binder Formulations**

Formulation	Major Binder	Minor Binder	Tackifier	Wax	Plasticizer
ECG 1	100	----	20	15	----
ECG 2	100	----	20	15	5
ECG 3	100	15	20	15	5
ECG 4	70	30	20	15	5
ECG 5	85	15	20	15	5
ECG 6	50	50	20	15	5
ECG 7	100	----	20	15	5
ECG 8	100	----	20	15	5
ECG 9	100	----	20	15	5
ECG 10	100	----	35	15	5

to the powder surface, thus allowing the remainder of the chain to provide steric hindrance to incoming particles. Since the average size, shape, and surface chemistry varies with the type of powder to be used, there is no guarantee that a surfactant suitable for  $\text{Si}_3\text{N}_4$  would be suitable in another powder system. Furthermore, the thermoplastic binder formulation used in this work is different from that of the previous  $\text{Si}_3\text{N}_4$  work.

The adsorption behavior of various hydrocarbons onto powder surfaces have been studied for many years<sup>3,4</sup>. Based on this earlier work, several trends have been established. In general, polar molecules tend to adsorb onto polar powder surfaces, while non-polar molecules tend to adsorb onto non-polar particle surfaces<sup>5</sup>. Oleyl alcohol, like other long-chain alcohols or fatty acids, contains a polar functional group at one end of the chain, and a non-polar hydrocarbon group at the other end. Therefore, these molecules can adsorb onto both non-polar and polar surfaces. A second trend can be seen in the rate at which molecules adsorb into surfaces. Adsorption from solution is strongly dependent on both the concentration of the adsorbing species, and the chemical nature of the medium in which the adsorption takes place. There are situations where the species of interest remains in solution rather than adsorbing onto the powder surface. This occurs when the species is more compatible with the solvent than the powder surface. The concentration of the adsorbing species in solution also plays a critical role.

Since the powders included in this study are oxide ceramics, they have a polar surface. Therefore, we can assume that the polar functional group of the surfactant will adsorb onto the powder surface. In the case of the surfactants tested (oleic acid, oleyl alcohol, stearic acid, and stearyl alcohol), this would be the COOH group of the acids, or the OH group of the alcohols.

The new thermoplastic binder formulation developed for the FDC process is comprised entirely of commercially available polymers, and exhibits properties adequate for usage in combination with lead zirconate titanate (PZT) and hydroxy apatite (HAp) ceramic powder filler. In this paper, the development of high-quality ceramic-loaded feedstock will be outlined. Rheological data from the raw binder will be presented, in addition to thermal and rheological data from a loaded system. Finally, photographs of functional components made using this binder formulation will be presented.

## Experimental

Formulations were batched and prepared using a parts-by-weight measuring system. Table 1 lists the various formulations tested within this system. Each formulation consists of at least one poly-olefin base binder, a hydrocarbon resin tackifier, a polyethylene wax, and a polybutylene plasticizer. The various binders, tackifiers, or waxes tested within this system vary primarily in molecular weight. For convenience, the iterations are labeled ECG-1 through ECG-9. The polymers were mixed at 150-175 °C using a high shear mixer, then de-aired until the entrapped air was removed. Viscosity measurements of the binder formulations were made at 190 °C using a Brookfield RVDV II+ rheometer with a number 27 spindle in conjunction with a Thermocel adapter.

The adsorption of four different surfactants was measured for the PZT and HAp systems. Oleyl alcohol, stearyl alcohol, oleic acid, and stearic acid were tested. Fifty g/l solutions of each surfactant were made by dissolving the appropriate amount of surfactant

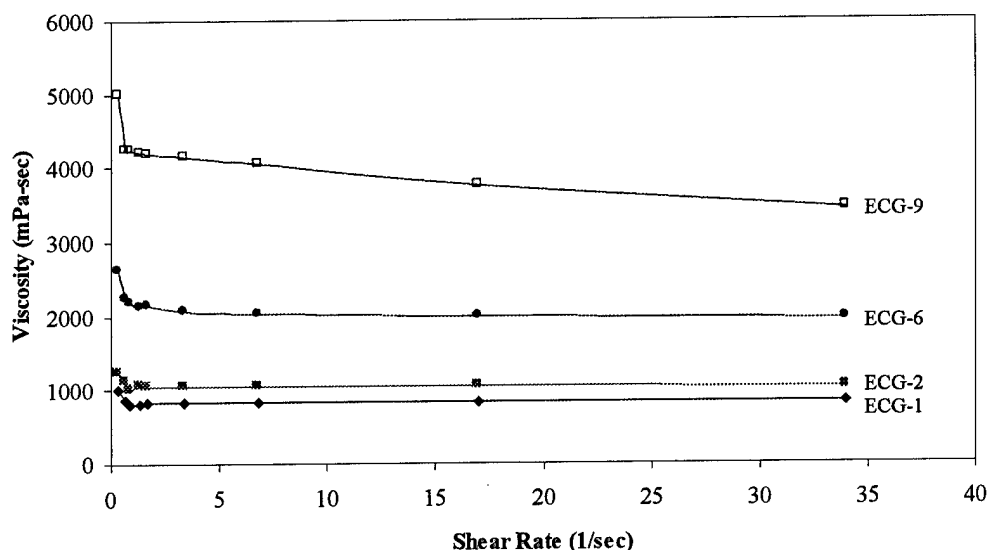


Figure 1: Viscosity vs. shear rate for selected ECG-series binder formulations

in toluene, and TGA analysis was performed to determine the exact concentration of each solution. In the case of PZT, 50 ml of the resultant solution was mixed with 50.0 g of ceramic powder (surface area =  $2.58 \text{ m}^2/\text{g}$ ) for 4 hours. For HAp, 50 ml of the solution was mixed with 10.0 g of ceramic powder (surface area =  $3.40 \text{ m}^2/\text{g}$ ). After mixing, the slurry was centrifuged for 90 min at 1000 rpm to extract the supernatant. TGA analysis was then performed on the supernatants to determine the concentration of surfactant still in solution after milling and centrifugation. Of the four surfactants, the one with the least surfactant remaining in the supernatant was chosen for further studies.

Once the suitable surfactant was chosen, the coated powder was mixed with the optimized binder, and rheological measurements were made. For this portion of the work, 300.0 g of PZT powder was milled for 4 hours with 300.0 ml of the surfactant solution. The slurry was then vacuum filtered to remove the solvent and any excess surfactant. After drying, 245.42 g of the coated powder was mixed with 19.27 g of binder using a Haake System 9000 torque rheometer in conjunction with a 70 cc mixing bowl. This corresponds to 55 vol% solids loading. The powder was added in 4 steps spaced 10 minutes apart, with the initial mixing temperature set at  $160 \text{ }^\circ\text{C}$ . High shear mixing was performed at  $140 \text{ }^\circ\text{C}$  for 20 minutes. Hydroxyapatite / thermoplastic compound was produced in a similar fashion. The viscosity of the PZT / thermoplastic compound was measured using a capillary rheometer. The capillary measured 1.016 mm in inside diameter, and 20.32 mm in length. Shear rates of 2.3 to  $230 \text{ sec}^{-1}$  were measured. Measurements were made at 160, 175, and  $190 \text{ }^\circ\text{C}$ .

The compounded mixtures were test-extruded at 1 mm / minute and a temperature range of 80 to  $95 \text{ }^\circ\text{C}$  into filament 1.75 mm in diameter, cut to lengths of approximately 50 cm. In the case of PZT, the purpose was to test the ability to FDC the compounded mixture. For HAp, this filament would be used as the actual feedstock for part production. Once the filament parameters were optimized, continuous lengths of PZT filament were produced using the Haake System 9000 torque rheometer in conjunction with a single screw extruder. Approximately 100 meters of continuous filament was

extruded and spooled. This filament was used as feedstock to create green ceramic parts with an upgraded Stratasys™ 3-D Modeler™ machine.

Fused deposition was performed with both materials using a liquefier temperature setpoint of 140-146 °C, and a build envelope temperature of 25-35 °C. Parts were made using both 250 and 300 µm nozzles, depending on part specifications. Build time was 1 to 4 hours, depending on the design. Compositions with 55 vol.% ceramic were used to make the trial parts.

Binder burnout (BBO) was performed in both types of samples using a ramp of 10.0 °C/hr to 550 °C, with a 4.0 hr soak at 550 °C. In each case, BBO was performed in air. After BBO, the materials were sintered at 1285 °C for PZT, and 1100 °C for HAp.

## Results and Discussion

Figure 1 shows the viscosity vs. shear rate plots for the binder formulations tested. In each case, the viscosity of the formulations are relatively low, with ECG-9 showing a viscosity approximately 4 times that of ECG-1. Based on viscosity alone, one may conclude that ECG-1 would make the best binder for FDC applications. Instead, ECG-9 was chosen as the binder to be used in future FDC work, primarily due to other factors such as strength and flexibility when mixed in a loaded-system. This point was covered in greater detail in an earlier publication.<sup>6</sup> Figure 2 shows the viscosity vs. shear rate for

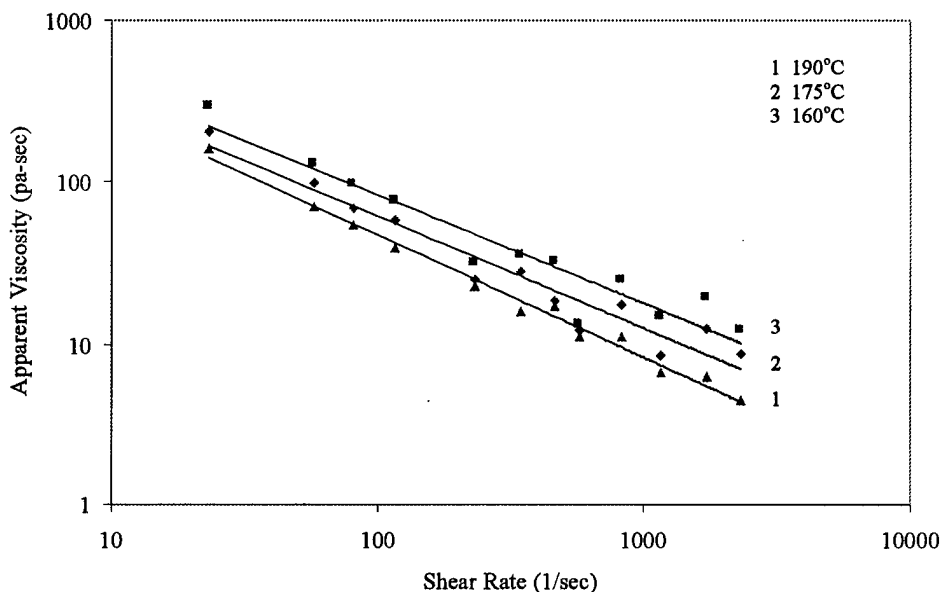


Figure 2: Viscosity vs. shear rate for 55 vol. % PZT / ECG-6 compound

55 vol.% PZT / ECG-6 compounded batch. As expected, the material is pseudoplastic, with the viscosity of the mix remaining below 1000 Pa-s throughout the range of shear rates tested.

Figure 3 shows the thermogravimetric analysis of the supernatant solutions after being mixed with PZT powder for 4 hours. Clearly, stearic acid adsorbed the most onto the powder surface after being mixed with the PZT powder. A total of 8.1 mg/m<sup>2</sup> of

stearic acid adsorbed onto the PZT powder surface from the solution. The data for HAp powder shows similar trends, with stearic acid clearly being the best surfactant of the 4 tested. A total of 26.38 mg/m<sup>2</sup> adsorbed onto the HAp powder surface.

Figure 4 is a thermogravimetric analysis plot of a 55 vol.% PZT / thermoplastic compounded mixture. The solid line denotes the weight % lost as a function of temperature, while the dashed line denotes the slope (ie. rate) of decomposition as a function of temperature. As shown in the plot, the decomposition profile shows a gradual loss of binder with increasing temperature. Of greatest importance is the existence of two

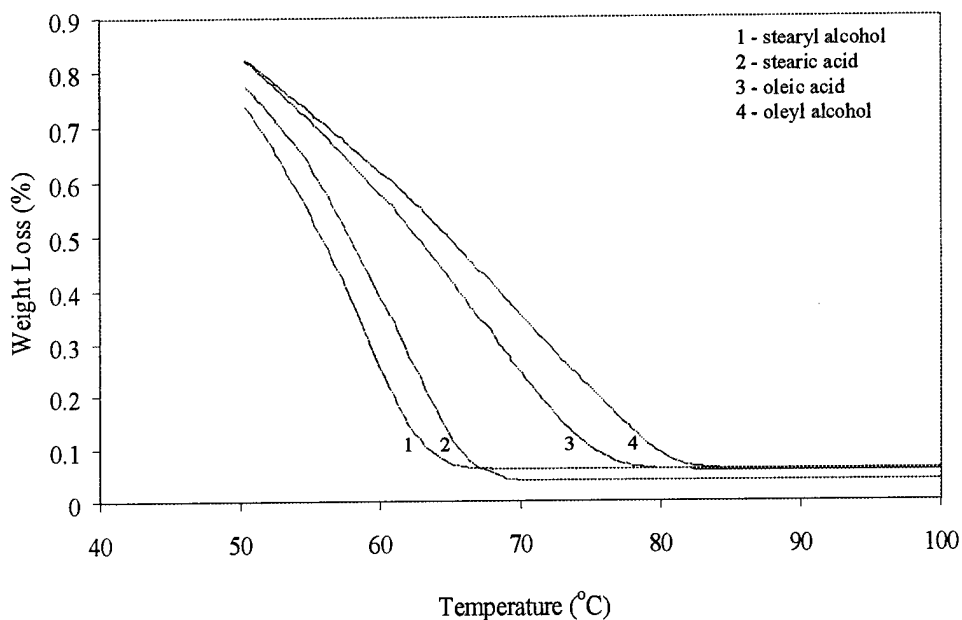


Figure 3: Thermogravimetric analysis of extracted supernatant after mixing with PZT powder

rapid increases in rate of decomposition profile. The smaller first spike, occurring at approximately 360 °C causes open channels to form in the otherwise dense green body. These open channels facilitate removal of the remainder of the binder at approximately 390 °C, without blistering or cracking which could present an obstacle to the successful BBO of complex ceramic bodies.

Using the new binder formulation along with PZT and HAp powder, multiple copies of complex designs have been produced using FDC. Figure 5 shows photographs of two such designs. Figure 5a is a photograph of a PZT ceramic part slated for use in Naval towed arrays. Figure 5b is a photograph of a green and sintered PZT design also for use in Naval towed arrays. In each case, the ceramic phase was sintered to near-theoretical density, and was free of defects resulting from FDC processing. In the case of PZT samples, total firing shrinkage averages 18 % in the radial direction, and 24 % in the z-direction.

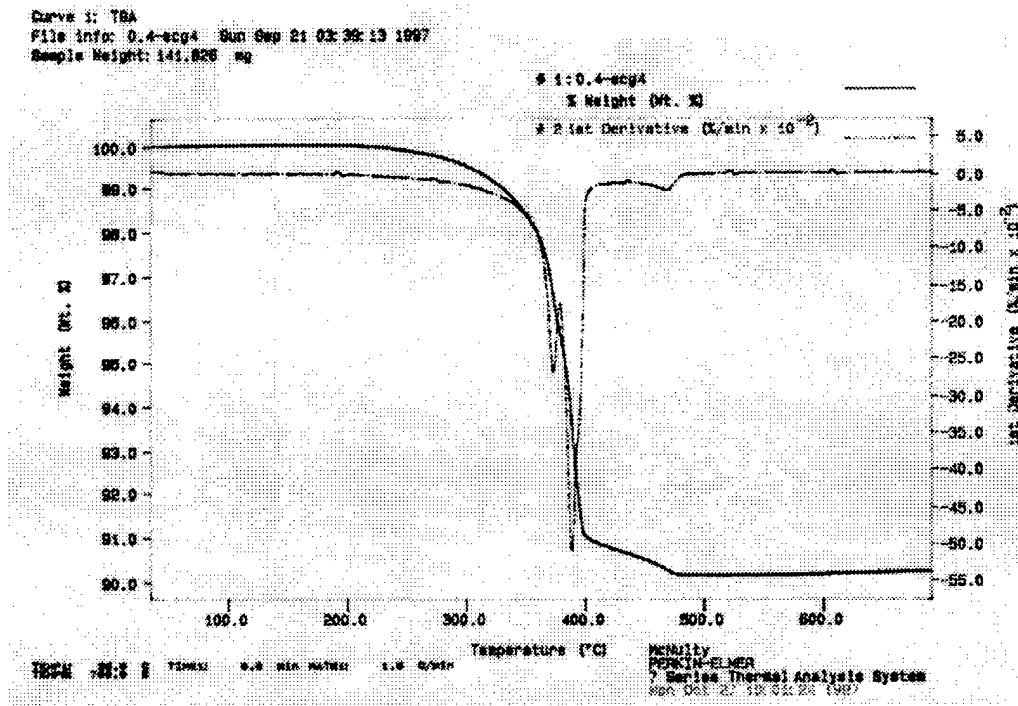


Figure 4: Thermogravimetric analysis of 55 vol.% PZT / thermoplastic compound

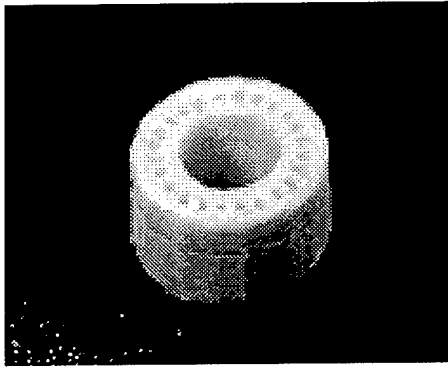
For HAp samples, shrinkage averages 13 % in the radial direction, and 14 % in the z direction.

### Conclusions

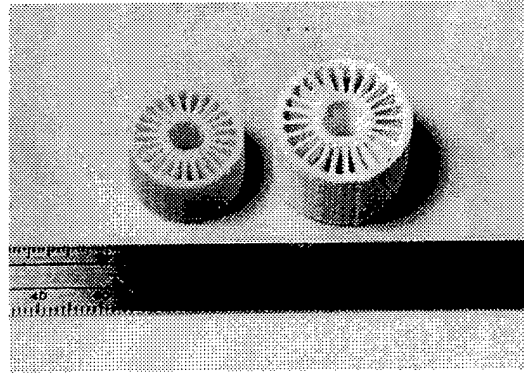
A new binder formulation has been developed for use in Fused Deposition of Ceramics (FDC). This binder formulation consists entirely of commercially available polymers, and exhibits rheological and thermal properties suitable for FDC applications. In addition, stearic acid has been found to provide adequate dispersion for both a lead zirconate titanate-based system and a hydroxyapatite-based system. In both cases, functional ceramic prototypes were manufactured using a Stratasys 3-D Modeler<sup>TM</sup>. Parts made using this new polymer were of high quality, and showed no signs of binder-related flaws after sintering.

### Acknowledgments

This work was made possible by ONR ASSERT grant No. N00014-94-0724. The authors would also like to thank D. Patel, S. Ocasio, A. Michaels, N. Venkataraman, E. Bianchi, S. Lee, T. McCarthy, and G. Lous whose contributions made this work possible.



a



b

Figure 5: a) Photograph of sintered PZT part made via FDC  
 b) Photograph of green and sintered PZT parts made via FDC

### References

1. S. Rangarajan, G. Qi, A. Bandyopadhyay, C. Dai, J. W. Han, P. Bharagava, S. Wu, A. Safari, and S. C. Danforth, "The Role of Materials Processing Variables in FDC Process," Proceedings of the Solid Freeform Fabrication Symposium, Edited by H. L. Marcus, J. J. Beaman, J. W. Barlow, D. Bourell, and R. Crawford, The University of Texas at Austin, Austin, Texas, pp. 431-440, 1997.
2. G. Qi, C. Dai, S. Rangarajan, S. Wu, A. Bandyopadhyay, N. Langarana, A. Safari and S. C. Danforth, "Properties of RU955 Si<sub>3</sub>N<sub>4</sub> Filament for Fused Deposition of Ceramics," Proceedings of the Solid Freeform Fabrication Symposium, Edited by H. L. Marcus, J. J. Beaman, J. W. Barlow, D. L. Bourell and R. H. Crawford, The University of Texas at Austin, Austin, Texas, pp. 421-430, 1997.
3. S. Miller, "Adsorption on Carbon: Solvent Effects on Adsorption," *Environmental Science & Technology*, vol. 14, No. 9, pp. 1037-1049, 1980.
4. T. Allen and R. M. Patel, "The Adsorption of Fatty Acids on Fine Divided Solids Using a Flow Microcalorimeter," *Journal of Colloid and Interface Science*, vol. 35, No. 4, pp. 647-655, 1971.
5. A. W. Adamson, Physical Chemistry of Surfaces, John Wiley and Sons, New York 1990.
6. T.F. McNulty, F. Mohammadi, A. Bandyopadhyay, S.C. Danforth, and A. Safari, "Development of a Binder Formulation for Fused Deposition of Ceramics (FDC)", *Rapid Prototyping Journal*, (In press).

## Materials for Biomedical Applications

N. K. Vail<sup>1</sup>, L. D. Swain<sup>1</sup>, W. C. Fox<sup>1</sup>, T. B. Aufdemorte<sup>2</sup>, G. Lee<sup>3</sup>, and J. W. Barlow<sup>3</sup>

<sup>1</sup> BioMedical Enterprises, Inc  
Texas Research Park  
14785 Omicron Drive, Suite 205  
San Antonio, Texas 78245

<sup>2</sup> Department of Pathology  
The University of Texas Health Science Center at San Antonio  
San Antonio, Texas 78284

<sup>3</sup> Department of Chemical Engineering  
The University of Texas at Austin  
Austin, Texas 78712

### Abstract

This paper discusses two ceramic material systems for selective laser sintering (SLS) that are being developed for biomedical applications for use in repair of bone defects. SLS is the preferred method of fabricating ceramic implants that exhibit well defined porous microstructures. Implants fabricated in this manner have proven effective *in-vivo* showing excellent biocompatibility as well as considerable osseous integration and remodeling of the implant material. (**Keywords** : selective laser sintering, porous, ceramic implant, biocompatible)

### Introduction

Selective laser sintering (SLS) is one of the few rapid prototyping (RP) technologies that can fabricate complex objects from a wide variety of materials, including ceramics and metals. This makes SLS, and other capable processes, very attractive to manufacturers with needs for custom parts in novel materials. Historically, RP has been most accepted by large volume manufacturers requiring low volume prototypes in non-production and production materials. However, as RP has gained acceptance and evolved to offer greater accuracy and access to engineering materials, it has become attractive to low volume manufacturers who can benefit from fabrication in production materials.

The medical field is a specific example of low volume manufacturing. This area has seen limited use of RP, primarily as a means of guiding surgical procedures using tactile models derived from patient computed tomography (CT) data. In a classical RP application, James, *et al.*,<sup>1</sup> used stereolithography (SLA) models to plan the surgical correction of a facial defect. Others have utilized tooling capabilities of RP to provide solutions to specific patient defects. Holle *et al.*,<sup>2</sup> discuss the use of an SLA model to plan surgical shaping and attachment of autograft implants. Erickson, *et al.*,<sup>3</sup> cast custom titanium orbital implants. However, these latter two examples have notable drawbacks related to either multistep manufacturing processes or multistep surgical procedures. Direct fabrication of custom anatomical implants offers

streamlined manufacturing and provides a more simple surgical implementation. This paper discusses on going work to commercialize RP fabrication of custom anatomical implants for bone defect repair.

### Ceramic Implants

Repair of skeletal defects is limited to commodity devices, formable pastes, and surgically sculpted grafts. Custom anatomical implants show promise to provide improved osseous defect repair modalities. Such implants would be designed and optimized for a target defect using anatomical information and surgeon input, fabricated from an appropriate material exhibiting desired properties, and then implanted to effect repair and to restore form and function. 3D implant models would be derived with the aid of CAD and measurement data such as tactile, optical, or medical imaging techniques.<sup>4</sup> The combination of RP fabrication technologies and 3D implant models makes available for the first time the capability to fabricate custom anatomical implants from novel biocompatible materials. The ability to form strong, complex ceramic implants would alleviate existing problems with current materials and would open a new realm in osseous defect treatments.

In the present work, porous ceramic implants are fabricated using the established SLS based method illustrated in Figure 1.<sup>5,6</sup> This method uses conventional SLS technology to readily fabricate objects from polymer based materials. A substrate material, such as a ceramic powder, is combined with a polymeric binder that serves to bind the substrate particles during SLS processing into a contiguous object. The resulting “green” part is then subjected to post-processing techniques to thermally debind the green object and to impart strength to the bisque shape. The binder is combined with the substrate material by one of two methods: either simple mixing or encapsulation. Both methods have been used and offer distinct advantages in certain applications. However, the encapsulation method provides a clear advantage with respect to minimizing binder requirements, offering improved green part strength, and providing compositional control. Due to the porous nature of SLS parts, post-processing can include steps to introduce additional materials into the green part that serve to alter material composition as well as help to control part stability.

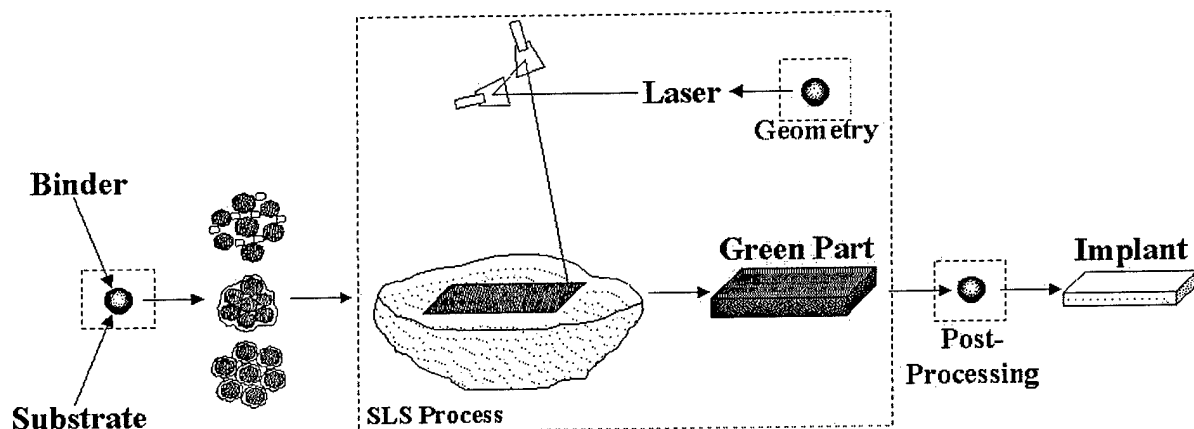


Figure 1. Fabrication of ceramic implants using indirect SLS technology.

### Calcium Phosphate Materials

Fabrication of calcium phosphate ceramic implants and preliminary biocompatibility results *in-vivo* have been discussed in previous work.<sup>7</sup> This benchtop process is currently being

commercialized to offer custom and commodity type implants as treatment modalities for bone defects resulting from trauma and disease. Present work is focused on materials formulation, implant properties quantification, and overall fabrication process control.

As noted above, SLS is used to create green ceramic implants. Feedstocks for SLS consist of polymer coated substrate ceramic particles. Current materials formulation uses fluidized bed coating, which yields discrete encapsulated particles with known polymer coating composition and is suitable for a broad range of particle sizes.

Two standard calcium phosphate substrate powder fractions, +45-63 $\mu\text{m}$  and +106-125 $\mu\text{m}$ , were encapsulated via fluidized bed processing using a latex based polymer.<sup>8</sup> Separate batches were prepared with different polymer contents in the range 10-40 vol. % (4-20 wt. %). Thermogravimetric analysis indicated polymer coating yields were greater than 90%. Particle size distribution analysis indicated the fluidized bed coating reduced the amount of fines present in the substrate material, probably either by material loss or by particle agglomeration (Figure 2). Agglomerated particles were prevalent in the smaller powder fraction as viewed by scanning electron microscopy (SEM). The particle size distributions suggested the majority of particles are uniformly coated since the distribution forms changed little and are uniformly shifted to larger particle sizes with increased polymer coating. There was little broadening of the distribution, suggesting little agglomeration of larger particles and no occurrence of polymer fines due to coating inefficiencies or interparticle abrasion.

SLS processing conditions were determined with a +106-125 $\mu\text{m}$  powder containing 20 vol. % (8.7 wt. %) polymer coating. Two sets of three point bend specimens 1in. x 3in. x 0.25in. were fabricated in different orientations. The first set was oriented with the long specimen axis parallel to the laser fast axis and the second set was oriented with the long specimen axis perpendicular to the laser fast axis. Each set was fabricated using applied energy densities 0.5-3.0cal/cm<sup>2</sup>, where the applied energy density is defined as<sup>9</sup>

$$\frac{37.05P}{bs * scsp} [=] \frac{\text{cal}}{\text{cm}^2} \quad \text{Eq. 1}$$

with  $P$  the laser power in watts,  $bs$  the scan speed in inches per second, and  $scsp$  the scan vector spacing in mils. Green strength analysis showed a linear strength increase with increasing applied energy density. Maximum strength was about 200psi (1.4MPa), although no plateau or decrease in strength was observed over the parameter range. As expected, specimens scanned with the long axis perpendicular to the laser fast axis showed a steeper strength development than the other sample set. This phenomena has been shown to be a result of differences in the average temperature of the scanned area.<sup>5</sup>

SLS shrinkage factors were determined using three-point bend specimens ranging in size from 0.25in. x 1.0in. x 0.125in. to 1.0in. x 3.0in. x 0.25in. Two sets, oriented orthogonal, were fabricated using a constant applied energy density of 2.0cal/cm<sup>2</sup>. Figure 3 shows shrinkages in the  $x$ - and  $y$ -directions to be similar at about 0.5%. However, laser beam size compensation is

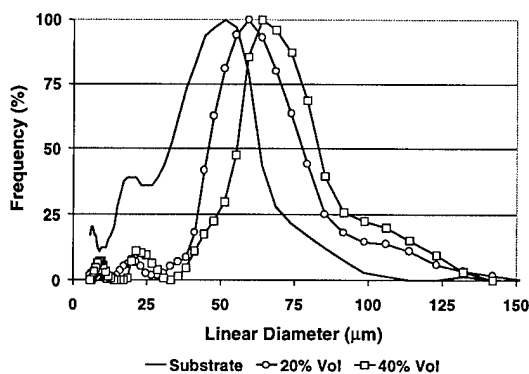
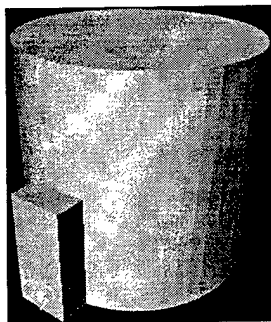


Figure 2. Particle size distributions for +45-63 $\mu\text{m}$  uncoated and coated calcium phosphate powders.

greater in the *x*-direction than in the *y*-direction (0.28mm vs. 0.15mm). The reason for this is not immediately clear, although the results are repeatable. Shrinkage and beam compensation do not vary significantly ( $p=0.01$ ) for similar specimens scanned with different applied energy densities. Verification of the process scaling parameters yielded parts with average nominal deviations of  $-0.06\pm 0.09$ mm, consistent with the material particle size.

In previous work, SLS green parts were post-processed using a sequence of infiltration, drying, and firing steps. Infiltrating solutions comprised of various compositions of calcium and phosphorous served to cement the particles and to alter the composition of the calcium phosphate material. Typical post-processing involved 3-4 infiltration steps to obtain a desired calcium phosphate composition, requiring 10-14 days of processing. In practice, implant delivery time is targeted for less than one week, and ideally 3-4 days once an implant design as been validated. Consequently, the post-processing has been refined and currently involves two infiltration/firing steps to obtain implants of a specific calcium phosphate composition and strength. To date, only the first infiltration step has been fully quantified.



**Figure 4.** Compression test specimen. Dimensions: 0.3in. x 0.3in.

Cylindrical compression test specimens were fabricated via SLS using an optimal applied energy density of  $2.0\text{cal/cm}^2$  (Figure 4). These specimens incorporated measurement markers to reduce data acquisition variation. The green specimens had a compression strength of about 400psi (2.8MPa). Polymer content of the samples was determined thermogravimetrically to be 8.10 wt. % (18.6 vol. %).

Green test specimens were infiltrated with a 50/50 w/w aqueous methanol solution that contained 6-16wt. %  $\text{P}_2\text{O}_5$ . Liquid uptake analysis indicated the specimens had a porosity of  $48\pm 1\%$ . The infiltrated specimens were dried 8hrs at  $25^\circ\text{C}$  and 75% R.H. At this point, liquid mass loss was  $\sim 90\%$  of theoretical. The specimens were further dried at  $40^\circ\text{C}$  and 50% R.H. for two hours. Measured liquid loss was  $96.3\pm 0.2\%$  of theoretical.

The dried specimens were fired in air at  $800^\circ\text{C}$  for 1 hour. The heat ramp consisted of  $5^\circ\text{C}/\text{min}$  ramp to  $400^\circ\text{C}$  and a hold of 1 hour, followed by a  $2^\circ\text{C}/\text{min}$  ramp to the sintering temperature, followed by  $5^\circ\text{C}/\text{min}$  ramp to ambient temperature. Material balances indicated the mass change to be  $4.6\pm 2.5\%$  of theoretical.

Figures 5 and 6 show results for dimensional shrinkage and compressive strength, respectively. Shrinkage is anisotropic in the *z*-direction and typically twice the shrinkage in the *xy*-plane. Strength increases with increased solids in the infiltrating solution suggesting a dependence on the final part density. In addition to a density increase, the infiltrating solution alters the calcium phosphate composition, effectively lowering the CaO to  $\text{P}_2\text{O}_5$  ratio thereby reducing the melting point.<sup>10</sup> Localized melting point depression probably induces liquid phase sintering and increases shrinkage of the part. The median composition infiltrating solution (12 wt. %  $\text{P}_2\text{O}_5$ ) was chosen for the first infiltration step due to its moderate shrinkage and good

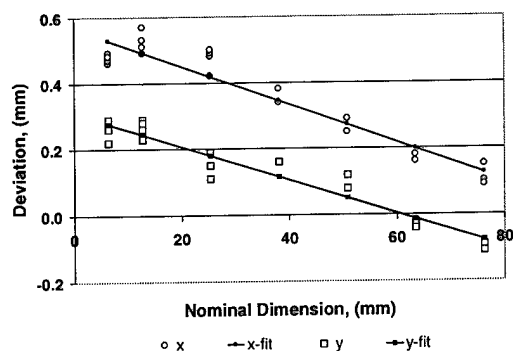


**Figure 3.** Shrinkage calibration for +106-125 $\mu\text{m}$  polymer coated calcium phosphate powder.

mechanical properties. These materials showed shrinkages of  $1.4 \pm 0.2\%$  in the  $xy$ -plane and  $2.7 \pm 0.4\%$  in the  $z$ -direction. Compressive strengths were  $5220 \pm 1090$ psi ( $36.0 \pm 7.5$ MPa) with a modulus of  $26000 \pm 6400$ psi ( $179.0 \pm 44.1$ MPa), suitable for low load applications.

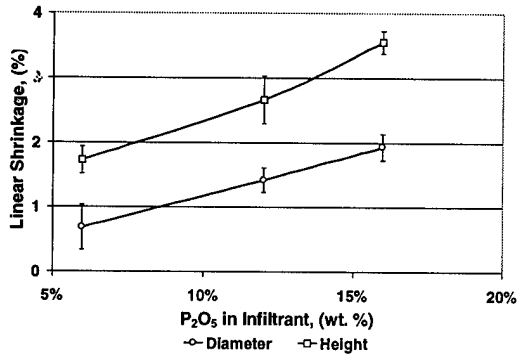


**Figure 5.** Shrinkage in the  $xy$ -plane and  $z$ -direction as a function of infiltrating solution composition for the first infiltration step in post-processing +106-125 $\mu$ m calcium phosphate SLS green parts. One hour at 800°C.

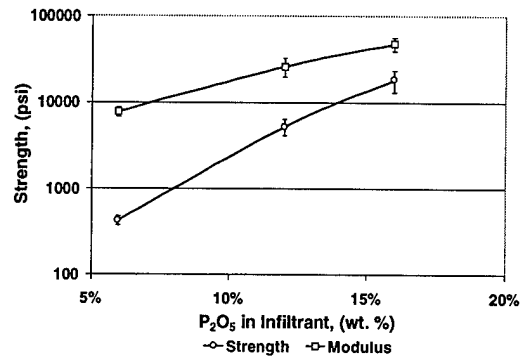


**Figure 6.** Strength and modulus as a function of infiltrating solution composition for the first infiltration step in post-processing +106-125 $\mu$ m calcium phosphate SLS green parts. One hour at 800°C.

Previous reports on this material system discussed the start of pre-clinical trials to assess the biocompatibility and efficacy of SLS formed calcium phosphate implants surgically placed in an alveolar ridge defect in canines.<sup>6</sup> Figure 7 shows the implant geometry used in these trials. Radiographic analysis showed the implants to be infiltrated with new bone (Figure 8). Some implant degradation was noted as changes in implant contour. The material showed a high degree of biocompatibility and mature mineralized bone was present throughout the implants, especially in the macropores (Figure 9).

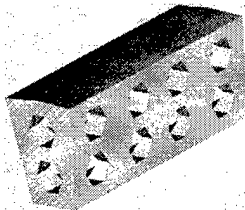


**Figure 7.** Implant model. Macropores are ~2mm in diameter. Dimensions: 3.3x6.6x15.3mm<sup>3</sup>.

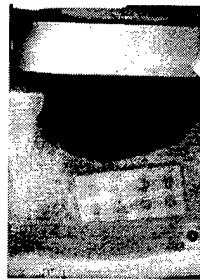


**Figure 8.** Radiograph of SLS formed implant *in-vivo*, at three months. Bone fills the macropores and covers the implant.

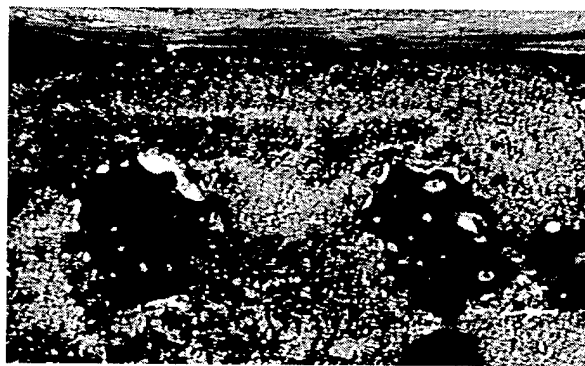


**Figure 9.** Histologic section showing new bone infiltration of macropores and microporous structure.

### Calcium Carbonate Materials

Natural calcium carbonate materials derived from marine corals have a history of use as osteoconductive scaffolds in bone defect repair.<sup>11</sup> These materials have two primary advantages in biomedical applications: 1) excellent biocompatibility, and 2) inherent microstructures very similar to natural bone (*i.e.* high porosity, well defined pore structures). Commercialized materials are either coarse granules or machined regular geometric shapes. Some materials have portions of the coral structure converted to hydroxyapatite. Machined shapes are brittle and, generally, are sculpted by the surgeon at the surgical site to fit the target defect. However,

failure to achieve close apposition to bone can lead to fibrous encapsulation and nonunion.<sup>12</sup> Hence, there is a need to examine alternative methods of forming site specific, strong coralline calcium carbonates that would facilitate their immediate use in osseous defect repair.

Coral (*pavona clavus*) was obtained in bulk from Tideline, Inc (Figure 10). Mercury intrusion porosimetry showed a narrow pore size distribution with a mean of about 100 $\mu$ m. The raw coral was broken into chunks, washed in a 5 wt. % Clorox solution followed by a water wash, then dried to constant weight. The cleaned material was crushed to powder and characterized by sieving. A single fraction +106-125 $\mu$ m was prepared. The mean particle diameter was 143.3 $\pm$ 35.5 $\mu$ m. X-ray diffraction (XRD) showed the coral to be aragonite, which, as confirmed by differential scanning calorimetry (DSC), is irreversibly converted to calcite on heating to 300 $^{\circ}$ C. A powder sample was polymer encapsulated via fluidized bed coating. Thermogravimetric analysis indicated a polymer content of 4.34 wt. % (9.98 vol. %). Mechanical strength specimens (1in. x 3in. x 0.25in. and 0.3in. dia. x 0.3in.) were molded from the encapsulated powder. Three point bend analysis showed a modulus of rupture (MOR) of 179 $\pm$ 42 psi (1.2 $\pm$ 0.3MPa). Compressive strength analysis showed 225 $\pm$ 28psi (1.6 $\pm$ 0.2MPa). Molded specimens had a mean density of 1.32 $\pm$ 0.03 g/cm<sup>3</sup> or an equivalent porosity of 52% assuming a theoretical density of 2.75 g/cm<sup>3</sup> for the composite encapsulated material.

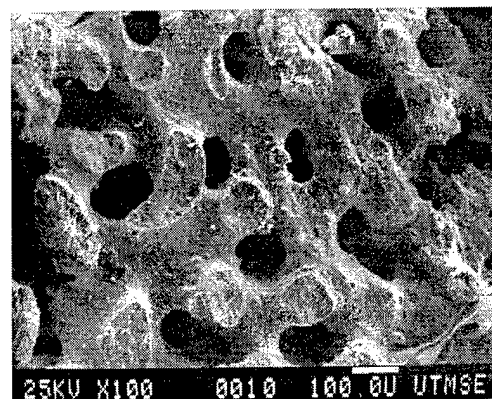
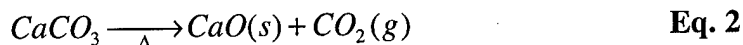


Figure 10. Microstructure of *pavona porites* coral at fracture surface.

To fabricate coralline calcium carbonate implants using the fabrication method of Figure 1, green parts must go through a post-processing step to remove the polymer binder and to impart strength. As with the calcium phosphate implants discussed above, infiltration is used to deposit material into the structure to control shrinkage and to bind the structure. However, the part must still go through a heat treatment cycle.

Calcium carbonate decomposes according to the following reaction:



Thermogravimetric analysis showed the conversion to calcium oxide becomes significant at about 600 $^{\circ}$ C under normal atmospheric conditions. Therefore, it is possible to remove the polymer binder using typical debind procedures. However, sintering above 600 $^{\circ}$ C in a controlled atmosphere may still be involved to achieve strong parts. Thermodynamic analysis of Eq. 2 shows the equilibrium CO<sub>2</sub> partial pressure approaches 1atm near 900 $^{\circ}$ C.

Ultrafine precipitated calcium carbonate (PCC) was used as an infiltrating material (OMYA, Inc., Proctor, VT). This material is a concentrated aqueous slurry (76.4 wt. % solids) and has a median particle size of 0.48 $\pm$ 0.19 $\mu$ m. The slurry was diluted to 20 wt. % solids with 1 wt. % aqueous sodium dodecyl sulfate (Aldrich) and used to infiltrate molded compression test specimens. The specimens were saturated, weighed, and dried at ambient conditions. Comparison of porosity calculations of the infiltrated specimens to measurements of control specimens indicated complete saturation. There was no indication of PCC deposit on part surfaces.

Dried specimens were divided into three groups. The first group was tested immediately for compressive strength. The second group was subjected to a polymer debind step conducted in air at 450°C for 30 minutes. The specimens were weighed and tested for compressive strength. The last group was subjected to the same debind step as the second group but with a continuous CO<sub>2</sub> purge of 225cc/min. Following the 30 minute debind step, the samples were heated to 900°C at 5°C/min, held for two hours, then allowed to cool to room temperature. The specimens were weighed and tested for compressive strength.

Figure 11 shows the compressive strengths of all groups compared to the compressive strength of the initial green parts. The compressive strength of the infiltrated and dried specimens is about 2.5 times greater than the original green compressive strength. This probably reflects the part density increase of ~14%. The compressive strength is decreased more than a factor of three following the polymer debind step. This is as expected due both to loss of the actual system binder and to the subsequent decrease in density. However, it is most interesting to note the increase in strength of the parts following heat treatment at 900°C. There is a three fold increase in compressive strength that strongly suggests an increased physical interlocking of the calcium carbonate particle network. Median strength was 460±50psi (3.2±0.2Mpa), which compares favorably with reported strengths for commercial coral implants (626±350psi).<sup>13</sup> SEM clearly shows particle bridging, although the discrete calcium carbonate particles are still discernable (Figure 12). Grain coarsening is also evident, which suggests refinement of the heat treatment could improve mechanical strength. Porosity is still present and porosimetry indicated a median pore diameter of 30-40µm. XRD showed the parts to be pure calcite.

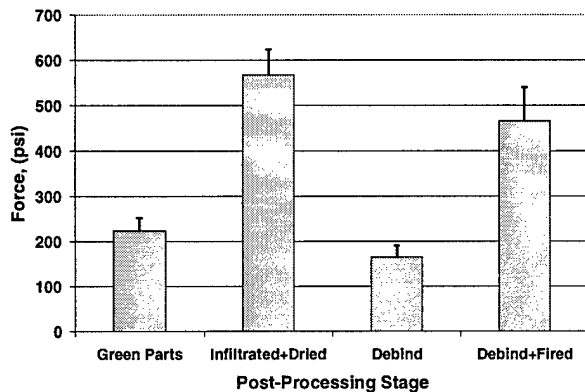


**Figure 11.** Comparison of compressive strengths of coralline calcium carbonate specimens at each step in the post-processing cycle.

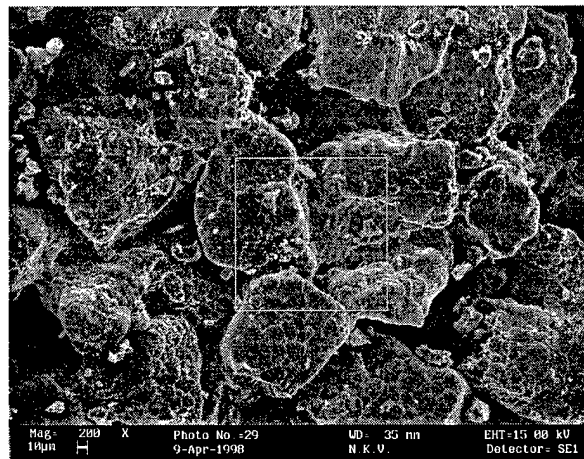


**Figure 12.** Fracture surface of completely post-processed coralline calcium carbonate part infiltrated with PCC

### Summary

Two ceramic material systems suitable for the fabrication of custom synthetic bone implants were presented. The first material system, comprised of calcium phosphate, has shown tremendous promise as an implant material. This material can be reproducibly processed to yield accurate parts with structures and strengths similar to natural bone. Work is continuing to refine the fabrication process and to more effectively control pore size of the final implant. Pre-clinical trials with SLS formed implants are very encouraging. Additional trials to demonstrate anatomical implants are planned precursory to clinical trials in humans.

The second material, comprised of coralline calcium carbonate, also shows promise as an implant material. Further work is required to refine the post-processing of this material to produce strong parts with controlled pore size. Pre-clinical trials to assess the biocompatibility and efficacy of SLS fabricated coralline calcium carbonate implants are planned.

### Acknowledgements

Portions of this work were supported under DoD STTR grants F41624-95-C-2008 and F41624-97-C-2000 and NIH SBIR grant 1-R43-DE-11749-01. The authors wish to thank Nicole Harlan of UT-Austin for assistance in preparing sintered calcium carbonate samples.

### References

- 1 James, W.J., M.A. Slabbekoorn, W.A. Edgin, and C.K. Hardin, "Correction of Congenital Malar Hypoplasia Using Stereolithography for Presurgical Planning," *J. Oral Maxillofac. Surg.*, **56**, 512-517, 1998.
- 2 Holle, J., K. Vinzenz, E. Würinger, K.-J. Kulenkampff, and M. Saidi, "The Prefabricated Combined Scapula Flap for Bony and Soft-Tissue Reconstruction in Maxillofacial Defects – A New Method", *Plastic and Reconstructive Surgery*, **98** [3], 542-552 (1996).
- 3 Erickson, D., Lt. Col., D.D.S., M.S., MacKown Dental Laboratory, Lackland Air Force Base, San Antonio, Texas, *personal communication*, 1997.
- 4 Vail, N.K., W. Wilke, H. Bieder, and G. Jünemann, in Marcus, H.L., *et al.* (Eds), "Interfacing reverse engineering data to rapid prototyping," in Marcus, *et al.* (Eds), *Solid Freeform Fabrication Symposium Proceedings*, **7**, 481-490, 1996.
- 5 Vail, N.K., Preparation and characterization of microencapsulated, finely divided ceramic materials for selective laser sintering, Ph.D. Dissertation, The University of Texas at Austin, 1994.
- 6 Balasubramanian, B., Study of the selective laser sintering of metal-polymer powders, Ph.D. Dissertation, The University of Texas at Austin, 1995.
- 7 Lee, G., W.C. Fox, T.B. Aufdemorte, and J.W. Barlow, "Biocompatibility of SLS-Formed Calcium Phosphate Implants", in Marcus, H.L., *et al.* (Eds), *Solid Freeform Fabrication Symposium Proceedings*, **7**, 15-21, 1996.
- 8 Vail, N.K., J.J. Beaman, D.L. Bourell, H.L. Marcus, and J.W. Barlow, "Development of a Poly(Methyl Methacrylate-co-n-Butyl Methacrylate) Copolymer Binder System, *J. Appl. Poly. Sci.*, **52**, 789-812, 1994.
- 9 Nelson, J.C., Selective Laser Sintering: A Definition of the Process and an Empirical Sintering Model, Ph.D. Dissertation, The University of Texas at Austin, 1992.
- 10 Faust, G.T., W.L. Hill, and D.S. Reynolds, "The Binary System  $P_2O_5-2CaO \cdot P_2O_5$ ," *Am. J. of Sci.*, **242**, 447-477, 1944.
- 11 Papacharalambous, S. and K. Anastasoff, "Natural coral skeleton used as onlay graft for contour augmentation of the face," *Int. J. Oral Maxillo. Surg.*, **22**, 260-269, 1993.
- 12 Holmes, R. and H. Hagler, "Porous hydroxyapatite as a bone graft substitute," *J. Oral Maxillo. Surg.*, **45**, 421-429, 1987.
- 13 White, E. and E.C. Shors, "Biomaterial Aspects of Interpore-200 Porous Hydroxyapatite," *Dental Clinics of N. Am.*, **30**, 49-67, 1986.

# PROCESSING OF BIOCERAMIC IMPLANTS VIA FUSED DEPOSITION PROCESS

Susmita Bose, Marisol Avila and Amit Bandyopadhyay

School of Mechanical and Materials Engineering  
Washington State University  
Pullman, WA 99164-2920

## Abstract

Porous ceramic structures have long been a subject of investigation as bone substitute. Most of these porous structures are typically made by techniques that result randomly arranged pores with a wide variety of pore sizes. In recent years, SFF methods are being used for the fabrication of porous bioceramic implants. Porous ceramic structures have been fabricated using indirect route where a polymeric mold is first created via fused deposition process. The mold was then infiltrated with ceramic slurry, dried and then subjected to a binder burn out and sintering cycle. In this paper, processing of 3D honeycomb porous alumina ceramic structures and some initial mechanical properties for bone implants will be discussed.

## Introduction

Development of specially designed ceramics and composites for the repair and reconstruction of diseased or damaged parts of the human body have been revolutionized the quality of human life during last five decades [1-5]. A number of different materials have been utilized for these purposes in various forms including collagen, metals, metal alloys, ceramics, glasses, carbon based materials and composites of the above materials. Among them, ceramic based materials are considered the most suitable artificial graft material [6]. The ceramic materials that are used for these purposes are called *bioceramics*. These bioceramic materials may be inert in nature (such as alumina, zirconia, titania), bioactive (such as hydroxyapatite, bioactive glasses or bioactive glass-ceramics) or resorbable (such as tricalcium phosphate, calcium phosphate salts). Bioceramic implants can again be classified into two categories including dense bioceramics and microporous bioceramics [1]. The potential for ceramics as biomaterials relies upon their compatibility with the physiological environment. Bioceramics are compatible because they are composed of ions commonly found in physiological environment and of ions showing limited toxicity to body tissues. Moreover, these materials are resistant to microbial attack, pH changes and solvent conditions and stable with temperature changes [7]. Applications of bioceramic materials include restoration of material in dentistry, spinal fusion, bone filling, maxillofacial reconstruction and hip, knee or other bone replacements.

Among the various bone substitutes that are currently being used that include: (1) autograft (bone from the another location from the body of the same person), (2) allograft (human bone from dead body), (3) xenograft (animal bone) and (4) bioceramic implant (artificial bone). Though autograft is probably the most suitable one, but it requires at least two operations and often causes problems with patient body from where the bone is taken (commonly hip or rib). In both, allograft and xenograft, rejection by the patient body and diseases transmitted by the foreign bone are of serious concern for their applicability. Naturally, applications of artificial

implants are becoming more and more popular. The increasing demand for bioceramic implants is evident from the growth of this field. In 1997, total estimated business was over \$50M and the projected sales for these implants for the year 2004 is over \$150M.

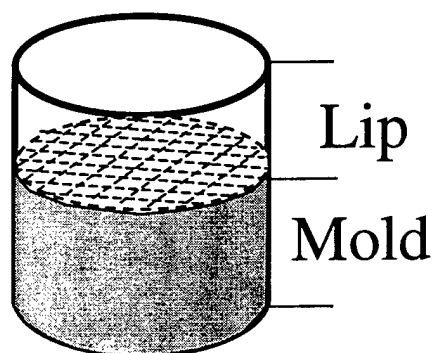
In recent years, rapid prototyping (RP) or solid freeform fabrication (SFF) techniques have shown potential for the fabrication of controlled porosity bioceramic implants. Selective laser sintering (SLS) [8-9], 3-D printing [10-11], stereolithography [12], ceramic filled stereolithography [13] and fused deposition (FDM) [14] processes have already been utilized to demonstrate the feasibility of processing controlled porosity ceramic implants for biomedical applications. In this work, polymeric molds were fabricated using an FDM 1650. Molds were infiltrated with alumina ceramic slurry, dried and then subjected to a binder burn out and sintering cycle. Processing and initial mechanical characterization of 3D honeycomb porous alumina ceramic preforms are described in this paper.

### Processing

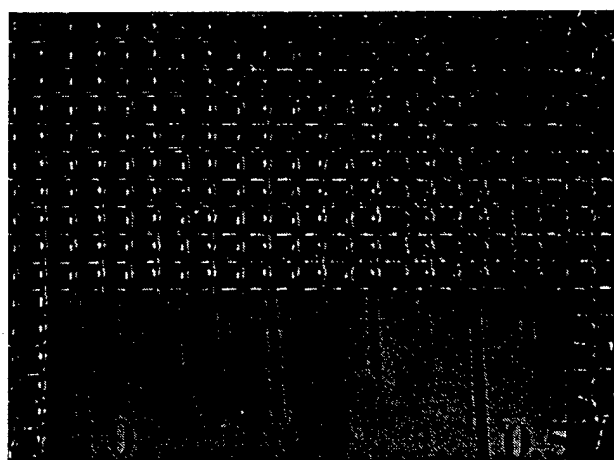
Processing of porous 3D honeycomb alumina ceramic preforms consists of three different types of development and optimization work. They are: (1) mold design, (2) development of ceramic slurry composition and (3) binder burn out and sintering cycle development for green ceramic structures.

#### Mold Design

Molds were designed and fabricated by FDM 1650 using ICW-06 filament material. Initially, 1" tall and 1" diameter cylindrical molds were designed and fabricated with a (45/-45) raster filling and varying the raster gap from 0.010 to 0.030". Top 0.3" of the mold had only perimeter but no raster filling, which is also called lip, to hold excess ceramic slurry during infiltration. Bottom four layers of the mold had no raster gap to avoid leaking of slurry during infiltration. Road width was varied from 0.015 to 0.025". Combination of raster gaps and road width control the volume fraction of ceramics and its pore sizes in the preform. Figure 1a and b show the schematic of mold design and top view of a polymeric mold.



(a)

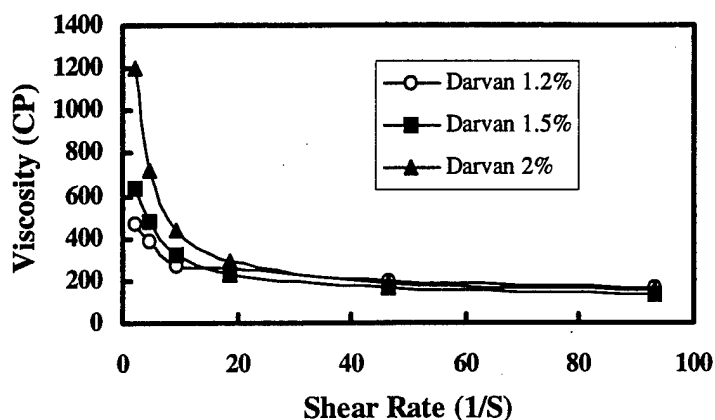


(b)

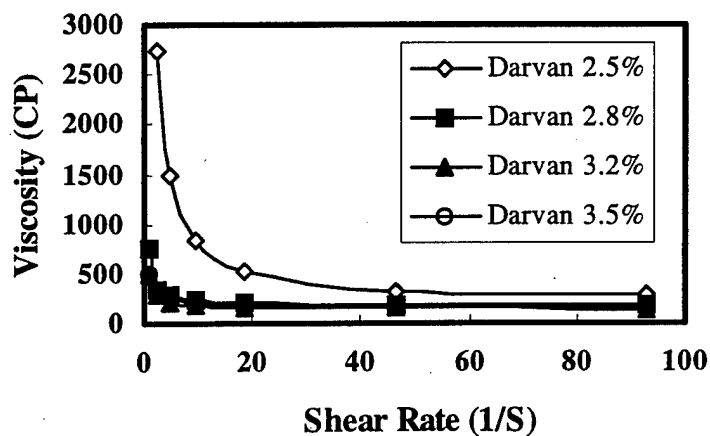
**Figure 1:** (a) Schematic presentation of polymeric mold design. (b) Optical image of the top view of a polymeric mold made by FDM 1650 using ICW06 material (scale 0 - 0.5").

### Development of Ceramic Slurry Composition

Development of ceramic slurry work started with different commercially available alumina powders. Finally most of the work has been performed with 10D and 30D alumina powders doped with 500 ppm of MgO from Baikowski International Corporation, N.C. Both 10D and 30D powders have submicron size particles (Sedigraph  $d_{50}$  for 10D =  $0.45 \mu\text{m}$  and for 30D =  $0.41 \mu\text{m}$ ), but specific surface area for 30D powder is  $26.6 \text{ m}^2/\text{gm}$  compared to  $8.6 \text{ m}^2/\text{gm}$  for 10D. High surface area of the 30D powder is also evident from higher slurry



(a)



(b)

**Figure 2:** Effect of dispersant amount on the viscosity of ceramic slurry with (a) 10D and (b) 30D powders.

viscosity compared to 10D powder at similar solids loading. Brookfield Viscometer was used to determine the optimum wt% of dispersant needed for the preparation of water based ceramic slurry by measuring the viscosity at different shear rates for each solution. 1-Butanol (Fisher Scientific) was used as an antifoaming agent for this ceramic slurry. Darvan 821 (R.T. Vanderbilt & Co., Norwalk, CT) was used as a dispersant. For the 10D alumina powder, 1.5

wt% darvan was found to be optimum and beyond that it increased the viscosity of the slurry a little bit. Whereas for the 30D alumina powder the optimum dispersant amount was 3 wt%. The viscosity vs. shear rate plots at different dispersant wt% for both the powders are shown in Figures 2a and b.

Viscosity of 10D and 30D ceramic slurry compositions at a fixed shear rate of 46 (1/S) were measured with increasing solid loading. The wt% of antifoaming agent and dispersant in the slurry were kept constant. Figure 3 shows the plot of viscosity vs. solids loading for both the powders. For the 10D powder, up to 63 wt% solid loading could be achieved, but for the 30D powder it was only 55 wt%.

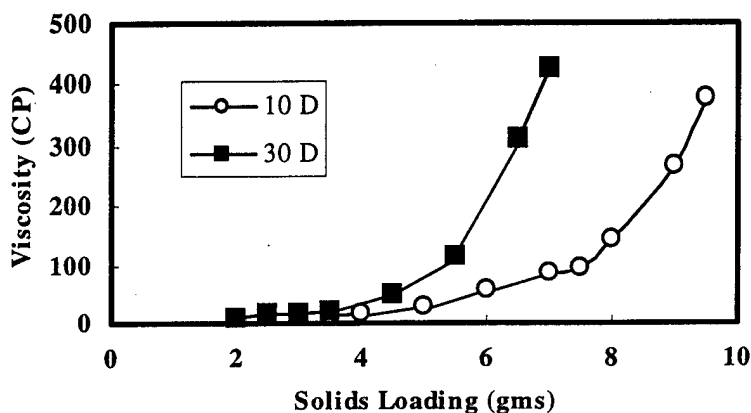


**Figure 3:** Effect of solids loading on the viscosity for 10D and 30D alumina ceramic powders.

For the present study, 10D and 30D both the powders were used to make water based ceramic slurry. Powder, antifoaming agent and dispersant were added to water and then mechanically stirred in a polyethylene boat for 10 minutes. The required amount of binder B-1035 (Rohm and Hass) was added to the mixture just before infiltration. Polymeric molds, produced via FDM, were infiltrated with the ceramic slurry using a vacuum oven. The infiltrated molds were dried at room temperature for 12 hours and then subjected to binder removal and sintering cycles.

#### Binder Removal and Sintering Cycle Development

Binder removal and sintering of dry ceramic powder loaded molds were carried out in a muffle furnace in furnace air environment. Samples were placed on top of a porous zirconia ceramic plate. Figure 4 shows the heating cycle. During the first part of the cycle (by 550°C), polymeric mold material and the binder evaporates. A slower heating rate is necessary up to this point to avoid cracking or distortion of the part. At higher temperature, densification of alumina ceramic occurs. A final sintering temperature of 1600°C and a hold time of 3 hours was used for all the samples.

#### Physical and Mechanical Characterization

The aim of this work was to investigate one of the most fundamental and general questions regarding bioceramic implants: what are the effects of pore size, pore volume and pore

distribution on the biomechanical properties of porous ceramic implants. During this initial part of the work, porous 3D honeycomb ceramic preforms were fabricated with various pore sizes and pore volumes. The 3D honeycomb structure has unique pore geometry that are inter-

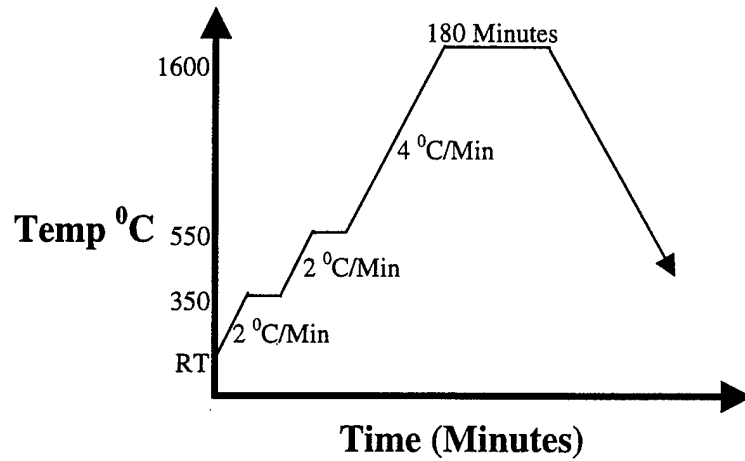


**Figure 4:** Schematic representation of the binder removal and sintering cycle for green ceramic parts.

connected in all three X, Y and Z directions. In this work, two types of ceramic preforms were fabricated. In the first type, the pore size was same in all the three directions or uniform pore geometry sample. But in the second type, pore sizes were different in X and Y compared to Z direction or non-uniform pore geometry. Similarly, a volume fraction gradient in porosity could also be achieved in pore distribution from top to bottom of the preform or from side to the center of the preform.

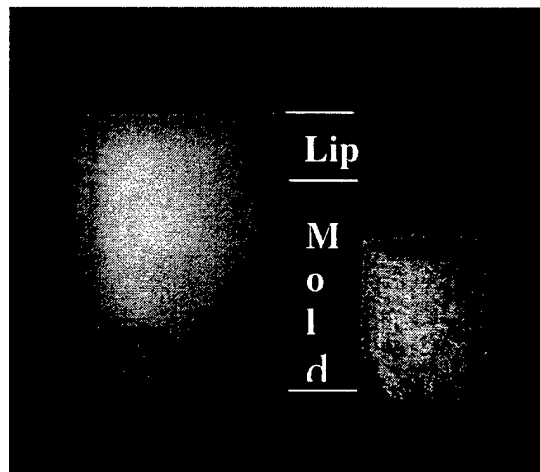


**Figure 5:** Optical photograph of a polymeric mold (with mold and lip) prepared via FDM and a sintered alumina ceramic preform.

Shrinkage is one of the most important factors during processing of these porous alumina ceramics. Initial data showed that linear shrinkage for the green to the sintered stage lie between

22 to 25%. Shrinkage data depends on the solids loading of the slurry and the particle size distribution of the ceramic powders. Figure 5 shows an optical photograph of a polymeric mold including the lip and a sintered ceramic preform fabricated using a similar mold.

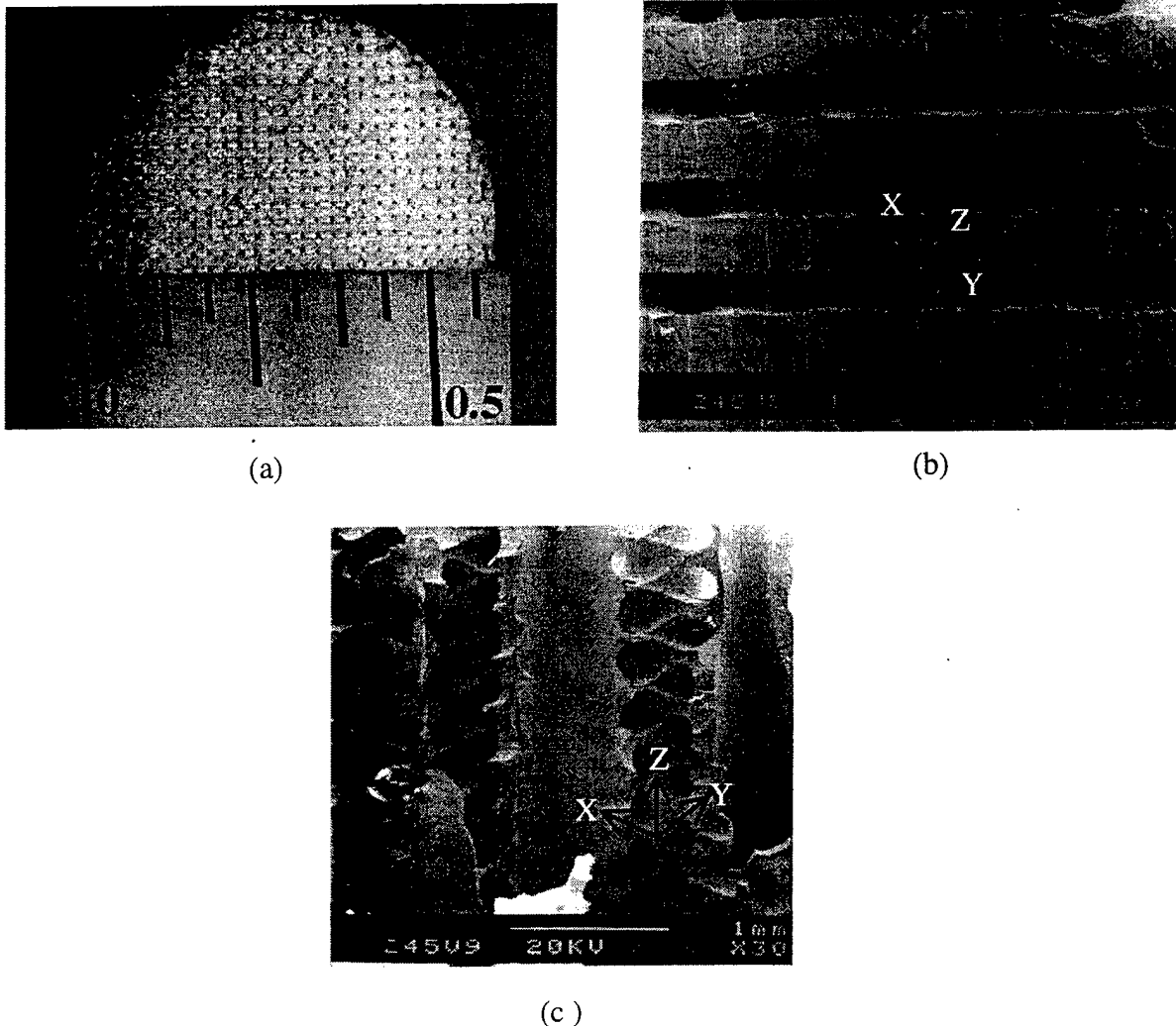


**Figure 6:** Optical and SEM micrographs of the sintered alumina ceramic preforms. (a) Top view of a cylindrical sample (~0.6" diameter). (b) Top view of a ceramic preform with *uniform pore sizes* in X, Y and Z directions (~ 300 $\mu$ m diameter). (c) Side view of a ceramic preform with *non-uniform pore sizes* in X, Y and Z directions (~ 300 $\mu$ m diameter in X and Y and 750 $\mu$ m in Z).

Figure 6 shows the optical and scanning electron micrographs of samples with uniform and non-uniform pore sizes. 3D honeycomb structures with 33% to 50% total pore volumes were fabricated with pore sizes varying from 300  $\mu$ m to 750  $\mu$ m. Figure 6 (b) shows the SEM micrograph of the uniform pore size sample where ~300  $\mu$ m diameter pores are interconnected in X, Y and Z directions. Figure 6 (c) shows another structure where pore sizes in Z direction is ~750  $\mu$ m and ~300  $\mu$ m in X and Y directions.

Initial compression tests were performed with some of these samples having 33% pore volume and uniform pore sizes using an MTS servo hydraulic machine. The compression test data is shown in Figure 7. These tests were performed with samples having a diameter vs. height ratio 1:1. The load vs. displacement curve showed a stepwise increase due to the failure of some of the pore walls during testing. The final fracture of these test samples occurred longitudinally with a multifaceted fracture surface. Final fracture stress varied between 2000 to 2500 MPa for samples with 33 volume% of porosity with pore sizes varying from 300 to 400  $\mu\text{m}$ . Further compression tests and four point flexural tests of these samples are currently under investigation.

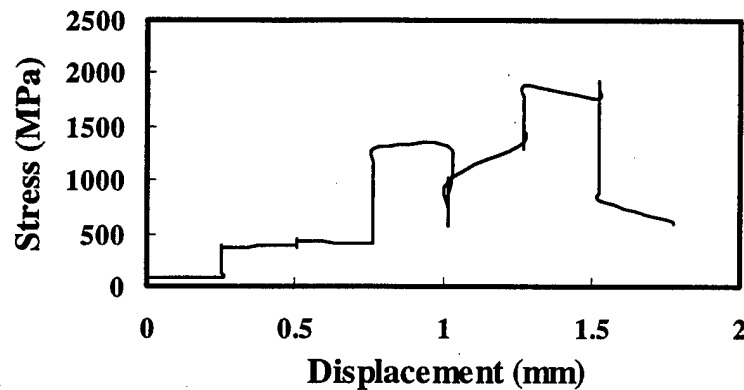


**Figure 7:** Displacement vs. stress plot for the 3-D honeycomb porous alumina ceramic preforms having 33% porosity.

### Conclusions

3D honeycomb porous alumina ceramic preforms were fabricated using indirect SFF route. Polymeric molds were fabricated using FDM 1650 with ICW06 filaments and then infiltrated with ceramic slurry and then dried. Dry molds were subjected to a binder burn out and sintering cycle. Structures with uniform and non-uniform pore sizes were fabricated via this method. Initial compression tests of 33 volume % porous structures showed that ultimate failure stress varied in the range of 2000 to 2500 MPa. Detailed mechanical characterization of these samples is currently under investigation.

### Acknowledgements

The authors would like to acknowledge John Merlino, Rubiela Diaz, Shinichi Sugiura and Sudharshan Rangaraj of the School of Mechanical and Materials Engineering at WSU for their help in SEM, and other materials processing work.

## References

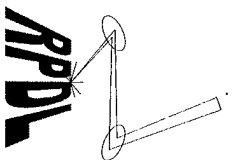
1. L. L. Hench, "Bioceramics: From Concept to Clinic," *J. Amer. Ceram. Soc.*, **74**[7], pp 1487-510 (1991).
2. L. L. Hench, "Bioceramics," *J. Amer. Ceram. Soc.*, **81**[7], pp 1705-28 (1998).
3. L. L. Hench and J. Wilson, "An Introduction to Bioceramics," World Scientific (1993).
4. A. Ravaglioli and A. Krajewski, "Bioceramics: Materials, Properties, Applications," Chapman and Hall, London, (1992).
5. K. deGroot, "Clinical Applications of Calcium Phosphate Biomaterials: A Review," *Ceramics International*, **19**, pp 363-66 (1993).
6. H. Alexander, J. R. Parsons, J. L. Ricci, P. K. Bajpai and A. B. Weiss, "Calcium Based Ceramics and Composites in Bone Reconstruction," *CRC Critical Reviews in Biocompatibility*, **4** [1], pp 44 (1987).
7. L. L. Hench and E. C. Ethridge, "Biomaterials: An Interfacial Approach," Academic Press, New York, (1982).
8. G. Lee and J. W. Barlow, "Selective Laser Sintering of Calcium Phosphate Powders," Proceedings of the Solid Freeform Fabrications 1993, The University of Texas at Austin, TX, pp 191-97 (1993).
9. G. Lee, J. W. Barlow, W. C. Fox and T. B. Aufdermorte, "Biocompatibility of SLS formed Calcium Phosphate Implants," Proceedings of the Solid Freeform Fabrications 1996, The University of Texas at Austin, TX, pp 15-21 (1996).
10. US patent 5,518,680.
11. US patent 5,490,962.
12. T. M. Chu and J. W. Halloran, "Hydroxyapatite Scaffolds with Controlled Porosity," presented at the Bioceramics: Materials and Applications Symposium at 100<sup>th</sup> Annual American Ceramic Society Meeting, Cincinnati, OH, May 2-6, 1998.
13. R. Garg, R. K. Prud'homme and I. A. Aksay, "Orthopaedic Implants by Ceramic Stereolithography," presented at the Bioceramics: Materials and Applications Symposium at 100<sup>th</sup> Annual American Ceramic Society Meeting, Cincinnati, Ohio, May 2-6, 1998.
14. P. Teung, R. K. Panda, S. C. Danforth and A. Safari, "Fabrication of Porous Hydroxyapatite Ceramics by Solid Freeform Fabrication Technique," presented at the Bioceramics: Materials and Applications Symposium at 100<sup>th</sup> Annual American Ceramic Society Meeting, Cincinnati, OH, May 2-6, 1998.

# Automated Fabrication of Nonresorbable Bone Implants Using Laminated Object Manufacturing (LOM)

Cheri Steidle<sup>1</sup>, Don Klosterman, Nora Osborne, George Graves, Richard Chartoff

<sup>1</sup>Master's thesis, Chemical Engineering, University of Dayton, May, 1998.

Rapid Prototype  
Development Laboratory

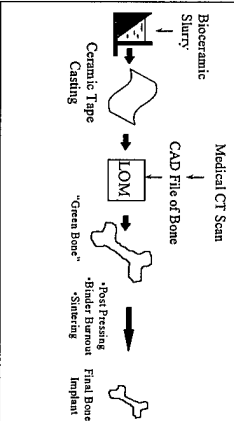


## Objective

Demonstrate Feasibility of Using Ceramic Tapes with the LOM Process to Fabricate Functional Bioceramic Parts for Use as Bone Implants.

- Bioceramic Material Formulation
- Tape Casting
- LOM Process Development
- High Temperature Ceramic Post Processing
- Mechanical Testing

## Bioceramic LOM Process Overview



## Step 1: Material System Selection

Hydroxyapatite (HA) :  $Ca_{10}(PO_4)_6(OH)_2$

- Proven biocompatibility
- Close resemblance to natural bone
- Used mostly for non-load-bearing applications
- general repair of bone defects
- augmentation of the alveolar ridge
- middle ear reconstruction
- plasma sprayed coating on metal implants
- However - HA is difficult to sinter!

## Material System Selection

- Composite system consisting of Hydroxyapatite and calcium phosphate glass was chosen. Calcium phosphate glass acts as a binding agent to hold the HA particles together
- Similar composite systems have been investigated

G. Graves et al.,  
J.C. Knowles et al.

increased porosity  
improved mechanical strength

## LOM Trials

- Lamination trials were conducted with a 2"x 4" part divided into eight one-inch squares
- Adjusted tape binder formula to produce adequate lamination
- Once a suitable tape formulation was achieved a CT file of a wrist bone was used to make a 3-D bone part

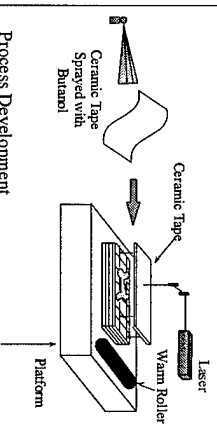
## LOM Parameters

Roller Speed	5.08 cm/sec
Roller Temperature	25°C
Roller Pressure	0.655 mm
Laser Power	9 - 20 %
Laser Speed	12.7 cm/sec
Laminating Solvent	Butanol

## Factors Involved in Lamination

- Type and amount of binder present in the tape
- Type and amount of solvent used for lamination
- Roller temperature, speed, and pressure

## Step 4: LOM of Bioceramic Tapes



## Step 5: High Temperature Ceramic Post Processing

- Pressing
- Binder Burnout
- Sintering

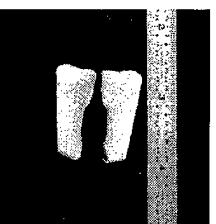
Post pressing is used to improve layer fusion and to prevent bloating during binder burnout



## Burnout and Sintering

Temperature (°C)	Time (hours)	Applied Pressure (MPa)	Apparatus
25 - 80	2	0.069 - 0.104	Com Meal BedPress
80 - 120	12	0.069 - 0.104	Com Meal BedPress
120 - 300	25	0	Humace
300 - 500	13	0	Humace
300 - 800	20	0	Humace
800 - 1050	2.5	0	Humace
1050 - 1050	5 minutes	0	Humace
1050 - 20	Free cool	0	Humace

## Bioceramic Wrist Bone Implants Made with LOM



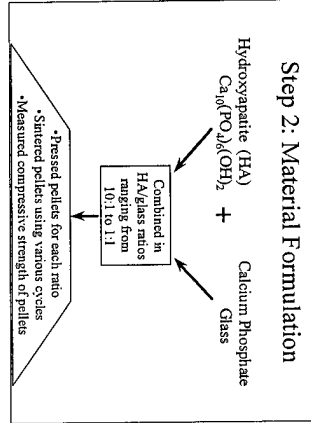
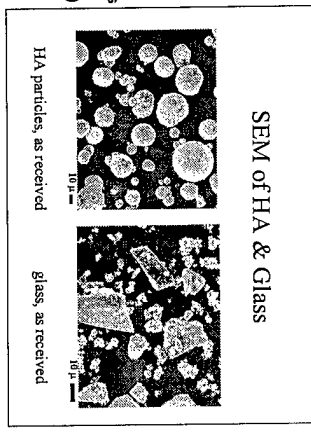
## Mechanical Test Results

Flexural Strength of Bone, Ceramics and LOM Samples

Bone	50 - 100 MPa (12)
HA	40 - 210 MPa (9)
TC <sup>1</sup>	90 - 154 MPa (4)
Bioglass	>120 MPa (4)
LOM Samples	18.8 MPa

(To next page, top row)

(From next page, middle row)



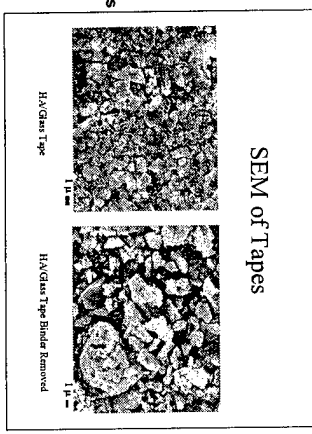
### Compression Test Results (sintered pressed pellets)

HA:glass ratio	Compressive Strength (MPa)
Grade 1 (100% Ca, 5 mm)	81.6
Grade 2 (90% Ca, 5 mm)	99.8
Grade 3 (80% Ca, 5 mm)	104.8
Grade 4 (70% Ca, 5 mm)	100.2
Grade 5 (60% Ca, 5 mm)	73.2
Grade 6 (50% Ca, 5 mm)	129.5
Grade 7 (40% Ca, 5 mm)	83.3
Grade 8 (30% Ca, 5 mm)	100-130

\*Taped test on grade (sample placed in on as prepared at 100°C) Heat up cycle = 5°C/min

### Formulation Selection

- 3:1 ratio was selected based on compressive strength
- However, FTIR analysis of sintered specimens revealed the presence of a reaction by-product, Tricalcium phosphate (TCP), at a level of 10%. Because TCP at this level is resorbed in the human body, the material system cannot be considered nonresorbable in a strict medical sense.
- Despite the presence of TCP, the current 3:1 HA:glass system was adopted to serve as a model system for use on the LOM

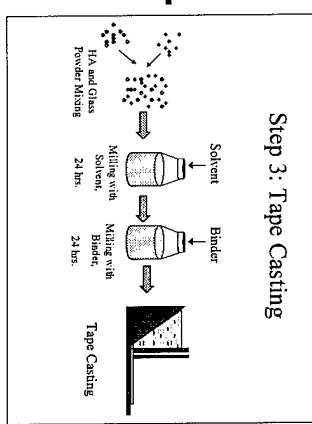


### Slurry Composition

Slurry Component	% of the total slurry weight	Role
HA	38 - 43	primary ceramic
Calcium phosphate glass	13 - 14	binding ceramic
Methacryl fish oil	1 - 1.5	deflocculant
Ethyl Alcohol	9.3 - 10	slurry solvent
Trichloroethylene	24 - 25	slurry solvent
Poly vinyl butyral	2.7 - 4.5	primary binder
Poly ethylene glycol (MW 400)	2.9 - 4.8	plasticizer
Benzyl benzoate	2.3 - 4.1	plasticizer
Stearic Acid	0 - 1.5	release agent

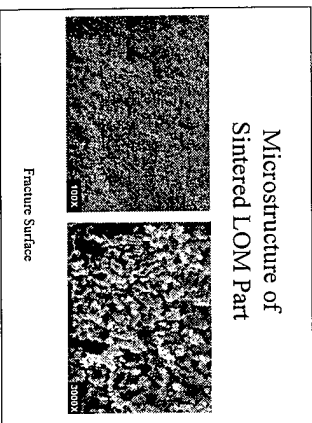
### Factors Involved in Tape Casting

- Slurry composition and viscosity
- Doctor blade setting
- Casting speed
- Drying conditions



### Other Properties of Sintered Bioceramic LOM Parts

- Compressive Strength = 30 MPa
- Specific Gravity = 2.77



### Conclusions

- HA:glass formulation can be cast into useable tapes for fabrication on the LOM
- HA:glass tapes are appropriate to form LOM shapes with acceptable adhesion between layers
- A 3-D bone shape was successfully produced from a CAD file taken from a medical CT Scan
- High temperature post-processing techniques were successfully used to densify the LOM bones without distorting the complex shape.

### Conclusions (cont.)

- The mechanical properties of the specimens made with the best HA:glass formulation (3:1 ratio) were lower than that of cortical bone and pure sintered HA by a factor of two or three.
- The mechanical properties are expected to rise with optimization of the various processes involved, particularly post-sintering (elimination of interlamellar voids) and sintering.
- Overall feasibility of producing bioceramic bone shapes from LOM has been established.

# Generation of Porous Structures Using Fused Deposition

Bertoldi M., Yardimci M. A., Pistor C. M., Güçeri S. I., Danforth S. C.  
University of Illinois at Chicago & Rutgers University

## *ABSTRACT*

The Fused Deposition Modeling process uses hardware and software machine-level language that are very similar to that of a pen-plotter. Consequently, the use of patterns with poly-lines as basic geometric features, instead of the current method based on filled polygons (monolithic models), can increase its efficiency.

In the current study, various toolpath planning methods have been developed to fabricate porous structures. Computational domain decomposition methods can be applied to the physical or to slice-level domains to generate structured and unstructured grids. Also, textures can be created using periodic tiling of the layer with unit cells (squares, honeycombs, etc). Methods based on curves include fractal space filling curves and change of effective road width within a layer or within a continuous curve. Individual phases can also be placed in binary compositions.

In present investigation, a custom software has been developed and implemented to generate build files (SML) and slice files (SSL) for the above-mentioned structures, demonstrating the efficient control of the size, shape, and distribution of porosity.

## *INTRODUCTION*

Two dimensional pattern generation capability of RP/SFF methods is not being fully utilized currently due to use of very limited set of toolpath generation algorithms and data representation problems associated with heterogeneous structures. Generation of controlled porosity structures with RP/SFF has been particularly challenging due to the need of defining the entire porous structure as a very complicated solid object.

Porosity generation within solid models with RP/SFF processes has been investigated in the context of investment casting with SLA fabricated constant pore size patterns. Two-dimensional equilateral triangular and square self-repeating patterns were developed by 3D Systems, three-dimensional laminated hexagonal structures by the University of Nottingham group [1] and three-dimensional tetragonal crystalline structures by Gervasi and coworkers [2].

Recently, rectangular porous interior structures were adopted by Stratasys in Fused Deposition and tetragonal patterns by Z-Corporation in 3D printing for build acceleration. The computational geometry definition problem of heterogeneous structures has been investigated [3]; however, this study does not address the generation of porous structures inside solid models.

Fused Deposition can be considered as a vector printing technique, in which the two-dimensional patterns are generated with poly-lines on a discretized  $x$ - $y$  plane. Boundary deposition and subsequent raster filling is employed during production; voids appear in the raster filling, due to the finite road width; this can be used to produce specific porosity. However, current Fused Deposition process planning software only allows for constant layer thickness across the entire part, constant road width within each layer, contour or rectilinear rasters, monolithic material composition, and constant air-gap between raster patterns. As a result, the variety of attainable porous structures is very limited.

A set of software tools has been developed and used to generate porous structures, showing the feasibility of the concepts presented. Since layer geometries are inherently two-dimensional, the remainder of the presentation will be focused on two-dimensional grid generation.

### *TWO DIMENSIONAL TEXTURES*

Basic texture structures employed by computer graphics methods, such as square blocks and honeycombs, can fill a plane by tiling the basic unit periodically. The variety of microstructures can be increased by recursively constructing higher-order unit cells that fill the plane through periodic tiling, as shown in Figure 1.

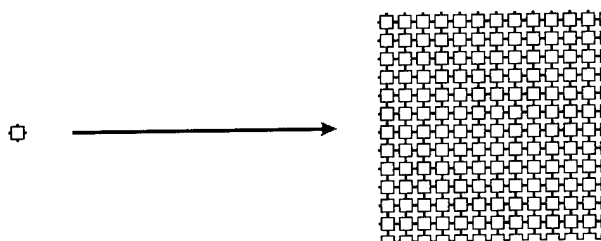


Figure 1 *Unit cell and resulting texture.*

Texture based patterns can be generated once the underlying unit cell is designed properly to fill the entire plane. The texture needs to be clipped to fit into the layer geometry described by the contours, which increases the computational requirements. The unit cell nature of the textures enforces a homogeneous pore size and microstructure distributions throughout the entire part, which limits the use of this technique.

## STRUCTURED GRID GENERATION

Structured grids are used in the simulation of complex physical processes, where discretization of the domain of interest into geometrically simple sub-structures is required. Systems of algebraic or ordinary differential equations representing the physical phenomena are defined over the discretized domain, with appropriate variable transformations [4]. Uniform Cartesian grids within rectangles and circular geometries can be generated, employing linear functions and coordinate transformations, as depicted in Figure 2.

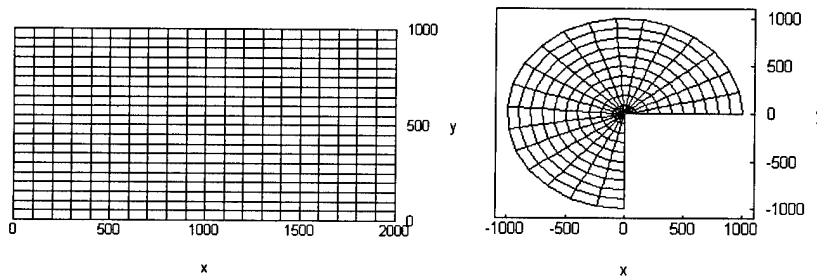


Figure 2 *Uniform Cartesian grids.*

The resultant grids have regular porosity distributions, which can be manipulated only by varying grid spacing independently along the coordinate axes. The porosity can be better controlled through use of nonlinear stretching functions as mapping functions from computational to physical space. One example of stretching functions to generate boundary clustering is:

$$\begin{cases} x \\ y \end{cases} = \begin{cases} (x_{\max} - x_{\min}) \frac{(2\alpha + \beta) \left[ (\beta + 1) / (\beta - 1) \right]^{(\xi - \alpha) / (1 - \alpha)} + 2\alpha - \beta}{(2\alpha + 1) \left\{ 1 + \left[ (\beta + 1) / (\beta - 1) \right]^{(\xi - \alpha) / (1 - \alpha)} \right\}} + x_{\min} \\ (y_{\max} - y_{\min}) \frac{(2\alpha + \beta) \left[ (\beta + 1) / (\beta - 1) \right]^{(\eta - \alpha) / (1 - \alpha)} + 2\alpha - \beta}{(2\alpha + 1) \left\{ 1 + \left[ (\beta + 1) / (\beta - 1) \right]^{(\eta - \alpha) / (1 - \alpha)} \right\}} + y_{\min} \end{cases} \quad (1)$$

where  $\xi$  and  $\eta$  denote coordinates in computational space. The generated grids are presented in Figure 3.

Although Cartesian grids are powerful geometric discretization tools for simple domains, they are not directly adaptable for arbitrary two-dimensional domains and have to be used as background textures with polygon clipping methods. Complex geometry physical simulation

necessitated the development of boundary conforming, or boundary fitted curvilinear grid methods [5].

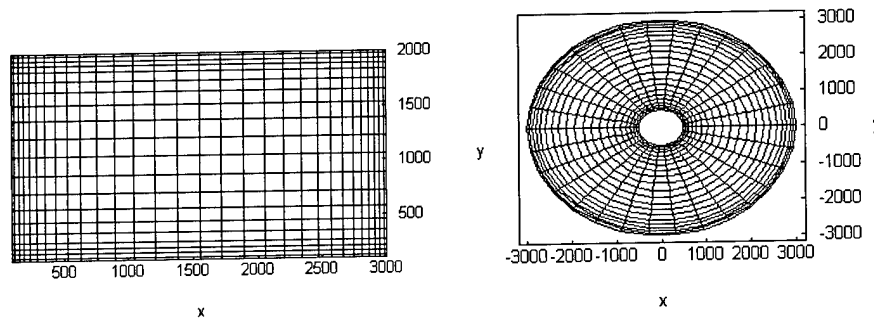


Figure 3 Non-uniform Cartesian grids with boundary clustering.

Boundary conforming structured grids can be efficiently produced by using algebraic interpolation methods. Portions of domain boundaries in physical space are associated with domain edges in computational space. Interpolation methods are utilized to generate coordinates of interior grid nodes; a two-boundary interpolation of a circle is presented in Figure 4.

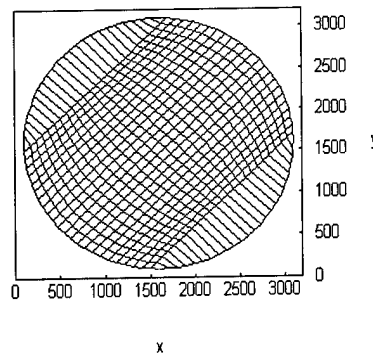


Figure 4. Boundary conforming grid generated with two-boundary interpolation.

Greater flexibility of boundary conformity can be obtained through higher order interpolation algorithms, e.g. transfinite interpolation:

$$\begin{aligned} \vec{r}_{i,j} &= P^i + P^j - P^{ij} \\ P^i &= f_i \vec{r}_{im,j} + (1-f_i) \vec{r}_{i,1} \quad , \quad P^j = g_j \vec{r}_{i,jm} + (1-g_j) \vec{r}_{i,1} \\ P^{ij} &= f_i g_j \vec{r}_{im,jm} + f_i (1-g_j) \vec{r}_{im,1} + (1-f_i) g_j \vec{r}_{i,jm} + (1-f_i) (1-g_j) \vec{r}_{i,1} \\ f_i &= \frac{i-1}{im-1} \quad , \quad g_j = \frac{j-1}{jm-1} \end{aligned}$$

(2)

The resultant grid for the same circular geometry is depicted in Figure 5. Regions around which grid nodes are concentrated and cells are distorted, correspond to the corners of the rectangle in physical space.

Porosity control on algebraic grids can be further enhanced through non-linear stretching functions or advanced mapping methods from the theory of complex variables. As an example, a simply connected arbitrary geometry polygon can be mapped onto a unit circle in the complex plane, i.e. computational space, through a series of conformal maps [6],[ 7].

Generation of boundary conforming curvilinear grids can also be formulated as a boundary or initial/boundary value problem (IVBP). IVBP's can be described by partial differential equation (PDE) as the governing equation over the domain and relevant initial and boundary conditions, where dependent variables are coordinates of the grid points. Since a variety of different PDE's can be used, greater control is achieved on pore sizes, clustering, continuity and orthogonality of grid lines.

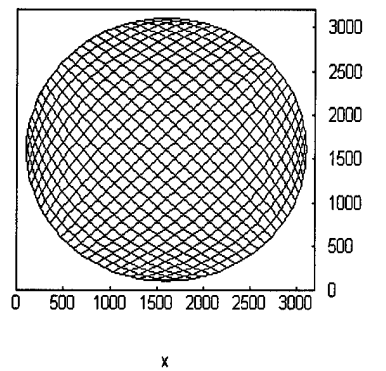


Figure 5: Boundary conforming grid generated with transfinite interpolation.

Mapping between computational and physical spaces is defined with a variable transformation, for effective construction of PDE based grid generation methods:

$$\begin{aligned}
 x &= x(\xi, \eta) \quad , \quad y = y(\xi, \eta) \\
 \xi &= \xi(x, y) \quad , \quad \eta = \eta(x, y)
 \end{aligned} \tag{3}$$

$$\begin{Bmatrix} d\xi \\ d\eta \end{Bmatrix} = \frac{1}{(x_\xi y_\eta - x_\eta y_\xi)} \begin{bmatrix} y_\eta & -x_\eta \\ -y_\xi & x_\xi \end{bmatrix} \begin{Bmatrix} dx \\ dy \end{Bmatrix}$$

where subscript denote partial differentiation of the dependent variable with respect to the independent variable. The most widely used PDE's are second order elliptic equations, written in the canonical form:

$$\Pi_1 \frac{\partial^2 \theta}{\partial x^2} + \Pi_2 \frac{\partial^2 \theta}{\partial y^2} + \Pi_3 \frac{\partial \theta}{\partial x} + \Pi_4 \frac{\partial \theta}{\partial y} + \Pi_5 = 0 \quad (4)$$

For grid generation, a system of elliptic PDE's can be constructed with grid coordinates as dependent variables in respective problem spaces:

$$\begin{aligned} \frac{\partial^2 \xi}{\partial x^2} + \frac{\partial^2 \xi}{\partial y^2} = P \quad , \quad \frac{\partial^2 \eta}{\partial x^2} + \frac{\partial^2 \eta}{\partial y^2} = Q \quad , \quad (\xi, \eta) = (\xi(\bar{r}), \eta(\bar{r})) \quad \bar{r} \in \Gamma_p \\ \text{or} \\ \begin{cases} L(x) \\ L(y) \end{cases} = \begin{cases} 0 \\ 0 \end{cases} \quad , \quad (x, y) = (x(\xi_0, \eta_0), y(\xi_0, \eta_0)) \quad (\xi_0, \eta_0) \in \Gamma_c \end{cases} \quad (5) \\ L \equiv A \left( \frac{\partial^2}{\partial \xi^2} + \phi \frac{\partial}{\partial \xi} \right) + 2B \frac{\partial^2}{\partial \xi \partial \eta} + C \left( \frac{\partial^2}{\partial \eta^2} + \varphi \frac{\partial}{\partial \eta} \right) \\ A = x_\eta^2 + y_\eta^2 \quad , \quad B = -(x_\xi x_\eta - y_\xi y_\eta) \quad , \quad C = x_\xi^2 + y_\xi^2 \end{aligned}$$

where (P,Q) are grid control parameters in physical space with their counterparts ( $\phi, \varphi$ ) in computational space. Since Dirichlet (constant value) type boundary conditions are specified for the BVP, the elliptic PDE's only need to be solved in the interior of the domain. The discretization of equations with central differences and employment of successive over-relaxation (SOR) iterative method, results in the following algebraic system:

$$\begin{aligned} i = 1 \dots im, \quad j = 1 \dots jm \\ x'_{i,j} = \frac{\omega}{2(A+C)} \left[ A \left( x_{i-1,j} + x_{i+1,j} + \frac{\phi}{2} (x_{i+1,j} - x_{i-1,j}) \right) + \frac{B}{2} (x_{i-1,j-1} - x_{i+1,j-1} - x_{i-1,j+1} + x_{i+1,j+1}) \right. \\ \left. + C \left( x_{i,j-1} + x_{i,j+1} + \frac{\varphi}{2} (x_{i,j+1} - x_{i,j-1}) \right) + (1-\omega)x_{i,j} \right] \quad (6) \\ y'_{i,j} = \frac{\omega}{2(A+C)} \left[ A \left( y_{i-1,j} + y_{i+1,j} + \frac{\phi}{2} (y_{i+1,j} - y_{i-1,j}) \right) + \frac{B}{2} (y_{i-1,j-1} - y_{i+1,j-1} - y_{i-1,j+1} + y_{i+1,j+1}) \right. \\ \left. + C \left( y_{i,j-1} + y_{i,j+1} + \frac{\varphi}{2} (y_{i,j+1} - y_{i,j-1}) \right) + (1-\omega)y_{i,j} \right] \\ A = \frac{(x_{i,j+1} - x_{i,j-1})^2 + (y_{i,j+1} - y_{i,j-1})^2}{4} \quad , \quad C = \frac{(x_{i+1,j} - x_{i-1,j})^2 + (y_{i+1,j} - y_{i-1,j})^2}{4} \\ B = - \frac{(x_{i+1,j} - x_{i-1,j})(x_{i,j+1} - x_{i,j-1}) - (y_{i+1,j} - y_{i-1,j})(y_{i,j+1} - y_{i,j-1})}{4} \quad (7) \end{aligned}$$

Four 51x31 grids with varying degrees of clustering were generated for a rectangular domain of which the upper boundary was replaced with the curve:

$$y = -1000 \cos\left(\frac{2\pi(x-100)}{3000}\right) + 3000 \quad (8)$$

The relaxation parameter,  $\omega$  (eq. 6), was set to 1.8 and iterations were stopped when the average cell-based residual was calculated to be less than % 0.1. The resulting grids are presented in Figure 6.

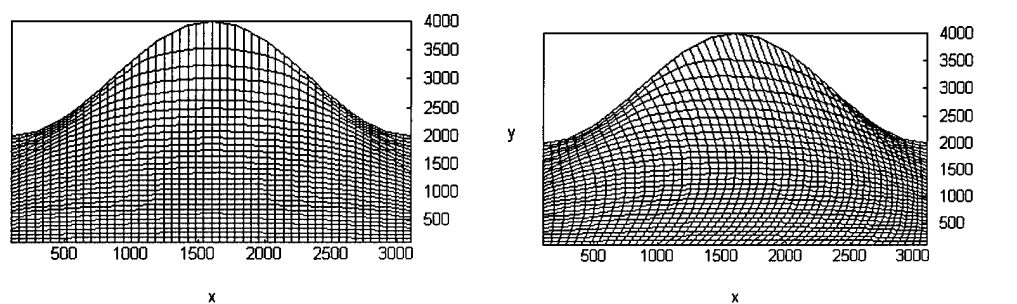


Figure 6 Curvilinear grids generated with second order elliptic PDE's: no clustering (a), clustering ( $\phi = 0.03$ ) in  $\xi$  direction (b).

### MULTI-GRID METHODS

If the solution of a computational problem requires higher grid node densities at specific locations within the domain, it is possible to generate an additional fine grid. Embedded grids, as shown in Figure 7-a, provide local density variations without distorting the base grid; however, the complexity of the algorithms is increased due to additional interpolation/interrogation steps. In analogy to computational physics simulations, embedded grids may provide refined porous structures.

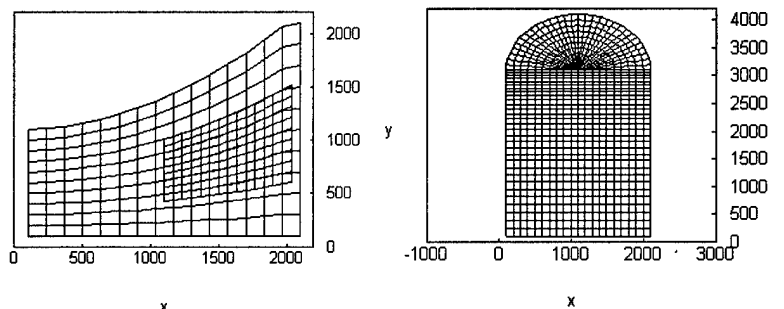


Figure 7 Sample embedded grid (a) and multi-block grid (b).

For complex geometry domains mapping of the Cartesian grid may result in severe distortion and low quality curvilinear grids, regardless of the particular method employed. Multi-block methods address grid quality by decomposing the domain into simpler geometry sub-domains, generating grids within each of them using any of the techniques described above. Multi-block grids are hybrid geometrical entities; each sub-domain is made of a structured grid but the overall grid topology is described in the context of unstructured grids (**Figure 7-b**). Multi-block grids offer increased geometric flexibility over single block structures; however, the algorithms are more complex and mostly semi-automatic.

### *UNSTRUCTURED GRIDS*

Unstructured grids discretize the problem domain into basic geometric features that do not have implicit topology. Their connectivity is defined explicitly as part of the data-structure, in contrast to structured grids. As a result, computational methods are less efficient due to additional overhead of calculating and storing information. On the other hand, unstructured grid generation methods are geometrically more flexible and robust, since the specification of domain boundaries with closed contours (2D), or closed surfaces (3D), is sufficient for initial grid generation [8]. Triangular grids are the most widely used type of unstructured grids and can be generated with different methods:

- Mapping of a pre-triangulated mesh onto the domain using structured grid generation methods, or conversion of two-dimensional structured grids, made of quadrilaterals, into triangles.
- Delaunay triangulation, which generates triangles for a pre-specified grid node distribution optimally. Optimality is defined with the conformity of the generated triangles to equilateral triangles [9].
- Advancing front method, in which the domain boundaries define a starting front. In contrast to Delaunay triangulation, advancing front method generates interior point cloud using a set of heuristic rules [10]. Parameters and transformations within the rules can be manipulated to obtain construct tailored triangulations with relatively high computational efficiency [8].

A dual tessellation of the polygon interior can be obtained for unstructured grids by generating new points at triangle center-points (type I), or by observing distance constraints (Voronoi tessellations, type II) and constructing polygons around the old grid nodes. Interior points of Voronoi polygon  $V_i$  are closer to old grid node  $P_i$  than any other node,  $P_j$ , in the original unstructured grid. For ideal equilateral triangular grids, both constructions produce identical hexagonal dual tessellations. For arbitrary grids there are considerable differences,

where type I reflects the underlying triangulations significantly better. Figure 8 depicts a constrained Delaunay triangulation, a dual center-point tessellation and the relative layer-wise superposition for a triply connected domain, showing as these algorithms can be effectively utilized for porosity generation.

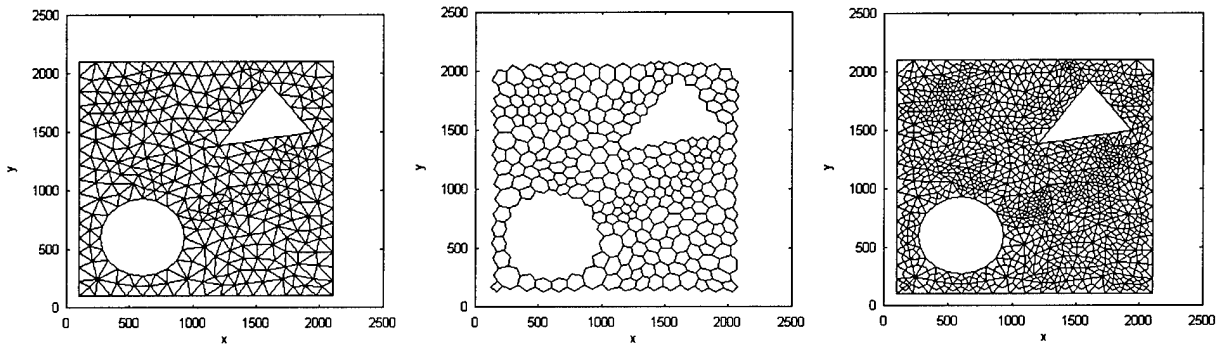


Figure 8 Triangulation (a), tessellation (b) and superposition of the two (c) on a triply connected domain.

### *DOMAIN DECOMPOSITION*

The capabilities of individual porosity generation methods can be further amplified utilizing domain decomposition tools on layer level geometry contours. Distributions of raster angles, road widths and air-gaps can be assigned to each sub-domain by automatically modifying the properties of individual polygons in the slice (SSL) file [9]. Although domain decomposition is not as geometrically flexible as direct toolpath generation techniques described above, it can be integrated into existing process planning chain more easily.

### *SPACE FILLING CURVES*

SFC's can be utilized as novel toolpath generation techniques in the generation of porous structures. The length of the unit steps within SFC's can be set to a value larger than width of the roads, to generate porosity. Three-dimensional porosity can be fabricated by stacking rotated or mirrored patterns of the original layer with respect to symmetry axes. See reference [9] for a more detailed description and some examples.

### *MULTI-MATERIAL DEPOSITION*

Fused Deposition hardware (e.g. Stratasys FDM 1650) is able to deposit two different materials (modeling and support), each of which has separate delivery systems and flow

controllers. In SML language, the material for each poly-line can be specified. Hence, it is possible to specify material distributions for the porous structures inside the toolpath generation algorithms. This can be done in different ways:

- Randomly, either by assigning the material to a particular polygon through random number generators, or using center-point coordinate of the polygon and utilizing two-dimensional binary random patterns.
- With a real valued function on a plane,  $f(x,y)$ : the function is evaluated at the center-point of individual polygons and the material is selected based on the digitization of the calculated function.

Figure 9 shows a part that has been fabricated based on an unstructured grid of a simply connected domain and having a material distribution assigned according to a function specified as

$$f = \cos\left(\frac{x}{1000}\right)\sin\left(\frac{3y}{2000}\right)$$

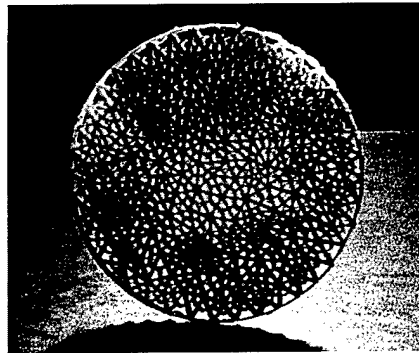


Figure 9 *Multimaterial porous structure.*

### *GENERATION OF POROUS STRUCTURES WITH FUSED DEPOSITION*

Porous structures are described with open or closed poly-lines. A routine has been developed for the translation of poly-lines with appropriate properties into SML files [9]. In contrast to transformation based RP/SFF methods, e.g. SLA and SLS, FD necessitates the use of non-intersecting toolpaths. The minimum feature size in FD is defined by nozzle diameter and attainable road width range is currently 0.014"-0.040" for the standard 0.012" nozzles. Since one micro-step corresponds to 0.001" in  $x$ - $y$  plane, the smallest controllable deposition is approximately 0.130" long. Although these bounds can be lowered using low deposition head speeds,

the minimum deposition length will not be shortened below 0.1" in the existing material delivery system, due to considerable inertia of the melt within the liquefier.

Also, due to limited communication between motion and flow controllers, straight lines, poly-lines with corners, and corners with small and large angles are not differentiated. As a result, excess material will be generated invariably at internal side of the corner, possibly closing the pores. For structures that rely on deposition of unsupported bridges, maximum pore size has been estimated as 0.150" for ABS material. However, for self-supporting structures the pore size is only bounded by the size of build domain.

### *SCAN-LINE DEPOSITION*

Structured grids and space filling curve patterns can be effectively achieved through deposition of open-ended poly-lines. Although structured grids can also be generated using polygon deposition methods, individual grid lines within the structures are natural building blocks for scan-line deposition. Structured grids can be generated via a number of ways:

- Families of grid lines,  $\xi$  and  $\eta$ , can be deposited on separate layers resulting in open porous structures along the side-walls, or on the same layer, resulting in laterally closed cells and excess material accumulation at grid nodes.
- Staggered grids can be inserted into layer stacking type a, in which  $\xi$  and  $\eta$  lines are produced on alternating layers. Considerably reduced sagging is expected to occur in comparison to type a, due to reduced bridging lengths.
- Staggered grid  $\xi$  and  $\eta$  lines are produced on the same layer. Although the overall structure will have open porosity along the wall surfaces, each layer will have closed boundaries.

### *CONCLUSIONS*

The work has presented the possibility of using Rapid Prototyping for the production of porous structures, using algorithms based on different computational approaches. Software tools have been developed and a number of porous structures has been built using a Stratasys FDM 1650 machine, showing the feasibility of all the proposed concepts. The future work will include use of polygon renumbering methods which are required for polygon-deposition of unstructured grids or their dual tessellation to shorten the deposition time as well as field adaptive unstructured grid generation techniques.

## REFERENCES

1. Hague R., Dickens P., "Design of new build structures for the successful autoclaving of stereolithography models," *The Seventh International Conference on Rapid Prototyping*, pp. 192-202, March 31-April 3 1997, San Francisco, California, USA.
2. Gervasi V. R., Brandt D. A., Shaffer S. D., Lim K., "Tetracast SLA buildstyle," *The Seventh International Conference on Rapid Prototyping*, pp. 309-317, March 31-April 3 1997, San Francisco, California, USA.
3. Sun W., Lau A. C., "Knowledge-enriched CAD modeling for Solid Freeform realization of heterogeneous material structures," *The Seventh International Conference on Rapid Prototyping*, March 31 - April 3 1997, pp. 79-84, San Francisco, California, USA.
4. Thompson J. F., "Grid generation," in Minkowycz W. J., Sparrow E. M., Schneide G. E., Pletcher R. H., (eds.) *Handbook of Numerical Heat Transfer*, ISBN 0-471-83093-3, 1988.
5. Eisemann P. R., "Grid generation for fluid mechanics computations," *Annual Review of Fluid Mechanics*, vol. 17, pp. 487-522, 1985.
6. Ives, D. C., "A modern look at conformal mapping including multi-connected regions," *AIAA Journal*, vol. 14, no. 8, pp. 1006-1011, 1976.
7. Davis R. T., "Numerical methods for coordinate generation based on Schwarz-Christoffel transformations," *Proceedings of 4<sup>th</sup> AIAA Computational Fluid Dynamics Conference*, pp. 1-15, 1979
8. Löhner R., "Unstructured grid generation," in *Handbook of Fluid Dynamics and Fluid Machinery vol. 2 Experimental and Computational Fluid Dynamics*, (eds. J. A. Schetz and A. E. Fuchs), pp. 1240-1257, John Wiley & Sons, ISBN 0-471-12597-0, 1996
9. Domain Decomposition and Space Filling Curves in Toolpath Planning and Generation  
M. Bertoldi, M. A. Yardimci, C. Pistor, S. I. Güçeri, Proceedings of the 1998 Solid Freeform Fabrication Symposium, The University of Texas at Austin, Austin, Texas 1998.
10. Peraire J., Vahdati M., Morgan K., Zienkiewicz O. C., "Adaptive remeshing for compressible flow computations," *Journal of Computational Physics*, vol. 72, pp. 449-466, 1987.

## A STUDY ON WEIGHT LOSS RATE CONTROLLED BINDER REMOVAL FROM PARTS PRODUCED BY FDC

Senol Pekin \* <sup>Ψ</sup>, John Bukowski <sup>δ</sup>, and Avigdor Zangvil \*,

\* Materials Research Laboratory, University of Illinois at Urbana-Champaign, Urbana, IL.

<sup>Ψ</sup> Energy Technology Division, Argonne National Laboratory, Argonne, IL.

<sup>δ</sup> Center for Cement Composite Materials, University of Illinois at Urbana-Champaign, Urbana, IL.

The binder removal schedule of a binder in the ethylene vinyl acetate-wax system was analyzed by automatically adjusting the soaking duration based on the monitored weight loss of the polymer. The thermolysis of several grades of microcrystalline wax and ethylene vinyl acetate have been analyzed by TGA and DSC to support the explanation of the weight loss rate controlled binder removal experiments. During the thermolysis of such binders in air, the degradation sequence is degradation and evaporation of hydrocarbons, degradation of the vinyl acetate, and degradation of the ethylene chain, all oxygen assisted. It was shown that the extent and the rate of the vinyl acetate degradation in air is determined by the molecular weight of the EVA, unlike its degradation in N<sub>2</sub>. It was concluded that thermolysis of light polymers is easier than that of the heavy ones and weight loss rate controlled binder removal technique can help in the optimization of binder removal schedule for a variety of polymers.

### I. Introduction

Fused deposition of ceramics (FDC) is a rapid prototyping technique in which a set of 3-D coordinate values can be used to manufacture a ceramic green body. While this method is not suitable for manufacturing an item in large quantities, it is ideal for manufacturing components for which the geometry needs to be tailored on a case by case basis, such as in the cases of biomedical implants and prototype development.

A typical process route in FDC involves milling of the ceramic powder, mixing the organic additives (binder) with the powder, extruding the filament feedstock, solid freeform manufacturing, binder removal and sintering. The binder used needs to have a low melting point (100-150°C), and low viscosity and tackiness upon melting [1]. In addition, since all organic additives are temporary additives in ceramic processing, physical and chemical phenomena that take place during binder removal must be considered for binder formulation. Several types of defects such as carbon retention, cracking, blistering, warping, anisotropic shrinkage and delamination of the sintered bodies can be introduced during the binder removal process [2, 3]. On the other hand, the binder removal process plays an important role in the through-put and the yield of the production [2].

In formulation of a binder system for FDC, four inter-conflicting issues arise:

a) since the FDC requires thermoplastic binders with low viscosity (perhaps the lowest among the paste shaping methods), a binder system with low molecular weight needs to be chosen,

- b) in order to minimize the binder content (to decrease volumetric shrinkage after binder removal) or to increase the handling strength of the filament feedstock, a binder system with high molecular weight needs to be considered,
- c) a binder with a low viscosity creates difficulties due to the possibility of deformation or slumping during the thermolysis [4], and
- d) since the rate of loss of molecular weight (number average) is nearly proportional to the square of the molecular weight, removal of a binder system with a high molecular weight creates difficulty during the thermolysis [5].

Strategies for binder removal include thermal debinding, wicking, solvent extraction and supercritical fluid extraction [2, 3, 6]. Complex chemical processes such as evaporation (endothermic process) of low molecular weight organic additives and degradation (generally exothermic process) of higher molecular additives, and physical processes such as redistribution of the binder throughout the green body take place during the removal process.

Several studies [7, 8, 9] have been conducted to monitor the changes that take place during the binder removal. These changes can include weight loss, heat exchange between the sample and the surroundings, and the dimensional change. Factors affecting the binder removal process include the polymer chemistry and structure, polymer loading, chemical interactions at polymer-ceramic interfaces, heat/mass transport, component geometry, firing atmosphere, and heating cycle [2, 8]. Therefore, optimization of binder removal schedule (i.e. temperature, time, and atmosphere) via analysis of the physico-chemical processes that occur during the thermolysis can be time consuming in rapid prototyping where ceramic powder, the exact binder formulation, and the part geometry need to be tailored within strict time limitations, due to the nature of the process. Therefore, a binder removal process in which the change in one or more of the parameters mentioned above will be automatically kept within the specified limits needs to be incorporated into rapid product development by FDC. The specific limits can be identified by trial-and-error design experiments [see, for example, 9].

In this study, a binder removal system based on monitoring the weight loss of the green component during thermolysis was developed, and incorporated into a research-scale process which aims at the rapid prototype development by FDC. The idea of rate controlled decomposition was suggested by Rouquerol [10] to study the apparent orders of reaction, energies of activation and differential enthalpies of dissociation, especially under high vacuum, and attempts have been made to employ such a technique in binder removal from ceramic green bodies. For example, a rate controlled extraction system [8] has been constructed which adjusts the (soaking) temperature of the furnace based on the weight-loss of the organic constituents. Following an evaluation of binder removal strategies and rate controlled binder removal systems, a rather complex procedure based on the PI (proportional-integral) control of the weight signal by means of the furnace temperature in an adaptive cascade configuration has been proposed [7]. However, the present study is different from the previous attempts, since a) it aims the determination of the soaking duration at each temperature reached, b) it is easy to incorporate into any vertical-tube furnace by the help of a data acquisition system capable of generating digital output signal, and c) it is used together with analysis of physico-chemical events that

occur during the pyrolysis in order to develop binder removal schedules in rapid ceramic prototype development.

## II. Experimental Procedure

A binder removal system based on monitoring the weight loss of the green component during thermolysis was constructed as described in Figure 1. The microcomputer commands the data acquisition system via a standard LPT port. The weight of the sample is monitored by a Mettler PJ300 digital balance equipped with a dedicated RS-232 board. The heart of the set up is a software (named DB3) developed specifically for this purpose and written in Labview. The software reads and averages the weight via the balance and converts this information into actual weight loss rate,  $(WLR)_{actual}$ , in each time interval, the duration of which is defined by the user. In this study, a two-minute long time interval was used. If the absolute value of  $(WLR)_{actual}$  is larger than a user defined value, the software sends a signal to a relay board which switches the furnace controller into “hold”; and therefore, initiates a soaking duration at that temperature. Once initiated, the number of intervals (hold period) that a hold command remains valid can also be entered by the user. During the hold period, if another  $(WLR)_{actual}$  value that falls outside the user defined limit is detected, the count-down of the hold period is re-started. If all of the  $(WLR)_{actual}$  values detected during a hold period remain within the user defined limits, the hold period lasts the number of intervals that was defined by the user.

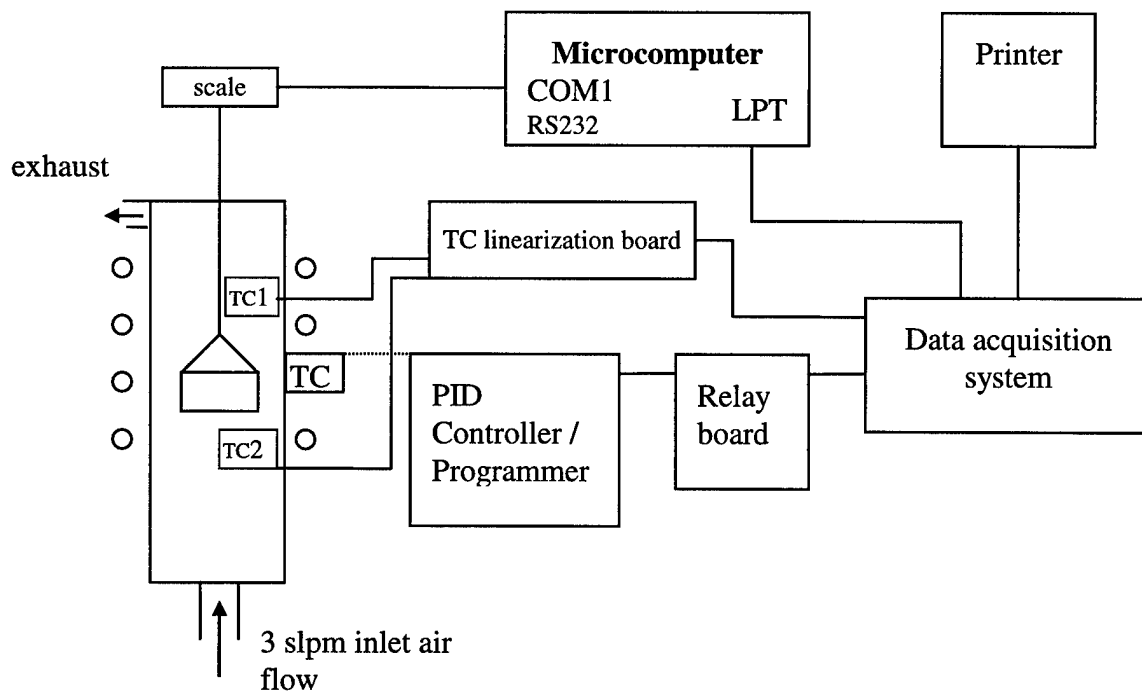


Figure 1. The schematic of the weight loss rate controlled binder removal system.

The sample was placed in a basket made of Inconel 601 alloy and was lowered into the hot zone of the furnace via the hook of the balance. In such a system oscillations cause sinusoidal

fluctuations in the balance readings. To overcome this effect a user defined value was introduced as the derivation interval as shown in figure 2.

A derivation interval of 7 was used in this study. The furnace was controlled by a PID controller which read the temperature of the furnace tube. The controller was programmed to heat the furnace at a rate of 15°C/hour up to 600°C. An upward air flow rate of 3 slpm was used. The direction of heat flow between the sample and the furnace atmosphere was monitored roughly by placing a thermocouple right below and another one right above the basket which contained the sample.

The samples used in this study contained 40 (wt.) % binder and 60% alumina. The binder itself contained 60% microcrystalline wax (blend of two different grades), 20% of an EVA grade that contains 20 % vinyl acetate, and 20 % of an EVA grade that contains 28 % vinyl acetate. The melt index of the former grade was 8 dg/min, whereas the melt index of the latter was varied between 2500-0.15 dg/min to study its effect in binder removal.

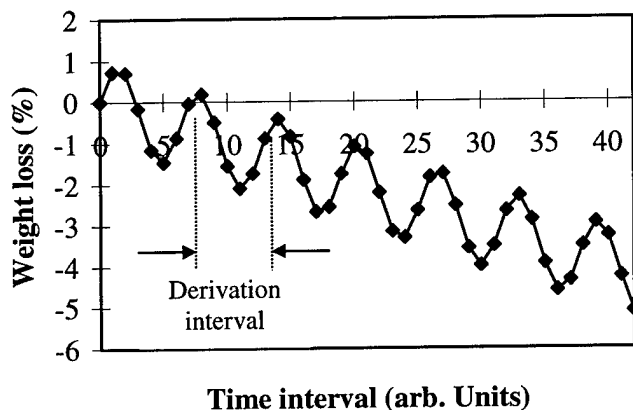


Figure 2: Explanation of the derivation interval. When sinusoidal oscillations are present, a normal derivation (derivation interval =1) would cause incorrect calculation of the weight loss rate.

Thermal analysis was done by using a Netzsch Model STA 409 simultaneous thermal analyzer, at a heating rate of 10°C/hour under flowing air. The solid freeform was fabricated by using a Stratasys FDM 3-D Modeler.

### III. Results and Discussions

Prior to the analysis of the data obtained from the rate controlled binder removal system, an understanding of the oxidative degradation of the organic components is needed. The TGA-DSC curves of the wax grades used are given in figure 3 and 4. A microcrystalline wax can be defined as a solid hydrocarbon mixture, of average molecular weight range of 490 to 800 ( i.e. appx. 17 - 44 carbons), considerably higher than that of paraffin wax (350 to 420) [11]. Hydrocarbons are formed by the decarboxylation of esters, the removal of the CO<sub>2</sub> resulting in a hydrocarbon with an odd number of carbons. Hydrocarbons found in waxes are mostly saturated open chain series

(alkanes), and to a lesser extent, unsaturated olefins (alkenes) [11]. These hydrocarbons have so low molecular weights that they can readily be evaporated without any chain scissioning. An analogy can be set here with the degradation of polyethylene,  $(\text{CH}_2)_n$ , which is nothing but a very large hydrocarbon chain. Iida et al. [12] reported that degradation of PE under  $\text{N}_2$  atmosphere provides products up to  $\sim\text{C}_{20}$ . Furthermore, it was reported [13] that molecules as large as  $\text{C}_{94}\text{H}_{190}$  can evaporate without decomposition in vacuum. Those molecules that are too large to evaporate decrease their chain length by undergoing an oxidative degradation process prior to evaporation. Jellinek [14] studied the mechanism of degradation of straight and branched type ethylene chains in vacuum, and proposed a mechanism in which the first or last monomer unit is broken off the chain. Dickens [15] studied the process in more detail and suggested that the end radicals extract hydrogen from the surrounding polymer matrix to form backbone radicals, and these backbone radicals undergo either  $\beta$  scission or disproportionation. Activation energy for the decomposition of polyethylene increases as the molecular weight of the polymer increases, and was reported to be in the range of 50-70 kcal/mole in vacuum [14, 15], and 20 kcal/mole for oxidation [15]. This argument is in good agreement with the results shown in figure 3 and 4. The microcrystalline wax given in figure 3 has more light hydrocarbons than the one given in figure 4, as the melting endotherms given in the insets indicate. Thus, the light hydrocarbons in the former wax can evaporate without much degradation which is proven by the large endothermic peak in the DSC curve.

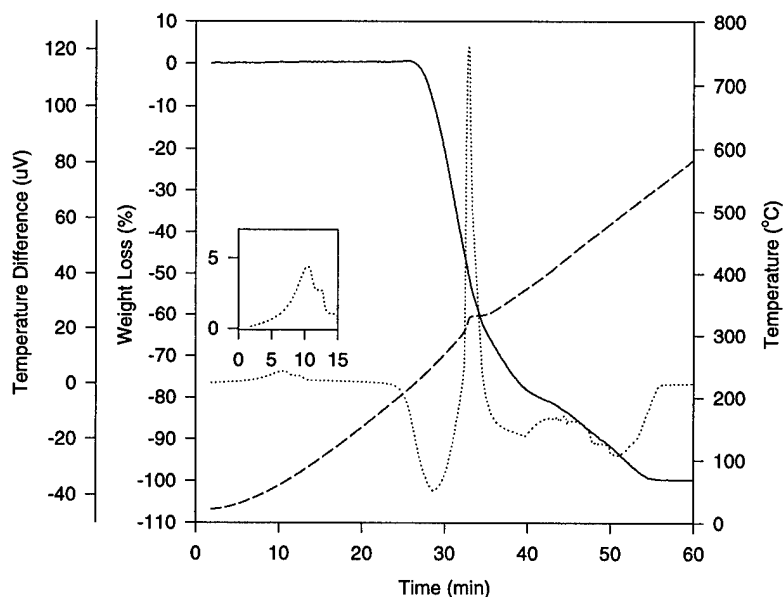


Figure 3: The TG (—) and DSC (.....) curves for the thermolysis of lower melting point grade microcrystalline wax. The first exotherm indicates the onset of the chain scissioning of the heavier hydrocarbons; whereas the following endotherms indicate the evaporation of the light components. The inset is a close-up of the melting endotherm of the DSC curve.

From a binder removal point of view, highly endothermic removal of a component can create a high temperature gradient between the furnace atmosphere and the remaining components of the binder system. It can be speculated that during the evaporation of the hydrocarbons in the microcrystalline wax, the next exothermic process would be suppressed. Once this endothermic

process is completed, the temperature of the sample would increase suddenly and the onset of the exothermic process would shift to higher temperatures. As far as the weight loss curves are concerned, it is obvious that the removal of microcrystalline wax is gradual and takes place between 250 and 450°C. This removal opens up free space in the green body, thus higher removal rates of the remaining organic components can be tolerated. A careful analysis of the TG curves reveals a weight gain at about 150°C right before the weight loss starts. This weight gain can be attributed to the oxygen uptake [16], and since this weight increase is more profound in the wax grade that contains heavy hydrocarbons, it verifies that oxygen assists in the chain scissioning process.

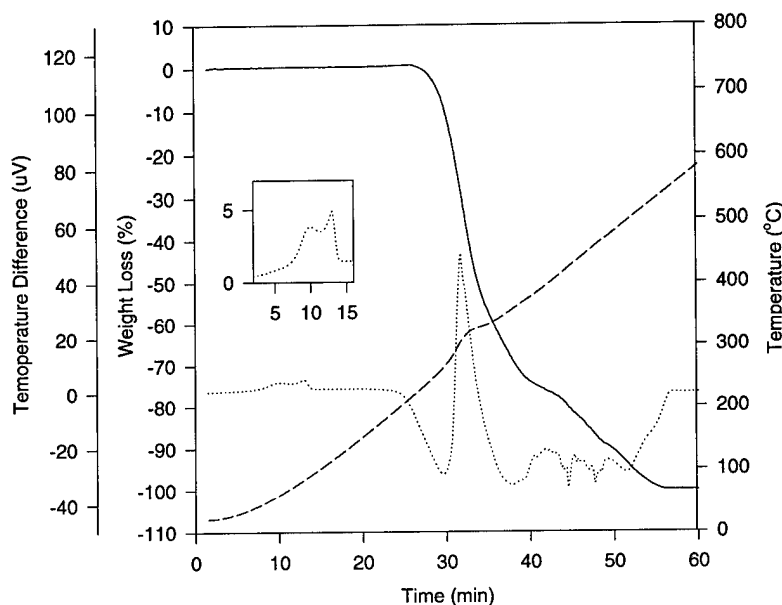


Figure 4: The TG (—) and DSC (.....) curves for the thermolysis of higher melting point grade microcrystalline wax. As shown in the inset, this wax has a significant amount of heavy hydrocarbons. The heat needed for evaporation is supplied by the exothermic oxidation reaction progressing in parallel. As a result, the range of the temperature difference, which is proportional to the change in heat flux, is smaller than the one in figure 3.

A typical TGA-DSC curve for degradation of EVA in flowing air is given in figure 5, for a 28% vinyl acetate containing grade. It has been shown [17, 18] that degradation of EVA in nitrogen atmosphere takes place in two steps: one for the degradation of the vinyl acetate chain and one for the degradation of the ethylene chain, as also shown in figure 5. The reported onset of the first step corresponds to 350°C whereas the maxima of the Gram-Schmidt intensity peak for the same step corresponds to 364°C [17]. It was also reported that the heating rate has no effect on the onset, rate or extent of this decomposition [18]. In this study, however, degradation studies carried out in air showed that molecular weight of the polymer has a significant effect on a) the extent and the rate of the pyrolysis of the vinyl acetate chain, and b) the rate of pyrolysis of the ethylene chain. The first step is slightly exothermic in general, whereas the second step displays first an exothermic and then an endothermic peak. The range of the temperature difference between the two opposite peaks was especially high for the high molecular weight grades. The

fact that the rate of the pyrolysis of the ethylene chain increases as the molecular weight increases can be explained by what Casassa had proposed [5]: If the degradation is a first-order reaction, the rate of destruction of the polymer links at some temperature is:

$$-\frac{dp}{dt} = kp$$

where  $p$  is the number of monomeric units held together by polymer linkages. Integration of this equation gives:

$$-\int_{p_{\infty}}^p \frac{dp}{p} = k \int_0^t dt, \text{ or } \ln\left(\frac{p_{\infty}}{p}\right) = kt,$$

where  $p_{\infty}$  is the number of polymer links in a given volume of a system consisting of polymer of (infinitely) high molecular weight. Since  $p = p_{\infty} \left(\frac{n-1}{n}\right)$ , where  $n$  is the number of monomer units per molecule [5];

$$-\left(\frac{dn}{dt}\right) = k(n^2 - n), \text{ or as a good approximation at high molecular weight; } -\left(\frac{dn}{dt}\right) = kn^2$$

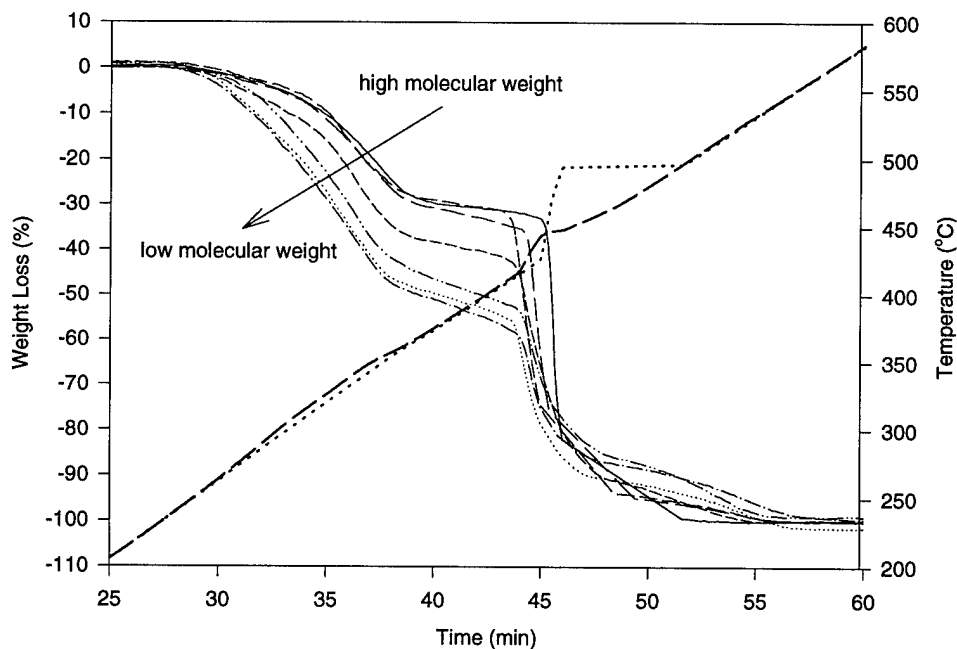


Figure 5: The TGA curves for the thermolysis of EVA (28% VA) with weight average molecular weight in the range from 29990 to 119900. The first weight loss step is due to oxy-degradation of the vinyl acetate and the second step is due to the oxy-degradation of polyethylene chain. The (.....) and (----) are the temperature vs. time curves for the highest and the lowest molecular weight polymers, respectively.

Thus, during a degradation reaction of the first order with respect to reacting groups, the rate of loss of molecular weight (number average) is nearly proportional to the square of the molecular weight. In the case of oxidative degradation, the rate of destruction of the polymer links may not be necessarily first order; however, Casassa also argued that the result would still be the same at high degree of polymerization without such an assumption.

The result of a pyrolysis experiment of a part produced by FDC [19] is given in figure 6. The molecular weight of the EVA (28% vinyl acetate) was 99360 [19]. In figure 6, it is clear that there is overall weight gain up to 200°C furnace temperature (TC). The feedback for the control of the furnace temperature is provided by a thermocouple that senses the temperature of the furnace chamber to avoid the interference from the pyrolysis heat. The weight gain is followed by evaporation of scissored or light hydrocarbons. Pyrolysis of rather heavy chains (ethylene chain of the EVA) takes place right above 400°C (TC) and at a narrow temperature range. As seen in figure 6, the DB3 algorithm was not able to control the weight loss rate during the EVA pyrolysis as strictly as it did during the pyrolysis of the wax, when the user defined value of the hold period was 4 intervals. However, the control of such rapid pyrolysis reactions can be improved by increasing the hold period via the DB3 software. The fluctuations in the TC2 thermocouple reading that started above 200°C (TC), were attributed to spattering of the polyethylene.

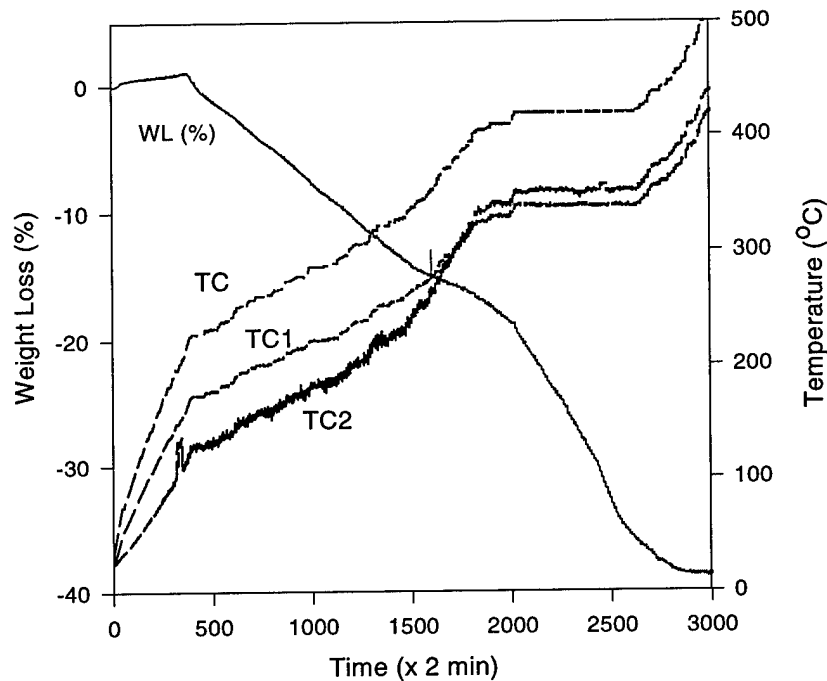


Figure 6: The controlled pyrolysis weight loss and the resulting temperature curves of a green body produced by FDC, and containing a binder in the EVA-wax system. The soaking duration at each temperature was controlled by specifically developed DB3 algorithm which allowed the temperature increase at 15°C/hour only if the measured weight loss rate was within the +/- 0.015 % per two-minute long interval (see figure 1 for details).

## IV. Conclusions

Thermal analysis of the organic components used in the binder system based on EVA-wax blends revealed that the degradation sequence is degradation and evaporation of hydrocarbons, degradation of the vinyl acetate, and degradation of the ethylene chain, respectively. It was shown that degradation of EVA in air is different than its degradation in N<sub>2</sub>. The extent and the rate of the vinyl acetate degradation in air is determined by the molecular weight of the EVA. It was also shown that degradation rate of the ethylene chain in EVA increases as its molecular weight increases. These thermal analyses were carried out to support the explanation of the weight loss rate controlled binder removal experiments.

A system that determines the soak duration at each temperature during heating up for binder removal has been set up. It was shown that, under given control parameters, removal of the wax can be done precisely, whereas controlled removal of the heavier components is rather difficult, and an example was given for the binder that contained EVA with a molecular weight of 99360.

A rate-controlled binder removal system can control chemical events taking place during the binder removal. Since low viscosity binders are used in FDC, physical events take place during binder removal from parts produced by FDC can be very important. Therefore, optimization of rate-controlled binder removal schedule, especially for parts produced by FDC, needs to be supported by an understanding of the physical phenomena as well.

## Acknowledgment

The authors would like to thank to Dr. Phillip Geil of Dept. of Materials Science and Engineering, UIUC for the fruitful discussions of issues related to polymer degradation.

## References:

- 1) M. K. Agarwala et. al., "Structural Ceramics by Fused Deposition of Ceramics", Proceedings of the Solid Freeform Fabrication Symposium, 1995, vol. 6, pp. 1-8, ed. by H. L. Marcus, J. J. Beaman, J. W. Barlow, D. L. Bourell, and R. H. Crawford, The University of Texas at Austin, Texas.
- 2) J. A. Lewis, "Binder Removal from Ceramics", *Annu. Rev. Mater. Sci.* 1997, 27:147-73
- 3) H. M. Shaw, and M. J. Edirisinghe, "Removal of Binder from Ceramic Bodies Fabricated Using Plastic Forming Methods", *Bull. Am. Ceram. Soc.*, 1993, vol. 72, 9: 94-99.
- 4) M. J. Cima, J. A. Lewis, and A. D. Devoe, Binder Distribution in Ceramic Greenware During Thermolysis", *J. Am. Ceram. Soc.*, 1989, 72 [7] 1192-99.
- 5) E. F. Casassa, "Degradation of High Polymers", *J. of Polymer Science*, 1949, vol. IV, pp. 405-7.
- 6) T. Chartier, M. Ferrato, and J. F. Baumard, "Supercritical Debinding of Injection Molded Ceramics", *J. Am. Ceram. Soc.*, 1995, 78[7] 1787-92.
- 7) H. Verwij, and W. H. M. Bruggink, "Reaction-Controlled Binder Burnout of Ceramic Multilayer Capacitors", *J. Am. Ceram. Soc.*, 1990, 73[2] 226-31.

- 8) A. Johnsson, E. Carlstrom, L. Hermansson, and R. Carlsson, "Rate-Controlled Extraction Unit for Removal of Organic Binders from Injection Molded Ceramics", *Ceramic Powders*, 1983, pp. 767-772, ed. By P. Vincenzini, Elsevier scientific Publishing Company, Amsterdam, The Netherlands.
- 9) V. N. Shukla, and D. C. Hill, "Binder Evolution from Powder Compacts: Thermal Profile for Injection-Molded Articles", 1989, *J. Am. Ceram. Soc.*, 72[10] 1797-803.
- 10) J. Rouquerol, "Critical Examination of Several Problems Typically Found in the Kinetic Study of Thermal Decomposition Under Vacuum", *J. of Thermal Analysis*, 1973, vol. 5, 203-216.
- 11) *The Chemistry and Technology of Waxes*, by A. H. Warth, 2<sup>nd</sup>. Ed., Reinhold Publishing Corporation, New York USA, 1956.
- 12) T. A. Iida, K. Honda, and H. Nozaki, *Bull. Chem. Soc. Jpn.*, 1973, 46, 1480.
- 13) L. A. Wall, J. H. Flynn, and S. Straus, *J. Phys. Chem.*, 1970, 74, 3237.
- 14) H. H. G. Jellinek, "Thermal Degradation of Polystyrene and Polyethylene. Part III", *J. of Polymer Science*, 1949, vol. IV, pp. 13-36.
- 15) B. Dickens, "Thermally Degrading Polyethylene Studied by Means of Factor-Jump Thermogravimetry", 1982, *J. of Polymer Science: Polymer Chemistry Edition*, vol. 20, 1065-1087.
- 16) G. Williams, M. R. Kamal, and D. G. Cooper, "Thermo-oxidative Degradation of Linear Low Density Polyethylene Melts", *Polymer Degradation and Stability*, 1993, 42, 61-68.
- 17) B. J. McGrattan, "Examining the Decomposition of Ethylene-Vinyl Acetate Copolymers Using TG/GC/IR", *J. of Applied Spectroscopy*, 1994, 48[12] 1472-76.
- 18) M. B. Maurin, L. W. Dittert, and A. Hussain, "Thermogravimetric Analysis of Ethylene-Vinyl Acetate Copolymers with Fourier Transform Infrared Analysis of the Pyrolysis Products", *Thermochimica Acta*, 1991, 186, 97-102.
- 19) S. Pekin, A. Zangvil, and W. Ellingson, "Binder Development in the EVA- wax System for Fused Deposition of Ceramics", *Proceedings of the Solid Freeform Fabrication Symposium*, 1998, to be published, The University of Texas at Austin, Texas.

## Binder Formulation in EVA-wax system for Fused Deposition of Ceramics

Senol Pekin \* <sup>Ψ</sup>, Avigdor Zangvil \*, and William Ellingson <sup>Ψ</sup>

\* Materials Research Laboratory, University of Illinois at Urbana-Champaign, Urbana, IL.

<sup>Ψ</sup> Energy Technology Division, Argonne National Laboratory, Argonne, IL.

Blends in the ethylene vinyl acetate (EVA) – wax system have been evaluated as potential binders to be used in fused deposition of ceramics (FDC). In order to obtain good handling strength, it was indicated that the melting point of the polymer needs to be lower than that of the wax. In this context, it was shown that the melting point of the EVA decreases as the vinyl acetate content in the copolymer increases. By measuring the viscosity as a macroscopic property, it was shown that 20 % vinyl acetate-containing EVA is miscible in microcrystalline wax up to, at least, 30 %. Binders used in FDC need to have low viscosity and it was pointed out that the slumping can be one main problem associated with binders with low viscosity. Thus, thermolysis of wax at low temperature is suggested as a solution. The volumetric thermal expansion and melt strength of an EVA-wax blend were displayed as a function of temperature, in the form of a penetration test.

### I. Introduction

Fused deposition of ceramics (FDC) has recently emerged as a new way of shaping ceramic components [1]. The method has advantages in the sense that it minimizes the product development time and cost; however, it also imposes several challenges regarding the ceramic processing. The main challenge lies in the binder development and in the optimization of the properties of the feed-stock material. Binder development has traditionally been a complex issue since it is related not only to the binder formulation but to optimization of the removal conditions as well. Therefore, mechanistic understanding of the physico-chemical processes that occur during thermolysis and information related to the rheology of the binder system are needed. In addition, the FDC method imposes several requirements for the binder system.

In this study, the requirements of a binder system to be used in FDC are classified into two categories: general and secondary. The general requirements are low melting point, low viscosity and tackiness. The secondary requirements are those that gain importance during specific processing stages (e.g.; extrusion, debinding, etc.) and are wetting ability ( $\gamma_{SL}$  and  $\gamma_{SV}$ ), melt strength, melt index, shear-thinning behavior, handling strength, (steric) stabilization ability, residue content, etc.

A typical processing sequence for FDC involves milling of the ceramic powder, mixing the organic additives with the powder, extrusion of the feed-stock filament, solid freeform fabrication, binder removal and sintering. For example, shear-thinning behavior and appropriate melt strength are required during the extrusion of the small-diameter (< 2 mm) filament. The FDC is the only ceramic shaping method that requires no die or mold, and, hence, the liquid-air interfacial energy of the binder system determines the surface finish of the sintered body. The requirement for the level of the paste viscosity upon melting is perhaps the lowest one among the ceramic shaping techniques. For example, in injection molding and extrusion, the acceptable

viscosity is higher than that for the FDC, since the former methods employ force for shaping the component. However, low viscosity of the binder above the melting point can cause deformation ("slumping") during the binder removal stage [2]. Below the melting point, strength of the binder is important for handling the filament.

These requirements limit the binder formulation to a thermoplastic one. Thermoplastic polymers can be semicrystalline (e.g.; polyethylene, polypropylene, nylon) or glassy (e.g.; polystyrene, polyvinyl chloride). A semicrystalline polymer becomes viscous liquid when melted, whereas a glassy polymer becomes a leathery or viscous dough-like material when heated above its glass temperature,  $T_g$  [3,4]. Thus, semicrystalline thermoplastic polymers are suitable as organic additives in FDC.

Since low viscosity is desired upon melting, wax has been the major component of the binder system. Wax is a general name for a variety of compounds that include paraffinic waxes, microcrystalline waxes, synthetic hydrocarbon waxes and oxidized polyethylene waxes [5]. Paraffinic and microcrystalline waxes are by-products of the petroleum industry, whereas synthetic hydrocarbon waxes and oxidized polyethylene waxes are produced by polymerization or oxidation of ethylene, respectively [5]. By adjusting the parameters during the polymerization of ethylene, not only the chain length (as represented by average molecular weight and molecular weight distribution), but also the degree of branching in the polymer (which determines the crystallinity and density) can be adjusted. The very low molecular weight (as low as 400) polyethylene (PE) is used as synthetic wax, whereas the very high end of the range (as high as 5 million) is known as ultra high  $M_w$  PE. The degree of branching, on the other hand, determines the crystallinity, and thus, the density of the polymer. The low density polyethylene (LDPE) is highly branched and has about 50 % crystallinity. The high density form (HDPE) has few side-chain branches and has about 90 % crystallinity [6, 7].

Olefins (propylene, 1-butene, 1-hexene, 1-octene) are copolymerized to improve selected properties of HDPE as the density is reduced. Low density copolymers containing varying amounts of vinyl acetate (EVA), maleic anhydride (EMA), ethyl acrylate (EEA) are produced to modify selected physical properties of LDPE homopolymers [6,7].

Properties of wax can be improved by the addition of PE homopolymer or copolymers containing PE. This blending process not only improves the properties of the wax, but also yields a graded volatility binder system. Despite the fact that every polymer has some solubility in every other polymer, the magnitude in most cases is extremely low [8, 9]. Compatibility of the wax with EVA depends on the melting points of the two, and on the vinyl acetate content of the copolymer.

In ceramic processing, organic additives not only aid in the shaping of the component, but also have significant influence on the microstructure, and thus, the properties of the ceramic component. The purpose of this study is to apply general ceramic processing science to FDC, by evaluating different grades of EVA-petroleum wax mixtures as a potential binder. The fact that EVA and the petroleum wax are commercially available in several different grades, make them

good candidates to be used as binder components for FDC; therefore, a discussion on the effect of their properties is given in this study.

## II. Experimental Procedure

Viscosity of the EVA-wax mixtures was measured by using a Brookfield viscometer with spindle #2. Since thermal gradients develop during non-isothermal viscosity measurement in viscous fluids, a sample holder which is slightly larger than the Brookfield LV2 spindle in diameter, was used. A cooling/heating rate of 30°C/hour was used, while the rotational speed of the spindle was selected depending on the viscosity range of the blend. Penetration tests were performed on the 1 g samples of the blends by using a 0.8 g/mm<sup>2</sup> contact pressure at a heating rate of 15°C/hour in a specially made penetration test apparatus. Melting endotherms of different grades of the EVA, wax, and their blends were characterized by using a Perkin-Elmer DSC-4 differential scanning calorimeter at 10°C/min heating rate, with 5 mg samples, and under flowing N<sub>2</sub>. The temperature scale was calibrated by using the melting endotherm of indium sample. Microstructural analysis of the extruded filaments were done by using a Hitachi S-800 SEM equipped with a thermoionic filament, at 10kV accelerating voltage.

The EVA used was supplied by DuPont and was a copolymer of vinyl acetate and polyethylene, whereas the microcrystalline wax used was supplied by IGI. The selected properties of the materials used as claimed by the supplier are given in table 1. The ceramic powder used was Alcoa A-17 grade alumina. The ceramic green bodies were fabricated by using a Stratasys FDM 3-D Modeler.

Table 1: Selected properties of the ethylene-vinyl acetate copolymer grades used, as claimed by the supplier.

V.A. wt. %	M.I. (dg/min)	Avg. M <sub>w</sub>	Tensile Strength (MPA)
20	500	49100	4.7
20	8		18
20	2.5	132000	23
25	400	51400	3.3
28	2500	29990	1.6
28	800	40840	2.6
28	400	44010	2.8
28	150		5.5
28	43	99360	9.7
28	25	112000	11
28	6	81900	24
28	3	119900	29
28	0.5		22
28	0.15		23

### III. Results and Discussions

In formulation of a binder system for FDC by using wax and EVA, the main factor that determines the handling strength of the filament feedstock are the melting points of the two components. To obtain good strength, the melting point of the weaker component (wax) needs to be higher than that of the stronger one (EVA). During cooling, the wax solidifies first and forms micro globes in the EVA melt, and eventually the polymer solidifies and forms a 3-dimensional network. During the early experiments in this study, it was observed that paraffinic wax-EVA blends don't display handling strength due to the low melting point of the paraffin wax. On the other hand, the melting point of the EVA can be adjusted by the vinyl acetate content, as shown in figure 1. The vinyl acetate disrupts crystallinity of the ethylene chain and decreases the melting temperature of the polymer. At a given vinyl acetate content, the rheological properties of EVA can be adjusted by changing the molecular weight of the polymer. As shown in figure 2, the change in the molecular weight of EVA influences the enthalpy of melting, but not the onset temperature of melting.

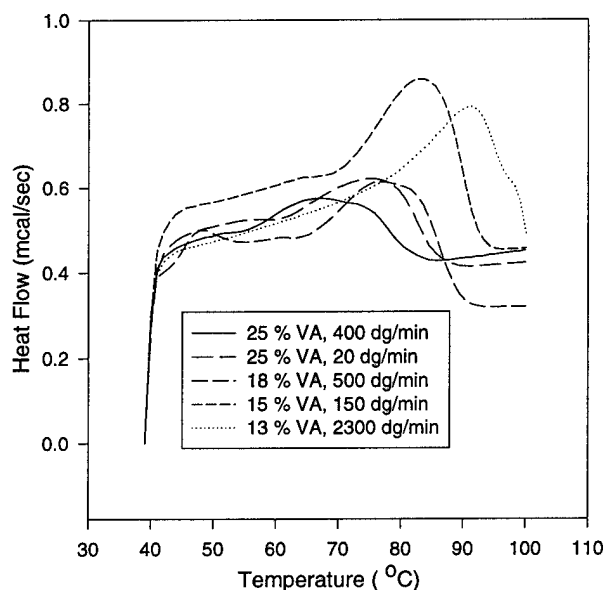


Figure 1: The effect of vinyl acetate content and the molecular weight (as represented by the melt index) on the melting endotherm of the EVA.

The compatibility of the wax-EVA mixtures were monitored by viscosity measurement during both cooling and heating. As shown in figure 3, the EVA containing 20 % vinyl acetate showed compatibility as the weight of the EVA was varied from 5 to 30 %. The fact that the slopes of the curves in the 5-20 % range are almost identical, reveal that the EVA can form a three dimensional network in the solvent wax and can dominate the viscoelastic/viscous flow. The increase in the activation energy at 30 % can be due to the entropic contribution.

Resistance to viscous flow is especially important during the binder removal step, since binders with too low viscosity can cause slumping of the green body. During the thermolysis, since the wax is removed at an earlier stage, the EVA content in the remaining of the binder will increase,

and viscosity decrease of the binder system due to temperature increase will be compensated to some extent. Figure 4 shows that the lower temperatures the wax is removed, the higher the

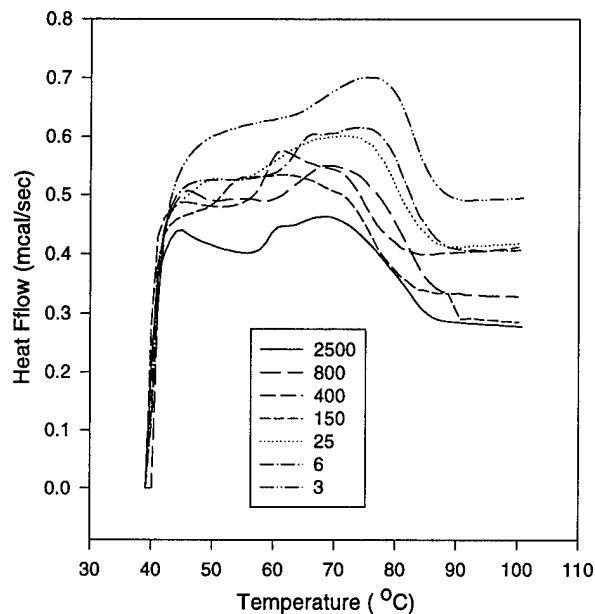


Figure 2: The effect of molecular weight(as represented by the melt index) on the melting endotherm of EVA, containing 28 % vinyl acetate.

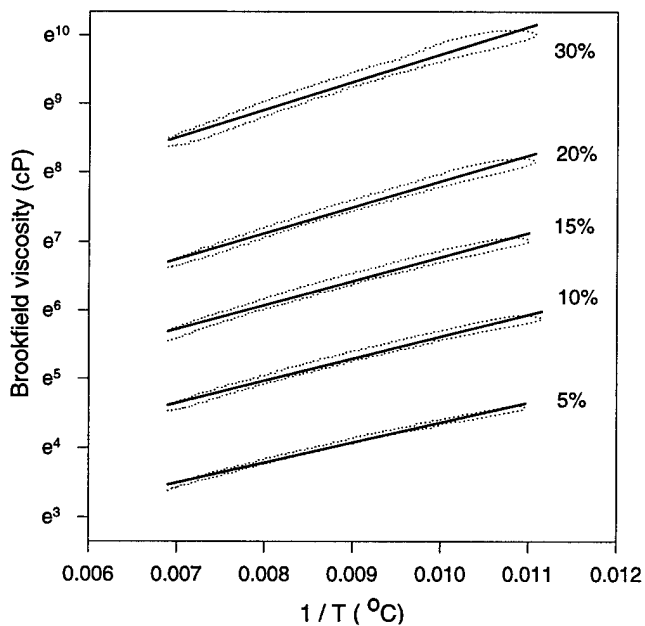


Figure 3: The Arrhenius plot of the viscosity change of the microcrystalline wax - 20 % vinyl acetate containing EVA blends during heating and cooling at a rate of  $1.5^{\circ}\text{C}/\text{min}$ . The increase in the hysteresis is due to the increase in viscosity, which in turn causes high thermal gradients in the sample cup during heating or cooling.

increase in the viscosity of the binder system. The viscosity of the binder system, together with the pore size distribution, will also affect the redistribution of the binder within the green body during the binder removal. It was stated that binder will be removed from larger pores first and it will be redistributed towards the smaller pores due to their high suction potential [2].

The dimensional change of the binder is also an important issue, since it can cause stress build up or warping in the green body. The thermal expansion of microcrystalline wax -EVA (20 % vinyl acetate) blends, which continues till the onset of the melting, is shown in figure 5 in the form of a penetration test. In figure 5, the fact that the penetration becomes more gradual as the EVA content increases reveal that melt strength increases as the EVA content is increased. This is to be expected, and a gradual decrease in the melt strength is desirable during the extrusion of the filament feedstock.

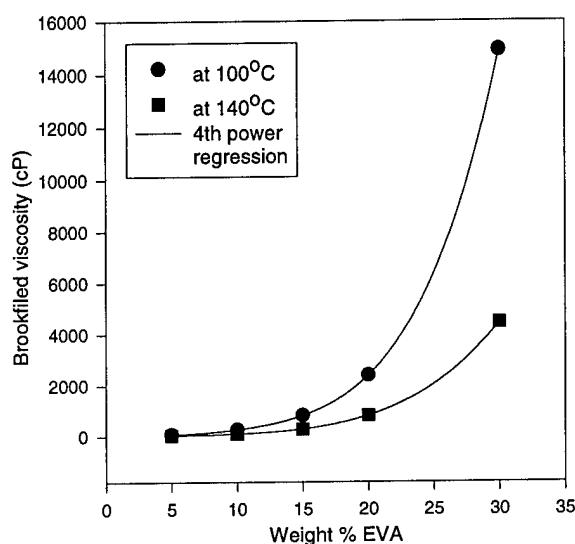


Figure 4: The effect of the EVA content on the viscosity of microcrystalline wax - 20 % vinyl acetate containing EVA blend.

A microstructural evaluation on the fracture surfaces of the filament feedstocks containing 60 % alumina support the previous arguments. The samples contained 24 % microcrystalline wax and 16 % EVA which had 24 % vinyl acetate on average. As shown in figure 6A, the binder that contains the higher molecular weight EVA forms a bulkier network, thus providing better handling strength as compared to the binder with lower molecular weight EVA.

Since all organic additives used in ceramic processing are temporary additives, their removal characteristics from the green body is as important as their functional properties. The pyrolysis characteristics of the binder systems in EVA- wax system developed for FDC is discussed in else where [10].

#### IV. Conclusions

Binder formulation is a complex issue and several factors need to be considered for intelligent formulation. Blends in the wax-EVA system have been evaluated as potential binders to be used

in fused deposition of ceramics. The fact that EVA and wax are available in several different grades make this system an excellent candidate as a potential binder for FDC, and the effect of some of the parameters have been discussed in this study. In order to obtain good handling

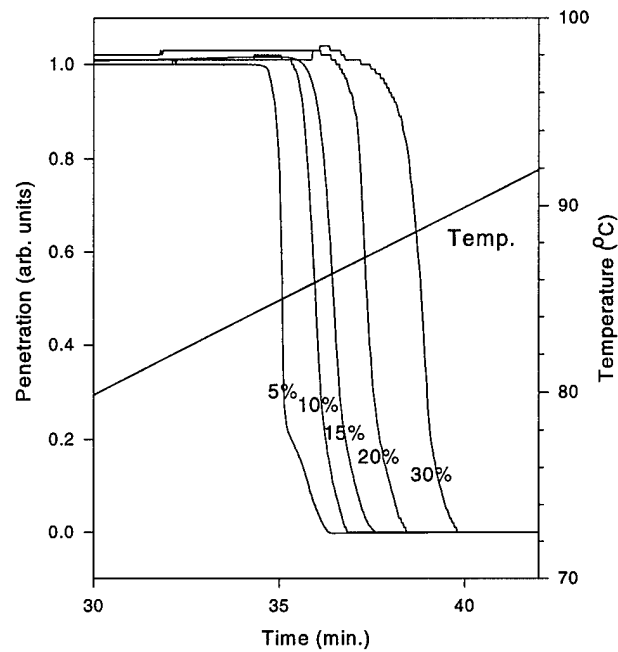


Figure 5: The effect of EVA content on the penetration test result of a microcrystalline wax – 20 % vinyl acetate containing EVA



A



B

Figure 6: Fracture surfaces of (A) alumina green body that contains low molecular weight EVA, (B) alumina green body that contains high molecular weight EVA.

strength, the melting point of the polymer needs to be lower than that of the wax. In this context, it was shown that as the vinyl acetate content in the EVA increases, the melting point of the polymer decreases. By measuring the viscosity as a macroscopic property, it was shown that 20 % vinyl acetate containing EVA is miscible in microcrystalline wax up to, at least, 30 %. Binders used in FDC needs to have low viscosity but their use may cause slumping during binder removal. Thus, thermolysis of wax at low temperature is suggested as a solution. The fact that volumetric change upon heating increases as the EVA content in the binder increases was displayed in the form of a penetration test, which also shows the increase in the melt strength (or softening point) as the EVA content in the binder increases.

Finally, the formulation of a binder system depends not only on the room temperature characteristics, but also on the degradation behavior of the binder. A study on the thermolysis characteristics of the binders in the EVA-wax systems is given in elsewhere [10].

### **Acknowledgment**

The authors would like to thank to Dr. Philip Geil of Dept. of Materials Science and Engineering, UIUC, and to Mr. John Bukowski of Center for Cement Composite Materials, UIUC, for the fruitful discussions of issues related to polymer degradation, and to Jason Carroll of Argonne National Laboratory for producing the test specimens.

This work is funded by the U.S. DOE, Office of Energy Research, Office of Computational and Technology Research.

### **References:**

- 1) M. K. Agarwala et al., "Structural Ceramics by Fused Deposition of Ceramics", Proceedings of the Solid Freeform Fabrication Symposium, 1995, vol. 6, pp. 1-8, ed. by H. L. Marcus, J. J. Beaman, J. W. Barlow, D. L. Bourell, and R. H. Crawford, The University of Texas at Austin, Texas.
- 2) M. J. Cima, J. A. Lewis, and A. D. Devoe, Binder Distribution in Ceramic Greenware During Thermolysis", J. Am. Ceram. Soc., 1989, 72 [7] 1192-99.
- 3) Ceramic Injection Molding, by B. C. Mutsuddy, and R. G. Ford, 1<sup>st</sup> Ed., Chapman & Hall, Cambridge, UK, 1995.
- 4) Polymers and Their Properties: vol.1 Fundamentals of Structure and Mechanics, by J. W. S. Hearle, Ellis Horwood Ltd., England, 1982
- 5) The Chemistry and Technology of Waxes, by A. H. Warth, 2<sup>nd</sup> Ed., Reinhold Publishing Corporation, New York USA, 1956.
- 6) Ethylene: Keystone to the Petrochemical Industry, by L. Kniel, O. Winter, and K. Stork, 2<sup>nd</sup> Ed., Marcel Dekker, Inc., USA, 1980.
- 7) High Polymers: vol. XI. Polyethylene, by R. A. V. Raff, and J. B. Allison, Interscience Publishers, , New York, USA, 1956
- 8) Lecture Notes, Polymer Blends Workshop, by D. J. Lohse et. al., Division of Polymeric Materials: Science and Engineering, ACS Spring Meeting, 1998, Dallas, USA.

- 9) Polymer-Polymer Miscibility, by O. Olabisi, L. M. Robeson, and M. T. Shaw, Academic Press, New York, USA, 1979.
- 10) S. Pekin, A. Zangvil, and W. Ellingson, "A Study on Weight Loss Rate Controlled Binder Removal from Parts Produced by FDC", Proceedings of the Solid Freeform Fabrication Symposium, 1998, to be published, The University of Texas at Austin, Texas.



## Curved Layer LOM of Ceramics and Composites

Donald A. Klosterman, Richard P. Chartoff, Nora R. Osborne, George A. Graves,  
Allan Lightman, Gyoowan Han, Akos Bezeredi, Stan Rodrigues  
Rapid Prototype Development Laboratory  
University of Dayton, Dayton, OH

Sung Pak, Gary Kalmanovich, Leon Dodin, Song Tu  
Helisys, Inc., Torrance, CA

### ABSTRACT

A novel rapid prototyping (RP) technology incorporating a curved layer building style has been developed. The new process, based on Laminated Object Manufacturing (LOM), is suited for efficient fabrication of curved layer structures made from ceramics and fibrous composites. A new LOM machine was developed that uses ceramic tapes and fiber prepregs as a feedstock and outputs a three dimensional green form. The green ceramic is then processed to a seamless, fully dense ceramic structure using traditional ceramic techniques. This report summarizes the new LOM process and necessary hardware. Also reviewed is the development of ceramic preforms and accompanying process technology for net shape fabrication of ceramic matrix composites (CMCs). Compared to making curved objects with the standard flat layer LOM process, the curved process affords the advantages of eliminated stair-step effect, increased build speed, reduced waste, reduced need for decubing, and the ability to maintain continuous fibers in the direction of curvature.

### CURVED LAYER LOM

Based on LOM, a novel RP technology has been developed to provide an enhanced capability for fabricating structural ceramic and composite articles. A comprehensive research program was recently completed that involved materials and process research, machine design, and system software adaptation [1, 2]. The envelope of available RP materials was expanded to include structural composites. In addition, an entirely new building paradigm was implemented: the *curved* layer building style. Instead of being limited to building with flat layers, the LOM machine is now capable of building in a curved-layer manner. The new curved layer LOM process allows continuous fiber composites to maintain fiber continuity in the plane of curvature in order to achieve optimum mechanical performance.

The curved layer LOM process originated from the need to fabricate fiber-reinforced structures containing sloping, curved surfaces, especially thin curved-shell components. An important factor in these structures is maintaining fiber continuity in the curved surfaces. All RP processes are capable of fabricating complex, curved geometries using thin flat layers in combination with post machining of the final part. However, flat

layer RP processes are incapable of addressing the larger geometrical issues involved with fiber composite fabrication, namely fiber orientation and continuity. In addition to the technical incentives for implementing a curved layer build style there is an economic incentive. Such a process will have a favorable cost benefit payoff because of the reduced raw material costs compared to flat layer processes (see Figure 1). This results from a dramatic reduction in the amount of waste material generated during processing.

The curved layer LOM process is illustrated in Figure 2. It begins with production of a matched tool or mandrel for the intended part. The temperature and pressure requirements for this mandrel are not demanding, so it can be made with the standard flat layer LOM process using LOM paper. The finished mandrel is mounted to the flat building platform in the curved layer LOM machine. Sheets of the desired build material are loaded onto a rotatable feed table, picked up with a vacuum chuck, and transported to the mandrel. A flexible thermoforming mechanism laminates each new layer to the curved mandrel with steady, uniform pressure. A laser cuts each layer accounting for the sloped surface. The fiber orientation can be varied from layer to layer by programming the rotatable feed table. The process proceeds one layer at a time until the part is finished. The part is then removed from the mandrel and the excess material is manually stripped away ("decubed"). The advantages of the curved layer process are elimination of stair step effect and improved surface quality, increased build speed, reduced waste, and easier decubing.

Since the new process is a significant departure from the flat layer LOM process, substantial new hardware and software development was necessary. The software issues are summarized in a previous report [3]. New hardware components included the material sheet feeding and rotating mechanism, curved layer bonding apparatus, and curved surface laser cutting. An automatic sheet feeding system rather than a roll feed was desired for two main reasons. First, many commercially available advanced materials, such as prepregs (preimpregnated fiber preforms) and ceramic tapes, are stiff at room temperature and/or available only in sheet form. Second, there is more material waste associated with the automatic roll feed system. Although this waste may be affordable when building LOM-paper parts, efficient use of material is critical when working with costly feedstocks such as fibrous composites and ceramics.

The curved layer bonding mechanism is a flexible, resistively heated pad that is backed with a silicone rubber frame (Figure 3). The frame consists of a top and bottom horizontal surface connected by vertical walls. The placement of the internal walls was custom designed to provide even pressure to the curved layer parts under consideration in this study. Vacuum cups protrude vertically through the rubber frame in order to pick up a new material layer. A single layer is held just underneath the heating surface as the entire assembly is moved over the mandrel via a rail system. The new layer is laminated by elevating the build platform up into the thermoformer and holding it in contact for about one minute. The bonding pressure is approximately 2 - 10 psi, which is adequate for laminating typical tapes and prepregs. Figure 4 shows a ceramic part that has been layed-up on a LOM paper tool.

Cutting curved layer parts required new computer algorithms for coordinating simultaneous control of the laser beam in the X, Y, and Z directions. In a conventional LOM machine, laser cutting is performed using a plotter system that transports a mirror and focusing lens over the X-Y envelope. The distance between the focusing lens and the top of the part is adjusted only once after placing each new layer, ensuring that the laser focus is maintained on the horizontal part surface. With the curved layer LOM machine, the build platform must be translated up and down dynamically in order to maintain the laser focus on the curved surface. An eight axis motion control card and new software algorithms were necessary to control this motion smoothly and quickly. A 225-Watt Diamond (pulsed) CO<sub>2</sub> laser was installed on the machine and proved effective in cutting SiC fibers and ceramic tapes. The quality of the fiber cuts was not as good as that obtained with a copper vapor laser as previously reported [1, 4], but the Diamond laser is more reliable, smaller, and less expensive than the copper vapor laser.

### CMC PREFORM DEVELOPMENT FOR LOM

SiC/SiC was used as a focus "model" material system for demonstrating curved layer, net shape CMC fabrication. A novel approach was used to fabricate CMCs that involved lay-up of separate, alternating layers of ceramic tape and fiber prepreg [1]. Green parts containing this alternating layer architecture were made using LOM, subsequently pyrolyzed, and densified through reaction bonding.

Fiber prepregs were fabricated with unidirectional SiC fiber tows (Nicalon<sup>TM</sup>, Dow Corning, carbon coated grade) and a furfural-phenolic thermosetting resin (FurCarb<sup>®</sup> UP440, QO Chemicals, Inc). The furfural resin served a dual role: as a binder and adhesive during the part fabrication and as a carbon source during the subsequent reaction bonding process. Descriptions of the reaction bonding process and monolithic SiC tapes are given in a previous report [1]. Alternating layers of the fiber prepreg and ceramic tape were delivered to the LOM machine as one single sheet, referred to as a "tape-preg" [1]. Tape-pregs, made by pre-adhering a prepreg layer to a tape layer, were stiff, non-tacky, and board like at room temperature, becoming soft and pliable at higher temperatures (130°C). The tape-preg contained approximately 25% fibers by weight, and overall it proved to be a robust sheet material suitable for the LOM process.

The advantages of the alternating layer technique are the relative ease of preparation of the preforms, elimination of fiber abrasion from the ceramic particles, reasonably high fiber volume fraction in the final CMC, and low cost resin binder. The tape-preg embodies several important characteristics of other commercially available CMC preforms. Key among these characteristics is the use of a fiber prepreg that contains a thermosetting, ceramic precursor resin. Based on this similarity, it is anticipated that LOM will accommodate other commercially available CMC preforms as easily as the "tape-preg".

Several parts were manufactured with curved layer LOM using SiC/SiC tape-pregs. Acceptable process parameters (e.g., temperature, pressure, time) were

determined through initial experimentation with a manual operation, mock-up system at the University of Dayton [4], and finally through operation of the actual curved layer LOM machine. A bonding time of 1 minute at 130-150°C was adequate for the tape-pregs; the bonding pressure was estimated to be 5 psi. Several curved layer parts were produced and successfully decubed. These green composites were not fully cured, but they were stiff and self-supporting. Curved layer LOM was also used to fabricate monolithic SiC parts by laminating only the ceramic tapes (no fibers). The temperature in this case was 90°C, and butanol was sprayed between the layers to act as a tackifier. Thus, the LOM process was successfully used to produce various types of green ceramic forms that were robust and handleable. Additional processing steps were required to convert them to full density.

## POST-LOM PROCESSING

It is not possible to execute all of the necessary ceramic processing steps within the LOM machine. The LOM machine is used only to produce the green form. Thus, post processing steps are needed. The overall process used for SiC/SiC is illustrated in Figure 5.

The first post-processing step combines binder burnout, pyrolysis, and pressing into a single operation. Although green LOM parts are sufficiently laminated to survive LOM processing, decubing, and handling, they require additional layer consolidation prior to the final densification step. Pressure must be applied during binder burnout and pyrolysis to counteract delamination and bloating that result from several sources such as outgassing and relaxation of residual stresses imparted during the lamination step. In order to maintain the complex geometry of green parts during pressure application, a technique involving quasi-isostatic powder pressing was developed.

Green parts from the LOM process were placed in a cylindrical chamber which was subsequently back filled with powder and fitted with a ram. Monolithic SiC was used as the powder medium in the chamber. For LOM parts that could be fitted with a porous Teflon bag, silica was used as the powder medium (i.e., sand pressing). A heated, programmable, uniaxial press was used to apply a heated pressure cycle to the enclosed chamber. The powder medium enabled pressure to be evenly distributed while allowing volatile degradation products to escape through a permeable bed. The various SiC/SiC and monolithic SiC parts were pressed at 60 psi and 30 psi, respectively, and at temperatures up to 325°C. Shrinkage of SiC/SiC and monolithic SiC parts during this step was  $7\% \pm 2\%$  and  $5\% \pm 2\%$  respectively, in the z direction (parallel to press movement), and zero in other directions. Appropriate scaling of the computer graphic file for part building in the z direction by 7% or 5% will compensate for this dimensional change due to compression.

An additional, freestanding binder burnout and pyrolysis step up to 700°C in argon was needed to achieve full chemical conversion of the organic resins to carbon. Because most of the total expected binder burnout and resin pyrolysis occurred during the powder pressing step, no part damage or shrinkage accrued during freestanding burnout.

The resulting porous structures were densified through reaction bonding. The final parts are shown in Figure 6.

The microstructure of flat LOM SiC/SiC panels prior to pyrolysis illustrates the alternating tape/fiber layer arrangement, excellent compaction, and minimal porosity (Figure 7, left). The photomicrograph of a specimen that has undergone reaction bonding indicates that there is some porosity, although much of this may be attributable to particle and fiber pull-out that occurred when the specimen was polished. It is clear, however, that the flatness, continuity, and integrity of the layers have been well maintained. The level of porosity is comparable to that of commercially available CMC systems.

Upon closer examination of the LOM SiC/SiC microstructure, it is evident that although the fibers are intact, there is fiber damage particularly at the fiber interface (Figure 8). This damage occurs as a result of the instability of Nicalon fibers at the temperatures encountered in the reaction bonding process (up to 1600°C). There are several potential solutions to this problem, such as developing superior fiber coatings and using silicon alloys that will infiltrate the composite at lower temperatures. However, the physical mating of the layers is intimate and the overall infiltration efficiency is quite good relative to commercial CMC systems.

Testing of final SiC/SiC specimens in four-point bend was not possible due to damage to specimens during cutting. The brittle behavior of the samples was expected, since the fiber coating problem has not been solved. The major result to report here is that the entire process, starting with fiber preforms and ending with a near net shape, densified part, has been fully demonstrated. Densified samples such as the flame holder and body armor are handleable, and photomicrographs illustrate that the microstructure compares quite favorably to commercial CMC systems. Further work with other material systems is being carried out to fully characterize and assess the overall process reproducibility and accuracy.

## SUMMARY AND CONCLUSIONS

The feasibility of using LOM for net shape, freeform fabrication of monolithic ceramics, continuous fiber CMCs, and curved layer composites has been fully demonstrated. Monolithic SiC and continuous fiber SiC/SiC were used as demonstration material systems. Commonly available preforms such as ceramic tapes and fiber preregs are entirely suitable as feedstocks to the process. The overall process methodology involves use of a LOM machine to produce dimensionally accurate green forms directly from CAD files, followed by post processing steps to bring the part to full density. Both flat layer and curved layer laminates can be built with this technology. The curved layer paradigm is critically important for fabricating continuous fiber, curved shell composites in order to maintain fiber continuity. Curved layer SiC/SiC composites were produced with good microstructure, although mechanical properties are not expected to be as high as commercial CMC systems due to ineffective fiber coatings. Inherent to the process of making the CMCs was the production of a precursor composite structure, consisting

essentially of a polymer matrix composite (PMC), which was subsequently converted to a CMC. Thus, the results demonstrate that PMC fabrication is also viable with the new LOM process. This also was demonstrated in our previous LOM processing studies using epoxy resin prepregs [5].

Although the parameters of the various processing steps are expected to change with different materials systems, the overall LOM process is expected to be generically applicable to a wide range of high performance materials. Thus, an entirely new fabrication capability is now available for designers and manufacturers. The new LOM process holds promise for lowering the cost of fabricating monolithic ceramic, CMC, and polymer matrix composite parts by virtue of its automation, which reduces fabrication time and eliminates the need for tooling. The process can best be applied by industry as a product development tool for fabricating molds, tools, or testable prototypes, or used directly for small lot production.

This is an ongoing effort. The immediate following steps are to improve the laminator design to achieve higher pressures and more flexibility, switch to working with commercially available CMC material systems, further investigate lasers that combine the advantages of the copper vapor laser and Diamond CO<sub>2</sub> laser, and investigate low cost tooling materials which would provide more robust mandrels for the curved layer process than LOM paper. Also, the laminator size envelope will be expanded to near or equal to that of a standard LOM2030 machine (32" x 22").

## REFERENCES

1. Klosterman, D., R. Chartoff, N. Osborne, G. Graves, "Automated Fabrication of Monolithic and Ceramic Matrix Composites via Laminated Object Manufacturing (LOM)," *Solid Freeform Fabrication Proceedings*, University of Texas at Austin, Austin, TX, Sept. 1997, pp.537-549.
2. Klosterman, D., R. Chartoff, G. Graves, N. Osborne, A. Lightman, G. Han, A. Bezeredi, S. Rodrigues, "Automated Fabrication of Monolithic Ceramics and Ceramic Matrix Composites (CMCs) Using a Novel Rapid Prototyping Method," *Proceedings of the 21<sup>st</sup> Annual Conference on Composites, Advanced Ceramics, Materials, and Structures*, The American Ceramic Society, Cocoa Beach, FL, Jan., 1998.
3. Kalmanovich, G., "'Curved-Layer' Laminated Object Manufacturing," *Solid Freeform Fabrication Proceedings*, University of Texas at Austin, Austin, TX, Sept. 1996, pp.273-279.
4. Lightman, A., G. Han, "Laser Cutting of Ceramic Composite Layers," *Solid Freeform Fabrication Proceedings*, University of Texas at Austin, Austin, TX, Sept. 1996, pp.291-298.
5. Klosterman, D., B. Priore, R. Chartoff, "Laminated Object Manufacturing of Polymer Matrix Composites," 7<sup>th</sup> International Conference on Rapid Prototyping, University of Dayton and Stanford University, San Francisco, CA, March 31-April 3, 1997, pp. 283-292.

ILLUSTRATIONS

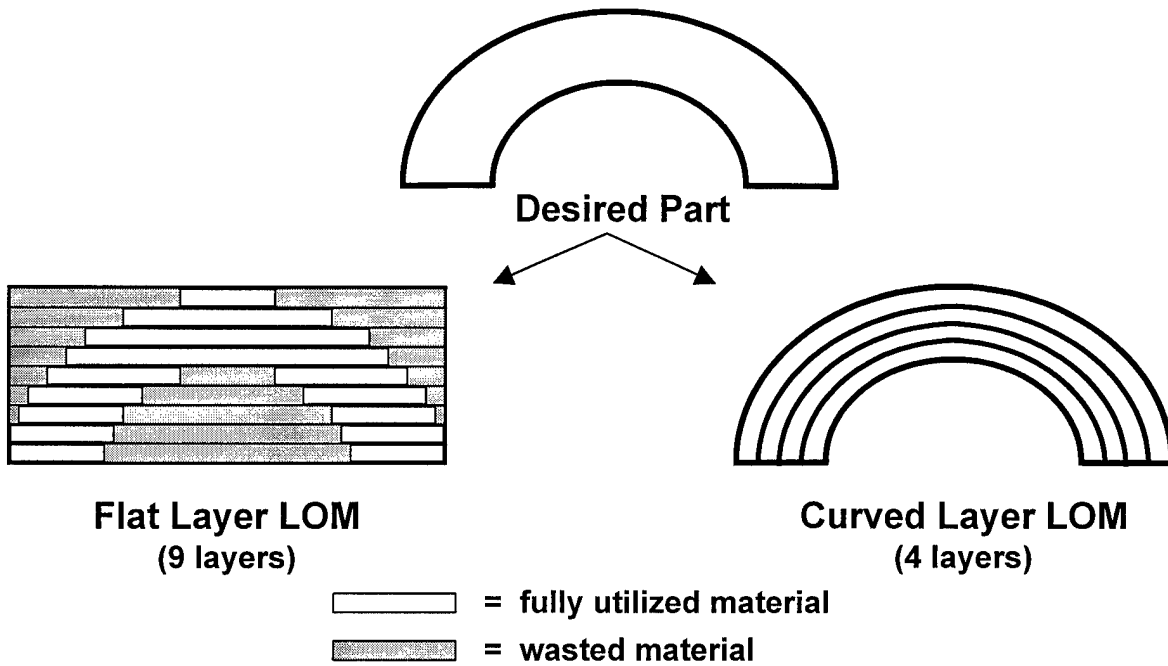


**Figure 1:** comparison of the flat layer and curved layer LOM processes for building a curved shell. Due to the mode of building, the curved layer process will require fewer layers of material to build the same part.

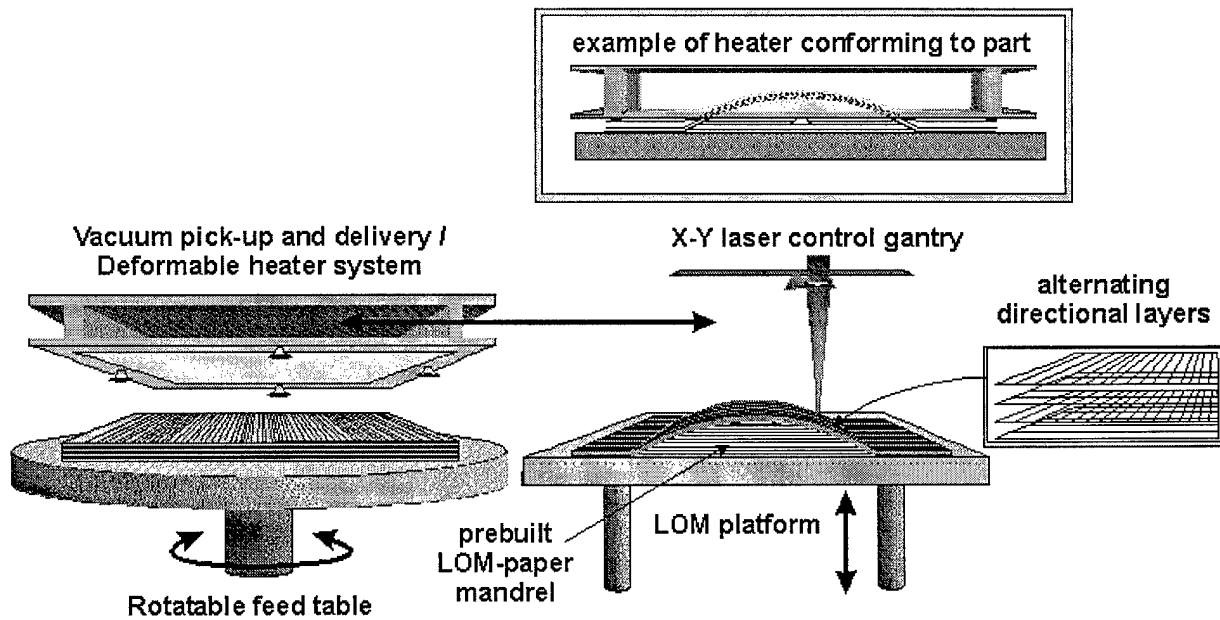


**Figure 2:** curved layer LOM process schematic.

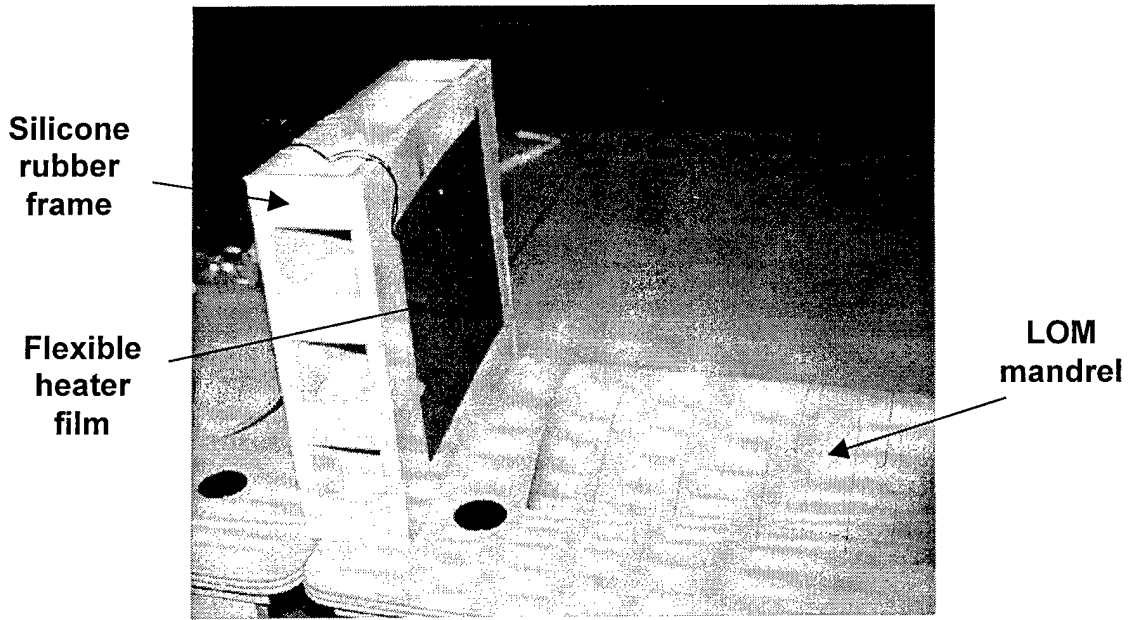


**Figure 3:** curved layer bonding apparatus (prior to installation in LOM machine). The vacuum cups, which protrude through the structure normal to the heater surface, are not installed on the unit in this picture.

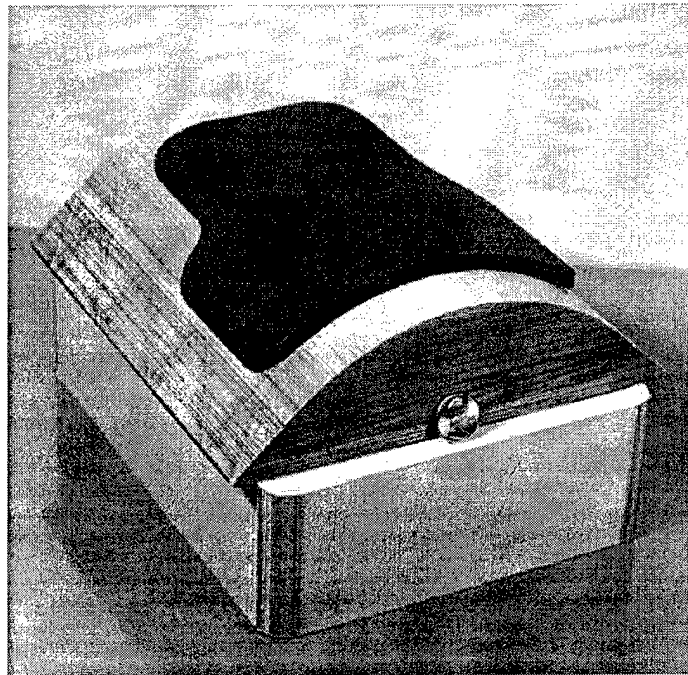


**Figure 4:** curved layer, monolithic SiC body armor panel, immediately after LOM processing. The piece has been fully decubed and placed back on the LOM-paper mandrel for illustration. Notice the smooth surface and lack of stair steps.

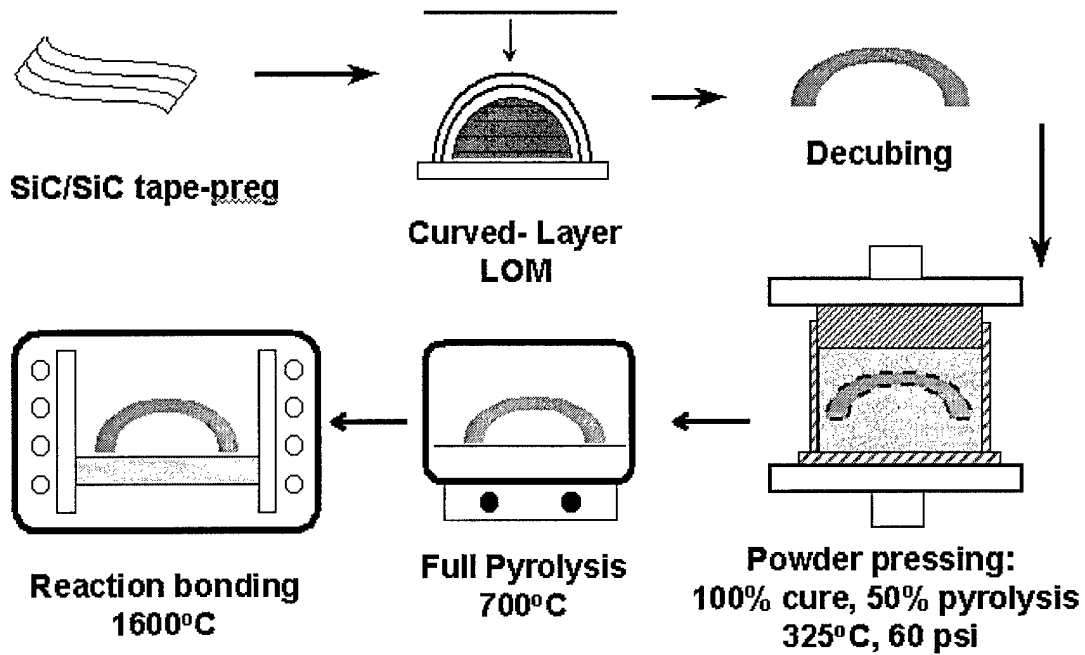


**Figure 5:** overall process flow chart for fabricating net shape CMCs with curved layer LOM process.

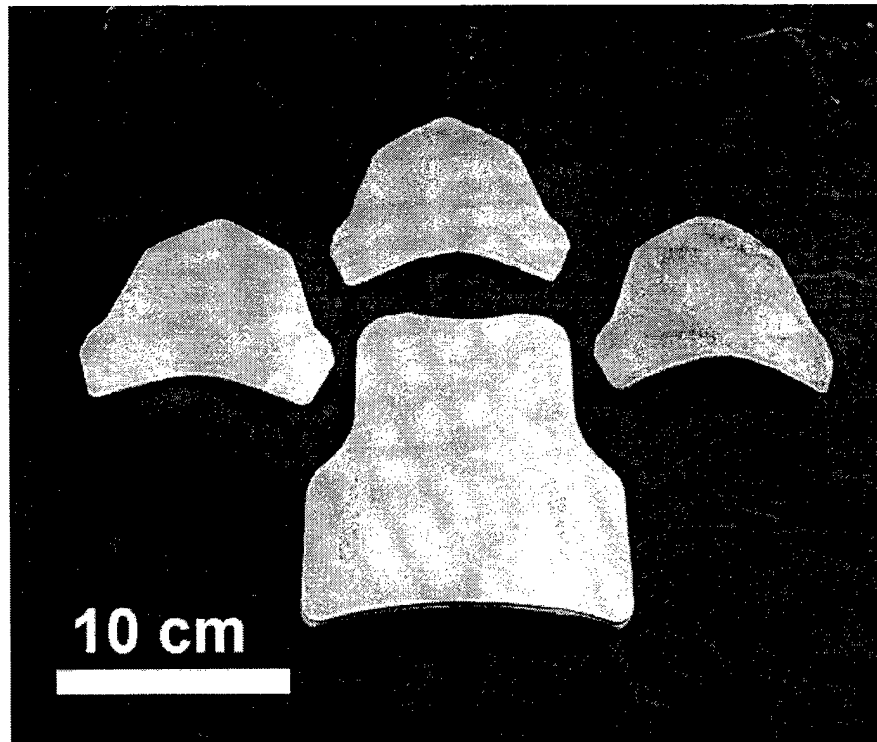


**Figure 6:** Reaction bonded SiC parts made with curved layer LOM process: three SiC/SiC aircraft engine flame holders of various curvature, and one small-scale monolithic SiC body armor panel.

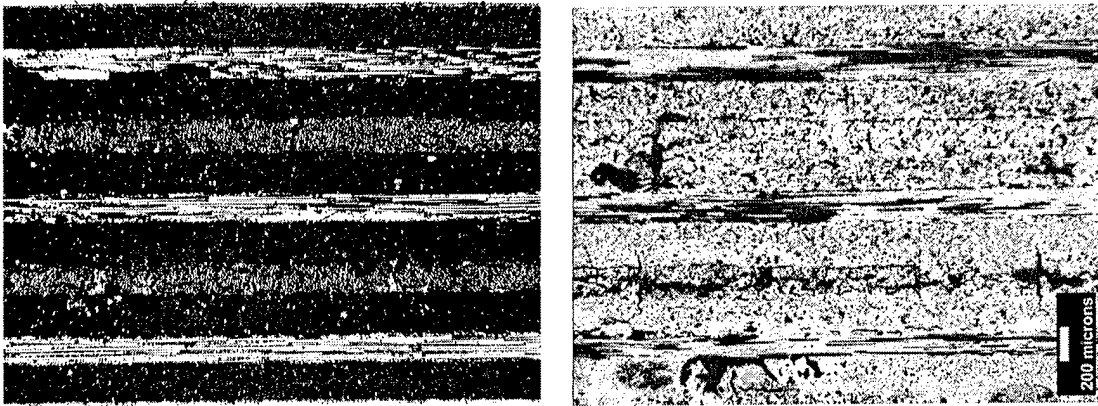


**Figure 7:** Polished cross section of (left) eleven-layer SiC/SiC LOM composite prior to pyrolysis, and (right) after pyrolysis and reaction bonding. From top to bottom the layers are: ceramic tape, 90° fiber layer, ceramic tape, 0° fiber layer, ceramic tape, etc.

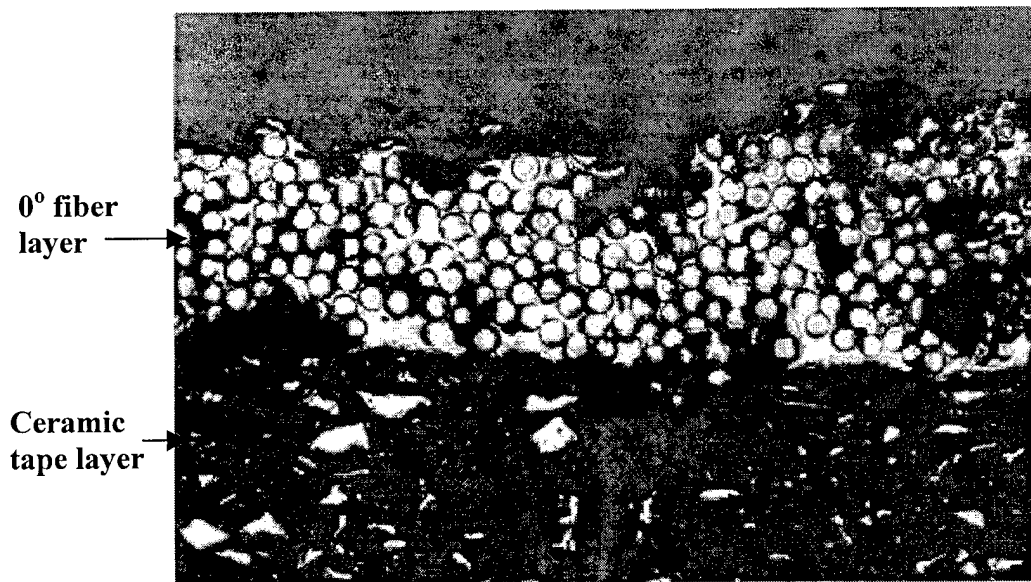


**Figure 8:** Photomicrograph of reaction bonded SiC/SiC microstructure showing mating of various layers, infiltration efficiency, and fiber condition.

# Virtual Simulation for Multi-material LM Process

Dan Qiu<sup>1</sup>, Noshir A. Langrana<sup>1</sup>, Stephen C. Danforth<sup>2</sup>,  
Ahmad Safari<sup>2</sup>, Mohsen Jafari<sup>3</sup>.

<sup>1</sup>Mechanical & Aerospace Engineering, <sup>2</sup>Ceramic & Materials Engineering, <sup>3</sup>Industrial Engineering, Rutgers - The State University of New Jersey, Piscataway, NJ, 08854-8058

## 1. Abstract

In an ONR funded MURI program, to improve quality of multi-material parts, we've been developing an advanced computer simulation for the multi-material layered manufacturing (LM) process. The CAD models and their .stl files are created using the commercially available software such as I-DEAS and ProE. Using this information, one tool path file per material is generated. Our file preparation algorithm, systematically, layer by layer, integrates all tool path files into one multi-material tool path file. The results of the multi-material tool path are graphically visualized using the simulation algorithm (written in C++ & SGI OpenGL). From a virtual simulation, we can check the LM process, and make the best selection of tool path parameters afterwards. After several trials from design to simulation, if the simulation result is acceptable, the real manufacturing can be started. And the part's quality should be better than a part manufactured without running simulation in advance. This paper will represent new studies on using real roadshapes to get more realistic simulation results. Many parts have been successfully simulated using our method.

## 2. Background

Layered Manufacturing (LM) technologies have been developed rapidly in the past decade. LM has significant differences from traditional fabrication technologies. LM refers to the process of fabricating three dimensional objects from CAD-generated solid models layer by layer [1]. A computer generated model of a part usually contains surface information. It is imported into a slicing program which mathematically slices the model into sequential horizontal layers, and the hardware specific toolpath for each layer is created. This toolpath file then is downloaded into the LM hardware, which fabricates the model layer by layer, following the specified path. It is different from traditional manufacturing in the sense that the part is produced by adding materials rather than removing materials. Using this technology, parts with a single (non support) material have been fabricated. Currently, there are mainly single component material LM technologies available. A representative listm [2] includes: 3D System's Stereolithography Apparatus(SLA) series, Stratasys's Fused Deposition Modeling Process(FDM), Sanders, and 3D Printing. Although those LM technologies may have multiple material options before starting the manufacturing process, they can only handle one component material during one building process. They are not true multi-material LM process.

Multi-material LM refers to a process of fabricating a part consisting of more than one material from a three dimensional CAD model layer by layer. A multi-material

CAD model consists of several different material blocks connected by interface boundaries. The LM system under development should be able to generate CAD model, slicing file, toolpath file and fabricate a multi-material part in a manufacturing process. The development of our multi-material LM system is still at the research stage. On the software development side, the CAD/CAM group at the university of Michigan has been investigating multi-material LM issues [3]. They are developing an integrated software system for LM process planning, which includes solid model building, part orientation, support structure generation, slicing, and path planning for multi-material solid models. In a Solid Model Builder module, the multi-material object will be represented by gray scale images, where a particular gray value is assigned to each individual material or it may also indicate material property such as density. There are several multi-material LM technologies under development currently. In Sandia National Laboratories, Robocasting technology, a freeform fabrication technique for dense ceramics and composites that is based on layer-wise deposition of highly load colloidal slurries, is being developed [7]. Mold Shape Deposition Manufacturing technology in Stanford University is a Solid Freeform Fabrication technique for producing complex fugitive wax molds which can fabricate multi-material parts [8].

### 3. Objective

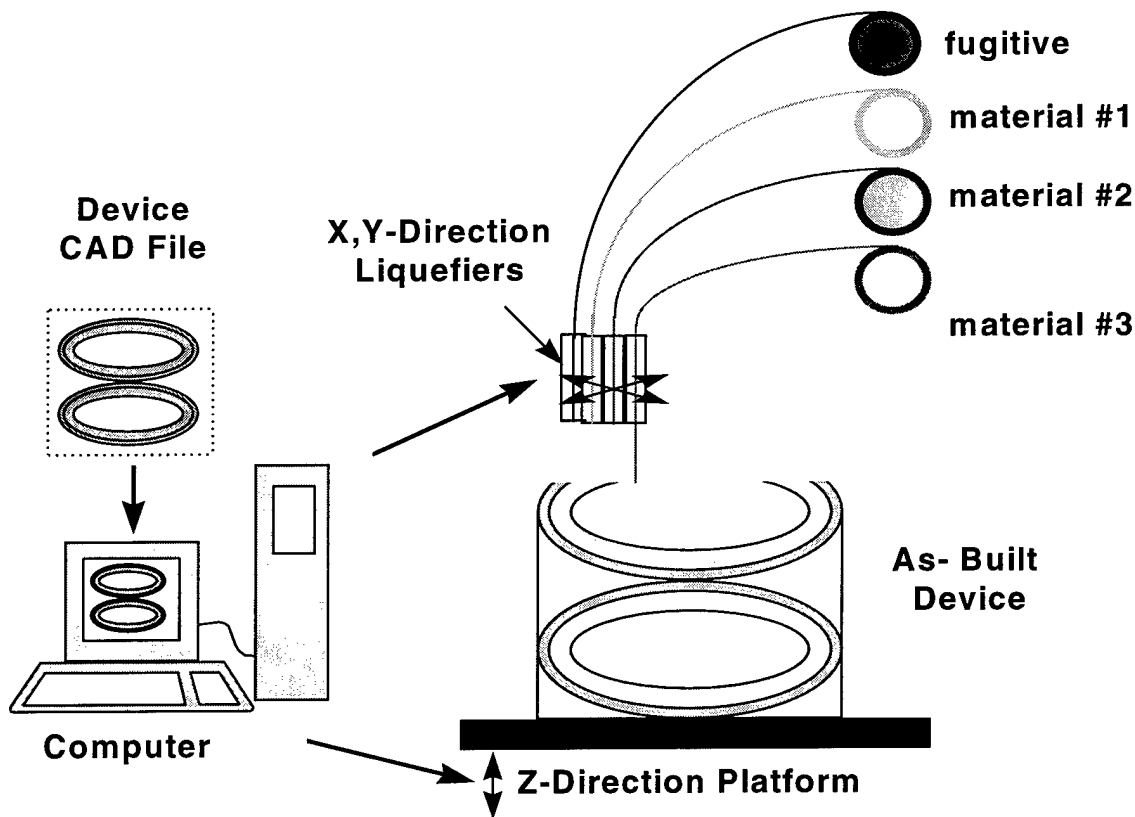


Fig 1 MURI multi-material LM system

Currently, at Rutgers University, under an ONR(Office of Navy Research) funded MURI program[4], An Intelligent Layered Manufacturing (LM) system (Fig 1) for fabrication of multiphase electromechanical parts has been developed. This program will require development of design and construction of an intelligent multi-material LM system, processing science for multi-material LM, CAD based design and manufacture of multi-phase electromechanical components. The intelligent multi-material LM system should include a high quality multi-material layered manufacturing machine (hardware), and a CAD based intelligent multi-material LM software system. In the recent past, the MURI hardware as well as corresponding software has been developed and several parts have been successfully fabricated.

To achieve the development of a multi-material LM software system, one of the necessary requirements is to perform the virtual simulation of the multi-material LM process. This paper discusses the implementation of the virtual LM simulation and its results. The objective of this study is to develop an advanced computer simulation for the multi-material LM process. In the present program, quality of a part is considered to be very important. We use the simulation to understand, and check the LM process before the real manufacturing. It is one of the steps to improve parts' quality. With computer simulation, it's possible to go through multiple design-simulation iterations within a short time, which can substantially improve the LM part quality.

## **4. Method**

The simulation package under development includes two main portions. The first one is a file preparation algorithm to generate the single multi-material toolpath file from multiple CAD solid models. The second one is the graphical simulation algorithm. The schematic flow and the simulation software development has been described in [5].

### **4.1. File preparation**

To perform a realistic simulation of a multi-material part fabrication, a multi-material toolpath file is required. The simulation process starts from a CAD model. Commercially available software such as I-DEAS or Pro-E can be used to create CAD models which represent different materials in a multi-material model. For each material a separate .stl file is created, while keeping its space location. These .stl files are then sliced and a toolpath is generated individually for each of them. Currently, we use QuickSlice software to create one toolpath file per material. This information is then used as the input to an in house file merge algorithm, which systematically, layer by layer, integrates all tool path build files into one multi-material toolpath build file.

### **4.2. Graphical simulation algorithm**

The simulation package includes an in house graphical simulation algorithm (written in C++ and OpenGL). The algorithm extracts critical information from a multi-

material toolpath build file, and utilizes SGI OpenGL to run the simulation, as it provides necessary graphical tools: coloring & shading, solid modeling, 3D viewing, and animation tools. The simulation opens a graphical window, specifies a color set for all materials, and starts the “material deposition” process along the tool path on the starting layer. When one material is finished, the simulation runs the “material deposition” process for other materials on the same layer. When one layer is finished, a new layer will be “deposited” on top of the finished layer, until all the layers of the part are stacked sequentially. That’s the graphical stacking process for multi-material parts, which simulates the physical multi-material LM process.

The shape and size of the deposited road in LM process using a nozzle is different from the nozzle cross sectional shape and size. This is due to the flow properties of the material as well as the shearing action of that translating nozzle. Considering a circular cross sectional nozzle, with a low viscosity and high surface tension material as wax, the road shape will remain close to a sphere. Where as, with high viscosity and low surface tension material such as ceramic or metal powder filled polymer, the road shape will be flatter. In addition, the shear action of the nozzle, and the adjacent road will alter the shape of the road. This implies that the virtual simulation should account for different road shapes for different materials. The current simulation have spherical roadshape as well as roadshapes obtained experimentally with specific toolpath parameters .

## 5. Previous Study

Several critical parameters for a build file were investigated [5]. They include roadwidth, offset (air gap between parallel roads), layer thickness, and raster angle. These parameters have different sensitivities in void creation or elimination. An idealized roadshape of sphere was considered. The relationships between parameters and void size have been studied, results can be summarized as follows:

1. Roadwidth is a sensitive parameter for sub-perimeter void size. However, the voids' sizes don't necessarily decrease when roadwidth decreases. The sub-perimeter void size depends on if the width in the perpendicular direction to the vector direction can be divided equally by the roadwidth.
2. Sub-parameter void size is directly related to boundary offset values. Similarly, vector road void size is directly related to vector offset size, But the vector angle has no apparent relationship with void size.
3. Slice thickness is not a sensitive parameter. But if the slice thickness is too big, there will be voids between layers.

In a parallel study, video microscopy [6] of the deposited road was performed. This information is utilized on the same experimental part to understand void & defect creation or elimination.

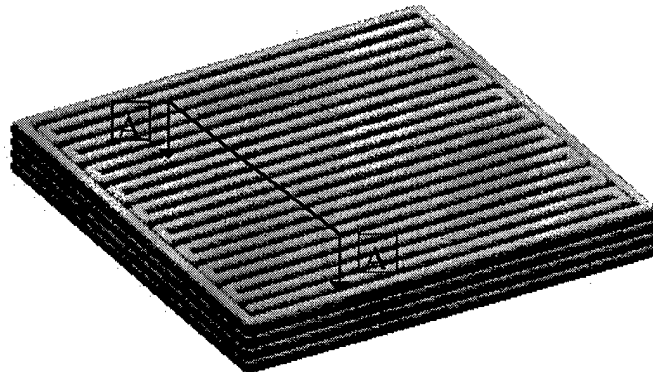
## 6. Simulation using Physical Roadshape

The above parametric study was on a spherical or idealized roadshape. To check a specified LM process in advance, a realistic way is to run the simulation using the actual roadshape, thus the simulation result will be more accurate, and the quantification of

voids will be more meaningful. The virtual simulation will be run before each fabrication to make adjustments in advance. The adjustments based on that result will also improve part's quality.

On the other hand, we use video microscopy to observe the real roadshape for a parameter-specified LM process [6]. The video microscopy uses CCD camera to capture the real time images of the experimental LM process. The actual roadshape can be identified from those images. HImage++ 97 has been utilized to quantify the void information.

To have a good understanding of the effect that toolpath parameters have on quality of the LM parts, a simple rectangular part (Fig 2) has been considered. The result on the idealized spherical roadshape [5] is shown here for comparison with real roadshape. The video microscopy data on PZT (Fig 3) were quantified and used in the simulation. The results of the deposited road at section A-A (Fig 2) for -4, 0, +4 mil offset were developed. Both the spherical roadshape and truncated ellipsoidal roads were used.



**Specifications:**

Roadwidth: 20 mil  
Offset: +4, 0, -4 mil  
Material: PZT

Nozzel size: 15 mil  
Slice thickness: 10 mil

Fig 2: A rectangular part with 0 degree Vector Angle

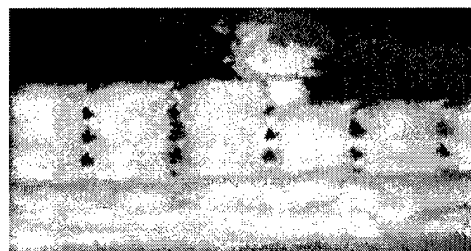


Fig 3 : Videomicroscopy image of a PZT rectangular part of Fig 2 (offset: 0 mil)

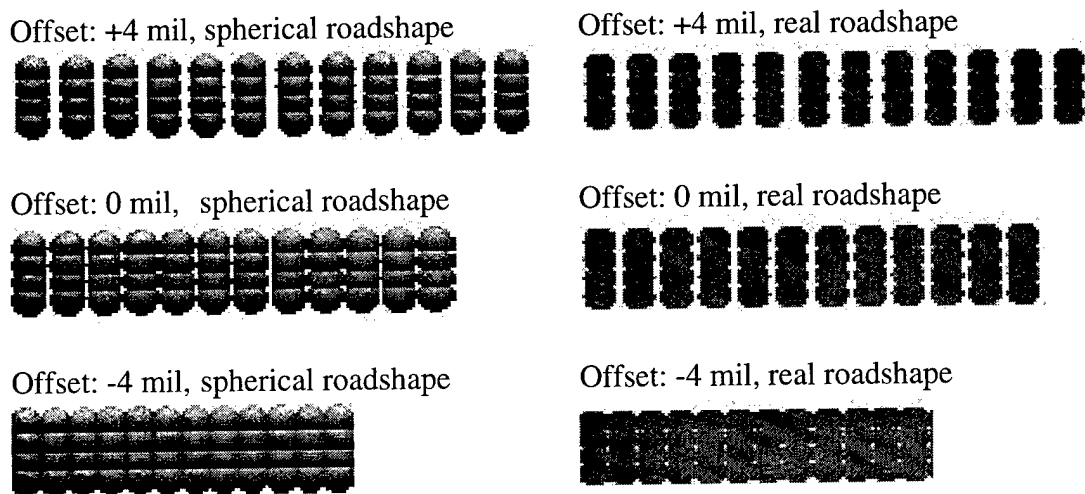


Fig 4: A-A cross section simulation images of this part.

The images of twelve deposited roads for each vector offset and each roadshape in the simulation are shown graphically (Fig 4). As the offset size changes from +4 mil to -4 mil, the width of twelve deposited roads reduces significantly. The deposited part is more dense.

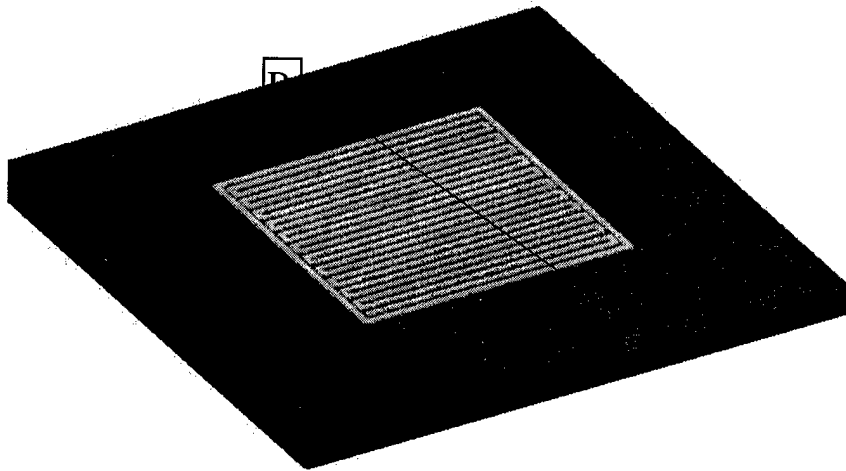
In the actual building experiment (Fig 3), to capture the voids between roads, the boundary was not build. The returns of the roads were kept, that's why the roadwidth in the video microscopy picture appears double size of the simulation roadwidth except at the nozzle tip(Fig 3).

As can be seen from the above images, the void shape and size for different roadshape are different. Using HImage++97 software, we quantified the void size. For 0 mil offset, the average void area in the video microscopy image (Fig 3) is  $40 \text{ mil}^2$ . The average void area from the corresponding simulation image (Fig 4, offset: 0 mil) using spherical roadshape is  $15 \text{ mil}^2$ , and for real roadshape is  $36 \text{ mil}^2$  (Fig 4). The simulation result using physical roadshape is closer to the real part's result.

## 7. Simulation of a two-material part

One of the desired goals of simulation software is to understand the interaction of materials in the LM process. The video microscopy will provide the needed data on the roadshape for each material. Utilizing that information, specifying roadshape specific to each material, will result in a more accurate simulation of multi-material parts.

A two material part was designed and simulated (Fig5). This part consists of two materials: PZT and fugitive wax phase. From a video microscopy experiment with the specifications, we captured the roadshapes for those two materials. The road shape for PZT is flatter and the roadshape for wax is almost spherical (Fig 6).



**Specifications:**      Roadwidth: 20 mil      Nozzel size: 15 mil  
                                  Slice thickness: 10 mil      Offset (for wax): -4 mil  
                                  Offset (for PZT): -4 mil

Fig 5 : A two material part (Wax: 1" x 1", PZT: 0.5" x 0.5")

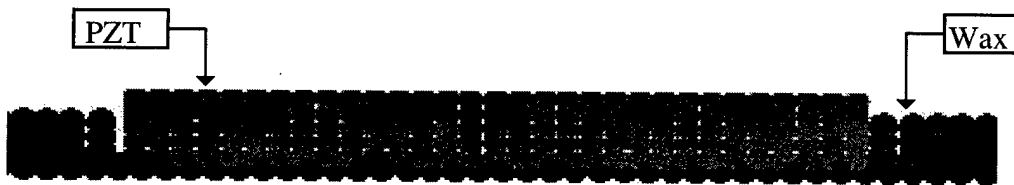


Fig 6 : The B-B cross section view of Fig 5 (amplified)



Fig 7 : Same view as Fig 6 with different offset for wax

The simulation of PZT-wax part demonstrate the potential applicability of the system (Figures 6 and 7). With -4 mil offset, each material in this part is almost void free. But when the interface offset between two adjacent materials is 0 mil, the interface void existed (Figure 6). Whereas the interface void vanished (Figure 7) when the interface offset changed to -4 mil. This experiment shows that in multi-material LM, not only the offset in each material, but also the interface offset between every two adjacent materials should be investigated.

As more information on the road shapes and the material interaction become available, the current simulation will become more intelligent.

## 8. Conclusion

A Multi-material Virtual Simulation System has been developed for LM. A variety of parts with interconnectivity have been simulated using roadshape information from videomicroscopy experiments. This study demonstrates that multi-material layered manufacturing simulationss can provide accurate and detailed information. Based on this information, we can make selections of part's parameters and make adjustments to the fabricating environment to get high quality parts.

## 9. Acknowledgments

This research reported here has been performed towards the partial fulfillment of the thesis of the first author. The authors would like to thank the Office of Naval Research (ONR) Drs. R.Wachter and G.Spanos, for the financial support under ONR MURI grant, #N00014-96-1-1175.

## 10. References

1. M. Agarwala, A. Bandyopadhyay, R. van Weeren, V. Jamalabad, P. Whalen, N. A. Langrana, A. Safari,, S. C. Danforth, "Fused Deposition of Ceramics", J. Rapid Prototyping, Vol. 2, 4, pp. 4-19, (1996).
2. X. Yan, P. Gu, "A Review of Rapid Prototyping Technologies and Systems", Computer-Aided Design, Vol. 28, No. 4, pp. 307-318, 1996.
3. A. L. Marsan, S. Allen, P. Kulkarni, and D. Dutta, "An Integrated Software System for Process Planning for layered Manufacturing", Proceedings of the Solid Freeform Fabrication Symposium, pp. 661-668, The University of Texas at Austin, Austin, TX, August 1997.
4. Office of Naval Research (ONR), # N00014-96-1-1175 Multidisciplinary Research Program of the Univ. Research Initiative (MURI): An Intelligent CAD Based System.
5. D. Qiu, N. Langrana, S. C. Danforth, A. Safari, M. Jafari, "Development of Multi-material Virtual Layered Manufacturing Simulation", the Proceedings of Third Pacific Rim International Conference on Advanced Materials and Processing, Hawaii, July, 1998.
6. E. Bossett, McCuiston, N. Langrana, Rangarajan, Venkataraman, S. C. Danforth, A. Safari, "Real Time Video Mcroscopy for the Fused Deposition Method", to be presented at the Ninth Solid Freeform Fabrication Symposium, August, 1998.
7. J. Cesarano III, B. King, H. Denham, "Recent Developments in Robocasting of Ceramics and Multi-material Deposition", to be presented at the Ninth Solid Freeform Fabrication Symposium, August, 1998.
8. A. Cooper, S. Kang, J. Kietzman, Fritz, "Automated Fabrication of Complex Molded Parts Using Mold SDM", to be presented at the Ninth Solid Freeform Fabrication Symposium, August, 1998.

# Features in Layered Manufacturing of Heterogeneous Objects

Xiaoping Qian  
xpqian@engin.umich.edu

Debasish Dutta  
dutta@engin.umich.edu

Dept. of Mechanical Engineering and Applied Mechanics  
The University of Michigan  
Ann Arbor, MI 48109-2125

## ABSTRACT

The usage of features in computer aided design and manufacturing has increased significantly over the last decade. By and large, all such features are geometric (form features).

In this paper, we shall discuss the need to go beyond current geometric features and consider material -- composition, and gradation -- within the object. This need has been brought about by layered manufacturing technologies which build up parts, layer by layer, under computer control. While industrial use of this new technology has been for making prototypes, functional metallic parts can/are being made by layered manufacturing. Furthermore, a variety of materials can be deposited to create multi-material and functionally graded components.

We consider features in this new domain (of layered manufacturing) and identify research topics and present an overview of our current focus on "material features" in the context of heterogeneous solid models.

## 1.0 Introduction

Layered manufacturing(LM) refers to the host of manufacturing technologies that deposit material, layer by layer, under computer control. It is also referred to as solid freeform fabrication (SFF) and in industry as rapid prototyping. Layered manufacturing methods can be used to make functional parts which have good surface quality and good material property. One distinguishing characteristic of LM is that it is capable of depositing multiple materials in a layer as well as varying the material composition. Harnessing this characteristic is the focus of our research.

In this paper, we consider heterogeneous objects i.e., objects made of different constituent materials and having continuously varying material composition and/or microstructure (See Fig. 1). The state-of-the-art design and analysis research indicates that heterogeneous objects naturally arise in the context of thermal expansion coefficients, mechanical strength, creep, thermal and electrical conductivity, etc. Applications of heterogeneous objects include automotive engineering, aerospace, and biomaterials, etc.

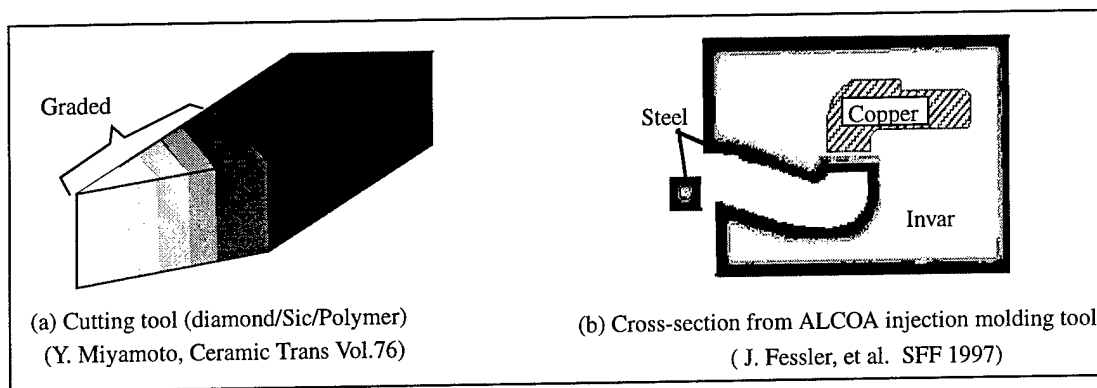


**FIGURE 1. Heterogeneous objects**

A key requirement for the fabrication of heterogeneous objects is their accurate representation in CAD systems. Solid modeling techniques for heterogeneous objects are just beginning to emerge [1][2]. However, there is a need for tools that can facilitate the fabrication process planning of such objects. Process planning for layered manufacturing can be a complicated task, involving the determination of orientation, slicing, deposition path planning, etc. In addition, fabrication of heterogeneous objects demands very delicate control of deposition to achieve desired material composition and gradient.

In our research, we explore the use of features to facilitate the high level conceptualizing of material composition and gradation and its downstream transforming to layered manufacturing instructions. Features were initially proposed to automate the link between design and NC path generation [3]. Since then, features have been widely and successfully used in CAD/CAM. Feature based design expedites the design process and feature recognition facilitates the fabrication process planning. A feature based product model also simplifies the assembly and inspection planning, etc. [4].

In this paper, we report on our ongoing work. We propose a feature based architecture for design and process planning for layered manufacturing. In this context, we present several feature related issues. We then describe how we propose to address these issues and conclude with a summary.

## **2.0 Feature-based design and process planning for LM**

Our proposed feature based design and fabrication integration approach is illustrated in Fig. 2. In this scheme, design can be carried out either by a feature based design method (explicit design whereby material composition is explicitly imposed over the geometry) or by an implicit design method (whereby material information is derived such as in homogenization design method). In feature based design method, the design features are mapped to fabrication feature. In implicit design method, a heterogeneous CAD model is employed to represent the design and a feature recognition module is adopted to extract the fabrication feature from this heterogeneous CAD model.

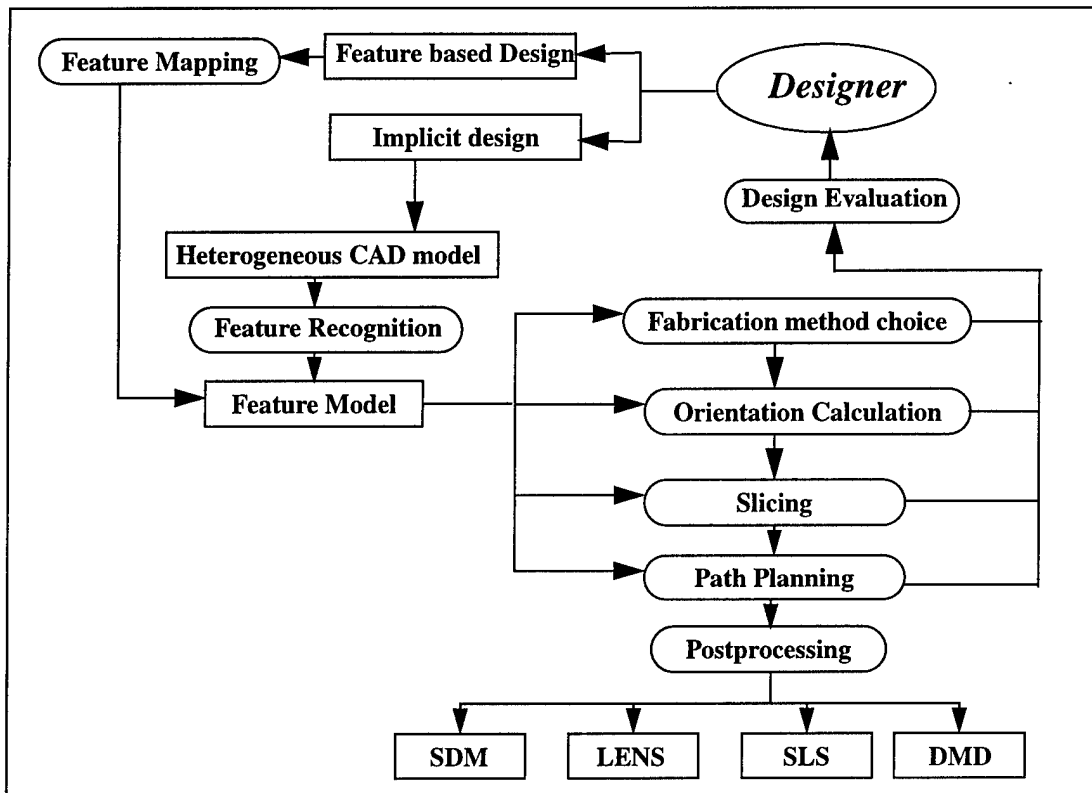


FIGURE 2. Feature based design and process planning for layered manufacturing

Understanding and characterizing the layered manufacturing processes is essential to generate the correct fabrication strategy. Feature based process planning is carried out on the basis of these characterization as well as the identified fabrication features. A set of mapping rules enable the identification of fabrication strategies, including orientation, slicing, road width, deposition path, etc., from the fabrication feature model. A final step might be post processing to generate the machine-specific data.

### 3.0 Features related issues in the LM domain

#### 3.1 Design feature and fabrication feature

Developing the concept of design feature in the context of heterogeneous object is of importance in the feature based design approach. In this context, a closer look at how heterogeneous object design is done will be helpful. Furthermore, methods representing the design feature is also an important issue. In addition, the interactions among features of different material compositions demand specific feature operators beyond the conventional boolean operators. Finally, a library of design features can be developed to support the feature based design approach.

Similarly, understanding and identifying fabrication features in the context of layered manufacturing processes is necessary for the automation of process planning. This fabrication feature identification will be at the core of the fabrication strategy generation. Also an efficient representation of the fabrication feature is important.

Implicit design schemes such as the homogenization design method yield heterogeneous objects[5]. Creating heterogeneous solid models from such density data is a topic of ongoing research. For processing such designs, feature recognition algorithms will be necessary to extract the fabrication features from the heterogeneous solid model.

### 3.2 Mapping from design feature to fabrication feature

Consider the heterogeneous object shown in Fig. 3. During its design (Fig. 3a), the groove would be a design feature. However, for layered manufacturing, the same groove, becomes a fabrication feature made of (sacrificial) support material (Fig. 3b). As illustrated by this simple example, there is a need to identify situations requiring design-to-fabrication feature mapping and develop efficient mapping methods.

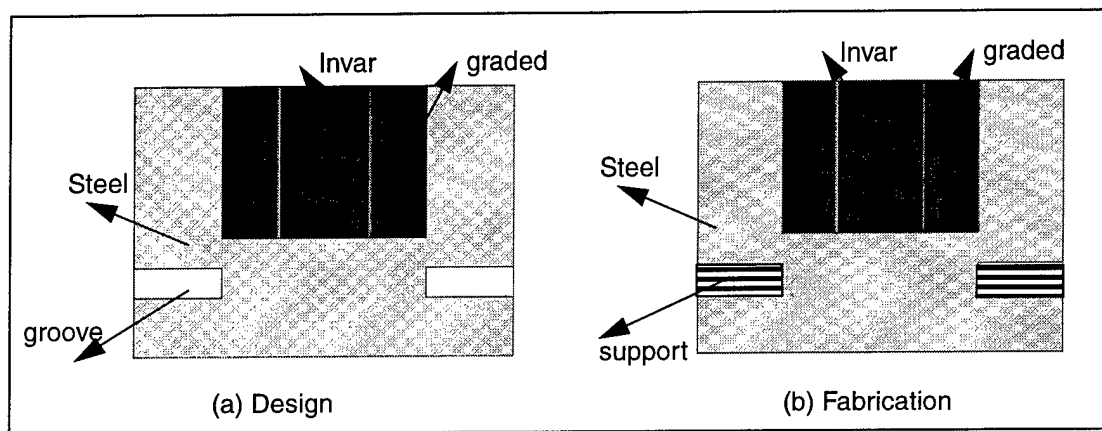


FIGURE 3. Mapping from design feature to fabrication feature

### 3.3 Co-existence of NC feature and LM feature

It is increasingly becoming evident that in the future, manufacturing will include both NC machining and layered manufacturing. Hence, it is important to develop methods that exploit the symbiotic relationship between NC and LM -- material removal and material deposition. Consequently, feature extraction should be looked at within an enlarged context -- the synthesis of NC machining and layered manufacturing. Based on the extracted NC features and LM features, the optimal balance between NC machining and layered manufacturing has to be determined.

## 4.0 Our current research

### 4.1 Characterization of material variation

Heterogeneous materials arises in shape and materially optimized structures. They can provide a smooth transition between materials which are otherwise incompatible because of their mechanical or chemical properties. They can also be used as a coating to modify the electrical, thermal, chemical or optical properties of a substrate [6]. The material variation is usually along some specific direction, based on the functionality and design intent and can be explicitly captured by a swept volume representation (See Fig. 4).

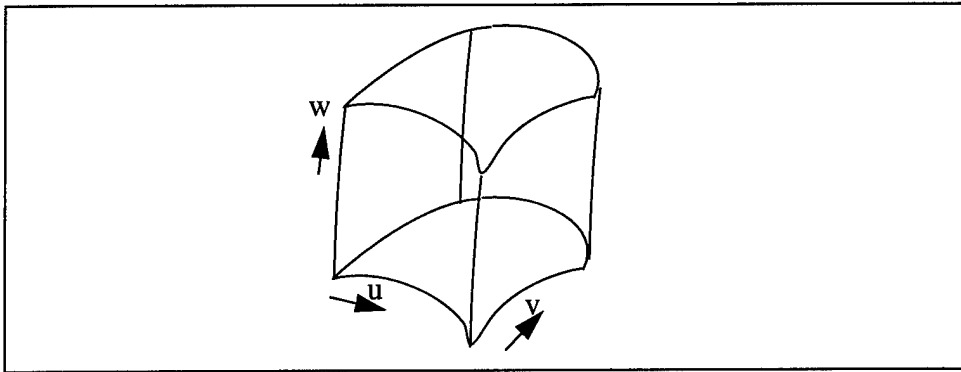


FIGURE 4. Swept Material Volume

**Swept Material Volume** [Working Definition]: *Swept Material Volume is composed of a cross-section and a path. The material could vary along the cross-section and/or along the path.*

Conventionally, a swept volume  $S$  (Fig. 4) is defined by sweeping a surface  $r(u,v)$  along path  $p(w)$ . If '\*' denotes sweep, the swept material primitive (Fig. 4) could be written as

$$SM(S, M) = ( r(u,v) * p(w), m(u,v,w) )$$

where  $S$  represents the geometric volume,  $M$  represents the material composition, and material variation function  $m(u,v,w)$  represents the material changes along the cross section  $r(u,v)$  and path  $p(w)$ . The material variation function could be any user defined function (e.g., constant, linear, step function, parabolic, exponential, etc.).

In practice, material variation typically would happen only along one of the  $u$ ,  $v$ ,  $w$  directions, denoted as  $m(u)$ ,  $m(v)$  and  $m(w)$ . The function  $m(u,v,w)$  would enable full three dimensional material variation.

This characterization of material variation provides a simple way to impose and manipulate material composition over geometry. The actual part could be composed of a combination of these *swept material volumes*. Similar to a CSG object in current solid modeling, material survival rules in the synthesis of such volumes is an issue of ongoing research.

## 4.2 Design feature

The design feature volume is composed of a *swept material volume*. The following (working) definition extends the conventional feature by adding the material dimension:

### Heterogeneous Design Feature

$$= (\text{Conventional}) \text{ Form Feature} + \text{Material Composition/Variation}$$

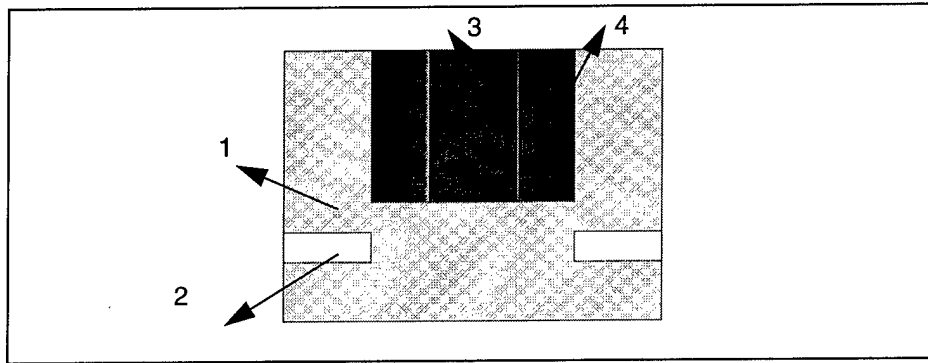


**FIGURE 5. Design Features for Heterogeneous Object**

In the sample part shown in Fig. 5, there are four design features (numbered 1 through 4). Each feature has a geometry and its own material composition (and fulfills a design function). Feature 1 is the base of the part and made of homogeneous material. Depression feature 2 is a groove. Feature 3 is made of another homogeneous material that is different from the base part material. Feature 4 provides the transition between 1 and 3 and makes the material property (e.g. coefficient of thermal expansion) transit smoothly from feature 3 to feature 1. In this way, feature based design can provide the designer an efficient way to synthesize heterogeneous objects.

### **4.3 Fabrication feature**

Layered manufacturing parameters for heterogeneous objects would consist of layer thickness, road width, material composition and its gradation. Based on this characterization, *fabrication feature* can be thought as a subvolume that can be produced by LM in the same deposition configuration (i.e., material composition and gradation, road width, and layer thickness, are kept “constant”). We have the following (working) definition:

#### **LM Fabrication Feature**

$$= \text{Subvolume} + \text{Deposition Configuration}$$

The fabrication feature is a subvolume of a part that is distinguished either by the material type, material gradation, or the fabrication method. Each fabrication feature element shares the same material composition or shares the same material gradient and is part of the same *swept material volume*.

### **4.4 Feature based slicing**

We envision fabrication features will facilitate the process planning for layered manufacturing. Here, we specifically look at how slicing information can be determined from the fabrication features under the assumption of simple geometry and compatibility of process resolution.

Denote the material composition at the height  $z$  as  $f(x,y,z)$ . Then the maximum allowable layer thickness ( $d$ ) could be derived from the maximum vertical gradient (Fig. 6) as:

$$d = \min \left[ \frac{\delta}{(\partial f)/(\partial z)} \right] \quad \text{where } \delta \text{ is the allowable material composition tolerance}$$

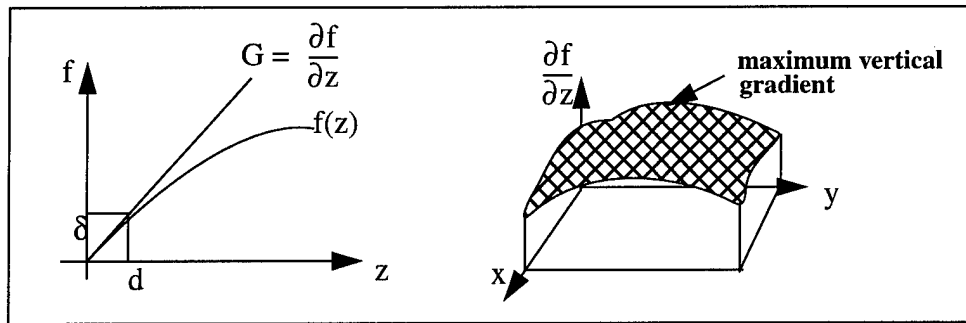


FIGURE 6. The vertical component of material gradient in one slice

Fig. 7 illustrates how material composition affects the slice thickness and road width.

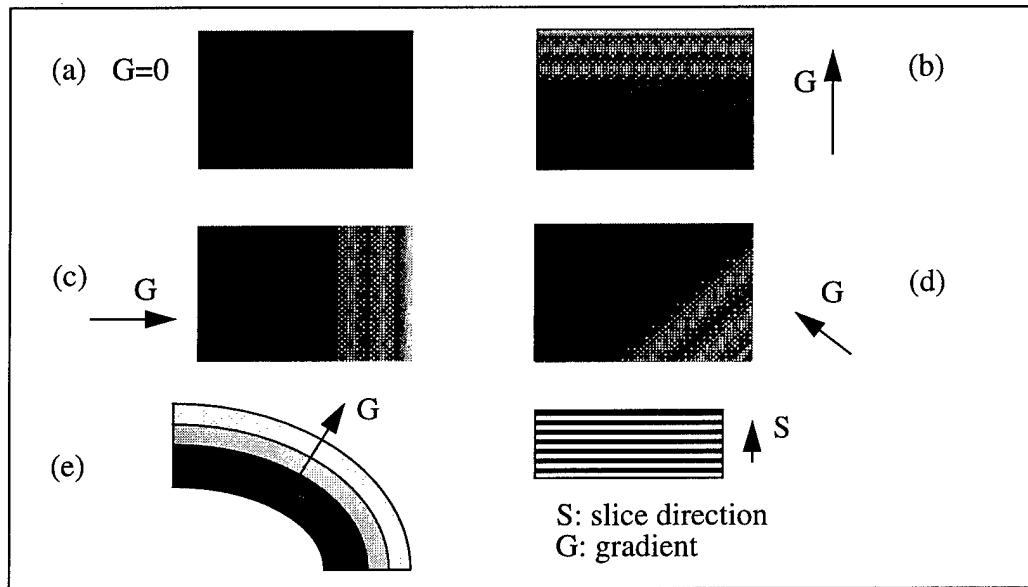


FIGURE 7. Material Gradation Direction versus Slice Direction

Denote the slice direction as  $S$ , the gradient as  $G$ ,  $\theta$  is the angle between  $S$  and  $G$ ,  $\delta$  is the allowed material composition tolerance. Then, the following rules can be used.

- If  $G=0$  (Fig. 7a), it is a homogeneous object and the material composition can be ignored.
- If  $G \parallel S$  (Fig. 7b), the slice thickness can be  $\delta/G$ , and the road width can be maximum.
- If  $G \perp S$  (Fig. 7c), the slice thickness can be maximum, the road width can be  $\delta/G$ .

- If  $\theta$  is the angle between S and G (Fig. 7d, e), the slice thickness can be  $\delta/G \cos\theta$ , and the road width can be  $\delta/G \sin\theta$ .

## 5.0 Summary

In this paper, we described feature related issues in the layered manufacturing of heterogeneous objects. An architecture for a feature based CAD/CAM system for layered manufacturing was presented. We proposed working definitions of *swept material volume*, *design feature* and *fabrication feature*. We also provided an overview of our ongoing work.

## 6.0 Acknowledgment

The authors gratefully acknowledge the support provided by ONR grant N00014-97-1-0245 and NSF grant MIP 9714951.

## 7.0 References

1. Kumar, V. and Dutta, D., "An Approach to Modeling and Representation of Heterogeneous Objects", accepted for publication in *ASME Journal of Mechanical Design*, available as technical report, 1998.
2. Marsan A. and Dutta D., "On the Application of Tensor Product Solids in Heterogeneous Solid Modeling", *1998 ASME Design Automation Conference*, Atlanta, GA, Sep. 1998.
3. Grayer, A., "A Computer Link between Design and Manufacture", Ph.D. Dissertation, University of Cambridge, UK, Sep. 1976.
4. Shah, J. J., Mantyla, M., and Nau, D. S., edited, *Advances in Feature Based Manufacturing*, Elsevier, 1994.
5. Bendsoe, M. P. and Kikuchi, N., "Generating Optimal Topologies in Structural Design Using a Homogenization Method", *Computer Methods in Applied Mechanics and Engineering*, Vol. 71, pp. 197-224, 1988.
6. Rabin, B. H., and Shiota, I., "Functionally Gradient Materials", *MRS Bulletin*, Jan. 1995.

# Recent Developments in Robocasting of Ceramics and Multimaterial Deposition

Joseph Cesarano III, Bruce H. King, and Hugh B. Denham  
Sandia National Laboratories, Albuquerque, NM.

## Abstract

Robocasting is a freeform fabrication technique for dense ceramics and composites that is based on layer-wise deposition of highly loaded colloidal slurries. The process is essentially binderless with less than 1% organics and parts can be fabricated, dried, and completely sintered in less than 24 hours. This overview will highlight recent materials developments for structural applications and modelling of slurry flow. Fabrication of preforms for alumina / metal composites will be discussed as well as techniques for multimaterial deposition in both graded structures and discrete placement of fugitive materials.

## Introduction

Robocasting is being developed at Sandia National Laboratories for the freeform fabrication of ceramics and composites. Robocasting uses robotics for the layerwise deposition of ceramic slurries through an orifice. Orifice openings can range from a couple of millimeters to tenths of millimeters. The process is based on the extrusion of highly loaded ceramic slurries that are typically 50 - 65 vol.% ceramic powder, < 1 vol.% organic additives, and 35 - 50 vol.% volatile solvent (usually water). Since binder burnout is not an issue, a dense ceramic part may be freeformed, dried, and sintered in less than 24 hours. Robocasting is described in detail in reference [1].

In general, a robocasting slurry must meet three criteria: 1) it must be pseudoplastic enough to flow through a small orifice at modest shear rates; 2) it must set-up into a nonflowable mass upon dispensing; and 3) it must be able to "accept" multiple layers without defects to form a uniform mass. Probably the most unique and interesting aspect of robocasting is the process by which the flowing pseudoplastic slurry transforms into a solid-like mass after deposition. In contrast to gel casting and other freeform fabrication techniques, robocasting does not require organic polymerization reactions or solidification of a polymeric melt for the solid transformation. On the contrary, in order to maintain structural integrity while building a component, robocasting relies on the rheology of the deposited slurry and on partial drying of the individual layers. This is explained below.

Typical ceramic powder slurries have an average particle size on the order of several microns and possess a relatively monosized distribution. Ceramic powders with this character, that are dried from a dispersed slurry, typically pack into a consolidated structure that is approximately 65% of the theoretical density. However, the character of flowable slurries with solids loadings just below the consolidated density is what is important for robocasting. Figure 1A depicts schematically the behavior of a typical dispersed alumina powder slurry. At low solids loadings, dispersed slurries have very low viscosity and are rheologically Newtonian. Around 40 volume percent solids, the slurries begin to show pseudoplastic shear-thinning behavior even though the viscosity is still relatively low. As the solids content approaches 60 volume percent, inter-particle interactions and inter-particle collisions become dominant;

viscosity begins to increase appreciably and the rheological behavior becomes highly shear-thinning. At approximately 63 volume percent solids, particle mobility becomes restricted and the slurry locks up into a dilatant mass. Therefore, it is desirable to robocast with slurries that have solids loadings close to the dilatant transition so that with minimal drying a robocasted layer becomes structurally sound and a foundation upon which more layers may be deposited.

Figure 1B schematically depicts how the pseudoplastic to dilatant transition must closely follow the build rate in order to maintain structural integrity for thick parts. Therefore, the drying kinetics of the freshly deposited beads determine the optimum build parameters. Typically, parts are built upon a platform heated between 30 and 60 degrees Celsius to assist the pseudoplastic to dilatant transition. For thick parts it is necessary to incorporate an additional heat source above the build platform. From Fig. 1B it is evident that if the drying rate is too slow, the pseudoplastic to dilatant transition is delayed and accumulated weight from several layers eventually surpasses the yield stress of the pseudoplastic layers. This condition can induce slumping and the creation of nonuniform walls. Conversely, if the drying rate is too fast, warping, cracking, and delamination may occur.

In general, proper robocasting requires a synergistic control of the : 1) percent solids in the ceramic powder slurry, 2) viscosity and rheology of the slurry, 3) dispensing rate of the slurry through the orifice, 4) drying kinetics of the dispensed bead of slurry, and 5) computer code for optimal machine instructions. When a proper balance of these variables is achieved, robocasting can be used to make intricate ceramic bodies that sinter into relatively strong, dense and defect free parts.

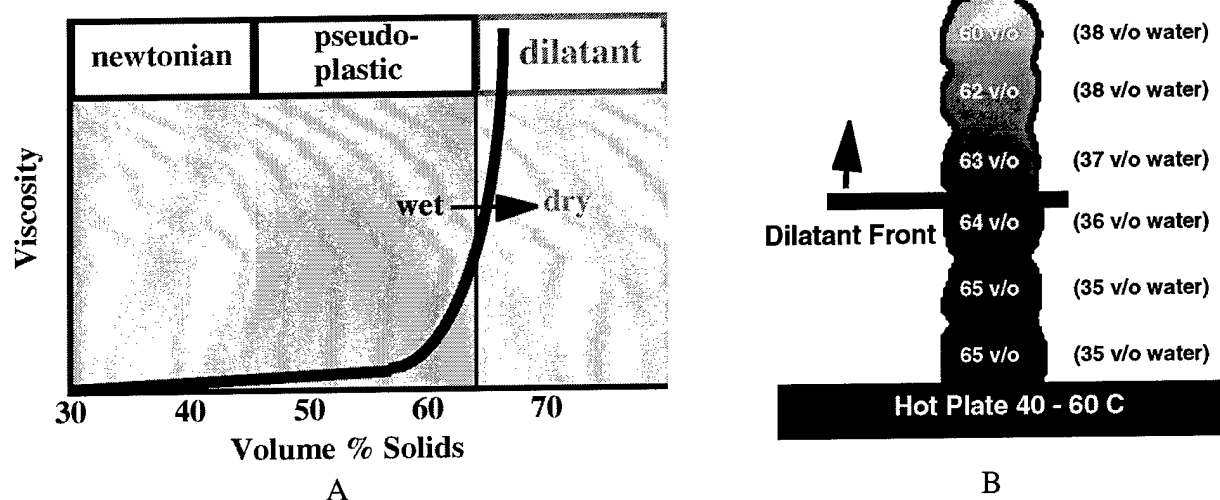


Figure 1: A) A schematic showing the typical viscosity versus volume percent solids behavior for dispersed alumina slurries. For optimal robocasting, work close to the dilatant transition. B) A schematic showing how a part "solidifies" during building through a pseudoplastic / dilatant rheological transition.

## Experimental

The slurries discussed throughout this paper were made and deposited in accordance with references [1] and [2]. The robotic slides used for the X, Y, Z and dispensing axes were purchased from Velmex, Inc. The slides were controlled with servo motors and controllers from

Galil Motion Control, Inc. The three-dimensional modelling of bead flow was based on finite element calculations developed by Thomas A. Baer at Sandia National Laboratories.

## Recent Developments and Discussion

Our current work is now being directed at characterizing and modelling the robocasting process in an effort to optimize build parameters for improved control and tolerance of part fabrication. Also, we are exploring new uses and opportunities related to materials fabrication to exploit the versatility of robocasting for nontraditional manufacturing methods and for multimaterial fabrication.

- **Modelling:** We have already shown that robocast alumina parts have densities and strengths comparable to alumina processed more traditionally [3]. However, there is a lot of room for improvement when looking at the dimensional tolerance and surface finish that robocasting provides. With that in mind, we are attempting to model the flow of beads of slurry to derive a knowledge-base for the exact shape of deposited beads as a function of build parameters. It is fortunate that it has already been determined that as the freshly deposited bead undergoes a dilatant transition into a solid-like mass, there is a minimal change in shape. There is appreciable flow and shape change as the slurry is being sheared during deposition. However, King et al [4] have shown with non-contact laser profilometry that alumina beads have minimal dimensional change after deposition. In fact, the entire dilatant transition takes approximately one minute to occur even at room temperature. With heat the transition occurs more rapidly.

Figure 2 is a schematic showing some results from the three-dimensional modelling of bead flow. The code is currently based on finite element analysis of a Newtonian slurry. Even though pseudoplasticity has not yet been taken into account, the bead shape predictions are very good for deposition onto a moving platform. However, the actual image in Figure 3C shows that the deposition behavior into a previously dispensed bead is very different than deposition onto a moving platform. The freshly dispensed bead wets the previously deposited bead. Therefore, the fresh slurry is pulled down and fills space over the entire top curved surface of the previously deposited bead. Also, the leading edge of the fresh slurry is now pulled even to the front of the orifice instead of lagging behind (Fig. 3A). This experiment shows the space filling behavior of slurries, that is beneficial for the fabrication of defect free parts. However, it also shows that the bead flow model will have to include calculations for deposition onto curved wetting surfaces in order to accurately predict part dimensions and tolerances.

- **Preforms for Alumina / Metal Composites:** In addition to fabricating single material parts, robocasting may have utility for the manufacture of intricate preforms for the fabrication of ceramic / metal joining composites. By robocasting various crosshatch patterns, intricate structures may be fabricated that can not obviously be manufactured by traditional fabrication techniques. Figure 4A shows a cross-section of a robocast alumina part fabricated with regions of closed porosity as well as open voids with large undercuts. This type of structure when infiltrated with a metal forms a mechanically bonded ceramic to metal join that has a graded composition on a macroscale. Figure 4B shows the cross-section of a similar preform that was infiltrated with an active metal (TiCuSi). This part not only showed exemplary bonding without cracking but was subsequently used as a platform upon which LENS [5] processed stainless steel was freeformed. In finality, a structurally sound crack-free part was fabricated that transitioned from 100% alumina to 100% stainless steel. Additionally, the part was mostly freeformed. The TiCuSi metal used to fabricate the composite in Fig. 4B is probably prohibitively expensive for any widespread application. Therefore, a method for infiltrating aluminum metal into a robocast alumina preform was developed. Figure 4C shows a cross-section of a structurally sound alumina / aluminum part that is macroscopically graded with some mechanical interlocking.

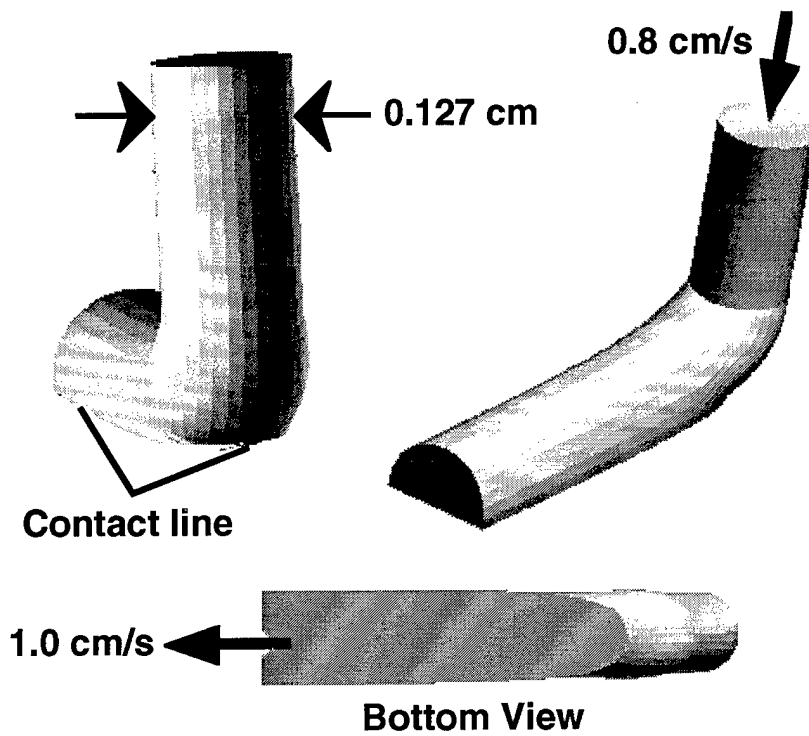


Figure 2: Three-dimensional modelling of bead flow. Three views of the same Newtonian bead laydown solution. The fluid enters the cylindrical nozzle at 0.8 cm/s and the web is moving at 1.0 cm/s.

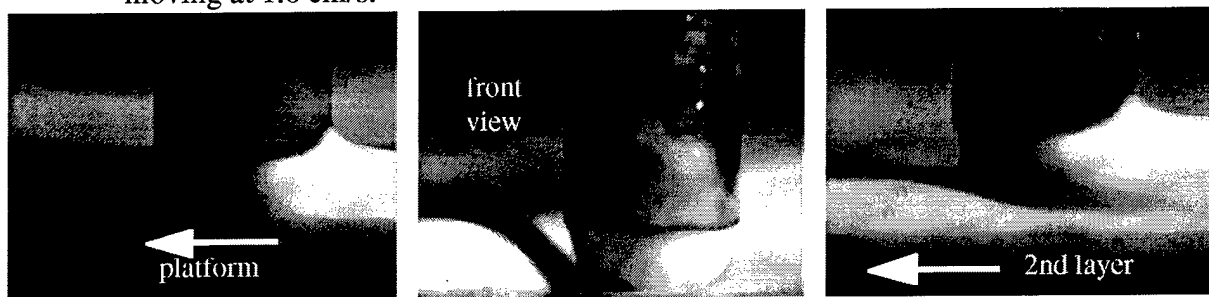


Figure 3: Images of an alumina slurry being deposited onto a moving platform (left and center) and the slurry being deposited onto a previously deposited alumina bead (right).

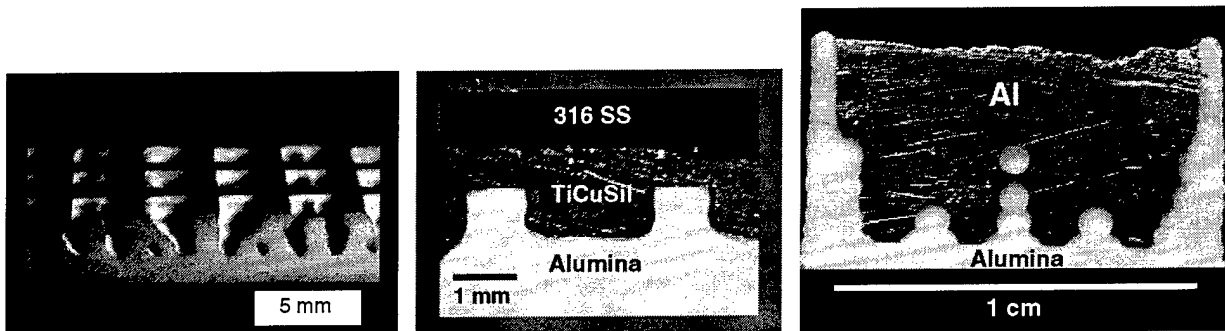


Figure 4: Robocast alumina preforms infiltrated with metal form graded interlocking composites.

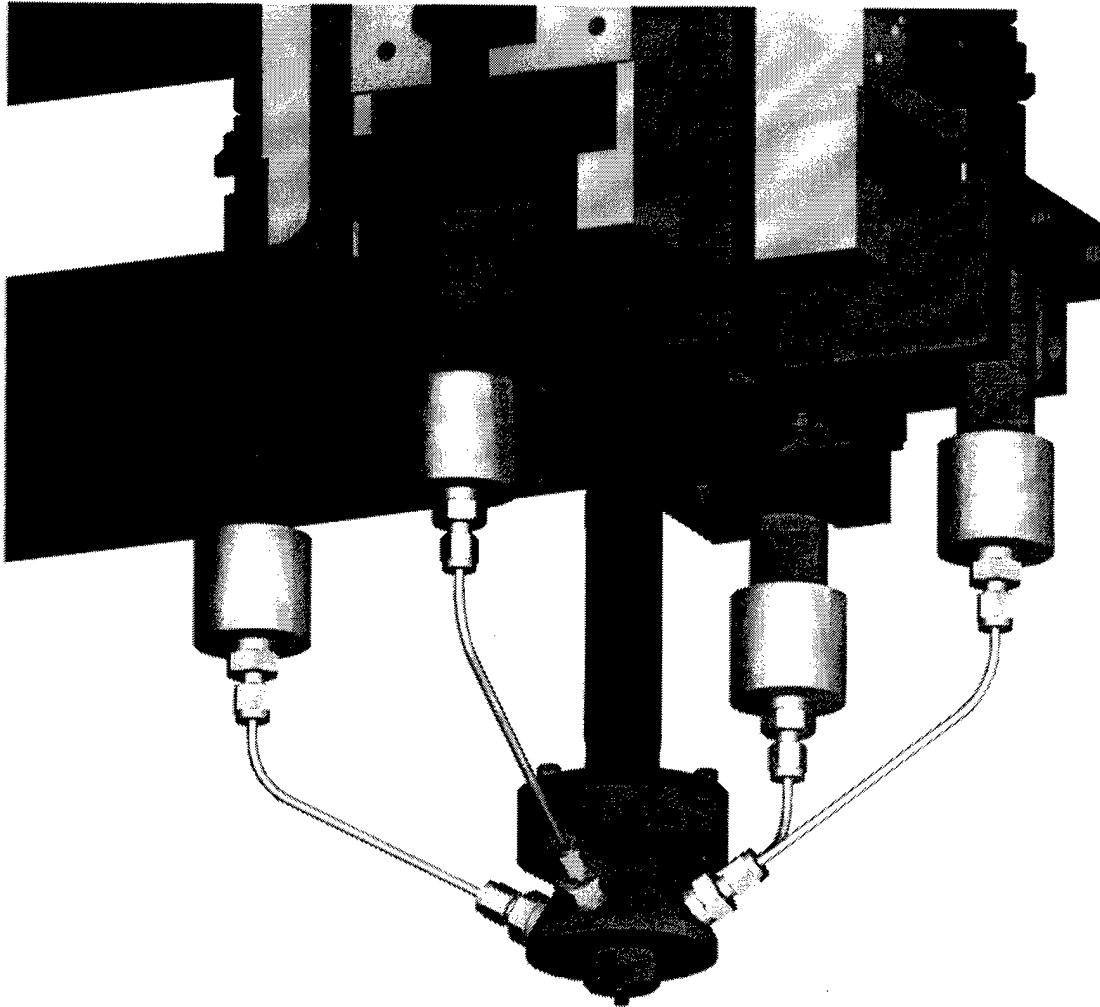


Figure 5: Mixing head capable of depositing four slurries simultaneously.

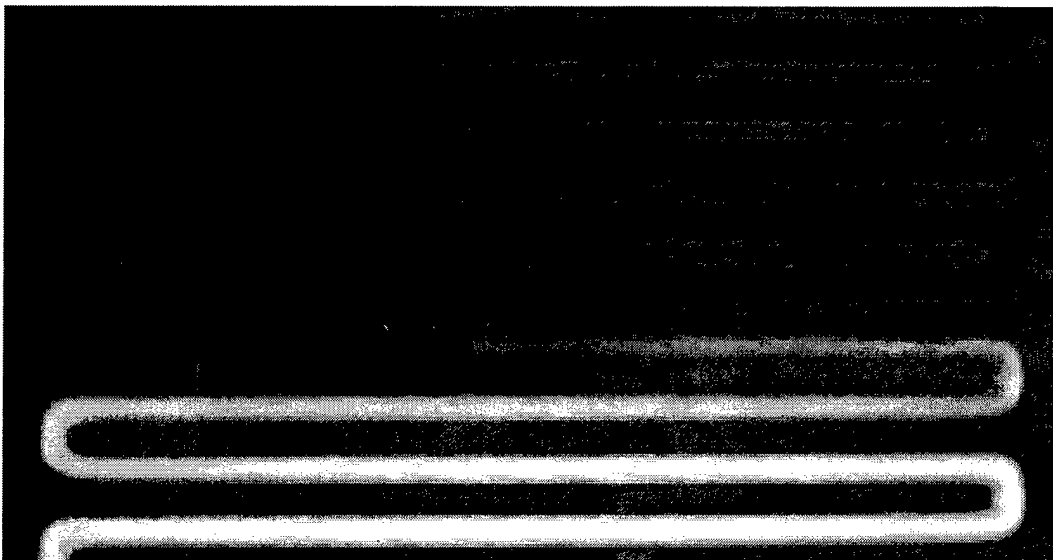


Figure 6: Demonstration of a graded transition between two slurries (bead width 1.5 mm).

• **Multimaterial Deposition:** The ability to deposit more than one material simultaneously through a single orifice is a recent advance for robocasting that should increase its versatility. Figure 5 shows a schematic of a mixing head that has the capability to dispense up to four different materials. Just before the orifice there is a miniature mixing chamber with a 3 mm rotatable paddle. When it is desired to deposit ratios of various materials the mixer can be turned on to ensure that a uniform mixture is dispensed through the orifice. For separate and discrete placement of materials, the mixer is automatically turned off.

Figure 6 shows a visual example of complete grading between two materials. This experiment was completed on a dual feed mixing head with a bead width of approximately 1.5 mm and shows a gradual 100 percent transition from one material to the other. However, in order to build truly three dimensional parts with overhangs, hidden features, and/or buried materials, robocasting must also have the capability to deposit multimaterials discretely. This capability is demonstrated in Fig. 7 for a part fabricated with a horizontal channel that is four bead widths wide. The part in Fig. 7 is made from a kaolin slurry using a fugitive support material. During the build the fugitive material supports the top two layers of kaolin. During drying the fugitive material deforms and is pulled into a thin layer by the surrounding kaolin matrix. During binder burnout and sintering the fugitive material is decomposed and the kaolin densifies. In conclusion, it was determined that for a fabrication technique such as robocasting (i.e., one in which liquid wicking and drying are part of the solidification process) an ideal fugitive material must have the following properties: 1) very low solids and organic contents; 2) a high enough yield strength to be an adequate supporting platform; and, 3) a low enough yield stress to deform during wicking and drying without disrupting neighboring materials.

Conceptually, this technique worked very well; however, a crack developed during binder burnout and can be seen on the left hand side of Fig. 7C. It is believed that the build parameters were slightly errant during the first layer of deposition for the fugitive material and some of the material was squeezed on top of the neighboring kaolin bead. This resulted in the crack upon fugitive decomposition. This experiment highlights the need for a knowledge-based ability to precisely predict the shape of deposited beads for all kinds of slurries. Also, there is a need to incorporate sensor controlled feedback for optimum adjustment of build parameters in real time.

Finally, Table I is included to show the current list of materials systems that have been made into robocasting slurries. Some have already been robocasted into samples and others are actively in development.

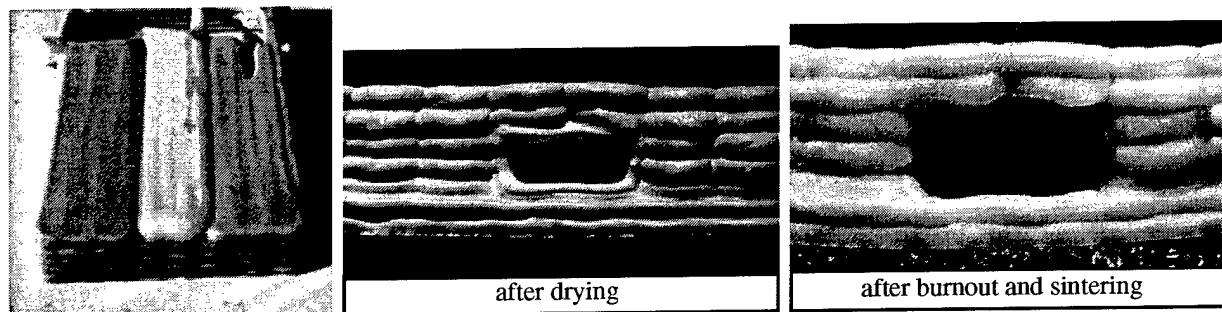


Figure 7: Robocasting a kaolin slurry along with a fugitive material to demonstrate how truly three dimensional parts may be freeformed. Both slurries were deposited with a dual feed mixer through a single orifice.

**Table I**  
A Current list of materials systems used with robocasting.

Alumina (dense and porous)	PZT
Al <sub>2</sub> O <sub>3</sub> / TiCuSil composites	ZnO
Al <sub>2</sub> O <sub>3</sub> / Al composites	Kaolin
Al <sub>2</sub> O <sub>3</sub> / Mo	

Thick film pastes, polymers, epoxy

In Development:	<ul style="list-style-type: none"> <li>* Mullite</li> <li>* Zirconia</li> <li>* Silicon Nitride</li> </ul>
-----------------	--

**Acknowledgment**

Sandia is a multiprogram laboratory operated by Sandia Corporation, a Lockheed Martin Company, for the United States Department of Energy under Contract DE-AC04-94AL85000.

**References**

- 1) Cesarano, Baer, and Calvert, Proceedings of the Solid Freeform Fabrication Symposium, Austin, TX, (1997) pp. 25 - 32.
- 2) Cesarano and Aksay, J. Amer. Ceram. Soc., (1988), **71**, 12, 1062-67.
- 3) Denham, Cesarano, King, and Calvert, "Mechanical Behavior of Robocast Alumina," Proceedings of the Solid Freeform Fabrication Symposium, Austin, TX (1998).
- 4) King, Morrisette, Denham, Cesarano, and Dimos, "The Influence of Rheology on Deposition Behavior of Slurry-Based Direct Fabrication Systems," Proceedings of the Solid Freeform Fabrication Symposium, Austin, TX (1998).
- 5) Griffith, Keicher, Atwood, Romero, Smugeresky, Harwell, and Greene, Proceedings of the Solid Freeform Fabrication Symposium, Austin, TX, (1996) p. 125.



## Functionally Optimized Ceramic Structures

C. Gasdaska, R. Clancy, M. Ortiz<sup>#</sup> and V. Jamalabad  
AlliedSignal, Inc. Research and Technology  
Morristown, NJ 07962

Anil Virkar  
Department of Materials Science and Engineering, University of Utah, UT

Dragan Popovitch  
Advanced Ceramics Research  
Tucson, AZ

*The feasibility of using the Fused Deposition of Ceramics (FDC) process to rapidly fabricate functional quality advanced ceramic components has been demonstrated. Multiple extrusion heads enable the deposition of spatially engineered ceramic microstructures on the scale of 250  $\mu\text{m}$ . This unique capability of FDC allows components to be built with combinations of materials and properties that are difficult or impossible to produce using conventional fabrication processes. Some concepts will be presented, along with examples of multiple material laminates produced using FDC. Strength data will be presented which demonstrates the performance improvement possible using spatially engineered microstructures.*

### Introduction

By suitably combining materials, it is possible to achieve improvements in properties such that the strength and toughness of the combination is greater than that for either material alone. Two multi-material approaches used for strengthening and flaw tolerance in brittle materials are development of residual surface compressive stresses due to coefficient of thermal expansion (CTE) mismatch<sup>1</sup>, and fabrication of silicon nitride/ boron nitride fibrous monolith composite structures<sup>2</sup>.

The concept of using combinations of ceramic materials with different coefficients of thermal expansion (CTE) to produce residual stresses on cooling from the fabrication temperature is well documented in the literature<sup>1</sup>. Systems which rely on phase changes to produce residual stresses have also been studied<sup>3</sup>. Strength increases of 300% have been observed in some of these systems. Reliability and flaw tolerance is also improved. In the present work, we are interested in pursuing multi-material combinations which are compatible and co-sinterable with silicon nitride, the leading candidate for high temperature structural applications such as gas turbine engine components. The 1-dimensional aspect of part building using FDC allows for structures more complicated than the simple laminates prepared using traditional methods<sup>4</sup>.

Fibrous monolith (FM) materials are essentially unidirectional composites in which the volume fraction of the matrix material is  $< 20\%$ . The most common example consists of a

---

<sup>#</sup> Located at AlliedSignal Engines Division, Phoenix, AZ

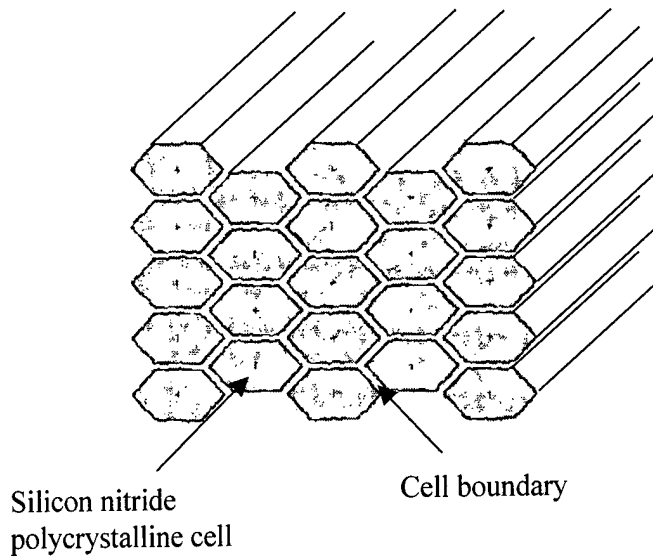


Figure 1. Cross-section of an idealized fibrous monolith microstructure.

structure containing silicon nitride filaments surrounded by a sheath of boron nitride (see Figure 1).

Cracking in these materials tends to be confined to the boron nitride layer, resulting in extensive delamination under bending stresses<sup>2</sup>. Alternatives to boron nitride are being investigated which would allow a greater amount of fiber pullout and work of fracture under tensile loading conditions. Typically, FM materials are produced using filament-winding techniques using fibers which have the FM structure. The FDC process offers a more cost effective method for producing these materials.

The solid freeform fabrication process we are using is based on the Stratasys machine. This technique uses solids loaded filament to deposit roads of a binder/ceramic powder mixture<sup>4</sup>. For multi-material parts, we are using a Stratasys 1650 dual-liquefier rapid prototyping machine.

### Laminates

In order to take advantage of the capability of FDC to spatially distribute materials, systems must be found which not only result in desirable material property combinations, such as residual stress production, but which are also capable of being co-sintered without excessive cracking or delamination. Toward this end, we have been examining the use of particulates dispersed in a silicon nitride matrix to increase the CTE. Two candidate material systems for use in silicon nitride are listed in Table 1.

Material	Melting/Decomposition Temperature (°C)	Coefficient of thermal expansion (°C x 10 <sup>6</sup> )	Young's Modulus (GPa)	Density (g/cm <sup>3</sup> )
SiC	2700	4.3	448	3.22
TiN	2940	9.35	260	5.22

Table 1. Properties of candidate particulate dispersants.

In order to evaluate the effectiveness of these materials in strengthening silicon nitride, bi-material laminates were prepared using slip-casting. The materials consisted of silicon nitride and silicon nitride plus up to 30 weight% of either TiN or SiC. The samples were sintered and dense samples were successfully prepared. Test bars were machined and room temperature bending strength measured. Results for samples containing SiC appear in Figure 2. The geometry of the samples is also illustrated. The results indicate that average strength can be increased by up to ~27%. In addition, the decrease in the amount of strengthening at 800 °C is consistent with the drop in residual stress as the test temperature approaches the temperature at which stresses start to set on cooling.

Verification that the increase in strength was due to residual stress was accomplished by a method of progressive material removal and strain measurement using strain gauges. In this technique<sup>3</sup> a strain gauge is mounted on a laminated sample and the build-up of strain is monitored as material is progressively removed from the opposite surface. A residual stress of ~157 MPa was measured using this technique. The differential strain between laminate materials

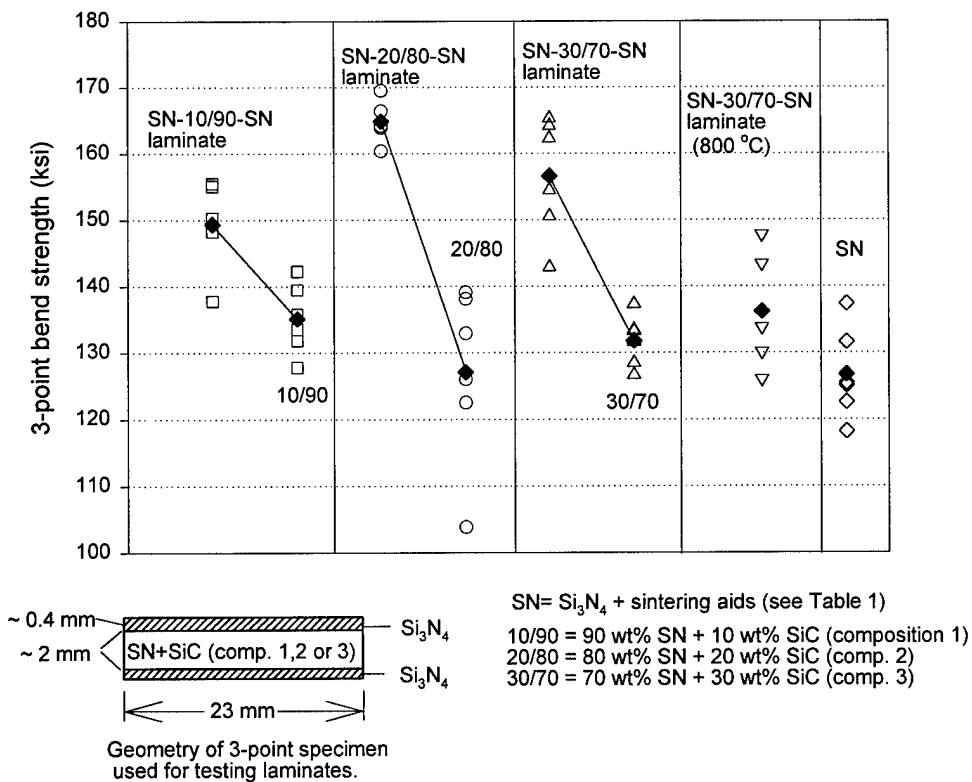


Figure 2. Strength data obtained in 3-point bending for laminates prepared from the indicated compositions. Data for both the laminates and the "core" materials are presented and connected by the lines. Individual data points are plotted, with the average strength for each group represented by the filled diamond symbol. In all cases, the average strength of the core (10/90, 20/80 or 30/70) is less than the laminate strength, indicating strengthening due to surface compressive stresses. The drop in strength at 800 °C is also consistent with the presence of residual stress due to thermal expansion mismatch between the core and outer skins. The strength of the outer skin by itself is shown by the group labeled SN.

was measured as  $5.4 \times 10^{-4}$ . If we assume that on cooling from the sintering temperature permanent stresses begin to set in at  $1300^\circ\text{C}$ , then a difference in CTE of  $0.42 \times 10^{-6}/^\circ\text{C}$  would produce a differential strain of  $\sim 5.4 \times 10^{-4}$ .

Using combinations of materials with CTE mismatch to produce residual stresses raises a number of issues. For example, residual stresses must not be so large as to induce spalling or delamination between materials. In addition, the bonding at the interface and the presence of interface defects are important characteristics in determining the ultimate degree of strengthening. The spalling and delamination question is strongly dependent on the interfacial bonding and Mode II fracture energy at the interface. Techniques for measuring interfacial fracture energy are under development. However, for the problem of failure from the surface versus failure at the interface – where residual tensile stresses develop – has been outlined for the case of bending. As an example, assuming a three layer laminate stressed in bending the corresponding fracture strengths (in flexure) are:

$$\sigma_{F(S)} = \sigma_{SF}^0 + \frac{d_2 E \Delta \epsilon_0}{(1 - \nu) d}$$

for failure from the surface, and

$$\sigma_{F(I)} = \frac{d}{d_2} \sigma_{IF}^0 - \frac{2d_1 E \Delta \epsilon_0}{(1 - \nu) d_2}$$

for failure from the interface. Where,  $\sigma_{SF}^0$  and  $\sigma_{IF}^0$  are the true fracture strengths for failure from surface and interface flaws, respectively,  $d_1$  is the outer layer thickness,  $d_2$  is the inner layer thickness,  $d = 2d_1 + d_2$  and  $\Delta \epsilon$  is the free strain difference between materials (related to the difference in CTE and  $\Delta T$ ).  $E$  is Young's modulus.

The preceding equations show that to maximize the strength as well as the damage resistance, the following are required: (1) high  $\sigma_{IF}^0$ : This can be achieved by improving processing such that interior flaws are kept to a minimum. (Failure from the interior may not be bad either); (2) the inner layer should be fully encapsulated in the outer layer such that there is no chance of introducing damage in the inner layer during service (complete confinement); (3) enhance  $\Delta \epsilon_0$  to as high a value as possible such that a high surface compressive stress exists. This provides damage resistance. However, the surface compressive stress should not be so large as to cause delamination; (4) decrease  $d_1$  to a value small enough (relative to  $d_2$ ) such that interior tensile stress is kept to a minimum, yet  $d_1$  is large enough to prevent contact-induced damage from penetrating too deep into the inner region. Preliminary calculations show an outer layer of thickness  $\sim 150$  to  $250 \mu\text{m}$  to be more than adequate for most applications. For a component of 5 mm thickness, the  $d_2/2d_1$  ratio is then between 9 and 15.67. For a component of 20 mm in thickness, with an outer layer thickness of  $\sim 500 \mu\text{m}$ , the ratio is 19. The corresponding tensile stress in the inner layer is very small. This latter example corresponds to the case of the SiC insert being examined by AlliedSignal Engines (see next section), where the insert is located  $\sim 380$  microns below the silicon nitride surface and the overall thickness is  $\sim 20$  mm.

## Design using FDC

While the preceding work has demonstrated the feasibility of using compatible, co-sinterable material combinations for strengthening, the ultimate goal is to use the unique spatial control capabilities of FDC to design and build components. As part of the project on solid freeform fabrication, the Engines division at AlliedSignal (ASE) has been working on designing a multi-material turbine blade which uses residual stress strengthening.

The design used for modeling consists of a ceramic blade inserted in an AF-2 alloy disk (Figure 3). In this initial work, design analysis was focussed on the attachment area since this region is known to experience the highest stresses and contains the area most likely to fail. Stresses in the attachment area were analyzed for a rotational speed of 33,500 RPM and a uniform temperature of 1450 °F. Based on these conditions a uniform stress of 24.1 ksi was imposed outside the attachment area. The coefficient of friction between blade and disk was assumed to be 0.6. This was based on previous experience with ceramic blade attachment systems. Using these inputs, a baseline condition was analyzed. The peak stress was calculated to be 105 ksi and located just outside the contact area between the blade and disk. It arises from the high frictional load between blade and disk.

Various design strategies were evaluated to reduce this peak stress and are illustrated in Figure 3. Although a silicon carbide material has been modeled as the higher CTE component, particulate based silicon nitride composites would provide nearly equivalent behavior. Three of the four geometries examined utilized combinations of SiC and Si<sub>3</sub>N<sub>4</sub> to produce residual compressive stresses in the contact area. The geometry illustrated in Figure 3d – a blade containing a central cavity to reduce weight – actually caused a 77% increase in peak stress. Figure 3c illustrates the most promising approach. A silicon carbide insert in the contact area significantly reduces the peak stress.

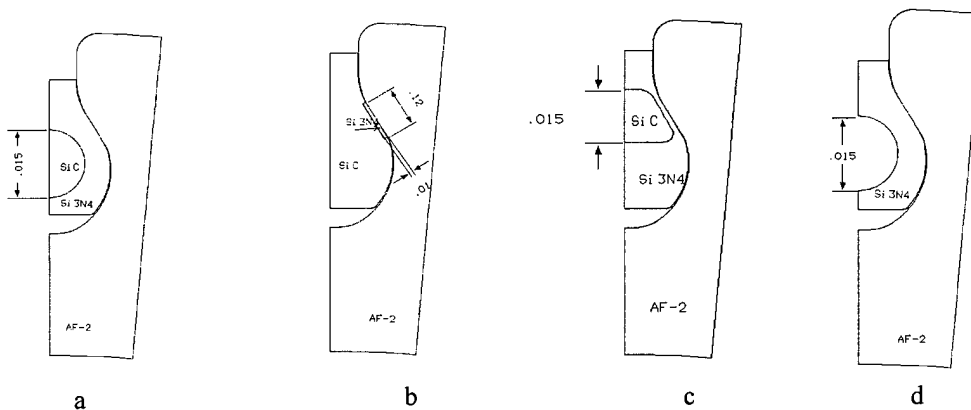


Figure 3. Various geometries evaluated for reducing the peak stress in the contact area.

The amount of the reduction is a function of set temperature; i.e., the temperature at which sufficient rigidity is obtained to start developing residual stress. The higher the set temperature, the larger the residual stress which can be produced by differential contraction. This is shown in

Figure 4, where the maximum stress at 787 C is given as a function of set temperature. Based on a set temperature of 1300 C, the peak stress is reduced from 105 ksi to 72.2 ksi.

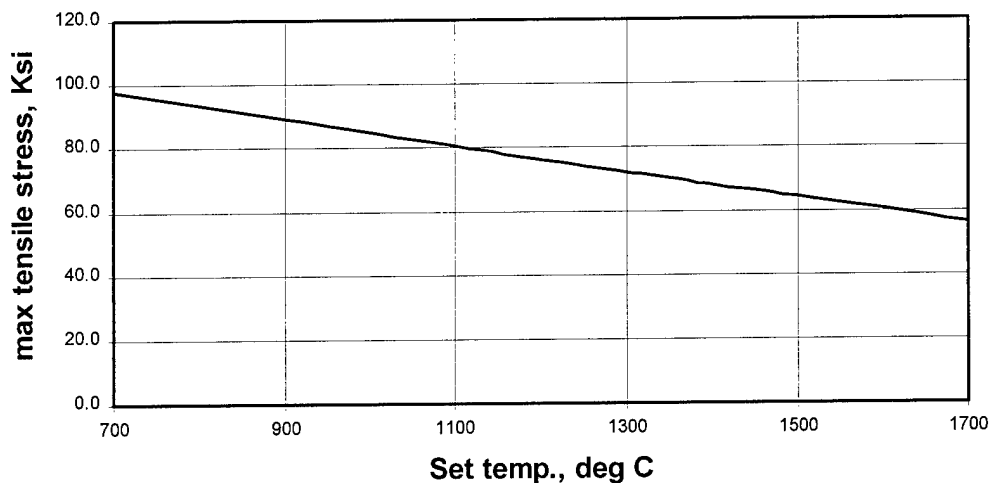


Figure 4. Variation in the maximum tensile stress in the blade attachment area as a function of set temperature.

Fabrication of a complete blade using multi-material FDC is expected to begin shortly. In the meantime, the feasibility of the process has been demonstrated in sub-element testing. Figure 5 shows a cross-section of a turbine blade with a narrow band of insert material at the attachment area.

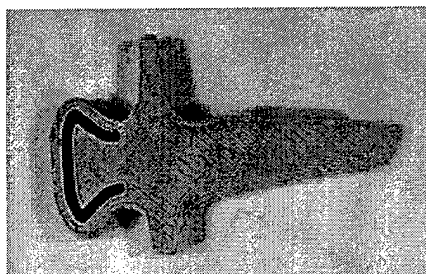


Figure 5. Cross-section of blade built with insert material in the attachment area (black line at right).

### Fibrous Monoliths

A major concern regarding the fused deposition of filaments with fibrous monolith structure was whether or not the fibrous monolith structure would be retained as the filament was melted in the liquefier and extruded. In order to address these concerns, Advanced Ceramics Research (ACR) fabricated a fibrous monolith filament containing a single core and sheath, using a model system containing alumina and carbon black for this evaluation. The core material was RU9

(Stratasys, Inc.) binder containing 55 vol% alumina while the sheath consisted of RU9 binder containing 42.75 vol% alumina and 2.25 vol% carbon black. The core and sheath constituted 82.5 and 17.5 vol% of the 0.070 inch diameter filament, respectively.

A number of test pieces were produced and a cross-section of one piece is shown in Figure 6. In order to more clearly discern the structure, the roads in this piece were laid down on

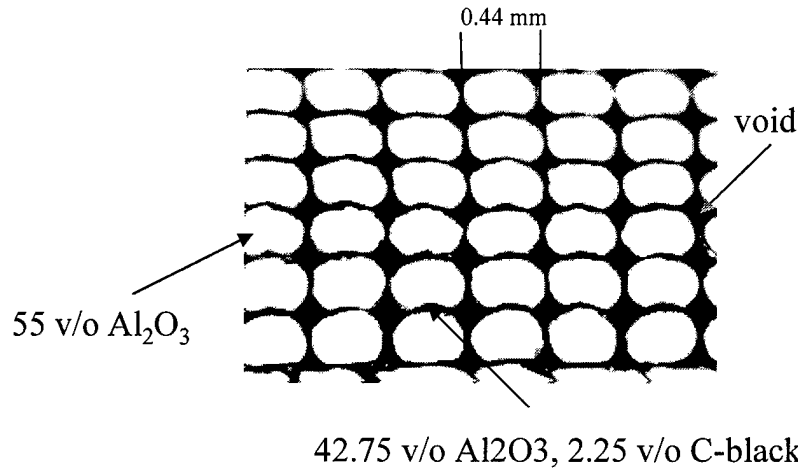


*Figure 6. Cross-section of single-cell fibrous monolith sample prepared by fused deposition of fibrous monolith filament.*

top of each other, resulting in the voids which appear in Figure 6. As seen in Figure 6, the fibrous monolith microstructure was retained during the deposition process. A 0.015 inch diameter nozzle was used for deposition, resulting in a road width of ~ 0.017 inches. ACR also prepared a 0.070 inch diameter filament containing 12 cells, each with a core and sheath, of alumina and carbon black respectively.

A micrograph of the filament cross-section is shown in Figure 7. The composition of the cell and cell walls was again alumina and alumina/C-black, respectively. The composition of the cell boundary material was adjusted slightly: the solids loading was increased from 45 to 54 volume % solids. Stearic acid was used as the dispersant for both cells and cell walls.

The cell structure retention is excellent after extrusion. Also shown in Figure 7 is a cross-section of a sample built with some overlap between adjacent rows. This overlap is commonly used in FDC to avoid the introduction of strength limiting voids. Though some loss of structure occurs when roads overlap during a build, the overall retention of the FM structure is quite good. Deposition parameters will need to be controlled closely to avoid excessive smearing under these conditions. However, it appears that the microstructural scale obtained (5 micron cell wall thickness) using single cell filament will be sufficient to get the advantages of the fibrous monolith microstructure.

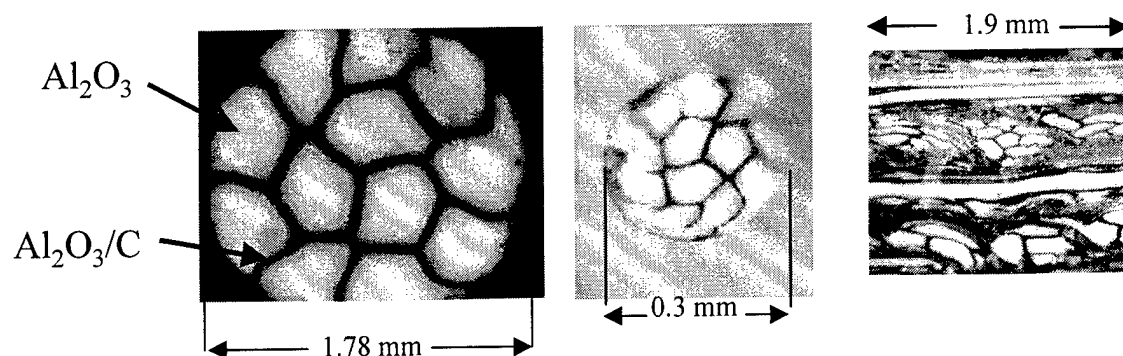


Figure 7. Micrographs of multi-cell fibrous monolith model material showing the structure in the as-prepared filament (left), after extrusion through a 0.3 mm nozzle (center) and after deposition with a 0.076mm overlap between roads (right).

The work on FM structures is being extended to materials based on silicon nitride as the core material and lanthanide glasses for the cell walls. Some promising lanthanide glass compositions have been prepared and will be used to manufacture filament in the next year.

#### Acknowledgements

The support of DARPA under contract N00014-97-C-0115 is gratefully acknowledged. Also, we would like to thank Sriram Rangarajan of Rutgers University for fabricating the part illustrated in Figure 6, and Don Baskin for his assistance in the preparation of the laminates.

#### References

1. R. Sathyamoorthy, A. V. Virkar, and R. A. Cutler, *J. Am. Ceram. Soc.*, **75** [5] 1136-1141 (1992).
2. D. Kovar, B. King, R. Trice and J. Halloran, *J. Am. Ceram. Soc.*, **80** [10] 2471-87 (1997)
3. A. Virkar et.al., *J. Am. Ceram. Soc.*, **71** [3] C-148-C-151 (1988)
4. M.K. Agarwala et.al., *Am. Ceram. Soc. Bull.*, **75** [11] 60-65 (1996)

# **Fabrication of Curved Ceramic / Polymer Composite Transducers for Ultrasonic Imaging Applications by Fused Deposition of Ceramics**

G.M. Lous, I.A. Cornejo, T.F. McNulty, A. Safari, S.C. Danforth

Rutgers, the State University of New Jersey,  
Department of Ceramic and Materials Engineering,  
607 Taylor road  
Piscataway, NJ

## **Abstract**

Fused Deposition of Ceramics (FDC), developed at Rutgers University, is a Solid Freeform Fabrication (SFF) technique where a three-dimensional green ceramic object is built layer by layer, starting from a Computer Aided Design (CAD) file of the object. This technique was used to build novel piezoelectric ultrasonic transducers for medical imaging applications. Curved ceramic skeletons for 2-2 (parallel ceramic / epoxy plates) composite transducers were built by FDC. The design's curvature can be tailored in the CAD file. Therefore, the final composite requires very little machining. In the FDC-built green parts, the ceramic plates were 500  $\mu\text{m}$  thick and the spacing between the plates was 1270  $\mu\text{m}$ . The FDC green samples were subjected to a slow binder burnout cycle at 550°C for 4 hours, using a heating rate of 8°C per hour, then sintered at 1285°C for 1 hour. Physical characterization of the samples revealed that 95% of the theoretical density was achieved. The ceramic plates shrunk 20% in height as well as in width. The shrinkage was of only 16% in the direction parallel to the plates. Optical microscopy and SEM were performed on green and sintered samples. The results of these characterizations are reported in this paper as well as the electromechanical properties of the final composites and of FDC bulk samples.

## **Introduction**

Fused Deposition of Ceramics [1] is a Solid Freeform Fabrication technique in which a green ceramic object can be built layer by layer, due to the deposition of roads by a liquefier moving in the x and y directions. The feedstock for this technique is a ceramic loaded, 1.78 mm diameter filament, which acts as a piston to push the material out of the nozzle. This technique was used to fabricate the ceramic portion of a piezoelectric ceramic / inactive polymer composite transducer for medical imaging applications. Composites are employed because they combine the property advantages of both polymer and ceramic transducers and thus have properties superior to the ceramic phase alone [2]. The material of choice was lead zirconate titanate (PZT) for the ceramic and Spurr epoxy for the polymer [3]. Ultrasound medical imaging transducers are used both as emitters and as receivers. For optimum efficiency in these two modes, the volume fraction of ceramic in the composite should be maintained between 20 and 30 volume percent [4]. This range is determined by compromising to achieve high piezoelectric charge coefficient ( $d_{33}$ ), moderate acoustic impedance and high thickness coupling coefficient ( $k_t$ ) [5]. For medical imaging applications, a curvature in the transducer's surface will allow for focusing the beam at a defined distance away from the transducer. This focusing ability leads to a better lateral

resolution, as the beam is smaller in the focal zone and therefore has a higher intensity; this increases the signal to noise ratio [6]. The design flexibility afforded by the FDC process allows the designer to freely choose the radius of curvature and all other transducer specifications without penalty of cost or manufacturing time associated with increased complexity of the design.

### Composite Design

Composites can have different “connectivities” as described by Newnham et al. [7], meaning that each phase can be self interconnected in either one, two or three dimensions. For this project, a 2-2 connectivity was chosen, where both the ceramic and the polymer are continuous in two directions (x and z), thus forming alternating parallel plates (Figure 1).

The minimum green ceramic plate width ( $w$ ) is dictated by the nozzle diameter used and the firing shrinkage. The volume fraction of ceramic then gives the spacing ( $s$ ) between these walls. In order to avoid lateral resonant waves between the plates (Lamb waves) [8], the thickness of the transducer should be larger than the pitch, which is defined as the sum of the width of one ceramic and one polymer plate. The resonant frequency of the transducer is inversely proportional to the transducer’s thickness [6].

In order to improve the resolution, it was chosen to use a curved transducer. The radius of curvature should be chosen depending on the application, i.e. the distance of the biological organ to image from the transducer. Two radii of curvature were chosen: 10 and 20 cm. Flat transducers (infinite radius of curvature) were also built for comparison.

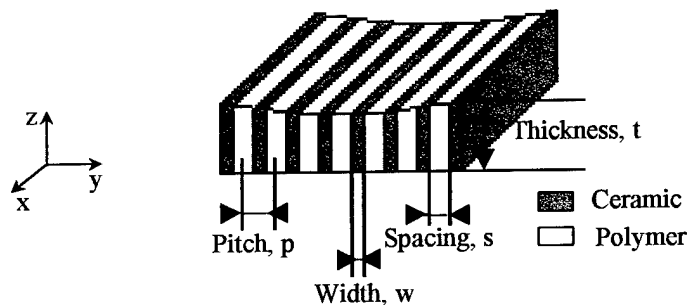


**Figure 1:** Schematic Representation of a Curved 2-2 Ceramic Composite Built by FDC Technique.

### Fused Deposition of Ceramics

The first step in making any structure by the FDC technique is to fabricate the raw material feedstock filaments. The generic processing sequence for PZT particle loaded filament fabrication was as follows: coating the PZT powder (non spray-dried, PZT-5H, TRS Ceramics, Inc., College Park, PA) with 1 wt. % stearic acid as a dispersant to lower the systems overall viscosity, compounding of coated powder (to 60 volume fraction of PZT ceramic) with binder, granulating the compounded material into mm sized pellets, and finally extrusion of filaments with close control over their diameter. Based on previous results, stearic acid was chosen as the dispersant. The binder used is a four component binder [9]. Several processing parameters were optimized to improve the quality of the filament. Capillary rheometer viscosity measurements

indicate a sufficiently low viscosity (at the actual FDC temperature of 166°C) for proper FDC behavior. These filaments were successfully used in the FDC process.

The next step was to create a CAD file of the desired transducer. In this project, the ceramic structure had to be curved on the top. However, since SFF techniques are layerwise techniques, the curvature had to be approximated by discrete steps. Figure 2 shows an example of the stepped surface.

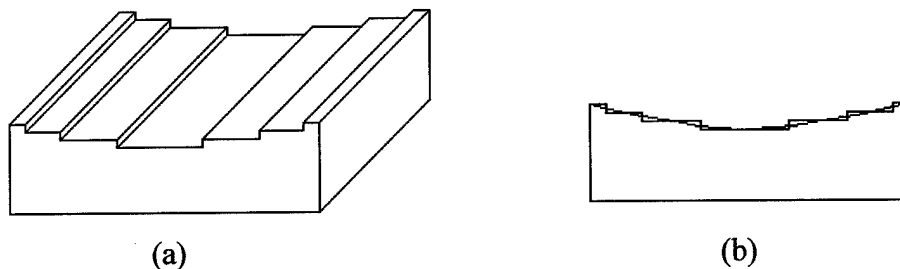


**Figure 2:** (a) Computer Aided Design of the 2-2 Composite Structure; (b) Side View of the CAD File Showing the Curvature Approximation by Steps.

Quickslice software was then utilized to slice the CAD file and to create the tool path. In order to create the parallel PZT plates for the 2-2 composite structure, a gap was left between the deposited ceramic roads. For the first parts, the nozzle diameter, road width and spacing between the roads were selected to be 508  $\mu\text{m}$ , 508  $\mu\text{m}$  and 1270  $\mu\text{m}$  respectively. The slice thickness was 254  $\mu\text{m}$ . Later, thanks to the development of a new binder formulation, it was possible to fabricate parts using a 254  $\mu\text{m}$  diameter nozzle; in these parts, the road width, spacing and slice thickness were respectively set at 330  $\mu\text{m}$ , 762  $\mu\text{m}$  and 127  $\mu\text{m}$ . In each case, the FDC build parameters such as liquefier temperature, envelope temperature, flow rate, etc., were optimized to improve part quality. The liquefier and envelope temperature were respectively set at 165 and 50°C. The flow rate was optimized in order to avoid overflow as well as underflow of material at the point where the nozzle starts depositing.

Figure 3 shows as-built ceramic structures for 2-2 composites fabricated by FDC with 508  $\mu\text{m}$  (a) and 254  $\mu\text{m}$  (b) diameter nozzles. It should be noted that the height of each of the parallel PZT plates is different, which results in the needed curvature for the focusing function of this transducer design.

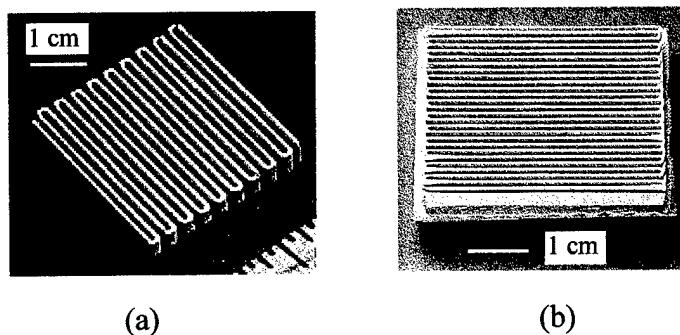


**Figure 3:** Images of Curved Green Ceramic Structures Built by the Direct FDC Technique; (a) Nozzle Diameter = 508  $\mu\text{m}$ , (b) Nozzle Diameter = 254  $\mu\text{m}$ .

## Post FDC Processing

The green PZT structure made by the direct FDC process was subjected to binder burnout (BBO) and sintering heat treatments after FDC. Since the part had fine features, the BBO cycle was modified to maintain part integrity: it was done by heat treating the part in static air atmosphere to 550°C for 4 hours with a heating rate of 10°C per hour. The set up was as follows: the sample was put in an alumina crucible on top of a coarse PZT bed; this bed eased the removal of the binder from the bottom of the sample. Sintering was performed at 1285°C for one hour in an excess PbO atmosphere (to prevent Pb loss during sintering) in a closed and sealed alumina crucible; the heating rate was 3.5°C per minute. The flow of oxygen inside the furnace was not controlled. This was followed by Corona poling of the ceramic using a voltage of 26 kV for 15 minutes. After aging for 24 hours, the ceramic structure was impregnated in Spurr epoxy polymer. The composites were then electroded, repled and the electromechanical properties were evaluated.

## Part Characterization

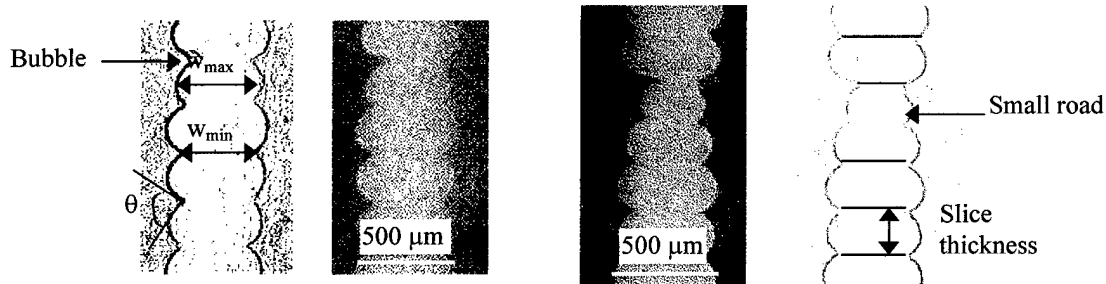


**Figure 4:** Optical Micrographs (and computer enhanced images) of Cross-Sections of Several Sintered FDC Plates made by FDC SFM Process.

Optical and scanning electron microscopy was performed on green and sintered PZT samples in order to characterize each part's micro- and macro-structure. Defects identified in the first iteration of the process (non-uniform road widths and porosity/bubbles) (Figure 4) were rectified through process improvements as can be seen from the micrograph shown in Figure 5.

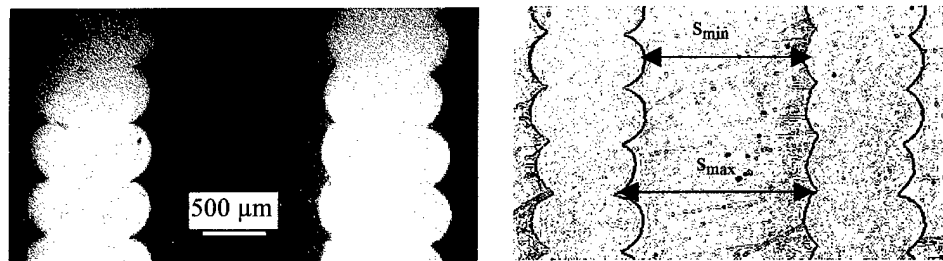


**Figure 5:** Optical micrographs (and computer enhanced image) of cross-sections of green PZT plates made by the FDC SFM process, showing that the defects such as small roads and bubbles were eliminated by improved processing.

Table 1 reports the measured values for road widths, slice thickness, pitch and the surface angles. The road width in the green state is what the FDC system builds and in the sintered state is after shrinkage during BBO and sintering. The surface angle refers to the angle that the material makes at the intersections of two successive layers. The main concern at this point is to decrease both the standard deviations of the values of road thickness, road width and inter-plate thickness (in both the as-built and as-sintered conditions), in order to maximize control over the component and insure that it accurately reproduces what is specified in the original CAD file. It is noted that, as with other ceramic materials made by SFF techniques, the green to sintered shrinkage measurements show anisotropy. For these parts, the shrinkage in the direction perpendicular to the roads (20%) was larger than in the direction parallel to the roads (16%). However, this can be incorporated into the original CAD design and can also be used to an advantage to obtain finer features. Scanning electron microscopy was performed on a fracture surface (Figure 6). These parts showed good layer to layer bonding and no delamination between the roads after sintering.

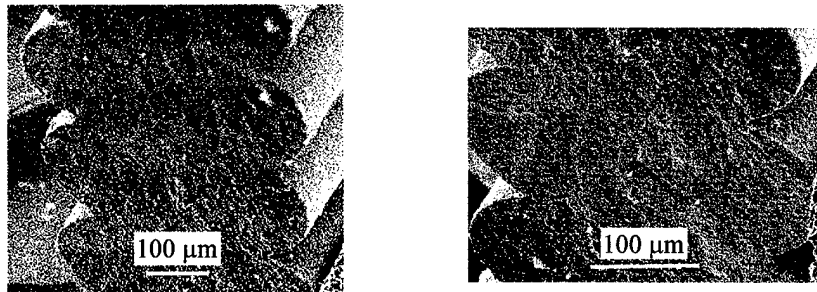


**Figure 6:** Scanning Electron Micrographs of fracture surfaces of sintered PZT plates showing good bonding between roads and high sintered density, i.e. no pores.

	Green part		Sintered part
	Measured values	CAD values	Measured values
<b>Slice thickness</b>	264 ± 7 μm	254 μm	212 ± 12 μm
<b>Left angle</b>	81 ± 15°		80 ± 13°
<b>Right angle</b>	71 ± 12°		81 ± 14°
<b>Maximum width</b>	553 ± 24 μm	508 μm	452 ± 39 μm
<b>Minimum width</b>	391 ± 34 μm		320 ± 44 μm
<b>(w<sub>max</sub>-w<sub>min</sub>)/2</b>	82 ± 12 μm		68 ± 24 μm
<b>Maximum spacing</b>	916 ± 15 μm		
<b>Minimum spacing</b>	751 ± 18 μm	813 μm	
<b>Pitch= w<sub>max</sub>+s<sub>min</sub></b>	1307 ± 21 μm	1321 μm	

**Table 1:** Statistical results regarding dimensional tolerances of green and sintered PZT plates made by FDC. The sintered parts were made before process improvements, the green parts were made after (See Figures 4 and 5).

Piezoelectric properties were measured on the flat PZT / polymer composites and on bulk samples made by FDC. The results are shown in Table 2. The values obtained are comparable with those obtained by conventional methods.

Sample	V <sub>f</sub> PZT (%)	k <sub>t</sub> (%)	k <sub>p</sub> (%)	K	tan δ	d <sub>33</sub> (pC/N)	ρ (g/cc)	Z (MRayls)
Flat FDC composite	27	68	32	627	0.023	397 ± 16	2.88	8.34
Dice-and-fill composite	25	63	---	780	0.085	355 ± 14	2.80	9.79
Bulk sample	100	54	71	3340	0.023	664 ± 4	7.7	30.54

**Table 2:** Piezoelectric Properties of Composites and Bulk Samples Made by FDC.

### Summary and conclusions

In summary, curved PZT composites with 2-2 connectivity have been designed and fabricated by the direct FDC technique. The curved 2-2 composite structure was successfully built by FDC using 508 micron and 254 micron diameter nozzles. Optical microscopy was performed on early samples, showing irregularities in the road widths for the green and sintered samples. Subsequent powder processing improvements have led to significantly better control over defects and road widths, etc. No significant irregularities were observed on recent samples as a result of these processing improvements. The slice thickness showed good uniformity. Scanning electron microscopy showed no delamination and good bonding of the roads. The shrinkage behavior of the FDC samples was shown to be anisotropic, as is the case for other ceramics made by the FDC process. The piezoelectric properties of the flat composites as well as those of bulk samples made by FDC were found to be similar to those obtained in samples made by conventional methods.

### Acknowledgments

The authors thank the New Jersey Commission on Science and Technology Multi-lifecycle Engineering Research Center and the New Jersey Institute of Technology for providing the funding for this project.

### References

- [1] S. C. Danforth, A. Safari, M. Agarwala, A. Bandyopadhyay, R. van Weeren, N. Langrana, V. Jamalabad and W. Priedeman, "Solid Freeform Fabrication Methods," U.S. Patent No. 5,738,817, April 14, 1998.
- [2] T.R. Gururaja, A. Safari, R.E. Newnham and L.E. Cross, ch. 2 in Electronic Ceramics, edited by L.M. Levinson, Marcel Dekker, Inc., New York, 1987.

- [3] V.F. Janas and A. Safari, "Overview of Fine-Scale Piezoelectric Ceramic / Polymer Composite Processing", *J. Am. Ceram. Soc.*, vol 78, No 11, 1995, p 2945.
- [4] D.D.N. Hall, J.T. Bennett and G. Hayward, "The Design and Evaluation of Ultrasonic Arrays Using 1-3 Connectivity Composites", *SPIE*, vol 1733, 1992, p 216.
- [5] W.A. Smith and B.A. Auld, "Modeling 1-3 Composite Piezoelectrics: Thickness-Mode Oscillations", *IEEE Trans. On Ultrasonics, Ferroelectrics and Frequency Control*, vol 38, No 1, 1991, p 40.
- [6] J.D. Wicks and K.S. Howe, Fundamentals of the Ultrasonographic Technique, Yearbook Medical Publishers, Chicago, 1983.
- [7] R.E. Newnham, D.P. Skinner, L.E. Cross, "Connectivity and Piezoelectric-Pyroelectric Composites", *Mat. Res. Bull.*, v 13, 1978, p 525.
- [8] W.A. Smith, "The Application of 1-3 Piezocomposites in Acoustic Transducers", *ISAF*, 1990, p 145.
- [9] T.F. McNulty, F. Mohammadi, A. Bandyopadhyay, D.J. Shanefield, S.C. Danforth and A. Safari, "Development of a binder formulation for Fused Deposition of Ceramics", *Rapid Prototyping Journal*, in Press.



# Automated Fabrication of Complex Molded Parts Using Mold SDM

A.G. Cooper<sup>1</sup>, S. Kang<sup>1</sup>, J.W. Kietzman<sup>1</sup>, F.B. Prinz<sup>1</sup>, J.L. Lombardi<sup>2</sup> and L. Weiss<sup>3</sup>

1. Stanford University, Stanford CA
2. Advanced Ceramics Research, Tucson AZ
3. Carnegie Mellon University, Pittsburgh PA

## ABSTRACT

Mold Shape Deposition Manufacturing (Mold SDM) is a Solid Freeform Fabrication technique for producing complex shaped fugitive wax molds. A variety of castable polymer and ceramic materials have been used to make parts from these molds. This paper describes the Mold SDM method and an automated mold building machine based on a commercial CNC mill. Process steps, material selection and equipment issues are explained. Alumina, silicon nitride, polyurethane and epoxy parts with feature sizes ranging from 0.5 to 30 mm will be shown, as well as pre-assembled mechanisms and multi-material parts.

## INTRODUCTION

Ceramic materials have excellent high temperature properties, high strength and stiffness, low density, and good chemical resistance. These properties make ceramic materials very attractive for a wide range of engineering applications. However, two principal factors currently limit the use of structural ceramics: the low toughness of ceramic materials and the difficulty of making high-quality complex shapes. The Mold SDM process addresses the latter issues.

Traditional ceramic manufacturing processes, such as machining of green ceramic blanks, work well for making simple shapes. Solid Freeform Fabrication (SFF) processes, based on layered manufacturing, can build up complex shapes but, in general, produce parts with poor surface finish, often displaying a stairstep effect on surfaces that are not vertical or horizontal. The layer boundaries are also potential sources of defects that can reduce the mechanical properties. Mold SDM was developed to address these issues. Mold SDM is a layered manufacturing process, so it can build complex shaped parts. However, it is also an additive-subtractive process which uses CNC milling to accurately shape all surfaces as they are built to minimize the stairstep effect. Although the mold is built in layers, there will be no layer boundaries in the finished part since the final part is cast monolithically.

In addition to ceramic parts, Mold SDM can be used to make parts from a variety of castable materials including polymers such as polyurethane and epoxy.

This paper describes two aspects of the Mold SDM process. First is the Mold SDM process itself in terms of process steps and the related materials and process issues. Second is the automation of the process and the construction of an automated machine that implements the mold building phase of the process.

## THE MOLD SDM METHOD

Mold SDM is a variation on Shape Deposition Manufacturing (SDM). SDM is an additive-subtractive layered manufacturing process which has been used to build a variety of metal and polymer parts [1,2]. Most SFF techniques decompose the model into relatively thin planar layers of uniform thickness. In SDM, however, the layers are three-dimensional, may be of arbitrary

thickness and do not need to be planar. This adaptive decomposition allows the number of layers to be minimized which in turn leads to reduced build times. In Mold SDM fugitive molds are built using SDM techniques and these are then used to cast a variety of part materials.

Figure 1 illustrates an example of the Mold SDM building sequence for a simple part with three layers. A mold is constructed from mold material surrounding temporary part material which defines the mold cavity. In steps 1 through 8 the mold is built up layer by layer. Removal of the temporary part material, in step 9, leaves a mold ready for casting in step 10. Once the part material has cured there are a range of processing options available. The figure shows two possible alternatives. In the first option (11a and 12a), the mold material is removed and then finishing operations, such as removal of runners and gates, are performed. In the second option (11b and 12b), the mold material is used as fixturing during finishing operations and is removed afterwards.

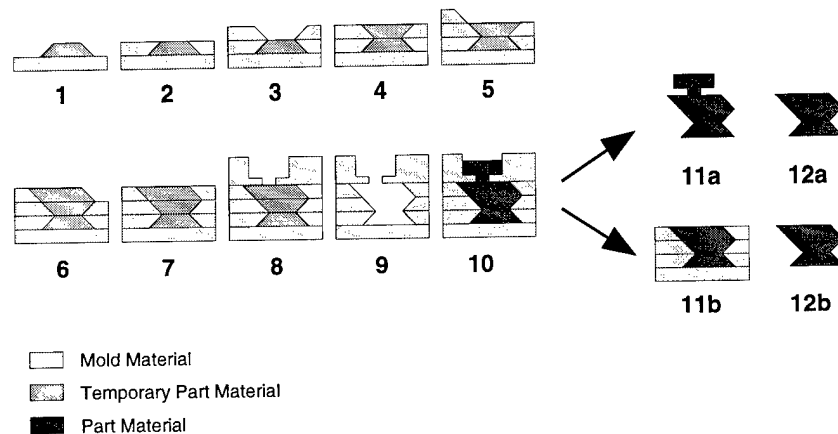


**Figure 1:** Example Mold SDM process sequence

The main advantage of Mold SDM over SDM and other layered processes is that since the final part is cast monolithically there will be no layer boundaries in the finished part. This is particularly advantageous for flaw sensitive materials, such as ceramics, or for materials with poor interlayer bonding. In comparison with direct machining of ceramic green materials, Mold SDM also minimizes the amount of part machining required which is an advantage for materials that are difficult or expensive to machine, such as ceramic green materials.

Mold SDM has several limitations over SDM. First, a third compatible material, the temporary part material, is required. The additional materials compatibility and processing requirements may restrict the range of materials that can be used. Second, there are the extra casting and mold removal steps which will increase processing time. Finally, mold filling issues may limit part geometry, although in many cases sprues and vents can be added to ensure complete mold filling.

### Materials Issues

The capability to make quality molds from which quality parts can be produced depends on a number of mold and temporary material properties [3]. The materials must have low shrinkage to reduce warping and distortion. They must bond to each other so that they do not delaminate and are able to withstand cutting forces. They must machine well so that good surfaces can be produced. They must be chemically compatible with each other so that they do not damage each other, both during the build phase and the two etching steps.

In addition to these basic requirements there are a number of other material properties which are desired to make the process more rapid or efficient. Being able to etch the temporary part

material and later the mold material quickly and easily saves time. Low cost, non-toxic materials make the process more economical.

The main issue with the mold material is the tradeoff between shrinkage and machinability. In general, machinable waxes have high shrinkage while low shrinkage waxes tend to machine poorly. Table 1 shows a range of waxes that have been tested for use in Mold SDM.

Wax	Melting Point (°C)	Shrinkage (linear %)
Kindt-Collins Master Protowax	60	0.46
Kindt-Collins Master File-a-wax	105	2.60
Freeman machinable	105	2.91
25% Kindt-Collins Master File-a-wax 75% Kindt-Collins Master Protowax	80	0.80

**Table 1:** Waxes tested for use in Mold SDM

Currently the preferred wax is the 25/75 mix of Kindt-Collins Master File-a-wax and Protowax. The File-a-wax is a machinable wax, the Protowax is a casting wax. By mixing the two it is possible to obtain a better tradeoff between machinability and shrinkage than is available in a commercially available wax.

Melting point and melt viscosity are two other important properties. A lower melting point wax is desired because this will reduce the heat input into the previous layers during wax casting thus reducing mold warpage. However, the wax must have a high enough melting point to be able to withstand the cure conditions for the final part material. Many materials require an elevated temperature cure or have an exothermic curing reaction. Low melt viscosity is beneficial since this will allow the wax to more easily fill fine features. It will also make wax removal by melting easier as the wax will run off the part more readily.

The temporary part material must be able to accurately define the mold cavity. To do this the temporary part material must be machinable so that fine features can be made and heat resistant so that it can withstand wax deposition conditions. Similar to the case for wax formulations, it was found that a better material could be obtained by mixing commercially available soldermask formulations. Mixing brittle and rubbery varieties produced a tougher, more machinable soldermask. One drawback of using this mixture, however, is that the viscosity gradually increases over time. This mixture also suffers from low heat resistance and low cure depth. Low heat resistance means that features are more likely to be distorted when hot wax is cast over the soldermask. Low cure depth reduces build rate because thick layers must be built up in several steps. The current formulation can be cured up to 1.5 mm deep in 2 minutes.

### Process Issues

In Mold SDM wax layers are deposited by mass casting. This enables much more rapid material deposition than is possible with bead extrusion systems. In order to prevent the wax from flowing away from the desired deposition area some sort of containment must be used. In Mold SDM this is done by building up thin wax walls around the deposition area. These walls are built up by extruding a higher melting point wax that has sufficient viscosity to form a narrow bead. The wax is deposited at a temperature only slightly above the melting point so that it will solidify rapidly and form precise walls. Once the walls have been formed, the lower melting point mold wax is mass cast inside the walled off areas and allowed to cool.

In order to reduce thermal stresses and minimize the potential of damage to previously built layers it is desirable to cast the wax layers at as low a temperature as possible. However at lower temperatures there will be less remelting of the previous layer, therefore the interlayer adhesion will not be as good. An option is to use preheating of the previous layer, using an IR lamp for example, to warm up the surface so that it will remelt more easily and reduce the required deposition temperatures. For example the Kindt-Collins Master File-a-wax deposition temperature can be reduced from 180°C to 160°C. One disadvantage of preheating is that interlayer discontinuities tend to be greater. This is believed to be due to softening of the surface layer that is then distorted as the new wax layer cools and shrinks above it.

The cooling time between wax deposition and machining accounts for a significant fraction of the total part build time. Wax layers must usually be allowed to cool for 2 hours for a typical 5-10 mm thick layer. Thicker layers will take longer. In order to reduce this time and increase the process rate, alternative ways of speeding the cooling of the wax are currently being investigated. By simply blowing cool air over the surface it is possible to reduce cooling times by a factor of 2-4.

## PROCESS AUTOMATION

To improve the rate of production and the quality of parts made by Mold SDM, an automated mold-making machine has been built. The machine, shown in Figure 2, is based on a commercially available Haas VF-0E 3-axis CNC milling machine. The mill was modified by the addition of material deposition and curing hardware. Ultimately one could produce either complete Mold SDM machines or retrofit kits that could be installed on existing CNC machines.

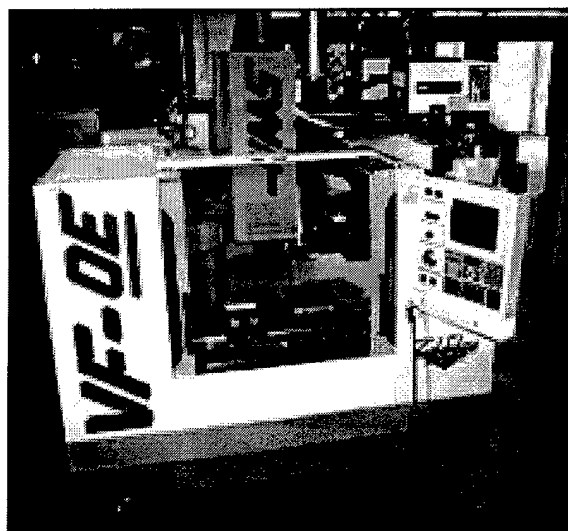
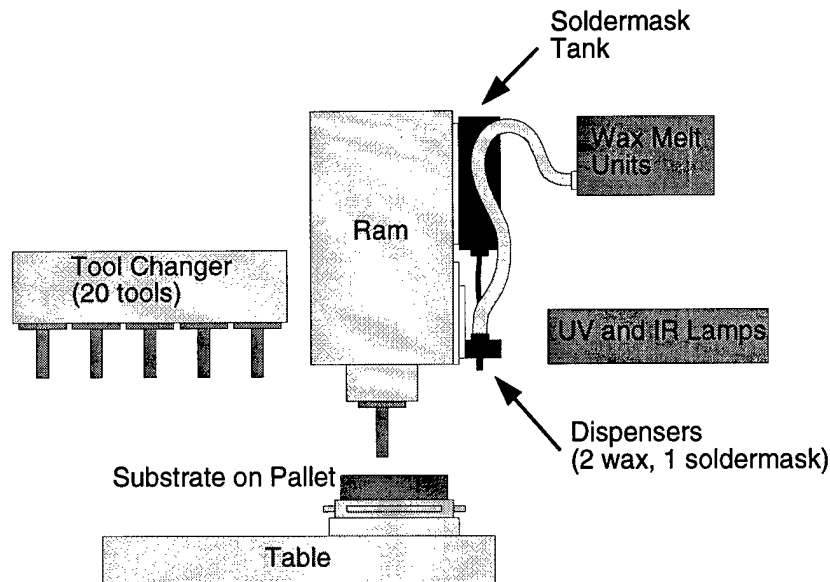


Figure 2: Automated Mold SDM machine picture

Figure 3 shows the main components of the Mold SDM machine. The CNC mill's machining functionality is used to perform all shaping operations. The add-on equipment together with the mill's positioning capabilities performs material deposition and curing.

The CNC mill is used to perform all XY motion, as well as the Z motion for the dispensers. The vertical positioning of the dispensers is critical since these need to be able to track the part surface accurately in order to deposit material in the right locations. By attaching the dispensers to the ram of the mill, one can use the Z positioning capabilities of the machine. This

makes implementation much easier since it is not necessary to build additional Z positioning hardware that is coordinated with the XY motion of the mill. The ram does have a weight limit, however, so the hardware attached to it should be as light as possible.



**Figure 3:** Automated Mold SDM machine schematic

The dispensers are attached to the ram via pneumatically actuated linear slides to produce an up and a down position. The dispensers are normally held in the up position to keep them clear of the part during machining. To deposit material, the appropriate dispenser is moved into the down position and material deposition begins. When finished the dispenser is retracted back to the up position.

The lights do not need to follow the surface of the part and so their Z positioning requirements are less strict. They are usually positioned at a set height above the surface and turned on while the part moves back and forth underneath. For these reasons, and to minimize the amount of equipment mounted on the ram, a separate linear actuator moves the lights up and down.

The Slautterback KB10 wax dispensers are commercially available hot melt dispense units which have a heated melt unit and a pump which forces the molten wax along a heated hose to a dispense valve. Since two types of wax must be deposited, one for building containment walls for casting and one for building the mold itself, two wax dispensers are required.

The soldermask dispenser consists of a pneumatically operated EFD 725DA-SS dispense valve. Soldermask is supplied from a pressurized reservoir.

The Uvexs OCU-12C ultraviolet light is used to cure the soldermask. It is a line source 12 inches long with a power intensity of 300 W/in. The light contains an IR filter to minimize the amount of IR light emitted. It is important to minimize the amount of IR light emitted because this will heat the previous layers and may cause warping, or even melting in extreme cases. The Research Inc. 4453-A-10-06 IR area heater is used to preheat the substrate before deposition of wax. This is an IR heat lamp with six 1000W bulbs that covers a 10 in. by 6 in. area. Since neither light covers the entire 12 in. by 12 in. area of a pallet, curing or preheating operations are performed by scanning the part back and forth under the light.

Control of the integrated CNC deposition/milling machine is performed using both the CNC mill's built-in controller and an external computer, as shown in Figure 4. The computer controls the deposition and curing apparatus via digital and analog I/O and sends motion commands to the CNC controller by downloading CNC program files via an RS232 serial line. The mill also has four relay closure outputs and a digital input that can be controlled and monitored from within the CNC program in order to synchronize the mill's motion with the deposition and curing operations. During a curing operation, for example, the mill will move the part below the UV light, set one of its outputs and wait. When the computer detects that output signal, it turns on the UV light and signals the mill to continue. The mill then begins to move the part back and forth under the light.

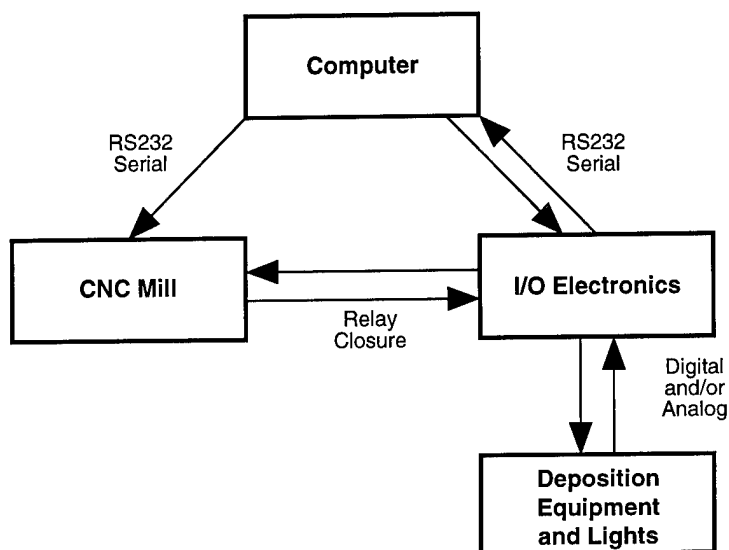


Figure 4: Machine control schematic

## EXAMPLE PARTS

A variety of castable part materials have been used to make parts using Mold SDM. Polymer parts have been made using polyurethanes and epoxy. Ceramic parts have been made using alumina and silicon nitride gelcasting formulations. Pre-assembled mechanisms have also been built in both polymer and ceramic materials.

Figure 5 shows three multi-material turbine assemblies. The epoxy rotor consists of eight curved blades between two discs. A captive polyurethane shaft passes through a hole in the center of the rotor. The rotor is free to spin around the shaft. The diameter of the rotors is 30 mm. These assemblies were built with radial clearances as small as 0.20 mm between the shaft and rotor.

In an effort to determine minimum feature sizes for Mold SDM a set of miniature alumina turbines were built. These are shown in Figure 6 in front of a full size part. The miniature turbines are 7 mm in diameter and 3 mm tall. The section thickness is 0.5 mm.

Figure 7 shows a simplified aircraft engine vane part made of alumina. This part is about 60 mm tall.

Figure 8 shows a part called the Inchworm. It features two pairs of wheels with ratchets mounted to a flexible backbone. The ratchets prevent the wheels from turning backwards. Pressing down on the backbone rolls the front wheels forward, releasing the backbone allows the rear wheels to roll forward in turn, thus moving the Inchworm forward. Unfortunately the wrong clearances were used in the actual parts and as a result the ratchets do not work. The Inchworms

were also the first Mold SDM parts made using multiple cavity molds. This allowed the wheels to be cast using colored polyurethane to distinguish them from the backbone.

The part shown in Figure 9 is a pitch shaft for a missile guidance system. This part demonstrates the ability of Mold SDM to build curved surfaces without stairsteps.



**Figure 5:** Multi-material turbines

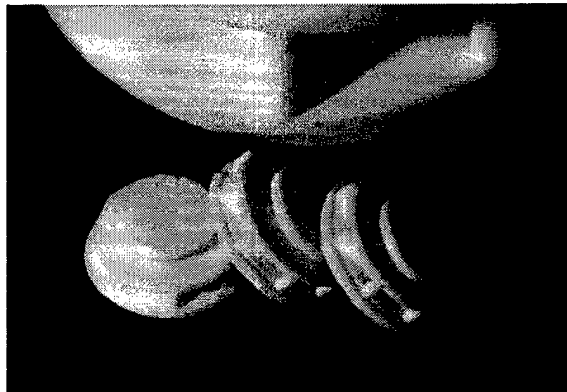


**Figure 6:** Miniature alumina turbines

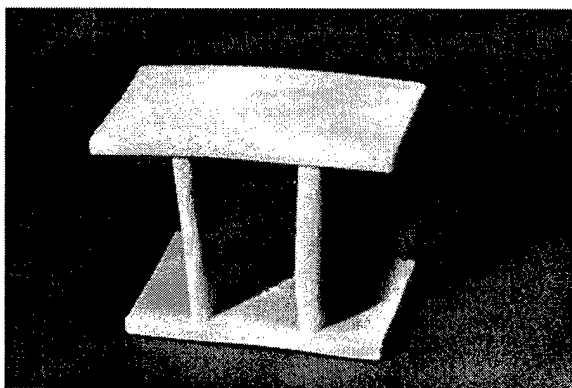


**Figure 7:** Alumina vane



**Figure 8:** Multicolor polyurethane Inchworm

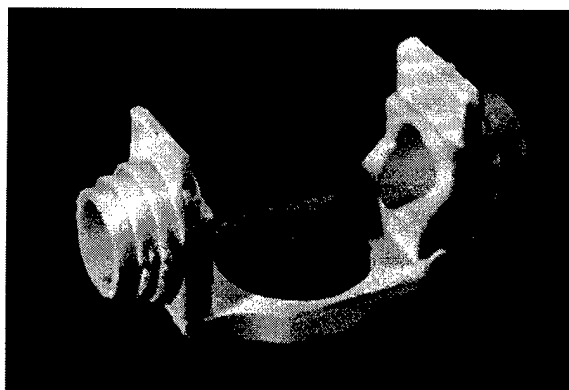


**Figure 9:** Alumina pitch shaft

## CONCLUSION

The Mold SDM process was developed to enable the fabrication of high quality complex ceramic parts. It is an additive-subtractive layered manufacturing process that builds complex fugitive molds. The use of CNC milling to shape all geometry results in smooth accurate surfaces. Since the final part material is cast monolithically there will be no layer boundaries in the finished part.

The Mold SDM process has been automated by the addition of deposition and curing hardware to a commercially available CNC milling machine. Parts have been made without manual intervention using this machine.

Alumina and silicon nitride ceramic parts have been made by gelcasting. Other castable materials, such as polyurethane and epoxy, have also been used successfully.

## ACKNOWLEDGMENTS

The authors would like to acknowledge Shelley Cheng for building the miniature turbine parts as well as David Miller and Brad Levin for building the Inchworm parts. The authors would also like to acknowledge Tom Hasler for his advice and help with all aspects of machining and CNC mill operation. The authors would also like to acknowledge Larry Schultz, Blake Tennison, and Mark Carter for their assistance with process automation equipment.

This work was supported by the Defense Advanced Research Projects Agency under contract N00014-96-1-0625. Additional support was provided by a Department of Energy Integrated Manufacturing Pre-Doctoral Fellowship.

## REFERENCES

- [1] R. Merz, F. B. Prinz, K. Ramaswami, M. Terk, and L. E. Weiss, "Shape Deposition Manufacturing," *Proceedings of the 1994 Solid Freeform Fabrication Symposium*, The University of Texas at Austin, August 1994, pp. 1-8.
- [2] F. Prinz and L. Weiss, "Method for Fabrication of Three-Dimensional Articles," U. S. Pat. No. 5,301,415, April 12, 1994.
- [3] J. W. Kietzman, A. G. Cooper, L. E. Weiss, L. Schultz, J. L. Lombardi, and F. B. Prinz, "Layered Manufacturing Material Issues for SDM of Polymers and Ceramics", *Proceedings of the 1997 Solid Freeform Fabrication Symposium*, The University of Texas at Austin, Austin, Texas, August 1997, pp. 133-140.

# COMPOSITES WITH GRADIENT PROPERTIES FROM SOLID FREEFORM FABRICATION

V.R. Gervasi, R.S. Crockett  
Rapid Prototyping Center  
Milwaukee School of Engineering, Milwaukee, WI

## Abstract

TetraCast is a build style developed by Milwaukee School of Engineering involving stereolithography patterns produced with an open cellular structure inside a surface shell. Composites are created using this pattern as a host for a filler material, generally epoxy matrices loaded with various fibers or microspheres. Regions within a single object may be separated by thin barriers, allowing filling with different matrix materials to create regions of differing local properties. The internal structure can also be continually graded in thickness to produce composites with properties ranging from that of the filler material to that of the TetraCast material (currently stereolithography epoxy or FDM ABS).

## Introduction

Functionally gradient materials (FGMs) transform from one material (part A) to another (part B), unlike traditionally bonded materials that have a distinctive seam. The goal of FGMs is generally to produce materials able to withstand extremely harsh environments. Examples include surviving temperatures as high as 2100 K and temperature gradients, within the FGM, as great as 1600 K over a very short region. FGMs also need to handle these temperatures while maintaining mechanical functionality. To accomplish this, the benefits of two or more materials are combined in a FGM to produce a non-traditional engineering material<sup>1</sup>. A good example is a FGM consisting of metal and ceramic, as illustrated in figure 1. The properties of the metal component are high strength, ductility, conductivity (electrically & thermally) and low chemical resistance. The properties of the ceramic are high hardness, insulating, brittle, chemically

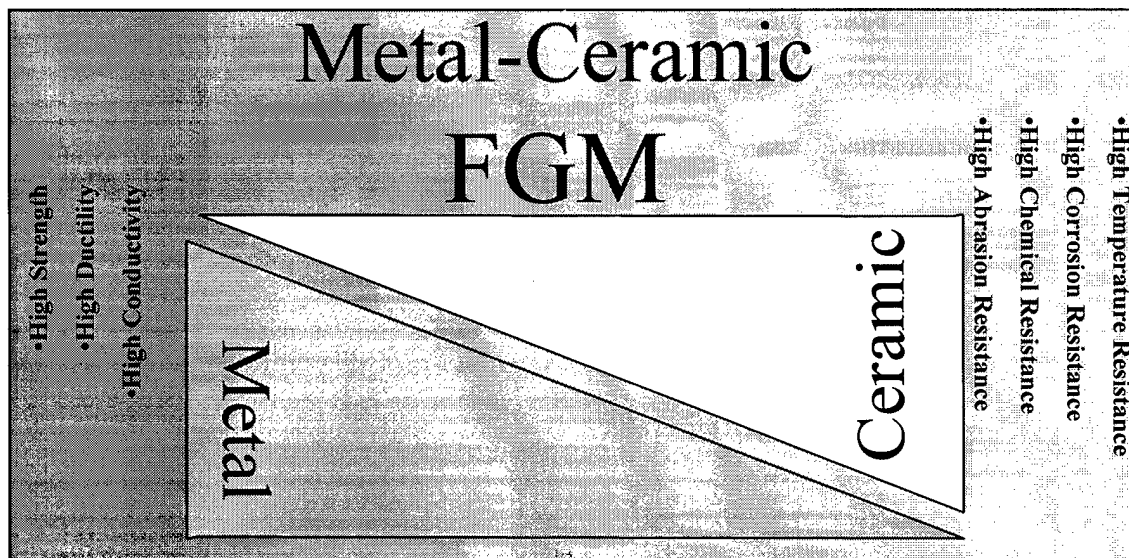


Figure 1. Metal-Ceramic FGM

resistant, and abrasion resistant. Now, if the advantages of both are combined in a FGM, the result is a material with high mechanical strength, conductivity, corrosion resistance, and abrasion resistance. Combinations being tested include: metal-ceramic, ceramic-ceramic, carbon-carbon, carbon-ceramic, and polymer-polymer.

Industries with applications for FGMs include aerospace, manufacturing, mining, nuclear power, architecture, automotive, biomedical, and electronics. In aerospace, leading edges and combustor cans could benefit from FGM properties. Whereas in manufacturing and mining, abrasive tools could be produced with a combination of wear resistant surfaces and shock absorbing surfaces such as those found in FGMs. Biomedically, bone implants could be generated with bio-compatible materials on one surface and mechanically functional materials on another surface.

The Production of FGMs is quite challenging, and numerous techniques are being tested and used. A technique, such as vapor deposition, creates gradient materials at the atomic or molecular level. Other techniques, on the micro-scale, produce gradients by combining powders or laminates to produce FGMs. A new approach uses a meso-scale gradient morphology. This morphology, discussed in this paper, is called Gradient Tetracast.

## Background

Before discussing the approach to this research, it is helpful to give some background on the TetraCast Build Style, the Gradient Tetracast Morphology, and the Rapid Composite Process.

TetraCast<sup>2</sup> is a SFF build style used to produce lattice-filled patterns for the Rapid Composite Process and investment casting. TetraCast patterns have many of the same benefits as QuickCast<sup>TM</sup> patterns. TetraCast uses an internal three-dimensional tetrahedron morphology modeled after the molecular bond geometry found in diamonds. The TetraCast internal lattice offers the outer surface or skin sufficient support with minimal density. Figure 2 illustrates the TetraCast Lattice.

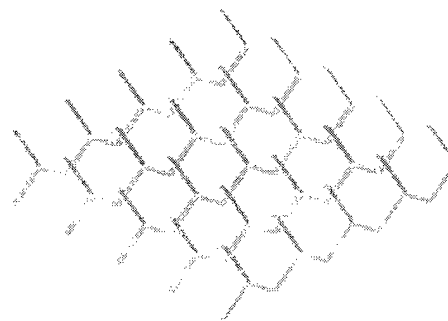


Figure 2. TetraCast Lattice

Gradient Tetracast (GTC) is a three-dimensional morphology, transforming from one material to another, in a controlled manner. This morphology can be likened to M.S. Esher art work in three dimensions. To create Gradient Tetracast, spacing between standard TetraCast units can remain constant while the branch thickness is increased in a controlled manner (as shown in figure 3). This controlled increase in branch thickness results in a proportional change in volume percentage of material combinations. In theory, this volume percentage will transform

from 100 percent of material A to 100 percent of material B at any rate, in any direction. With Gradient Tetracast the transformation is three dimensional and mechanically interlinked. GTC becomes two TetraCast lattices with varying branch thickness. Part A is the mirrored negative of part B and GTC can be stacked as shown in figure 4.

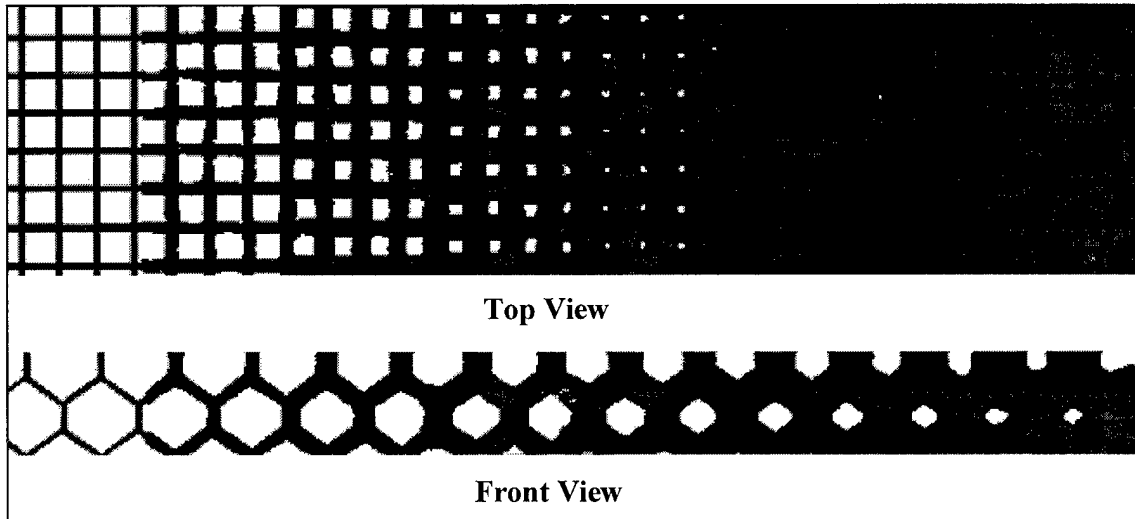


Figure 3. Gradient Tetracast

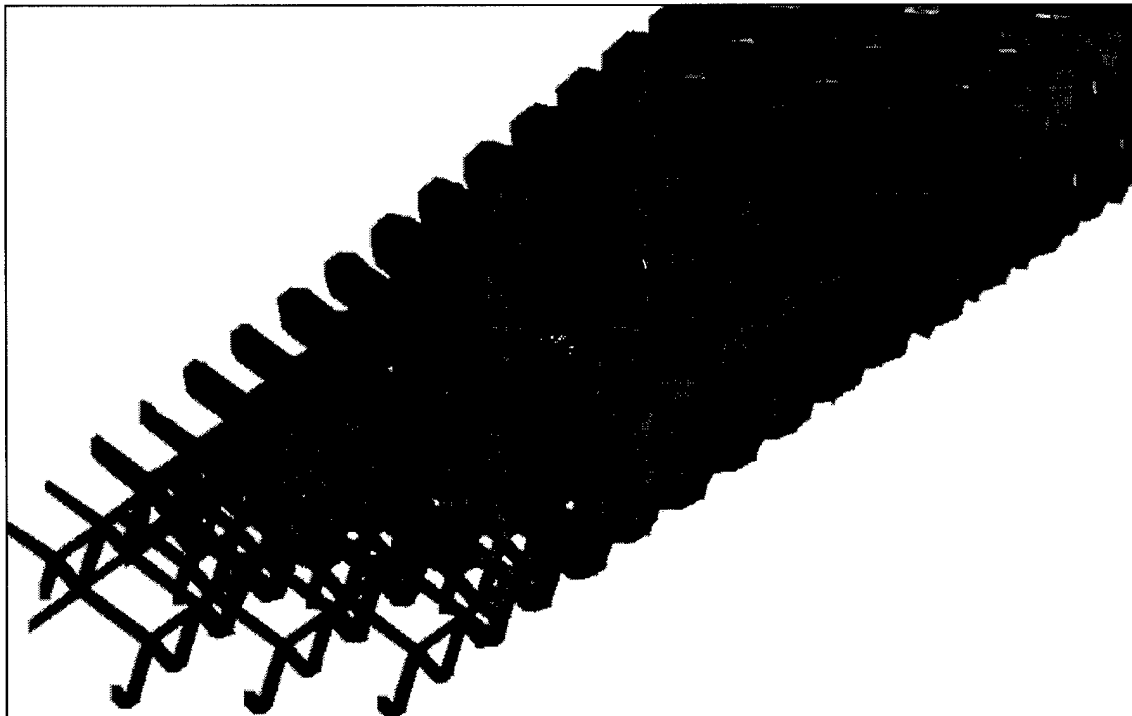


Figure 4. Stacked Gradient Tetracast

The Rapid composite Process<sup>3</sup> (RCP) is used to create composite parts from TetraCast patterns. With this method, the TetraCast pattern becomes part of the final composite, as it both

defines the net-shape of the desired geometry and embodies the composite material during matrix solidification. The composite material is introduced into the TetraCast pattern as chopped fibers, flakes, and/or particles suspended in a liquid matrix (typically epoxy). After the TetraCast pattern is completely filled, the matrix solidifies, resulting in a net-shape functional composite part.

Through this method, the composite material properties can be tailored to meet application requirements of the composite. Parts of virtually any geometry can be produced. This process may be especially well suited for custom-manufacturing of complex, one-of-a-kind, components for testing or end usage. The Rapid Composite Process was applied to GTC for the first experiment. The Rapid Composite process functions well to fill small features such as those found in the first GTC samples.

### **Objective**

The main objective of this research was to introduce a new gradient morphology that uses GTC as the transitional structure. To accomplish this a simple GTC material was produced consisting of part A (SLA photopolymer) transitioning into part B (glass filled epoxy). Sample Functionally Gradient Materials were produced within a class III tensile geometry profile.

### **Approach**

The approach to studying GTC began with the production of plastic-composite GTC tensile samples. The material combination was 50 percent SLA photopolymer and 50 percent glass filled epoxy. The main objective was to produce a visual sample of GTC to be used for discussion and analysis. The modulus of elasticity as a function of percentage composition was also analyzed. The approach used to produce the first GTC sample consisted of: CAD modeling, SLA production, RCP, sample slicing, and Testing.

The GTC tensile bar CAD model was designed to include five distinctive TetraCast percentage combinations to form a gradient. The first TetraCast region was less than 10 percent by volume increasing to greater than 90 percent in the final region. Each TetraCast section was 0.45 inches in thickness to allow machine stock for later slicing and sanding. All five TetraCast regions were combined within a thin shell. One hundred percent SLA photopolymer and composite samples were produced separately.

Two GTC samples were produced on an SLA 250, using ACES build style. Uncured photopolymer was removed in a centrifuge, leaving a 50 percent graded air void and 50 percent graded photopolymer. SLA Photopolymer was chosen because of the fine detail, ease of uncured resin removal, clarity, and homogeneous mechanical properties (specifically Young's Modulus of Elasticity).

The RCP was used to fill the 50 percent graded void with glass filled epoxy as shown in Figures 5. Glass filled Epoxy was chosen for its high modulus and grey color.

Samples were sliced, polished, and tested for Young's modulus of elasticity. Figure 6 illustrates the sectioned GTC sample.

### Results/Discussion

As shown in Figure 5, a gradient material was successfully produced using the GTC morphology. The tensile samples produced with GTC had a volume percentage range from 95 percent photopolymer/5 percent composite to 28 percent photopolymer/72 percent composite. Low volume percentage photopolymer sections collapsed during RCP filling and were not used. This section would have been 95 percent composite/ 5 percent Photopolymer.

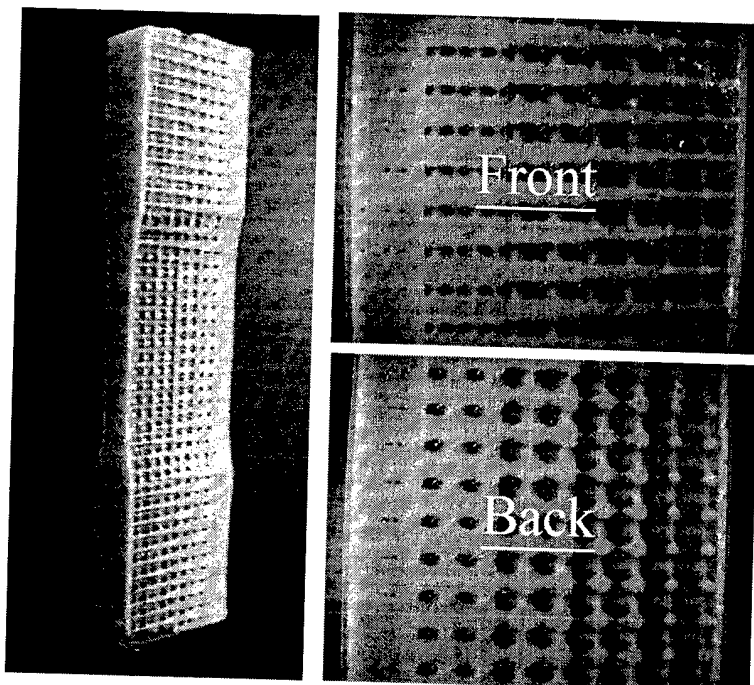


Figure 5. Filled Gradient Tetracast

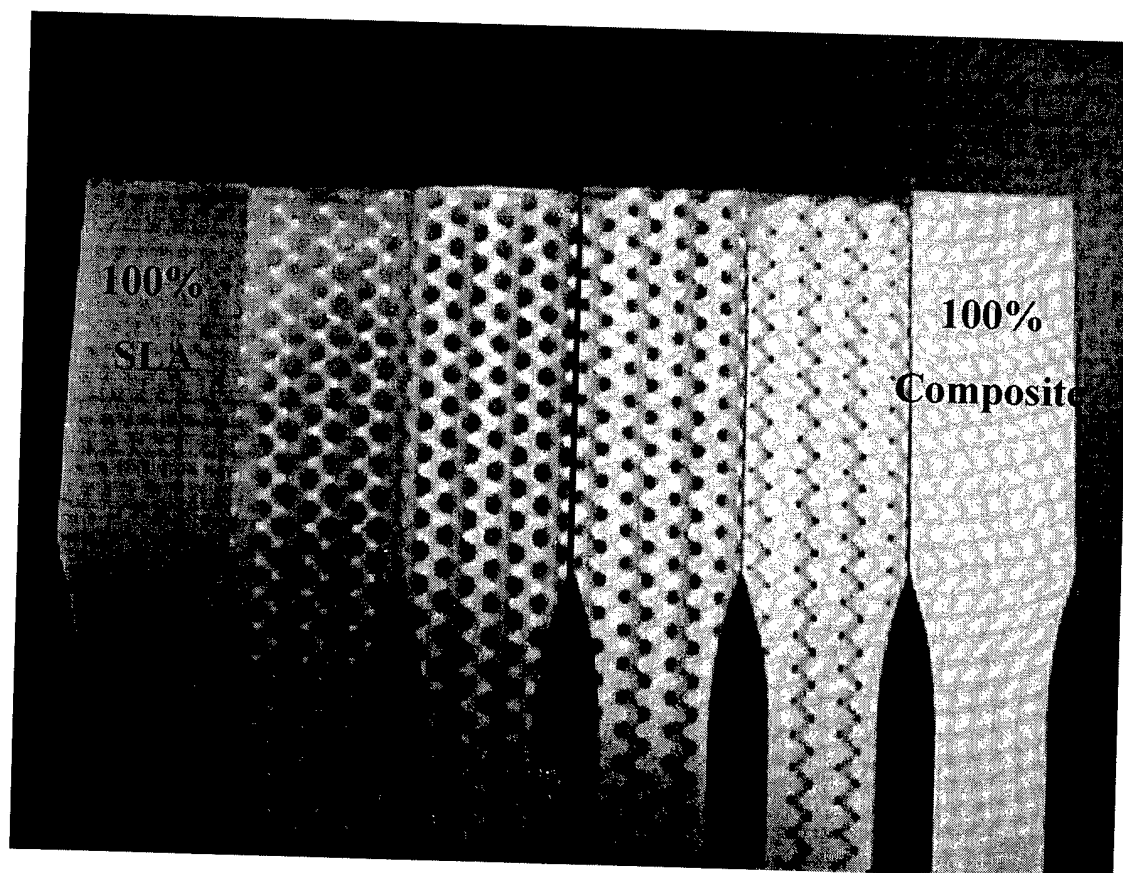


Figure 6. Sliced Samples

After sample slicing (figure 6), tensile testing was performed to determine the modulus of each section. Figure 7 illustrates the resulting stress-strain curves, clearly displaying an increase in stiffness as percentage volume of composite increased. Figure 8 illustrates the change in modulus as a function of material composition. The samples were expected to act similar to that of a particulate composite. The Upper Limit shown is the predicted moduli applying the rule of mixtures. The Lower Limit is what would be expected if the composite was loaded in the weakest possible direction, GTC fell below the Lower Limit. One reason for this could be a weak photopolymer-composite interface caused by uncured photopolymer between the two materials.

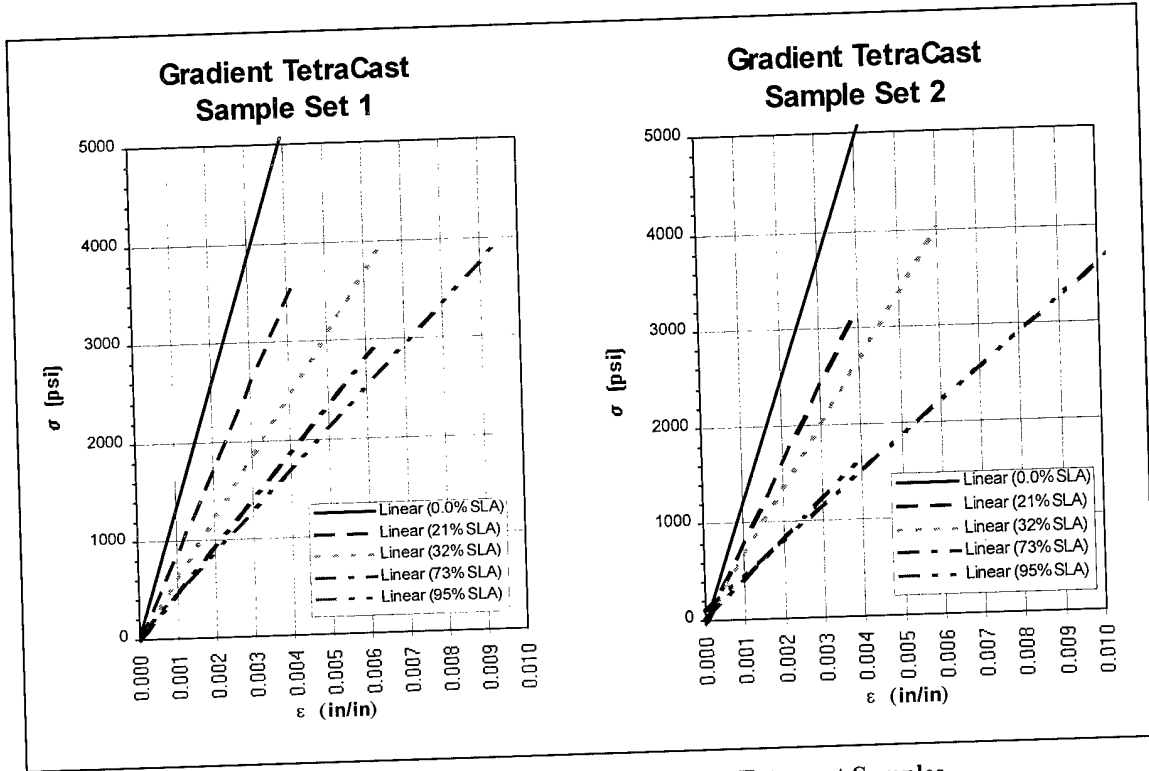


Figure 7. Stress Strain Curves for Gradient TetraCast Samples

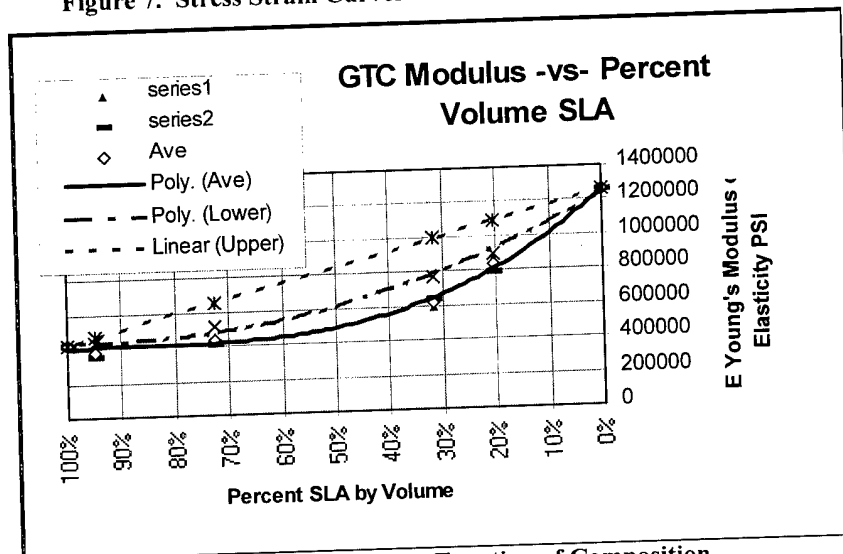


Figure 8. Modulus as a Function of Composition

## **Conclusions**

Functionally Gradient Materials can be created using Gradient TetraCast as a transformational morphology. Gradient TetraCast has the potential to be stackable, allowing for two or more materials in Functional Gradient Materials. Gradient TetraCast is a continuous structure providing thermal and electrical conductivity through metallic portions of Functional Gradient Materials.

## **Future Work**

Much work is required before the usefulness of Gradient TetraCast for Functional Gradient Materials is determined. In the future, metal-ceramic Functional Gradient Materials will be attempted along with other suitable material combinations. Applying Finite Element Analysis (FEA) to both the mechanical analysis and Gradient TetraCast unit design will also be considered for optimizing design and production. The production of simple to complex shapes will be attempted.

## **Acknowledgements**

The authors gratefully acknowledge the support of the Rapid Prototyping Consortium on this and other research.

The Authors also extend their thanks to the Rapid Prototyping Center Staff at Milwaukee School of Engineering for their contribution to this research.

Special thanks to Tom Bray, Dean of Applied Research, for his SFF insight and encouragement towards gradient material synthesis.

## **Bibliography**

1. Holt, J. Birch, Mitsue Koizuma, Toshio Hirai, Zuhair A. Munir, "Functionally Gradient Materials," American Ceramics Society, 1993, chaps 1 & 2
2. Gervasi, Vito R., Dr. Daniel A. Brandt, Steven D. Shaffer, King Lim, *TetraCast SLA Build Style*, International Conference on RP, 1997, pp 309-317
3. Gervasi, Vito R., *Net Shape Composites using SLA TetraCast Patterns*, Solid Freeform fabrication Symposium, 1997, pp 149-157



## Properties of a High Temperature Liquid Crystal Stereolithography Resin

R.P. Chartoff, J.W. Schultz\*, J. Bhatt\*\*, and J.S. Ullett

The University of Dayton  
Rapid Prototype Development Laboratory,  
Ohio Rapid Prototype Process Development Consortium, and  
Center for Basic and Applied Polymer Research  
Dayton, Ohio 45469-0130

\*Georgia Tech Research Institute

Atlanta, Georgia

\*\*Polaroid Corporation

Waltham, Mass

### Abstract

A liquid crystal monomer has been developed that contains both acrylate and acetylene reactive groups. The curing behavior and mechanical properties of the polymers formed from this monomer have been characterized in this study. Complete cure can be carried out in two separate steps, combining both photo and thermal polymerization. The initial photo-polymerization to form a robust "green" polymer involves crosslinking through the acrylate groups and the subsequent thermal polymerization to increase the crosslink density is accomplished by reaction of the acetylene groups. After the thermal postcure the polymer has an unusually high glass transition, in excess of 300°C. In addition, the monomer exhibits an ordered liquid crystalline (LC) phase. Photopolymerization while in the LC phase locks in the molecular ordering. Mechanical property data and additional information on curing in both the isotropic and LC phases are reviewed in the following presentation.

### Introduction

In order to expand the usefulness of stereolithography, new resins must be developed that have better functional mechanical properties at high temperatures. Current stereolithography resins have softening temperatures well under 100°C. As a result, they have limited value as high temperature structural materials. By increasing their high temperature mechanical stiffness and strength, stereolithography resins will find new and expanded applications in areas such as direct injection molding, wind tunnel testing, and under-the-hood automotive applications.

One way to increase the high temperature mechanical capability of a resin is to modify its molecular structure. Liquid crystal monomers represent a new class of stereolithography resins that incorporate rigid, rod-shaped molecular segments. The rigid molecular segment lends itself to two important properties: high glass transition temperature ( $T_g$ ), and the possibility of liquid crystalline order. Rigid-rod monomers can produce polymer networks with glass transition temperatures exceeding 100°C. In addition, their anisotropic molecular shape provides the possibility of liquid crystalline phase behavior, which can result in anisotropic physical and mechanical properties. At the University of Dayton, we have recently investigated a variety of rigid-rod photo-reactive resins. Four of these resins had liquid crystal phases. Some of the resins were cured with UV light, and some were cured with visible light. Table 1 summarizes  $T_g$  and elastic modulus data for these materials. The anisotropic physical and mechanical property characteristics of these materials are the subject of several previous papers [1- 4].

**Table 1 Summary of rigid-rod resin characteristics**

Resin	LC Phase	Cure Wavelength	T <sub>g</sub> (°C) (with postcure)	E' (GPa) (modulus at room temperature)
N1	Yes	364 nm	103	1 GPa
N2	Yes	364 nm	150	2 GPa
S1	Yes	Broadband, visible	150	2 GPa
S2	Yes	Broadband, visible	>350	2.2 GPa
I1	No	Broadband, visible	130	1.9 GPa
I2	No	Broadband, visible	158	1.75 GPa

In order to take advantage of such potentially useful properties, it is important to have a good understanding of the effects of monomer properties, polymerization conditions and postcure on the crosslink network formation and glass transition of these new materials. In this paper we consider resin S2, one that develops a particularly high apparent glass transition temperature, in excess of 300°C. This resin consists of a monomer that is both liquid crystalline and has two reactive acetylene groups. In addition to the acetylene groups, the monomer contains terminal acrylate groups that give it a "dual" curing capability. The network formation can proceed by first photo-curing through the acrylate groups, and then thermally postcuring the acetylene groups. This dual-curing capability allows increased flexibility in the processing of these materials for various applications.

## Experimental

### Material Preparation

Shown in Figure 1 is the monomer of interest, S2, which is a diacrylate with a rigid, rod-shaped core. The rigid core consists of a biphenyl moiety surrounded by acetylene bonds. On either side of the core are 3-carbon aliphatic spacers that connect to the reactive acrylate end groups.

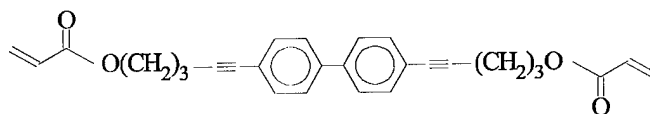


Figure 1 Chemical structure of monomer S2 showing two sets of reactive groups: acrylate and acetylene.

S2 has a smectic LC phase with a crystalline to smectic melting transition at 49°C and a smectic to isotropic transition at 64°C. These transition temperatures were measured by differential scanning calorimetry at a 10°C/min heating rate. To enable photopolymerization, the monomer was mixed with a photoinitiator, 2-benzyl-2-N,N-dimethylamino-1-(4-morpholinophenyl)-1-butanone (Irgacure 369, Ciba-Geigy), at 0.5 % concentration (by weight). Photopolymerization was carried out with a 100 Watt, broadband mercury lamp. Thermal post-curing was carried out without any additional initiator. Samples of polymer also were prepared from the monomer by thermal polymerization, either in its pure form or with a thermal initiator, dicumyl peroxide, at a concentration of 0.5 % (by weight).

### Characterization Methods

Differential scanning calorimetry (DSC) was used to identify phase transitions and to determine thermal cure temperature ranges for S2. The DSC instrument was a TA Instruments 2910 DSC, operated at a heating rate of 10°C/min. Thermo-gravimetric analysis (TGA) was used to identify thermal degradation of the polymer. The TGA instrument was a TA Instruments 2950 TGA, operated at a heating rate of 5°C/min.

Infrared spectra were measured in the transmission mode with a Nicolet 20DXB Fourier transform infrared (FTIR) spectrometer. To ensure sufficient signal from the instrument, the samples were kept very thin – approximately 10 microns. These thin-film samples were manufactured by sandwiching a small amount of LC monomer between glass slides. After photopolymerization, the films were carefully separated from the glass slides and were mounted, free standing in the FTIR spectrometer.

Linear viscoelastic characterization by dynamic mechanical analysis (DMA) was conducted with a Rheometrics RSA II instrument, using a thin film fixture. The measurements were made in the tension mode. All the samples were heated to 150°C and uniformly cooled immediately before testing to ensure a common thermal history and to minimize internal stresses caused by cure shrinkage.

### Results and Discussion

Network formation of S2 can occur via free-radical polymerization of the acrylate groups, the acetylene groups, or both. Without an initiator, thermal polymerization of the pure monomer occurs at a temperature of approximately 240°C. Addition of a free radical thermal initiator can substantially lower the polymerization temperature. This is shown in Figure 2, which plots the heat flow as a function of temperature for both pure monomer and monomer that is mixed with dicumyl peroxide. These data show that at room temperature, the monomer is in crystalline form. As the monomer is heated to a temperature of 49°C, it melts from a solid crystalline phase to a liquid crystalline (smectic) phase as shown by the first endothermic peak in Figure 2. At 69°C, the monomer undergoes a second melting transition from liquid crystalline to isotropic liquid as indicated by the second endothermic peak in Figure 2. For the pure monomer, the large exothermic peak at 240°C indicates the main polymerization reaction. This polymerization reaction is centered at 167°C for the monomer mixed with dicumyl peroxide. There is also a much smaller but repeatable exothermic peak at 175°C in the pure monomer sample. It is possible that this exotherm results from impurities, however the exact origin of this reaction peak is unclear.

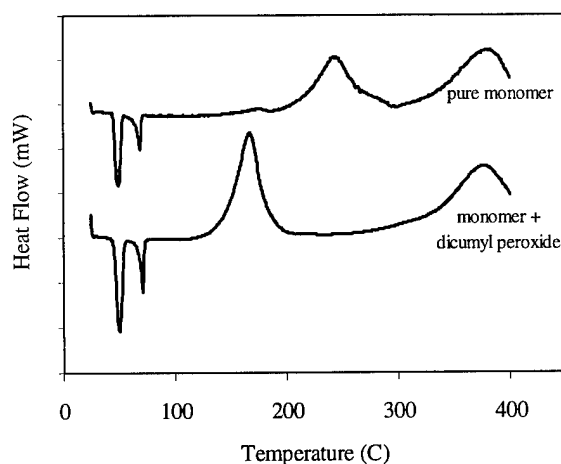


Figure 2 Differential scanning calorimetry data of monomer S2 in pure form and mixed with peroxide

At a temperature of 380°C, there is another large exothermic peak that occurs for both samples. This peak is caused by thermal degradation of the polymer. Confirmation that the 380°C peak is caused by degradation of the polymer is given by the thermo-gravimetric data of Figure 3. These data show the weight of monomer S2 as a function of temperature in an inert atmosphere. The temperature in this experiment was ramped at a linear rate of 5°C/min except at 250°C, where the temperature was held constant for 120 minutes before continuing the linear temperature ramp. The hold at 250°C allowed time for more complete network formation via thermal polymerization.

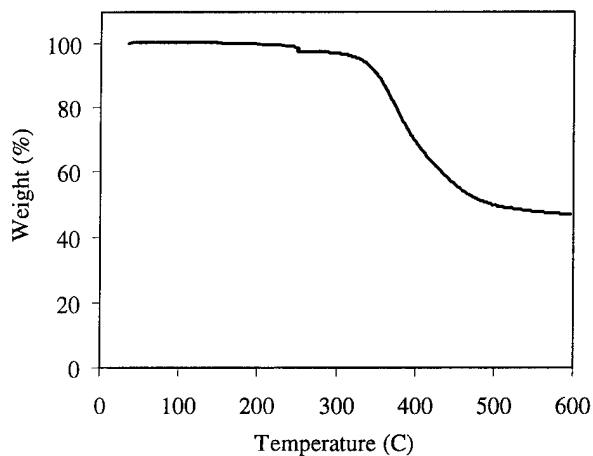


Figure 3 Thermo-gravimetric data for monomer S2 at 5°C/min in Argon atmosphere

The DSC data of Figure 2 show single polymerization peaks, which imply that when thermally polymerized, both sets of reactive groups (i.e. the acrylate and acetylene groups) undergo crosslinking simultaneously. However, this monomer is interesting because network formation can also occur by two separate cure steps: 1) UV photo-cure and 2) subsequent thermal postcure. Furthermore, the UV cure step is apparently dominated by acrylate crosslinking and the thermal postcure is then dominated by acetylene crosslinking. This last assertion is supported by FTIR spectra of the material at different stages during the cure.

The infrared spectrum of the pure monomer has IR absorption peaks centered at wavenumbers of 2230  $\text{cm}^{-1}$  and 1638  $\text{cm}^{-1}$ . The 2230  $\text{cm}^{-1}$  peak is relatively weak. It can be attributed to absorption by the  $\text{C} \equiv \text{C}$  (acetylene) stretch, while the 1638  $\text{cm}^{-1}$  absorption is most likely due to a  $\text{C} = \text{C}$  stretch in the acrylate moiety [5]. This is supported by the fact that the 1638  $\text{cm}^{-1}$  band disappears after photopolymerization.

The infrared spectra of polymerized films are shown in Figure 4. This Figure compares the infrared spectra of a film sample of S2 after photopolymerization at a temperature of 80°C (before thermal postcure), and after subsequent thermal treatment at 250°C (after thermal postcure). As in the monomer spectra, the UV cured sample shows a weak absorption at 2230  $\text{cm}^{-1}$ , which can be attributed to the acetylene moiety. This band is shown more clearly in Figure 4b. In addition, the 1638  $\text{cm}^{-1}$  band associated with the acrylate group in the monomer is almost non-existent in the UV cured sample. Thus UV photopolymerization results in crosslinking through the acrylate groups while leaving the acetylene groups intact. After thermal postcure at 250°C, the acetylene absorption disappears. Furthermore, a new band at 1605  $\text{cm}^{-1}$  becomes apparent. This band likely can be attributed to a  $\text{C} = \text{C}$  olefin stretch. Hence the IR spectra indicate that upon thermal postcure, there is a disappearance of the acetylene moiety and an appearance of a new carbon-carbon double bond. Such double bonds may be expected as a result of the acetylene reaction [6,7].

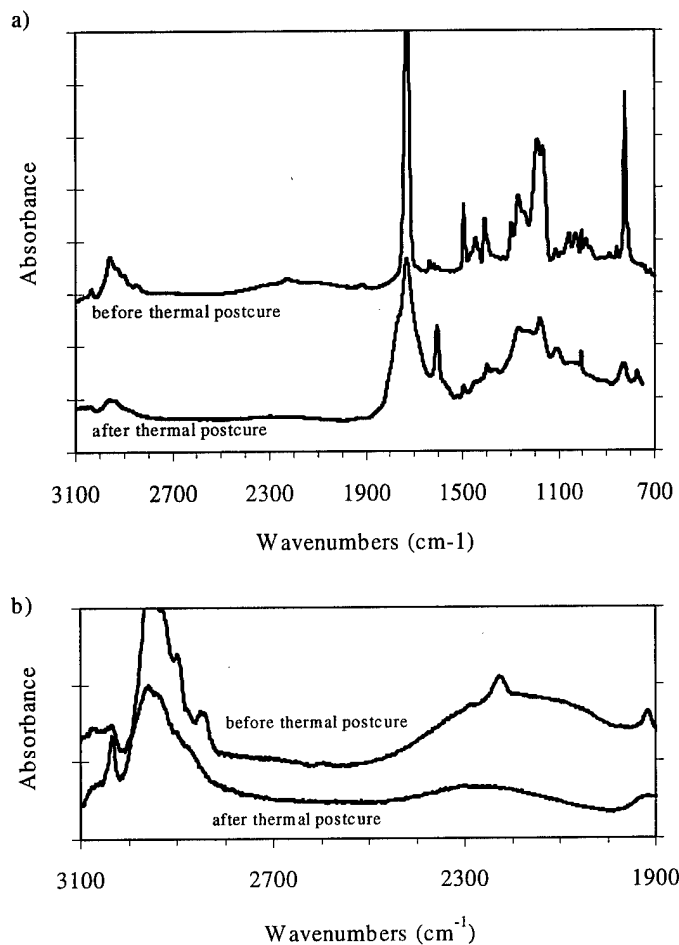


Figure 4 Fourier transform infrared spectra of networks formed from S2 i) after UV photopolymerization and ii) after subsequent thermal postcure at 250°C for 3 hours. Figure 4b shows the same spectra with an expanded scale.

Thus, the use of both photopolymerization and thermal postcuring allows the network formation to occur in two steps. This enables flexibility over the initial polymerization temperature so that the network can be formed by photo-curing the monomer in either the isotropic liquid state or liquid crystalline state. When the initial cure temperature is above the liquid crystalline to isotropic melting temperature of 69°C, the resulting polymer network shows no birefringence (when observed between crossed optical polarizers) and is, therefore, also isotropic. Conversely, when the initial cure temperature is below the 69°C melting temperature, the resulting network shows a birefringent texture, retaining the local ordering and liquid crystalline morphology of the monomer.

#### Viscoelastic Behavior

When viewed with polarized optical microscopy, polymers cured while in different phases can have drastically different appearances. Thus it is interesting to see what effect an ordered network has on the viscoelastic properties. If, for example, a polymer is cured in a non-aligned liquid crystalline state, then it has molecular order on a local level but no macroscopic alignment. A polymer cured from a liquid crystalline state might be expected to have different mechanical properties from a polymer cured from an isotropic state, where there is no local molecular order. Such a comparison is made in Figures 5 and 6.

Figure 5 compares the dynamic mechanical behavior of S2 after UV cure in the isotropic state and in the non-aligned liquid crystal state. The isotropic sample was cured for 30 minutes under a 100-watt UV lamp while being held at a temperature of 80°C. The liquid crystal sample was cured at room temperature under a UV lamp for 3 days. The networks that resulted from cure in the two different phases (and at two different temperatures) have considerably different characteristics. Based solely on the positions of the loss modulus peaks, the isotropic sample appears to have a lower glass transition temperature than the liquid crystal sample. The glass transition temperature,  $T_g$ , is often used as an empirical measure of the crosslink density [8, 9]. However, because of the influence of the network structure on the characteristics of the glass transition,  $T_g$  is not necessarily a reliable measure in highly crosslinked networks. The differences in network structure between the isotropic and liquid crystalline samples are reflected in the shapes of the loss modulus curves of Figure 5, where the loss modulus peak is broad for the isotropic polymer and narrow for the liquid crystal polymer. A possible explanation for these dramatically different shapes is that the *distribution* of molecular weights between crosslinks is much narrower in the liquid crystal network than in the isotropic network.

As shown by the FTIR data, monomer S2 has two different sets of reactive groups, which can be reacted separately. While the free-radical reaction initiated by UV exposure causes the acrylate end-

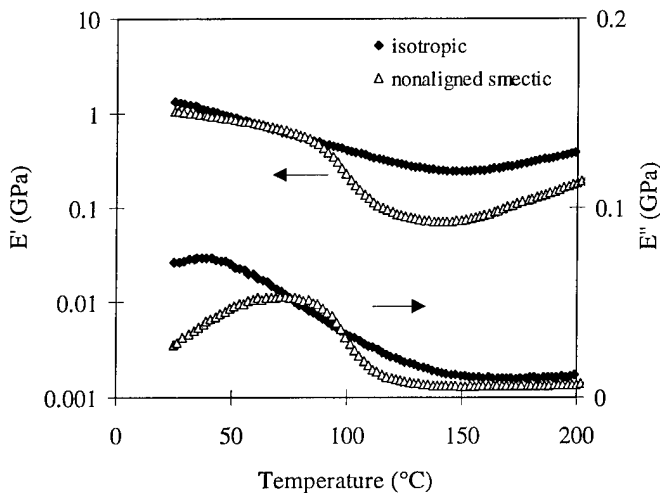


Figure 5 Comparison of storage and loss moduli at 1 Hz of polymer films formed from S2 after photo-cure but before thermal postcure.

groups to polymerize, there are acetylene groups in each monomer unit which crosslink only after heating to higher temperatures. This acetylene crosslinking is also illustrated in the modulus data of Figure 5. As described previously, these two samples were UV cured at relatively low temperatures. Figure 5 shows that as they are heated above 150 °C, the plateau modulus values begin to rise again indicating additional crosslinking. Thus by heating to high temperatures and holding there, these polymers can be thermally postcured to an even greater extent of polymerization.

Figure 6 shows the storage moduli of isotropic and liquid crystalline polymer samples after they have undergone thermal postcuring. Both samples were postcured at 250 °C for three hours. Figure 6 shows that from a practical standpoint, there is only a modest difference between the modulus of the sample cured in the isotropic state and that of the sample cured in a non-aligned liquid crystal state. The isotropic polymer modulus is approximately 23% higher than the modulus of the liquid crystalline polymer. Comparisons of the loss modulus data also show only minor differences in the glassy state. The apparent transition (loss modulus peak) at 375°C in Figure 6 corresponds to high temperature degradation of the polymer, which was verified by the thermo-gravimetric data of Figure 3. Thus, the glass transition

behavior can not be measured in the postcured polymers because they are highly crosslinked enough so that thermal degradation occurs first.

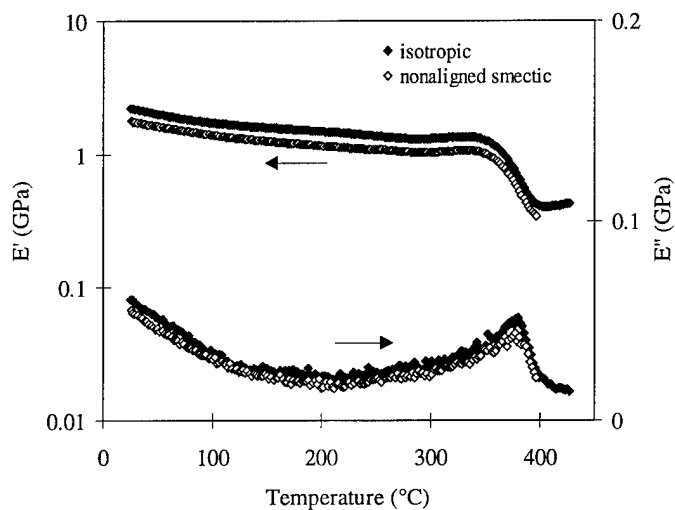


Figure 6 Comparison of storage and loss moduli at 1 Hz of polymer films formed from S2 after thermal postcure.

### Conclusions

The crosslink network formation of a rigid-rod shaped, liquid crystalline monomer was studied using various methods. The monomer contained two sets of reactive groups, acrylate and acetylene, and exhibited a dual-curing capability. In particular, the monomer was initially photopolymerized and subsequently thermally postcured. DSC and FTIR spectroscopy showed that the photopolymerization step was dominated by reaction of the acrylate groups while the subsequent thermal postcure caused additional crosslinking through the acetylene groups. Because of this dual curing capability, the monomer could be polymerized from either the liquid crystalline phase or the isotropic phase. Birefringence microscopy showed that the molecular order of the monomer when cured in the LC state was locked into the network of the formed polymer. The postcured polymer has a high crosslink density resulting in an apparent  $T_g$  in excess of 350°C

Dynamic mechanical analysis was used to study the viscoelastic behavior of networks formed from either isotropic or liquid crystalline monomers. The storage modulus ( $E'$ ) and loss modulus ( $E''$ ) indicated that the liquid crystalline-cured polymer appeared to have a lower crosslink density and a narrower distribution of molecular weights between crosslinks, while the isotropic-cured polymer had a higher crosslink density and a broader distribution (more heterogeneous network). After postcure both isotropic and liquid crystalline networks thermally degraded before reaching their ultimate glass transitions. The only observable viscoelastic difference between the postcured networks was that the isotropic network showed a 23% higher glassy state modulus than the liquid crystalline network.

### Acknowledgments

The authors are pleased to acknowledge that this research was supported by the U.S. National Science Foundation through NSF Grant # DMR-9420357, from the Polymer Program, Division of Materials Research. Dr. Andrew Lovinger was program manager. We also thank

Mary Galaska, from the University of Dayton, for assistance with sample preparation and in setting up the experiments.

### References

1. J.W. Schultz, R.P. Chartoff, *Polymer*, **39**(2), 319-325, (1998)
2. J.W. Schultz, J. S. Ullett, R.P. Chartoff, *Prototyping Technology International '98*, UK and International Press, Surrey, UK, 178(1998)
3. J.W. Schultz, R.P. Chartoff, J.S. Ullett, *J. Polym. Sci.: Part B: Polym. Phys.*, **36**(6), 1081-1089, (1998)
4. J.W. Schultz, R.T. Pogue, J.S. Ullett, and R.P. Chartoff, *J. Thermal Analysis*, **49**, 155-160 (1997)
5. R.H. Silverstein, G.C. Bassler, *Spectrometric Identification of Organic Compounds*, John Wiley & Sons, New York, (1967)
6. R.F. Kovar, G.F.L. Ehlers, F.E. Arnold, *J. Polym. Sci.: Polym. Chem. Ed.*, **15**, 1081-1095, (1977)
7. P.T. Hammond, M.F. Rubner, *Macromolecules*, **28**(4), 795-805, (1995)
8. E.A. DiMarzio, *J. Res. Natl. Bur. Stds.*, **68A**(6), 611-617, (1964)
9. K. Ueberreiter, G. Kanig, *J. Chem. Phys.*, **18**(4), 399-406, (1950)

## Net Shape Fabrication of SiC and SiC/SiC Components Using Laminated Object Manufacturing (LOM)

### Overall Process Flowchart

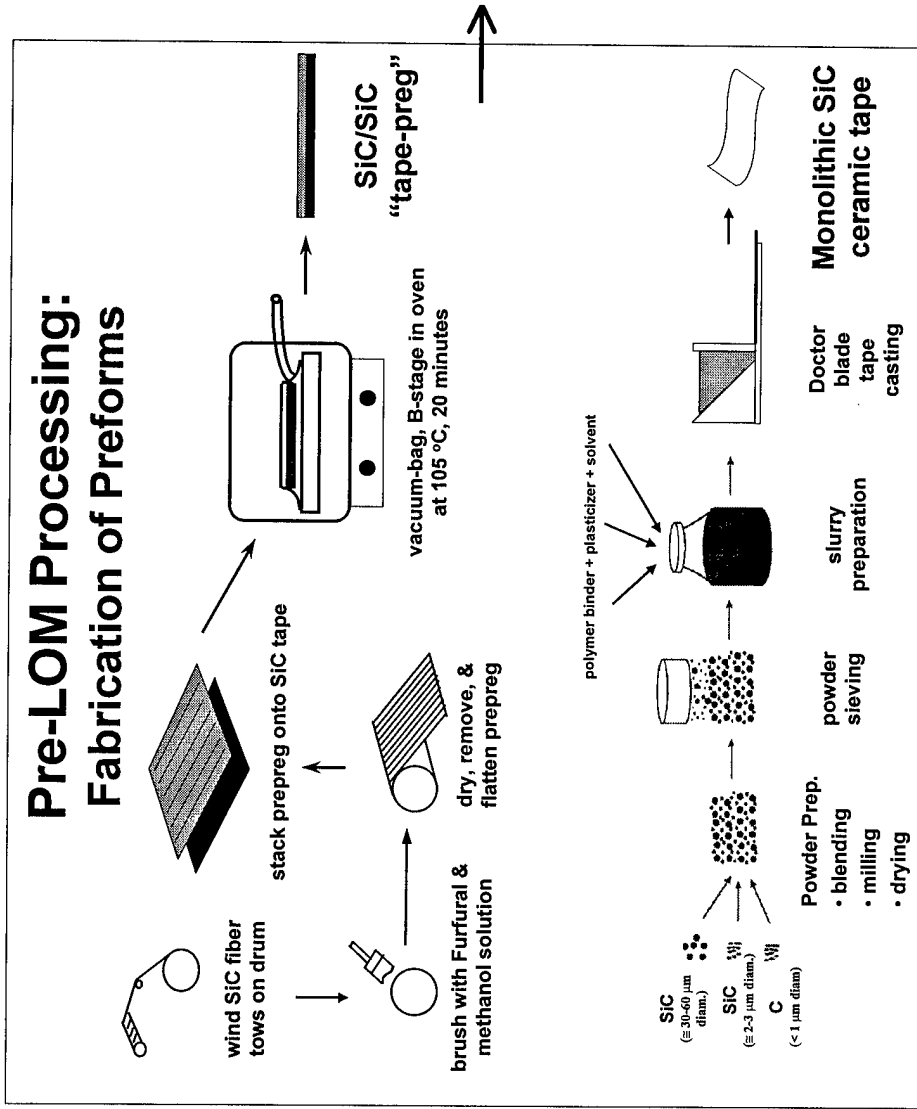
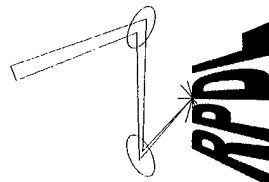
Don Klosterman, Richard Chartoff, Nora Osborne,  
George Graves, Allan Lightman, Akos Bezeredi

University of Dayton  
300 College Park  
Dayton, Ohio 45469-0130  
937-229-2517

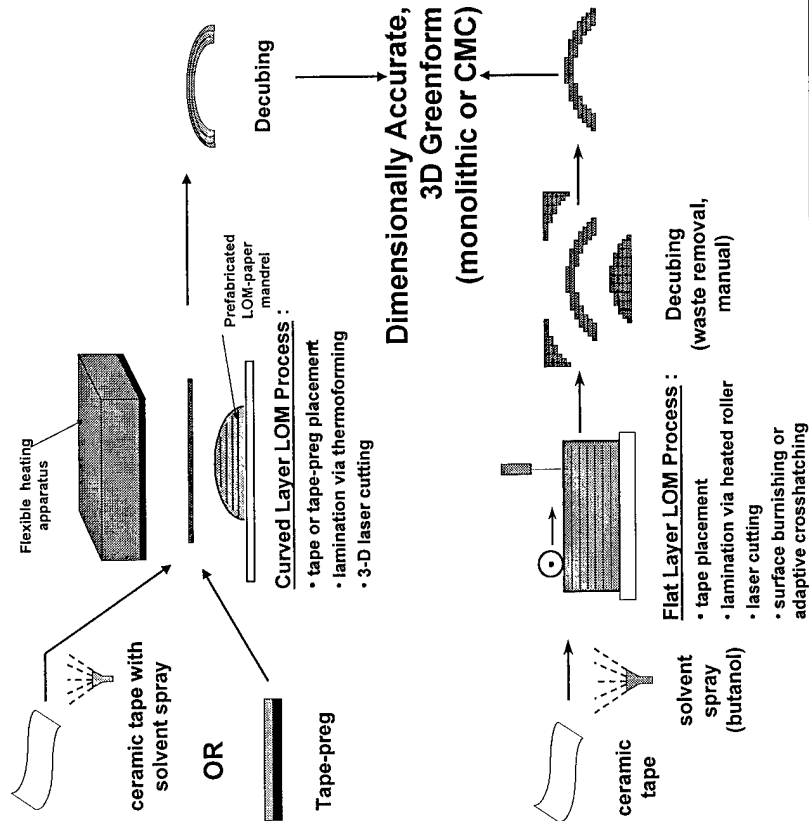
For more information on rapid prototyping of  
ceramics, see our website, containing several  
on-line technical papers :

[www.udri.udayton.edu/rpd/](http://www.udri.udayton.edu/rpd/)

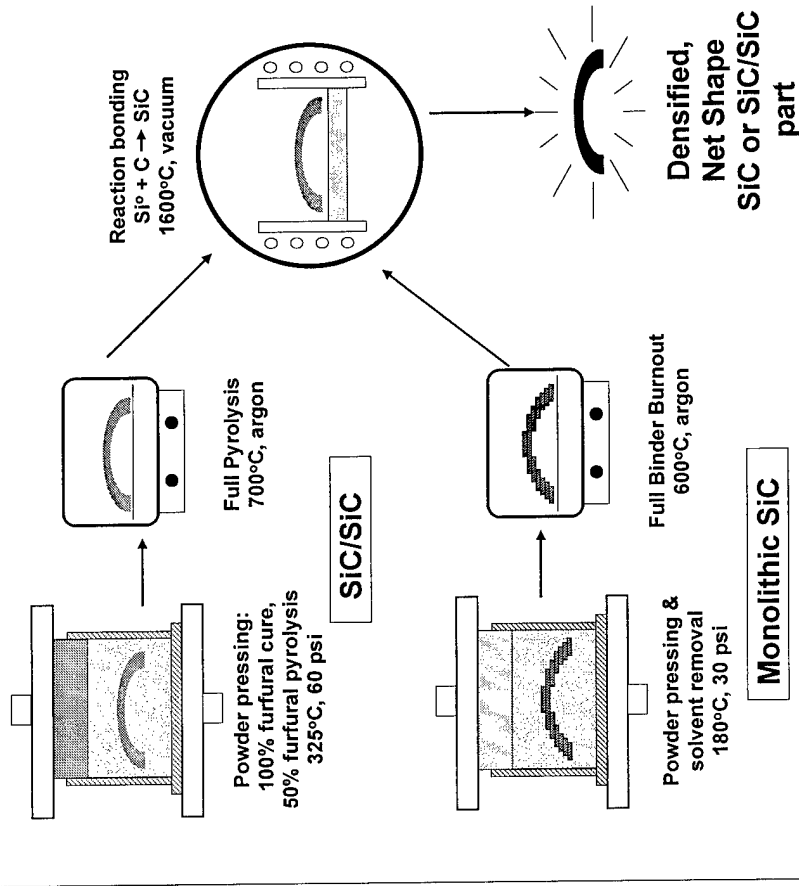
Rapid Prototype  
Development Laboratory



# LOM Processing: Lamination, Cutting, Decubing



# Post-LOM Processing: Binder Removal and Densification



# Solid Freeform Fabrication Symposium - 1998

## Author/Attendee List

Mukesh Agarwala  
University of Dayton Research Institute  
300 College Park  
Dayton, OH 45469-0150  
Phone: (937)229-3965  
Fax: (937)229-3433  
Email: agarwala@udri.udayton.edu

David Alexander  
Pratt & Whitney  
P.O. Box 109600  
West Palm Beach, Fl 33410-9600  
Phone: (561)796-6149  
Fax: (561)796-7454  
Email: alexnder@pwfl.com

Clint Atwood  
Sandia National Laboratories  
P. O. Box 5800  
MS 0958  
Albuquerque, NM 87185  
Phone: 505-844-0816  
Fax: (505)844-5589  
Email: clatwood@sandia.gov

Amit Bandyopadhyay (351, 629)  
Washington State University  
School of Mechanical & Materials  
Engineering  
PO Box 642920  
Pullman, WA 99164-2920  
Phone: (509)335-4862  
Fax: (509)335-4662  
Email: amitband@mme.wsu.edu

Joel Barlow (621)  
The University of Texas at Austin  
Department of Chemical Engineering  
Austin, TX 78712  
Phone: (512)471-6909  
Fax: (512)471-1271

Joseph Beaman (1, 19, 37, 469, 597)  
The University of Texas at Austin  
Department of Mechanical Engineering  
Professor  
Austin, TX 78712  
Phone: (512)471-3058  
Fax: (512)471-8727  
Email: jbeaman@mail.utexas.edu

Raphael Berge  
Concordia University  
Institute for Micromanufacturing, LA Tech  
911 Ergot Ave.  
Ruston, LA 71272  
Email: raf64@yahoo.com

Maurizio Bertoldi (267, 557, 639)  
University of Illinois at Chicago  
Department of Mechanical Engineering  
867 W. Taylor St..  
Chicago, IL 60607  
Phone: (312)413-7408  
Fax: (312)413-0447  
Email: bertoldi@uic.edu

J. Beuth (367)  
Carnegie Mellon University  
Dept. of Mechanical Engineering  
5000 Forbes Ave.  
Pittsburgh, PA 15213  
Phone: (412)268-3873  
Fax: (412)268-3348  
Email: beuth@andrew.cmu.edu

Jan Helge Bøhn (375)  
Virginia Tech  
Department of Mechanical Engineering  
Blacksburg, VA 24061-0238  
Phone: (540)231-3276  
Fax: (540)231-9100  
Email: bohn@vt.edu

Klas Boivie  
The Royal Institute of Technology  
Brinellvagen 68  
Stockholm, Sweden  
SWEDEN  
Phone: 46 8 21 98 64  
Fax: 46 8 20 79 19  
Email: klasbv@admin.kth.se

Susmita Bose (629)  
Washington State University  
School of Mechanical & Materials  
Engineering  
PO Box 642920  
Pullman, WA 99164-2920  
Phone: (509)335-4862  
Fax: (509)335-4662  
Email: sbose@mme.wsu.edu

# Solid Freeform Fabrication Symposium - 1998

## Author/Attendee List

Dave Bourell (469, 597, 1, 37)  
The University of Texas at Austin  
Department of Mechanical Engineering  
Austin, TX 78712  
Phone: (512)471-3170  
Fax: (512)471-7681  
Email: dbourell@mail.utexas.edu

Robert Brown  
The Gillette Company  
The Prudential Tower Bldg., 49th Floor  
800 Boylston St.  
Boston, MA 02199  
Phone: (617)421-7604  
Fax: (617)421-8484  
Email: robert\_brown@gillette.com

Marshall Burns  
Ennex Corporation  
10911 Weyburn Ave., Ste. 332  
Los Angeles, CA 90024  
Phone: (310)824-8700  
Fax: (310)824-5185  
Email: fabbers@ennex.com

Zbigniew Bzymek (285, 399)  
University of Connecticut at Storrs  
Department of Mechanical Engineering  
191 Auditorium Road  
Storrs, CT 06269-3159  
Phone: (860)486-2275  
Fax: (860)486-5088  
Email: bzymek@uconnvm.uconn.edu

Henry Cataldo  
Gillette Company  
Prudential Tower Bldg. - 49  
Boston, MA 02119  
Phone: (617)721-7602  
Fax: (617)421-8484  
Email: henry\_cataldo@gillette.com

James D. Cawley (335, 503)  
Case Western Reserve Univ.  
500 White Bldg.  
10900 Euclid Ave.  
Cleveland, OH 44106  
Phone: (216)368-6482  
Fax: (216)368-3209  
Email: jxc41@po.cwru.edu

Joe Cesarano (391, 589, 697)  
Sandia National Labs  
1001 University Blvd. SE  
Albuquerque, NM 87106  
Phone: (505)272-7624  
Fax: (505)272-7304  
Email: jcesara@sandia.gov

Peter Chamberlain (311, 435))  
University of Utah  
50 South Central Campus Dr. #2202  
Salt Lake City, UT 84112  
Phone: (801)585-9752  
Fax: (801)585-9826  
Email: P.Chamberlain@m.cc.utah.edu

Richard Chartoff (671, 737, 407, 519, 745, 437)  
University of Dayton  
Rapid Prototype Development Lab  
300 College Park Avenue  
Dayton, OH 45469-0130  
Phone: (937)229-2517  
Fax: (937)229-2503  
Email: Chartoff@udri.udayton.edu

Jon Christensen (351)  
Washington State University  
School of Mechanical & Materials  
Engineering  
P.O. Box 642920  
Pullman, WA 99164-2920  
Phone: (509)335-4862  
Fax: (509)335-4662  
Email: chrijon@mme.wsu.edu

Paul Cilino  
University of Texas at Austin  
Austin, TX  
Phone: (512)495-5503  
Email: fourier@mail.utexas.edu

Michael J. Cima (131, 259)  
MIT  
77 Massachusetts Avenue, MIT Rm 12-011  
Cambridge, MA 01239  
Phone: (617)253-6877  
Fax: (617)258-6936  
Email: mjcima@mit.edu

# Solid Freeform Fabrication Symposium - 1998

## Author/Attendee List

Adam Cohen (161)  
University of Southern California  
Information Sciences Institute  
4676 Admiralty Way, Ste. 1001  
Marina del Rey, CA 90292  
Phone: (310)822-1511  
Fax: (310)823-6714  
Email: acohen@isi.edu

Alexander Cooper (721)  
Stanford University  
Mechanical Engineering  
Bldg. 530, Rm. 128  
Stanford, CA 94305-3030  
Phone: (415)723-0565  
Fax: (415)723-5034  
Email: agcooper@leland.stanford.edu

Richard Crawford  
The University of Texas at Austin  
Department of Mechanical Engineering  
Austin, TX 78712  
Phone: (512)471-3030  
Fax: (512)471-7682  
Email: rhc@mail.utexas.edu

James Crocker (543)  
University of Connecticut  
Institute of Materials Science  
U-136, IMS, Uconn  
Storrs, CT 06268-3136  
Phone: (860)486-4410  
Fax: (860)486-4745  
Email: jec96001@uconnvm.uconn.edu

Robert Crockett (789, 229)  
Milwaukee School of Engineering  
1025 N. Broadway  
Milwaukee, WI 53202  
Phone: (414)277-7275  
Fax: (414)277-7470  
Email: crockett@msoe.edu

Suman Das (1, 19, 469)  
The University of Texas at Austin  
Laboratory for Freeform Fabrication  
Austin, TX 78712  
Phone: (512)471-5838  
Fax: (512)471-8727  
Email: das@sffoffice.me.utexas.edu

Hugh Denham (589, 391, 697)  
Sandia National Laboratories  
Advanced Materials Lab  
1001 University Blvd., SE Ste. 100  
Albuquerque, NM 87106  
Phone: (505)272-7623  
Fax: (505)272-7304  
Email: hbdenha@sandia.gov

Phill Dickens (65)  
De Montfort University  
Dept. of Mechanical & Manufacturing  
Engineering  
Queens Building, The Gateway  
Leicester, LE1 9BH  
UK  
Phone: 44 116 2577 689  
Fax: 44 116 2577 052  
Email: pdickens@dmu.ac.uk

Kristin Dudash  
Rapid Prototyping Assoc. Of SME  
One SME Drive  
P.O. Box 930  
Dearborn, MI 48721  
Phone: (313)271-1500x532  
Fax: (313)271-2861  
Email: dudakri@sme.org

Chad Duty  
Georgia Tech  
MARC 460  
813 Ferst Dr.  
Atlanta, GA 80332  
Phone: (404)894-1836  
Fax: (404)894-0957  
Email: chad.duty@rpm.marc.gatech.edu

Jason Engler  
Concordia University  
Institute for Micromanufacturing, LA Tech  
P. O. Box 10137  
Ruston, LA 71272  
Email: j-eng-31@hotmail.com

# Solid Freeform Fabrication Symposium - 1998

## Author/Attendee List

Mark Ensz (89, 359)  
Sandia National Labs  
P. O. Box 5800, MS 0958  
Albuquerque, NM 87185  
Phone: (505)844-6873  
Fax: (505)844-5589  
Email: mtensz@sandia.gov

Marcelino Essien (89)  
Sandia National Labs  
Dept. 1831 MS 1411  
Albuquerque, NM 87185  
Phone: (505)845-0574  
Fax: (505)844-9781  
Email: messien@sandia.gov

Georges Fadel (236)  
Clemson University  
202 Fluor Daniel Building  
Clemson, SC 29634  
Phone: (864)656-5620  
Fax: (864)656-4435  
Email: gfadel@ces.clemson.edu

Steffi Finke  
TNO Industry, Delft  
P. O. Box 5073  
Oostsingel 209  
2600 GB Delft  
The Netherlands  
Phone: 31 15 2608 762  
Fax: 31 15 2608 725  
Email: s.finke@ind.tno.nl

John Forsyth  
SDI  
Pine Valley Mill  
Wilton, NH

Charles Gasdaska (319, 705)  
AlliedSignal Research & Technology  
101 Columbia Road  
Morristown, NJ 07960-4638  
Phone: (973)455-4022  
Fax: (973)455-3008  
Email: charles.gasdaska@alliedsignal.com

Erik Geiss  
University of Connecticut  
Institute of Materials Science  
97 North Eagleville Rd.  
U-Box 136  
Storrs, CT 06269-3136  
Phone: (860)486-4410  
Email: geiss@main.phys.uconn.edu

Vito Gervasi (789, 229)  
Milwaukee School of Engineering  
1025 N. Broadway  
Milwaukee, WI 53202  
Phone: (414)277-4554  
Fax: (414)277-7470  
Email: gervasi@msoe.edu

Ian Gibson (343, 27)  
University of Hong Kong  
Dept. of Mechanical Engineering  
Pok Fu Lam Road.  
Hong Kong  
Phone: 28 59 7901  
Fax: 28 58 5415  
Email: igibson@hkucc.hku.hk

R. E. Glardon (79)  
Swiss Federal Institute of Technology  
DGM-ICAP-LGPP  
Lausanne 1015  
Switzerland  
Phone: 41 21 693 3861  
Fax: 41 21 693 3509  
Email: remy.glardon@epfl.ch

Mike Gou  
Cryco Quartz, Inc.  
8107 Altoga Dr.  
Austin, TX 78724  
Phone: (512)926-8931  
Fax: (512)929-8257  
Email: mgou@cryco.com

Damien Gray  
DTM Corporation  
1611 Headway Circle, Bldg. 2  
Austin, Tx 78754  
Phone: (512)425-2871  
Fax: (512)339-0634  
Email: grayd@dtm-corp.com

# Solid Freeform Fabrication Symposium - 1998

## Author/Attendee List

Michelle Griffith (359, 89, 205)  
Sandia National Labs  
P. O. Box 5800, MS 0958  
Albuquerque, NM 87185  
Phone: (505)284-2096  
Fax: (505)844-5589  
Email: mlgriff@sandia.gov

Richard Hague  
De Montfort University  
Mechanical & Manufacturing Dept.  
Queens Building  
The Gateway  
Leicester LE1 9BH  
UK  
Phone: 44 116 2577 064  
Email: rhague@dmu.ac.uk

Nicole Harlan (597)  
The University of Texas at Austin  
Department of Mechanical Engineering  
Austin, TX 78712  
Phone: (512)471-3146  
Fax: (512)471-7681  
Email: la-inka@mail.utexas.edu

David Harrison (537)  
Glasgow Caledonian University  
Department of Engineering  
Glasgow  
G4-0BA  
United Kingdom  
UK  
Phone: 44 141 331 3745  
Fax: 44 141 331 3690  
Email: dha2@gcal.ac.uk

Shay Harrison (537)  
University of Connecticut at Storrs  
Institute of Materials Science  
U-Box 136  
97 N. Eagleville Road  
Storrs, CT 06269  
Phone: (860)486-4410  
Fax: (860)486-4745  
Email: slh95001@uconnvm.uconn.edu

Marge Hartfel  
3M Center  
Building 42-3E-02  
St. Paul, MN 55144  
Phone: (651)778-6950  
Fax: (651)778-6906  
Email: mahartfel@mmm.com

Matthew Hegler  
LA Tech  
Institute for Micromanufacturing  
P. O. Box 10137  
Ruston, LA 71272

Mark Henderson (221, 327)  
Arizona State University  
Industrial Engineering Dept.  
Box 875906  
Tempe, AZ 85287-5906  
Phone: (602)965-2899  
Fax: (602)965-8692  
Email: mark.henderson@asu.edu

Kurt Hertzog  
General Motors  
P. O. Box 20366  
Rochester, NY 14602  
Phone: (716)359-6735  
Fax: (716)359-6578  
Email: khertzog@worldnet.att.net

Kathryn Higgins (383)  
Rutgers, The State University of New Jersey  
Department of Mechanical & Aerospace Eng.  
98 Brett Road  
Piscataway, NJ 08854-8058  
Phone: (732)445-5055  
Fax: (732)445-3124  
Email: kbhiggin@caip.rutgers.edu

K.K.B. Hon (147)  
University of Liverpool  
Department of Engineering  
Liverpool L69 3BX  
UK  
Phone: 44 151 794 4680  
Fax: 44 151 794 4693  
Email: hon@liv.ac.uk

# Solid Freeform Fabrication Symposium - 1998

## Author/Attendee List

Paul Hooge (529)  
712 Kay Drive  
Longview, TX 75601  
Phone: (903)758-9443  
Email: puhooge@linknet.net

Neil Hopkinson (65)  
De Montfort University  
Queens Building  
The Gateway  
Leicester LE1 9BH  
UK  
Phone: 44 115 2551551x8093  
Fax: 44 115 2577052  
Email: nhopkins@dmu.ac.uk

Todd Jackson (259)  
MIT  
Room 5-430  
77 Massachusetts Ave.  
Cambridge, MA 02139  
Phone: (617)253-7799  
Email: trjackso@mit.edu

Paul Jacobs  
Express Tool, Inc.  
300 Metro Center Blvd.  
Warwick, RI 02886  
Phone: (401)737-7900  
Fax: (401)737-8223  
Email: pjacobs@expresstool.com

Kevin Jakubenas  
Westinghouse - Bettis  
P.O. Box 79  
West Mifflin, Pa 15122-0079  
Phone: (412)476-6749  
Fax: (412)476-5151

Vikram Jamalabad (705, 319)  
AlliedSignal Research & Technology  
101 Columbia Road  
Morristown, NJ 07960-4638  
Phone: (973)455-3668  
Fax: (973)455-5991  
Email: vikram.jamalabad@alliedsignal.com

Dan Jean  
Georgia Tech  
MARC 460  
813 Ferst Dr.  
Atlanta, GA 80332  
Phone: (404)894-1836  
Fax: (404)894-0957  
Email: gte815f@prism.gatech.edu

Jon Jeffries  
Air Force Research Lab  
2977 "P" St. Suite 6  
Wright-Patterson AFB, OH 45433  
Phone: (937)255-7371  
Fax: (937)656-4269  
Email: jeffrijf@ml.wpafb.af.mil

Ken Johnson  
University of Michigan  
5667 High Ridge Dr.  
Ypsilanti, MI 48197  
Phone: (734)995-4977  
Fax: (734)995-1150  
Email: kenj@ncms.org

Sangkyun Kang (721)  
Stanford University  
Mechanical Engineering  
Bldg. 530, Rm. 128  
Stanford, CA 94305-3030  
Phone: (650)725-0107  
Fax: (650)723-5034  
Email: kangsk@leland.stanford.edu

Yeon-Sik Kang  
Institute for Advanced Engineering  
Yongin P. O. Box 25  
Kyonggi-Do, 449-820  
Kyonggi, Korea  
KOREA  
Phone: 82 335 30 7360  
Fax: 82 335 30 7113  
Email: kangys@iae.re.kr

# Solid Freeform Fabrication Symposium - 1998

## Author/Attendee List

Ju-Hsien Kao (245)  
Stanford University  
Dept. of Mechanical Engineering  
Bldg. 530, Room 128  
Rapid Prototyping Lab  
Stanford, CA 94305-3030  
Phone: (650)723-1301  
Fax: (650)723-5034  
Email: jhkao@stanford.edu

Nakis Karapatis (79)  
Swiss Federal Institute of Technology  
DGM-ICAP-LGPP  
Lausanne, 1015  
SWITZERLAND  
Phone: 41 21 693 3861  
Fax: 41 21 693 3509  
Email: nakis.karapatis@epfl.ch

Gautham Kattethota (327)  
Arizona State University  
Dept. of Mechanical Engineering  
950, S. Terrace Rd., #C349  
Tempe, AZ 85281  
Phone: (602)965-7830  
Fax: (602)965-8692  
Email: gautham@asu.edu

Dave Keicher  
Optomec Design  
2701-D Pan American Freeway NE  
Albuquerque, NM 87107  
Phone: (505)761-8250  
Fax: (505)761-6638  
Email: dkeicher@optomec.com

Thomas Kenney  
Nichols Aircraft Division  
Parker Hannifin Corp.  
14 Robbins Pond Rd.  
Ayer, MA 01432  
Phone: (978)784-1217  
Fax: (978)784-1400  
Email: tk34249@nichpark.attmail.com

John Kietzman (567, 721)  
Stanford University  
Mechanical Engineering  
Bldg. 530, Rm. 128  
Stanford, CA 94305-3030  
Phone: (415)723-0565  
Fax: (415)723-5034  
Email: kietzman@leland.stanford.edu

Lena A. Killander  
IVF  
The Swedish Institute of Production Eng.  
Research  
Brinellvagen 68  
Stockholm, Sweden  
SWEDEN  
Phone: 46 8 21 98 64  
Fax: 46 8 20 79 19  
Email: lenaak@cadcam.kth.se

Bruce H. King (391, 697)  
Sandia National Labs  
1001 University Blvd. SE Suite 100  
Albuquerque, NM 87106  
Phone: (505)272-7125  
Fax: (505)272-7304  
Email: bhking@sandia.gov

Donald Klosterman (407, 745, 437, 671)  
University of Dayton  
Rapid Prototype Development Laboratory  
300 College Park  
Dayton, OH 45469-0130  
Phone: (937)229-2794  
Fax: (937)229-2503  
klosterman@udri.udayton.edu

Kai Uwe Koch (105)  
Fraunhofer Institut  
Produktionstechnik und Automatisierung  
Nobelstrasse 12  
70569 Stuttgart  
Fed. Rep. Of Germany  
GERMANY  
Phone: 49(711)970-1856  
Fax: 49(711)970-1004  
Email: kuk@ipa.fhg.de

# Solid Freeform Fabrication Symposium - 1998

## Author/Attendee List

Radovan Kovacevic (57)  
Southern Methodist University  
3160 SMU Blvd.  
Dallas, TX 75275  
Phone: (214)768-4865  
Fax: (214)768-2116  
Email: kovacevi@seas.smu.edu

Ashok Kumar (169)  
University of Florida  
Department of Mechanical Engineering  
MEB 237  
Gainesville, FL 32611-6300  
Phone: (352)392-0816  
Fax: (352)392-1071  
Email: akumar@cimar.me.ufl.edu

Noshir Langrana (383, 479, 681, 113)  
Rutgers, The State University of New Jersey  
Department of Mechanical & Aerospace  
Engineering  
98 Brett Road  
Piscataway, NJ 08854-8058  
Phone: (732)445-3618  
Fax: (732)445-3124  
Email: langrana@caip.rutgers.edu

Mathias Le Saux  
Concordia University  
Institute for Micromanufacturing, LA Tech  
911 Ergot Ave.  
Ruston, LA 71272  
Email: mle\_saur@hotmail.com

Lex Lennings (97)  
Delft University of Technology  
Subfaculty of Industrial Design Engineering  
Jaffalaan 9, 2628 BX Delft  
The Netherlands  
Phone: 31 15 278 1197  
Fax: 31 15 278 7316  
Email: a.f.lennings@io.tudelft.nl

Ming Leu (185, 427)  
New Jersey Institute of Technology  
Dept. of Mechanical Engineering  
210 Central Ave., ITC 2400, Dept. of M.E.  
Newark, NJ 07102  
Phone: (973)596-3335  
Fax: (973)596-5601  
Email: mleu@nsf.gov

John Lombardi (511, 721)  
Advanced Ceramics Research Inc.  
3292 East Hemisphere Loop  
Tucson, AZ 85706-5013  
Phone: (520)573-6300  
Fax: (520)573-2057  
Email: j.lombardi@acrtucson.com

Kai Loose (177)  
The Institute of Physical & Chemical  
Research (RIKEN)  
2-1 Hirosawa  
Wako-shi, Saitama 351-0111  
Japan  
Phone: 81 48 467 9581  
Fax: 81 48 462 4639  
Email: kai@postman.riken.go.jp

James Love  
Optomec Design Co.  
2701-D Pan American Freeway NE  
Albuquerque, NM 87107  
Phone: (505)761-8250  
Email: jlove@optomec.com

Charity Lynn (293)  
Georgia Institute of Technology  
George W. Woodruff School of Mechanical  
Eng.  
813 Ferst Drive  
Atlanta, GA 30332-0405  
Phone: (404)894-9158  
Fax: (404)894-9342  
Email: gt0658a@prism.gatech.edu

Harris Marcus (537, 543)  
University of Connecticut at Storrs  
Institute of Materials Science  
U-136, IMS, UConn  
97 N. Eagleville Road  
Storrs, CT 06268-3136  
Phone: (860)486-4623  
Fax: (860)486-4745  
Email: hmarcus@mail.ims.uconn.edu

Ray Meilunas  
Northrop Grumman Corp.  
MS A01-26  
Bethpage, NY 11714  
Phone: (516)346-6247  
Fax: (516)346-3670  
Email: ray-meilunas@atdc.northgrum.com

# Solid Freeform Fabrication Symposium - 1998

## Author/Attendee List

Gert Mensing (343)  
University of Hong Kong  
Dept. of Mechanical Engineering  
Pok Fu Lam Road  
Hong Kong  
Phone: 28 592 626  
Fax: 28 585 415  
Email: mgeert@hkusua.hku.hk

Jason R. Mock (575)  
Louisiana Tech University  
P.O. Box 10137  
911 Hergot Street  
Ruston, LA 71272  
Phone: (318)257-5100  
Fax: (318)257-5104  
Email: jrm008@engr.latech.edu

Edmund H. Moore  
AFRL  
AFRL/MLLM Bldg. 655  
2230 Tenth St. Suite 1  
Wright-Patterson AFB, OH 45433  
Phone: (937)255-9834  
Fax: (937)255-3007  
Email: mooreeh@ml.wpafb.af.mil

Sherry Morissette (391)  
Sandia National Laboratories  
1001 University Blvd. SE  
Albuquerque, NM 87106  
Phone: (505)272-7608  
Fax: (505)272-7304  
Email: [slmoris@sandia.gov](mailto:slmoris@sandia.gov)

Amit Kumar Muraleedharan  
600 W. 26th Street, # E339  
Austin, TX 78705

Kesh Narayanan  
National Science Foundation  
4201 Wilson Blvd.  
Arlington, VA 22230  
Phone: (703)306-1330  
Fax: (703)306-0298  
Email: knarayan@nfs.gov

Christian Nelson (451)  
DTM Corporation  
1611 Headway Circle, Bldg. 2  
Austin, TX 78754  
Phone: (512)425-2934  
Fax: (512)832-6735  
Email: nelson@dtm-corp.com

Olli Nyrhila (487)  
Electrolux Rapid Development  
Aholantie 17  
FIN-21290 Rusko  
Finland  
Phone: 35 82 4365611  
Fax: 35 82 4399620  
Email: olli.nyrhila@notes.electrolux.fi

Chris O'Neill  
United Technologies – Pratt & Whitney  
400 Main Street M/S 118-40  
East Hartford, CT 06108  
Phone: (860)565-2729  
Fax: (860)565-5611  
Email: oneillcf@pweh.com

Harald Okruch  
Bombardier-Rotax GMBH  
Welser Strasse 32  
Gunskirchen  
AUSTRIA  
Phone: 43 7246 601 342  
Fax: 43 7246 601 275  
Email: okh@rotax.bombardier.com

Seok-Min Park  
The University of Texas at Austin  
Department of Mechanical Engineering  
C2200  
Austin, TX 78712  
Phone: (512)471-5838  
Email: smpark@mail.utexas.edu

Joseph Pegna  
Concordia University  
Department of Mechanical Engineering  
1455 De Maisonneuve Blvd.  
Montreal, PQ H3G1M8  
Canada  
Phone: (514)848-4193  
Fax: (514)848-3175  
Email: pegna@me.concordia.ca

# Solid Freeform Fabrication Symposium - 1998

## Author/Attendee List

Senol Pekin (651, 661)  
University of Illinois at U-C  
Materials Research Lab & Dept. of MS&E  
104 S. Goodwin Ave.  
Urbana, IL 61801  
Phone: (217)333-8029  
Fax: (217)244-2278  
Email: pekin@uimrl7.mrl.uiuc.edu

Chadee Persad  
University of Texas  
Institute for Advanced Technology  
4030-2 West Braker  
Austin, TX 78759  
Phone: (512)471-9060  
Fax: (512)471-9096  
Email: persad@email.utexas.edu

Rolf Pfeifer (549)  
Inst. of Polymer Testing and Polymer  
Science  
IKP, University of Stuttgart  
Bölingerstrasse 78E  
Stuttgart 70199  
Germany  
Phone: 49 711 641 2269  
Fax: 49 711 641 2264  
Email: pfeifer@ikp2.uni-stuttgart.de

Paul Pilling  
University of Leeds  
School of Mechanical Engineering  
Woodhouse Lane  
Leeds, West Yorkshire LS 2 9 JT  
UK  
Phone: 44 113 233 2228  
Fax: 44 113 233 2150  
Email: menpjp@leeds.ac.uk

J. Miguel Pinilla (245)  
Stanford University  
Dept. of Mechanical Engineering  
Bldg. 530, Room 128  
Rapid Prototyping Lab  
Stanford, CA 94305-3030  
Phone: (650)723-1301  
Fax: (650)723-5034  
Email: jmp@stanford.edu

Reginald Ponder  
Georgia Institute of Technology  
Manufacturing Research Center  
813 Ferst Dr.  
Atlanta, GA 30332  
Phone: (404)894-7688  
Fax: (404)894-7689  
Email: reginald.ponder@marc.gatech.edu

Fritz Prinz (721, 245, 567)  
Stanford University  
Dept. of Mechanical Engineering  
Bldg. 530, Room 128  
Rapid Prototyping Lab  
Stanford, CA 94305-3030  
Phone: (650)723-0084  
Fax: (650)723-5034  
Email: fbp@cdr.stanford.edu

Xiaoping Qian (689)  
Univ. of Michigan  
Mechanical Engineering  
2225 G.G. Brown  
Dept. of MEAM  
Ann Arbor, MI 48109  
Phone: (734)763-4056  
Email: xpqian@engin.umich.edu

Sriram Rangarajan (113, 479)  
Rutgers, The State University of New Jersey  
Department of Ceramic and Materials  
Engineering  
607 Taylor Road  
Piscataway, NJ 08854-8065  
Phone: (732)445-5616  
Fax: (732)445-2893  
Email: rangers@rci.rutgers.edu

Anshuman Razdan (221, 277)  
Arizona State University  
PRISM  
Box 875106  
Tempe, AZ 85287-5106  
Phone: (602)965-5368  
Fax: (602)965-2910  
Email: razdan@asu.edu

# Solid Freeform Fabrication Symposium - 1998

## Author/Attendee List

Gerard Ryder  
Strathclyde University  
DMEM, CAD Centre, James Weir Bldg.  
75 Montrose St.  
Glasgow, Scotland G1 1XT  
SCOTLAND  
Phone: 0141 548 3056  
Fax: 0141 552 3148  
Email: gerard@cad.strath.ac.uk

Emanuel Sachs (131, 259)  
MIT  
77 Massachusetts Avenue, Room 35-136  
Cambridge, MA 02139-4307  
Phone: (617)253-5381  
Email: sachs@mit.edu  
Fax: (617)253-0209

Roy Sanders (205, 89)  
SDI  
Pine Valley Mill  
P.O. Box 550  
Wilton, NH 03086  
Phone: (603)654-6100x203  
Fax: (603)654-2616

Eric Schlienger (89, 205)  
Sandia National Labs  
P.O. Box 5800, MS 1411  
Albuquerque, NM 87185-1411  
Phone: (505)845-3497  
Fax: (505)844-9871  
Email: meschli@Sandia.Gov

Wayde Schmidt  
United Technologies Research Center  
411 Silver Lne  
MS 129-26  
East Hartford, CT 06108  
Phone: (860)610-1660  
Fax: (860)610-1697  
Email: schmidwr@utrc.utc.com

Jonathan Schneider  
Lockheed Martin - KAPL, Inc.  
P. O. Box 1072  
Bin #102  
Schenectady, NY 12301  
Phone: (518)395-6097  
Fax: (518)395-6136  
Email: schneiman@aol.com

Jubin Shah (575, 529)  
Louisiana Tech University  
10869 Gambriel Dr. #14  
Manassas, VA 20109  
Phone: (703)365-0312  
Email: jshah@dominionsc.com

Dongping Shi (27)  
University of Hong Kong  
Dept. of Mechanical Engineering  
Pokfulam Road  
Hong Kong  
Phone: 852 2859 2626  
Fax: 852 2547 4699  
Email: dpshi@hkusua.hku.hk

Geoff Smith-Moritz  
Rapid Prototyping Report  
CAD/CAM Publishing, Inc.  
1010 Turquoise St., Ste. 320  
San Diego, CA 92109  
Phone: (619)488-0533  
Fax: (619)488-6052  
Email: www.cadcarnet.com

John E. Smugeresky (89, 205)  
Sandia National Labs  
MS9403 / Bldg. 940 / Rm 1191  
7011 East Ave.  
Livermore, Ca 94551-0969  
Phone: (925)294-2910  
Fax: (925)294-3410  
Email: smug@sandia.gov

Yong Ak Song (495)  
KIST  
Cheongryang P.O. Box 131  
Seoul  
Korea  
Phone: 82 2 958 5638  
Fax: 82 2 958 5649  
Email: yongak@kistmail.kist.re.kr

Ben Steinberg (277)  
Arizona State University  
PRISM  
Box 875106  
Tempe, AZ 85287-5106  
Phone: (602)965-2771  
Fax: (602)965-2910  
Email: asbms@imapl.asu.edu

# Solid Freeform Fabrication Symposium - 1998

## Author/Attendee List

Todd Stewart (443)  
The University of Leeds  
The School of Mechanical Engineering  
Woodhouse Lane  
Leeds, Yorkshire LS2 9JT  
UK  
Phone: 44 113 2332 228  
Fax: 44 113 2332 150  
Email: T.D.Stewart@Leeds.ac.uk

Peter Stierlen (581)  
Inst. for Polymer Testing & Polymer Science  
Inst. für Kunststoffprüfung und  
Kunststoffkunde  
Pfaffenwaldring 32  
Stuttgart 70569  
Germany  
Phone: 49 711 641 2276  
Fax: 49 711 6412 264  
Email: stierlen@ikp2.uni-stuttgart.de

Brent Stucker  
University of Rhode Island  
Dept. of Ind. & Mfg. Engineering  
2 East Alumni Ave.  
Gilbreth Hall  
Kingston, RI 02892  
Phone: (401)874-5187  
Fax: (401)874-5540  
Email: stucker@egr.uri.edu

Douglas Taft  
Molecular Geodesics, Inc.  
300 Metro Center Blvd.  
Warwick, RI 02886  
Phone: (401)737-7900  
Fax: (401)737-8223  
Email: dtaft@molec-geodesics.com

Jill Ullett (519, 737)  
University of Dayton  
Rapid Prototype Dev. Lab. & OH Rapid  
Prototype  
300 College Park Avenue  
Dayton, OH 45469-0130  
Phone: (937)229-3609  
Fax: (937)229-2503  
Email: Ullett@udri.udayton.edu

Ranji Vaidyanathan (511)  
Advanced Ceramics Research, Inc.  
3292 E. Hemisphere Loop  
Tucson, AZ 85706-5013  
Phone: (520)434-6392  
Fax: (520)573-2057  
Email: vaidyanalhan@acrucson.com

Neal Vail (621)  
BioMedical Enterprises, Inc.  
Texas Research Park  
14785 Omicron Drive, Suite 205  
San Antonio, TX 78245  
Phone: (210)677-0354  
Fax: (210)677-0355  
Email: vail@bme-tx.com

Mark Van Roosendaal (435, 311)  
University of Utah  
MEB 2202  
Salt Lake City, UT 84112  
Phone: (801)585-9752

Hubert Vander Plas  
Hewlett-Packard Laboratories  
1501 Page Mill Rd., MS 1L-6  
Palo Alto, CA 94304  
Phone: (650)857-8722  
Fax: (650)236-9885  
Email: hvp@ieee.org

Ravi Venkataramani (19, 113)  
The University of Texas at Austin  
Laboratory for Freeform Fabrication  
Austin TX 78712-1063  
Phone: (512)471-5838  
Fax: (512)471-8727  
Email: rvenka@mail.utexas.edu

Craig Wadham  
DTM Corporation  
1611 Headway Circle, Bldg. 2  
Austin, TX 78754  
Phone: (512)425-2870  
Fax: (512)339-0634  
Email: wadhamc@dtm/corp.com

# Solid Freeform Fabrication Symposium - 1998

## Author/Attendee List

Daniel Walczyk (121)  
Rensselaer Polytechnic Institute  
Dept. of ME, AE & M  
110 8th St.  
Troy, NY 12180-3590  
Phone: (518)276-2397  
Fax: (518)276-2623  
Email: walczd@rpi.edu

Hongyun Wang(37)  
The University of Texas at Austin  
Department of Mechanical Engineering  
Austin, TX 78712  
Phone: (512)471-3578  
Fax: (512)471-7681  
Email: hongyunwang@mail.utexas.edu

Jianguo Wang (211)  
Dept. of Mechanical & Production Eng.  
National Univ. of Singapore  
10 Kent Ridge Crescent  
Singapore 119260  
Singapore  
Phone: (65)874-3490  
Fax: (65)874-1459  
Email: mpewjg@nus.edu.sg

Wanlong Wang (417)  
Northwestern University  
Dept. of Mechanical Engineering  
2145 Sheridan Rd.  
Evanston, IL 60202  
Phone: (847)467-3291  
Fax: (847)491-3915  
Email: wwang@nwu.edu

Doug Watson  
University of Texas at Austin  
Dept. of Mechanical Engineering  
Austin, TX  
Phone:  
Fax: (512)471-7681  
Email: dwatson@mail.utexas.edu

Timothy Weaver (461)  
Pennsylvania State University  
118 Research West  
University Park, PA 16802-6809  
Phone: (814)865-1308  
Fax: (814)863-8211  
Email: tjw112@psu.edu

Lee Weiss (721)  
Carnegie Mellon University  
207 Smith Hall  
Pittsburgh, PA 15213  
Phone: (412)268-7657  
Fax: (412)268-5570  
Email: lew@cs.cmu.edu

Bernhard Wiedemann  
Daimler-Benz  
Wilhelm-Runge-Strasse 11  
Ulm, 89077  
Germany  
Phone: 49 731 505 2925  
Fax: 49 731 505 4212  
Email:  
bernhard.wiedemann@dbag.ulm.DaimlerBen  
z.com

David Winmill (303)  
DuPont Somos  
Two Penn's Way, Suite 401  
New Castle, DE 19720  
Phone: (302)328-8542  
Fax: (302)328-5693  
Email: david.l.winmill@usa.dupont.com

Holger Wirtz (605)  
Fraunhofer-Institut IPT  
Steinbachstr. 17  
Aachen 52074  
Germany  
Phone: 49 241 8904 120  
Fax: 49 241 8904 198  
Email: wizeipt.rwth-aachen.de

Martin Wohlert (469)  
The University of Texas at Austin  
Laboratory for Freeform Fabrication  
Austin, TX 78712  
Phone: (512)232-2197  
Fax: (512)471-7681  
Email: mwohlert@mail.utexas.edu

Joe Wright  
Lockheed Martin Vought Systems  
P. O. Box 650003, M/S: SK-0003  
Dallas, TX 75265  
Phone: (972)603-2507  
Fax: (972)603-0419  
Email: joe.m.wright@lmco.com

# Solid Freeform Fabrication Symposium - 1998

## Author/Attendee List

Xiaorong Xu (131)  
MIT  
Rm. 35-011, MIT  
Cambridge, MA 02139  
Phone: (617)253-7274  
Fax: (617)258-0209  
Email: xiaorong@mit.edu

Wei Zhang (185)  
New Jersey Institute of Technology  
Mechanical Engineering Department  
210 Central Ave., ITC 2400, M.E. Dept.  
Newark, NJ 07102  
Phone: (973)642-4994  
Fax: (973)596-5601  
Email: zhangwei@oak.njit.edu

## Keyword Index

17-4PH Stainless Steel	479	Conformal cooling	131, 495
3D Printing (3DP)	259, 131	Controller	236
5-axis milling	495	Cooling passages	205
Abrasive blade tip	1	Copper-polyamide	451
Abrasive water jet cutting	121	Cure depth	177
ABS	375	Curriculum	221
Absorption coefficient	549	Curve matching	97
Accuracy	303	Curved layer build style	671
Adaptive Slicing	97, 105, 375, 435	Decision Support	293
Additive/subtractive SFF	245	Density	285
Adhesion	567	Deposition	205
Adjacency graph	245	Design of experiments	293
Alumina	721	Design window	131
Anisotropy	519, 567	Design	705
Architecture	229	Desk-Top SFF Fabrication	285
Automation	245, 721	Devices	543
B spline	19, 277	Dilatant	697
Base-line method	549	Dimensional Changes	79
Batch fabrication	161	Dimensions	303
Bevel cutting	121	Direct AIM	65
Binder Burn Out (BBO)	479	Direct fabrication	205
Binder	613, 651, 661	Direct laser-sintering	487
BioCeramic implants	629	Direct metal tooling	495
Biocompatible	621	Direct Rapid Tooling	105
Biomedical	229	Direct SLS	1
Bronze powder	487	Directional solidification	1
Build parameters	319	Direct-writing	529
Build strategy	193	DLR-German Aerospace Center, Stuttgart	581
Build Style	293	DMLS	79
Build time estimators	343	Domain decomposition	267
Building alternative tree	245	Droplet transfer	57
Building graph	245	Dry pressing	589
CO <sub>2</sub> -laser	549	Drying	697
CAD	205	Dual curing monomers	737
Calibration	375	Dynamic Control	47
CAM-LEM	335, 503	Education	229
Carbon	529	EFF	511
Casting molds	597	Ejection Force	65
Ceramic implant	621	Electrodeposition	161
Ceramic Joining	537	Electronic materials	391
Ceramic slurry	629	Environment	303
Ceramics	319, 391, 407, 503, 589, 671, 697, 705, 721	Epoxy	567, 721
Cermets	1	Execution system	245
CNC machining	245	Exposure	303
Color-coding	327	Extrusion	589, 697
Composites	229, 671, 697, 789	FDM	327, 375, 511, 629
Computer aided design (CAD)	259, 383, 681	FDMet	479
Concept modelling	177	Fibers	575
		Fibrous monolith	705
		Fill patterns	359
		Filled	169
		Flexible cutting blade	97

## Keyword Index

Flexible resin	303	Laser digitizer	277
Fractal space filling curves	267	Laser path pattern	285, 399
Fracture toughness, in stereolith resins	519	Laser profilometry	391
Freeform front faces	97	Laser sintering	487, 549
Freeform growth	529, 575	Laser	205
Freeform thick layers	97	Layered manufacturing	113, 185, 383, 435, 689
Frequency analysis	435	Lead zirconate titanate	613
Fugitive materials	335, 697	Lens	89, 205, 359
Fugitive mold	721	Line width	177
Fugitive support	511	Liquid crystal resins	519
Fully-dense parts	161	Liquid silicon infiltration process (LSI)	581
Functional parts	161	Local composition control (LCC)	259
Functionally graded materials (FGM)	259	Machining	495
Functionally Gradient Materials (FGMs)	789	Manufacturing information system	245
Fused deposition modeling	169, 267, 375, 383, 557, 639, 681, 705	Material deposition	245
Fused deposition of ceramics (FDC)	319, 613, 651, 661, 713	Material features	689
Galvanometers	236	Mechanical properties	567, 589
Geometric Tolerances	293	Mechanical-thermal characterization	557
Graded	697	Mechanisms of selective laser sintering	605
Gradient	789	Medical imaging	713
H13 steel	89	Metal parts	161, 205, 605
Hardness	79	Metal powder	487
Heat transfer	549	Metal tooling	461
Hermetic Sealing	537	Metal	205
Heterogeneous composition	259	Microcoils	529
High speed videography	605	Microelectromagnet	529
High temperature resins	737	Microelectromechanical systems	161, 229, 575
Hot isostatic pressing	19, 469	Microfabrication	161
Humidity	303	Microgravity	229
Hydrophones	613	Micromachining	161
Hydroxyapatite	613	Micropen	391
Ice patterns	185	Microsolenoid	529
IKP-Institute of Polymer Testing and Polymer Science, University Stuttgart	581	Microsprings	529
Indirect SFF	629	Milling	343
Infiltration	443	Modeling	367, 407, 549
Injection molding	65, 131	Mold SDM	721
Injection welding	451	Monolithic Joints	537
Interactive tool	327	MRI	229
Investment casting	427, 605	Multicriteria optimization	399
IR-spectroscopy	549	Multi-material layered manufacturing	681
Laminated object manufacturing	407, 417, 503, 671	Multi-material parts	721
Laminated tooling	121	Multi-material solid modeling	259
Laminates	705	Multiple LED photographic curing	177
Lamination	503	Multiple materials	335, 697
Large scale rapid prototyping	343	Multi-spot exposure	177
Large sized objects	97	Near-net Slice	105
Laser beam welding	495	NURBS	19, 277
Laser cutting	121, 503	Object reconstruction	211
Laser deposition	529, 575	Offset curves	19

## Keyword Index

Optimal control	236	Rheology	391, 697
Orthotropic material	557	Rigid-rod molecules	737
Overhang	205	Robocasting	391, 589, 697
Part decomposition	245	Robot	27
Part Ejection	65	Roughness	285
Part orientation	327	RTV mold	479
Phenol	581	Rubber mold	461
Photogrammetry	229	Ruled edges	435
Piezoelectricity	713	Sacrificial Material	205
Polishing	37	SALD Joining	537
Polyethylene	303	SALDVI	543
Polymer parts	351	Sand casting	417
Polymer powder	549	Scanning	47
Polymer thick films	391	Selective area laser deposition (SALD)	399, 543
Polyurethane	567, 721	Selective Laser Sintering	19, 27, 37, 47, 79, 443, 451, 469, 597, 605, 621
Porosity	79	Shape deposition manufacturing	245, 567, 721
Porous structures generation	621, 639	Shape deposition modeling	367
Post processing	417	Shell	169
Powder metallurgy	461, 503	Shop scheduling	245
Powder	205	Si/SiC-ceramic	581
Precedence graph	245	Silicon Carbide	113, 537, 543, 705, 721
Precursor	581	Silicone Carbide	581
Probes	529	Siliconization	581
Process control	407	Simulation	407
Process description language	245	Sintering	461, 479
Process planning	245, 293, 689	Slip casting	589
Process Simulation	27	Slurry	391, 589, 697
Profiled edge laminated tooling	121	Software development	359
Prototyping	245	Solid freeform fabrication (SFF)	185, 285, 383, 399, 427, 713
Pseudoplastic	697	Somos	303
Pyrolysis	581	Staircase Effect	105
PZT	113	Steel powder	487
Quantity	37	Stereolithography resin	737
Rapid composite process (RCP)	789	Stereolithography	177, 193, 293, 303, 383, 519
Rapid freezing prototyping	185	Stereometric design	285
Rapid Prototyping & Tooling	105	Strength	285, 567
Rapid prototyping (Metal or Cermaic)	461	Superalloy	1
Rapid Prototyping (RP)	27, 185, 211, 236, 383, 427, 479, 589	Surface definition	435
Rapid tooling	65, 79, 185, 383, 417, 427, 461	Surface deviation	327
RapidSteel	443	Surface finish	27, 327
RapidTool	451	Surface fitting	277
Raster scanning	177	Surface modeling	211
Reactive liquid crystals	737	Surface quality	327
Refractive Index Matching (RIM)	351	Surface roughness	65, 193, 327
Residual stress	79, 367, 705	Temperature dependent optical properties	549
Resin	303	TetraCast	789
Resolution	229		
Response surface methodology	293		
Reverse engineering	211, 277, 351		

## Keyword Index

Theoretical model	399
Thermal analysis	651
Thermal modeling	89
Thermal stresses and deformations	399
Thermal-expansion, designable	519
Thermocouple	543
Thermoset polymer	567
Thick Layered Object Manufacturing	97
Time parameterization	236
Titanium casting	597
Titanium nitride	575
Titanium	469
Tooling	451
Toolpath	267, 319
Trajectory control	121
Transducer	713
Tungsten	529
University activities	221
Video microscopy	113, 681
Virtual simulation	681
Viscosity	697
Vision system	57
Visualization	327
Warping	367
Water soluble support	511
Wavelet transforms	435
Wax	651, 661
Wear resistance	461
Welding	495
Welding	57, 495
Working curves	549
Zirconia	597
Zirconium silicate	605